

**Comparative Embryonic Morphogenesis
of Emerging Insect Model Organisms
• Volume I of III •**

Dissertation

**zur Erlangung des Doktorgrades
der Naturwissenschaften**

**vorgelegt beim Fachbereich 15 – Biowissenschaften
der Johann Wolfgang Goethe-Universität**

**von
Frederic Strobl
aus Frankfurt am Main**

Frankfurt am Main, 2017

(D30)

Vom Fachbereich 15 – Biowissenschaften der

Johann Wolfgang Goethe-Universität als Dissertation angenommen.

Dekanin: Prof. Dr. Meike Piepenbring

1. Gutachter: Prof. Dr. Ernst H.K. Stelzer

2. Gutachter: Prof. Dr. Bernd Grünewald

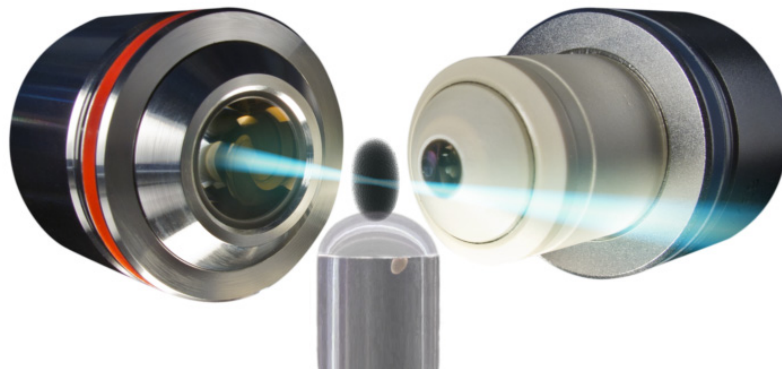
Datum der Disputation:



Buchmann Institute
for Molecular Life Sciences



**Comparative Embryonic Morphogenesis
of Emerging Insect Model Organisms
• Volume I of III •**



Frederic Strobl

Matrikel-Nummer 3326422

Physical Biology / Physikalische Biologie

Buchmann Institute for Molecular Life Sciences

Cluster of Excellence – Macromolecular Complexes

Johann Wolfgang Goethe-Universität – Frankfurt am Main

2012 – 2017

About the Volumes

The style of my PhD thesis is 'publication-based'. Due to the scope, my thesis is divided into three volumes:

- Volume I contains the Extended Summary divided into seven chapters, 1. Summary, 2. Insect Development in a Nutshell, 3. Unpublished Results, 4. Future Trends, 5. Teaching Efforts, 6. Publications and Applications and 7. Trivia.
- Volume II contains the published manuscripts Strobl & Stelzer 2014 (#1), Nollmann *et al.* 2015 (#2), Strobl *et al.* 2015 (#3), Strobl & Stelzer 2016 (#4), Strobl *et al.* 2017A (#5), Strobl *et al.* 2017B (#6) and their respective supplementary material as summarized in Publication Table 1 and Publication Table 2 (Subchapter 6.1) as well as the submitted but not yet accepted manuscripts Strobl *et al.* 2017C (#7), Strobl *et al.* 2017D (#8) and their respective supplementary material as summarized in Publication Table 3 (Subchapter 6.2).
- Volume III contains the submission-ready manuscripts Strobl *et al.* 2017E (#9), Strobl *et al.* 2017F (#10) and their respective supplementary material as summarized in Publication Table 3 (Subchapter 6.2) as well as the patent and grant applications (Subchapter 6.3).

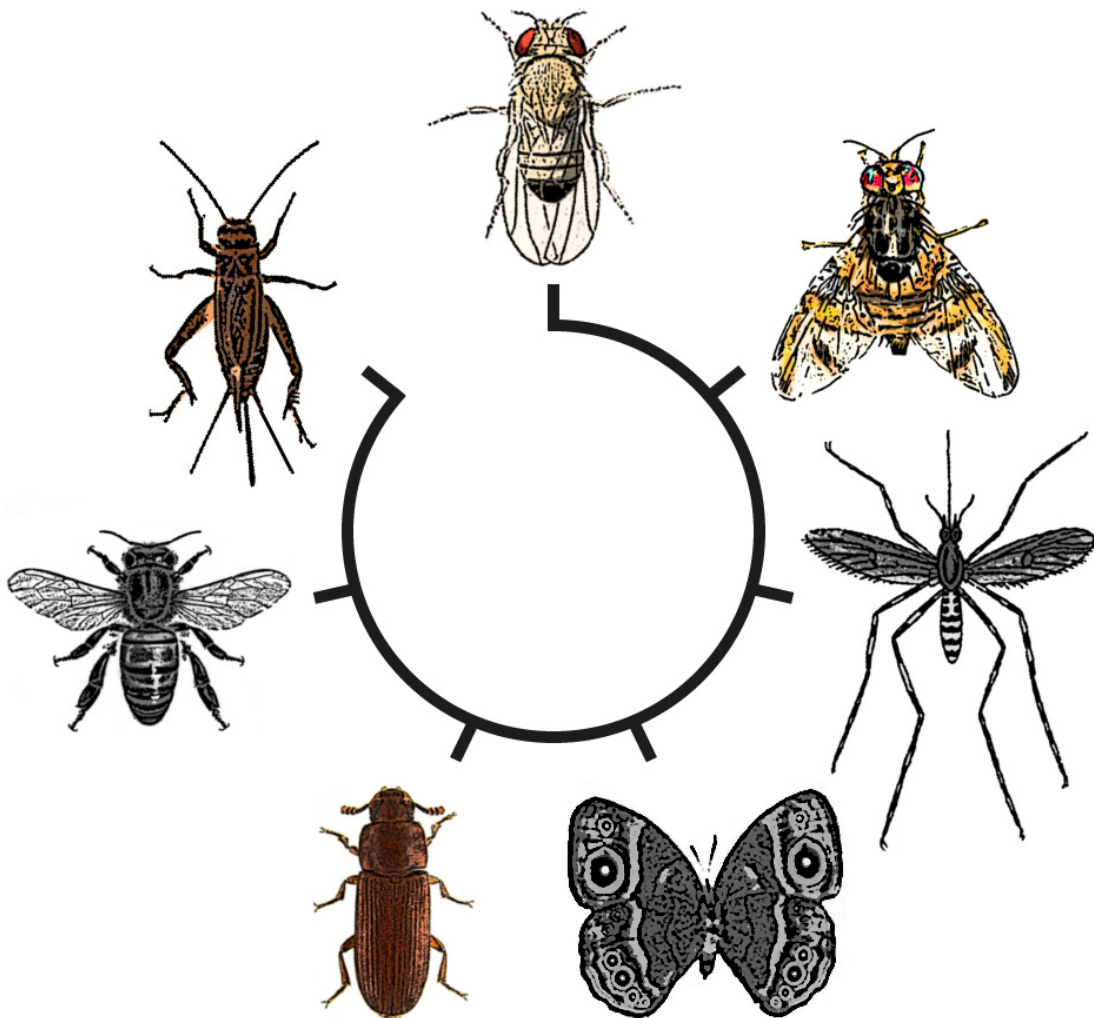


Table of Contents

1. Summary	8
1.1. Deutsche Zusammenfassung	9
1.2. Deutsche Kurzfassung	10
1.2.1. Haltemethoden für <i>Tribolium</i> -Embryos in der Lichtblatt-Fluoreszenzmikroskopie	10
1.2.2. Die Embryonale Morphogenese von <i>Tribolium castaneum</i>	11
1.2.3. Die Embryonale Morphogenese von <i>Ceratitis capitata</i> und <i>Gryllus bimaculatus</i>	11
1.2.4. Ein Vektorkonzept für die Systematische Herstellung von Homozygot Transgenen Linien	11
1.2.5. Schlussfolgerung und Blick in die Zukunft	14
1.3. English Abstract	15
1.4. English Summary	16
1.4.1. Mounting Methods for <i>Tribolium</i> Embryos in Light Sheet-Based Fluorescence Microscopy	16
1.4.2. The Embryonic Morphogenesis of <i>Tribolium castaneum</i>	17
1.4.3. The Embryonic Morphogenesis of <i>Ceratitis capitata</i> and <i>Gryllus bimaculatus</i>	17
1.4.4. A Vector Concept for the Systematic Creation of Homozygous Transgenic Lines	17
1.4.5. Conclusion and Future Trends	20
2. Insect Development in a Nutshell	21
2.1. Introduction	22
2.1.1. Insects and Developmental Biology	22
2.1.2. Developmental Biology and Advanced Fluorescence Live Imaging Techniques	25
2.1.3. Advanced Fluorescence Live Imaging Techniques and Functional Genetics	27
2.1.4. Aim of my PhD Project	29
2.2. Achievements	30
2.2.1. Long-Term Live Imaging of the ‘Gold Standard’ <i>Drosophila melanogaster</i>	30
2.2.2. Non-Invasive Long-Term Fluorescence Live Imaging of <i>Tribolium castaneum</i> Embryos	33
2.2.3. Side-By-Side Comparison of <i>Drosophila</i> and <i>Tribolium</i> Embryonic Morphogenesis	39
2.2.4. Standard Operating Procedures for Fluorescence Microscopy of <i>Tribolium</i> Embryos	41
2.2.5. The Embryonic Morphogenesis of <i>Ceratitis capitata</i> – A Fairly Complete Description	48
2.2.6. Side-By-Side Comparison of <i>Drosophila</i> and <i>Ceratitis</i> Embryonic Morphogenesis	55
2.2.7. AGameOfClones – Systematic Creation of Homozygous Transgenic Lines	57
3. Unpublished Results	67
3.1. Non-Invasive Long-Term Live Imaging of <i>Gryllus bimaculatus</i> Embryos	68
3.1.1. Imaging Large Specimens with Light Sheet-Based Fluorescence Microscopy	68
3.1.2. The Morphogenetic Dynamics of Katatrepsis and Dorsal Closure in <i>Gryllus</i>	69
3.2. Registration and Fusion of <i>Tribolium</i> Long-Term Live Imaging Datasets	73
3.2.1. Compensating the Shadowing Effect by Reconstructing the Specimen	73
3.2.2. Evaluation of the Bead-Based / Landmark-Based Registration and Fusion Method	74
3.3. The BugCube Project – Sharing of Image Data with the Community	77
3.3.1. Theoretical Background and Current Implementation	77
3.3.2. Anticipated Scope – Fluorescence Channels, More Directions and JPEG2000	79
3.4. AClashOfStrings – Systematic Creation of Double Homozygous Transgenic Hybrid Lines	79
3.4.1. Nota Bene	79
3.4.2. The AClashOfStrings Vector Concept – From the F3 to the F7	80
3.4.3. The AClashOfStrings Vector Concept – From the F7 to the F10	86
3.4.4. Advantages of the AClashOfStrings Vector Concept	88
3.5. AStormOfRecords – Systematic Creation of Triple Homozygous Transgenic Hybrid Lines	89
3.5.1. The AStormOfRecords Vector Concept	89
3.5.2. Preliminary Experiments and Further Considerations	90

4. Future Trends	91
4.1. Outlook	92
4.1.1. Nota Bene	92
4.1.2. Outlook I – A Comparative Approach to Embryonic Robustness	93
4.1.3. Outlook II – Functional Genetics	95
4.1.4. Outlook III – Biological Questions	96
4.1.5. Outlook IV – Universalizing AGameOfClones	103
4.1.6. Outlook V – Side Projects	103
4.2. Perspective	107
4.2.1. The Primary Level – Developmental Biology	107
4.2.2. The Secondary Level – Evolutionary Developmental Biology	111
4.2.3. The Tertiary Level – Ecological Evolutionary Developmental Biology	114
4.2.4. Imaging Insect Morphogenesis – Ongoing Technical Challenges and Potential Synergies	114
4.2.5. Imaging Insect Morphogenesis – From On-Demand to Systematic Data Acquisition	118
4.2.6. Closing Summary and Concluding Remarks	120
5. Teaching Efforts	121
5.1. Alexander Ross – Master Thesis in <i>Cell Biology and Physiology</i>	122
5.2. David Kleinhans – Master Thesis in <i>Cell Biology and Physiology</i>	123
5.3. Anita Anderl – Master Thesis in <i>Biophysics</i>	124
5.4. Selina Klees – Bachelor Thesis in <i>Bioinformatics</i>	125
5.5. Franziska Krämer – Bachelor Thesis in <i>Bioinformatics</i>	126
5.6. Henrik Tonner – Master Thesis in <i>Biochemistry</i>	127
6. Publications and Applications	128
6.1. Published Manuscripts	129
6.1.1. Nota Bene	129
6.1.2. Strobl & Stelzer 2014 (#1) – <i>Development</i> (Research Article)	130
6.1.3. Nollmann <i>et al.</i> 2015 (#2) – <i>ChemBioChem</i> (Research Article)	131
6.1.4. Strobl <i>et al.</i> 2015 (#3) – <i>Nature Protocols</i> (Research Article)	132
6.1.5. Strobl & Stelzer 2016 (#4) – <i>Current Opinion in Insect Science</i> (Invited Review Article)	133
6.1.6. Strobl <i>et al.</i> 2017A (#5) – <i>Journal of Visualized Experiments</i> (Invited Research Article)	134
6.1.7. Strobl <i>et al.</i> 2017B (#6) – <i>Nature Protocols</i> (Invited Review Article)	135
6.2. Submitted and Submission-Ready Manuscripts	136
6.2.1. Nota Bene	136
6.2.2. Strobl <i>et al.</i> 2017C (#7) – <i>To Be Determined</i> (Research Article)	137
6.2.3. Strobl <i>et al.</i> 2017D (#8) – <i>To Be Determined</i> (Research Article)	138
6.2.4. Strobl <i>et al.</i> 2017E (#9) – <i>To Be Determined</i> (Research Article)	139
6.2.5. Strobl <i>et al.</i> 2017F (#10) – <i>To Be Determined</i> (Research Article)	140
6.3. Patent and Grant Applications	141
6.3.1. Patent Application – The AGameOfClones Vector Concept	141
6.3.2. Grant Application – The ‘Reinhart Koselleck-Projekt’	143
7. Trivia	145
7.1. Erklärung bezüglich bereits abgelegter Doktorprüfungen	146
7.2. Eidesstattliche Versicherung	146
7.3. Curriculum Vitae	146
7.4. Danksagung	147
7.5. Quellenverzeichnis	148

Prolog

Manchmal braucht es nicht mehr als einen noch fast unbenutzten Insekten-Inkubator, ein doch noch relativ jungfräuliches Mikroskop und ein kleines bisschen Geduld, um selbst ohne großartiges Vorwissen zumindest einigermaßen professionelle Forschung machen zu können und deren Resultate auch an den motivierten Nachwuchs weitergeben zu können. Da eine Doktorarbeit für gewöhnlich nur das wissenschaftliche Destillat von 3-5 Jahren praktischer Arbeit beinhaltet, man aber von dem was Drumherum geschieht nur selten etwas mitbekommt, habe ich mich entschlossen, eine Abbildung oder Tabelle an den Anfang von jedem der sieben Kapitel zu setzen, die darauf hinweisen sollen, dass während jeder Doktorarbeit immer mehr geschieht, als sich in gut 150 Seiten pressen lässt. Eine Erinnerung für all die Studenten, egal ob meiner oder anderer, die noch nicht wissen, ob sie sich auch auf dieses Abenteuer einlassen sollen.

Gewidmet sei diese Arbeit

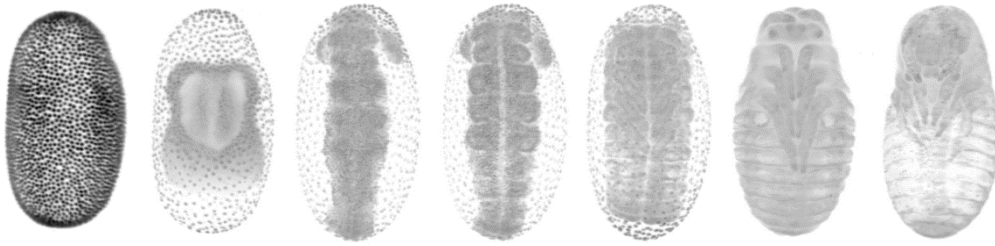
Alexander, David, Anita, Selina, Franziska, Henrik

und allen, die noch kommen werden.

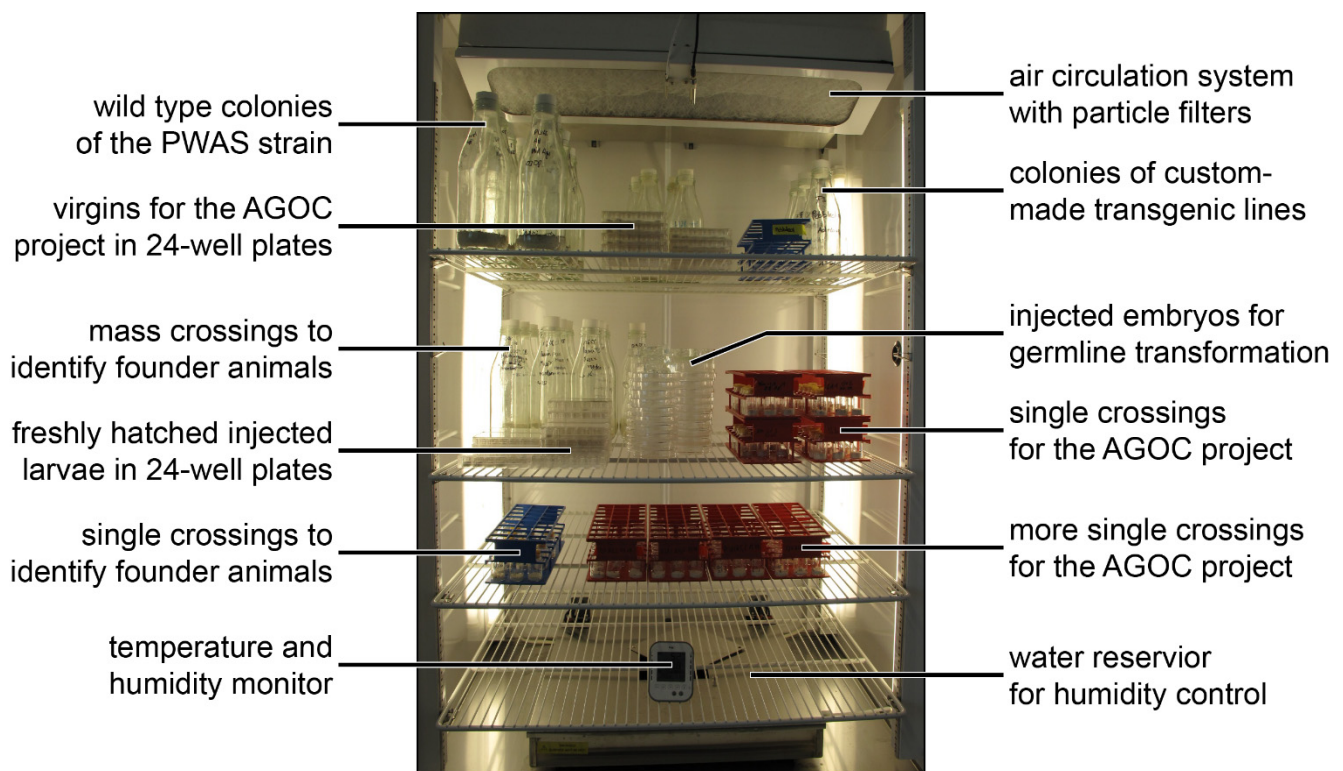
• Valar Morghulis •



1. Summary



*This chapter summarizes the major achievements of my PhD project in German and English. According to the doctorate regulations of the Johann Wolfgang Goethe-Universität, two German versions are required: The first version, entitled *Deutsche Zusammenfassung*, spans only one page. It will be also handed in separately in addition to the thesis books. The second version, entitled *Deutsche Kurzfassung*, explains ‘the whole story’ slightly abbreviated within five pages. It also contains four figures. The English Abstract and the English Summary are analogous translations of the German versions and were added for convenience.*



An insect incubator during the fifth year of my PhD project, anno 2016. Insect incubators are essential to rear insect model organisms in the laboratory, as they control temperature, humidity and provide a controlled day/night cycle. At this time, there were already two insect incubators in the laboratory. While this incubator runs at 32°C to minimize the generation time of *Tribolium*, the second incubator runs at 25°C to maintain the majority of custom-made transgenic lines. This chapter figure should show how certain projects evolve over the years. At the end of the first year, I had only two to three cultures of the same transgenic line in the incubator, at the end of my PhD project, I am nearly running short of space.

1.1. Deutsche Zusammenfassung

Die Fruchtfliege *Drosophila melanogaster* gehört zu den wichtigsten biologischen Modellorganismen, doch ausschließlich der vergleichende Ansatz mit nahe verwandten Spezies erlaubt Aussagen über die evolutionäre Diversifikation der Insekten. Eine besondere Stellung nimmt die Fluoreszenzmikroskopie von lebenden, sich entwickelnden Embryonen ein, mit deren Hilfe die dreidimensionale Morphogenese als Funktion der Zeit erfasst, beschrieben und verglichen werden kann. Allerdings gibt es für Spezies außer *Drosophila*, zum Beispiel den Rotbraunen Reismehlkäfer *Tribolium castaneum*, bislang kaum etablierte Standards und die verfügbaren Daten und Ressourcen sind vergleichsweise gering. Ziel meiner Doktorarbeit war es, diese Limitierungen aufzuheben. Die folgenden sechs Meilensteine konnten erreicht werden:

- Entwicklung der Hemisphäre- und Netzhaltermethoden für nicht-invasive Langzeitaufnahmen von *Tribolium*-Embryos in Lichtblatt-Fluoreszenzmikroskopen und Charakterisierung der wichtigsten embryonalen Ereignisse.
- Ausführliche protokollarische Dokumentation dieser Methoden, die unter anderem (i) die Haltung im Labor, (ii) die Vorbereitung der Embryonen, (iii) die Konfiguration des Lichtblatt-Fluoreszenzmikroskops, (iv) das Durchführen der Aufnahme über mehrere Tage, (v) die Rettung der erfassten Embryos zur Qualitätskontrolle sowie (vi) das Prozessieren der Daten beschreiben.
- Umfangreiche Adaptionen dieser Methoden, um die embryonale Morphogenese der mediterranen Fruchtfliege *Ceratitis capitata* und der Mittelmeer-Feldgrille *Gryllus bimaculatus* zu beschreiben, zu analysieren und in einen evolutionären Kontext zu setzen.
- Weiterentwicklung der Hemisphäremethode, die die Referenzpunkt-basierte Fusion von dreidimensionalen Bildern erlaubt, welche entlang mehrerer Richtungen aufgenommen wurden, um so den Schattenwurf-Effekt zu kompensieren.
- Erstellen des BugCubes, eines Web-basierten Computerprogramms, mit dem Bilddaten, die mit Hilfe der Lichtblatt-Fluoreszenzmikroskopie erfasst wurden, mit Kollegen geteilt werden können.
- Entwicklung und experimenteller Beweis der Funktionalität des (i) AGameOfClones Vektorkonzeptes um homozygote transgene Insektenlinien systematisch herzustellen. Weiterentwicklung und teilweiser experimenteller Beweis der Funktionalität des (ii) AClashOfStrings Vektorkonzeptes um doppelt homozygote transgene Insektenlinien systematisch herzustellen, sowie eine vorläufige Evaluierung des (iii) AStormOfRecords Vektorkonzeptes um dreifach homozygote transgene Insektenlinien systematisch herzustellen.
- Erschaffung und Eignungsprüfung von mehr als fünfzig transgenen *Tribolium*-Linien für die Langzeitaufnahme der Embryonalentwicklung in Fluoreszenzmikroskopen, unter anderem die ersten Lifeact- und Histon-basierten Linien.

Meine primären Resultate leisten einen signifikanten Beitrag zur erweiterten Fluoreszenzmikroskopie von Insektenpezies jenseits von *Drosophila*. Sie erlauben es, verschiedene Strategien der embryonalen Insektenmorphogenese zu vergleichen und damit in einen phylogenetischen Kontext zu setzen. Meine technischen Entwicklungen erweitern das methodologische Arsenal für Insekten beachtlich.

In meiner Perspektive erörtere ich die Wichtigkeit von nicht-invasiven Fluoreszenz-Langzeitaufnahmen zur Erstellung von spezies-spezifischen morphogenetischen Standards, diskutiere die Praktikabilität einer morphologischen Ontogenie auf dem zellulären Level, schlage einen ‘verschachtelten linear abnehmenden Verwandtschaftsverhältnis’-Ansatz für die evolutionäre Entwicklungsbiologie vor, suggeriere Lebendaufnahmen von Spezieshybriden um das Entstehen neuer Arten zu untersuchen und skizziere zuletzt den Betrag der Lichtblatt-Fluoreszenzmikroskopie zur Umstellung auf systematische Datenakquise.

Aus meiner Doktorarbeit gehen zehn Fachartikel hervor, von denen sechs bereits in wissenschaftlichen Zeitschriften mit Begutachtungsverfahren publiziert wurden, außerdem habe ich vier Masterarbeiten und zwei Bachelorarbeiten betreut, deren wissenschaftliche Fragestellungen an mein Promotionsthema angelehnt waren.

1.2. Deutsche Kurzfassung

Um die Evolution der Insekten zu verstehen, muss die Entwicklung der Fruchtfliege *Drosophila melanogaster* mit der von anderen Spezies, zum Beispiel der des Rotbraunen Reismehlkäfers *Tribolium castaneum*, verglichen werden. Das Spektrum verfügbarer Methoden und Ressourcen, besonders an Protokollen für und Daten von Fluoreszenz-Lebendaufnahmen, ist jedoch sehr gering. Meine Aufgabe war es, diese Limitierungen aufzuheben und die embryonale Morphogenese neuer Insektenmodellorganismen vergleichbar zu machen.

1.2.1. Haltemethoden für *Tribolium*-Embryos in der Lichtblatt-Fluoreszenzmikroskopie

Der Rotbraune Reismehlkäfer *Tribolium castaneum* gehört zu den Coleoptera, die sich in etwa vor 330 Millionen Jahren von den Diptera abgespalten haben. Er ist der zweitwichtigste Insektenmodellorganismus in der Entwicklungsgenetik. Allerdings sind bisher kaum morphogenetische Daten verfügbar. Als ersten Schritt etablierte ich Haltemethoden, um nicht-invasive Langzeitaufnahmen von *Tribolium*-Embryos im Lichtblatt-Fluoreszenzmikroskop durchzuführen. Zunächst adaptierte ich die Agarosesäulemethode, welche schon erfolgreich an *Drosophila*-Embryos angewendet wurde. Allerdings bricht die Entwicklung von vollständig in Agarose eingebetteten *Tribolium*-Embryonen nach einigen Stunden ab. Deshalb erfand ich die Hemisphäre- und Netzhaltermethoden (Abbildung 1-1).

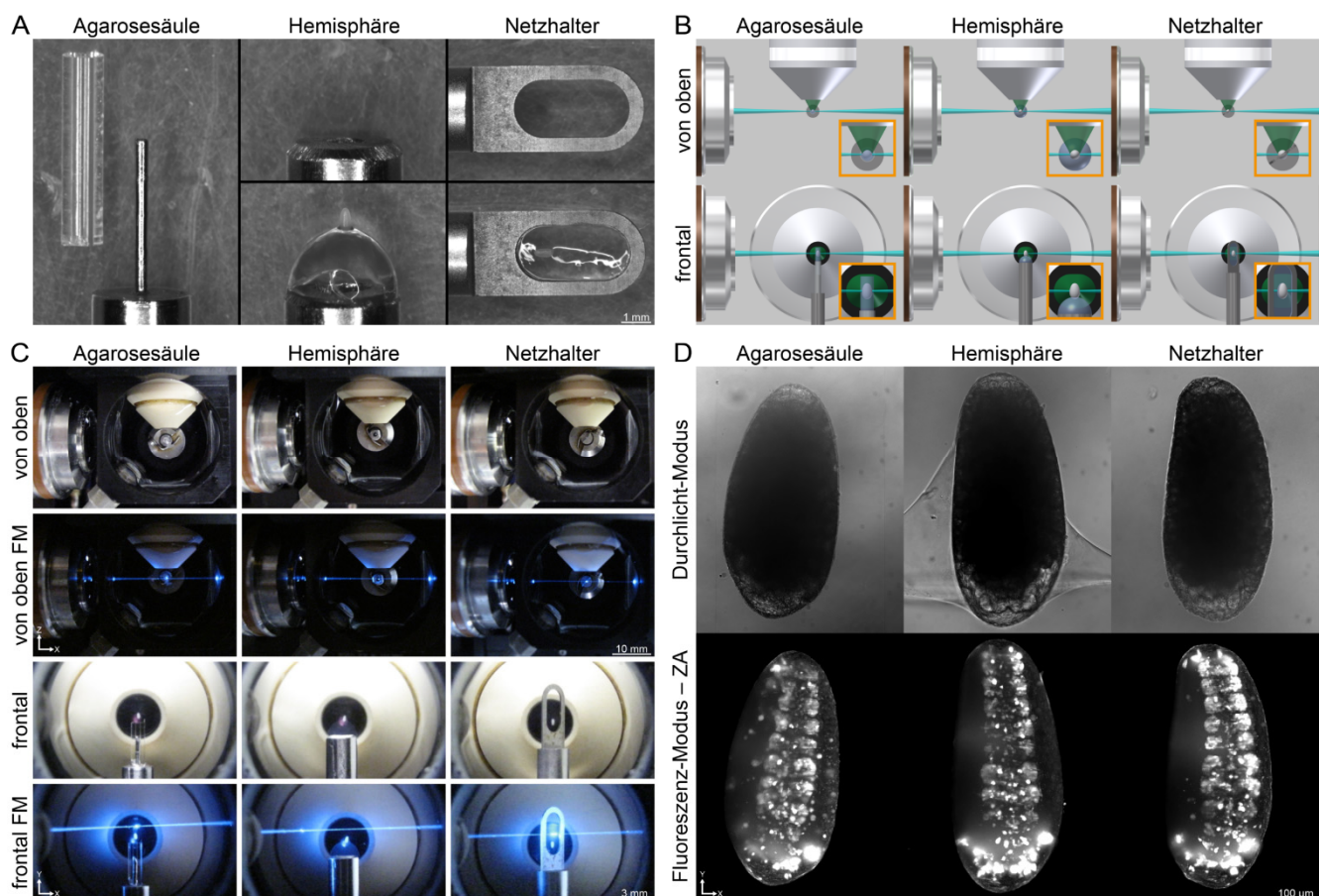


Abbildung 1-1 – Drei unterschiedliche Haltemethoden, die verwendet wurden um die Embryogenese von *Tribolium castaneum* im Lichtblatt-Fluoreszenzmikroskop zu erfassen. (A) Agarosesäule, Hemisphäre und Netzhalter. **(B)** Schemata der drei Haltemethoden während der Aufnahme. **(C)** Verwendung der Haltemethoden in einem Lichtblatt-Fluoreszenzmikroskop mit digital abtastendem Laser. **(D)** Beispielbilder von *Tribolium*-Embryonen der transgenen Glia-Blue-Linie. FM, Fluoreszenz-Modus; ZA, Z-Maximum-Projektion mit nachträglicher Intensitätsanpassung. Abbildung und/oder Abbildungsbeschreibung vollständig und/oder teilweise reproduziert von Strobl *et al.* 2017A, #5 in Publication Table 2.

1.2.2. Die Embryonale Morphogenese von *Tribolium castaneum*

Bei den Hemisphäre- und Netzhaltermethoden ist die Oberfläche des Embryos nur partiell in Kontakt mit der Agarose während der größte Teil dem Puffer ausgesetzt ist. Das reduziert die mechanische Behinderung und fördert den Gasaustausch. Dadurch konnte ich annäherungsweise die gesamte Embryonalentwicklung von *Tribolium* erfassen (Abbildung 1-2) und eine bisher unbekannt Struktur, die Serosanarbe (engl. serosa scar), identifizieren. Sie stellt eine Verbindung zwischen dem Serosa-Fensterschluss während der Gastrulation und dem Aufreißen der Serosamembran während des Dorsalsschlusses da. Um die Lücke zwischen den technisch- und biologisch-orientierten Laboratorien zu verringern sind alle entsprechenden Datensätze als Ressource verfügbar und die beschriebenen Methoden umfassend in Form von Protokollen niedergelegt.

1.2.3. Die Embryonale Morphogenese von *Ceratitis capitata* und *Gryllus bimaculatus*

Die Signifikanz des vergleichenden Ansatzes steigt mit der Zahl untersuchter Spezies erheblich an. Deshalb führte ich im Anschluss nicht-invasive Langzeit-Lebendaufnahmen von transgenen *Ceratitis capitata* und *Gryllus bimaculatus* Embryonen mit Hilfe der Lichtblatt-Fluoreszenzmikroskopie durch (Abbildung 1-3).

Die Mediterrane Fruchtfliege *Ceratitis capitata* ist der Hauptüberträger der Feuerbrand-Pflanzenkrankheit und deshalb ein etablierter Modellorganismus in den Agrarwissenschaften. Mit einem evolutionären Abstand von etwa 80 Millionen Jahren ist sie sehr nah mit *Drosophila* verwandt. Durch Adaption der Netzhaltermethode gelang es, ungefähr 97% der gesamten Embryonalentwicklung zu erfassen, was es wiederum ermöglichte die Gesamtembryogenese in einem sehr hohen Detailgrad zu beschreiben. Die Mittelmeer-Feldgrille *Gryllus bimaculatus* ist der primäre Modellorganismus für die Entwicklung von hemimetabolen Insekten. Da die anterior-posterior Länge der Eier von ungefähr 3 mm eine große Herausforderung für die Erfassung der gesamten Embryos auf dem zellulären Level darstellt, mussten diese für jede Aufnahmerichtung entlang vier überlappender Z-Stapel aufgenommen und anschließend in drei Dimensionen zusammengefügt werden. Die Anwendung dieser Strategie erlaubte es mir, zwei embryonale Ereignisse zu dokumentieren, Katatrepsis und Dorsalschluss.

Auch nach dreidimensionalem Zuschneiden und verlustfreier Kompression haben meine Bilddaten noch ein Volumen von mehreren Terabytes. Um diese mit Kollegen teilen zu können habe ich den BugCube, ein Web-basiertes Computerprogramm, erstellt, mit dem sich alle Datensätze, die ich während meiner Doktorarbeit aufgenommen habe, ansehen und einzelne Bilder, Z-Maximum-Projektionen, Z-Stapel sowie Z-Maximum-Projektionen-Zeit-Stapel herunterladen lassen.

1.2.4. Ein Vektorkonzept für die Systematische Herstellung von Homozygot Transgenen Linien

Transgene Insekten und ihre Nachkommen, die in den oben beschriebenen Versuchen verwendet werden, sind entweder hemi- oder homozygot für das Transgen. Sie werden typischerweise als hemizygot/homozygote Mischkulturen gehalten oder zeitaufwändig gekreuzt, um homozygote Kulturen zu bekommen. Um hochwertige und reproduzierbare Ergebnisse zu erhalten sollte in der Fluoreszenzmikroskopie nur mit den Letztgenannten gearbeitet werden. Erstens wird das Halten und Züchten der Kulturen vereinfacht, da das Transgen nicht mehr angereichert werden muss. Zweitens sind die experimentellen Bedingungen eher vergleichbar, da nur ein Genotyp präsent ist. Drittens ist das durchschnittliche Fluoreszenzsignal stärker. Allerdings bedarf es weiterer Assays um homozygote Kulturen herzustellen. Das kostet Arbeitskraft, Verbrauchsgüter sowie Zeit und kann invasiv oder inkompatibel mit dem experimentellen Arbeitsplan sein. Deshalb erfand ich das AGameOfClones Vektorkonzept, in dem zwei phänotypisch klar unterscheidbare Transformationsmarker in miteinander verwobenen, aber inkompatiblen Lox-Sequenzen eingebettet sind (Abbildung 1-4A). Eine solche Vektorarchitektur erlaubt die systematische Herstellung von homozygoten transgenen Insektenlinien. Nach Cre-vermittelten Rekombination (Abbildung 1-4B) werden Individuen, die beide Marker exprimieren, als heterozygot identifiziert. Anschließend können in der folgenden Generation homozygote Nachkommen durch Wegfall eines Markers selektiert werden. Weiterhin erlauben die AClashOfStrings und AStormOfRecords Vektorkonzepte, die farbverschobene Weiterentwicklung des AGameOfClones Vektorkonzeptes sind, die systematische Herstellung von doppelt homozygoten sowie dreifach homozygoten transgenen Linien.

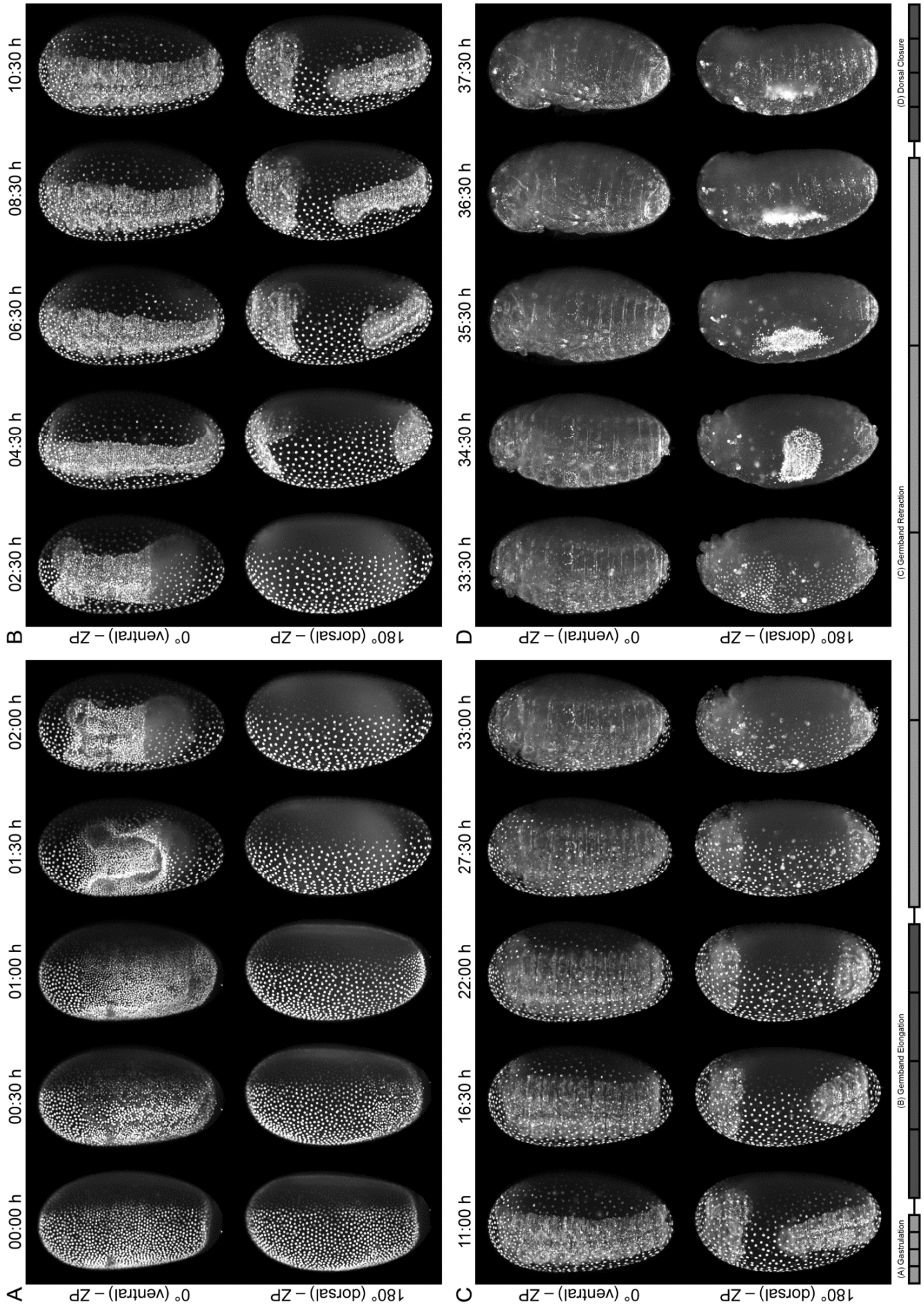


Abbildung 1-2 – Embryogenese von *Tribolium castaneum*. Vier embryonale Ereignisse, (A) Gastrulation, (B) Keimbandelongation, (C) Keimbandrückzug und (D) Dorsalschluss, sind gezeigt. Der Fortschrittsbalken zeigt den zeitlichen Rahmen der Aufnahmen. ZP, Z-Maximum-Projektion mit Anpassung. Abbildung und/oder Abbildungsbeschreibung vollständig und/oder teilweise reproduziert von Strobl & Stelzer 2014, #1 in Publication Table 1.

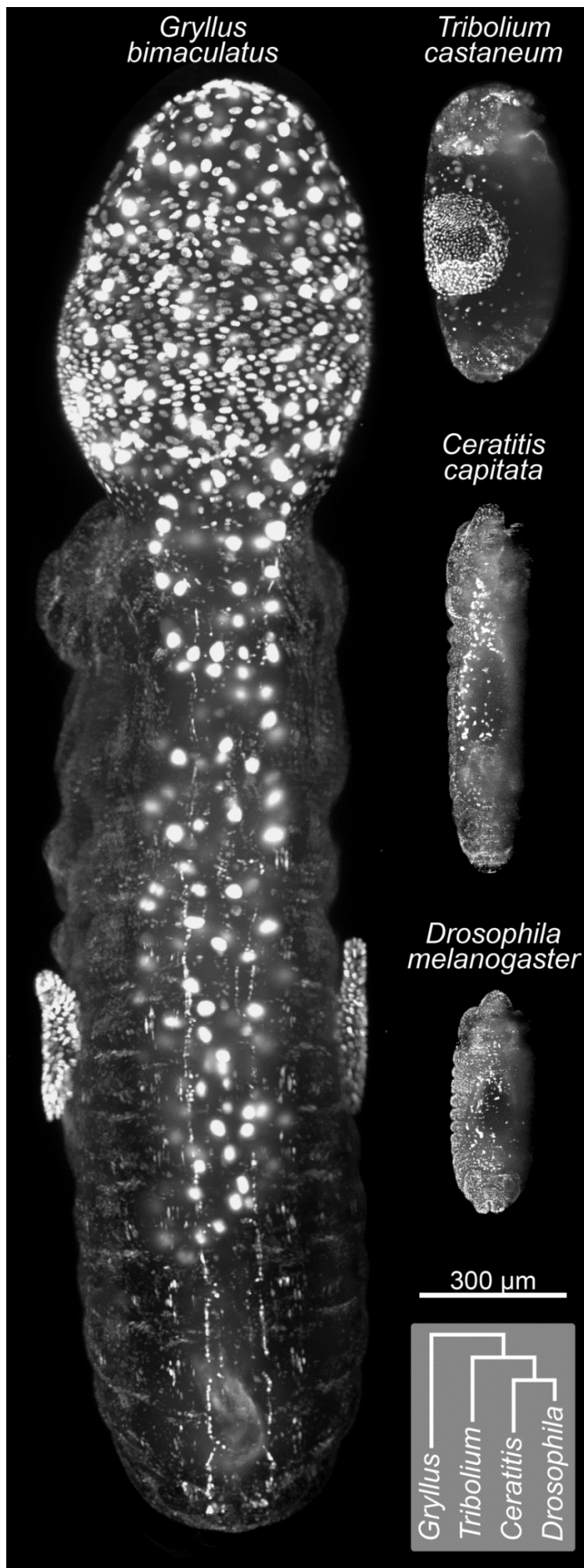
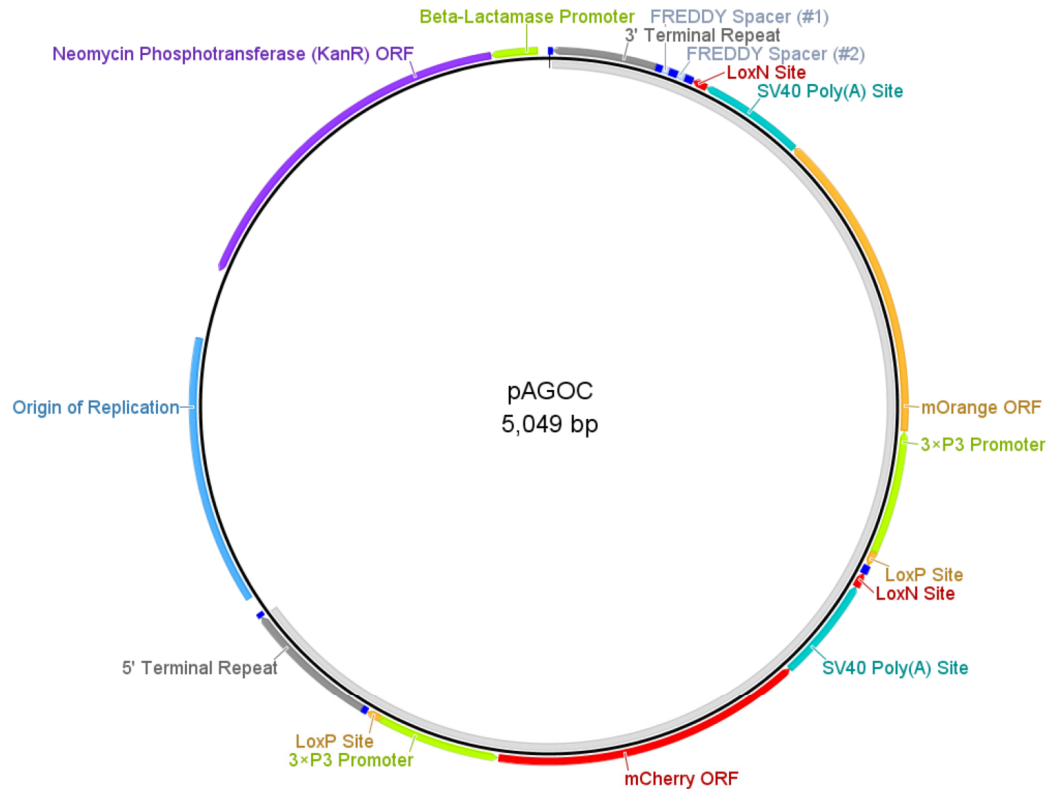


Abbildung 1-3 – Beispielbilder lebender transgener Embryos von vier verschiedenen Insektenpezies gezeigt als Z-Maximum-Projektionen während des Dorsalschlusses. Alle Embryos exprimieren entweder ein nuklear-lokalisiertes Fluoreszenzprotein oder ein Histon-Untereinheit-gekoppeltes Fluoreszenzprotein unter Kontrolle eines ubiquitären Promoters. Die Box in der unteren rechten Ecke veranschaulicht die phylogenetische Verwandtschaft der Spezies. Während *Tribolium castaneum* (Rohbrauner Reismehlkäfer), *Ceratitis capitata* (Mediterrane Fruchtfliege) und *Drosophila melanogaster* (Fruchtfliege) vollständig mit einem einzigen Aufnahmevolumen erfasst werden konnten, musste *Gryllus bimaculatus* (Mittelmeer-Feldgrille) mit vier vertikal überlappenden Aufnahmevolumen erfasst werden, die anschließend in drei Dimensionen fusioniert wurden. Alle Embryonen überlebten den Aufnahmeprozess. Abbildung und/oder Abbildungsbeschreibung vollständig und/oder teilweise reproduziert von Strobl *et al.* 2017B, #6 in Publication Table 2.

A



B

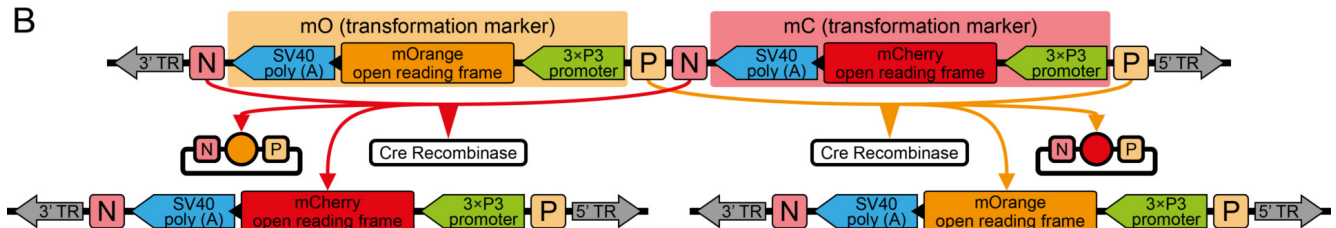


Abbildung 1-4 – Das AGameOfClones Vektorkonzept. (A) Vektorkarte von pAGOC in der minimalen funktionierenden Konfiguration. Die innere hellgraue Bande zeigt das Transgen an, die dunkelblauen Abschnitte zeigen einmalige Schnittstellen. Zusätzliche Fracht kann in die #1 und #2 Steckplätze eingefügt werden, in denen sich standardmäßig FREDDY-Platzhalter befinden. (B) Nach erfolgreicher Integration in das Zielgenom führt Cre-vermittelte Rekombination zum Verlust von entweder mO oder mC. Wenn ein Marker entfernt wird, dann verbleibt der andere im Genom, weil die beiden residualen Lox-Sequenzen inkompatibel sind. ORF, Offener Leserahmen; TR, Terminale Wiederholungen; SV40, Simian Virus 40; P, LoxP-Sequenz; N, LoxN-Sequenz. Abbildung und/oder Abbildungsbeschreibung vollständig und/oder teilweise reproduziert von Strobl *et al.* 2017D, #8 in Publication Table 3.

1.2.5. Schlussfolgerung und Blick in die Zukunft

Meine Methoden und Protokolle, meine Mikroskopiedaten sowie meine Vektorkonzepte leisten einen wichtigen Beitrag zum derzeitigen Wissensstand und zukünftigen Verständnis der Morphogenese der Insekten und, gleichsam wichtig, ihrer Evolutionsgeschichte. Die wichtigste Neuerung ist hierbei, dass meine Lebendaufnahmen, die direkt nach der Fertilisation beginnen und kurz vor dem Schlüpfen enden, in systematisch akquirierten Daten resultieren, die als ‘Ground Truth’ in Studien verwendet werden können, die Aberrationen induzieren oder um Merkmale als apo- oder plesiomorphic zu charakterisieren.

In meiner Perspektive schlage ich vor, die Lichtblatt-Fluoreszenzmikroskopie zu verwenden, um (i) erweiterte spezies-spezifische Stadiensysteme zu definieren, (ii) eine morphologische Ontologie auf dem zellulären Level zu erstellen, (iii) mit Hilfe des ‘verschachtelten linear abnehmenden Verwandtschaftsverhältnis’-Ansatzes die Morphogenese der Insekten in einem breiteren evolutionären Kontext zu verstehen, (iv) Spezieshybride zu untersuchen um die Prinzipien der Artentstehung zu entschlüsseln und (v) das Potential von erweiterten funktionellen genetischen Konzepten auszunutzen.

Während meiner Doktorarbeit habe ich zehn Fachartikel verfasst, von denen sechs – vier Forschungsbeiträge und zwei Rückblicke – in wissenschaftlichen Zeitschriften publiziert wurden, und habe zu einem groß angelegten Forschungsantrag sowie einem Patentantrag beigetragen. Weiterhin habe ich vier Master- und zwei Bachelorstudenten betreut.

1.3. English Abstract

The fruit fly *Drosophila melanogaster* is one of the most important biological model organisms, but only the comparative approach with closely related species provides insights into the evolutionary diversification of insects. Of particular interest is the live imaging of fluorophores in developing embryos. It provides data for the analysis and comparison of the three-dimensional morphogenesis as a function of time. However, for all species apart from *Drosophila*, for example the red flour beetle *Tribolium castaneum*, essentially no established standard operation procedures are available and the pool of data and resources is sparse. The goal of my PhD project was to address these limitations. I was able to accomplish the following milestones:

- Development of the hemisphere and cobweb mounting methods for the non-invasive imaging of *Tribolium* embryos in light sheet-based fluorescence microscopes and characterization of most crucial embryogenetic events.
- Comprehensive documentation of methods as protocols that describe (i) beetle rearing in the laboratory, (ii) preparation of embryos, (iii) calibration of light sheet-based fluorescence microscopes, (iv) recording over several days, (v) embryo retrieval as a quality control as well as (vi) data processing.
- Adaption of the methods to record and analyze embryonic morphogenesis of the Mediterranean fruit fly *Ceratitis capitata* and the two-spotted cricket *Gryllus bimaculatus* as well as integration of the data into an evolutionary context.
- Further development of the hemisphere method to allow the bead-based / landmark-based registration and fusion of three-dimensional images acquired along multiple directions to compensate the shadowing effect.
- Development of the BugCube, a web-based computer program that allows to share image data, which was recorded by using light sheet-based fluorescence microscopy, with colleagues.
- Invention and experimental proof-of-principle of the (i) AGameOfClones vector concept that creates homozygous transgenic insect lines systematically. Additionally, partial proof-of-principle of the (ii) AClashOfStrings vector concept that creates double homozygous transgenic insect lines systematically, as well as preliminary evaluation of the (iii) AStormOfRecords vector concept that creates triple homozygous transgenic insect lines systematically.
- Creation and performance screening of more than fifty transgenic *Tribolium* lines for the long-term imaging of embryogenesis in fluorescence microscopes, including the first Lifeact and histone subunit-based lines.

My primary results contribute significantly to the advanced fluorescence imaging approaches of insect species beyond *Drosophila*. The image data can be used to compare different strategies of embryonic morphogenesis and thus to interpret the respective phylogenetic context. My technological developments extend the methodological arsenal for insect model organisms considerably.

Within my perspective, I emphasize the importance of non-invasive long-term fluorescence live imaging to establish species-specific morphogenetic standards, discuss the feasibility of a morphologic ontology on the cellular level, suggest the ‘nested linearly decreasing phylogenetic relationship’ approach for evolutionary developmental biology, propose the live imaging of species hybrids to investigate speciation and finally outline how light sheet-based fluorescence microscopy contributes to the transition from on-demand to systematic data acquisition in developmental biology.

During my PhD project, I wrote a total of ten manuscripts, six of which were already published in peer-reviewed scientific journals. Additionally, I supervised four Master and two Bachelor projects whose scientific questions were inspired by the topic of my PhD work.

1.4. English Summary

To understand the evolution of insects, the development of the fruit fly *Drosophila melanogaster* has to be compared to that of other species, for example the red flour beetle *Tribolium castaneum*. However, the arsenal of available methods and resources, especially fluorescence live imaging protocols and data, is quite small. It was my task to overcome these limitations and to compare the embryonic morphogenesis of several emerging insect model organisms.

1.4.1. Mounting Methods for *Tribolium* Embryos in Light Sheet-Based Fluorescence Microscopy

The red flour beetle *Tribolium castaneum* belongs to the Coleoptera, which diverged from the Diptera approximately 330 million years ago. It is the second most important insect model organism and frequently used in developmental genetics. However, morphogenetic data were sparse. My first task was to establish mounting techniques for non-invasive long-term live imaging of *Tribolium* embryos in light sheet-based fluorescence microscopes. Initially, I adapted the agarose column method, which was already successfully applied to *Drosophila* embryos. However, development arrested several hours after when *Tribolium* embryos had been embedded. Thus, I invented the hemisphere and the cobweb holder methods (Figure 1-1).

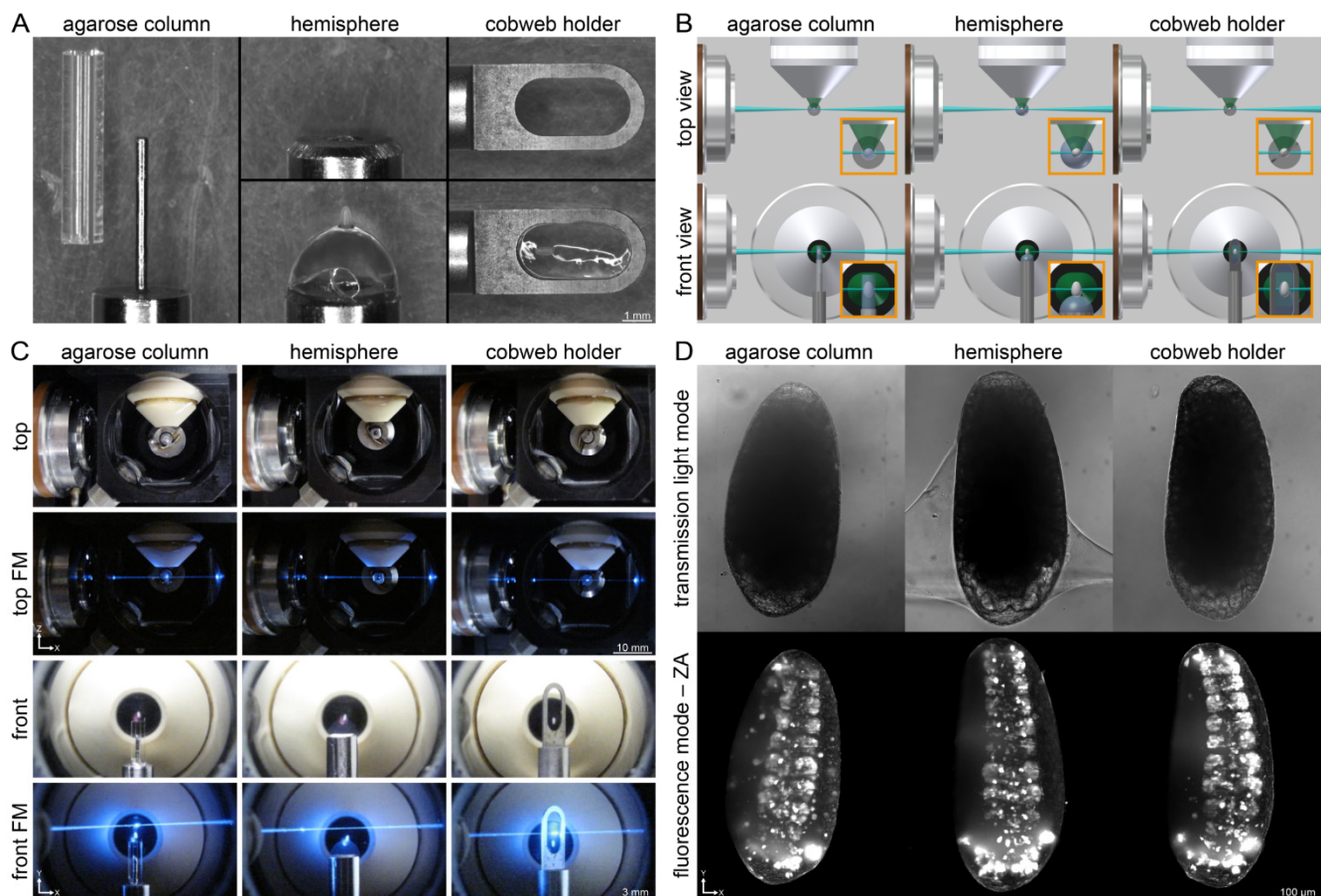


Figure 1-1 – Three different mounting methods used in the recording of the embryonic development of *Tribolium castaneum* with light sheet-based fluorescence microscopy. (A) Agarose column, hemisphere and cobweb holder. **(B)** Schematics of the three mounting methods during the recording process. **(C)** The three mounting methods applied within a digital scanned laser light sheet-based fluorescence microscope. **(D)** Exemplary images recorded with *Tribolium* embryos of the Glia-blue transgenic line. FM, fluorescence mode; ZA, Z maximum projection with intensity adjustment. Figure and/or figure description fully and/or partially reproduced from Strobl *et al.* 2017A, #5 in Publication Table 2.

1.4.2. The Embryonic Morphogenesis of *Tribolium castaneum*

With the hemisphere and cobweb holder methods, the surface of the embryo is only partially in contact with agarose while the major fraction remains exposed to the imaging buffer. This reduces the mechanical constriction and favors gas exchange. Thus, I was able to record nearly the entire embryonic morphogenesis of *Tribolium* (Figure 1-2) and discovered a previously undescribed structure, the serosa scar. It operates as a functional link between serosa window closure during gastrulation and serosa rupture during dorsal closure. To reduce the gap between the technically orientated laboratories, which primarily aim to improve the microscopy methodology, and the life science laboratories, all live imaging datasets are provided as a resource for the community and the methods are comprehensively documented as protocols.

1.4.3. The Embryonic Morphogenesis of *Ceratitidis capitata* and *Gryllus bimaculatus*

The significance of the comparative approach increases strongly with an increasing number of species. Thus, I performed non-invasive long-term live imaging of transgenic *Ceratitidis capitata* and *Gryllus bimaculatus* embryos by using light sheet-based fluorescence microscopy (Figure 1-3).

The Mediterranean fruit fly *Ceratitidis capitata* is the main vector of the fire blight plant disease and thus an established model organism in agricultural- and pest-related research. With an evolutionary gap of about 80 million years, it is a close relative of *Drosophila*. I adapted the cobweb holder method for *Ceratitidis* and was able to record five datasets that cover about 97% of the total embryonic development, which allowed me to describe the whole embryogenesis with a very high level of detail. The two-spotted cricket *Gryllus bimaculatus* is the primary model organism for hemimetabolous insect development. The eggs have an anterior-posterior length of about 3 mm, thus imaging the whole embryo on the cellular level imposed a serious challenge. For each direction, the embryos were recorded along four overlapping Z stacks, which were stitched in three dimensions. Finally, I was able to document two embryogenetic events, katatrepsis and dorsal closure.

Even after three-dimensional cropping and lossless compression, my acquired image data have a volume of several terabytes. To share the data with colleagues, I created the BugCube, a web-based computer program, which allows to browse through all datasets that were generated during my PhD project and to selectively download single planes, Z maximum projections, Z stacks as well as Z maximum projection time stacks.

1.4.4. A Vector Concept for the Systematic Creation of Homozygous Transgenic Lines

Transgenic insects and their progeny, which are used in the live imaging assays outlined above, are either hemizygous or homozygous. They are typically kept as either hemizygous/homozygous mixed cultures or are comprehensively crossed to create homozygous cultures, which is usually a time-consuming process. However, it is favorable to create and work with homozygous cultures. Firstly, culture rearing is simplified, since no curation is necessary. Secondly, the overall experimental conditions are better defined, since only one genotype is present. Thirdly, the mean fluorescence signal is stronger. However, to create homozygous cultures, additional assays are necessary, which require manpower, consumables and time and may be invasive or incompatible with the experimental workflow. Thus, I invented the AGameOfClones vector concept, in which two phenotypically clearly distinguishable transformation markers are embedded in interweaved, but in compatible Lox site pairs (Figure 1-4A). This vector architecture allows a systematic creation of homozygous transgenic lines. After Cre-mediated recombination (Figure 1-4B), individuals that express both markers are identified as heterozygous and in the next generation, homozygous progeny can be selected by the omission of one marker. Further, the AClashOfStrings and AStormOfRecords vector concepts, which are color-shifted variants of the AGameOfClones vector concept, can be used to create double homozygous and triple homozygous transgenic lines, respectively.

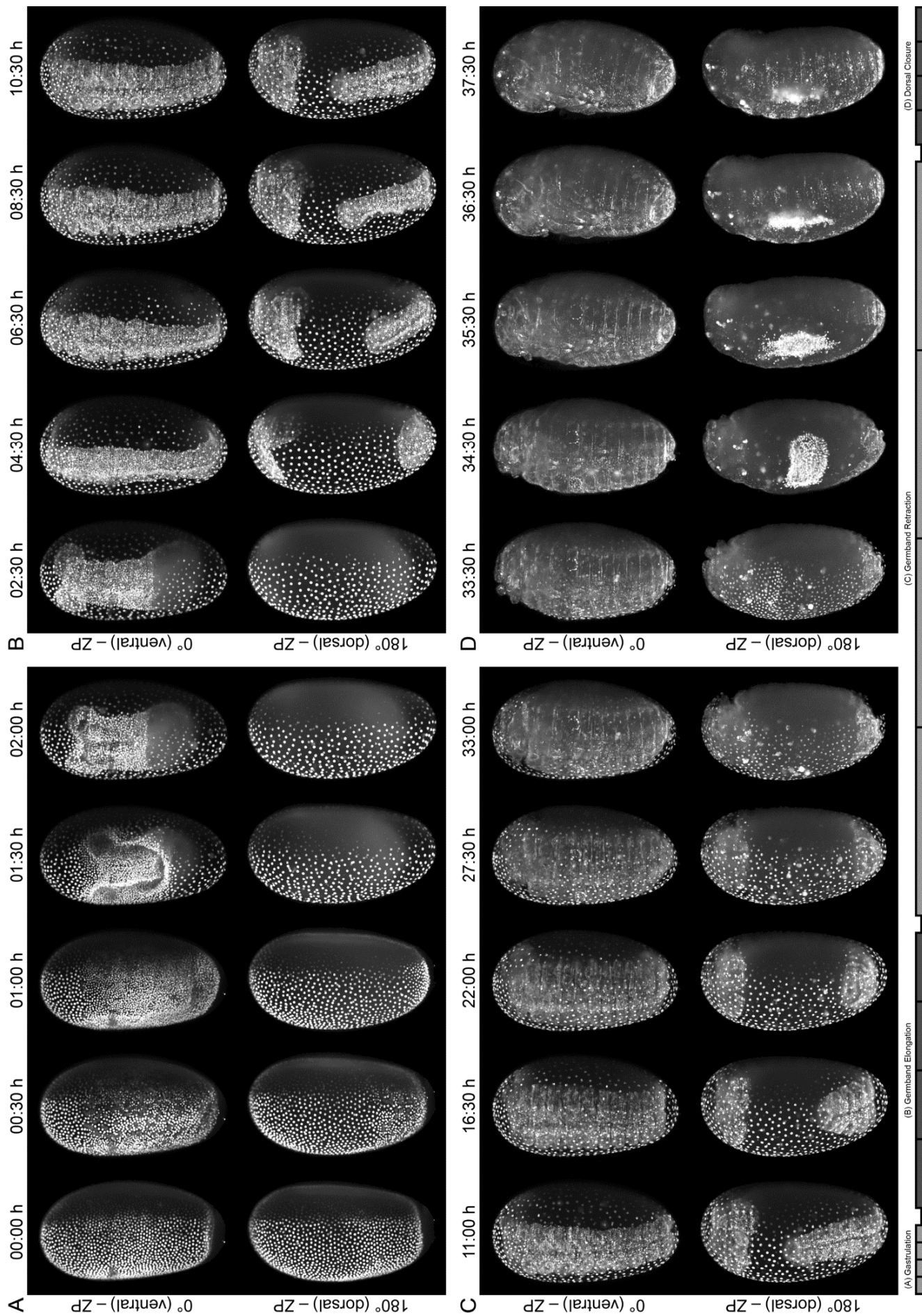


Figure 1-2 – Embryogenesis of *Tribolium castaneum*. Four embryogenetic events, (A) gastrulation, (B) germband elongation, (C) germband retraction and (D) dorsal closure, are shown. The progress bar at the bottom indicates the temporal frame of the images. ZP, Z maximum projection with image processing. Figure and/or figure description fully and/or partially reproduced from Strobl & Stelzer 2014, #1 in Publication Table 1.

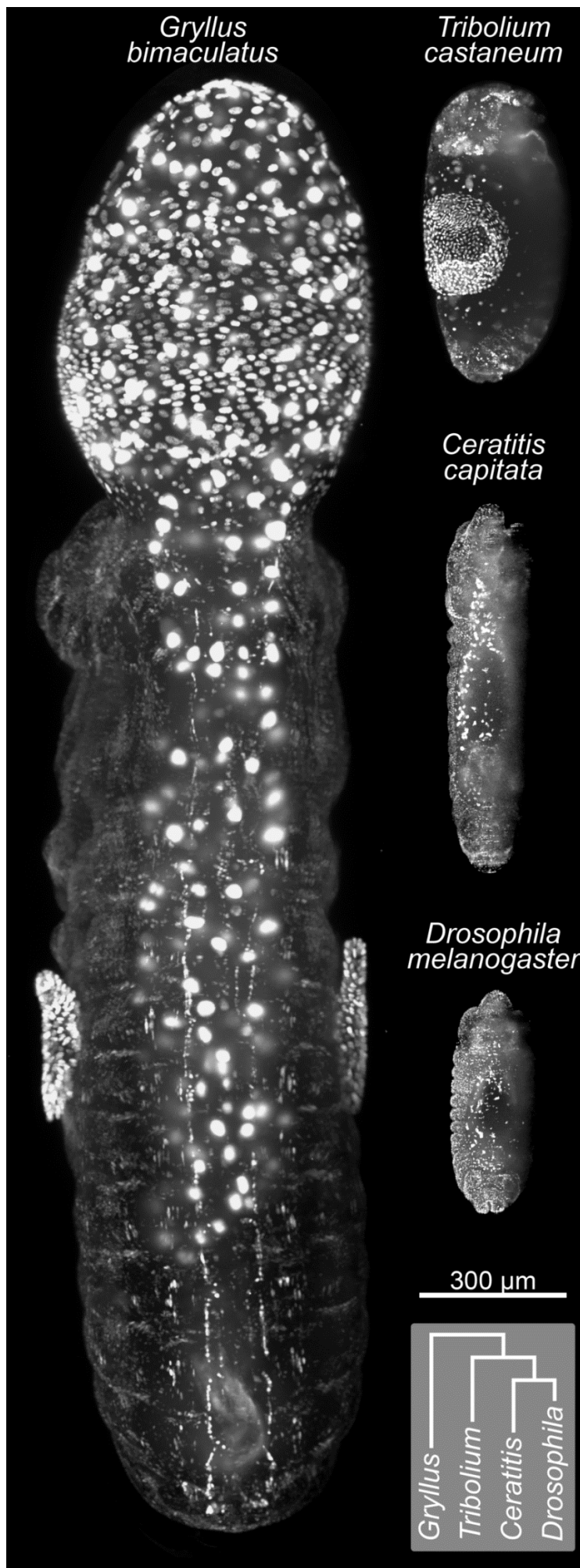


Figure 1-3 – Images of live transgenic embryos of four different insect species shown dorsally as z maximum projections during dorsal closure. All embryos expressed either a nuclear-localized fluorescent protein or a histone subunit-linked fluorescent protein under the control of a ubiquitous promoter. For convenience, the phylogenetic relationship is provided in the lower right corner. Whereas the *Tribolium castaneum* (red flour beetle), *Ceratitis capitata* (Mediterranean fruit fly), and *Drosophila melanogaster* (fruit fly) embryos were acquired *in toto* within a single volume of view, the *Gryllus bimaculatus* (two-spotted cricket) embryo was acquired with four vertically continuous volumes of view, which were stitched and fused in three dimensions. Please note that the volume of the *Gryllus* embryo is approximately 80× that of the *Drosophila* embryo. All embryos shown in this figure survived the recording process and could be raised to healthy adults. Figure and/or figure description fully and/or partially reproduced from Strobl *et al.* 2017B, #6 in Publication Table 2.

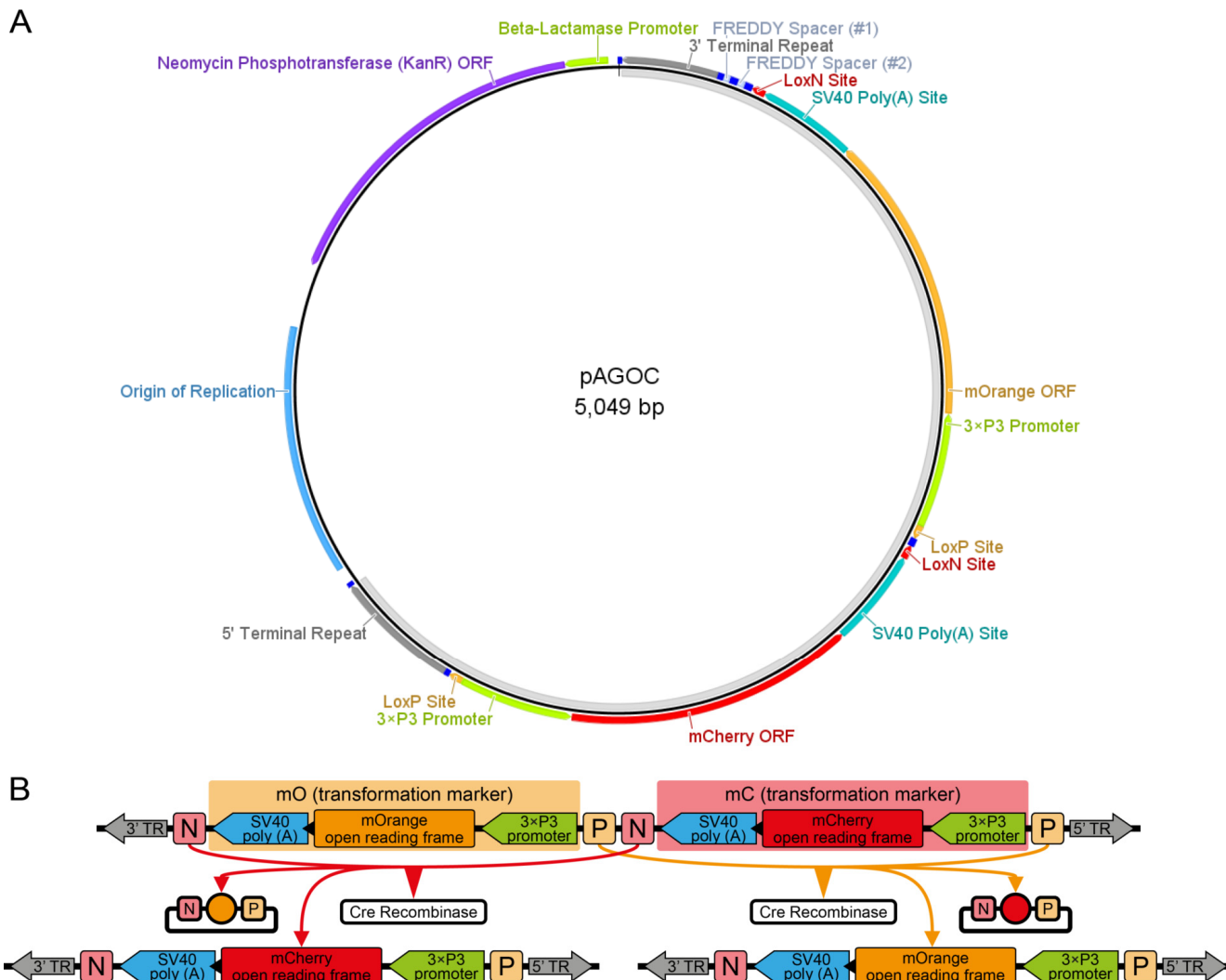


Figure 1-4 – The AGameOfClones vector concept. (A) Vector map of pAGOC in the minimal functional configuration. The light gray band on the inside indicates the transgene. The non-annotated dark blue boxes represent unique restriction enzyme sites. Additional cargo can be inserted into the #1 and #2 slots, which are per default occupied by FREDDY spacers. **(B)** After successful integration into the target genome, Cre-mediated recombination leads to the excision of either mO or mC. When one marker is removed, the other marker remains within the genome, since the two remaining Lox sites are incompatible. ORF, open reading frame; TR, terminal repeats; SV40, simian virus 40; P, LoxP Site; N, LoxN Site. Figure and/or figure description fully and/or partially reproduced from Strobl *et al.* 2017D, #8 in Publication Table 3.

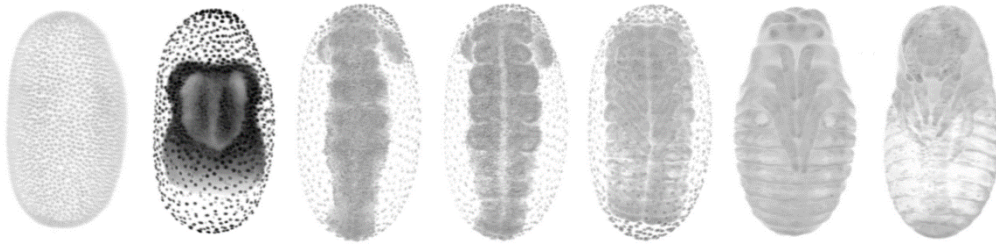
1.4.5. Conclusion and Future Trends

The methods and protocols that I established, the microscopy data that I recorded as well as the vector concepts that I invented, contribute significantly to the current knowledge and future understanding of insect morphogenesis and, equally important, also their evolutionary history. The most important novelty is that my live imaging assays, which usually begin directly after fertilization and end shortly before hatching, result in systematically acquired data, which can be used as a ‘ground truth’ for studies that induce aberrations or in the comparative approach to characterize traits as apo- and plesiomorphic.

Within my perspective, I suggest to use light sheet-based fluorescence microscopy to (i) define extended species-specific morphogenetic staging systems, (ii) establish a morphologic ontology on the cellular level, (iii) follow the ‘nested linearly decreasing phylogenetic relationship’ approach to investigate insect morphogenesis in a broader evolutionary context, (iv) analyze species hybrids to understand the principles of speciation and (v) exploit the potential of advanced functional genetic concepts.

Throughout my PhD project, I authored ten manuscripts, of which six – four research articles and two review articles – were already published in peer-reviewed scientific journals, and contributed to a large-scale grant application and a patent application for the AGameOfClones vector concept. Further, I supervised four Master and two Bachelor students.

2. Insect Development in a Nutshell



This chapter begins with a brief overview of insect-associated developmental biology and further illustrates the essential role that advanced fluorescence live imaging methods and functional genetics play for the characterization of morphogenetic processes. Since my PhD thesis is ‘publication-based’, I kept the introduction, on purpose, conveniently short and provide only the minimal background information to understand the achievements, unpublished result and future trends. Instead of being repetitive, the introduction is designed to complement the narrations that are found within other chapters as well as the published, submitted and submission-ready manuscripts. An overview is given in the table below. The achievements subchapter summarizes only the results of the manuscripts, while all unpublished results are described in Chapter 3. Throughout this and all the remaining chapters, I decided to also take advantage of boxes to explain more complex circumstances without disturbing the reading flow.

List of topics for which a detailed explanation or discussion is found within either the unpublished results or the manuscripts. The numbers refer to Publication Table 1 (#1 to #3), Publication Table 2 (#4 to #6) and Publication Table 3 (#7 and #10) in Subchapters 6.1 and 6.2. The type column indicates how the information is provided: LSFM, light sheet-based fluorescence microscopy; D, description; F, figures; T, tables.

topic (subdivided by genre)	Unpublished Results (Chapter 3) or Publications (Chapter 6)	type
the red flour beetle <i>Tribolium castaneum</i>	Strobl & Stelzer 2014 (#1), Strobl & Stelzer 2016 (#4)	D
the Mediterranean fruit fly <i>Ceratitidis capitata</i>	Strobl <i>et al.</i> 2017E (#9), Strobl <i>et al.</i> 2017I0 (#10)	D
the two-spotted cricket <i>Gryllus bimaculatus</i>	Subchapter 3.1, Strobl <i>et al.</i> 2017F (#10)	D
the comparative approach in developmental biology	Strobl & Stelzer 2016 (#4), Strobl <i>et al.</i> 2017B (#6)	D, F
the methodological arsenal for <i>Tribolium</i>	Strobl <i>et al.</i> 2015 (#3), Strobl <i>et al.</i> 2017A (#5)	D
genetics and germline transformation in <i>Tribolium</i>	Subchapters 2.2.7 and 3.4, Strobl <i>et al.</i> 2017C (#7), Strobl <i>et al.</i> 2017D (#8)	D
principle, technical background and benefits of LSFM	Strobl <i>et al.</i> 2015 (#3), Strobl & Stelzer 2016 (#4), Strobl <i>et al.</i> 2017B (#6)	D, F
comparison of LSFM to other fluorescence microscopes	Strobl <i>et al.</i> 2017A (#5)	D, F, T
mounting of insect embryos for live imaging	Strobl <i>et al.</i> 2015 (#3), Strobl <i>et al.</i> 2017A (#5), Strobl <i>et al.</i> 2017E (#9)	D, F, T
image data processing and distribution	Subchapters 3.2 and 3.3, Strobl <i>et al.</i> 2015 (#3), Strobl <i>et al.</i> 2017E (#9)	D, F
quality control in live imaging assays	Subchapter 4.1.6, Strobl <i>et al.</i> 2015 (#3), Strobl <i>et al.</i> 2017A (#5)	D, F

2.1. Introduction

2.1.1. Insects and Developmental Biology

With more than one million described and about twenty million assumed species, insects are considered the evolutionary most successful metazoan class [1]. They are found on every continent, occupy every ecological niche and exploit all modes of locomotion. Although constant adaptation to the ever changing environment has resulted in a remarkable biodiversity, three general challenges can be stated that have to be addressed by every insect species in order to persist within the constant struggle of natural selection:

- **The ‘gather energy’ challenge:** Most insect species are oviparous, *i.e.* their embryos develop inside eggs with only a limited initial nutrient supply. At the end of embryogenesis, nearly all resources are consumed and the hatched larva has to exploit the environment.
- **The ‘reproduction’ challenge:** To ensure the survival of the respective species, adult insects have to produce progeny. While males only pass on their genetic information, females also have to provide the initial nutrient supply for the egg.
- **The ‘self-defense’ challenge:** Insect have to be able to avoid extinction due to organic and inorganic threats until they have reproduced successfully.

To cope with these challenges, insects develop relatively large somatic bodies that are equipped with complex sensory organs [2,3], highly specialized locomotion systems [4,5], powerful reproductive organs [6,7] and efficient defensive structures such as spikes or stings to combat predators and competitors [8]. These large somatic bodies contain a relatively small number of germ cells that produce haploid gametes. Fusion of two parental gametes results in a single diploid cell, *i.e.* the zygote, which develops a potentially superior somatic body that may be slightly better adapted to handle the aforementioned challenges.

Insect developmental biologists are interested in the underlying morphogenetic, cellular, genetic, molecular, biochemical and biophysical principles how zygotes utilize their genetic information and limited initial nutrient supply to produce complex somatic bodies that consist of millions of precisely arranged cells and hundreds of cell types with completely different specializations. Research is thereby performed on multiple levels:

- **The *in toto* and the tissue-and-organ levels:** In their entirety, *i.e. in toto*, individual insects can be seen as a ‘closed biological systems’ that consists of many ‘higher order biological units’, *i.e.* certain tissues and distinct organs. These units may be present only one or multiple times, *e.g.* brain tissue, head appendices or legs.
- **The cellular level:** Abstractly seen, individual cells of a multicellular organism can be considered as the ‘smallest functional biological units’ and their behavior can be described as a complex sequence of three highly stereotypic processes, (i) proliferation, (ii) migration and (iii) differentiation.
- **The subcellular and molecular levels:** The subcellular and molecular processes that occur within cells are highly diverse. Some of these processes are involved in mediating the aforementioned highly stereotypic processes while the remaining processes provide specifically differentiated cells with their respective functions.

Research on the fruit fly *Drosophila melanogaster*, the ‘gold standard’, has contributed significantly to our current knowledge within many biological disciplines [9–13]. However, when the effort is focused on only one model organism, the information cannot be embedded into the phylogenetic context. Only the comparative approach, *i.e.* determining the similarities and differences within the development of at least two species, allows to characterize specific traits as either apomorphic or plesiomorphic and thus gain insights into the evolution of development. For example, the red flour beetle *Tribolium castaneum* (Figure 2-1) is considered the second most important insect species for biological research and was chosen as one of the eight emerging model organisms to represent the arthropods in the avantgardistic *Emerging Model Organisms* books [14,15]. In comparison to *Drosophila*, *Tribolium* shows remarkable differences during morphogenesis – the embryos employ the short-germ mode of development [16–18], do not involute the head [19–21] and develop fully functional legs [22,23].

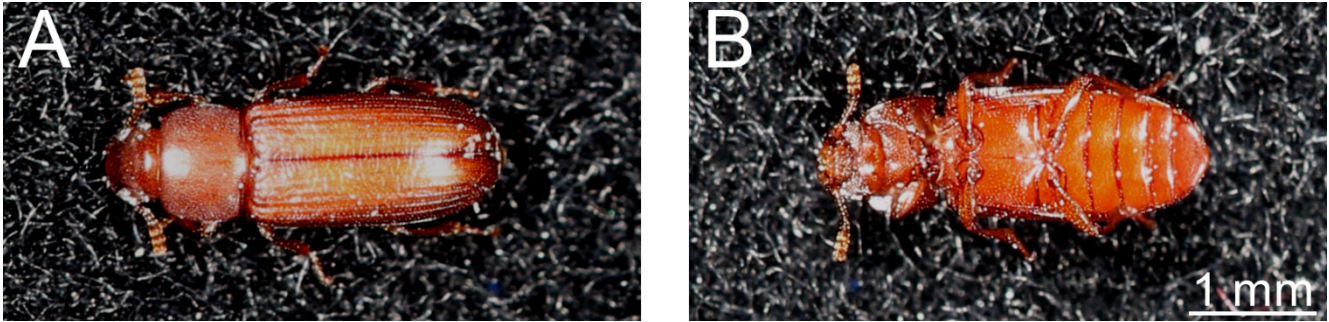


Figure 2-1 – The red flour beetle *Tribolium castaneum*, the second most important insect species for biological research. (A) Adult individual shown along the dorsal side. (B) Same adult individual shown along the ventral side.

Insects originated during the late Paleozoic era and have acquired a remarkable morphogenetic diversity on the tissue-and-organ level [24] throughout their 480 million years of evolution [25–27]. Surprisingly, the morphogenetic principles on the cellular level are particularly well conserved – the complex sequences of the aforementioned highly stereotypic processes, *i.e.* proliferation, migration and differentiation, which are responsible for the basic morphology of the larva, are astoundingly similar. Consequently, the morphogenesis from the zygote to the larva can be divided into six consecutive embryogenetic events (Table 2-1), which are more or less evident in all insect species (Table 2-2) regardless whether the respective species belong to the Hemimetabola or the Holometabola (Box 2-1).

Thus, embryogenetic events can be considered fundamental throughout the insect class and serve as a common ground for research motivated by evolutionary question. In the very few morphology-based comparative studies that have been published to date [28–32], gene expression patterns of *Drosophila* and one or two other insect species have been aligned throughout certain embryogenetic events, but comprehensive side-by-side comparisons of morphogenetic processes on the cellular or subcellular levels have not yet been feasible due to a lack of appropriate methodology – previous imaging-based studies were either based on (i) electron microscopy, which is does not allow live imaging, (ii) reflected light and transmission light live imaging, which resolves even structures on the tissue-and-organ level quite poorly, or (iii) fluorescence microscopy of fixed and stained samples, since long-term fluorescence live imaging assays require appropriately prepared specimen and advanced technology (Table 2-2, fourth column).

Table 2-1 – Brief description of the six consecutive embryogenetic events that are considered fundamental throughout the insect class. Since the embryogenetic events reappear relatively frequently within the figures of Subchapters 2.2, 3.1, 3.2, 4.1 and 4.1, they are, for convenience, color-coded.

#	embryogenetic events	rationale
I	blastoderm formation	After fusion of the gametes, the zygote proliferates multiple times. The nuclei migrate to the surface of the egg, undergo several more rounds of synchronous proliferation and give rise to the cellular blastoderm.
II	gastrulation	The cellular blastoderm, which surrounds the yolk, reorganizes into the ventrally located germband, consisting of an ectodermal, mesodermal and endodermal germ layer, as well as the extra-embryonic membranes.
III	germband elongation	The posterior tip of the germband curls around the posterior pole and migrates anterior along the dorsal side of the egg until it reaches a certain extend and remains quiescent for a certain period of time.
IV	germband retraction	The posterior tip of the germband migrates posteriad along the dorsal side of the egg and eventually flips into the posterior pole. Typically, segmentation and, if applicable, also the developing legs become evident.
V	dorsal closure	The flanks of the ventrally located germband extend towards the dorsal midline and begin with epidermal zippering. The remaining yolk and the extra-embryonic membranes are internalized into the digestive system.
VI	muscular movement	Shortly after the germband has finished the zippering process, irregular muscle twitching begins, which turns later on into regular muscular movement. Eventually, the larva hatches from the egg.

Box 2-1 – Hemimetabolous and holometabolous insect species

The life cycle of hemimetabolous insect species includes three phases, (i) egg, (ii) nymph and (iii) imago. Except for missing wings and immature reproductive organs, the nymph already resembles the adult. Hemimetabolism, also termed incomplete metamorphosis, is considered an ancestral trait and thus found within the basally located insect species. Hemimetabolous insects also undergo anatrepsis and katatrepsis during their embryogenesis, *i.e.* entry into and exit from the yolk. In contrast, the life cycle of holometabolous insect species, *e.g.* *Drosophila* or *Tribolium* includes four phases, (i) egg, (ii) larva, (iii) pupae and (iv) adult. Holometabolism, also termed complete metamorphosis, is considered a derived trait, and the Holometabola form a monophyletic group.

Table 2-2 – Methodological and structural summary of selected articles that, in their entirety, describe the embryogenesis of twenty-two insect species from ten orders. Entries are ordered primarily by phylogenetic distance and secondarily alphabetically. For a brief summary of embryogenetic events, see Table 2-1. Table and/or table description fully and/or partially reproduced from Strobl *et al.* 2017F, #10 in Publication Table 3.

species (order:family)	common name	references	methods	embryogenetic events / staging
<i>Drosophila melanogaster</i> (Diptera:Drosophilidae)	fruit fly (holometabolous)	[33]	non-fluorescence live imaging; fixation, mechanical sectioning and staining with non-fluorescent dyes	staging system (17)
<i>Megaselia abdita</i> (Diptera:Phoridae)	scuttle fly (holometabolous)	[34]	non-fluorescence live imaging; fixation and staining with fluorescent dyes followed by widefield microscopy	staging system (17)
<i>Aedes aegypti</i> (Diptera:Culicidae)	yellow fever mosquito (holometabolous)	[35,36]	fixation, mechanical sectioning and staining with non-fluorescent dyes	staging system (26, time points)
<i>Aphidoletes aphidimyza</i> (Diptera:Cecidomyiidae)	predatory gall midge (holometabolous)	[37]	non-fluorescence live imaging	staging system (10)
<i>Clogmia albipunctata</i> (Diptera:Psychodidae)	moth midge, drain fly (holometabolous)	[38]	non-fluorescence live imaging; fixation and staining with fluorescent dyes followed by widefield microscopy	staging system (17)
<i>Nemotaulius admorsus</i> (Trichoptera:Limnephilidae)	caddis fly (holometabolous)	[39]	fixation, mechanical sectioning and staining with non-fluorescent dyes, scanning electron microscopy	staging system (10)
<i>Philanisus plebeius</i> (Trichoptera:Chathamidae)	marine caddis fly (holometabolous)	[40]	fixation and non-stained observation	no staging system
<i>Bombyx mori</i> (Lepidoptera:Bombycidae)	domestic silkworm (holometabolous)	[41]	fixation and staining with fluorescent dyes followed by confocal microscopy	description ends after III no staging system
<i>Endoclyta signifier</i> and <i>Endoclyta excrescens</i> (Lepidoptera:Hepialodae)	primitive moth (holometabolous)	[42]	fixation, mechanical sectioning and staining with non-fluorescent dyes	description ends after II no staging system
<i>Nemophora albi antennella</i> (Lepidoptera:Adelidae)	fairy moth (holometabolous)	[43]	fixation and non-stained observation; fixation, mechanical sectioning and staining with non-fluorescent dyes; scanning electron microscopy	staging system (12)
<i>Neomicropteryx nipponensis</i> (Lepidoptera:Micropterygidae)	primitive moth (holometabolous)	[44]	fixation, mechanical sectioning and staining with non-fluorescent dyes	staging system (14)
<i>Rhagophthalmus ohbai</i> (Coleoptera:Rhagophthalmidae)	glowworm (holometabolous)	[45]	fixation, mechanical sectioning and staining with non-fluorescent dyes; scanning electron microscopy	description ends after III staging system (8, not numbered)
<i>Xyleborus ferrugineus</i> (Coleoptera:Scolytidae)	ambrosia beetle (holometabolous)	[46]	non-fluorescence live imaging	staging system (12, time points)
<i>Apis mellifera</i> (Hymenoptera:Apidae)	honeybee (holometabolous)	[47–49]	scanning electron microscopy	staging system (6)

species (order:family)	common name	reference	methods	embryogenetic events / staging
<i>Nasonia vitripennis</i> (Hymenoptera:Pteromalodae)	jewel wasp (holometabolous)	[50]	non-fluorescence live imaging; fixation and staining with non- fluorescent dyes	staging system (8)
<i>Acyrtosiphon pisum</i> (Hemiptera:Aphididae)	pea aphid (hemimetabolous)	[51]	fixation and staining with fluorescent dyes/antibodies followed by confocal microscopy	V not properly described staging system (20)
<i>Galloisiana yuasai</i> (Grylloblattoidea:Grylloblattidae)	- (hemimetabolous)	[52]	fixation and staining with fluorescent dyes followed by wide field microscopy; fixation, mechanical sectioning and staining with non- fluorescent dyes; scanning electron microscopy; transmission electron microscopy	staging system (11)
<i>Gryllus bimaculatus</i> (Orthoptera:Gryllidae)	two-spotted cricket (hemimetabolous)	[53]	non-fluorescence live imaging, fixation and non-stained observation, fixation, germband preparation and staining with fluorescent dyes followed by confocal microscopy	staging system (23)
<i>Kamimuria tibialis</i> (Plecoptera:Perlidae)	stonefly (hemimetabolous)	[54]	fixation, mechanical sectioning and staining with non- fluorescent dyes; scanning electron microscopy	staging system (12)
<i>Rhodnius prolixus</i> (Hemiptera:Redivividae)	kissing bug (hemimetabolous)	[55]	fixation and staining with fluorescent dyes followed by wide field microscopy; fixation, mechanical sectioning and staining with non- fluorescent dyes; scanning electron microscopy; transmission electron microscopy	staging system (4, not numbered)
<i>Ephemera japonica</i> (Ephemeroptera:Ephemeridae)	mayfly (hemimetabolous)	[56,57]	fixation, mechanical sectioning and staining with non- fluorescent dyes; scanning electron microscopy	staging system (13)

2.1.2. Developmental Biology and Advanced Fluorescence Live Imaging Techniques

Fluorescence microscopy provides the unique advantage that the subcellular structures of interest, for example the nucleus, the membranes or certain elements of the cytoskeleton, can be selectively labeled and has thus become one of the most frequently applied techniques in developmental biology and associated disciplines [58]. In principle, each fluorescence microscopy technique measures the fluorophore distribution within a given specimen, optionally as a function of time.

In conventional wide-field fluorescence microscopy, which has been invented about a century ago [59,60], all fluorophores within the specimen are simultaneously illuminated and detected through the same objective. The signal is collected in parallel with modern CCD or sCMOS cameras. Thus, respective implementations have a very high acquisition speed but no optical sectioning capability since out-of-focus signal from above and below the focal volume obscure the axial resolution. Thus, wide-field microscopes are primarily used to acquire two-dimensional images of very thin samples, for example monolayers of cells that were grown on coverslips [61]. In confocal fluorescence microscopy, which has been developed about three decades ago [62–64], a focused laser beam is scanned through the specimen and the signal is collected point-by-point with photomultiplier tubes. The optical sectioning capability is based on rejection of out-of-focus signal from above and below the focal volume by using a spatial filter, *i.e.* a pinhole. Thus, confocal microscopes have a satisfactory axial resolution and can be used to acquire three-dimensional images, *i.e.* Z stacks of two-dimensional images, by moving the specimen plane-wise through the focal volume. However, point scanning approaches are, due the sequential detection, inconveniently slow for live imaging assays. Both approaches also have in common that all fluorophores within the specimen are excited for each acquired two-dimensional image. Especially in live imaging assays, where it is necessary to avoid detrimental side-effects caused by light irradiation (Box 2-2), this principle strongly limits the amount of images that can be taken.

Box 2-2 – Light irradiation: photo-bleaching and photo-toxicity

In fluorescence microscopy, it is inevitable that the specimens are influenced by the observation technique since irradiation with light of a specific wavelength, *i.e.* influx of additional energy, is necessary to get fluorescence signal. Typically, two undesired side effects may occur, (i) photo-bleaching, *i.e.* the irreversible photochemical destruction of a fluorophore by breaking the respective covalent bonds within the molecule, and (ii) photo-toxicity, *i.e.* the reduction of cellular viability mainly due to the generation of large amounts of reactive oxygen species [65,66]. In live imaging assays, it is recommended to keep the light irradiation at a level where the influence on the specimen is negligible so that the assay can be considered non-invasive.

In light sheet-based fluorescence microscopy, which was invented about a decade ago [67], illumination and detection are decoupled [68,69]. In the excitation light path, the laser beam is shaped by specific optical components and a low-aperture illumination objective into a several micrometer thin light sheet. The sheet excites only the fluorophores located within the focal volume of a perpendicular arranged high-aperture detection objective while the out-of-focus regions remain dark. This illumination principle provides light sheet-based fluorescence microscopes with an optical sectioning capability comparable to confocal microscopes [70] but due to the plane-wise illumination, two-dimensional images can be acquired in parallel with modern CCD or sCMOS, resulting in very fast acquisition speeds. Thus, by moving the specimen step-by-step through the light sheet, Z stacks of very large samples can be recorded within only a few seconds [65]. Light sheet-based fluorescence microscopes are powerful tools in developmental biology:

- Depending on the objective and camera combination, it is possible to cover the *in toto*, tissue-and-organ, cellular and subcellular levels (Table 2-3) simultaneously and thus characterize the behavior of the ‘smallest functional biological units’ forming ‘higher order biological units’ as part of a ‘closed biological system’.
- Due to the plane-wise illumination, the signal-to-noise ratio is excellent and photo-bleaching and photo-toxicity are kept at a minimum (Box 2-2). In conjunction with the high imaging speed and the obligatory sample rotation feature, embryos can be imaged more than hundred times during their embryonic development period along multiple embryonic axes.
- Customized mounting methods preserve the three-dimensional integrity of living specimen and allow unimpeded gas and ion exchange. For example, explanted mouse embryos can be imaged for several days when embedded in a Reichert’s membrane [71], rectangular fluorinated ethylene propylene capillaries filled with low-concentration agarose are used to observe zebrafish embryos without physical constrictions [72] and *Drosophila* embryos are conveniently mounted by using the agarose column method [73,74]. Additionally, respective setups are equipped with large sample chambers, which allow full control over the imaging environment, *e.g.* composition and temperature of the imaging buffer.

Table 2-3 – The biologically relevant microscopic scale: Characteristics of the *in toto*, tissue-and-organ, cellular, subcellular and molecular levels.

level	<i>in toto</i>	tissue-and-organ	cellular	subcellular	molecular
abstractly seen	‘closed biological system’	‘higher order biological unit’	‘smallest functional biological unit’	-	-
example	individual embryos	antennae, legs or the midgut	epithelial, neuronal or muscle cells	organelles, cytoskeleton	proteins, lipids or carbohydrates
range	about 1,000 to 100 μm	about 100 to 10 μm	about 10 to 1 μm	about 1 to 0.1 μm	smaller than 0.1 μm
fluorescence imaging	wide-field confocal light sheet	wide-field confocal light sheet	wide-field confocal light sheet	confocal light sheet super-res [75,76]	super-res [75,76]
other imaging techniques	mini CT [77]	micro CT [77]	micro CT [77]	nano CT [77] electron-based [78]	electron-based [78]

Due to the above mentioned advantages, light sheet technology permits comprehensive imaging assays that are not feasible with wide-field or confocal microscopes. This is especially evident in developmental biology and associated disciplines, in which large living samples have to be analyzed on multiple biologically relevant microscopic levels for many hours or even several days without affecting their viability. Light sheet-based fluorescence microscopy has already been used to investigate the embryonic development – primarily the migration, proliferation and differentiation patterns (Subchapter 2.2.1) on the cellular level – of all established metazoan model organisms:

- For mouse, comprehensive quantitative information on cell migration patterns from the zygote to the blastocyst [79] and during gastrulation [80] is available.
- For zebrafish, large image databases on the cellular dynamics during germ layer formation [81] as well as microscopy data on the already functional but still developing embryonic heart [82,83] and the morphogenetic principles of eye formation [84] are available.
- For *Drosophila*, massive amounts of data on the whole embryonic development of wild-type are available [85–88] that cover all six insect-specific embryogenetic events (Subchapter 2.2.1). Additionally, several aberration phenotypes have been analyzed, for example knock-down mutants of *schurri* [89] and *twist* [90].

Aside from *Drosophila* and the three model organisms that are part of my PhD project, *Megaselia* is the only insect species whose embryogenesis has been characterized with light sheet-based fluorescence microscopy [91]. Apart from imaging the embryonic development of metazoans, light sheet technology has also been applied in three-dimensional cell biology [61,92], neurosciences [93–97] and plant research [98–100].

In summary, light sheet-based fluorescence microscopy combines the fast acquisition speed of wide-field microscopes with an optical section capability comparable to that of confocal microscopes. By illuminating only the fluorophores within the focal volume, a very high signal-to-noise ratio is achieved while photo-bleaching and photo-toxicity are kept on a negligible level. This is especially important in developmental biology, in which long-term live imaging assays are very common.

2.1.3. Advanced Fluorescence Live Imaging Techniques and Functional Genetics

For fluorescence live imaging, it is necessary that fluorophores are present within the specimen. However, this is a non-trivial challenge. For emerging insect model organisms, three strategies have been suggested, two injection-based as well as one functional genetics-based approach, which have a different combination of advantages and disadvantages (Table 2-4).

Due to the spatiotemporal flexibility of fluorophore expression and the low preparation effort per imaging assay, functional genetics is the most powerful approach. However, the creation procedure for custom-made transgenic lines is tedious:

- Firstly, the properties of the fluorophore expression cassette have to be defined by carefully choosing a suitable promoter and, optionally, an appropriate intracellular label (Box 2-3).
- Secondly, the architecture of the expression cassette, *i.e.* the fluorescent protein and the intracellular labeling strategy (Box 2-4), has to be defined and a respective transformation-ready vector has to be created via molecular cloning. This procedure can be, depending on the starting material and complexity of the desired fluorophore expression cassette, rather laborious since for each subcloning step, a certain chain of assays, *e.g.* editing of the nucleotide sequences followed by transformation into a bacterial host and screening of potential carriers of the respective vector, has to be done.
- Thirdly, the respective vector has to be injected, typically in conjunction with a helper vector that mediates the insertion process, into preblastoderm embryos, where the transgene has to integrate into germline progenitor cells.
- Fourthly, all transgenic sublines, *i.e.* lines that carry the same transgene but at a different genomic location, have to be characterized. Further, it is scientifically very reasonable, but very laborious, to cross suitable sublines homozygous.

Table 2-4 – Rationale, advantages and disadvantages as well as other characteristics of three techniques for the fluorescent labeling of emerging insect model organisms. Table and/or table description fully and/or partially reproduced from Strobl & Stelzer 2016, #4 in Publication Table 2.

critereon	injection of fluorescent dyes	injection of mRNA	custom-made transgenic lines
rationale	The respective fluorescent dye is directly injected into early preblastoderm embryos.	The respective plasmids carry a viral promoter (typically T7) that allows <i>in vitro</i> transcription of mRNA coding for the respective fluorescence protein. The mRNA is injected into early preblastoderm embryos.	Donor plasmids typically contain the coding sequence for a fluorescence protein under control of a specific endogenous promoter as well as a transgenesis marker. Both cassettes are inserted into transposase recognition sites, which allows the transfer of the cassette to the genome when the donor plasmid is co-injected with a helper plasmid that expresses the respective transposase, for example <i>piggyBac</i> [101].
example (in <i>Tribolium</i>)	Fluoro-ruby [102]	mRNA encoding RFP-labeled endogenous histone 2B subunits [103]	EFA-nGFP [104] transgenic line
advantages (+) and disadvantages (-)	(+) low overall effort (-) embryo manipulation necessary (-) only spatiotemporal ubiquitous and constitutive fluorescence possible (-) not all intracellular structures can be targeted with fluorescent dyes	(+) co-injection with constructs for RNA interference possible (+) fluorescent protein can be linked to tags or proteins that will lead to a certain intracellular localization (-) embryo manipulation necessary (-) only spatiotemporal ubiquitous and constitutive fluorescence possible	(+) fluorescent protein can be linked to tags or proteins that will lead to a certain intracellular localization (+) spatiotemporal expression control available via choice of the promoter (+) no embryo manipulation necessary (+) continuous production of fluorophores (-) long and laborious effort to create custom-made transgenic lines
initial effort for the establishment	Dyes can be purchased.	Several plasmid are available from the respective laboratories [103,105,106]. If new constructs are needed, several days to a few weeks are necessary for cloning.	Several days to a few weeks for molecular cloning, several weeks for injection and screening of founders, a few month to establish an appropriate culture for egg collection.
preparation for each imaging assay	Few hours for injection of the embryos.	Several hours for the preparation and purification of the mRNA and injection of the embryos, fluorescence signal is detectable a few hours after injection.	No preparation necessary.
total required work and time	Initial work and time requirements are very low, but work and time necessary per live imaging assay are high (the embryos have to be injected every time an assay should be performed).	Initial work and time requirements are low (plasmid already available) to medium (molecular cloning is required), but work and time necessary per live imaging assay are high (the embryos have to be injected every time an assay should be performed).	Initial work and time requirements are very high, but work and time necessary per live imaging assay are low.

Box 2-3 – Transgenic lines for fluorescence live imaging: promoter and label

Whenever custom-made transgenic lines specifically designed for fluorescence live imaging assays are created, the most obvious consideration might be the fluorescent proteins, since this choice defines which laser lines and spectral filters have to be used during microscopy. However, in developmental biology, there are two more important considerations, the promoter and the label:

- The promoter (or upstream regulatory sequence) determines the spatiotemporal expression pattern on the cellular level. They are either ubiquitously active or alternatively only in a certain subset of cells, and they are either constitutively active or alternatively only during certain developmental periods.
- The label defines the intracellular localization of the fluorescent protein. Typically and most frequently labeled are the nucleus, *e.g.* by using the simian virus 40 nuclear localization signal [107], the membranes, *e.g.* by using the human *GAP43* membrane anchor [108] as well as the actin cytoskeleton, *e.g.* by using the yeast Lifeact tag [109].

For *Drosophila*, the Bloomington Stock Center (flystocks.bio.indiana.edu) in the United States, a non-profit repository, offers more than 3,200 custom-made transgenic lines specifically designed for fluorescence live imaging, which are typically very well characterized and either carry a transgene/balancer combination (Subchapter 2.2.7) or are homozygous for the transgene. However, for emerging insect model organisms, only very few suitable lines are available, which is the largest limiting factor for the practicability of fluorescence live imaging in insect developmental biology.

Box 2-4 – Intracellular labeling strategies: fusion proteins, tags and nanobodies

There are three major strategies on how certain intracellular structures can be labeled when transgenic lines for fluorescence live imaging assays should be created:

- Fluorescent proteins can be linked to endogenous proteins or protein fragments that mediate localization to certain intracellular structures or organelles [110]. These constructs are termed fusion proteins and the endogenous remnant is usually still fully or partially functional. One of the most prominent examples is fusion to histone subunits, which are translocated to the nucleus and become part of fully functional histones that bind the chromosomal DNA [111].
- Tags are very short peptide sequences (usually four to twenty amino acids). They derive from functional proteins but have no biological function anymore except to mediate correct localization. One of the most important characteristics is their universality, as they function in nearly all eukaryotic model organisms. For example, a frequently used tag is the yeast Lifeact peptide with a length of 17 amino acids [109].
- Nanobodies are extremely small antibodies that derive from members of the Camelidae family and also function properly when expressed intracellularly [112]. When linked to a fluorescent protein, Nanobodies are termed chromobodies. Chromobodies have the advantage that they can be used visualize endogenous cellular structures without disturbing the cellular equilibrium too heavily.

For tags and nanobodies, it is usually not important if the respective fluorescent protein is linked to the N-terminal or C-terminal end. However, it matters for certain fusion proteins either because the fluorescent protein may influence the protein or protein fragment, or because the remnant may have a protein cleavage site [113].

2.1.4. Aim of my PhD Project

The overall aim of my PhD project was relatively open. In principle, I should characterize the embryonic morphogenesis of several other emerging insect model organisms and compare my insights to the ‘gold standard’ *Drosophila*.

- To gain a broad overview about the heterogenic pool of morphogenetic strategies within the insect class, I should choose three further insect species with a decreasing phylogenetic relationship to *Drosophila*.
- Since the methodological arsenal for emerging insect model organisms is typically quite limited, I should establish or adapt all necessary and/or convenient techniques and resources for the chosen species. Especially, I should focus on the creation of functional transgenic lines specifically designed for fluorescence live imaging.
- In more detail, I should establish imaging protocols for light sheet-based fluorescence microscopy that allow to image the embryonic development the chosen species as long as possible under similar conditions.

2.2. Achievements

2.2.1. Long-Term Live Imaging of the ‘Gold Standard’ *Drosophila melanogaster*

For the comparative approach in insect developmental biology, it is necessary to have comprehensive data on the ‘gold standard’ *Drosophila* available. Thus, as the first task of my PhD project, I recorded nearly the entire embryonic development of three different transgenic *Drosophila* lines that exhibit fluorescence signal from the nucleus by using light sheet-based fluorescence microscopy. One line expresses an EGFP-labeled histone 2A variant, while the two other lines express nuclear-localized GFP (Table 2-5). Both labels behave slightly different in live imaging assays (Box 2-5).

Table 2-5 – Transgenic *Drosophila* lines recorded in live imaging assays by using light sheet-based fluorescence microscopy. All lines were obtained from the Bloomington *Drosophila* Stock Center, Indiana, United States of America. NLS, nuclear localization signal.

line	genotype	fluorophore expression
#24163	w[*]; P{w[+mC]=His2Av-EGFP.C}2/SM6a	EGFP-labeled histone 2A variant in all cells
#01691	y[1] w[67c23]; P{w[+mC]=Ubi-GFP.nls}ID-2; P{Ubi-GFP.nls}ID-3	NLS-GFP under control of the <i>polyubiquitin</i> promoter
#29724	w[*]; P{w[+mC]=Tub84B-EGFP.NLS}3	NLS-GFP under control of the <i>alpha-tubulin 84B</i> promoter

Collection, preparation and imaging were performed at room temperature and as described previously [73,85]. Embryos were collected for 10 minutes, embedded into agarose columns and inserted into the sample chamber within the next 30 minutes so that the embryonic morphogenesis could be recorded from the middle of blastoderm formation to the moment of hatching, which equals to about 95% of the total embryonic development [33]. For each line, three datasets were recorded in the same light sheet-based fluorescence microscope under similar conditions, which allows a morphogenetic side-by-side comparison (Figure 2-2). With uniform signal strength, high signal-to-noise ratio and low degree of photo-bleaching (Figure 2-3), the #24163 transgenic line showed the best overall performance and thus became the favored candidate to represent *Drosophila* in the comparative approach (Subchapters 2.2.3, 2.2.6 and 4.2.2).

Box 2-5 – Fluorescently labeled nuclei: nuclear localization signal and histone subunits

Ubiquitous and constitutive labeling of the nucleus became standard for transgenic organisms in fluorescence live imaging assays. There are two major strategies to achieve this, either via the nuclear localization signal, a universal tag that derives from the simian virus 40 [107], or by fusing the fluorescent protein to an endogenous histone subunit, for example the histone 2A variant for *Drosophila* [111,114] or the histone 2B subunit for *Tribolium* [103]. Usage of the nuclear localization signal provides a fairly homogenous signal, but when histone-based fusion proteins are expressed, regions with stronger as well as weaker signal are seen within the nucleus. However, during the M-phase of the mitotic cycle, in which the nuclear envelope temporarily dissipates, the fluorophores linked to the nuclear localization signal tag spread through the whole cell, while the fluorophores linked to histone subunits remain with the condensed chromatin. See also Strobl & Stelzer 2016, #4 and Strobl *et al.* 2017B, #6 in Publication Table 2.

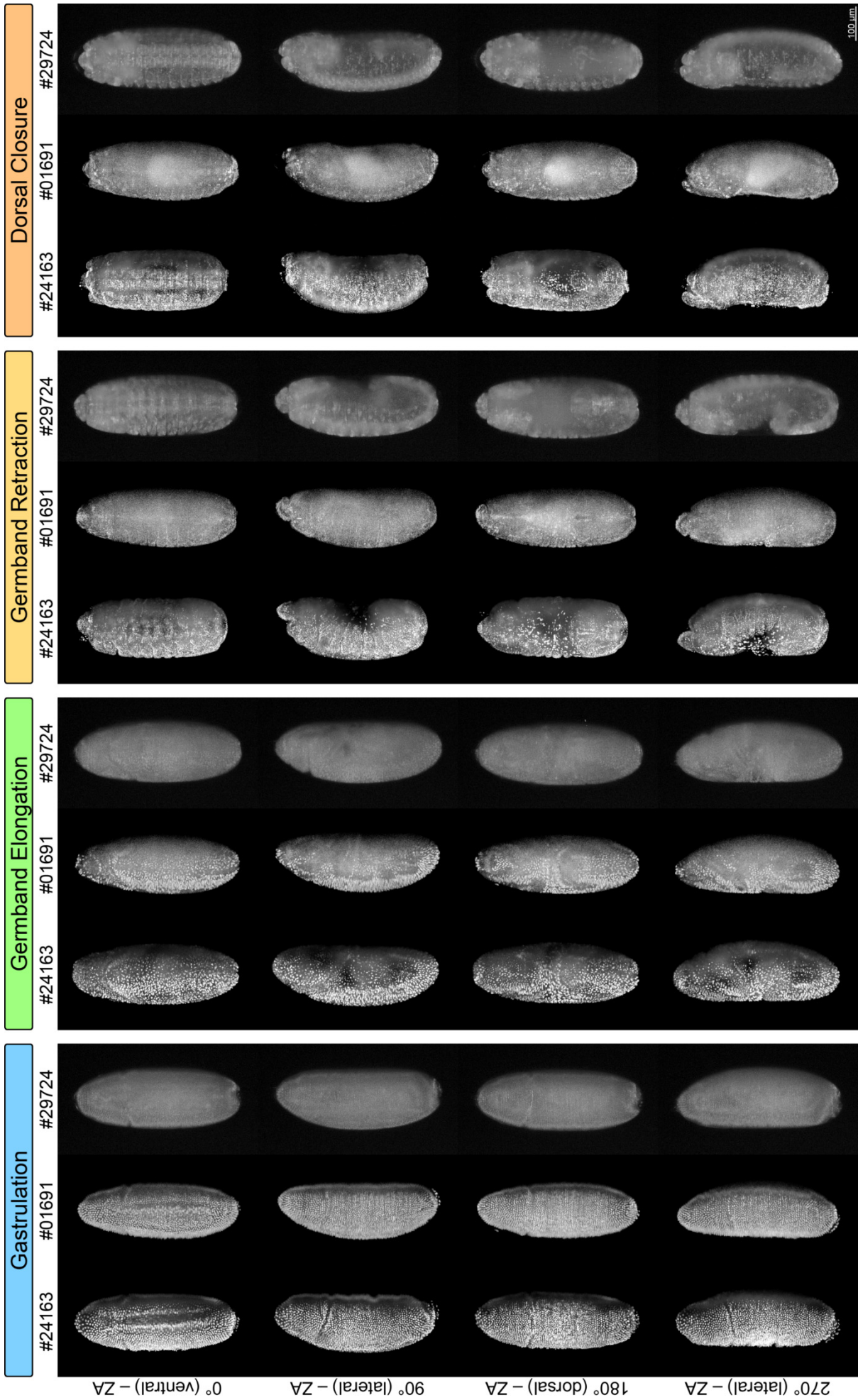


Figure 2-2 – Embryonic morphogenesis of *Drosophila* from gastrulation to dorsal closure along four directions by using the #24163, #01691 and #29724 (Table 2-5) transgenic lines. For a brief summary of embryogenetic events, see Table 2-1. ZA, Z maximum projection with intensity adjustment. Figure and/or figure description fully and/or partially reproduced from Strobl & Stelzer 2016, #4 in Publication Table 2.

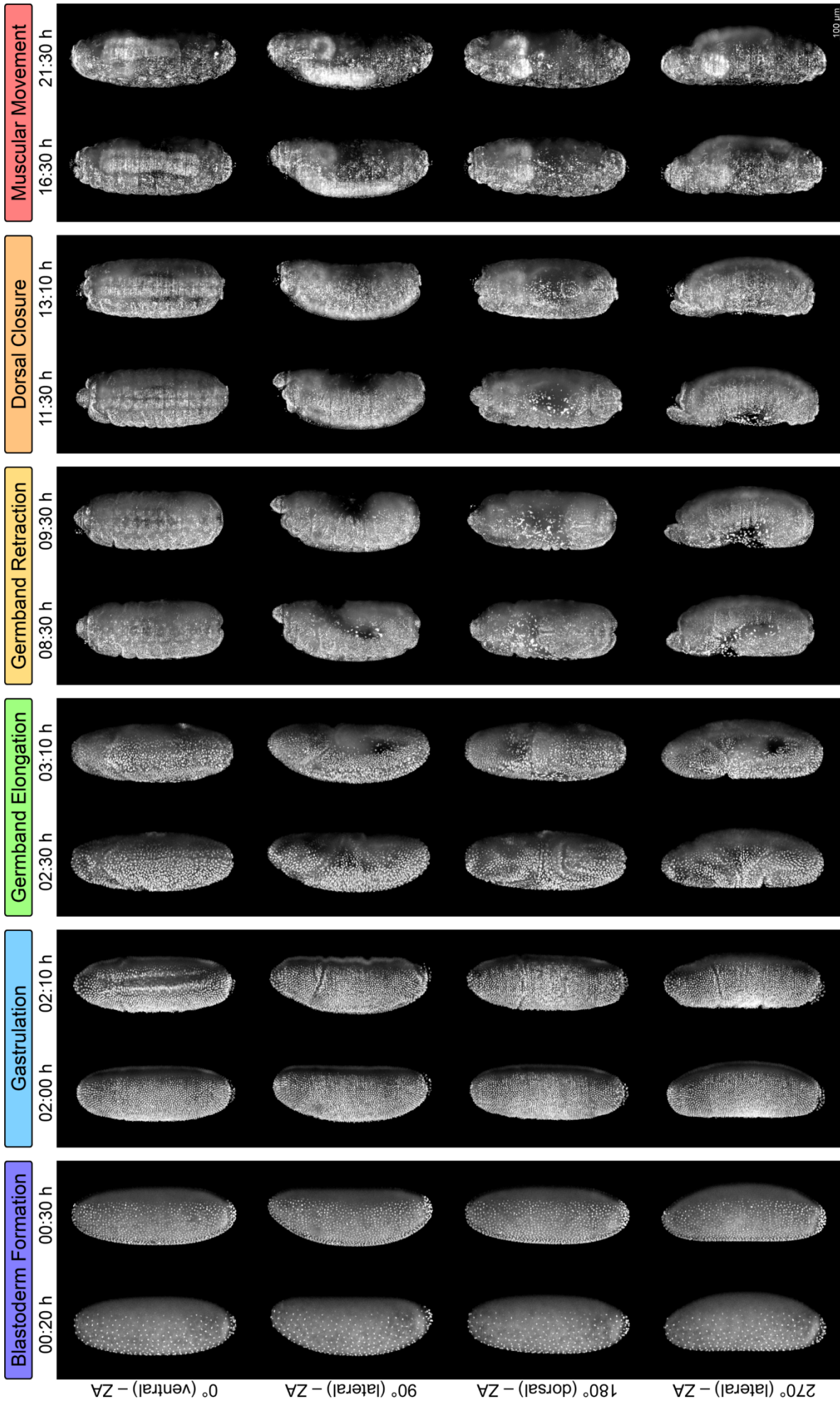


Figure 2-3 – Embryonic morphogenesis of *Drosophila* during all six consecutive embryogenetic events along four directions. For a brief summary of embryogenetic events, see Table 2-1. Z.A. The data were acquired by using the P{His2Av-EGFP-C}2 (Table 2-5) transgenic line. Z. maximum projection with intensity adjustment. Figure and/or figure description fully and/or partially reproduced from Strobl & Stelzer 2016, #4 in Publication Table 2.

2.2.2. Non-Invasive Long-Term Fluorescence Live Imaging of *Tribolium castaneum* Embryos

At the beginning of my PhD project, there have been large amounts of morphogenetic data for *Drosophila* [85–88] available, but nearly none for *Tribolium*. Fortunately, the EFA-nGFP [104] transgenic line, which expresses nuclear-localized GFP under control of the *elongation factor 1 alpha 1 subunit* promoter, has already been established. This line has fairly similar characteristics as the three investigated transgenic *Drosophila* lines. For my fluorescence live imaging assays, I adapted at first the agarose column method, which performs well for *Drosophila* embryos [73,85]. However, development of *Tribolium* embryos arrested after several hours, which was probably caused by mechanical constriction, impeded gas and ion exchange or a combination of both factors. Thus, I invented a novel mounting method in which the embryo is attached with only the anterior end to the pole of an agarose hemisphere, while the remaining surface is exposed to the imaging buffer (Figure 2-4A). With this mounting method, I was able to record the embryonic morphogenesis (Figure 2-4B) from the rearrangement of the cellular blastoderm during gastrulation to the first irregular twitches during muscular movement (Figure 2-4C) continuously in one specimen and publish the first study on long-term live imaging in *Tribolium* (Subchapter 6.1.2).

After the recording process was completed, I retrieved the embryos from the microscope and cultivated them in a water-saturated atmosphere until they hatched successfully (Figure 2-4D). After hatching, I transferred the larvae to individual wells of a 24-well plate and cultivated them under standard conditions. They developed into morphologically inconspicuous adults that produced fertile progeny, a quality control which approves that the recording process with light sheet-based fluorescence microscopes under appropriate conditions does not have any detrimental effect on *Tribolium* embryos, even when they are recorded over very long time periods.

In total, I acquired three long-term datasets at an imaging temperature of 35°C by using a perfusion system to warm the imaging buffer (Figure 2-5). At this temperature, embryonic development of *Tribolium* takes around 60 hours [115]. Since my data covered periods of more than 50 hours, I was able to document more than 80% of the total embryonic development (Figure 2-6), including full coverage of four of the six consecutive embryogenetic events – gastrulation, germband elongation, germband retraction and dorsal closure.

In brief, the uniform blastoderm rearranges and thus differentiates into the serosa, the amnion and the embryonic rudiment during gastrulation. The embryonic rudiment condenses remarkably and sinks into the yolk while becoming covered ventrally by the amnion and the serosa. Once the serosa window closes, the embryonic rudiment differentiates into the germband and is released, together with the amnion, into the interior of the serosa. At the growth zone, which is located at the posterior tip of the germband, additional abdominal segments are added sequentially during germband elongation. The anterior and posterior tips of the germband curl around both poles and approach each other on the dorsal side while segmentation becomes more pronounced and leg buds emerge at the thoracic segments. During germband retraction, the flanks broaden significantly and the legs reach their maximum extend. Also, pleuropodia become visible at the first abdominal segment and a moderate furrow between head and thorax emerges. When the posterior tip of the germband flips into the posterior pole, dorsal closure begins. After rupture, the serosa migrates over both poles and turns inside-out, giving rise to the dorsal organ, which becomes internalized together with the yolk into the midgut when both flanks of the germband fuse along the dorsal midline. Several hours after dorsal closure, the embryo shows the first, irregular twitches.

Within the brief summary above, I have described only structures and processes that can be seen within the Z maximum projections. However, by using light sheet-based fluorescence microscopy, three-dimensional volume data is recorded, and optical sections may reveal previously unrecognizable details, for example the emergence and growth of the leg buds during germband elongation (Figure 2-7). To prove the universality of the hemisphere method, I also imaged the Brainy [32] double transgenic line. This line expresses ECFP under control of the artificial 6×P3 promoter, which labels glia cells, and DsRed under control of the *elongation factor 1 alpha B* promoter, which is only active in neuronal cells. Also with this line, long-term live imaging could be successfully performed, providing a brief glimpse on the complex cellular processes occurring during germband elongation and retraction that are necessary to build a functional neuronal network (Figure 2-8).

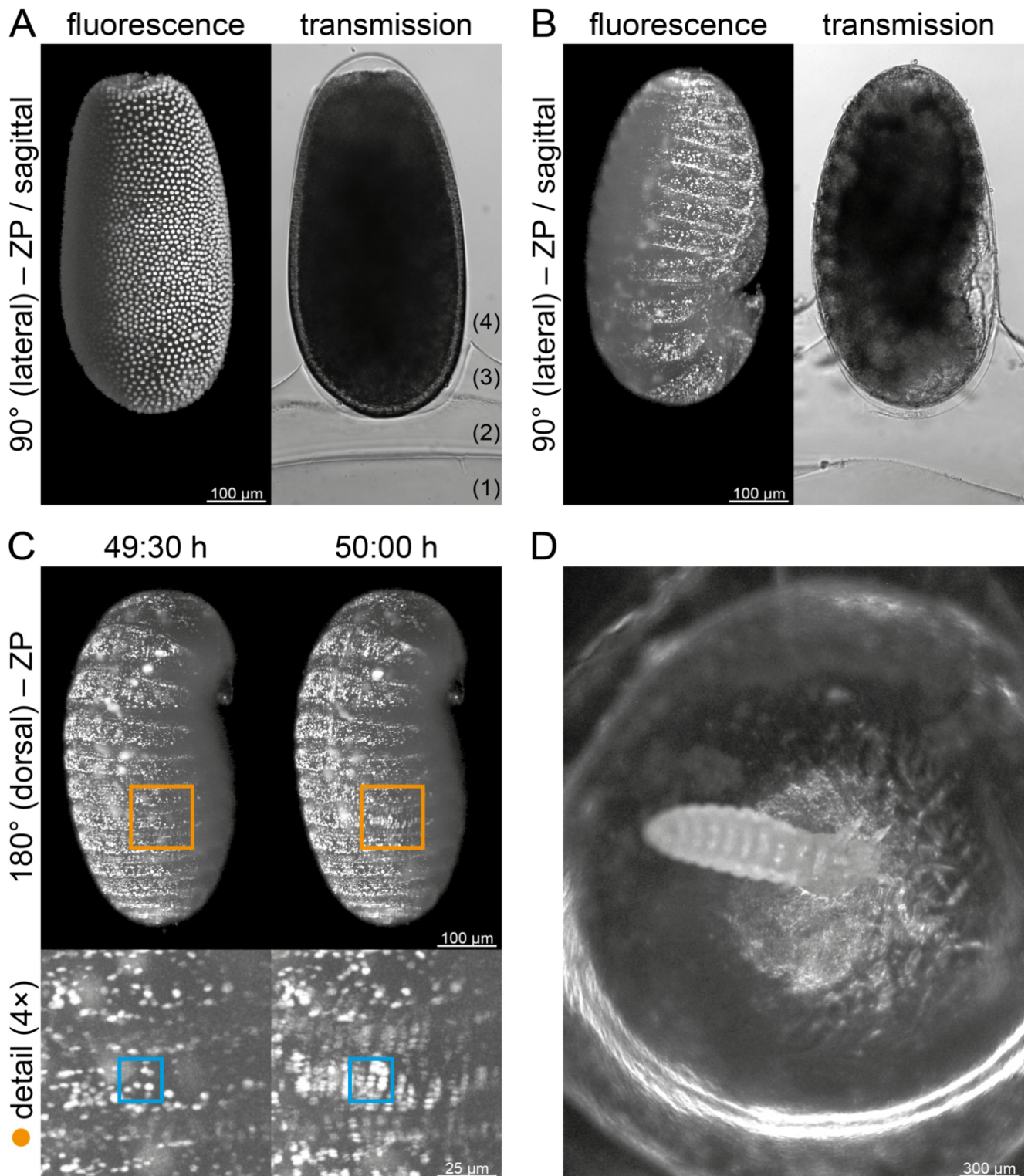


Figure 2-4 – Mounting and imaging of *Tribolium* embryos within light sheet-based fluorescence microscopes by using the hemisphere method. The data were acquired by using the EFA-nGFP [104] transgenic line, which expresses nuclear-localized GFP under control of the *elongation factor 1 alpha 1 subunit* promoter. **(A)** Embryo at the beginning of the imaging process at the uniform blastoderm stage. The anterior pole is at the bottom. In the transmission light image, (1) marks the hemisphere layer, (2) marks the mounting layer, (3) marks the stability layer and (4) marks the imaging buffer. **(B)** Embryo at the end of the imaging process when embryonic morphogenesis is completed. The anterior pole is at the bottom. **(C)** Onset of regular muscular movement. The blue box marks five superficial nuclei, which show motion blur at 50:00 h. **(D)** Hatched larva after long-term imaging. View from the top on the dried-out hemisphere. The larva could be retrieved and raised to a healthy and fertile adult. ZP, Z maximum projection with image processing. Figure and/or figure description fully and/or partially reproduced from Strobl & Stelzer 2014, #1 in Publication Table 1.

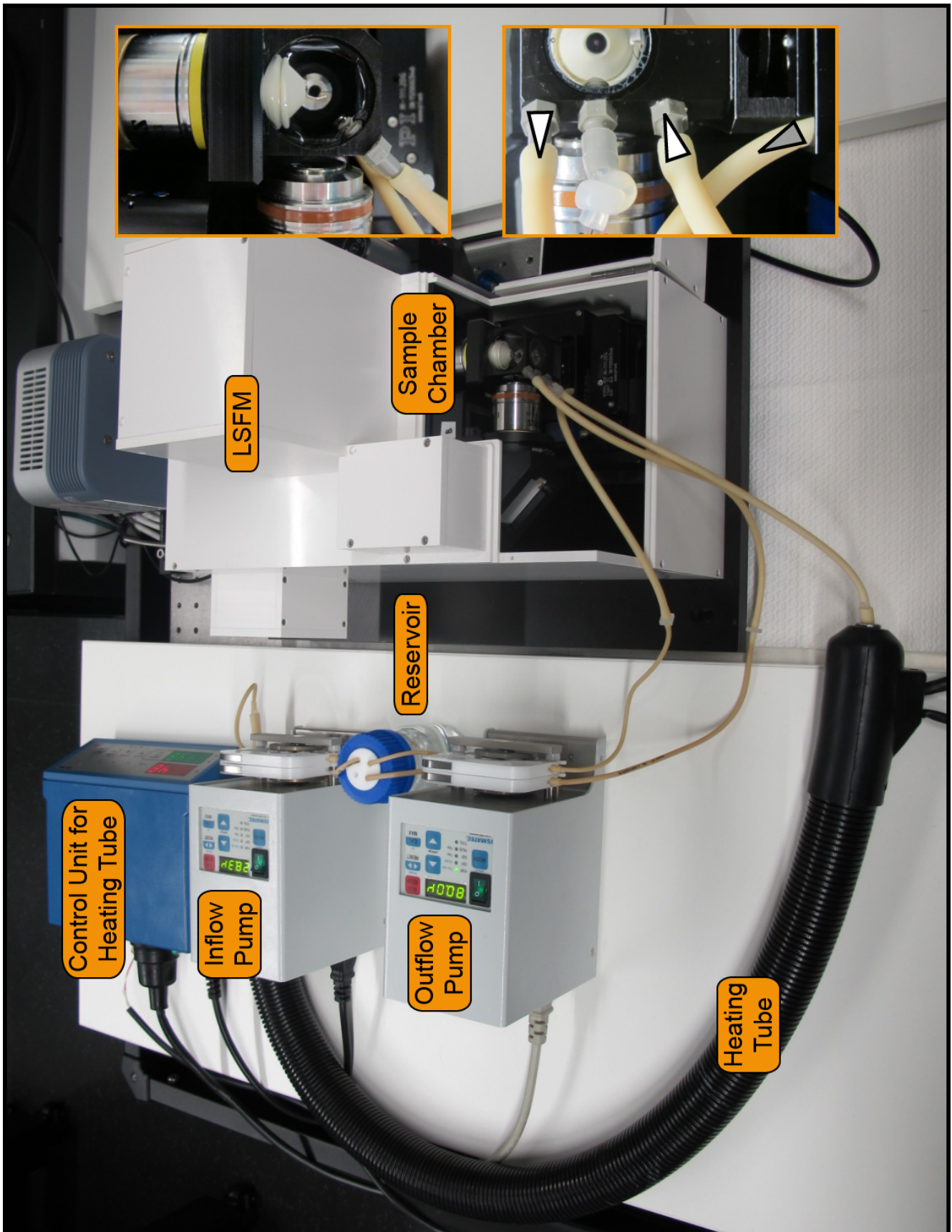


Figure 2-5 – Light sheet-based fluorescence microscope with connected perfusion system. The main elements of the circulatory perfusion system are labeled. Controlled transfer of imaging buffer from the reservoir is achieved via the inflow pump through the heating tube into the sample chamber. From the chamber, excessive imaging buffer is transferred via the outflow pump back into the reservoir. The upper detail box shows a top view of the sample chamber. The perfusion system connects to the periphery of the sample chamber and, therefore, does not impair the imaging process. The lower detail box shows the front view of the sample chamber with connected inflow and outflow tubes. The inflow tube connects to the lower and the outflow tube to the upper joint of the sample chamber. Therefore, the imaging buffer outflow rate is limited by the inflow rate. Directions of flow are indicated with white arrowheads. The gray arrowhead indicates a safety outflow tube connected to a catch basin in case of image buffer leakage. LSFM, light sheet-based fluorescence microscope. Figure and/or figure description fully and/or partially reproduced from Strobl *et al.* 2015, #3 in Publication Table 1.

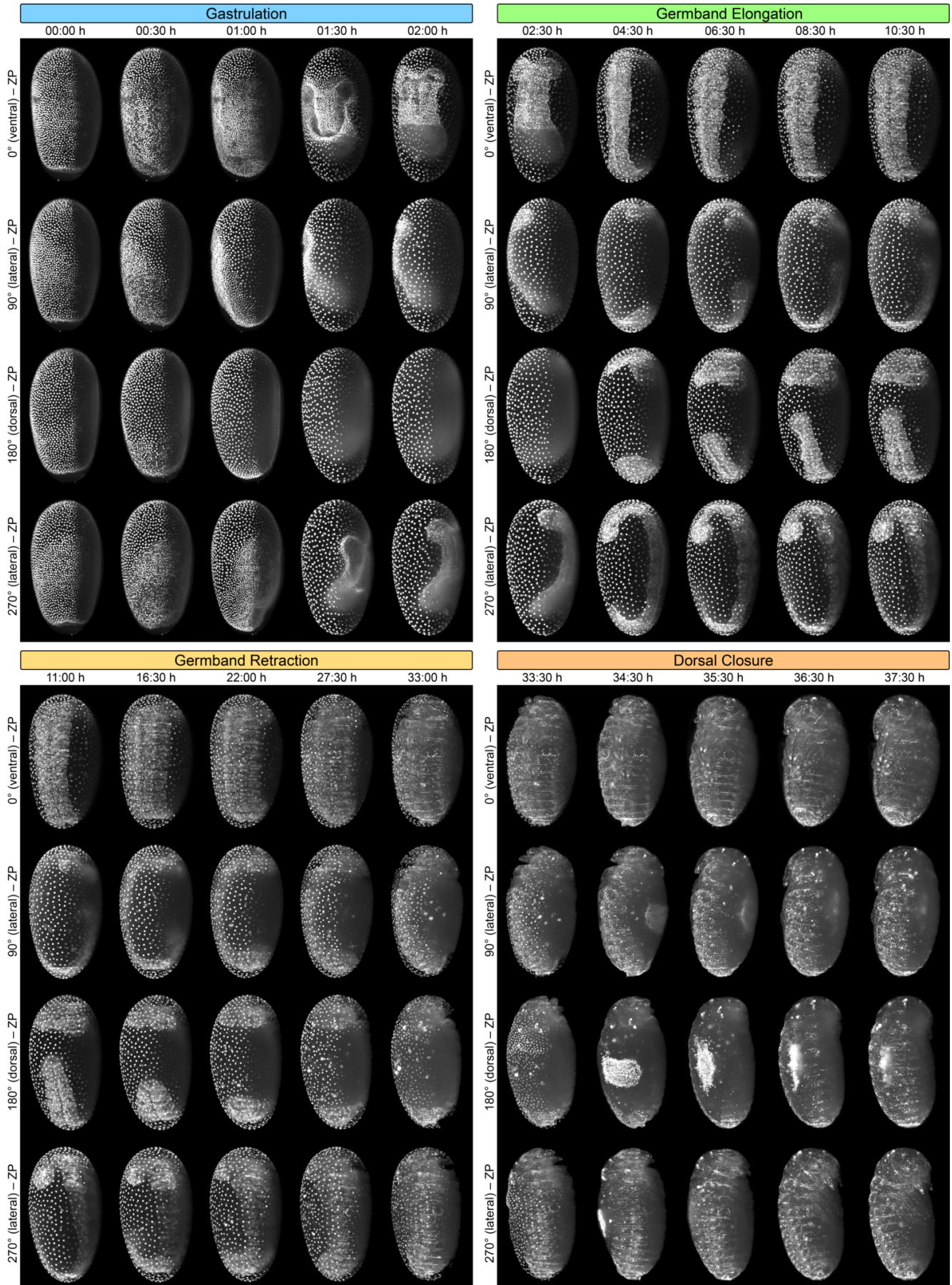


Figure 2-6 – Embryonic morphogenesis of *Tribolium* from gastrulation to dorsal closure along four directions by using the hemisphere method. For a brief summary of embryogenetic events, see Table 2-1. The events are shown with different temporal intervals. The data were acquired by using the EFA-nGFP [104] transgenic line, which expresses nuclear-localized GFP under control of the *elongation factor 1 alpha 1 subunit* promoter. ZP, Z maximum projection with image processing. Figure and/or figure description fully and/or partially reproduced from Strobl & Stelzer 2014, #1 in Publication Table 1.

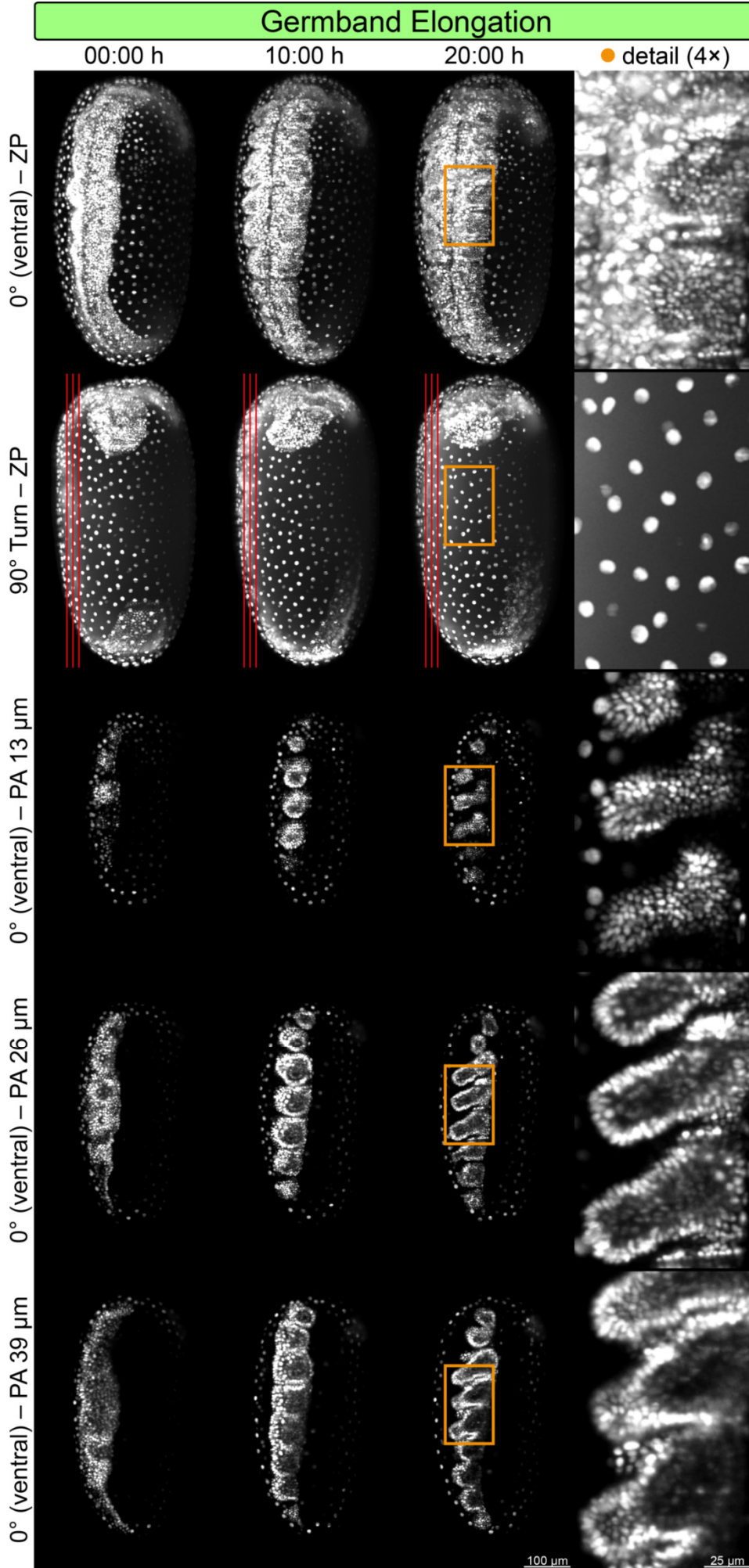


Figure 2-7 – Optical sectioning of a *Tribolium* embryo during germband elongation along the 0° (ventral) direction. For a brief summary of embryogenetic events, see Table 2-1. The data were acquired by using the EFA-nGFP [104] transgenic line, which expresses nuclear-localized GFP under control of the *elongation_factor 1 alpha 1 subunit* promoter. Z spacing is 13 μm. Detail images show the leg primordia at the thoracic segments. The locations of the single planes are indicated by the red lines. ZP, Z. maximum projection with image processing; PA, single plane with intensity adjustment. Figure and/or figure description fully and/or partially reproduced from Strobl *et al.* 2015, #3 in Publication Table 1.

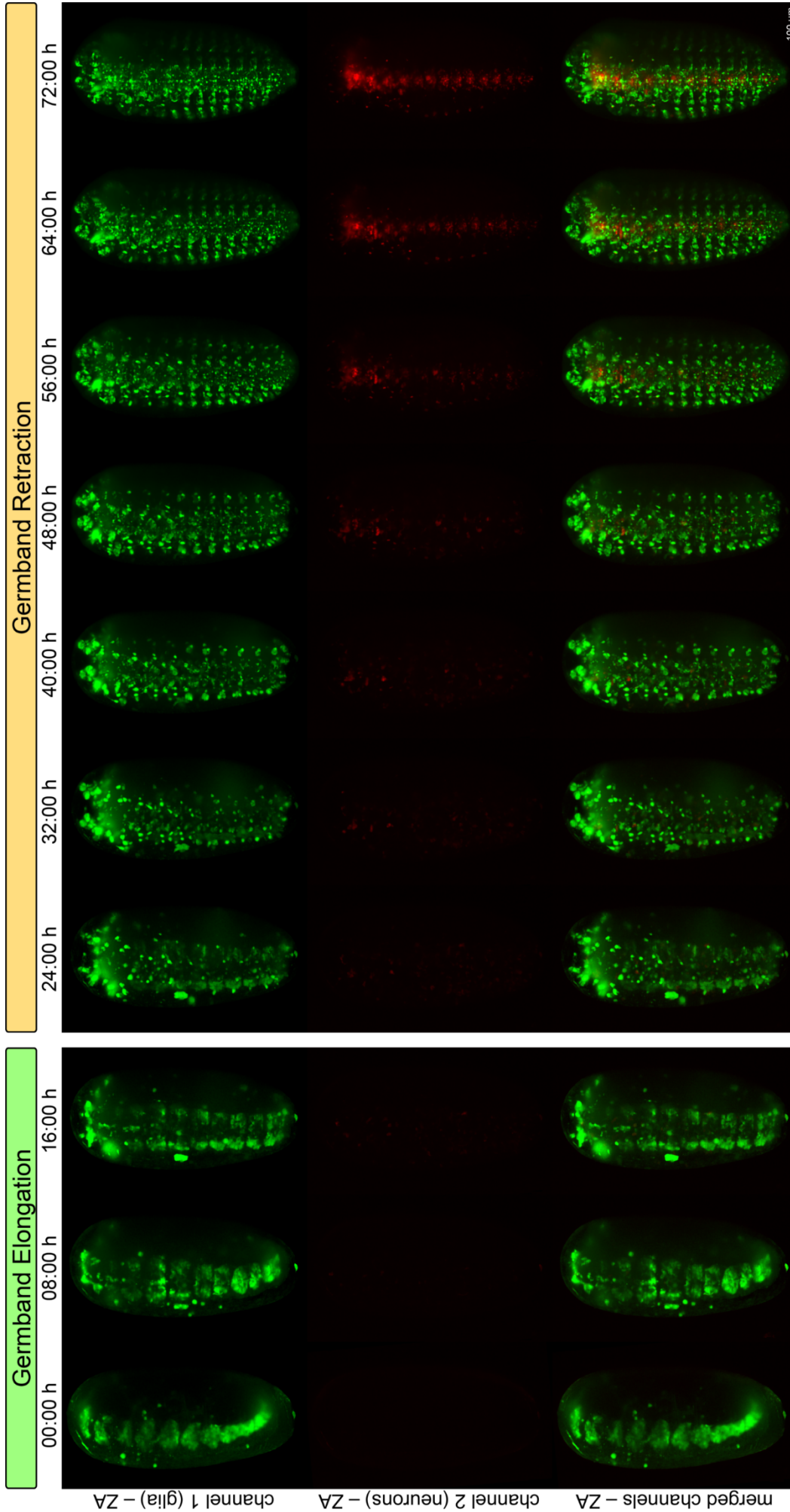


Figure 2-8 – Neuronal development of *Tribolium* during germband elongation and germband retraction along the 0° (ventral) orientation in two spectral channels. For a brief summary of embryogenetic events, see Table 2-1. The data were acquired by using the Brainy [32] double transgenic line, which expresses ECFP under control of the artificial 6×P3 promoter (channel 1, labeling the glia cells) and DsRed under control of the *elongation factor 1 alpha B* promoter (channel 2, labeling the neurons). While many glia cells can already be seen during germband elongation, signal in the neuronal cells can be detected not until the beginning of germband retraction. ZA, Z maximum projection with intensity adjustment. Figure and/or figure description fully and/or partially reproduced from Strobl & Stelzer 2016, #4 in Publication Table 2.

2.2.3. Side-By-Side Comparison of *Drosophila* and *Tribolium* Embryonic Morphogenesis

The comparative approach, *i.e.* analyzing similarities and differences in the embryonic development of at least two species, allows the interpretation of developmental principles within their phylogenetic context [116]. Typically, such comparisons are done on the genomic [25,117,118], the transcriptomic [31,119,120] or the morphologic level [32,121,122]. Now, as long-term fluorescence live imaging datasets of *Drosophila* and *Tribolium* are available, comparisons can also be performed on the morphogenetic level. For *Drosophila*, I used data from the #24163 transgenic line (Subchapter 2.2.1), which expresses an EGFP-labeled histone 2A variant in all cells. For *Tribolium*, I used data from the EFA-nGFP [104] transgenic line, which expresses nuclear-localized GFP under control of the *elongation factor 1 alpha 1 subunit* promoter.

Although both species separated approximately 327 million years ago [25–27] and thus belong to different insect orders, a morphogenetic side-by-side comparison (Figure 2-9) reveals a moderate similarity between the course of the six consecutive embryogenetic events (Subchapter 2.1.1):

- At the end of blastoderm formation, after the 12th synchronous nuclear division, the blastoderm nuclei are distributed homogeneously on the surface (Figure 2-9, upper left panel) of the egg before the ventral furrow emerges ventrally during gastrulation (Figure 2-9, upper right panel).
- During germband elongation and retraction, the germband tip migrates towards the anterior pole on the dorsal side of the embryo. Additionally, segmentation becomes evident during elongation (Figure 2-9, middle left panel) and prominent during retraction (Figure 2-9, middle right panel).
- During dorsal closure, the extra-embryonic membranes fold at the dorsal side of the embryo and internalize, together with the remaining yolk, into the digestive tract before the dorsal epidermal primordia begin with the zippering process to form the dorsal seam (Figure 2-9, lower left panel).

On the other side, crucial morphogenetic differences can be spotted. For example, *Drosophila* embryos give rise to only one heavily degenerated extra-embryonic membrane, the amnioserosa, on the dorsal side of the embryo, while *Tribolium* embryos become ventrally covered by the amnion and completely enveloped by the serosa (Figure 2-9, middle right and lower left panels). Further, *Drosophila* embryos do not grow legs during germband retraction and undergoes head involution during dorsal closure, while *Tribolium* embryos develop all thorax and head appendices, which are also present in the adults, already during embryogenesis (Figure 2-9, lower right panel).

Additionally, begin, duration and end of the respective consecutive embryogenetic events differ heavily between both species. For example, germband retraction begins, on a relative scale, slightly earlier in *Tribolium*, but takes about three times as long, so that it ends about the same relative moment when dorsal closure has already completed in *Drosophila* (Figure 2-9, progression bar at the bottom of the figure).

This subchapter, as well as the associated review (Subchapter 6.1.5), are only intended as a superficial evaluation. A detailed comparison between *Drosophila* and *Tribolium*, ideally based on a morphogenetic ontology on the cellular level (Subchapters 4.2.1 and 4.2.2), lies far beyond the scope of this PhD thesis and the respective review and will be the topic of future studies, as described within Outlook I (Subchapter 4.1.2).

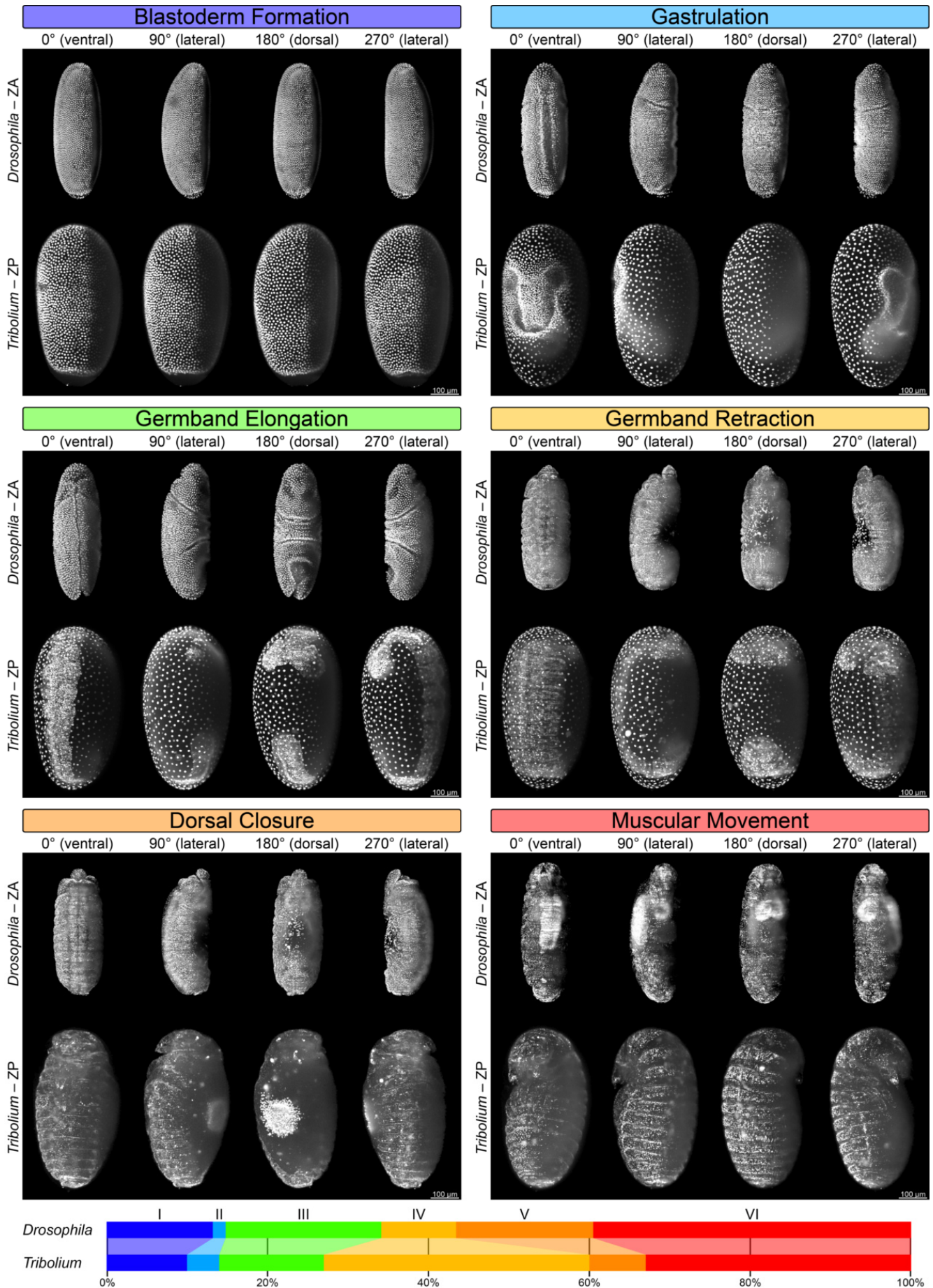


Figure 2-9 – Side-by-side comparison of *Drosophila* and *Tribolium* embryonic morphogenesis during all six consecutive embryogenic events along four directions. For a brief summary of embryogenic events, see Table 2-1. All data were acquired by using the *Drosophila* P{His2Av-EGFP.C}2 (Table 2-5) and the *Tribolium* EFA-nGFP [104] transgenic lines. The normalized progression bar below the images shows the temporal frame of the embryogenic events relative to the complete embryonic development. ZA, Z maximum projection with intensity adjustment; ZP, Z maximum projection with image processing. Figure and/or figure description fully and/or partially reproduced from Strobl & Stelzer 2016, #4 in Publication Table 2.

2.2.4. Standard Operating Procedures for Fluorescence Microscopy of *Tribolium* Embryos

Before 2012, most studies that contained fluorescence microscopy data of *Tribolium* embryos had applied the fixation-and-staining approach [22,123–126]. When I started my PhD project in summer 2012, the live imaging approach within the *Tribolium* community was still very young – only one study was published at that time [104]. This study introduced the EFA-nGFP transgenic line (Subchapter 2.2.2) and the authors applied spinning disk confocal fluorescence microscopy to image living embryos during germband elongation over a period of about 7 hours.

Whenever a new element is added to the methodological toolkit of a scientific community, the definition of standard operating procedures offers two significant advantages: Firstly, the chances that two or more quasi-identical experimental workflows with a confusing plethora of homonyms and synonyms arise are reduced. Secondly, since the establishment effort is reduced, adaption of the technique becomes more attractive for interested laboratories.

Since I published the first methodological study on this topic (Subchapter 6.1.2) and since preparation of insect embryos for live imaging in light sheet-based fluorescence microscopes is a non-trivial task, it was convenient to streamline my approach in the form of protocol-like studies (Box 2-6). A comprehensively documented workflow helps non-initiated colleagues to avoid numerous pitfalls that may either result in low quality data or death of the embryo during the imaging process.

During my PhD project, I authored two self-contained and peer-reviewed protocol-like studies. Each study is fully sufficient to reproduce the hemisphere method, but both have complementary additional information that emphasize certain aspects on a higher level of detail.

The first protocol (Subchapter 6.1.4) thoroughly describes a two-step calibration routine for light sheet-based fluorescence microscopes and is accompanied by a comprehensively illustrated guide how *Tribolium* embryos are dechorionated (Figure 2-10A to D, Box 2-7), mounted (Figure 2-10E to O), inserted into the sample chamber and retrieved after imaging has ended. Furthermore, it describes how the recorded data can be processed to perform a quick evaluation of the imaging assay.

Box 2-6 – Methodological studies versus protocol-like studies

Significant parts of my PhD project are one methodological and two protocol-like studies about non-invasive long-term fluorescence live imaging of *Tribolium* embryos by using light sheet-based fluorescence microscopy. Although both publication types subject novel or refined techniques, their purpose is different. Methodological studies usually introduce the respective scientific communities to the new invention or significant advantage. Typical journals are for example *Nature Methods* or the *Journal of Biological Methods*, but smaller journals such as *Development* also publish methodological work along with classical studies. In contrast, Protocol-like studies are usually based on preceding methodological studies and outline the techniques in more detail. They usually contain a comprehensive illustrated workflow in the form of bullet points, elucidate options and pitfalls, discuss optimization strategies and provide troubleshooting information. Typical journals are for example *Nature Protocols* and *Cold Spring Harbor Protocols*.

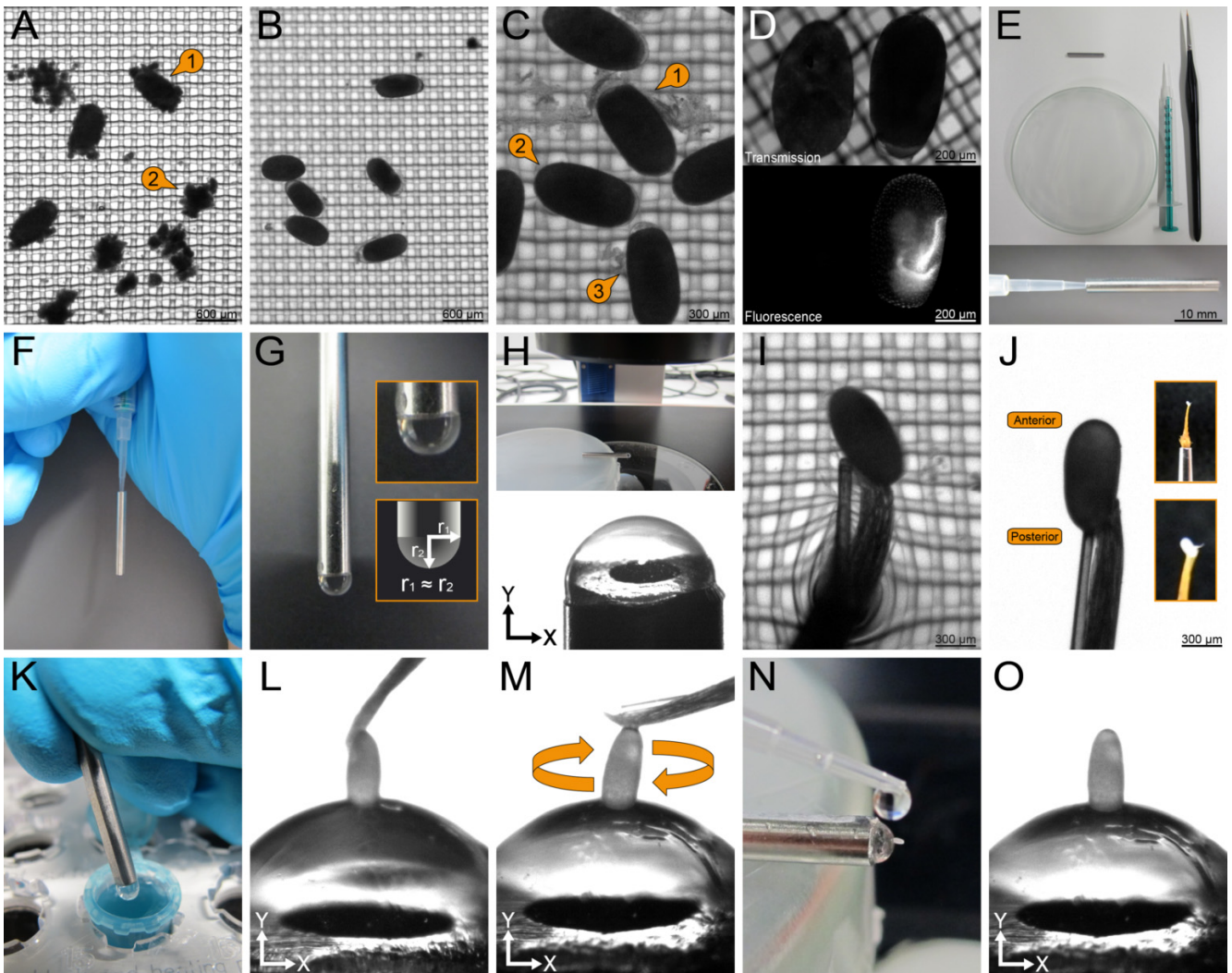


Figure 2-10 – Preparation of *Tribolium* embryos for light sheet-based fluorescence microscopy. (A) Embryos before dechoriation in a cell strainer with 100 μm mesh size. (B) Embryos during dechoriation in sodium hypochlorite solution. Flour particles are degraded. (C) Washing step after dechoriation in PBS. Three cases have to be distinguished: (1) incomplete dechoriation, (2) complete detachment of chorion from embryo and (3) small parts of the chorion still sticking to the embryo. (D) Distinction between non-fertilized (left) and fertilized (right) embryos in transmission light (top row) and between non-fluorescent and fluorescent embryos with the respective fluorescence filter set (bottom row). (E) Tools for mounting the embryo onto the sample holder (top row). Shown are the steel pipe, the modified syringe, a paintbrush and the Parafilm-covered glass Petri dish. Insertion of modified syringe to the steel pipe (bottom row). (F) Preparation of agarose hemisphere. The steel pipe aligned along gravity and filled from the top with liquid agarose to create the hemisphere at the bottom. (G) Detail of the hemisphere on the steel pipe. Detail boxes show the optimal hemisphere geometry. The semi-axes r_1 and r_2 should have similar lengths. (H) Under the stereo microscope, the hemisphere should appear uniformly smooth and transparent. (I) Picking of embryo with the brush. (J) Correct positioning of the embryo on brush. Attach the embryo with the posterior end on the tip of the brush so that the anterior end is accessible. Detail boxes show the positioning on a macroscopic level. (K) Creation of the mounting agarose layer. Dip the agarose hemisphere into liquid agarose. (L) Placement of the embryo in mounting agarose layer. The embryo should be placed on the pole of the hemisphere. (M) Correction of the embryo position on hemisphere. Gradually correct the position of the embryo on the hemisphere by rotating the steel pipe and carefully brushing along the posterior end of the embryo. (N) Preparation of the stability agarose layer. (O) Correctly mounted embryo on the hemisphere. The embryo is positioned upright at the pole so that the major fraction of the embryo surface is not covered by agarose and is in contact with the air and later on with PBS. Figure and/or figure description fully and/or partially reproduced from Strobl *et al.* 2015, #3 in Publication Table 1.

In the exemplary results, *Tribolium* embryos are shown with different varying degrees of freedom. While the two laterally acquired spatial dimensions (X and Y) are always shown, the figures show either the direction and the time, the direction and the third spatial dimension (Z), or the third spatial dimension (Z) and the time. Three aspects are emphasized in this protocol: Firstly, quality control. The protocol explains in detail how the embryo has to be further cultivated after retrieval to ensure that the live imaging assay can be truly considered non-invasive. Secondly, troubleshooting. The protocol is accompanied by a comprehensive table that lists more than thirty possible pitfalls, of which eleven are visualized in a supplementary figure. Thirdly, the protocol presents three imaging options with broad relevance (Table 2-6 and Figure 2-11).

Box 2-7 – Architecture of the insect egg shell and the function of the chorion

Beside the yolk and cellular components, the insect egg also consists of two non-cellular layers:

- The inner vitelline membrane is a very thin layer that consists of several different protein types which are crosslinked to form a structural matrix that functions as a barrier against harmful extrinsic factors, prevents the embryo from desiccation and plays an important role in embryonic patterning [127,128].
- The outer chorion is a rigid proteinaceous structures that protects the embryo from pathogens and provides a certain degree of mechanical stability [129]. In *Tribolium*, the chorion additionally provides protection against desiccation, but is highly light absorbent. However it is not necessary for proper embryonic development as long as the embryos are kept in a humid atmosphere after dechorionation. It can be gently removed by incubating the embryos for a short time in diluted sodium hypochlorite solution.

Table 2-6 – Imaging Options. Table and/or table description fully and/or partially reproduced from Strobl *et al.* 2015, #3 in Publication Table 1.

option	advantages (+) and disadvantages (-)	rationale
imaging at room temperature (Figure 2-11A)	(+) high relative temporal resolution (+) higher efficiency of fluorescent proteins (+) no heating system required (-) longer development time (approximately factor 3) (-) lower survival rate	<ul style="list-style-type: none"> • detailed temporal observation of morphogenesis • use of short-term imaging • not recommended for high-throughput long-term imaging
structured illumination (Figure 2-11B)	(+) higher contrast in focal plane (+) reduced background in dense regions (-) higher laser energy exposure (-) longer recording time per image / Z stack	<ul style="list-style-type: none"> • required for accurate segmentation • not recommended for high temporal resolution • not recommended for long-term imaging
20× objective / sCMOS camera (Figure 2-11C)	(+) higher spatial resolution (-) longer recording time per Z stack (-) larger data volume (approximately factor 8)	<ul style="list-style-type: none"> • required for accurate segmentation • not recommended for high temporal resolution • not recommended for long-term imaging

Beside a rigorous technical description of the agarose column method, which is only suitable for short-term live imaging or data acquisition of fixed and stained embryos, and the hemisphere method, which needs some training before it can be applied successfully, the second protocol (Subchapter 6.1.6) introduces a third mounting method, the cobweb holder (Figure 2-12). In this option, a steel cylinder is equipped with a thin metal sheet that contains a slotted hole to which a very thin agarose film is applied. As long as the agarose is still liquid, the embryo is placed onto the film and remains in its initial position after solidification. This mounting method has multiple advantages: Firstly, the embryo is only partially covered by a very thin agarose film, which favors gas and ion exchange and simplifies embryo retrieval. Secondly, the effort to master this method is low, students are able to apply it after only a few hours of training. Thirdly, the method supports parallelization, as up to six embryos can be mounted onto one cobweb holder. The most crucial drawback is that the embryos can only be properly recorded along four directions in the orientations 0°, 90°, 180° and 270°.

The protocol also introduces two custom-made transgenic lines specifically designed for long-term fluorescence live imaging, AGOC{ATub'H2B-mEmerald} #1 and #2, which were created via the AGameOfClones vector concept (Subchapter 2.2.7). Since the number of custom-made fluorophore-expressing transgenic lines is still low, it also describes a workflow for the fixation, permeabilization, staining and imaging of *Tribolium* embryos in light sheet-based fluorescence microscopes. In total, five dyes that stain either the nucleus, the nuclear envelope or the actin cytoskeleton are described. The procedure can be applied to wild-type as well as transgenic embryos that already express fluorophores (Figure 2-13).

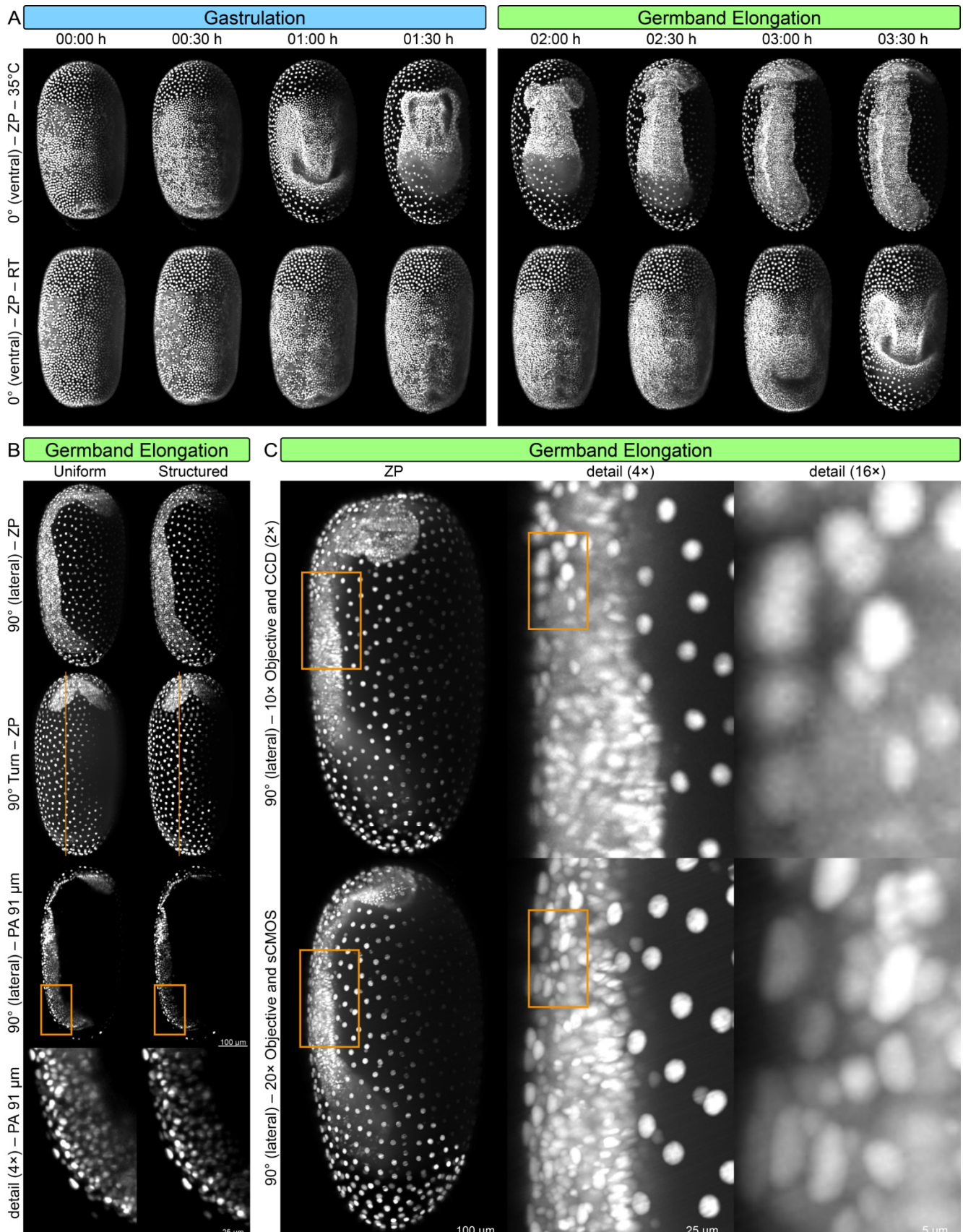
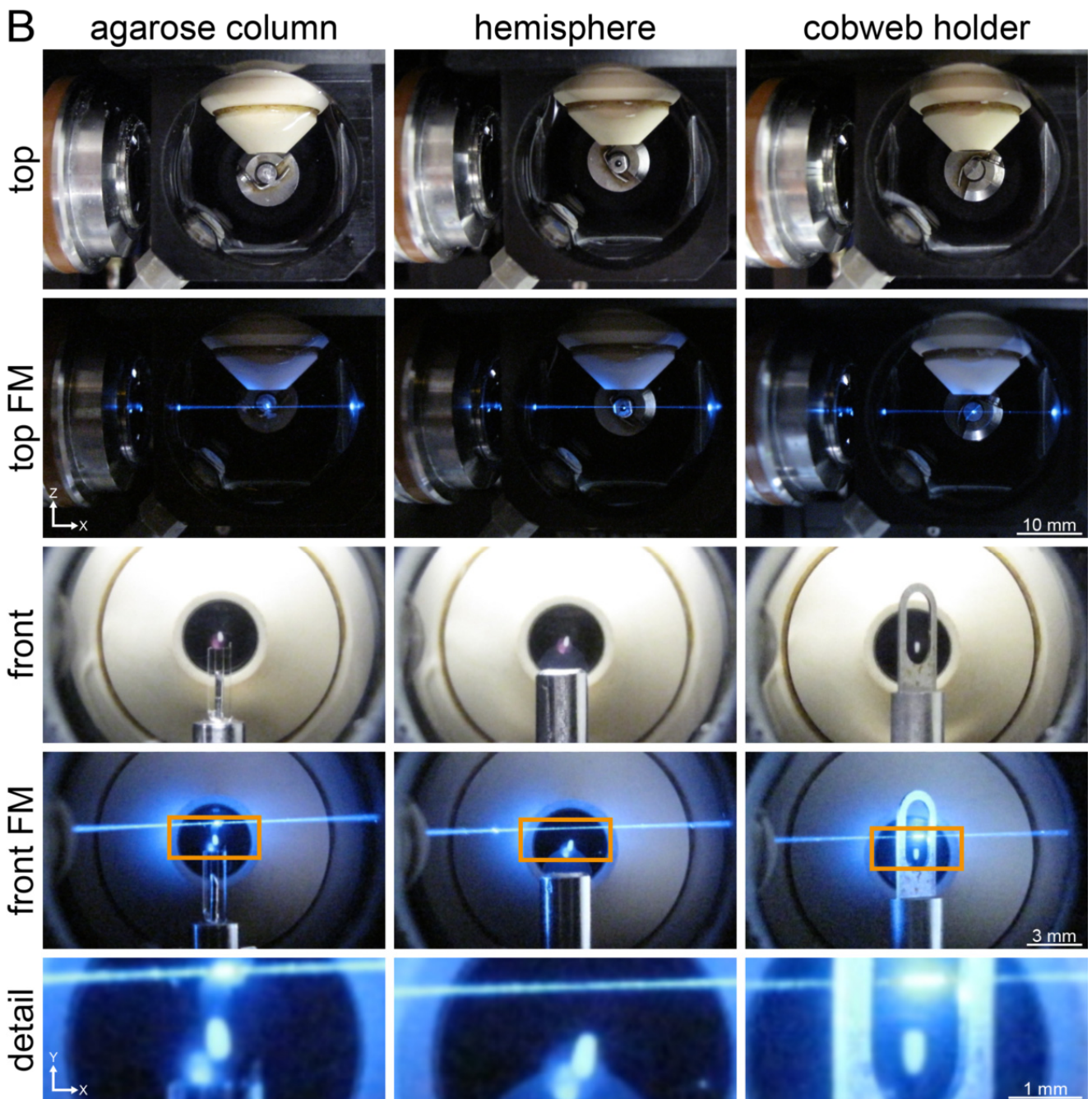
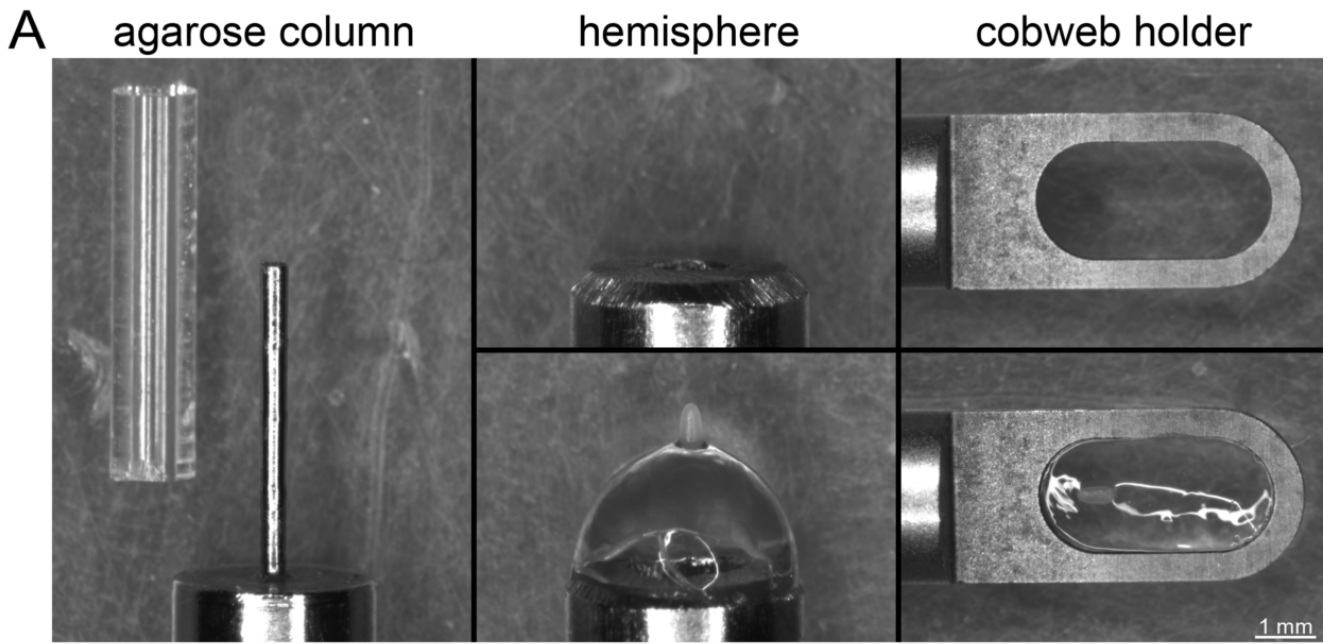


Figure 2-11 – Effect of imaging options on the acquired data. All data were acquired by using the EFA-nGFP [104] transgenic line. **(A)** Comparison of the development speed of *Tribolium* embryos at different temperature conditions. **(B)** Comparison of uniform versus structured illumination light-sheet modes. Dense structures such as the germband might appear blurry when the uniform illumination light-sheet mode is used. Structured illumination light-sheet mode leads to an increased image contrast by eliminating most of the blur from out-of-focus structures. The location of the single plane is indicated by the red line. **(C)** Comparison of images acquired with the 10× objective/CCD camera combination versus images acquired with the 20× objective/sCMOS camera combination. Although the volume of view remains approximately equal, an eightfold-higher spatial resolution can be obtained by a combination of a 20× objective with a sCMOS camera. RT, room temperature; ZP, Z maximum projection with image processing; PA, single plane with intensity adjustment. Figure and/or figure description fully and/or partially reproduced from Strobl *et al.* 2015, #3 in Publication Table 1.



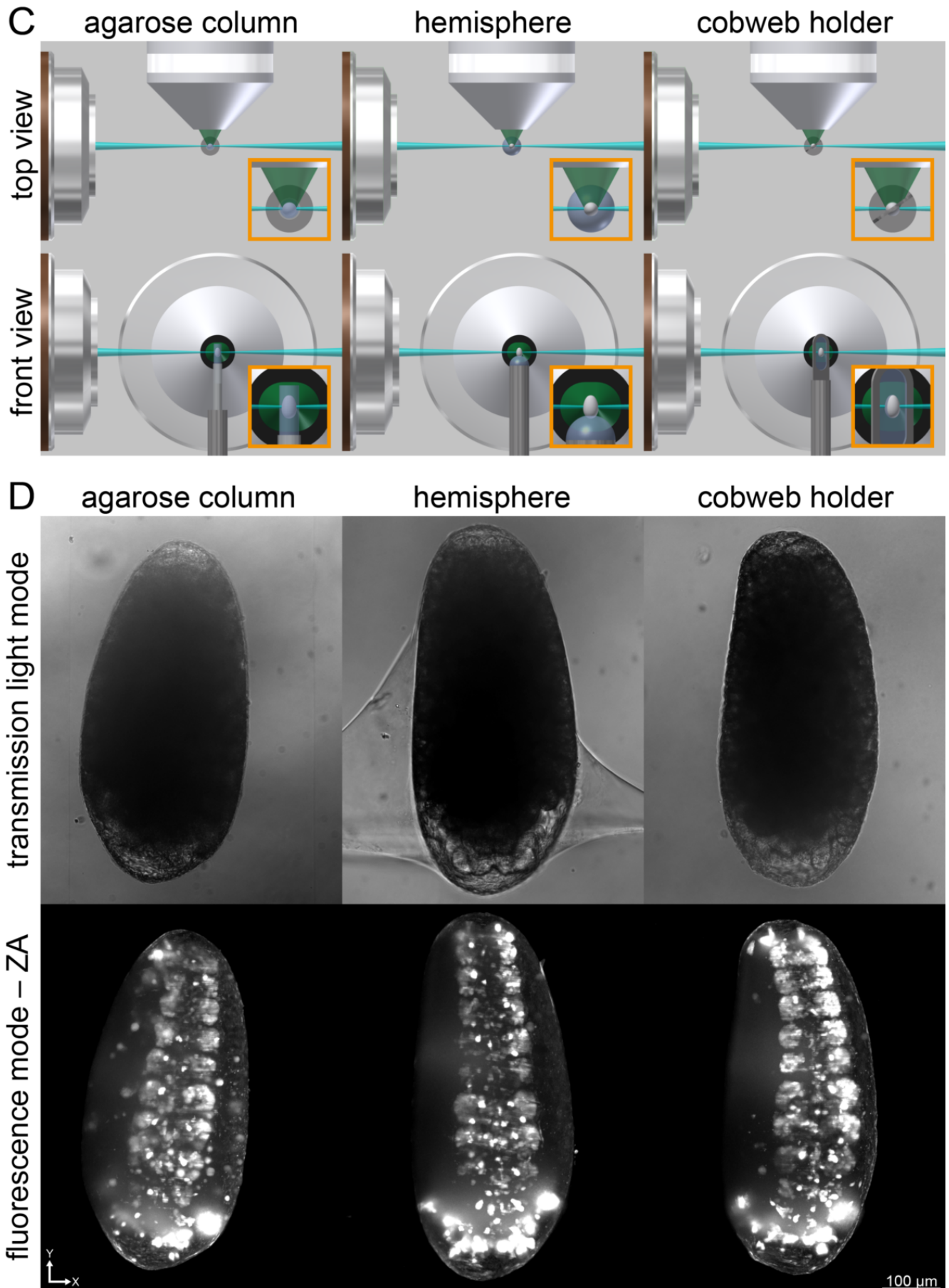


Figure 2-12 – Three mounting methods for the recording of the embryonic morphogenesis of *Tribolium* by using light sheet-based fluorescence microscopy. (A) Stereo microscope images of the agarose column, hemisphere and cobweb holder. (B) The three mounting methods applied within a digital scanned laser light sheet-based fluorescence microscope. (C) Schemes of the three mounting methods during the recording process. (D) Exemplary images from *Tribolium* embryos of the Glia-blue [32] transgenic line. FM, fluorescence mode, ZA, Z maximum projection with intensity adjustment. Figure and/or figure description fully and/or partially reproduced from Strobl *et al.* 2017A, #5 in Publication Table 2.

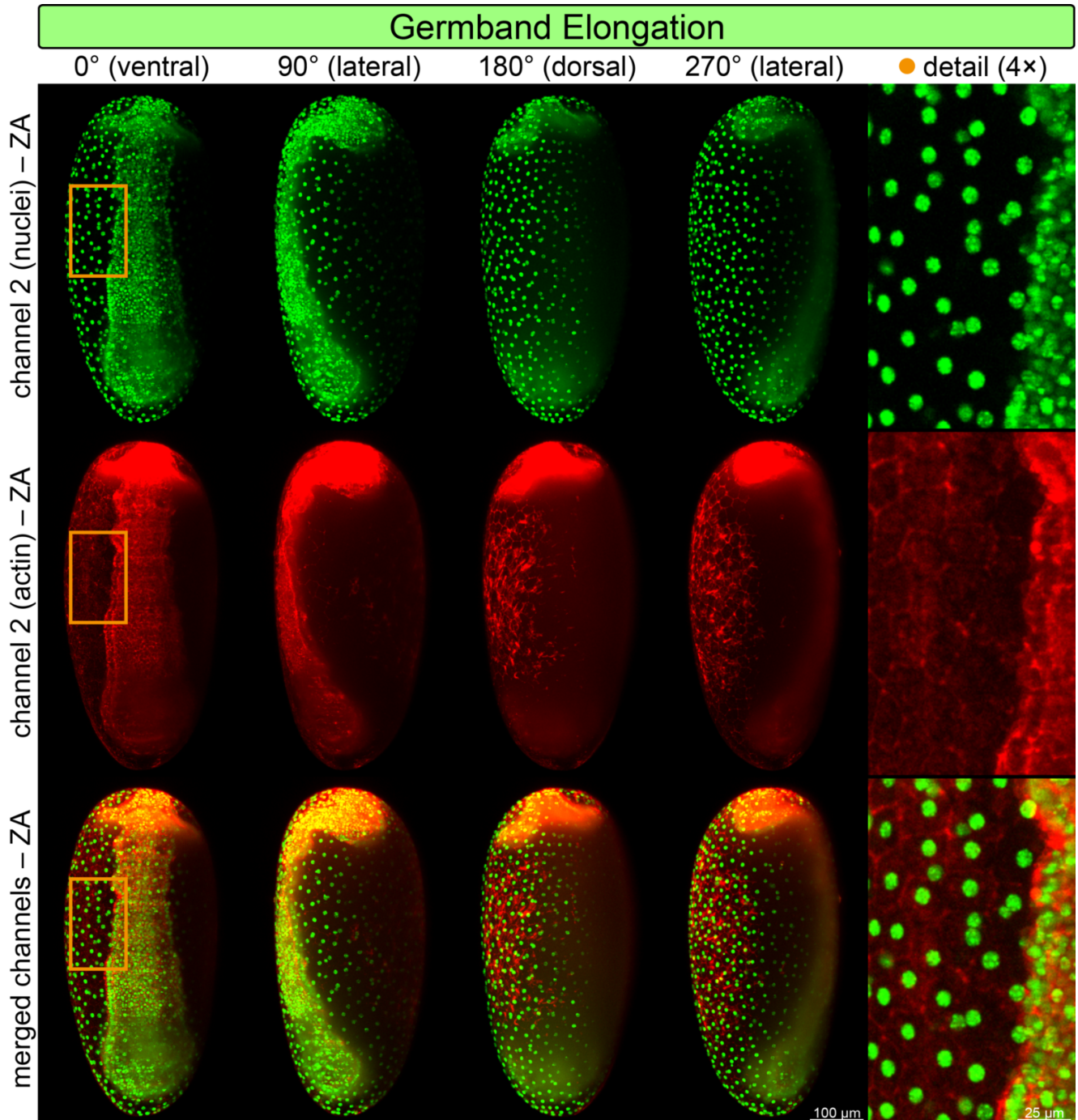


Figure 2-13 – Fixed and stained *Tribolium* embryo during germband elongation along four directions in two spectral channels. The data were acquired by using the AGOC{ATub'H2B-mEmerald} #1, which expresses mEmerald-labeled histone 2B subunits under control of the *alpha-tubulin 1* promoter. The embryo was further stained with Alexa Fluor 546 Phalloidin, which labels the actin cytoskeleton. ZA, Z maximum projection with intensity adjustment. Figure and/or figure description fully and/or partially reproduced from Strobl *et al.* 2017A, #5 in Publication Table 2.

2.2.5. The Embryonic Morphogenesis of *Ceratitis capitata* – A Fairly Complete Description

After documenting nearly the whole embryonic morphogenesis of *Drosophila* and *Tribolium*, I moved on to investigate the developmental principles of the Mediterranean fruit fly *Ceratitis capitata*, an established insect model organism in pest- and agricultural-related research. *Ceratitis* is a member of the Diptera and diverged from *Drosophila* approximately 80 million years ago [25,130,131].

To perform long-term live imaging of *Ceratitis* embryos by using light sheet-based fluorescence microscopy, I adapted the cobweb holder method (Figure 2-14) and recorded nine datasets by using the TREhs43-hidA1a5_F1m2 [132] transgenic line, which expresses nuclear-localized EGFP under control of the *Drosophila polyubiquitin* promoter. In six of these datasets, I recorded the embryo *in toto* under similar conditions for time periods of more than 60 hours, which equals to more than 97% of the total embryonic development. These data show blastoderm formation partially and the five following embryogenetic events completely. However, only five of these embryos developed to healthy adults, so one dataset was considered invalid. Two of these remaining datasets show the embryo in ventrolateral as well as dorsolateral orientation, the other three remaining datasets show the embryo in ventral, lateral as well as dorsal orientation (Figure 2-15). The other datasets are spatiotemporally limited to certain regions and developmental phases and cover specific embryonic processes, for example formation of the pole cells or head involution.

Due to the large volume of the datasets (Box 2-8) and the high level of recognizable morphogenetic detail, I decided to split the study into two *Ceratitis*-associated articles, one data publication and one classical biological publication that describes the embryonic development.

The data article (Subchapter 6.2.4) describes the embryo preparation workflow, the mounting method, microscopy modalities, image processing, technical validation and provides usage notes and access information for the datasets. It also briefly introduces a two-level staging system that is picked up in the second article.

The classical article (Subchapter 6.2.5) provides a fairly complete description of the *Ceratitis* embryonic development. Since hardly any morphogenetic data and thus no staging system for the embryonic development of *Ceratitis* was available, I implemented a comprehensive two-level staging system, which is summarized in Figure 2-16, Figure 2-17 and Figure 2-18. The system relies on the five valid *in toto* datasets and is solely based on morphogenetic criteria.

Box 2-8 – Large data volumes and the inevitable rise of data journals

Due to rapid technological advances over the last decade, the amount of data that can be acquired in some biological disciplines has increased by multiple orders of magnitude. Prime examples are genetics, where next-generation approaches have dramatically decreased the time and cost for acquiring sequence data [133], and microscopy, where state-of-the-art techniques such as light sheet-based fluorescence microscopes acquire millions of images in several days [69].

Within the last years, several large scientific publishing groups established a new journal type: data journals exclusively publish studies that present and describe very large datasets. These articles contain only a brief introduction and a comprehensive methodological section, but purposely lack any biological interpretation. Instead, the data is conveniently formatted and deposited at an open access repository, for example the Dryad Digital Repository (datadryad.org). Examples for data journals are *Scientific Data* and *Data in Brief*.

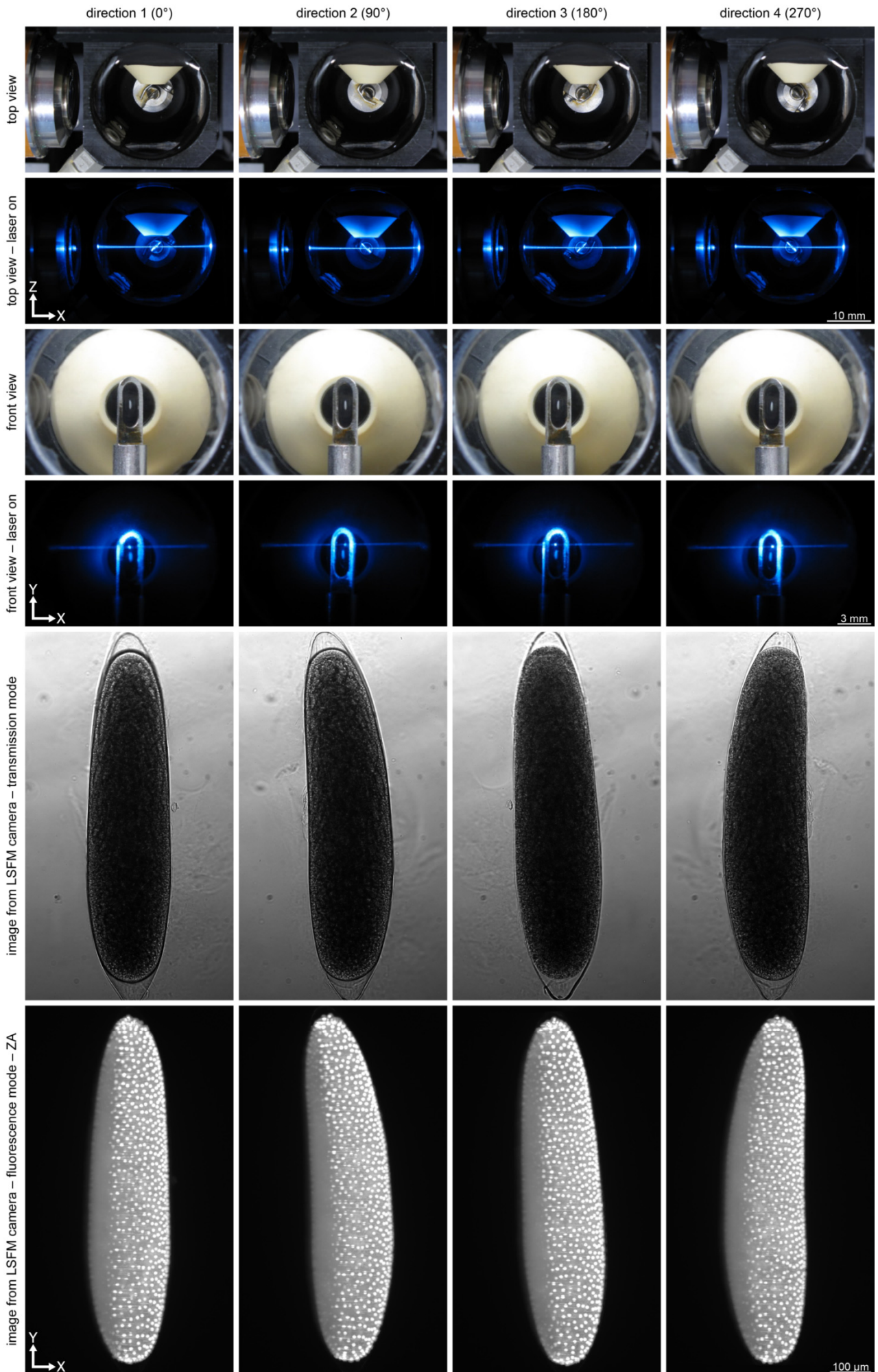


Figure 2-14 [↑] – Mounting of *Ceratitis* embryos with the cobweb holder for live imaging by using light sheet-based fluorescence microscopy along four directions. The fifth and sixth row show a *Ceratitis* embryo during blastoderm formation. The data were acquired by using the TREhs43-hidAla5_F1m2 [132] transgenic line, which expresses nuclear-localized EGFP under control of the *Drosophila polyubiquitin* promoter. ZA, Z maximum projection with intensity adjustment. Figure and/or figure description fully and/or partially reproduced from Strobl & Stelzer 2017E, #9 in Publication Table 3.

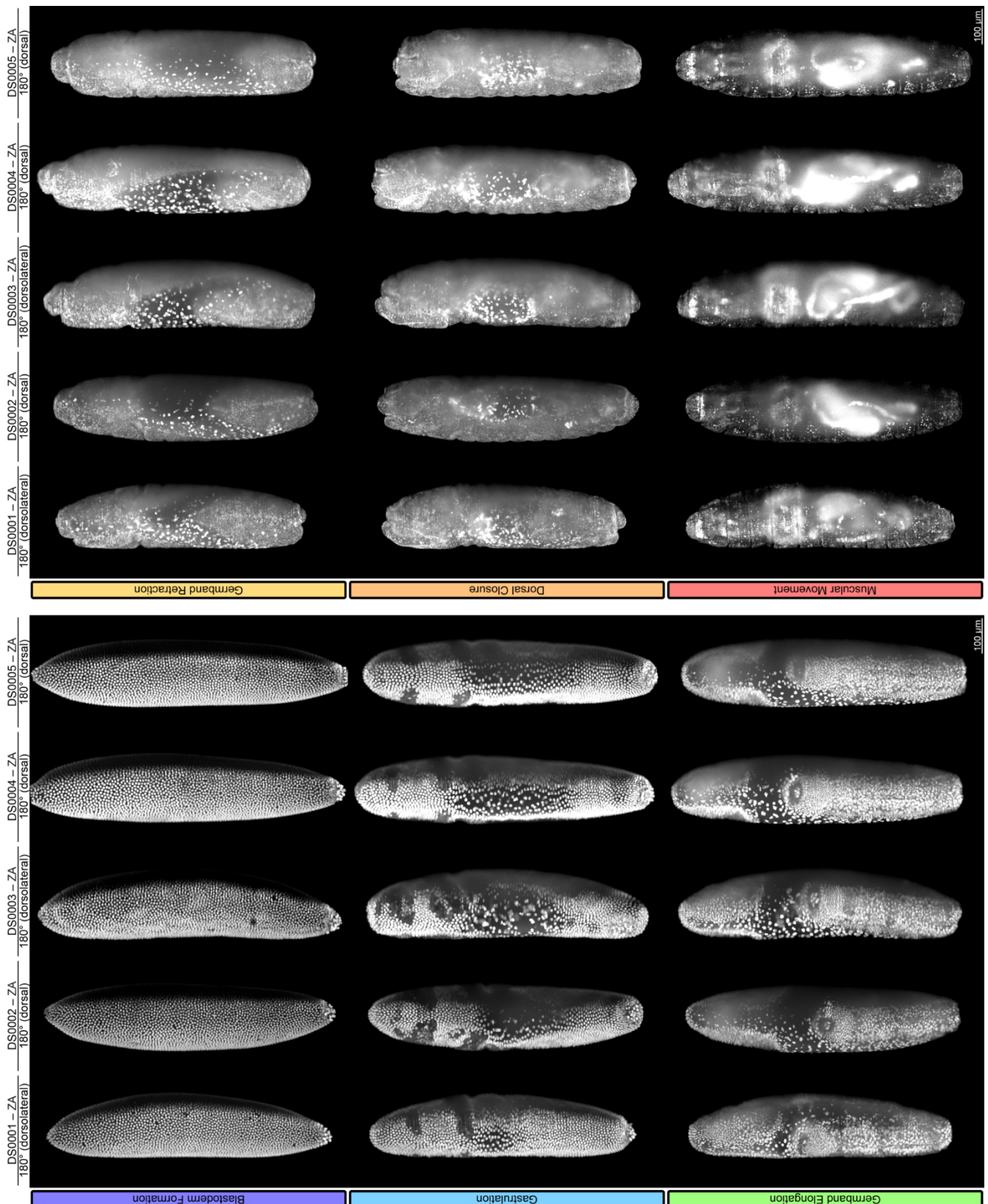


Figure 2-15 – Comparison of all five *Ceratitis* datasets for all six consecutive embryogenetic events shown along the 180° (dorsolateral for DS0001 and 0003, dorsal for DS0002, 0004 and 005) direction. For a brief summary of embryogenetic events, see Table 2-1. The data were acquired by using the TREhs43-hidAla5_F1m2 [132] transgenic line. Time points depict characteristic structures for the respective embryogenetic events. ZA, Z maximum projection with intensity adjustment. Figure and/or figure description fully and/or partially reproduced from Strobl *et al.* 2017E, #9 in Publication Table 3.

- The upper level derives from the six consecutive embryogenetic events that are considered fundamental throughout the insect class (Subchapter 2.1.1). This level is intended to compare the morphogenesis of *Ceratitis* with distantly related insect species of different orders, for example *Tribolium* or *Gryllus*.
- Due to the high degree of morphological similarity, I adopted the seventeen stages that have already been established for *Drosophila* [33] for the lower level. This level is intended to compare the morphogenesis of *Ceratitis* with closely related insect species within the same order.

In brief, blastoderm formation begins with egg fertilization. Subsequently, the zygotic nuclei undergo nine synchronous rounds of nuclear division, migrate to the surface of the egg and turn into blastoderm nuclei that undergo four more nuclear divisions to form a large uniform syncytium. After synthesis of cell membranes is completed, gastrulation begins. The cellular blastoderm differentiates into the head, the thorax, the abdomen and the amnioserosa, and the first asynchronous cell divisions occur. In addition, formation of the three germ layers, the ectoderm, the mesoderm and the endoderm, is orchestrated mainly by the ventral furrow (Figure 2-16). During germband elongation, the posterior tip of the germband curls around the posterior pole and migrates anteriorly along the dorsal surface of the egg before remaining in a quiescent position close to the head (Figure 2-16 and Figure 2-17). During germband retraction, the anterior movement is reversed, and the posterior tip of the germband returns eventually to the posterior pole. In parallel, the amnioserosa unfolds at the dorsal side of the embryo and segmentation in the germband becomes evident (Figure 2-17 and Figure 2-18). During dorsal closure, the dorsal epidermal primordia approach each other and form a tight seam along the dorsal midline in a zipper-like closing process while the amnioserosa is internalized and degraded. At the same time, the clypeolabrum retracts dorsad as part of the head involution process. Afterwards, muscular movement begins, during which the digestive tract forms, the ventral cord retracts and the first irregular muscle twitches are detected (Figure 2-18). Finally, when embryonic development is completed, the larva hatches from the egg.

Previous studies that used to describe the development of certain insect species usually applied methods where fixation of the embryo and oftentimes also some sort of staining is necessary (Subchapter 2.1.1). Besides the high demand on manpower and consumables, these approaches also suffer from the limitation that any correlations between data from two different specimen at close, but not identical developmental stages have to be done with great care – for example, does the size of a specific tissue or organ change during this particular developmental period, or is it just subject to natural variance?

One of the most remarkable features of my work is that high-resolution image data from fertilization to hatching is acquired in the same specimen, which is only possible due to the high recording speed and low photo-toxicity of light sheet-based fluorescence microscopy. For each time point, three-dimensional images with half a billion voxels are acquired, and the embryos were sampled more than a hundred times during their development. Since the data derive from the same specimen, correlations between different developmental phases are convenient. Live imaging also allows me to focus on quantitative analyses, for example by calculating not only the temporal standard deviations for the begin, end and length of all stages, but also for each single time point that was recorded during the imaging process.

My staging system serves as a convergence point for previous studies on the morphogenesis of *Ceratitis* and can in future be used as an integrative framework. My approach – imaging an appropriate transgenic line with light sheet-based fluorescence microscopy – is also a template for future attempts that aim to describe the morphogenesis of other species. Although it is a laborious initial task to create a convenient transgenic line, high quantities of high quality data can be acquired afterwards with only moderate effort, and the respective lines can also be used in further studies, for example when gene knock-downs, mutations or the appliance of extrinsic factors are believed to cause morphological aberrations.

stage	0° (ventrolateral) – ZA	timing	description
1/2		start 02:00 h } 01:30 h end 03:30 h } start 3.2% } 2.4% end 5.6% }	<ul style="list-style-type: none"> egg fertilization results in the <i>zygote</i>, which consists of the <i>yolk</i> and the <i>zygotic nuclei</i> the <i>yolk</i> begins withdrawing from both poles (<i>repeated withdrawal</i>) the respectively allocated <i>zygotic nuclei</i> begin protruding towards the surface (<i>peripheral migration</i>)
Blastoderm Formation			
3		start 03:30 h } 01:00 h end 04:30 h } start 5.6% } 1.6% end 7.2% }	<ul style="list-style-type: none"> the <i>yolk</i> withdrawal at both poles reaches a relative maximum and starts reversing (<i>repeated withdrawal</i>) the first <i>zygotic nuclei</i> reach the surface (<i>peripheral migration</i>) and undergo two synchronous nuclear divisions the <i>pole buds</i> emerge at the posterior tip of the <i>zygote</i> from the <i>zygotic nuclei</i> (<i>germ cell dynamics</i>)
Blastoderm Formation			
4		start 04:30 h } 02:30 h end 07:00 h } start 7.2% } 4.0% end 11.2% }	<ul style="list-style-type: none"> the last <i>zygotic nuclei</i> reach the surface (<i>peripheral migration</i>), turn into <i>blastoderm nuclei</i> and undergo two synchronous nuclear divisions the <i>zygote</i> turns into the <i>syncytial blastoderm</i> (<i>peripheral migration</i>) the <i>pole cells</i> derive at the posterior tip of the <i>syncytial blastoderm</i> from the <i>pole buds</i> (<i>germ cell dynamics</i>)
Blastoderm Formation			
5		start 07:00 h } 04:30 h end 11:30 h } start 11.2% } 7.2% end 18.4% }	<ul style="list-style-type: none"> the <i>blastoderm nuclei</i> synthesize cell membranes (<i>cellularization</i>) the medio-ventral <i>blastoderm nuclei</i> exhibit a slight wavy appearance
Blastoderm Formation			
6		start 11:30 h } 02:00 h end 13:30 h } start 18.4% } 3.2% end 21.6% }	<ul style="list-style-type: none"> the <i>blastoderm nuclei</i> complete the synthesis of cell membranes, the <i>syncytial blastoderm</i> turns into the <i>cellular blastoderm</i> (<i>cellularization</i>) the <i>ventral furrow</i> and <i>cephalic furrow</i> arise in the <i>cellular blastoderm</i> the <i>posterior plate</i>, to which the <i>pole cells</i> adhere, emerges at the posterior tip of the <i>cellular blastoderm</i> (<i>germ cell dynamics</i>)
Gastrulation			
7		start 13:30 h } 01:00 h end 14:30 h } start 21.6% } 1.6% end 23.2% }	<ul style="list-style-type: none"> the <i>anterior midgut primordium</i> emerges and invaginates at the anterior tip of the <i>ventral furrow</i> (<i>germ layer specification</i>) the <i>cellular blastoderm</i> differentiates into the <i>head</i>, the <i>thorax</i>, the <i>abdomen</i> and the <i>amnioserosa</i> (<i>extra-embryonic membrane folding</i>) the <i>ventral furrow</i> differentiates into the superficial <i>ectodermal layer</i> and the internal <i>mesodermal layer</i> (<i>germ layer specification</i>)
Gastrulation			
8		start 14:30 h } 02:00 h end 16:30 h } start 23.2% } 3.2% end 26.4% }	<ul style="list-style-type: none"> the posterior tip of the <i>germband</i> begins elongation along the dorsal side towards the anterior pole with high speed the <i>stomodaeal cell plate</i> emerges from the <i>procephalon</i> the <i>dorsal plate</i> internalizes and turns into the <i>posterior midgut primordium</i> (<i>germ cell dynamics</i> and <i>germ layer specification</i>)
Germband Elongation			

Figure 2-16 – Chronological staging table of *Ceratitis* embryogenesis for the stages 1 to 8. The first column indicates the stage and the embryogenetic event. The second column shows exemplary Z maximum projections of embryos in the 0° (ventrolateral) orientation. The third column summarizes start, duration and end of the given stage in hours (blue) and in percent of total development (purple). The fourth column outlines up to four developmental processes during the respective stage. ZA, Z maximum projection with intensity adjustment. Figure and/or figure description fully and/or partially reproduced from Strobl *et al.* 2017F, #10 in Publication Table 3, to which also the key terms (in *italics*) in the fourth column refer.

stage	180° (dorsolateral – ZA)	timing	description
II–7 Gastrulation		start 13:30 h } 01:00 h end 14:30 h } start 21.6% } 1.6% end 23.2% }	<ul style="list-style-type: none"> the anterior midgut primordium emerges and invaginates at the anterior tip of the ventral furrow (<i>germ layer specification</i>) the cellular blastoderm differentiates into the head, the thorax, the abdomen and the amnioserosa (<i>extra-embryonic membrane folding</i>) the ventral furrow differentiates into the superficial ectodermal layer and the internal mesodermal layer (<i>germ layer specification</i>)
III–8 Germband Elongation		start 14:30 h } 02:00 h end 16:30 h } start 23.2% } 3.2% end 26.4% }	<ul style="list-style-type: none"> the stomodeal cell plate turns into the stomodeal invagination the amnioproctodeal invagination emerges around the invaginating posterior midgut primordium from the ectodermal layer the ectodermal layer differentiates into the ventral epidermal primordium and the lateral epidermal primordium
III–9 Germband Elongation		start 16:30 h } 01:30 h end 18:00 h } start 26.4% } 2.4% end 28.8% }	<ul style="list-style-type: none"> the posterior tip of the germband continues elongation along the dorsal side towards the anterior pole with moderate speed the stomodeal invagination turns into the stomodeum, which becomes the anteromedial part of the digestive tract (<i>digestive system formation</i>) the amnioproctodeal invagination differentiates into the proctodeum and the proctodeal opening (<i>digestive system formation</i>)
III–10 Germband Elongation		start 18:00 h } 04:00 h end 22:00 h } start 28.8% } 6.4% end 35.2% }	<ul style="list-style-type: none"> the posterior tip of the germband continues elongation along the dorsal side towards the anterior pole with low speed the ventral midline emerges ventrally along the thorax and abdomen from the ventral epidermal primordium
III–11 Germband Elongation		start 22:00 h } 02:30 h end 24:30 h } start 35.2% } 4.0% end 39.2% }	<ul style="list-style-type: none"> the posterior tip of the germband completes elongation towards the anterior pole and remains in a quiescent position the amnioserosa folds (<i>extra-embryonic membrane folding</i>) the gnathal protuberances emerge from the gnathocephalon (<i>metamerization</i>)
IV–12 Germband Retraction		start 24:30 h } 07:30 h end 32:00 h } start 39.2% } 12.0% end 51.2% }	<ul style="list-style-type: none"> the posterior tip of the germband begins retraction along the dorsal side towards the posterior pole the amnioserosa unfolds again (<i>extra-embryonic membrane folding</i>) the dorsal epidermal primordia emerge laterally from the lateral epidermal primordia
V–13 Dorsal Closure		start 32:00 h } 02:30 h end 34:30 h } start 51.2% } 4.0% end 55.2% }	<ul style="list-style-type: none"> the posterior tip of the germband completes retracting the ventral epidermal primordium and lateral epidermal primordia of the thorax begin migration towards the anterior pole (<i>head involution</i>) the dorsal epidermal primordia begin migration dorsolaterally over the amnioserosa (<i>dorsal zipping</i>) the dorsal fold emerges from the gnathocephalon (<i>head involution</i>)

Figure 2-17 – Chronological staging table of *Ceratitis* embryogenesis for the stages 7 to 13. The first column indicates the stage and the embryogenetic event. The second column shows exemplary Z maximum projections of embryos in the 180° (dorsolateral) orientation. The third column summarizes start, duration and end of the given stage in hours (blue) and in percent of total development (purple). The fourth column outlines up to four developmental processes during the respective stage. ZA, Z maximum projection with intensity adjustment. Figure and/or figure description fully and/or partially reproduced from Strobl *et al.* 2017F, #10 in Publication Table 3, to which also the key terms (in *italics*) in the fourth column refer.

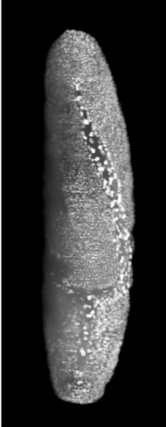
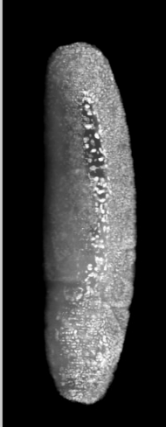
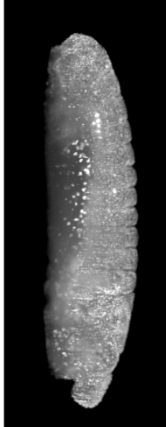
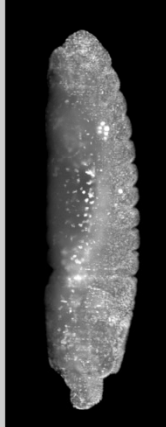
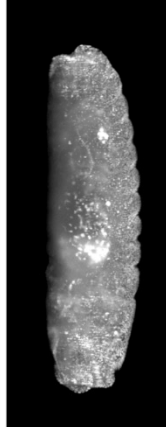
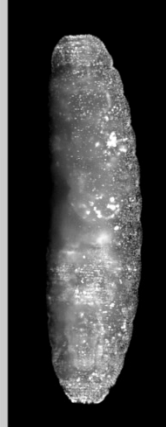
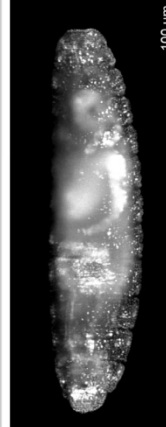
stage	90° (dorsolateral – ZA)	timing	description
III–11 Germband Elongation		start 22:00 h } 02:30 h end 24:30 h } start 35.2% } 4.0% end 39.2% }	<ul style="list-style-type: none"> the posterior tip of the <i>germband</i> completes elongation towards the anterior pole and remains in a quiescent position the <i>amnioserosa</i> folds (<i>extra-embryonic membrane folding</i>) the <i>gnathal protuberances</i> emerge from the <i>gnathocephalon</i> (<i>metamerization</i>)
IV–12 Germband Retraction		start 24:30 h } 07:30 h end 32:00 h } start 39.2% } 12.0% end 51.2% }	<ul style="list-style-type: none"> the <i>clypeolabrum</i> emerges antero-dorsally from the <i>procephalon</i> and becomes thinner and more pronounced the <i>intersegmental grooves</i> arise and separate the <i>thorax</i> into three and the <i>abdomen</i> into nine segments (<i>metamerization</i>)
V–13 Dorsal Closure		start 32:00 h } 02:30 h end 34:30 h } start 51.2% } 4.0% end 55.2% }	<ul style="list-style-type: none"> the posterior tip of the <i>germband</i> completes retracting the <i>ventral epidermal primordium</i> and <i>lateral epidermal primordia</i> of the <i>thorax</i> begin migration towards the anterior pole (<i>head involution</i>) the <i>dorsal epidermal primordia</i> begin migration dorsolaterally over the <i>amnioserosa</i> (<i>dorsal zipping</i>) the <i>dorsal fold</i> emerges from the <i>gnathocephalon</i> (<i>head involution</i>)
V–14 Dorsal Closure		start 34:30 h } 03:30 h end 38:00 h } start 55.2% } 5.6% end 60.8% }	<ul style="list-style-type: none"> the <i>clypeolabrum</i> turns from an antero-dorsal to an antero-ventral orientation (<i>head involution</i>) the <i>dorsal epidermal primordia</i> begin with fusion (<i>dorsal zipping</i>) the <i>gnathal protuberances</i> differentiate into the <i>mandibular buds</i>, the <i>maxillary buds</i> and the <i>labial buds</i> (<i>head involution</i>)
V–15 Dorsal Closure		start 38:00 h } 07:00 h end 45:00 h } start 60.8% } 11.2% end 72.0% }	<ul style="list-style-type: none"> the <i>abdomen</i> withdrawal at the posterior pole reaches the absolute maximum (<i>repeated withdrawal</i>) the <i>antennomaxillary</i> complexes originate from the fusion of the <i>maxillary buds</i> and the <i>procephalon</i> (<i>head involution</i>) the <i>amnioserosa</i> internalizes (<i>extra-embryonic membrane dynamics</i>)
VI–16 Muscular Movement		start 45:00 h } 09:30 h end 54:30 h } start 72.0% } 15.2% end 87.2% }	<ul style="list-style-type: none"> the <i>dorsal epidermal primordia</i> complete fusion and turn into the <i>dorsal epidermis</i> (<i>dorsal zipping</i>) the posterior tip of the <i>ventral cord</i>, which extends to the eighth segment of the <i>abdomen</i>, begins shortening the <i>dorsal fold</i> turns into the <i>dorsal pouch</i> (<i>head involution</i>) the <i>atrium</i> forms anteriorly (<i>digestive system formation</i>)
VI–17 Muscular Movement		start 54:30 h } 08:00 h end 62:30 h } start 87.2% } 12.8% end 100.0% }	<ul style="list-style-type: none"> the posterior tip of the <i>ventral cord</i> shortens to the fifth segment of the <i>abdomen</i> the <i>embryo</i> begins with regular muscular movement, completes embryonic development, hatches and turns into the larva

Figure 2-18 – Chronological staging table of *Ceratitis* embryogenesis for the stages 11 to 17. The first column indicates the stage and the embryogenetic event. The second column shows exemplary Z maximum projections of embryos in the 90° (dorsolateral) orientation. The third column summarizes start, duration and end of the given stage in hours (blue) and in percent of total development (purple). The fourth column outlines up to four developmental processes during the respective stage. ZA, Z maximum projection with intensity adjustment. Figure and/or figure description fully and/or partially reproduced from Strobl *et al.* 2017F, #10 in Publication Table 3, to which also the key terms (in *italics*) in the fourth column refer.

2.2.6. Side-By-Side Comparison of *Drosophila* and *Ceratitis* Embryonic Morphogenesis

In contrast to *Drosophila* and *Tribolium*, which have a quite distant phylogenetic relationship and can thus only be properly compared on the level of embryogenetic events (Subchapter 2.1), *Drosophila* and *Ceratitis* are very closely related and hence show a high degree of similarity throughout their embryonic morphogenesis. However, I was able to identify one temporary deviation of great interest within the emergence of the amnioserosa, the only extra-embryonic membrane (Box 2-9) that differentiates in higher Dipterans.

At the beginning of blastoderm formation, the *Drosophila* and *Ceratitis* embryos appear extremely similar (Figure 2-19, first column). However, during the transition from gastrulation to germband elongation, the primordial amnioserosa cells of the *Drosophila* embryo become compressed between the posterior tip of the germband and the posterior transversal fold and do not obtain their characteristic morphology until the germband has nearly completed the elongation process (Figure 2-19, first row). On the contrary, the amnioserosa differentiates in the *Ceratitis* embryo already during gastrulation as a monolayer of widely spaced cells on the dorsal side between the head and the posterior plate. During germband elongation, the shape of the amnioserosa changes comprehensively – the cells become dorsally compressed and expand over the lateral flanks of the embryo as the germband tip migrates anteriorly (Figure 2-19, second row). The anterior and posterior transverse folds, which emerge as characteristic transient structures for other Diptera [33,91] during gastrulation and early germband elongation, are absent in *Ceratitis*. Surprisingly, after germband elongation is nearly completed, both embryos once again have a strikingly similar appearance (Figure 2-19, ninth column). I assume that such a ‘premature’ differentiation process of the amnioserosa in *Ceratitis*, which begins already during gastrulation, is an apomorphic trait, since other, more basally located Diptera such as *Megaselia* [34,134–136] and *Clogmia* [38] specify, similar to *Drosophila*, their respective extra-embryonic membranes not before germband elongation has begun.

As a final remark, it is an interesting fact that the embryos of both species have transiently a very different appearance, while the initial and final morphology look astoundingly alike, which indicates that there may be more than one phylotypic stage during the embryonic development of insect (Subchapter 4.2.2).

Box 2-9 – Extra-embryonic membranes in insects: amnion, serosa and amnioserosa

The current assumption about the evolutionary history of extra-embryonic membranes in insects is that the last common ancestor has had an amnion and a serosa, since both membranes are found in all recent hemimetabolous as well as nearly all recent holometabolous insect species [137,138]. The only currently known exception are higher Dipterans, which develop only a single extra-embryonic membrane. Since it shows mixed characteristics, it is considered a ‘fusion’ of the amnion and the serosa found in lower Dipterans – thus, this membrane was designated with the portmanteau term ‘amnioserosa’.

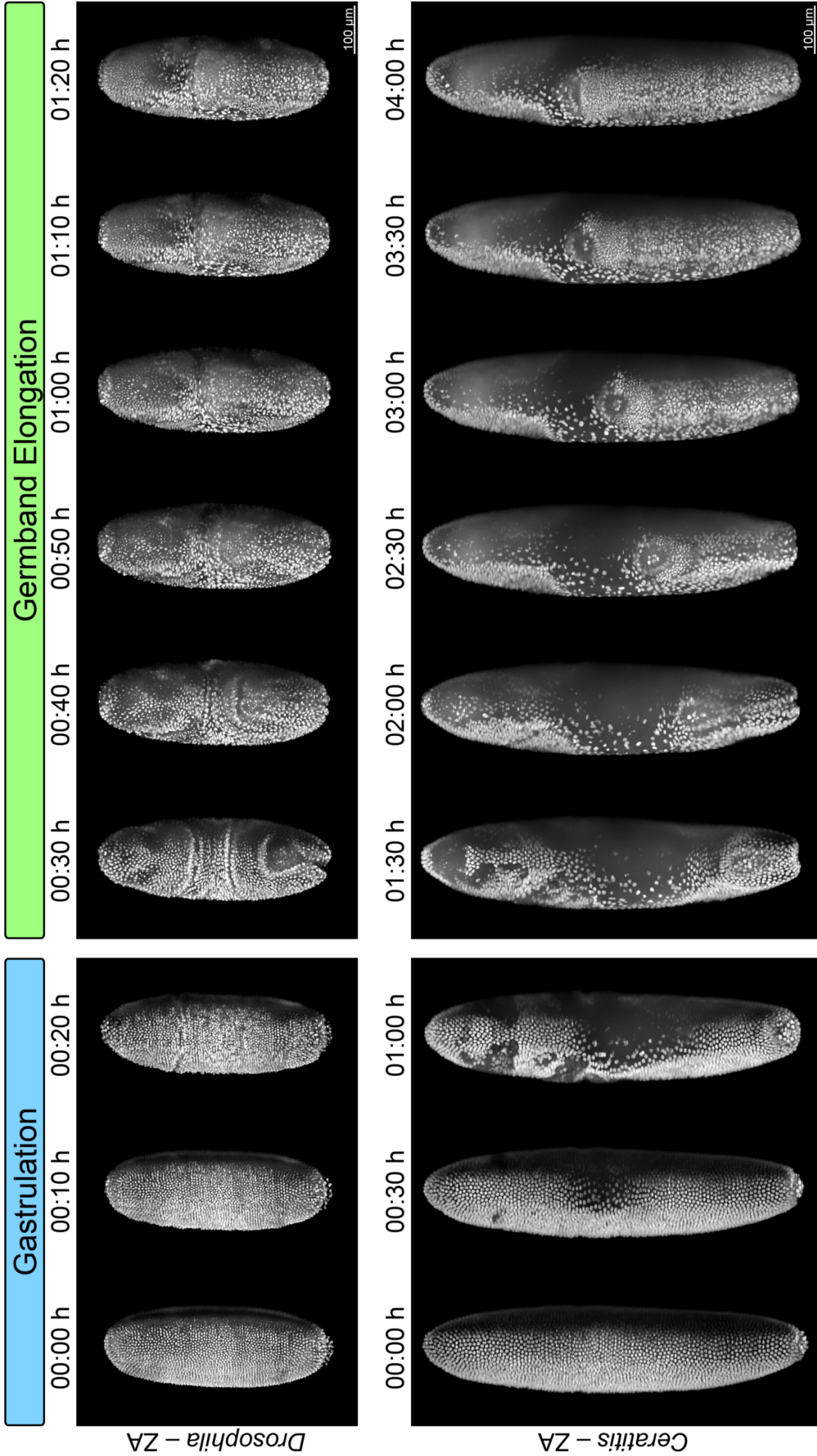


Figure 2-19 – Side-by-side comparison of *Drosophila* and *Ceratitis* embryonic morphogenesis during gastrulation and germband elongation along the 180° (dorsal) direction. For a brief summary of embryogenetic events, see Table 2-1 All data derive from the *Drosophila* P{His2Av-EGFP.C}2 (Table 2-5) and the *Ceratitis* TREhs43-hidA1a5_F1m2 [132] transgenic lines in approximately the same development phase. In *Drosophila*, the amnioserosa becomes apparent during germband elongation, while in *Ceratitis*, the amnioserosa already differentiates as a membrane of widely spaced cells on the dorsal side between the posterior plate and the head. ZA, Z maximum projection with intensity adjustment. Figure and/or figure description fully and/or partially reproduced from Strobl & Stelzer 2016, #4 in Publication Table 2 and Strobl *et al.* 2017E, #9 in Publication Table 3.

2.2.7. AGameOfClones – Systematic Creation of Homozygous Transgenic Lines

Nearly all frequently used model organisms in cell and developmental biology, including *Drosophila*, *Tribolium* and most other insect species, are diploid. This results in a certain experimental complexity when custom-made transgenic lines specifically designed for fluorescence live imaging assays should be created since the genotype has also to be taken into consideration [139]. Transgenic individuals can be either hemizygous, that is either the maternal or the paternal chromosome carry the transgene, or homozygous, that is both parental chromosomes carry the transgene, but only if the transgene is not recessively lethal [140]. In practice, transgenic *Tribolium* lines are usually kept in two culture types:

- Mixed cultures consist of wild-type, hemizygous and homozygous individuals and both, the wild-type allele and the transgenic allele, are present in a certain ratio. This culture type results directly from the transformation assays – after injection, heterozygous founders, which can be typically identified by a dominant transformation marker, are outcrossed against wild-types to create several heterozygous individuals that carry the transgene, and these hemizygous individuals are crossed *inter pares*, which results in 25% wild-type, 50% hemizygous and 25% homozygous progeny. Mixed cultures can be used during the egg collection step in fluorescence live imaging assays, but several disadvantages compared to homozygous cultures are evident (Table 2-7).
- Homozygous cultures can be obtained from mixed cultures, but this procedure is experimentally challenging, since hemizygous and homozygous transgenic individuals cannot be distinguished when dominant transformation markers are used. Either extensive test crossings or genetic assays, e.g. PCR-based genotyping, are necessary to create homozygous cultures, which requires manpower, time and consumables. Homozygous cultures have several crucial advantages over mixed cultures (Table 2-7).

The *Drosophila* community uses balancer chromosomes [141] as a straightforward and elegant strategy to create homozygous transgenic lines specifically designed for fluorescence live imaging (Box 2-10), but this approach is not convenient for *Tribolium* since only a limited choice of balancer chromosomes are available to date [115].

Table 2-7 – Transgenic lines: advantages of homozygous cultures over mixed cultures.

advantage	rationale	comment
no continuous culture curation necessary	Since there is only the transgenic allele present, it cannot get lost throughout continuous reproduction cycles since no competition with the wild-type allele occurs. The wild-type allele usually has a higher fitness value, since the individual does not have to spend energy and resources on the production of proteins that do not have a biological function.	Massively saves manpower during the rearing routine.
no curation after egg collection necessary	When homozygous cultures are used for egg collection, each embryo carries the transgene on both chromosomes and thus express the fluorescent protein. On the contrary, mixed cultures always result in a certain number of wild-type embryos which have to be removed after dechoriation, but before the mounting procedure begins with the aid of the stereo microscope that is equipped with a fluorescence unit.	Ratio of wild-type embryos varies with the degree of culture curation.
higher fluorescent protein expression	Since the transgenic allele in homozygous individuals is present on the maternal and on the paternal allele, the expression level is usually slightly higher in comparison to heterozygous individuals.	I discretely estimate that the expression is increased by a factor of about 1.3 to 1.7.
narrow experimental conditions	Egg collection from mixed cultures results in wild-type, hemizygous and homozygous embryos. While wild-types can be removed during embryo preparation due to the lack of fluorescence signal or the transformation marker, hemizygotes and homozygotes cannot be distinguished from each other. This results in an additional, unnecessary experimental parameter, which can usually not be determined before or during the live imaging assay.	A crucial difference between hemi- and homozygotes must not necessarily occur and is most probably line-specific.
other phenomena	Usage of mixed cultures for egg collection may result in certain phenomena that do not occur when homozygous cultures are used. For example, in <i>Tribolium</i> , expression from the <i>ubiquitin</i> promoter lines results in a different spatiotemporal fluorescence pattern depending on if it was inherited only maternally, only paternally or from both parents.	Hardly predictable.

Box 2-10 – Balancer chromosomes for insect model organisms

Balancer chromosomes are artificially modified wild-type chromosomes that are typically utilized to maintain transgenes or homozygous lethal mutations in insect cultures without the need to constantly screen for carriers [142]. These chromosomes have three crucial properties:

- They suppress homologous recombination during meiosis (via multiple nested inversions)
- They carry a dominant marker for quick phenotypic identification (for example eye pigmentation)
- They are recessively lethal (individuals with two balancer chromosomes are not viable)

Balancer chromosomes can also be used to create homozygous transgenic cultures specifically designed for fluorescence live imaging: Firstly, founder individuals are crossed against an appropriate partner that carries a suitable balancer chromosome. Secondly, the progeny that carries the transgene and the balancer chromosome are crossed *inter pares*. Thirdly, individuals homozygous for the transgene are identified by the omission of the balancer chromosome-specific dominant marker.

To overcome this issue, I invented the AGameOfClones (AGOC) vector concept, which allows the systematic creation of homozygous transgenic lines without the need of test crossing, genetic assays or balancer chromosomes. In this concept, the respective transgene is accompanied by two phenotypically clearly distinguishable dominant transformation markers. Both markers are based on the artificial and eye-specific $3\times P3$ promoter [143], but rely on two different fluorescent proteins, mOrange [144] and mCherry [145] and are thus termed mO and mC, respectively. The signal from both fluorophores can be spectrally separated when appropriate excitation and emission filters are used [146]. Thus, hemizygous individuals that carry such a transgene show the phenotype of both markers.

Both markers are embedded into interweaved LoxP [147] and LoxN [148] site pairs (Figure 2-20A). These lox site pairs are incompatible with each other but stochastically equitable targets for the Cre recombinase [149]. Consequently, recombination leads to the excision of only one of both markers while the other marker remains within the transgene due to the lack of compatible lox sites (Figure 2-20B). This results in post-recombination hemizygotes that carry either only mO or only mC and can thus be phenotypically distinguished from each other as well as the pre-recombination hemizygotes. In the following generation, heterozygous progeny can be identified since they once again carry both markers, and a final cross results in homozygous progeny that can be selected by the omission of one marker.

To verify the functionality of my vector concept, I created a piggyBac-based transformation vector that should work in all insect species for which the piggyBac transformation system (Box 2-11) has been proven functional [101]. The 5,049 bp-long vector, termed pAGOC (Figure 2-21A), contains the minimal inverted terminal repeat sequences that are necessary for transposition [150] as well as mO and mC embedded in interweaved, but incompatible LoxP and LoxN site pairs (Figure 2-21B). I injected this vector together with a piggyBac transposase-expressing helper vector into pre-blastoderm *Tribolium* embryos and obtained several F2 hemizygous founder females that were used to establish six independent sublines, which were termed AGOC #1 to #6. All sublines carry the same transgene, but at a different genomic location.

Box 2-11 – The piggyBac transposon and transformation system

The piggyBac transformation system is based on the piggyBac transposon that was initially discovered in the cabbage looper *Trichoplusia ni* [151]. The transposon consists of two inverted terminal repeats [152] that flank a single functional expression cassette which contains an 1,785 base pair open reading frame encoding the piggyBac transposase [153]. In the transformation system, the expression cassette is replaced by the desired cargo and the transposase is delivered externally, for example by using a helper vector or via mRNA. The piggyBac transposase targets exclusively 5'-TTAA-3' sites that statistically occur every 256 bp within typical eukaryotic genomes. Insertion and excision are performed scarless. A highly efficient piggyBac-based germline transformation protocol for *Tribolium* was published in 2003 [154]. Besides *Tribolium*, a broad variety of insect species have been successfully transformed by using the piggyBac transformation system, for example the yellow fever mosquito *Aedes aegypti* [155] and the silkworm *Bombyx mori* [156].

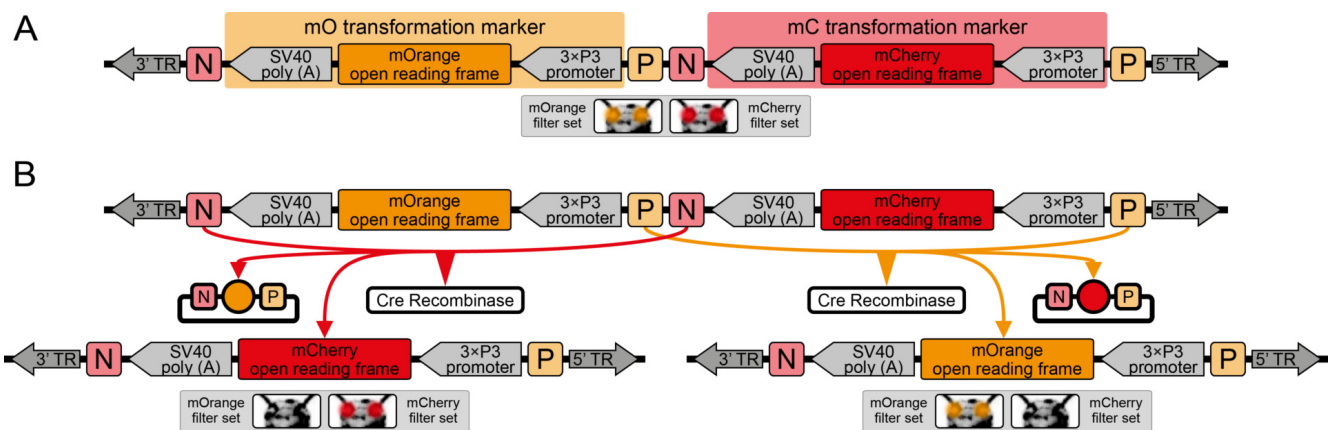


Figure 2-20 – The AGameOfClones vector concept. (A) Two spectrally separable fluorescence-based transformation markers are embedded into a shuttle vector that is characterized by 3' and 5' terminal repeats necessary for integration into the target genome. The transformation markers are based on the artificial eye-specific 3xP3 promoter, the open reading frames for mOrange or mCherry, respectively, and the SV40 poly (A) site. Each marker is flanked upstream by a LoxP and downstream by a LoxN site, which results in interweaved LoxP/LoxN site pairs. Phenotypically, fluorescence can be detected in the eyes by using the appropriate filter sets. (B) Cre-mediated recombination leads to the excision either mO or mC. When one marker is removed, the other marker remains within the genome, since the two remaining lox sites are incompatible. Individuals in which recombination occurred give rise to progeny where only one marker is detectable in the eyes. TR, terminal repeats; P, LoxP site; N, LoxN site; SV40, simian virus 40. Figure and/or figure description fully and/or partially reproduced from Strobl *et al.* 2017D, #8 in Publication Table 3.

The systematic creation of homozygous transgenic lines requires four more generations (Figure 2-22) and was successfully performed with all six AGOC sublines. In brief, F3 mO-mC pre-recombination hemizygous females were crossed against males from the homozygous ICE{HSP68'NLS-Cre} #1 transgenic helper line. This line expresses a nuclear-localized Cre recombinase [157] under control of the endogenous *HSP68* promoter [158] and also carries a mCerulean-based [159] eye-specific transformation marker, termed mCe, which can be spectrally separated from mO and mC [146]. This cross resulted in F4 mCe×mO-mC double hemizygous hybrids, which undergo recombination. To remove the transgene that carries the Cre expression cassette and to separate the markers, the F4 mCe×mO-mC double hemizygous females were outcrossed against wild-type males, resulting in F5 mO- and mC-only post-recombination hemizygotes. Subsequently, a brother-sister cross of individuals with different markers gave rise to F6 mO/mC heterozygotes, and a cross *inter pares* finally resulted in F7 mO- and mC-only homozygotes, which were used to establish the respective homozygous lines. For each of the six AGOC sublines, all expected phenotypes, and thus all expected genotypes, were found in the respective generations. The complete crossing procedure was phenotypically documented for the AGOC #5 and #6 sublines (Figure 2-23).

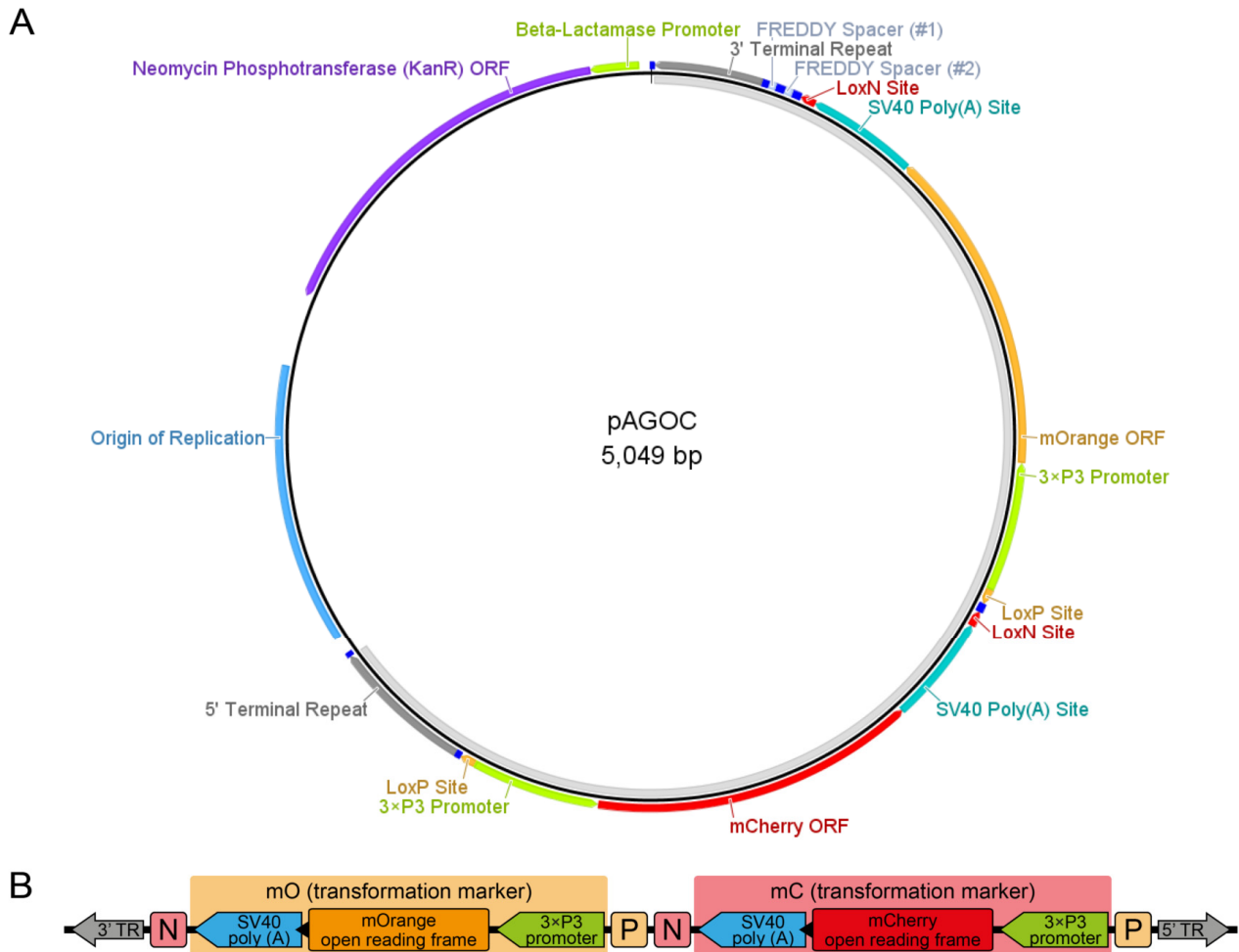


Figure 2-21 – The pAGOC vector. (A) Vector map of pAGOC, the minimal functional configuration. The light gray band on the inside indicates the transgene, which contains mO and mC embedded into interweaved, but incompatible lox site pairs. The non-annotated dark blue boxes represent unique restriction enzyme sites. Additional cargo can be inserted into the #1 and #2 slots, which are per default occupied by FREDDY spacers. (B) Scheme of mO and mC embedded into interweaved but incompatible Lox and LoxP site pairs. Sizes of genetic elements are not to scale. ORF, open reading frame; SV40, simian virus 40; TR, terminal repeat; N, LoxN site; P, LoxP site. Figure and/or figure description fully and/or partially reproduced from Strobl *et al.* 2017D, #8 in Publication Table 3.

After the proof-of-principle experiments with the AGOC #1 to #6 sublines were completed successfully, I established an advanced version of the AGOC vector concept that can be used to create functional homozygous transgenic lines specifically designed for fluorescence live imaging assays. Therefore, I inserted the #P'#O(LA)-mEmerald two-slow cloning site into the #2 slot of pAGOC, which has a slot for a promoter or upstream regulatory sequence (#P) and a slot for an intracellular label (#O) that contains the Lifeact (LA) tag [109] per default. The slot for the intracellular label is directly linked to the open reading frame of mEmerald [146] and followed by an extended simian virus 40 poly (A) site. The resulting 6,852 bp-long vector (Figure 2-24A) was termed pAGOC{#P'#O(LA)-mEmerald} and used as a convenient intermediate vector for further cloning operations (Figure 2-24B).

I used the pAGOC{#P'#O(LA)-mEmerald} vector to create several transformation-ready vectors with various promoters and intracellular labels. In total, I obtained thirteen transgenic lines and sublines from which twelve successfully went through the F3 to F7 crossing procedure outlined above. Throughout the crossing procedure, the experimentally obtained phenotype ratios occasionally deviated from the theoretical Mendelian values, but all expected phenotypes, and thus also all expected genotypes, were found in the F3 to F7 generations, and both, mO- and mC-only homozygotes, could be obtained in the F7, as exemplarily shown for four sublines (Table 2-8).

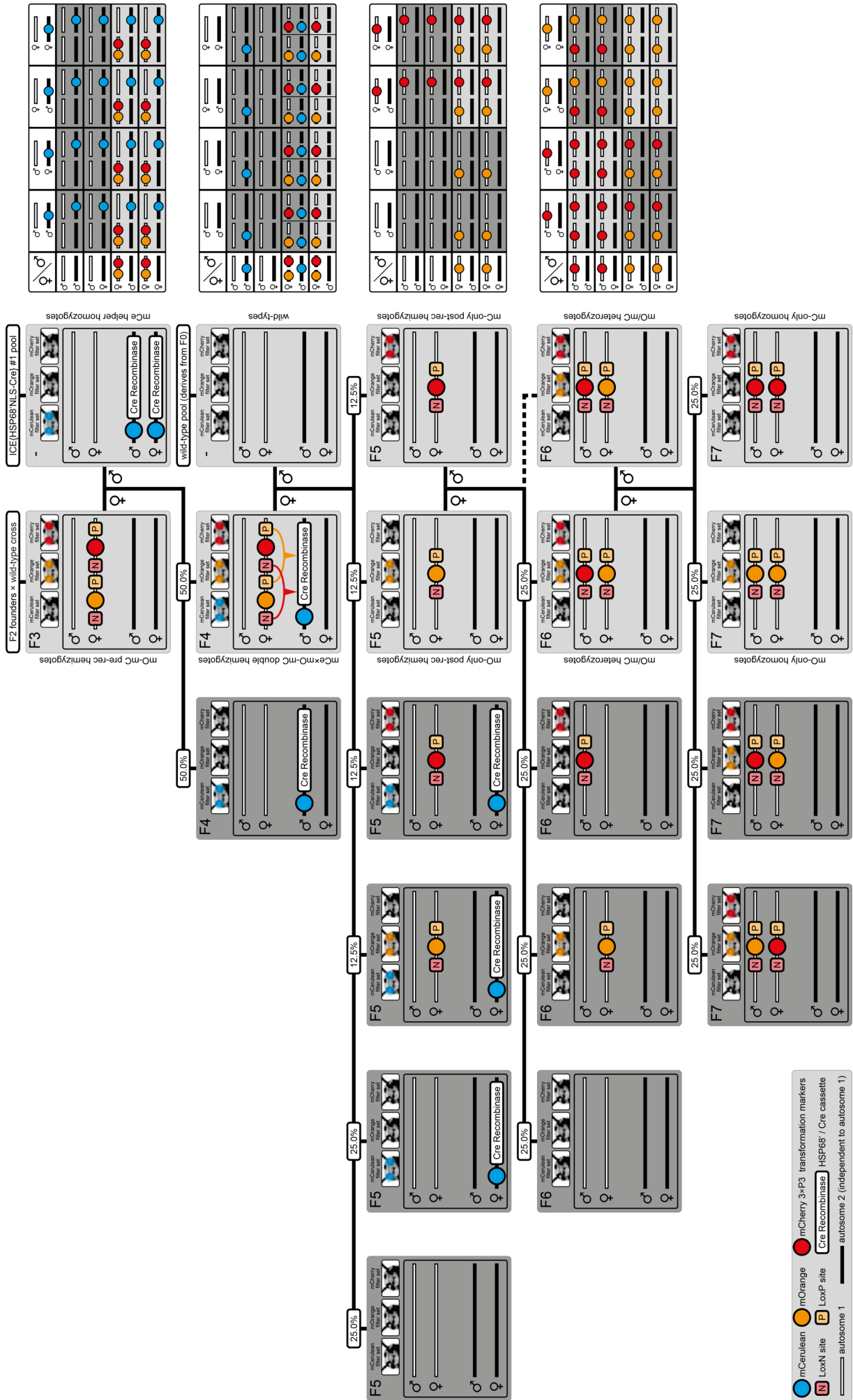


Figure 2-22 – The AGameOfClones F3 to F7 crossing procedure with respective F3 to F6 Punnett squares. The light gray background indicates F3 to F6 outcomes that are either further used within the procedure or the desired F7 mO- and mC- only homozygotes, while the dark gray background indicates progeny that can be disregarded. Figure and/or figure description fully and/or partially reproduced from Strobl *et al.* 2017D, #8 in Publication Table 3.

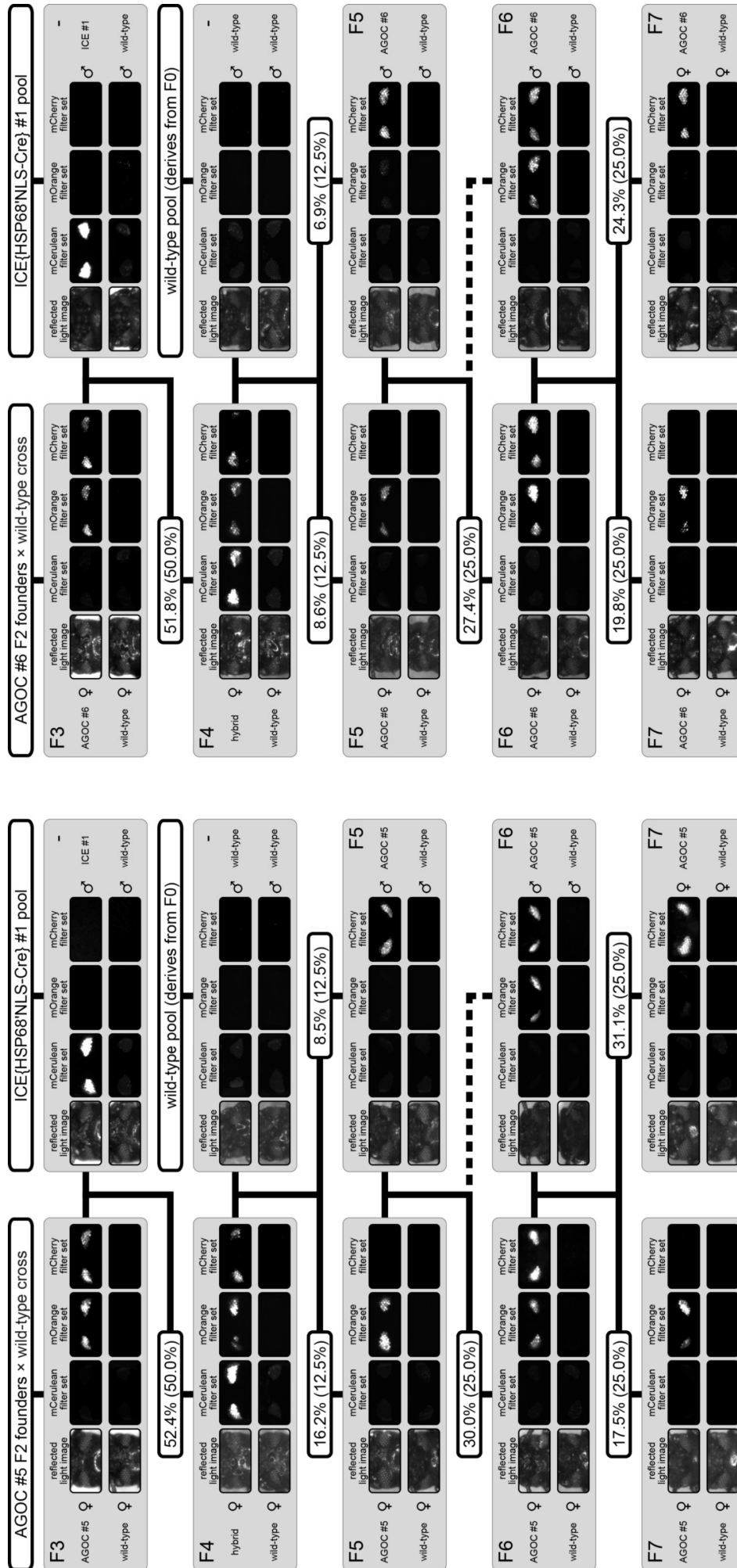








































































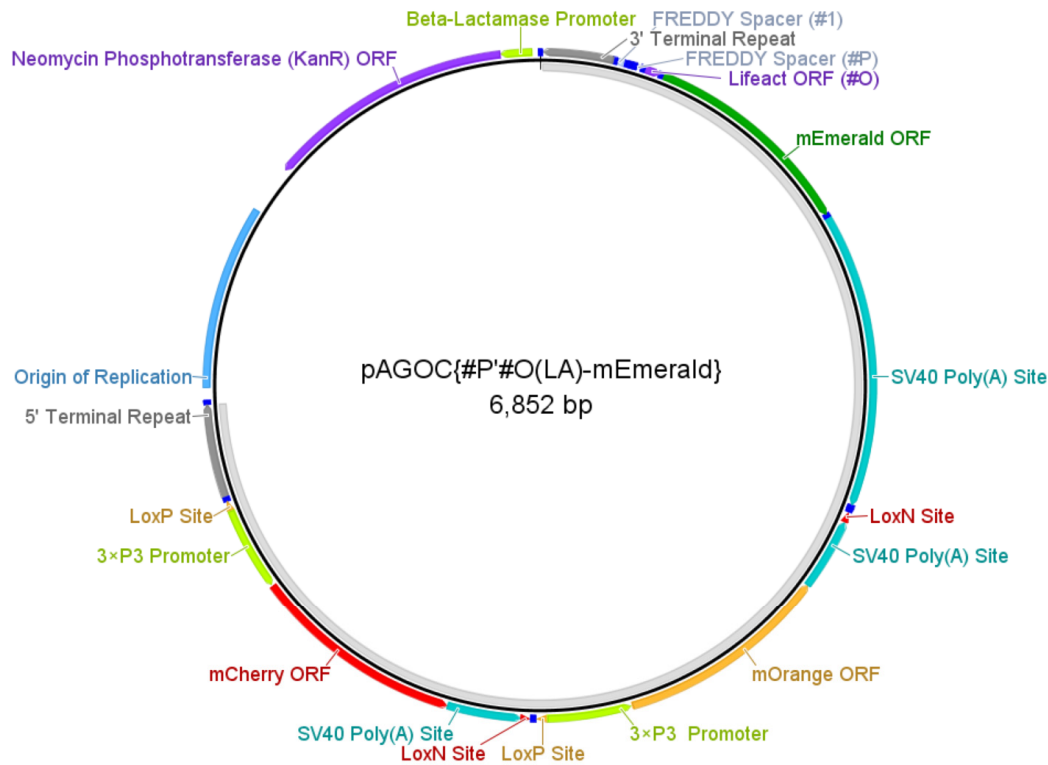


Figure 2-23 – The AGameOfClones F3 to F7 crossing procedure shown for the AGOC #5 and #6 sublines. From the F3 to the F7 generation, the genotype was phenotypically determined by monitoring mCe, mO and mC. For both sublines, F7 mO- and mC-only homozygotes were obtained by following the systematic procedure outlined in Figure 2-22. For each individual, a wild-type control of the same gender is shown. The percentage boxes show the experimental (and theoretical) ratios of the progeny with the respective phenotype. Figure and/or figure description fully and/or partially reproduced from Strobl *et al.* 2017D, #8 in Publication Table 3.

Table 2-8 – Crossing results for functional AGOC lines from the F3 to F7 generation. Bold entries mark progeny that was used in the subsequent cross, the F6-S, F7-O and F7-C entries mark control crosses.

gen	cross	subline	progeny							number
	♀ ♂		●●●	●●●	●●●	●●●	●●●	●●●	●●●	
F3	♂  ♀ 	Theoretical	-	-	-	-	-	-	-	-
	♂  ♀ 	AGOC {ATub#O(LA)-mEmerald} #1	-	-	-	-	-	-	-	-
	♂  ♀ 	AGOC {ARP5#O(LA)-mEmerald} #1	-	-	-	-	-	-	-	-
	♂  ♀ 	AGOC {ATub#H2B-mEmerald} #1	-	-	-	-	-	-	-	-
F4	♂  ♀ 	AGOC {ATub#H2B-mEmerald} #3	-	-	-	-	-	-	-	-
	♂  ♀ 	Theoretical	25.0%	25.0%	12.5%	12.5%	12.5%	12.5%	12.5%	-
	♂  ♀ 	AGOC {ATub#O(LA)-mEmerald} #1	31.6%	29.2%	15.0%	2.5%	20.0%	1.7%	20.0%	110
	♂  ♀ 	AGOC {ARP5#O(LA)-mEmerald} #1	32.4%	27.8%	6.5%	14.8%	7.4%	11.1%	7.4%	108
F5	♂  ♀ 	AGOC {ATub#H2B-mEmerald} #1	29.4%	23.9%	11.9%	16.5%	5.5%	12.8%	5.5%	109
	♂  ♀ 	AGOC {ATub#H2B-mEmerald} #3	35.8%	25.3%	10.5%	8.4%	14.7%	5.3%	14.7%	95
	♂  ♀ 	Theoretical	25.0%	-	25.0%	25.0%	-	-	-	25.0%
	♂  ♀ 	AGOC {ATub#O(LA)-mEmerald} #1	27.2%	-	24.6%	26.3%	-	-	-	21.9%
F6-S	♂  ♀ 	AGOC {ARP5#O(LA)-mEmerald} #1	26.6%	-	16.8%	33.5%	-	-	-	23.1%
	♂  ♀ 	AGOC {ATub#H2B-mEmerald} #1	29.2%	-	28.3%	23.9%	-	-	-	18.6%
	♂  ♀ 	AGOC {ATub#H2B-mEmerald} #3	22.6%	-	25.8%	20.4%	-	-	-	31.2%
	♂  ♀ 	Theoretical	-	-	50.0%	50.0%	-	-	-	-
F6	♂  ♀ 	AGOC {ATub#O(LA)-mEmerald} #1	-	-	44.4%	55.6%	-	-	-	81
	♂  ♀ 	AGOC {ARP5#O(LA)-mEmerald} #1	-	-	43.9%	56.1%	-	-	-	66
	♂  ♀ 	AGOC {ATub#H2B-mEmerald} #1	-	-	40.6%	59.4%	-	-	-	69
	♂  ♀ 	AGOC {ATub#H2B-mEmerald} #3	-	-	50.9%	49.1%	-	-	-	108
F7-Ce	♂  ♀ 	Theoretical	-	-	25.0%	25.0%	-	-	-	50.0%
	♂  ♀ 	AGOC {ATub#O(LA)-mEmerald} #1	-	-	27.6%	25.5%	-	-	-	46.9%
	♂  ♀ 	AGOC {ARP5#O(LA)-mEmerald} #1	-	-	25.7%	18.1%	-	-	-	56.2%
	♂  ♀ 	AGOC {ATub#H2B-mEmerald} #1	-	-	41.1%	12.5%	-	-	-	46.4%
F7-Ve	♂  ♀ 	AGOC {ATub#H2B-mEmerald} #3	-	-	28.3%	27.5%	-	-	-	44.2%
	♂  ♀ 	Theoretical	-	-	100%	-	-	-	-	-
	♂  ♀ 	AGOC {ATub#O(LA)-mEmerald} #1	-	-	100%	-	-	-	-	99
	♂  ♀ 	AGOC {ARP5#O(LA)-mEmerald} #1	-	-	100%	-	-	-	-	98
F7-Ve	♂  ♀ 	AGOC {ATub#H2B-mEmerald} #1	-	-	100%	-	-	-	-	103
	♂  ♀ 	AGOC {ATub#H2B-mEmerald} #3	-	-	100%	-	-	-	-	103
	♂  ♀ 	Theoretical	-	-	100%	-	-	-	-	-
	♂  ♀ 	AGOC {ATub#O(LA)-mEmerald} #1	-	-	100%	-	-	-	-	64
F7-Ve	♂  ♀ 	AGOC {ARP5#O(LA)-mEmerald} #1	-	-	100%	-	-	-	-	101
	♂  ♀ 	AGOC {ATub#H2B-mEmerald} #1	-	-	100%	-	-	-	-	134
	♂  ♀ 	AGOC {ATub#H2B-mEmerald} #3	-	-	100%	-	-	-	-	71
	♂  ♀ 	Theoretical	-	-	100%	-	-	-	-	-

A



B

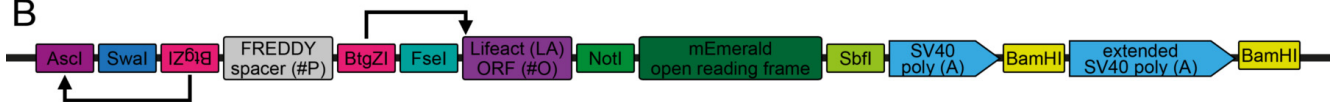


Figure 2-24 – The pAGOC{#P'#O(LA)-mEmerald} vector. (A) Vector map of pAGOC{#P'#O(LA)-mEmerald}, which is based on the pAGOC vector shown in Figure 2-21. The light gray band on the inside indicates the transgene, which contains the modular #P'#O(LA)-mEmerald two-slot cloning site as well as mO and mC embedded into interweaved, but incompatible lox site pairs. The non-annotated dark blue boxes represent unique restriction enzyme sites. Additional cargo can be placed into the #1 slot, which is per default occupied by a FREDDY spacer. (B) Scheme of the #P'#O(LA)-mEmerald two-slot cloning site. To insert a promoter, the #P slot can be accessed by the AsclI/FseI restriction enzyme site pair, but alternatively also by the double BtgZI restriction enzyme site pair, which flanks a FREDDY spacer. BtgZI is a type I restriction enzyme with a non-palindromic recognition sequence. It cuts the sequence several bp (10/14) downstream, resulting in a 4 bp sticky end. In this vector, the upstream BtgZI restriction enzyme site (in reverse orientation) allows opening of the AsclI restriction enzyme site, while the downstream BtgZI restriction enzyme site (in forward orientation) allows opening of the Lifeact (LA) open reading frame start codon and the first bp of the subsequent codon, which allows scarless insertion of respectively digested promoter sequences (indicated by arrows). The Lifeact open reading frame, which is in the #O slot per default, can be substituted with another open reading frame to change the intracellular localization by the FseI/NotI restriction enzyme site pair, while the mEmerald open reading frame can be substituted with another fluorescence protein open reading frame by the NotI/SbfI restriction enzyme site pair. ORF, open reading frame; SV40, simian virus 40. Figure and/or figure description fully and/or partially reproduced from Strobl *et al.* 2017D, #8 in Publication Table 3.

Three of these functional mC-only homozygous sublines were used in fluorescence live imaging assays as described above (Subchapter 2.2.2). The AGOC{Zen1'#O(LA)-mEmerald} #2 subline can be used to observe and describe actin dynamics within the amnion and serosa during gastrulation and early germband elongation (Figure 2-25). The AGOC{ARP5'#O(LA)-mEmerald} #1 subline surprisingly shows a strong signal within neuronal cells but only moderate signal throughout the non-neurogenic tissue (Figure 2-26A), which stands in strong contrast to the AGOC{ARP5'#O(LA)-mEmerald} #2 subline, in which the neuronal cells so not shown a particularly strong signal (Figure 2-26B).

The AGOC vector concept has the unique feature that all genotypes can be immediately and accurately identified by purposely produced distinct phenotypes. This allows not only to systematically create homozygous transgenic lines but also individuals with any relevant genotype. In consequence, my approach has multiple advantages that apply to *Tribolium* as well as other model organisms, for which the AGOC vector concept can be adapted (Subchapter 4.1.5), alike:

- My approach strongly reduces the manpower necessary for genotyping and is less error-prone. More than two hundred individuals can be reliably genotyped in about one hour.
- In contrast to genetic assays, my vector concept does not require any further consumables. A stereo microscope with the respective filter sets, which is a one-time investment, suffices.
- The AGameOfClones vector concept supports desynchronized genotyping, which is an arduous task when the genotype should be determined via genetic assays. It also fosters automatization approaches.
- Handling of transgenic lines is simplified, since the respective individuals can be directly quantified, selected, crossed and/or grouped according to their genotype during nearly all life stages.
- The approach is non-invasive and thus a convenient choice when invasive procedures would influence the experimental workflow.
- The vector concept also works when the insertion location of the transgene is unknown, which would strongly support assays with extended scopes, *e.g.* large-scale insertional mutagenesis screens [160].
- Broad adaption of the vector concept to established and emerging vertebrate model organisms, *e.g.* zebrafish and mouse, will contribute significantly to the ethically motivated endeavor to minimize the number of wasted animals, since efforts can be narrowed down to the relevant samples and controls.

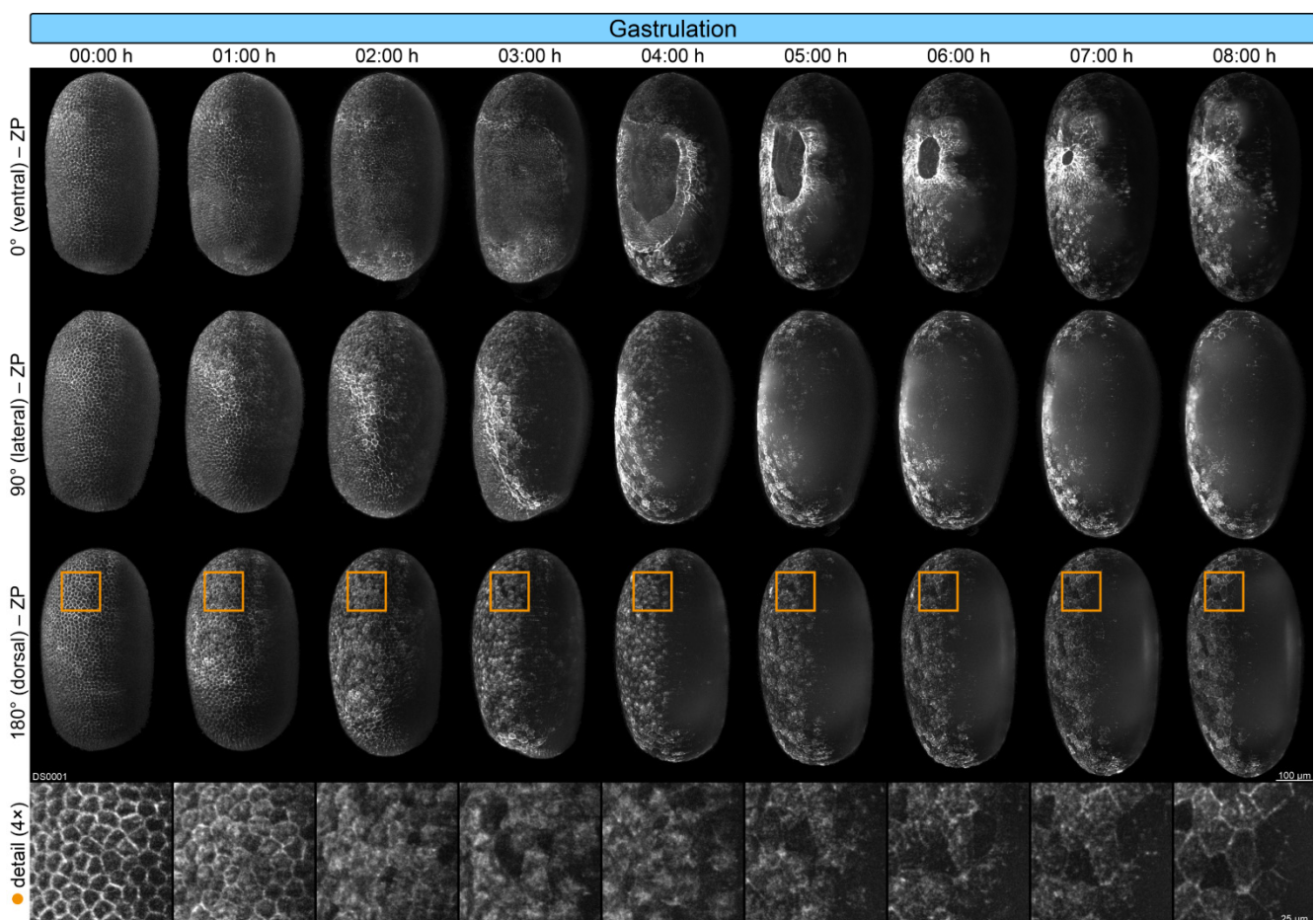


Figure 2-25 – Long-term live imaging of an AGOC{Zen1[#]O(LA)-mEmerald} #2 mC-only homozygous *Tribolium* embryo by using light sheet-based fluorescence microscopy during gastrulation along three directions. The embryo expresses mEmerald-labeled Lifeact under control of the *zerknullt 1* promoter, which is primarily active within the emerging extra-embryonic membranes, *i.e.* the amnion and the serosa, during gastrulation and early germband elongation. ZP, Z maximum projection with image processing. Figure and/or figure description fully and/or partially reproduced from Strobl *et al.* 2017D, #8 in Publication Table 3.

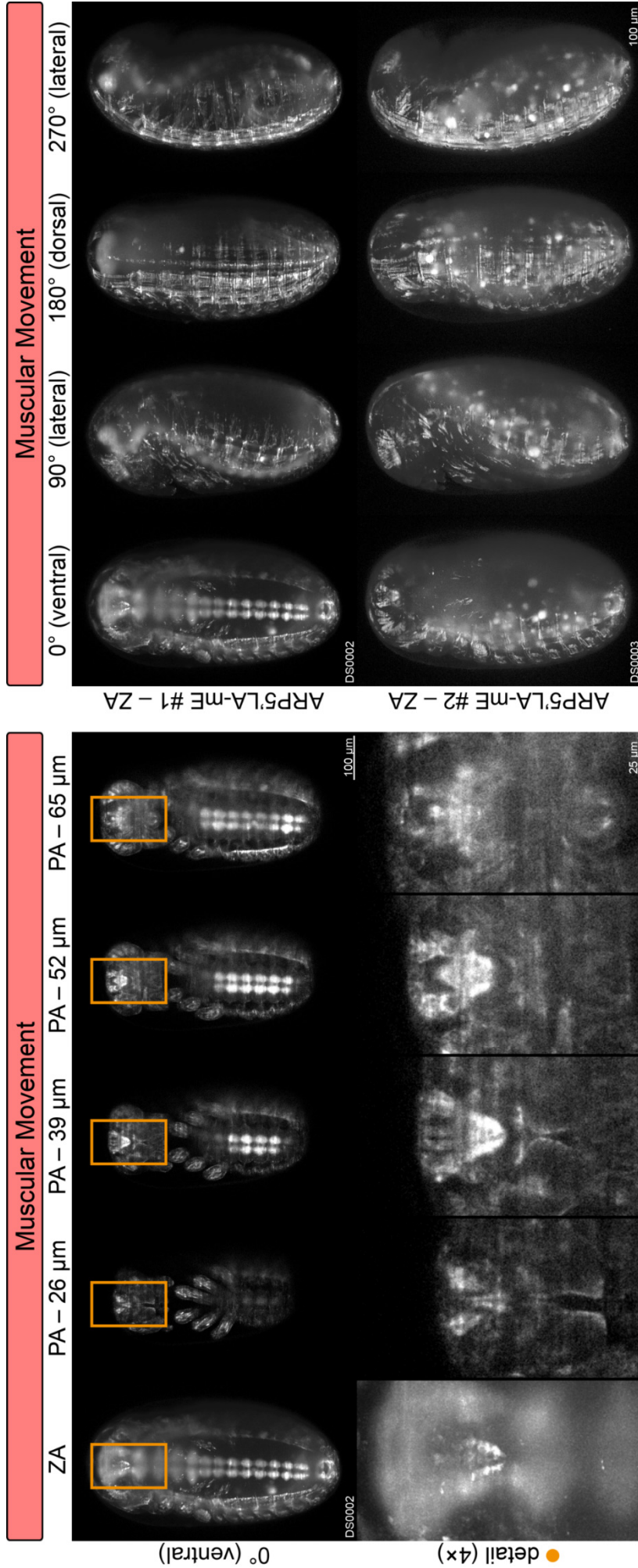
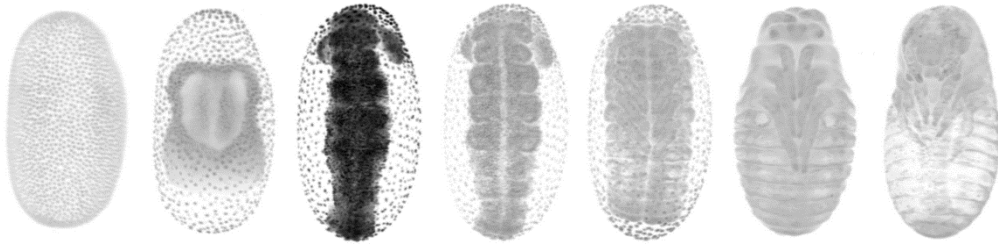
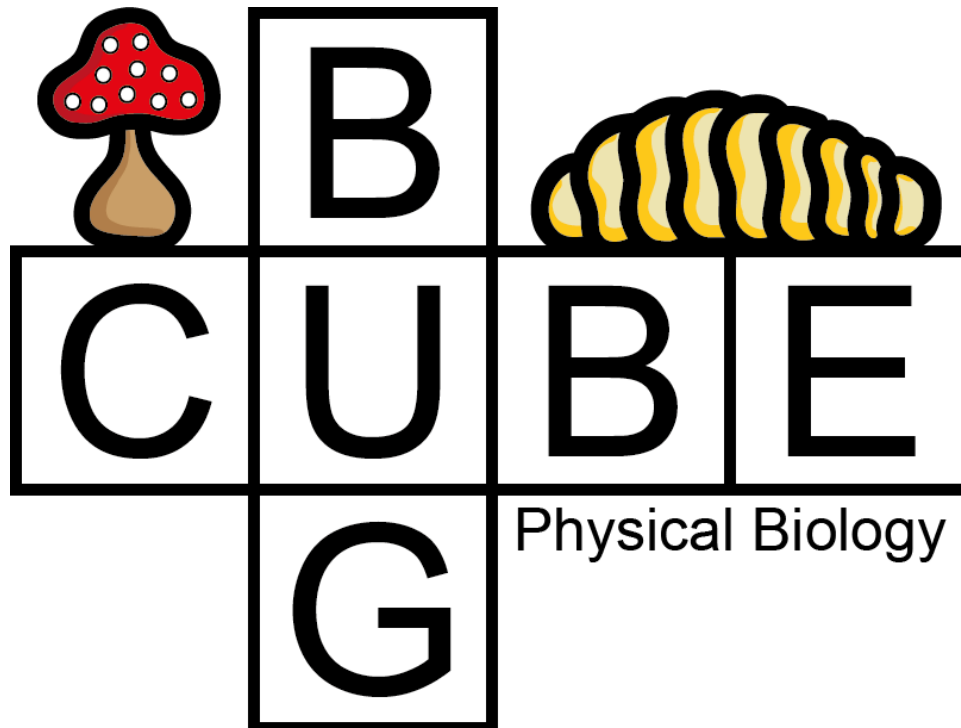


Figure 2-26 – Optical sectioning of a AGOC{ARP5{#O(LA)-mEmerald} #1 mC-only homozygous *Tribolium* embryo and comparison of the expression pattern between the #1 (ARP5{LA-mE #1) and #2 (ARP5{LA-mE #2) sublines during muscular movement. Both sublines carry the same transgenic construct, but at a different genomic location. The embryos express mEmerald-labeled Lifeact under control of the *actin related protein 5* promoter. In contrast to the expression level in the #1 subline, the Lifeact-mEmerald expression level of the AGOC{ARP5{#O(LA)-mEmerald} #2 subline in the nervous system is very low. ZA, Z maximum projection with intensity adjustment; PA, single plane with intensity adjustment. Figure and/or figure description fully and/or partially reproduced from Strobl *et al.* 2017D, #8 in Publication Table 3.

3. Unpublished Results



Within this chapter, I present an extremely brief summary of my yet unpublished results that are strongly associated with the achievements presented within Subchapter 2.2. In addition to the projects shown here, I am also involved in several still ongoing cooperations with other Tribolium-associated laboratories, which are not listed here due to space restrictions.



The BugCube logo. The BugCube is a web-based computer program that can be used to share multidimensional microscopy image data in a comfortable way. The program was coded together with Alexander Schmitz and is described in detail within Subchapter 3.3. Even in the life sciences, the usage of logos is well spread, as they are used by institutes, groups or large-scale projects. The advantage of logos are their recognition value, especially during conferences. The BugCube logo features an unfolded cube, in which the word Bug and Cube share the U letter. In the top right corner, a stylistic insect larva is shown, while the name of our group, Physical Biology, is placed in the bottom right corner. The mushroom was just added randomly.

3.1. Non-Invasive Long-Term Live Imaging of *Gryllus bimaculatus* Embryos

3.1.1. Imaging Large Specimens with Light Sheet-Based Fluorescence Microscopy

Within the previous chapter, I have presented my live imaging results for three holometabolous insect model organisms, *Drosophila*, *Tribolium* and *Ceratitis*. All of these species have in common that their embryos are relatively small and can be imaged within one volume of view when low magnification objectives are used. Furthermore, I was also interested in looking at the embryonic development of hemimetabolous insects. One of the most commonly used emerging model organisms to investigate the embryonic development of hemimetabolous insects is the two-spotted cricket *Gryllus bimaculatus* [161].

Fortunately, a transgenic *Gryllus* line that expresses EGFP-labeled histone 2B subunits under control of the *actin 5c* promoter was available [162]. However, due to the large size of the eggs, *i.e.* a lateral width of about 600 μm and anterior-posterior length of about 3 mm, it is not possible to perform *in toto* fluorescence live imaging within one volume of view even when low magnification objectives and cameras with very large detector chips are used. Thus, Alexander Ross, a Master student of mine, developed an experimental workflow to capture the embryo *in toto* with cellular resolution during his Master project (Subchapter 5.1). In brief, dechorionated embryos were mounted by adapting the cobweb holder method (Subchapter 2.2.3 and Figure 3-1) for usage within the Lightsheet Z.1 from Carl Zeiss, a commercial light sheet-based fluorescence microscope with double-sided illumination [163]. Then, four ‘tiles’, *i.e.* four Z stacks with a partial overlap along the Y axis, were acquired and the Z maximum projections were calculated. Subsequently, the Z stacks and Z maximum projections were stitched in three and two dimensions (Figure 3-2), respectively, by using the previously published phase correlation-based alignment algorithm [164], which is available as a Fiji plugin (imagej.net/Image_Stitching).

In cooperation with Alexander, I advanced this workflow for non-invasive long-term live imaging along multiple directions. Briefly, four partially overlapping Z stacks along four directions, *i.e.* a total of sixteen Z stacks, were recorded for each time point and processed with a custom Fiji plugin that automatically performed the above outlined steps.

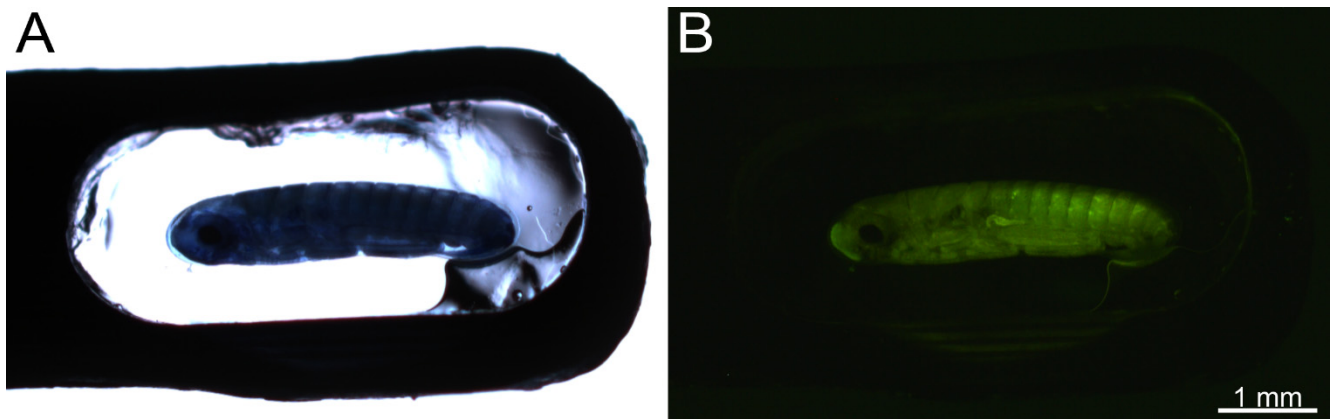


Figure 3-1 – Mounting of a transgenic *Gryllus* embryo for *in toto* fluorescence live imaging by adapting the cobweb holder method. (A) Transmission light image of a *Gryllus* embryo during dorsal closure within the slotted hole of the Lightsheet Z.1 adaption of the cobweb holder. **(B)** Same embryo recorded with widefield fluorescence microscopy. The embryo expresses EGFP-labeled histone 2B subunits under control of the ubiquitous *actin 5c* promoter [162].

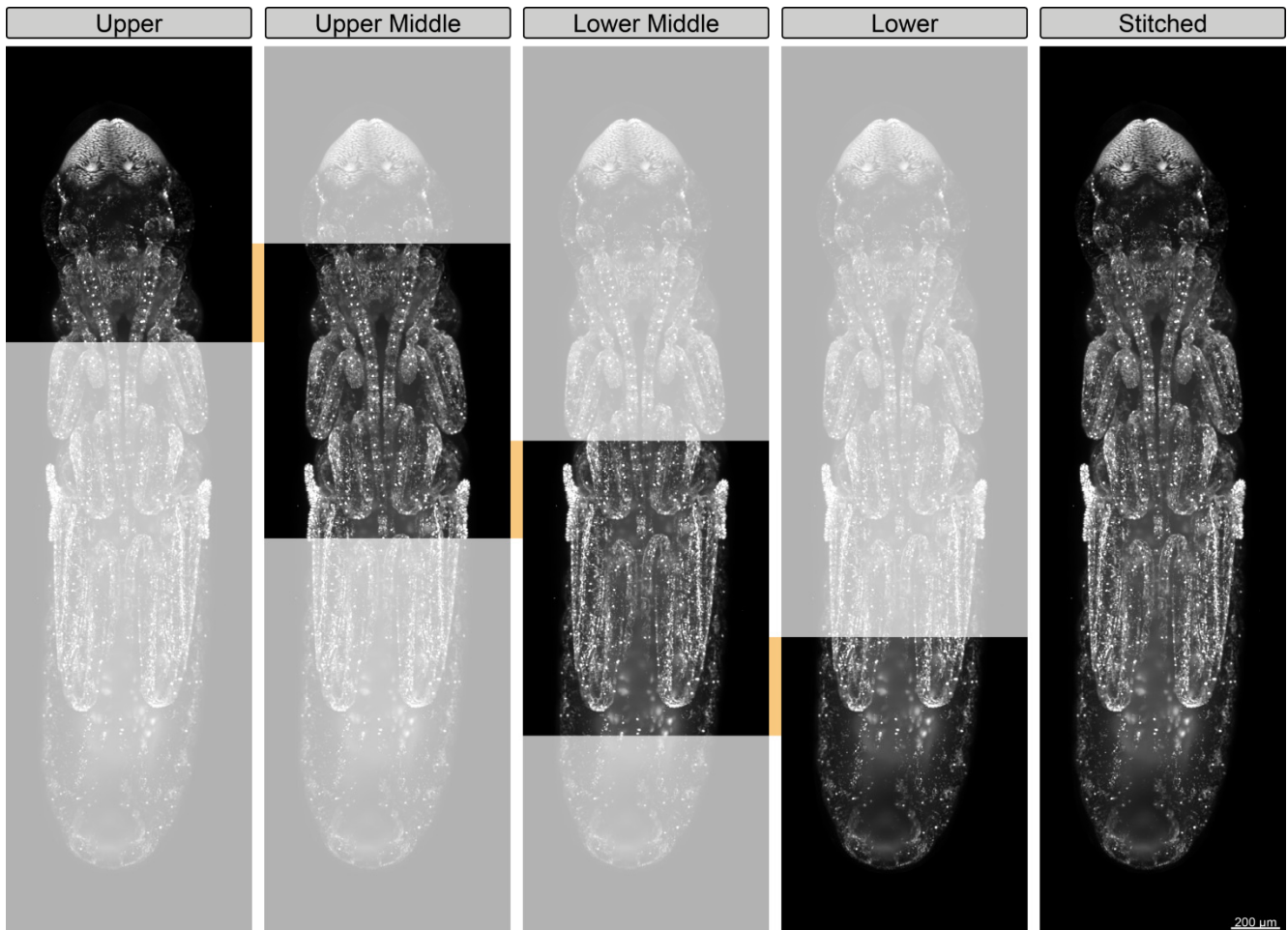


Figure 3-2 – Z maximum projections of four Z stacks and the stitched Z maximum projection of a *Gryllus* embryo during muscular movement. The Z stacks have an approximately 33% overlap, indicated by the orange bars, along the anterior-posterior axis of the embryo, which is aligned with the Y axis, *i.e.* the rotation axis, of the microscope. The embryo expresses EGFP-labeled histone 2B subunits under control of the ubiquitous *actin 5c* promoter [162].

3.1.2. The Morphogenetic Dynamics of Katatrepsis and Dorsal Closure in *Gryllus*

With the advanced workflow, we were able to record *Gryllus* embryos for more than four days. The stitching algorithm performed with a high precision over the whole recording period and without any ‘tile’ misalignment errors, independently if the Z stacks or Z maximum projections were stitched in three or two dimensions, respectively. This allowed us to capture two important embryogenetic events:

- During katatrepsis, which is an embryogenetic event exclusive to hemimetabolous insects and that happens between germband retraction and dorsal closure, the embryo everts within the egg and subsequently exits the yolk (Box 2-1). At the beginning of katatrepsis, the serosa opens posteriorly and the embryo curls – backwards and head first – around the posterior pole (Figure 3-3). Even though we recorded the embryo *in toto*, single nuclei are still identifiable (Figure 3-3, seventh column).
- In *Gryllus*, katatrepsis is followed immediately by dorsal closure, during which the extra-embryonic membranes are internalized together with the remaining yolk into the digestion tract (Figure 3-4).

This is the first time that katatrepsis and dorsal closure were documented with fluorescence live imaging in a hemimetabolous insect species. Due to space restrictions, it is not possible to perform an in-depth comparison between *Gryllus* and *Drosophila*, *Tribolium* and *Ceratitis* within my PhD thesis.

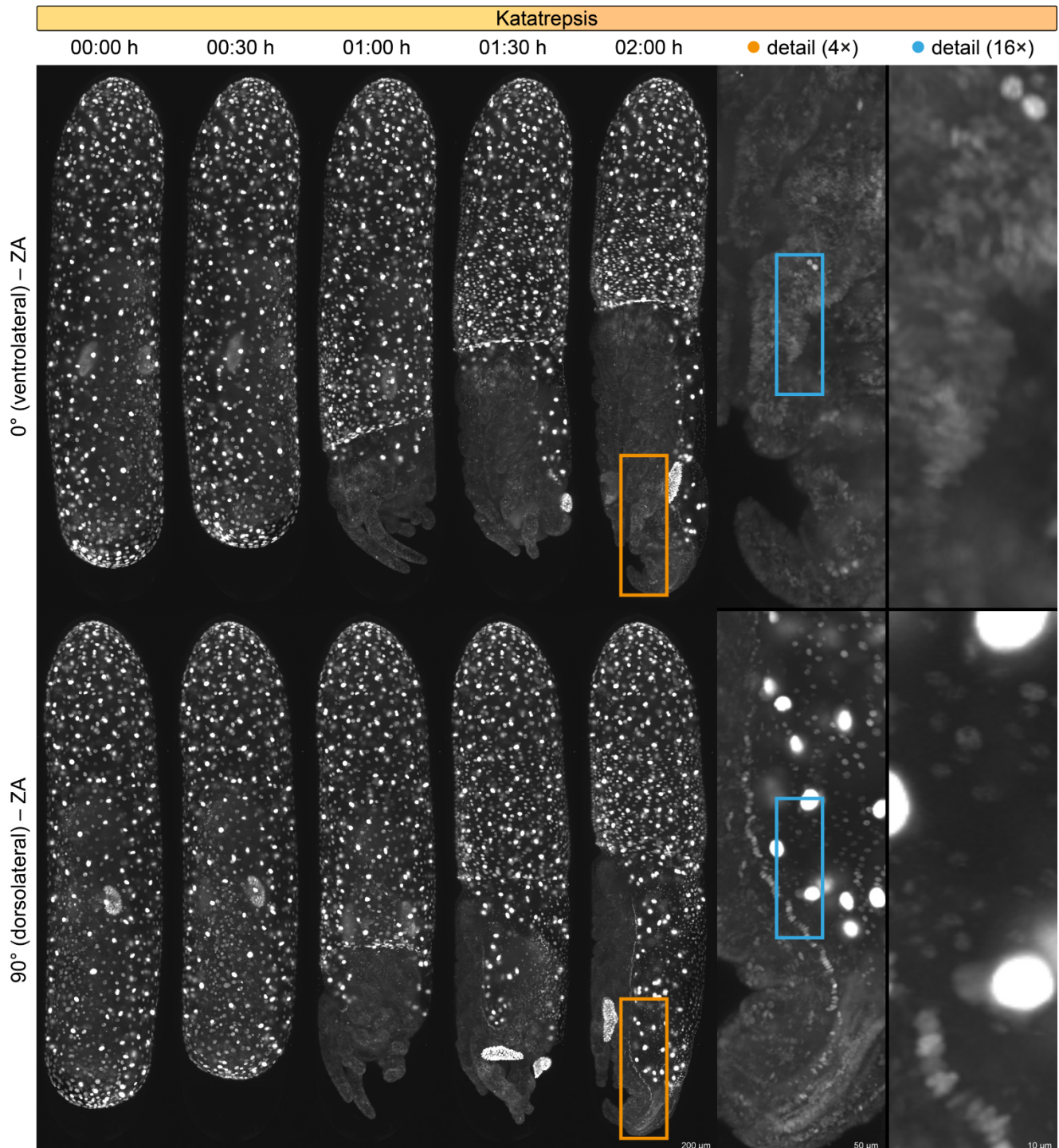
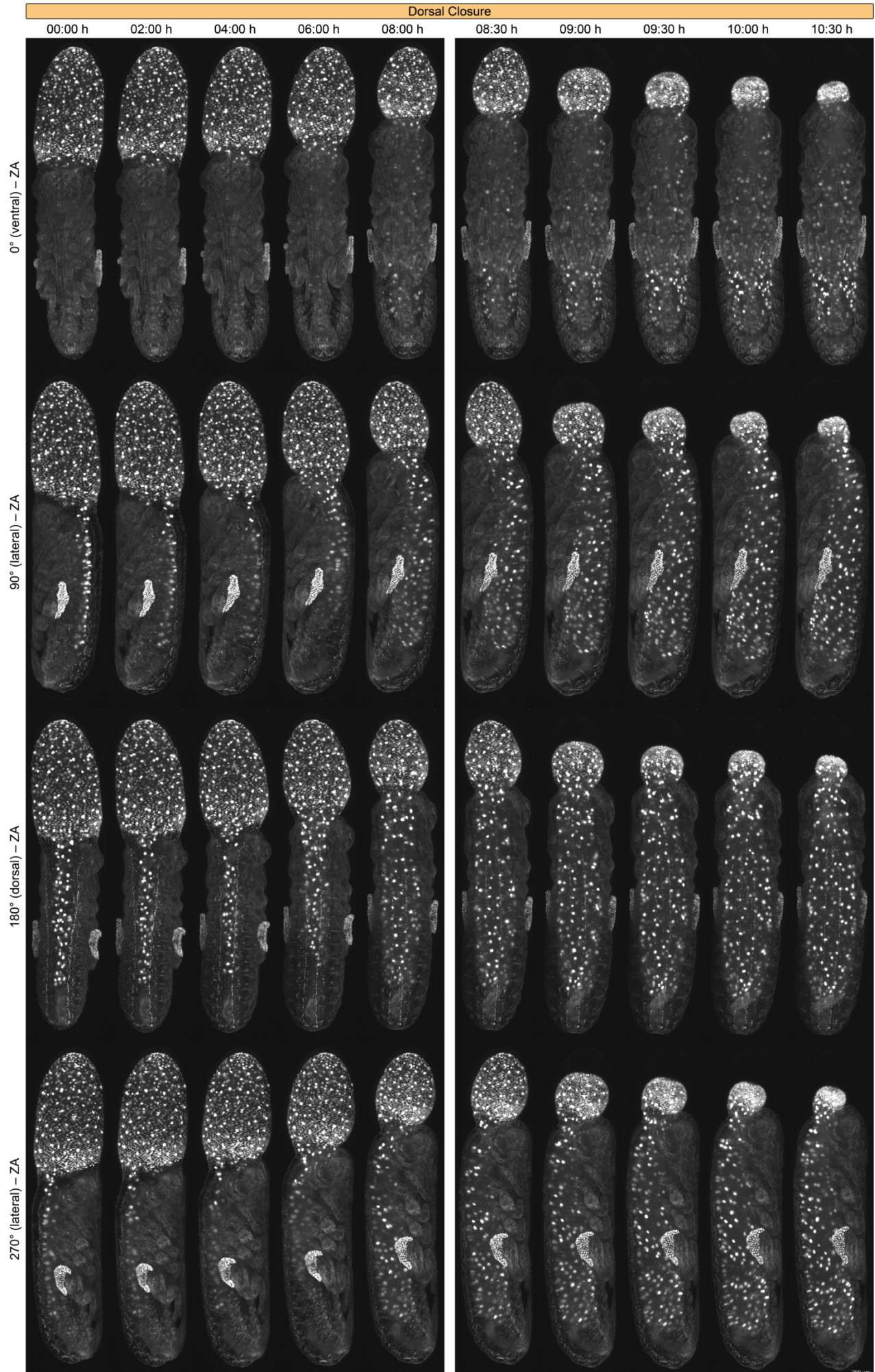


Figure 3-3 – Katatrepsis in *Gryllus* shown along two directions over a period of 02:00 h. Even though the embryo was captured *in toto*, single nuclei are still identifiable within the detail images. ZA, stitched Z maximum projection with image adjustment. The embryo expresses EGFP-labeled histone 2B subunits under control of the ubiquitous *actin 5c* promoter [162].

In conclusion, we showed that by using light sheet-based fluorescence microscopy, even embryos with an anterior-posterior length of several millimeters can be imaged for long time periods – our workflow serves as a guideline whenever very large specimens should be live imaged for several days.

There are several more datasets available from *Gryllus* embryos that were mounted and recorded as described above, but the thin mounting agarose film was enriched with fluorescent beads. Thus, the four stitched Z stacks, which were acquired along multiple directions, could be registered and fused – in cooperation with Alexander Schmitz – to create superior image stacks as described below in detail for *Tribolium* (Subchapter 3.2). Due to space restrictions, the data is not shown here, but can be found in the PhD thesis of Alexander Schmitz.



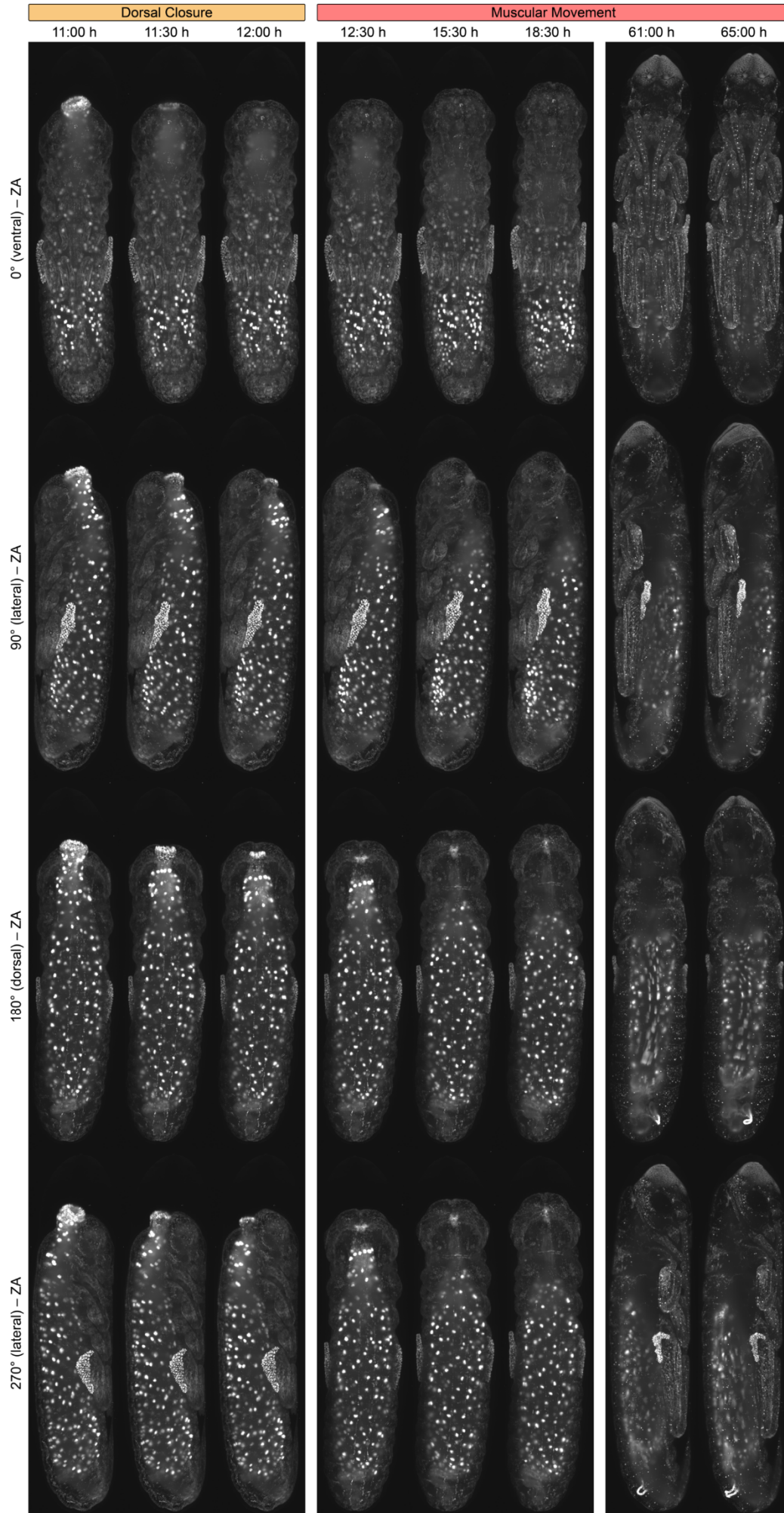


Figure 3-4 – Dorsal closure in *Gryllus* shown along four directions over a period of 65:00 h. During *Gryllus* dorsal closure, the extra-embryonic membranes are internalized with the remaining yolk into the digestion tract. The dorsal epidermal flanks, in *Gryllus* located at the dorsal side of the head fuse to form the dorsal seam before irregular twitching during muscular movement begins. ZA, stitched Z maximum projection with image adjustment. The embryo expresses EGFP-labeled histone 2B subunits under control of the ubiquitous *actin 5c* promoter [162].

3.2. Registration and Fusion of *Tribolium* Long-Term Live Imaging Datasets

3.2.1. Compensating the Shadowing Effect by Reconstructing the Specimen

Three-dimensional live imaging datasets acquired from relatively large and opaque specimen such as insect embryos usually suffer from the so called ‘shadowing effect’, a fundamental problem that occurs independently no matter if confocal or light sheet-based fluorescence microscopes are used. The signal quality declines proportionally to the amount of tissue that has to be passed by the excitation as well as the emission light (Figure 3-5). One of the unique features of basically all light sheet-based fluorescence microscopy setups used in developmental biology is sample rotation, *i.e.* the embryo is revolved around the Y axis, which is perpendicular to the X axis, *i.e.* the illumination axis, as well as the Z axis, *i.e.* the detection axis. Thus, Z stacks can be recorded along multiple directions – consequently, always a different region of the embryo is imaged with high quality. There are two options how to proceed with the data:

- The different Z stacks can be considered as merely independent coverages the same volume of view at nearly identical time points. For further analyses, the most suitable stacks are chosen.
- The Z stacks can be registered and fused to ‘reconstruct’ a single, superior image stack by detecting and combining the regions image high quality from each direction.

However, registration and fusion of the Z stacks is a non-trivial task and multiple complex algorithms have been published that address this issue (Table 3-1). Due to the high accuracy as well as the technical robustness, we decided for the bead-based / landmark-based registration and fusion approach. In brief, the algorithm identifies homogenous landmarks, *e.g.* fluorescent beads with similar sizes and intensities, by their unique constellations of neighbors within all Z stacks recorded along multiple directions. The coordinates of these landmarks are used to calculate affine transformation matrices to align all directions from the second to the last with the first direction by following an iterative optimization procedure.

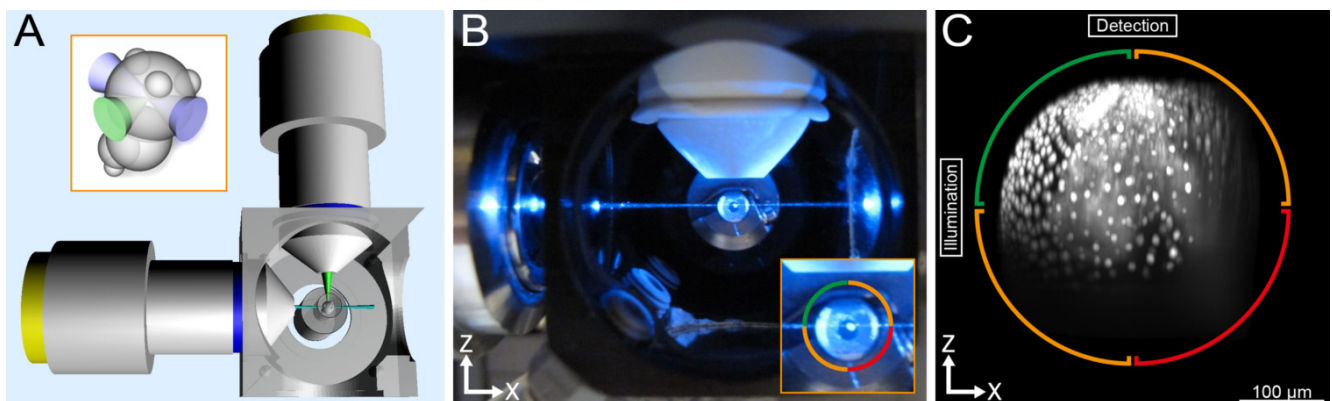


Figure 3-5 – The shadowing effect in light sheet-based fluorescence microscopy. (A) Scheme showing the arrangement of the illumination and detection objectives in light sheet-based fluorescence microscopy. The inset depicts excitation of a single line and detection of fluorescence signal from a single point source within a given specimen. (B) Top view of the objective arrangement in a monolithic digital scanned laser light sheet-based fluorescence microscope. In the inset, image quality indicators are provided as colored arcs. The green arc marks the quarter with an expected high quality, the orange arcs the quarters with an expected moderate quality and the red arc the quarter with an expected low quality. (C) Y maximum projection of a Y stack annotated with the previously introduced image quality indicators. The regions with strong quality reduction caused by the shadowing effect are clearly visible. Figure and/or figure description fully and/or partially reproduced from Strobl *et al.* 2015, #3 in Publication Table 1.

Table 3-1 – Overview of registration and fusion methods for the ‘reconstruction’ of superior image stacks.

registration and fusion method	references	comment
non-blind shift-invariant	[165]	In conjunction with different deconvolution (Subchapter 5.5) methods [166,167].
bead-based / landmark-based	[168]	In conjunction with a Lucy-Richardson deconvolution (Subchapter 5.5) method [169].
content-based	[86,88,170,171]	Algorithm can process the data in real-time when the appropriate hardware is available.

3.2.2. Evaluation of the Bead-Based / Landmark-Based Registration and Fusion Method

At first, I modified the agarose hemisphere mounting method by adding fluorescent beads to the hemisphere layer (Figure 3-6A, first column) and decided to image embryos of the EFA-nGFP [104] transgenic line, which expresses nuclear-localized GFP under control of the ubiquitous *elongation factor 1 alpha 1 subunit* promoter. In contrast to the study that introduced the bead-based / landmark-based registration and fusion method, our adaption has the advantage that the beads do not mask the specimen. Similar to my previous results (Subchapter 2.2.2), the beads-containing hemisphere was stable enough to record the embryo along eight equally spaced directions for more than seven days (Figure 3-6A, second column). In cooperation with Alexander Schmitz, I subsequently processed the eight Z stacks by using the respective algorithm (Figure 3-6B), which is available as a Fiji plugin (imagej.net/Multiview-Reconstruction). The algorithm performed with a high degree of accuracy and without any Z stack misalignment errors over the whole recording period, resulting in superior image stacks in which the shadowing effect was properly compensated (Figure 3-7) and that also performed properly in volume renderings (Box 3-1) by using the commercial Arivis Vision 4D image processing software (Figure 3-8).

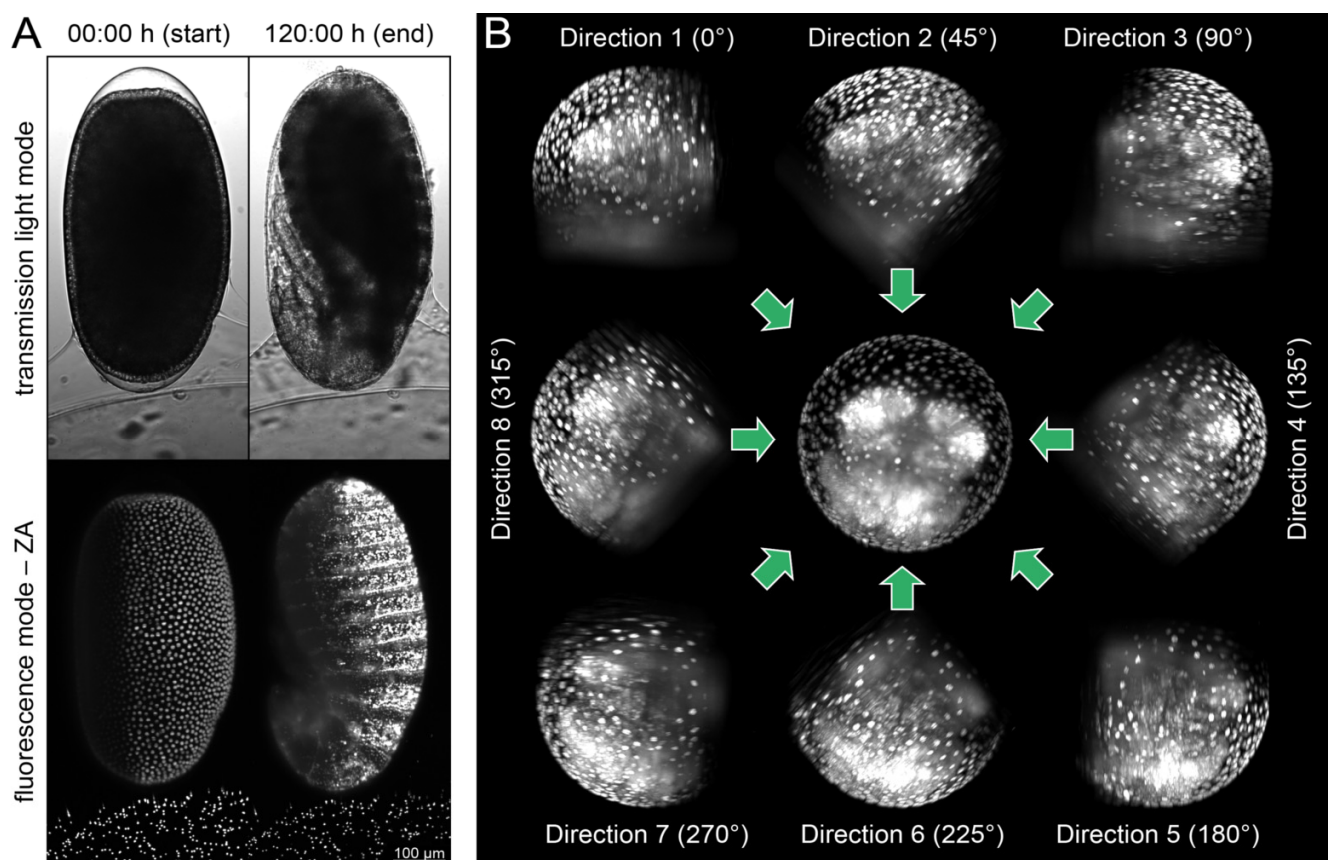


Figure 3-6 – Data acquisition for registration and fusion. (A) Mounting by using the agarose hemisphere method with fluorescent beads added to the hemisphere layer, which can be used to determine the transformation matrices when the embryo is recorded along multiple directions. The major advantage of this approach is that the embryo is not masked by beads. Mounting is stable throughout the whole imaging procedure, the embryo and the beads are still in the same position even after 120:00 h of constant imaging. (B) Y maximum projections of eight Z stacks recorded along eight equally spaced directions (outer images) and the reconstructed superior image stack (center). Registration and fusion results in a strongly reduced shadowing effect since the low quality region of a Z stack acquired along a certain direction is compensated by the high quality regions of another Z stack acquired along another direction.

Our results show that registration and fusion followed by volume rendering is a powerful strategy that strongly aids with visualization of multidimensional image data and facilitates biological interpretation. The additional effort, *i.e.* supplementing the hemisphere with fluorescent beads and running the Fiji plugin, is moderate, but the benefit of reconstructed datasets is convenient:

- The shadowing effect is noticeably compensated and the signal intensity appears homogenous throughout the whole embryo, which will facilitates both, qualitative and quantitative evaluations.
- The axial resolution of a Z stack along a certain direction, which is usually worse by a factor of around four compared to the lateral resolution [70], is replaced by the lateral resolution of a Z stack acquired along the perpendicular orientated direction, leading to isotropic superior image stacks.
- In comparison to a dataset consisting of eight non-fused directions, the volume of a reconstructed dataset is reduced to approximately 25%, thus significantly lowering the need for storage capacity.

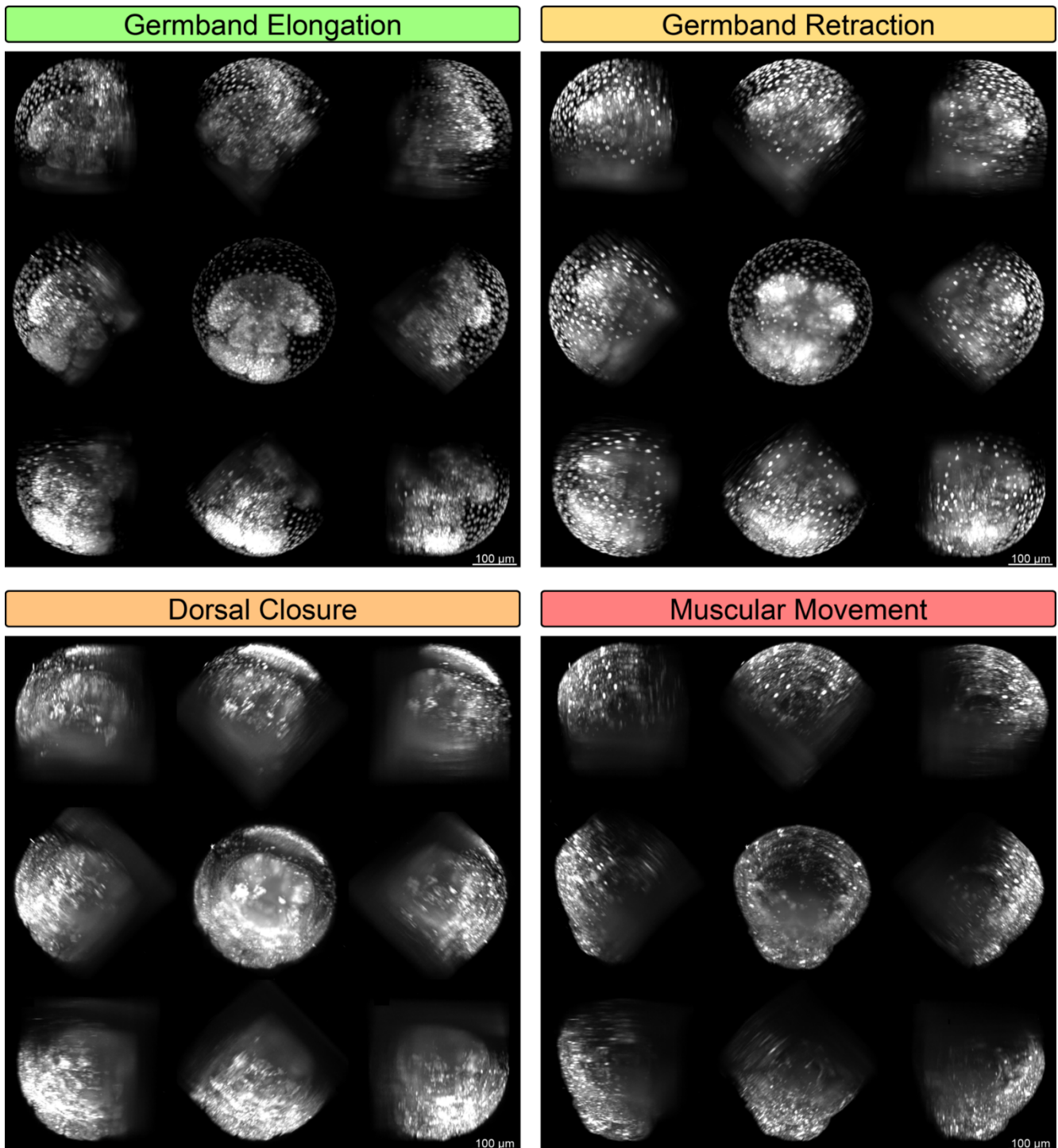


Figure 3-7 – Y maximum projections of eight Z stacks and superior image stacks of a *Tribolium* embryo from the EFA-nGFP transgenic line during four embryogenetic events. The embryo was recorded for more than seven days at room temperature along eight equally spaced directions (outer images) and subsequently reconstructed with the beads-based / landmark-based registration and fusion method (center) without any Z stack misalignment errors.

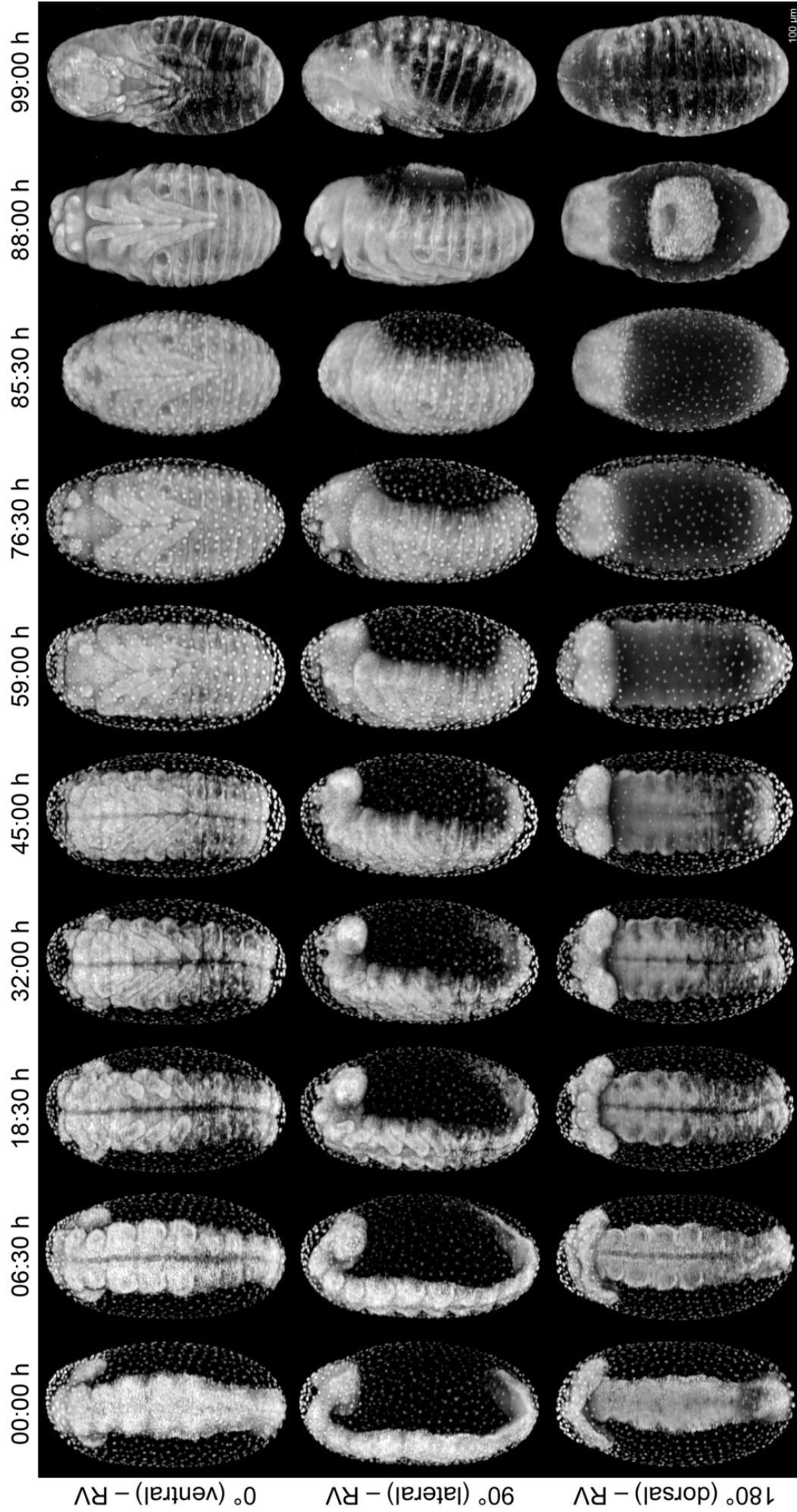


Figure 3-8 – Volume rendering of a registered and fused dataset. The data were acquired by using the EFA-nGFP [104] transgenic line, which expresses nuclear-localized GFP under control of the *elongation_factor 1 alpha 1 subunit* promoter. The embryo is shown along three directions over a course of 99:00 h, covering the embryogenetic events germband elongation (first and second column), germband retraction (third to seventh column), dorsal closure (eighth and ninth column) and muscular movement (tenth column). RV, Aravis-based volume rendering.

Box 3-1 – Rendering of microscopy data with dedicated software

In microscopy, rendering is a post-processing algorithm that adds colors, shades and textures to a three-dimensional image which is usually performed with dedicated commercial software such as Arivis Vision 4D (arivis.com/de/imaging-science/arivis-vision4d), Bitplane Imaris (bitplane.com/imaris/imaris) and FEI Amira (fei.com/software/amira-3d-for-life-sciences). After registration and fusion, Z maximum projections of superior image stacks appear ‘slightly odd’ due to the fact that compensation of the shadowing effect is counterintuitive to the customary visual perception. Rendering adds a certain plasticity and allows an intuitive perception of the respective data [172]. While animated movies and modern video games typically rely on surface renderings, both surface and volume rendering approaches are typically used in microscopy [173].

In conclusion, registration and fusion of *Tribolium* datasets acquired with light sheet-based fluorescence microscopy is a powerful post-processing procedure. I expect that respective datasets perform very well in segmentation and tracking approaches, especially when complex cell movements, *e.g.* from a ventral to a dorsal position, should be followed. The project was continued by Franziska Krämer, a Bachelor student of mine. She tested in how far the deconvolution option of the beads-based / landmark-based registration and fusion method (Table 3-1) further increases the image quality (Subchapter 5.5).

3.3. The BugCube Project – Sharing of Image Data with the Community

3.3.1. Theoretical Background and Current Implementation

Light sheet-based fluorescence microscopy is one of the key elements for the transition from on-demand to systematic data acquisition in fluorescence live imaging (Subchapters 4.2.5 and 6.1.7). Typically, systematically acquired data are provided as a resource to the respective communities and serve as a gateway and inspiration for many futures studies. Consequently, straightforward access to the data is of great importance:

- One of the most crucial considerations is logical and consistent data structuring. This is especially important for data acquired with light sheet-based microscopes, since live imaging datasets explore up to six degrees of freedom (three spatial dimensions, the direction, the fluorescence channel and the time point).
- Data exchange between laboratories is nowadays nearly exclusively done via the internet. For most types of scientific data, the volume is usually in the range of several megabytes to a few gigabytes. Therefore, it takes usually only a few minutes for data transfer and also storage is also not an issue. Light sheet-based fluorescence microscopy results in datasets that have volumes of up to several terabytes, thus transfer of the entire data is cumbersome and inefficient. Consequently, it is required that the datasets of interest can be browsed efficiently to gain an overview and then to decide which parts are finally transferred.
- To support colleagues that are not familiar with image data from advanced microscopy setups, it is helpful to provide a ‘point-and-click’ working interface that facilitates data access. It is especially important that navigation through the six aforementioned degrees of freedom is as intuitive as possible.
- For proper interpretation of microscopy data, comprehensive meta information about the acquisition process is essential. In developmental biology-associated fluorescence imaging assays, the meta information should contain (i) all essential background information on the specimen, (ii) a brief overview of the preparation, mounting and recording procedure and (iii) a comprehensive list of all imaging parameters.

In cooperation with Alexander Schmitz, I developed the BugCube, a web-based computer program that allows to share the image data with the community. It is coded in Wolfram *Mathematica* Version 9.0.1 and provided in the computable document format, which can be embedded into hypertext markup language documents and thus incorporated into websites. The program is basically an FTP client with a user interface (Figure 3-9) that provides the following functions:

- In the main menu, the user can select a publication, access the meta information and load respective datasets as size-reduced Z maximum projection time stacks into the time browser. The time browser supports four directions and one fluorescence channel and also allows to download the entire Z maximum projection time stack in full resolution.
- The time browser is equipped with a function to load the respective Z stacks of the currently displayed Z maximum projections into the Z stack browser. It also confers the option to download the whole Z stack in full resolution.
- Both, Z maximum projections from the time stacks and single planes from the Z stack can be loaded in their full resolution into either the left or right image slot.
- Each image slot has an information and task bar, which can be used to adjust brightness and contrast, to activate a magnification glass option, and to download the respective image in full resolution.

The BugCube can be accessed by any modern web browser at physikalischebiologie.de/bugcube. The program itself, which is fairly small (around 400 kilobytes), is embedded on the website. To run it properly, the computer of the end user needs the Wolfram computable document format player, which can be downloaded at wolfram.com/cdf-player. Additionally, in several web browsers, protection has to be disabled before the BugCube may start. The image data is deposited on the ftpbugcube FTP server, which is located here at the Johann Wolfgang Goethe-Universität. When one of the download options is used, the BugCube emulates a standard web browser-mediated download. Currently, the live imaging datasets from four studies as well as their respective meta information are accessible in the BugCube (Subchapters 6.1.2, 6.1.4, 6.1.5 and 6.1.6).

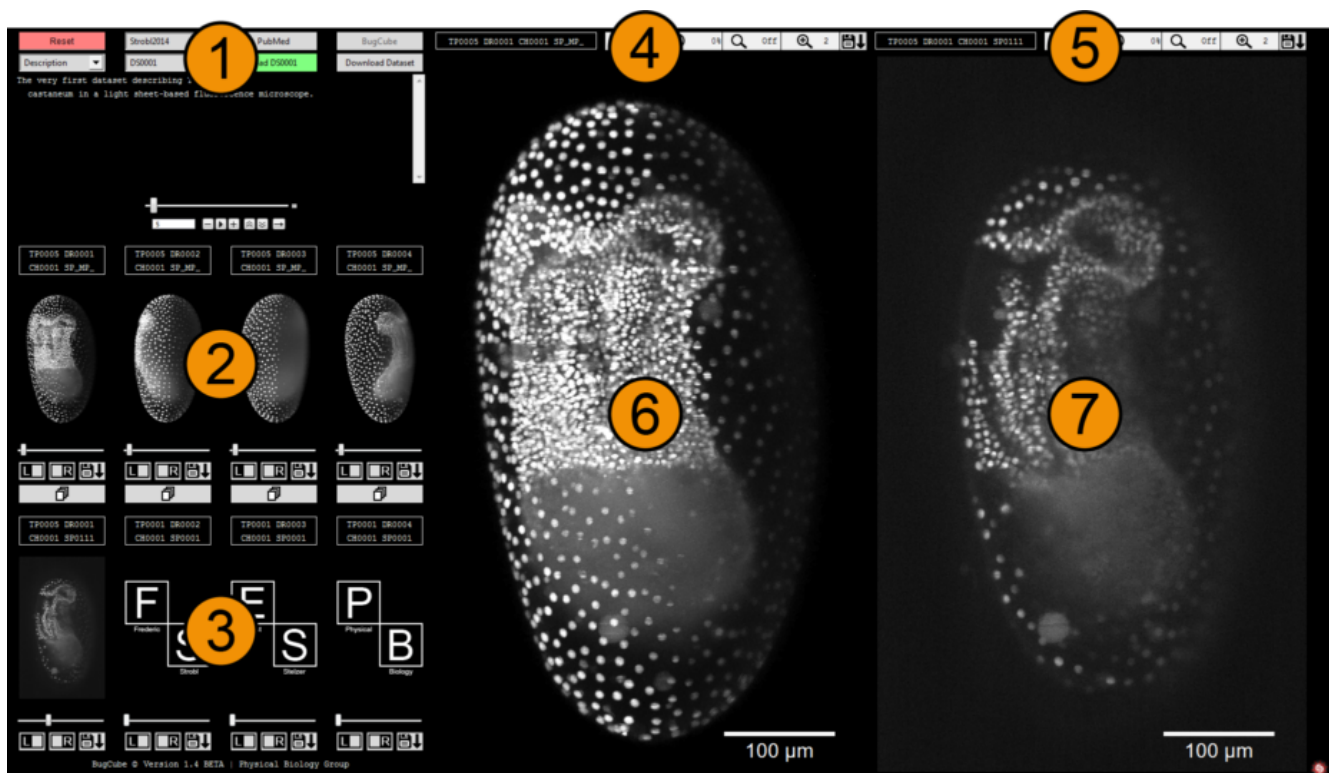


Figure 3-9 – BugCube user interface. (1) Main menu, in which the publications and datasets are selected and loaded. Also links to the meta data and the respective PubMed entry. (2) Time browser to move through the time points along four directions and load the respective Z stack for the desired time point. (3) Z stack browser to move through Z for a respective time points along four directions. (4) Information and task bar for the left image slot. (5) Information and task bar for the right image slot. (6) Left image slot, currently showing a Z maximum projection. (7) Right image slot, currently showing a single plane.

3.3.2. Anticipated Scope – Fluorescence Channels, More Directions and JPEG2000

The BugCube is currently still in the beta version. All basic functions are working properly and most bugs have been fixed, but several advanced functions are still missing. The following features will be added to the program in future:

- A dropdown menu that allows the selection of the fluorescence channel. Either, the fluorescence channel images can be loaded individually, then the image is shown as grayscale. Alternatively, merged fluorescence channel images can be loaded, then the BugCube will use the red-green-blue system to display the individual channels. Two-channel overlaps will appear in yellow, cyan or magenta, three-channel overlaps in white.
- A dropdown menu that allows the selection of more options for the directions. This is necessary for datasets with more than four directions but also for reconstructed datasets (Subchapter 3.2).
- A dropdown menu that allows access to the data in the lossless TIFF format or alternatively in the lossy, but smaller JPEG2000 format, which speeds up the download process.

In addition to the four published studies that contain BugCube-associated live imaging datasets (Subchapters 6.1.2, 6.1.4, 6.1.5 and 6.1.6), two more manuscripts with associated live imaging datasets have been submitted and are under review (Subchapters 6.2.3 and 6.2.4). As soon as the aforementioned features have been added and ten to fifteen studies with associated live imaging datasets are available, the BugCube will be overhauled and an explanatory manuscript will be written. The program should then confer access to around forty to fifty datasets with a total count in the range of 10^7 to 10^8 images and a total data volume of around twenty to thirty terabytes. The BugCube source code will be provided as open access for the community. It is annotated properly, and can be adapted easily with only moderate programming knowledge.

I anticipate that comprehensive imaging databases such as flybase (flybase.org) [174–176] for *Drosophila*, worm atlas (wormatlas.org) as well as worm image (wormimage.org) for the nematode *Caenorhabditis elegans*, Bio-Atlas for zebrafish (zfatlas.psu.edu), eMouseAtlas for mouse (emouseatlas.org) [177,178] and soon the BugCube for emerging insect model organisms will become an important resource for any morphogenesis-related studies in developmental biology. The BugCube is slightly outstanding from the other mentioned databases, since it does not focus on only one species, but follows the basic idea of the comparative approach and contains comprehensive information on at least three, *i.e.* *Ceratitis*, *Tribolium* and *Gryllus*, but preferable six, *i.e.* the aforementioned species as well as the Asian tiger mosquito *Aedes albopictus*, the squinting bush brown *Bicyclus anynana* and the western honeybee *Apis mellifera* (Subchapter 4.1.2) or even more species with ideally a linear decreasing phylogenetic relationship to the ‘gold standard’ *Drosophila*. Therefore, the BugCube will be a valuable resource also for evolutionary developmental biology.

3.4. AClashOfStrings – Systematic Creation of Double Homozygous Transgenic Hybrid Lines

3.4.1. Nota Bene

The AClashOfStrings (ACOS) vector concept is a highly complex invention. Similar to the AGOC vector concept, it can be independently used to systematically create homozygous transgenic lines, but it can also be used in conjunction with the AGOC vector concept to systematically create double homozygous transgenic hybrid lines. To appreciate the whole story, several arguments have to be considered:

- The ACOS vector concept can only be properly understood in context of the AGOC vector concept. It is therefore highly recommended to read the AGOC vector concept summary (Subchapter 2.2.7), the AGOC vector concept manuscript summary (Subchapter 6.2.3) and AGOC vector concept manuscript (Strobl *et al.* 2017D, #8 in Publication Table 3) before reading this subchapter.
- The paragraphs within this subchapter are already written in ‘publication’ style – it is planned to simply copy & paste several text passages from my PhD thesis into the respective manuscript.

- Several of the text passages, tables and figures in this subchapter have a very high degree of similarity to text passages, tables and figures within the AGOC vector concept manuscript (Strobl *et al.* 2017D, #8 in Publication Table 3). This is inevitable since the ACOS vector concept is a color-shifted variant of the AGOC vector concept – the vector architecture is nearly identical, basically only the transformation markers and the modular two-slot cloning site were exchanged. Thus, the crossing procedure from the F3 to the F7 generation is very similar (Subchapter 3.4.2). The true novelty of the ACOS vector concept lies within the creation of double homozygous transgenic hybrid lines within three additional generations, *i.e.* from the F7 to the F10 (Subchapter 3.4.3).
- The experimental phase is not finished yet. I was able to show that the ACOS vector concept works as well as the AGOC vector concept for the systematic creation of homozygous transgenic lines (Subchapter 3.4.2), and further to perform a preliminary proof-of-principle for the combined AGOC/ACOS vector concept from the F7 to the F10 generation (Subchapter 3.4.3) by systematically creating one double homozygous transgenic hybrid line, but additional experiments have to be performed to prove the functionality beyond any doubt. They are scheduled for fall 2017.
- I created many more ACOS lines and sublines than presented in the following subchapters. To save space, I only show a convenient selection of these lines that is necessary to understand the functionality and the proof-of-principle.
- Some of the ACOS sublines that I created (Subchapter 3.4.2) have already been used in live imaging assays by two of my students during their Bachelor projects, Selina Klees (Subchapter 5.4) and Franziska Krämer (Subchapter 5.5).

3.4.2. The AClashOfStrings Vector Concept – From the F3 to the F7

Transgenesis of established and emerging model organisms is a core method in cell and developmental biology [139]. Since nearly all metazoan model organism are diploid, hemizygous partners produce progeny that is either wild-type, hemizygous or homozygous. The complexity rises considerably when hybrid lines with two independent transgenes are required, since typical breeding setups, *i.e.* crosses of two double hemizygous individuals, result in up to nine genotypes:

- double wild-type, *i.e.* both transgenes are absent, the individual fully resembles the wild-type
- hemizygous/wild-type, *i.e.* only the first transgene is present one time, the second transgene is absent
- wild-type/hemizygous, *i.e.* the first transgene is absent, only the second transgene is present one time
- double hemizygous, *i.e.* both transgenes are present one time, the individual resembles the parents
- homozygous/wild-type, *i.e.* only the first transgene is present two times, the second transgene is absent
- wild-type/homozygous, *i.e.* the first transgene is absent, only the second transgene is present two times
- homozygous/hemizygous, *i.e.* the first transgene is present two times, the second transgene present one time
- hemizygous/homozygous, *i.e.* the first transgene is present one time, the second transgene present two times
- double homozygous, *i.e.* both transgenes are present two times

The genotype of double transgenic hybrid individuals can almost never be identified by considering the phenotype since transformation markers are usually not sufficient to determine whether the respective transgenes are present on only one or both chromosomes. Therefore, comprehensive genetic assays have to be performed, which are laborious and error-prone.

I have already established the AGameOfClones (AGOC) vector concept in the emerging insect model organism *Tribolium castaneum* (Subchapter 2.2.7). The concept allows the systematic creation of homozygous transgenic lines by using two clearly distinguishable transformation markers. These markers, termed mO and mC, are based on the 3×P3 eye-specific promoter [143] and the fluorescent proteins mOrange [144] and mCherry [145] which are embedded into interweaved, but incompatible lox site pairs [147,148].

After Cre-mediated recombination, hemizygous descendants are available that carry the transgene with only one of both markers. When such individuals are crossed, heterozygous progeny are identified by the presence of both markers, and in the following generation, homozygous individuals can be selected by omission of one marker. Throughout the whole procedure, all genotypes are identified by purposely produced distinct phenotypes.

The ACLashOfStrings (ACOS) vector concept is a color-shifted variant of the AGOC vector concept. The vector architecture is similar, but two different transformation markers are used. These markers, termed mCe and mVe, are also based on the artificial 3×P3 eye-specific promoter but use the fluorescent proteins mCerulean [159] and mVenus [179], respectively, and are thus clearly distinguishable from each other and the mO and mC markers used in the AGOC vector concept. Derivates of both vector concepts are independently used in germline transformation assays, thus inserting in two different genomic locations. Independent Cre-mediated recombination results in four phenotypes that can be distinguished from each other and from the wild-type (Figure 3-10, compare to Figure 2-20). Individuals that carry all four transformation markers can be identified as double heterozygous for both transgenes. A further cross results in double homozygous progeny that carry both transgenes with the same markers on both chromosomes.

First, I assayed if the ACOS vector concept performs as well as the AGOC vector concept. Thus, I created an intermediate vector, termed pACOS{#P'#O(MEM)-mRuby}, which contains the modular #P'#O(MEM)-Ruby two-slot cloning site as well as mCe and mVe embedded in interweaved, but incompatible lox site pairs. The cloning site contains the human *GAP43* membrane anchor [103] and the open reading frame for the mRuby fluorescent protein [110] per default (Figure 3-11). The intermediate vector was used to create two transformation-ready vectors that express either the default membrane tag or the histone 2B subunit under control of the *alpha-tubulin 1* promoter [180]. Injection of these vectors into preblastoderm embryos resulted in two transgenic *Tribolium* lines with two sublines each. I sequenced the insertion junctions (Table 3-2) and created a helper line, termed FIRE{HSP68'NLS-Cre} #1. This line expresses a nuclear-localized Cre recombinase [157] under control of the *HSP68* promoter [158] and also carries a mCherry-based eye-specific transformation marker. All four sublines successfully went through the recombination procedure (Figure 3-12), which was phenotypically documented for two sublines (Figure 3-13), and resulted in F7 mCe- and mVe-only homozygotes that carry either only mCe or mVe on both, the maternal and paternal chromosomes (Table 3-3). Similar to the F4 generation of the AGOC vector concept, the F4 generation of the ACOS vector concept also showed a patchy expression pattern in the compound eyes (Figure 3-14).

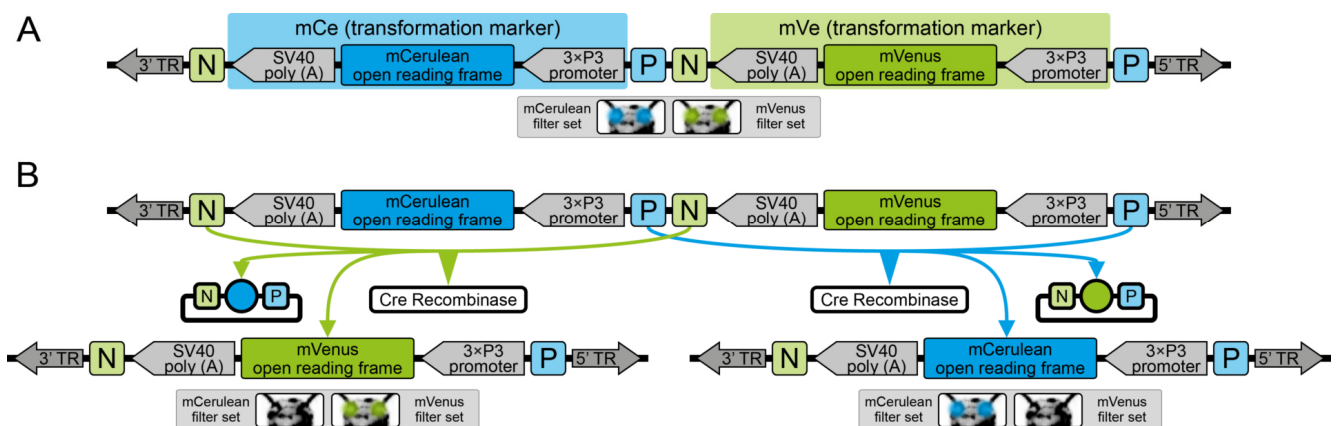
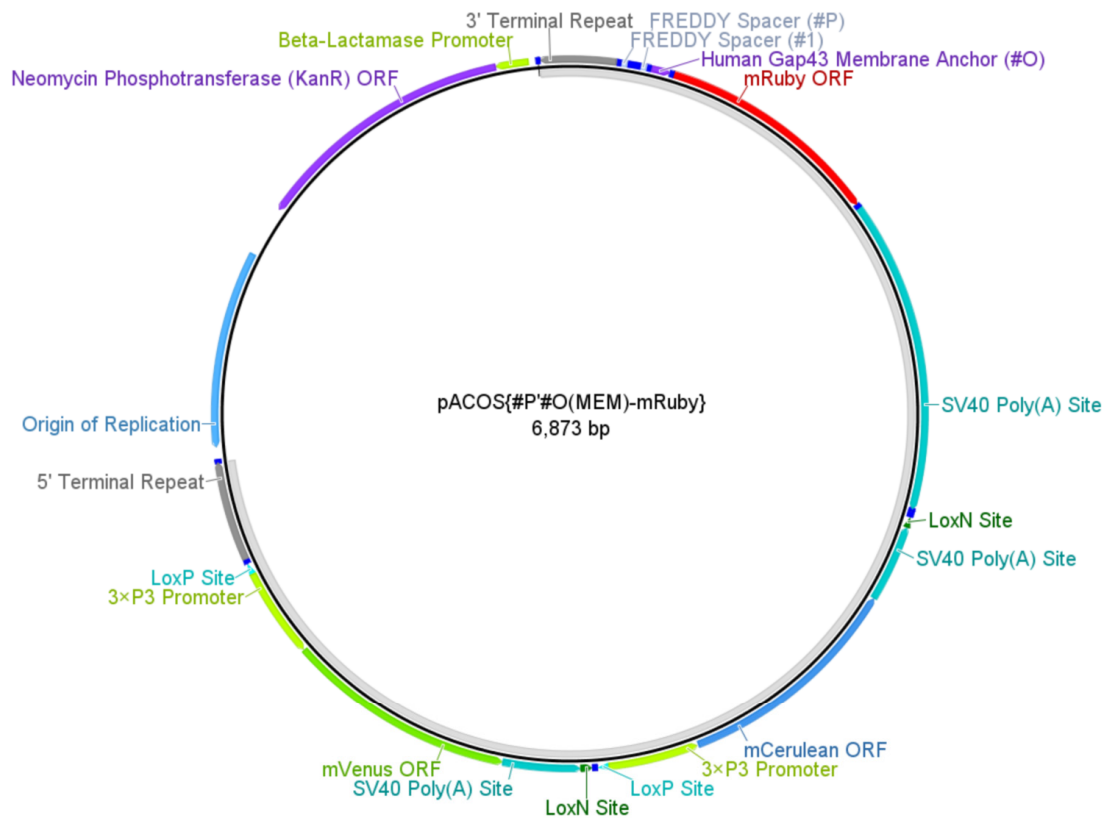
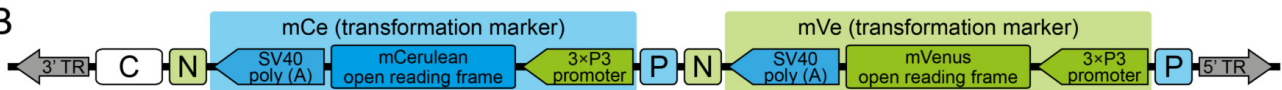


Figure 3-10 – The ACOS vector concept within the piggyBac-based pACOS transformation vector for *Tribolium*. (A) Two spectrally separable fluorescence-based transformation markers, mCe and mVe, are embedded into a piggyBac-based transformation vector that is characterized by 3' and 5' terminal repeats (TR) necessary for genomic integration. The markers are based on the artificial 3×P3 promoter, which drives expression in the neuronal system, the open reading frame for respective fluorescence protein, *i.e.* mCerulean or mVenus, and the SV40 poly (A) site. Each transformation marker is flanked upstream by a LoxP and downstream by a LoxN site, which results in interweaved lox site pairs. In *Tribolium* adults, the fluorescence phenotype can be detected in the eyes by using the appropriate filter sets. (B) Cre-mediated recombination leads to the excision of one of both markers from the genome. When one marker is removed, the other marker remains within the genome, since the two remaining lox sites, *i.e.* a LoxP and a LoxN site, are incompatible. *Tribolium* adults that underwent recombination give rise to progeny where only one marker is present in the eyes.

A



B



C

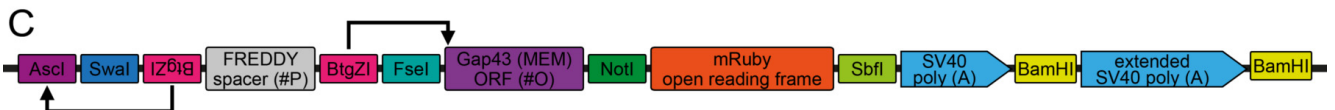


Figure 3-11 – The pACOS{#P'#O(MEM)-mRuby} vector. (A) Vector map of pACOS{#P'#O(MEM)-mRuby}. In this vector, the #1 slot remains empty, while the #P'#O(MEM)-mRuby two-slot cloning site was inserted into the #2 slot. The non-annotated dark blue boxes represent the same restriction enzyme sites as shown for the pAGOC{#P'#O(LA)-mEmerald} vectors (Figure 2-24). The light gray band on the inside indicates the transgene. (B) Scheme of mCe and mVe that are embedded into interweaved but incompatible LoxN and LoxP site pairs. Restriction enzyme sites are not shown. Sizes of genetic elements are not to scale. The white box on the left indicates that the genetic elements shown in panel C are positioned at that location. (C) Scheme of the #P'#O(MEM)-mRuby two-slot cloning site. To insert a promoter, the #P slot can be accessed wither by the AscI/FseI restriction enzyme site pair, but alternatively by the double BtgZI restriction enzyme site pair, which flanks a FREDDY spacer. BtgZI is a type I restriction enzyme with a non-palindromic recognition sequence. It cuts the sequence several bp (10/14) downstream, resulting in a 4 bp sticky end. In this vector, the upstream BtgZI restriction enzyme site (in reverse orientation) allows the opening of the AscI restriction enzyme site, while the downstream BtgZI restriction enzyme site (in forward orientation) allows the opening of the *GAP43* open reading frame start codon and the first bp of the subsequent codon, which allows scarless insertion of respectively digested promoter sequences (indicated by arrows). The human *GAP43* membrane anchor (MEM) open reading frame, which is in the #O slot per default, can be substituted with another open reading frame to change the intracellular localization by the FseI/NotI restriction enzyme site pair, while the mRuby open reading frame can be substituted with another fluorescence protein open reading frame by the NotI/SbfI restriction enzyme site pair. TR, piggyBac terminal repeat; ORF, open reading frame.

Table 3-2 – Overview of the four ACOS sublines, their insertions junctions and closest neighbors.

ACOS subline	chromosome	insertion junction	nearest neighbor
ACOS{ATub'#O(MEM)-mRuby} #1	ChLG3 (reverse orientation)	5' -TAATCTTATTTAAATAAATAA-3'	NC_007418.2
ACOS{ATub'#O(MEM)-mRuby} #2	ChLG9 (forward orientation)	5' -GTCTAAGCTCTTAAATAACAAGA-3'	NC_007424.2
ACOS{ATub'H2B-mRuby} #1	ChLG6 (forward orientation)	5' -GCGCGTTAACTTAAATAAGCCATCG-3'	NC_007421.2
ACOS{ATub'H2B-mRuby} #2	ChLG7 (forward orientation)	5' -TGAATAATCATTAATCCTTTTGC-3'	NC_007422.4

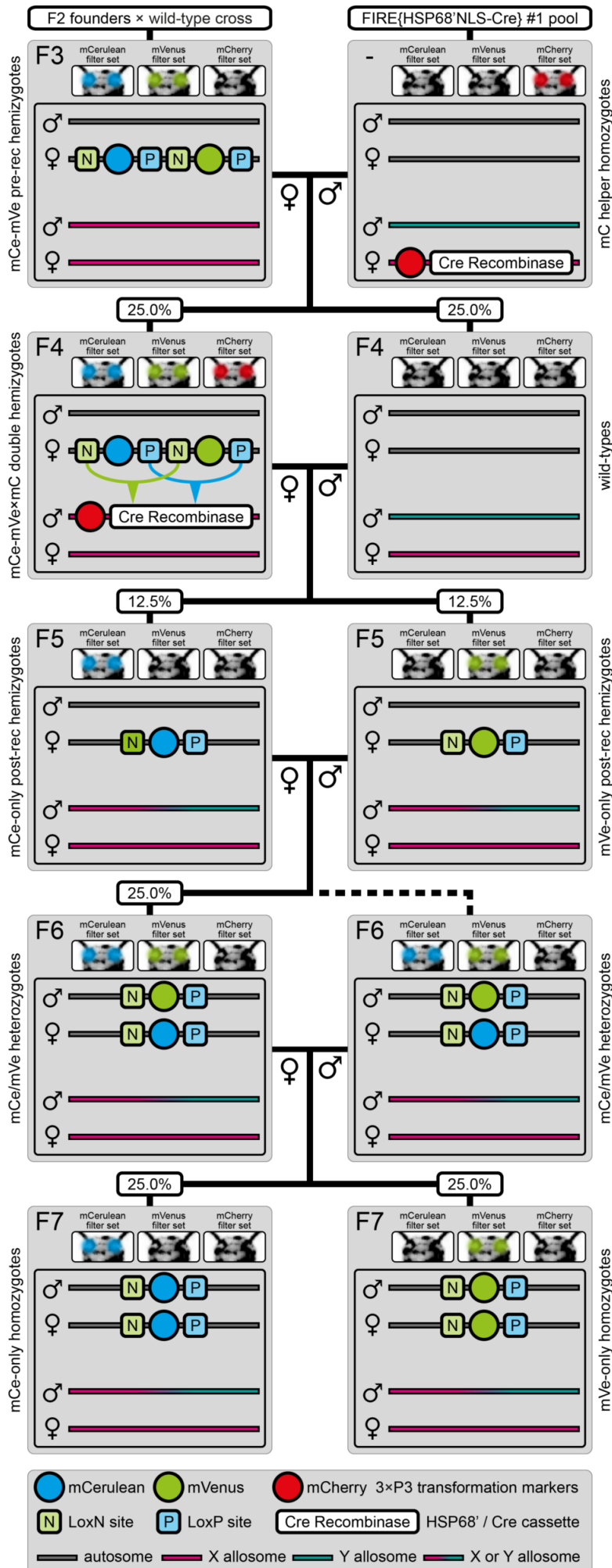


Figure 3-12 – The ACOS F3 to F7 crossing procedure that allows the systematic creation of homozygous transgenic lines. The rounded rectangle illustrates the genotype for one autosome and both allosomes, gray bars represent the ACOS transgene location, pink bars represent the helper transgene location on the X allosome and teal bars represent the Y allosome. A F2 mCe/mVe heterozygous founder female × wild-type male outcross results in the F3 mCe/mVe pre-recombination heterozygotes that carry mCe and mVe consecutively on one chromosome. A F3 mCe/mVe pre-recombination heterozygous female × FIRE(HSP68'NLS-Cre) #1 male (which carries the transgene only on the X allosome) cross gives rise to F4 mCe/mVe patchy eye hybrids, in which one marker is removed through Cre-mediated recombination. A F4 mCe/mVe patchy eye hybrid female × wild-type male outcross generates F5 mCe- and mVe only post-recombination heterozygotes. Next, a F5 mCe-only post-recombination heterozygous female × F6 mCe/mVe semi homozygous male brother-sister-cross results in a certain fraction of F6 mCe/mVe semi homozygous progeny. Finally, a F6 mCe/mVe semi homozygous female × F6 mCe/mVe semi homozygous male brother-sister-cross creates F7 mCe- and mVe-only full homozygous progeny. The percentage boxes show the theoretical ratio of the progeny that carry the respective genotype.

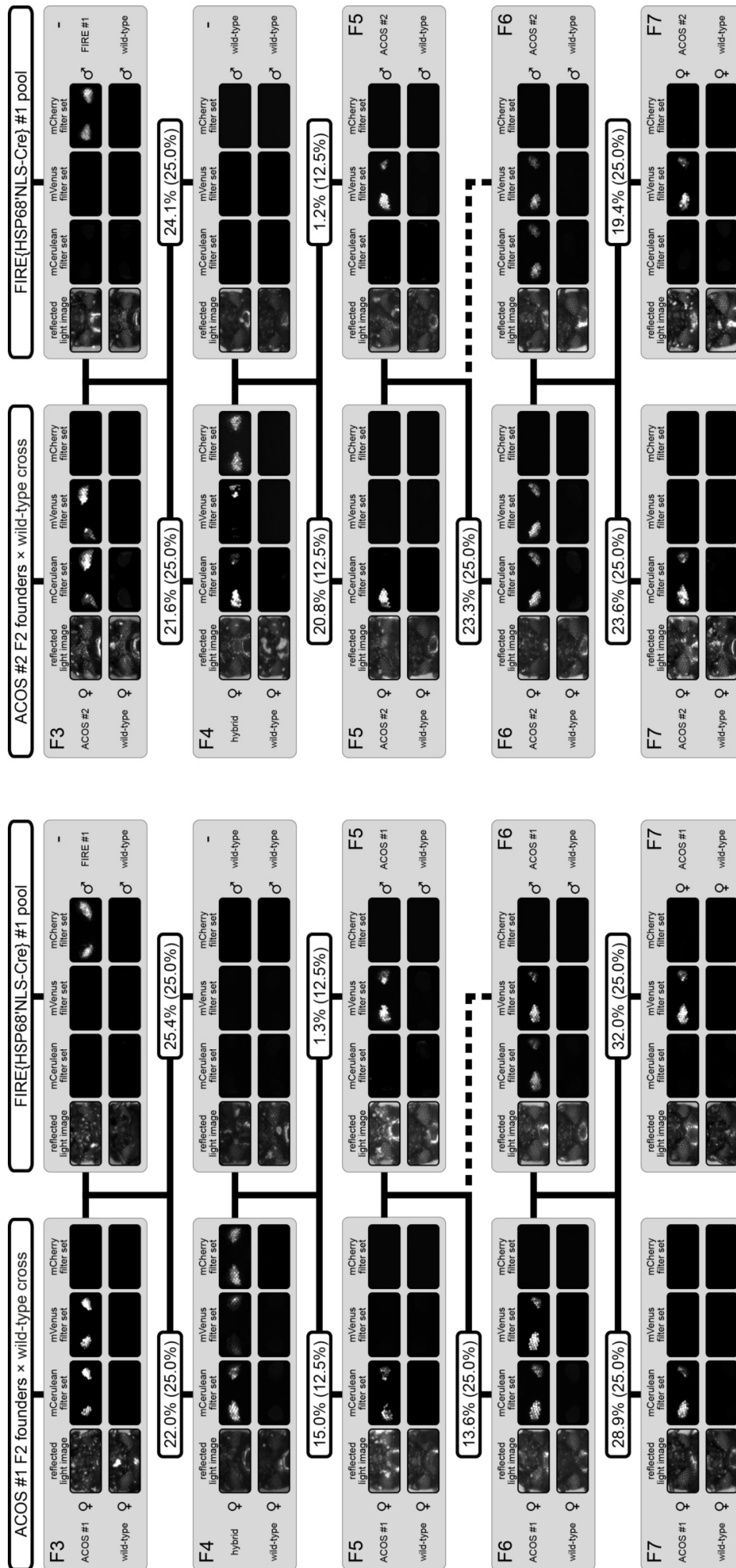


Figure 3-13 – The ACOS strings F3 to F7 crossing procedure shown for the ACOS{A Tub#O(MEM)-mRuby} #1 (ACOS #1) and #2 (ACOS #2) sublines. From the F3 to the F7 generation, the genotype was phenotypically determined by monitoring mCe, mVe and mC. Both sublines could be systematically crossed to obtain F7 mCe- and mVe-only full homozygotes. For each individual, a wild-type control of the same gender is shown. The percentage boxes show the experimental (and theoretical) ratios of the progeny with the respective phenotype.

Table 3-3 – Crossing results for four functional ACOS lines from the F3 to F7 generation. Bold entries mark progeny that was used in the subsequent cross, the F6-S, F7-Ce and F7-Ve entries mark control crosses.

gen	cross	subline	progeny								number
	♀	♂	●●●	●●●	●●●	●●●	●●●	●●●	●●●	●●●	
F3	♂	♂	25.0%	-	-	-	-	-	-	-	-
	♀	♀	25.4%	-	-	-	-	-	-	-	-
	♂	♂	24.1%	-	-	-	-	-	-	-	-
	♀	♀	29.8%	-	-	-	-	-	-	-	-
F4	♂	♂	23.3%	-	-	-	-	-	-	-	-
	♀	♀	25.0%	12.5%	12.5%	25.0%	25.0%	12.5%	12.5%	-	-
	♂	♂	34.3%	15.0%	1.3%	36.9%	36.9%	10.3%	2.2%	-	233
	♀	♀	30.0%	20.8%	1.2%	22.1%	22.1%	24.2%	1.7%	-	240
F5	♂	♂	23.0%	21.3%	2.5%	31.1%	31.1%	20.0%	2.1%	-	235
	♀	♀	37.9%	14.3%	3.6%	32.1%	32.1%	6.4%	5.7%	-	140
	♂	♂	25.0%	25.0%	25.0%	-	-	25.0%	-	-	-
	♀	♀	33.0%	27.1%	26.3%	-	-	13.6%	-	-	118
F6-S	♂	♂	23.3%	25.5%	27.9%	-	-	23.3%	-	-	43
	♀	♀	29.7%	23.4%	26.6%	-	-	20.3%	-	-	64
	♂	♂	30.8%	23.5%	24.7%	-	-	21.0%	-	-	81
	♀	♀	-	50.0%	50.0%	-	-	-	-	-	-
F6	♂	♂	-	50.5%	49.5%	-	-	-	-	-	95
	♀	♀	-	53.8%	46.2%	-	-	-	-	-	78
	♂	♂	-	51.7%	48.3%	-	-	-	-	-	118
	♀	♀	-	53.7%	46.3%	-	-	-	-	-	54
F7-Ce	♂	♂	-	25.0%	25.0%	-	-	50.0%	-	-	-
	♀	♀	-	28.9%	32.0%	-	-	39.1%	-	-	128
	♂	♂	-	23.6%	19.4%	-	-	57.0%	-	-	93
	♀	♀	-	30.0%	24.4%	-	-	45.6%	-	-	90
F7-Ve	♂	♂	-	29.4%	24.5%	-	-	46.1%	-	-	143
	♀	♀	-	100%	-	-	-	-	-	-	-
	♂	♂	-	100%	-	-	-	-	-	-	-
	♀	♀	-	100%	-	-	-	-	-	-	-
F7-S	♂	♂	-	100%	-	-	-	-	-	-	-
	♀	♀	-	100%	-	-	-	-	-	-	-
	♂	♂	-	100%	-	-	-	-	-	-	-
	♀	♀	-	100%	-	-	-	-	-	-	-
F7-Ve	♂	♂	-	100%	-	-	-	-	-	-	-
	♀	♀	-	100%	-	-	-	-	-	-	-
	♂	♂	-	100%	-	-	-	-	-	-	-
	♀	♀	-	100%	-	-	-	-	-	-	-

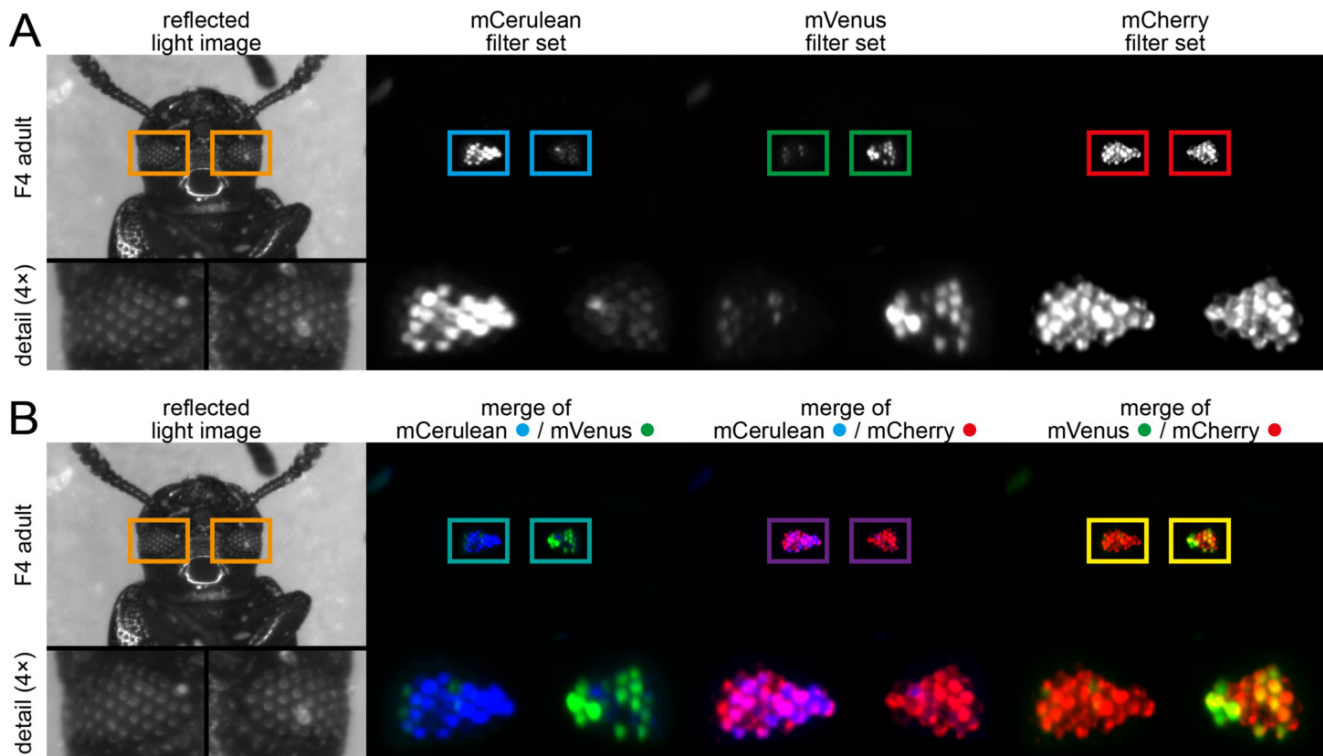


Figure 3-14 – The F4 mCe-mVe×mC double hemizygous generation. (A) The F4 hybrid generation is hemizygous for both the ACOS transgene, which carries both mCe and mVe embedded into interweaved lox site pairs, and for the helper transgene, which carries mC and the Cre recombinase expression cassette. Within this cassette, expression of a nuclear-localized Cre recombinase is driven by the endogenous *HSP68* promoter. During the development of the F4 generation from the zygote to the fertile adult, the *HSP68* promoter exhibits a slightly leaky expression. Over time, this leads to recombination in germ cells (*i.e.* the prerequisite for the ACOS vector concept) but also in certain somatic progenitor cells that later on give rise to distinct, typically spatially clustered cell populations. This effect is evident in the compound eyes of adults in all ACOS sublines, where certain cluster of ommatidia show either expression of mCe or mVe. (B) Within the merged images, it is evident that most of the ommatidia express either only mCe or mVe.

In conclusion, the ACOS vector concept performs as well as the AGOC vector concept and can be used as an alternative to systematically create homozygous transgenic lines whenever expression of mEmerald or the mOrange- and mCherry-based transformation markers are an inconvenient choice or stand in conflict with the experimental strategy.

3.4.3. The AClashOfStrings Vector Concept – From the F7 to the F10

In combination, the AGOC and ACOS vector concepts allow the systematic creation of double homozygous transgenic hybrid lines by following a certain crossing procedure (Figure 3-15), which is completed within three further generations:

- Firstly, F7 mCe-only homozygous females (ACOS), which carry only mCe on both the maternal and paternal chromosome, are crossed against F7 mO-only homozygous males (AGOC), which carry only mO on both the maternal and paternal chromosome (Figure 3-15, first row, left). In parallel, F7 mVe-only homozygous females (ACOS), which carry only mVe on both the maternal and paternal chromosome, are crossed against F7 mC-only homozygous males (AGOC), which carry only mC on both the maternal and paternal chromosome (Figure 3-15, first row, right). Together, both crosses result in F8 mCe×mO- and mVe×mC-only double hemizygous progeny.
- Secondly, F8 mCe×mO-only double hemizygous females are crossed against F8 mVe×mC-only double hemizygous males (Figure 3-15, second row) resulting in F9 mCe/mVe×mO/mC double heterozygotes that carry all four markers.
- Thirdly, F9 mCe/mVe×mO/mC double heterozygous females are brother-sister crossed against genotypic identical F9 males (Figure 3-15, third row), resulting in F10 mCe×mO-, mCe×mC-, mVe×mO- and mVe×mC-only double homozygotes (Figure 3-15, fourth row).

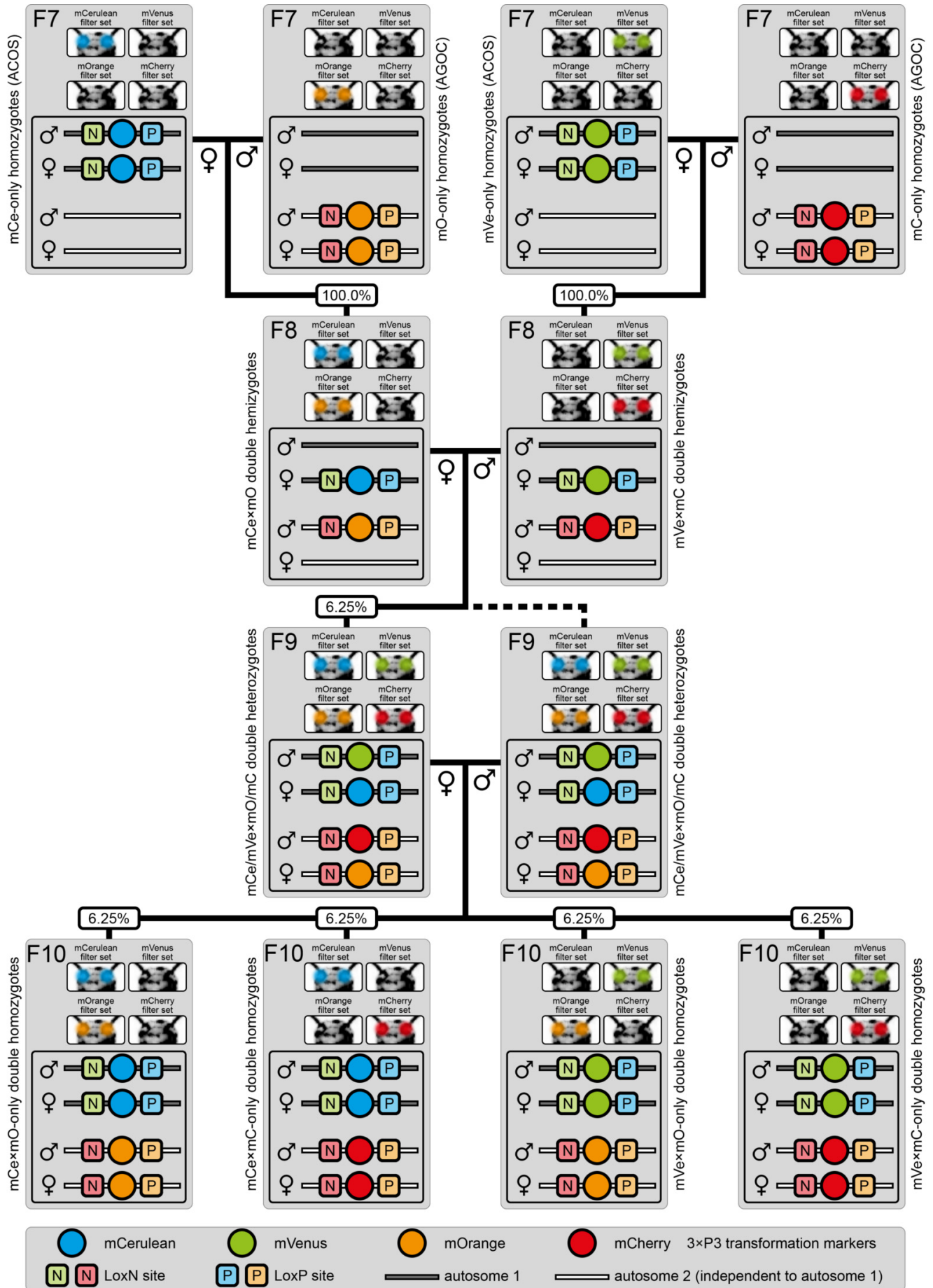


Figure 3-15 - The ACOS F7 to F10 crossing procedure for the systematic creation of double homozygous transgenic hybrid lines. The rounded rectangle illustrates the genotype for two independent autosomes, gray bars represents the ACOS transgene location and white bars represent the AGOC transgene location.

In contrast to the F8 mCe×mO- and mVe×mC-only double hemizygotes, which show the same phenotype but carry mCe or mVe on the maternal and mO or mC on the paternal chromosomes, the F10 mCe×mO- and mVe×mC-only double homozygotes carry the respective markers on the maternal and paternal chromosomes, while the respective other two markers are omitted. The F10 mCe×mC- and mVe×mO-only double homozygotes do not have a phenotypic counterpart in the F8 generation.

I was already able perform a preliminary proof-of-principle of the functionality of the combined AGOC/ACOS vector concept by systematically creating one double homozygous transgenic hybrid line using the AGOC{ARP5’#O(LA)-mEmerald} #1 (Subchapter 6.2.3) and the ACOS{ATub’H2B-mRuby} #1 (Table 3-2) sublimes. Within the F10, all four double homozygous variants were obtained, which was proven by outcrossing respective females against the wild-type males (Table 3-4). The functionality will be proven beyond and doubt by creating at least five more double homozygous transgenic hybrid lines, and selected functional lines will be analyzed in fluorescence live imaging assays.

Table 3-4 – Crossing results for hybridization of the AGOC{ARP5’#O(LA)-mEmerald} #1 and the ACOS{ATub’H2B-mRuby} #1 sublimes. The ‘other’ column summarizes eleven other phenotypes (wild-type, both parental phenotypes, four times one and four times three transformation markers).

generation	cross		progeny					other	number
	♀	♂	●●●●	●●●●	●●●●	●●●●	●●●●		
F7 mCe and mO	ACOS mCe	AGOC mO	100%	-	-	-	-	-	80
F7 mVe and mC	ACOS mVe	AGOC mC	-	-	100%	-	-	-	72
F8	●●●●	●●●●	7.9%	5.6%	7.6%	4.0%	7.6%	67.3%	251
F9-S	●●●●	●●●●	22.0%	22.9%	24.8%	30.3%	-	-	109
F9	●●●●	●●●●	11.0%	2.5%	10.1%	3.0%	31.7%	41.7%	199
F10-mCe×mO	●●●●	●●●●	100%	-	-	-	-	-	87
F10-mCe×mC	●●●●	●●●●	-	100%	-	-	-	-	101
F10-mVe×mO	●●●●	●●●●	-	-	100%	-	-	-	71
F10-mVe×mC	●●●●	●●●●	-	-	-	100%	-	-	76

3.4.4. Advantages of the AClashOfStrings Vector Concept

Similar to the AGOC vector concept, the ACOS vector concept has several advantages over traditional approaches and the effort reduction is even more significant. They arise from the unique feature that from the F1 potential mosaics to the F10 double homozygous hybrids, the genotype of each individual can be identified by considering the phenotype. Genetic assays to genotype two transgenes requires even more manpower and material and is also more error-prone due to the fact that the fraction of suitable progeny decreases the more transgenes are involved. Similar to the AGOC vector concept, the ACOS vector concept should also work in all model organisms for which Cre-mediated recombination was proven functional.

The procedure that I describe involves the independent creation of homozygous transgenic lines with the AGOC and ACOS vector concept before double homozygous hybrid lines are created, which takes a total of ten generations. However, it is also possible to cross F5 mO- and mC-only post-recombination hemizygotes (AGOC) against F5 mCe- and mVe-only post-recombination hemizygotes (ACOS), respectively. This results immediately in F6 (‘F8’) mCe×mO and mVe×mC double hemizygotes. Within two additional generations, F8 (‘F10’) mCe×mO-, mCe×mC-, mVe×mO- and mVe×mC-only double homozygotes are obtained.

I have proven the functionality of the combined AGOC/ACOS vector concept in *Tribolium* by creating a double homozygous transgenic hybrid lines designed primarily for fluorescence live imaging. The combined AGOC/ACOS vector concept can also be used to create double homozygous organisms that have either (i) a knock-in and a knock-out or (ii) two knock-outs.

Especially the latter case is of high interest, since at a certain point in future, there will be data available on every single gene knock-out. However, this information will not suffice to decipher all fundamental developmental processes and the next higher experimental order is a systematic knock-out of two genes at the same time followed by an analysis of the ‘cumulative’ phenotype. The combined AGOC/ACOS vector system is a convenient approach for such experiments.

Double knock-in homozygous transgenic hybrid lines are also very suitable for certain advanced genetic approaches such as the GAL4/UAS system [181]. In brief, a driver line, which expresses the GAL4 peptide under control of a promoter of choice, is crossed against a reporter line that expresses, for example, a fluorescent protein under control of the GAL4-controlled upstream activation sequence (UAS). With this binary expression system, a quadratic increasing number of reporter patterns can be created with a linear increasing number of driver and reporter lines. However, to conveniently work with the transgenic hybrid line, it has to be double homozygous, which can be achieved with the combined AGOC/ACOS vector concept.

3.5. AStormOfRecords – Systematic Creation of Triple Homozygous Transgenic Hybrid Lines

3.5.1. The AStormOfRecords Vector Concept

The AStormOfRecords (ASOR) vector concept is an even further development of the combined AGOC/ACOS vector concept and allows the systematic creation of triple homozygous transgenic hybrid lines. The basic vector architecture is similar to the ACOS and AGOC (Subchapters 3.4 and 2.2.7, respectively) vectors, but ASOR-derived vectors carry mVe (which is also part of the ACOS vector concept) and mO (which is also part of the AGOC vector concept) as the eye-specific transformation markers. Similar to both other concepts, respective vectors can be used in independent *Tribolium* germline transformation assays and as soon as appropriate F3 subline cultures are established, a certain crossing procedure has to be followed:

- The F3 to F7 procedure is similar to the procedures for the AGOC and ACOS vector concepts and is initiated by crossing F3 mVe-mO heterozygous females against appropriate Cre-expressing helper males. Conveniently, both helper lines that are used for the AGOC and ACOS vector concepts, ICE{HSP68’NLS-Cre} and FIRE{HSP68’NLS-Cre}, are valid choices since they carry mCe and mC, respectively. After Cre-mediated recombination and three more generations, F7 mVe-only and mO-only homozygotes are obtained.
- Respective F7 mVe-only and mO-only homozygotes can be hybridized with individuals deriving from independent transformations with both the AGOC and ACOS vectors concept to create F10 mCe×mVe- and mO×mC-only double homozygous hybrids, although the crossing procedure differs moderately from the scheme shown for the combined AGOC/ACOS vector concept (Subchapter 3.4.3) since only three but not four markers are available. To continue, also F10 mCe×mC-only double homozygotes are necessary that derive from the same AGOC and ACOS sublines as the mCe×mVe- and mO×mC-only double homozygous individuals.
- The creation of triple homozygous transgenic hybrid lines begins by crossing F10 mCe×mVe- and mO×mC-only double homozygous females against F10 mCe×mC-only double homozygote males, *i.e.* by three-way hybridizing two hybrids. Throughout four more crosses, F15 mVe×mCe×mC- and mO×mCe×mC-only triple homozygous transgenic individuals are obtained. These hybrids always carry mC, which marks the AGOC transgene, and mCe, which marks the ACOS transgene, but either mVe or mO, which marks the ASOR transgene.

While marker choice and crossing procedure are unambiguous, the question of the fluorescence protein remains. Since the AGOC vector concept uses mEmerald [146] with a 487 nm excitation and 509 nm emission peak and the ACOS vector concept uses mRuby [110] with a 559 nm excitation and 600 nm emission peak, the most convenient choice was to use a near infrared fluorescent protein. With a 643 nm excitation peak, a 670 nm emission peak and a brightness of 12.5, iRFP670 [182] was chosen. Further, as the default tag, the SV40 nuclear localization signal was taken.

3.5.2. Preliminary Experiments and Further Considerations

Based on these considerations, an intermediate vector termed pASOR{#P'#O(NLS)-iRFP670} was created, which can be used in a similar manner for cloning as the ACOS and AGOC intermediate vectors (Subchapters 2.2.7 and 3.4.2). Further cloning steps were performed to create two transformation-ready vectors:

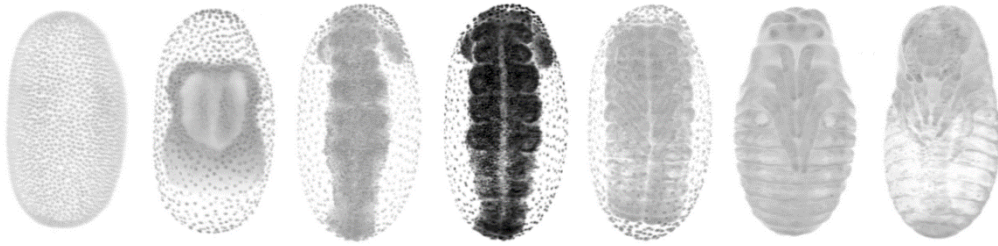
- The pASOR{ATub'#O(NLS)-iRFP670} vector allows expression of nuclear-localized iRFP670 under control of the *alpha-tubulin 1* promoter [180].
- The pASOR{ATub'H2B-iRFP670} vector allows expression of iRFP670-labeled histone 2B subunits under control of the *alpha-tubulin 1* promoter.

Subsequent germline transformation resulted in twenty-four and five sublines, respectively. I characterized nearly all of these lines together with Selina Klees and Franziska Krämer by using light sheet-based fluorescence microscope, but only embryos from the pASOR{ATub'H2B-iRFP670} #3 subline showed a very faint signal during germband retraction in the serosa cells when imaged with 3 mW laser power and 100 ms exposure time. These preliminary results indicate that iRFP670 is not a reasonable choice for *Tribolium*. Thus, the vector architecture has to be changed by replacing the open reading frame of the iRFP670 with a variant that can be excited with a near ultra violet laser and emits blue light, e.g. mTagBFP [183].

Initially, the ASOR vector concept, which is a further development of the combined AGOC/ACOS vector concept, was invented to systematically create triple homozygous transgenic hybrid lines designed primarily for fluorescence live imaging. However, it is also possible to use the vector concept in other experimental strategies:

- The concept can be used to create triple knock-outs by rendering the first target gene inoperative with the AGOC vector concept, the second target gene with the ACOS vector concept and the third target gene with the ASOR vector concept. However, double knock-out combination have to be homozygous viable to reach the triple knock-out generation.
- Further, double knock-outs in combination with single knock-ins are possible. However, one of these knock-outs has to be homozygous viable to reach the double knock-out / single knock-in generation. Similarly, also single knock-outs in combination with double knock-ins can be created without restrictions.
- With the ASOR vector concept, it is possible to add another experimental order to the GAL4/UAS binary expression system [181]. In brief, a 'driver' line is created that expresses the GAL4 peptide under control of a promoter of choice. Respective individuals are crossed against a reporter line, which express a protein of choice, e.g. a fluorescent protein, under control of the GAL4-activatable UAS promoter. Thus, the resulting hybrids express the chosen reporter under the spatiotemporal control of the respective promoter. With the combined AGOC/ACOS/ASOR vector system, it is possible to build a 'ternary' expression system, in which either two promoter transgenes can be combined with one reporter transgene, or alternatively, one promoter transgene drives expression of two reporter transgenes.

4. Future Trends



In this chapter, I provide a comprehensive outlook and a concise perspective. While the outlook subchapters give a practical working outline how the already completed and still ongoing projects can be continued, the perspective subchapters illustrate my thoughts on the general future of insect-associated developmental biology and related disciplines.

PWAS
wild type

VDAC
mutant



The Vicious-Dark-As-Coal (VDAC) *Tribolium* mutant strain. Compared to the Plain-White-As-Snow (PWAS) wild-type strain, which I primarily used during my PhD project, the VDAS mutant strain has a conspicuously darker cuticle color. As this line spontaneously originated from the PWAS strain, it also carries loss-of-function mutations in the *Pearl* and the *Light Ocular Diaphragm* genes, which results in completely transparent eyes. Over a period of more than four years, this was the only mutant with a noticeable phenotype that was found. The mutation has not been analyzed to date, and the strain has not been used in experiments yet. This chapter figure shows that even when the everyday laboratory work is conducted with maximum diligence to keep the amount of variation and experimental errors such as cross contamination at a minimum, some uncontrollable factors always remain when working in the field of life sciences.

4.1. Outlook

4.1.1. Nota Bene

Similarly to all disciplines in the natural sciences, acquisition and interpretation of data inevitably leads to follow-up questions and hypotheses. This subchapter summarizes the most important thoughts, ideas and concerns that arose during the experimental and analytical phase of my PhD project. Five outlooks, classified by research type and feasibility, (Table 4-1), are provided:

- Outlook I describes a large, self-contained project outline that provides comprehensive insights on all three perspective levels discussed in Subchapter 4.1 – developmental biology, evolutionary developmental biology and ecological evolutionary developmental biology. However, due to the large scope of the project, extensive funding is necessary. Thus, the project outline was transcribed into a grant application (Subchapter 6.3.2) and the following subchapter only provides a very brief summary.
- Outlook II outlines concepts and ideas for further functional genetic approaches that synergize well with non-invasive long-term fluorescence live imaging and thus aid in deciphering developmental processes. The described projects do not address biological hypotheses directly but rather establish new methods and proof their functionality.
- Outlook III describes all major biological questions that arose during my PhD project. For each question, a scientific hypothesis is provided and multiple verification approaches are described in detail, including a preliminary experimental workflow.
- Outlook IV explains my notion to transfer the AGameOfClones vector concept to vertebrate or other eukaryotic species. However, such an extensive project is not feasible without dedicated co-operations.
- Outlook V illustrates several side projects. These projects are usually methodological in character and either aim to (i) adapt certain techniques to specific biological models, (ii) simplify the everyday laboratory work or (iii) propose standard operation procedures.

While Outlook I has been transcribed into a grant application, the text passages and figures for Outlook II to V are written in a concise and autonomous style to convert them into proposals. Typically, two suggestions from Outlook II and III and a variable number of smaller side projects should occupy an ambitious PhD student for 3 to 3½ years.

Table 4-1 – Research type, feasibility and priority overview of Outlook I to V. The priority column states my personal preferences (how I would allocate time, resources and manpower) and does not claim universal validity. For the grant application related to Outlook I, see Subchapter 6.3.2.

outlook	rationale	research Type	feasibility	priority
I	A Comparative Approach to Embryonic Robustness	biological hypotheses	grant/funding necessary	high
II	Functional Genetics	mainly methodological	time and effort moderate	high
III	Biological Questions	biological hypotheses	time and effort moderate	moderate
IV	Universalizing AGameOfClones	mainly methodological	co-operations necessary	low
V	Side Projects	mainly methodological	usually by/with students	low

4.1.2. Outlook I – A Comparative Approach to Embryonic Robustness

During my PhD project, I was able to document a large part of the embryonic morphogenesis of three emerging insect model organisms, (i) the red flour beetle *Tribolium castaneum*, which belongs to the Coleoptera, (ii) the Mediterranean fruit fly *Ceratitis capitata*, which belongs to the Diptera, and (iii) the two-spotted cricket *Gryllus bimaculatus*, which belongs to the Orthoptera. Insects are considered one of the most successful metazoan groups [1], but the amount of morphogenetic data for species of other important insect orders is still quite limited. Therefore, a comprehensive research outline for a large-scale interdisciplinary project was prepared that provides profound insights in developmental biology, evolutionary developmental biology and ecological evolutionary developmental biology. The embryonic morphogenesis as well as the developmental robustness under certain crucial environmental factors of the ‘gold standard’ *Drosophila* and six more candidates with a linear decreasing phylogenetic relationship should be characterized, quantitatively described and compared. Besides the three aforementioned emerging insect model organisms, also (iv) the Asian tiger mosquito *Aedes albopictus*, which belongs to the Diptera, (v) the squinting bush brown *Bicyclus anynana*, which belongs to the Lepidoptera, and (vi) the western honeybee *Apis mellifera* qualify as suitable candidates due to their scientific and economic relevance (Figure 4-1).

Due to the anticipated extensive scope of the project, additional funding is necessary, so the outline was transcribed into a ‘Reinhart Koselleck-Projekt’ grant application (Subchapter 6.3.2) that comprises three subsequent phases:

- During Phase 1, for all seven species, the ‘missing’ resources, *i.e.* appropriate protocols and suitable transgenic lines, which are essential to perform non-invasive long-term live imaging under comparable conditions with light sheet-based fluorescence microscopy, are established (Table 4-2).
- During Phase 2, the development of all seven species is recorded with a statistically significant number of repetitions so that processes can be described quantitatively. Similarities and differences between the species will provide profound insights into the evolution of development.
- During Phase 3, the effective thresholds of four environmental factors, *i.e.* temperature, pH value, UV irradiation and ion concentration, on the embryonic morphogenesis are characterized within a three-dimensional experimental matrix (species • environmental factor • variance of factor). This systematical setup allows estimations and comparisons of the developmental robustness with a high degree of detail.

Table 4-2 – Overview of the ‘missing’ protocols and resources that have to be established during Phase 1. Green shows already established resources, yellow and red indicate not yet established resources that are considered either a moderate or an ambitious challenge, respectively. Table/and or table description fully and/or partially reproduced from the ‘Reinhart Koselleck-Projekt’ grant application (Subchapter 6.3.2).

resource	<i>Drosophila</i>	<i>Ceratitis</i>	<i>Aedes</i>	<i>Bicyclus</i>	<i>Tribolium</i>	<i>Apis</i>	<i>Gryllus</i>
rearing routine	established ¹	established ²	established ³	not established ⁵	established ⁷	established ⁸	established ¹⁰
transgenic line	established ¹	established ²	not established ⁴	not established ⁶	established ⁷	not established ⁹	established ¹⁰
live imaging protocol	established ¹	established ²	not established	not established	established ⁷	not established	partially ¹¹

¹ see also Subchapter 2.2.1, transgenic lines derive from the Bloomington *Drosophila* Stock Center (Indiana, United States of America). ² see also Subchapter 2.2.5. ³ in cooperation with Dr. Ruth Müller, see also Subchapter 6.3.2. ⁴ potentially working transformation vectors with suitable promoter available [184] that have to be tested, transformation protocol available [185]. ⁵ protocol available [186]. ⁶ suitable promoters not known, transformation protocol available [187]. ⁷ see also Subchapter 2.2.2. ⁸ in cooperation with Prof. Dr. Bernd Grünwald, see also Subchapter 6.3.2. ⁹ suitable promoter available [188], transformation protocol available [189]. ¹⁰ see also Subchapter 3.1. ¹¹ the current protocol allows to image only a certain period of the embryogenesis.

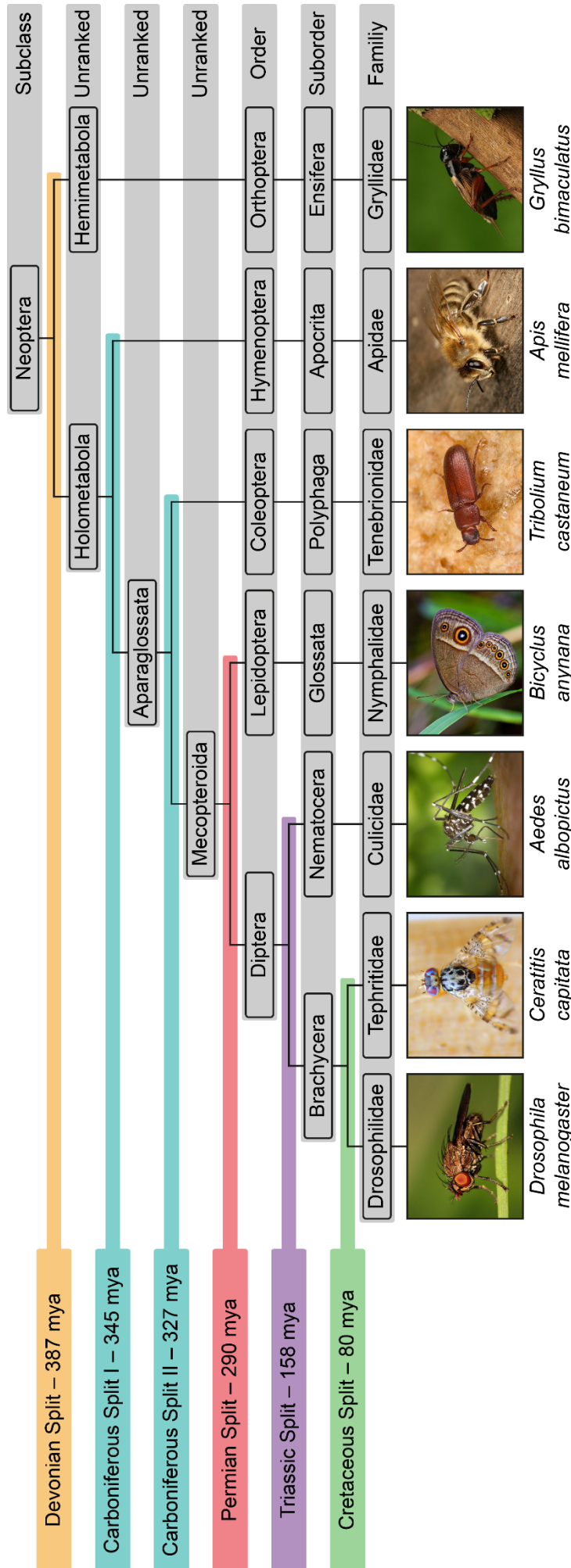


Figure 4-1 – Phylogenetic tree of the ‘gold standard’ *Drosophila* and the six additional insect species. Evolutionary ‘splits’ have been termed according to their geological period. The Mediterranean fruit fly *Ceratitis capitata* belongs to the Diptera and is one of the most important agricultural pests in the southern regions of the United States of America [190,191], and the species has been subject to the sterile insect technique [132,192,193]. The Asian tiger mosquito *Aedes albopictus* also belongs to the Diptera, serves as a vector for several human pathogenic viruses such as Chikungunya [194,195] and Dengue [194,196] and has begun to invade Europe [197–199]. The squinting bush brown *Bicyclus anynana* represents the Lepidoptera and is a model organism for biological mechanisms of color pattern formation [200]. The red flour beetle *Tribolium castaneum* is a member of the Coleoptera, infests wheat silos and grain storage facilities and has become the second most important insect model organism [115,201,202]. The western honeybee *Apis mellifera*, which belongs to the Hymenoptera, is of crucial economic relevance as a pollinator and producer of honey and wax [203]. A germline transformation protocol was recently established [189]. The two-spotted cricket *Gryllus bimaculatus* is an Orthoptera and the only hemimetabolous species. It is an emerging model organism for developmental and regenerative studies [161]. Figure and/or figure description fully and/or partially reproduced from the ‘Reinhardt Kosselack-Projekt’ grant application (Subchapter 6.3.2).

4.1.3. Outlook II – Functional Genetics

One of the best synergizing co-disciplines for fluorescence live imaging in developmental biology is functional genetics. Although it is possible to inject fluorescent dyes into embryos to observe their development over time [102] and thus bypass genetics completely, this approach has several limitations: (i) only spatiotemporal ubiquitous labeling is possible, (ii) not all intracellular structures can be stained, and (iii) embryo manipulation is necessary. The creation of custom-made transgenic lines – one of the primary applications of functional genetics – overcomes these issues. In my PhD thesis, I present the AGOC (Subchapter 2.2.7), ACOS (Subchapter 3.4) and ASOR (Subchapter 3.5) vector concepts, which allow the systematic creation of homozygous, double homozygous and in theory also triple homozygous transgenic lines. However, functional genetics have a much higher potential. The following listing (i) briefly suggests improvements, (ii) explains a ternary variant of the GAL4/UAS system and (iii) presents a completely novel concept for the stochastic labeling of cells within embryos:

- The AGOC, ACOS and ASOR vector concepts are the first versions of their kind. Their functionality has been proven (AGOC), partially proven (ACOS) or suggested (ASOR), but the vector architecture can be improved. The following improvement suggestions apply to all three vector concepts alike:
 - The FREDDY spacer in the #1 slot, which has not yet been used, will be replaced by a 23 bp attB acceptor site. This allows a site-specific nested integration of a second transgene into the initial transgene. The second transgene has to carry a 23 bp attP site for integration [204]. This is especially useful when the initial transgene integrated close to an enhancer and mimics the respective expression pattern.
 - Currently, the vectors come with an empty promoter/upstream regulatory sequence slot (#P). In the next version, the viral *IE1* promoter [205], which was initially discovered in the silkworm *Bombyx mori*, will be inserted in the #P slot by default. The sequence will be slightly adjusted so that the *IE1* promoter can be replaced scarlessly by other promoters or upstream regulatory sequences by performing a single enzyme digest with only the BtgZI restriction enzyme as already possible. The *IE1* promoter has been tested in *Drosophila* and should lead to a strong ubiquitous spatiotemporal expression in a variety of insect species and is therefore properly qualified as the default promoter. Respective vectors can be used directly in other candidate species for the comparative approach (Subchapter 4.2.2) without any need for molecular cloning, ideally with mRNA as the piggyBac transposase source.
 - The fluorescent protein open reading frames will be replaced by optimized derivatives, for example, mRuby2 in the ACOS vector concept will be replaced by mRuby3 [206], which has a 35% higher brightness and photo-stability. It is also possible to create vector derivatives that carry open reading frames for photo-activatable fluorescent proteins such as PA-GFP [207] and PA-mKate [208], photo-convertible fluorescent proteins such as mEos2 [209] or photo-switchable fluorescent proteins such as Dronpa [210].
 - The transformation marker cassettes, currently in the #3 and #4 slots, will be merged into one hybrid cassette, which will be placed in the #3 slot. The current concept uses two interweaved, but incompatible lox site pairs (LoxP and LoxN) in tail-to-head orientation, which leads to excision of one transformation marker. The improved version will use only one 3×P3 promoter, followed by a LoxP site pair in tail-to-tail orientation. This lox site arrangement allows inversion instead of excision. Within the LoxP site pair, two fluorescent protein open reading frames and their respective poly (A) sites are placed in tail-to-tail orientation. Before recombination, only the first fluorescent protein is expressed. After Cre-mediated recombination, there will be individuals that express only the second fluorescent protein. Advantages are (i) shorter overall length of the plasmids, (ii) usage of only one lox site, (iii) no sequence loss during recombination and (iv) the #4 slot is unoccupied now and will carry a FREDDY spacer by default.

- As the #1 and #4 slots are now unoccupied, insulators can be used [211]. Insulators that flank expression cassettes dramatically reduce the enhancing/silencing effect that the surrounding genomic sequence around the insertion locus may have on the expression cassettes of the transgene. Insulators will not be included by default, as in certain experimental approaches, an enhancer-trap pattern is either desired [160] or an interesting by-product which usually cannot be created on purpose, as it occurred in the AGOC {ATub'H2B-mEmerald} #1 subline (Subchapter 6.1.6).
- The ACOS vector concept is a further development of the AGOC vector concept and allows the creation of double homozygous transgenic hybrid lines (Subchapter 3.4). I already elaborated the synergy with the binary GAL4/UAS expression system (Subchapter 3.4.4). However, when the ASOR vector concept is used, a ternary GAL4/UAS system can be built. A triple homozygous transgenic hybrid line can be created that either consist of (i) two driver lines and one reporter line or (ii) one driver line and two reporter lines. In the former case, the fluorescence reporter will show a mixed pattern, in the latter case, two different intracellular structures can be labeled within the same cell populations.
- The AFestForCres vector concept allows the stochastic labeling of cells in an embryo. The transformation-ready vector, which is already designed *in silico*, carries a mCe transformation marker in slot #4. In slot #2 and #3, two expression cassettes will be placed in tail-to-tail orientation, initially expressing either mEmerald-labeled histone 2B subunits or mRuby-labeled histone 2B subunits under control of a spatiotemporal ubiquitous promoter. Similar to the AGOC, ACOS and ASOR vector concepts, the expression cassettes are placed in interweaving, but incompatible lox site pairs. However, one and only one lox site pair has 'stacked', *e.g.* duplicated, triplicated or quadruplicated, lox sites before and behind the expression cassettes. I hypothesize that an arrangement like this will shift the recombination ratio from approximately 1:1 to 1:4 (duplicates on both sides), 1:9 (triplicates on both sides) or 1:16 (quadruplicates on both sides). Currently, there is no data about the effect of 'stacked' lox sides on the recombination ratio.

4.1.4. Outlook III – Biological Questions

Due to the sheer mass of image data that was acquired for insect species for which almost no morphogenetic data was previously available, it is inevitable that novel phenomena are discovered and respective biological questions arise. Within this subchapter, several of these questions are described and substantiated with preliminary imaging data, while additionally, concrete experimental suggestions are provided:

- It has been demonstrated that the extra-embryonic membranes of *Tribolium* – the amnion, which covers the embryo on the ventral side and the serosa, which envelops the embryo completely – have a broad variety of functions. They protect the embryo from desiccation [212], contribute to the immune response when the embryo is confronted with pathogenic microorganisms [105,213] and play an important morphogenetic function during dorsal closure [214]. Due to the vast spatio-temporal reorganization processes of the serosa during the embryonic development – it emerges already during gastrulation, envelops the embryo completely during germband elongation and retraction and forms a complex transient structure, called the dorsal organ, in the middle of dorsal closure, before it is internalized – I hypothesize that the serosa has also a physical compartmentation function to isolate and combat pathogenic microorganisms. The theory is based on the morphogenetic dynamics of the serosa after the rupture of the extra-embryonic membranes during dorsal closure. The serosa turns inside-out and closes the opening nearly completely again during the formation process of the dorsal organ (Figure 4-2). Potential pathogens, which were attached to the former outside of the serosa are now confined to the inside, so that the immune response of the serosa can be maximized. Especially when the dorsal ridge closes, it is of great importance that no pathogens get into contact with the internal, *i.e.* endothelial, tissue. Additionally, the pathogens are moved to the digestion system of the embryo during the internalization process, which is – by design – prepared to combat microorganisms (Figure 4-3). To prove this hypothesis, I suggest the following initial experiments:

- Injection of fluorescent beads into the cavity between the vitelline membrane and the serosa after serosa window closure completed. The respective embryo is monitored via live imaging until the end of dorsal closure. During dorsal closure, the beads become trapped in the dorsal organ.
- Injection and monitoring as described above, but not of fluorescent beads but fluorescently labeled microorganisms, for example DsRed-expression *Escherichia coli* [215] and certain insect pathogenic bacteria [216]. The survival rate in relation to the number of bacteria is determined.
- Injection of fluorescently labeled bacteria as described above, but into embryos in which *zerknüllt 1* is knocked down via parental RNA interference [125,217]. Respective knock-down embryos are viable, but develop no serosa. The amnion emerges on the dorsal side and is solitarily internalized during dorsal closure. Also for these embryos and respective RNA interference control, the survival rate in relation to the number of bacteria should be calculated.

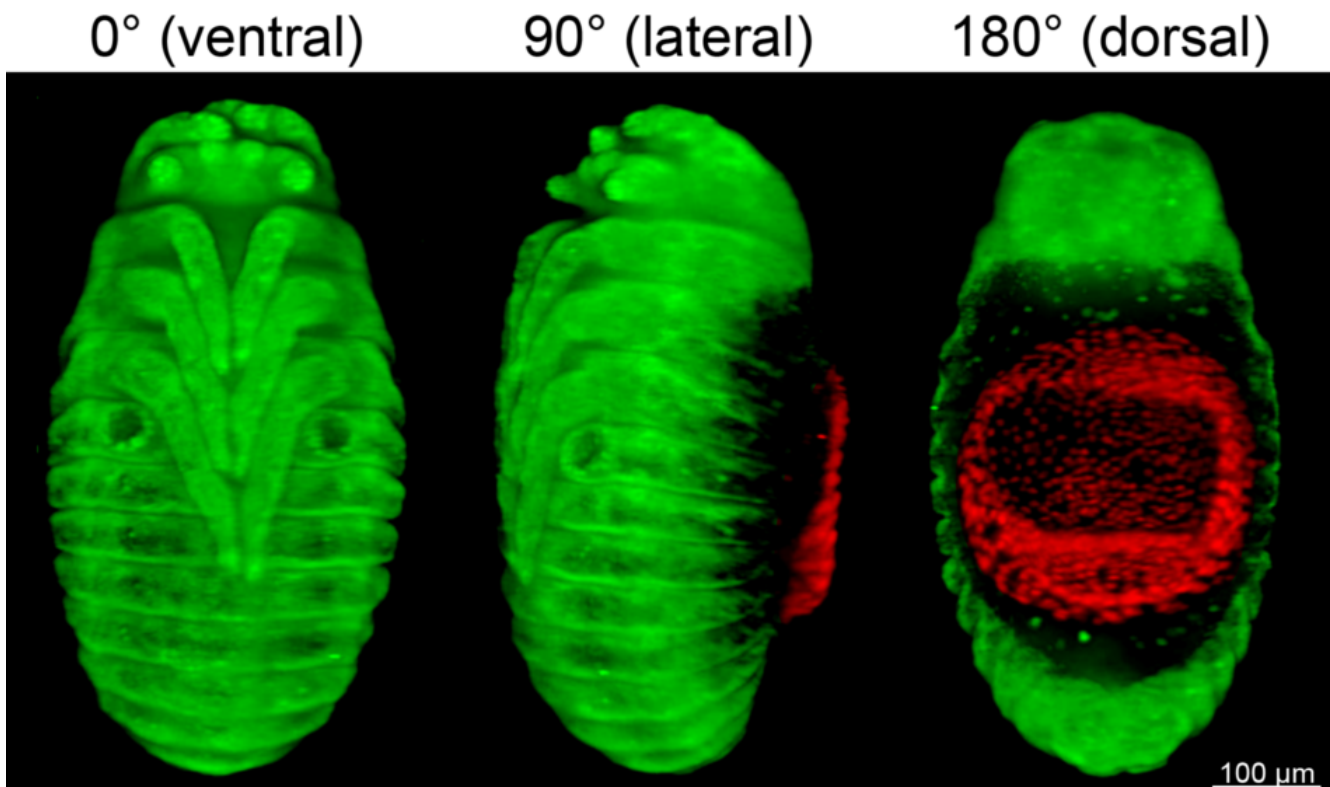
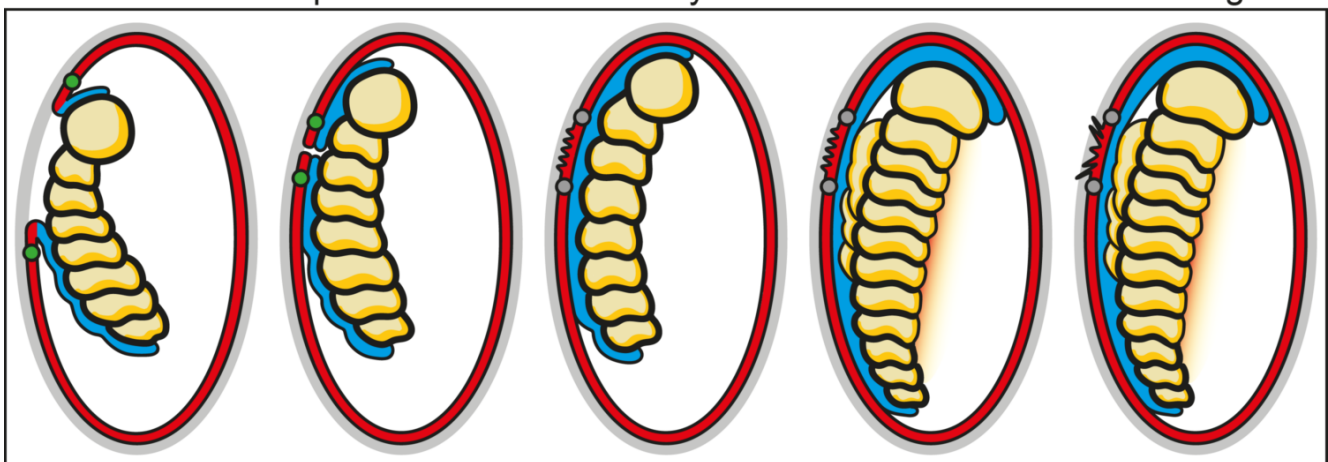


Figure 4-2 – Dorsal organ of *Tribolium castaneum*. The dorsal organ (red) is a transient structure that is formed on the dorsal side of the embryo (green) when the serosa turns inside-out during dorsal closure. Images derive from a registered and fused dataset (Subchapter 3.2) and are false-colored.

- During serosa window closure, which occurs at the end of gastrulation, the *Tribolium* embryo utilizes an actomyosin cable within a certain sub-population of serosa cells to constrict the opening in both extra-embryonic membranes and finally provoke a serosa-amnion inter-tissue separation and a serosa and amnion intra-tissue fusion. I already described the serosa scar, a functional link between serosa window closure and serosa opening (Subchapters 2.2.2 and 6.1.2), which emerges at the point of closure and marks the region where the serosa reopens after germband retraction is completed. I hypothesize that the actomyosin cable is not degraded after gastrulation, but remains quiescent within the respective cells. Later on, when dorsal closure has begun and the serosa has moved across the anterior and posterior poles, the cable is reactivated and used to turn the serosa inside-out and form the dorsal organ (Figure 4-3). To prove this hypothesis, I suggest the following initial experiments:

- Establishment of a custom-made transgenic line that expresses mRuby-labeled myosin under control of either a ubiquitous [180,218] or the serosa-specific *zerknüllt 1* promoter (Subchapters 2.2.7 and 6.2.3) by using the ACOS vector concept (Subchapter 3.4).
- Creation and subsequent live imaging of two hybrid lines by crossing the aforementioned transgenic line against either the AGOC{ATub'LA)-mEmerald} #1 subline, which expresses mEmerald-labeled Lifeact under control of the *alpha-tubulin 1* promoter, or alternatively the AGOC{ATub'H2B-mEmerald} #3 subline, which expresses mEmerald-labeled histone 2B subunits under control of the *alpha-tubulin 1* promoter (Subchapter 6.2.3).
- The hybrid lines are monitored via live imaging until the end of dorsal closure. The first hybrid line allows to observe the actomyosin cable in detail, while the second hybrid line provides information on the cellular context of the actomyosin cable.

inactivation and quiescence of the actomyosin cable until dorsal closure begins



actomyosin cable reactivation and formation of the dorsal organ compartment

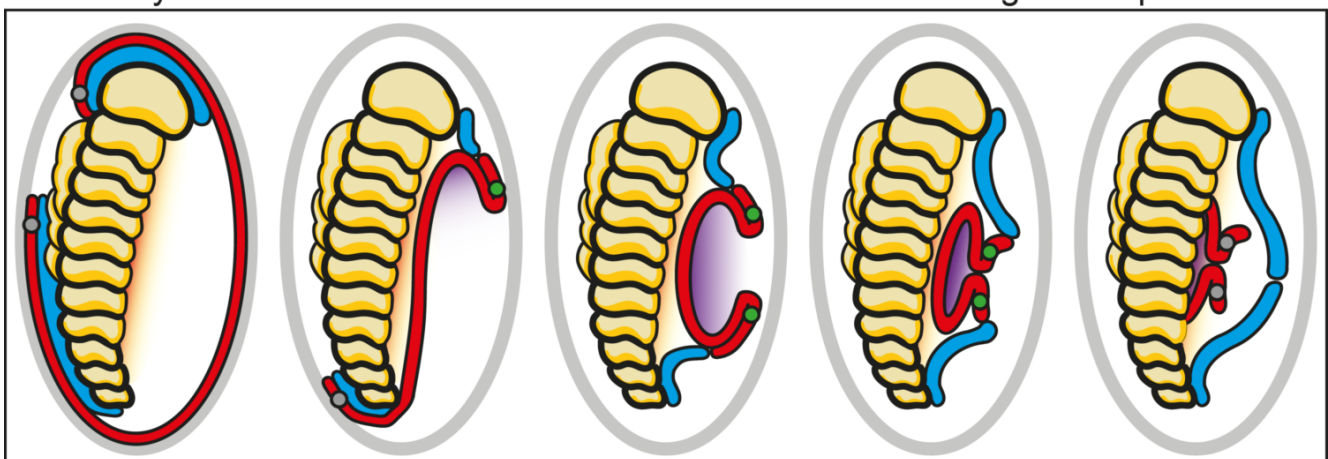


Figure 4-3 – Hypothesized morphogenetic procedure how the activation-quiescence-activation sequence of the actomyosin cable turns the serosa into a physical compartment by forming the dorsal organ. During gastrulation (upper row), an actomyosin cable is used to close the serosa window in a purse-string fashion. This results in a serosa and amnion and inter-tissue separation intra-tissue fusion, leaving the serosa scar behind. Throughout germ band elongation and retraction, the cable remains inactive. At the beginning of dorsal closure, the serosa scar is pulled apart, and the serosa reopens (lower row). Together with the amnion, the serosa is initially dragged over the anterior pole, then over the posterior pole. The actomyosin cable reactivates and turns the serosa inside-out, leading to the formation of the dorsal organ on the dorsal side of the embryo. In consequence, potential pathogenic microorganisms, which gathered on the outside of the serosa are now isolated on the inside within a physical compartment formed by extra-embryonic membranes. At the end of dorsal closure, the compartment is internalized into the digestive system, which is a favorable position to combat pathogens.

- During several independent microscopy experiments, in which *Tribolium* embryos of different transgenic lines were observed, I noticed the formation of a previously undescribed cell population. At the transition from blastoderm formation to gastrulation, the superficially located cells rearrange. A certain fraction spreads into a dorsally tilted anterior cap, which represents the future extra-embryonic membranes. The remaining cells cluster into a ventrally tilted posterior cap, which represents the future germband. While the condensing germband sinks into the yolk, the presumptive serosa extends and migrates over the germband. Thereby, the amnion forms at the serosa-germband intersection, which results in a serosa-amnion-germband tissue tri-layer [103,123,219]. During this process, a very small number of blastoderm cells (estimated 30 to 50) around the serosa-germband intersection ‘dive’ into the yolk and migrate away from the germband, but remain in close proximity to the surface, directly under the presumptive serosa cells. After serosa window closure, when the head lobes curl around the anterior pole, these cells move in concert with the germband and loosely cluster at the dorsal side of the embryo, right below the serosa.

The formation process was first witnessed during the analysis of a long-term fluorescence live imaging dataset from a hemizygous embryo from the FNL line (Subchapter 6.1.5). The recoding was performed with high temporal resolution (time interval 00:06 h), which allows the identification of progenitor nuclei during blastoderm formation, shortly before they proceed through the 12th synchronous proliferation cycle. The behavior of respective candidates was followed for several hours until the end of gastrulation (Figure 4-4). It can be excluded that these cells are vitellophages (Box 4-1) and therefore, they must have a different function during development. These diving cells could be detected also during later stages of development. Imaging of a double hemizygous hybrid embryo, in which the nuclei and membranes are fluorescently labeled, at the transition from germband elongation to germband retraction confirmed the presence of these diving cells, which now have a ‘cushion-like’ appearance, right below the serosa (Figure 4-5). Furthermore, data acquired from a double hemizygous hybrid embryo at the same developmental stage, in which the nuclei are fluorescently labeled and that expresses a fluorescent protein-labeled nanobody against proliferation cell nuclear antigen (PCNA), roughly outlines the cellular and subcellular morphology of these cells and their developmental context (Figure 4-6).

Based on the available information, I hypothesize that these cells have a biomechanical function during development. Serosa window closure, which occurs at the transition from gastrulation to germband elongation, leads to a separation of serosa and amnion. While the serosa remains attached to the inner side of the vitelline membrane, the amnion is linked to the germband and both sink into the yolk. However, the plethora of available microscopy data shows that the germband does not move freely through the yolk – its ventral side always remains in close proximity with the ventral serosa.

Box 4-1 – Vitellophages in the embryonic development of insects

Besides the cells that form the extra-embryonic membranes and the germband, it is well known that certain insect species, such as *Drosophila* [220,221] and *Tribolium* [123,222], transiently generate a small number of vitellophages, a subpopulation of cells that play an important role for yolk degradation. They are also known as yolk nuclei or yolk energids. During blastoderm formation, when the nuclei migrate to the surface, several cells remain in the interior. For several mitotic circles, they still divide in parallel with the superficial cells, but become polyploid at the beginning of gastrulation. Later on, they are internalized into the digestive system during dorsal closure. They differ from the newly discovered cell population in two important aspects: vitellophages (i) do not leave the interior during germband formation, (ii) have much larger nuclei (FIG, middle right panel) and (iii) move freely through the yolk and are thus only found occasionally around the surface region.

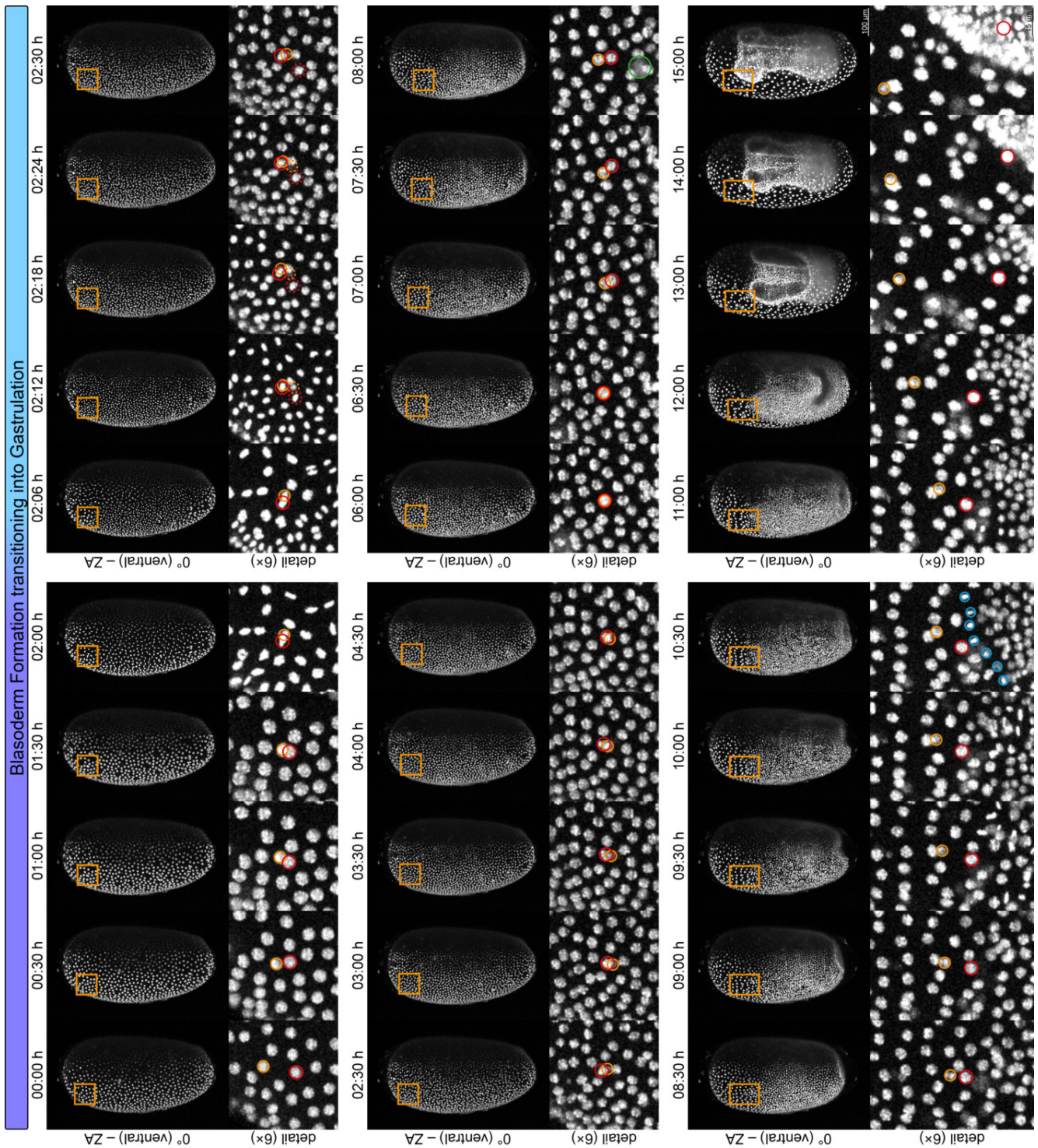


Figure 4-4 – Movement and behavior of diving cells from the end of blastoderm formation to the end of gastrulation. After the 11th proliferation wave, a nucleus of a diving cell (orange circle) and a prospective serosa nucleus (red circle) establish contact, since no cell membranes have formed yet (upper left panel). During the 12th mitotic proliferation wave, the diving nucleus and the associated serosa nucleus divide in close proximity. Only one of both daughter nuclei stays attached to the other nucleus, the remaining serosa nucleus (blue dashed circle) becomes independent, while the remaining diving nucleus (red dashed circle) seems to degrade (upper right panel). After cell division, the contact is reestablished (middle left panel). Gastrulation begins and both nuclei diverge. For a short time, a vitellophage (green circle) can be seen close to the surface (middle right panel). The nuclei reposition while the anterior amniotic cells (blue circles) emerge (lower left panel). The diving nucleus migrates anterior below the serosa, while the serosa nucleus moves posterior on top of the germband (lower right panel). Figure and/or figure description fully and/or partially reproduced from Strobl & Stelzer 2016, #4 in Publication Table 2.

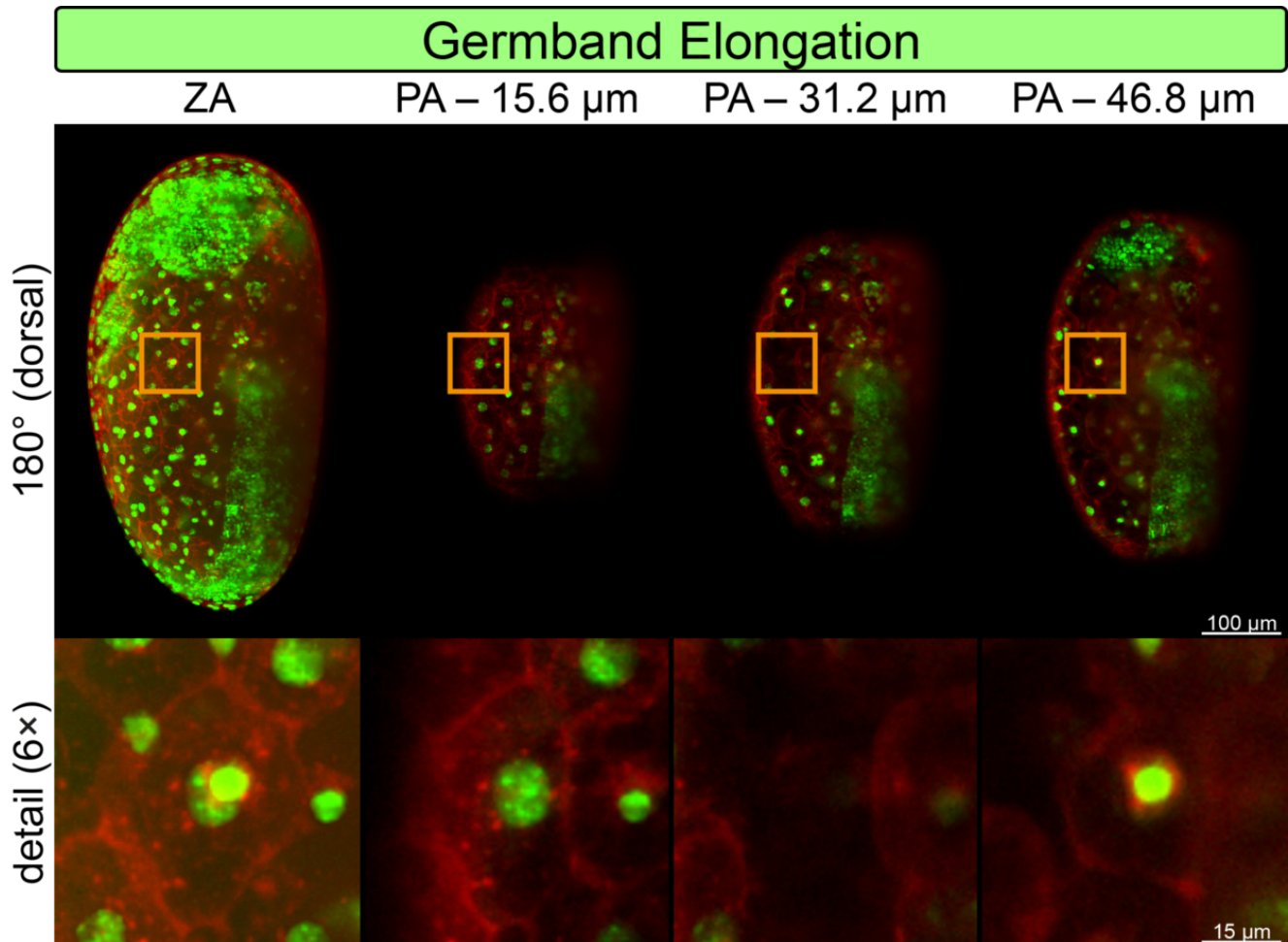


Figure 4-5 – Extra-embryonal cell types at the dorsal side of the embryo during the transition from germband elongation to germband retraction. An AGOC{ATub^{H2B}-mEmerald} #4 × ACOS{Ub^{O(MEM)}-mRuby} #2 double hemizygous hybrid embryo is shown in the merged channel as a Z maximum projection and as single planes in three different depths along the 180° (dorsal) orientation. The embryo expresses mEmerald-labeled histone 2B subunits under control of the *alpha tubulin 1* promoter (green) and mRuby-labeled *GAP43* membrane anchor (red) under control of the polyubiquitin promoter. During this developmental stage, two different extra-embryonal cell types are found on the dorsal side of the embryo: Firstly, the superficial serosa cells, which are organized as a single cell layer, are characterized by their rectangular shape and the large nuclei with their moderate and inhomogeneous signal (second column, detail image). Secondly, below these serosa cells, a previously undescribed cell population is found, which are not organized as a single, membrane-like cell layer. These cells have a cushion-like appearance and are clustered, but most of these cells appear to partially border the circumfluent yolk. Their nuclei are smaller and exhibit a strong, uniform signal (fourth column, detail image). The AGOC{ATub^{H2B}-mEmerald} #4 transgene was inherited paternally, the ACOS{Ub^{O(MEM)}-mRuby} #2 transgene maternally.

I assume that the diving cells function as hydroskeletal-like elements. They loosely envelop the yolk in a net-like fashion while staying in contact with the dorsal serosa and thus keep the germband in place during germband elongation and germband retraction. Later on, during dorsal closure, the diving cells are, together with the serosa, the amnion and the remaining yolk, internalized into the digestive system. The following experiments should be considered:

- After establishing a suitable clearing technique for insect eggs (Subchapters 4.1.6 and 5.4), embryos at multiple different developmental stages are cleared. Subsequently, they should be imaged with a multitude of different labels to determine the number, morphology and relative locations of the diving nuclei and describe their behavior during gastrulation and germband elongation.
- Several appropriately labeled embryos should be imaged for long periods of time with high spatiotemporal resolution (voxel size around $0.3 \times 0.3 \times 1.2 \mu\text{m}$, interval of 00:03 h) along multiple directions by using a double-sided light sheet-based fluorescence microscope. Imaging will begin after the 9th synchronous proliferation cycle until the embryo hatches and the image data are subsequently registered and fused (Subchapters 3.2 and 5.5). This allows to quantitatively describe the spatiotemporal differentiation and migration pattern of the diving cells.

- Creation of a transgenic *zerknüllt 1* knock-out line, in which parts or the whole *zerknüllt 1* gene is replaced by an AGOC vector concept-based element (Subchapter 2.2.7). The knock-out line should be homozygously viable, since knock-down of *zerknüllt 1* via parental RNAi results in embryos that do not generate a serosa, but develop properly as long as they stay in atmosphere with 60% to 80% relative humidity [212]. In conjunction with the ACOS vector system (Subchapter 3.4), this allows the creation of a double homozygous transgenic hybrid line in which the cell migration and proliferation dynamics of *zerknüllt 1* knock-out embryos can be analyzed to see if deletion of this gene also leads to a respecification of the diving cells.

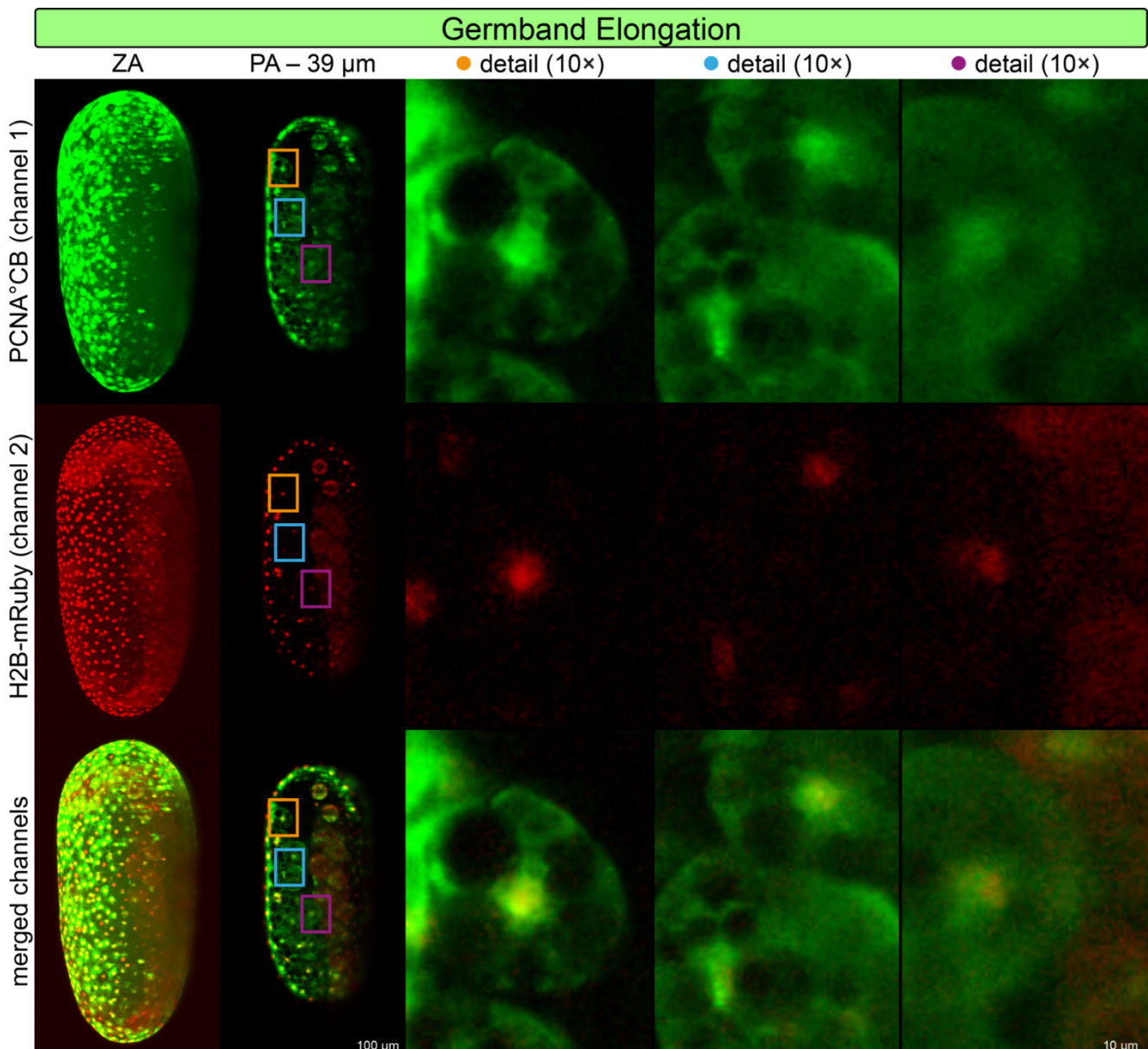


Figure 4-6 – Cellular and subcellular morphology of the diving cells during the transition from germband elongation to germband retraction. An AGOC{Ub°PCNA°CB-mEmerald} #2 × ACOS{ATub°H2B-mRuby} #1 double hemizygous hybrid embryo is shown in the green, red and merged channel as a Z maximum projection and as a single plane along the 270° (lateral) orientation. The embryo expresses mEmerald-labeled α -PCNA nanobodies under control of the *polyubiquitin* promoter (green) and mRuby-labeled histone 2B subunits (red) under control of the *alpha tubulin 1* promoter. Although the α -PCNA chromobodies do not localize as intended, the obtained pattern can be used to characterize the cellular and subcellular morphology of the diving cells (detail images). They have a round shape and contain several non-fluorescent, vacuole-like regions. The nucleus is usually in the center of the cell and, due to the size and signal strength, most probably polyploid. The cells have a cushion-like appearance and are attached or in close proximity to the serosa cells (third column) and form a large, but slightly loose cluster (third and fourth column). Most of them are in contact with the yolk, and the laterally located cells appear to be also connected to the germband (fifth column). The mEmerald-labeled α -PCNA nanobody-expressing transgenic *Tribolium* line was created by Henrik Tonner (Subchapter 5.6), the AGOC{Ub°PCNA°CB-mEmerald} #2 transgene was inherited paternally and the ACOS{ATub°H2B-mRuby} #1 transgene maternally.

4.1.5. Outlook IV – Universalizing AGameOfClones

The AGOC vector concept manuscript (Subchapter 6.2.3) describes the genetic architecture and proves the functionality of the AGOC vector concept in the emerging insect model organism *Tribolium castaneum*. Although the concept was initially developed for arthropods, it should work in all diploid species in which the Cre/Lox system has been proven functional. Greatly attractive are the two established vertebrate model organisms mouse (*Mus musculus*) and zebrafish (*Danio rerio*). If the vector concept is adapted to these species, it would facilitate work in many laboratories, especially these with large numbers of animals.

For mouse, eye-specific transformation markers, which use the *Alpha-A-Crystallin* promoter, have been used already [223], but are not the optimal choice due to the different habitus and the eye pigmentation in non-albino mice. Thus, I recommend to use a promoter that is specific for epidermal cell layers in either the tail or alternatively the ears, as these tissues are not as heavily covered by hair. Additionally, the promoter should already be active as early as possible during the embryonic development, so that homozygous transgenic mice can be identified already during this stage. A promising candidate is the promoter from the *Spr2b* gene, which encodes the small proline-rich protein 2B. Its expression strength in adult mice is approximately sixty times higher in the tail than in the dorsal anagen and dorsal telogen skin, but the embryonal expression pattern and strength is not known [224]. Fur color markers such as the tyrosinase minigene are an alternative to fluorescence-based markers for mouse [225].

For zebrafish, it might be reasonably assumed that the 3×P3 promoter works properly, which is essential for both eye-specific transformation markers in the AGameOfClones vector concept. I therefore suggest the following modifications:

- The current open reading frames for mOrange and mCherry are codon-optimized for arthropods and should be exchanged for variants that are codon-optimized for vertebrates.
- The transposon system has to be changed from piggyBac to a system that works reliably in zebrafish, for example Tol2 or Sleeping Beauty [226].
- Available Cre-expressing transgenic zebrafish lines [227] have to be tested whether they can be properly used to drive recombination in the adapted AGameOfClones vector concept.

Adaption of the AGOC vector concept to plant species is also possible. It has been shown that the Cre/Lox system works reliably in the thale cress *Arabidopsis thaliana* [228]. Theoretically, the vector concept can also be adapted to species with a higher degree of ploidy, for example hexaploid wheat species (*e.g. Triticum aestivum*), that have huge economical relevance. However, the transformation marker setup has to be enlarged so that six different phenotypes can be obtained after recombination. For this, at least three different lox site pairs have to be used (*e.g. LoxP, LoxN and Lox2272*).

4.1.6. Outlook V – Side Projects

This subchapter describes three side projects that do not fit into any other outlook category. They usually have a rather moderate scope and can thus be handed out to Bachelor and Master students.

- One of the major limitations in fluorescence microscopy is the penetration depth into deeper tissue regions when large three-dimensional specimens such as insect embryos are observed. Due to differences in the refractive indices between biological structures and the surrounding imaging media, the signal becomes blurry and the resolution decreases when internal cellular structures are imaged. Current approaches to address this issue include: (i) creation of specific mutant lines that have a higher degree of transparency, as shown for *Drosophila* [229], (ii) usage of near-infrared fluorescent proteins such as iRFP670 [182] and (iii) working with an adaptive microscopy setup that can partially compensate refractive index mismatches [230]. Another approach, which requires the fixation of the specimen, is optical tissue clearing [231–233]. The principle of most established clearing techniques is identical – the water within a fixed and

permeabilized specimen is replaced by an organic solution such as benzyl alcohol-benzyl benzoate with a refractive index similar to the average refractive index of the residual tissue. To my knowledge, there are currently no studies that have dealt with adapting clearing protocols to insect embryos. Selina Klees, a Bachelor student of mine, has investigated the effect of the SeeDP fructose-based clearing method [234] on *Tribolium* embryos during gastrulation and germband elongation (Subchapter 5.4). Her results show that clearing techniques have a huge potential for insect developmental biology. For *Tribolium* embryos, which have a lateral width of 300 to 330 μm , signal from the surface that opposes the detection objective could be detected and nuclei in inner regions were found that are impossible to spot in non-cleared specimen. However, the scope of a Bachelor project is limited, and a more comprehensive evaluation of clearing techniques is necessary. I suggest the following workflow:

- Comparison of several clearing techniques such as 3DISCO [235], iDISCO [236], FocusClear [237], ClearT [238], CUBIC [239] and CLARITY [240] for multiple developmental stages of *Tribolium* embryos. The stages should be widely spread throughout the whole embryonic development process, ideally covering all six embryogenetic events.
- Comprehensive quantitative evaluation of (i) the increase in depth penetration and (ii) the magnitude of potential issues such as fluorescence quenching and alteration in tissue morphology, *i.e.* expansion or shrinkage.
- Establishment of an ease-of-use protocol for light sheet-based fluorescence microscopes that allows at least medium-throughput, *i.e.* twenty to forty embryos per week.
- Quick assessment if the protocols established for and conclusions drawn from the *Tribolium* experiments are also applicable to other insect species such as *Ceratitis* or *Gryllus*.
- Discrimination between female and male individuals in *Tribolium* is a tedious task. The gender cannot be specified at all by the phenotype during the embryonic and larval stages. During the pupal stage, the female pupae develop urogomphi, *i.e.* a pair of short spines, on the ventral side of the last abdominal segment. During the adult stage, male beetles have ‘sex patches’ on the femur of the first leg pair. In both stages, the gender can only be determined with the aid of a stereo microscope. It would be convenient to establish a genetic marker that allows to determine the gender (i) during the larval stage and (ii) without the help of a stereo microscope. A convenient approach would be to change the cuticle color by creating transgenic males that carry an expression cassette to alter the enzymatic equilibrium of the cuticle pigmentation pathway. Such a procedure has already been shown in the silkworm *Bombyx mori* – overexpression of endogenous *aaNAT* (Arylalkylamine-N-acetyl transferase) or *ebony* (*N*-Beta-alanyldopamine synthase) lightens the pigmentation in a black-striped background strain strongly [241]. If a similar expression cassette is inserted into the Y allosome of *Tribolium*, only male individuals would be transgenic and show a change in their cuticle color while the female individuals would remain non-transgenic and show the wild-type phenotype.

The cuticle tanning pathway in *Tribolium* is well understood: Within the epidermal cells, the proteinogenic amino acid Tyrosine is converted to four pigments: (i) DOPA-melanin, (ii) Dopamine-melanin, (iii) NADA-pigment and (iv) NBAD-pigment [242–244]. The expression equilibrium of enzymes involved in the conversion process results in a certain ratio of pigments. Thus, any shift, for example via overexpression or knock-down, should result in a deviant ratio of pigments and therefore in a different phenotype – usually lighter or darker cuticles in the larval, pupal and/or adult stages. It has already been shown that RNA interference-based knock-down of *ADC* (Aspartate 1-decarboxylase) [242] and *aaNAT* [244] result in a darker cuticle, while knock-down of *DDC* (3,4-dihydroxyphenylalanine) results in a lighter cuticle [242]. Two more promising candidate genes, *tan* and *ebony*, have not been investigated in *Tribolium* via knock-down yet (Figure 4-7).

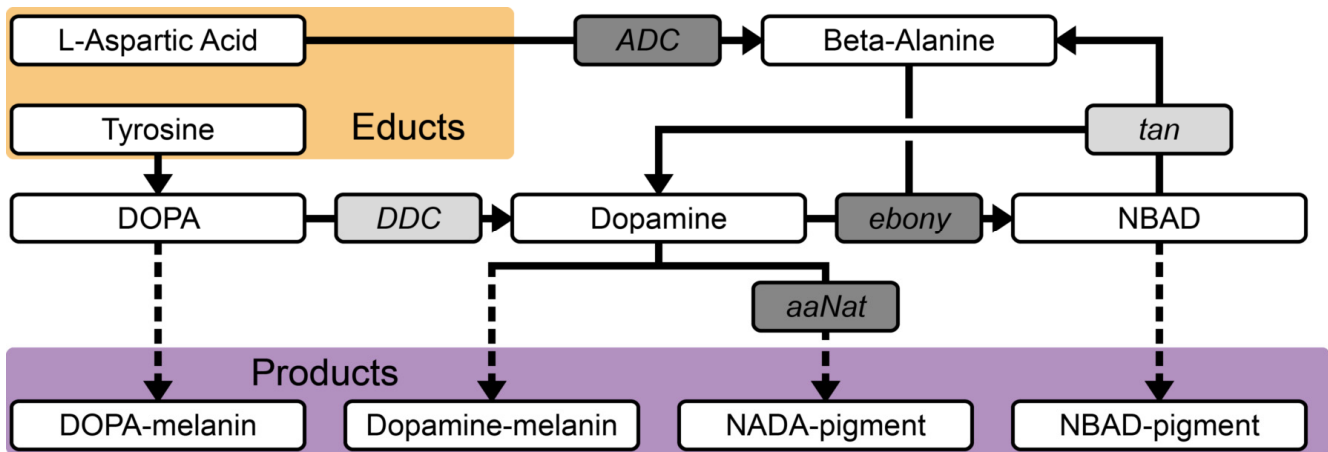


Figure 4-7 – Cuticle pigmentation metabolic pathway in *Tribolium*. Candidates that are expected to lighten or darken the cuticle when overexpressed are shown in light or dark gray, respectively. Dashed lines indicate that several more processes are necessary to reach the indicated product.

I already identified, extracted and verified the sequence integrity of the open reading frame sequence of these five candidates (Table 4-3, second column) and suggest the following workflow to create a transgenic line which allows gender determination without a stereo microscope:

- Creation of five transformation vectors that contain an expression cassette for each of the five candidates under control of a ubiquitous promoter [180,218]. With these vectors, transgenic *Tribolium* lines are established and any phenotypical change is characterized (Table 4-3, fourth column).
- Insertion of respective expression cassettes onto dedicated location of the Y allosome via homology-directed repair or non-homologous end joining by using the CRISPR/Cas9-based genome editing approach, which has recently been established for *Tribolium* [245,246].

Table 4-3 – Candidate genes to influence cuticle pigmentation in *Tribolium*. ORF, open reading frame.

candidate	ORF size	knock-down phenotype	overexpression phenotype	comment
ADC	1,623 bp	darker [242,247]	lighter (expected)	may affect mechanical properties of the cuticle [242]
aaNAT	756 bp	darker [244]	lighter [241]	may affect exoskeletal surface [244]
DDC	1,428 bp	lighter [242]	darker (expected)	-
tan	1,158 bp	lighter (expected)	darker (expected)	-
ebony	2,583 bp	darker (expected)	lighter [241]	-

- With the advent of light sheet-based fluorescence microscopy, non-invasive long-term live imaging was added to the experimental toolbox of developmental biology, which contributes significantly to the transition from on-demand to systematic data acquisition (Subchapters 4.2.5 and 6.1.7). Data obtained from live imaging assays has the potential to provide more profound insights compared to ‘morphological snapshots’, *i.e.* traditional fixation-and-staining microscopy approaches, but the data are only reliable when stringent quality control is conducted. About a little more than one decade after its invention [67], light sheet technology has boundlessly radiated and is about to become standard in developmental biology laboratories. Besides the establishment of standard operation procedures on how to calibrate the microscope and mount specimen (Subchapter 6.1.4), similar standards are also necessary for the quality control in live imaging assays. Within the following list, I propose different quality control steps for the most important application of fluorescence live imaging, the usage of custom-made transgenic lines to record wild-type development or aberrational phenotypes. The considerations primarily concern *Tribolium*, but can be easily adapted to other model organisms.

- A major factor in fluorescence live imaging is that all working cultures, either background strains for germline transformation or transgenic lines for live imaging are healthy, well-fed and not too old: Firstly, they should be free of germs, protozoans, fungi and pathogenic metazoans such as mites. Secondly, the growth medium should be exchanged regularly, ideally before any obvious signs of pollution become evident. Thirdly, it is also necessary to replace the working cultures with progeny cultures on a regular schedule. For *Tribolium*, this is typically done after six to eight weeks. It is advantageous if profound knowledge about the background strain is available.
- Newly established custom-made transgenic lines should be thoroughly characterized before they are used in any important experiment. For transgenic lines that are created with transposase-based systems and thus have a semi-random integration site and eventually multiple inserts, I suggest the following preliminary checks: (i) determination of the insert number via test crossing (Subchapter 6.2.3), (ii) a homozygous viability cross (Subchapter 6.2.3), (iii) determination of the genomic location where the transgene has inserted, (iv) documentation of the fluorescence and morphological phenotype for a standardized developmental stage, for example first instar larva and (v) a comparison of the total embryonic development time of the transgenic line and the background strain (Subchapter 6.1.4). The AGameOfClones vector concept (Subchapter 2.2.7) allows to determine homozygous viability without the need of a homozygous viability cross.
- For transgenic lines that are created with transposase-based transformation systems and therefore have semi-random integration sites, it is strongly recommended to work with at least two different sublines, especially if a previously uncharacterized promoter is used. By comparing the expression pattern of both sublines, it can be evaluated if any enhancer trap effect occurred or if the expression is reasonably similar to the expectations. Such an approach also allows to select the subline with the appropriate expression strength. Additionally, I suggest to evaluate if heterozygous and homozygous transgenic individuals have a different phenotype.
- One of the most important factors is that the genotype of the imaged embryo is known. Ideally, this is achieved by working with homozygous imaging cultures that produce only homozygous progeny. There are also several other imaging culture setups that result in progeny with known phenotypes, but some setups should be avoided, for example working with an imaging culture that contains heterozygous and homozygous individuals, as the genotype of any fluorescence embryo is not automatically evident. The AGOC vector concept (Subchapter 2.2.7) allows the systematic creation of homozygous transgenic lines. This argument is also crucial for cultures that produce hybrid lines by bringing two transgenes together – the genotype for both transgenes should be known. The ACOS vector concept (Subchapter 3.4) allows the systematic creation of double homozygous transgenic lines.
- Whenever live imaging is performed, I suggest to run non-imaged controls in parallel ideally deriving from the same imaging culture and embryo collection. The incubation condition of these controls are synchronized to the imaged embryo. Any significant delay between the development time of the imaged and controls indicates that the laser irradiation was too high (Subchapter 6.1.4). This control is important for assays that aim to characterize wild-type development, but also for experiments that induce developmental aberrations. For the latter case, also several other controls are necessary (see below).
- Many insights in gene function or morphogenesis can only be obtained by interfering with the wild-type processes. The most frequently used approaches to provoke developmental aberrations are (i) gene knock-down via embryonic [103,248] or parental [249,250] RNA interference, (ii) usage of recessive embryonic lethal mutant lines [140,251–254] and (iii) applications of extrinsic factors [255,256]. For each experimental strategy, an individual concept for the controls is necessary (Subchapter 6.1.6).

- Fluorescence live imaging assays always affect the specimen, but they can be considered non-invasive when the imaged embryo is carefully retrieved from the microscope after imaging, hatches and develops into a healthy and fertile adult (Subchapters 6.1.4 and 6.1.6). Especially the fertility control is crucial, as sterility is one of the first deficiencies that emerge when the sample is influenced detrimental extrinsic factors. As an additional control, it might also be convenient to evaluate the fertility of the progeny.
- Especially for studies that provide systematically acquired microscopy data as a resource for the community, comprehensive documentation of the meta data is inevitable: they (i) outline the experimental context, (ii) are part of the quality control, (iii) ensure reproducibility, (iii) allow proper comparison of datasets and (v) contain values that are necessary for dedicated post-processing approaches. The meta data can be subdivided into three sections: Firstly, it should provide essential background information on the specimen. This includes information on the species, the respective line and/or subline, the genotype, the imaging culture as well as the embryo collection and incubation procedure. Secondly, preparation, mounting and recording should be outlined shortly. Major elements are the mounting method and the microscope setup. Additionally, specifications of optical key components, such as the objective, lenses and filters should be stated in detail. Thirdly, primary and secondary imaging parameters should be listed for all degrees of freedom. Primary imaging parameters should rather be given as absolute instead of relative values, for example for laser power in watt instead of as a proportion of the maximum power. For convenience, primary imaging parameters, *e.g.* the number of planes and the Z spacing, can be used to calculate secondary imaging parameters, *e.g.* the Z distance.
- Typically, raw imaging data need processing before they are ‘print-ready’. The spectrum of processing options is large – ranging from adjustments in brightness and contrast over filtering or photo-bleaching corrections to more complex approaches such as deconvolution – and in some cases, these processing options need to be queued. It is therefore essential to (i) keep a copy of the raw image data and (ii) carefully document all processing steps that have been performed.

4.2. Perspective

4.2.1. The Primary Level – Developmental Biology

Insect developmental biologists are interested in the genetic and morphogenetic processes how a single copy of the genome utilizes the information and resources to develop into a fully functional organism that is able to gather energy, to defend itself against environmental threats and to reproduce (Subchapter 2.1.1). Within the next paragraphs, I outline my thoughts and expectations on how developmental biology – and not only the insect community in particular – benefits from advanced fluorescence microscopy techniques. Each of the arguments discussed below thereby fits into one or more of three elementary experimental categories stated already in two of my publications (Subchapters 6.1.4 and 6.1.5): (i) analysis of wild-type embryogenesis to define ‘normal’ development, (ii) induction of aberrations to investigate the function of genes, proteins and other factors as well as to localize the developmental ‘robustness’ window or (iii) quantitative analysis of cellular dynamics to establish bio-mathematical models:

- **The ‘ground truth’ argument:** Ideally, sufficient information about the ‘normal’ development of a given species should be available before aberration-inducing studies are performed. Since this is not always the case, most studies compare their aberrational phenotype to controls performed within the same spatiotemporal, and thus contextually strongly limited, frame. Countless studies show only a ‘spatial snippet’ instead of the whole embryo and a ‘morphologic snapshot’ instead of a time series. Thus, the broader morphogenetic context is missing. This immensely complicates subsequent analyses and interpretations. For example, it has been well known for more than a decade that knock-down of *zerknüllt 1* in *Tribolium* via parental RNA interference leads to a loss of the serosa [103,125,213,214,217,257–259], but the embryos develop properly as long as the relative humidity does not drop below a certain level [212]. However, even until today,

the moment of manifestation and morphogenetic course of the aberration remain unknown, since respective embryos were never imaged during the first two embryogenetic events, *i.e.* blastoderm formation and gastrulation (Subchapter 2.2.2). This argument is related to the more generalized considerations about light sheet-based fluorescence microscopy and the transition from on-demand to systematic data acquisition (Subchapter 4.2.5).

- **The ‘paired correlations’ argument:** The tissue-and-organ level is of particular interest in developmental biology, since research on differentiation, growth and function of ‘higher order biological units’ bridges the gap between the *in toto* and the cellular level (Subchapter 2.1.1). However, imaging assays based on fixed samples suffer from issues when quantitative correlations over a certain developmental period should be done. For example, if the growth of a certain organ should be analyzed, a statistically significant number of embryos have to be fixed at two time point since only one ‘morphologic snapshot’ can be taken of each individual. Consequently, all correlations will be non-paired and are thus affected by natural plasticity, which occurs even under similar rearing conditions and in genetically quite homogenous populations [260]. Usually, quantifications based on non-paired correlations are affected by large standard deviations and thus complicate the analytical process. Long-term fluorescence live imaging has the particularly elegant advantage that the same developing individual can be imaged at multiple time points [261]. Thus, statistical analysis and subsequent interpretation can be based on paired correlations, which strongly increases the sensitivity of the imaging assay.
- **The ‘standardization’ argument:** As already stated above, an extensive description of ‘normal’ development is essential for the proper characterization of aberrational phenotypes. For scientific communities that are associated with specific species, it is convenient to establish a universally accepted integrative framework, *i.e.* a comprehensive and standardized staging system, before extensive morphogenetic studies are performed. Such systems are readily available for established model organisms, *e.g.* mouse [262–265], zebrafish [266] and *Drosophila* [33,267] and considered as text book knowledge. They are frequently used without referencing original publications. The level of detail is very high, which usually results from years of cumbersome work. For the *Drosophila* standard – ‘The Embryonic Development of *Drosophila melanogaster*’ [33] – more than 400 embryos had been fixed, stained, manually sectioned and the slices were separately photographed and annotated. Many staging systems are also available for emerging and exotic insect model organisms (Table 2-2), but their scope is typically quite limited – the invested manpower is kept on a mediocre level since the ‘scientific impact’ is generally considered low and the studies are rated as ‘too descriptive’.

Compared to previous studies, in which primarily classical fixation-based techniques were used (Table 2-2, fourth column), light sheet-based fluorescence microscopy allows live imaging of the entire embryonic development process. It will, therefore, lead to a renaissance of staging system studies: Firstly, the ratio between the amount of image data and invested resources is reasonable – a comprehensive staging system can be established with only moderate experimental effort. Secondly, the quintessence of the ‘paired correlation’ argument, as discussed above, also applies to studies that aim to establish staging systems – the inconvenient effects of phenotypic plasticity on quantitative evaluation are minimized. Thirdly, live imaging facilitates the calculation of temporal values and the respective standard deviations – beginning, duration and end of all stages are precisely calculated and averaging is only necessary between the datasets.

During my PhD project, I established the first staging system for *Ceratitis* (Subchapter 6.2.5). My study – as far as I know the first staging system employing fluorescence live imaging – is based on nine long-term live imaging datasets and was conceived with a much larger scope compared to previous studies on other emerging insect model organisms (Table 2-2). I assume that my work will be used as an integrative framework for many *Ceratitis*-associated studies – not only for developmental biology but also agricultural-related research – but also serves as a template for other studies that aim to employ a staging system on fluorescence live imaging data.

However, I still did not exploit the full potential that can be put into staging system studies, partially as a result of ongoing technological challenges, *e.g.* the limited penetration depth, and partially as a consequence of the manpower that I invested into this part of my PhD project. For future staging system studies that will be based on fluorescence live imaging, also with regard to the comparative approach (Subchapter 4.2.2), I suggest the following assay types:

- Long-term fluorescence live imaging of functional transgenic hybrid lines with multiple labels should be considered. Other standards, *e.g.* membrane and cytoskeletal labels (Box 2-4), provide information that cannot be obtained when only nuclear labeling is available. Additionally, transgenic reporter lines can be used to analyze specific processes in detail.
- The long-term imaging assays should be complemented by a non-fluorescence imaging technique, for example transmission light microscopy or optical tomography [268] to obtain additional structural information that can be used as a spatiotemporal frame for the fluorescence data.
- For stages of particular interest, which are determined by considering the live imaging data, embryos should be fixed and optically cleared so that also the inner regions can be captured properly. This also allows the usage of dyes or antibodies to stain structures for which no appropriate transgenic line is available.
- Optionally, an automated staging program based on machine learning would be useful to remove the manual and thus partially arbitrary component from the data analysis workflow.
- **The ‘increasing horizon’ argument:** Only long-term fluorescence live imaging allows the identification of functional links between processes that are temporally separated. Developing embryos constantly change their three-dimensional morphology and thus transit many complex intermediate stages which may have no other purpose except for triggering downstream processes. This *modus operandi* is commonly found throughout metazoan development and is, in many cases, associated with apoptosis [269]. For example, male zygotes of *Caenorhabditis* give rise to a total of 1,178 cells, but 147 of these cells undergo apoptosis, so that male adults only have 1,031 cells. Another example that does not involve apoptosis is the formation of the serosa scar during *Tribolium* embryogenesis, where serosa window closure during gastrulation marks the spot where the serosa opens during dorsal closure (Subchapters 2.2.2 and 6.1.2). Thus, it can be reasonably assumed that essential but temporary interactions occur that cannot be reconstructed by considering only the later stages of development. Instead, the actual morphogenetic processes have to be captured to understand the whole principle. Long-term fluorescence live imaging is not only a powerful approach to discover such links during wild-type development, but also when aberrations are induced, *e.g.* via the application of extrinsic factors or gene knock-down, since manipulative procedures may have multiple, partially non-obvious but causally connected effects.
- **The ‘self-containment’ argument:** In developmental biology, one of the convenient advantages of light sheet-based fluorescence microscopy is that up to four orders of spatial magnitude, *i.e.* from the millimeter to the micrometer range, can be covered simultaneously (Table 2-3). Thus, it is possible to investigate the development of whole insect embryos, *i.e.* ‘closed biological systems’ (Box 2-4), on the *in toto* level by analyzing individual cells, *i.e.* their ‘smallest functional biological units’, on the tissue-and-organ, cellular and subcellular levels (Subchapter 2.1.1). Consequently, conservation laws, *i.e.* energy and mass, can be used to describe the dynamics and ultimately the mechanics of complex morphogenetic processes and establish physical-mathematical models for the biophysical behavior of single cells and certain cluster of cells as part of a developing multicellular organism.

Box 4-2 – Insect embryos as ‘closed biological systems’ on the *in toto* level

In physical sciences, the subset that is chosen for analysis is defined as the ‘system’ while everything else is regarded as the ‘environment’ and, for reasons of simplification, partially or completely ignored. While ‘isolated systems’ are purely hypothetical setups that do not allow any type of transfer, *e.g.* not even energy, ‘closed systems’ are experimental setups that do not allow certain types of transfers, *e.g.* mass, into or out of the system. One of the major advantages of these systems is that conservation laws can be applied.

Abstractly, insect embryos – from the moment of fertilization to the point of hatching – within a thermal reservoir can be considered as ‘closed systems’ on the *in toto* level (Table 2-3). In strong contrast to mammals, embryonic development of egg-laying species is a self-contained process: resources and energy are provided only once at the beginning, the exchange of particles is negligibly low and the majority of the energy can be assumed to remain within the embryo until hatching.

As already suggested by many laboratories that work primarily on the technical aspects of light sheet-based fluorescence microscopy [65,170,270,271], fully automated cell tracking algorithms will become very important for quantitative analyses of developmental processes. In my opinion, it would be advisable to embed these tracking approaches into an ontological background (Box 4-3) – also with regard to the comparative approach (Subchapter 4.2.2). Currently, all ontologies that describe morphologic elements of insects, *e.g.* FBbt for *Drosophila* [272], TrON for *Tribolium* [273] and HAO for several hymenopteran species [274], categorize the morphology only on the tissue-and-organ level (Subchapter 2.1.1). Within the next years, once light sheet-based fluorescence microscopy and dedicated processing software become even more advanced, the respective ontologies can be extended systematically to the cellular level. This has been done already for multicellular organisms with a lower degree of complexity, for example *Caenorhabditis* with its highly stereotypic development. During embryonic development, the zygote gives rise to exactly 1,178 somatic cells in male individuals and size differences between eutelic individuals result from variances in the cell volumes [275].

About three decades ago, the *Caenorhabditis* community established an ontologic database that lists every individual cell including its lineage and function [276] (wormatlas.org/celllistsulston.htm). The ontological approach on the cellular level is also possible for the morphogenesis of insects, but several challenges have to be faced:

Box 4-3 – Ontologies in the life sciences

In information science, ontologies described the categorization of specific groups of elements by establishing a controlled vocabulary and defining their relationship to each other.

In the life sciences, a highly decentralized working style prevails. The respective communities consist of many loosely associated laboratories, and scientific questions are typically addressed either independently or at best in cooperation with a few other laboratories. Furthermore, results are communicated primarily in the form of research articles – scientific distillates of several years that are not subject to larger changes anymore. Thus, for proper correlation and unification of data originating from sources that communicate only sporadically, ontologies are necessary. One of the most comprehensive and formidable examples is the gene ontology project [277], which aims to define functional concepts and classes of genes along the aspects ‘molecular function’, ‘cellular component’ and ‘biological process’.

- The limited penetration depth is an issue when individual cells within the internal regions should be segmented. Unfortunately, no promising approaches are available yet (Subchapter 4.2.4).
- Insect species are, in general, non-eutelic, *i.e.* the total number of cells, and thus also the number of cells that form a given tissue or organ, vary slightly amongst individual embryos. Therefore, the ontology has to be designed with a certain flexibility to handle a range of cell numbers.
- As a consequence of the challenge outlined above, it is of great importance that cell differentiation processes can be reliably detected. However, this is, compared to cell migration and proliferation, the most difficult task when working on the cellular level (Subchapter 2.1.1) since the only feasible option is ‘retrospective’ annotation by considering the relative position and morphologic changes of the cells.

I assume that the ontological approach will eventually become an integrated element of advanced imaging systems. Once the respective databases are established, the operation software of the microscope will automatically identify the developmental stage of the embryo, annotate the cells and track them and their daughter cells throughout further development. Furthermore, in assays that induce aberrations, the microscope will automatically recognize significant deviations and provide lower order and higher order quantitative information: When did the aberration manifest? Which and how many cells are affected? To which extent do cell migration, proliferation and differentiation patterns change? Are there different reaction patterns between multiple individuals?

4.2.2. The Secondary Level – Evolutionary Developmental Biology

Developmental biologists typically decipher the developmental principles of one species with only negligible consideration of its phylogenetic position. In contrast, evolutionary developmental biologists focus on the comparative approach – homologies in gene expression pattern and morphogenesis between at least two species are identified, analyzed and interpreted within their phylogenetic context.

In the previous subchapter, within the ‘standardization’ argument, I already illustrated my thoughts how light sheet-based fluorescence microscopy may affect staging system studies. A reasonably coordinated establishment of comprehensive staging systems for two or more insect species will be a substantial benefit for evolutionary developmental biology. These systems will be preferably based on the same assay types and ideally performed by using similar microscope setups. The respective raw data, when provided as a resource for the community (Subchapters 3.3 and 4.2.5), can be ‘recycled’ for detailed side-by-side comparisons [32], quantitative evaluation of similarities and differences or data mining approaches [278,279]. The two-level staging system that I suggest for *Ceratitis* (Subchapters 6.2.4 and 6.2.5) will be a for both, comparison between closely related species, *i.e.* within the same order, by using the species-specific stages on the lower level, and comparison between distantly related species, *i.e.* between orders, by using the embryogenetic events on the upper level.

In evolutionary developmental biology, long-term live imaging with advanced fluorescence microscopy techniques provide the advantage that comparisons can be conveniently performed on the cellular level by aligning cell migration, proliferation and differentiation patterns (Subchapter 2.1.1). In contrast to interpreting static ‘morphologic snapshots’, comprehensive analyses of dynamic processes will provide more profound insights into the question if the hourglass model, *i.e.* the existence of one or more phylotypic stages [280,281], is also applicable to insect. Or, to use the words of Karl Ernst von Baer, to figure out if the ‘ontogeny recapitulates phylogeny’ [282] theory is not only true for vertebrates but also for insects. However, I assume that this is a non-trivial task that will require a profound strategy and an interdisciplinary mindset to be able to address a very diverse spectrum of challenges, of which two are exemplarily illustrated below:

- The most elegant style to perform a comparative experiment is to vary only a single parameter. While this is almost dogmatic for physicists, life scientist cannot always comply with this practice. In the comparative approach, the parameter of choice is the species, while all other factors, *e.g.* the setup of the microscope, remain constant. For some factors, *e.g.* the imaging buffer, a compromise can be found, but other factors inevitably add a second parameter. For example, by varying the species, also the architecture of the transgene has to be altered, since the interpretation of certain genetic elements, *e.g.* the promoter, may be inconsistent. The challenge will be to design transgenes that have a very similar expression pattern within species that have a phylogenetically decreasing relationship.
- Within the previous subchapter, in which I illustrate my anticipations for developmental biology, I suggest to establish an ontology on the cellular level (Subchapter 4.2.1). For an in-depth comparison of morphogenetic strategies, it will be necessary to define a universal ontology that is valid for all considered species. This ontology has to be highly flexible since it has to cover functionally similar cells even though their migration, proliferation and differentiation principles may vary considerably between species.

Within Outlook I, the ‘Reinhart Koselleck-Project’ (Subchapter 4.1.2), I propose a complete working outline with the ultimate goal to compare the morphogenesis of the ‘gold standard’ *Drosophila* to six species with a linearly decreasing phylogenetic relationship, but even for such an exhaustive project, the insight potential will converge sooner or later towards a hard cap. For an in-depth understanding of the evolution of insect development, I suggest to consider the two following more general approaches:

- **The ‘nested linearly decreasing phylogenetic relationship’ approach:** The comparative approach outlined above, *i.e.* defining only *Drosophila* as the absolute ‘gold standard’, is on the long term too simple. I therefore suggest to define a relative morphogenetic ‘gold standard’ also for the lepidoptera, coleoptera and hymenoptera and to choose, for each of these groups, three more model organisms (Table 4-4) that allow a ‘lower tier’ morphogenetic comparison within these holometabolic orders (Subchapter 2.1.1). Upon evaluation, the data will be used to determine the apomorphic traits of the individual species as well as the plesiomorphic traits of the respective order. In turn, when the plesiomorphic traits of the orders are known, it will be possible to perform a ‘higher tier’ morphogenetic comparison and to determine the apomorphic traits of the individual orders and the plesiomorphic traits of the holometabolic insects. Theoretically, this ‘increasing tier’ approach – based on the analyses of nested phylogenetic relationships – is iteratively increased, at first by comparing holometabolic insects and hemimetabolic insects, and finally by looking at the similarities and differences between insects and non-insect arthropods.

Table 4-4 – Insect species suggestions for the ‘nested linearly decreasing phylogenetic relationship’ approach. Green indicates species that are already part of my PhD project, blue indicates species that are part of the ‘Reinhart Koselleck-Project’ grant application, yellow indicated species described in the ‘Emerging Model Organisms’ books [14,15], orange indicates emerging insect model organisms and gray indicates exotic insect model organisms.

order	evolutionary distance to Diptera	‘gold standard’ of the respective order			
		‘gold standard’ of the respective order	phylogenetic relationship to the respective close	moderate	distant
Diptera	-	<i>Drosophila melanogaster</i>	<i>Ceratitis capitata</i>	<i>Megaselia abdita</i> ¹	<i>Aedes albopictus</i>
Lepidoptera	290 million years	<i>Bicyclus anynana</i>	<i>Heliconius melpomene</i> ²	<i>Danaus plexippus</i> ³	<i>Bombyx mori</i> ⁴
Coleoptera	327 million years	<i>Tribolium castaneum</i>	<i>Tenebrio molitor</i>	<i>Dendroctonus ponderosae</i> ⁵	<i>Onthophagus taurus</i> ⁶
Hymenoptera	345 million years	<i>Apis mellifera</i>	<i>Bombus terrestris</i> ⁷	<i>Nasonia vitripennis</i> ⁸	<i>Monomorium pharaonis</i> ⁹

¹ transformation protocol available [91]. ² genome sequenced [283]. ³ genome sequenced [284] and cell line available [285] that is used for complex N-glycosylation and sialylation of recombinant proteins [286]. ⁴ genome sequenced [287] and transformation protocol available [156]. ⁵ genome sequenced [288]. ⁶ genome sequenced, but not specific publication available yet [289]. ⁷ genome sequenced [287]. ⁸ genome sequenced [290]. ⁹ genome sequenced, but not specific publication available yet [289].

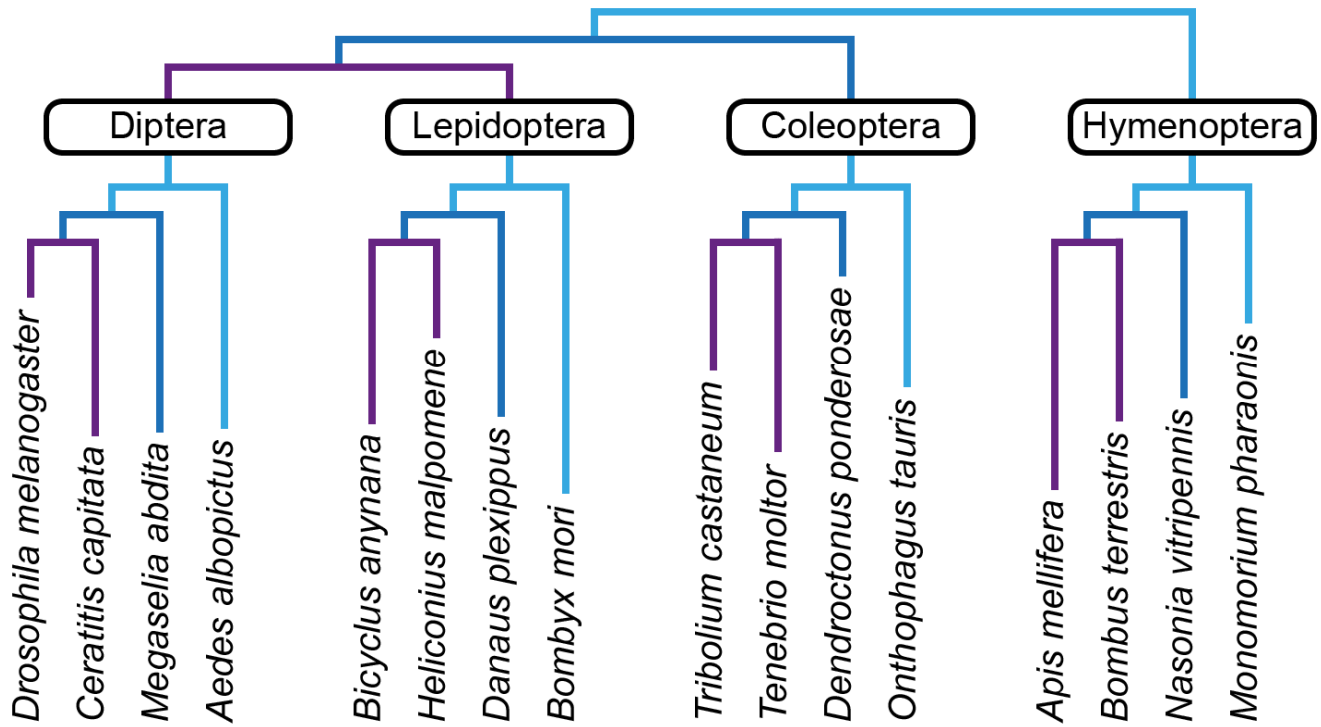


Figure 4-8 – Phylogenetic tree for the ‘nested linearly decreasing phylogenetic relationship’ approach. The colored lines indicate the increasing evolutionary distance: purple indicates a close, blue a moderate and teal a distant relationship either within the orders (the ‘lower tier’ is shown at the bottom) or between the orders (the ‘higher tier’ is shown at the top). The repetition of the color line pattern indicates the ‘nesting’.

- The ‘speciation’ approach:** The analysis of insect species hybrids has a long history in evolutionary developmental biology, especially for the Drosophilidae family [291], but inter-specific crossing has, for example, also been done with lepidopteran, coleopteran and hymenopteran species (Table 4-5). However, the embryonic morphogenesis of hybrid embryos from two closely related insect species has never been characterized with advanced fluorescence microscopy techniques. Such an approach will provide insights about the origins of novel species – one of the most crucial aspects of evolution. The rise of a species is a gradual process with several intermediate steps – at first, they produce fertile progeny, then only infertile but viable progeny, and finally no progeny at all [292,293]. A comparison between hybrid embryos and embryos of both parental species on the cellular level (Subchapter 2.1.1) will allow to investigate speciation based on morphogenetic data.

Table 4-5 – Selection of hybridization studies within evolutionary developmental biology of insects. Entries are ordered primarily by first species in order of decreasing phylogenetic relationship to *Drosophila melanogaster* and secondarily by publication year.

first species	second species	rationale (techniques)	reference
<i>Drosophila melanogaster</i>	<i>Drosophila simulans</i> <i>Drosophila mauritania</i>	Female hybrids have agametic ovaries, which can be rescued by mutations in the <i>male rescue</i> gene (ovary dissection and counting of mature eggs).	[294]
<i>Drosophila virilis</i>	<i>Drosophila lummei</i>	Hybrids lose the sixth <i>Drosophila lummei</i> chromosome during development and suffer from aberrations (karyotyping, visual inspection of adults).	[295]
<i>Heliconius melpomene</i>	<i>Heliconius cydno</i>	The hybrids do not show any defects, but show an intermediate wing color pattern (visual inspection of adults).	[296]
<i>Bombyx mori</i>	<i>Bombyx mandarina</i>	Inter-specific crossing leads to progeny that have a mixed pigmentation pattern during their larval stage (visual inspection of larvae).	[297]
<i>Tribolium castaneum</i>	<i>Tribolium freemani</i>	Depending on the respective strains, the hybrids show different aberrations, e.g. antennal defects or limb segment loss (visual inspection of adults).	[298]
<i>Nasonia vitripennis</i>	<i>Nasonia longicornis</i>	The courtship behavior of hybrids were intermediates between the style of the respective parents (visual inspection of adult behavior).	[299]

4.2.3. The Tertiary Level – Ecological Evolutionary Developmental Biology

Ecological evolutionary developmental biologists go even one step further and investigate how abiotic and biotic environmental factors, *e.g.* temperature, biosphere composition, predators or competitors, have influenced the evolution of development and how natural selection has resulted in the currently prevalent biodiversity [300]. I am convinced that state-of-the-art imaging techniques support this discipline in the following scenarios:

- Adaptation to changing environmental factors happens either on the subcellular and molecular level, *e.g.* when species evolve enzyme-based resistances against certain bioactive agents [301], or on the tissue-and-organ level (Subchapter 2.1.1), *e.g.* by evolving appropriate morphologic structures that provide an increase in fitness. Long-term live imaging can be used to characterize and compare the morphogenesis of these structures considering their respective phylogenetic context. One interesting example is *Drosophila sechellia*, which has specialized to feed preferably on the fruit of the noni tree *Morinda citrifolia*. In contrast to most other fruit fly species, this species does not grow fine hairs anymore at the dorsal side of most segments, which is believed to be beneficial for the larvae when they attempt to penetrate the exterior of verdant *Morinda* fruits [302].
- Comparing the tolerance windows of multiple species by varying certain environmental factors along one or more degrees of freedom provides insights into the biophysical level of ecological evolutionary developmental biology. For example, a comparative study based on transmission light microscopy of eleven members of the Drosophilidae family has shown that the temperature optimum for development corresponds nearly optimally to the respective habitats [303], but the imaging technique did not provide any information on the cellular level. Light sheet-based fluorescence microscopy is particularly well suited for a detailed long-term side-by-side comparison since respective setups are typically ‘built around the sample’, *i.e.* not only the viability and three-dimensional integrity are generally preserved, the embryo also remains accessible for external manipulation. Simple conditions, *e.g.* presence of insecticides, ion concentrations of the effect of bioactive agents, can be tested by filling the sample chamber with the appropriately prepared imaging buffer. For more advanced test procedures, *e.g.* changing the magnitude of a factor gradually over time, the sample chambers can be equipped with a heating unit or a perfusion system. A good example of such assays is the cooperation with Prof. Dr. Helge Bode, in which we analyzed the effect of hormone-like agents such as methoprene on *Tribolium* embryos (Subchapters 5.2 and 6.1.3). The ‘Reinhard Koselleck-Projekt’ also aims to determine the tolerance windows of seven insect species (Subchapter 4.1.2).
- One of the evolutionary and ecologically most interesting phenomena are symbioses, probioses, parabioses and antibioses. However, it is especially challenging to characterize relationships of species with large size differences, *e.g.* insects and microorganisms, using imaging techniques. As stated above within the ‘self-containment’ argument (Subchapter 4.2.1), one of the major advantages of light sheet technology is that multiple levels (Table 2-3) on the ‘microscopic scale’ are covered simultaneously.

4.2.4. Imaging Insect Morphogenesis – Ongoing Technical Challenges and Potential Synergies

Studies by colleagues as well as my PhD project show that light sheet-based fluorescence microscopy is a valuable tool in insect developmental biology. However, there are technical challenges that have to be addressed, especially when live imaging assays will be performed:

- The technical performance, *e.g.* the spatiotemporal resolution, of the microscopes can be improved, but this depends mainly on the research progress of the companies that manufacture the respective building blocks, *e.g.* the micro-translation stages, the objectives and the cameras. During the next years, significant progress can be expected here, and the main goals will be to achieve a spatial resolution below the diffraction limit [304] and a temporal resolution that allows the description of subcellular processes [305] while imaging the insect embryo *in toto* over very long time periods.

- The throughput is still limited, since only a few insect embryos can be observed at the same time within one microscope (Subchapter 2.2.4) and current parallelization approaches are mainly optimized for the imaging of cells [306,307], zebrafish embryos [308], the nematode *Caenorhabditis elegans* [307,309] or phytoplankton [310]. For large-scale screening assays, parallel imaging of around 50 to 100 embryos is necessary, but no satisfactory solution is currently available.
- One of the most crucial issues is the limited penetration depth. In live imaging assays of *Tribolium*, *Ceratitis* and *Gryllus*, the fluorescence signal becomes blurry when deeper regions are imaged, *i.e.* around 50 to 90 μm below the surface, the nuclei of respectively labeled lines are not properly resolved. Several approaches claim to overcome this limitation, but either the benefit is only mediocre or comes with disadvantages:
 - In adaptive light sheet-based fluorescence microscopy [230], the light sheet is digitally translated and rotated to compensate the varying optical properties of large living biological specimens. However, for the automatized real-time correction algorithm, it is necessary to illuminate several ‘reference planes’ multiple times, firstly to calculate the compensation parameters and secondly to actually acquire the data.
 - In two-photon light sheet-based fluorescence microscopy [86,311], fluorophores absorb two photons with approximately twice the wavelength of their respective excitation peak. Depth penetration in biological tissue increases exponentially with a linearly increasing illumination light wavelength [312,313], but adequate signal is only obtained with an exorbitant high photon density, *i.e.* a disproportionately high integrated energy load, since both photons have to hit the fluorophore within a very short time period.
 - Near-infrared and infrared fluorescent proteins also profit from the increased depth penetration of light with relatively high wavelengths [314–316]. However, preliminary experiments have shown that the fluorescence signal of transgenic *Tribolium* embryos that express iRFP670 under control of the *alpha tubulin 1* promoter is rather weak (Subchapter 3.5). In that specific experimental period, iRFP670 was the optimal choice, since its excitation peak at 643 nm is close to the maxima of typical red diode lasers and its quantum yield of 11% was the highest among the arsenal of iRFPs at that time, but even more recent variants suffer from severe drawbacks. For example, smURFP has a quantum yield of 18%, but depends on biliverdin as a cofactor [317], which is most likely not abundantly available within insect embryos. The search for high performance near-infrared and infrared fluorescent proteins is still ongoing, but it remains questionable if variants with comparable quantum yields as green and red fluorescent proteins will ever become available.
 - Optical clearing [232] is a powerful procedure to increase the penetration depth (Subchapters 4.1.6 and 5.4). Many sophisticated techniques have been established [231], but they are obviously not compatible with live imaging.
 - In *Drosophila*, it has been shown that homozygous knock-out of *klarsicht*, which is not lethal, alters the apical distribution of lipid bodies and thus significantly reduces light scattering [229]. However, data on the knock-out of respective homologues in other insect species is not yet available.

The most promising technical advancements in light sheet-based fluorescence microscopy for insect developmental biology are additional, *i.e.* two [86,87] or four [88], illumination and detection arms to combat the shadowing effect and parallelize the detection process. The benefits of other enhancements are questionable. For example, beam-shaping approaches such as illumination with a Bessel [318] or Airy [319] beam result in a very high laser irradiation level and in ‘tiled’ light sheet-based microscope setups [320] more uniform illumination of large samples comes at the expense of imaging speed.

Importantly, also the demand for sophisticated image quality enhancement and data extraction software and the appropriate hardware for computation and data storage rises in parallel. Three of the major post-processing topics that are important for insect developmental biology are:

- Registration and fusion of image data acquired along multiple directions, for which already multiple solutions are available [88,166–169]. The ‘multiview reconstruction’ plugin [169] already yields promising results (Subchapters 3.2 and 5.5) but requires landmarks within the imaging volumes. In future, improved algorithms are ideally landmark-independent, runtime-optimized and provide results with only minimal alignment errors.
- Deconvolution algorithms (Box 4-4) can be used to improve the resolution of imaging data acquired with light sheet-based fluorescence microscopy. Primarily, Lucy/Richardson-based [321,322] approaches are used and the respective computer codes are designed to run primarily on graphics processing units instead of on central processing units. The rationale of the algorithms has not changed since the early 1970s, and progress is mainly expected in the fields of automatization and processing speed.
- Image segmentation and data mining is a wide-ranging field with a heterogeneous arsenal of complex algorithms that allow to extract massive amounts of quantitative information from multidimensional datasets [323,324]. Such software is particularly important in insect developmental biology, since precise segmentation solutions are necessary to draw conclusion about the biophysical mechanisms of development, *e.g.* cell shape changes that lead to a spatial rearrangement and consequently a differentiation of certain cell populations during specific developmental stages [325]. Appropriate segmentation algorithms are also the prerequisite for nuclei tracking and cell lineage reconstruction software [170,326].

My PhD project contributes to the effort to close the gap between the technically motivated laboratories that concentrate primarily on technical developments and the biologically motivated laboratories that need easily comprehensible imaging solutions. In the future, light sheet-based fluorescence microscopy will become more and more automatized – while the technology and performance levels and thus the quality and amount of data increases, the time and effort for the end user will decrease significantly to the extent where the microscope will almost turn into a ‘plug-and-play’ solution. Error sources such as manual microscope calibration will be eliminated and modularized pipelines with optimized algorithms for the timely and standardized post-processing of the recorded data will become available. In this way, the experimenter can concentrate completely on the biological question.

Box 4-4 – Improving image quality via deconvolution

In microscopy, deconvolution describes the mathematical process that is used to (partially) reverse the effects of optical distortions in raw image data [327]. The procedure typically results in images with higher contrast and less blur. In optical physics, point spread functions describe the spatial dispersal of a point source of light in a three-dimensional image. Since the dispersion depends on multiple, usually well-known, factors such as the wavelength peak of the emitted light and the properties of the illumination and detection objectives, the point spread functions can be determined and used to calculate the complimentary functions. These functions are, in turn, used to perform the deconvolution operation and obtain an image that is more similar to the theoretical original. The Lucy/Richardson approach belongs to the group of iterative deconvolution algorithms, *i.e.* the mathematical operation is repeated a certain number of times. The iteration number depends on a variety of considerations [328].

When regarded from the developmental biology perspective, performing long-term live imaging of the morphogenesis of insect embryos with light sheet-based fluorescence microscopy synergizes strongly with other sophisticated techniques, especially from genetics, as illustrated by two examples:

- In genome editing assays, engineered nucleases are used to insert, delete or replace sequences within the genomes of model organisms (Box 4-5). This approach allows to characterize the function of any gene by creating an appropriate knock-in or knock-out transgenic line. Due to its high efficiency and low cost, the CRISPR/Cas9 system [329–331] has become the most frequently used genome editing method. In developmental biology (Subchapter 4.2.1), genome editing is used to analyze the function and interaction of genes and gene families to understand how a single cell develops into a functional multicellular organism. In evolutionary developmental biology on the other hand (Subchapter 4.2.2), knock-out of homologous genes in two or more species provides insights into the evolutionary history and potential ancient function of that gene. However, in both disciplines, an appropriate readout technique is necessary to characterize and compare the phenotypes. For this, long-term live imaging with light sheet-based fluorescence microscopy is a convenient choice. The affected specimen can be imaged from fertilization through the period of normal development to the moment when the aberration manifests, and the time course of the manifestation can also be documented without having to consider if the phenotype was induced by photo-toxicity. The CRISPR/Cas9 system has been successfully established for many insect species [332,333]. Protocols as well as resources are available for six of the seven candidates that are part of the ‘Reinhard Koselleck-Projekt’ (Subchapter 4.1.2): *Drosophila* [334–336], *Ceratitis* [337], *Bicyclus* [338], *Tribolium* [246], *Apis* [339] and *Gryllus* [340].

Box 4-5 – Genome editing using engineered nucleases

All commonly used genome editing methods follow basically the same principle: either by editing the respective amino acid sequence or by providing a specific guide RNA, nucleases are directed more or less precisely to the desired location on the respective chromosome to induce a site-specific double strand break. Affected cells try to correct the defect by activating one of two intrinsic repair mechanisms, non-homologous end joining or homology directed repair. The first mechanism is error-prone and can be used to provoke either a short deletion or the insertion of exogenous DNA at the target site. The second mechanism can be used for precise insertions into the desired location, but works only when homologous arms with specific lengths are present within the exogenous DNA [245,341,342]. Using genome editing approaches to create knock-out organisms of candidate genes subsequent analysis of the phenotype is also known as ‘reverse genetics’ [343]. The most crucial issue with genome editing methods is off-targeting [344,345].

- Advanced genetic concepts for fluorescence labeling of model organisms provide insights that are not obtainable with basic genetic concepts. For example, in the fluorescent ubiquitination-based cell cycle indicator system [346,347], cells that carry the respective transgene express a different fluorescent protein depending on their cell cycle phase, e.g. red during the G1, but green during the S, G2 and M phases. The system is frequently used in cell biology, for example to measure the effect of certain factors and agents on the proliferation frequency [348–350], but has also been successfully established for mouse [351], zebrafish [352] and *Drosophila* [353] and has the potential to become a powerful tool for developmental biology when used in conjunction with long-term live imaging. By recording the morphogenesis of wild-types with advanced fluorescence microscopy techniques, three-dimensional ‘reference’ proliferation maps over the whole embryonic development can be established and compared to specimen in which aberrations are induced.

Alternatively, such proliferation maps can be used in the comparative approach to detect and characterize evolutionary conserved mitotic hot spots.

Other developmental biology-exclusive advanced genetic concepts for fluorescence labeling assign different fluorescence protein expression patterns to individual cells within the same individual – an approach that also synergizes very reasonably with advanced live imaging techniques. One of the first and most impressive examples is the ‘Brainbow’ system (Box 4-6), but appropriately adapted derivatives are also used to investigate non-neuronal cellular dynamics [354–357] and to perform cell lineage reconstruction [358–360]. The AFeastForCres vector concept that I propose within my Outlook II (Subchapter 4.1.3) is inspired by the Brainbow system but has the advantage that theoretically, variants with different recombination probabilities can be created.

Box 4-6 – Visualization of synaptic circuits with the ‘Brainbow’ concept

The Brainbow system, a portmanteau term that derives from ‘brain’ and ‘rainbow’, is an advanced genetic labeling concept used to investigate the architecture and functionality of complex neuronal networks [361]. Independent Cre-mediated recombination in a given population of neurons results in the expression of one, or alternatively a combination of several, randomly chosen fluorophores per neuron – the recombination process follows purely stochastic principles for each individual cell. Thus, within that cell population, neighboring neurons that underwent recombination will most probably express a different fluorophore or combination of fluorophores and can thus be easily distinguished from each other, which is especially crucial when dendrites and axons should be allocated to their respective cells. The number of resulting color combinations depends on the transgene architecture and number of transgene copies in the genome. The Brainbow concept has been successfully established for mouse [148,362], zebrafish [363,364] and *Drosophila* [365,366].

4.2.5. Imaging Insect Morphogenesis – From On-Demand to Systematic Data Acquisition

The advent and continuous improvement of light sheet-based fluorescence microscopy has already begun and will continue to influence analyses of the embryonic morphogenesis of insects. Three-dimensional imaging with confocal microscopes is spatially restricted to certain regions of the embryo due to the shadowing effect and temporally to a small number of time points due to the high integrated energy load. In contrast, light sheet-based fluorescence microscopy overcomes these limitations due to several unique features:

- Respective setups used in developmental biology typically come with a sample rotation feature. In conjunction with the very high acquisition speed, embryos can be recorded along multiple directions without significant delays. By using algorithms for registration and fusion, a superior dataset can be calculated to compensate the shadowing effect and obtain isotropic resolution (Subchapter 3.2). Thus, the embryo is truly captured *in toto*, since high quality data along all embryonic axes, *i.e.* anterior, posterior, ventral, lateral, dorsal as well as intermediates thereof, are available.
- Since only the observed plane is illuminated in light sheet-based fluorescence microscopy, the integrated energy load is reduced by several orders of magnitude compared to confocal fluorescence microscopy. This approach strongly reduces photo-bleaching and photo-toxicity, two crucial factors that have to be minimized in long-term live imaging assays.

Until now, imaging assays in insect developmental biology have been performed primarily on-demand. The processes of interest, *e.g.* the cellular dynamics of certain organs, were recorded for short periods in an isolated fashion so that a broader contextual interpretation was impossible. However, as shown exhaustively throughout my PhD thesis (Subchapters 2.2 and 3.1), light sheet technology permits imaging assays that fulfill the two crucial criteria for systematic data acquisition:

- **The ‘massive-but-finite’ criterion:** systematic data acquisition procedures have a large, but self-contained and scientifically reasonable scope. In insect developmental biology, the scope can be defined as the moment of fertilization, to the point of hatching, *i.e.* from a single cell – which can be considered the ‘smallest biological unit’ – to an autonomous organisms that is able to gather energy, to defend itself against predators and, later on, to reproduce (Subchapter 2.1.1).
- **The ‘universality’ criterion:** the benefit of systematically acquired data is inversely proportional to the number of relevant acquisition parameters. Fortunately, for imaging assays of insect embryos, ‘common sense’ solutions for all relevant acquisition parameters can be found:
 - The influence of most environmental factors, *e.g.* the temperature or the composition of the imaging buffer, is negligible as long as certain effect thresholds are not transgressed (Subchapter 4.1.2).
 - The spatiotemporal resolution that is achievable with light sheet-based fluorescence microscopy usually heavily exceeds the ‘interest threshold’ – insect embryos can be sampled with reasonable sub-cellular spatial resolution a thousand or more times during their embryonic development.
 - The genetic architecture of the cassette that expresses the fluorescent protein and thus the nature of the signal is the most debatable parameter. However, ubiquitous and constitutive labeling of the cell nuclei is the most convenient solution. It allows the identification of organs and tissues and can be used to estimate the current cell number at any developmental stage.

Usually, systematic data acquisition approaches do not directly address hypotheses but serve as scientific convergence and divergence points. Hence, they provide an integrative framework by linking previously unrelated ‘puzzle pieces’ that were obtained in on-demand studies and serve as a starting point for many further studies that directly utilize the provided resources or use the given data as a suggestive gateway to develop novel hypotheses.

Image data acquisition in insect developmental biology will become systematic. In particular, light sheet-based fluorescence microscopy allows the experimenter to kill two birds with one stone – systematic imaging assays can answer specific scientific questions equally well or even better than on-demand approaches, while the data can also be provided as a valuable resource for the community by submitting it to an appropriate repository and by describing the metadata and experimental conditions in a data article (Box 2-8).

Further, I presume that such repositories will have a similar benefit for the insect developmental biology community as sequences databases, *e.g.* NCBI (ncbi.nlm.nih.gov), have for the genetic community and satellite image databases, *e.g.* Landsat (landsat.usgs.gov), have for the geosciences community. In these two disciplines, both above mentioned criteria are fulfilled properly and therefore, a transition from on-demand to systematic data acquisition has occurred as soon as the technological progress allowed it (Table 4-6). Within the next decade, it should be possible to document, characterize and compare the embryonic morphogenesis of many emerging insect model organisms on a similar scale as their genomes are sequenced, analyzed and assembled within i5K project (Box 4-7).

Table 4-6 – Systematic data acquisition criteria in genetics, geosciences and insect developmental biology.

critterion	genetics	geosciences	insect developmental biology
on-demand data	short and unrelated sequences in the range of 10^2 to 10^3 base pairs	snapshots of certain areas in the range of a few square kilometers	several (10^1 to 10^4) ‘morphogenetic snapshots’
‘massive-but-finite’	whole eukaryotic genome, <i>e.g.</i> 3.2×10^9 base pairs for human	whole surface of the Earth, <i>i.e.</i> 5.1×10^8 square kilometers	whole embryonic morphogenesis from fertilization to hatching
‘universality’	no parameters, genome data is absolute	spatiotemporal resolution	spatiotemporal resolution, nature of the signal
technological progress	next-generation sequencing [133], <i>e.g.</i> pyrosequencing [367]	mainly progress in camera and data transmission / storage technology	light sheet-based fluorescence microscopy

Consequently, I anticipate a certain change of mind within the insect developmental biology community. Systematic imaging will become such an important factor that, whenever an emerging insect model organism is introduced to a non-initiated audience as part of a scientific study or during a conference presentation, the obligatory species-related statements such as ‘the genome is sequenced’ or ‘important techniques such as transgenesis and genome editing are established’ will be accompanied by ‘systematic microscopy data on the whole embryonic morphogenesis is available’.

Box 4-7 – The i5K project: sequencing the genome of 5,000 arthropod species

Unsurprisingly, the first and second sequenced insect genomes belong to *Drosophila* [368] and to *Tribolium* [202] and were published in 2000 and 2008, respectively, when sequencing was still relatively expensive and required the combined efforts of a large community, *i.e.* several hundreds of people.

The i5K project (hgsc.bcm.edu/arthropods/i5k), which was initiated in 2011, is a large-scale endeavor that aims to sequence, analyze and compare the genomes of 5,000 arthropod species within the next few decades by using next-generation sequencing approaches. The project is expected to contribute substantially to the overall goal of understanding the molecular architecture and diversity of arthropods [369]. Besides life sciences, the data is will be of considerable relevance for medicine, agriculture and economics. During the recently completed pilot phase, the genomes of 28 insect species have already been sequenced, including *Ceratitis* [191], while *Aedes*, *Bicyclus*, *Apis* and *Gryllus* will be under consideration with the next years.

4.2.6. Closing Summary and Concluding Remarks

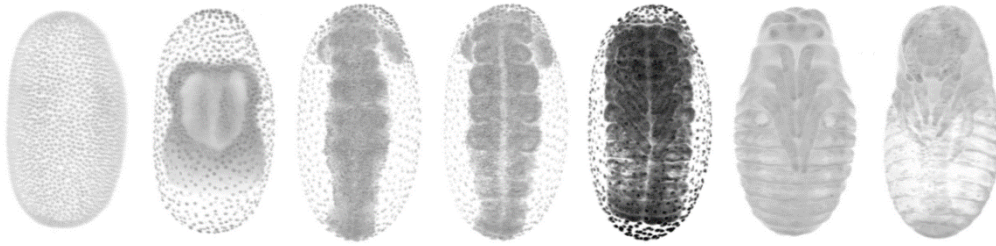
Previously, insect developmental biology focused mainly on the fruit fly *Drosophila melanogaster* and thus only little data on the embryonic morphogenesis of other model organisms was available. The goal of my PhD project was to address this limitation, and I was accomplish the following milestones:

- Invention and comprehensive documentation of the hemisphere and cobweb holder mounting methods for light sheet-based fluorescence microscopes that allow non-invasive long-term live imaging of insect embryos.
- Long-term live imaging of almost the whole embryonic morphogenesis of the red flour beetle *Tribolium castaneum*, the Mediterranean fruit fly *Ceratitis capitata* and the two-spotted cricket *Gryllus bimaculatus*.
- Invention and proof-of-principle of the AGameOfClones and AClashOfStrings vector concepts that allow the systematic creation of homozygous and double homozygous transgenic insect lines, respectively.

My achievements are important milestones in the quite long but oddly fascinating journey to unravel the ‘big picture’ of developmental biology – to understand the molecular processes how the genomic information orchestrates a highly complex sequence of cell proliferation, migration and differentiation to turn a single cell into a fully functional multicellular organism.

Then again, my work also contributes considerably to the even ‘bigger picture’ of evolutionary developmental biology – to understand how evolution has affected development – simply because, in my opinion, morphogenetic processes can only be properly understood in the context of their phylogenetic history. Or, to use the words of Theodosius Dobzhansky, ‘Nothing in Biology Makes Sense Except in the Light of Evolution’ [370].

5. Teaching Efforts



During my PhD project, I supervised a total of six students in four Master and two Bachelor projects. The background of these students was quite diverse, as they came from cell biology and physiology, biophysics, bioinformatics and biochemistry, which also reflects the interdisciplinary approach to developmental biology that was pursued. All projects focused on individual, self-contained scientific questions, but were thematically linked to my PhD project. Whenever a significant amount of data were or will be used in a manuscript, the students became or will become co-authors (Subchapters 6.1 and 6.2). Within in this chapter, each of these projects is described on one page, and the most striking result from the respective project is summarized in a figure. The subchapters are presented in chronological order of thesis submission.



The Fluorescence of the ACOS{Ub[#]O(MEM)-mRuby} #2 transgenic *Tribolium* subline is visible without appropriate excitation light and emission filters. Observation under reflected light is sufficient to discriminate wild-type (left) and ACOS{Ub[#]O(MEM)-mRuby} #2 (right) pupae since transgenic individuals have a brief red glow. This phenomenon occurs when the level of fluorophore expression is extremely high. The ACOS{Ub[#]O(MEM)-mRuby} #1 and #3 sublines, which carry the same transgene, but at a different genomic location, do not show this effect. The 3×P3 eye-specific transformation markers can be seen in the green channel, while the very high level of mRuby expression is clearly evident in the red channel. This chapter figure shows the result of continuous fluorescence signal yield optimization: (i) screening for a strong spatiotemporal ubiquitous upstream regulatory sequence, (ii) scarless connection of the upstream regulatory sequence to the open reading frame, (iii) choice of the most suitable red fluorescent protein mRuby, (iv) removal of triplets that translate into unnecessary amino acids, (v) codon optimization of the coding sequence and (vi) usage of an extended version of the SV40 poly(A) site. The ACOS vector concept is described in detail in Subchapter 3.4 – the chapter figure is shown here because the phenomenon was discovered by Selina.

5.1. Alexander Ross – Master Thesis in *Cell Biology and Physiology*

The aim of Alexander's Master project was to develop the experimental framework for *in toto* fluorescence live imaging of transgenic embryos of the two-spotted cricket *Gryllus bimaculatus* (Figure 5-1A). Therefore, Alexander established the transgenic H2B-EGFP *Gryllus* line [162] in our laboratory, adapted the cobweb holder mounting method for cricket embryos (Figure 5-1B) and evaluated the appropriate conditions necessary for non-invasive live imaging within the Lightsheet Z.1 microscope.

The challenge within his project was the very large size of the embryos – they have a lateral width of about 600 μm and an anterior-posterior length of about 3,000 μm . Thus, the embryos did not fit completely in one volume of view and had to be imaged in four partially overlapping Z-stacks per direction (anterior, anterior-medial, posterior-medial and posterior). During post-processing, these Z stacks were stitched together to regain an *in toto* three-dimensional image of the embryo (Figure 5-1C).

Alexander's work was the foundation for the non-invasive long-term live imaging of *Gryllus bimaculatus* embryos project (Subchapter 3.1). Currently, Alexander works as a PhD student with retroviral infection mouse models at the Universität Duisburg-Essen.

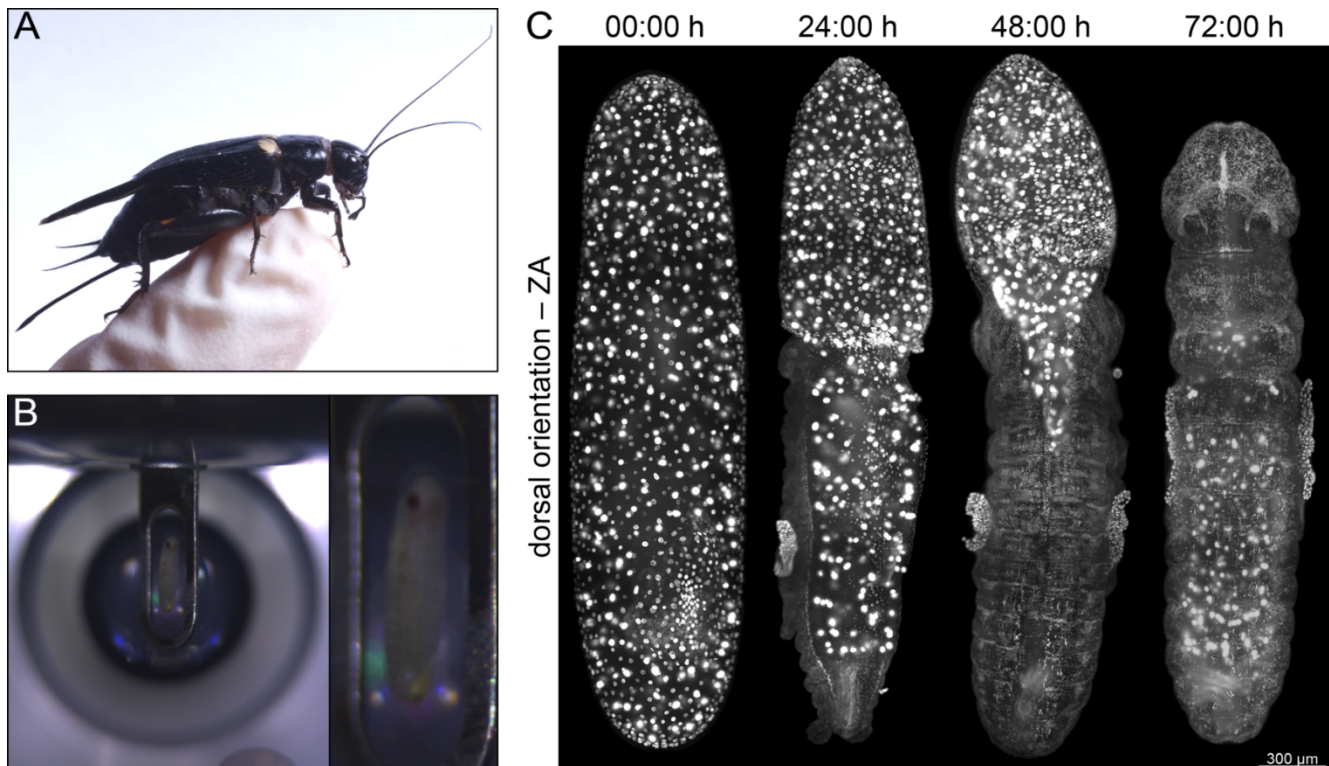


Figure 5-1 – Live imaging of *Gryllus bimaculatus* embryos. (A) The two-spotted cricket *Gryllus bimaculatus* has become a powerful and popular model organism for embryonic development of hemimetabolous insects. (B) Adaption of the cobweb holder mounting method for the Lightsheet Z.1. In contrast to the custom-build light sheet-based fluorescence microscopes that were used in all other experiments described in this thesis, the sample is held from above. The detail image shows the embryo within the holder. (C) Four *Gryllus* embryos imaged along the dorsal direction. The embryo shown in the first column is at the beginning of katarrepsis, the embryos in the second and third column are in the middle of dorsal closure, while the embryo in the fourth column is in the muscular movement phase. Figure and/or figure description fully and/or partially reproduced from the Master thesis of Alexander Ross.

5.2. David Kleinhans – Master Thesis in *Cell Biology and Physiology*

The aim of David's Master project was to investigate the effect of small organic substances (800 gram per mole or less) on the morphogenesis of *Tribolium* embryos. Hence, David developed a microscopy-based screening pipeline: Firstly, he applied spinning disk confocal microscopy to evaluate the effects quantitatively by determining the manifestation point and course of the aberrations. Secondly, he used light sheet-based fluorescence microscopy to characterize the extent of the aberrations in detail. In this experimental work, David investigated the effects of (i) methoprene (Figure 5-2A), a juvenile hormone analog, (ii) HB71 (Subchapter 6.1.3), a juvenile hormone epoxide hydrolase inhibitor, (iii) methanol, (iv) acetic acid and (v) maleic acid. Out of these substances, methoprene, which is commonly used as an insecticide [371], had the most obvious morphogenetic consequences (Figure 5-2B).

David's work contributes to our efforts to establish standard operation procedures for microscopy-based screens to evaluate the effect of environmental factors on insect development. While David was working with a two-dimensional experimental matrix (factor • concentration), we are looking forward to add a third dimension (species • factor • concentration) and thus gain a deeper understanding of the developmental robustness in context of ecological evolutionary developmental biology (Subchapter 4.1.2 and 4.2.3). David remained at the Johann Wolfgang Goethe-Universität as a PhD student and investigates lateral line organ formation in zebrafish.

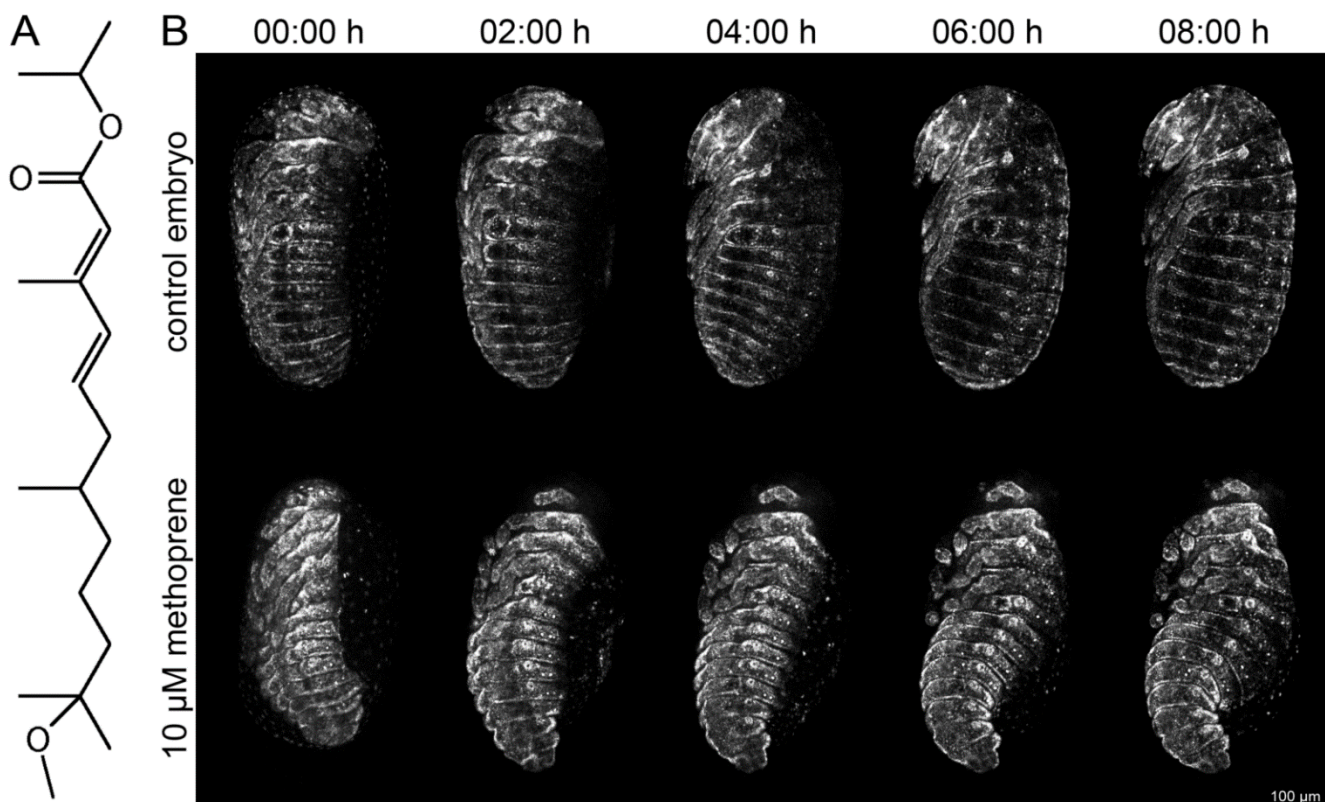


Figure 5-2 – The effect of methoprene on the embryonic development of *Tribolium*. (A) Structural formula of methoprene. The substance mimics the natural insect growth regulator juvenile hormone. (B) Extrinsic application of methoprene leads, beside others, mainly to a seahorse-like aberration. During dorsal closure, the germband flanks fail to initiate epidermal zippering, and the yolk sac cannot be internalized properly. Figure and/or figure description fully and/or partially reproduced from Nollmann *et al.* 2015, #2 in Publication Table 1.

5.3. Anita Anderl – Master Thesis in *Biophysics*

The aim of Anita's Master project was to create custom-made transgenic *Tribolium* lines suitable for long-term live imaging. Thus, she further developed the AGameOfClones vector concept (Subchapter 2.2.7) and created two transformation-ready vectors that allow expression of mEmerald-labeled Lifeact [109] under control of either the *alpha-tubulin 1* promoter [180] or the *zerknüllt 1* promoter, which had not been described previously. With these vectors, she created two transgenic lines with one and three sublimes, respectively. The AGOC{ATub'#O(LA)-mEmerald} #1 subline is fairly interesting: individuals show green fluorescence throughout the whole body (Figure 5-3A) and, as expected, orange and dark red fluorescence of the transformation markers in the eyes (Figure 5-3B). When imaged with light sheet-based fluorescence microscopy, this line allows the visualization of certain processes that cannot be properly described with transgenic lines in which the nuclei are labeled, for example dorsal seam formation (Figure 5-3C).

Anita's work contributed considerably to the AGameOfClones vector concept (Subchapter 2.2.7) and the vectors as well as transgenic lines that she created are featured in the respective publication (Subchapter 6.2.3), which she also co-authors. She is currently a PhD student at the Hochschule Darmstadt.

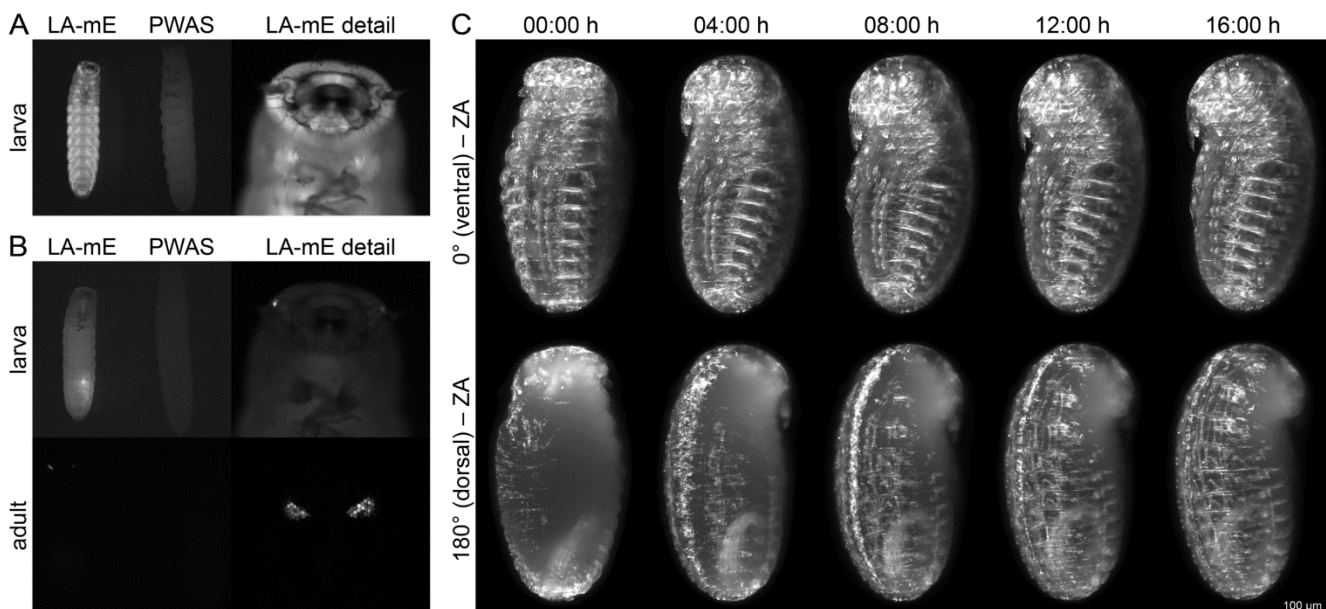


Figure 5-3 – Characterization of the AGOC{ATub'#O(LA)-mEmerald} #1 transgenic *Tribolium* subline. (A) Wide-field fluorescence microscope images with the F38 filter set (Carl Zeiss), visualizing Lifeact-mEmerald. Muscular structures, for example in the legs, are recognizable. The Plain-White-As-Snow (PWAS) background strain is shown as control. (B) Wide-field fluorescence microscope images with the F43 filter set (Carl Zeiss), simultaneously visualizing the mOrange and mCherry-based eye-specific transformation markers, which are based on the artificial 3×P3 promoter. The Plain-White-As-Snow (PWAS) background strain is shown as control. (C) The AGOC{ATub'#O(LA)-mEmerald} #1 subline is well-suited to characterize complex morphogenetic processes such as epidermal zippering and dorsal seam formation during dorsal closure with light sheet-based fluorescence microscopy. Figure and/or figure description fully and/or partially reproduced from the Master thesis of Anita Anderl.

5.4. Selina Klees – Bachelor Thesis in *Bioinformatics*

The aim of Selina's Bachelor project was to adapt and optimize the SeeDB fructose-based optical clearing protocol [234], which was initially developed for mouse brain tissue, for *Tribolium* embryos. Furthermore, the protocol also had to be customized for light sheet-based fluorescence microscopes. The clearing approach is based on the idea that the refractive index of water-based sugar solutions and biological tissue are nearly identical. The increase in transparency can already be seen in the transmission light mode. Before optical clearing, embryos are nearly uniformly dark, but after clearing, they appear considerably brighter (Figure 5-4A). When images are acquired in the fluorescence mode, the benefit of clearing becomes evident. In non-cleared embryos, the signal becomes blurry in regions deeper than 50 μm , and structures cannot be recognized properly (Figure 5-4B, upper row). After clearing, the image quality in these regions increases considerably (Figure 5-4B, lower row). Although clearing is not compatible with live imaging, it is a promising approach when structures in inner regions of the embryo have to be resolved.

Selina's work contributes to a future project in which the performance of multiple clearing techniques on *Tribolium* embryos should be comprehensively evaluated (Subchapter 4.1.6). She is now doing her Master in computer science at the Georg-August-Universität Göttingen.

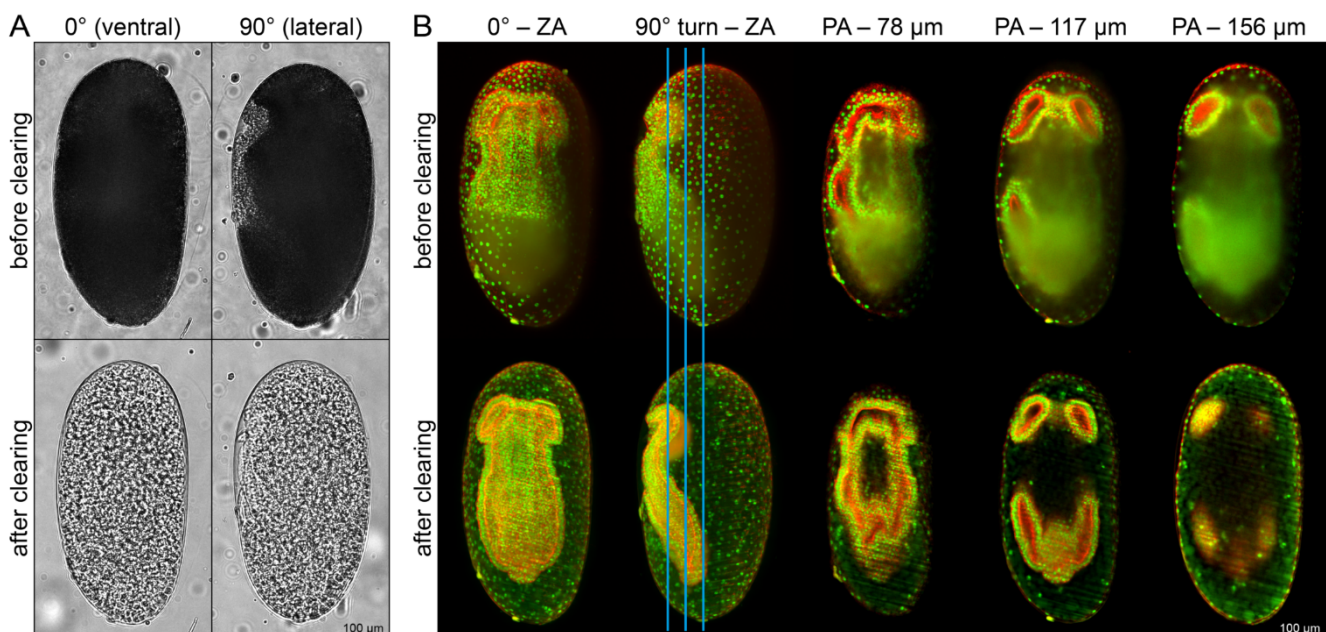


Figure 5-4 – Increasing the transparency of *Tribolium* embryos with the SeeDB fructose-based optical clearing protocol. The embryo derives from the AGOC{ATub'H2B-mEmerald} #4 subline and was additionally stained with Phalloidin 546. (A) The same embryo before and after optical clearing recorded in transmission light mode. A strong increase in transillumination is evident. **(B)** Comparison of fluorescence image quality increase after the clearing procedure. After clearing, the complete shape of the germband, also the posterior region that is covered by the yolk sac fold, can be recognized properly (first and second column). The optical sections show that also structures deep within the embryo can be resolved even in depths of more than 100 μm (third to fifth column). The blue lines in the second column indicate single planes shown in the third to the fifth column. Figure and/or figure description fully and/or partially reproduced from the Bachelor thesis of Selina Klees.

5.5. Franziska Krämer – Bachelor Thesis in *Bioinformatics*

The aim of Franziska's Bachelor project was to apply landmark-based fusion to long-term live imaging datasets of *Tribolium* embryos, eventually in conjunction with deconvolution, and evaluate in how far this approach compensates the shadowing effect. Therefore, she created a hybrid line that expresses mEmerald-labeled Lifeact in the serosa cells and mRuby-labeled histone 2B subunits ubiquitously and advanced the cobweb mounting technique by placing an agarose-embedded fluorescent beads column below the embryo, which provides the landmarks for registration and fusion. Finally, Franziska applied the Multiview Reconstruction plugin [169] to the recorded data, which allowed her to describe the serosa window perimeter and area quantitatively as a function of time (Figure 5-5).

Franziska's work contributes significantly to our efforts to compensate the shadowing effect, a fundamental problem in fluorescence microscopy (Subchapter 3.2). She continued her studies as a Master student in bioinformatics at the Johann Wolfgang Goethe-Universität.

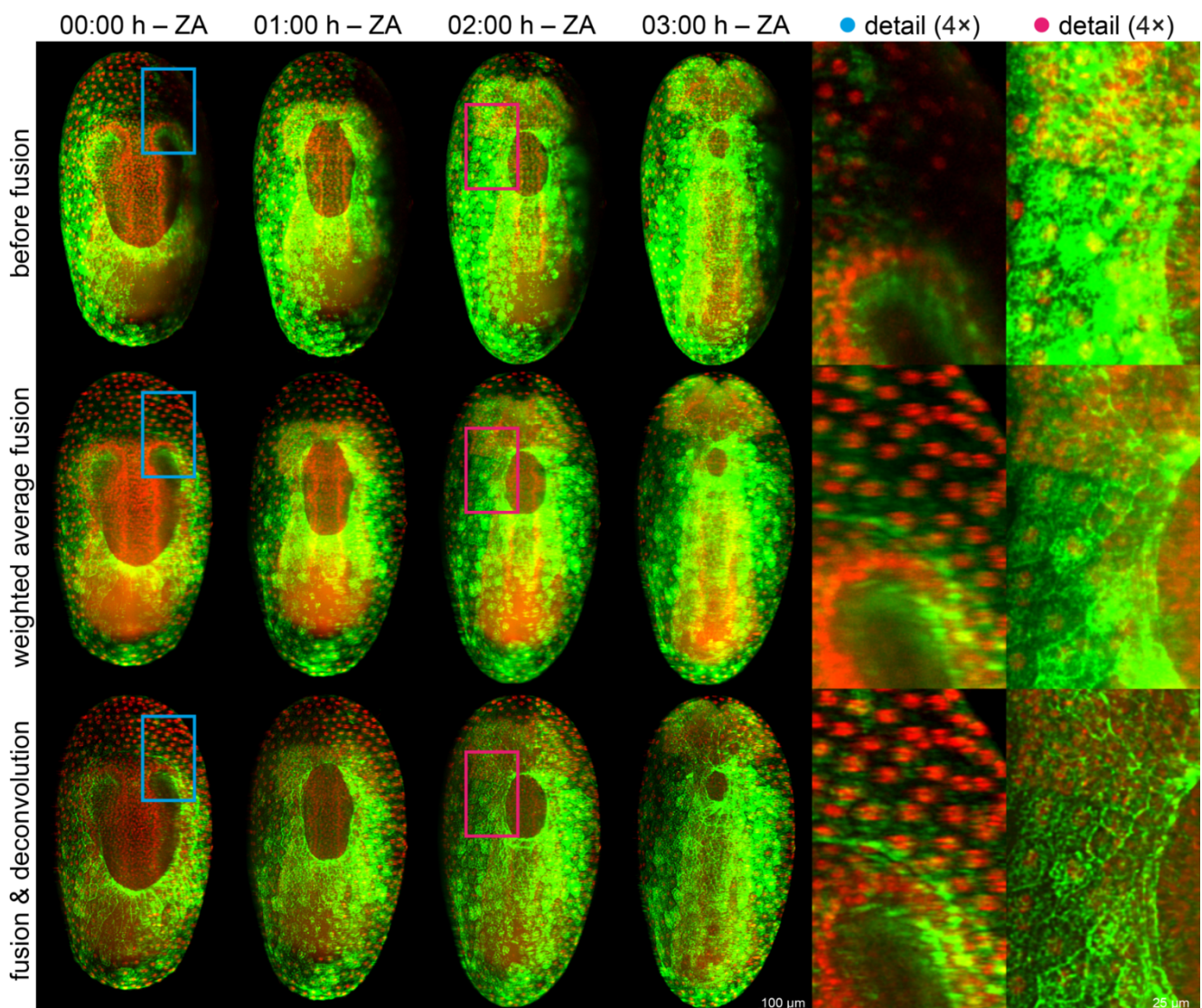


Figure 5-5 – Registration and fusion of image data acquired from a *Tribolium* hybrid embryo during gastrulation. The hybrid embryo received the AGOC {Zen1' #O(LA)-mEmerald} #2 allele maternally and the ACOS {ATub'H2B-mRuby} #2 allele paternally and thus is double hemizygous. Weighted average fusion removes the shadowing effect on the right side of the embryo that is caused by the unique illumination principle of light sheet-based fluorescence microscopy (blue detail image). Fusion & deconvolution compensates the shadowing effect and thus improves image quality in certain regions (pink detail image). Figure and/or figure description fully and/or partially reproduced from the Bachelor thesis of Franziska Krämer.

5.6. Henrik Tonner – Master Thesis in *Biochemistry*

The aim of Henrik's Master project was to evaluate if nanobodies, *i.e.* extremely small intracellular functional antibodies, raised against antigens of certain vertebrate proteins also localize properly in *Tribolium*. Nanobodies derive from Camelidae heavy chain antibodies, specifically from the V_HH antigen binding domain. They can be encoded in less than 400 bp and C-terminally linked to a fluorescent protein without disturbing its binding capacity [112]. Through his Master project, Henrik created several transgenic *Tribolium* lines that ubiquitously and constitutively express fluorescent protein-linked nanobodies, *i.e.* chromobodies, against proliferating cell nuclear antigen and lamin and analyzed respective embryos with light sheet-based fluorescence microscopy. Although the expected subcellular localization patterns were found for neither chromobody, the transgenic lines can be used to describe developmental processes on the cellular and tissue-and-organ level (Figure 5-6). Henrik's work contributes to our efforts to find alternatives to the fusion protein- and tag-based labeling strategies (Box 2-4). He became a PhD student at the Johannes Gutenberg-Universität Mainz.

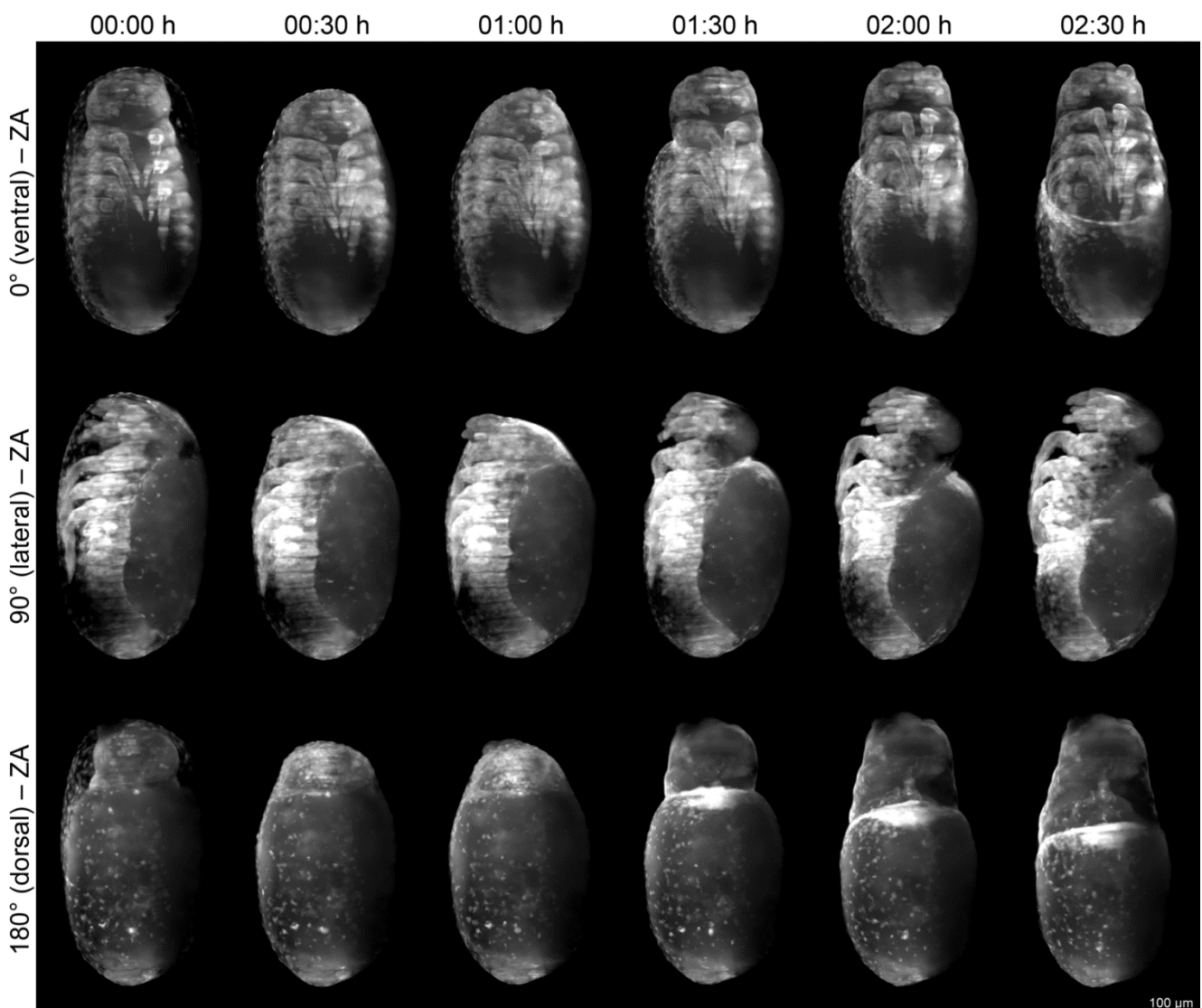
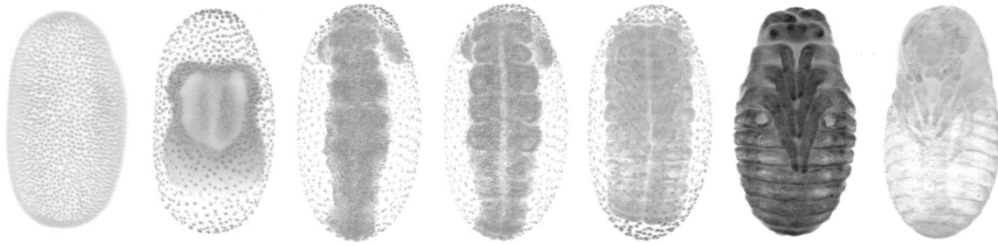


Figure 5-6 – Live imaging of the ACOS{Ub⁺Lamin[°]CB-mRuby} #1 subline at the beginning of dorsal closure along three directions. The mainly cytosolic/nuclear dispersed signal obtained from the mRuby-labeled α -lamin nanobody fluorescence fusion protein is particularly well-suited to document the morphogenesis of *Tribolium* embryos during phases of rapid cellular movements, such as serosa opening and migration at the beginning of dorsal closure. Figure and/or figure description fully and/or partially reproduced from the Master thesis of Henrik Tonner.

6. Publications and Applications



This chapter briefly summarizes the scope and major achievements of the ten manuscripts that were prepared during my PhD project. Six are already published, two are under review, and the last two are submission-ready, but the choice of appropriate journals and thus the respective formatting work has not yet been performed. The chapter also gives background information about the patent application for the AGameOfClones vector concept and the grant application for the 'Reinhart Koselleck-Project' to which I contributed substantially. It might be debatable in how far patent and grant applications belong in a PhD thesis. However, life sciences, like all modern academic fields, constantly evolve and thus do the overall demands towards the scientists. Besides the actual research (Chapters 2 and 3) and teaching efforts (Chapter 5), it is nowadays quite advisable for 'junior researchers' who pursue an 'academic career' to consider and exploit the economic potential of scientific inventions and to learn as early as possible how build and retain the 'financial momentum', since publications seem to be not the only factor that contribute to the 'qualification level' of a young scientist.



Picture of the AGameOfClones vector concept recombination principle re-enacted with candies. The chapter figure shows a slide out of my BMLS Student Symposium 2014 presentation during which I explained the principle and background of the AGameOfClones vector concept to a BMLS-internal audience. Together with Alexander Ross, who at that time did his Master project with me, I spent a whole evening taking pictures of precisely arranged candies that represent all genetic elements necessary for the vector concept to work. In the particular situation that is shown above, the Cre recombinase has attached to the LoxP sites and will excise the mOrange transformation marker and a 'stitched equivalent' of a LoxN site. The whole presentation did not contain any proper scientific image, but I still won the 'Best Talk' award.

6.1. Published Manuscripts

6.1.1. Nota Bene

In this subchapter, the scope and major achievements of my six already published research and review articles (#1 to #6) are summarized. The final manuscripts, in their formatted and typeset versions, are found in Volume II of my PhD thesis. Meta data of the publications are given in Publication Table 1 for the manuscripts that were published in 2014 and 2015 and in Publication Table 2 for the manuscripts that were published in 2016 and 2017. The denomination is final and will not change anymore. The microscopy data can be found within the BugCube (Subchapter 3.3) by using the respective identifier.

Publication Table 1 – Meta data of the published manuscripts in 2014 and 2015.

Publication	Strobl & Stelzer 2014	Nollmann <i>et al.</i> 2015	Strobl <i>et al.</i> 2015
Number	#1	#2	#3
Epub	May 2014	February 2015	September 2015
Print Date	June 2014	March 2015	October 2015
Journal	<i>Development</i>	<i>ChemBioChem</i>	<i>Nature Protocols</i>
Publisher	Company of Biologists	Wiley	Nature Publishing Group
Pages	15 (with supplements)	32 (with supplements)	38 (with supplements)
PubMed ID	24803590	25711603	26334868
BugCube	Strobl2014A	-	Strobl2015A
Datasets	3 (DS0001-DS0003)	-	3 (DS0001-DS0003)
Type	Research Article	Research Article	Research Article
Subtype	Methods & Resources	Classical	Protocol
Open Access	Yes	Yes (PMC)	No
Invitation	No	No	No
Cooperation	No	Yes ¹	No
Volume	Volume II	Volume II	Volume II
Authorship	First Author	Co-Author	First Author
Authors	2	2 ²	3
Text	50%	2%	33.3%
Boxes	-	-	33.3% (2 in total)
Experiments	100%	2%	100% (anticipated results)
Figures	100% (3 of 3)	-	100% (12 of 12) ³
Tables	100% (1 of 1)	-	100% (2 of 2)
SFigures	100% (3 of 3)	~15% (1 of 7)	100% (11 of 11) ³
STables	100% (1 of 1)	-	100% (1 of 1)
SMovies	100% (3 of 3)	100% (1 of 1)	100% (6 of 6)
Comment	-	see Subchapter 5.2	-

¹the project was primarily performed in the laboratory of Prof. Dr. Helge Bode, Johann Wolfgang Goethe-Universität. ²the co-author David Kleinhans was a Master student of mine. ³several raw photos and microscopy images were acquired together with the co-author Alexander Schmitz.

Publication Table 2 – Meta data of the published manuscripts in 2016 and 2017.

Publication	Strobl & Stelzer 2016	Strobl <i>et al.</i> 2017A	Strobl <i>et al.</i> 2017B
Number	#4	#5	#6
Epub	August 2016	April 2017	May 2017
Print Date	December 2016	-	June 2017
Journal	<i>Current Opinion in Insect Science</i>	<i>Journal of Visualized Experiments</i>	<i>Nature Protocols</i>
Publisher	Elsevier	MyJove Corporation	Nature Publishing Group
Pages	12 (with supplements)	22 (with supplements)	7 (no supplements)
PubMed ID	27939706	28518097	28471459
BugCube	Strobl2016A	Strobl2017A	-
Datasets	3 (DS0001-DS0003)	3 (DS0001-DS0003)	-
Type	Review Article	Research Article	Review Article
Subtype	Classical	Methods & Resources	Commentary
Open Access	No	No	No
Invitation	Yes	Yes	Yes
Cooperation	No	No	No
Volume	Volume II	Volume II	Volume II
Authorship	First Author	First Author	First Author
Authors	2	3 ²	3
Text	50%	75%	75%
Boxes	50% (1 in total)	-	-
Experiments	100% (example datasets)	90% ³	-
Figures	100% (3 of 3) ¹	100% (6 of 6) ⁴	50% (1 of 2)
Tables	100% (1 of 1)	100% (4 of 4)	100% (1 of 1)
SFigures	-	-	-
STables	100% (1 of 1)	100% (1 of 1)	-
SMovies	100% (1 of 1)	100% (2 of 2)	-
Comment	-	see Subchapter 5.4	-

¹Inventor-based raw images for Figure 1 were generated by Sven Plath. ²the co-author Selina Klees was a Bachelor student of mine. ³the other 10% were contributed by Selina Klees. ⁴Inventor-based raw images for Figure 2 were generated by Sven Plath.

6.1.2. Strobl & Stelzer 2014 (#1) – *Development* (Research Article)

This study provides a methodological outline to perform non-invasive long-term fluorescence live imaging of *Tribolium* embryos by using a novel mounting method that minimizes the amount of agarose necessary to keep the embryo in position during the observation process. The publication was shortened to the *Development* ‘report’ format, which allows a maximum of four display items and 7,000 words. The purpose of the report was straightforward – the *Tribolium* community should be made aware that light sheet-based fluorescence microscopy is a promising tool to observe the embryonic morphogenesis over very long time periods while the embryo remains healthy – after observation, it hatches, develops into a healthy adult and is even fertile. This is the first study that shows more than 80% of the whole *Tribolium* embryonic development period. Observation starts with the rearrangement of the uniform blastoderm and ends once muscular movement sets in. It covers the embryogenetic events gastrulation, germband elongation, germband retraction and dorsal closure entirely and along four directions.

In the second part of the report, we show the potential of light sheet technology to detect and characterize biological phenomena. We were able to link the serosa window closure process that occurs at the end of gastrulation to the serosa rupture process that happens when dorsal closure begins (Figure 6-1). Both processes are temporally considerably separated from each other – about 40% of the total embryonic development time lies between both processes.

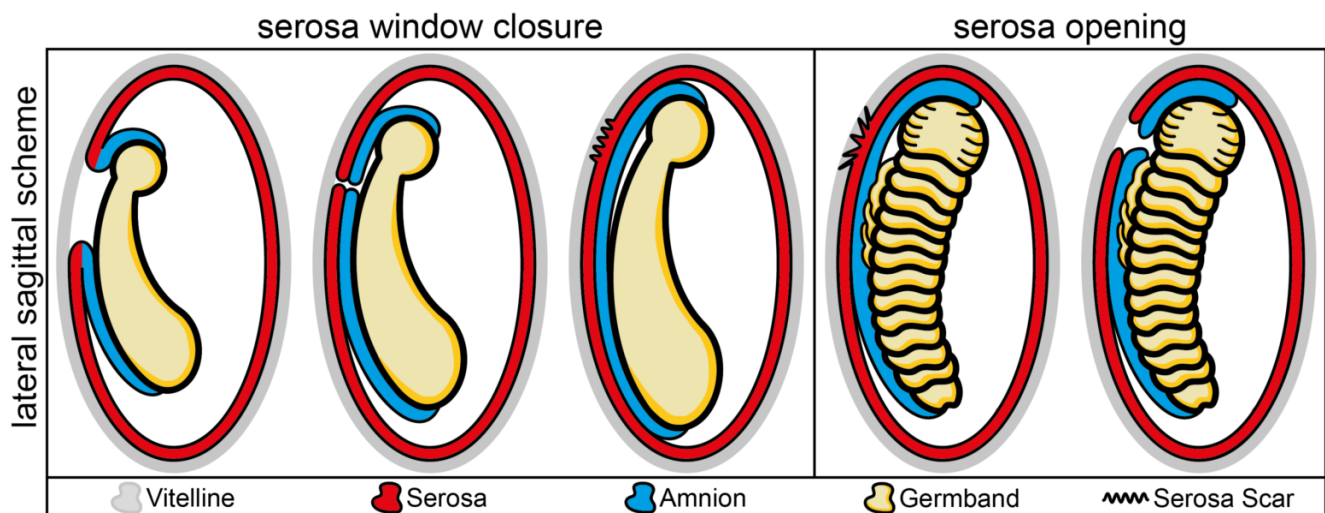


Figure 6-1 – Scheme of serosa scar formation and serosa opening. During gastrulation, the amnion and the serosa undergo an inter-tissue separation and an intra-tissue fusion during serosa window closure, leaving the serosa scar behind on the location where the window closed. The scar remains quiescent during germband elongation and retraction. During dorsal closure, the serosa scar gets pulled apart and turns into the serosa opening. This link between two spatiotemporally and functionally distinct morphogenetic processes could only be described by using light sheet-based fluorescence microscopy, which allows non-invasive long-term live imaging. Figure and/or figure description fully and/or partially reproduced from Strobl & Stelzer 2014, #1 in Publication Table 1.

6.1.3. Nollmann *et al.* 2015 (#2) – *ChemBioChem* (Research Article)

The publication describes the identification, biosynthesis and/or bioactivity of simple urea compounds and related synthetic substances deriving from the entomopathogenic bacterium *Photorhabdus luminescens*. They are believed to interfere with the function of the juvenile hormone epoxide hydrolase, a key enzyme during all stages of insect development. In *in vitro* experiments, it was observed that the synthetic compound HB71 has a strong inhibitory potential, which led to the question if a concurrent effect could be shown in *in vivo* experiments. Consequently, HB71 was applied ectopically to transgenic *Tribolium* embryos of the EFA-nGFP line that were at the beginning of germband elongation and their further morphogenetic development was observed with spinning disk confocal microscopy. The experiments were performed together with David Kleinhans (Subchapter 5.2). However, in contrast to the methoprene positive control (Figure 5-2B), HB71 did not lead to any aberrational phenotypes (Figure 6-2).

This study was primarily conducted in the laboratory of Prof. Dr. Helge Bode, who also initiated the cooperation with our group. The greater goal of this joint venture was to see if the effects of toxic metabolic products from bacteria or other small organic substances on insects can be properly analyzed with fluorescence microscopy – and to visualize the respective aberrations.

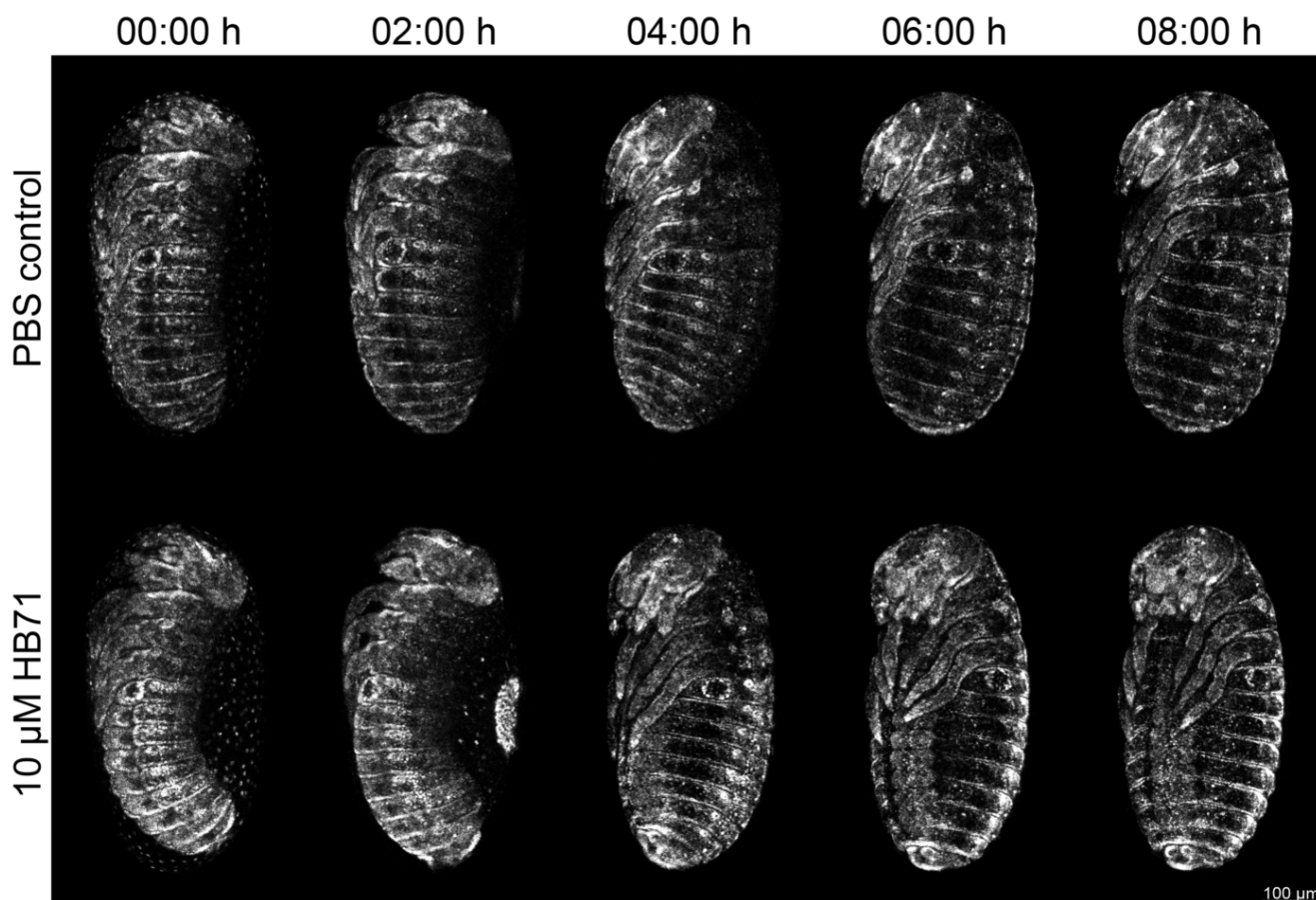


Figure 6-2 – Fluorescence live imaging of *Tribolium* embryos of the EFA-nGFP line under the effects of HB71. HB71 did not affect the embryonic development of *Tribolium* embryos, as no aberrations were found. Figure and/or figure description fully and/or partially reproduced from Nollmann *et al.* 2015, #2 in Publication Table 1.

6.1.4. Strobl *et al.* 2015 (#3) – *Nature Protocols* (Research Article)

While the methodological publication (Subchapter 6.1.2) about non-invasive long-term live imaging of *Tribolium* embryos with light sheet-based fluorescence microscopy only briefly describes technical details, this protocol provides comprehensive and well-illustrated guidelines on embryo collection, sample mounting (Figure 6-3), experimental options, imaging modalities, embryo retrieval, data processing and potential pitfalls. Especially detailed is the troubleshooting table, which addresses a broad variety of issues and is accompanied by a large figure that outlines correct and incorrect microscope calibration and sample handling. Thus, this protocol is not only of use for the *Tribolium* community, but serves as a general guideline for the application of light sheet-based fluorescence microscopy in insect developmental biology.

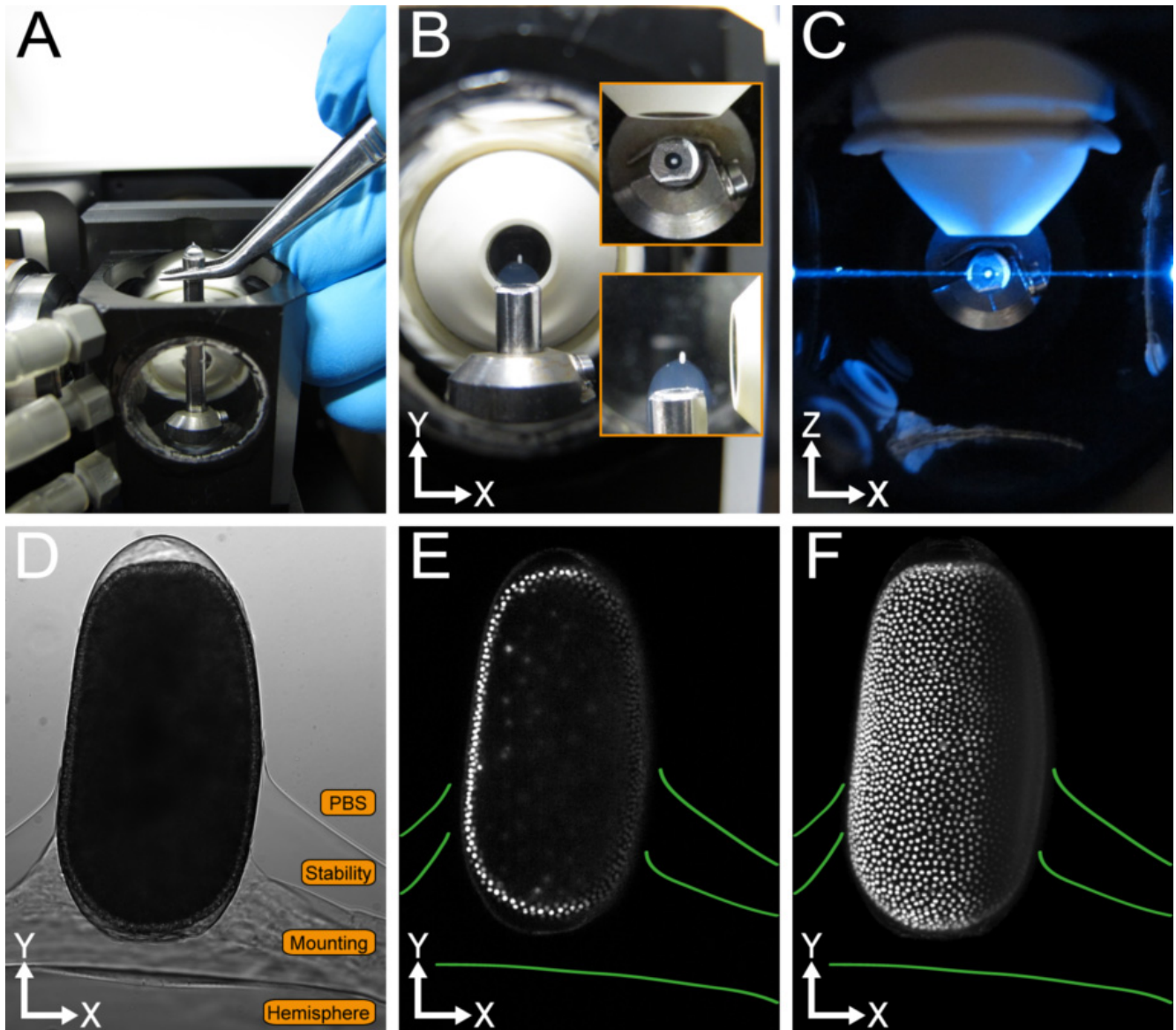


Figure 6-3 – *Tribolium* embryo mounted by using the hemisphere method. (A) Embryo insertion into the sample chamber. (B) Positioning of the embryo in front of the detection objective. (C) View from the top with light sheet. (D) Embryo in transmission light mode. Agarose layers and PBS are annotated. (E) Single plane from the center of the embryo. (F) Z maximum projection. The boundaries of the agarose layers are outlined in green. Figure and/or figure description fully and/or partially reproduced from Strobl *et al.* 2015, #3 in Publication Table 1.

6.1.5. Strobl & Stelzer 2016 (#4) – *Current Opinion in Insect Science* (Invited Review Article)

This invited review article attempts to increase the attractiveness of light sheet-based fluorescence microscopy within the insect developmental biology community. Firstly, it explains the principle (Figure 6-4) and benefits of light sheet technology for imaging assays involving living specimens, *i.e.* strongly reduced photo-toxicity, nearly no photo-bleaching, a supreme signal-to-noise ratio and extremely fast acquisition speed. Secondly, it summarizes all currently available labeling options for *Tribolium* embryos and describes the respective advantages and disadvantages. Thirdly, it highlights state-of-the-art scientific questions and outlines how light sheet technology may be used to address these challenges. Fourthly, it discusses the comparative approach to investigate the embryonic morphogenesis of insects by considering their evolutionary context (Subchapter 4.2.2).

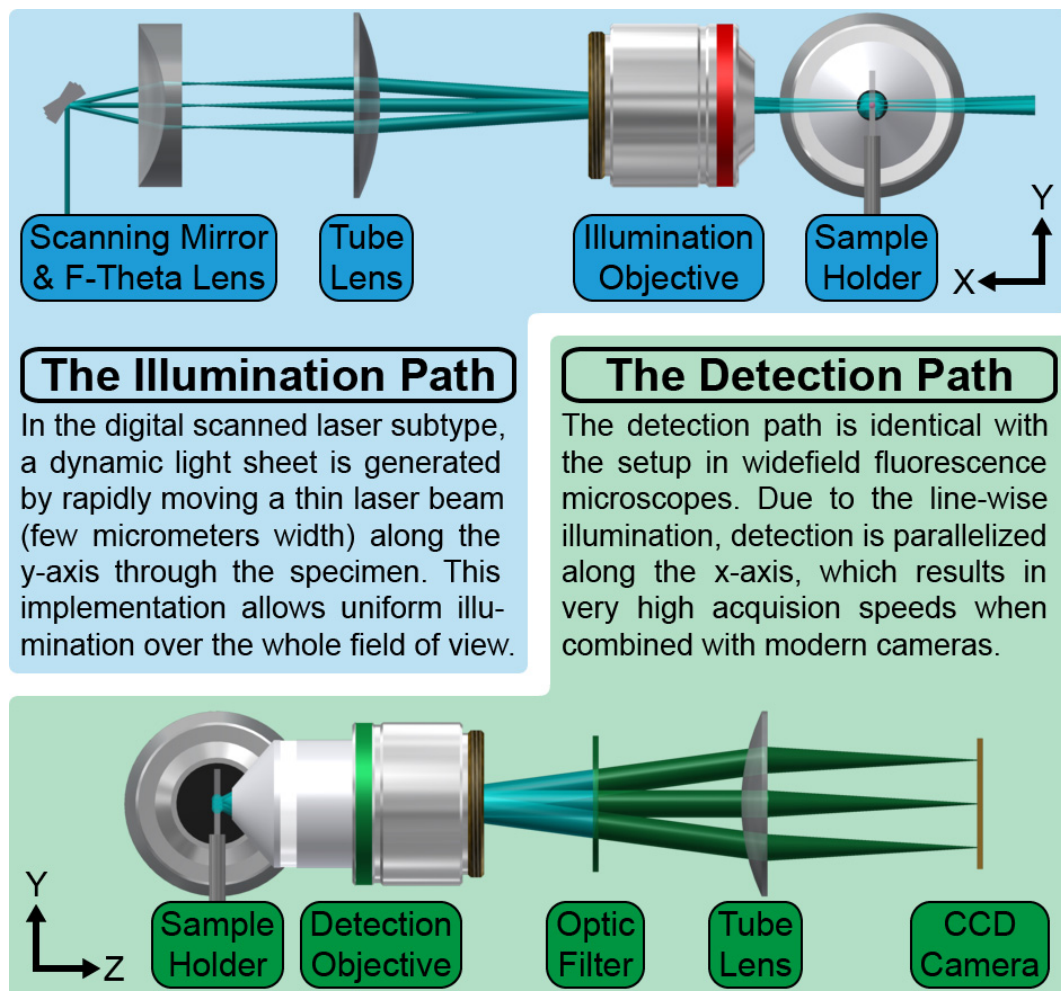


Figure 6-4 – Scheme of the illumination and detection arms of a digital scanned laser light sheet-based fluorescence microscope. This light sheet-based fluorescence microscopy implementation generates a dynamic light sheet by rapidly scanning the laser beam along the Y axis. Figure and/or figure description fully and/or partially reproduced from Strobl & Stelzer 2016, #4 in Publication Table 2.

6.1.6. Strobl *et al.* 2017A (#5) – *Journal of Visualized Experiments* (Invited Research Article)

Similar to the first protocol (Subchapter 6.1.4), this manuscript also explains the procedure on how *Tribolium* embryos can be imaged with light sheet technology in a complementary way instead of repeating the arguments and conclusions. The manuscript outlines classic and state-of-the-art fluorescence microscopy techniques (Figure 6-5), introduces two novel transgenic lines, presents three mounting techniques with different experimental purposes and explains their advantages, extends the imaging guidelines also to fixed and stained *Tribolium* embryos and provides comprehensive guidelines for quality control in live imaging assays, especially for approaches that provoke developmental aberrations such as RNA interference or application of extrinsic bioactive factors.

The peculiarity of the *Journal of Visualized Experiments* is that in addition to the publication, also a high quality, highly engaging scientific video is produced that should increase reproducibility. The video features documentary scenes filmed within the laboratories, schematic visualizations, movies generated from the respective data and interviews with the authors.

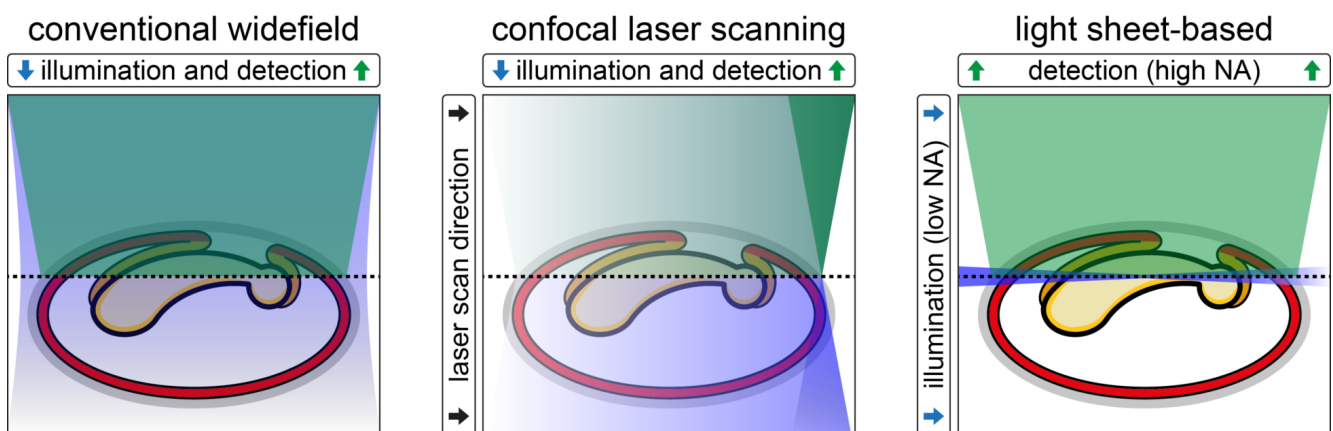


Figure 6-5 – Comparison of conventional widefield, confocal laser scanning and light sheet-based fluorescence microscopy. Conventional wide-field microscopes use xenon arc/mercury-vapor lamps with appropriate fluorescence filters or high-power light emitting diodes as excitation light sources. For each two-dimensional image that is acquired, the whole specimen has to be illuminated. In confocal laser scanning microscopy, a Gaussian laser beam is scanned through the specimen and fluorescence is detected point-by-point. Similar to conventional widefield microscopes, the whole specimen is illuminated for each two-dimensional image that is acquired. In contrast, light sheet-based fluorescence microscopes guide a Gaussian laser beam perpendicularly to the detection axis through the specimen and fluorescence is detected either plane-by-plane or line-by-line. During the acquisition of a two-dimensional image, only a small volume centered on the focal plane of the detection objective is affected by the excitation light. The remaining volume is not illuminated, does not contribute to out-of-focus blur, and does not suffer from photo-toxicity or photo-bleaching. Figure and/or figure description fully and/or partially reproduced from Strobl *et al.* 2017A, #5 in Publication Table 2.

6.1.7. Strobl *et al.* 2017B (#6) – *Nature Protocols* (Invited Review Article)

For the tenth anniversary, *Nature Protocols* launched an editorial about ten technological areas in which there has been particular methodological progress over the last decade, one of them being light sheet-based fluorescence microscopy, and invited relevant scientists to write short opinionated commentaries.

Obligatory, the commentary explains the history, principle and technological radiation of light sheet-based fluorescence microscopy, but also points out the benefits for two subdisciplines within life sciences. For cell biology, light sheet-based fluorescence microscopy synergizes well when combined with advanced sample preparation techniques such as optical clearing (Figure 6-6A). This improves the segmentation performance of subcellular structures such as cell nuclei (Figure 6-6B) and allows a quantitative evaluation of complex multicellular such as acini (Figure 6-6C). For insect developmental biology, the commentary compares the transition from on-demand to systematic data acquisition with a similar procedure that occurred in eukaryotic genomics some decades ago and outlines the how large-scale image databases support the comparative approach (Subchapter 4.2.2).

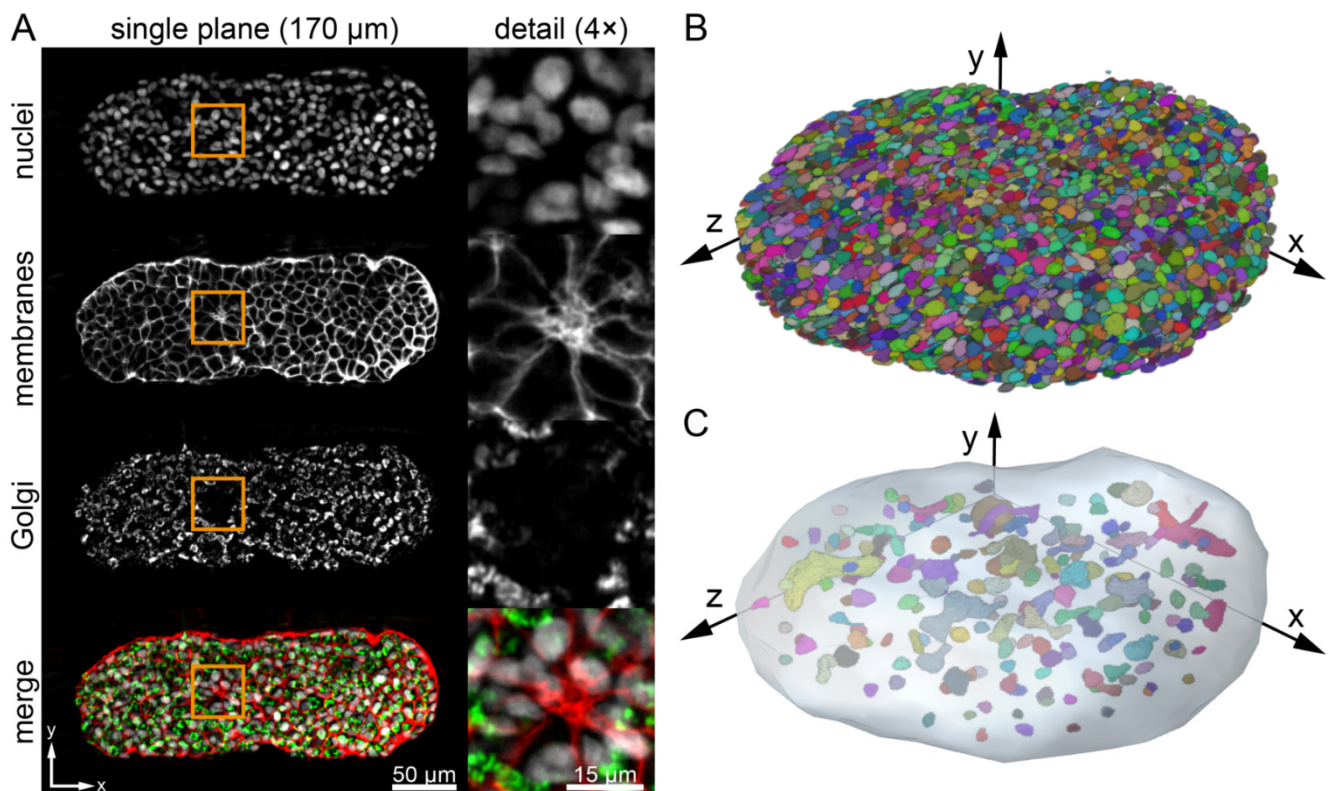


Figure 6-6 – Light sheet-based fluorescence microscopy in three-dimensional cell biology. (A) Single plane of an optically cleared and triple-stained (nuclei, membranes and Golgi apparatus) spheroid (2,000 seeded T47D breast cancer cells, ten days formation). The detail images in the right column show an acinus during the initiation phase. (B) Cell nuclei segmentation and volume rendering of the same spheroid. (C) Acini segmentation and volume rendering of the same spheroid. The light blue shading is the approximated surface of the spheroid based on the cell nuclei segmentation. Images were acquired by Katharina Hötte, segmentation was performed by Alexander Schmitz. Figure and/or figure description fully and/or partially reproduced from Strobl *et al.* 2017B, #6 in Publication Table 2.

6.2. Submitted and Submission-Ready Manuscripts

6.2.1. Nota Bene

In this subchapter, the scope and major achievements of my four submitted and submission-ready research articles (#7 to #10) are summarized. The manuscripts are found in Volume II and III of my PhD thesis. Meta data of the publications are given in Publication Table 3. Please note the following:

- The manuscripts are formatted according to the respective guidelines provided by the favored journal and the denomination is yet provisional and may change according to the publication order.
- All four manuscripts presented here were just recently or not yet submitted. Thus, all text passages, figures and tables are still subject to change.
- Although data acquisition for the long-term live imaging of *Gryllus bimaculatus* (Subchapter 3.1) and the registration and fusion of *Tribolium* long-term live imaging datasets (Subchapter 3.2) projects is completed, the results have not yet been summarized in the form of a presentable manuscript. Writing is scheduled for fall 2017. The BugCube (Subchapter 3.3), AClashOfStrings (Subchapter 3.4) and AStormOfRecords (Subchapter 3.5) projects require additional work.

Publication Table 3 – Meta data of the four submitted and submission-ready manuscripts.

Publication	Strobl <i>et al.</i> 2017C	Strobl <i>et al.</i> 2017D	Strobl <i>et al.</i> 2017E	Strobl <i>et al.</i> 2017F
Number	#7	#8	#9	#10
Submitted	January 2017	August 2017	Not Yet Submitted	Not Yet Submitted
Status	Under Review (2 nd round)	Under Review (1 st round)	-	-
Pages	30 (raw manuscript)	55 (raw manuscript)	39 (raw manuscript)	54 (raw manuscript)
BugCube	-	Strobl2017D	Strobl2017E	-
Datasets	-	3 (DS0001-DS0003)	9 (DS0001-DS0009)	-
Type	Research Article	Research Article	Research Article	Research Article
Subtype	Methods & Resources	Biotechnology	Data Publication	Classical
Invitation	No	No	No	No
Cooperation	No	No	Yes ⁶	Yes ⁶
Volume	Volume II	Volume II	Volume III	Volume III
Authorship	First Author	First Author	First Author	First Author
Authors	3 ¹	3 ⁴	4	4
Text	75%	95%	95%	95%
Boxes	-	-	-	-
Experiments	60% ²	95% ⁵	100%	-
Figures	100% (4 of 4) ³	100% (5 of 5)	100% (2 of 2)	100% (7 of 7)
Tables	-	100% (1 of 1)	100% (2 of 2)	100% (2 of 2)
SFigures	100% (2 of 2)	100% (11 of 11)	100% (4 of 4)	100% (1 of 1)
STables	100% (1 of 1)	100% (17 of 17)	100% (1 of 1)	100% (3 of 3)
SMovies	-	100% (3 of 3)	100% (1 of 1)	100% (2 of 2)
Comment	-	-	back-to-back with #10	back-to-back with #9

¹ the co-author Alexander Ross was a Master student of mine. ² the other 40% were contributed by Alexander Ross. ³ several raw photos and microscopy images were acquired together with the co-author Alexander Ross. ⁴ the co-author Anita Anderl was a Master student of mine. ⁵ the other 5% were contributed by Anita Anderl and two technical assistants of the group, Berit Reinhardt and Sigrun Becker. ⁶ the project was primarily performed in our laboratory, but with support from Dr. Marc F. Schetelig, Justus-Liebig-Universität, Gießen.

6.2.2. Strobl *et al.* 2017C (#7) – *To Be Determined* (Research Article)

This manuscript describes the extraction of genomic DNA from *Tribolium* wing tissue, which can be used in PCR-based genotyping assays. The wing tissue is dissected from paralyzed adults, which typically survive this procedure and are thus available for further experiments or as crossing partners. This protocol was adapted from studies already available for *Drosophila* [372] and *Apis* [373], but came with an additional challenge, as the hindwing of *Tribolium* is covered by protective elytra. The obtained DNA is sufficient for up to ten PCR-based assays and is even adequate for sequencing (Figure 6-7).

Adaption of convenient protocols is an important step to enlarge the arsenal of techniques for emerging model organisms, and our guideline simplifies large-scale rearing and the conceptualization of experimental workflows in which the genotype of individual beetles has to be determined without sacrificing them. The idea for this side project emerged before the AGOC vector concept (Subchapter 2.2.7) was invented. By using the AGOC vector concept, molecular biology-based assays are not necessary anymore and the genotype can already be non-invasively determined during the latter stages of embryogenesis, but unlike technique presented in this study, it works only when individuals should be genotyped for transgenes.

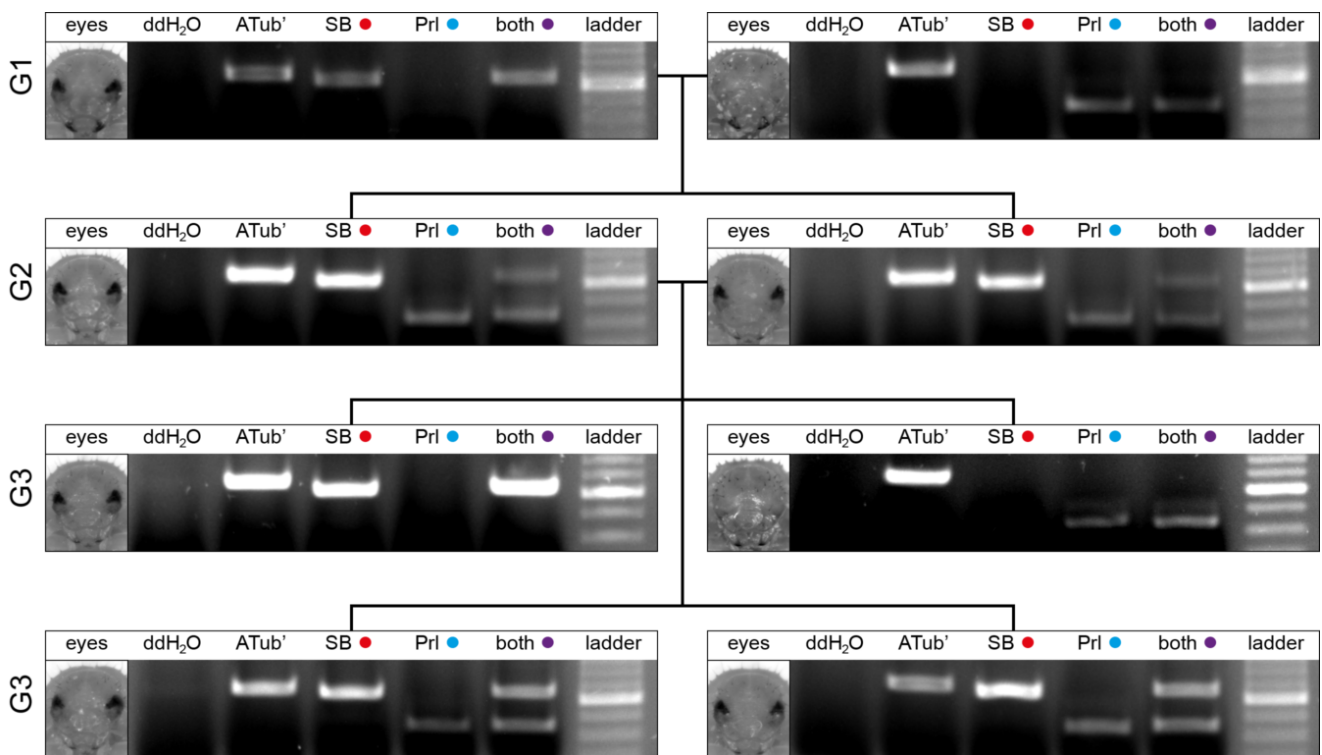


Figure 6-7 – Proof-of-principle over three generations for the established non-lethal genotyping method. Exemplary results from the proof-of-principle PCR-based genotyping assay for the white allele from the G1 to G3. Estimated PCR product size is 616 bp for the *alpha-tubulin 1* control (ATub'), 577 bp for the San Bernadino primer group, 349 bp for the Pearl primer group and 577 and 349 bp for the primer group that contains both forward primers. Bright DNA ladder band represents 500 bp. Figure and/or figure description fully and/or partially reproduced from Strobl *et al.* 2017C, #7 in Publication Table 3.

6.2.3. Strobl *et al.* 2017D (#8) – *To Be Determined* (Research Article)

This manuscript explains the principle and the genetic background of the AGameOfClones vector concept in comprehensive detail. In brief, it allows the systematic creation of homozygous transgenic lines by performing Cre-mediated recombination of two transformation markers embedded in interweaved, but incompatible lox site pairs, which results in two clearly distinguishable phenotypes. Consequently, individuals that carry both markers can be identified as homozygous.

While the main text is short and concise, the study is accompanied by a broad variety of supplementary material that underlines the conclusions. One of the most impressive figures shows the fluorescence in the compound eyes of the F4 mCe×mO-mC double hemizygous hybrid generation (Figure 6-8A). While mCe, which accompanies the Cre-expressing cassette, is uniformly detected throughout the whole compound eyes, single ommatidia express either only mO or mC (Figure 6-8B) due to recombination in the somatic neuronal progenitor cells during embryonic development.

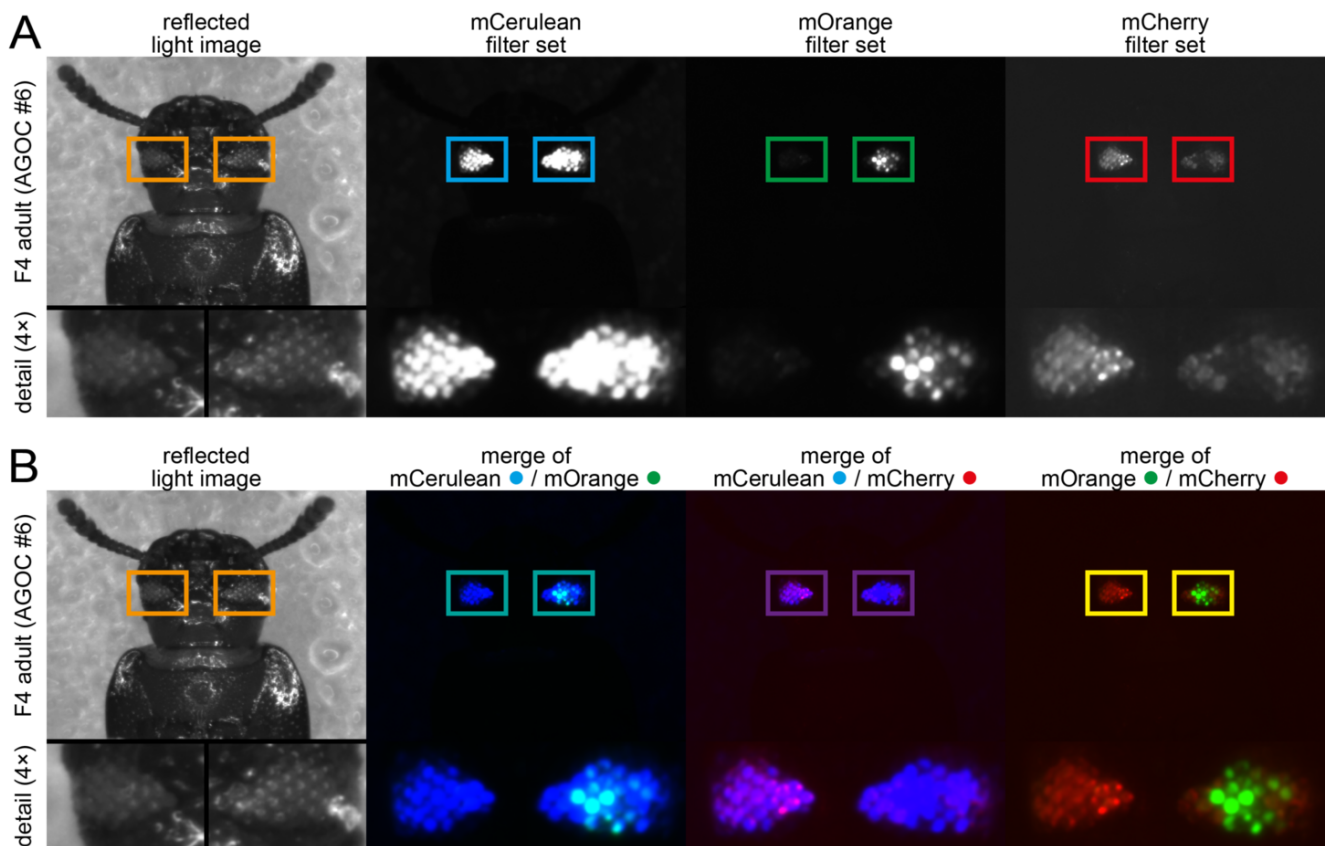


Figure 6-8 – F4 mCe×mO-mC double hemizygous generation. (A) The F4 hybrids are hemizygous for both the AGOC and the Cre-expressing helper transgene and thus carries mCe, mO and mC. In these individuals, recombination occurs in germ cells but also in certain somatic progenitor cells that later on give rise to distinct, typically spatially clustered cell populations. This effect is evident in the compound eyes, where certain cluster of ommatidia show either expression of mO or mC. (B) Within the merged images, it becomes evident that most of the ommatidia express either exclusively mO or mC in a quite random pattern. Figure and/or figure description fully and/or partially reproduced from Strobl *et al.* 2017B, #6 in Publication Table 3.

6.2.4. Strobl *et al.* 2017E (#9) – *To Be Determined* (Research Article)

This data article manuscript outlines sample preparation (Figure 6-9), non-invasive long-term fluorescence live imaging and data processing for nine datasets that document the embryonic development of *Ceratitis*. Six of the datasets show the embryo *in toto* and document approximately 97% of the time period between fertilization and hatching, while the three remaining datasets document specific processes with a higher spatial resolution. Additionally, a two-level staging system for *Ceratitis* is proposed. The decision to split the *Ceratitis* study into two publications derived from the idea to decouple the raw data from subjective description and/or interpretation and make them available as an open access resource for the developmental biology community. This project was a cooperation with Dr. Marc F. Schetelig, Justus-Liebig-Universität Gießen.

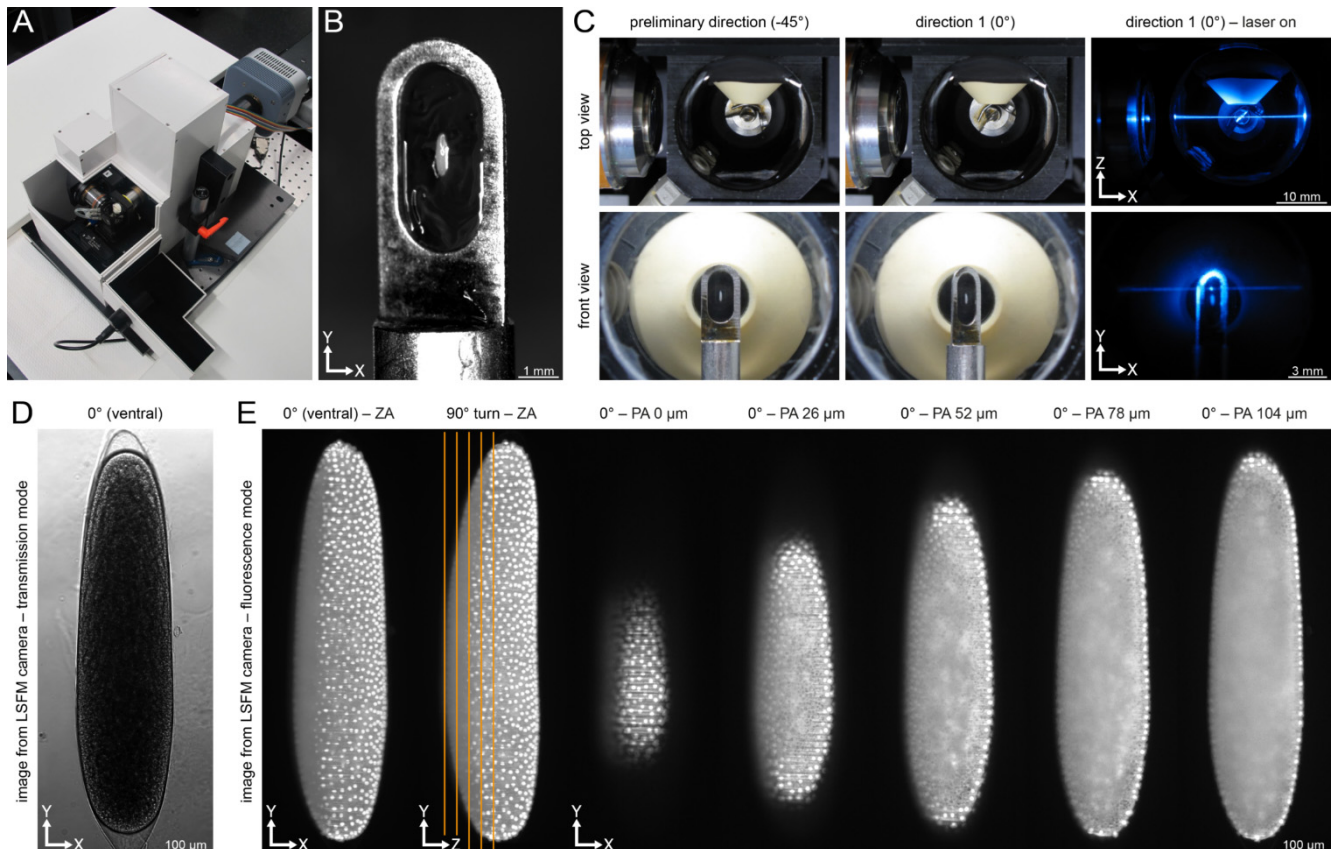


Figure 6-9 – Mounting of *Ceratitis* embryos to the cobweb holder and insertion into the sample chamber. (A) Diagonal view of the microscope. **(B)** Cobweb holder with *Ceratitis* embryo embedded into an agarose film. **(C)** Top view (upper row) and front view (lower row) of the sample chamber. Firstly, the embryo is centered in front of the detection objective (first column), which is defined as the preliminary direction (-45°). Afterwards, the embryo is rotated by 45° (second column), which is defined as direction 1 (0°). This setup allows illumination of the embryo with the laser beam and simultaneous acquisition of images with the detection objective (third column). **(D)** Transmission light image of a *Ceratitis* embryo. **(E)** Example fluorescence images of an acquired image stack. The locations of the planes are indicated by orange lines. ZA, Z maximum projection with image adjustment; PA, plane with image adjustment. Figure and/or figure description fully and/or partially reproduced from Strobl *et al.* 2017E, #9 in Publication Table 3.

6.2.5. Strobl *et al.* 2017F (#10) – *To Be Determined* (Research Article)

As already described for the data article manuscript (Subchapter 6.2.4), it is convenient to decouple the raw data from subjective description and interpretation. While the staging system was already proposed in the data article manuscript, this manuscript aims to extract biologically relevant information from the raw data (Figure 6-10). It (i) contains a comprehensive and well-illustrated description of the whole embryonic morphogenesis of *Ceratitis*, (ii) is supported by a large, chronological table of all observable developmental processes, (iii) provides quantitative values whenever appropriate, including temporal standard deviations, (iv) highlights phylogenetic derived traits, (v) discusses *Ceratitis* as a model organism for developmental biology, (vi) compares our workflow to traditional approaches and (vii) ends by outlining the importance of professionally established staging systems for emerging insect model organisms. This project was a cooperation with Dr. Marc Schetelig, Justus-Liebig-Universität Gießen.

This manuscript, together with the back-to-back submitted data article manuscript, should serve as a working guideline for any further similar work in developmental biology (Subchapter 4.2.1). This description as well as any similar future studies contribute to the transition from on-demand to systematic microscopy data acquisition of the embryonic development of emerging insect model organisms (Subchapter 4.2.5). If the ‘Reinhart Koselleck-Projekt’ becomes feasible (Subchapter 4.1.2), it is planned to write similar articles for *Aedes*, *Bicyclus*, *Tribolium*, *Apis* and *Gryllus*.

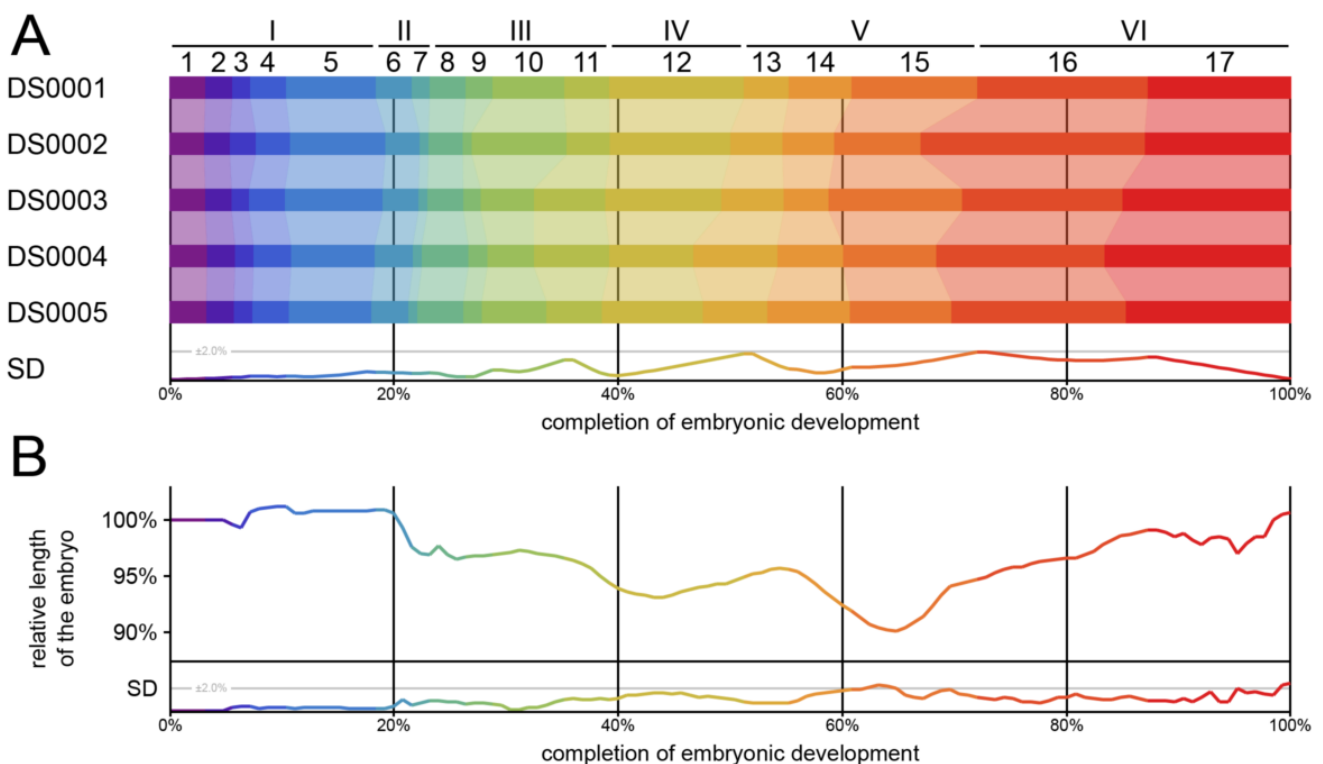


Figure 6-10 – Staging of *Ceratitis* embryogenesis and morphological analysis of five datasets. (A) Individual dataset staging and standard deviation (SD) in percent of total development. **(B)** Average relative length with standard deviation as a function of embryonic development. Figure and/or figure description fully and/or partially reproduced from Strobl *et al.* 2017F, #10 in Publication Table 3.

6.3. Patent and Grant Applications

6.3.1. Patent Application – The AGameOfClones Vector Concept

It is not unusual that biotechnological inventions are of economic relevance. The AGOC vector concept (Subchapter 2.2.7) has immense potential to save resources, simplify experimental workflows and contribute to the ethically motivated endeavor to reduce the number of wasted animals. Thus, with the support of Innovectis, a subsidiary of the Johann Wolfgang Goethe-Universität specialized on the commercialization of inventions, a patent application for the AGOC vector concept, with the identification number 2017061214242700DE, was filed.

The concept was initially developed for *Tribolium*, an emerging insect model organism in developmental biology that is also considered a pest species since it feeds on stored grain and other agricultural products [115,202]. The AGOC vector concept could strongly reduce the workload during the establishment of molecular biology-based pest management strategies for *Tribolium* [374] and other insects such as *Ceratitis* [375] and various mosquito species [376–381], which usually demand experimental workflows based on large-scale germline transformation and management of an immense number of transgenic lines and sublines.

However, the AGOC vector concept is not limited to insect species. With respective modifications, the concept can be adapted to basically every diploid eukaryotic organism for which germline transformation has been established, including – but not limited to – mouse, rat, zebrafish and various plants (Subchapter 4.1.5). Commercial potential of our concept is expected in the following scenarios:

- A broad variety of standard vectors for germline transformation of various animal species can be purchased from respective companies. It might be convenient to also offer variants of these vectors that are based on the AGOC vector concept.
- Several providers offer all-in-one (strategy design, cloning, injection and screening) services for the creation of custom transgenic mouse [382,383] and rat [384] lines. In classical knock-in assays, an AGOC vector concept-based element can be placed upstream or downstream relative to the transgene of interest, while in classical knock-out assays, the gene of interest can be replaced fully or partially by an AGOC vector concept-based element. At first, the provider creates the respective transgenic lines and supplies the customer with several pre-recombination individuals to perform preliminary experiments. Subsequently, the provider carries out recombination procedure, and after completion, the customer also receives several post-recombination individuals.
- The AGOC vector concept also supports the trend to automatize certain processes in the laboratory. As an example, two hands-off strategies for the allocation of zebrafish embryos to 96-well plates have been suggested [385,386], but they do not support sorting by genotype. The AGOC vector concept would synergize well with a sorting system that is equipped with a fluorescence detection unit. When the concept becomes broadly adapted, standardized commercial versions of such sorting systems would be convenient.
- Considerable effort goes into the creation of transgenic plants that are resistant against herbicides [387,388] or certain pathogens, for example insects [389–393], microorganisms [394,395] and viruses [396–398] and several companies are specialized on the creation of genetically modified crops that withstand harsh environmental conditions. The AGOC, ACOS (Subchapter 3.4) and ASOR (Subchapter 3.5) vector concepts can be used to create transgenic crop lines that are resistant against a specific detrimental factor. Then, depending on the specific requirements of the customer, double or triple transgenic hybrid lines can be created that withstand multiple detrimental factors. Since the lines are homozygous, the transgenes are not subject to allele frequency dynamics [399].

The claims are the centerpiece of every patent application. The primary claim of our vector concept is straightforward – it simply states the structural arrangement of six genetic elements that constitute the interweaved but incompatible arrangement of the lox site pairs (termed 5' and 3' donor/acceptor nucleic acid sequence) and the respective transformation markers (termed transgenes). The figures within the patent application are reproduced from display items originally generated for the manuscript (Subchapter 6.2.3) which were optimized for black-and-white-printing. However, especially in genetics, it is of great importance that claims in patent applications are as broad as possible so that the functionality cannot be reproduced by trivial changes in the architecture. Thus, the patent application contains an additional figure that illustrates eight additional vector architecture suggestions that result in a similar function (Figure 6-11). The patent application can be found in Volume III of my PhD thesis.





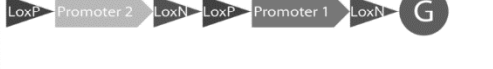

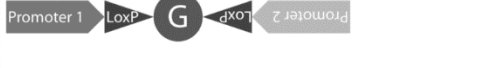


	Hemizygotes Pre-R	Hemizygotes Post-R	Heterozygotes	Homozygotes	Rationale
	(i) 1 - G and 1 - R (ii) - - - - -	(i) 1 - G (i) 1 - R (ii) - - - (ii) - - -	(i) 1 - G (ii) 1 - R	(i) 1 - G (i) 1 - R (ii) 1 - G (ii) 1 - R	Two identical promoters, two different proteins. Similar to Figure 1.
	(i) 1 - G and 2 - G (ii) - - - - -	(i) 1 - G (i) 2 - G (ii) - - - (ii) - - -	(i) 1 - G (ii) 2 - G	(i) 1 - G (i) 2 - G (ii) 1 - G (ii) 2 - G	Two different promoters, two identical proteins.
	(i) 1 - G and 2 - R (ii) - - - - -	(i) 1 - G (i) 2 - R (ii) - - - (ii) - - -	(i) 1 - G (ii) 2 - R	(i) 1 - G (i) 2 - R (ii) 1 - G (ii) 2 - R	Two different promoters, two different proteins.
	(i) 1 - G (ii) - - -	(i) 1 - G (i) 1 - R (ii) - - - (ii) - - -	(i) 1 - G (ii) 1 - R	(i) 1 - G (i) 1 - R (ii) 1 - G (ii) 1 - R	One promoter, two different proteins. Shorter than the systems above.
	(i) 1 - G (ii) - - -	(i) 1 - G (i) 2 - G (ii) - - - (ii) - - -	(i) 1 - G (ii) 2 - G	(i) 1 - G (i) 2 - G (ii) 1 - G (ii) 2 - G	Two different promoters, one protein. Shorter than the systems above.
	(i) 1 - G (ii) - - -	(i) 1 - G (i) 1 - R (ii) - - - (ii) - - -	(i) 1 - G (ii) 1 - R	(i) 1 - G (i) 1 - R (ii) 1 - G (ii) 1 - R	One promoter, two different proteins. Even shorter.
	(i) 1 - G (ii) - - -	(i) 1 - G (i) 2 - G (ii) - - - (ii) - - -	(i) 1 - G (ii) 2 - G	(i) 1 - G (i) 2 - G (ii) 1 - G (ii) 2 - G	Two different promoters, one protein. Even shorter.
	(i) 1 - G (ii) - - -	(i) 1 - G (i) 1 - R (ii) - - - (ii) - - -	(i) 1 - G (ii) 1 - R	(i) 1 - G (i) 1 - R (ii) 1 - G (ii) 1 - R	One promoter, two different proteins. Even shorter.
	(i) 1 - G (ii) - - -	(i) 1 - G (i) 2 - G (ii) - - - (ii) - - -	(i) 1 - G (ii) 2 - G	(i) 1 - G (i) 2 - G (ii) 1 - G (ii) 2 - G	Two different promoters, one protein. Even shorter.

Figure 6-11 – The initial AGameOfClones vector concept and eight additional vector architecture suggestions resulting in a similar function. Suggestion 1 is identical to the AGOC vector concept (Subchapter 2.2.7). Suggestions 1 to 5 are based on recombination-excision, while 6 to 9 are based on recombination-inversion. Promoter 1 and 2 resemble two regulatory sequences with a different spatiotemporal expression pattern. G and R resemble two different transgenes, for example fluorescent proteins with non-overlapping excitation and emission maxima. Pre-R, pre-recombination; Post-R, post-recombination. Figure and/or figure description fully and/or partially reproduced from patent application 2017061214242700DE.

6.3.2. Grant Application – The ‘Reinhart Koselleck-Projekt’

By successfully imaging large periods of the embryonic development of three emerging insect model organisms, my PhD thesis contributes considerably to insect developmental biology and evolutionary developmental biology, but does not yet consider ecological criteria. To obtain further insights into the evolution of development, also with noticeable consideration of several crucial environmental factors, a grant application entitled ‘Morphotypic-quantitative embryonic variability of prominent beneficial and detrimental insects influenced by intrinsic and extrinsic factors’ was prepared to finance additional research personnel, novel light sheet-based fluorescence microscopes and the necessary infrastructure. Biological background and scientific rationale are described in Outlook I (Subchapter 4.1.2).

One of the non-trivial questions during the planning phase of the project was how many insect species besides the ‘gold standard’ *Drosophila* should be taken into consideration. The number of side-by-side comparisons (c) that can be performed increases according to the Gaussian sum formula with a linearly increasing number of additional species (n):

$$c = \frac{n^2 + n}{2}$$

If for example six additional species are selected, a total of twenty-one side-by-side comparisons can be performed. However, the total number and choice of additional species has to be carefully considered:

- It is scientifically both convenient and elegant to select candidates that form a phylogenetic tree with an approximately linearly decreasing relationship to *Drosophila*. Preferably, evolutionary splits in certain prominent geologic periods, e.g. Devonian, Carboniferous and Cretaceous, are covered.
- It is also reasonable to choose candidates from insect orders that are considered evolutionary very successful. The most commonly used criterion for success is typically the total count of described species within that order, which applies specifically to the Diptera (flies and mosquitos), Lepidoptera (butterflies and moths), Coleoptera (beetles) and Hymenoptera (bees, wasps and ants) orders, which are all part of the Holometabola.
- The significance of the project rises considerably when species with a certain agricultural and medical relevance are chosen. For agricultural aspects, both beneficial species such as honeybees and butterflies as well as detrimental species such as certain beetles can be considered, while for medical aspects, usually only detrimental species such as mosquitoes are of relevance.
- The candidates should also be selected in compliance with the current broader scientific ‘big picture’ on emerging insect models as witnessed by the avantgardistic *Emerging Model Organisms* books [14,15].
- One of the most crucial criteria is the compatibility of the eggs with fluorescence microscopy assays, i.e. they have to be at least moderately transparent, they have to be small enough so that they can be imaged *in toto* and they should develop properly in aqueous imaging buffers.
- It is also of vast importance to estimate the efforts that have to be invested into each candidate before the actual fluorescence microscopy assays can be performed. Expenditure is expected on different levels:
 - The efforts to rear differ strongly from species to species. While *Drosophila*, *Ceratitis*, *Tribolium* and *Gryllus* can be easily cultivated in incubators, mosquitoes need to feast on warm blood before they reproduce, butterflies need large hanging cages and fresh plants and the most relevant Hymenoptera, the honeybee, is a social insect that builds large hives.

- For each species, a vector for germline transformation has to be created. The major difficulty lies within the upstream regulatory sequences, *i.e.* the promoters, which are necessary for proper expression of the fluorescent proteins during embryonic development. If the genome sequence is not yet available, respective sequences have to be obtained with inconvenient methods, for example via degenerate PCR.
- Except for *Drosophila* [73,74] and *Tribolium* (Subchapters 2.2.1 and 2.2.2), live imaging protocols for light sheet-based fluorescence microscopes are not available and have to be established. Presumably, imaging modalities have to be carefully optimized for each species.

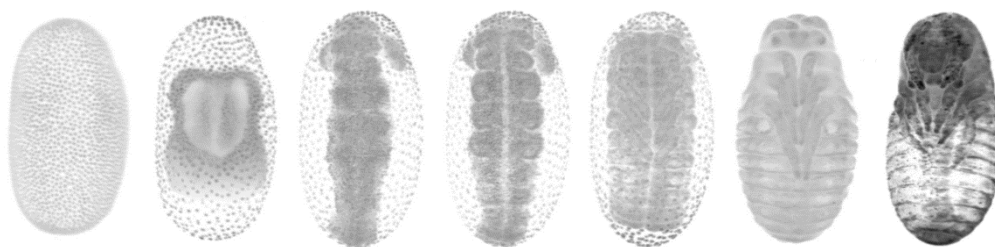
In addition to the four species that have already been investigated, the choice fell on three additional candidates of particular interest: The squinting bush brown *Bicyclus anynana* is an established model organism for evolutionary genetics and color pattern formation [400] can be cultivated and transformed within our laboratory. In contrast, the Asian tiger mosquito *Aedes albopictus* and the honeybee *Apis mellifera* are cultivated in cooperation with the groups of Dr. Ruth Müller and Prof. Dr. Bernd Grünewald, which are both also located at the Johann Wolfgang Goethe-Universität.

The second non-trivial question concerns the environmental factors that should be altered to test the developmental robustness. Four factors were chosen by thoughtfully considering their ecological relevance, the technical feasibility and their proximity to contemporary geopolitical issues, *e.g.* climate change and environmental pollution: temperature, pH value, UV irradiation and ion concentration.

Both questions outlined above indicate the high interdisciplinary level of the project, since it combines elements of optical physics, genetics, developmental biology, evolution, ecology and bioinformatics, and is estimated to occupy about three to five scientists over a period of up to five years.

Due to the fairly unrestricted regularities concerning the scope of the project, the temporal schedule and the financial frame, the ‘Reinhard Koselleck-Projekt’ program of the Deutsche Forschungsgemeinschaft appeared to be the ideal choice for the grant application. The application was submitted in March 2016, rejected in October 2016 by the Fachkollegium Zoologie and is now prepared for re-submission in fall 2017 with the request to forward the proposal to a more interdisciplinary orientated Fachkollegium. The grant application, to which I contributed significantly, can be found in Volume III of my PhD thesis.

7. Trivia

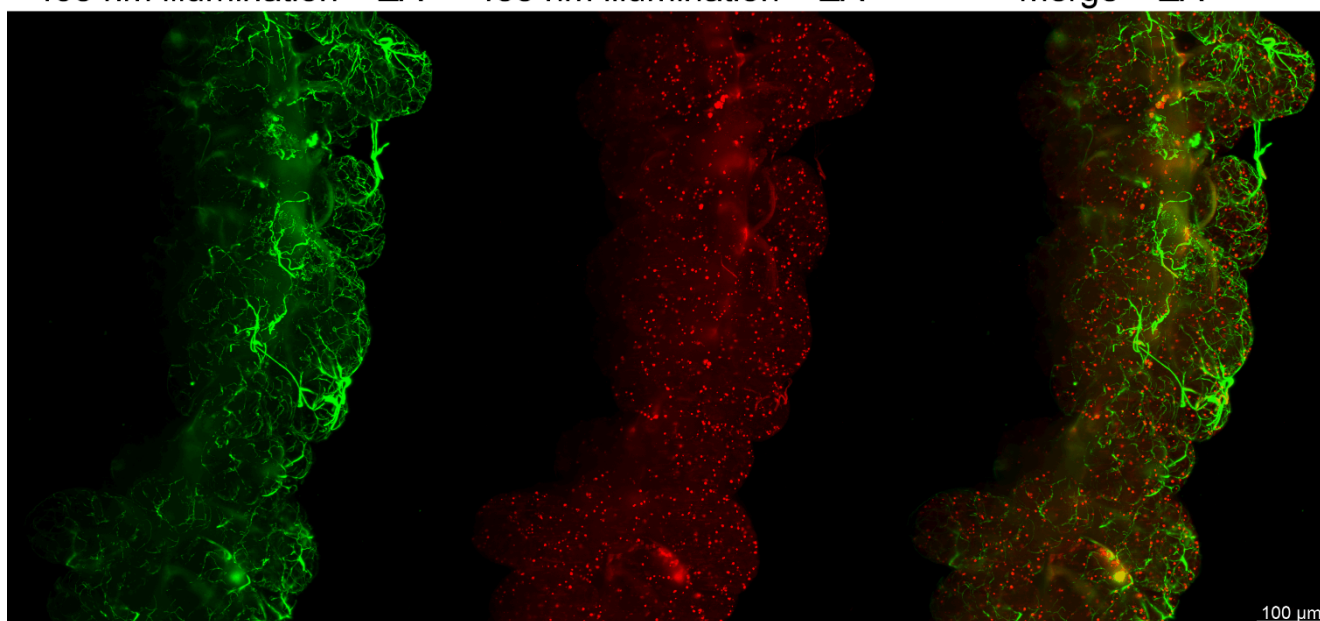


In diesem Kapitel findet sich die gesamten erforderlichen und optionalen Metainformationen zu meiner Doktorarbeit. Aus Platzgründen sehe ich bewusst davon ab, alle Abbildungen und Tabellen aufzulisten und auch ein Abkürzungsverzeichnis ist bei der absichtlich gering gehaltenen Anzahl nicht wirklich praktikabel. Mein Lebenslauf ist ebenfalls so kurz wie möglich gehalten. Ich verzichte außerdem darauf, alle Konferenzen aufzulisten, die ich im Laufe meiner Doktorarbeitszeit besucht habe. Die EuroEvoDevo-Treffen in Wien 2014 und Uppsala 2016 waren wohl die mit Abstand lehrreichsten Abenteuer, die ich im Laufe der Zeit beschritten habe, und ich gehe stark davon aus, dass meine derzeitige und zukünftige Forschung dort immer sehr gut aufgehoben sein wird.

405 nm illumination – ZA

488 nm illumination – ZA

merge – ZA



Autofluorescence of a freshly dissected nectary gland of an *Apis* adult worker recorded by using light sheet-based fluorescence microscopy. The gland was illuminated either with the 405 nm laser (447/55 bandpass filter) or the 488 laser (525/50 bandpass filter). In both spectral channels, a totally different fluorescence pattern was obtained. The nectary glands were imaged in cooperation with the Bieneninstitut of the Johann Wolfgang Goethe-Universität (Paul Siefert and Prof. Dr. Bernd Grünewald). This chapter figure is representative for all collaborations in which I contributed, but were not yet published or became part of Bachelor, Master or PhD projects. ZA, Z maximum projection with intensity adjustment.

7.1. Erklärung bezüglich bereits abgelegter Doktorprüfungen

Ich erkläre hiermit, dass ich mich bisher keiner Doktorprüfung im Mathematisch-Naturwissenschaftlichen Bereich unterzogen habe.

Frankfurt am Main, den 14.09.2017

7.2. Eidesstattliche Versicherung

Ich erkläre hiermit, dass ich die vorgelegte Dissertation über ‘Comparative Embryonic Morphogenesis of Emerging Insect Model Organisms’ selbständig angefertigt und mich anderer Hilfsmittel als der in ihr angegebenen nicht bedient habe, insbesondere, dass alle Entlehnungen aus anderen Schriften mit Angabe der betreffenden Schrift gekennzeichnet sind. Ich versichere, die Grundsätze der guten wissenschaftlichen Praxis beachtet, und nicht die Hilfe einer kommerziellen Promotionsvermittlung in Anspruch genommen zu haben.

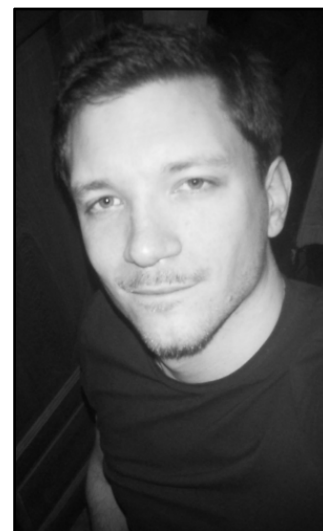
Frankfurt am Main, den 14.09.2017

7.3. Curriculum Vitae

Frederic Strobl

born on 12 June 1985
in Frankfurt am Main

Nibelungenallee 19a
60318 – Frankfurt am Main
fdrdc.strobl@t-online.de / fstrobl@stud.uni-frankfurt.de



June 2012 – Ongoing	PhD Student in Biology Group of Prof. Dr. Ernst H.K. Stelzer (Physical Biology / Physikalische Biologie) FB15 – Institute for Cell Biology and Neurosciences Buchmann Institute for Molecular Life Sciences (BMLS) Cluster of Excellence Frankfurt – Macromolecular Complexes (CEF – MC) Johann Wolfgang Goethe-Universität – Frankfurt am Main Supervisors: Prof. Dr. Ernst H.K. Stelzer & Prof. Dr. Bernd Grünewald
July 2011 – May 2012	Diploma Thesis in Biology (Cell and Developmental Biology) Group of Dr. Felix B. Engel (Heart Development and Regeneration) Max Planck Institute for Heart and Lung Research – Bad Nauheim & Johann Wolfgang Goethe-Universität – Frankfurt am Main Thesis Title: The TWEAK/FN14 Axis in Fibrotic Disease Supervisors: Prof. Dr. Dr. T. Braun & Prof. Dr. A. Starzinski-Powitz
Oct 2006 – May 2012	Diploma Student in Biology Johann Wolfgang Goethe-Universität – Frankfurt am Main Major Subjects: Animal Physiology, Neurobiology, Genetics, Cell and Developmental Biology
Nov 2004 – Aug 2006	Civil and Volunteer Services Universitätsklinikum Frankfurt am Main & Sozialwerk Main-Taunus
June 2004	Graduation from High School Musterschule, Frankfurt am Main

7.4. Danksagung

Zu allererst möchte ich mich bei Ernst bedanken, der mit die Chance gegeben hat, meine Doktorarbeit in seinem Labor durchzuführen und mit mich seinem immensen Wissen, welches an der ansonsten viel zu sehr vernachlässigten Schnittschnelle zwischen Physik und Biologie angesiedelt ist, sowie seiner langjährigen Erfahrung in der Forschung unterstützt hat. Dafür, dass ich eigentlich machen konnte, was ich wollte, solange was Produktives bei raus kam. Und auch für die Anekdoten aus der Wissenschaft und für den zweiten Insekteninkubator, für dessen Preis man auch locker einen Neuwagen eines mittelguten Autoherstellers hätte erwerben können. Und natürlich dafür, dass ich den Todesstern hier aufstellen durfte (es war eigentlich eher eine vollendete Tatsache). Besonderer Dank gebührt außerdem Prof. Dr. Grünewald, der sich bereiterklärt hat, das Zweitgutachten zu übernehmen, der Dekanin Fr. Prof. Dr. Meike Piepenbring, sowie meinem Prüfungskomitee.

Besonderer Dank gebührt auch der Goethe Universität und allen anderen Förderern des BMLS, insbesondere dem Ehepaar Buchmann. Hätten mir die entsprechenden Mittel nicht in diesem Umfang zur Verfügung gestanden, hätte ich vermutlich niemals das erreichen können, was jetzt hier in diesem Buch (und den zwei anderen Bänden) vorzufinden ist. Selbst wenn Tribolium nur Mehl mit etwas Trockenhefe futtert, irgendjemand muss ja für die geschätzten 250 Kilogramm Mehl, die ich in den vergangenen fünf Jahren besorgt und gesiebt habe, aufkommen.

Ebenfalls möchte ich der gesamten Arbeitsgruppe danken, besonders Alexander, ohne den ich nicht halb so weit gekommen wäre, wie ich bin, sowie Katharina, die sich die Betreuung von Henrik mit mir geteilt hat. Dann wären da noch Sven und Heinz, die so ziemlich jedes Problem mit den Mikroskopen lösen konnten. Michaela, die sich wirklich um alle Formalitäten gekümmert hat, besonders bezüglich meiner Abstecher in fremde Länder. Und selbstverständlich Berit und Sigg, zwei der fünf besten technischen Assistentinnen der Welt, für all die Bestellungen, die zahllosen guten Taten im Labor, den GVO-Kram und natürlich für die Hilfe bei der Käferauszählung. ♥

Außerdem danke ich ganz besonders Bettina aus dem Stockwerk obendrüber für die netten Gespräche zwischendurch, den internen Arbeitsgruppen Bode, Oehlmann und Pohl für die interessanten Einsichten in andere Forschungszweige sowie den externen Arbeitsgruppen Schoppmeier und Bucher für die Chance, ihre Labore zu besuchen und mir dort Wissen anzueignen. Auch der gesamten BMLS-Administration ist zu danken und nicht zu vergessen sind weiterhin Dr. Marc F. Schetelig, Dr. Ruth Müller, Paul Siefert und nochmals Prof. Dr. Bernd Grünewald, die sich bereit erklärt haben, bei unserem Fördergelder-Antrag mitzumachen, um noch viel mehr Geheimnisse der Insekten-Embryogenese zu entschlüsseln.

Weiterhin Danke ich meiner BMLS-Skat-Runde, bestehend aus Kenny, Stanny und Henny, sowie meiner gesamten WG, es sei einfach mal stellvertretend die letzte Besetzung mit Maxi, Laura und Adriana genannt. Und natürlich Steffie für die großartige Käferzeichnung.

Fast zum Schluss natürlich noch der Dank an Roberta und Jürgen für die wunderbare Unterstützung. Hiermit habe ich endlich das inoffizielle Familienrecht erworben, mit unglaublich grauenhafter Handschrift schreiben zu dürfen.

Und nochmals ein ganz besonderer Gruß an M., für die ich zwar einen neuen Keramiklöffel für ihre Tetris-Tasse finden konnte, aber die ich selber verloren habe. Und so begann das Chaos.

Und dann kam Anna.

7.5. Quellenverzeichnis

1. Patel, N. H. It's a bug's life. *Proceedings of the National Academy of Sciences* **97**, 4442–4444 (2000).
2. Hartenstein, V. Introduction to Insect Sensory Organs as a Model System in Sensory Physiology and Developmental Biology. *Microscopy Research and Technique* **39**, 467–469 (1997).
3. Nation, J. L. *Insect Physiology and Biochemistry*. 3rd edition (CRC Press, 2002).
4. Herreid, C. F. (Editor). *Locomotion and Energetics in Arthropods*. 1st edition (Springer, 1981).
5. Gullan, P. J. & Cranston, P. S. *The Insects: An Outline of Entomology*. 5th edition (Wiley, 2014).
6. Resh, V. H & Cardé, R.T (Editors). *Encyclopedia of Insects*. 2nd edition (Elsevier, 2009).
7. O'woma., O. O., Chigozirim., U. P., Emmanuel, O. & Chukwuebuka, E. M. Reproductive and Survival Strategies Utilized by Insect. A Review. *American Journal of Zoological Research* **4**, 1–6 (2016).
8. Evans, D. L. & Schmidt, J. O (Editors). *Insect Defenses: Adaptive Mechanisms and Strategies of Prey and Predators*. 1st edition (State University of New York Press, 1990).
9. Bodmer, R. & Venkatesh, T. V. Heart Development in *Drosophila* and Vertebrates: Conservation of Molecular Mechanisms. *Developmental Genetics* **22**, 181–186 (1998).
10. Kumar, J. P. Signalling Pathways in *Drosophila* and Vertebrate Retinal Development. *Nature Reviews Genetics* **2**, 846–857 (2001).
11. Bellen, H. J., Tong, C. & Tsuda, H. 100 Years of *Drosophila* Research and its Impact on Vertebrate Neuroscience: A History Lesson for the Future. *Nature Reviews Neuroscience* **11**, 514–522 (2010).
12. Jennings, B. H. *Drosophila – A Versatile Model in Biology & Medicine*. *Materials Today* **14**, 190–195 (2011).
13. Gonzalez, C. *Drosophila melanogaster: A Model and a Tool to Investigate Malignancy and Identify new Therapeutics*. *Nature Reviews Cancer* **13**, 172–183 (2013).
14. Crotty D. A. & Gann A (Editors). *Emerging Model Organisms: A Laboratory Manual, Volume 1*. 1st editon (Cold Spring Harbor Laboratory Press, 2009).
15. Crotty D. A. & Gann A (Editors). *Emerging Model Organisms: A Laboratory Manual, Volume 2*. 1st editon (Cold Spring Harbor Laboratory Press, 2010).
16. Liu, P. Z. & Kaufman, T. C. Short and Long Germ Segmentation: Unanswered Questions in the Evolution of a Developmental Mode. *Evolution and Development* **7**, 629–646 (2005).
17. Roth, S. & Hartenstein, V. Development of *Tribolium castaneum*. *Development Genes and Evolution* **218**, 115–118 (2008).
18. Schröder, R., Beermann, A., Wittkopp, N. & Lutz, R. From Development to Biodiversity – *Tribolium castaneum*, an Insect Model Organism for Short Germband Development. *Development Genes and Evolution* **218**, 119–26 (2008).
19. Peel, A. D. The Evolution of Developmental Gene Networks: Lessons from Comparative Studies on Holometabolous Insects. Published in *Animal Evolution: Genomes, Fossils, and Trees*. 1st edition (Oxford University Press, 2008).
20. Schinko, J. B. *et al.* Divergent Functions of *orthodenticle*, *empty spiracles* and *buttonhead* in Early Head Patterning of the Beetle *Tribolium castaneum* (Coleoptera). *Developmental Biology* **317**, 600–613 (2008).
21. Posnien, N. & Bucher, G. Formation of the Insect Head Involves Lateral Contribution of the Intercalary Segment, which depends on Tc-*labial* Function. *Developmental Biology* **338**, 107–116 (2010).

22. Lewis, D. L., DeCamillis, M. & Bennett, R. L. Distinct Roles of the Homeotic Genes *ubx* and *abd-A* in Beetle Embryonic Abdominal Appendage Development. *Proceedings of the National Academy of Sciences* **97**, 4504–4509 (2000).
23. Grossmann, D. & Prpic, N. M. *Egfr* Signaling Regulates Distal as well as Medial Fate in the Embryonic Leg of *Tribolium castaneum*. *Developmental Biology* **370**, 264–272 (2012).
24. Stork, N. E. Biodiversity: World of Insects. *Nature* **448**, 657–658 (2007).
25. Misof, B. *et al.* Phylogenomics Resolves the Timing and Pattern of Insect Evolution. *Science* **346**, 763–767 (2014).
26. Tong, K. J., Duchêne, S., Ho, S. Y. W. & Lo, N. Comment on ‘Phylogenomics Resolves the Timing and Pattern of Insect Evolution’. *Science* **349**, 487 (2015).
27. Kjer, K. M. *et al.* Response to Comment on ‘Phylogenomics Resolves the Timing and Pattern of Insect Evolution’. *Science* **349**, 487 (2015).
28. Schetelig, M. F., Schmid, B. G. M., Zimowska, G. & Wimmer, E. A. Plasticity in mRNA Expression and Localization of *orthodenticle* within Higher Diptera. *Evolution & Development* **10**, 700–704 (2008).
29. Nunes da Fonseca, R., van der Zee, M. & Roth, S. Evolution of Extracellular Dpp Modulators in Insects: The Roles of *tolloid* and *twisted-gastrulation* in Dorsventral Patterning of the *Tribolium* Embryo. *Developmental Biology* **345**, 80–93 (2010).
30. Kalinka, A. T. *et al.* Gene Expression Divergence Recapitulates the Developmental Hourglass Model. *Nature* **468**, 811–814 (2010).
31. Lynch, J. A., El-Sherif, E. & Brown, S. J. Comparisons of the Embryonic Development of *Drosophila*, *Nasonia*, and *Tribolium*. *Wiley Interdiscip. Rev. Developmental Biology* **1**, 16–39 (2012).
32. Koniszewski, N. D. B. *et al.* The Insect Central Complex as Model for Heterochronic Brain Development – Background, Concepts, and Tools. *Development Genes and Evolution* **226**, 209–219 (2016).
33. Campos-Ortega, J. A. & Hartenstein, V. *The Embryonic Development of Drosophila melanogaster*. 2nd edition (Springer, 1997).
34. Wotton, K. R., Jiménez-Guri, E., García Matheu, B. & Jaeger, J. A Staging Scheme for the Development of the Scuttle Fly *Megaselia abdita*. *PLoS One* **9**, e84421 (2014).
35. Raminani, L. N.; Cupp, E. W. Early Embryology of *Aedes aegypti* (L.) (Diptera:Culicidae). *International Journal of Insect Morphology and Embryology* **4**, 517–528 (1975).
36. Raminani, L. N. & Cupp, E. W. Embryology of *Aedes aegypti* (L.) (Diptera:Culicidae): Organogenesis. *International Journal of Insect Morphology and Embryology* **7**, 273–296 (1978).
37. Havelka, J., Landa, V. & Landa, V. Embryogenesis of *Aphidoletes aphidimyza* (Diptera: Cecidomyiidae): Morphological Markers for Staging of Living Embryos. *European Journal of Entomology* **104**, 81–87 (2007).
38. Jiménez-Guri, E., Wotton, K. R., Gavilán, B. & Jaeger, J. A Staging Scheme for the Development of the Moth Midge *Clogmia albipunctata*. *PLoS One* **9**, e84422 (2014).
39. Kobayashi, Y. & Ando, H. Early Embryonic Development and External Features of Developing Embryos of the Caddisfly, *Nemotaulius admorsus* (Trichoptera:Limnephilidae). *Journal of Morphology* **203**, 69–85 (1990).
40. Anderson, D. T. & Lawson-Kerr, C. The Embryonic Development of the Marine Caddis Fly, *Philanisus plebeius* Walker (Trichoptera:Chathamidae). *The Biological Bulletin* **153**, 98–105 (1977).

41. Nagy, L., Riddiford, L. & Kiguchi, K. Morphogenesis in the Early Embryo of the Lepidopteran *Bombyx mori*. *Developmental Biology* **165**, 137–151 (1994).
42. Ando, H. & Tanaka, M. Early Embryonic Development of the Primitive Moths, *Endoclyta signifer* Walker and *E. excrescens* Butler (Lepidoptera:Hepialidae). *International Journal of Insect Morphology and Embryology* **9**, 67–77 (1980).
43. Kobayashi, Y. Embryogenesis of the Fairy Moth, *Nemophora albiantennella* Issiki (Lepidoptera:Adelidae), with Special Emphasis on its Phylogenetic Implications. *International Journal of Insect Morphology and Embryology* **27**, 157–166 (1998).
44. Kobayashi, Y. & Ando, H. The Early Embryonic Development of the Primitive Moth, *Neomicropteryx nipponensis* Issiki (Lepidoptera:Micropterygidae). *Journal of Morphology* **172**, 259–269 (1982).
45. Kobayashi, Y., Suzuki, H. & Ohba, N. Embryogenesis of the Glowworm *Rhagophthalmus ohbai* Wittmer (Insecta, Coleoptera:Rhagophthalmidae), with Emphasis on the Germ Rudiment Formation. *Journal of Morphology* **253**, 1–9 (2002).
46. Beeman, S. L. & Norris, D. M. Embryogenesis of *Xyleborus ferrugineus* (Fabr.) (Coleoptera, Scolytidae). II. Developmental Rates of Male and Female Embryos. *Journal of Morphology* **152**, 221–227 (1977).
47. Fleig, R. & Sander, K. Blastoderm Development in Honey Bee Embryogenesis as Seen in the Scanning Electron Microscope. *International Journal of Invertebrate Reproduction and Development* **8**, 279–286 (1985).
48. Fleig, R. & Sander, K. Embryogenesis of the Honeybee *Apis mellifera* L. (Hymenoptera:Apidae): An SEM Study. *International Journal of Insect Morphology and Embryology* **15**, 449–462 (1986).
49. Fleig and Sander. Honeybee Morphogenesis: Embryonic Cell Movements that Shape the Larval Body. *Development* **103**, 525–534 (1988).
50. Bull, A. L. Stages of Living Embryos in the Jewel Wasp *Mormoniella (Nasonia) vitripennis* (Walker) (Hymenoptera:Pteromalidae). *International Journal of Insect Morphology and Embryology* **11**, 1–23 (1982).
51. Miura, T. *et al.* A Comparison of Parthenogenetic and Sexual Embryogenesis of the Pea Aphid *Acyrtosiphon pisum* (Hemiptera:Aphidoidea). *Journal of Experimental Zoology Part B: Molecular and Developmental Evolution* **295**, 59–81 (2003).
52. Uchifune, T. & Machida, R. Embryonic Development of *Galloisiana yuasai* Asahina, with Special Reference to External Morphology (Insecta:Grylloblattodea). *Journal of Morphology* **266**, 182–207 (2005).
53. Donoughe, S. & Extavour, C. G. Embryonic Development of the Cricket *Gryllus bimaculatus*. *Biol.* **441**, 140–156 *Developmental Biology* (2015).
54. Kishimoto, T. & Ando, H. External Features of the Developing Embryo of the Stonefly, *Kamimuria tibialis* (Pictet) (Plecoptera:Perlidae). *Journal of Morphology* **183**, 311–326 (1985).
55. Kelly, G. M. & Huebner, E. Embryonic Development of the Hemipteran Insect *Rhodnius prolixus*. *Journal of Morphology* **199**, 175–196 (1989).
56. Tojo, K. & Machida, R. Embryogenesis of the Mayfly *Ephemera japonica* McLachlan (Insecta, Ephemeroptera:Ephemeridae), with Special Reference to Abdominal Formation. *Journal of Morphology* **234**, 97–107 (1997).
57. Tojo, K. & Machida, R. Early Embryonic Development of the Mayfly *Ephemera japonica* McLachlan (Insecta, Ephemeroptera:Ephemeridae). *Journal of Morphology* **238**, 327–335 (1998).

58. Lichtman, J. W. & Conchello, J. A. Fluorescence Microscopy. *Nature Methods* **2**, 910–919 (2005).
59. Combs, C. A. Fluorescence Microscopy: A Concise Guide to Current Imaging Methods. *Current Protocols in Neuroscience* Chapter 2, Unit 2.1 (2010).
60. Renz, M. Fluorescence Microscopy – A Historical and Technical Perspective. *Cytometry Part A*. **83**, 767–779 (2013).
61. Pampaloni, F., Reynaud, E. G. & Stelzer, E. H. K. The Third Dimension Bridges the Gap between Cell Culture and Live Tissue. *Nature Reviews Molecular Cell Biology* **8**, 839–845 (2007).
62. Resandt, R. W. W. *et al.* Optical Fluorescence Microscopy in Three Dimensions: Microtomoscopy. *Journal of Microscopy* **138**, 29–34 (1985).
63. White, J. G., Amos, W. B. & Fordham, M. An Evaluation of Confocal versus Conventional Imaging of Biological Structures by Fluorescence Light Microscopy. *Journal of Cell Biology* **105**, 41–48 (1987).
64. van Meer, G., Stelzer, E. H., Wijnaendts-van-Resandt, R. W. & Simons, K. Sorting of Sphingolipids in Epithelial (Madin-Darby Canine kidney) Cells. *Journal of Cell Biology* **105**, 1623–1635 (1987).
65. Daetwyler, S. & Huisken, J. Fast Fluorescence Microscopy with Light Sheets. *The Biological Bulletin* **231**, 14–25 (2016).
66. Icha, J., Weber, M., Waters, J. C. & Norden, C. Phototoxicity in Live Fluorescence Microscopy, and how to Avoid it. *BioEssays* **39**, 1700003 (2017).
67. Huisken, J., Swoger, J., Del Bene, F., Wittbrodt, J. & Stelzer, E. H. K. Optical Sectioning Deep Inside Live Embryos by Selective Plane Illumination Microscopy. *Science* **305**, 1007–1009 (2004).
68. Huisken, J. Slicing Embryos gently with Laser Light Sheets. *BioEssays* **34**, 406–411 (2012).
69. Stelzer, E. H. K. Light Sheet Fluorescence Microscopy for Quantitative Biology. *Nature Methods* **12**, 23–26 (2015).
70. Engelbrecht, C. J. & Stelzer, E. H. Resolution Enhancement in a Light Sheet-Based Microscope (SPIM). *Optics Letters* **31**, 1477–1479 (2006).
71. Ichikawa, T. *et al.* Live Imaging and Quantitative Analysis of Gastrulation in Mouse Embryos Using Light Sheet Microscopy and 3D Tracking Tools. *Nature Protocols* **9**, 575–85 (2014).
72. Kaufmann A, Mickoleit M, Weber M, Huisken J. Multilayer Mounting Enables Long-Term Imaging of Zebrafish Development in a Light Sheet Microscope. *Development* **139**, 3242–3247 (2012)
73. Keller, P. J., Schmidt, A. D., Wittbrodt, J. & Stelzer, E. H. K. Digital Scanned Laser Light Sheet Fluorescence Microscopy (DSLM) of Zebrafish and *Drosophila* Embryonic Development. *Cold Spring Harbor Protocols*. **2011**, 1235–1243 (2011).
74. Schmied, C. & Tomancak, P. Sample Preparation and Mounting of *Drosophila* Embryos for Multiview Light Sheet Microscopy. Published in *Methods in Molecular Biology – Volume 1478*. 1st edition (Springer, 2016).
75. Schermelleh, L., Heintzmann, R. & Leonhardt, H. A Guide to Super-Resolution Fluorescence Microscopy. *Journal of Cell Biology* **190**, 165–175 (2010).
76. Leung, B. O. & Chou, K. C. Review of Super-Resolution Fluorescence Microscopy for Biology. *Applied Spectroscopy* **65**, 967–980 (2011).
77. Ritman, E. L. Current Status of Developments and Applications of Micro-CT. *Annual Review of Biomedical Engineering* **13**, 531–52 (2011).

78. Frank, J. Advances in the Field of Single-Particle Cryo-Electron Microscopy over the Last Decade. *Nature Protocols* **12**, 209–212 (2017).
79. Strnad, P. *et al.* Inverted Light Sheet Microscope for Imaging Mouse Pre-Implantation Development. *Nature Methods* **13**, 139–142 (2016).
80. Ichikawa, T. *et al.* Live Imaging of Whole Mouse Embryos During Gastrulation: Migration Analyses of Epiblast and Mesodermal Cells. *PLoS One* **8**, e64506 (2013).
81. Keller, P. J., Schmidt, A. D., Wittbrodt, J. & Stelzer, E. H. K. Reconstruction of Zebrafish Early Embryonic Development by Scanned Light Sheet Microscopy. *Science* **322**, 1065–1069 (2008).
82. Arrenberg, A. B., Stainier, D. Y. R., Baier, H. & Huisken, J. Optogenetic Control of Cardiac Function. *Science* **330**, 971–974 (2010).
83. Mickoleit, M. *et al.* High-Resolution Reconstruction of the Beating Zebrafish Heart. *Nature Methods* **11**, 919–922 (2014).
84. Icha, J. *et al.* Using Light Sheet Fluorescence Microscopy to Image Zebrafish Eye Development. *Journal of Visualized Experiments* **110**, e53966 (2016).
85. Keller, P. J. *et al.* Fast, High-Contrast Imaging of Animal Development with Scanned Light Sheet-Based Structured-Illumination Microscopy. *Nature Methods* **7**, 637–642 (2010).
86. Tomer, R., Khairy, K., Amat, F. & Keller, P. J. Quantitative High-Speed Imaging of Entire Developing Embryos with Simultaneous Multiview Light Sheet Microscopy. *Nature Methods* **9**, 755–763 (2012).
87. Krzic, U., Gunther, S., Saunders, T. E., Streichan, S. J. & Hufnagel, L. Multiview Light Sheet Microscope for Rapid *in toto* Imaging. *Nature Methods* **9**, 730–733 (2012).
88. Chhetri, R. K. *et al.* Whole-Animal Functional and Developmental Imaging with Isotropic Spatial Resolution. *Nature Methods* **12**, 1171–1178 (2015).
89. Beira, J. V. *et al.* The *Dpp/TGFβ*-Dependent Corepressor *Schnurri* Protects Epithelial Cells from JNK-Induced Apoptosis in *Drosophila* Embryos. *Developmental Cell* **31**, 240–7 (2014).
90. Lye, C. M. *et al.* Mechanical Coupling between Endoderm Invagination and Axis Extension in *Drosophila*. *PLoS Biology* **13**, e1002292 (2015).
91. Caroti, F., Urbansky, S., Wosch, M. & Lemke, S. Germ Line Transformation and *in vivo* Labeling of Nuclei in Diptera: Report on *Megaselia abdita* (Phoridae) and *Chironomus riparius* (Chironomidae). *Development Genes and Evolution* **225**, 179–186 (2015).
92. Pampaloni, F., Chang, B. J. & Stelzer, E. H. K. Light Sheet-Based Fluorescence Microscopy (LSFM) for the Quantitative Imaging of Cells and Tissues. *Cell and Tissue Research* **360**, 129–141 (2015).
93. Ahrens, M. B., Orger, M. B., Robson, D. N., Li, J. M. & Keller, P. J. Whole-Brain Functional Imaging at Cellular Resolution Using Light Sheet Microscopy. *Nature Methods* **10**, 413–420 (2013).
94. Keller, P. J., Ahrens, M. B. & Freeman, J. Light Sheet Imaging for Systems Neuroscience. *Nature Methods* **12**, 27–29 (2015).
95. Keller, P. J. & Ahrens, M. B. Visualizing Whole-Brain Activity and Development at the Single-Cell Level Using Light Sheet Microscopy. *Neuron* **85**, 462–483 (2015).

96. Lemon, W. C. *et al.* Whole-Central Nervous System Functional Imaging in Larval *Drosophila*. *Nature Communications* **6**, 7924 (2015).
97. Lemon, W. C. & Keller, P. J. Live Imaging of Nervous System Development and Function Using Light Sheet Microscopy. *Molecular Reproduction and Development* **82**, 605–618 (2015).
98. Maizel, A., Von Wangenheim, D., Federici, F., Haseloff, J. & Stelzer, E. H. K. High-Resolution Live Imaging of Plant Growth in Near Physiological Bright Conditions Using Light Sheet Fluorescence Microscopy. *Plant Journal* **68**, 377–385 (2011).
99. Von Wangenheim, D. *et al.* Rules and Self-Organizing Properties of Post-embryonic Plant Organ Cell Division Patterns. *Current Biology* **26**, 439–449 (2016).
100. Berthet, B. & Maizel, A. Light Sheet Microscopy and Live Imaging of Plants. *Journal of Microscopy* **263**, 158–164 (2016).
101. Handler, A. M. Use of the piggyBac Transposon for Germ-Line Transformation of Insects. *Insect Biochemistry and Molecular Biology* **32**, 1211–1220 (2002).
102. Nakamoto, A. *et al.* Changing Cell Behaviours during Beetle Embryogenesis Correlates with Slowing of Segmentation. *Nature Communications* **6**, 6635 (2015).
103. Benton, M. A., Akam, M. & Pavlopoulos, A. Cell and Tissue Dynamics during *Tribolium* Embryogenesis Revealed by Versatile Fluorescence Labeling Approaches. *Development* **140**, 3210–20 (2013).
104. Sarrazin, A. F., Peel, A. D. & Averof, M. A Segmentation Clock with Two-Segment Periodicity in Insects. *Science* **336**, 338–341 (2012).
105. Jacobs, C. G. C., Spink, H. P. & van der Zee, M. The Extraembryonic Serosa is a Frontier Epithelium Providing the Insect Egg with a Full-Range Innate Immune Response. *eLife* **3**, 04111 (2014).
106. Benton, M. A. *et al.* *Toll* Genes Have an Ancestral Role in Axis Elongation. *Current Biology* **26**, 1609–1615 (2016).
107. Kalderon, D., Roberts, B. L., Richardson, W. D. & Smith, A. E. A Short Amino Acid Sequence able to Specify Nuclear Location. *Cell* **39**, 499–509 (1984).
108. Zuber, M. X., Strittmatter, S. M. & Fishman, M. C. A Membrane-Targeting Signal in the Amino Terminus of the Neuronal Protein *GAP43*. *Nature* **341**, 345–348 (1989).
109. Riedl, J. *et al.* Lifeact: A Versatile Marker to Visualize F-Actin. *Nature Methods* **5**, 605–7 (2008).
110. Lam, A. J. *et al.* Improving FRET Dynamic Range with Bright Green and Red Fluorescent Proteins. *Nature Methods* **9**, 1005–1012 (2012).
111. Clarkson, M. & Saint, R. A His2AvDGFP Fusion Gene Complements a Lethal *His2AvD* Mutant Allele and Provides an *in vivo* Marker for *Drosophila* Chromosome Behavior. *DNA and Cell Biology* **18**, 457–462 (1999).
112. Rothbauer, U. *et al.* Targeting and Tracing Antigens in Live Cells with Fluorescent Nanobodies. *Nature Methods* **3**, 887–889 (2006).
113. Snapp, E. Design and Use of Fluorescent Fusion Proteins in Cell Biology. *Current Protocols in Cell Biology* Chapter 21, Unit 21.4 (2005).
114. Chinta, R. & Wasser, M. Three-Dimensional Segmentation of Nuclei and Mitotic Chromosomes for the Study of Cell Divisions in Live *Drosophila* Embryos. *Cytometry Part A*. **81**, 52–64 (2012).

115. Brown, S. J. *et al.* The Red Flour Beetle, *Tribolium castaneum* (Coleoptera): A Model for Studies of Development and Pest Biology. *Cold Spring Harbor Protocols* **4**, pdb.emo126 (2009).
116. Heffer, A. & Pick, L. Conservation and Variation in Hox Genes: How Insect Models Pioneered the Evo-Devo Field. *Annual Review of Entomology* **58**, 161–179 (2013).
117. Bergman, N. H (Editor). *Comparative Genomics: Volumes 1 and 2*. 1st edition (Humana Press, 2007).
118. Cameron, S. L. Insect Mitochondrial Genomics: Implications for Evolution and Phylogeny. *Annual Review of Entomology* **59**, 95–117 (2014).
119. Oppenheim, S. J., Baker, R. H., Simon, S. & DeSalle, R. We Can't All be Supermodels: The Value of Comparative Transcriptomics to the Study of Non-Model Insects. *Insect Molecular Biology* **24**, 139–154 (2015).
120. Roux, J., Rosikiewicz, M. & Robinson-Rechavi, M. What to Compare and How: Comparative Transcriptomics for Evo-Devo. *Journal of Experimental Zoology Part B: Molecular and Developmental Evolution* **324**, 372–382 (2015).
121. Chapman, R. F. *The Insects – Structure and Function*. 5th edition (Cambridge University Press, 2013).
122. Wanninger, A. Morphology is Dead – Long Live Morphology! Integrating Morpho-Evo-Devo into Molecular Evo-Devo and Phylogenomics. *Frontiers in Ecology and Evolution* **3**, 54 (2015).
123. Handel, K., Grünfelder, C. G., Roth, S. & Sander, K. *Tribolium* Embryogenesis: A SEM Study of Cell Shapes and Movements from Blastoderm to Serosal Closure. *Development Genes and Evolution* **210**, 167–179 (2000).
124. Handel, K., Basal, A., Fan, X. & Roth, S. *Tribolium castaneum* Twist: Gastrulation and Mesoderm Formation in a Short-Germ Beetle. *Development Genes and Evolution* **215**, 13–31 (2005).
125. van der Zee, M., Berns, N. & Roth, S. Distinct Functions of the *Tribolium* Zerknullt Genes in Serosa Specification and Dorsal Closure. *Current Biology* **15**, 624–636 (2005).
126. Schoppmeier, M., Fischer, S., Schmitt-Engel, C., Löhr, U. & Klingler, M. An Ancient Anterior Patterning System Promotes Caudal Repression and Head Formation in Ecdysozoa. *Current Biology* **19**, 1811–1815 (2009).
127. Konrad, K. D., Wang, D. & Marsh, J. L. Vitelline Membrane Biogenesis in *Drosophila* Requires the Activity of the Alpha-Methyl Dopa Hypersensitive Gene (*I(2)Amd*) in Both the Germline and Follicle Cells. *Insect Molecular Biology* **1**, 179–187 (1993).
128. Wu, T., Manogaran, A. L., Beauchamp, J. M. & Waring, G. L. *Drosophila* Vitelline Membrane Assembly: A Critical Role for an Evolutionarily Conserved Cysteine in the 'VM Domain' of *SV23*. *Developmental Biology* **347**, 360–368 (2010).
129. Pascucci, T., Perrino, J., Mahowald, A. P. & Waring, G. L. Eggshell Assembly in *Drosophila*: Processing and Localization of Vitelline Membrane and Chorion Proteins. *Developmental Biology* **177**, 590–598 (1996).
130. Pane, A., De Simone, A., Saccone, G. & Polito, C. Evolutionary Conservation of *Ceratitis capitata* Transformer Gene Function. *Genetics* **171**, 615–624 (2005).
131. Gabrieli, P. *et al.* Sex and the Single Embryo: Early Development in the Mediterranean Fruit Fly, *Ceratitis capitata*. *BMC Developmental Biology* **10**, 12 (2010).
132. Schetelig, M. F., Caceres, C., Zacharopoulou, A., Franz, G. & Wimmer, E. A. Conditional Embryonic Lethality to Improve the Sterile Insect Technique in *Ceratitis capitata* (Diptera:Tephritidae). *BMC Biology* **7**, 4 (2009).
133. Mardis, E. R. Next-Generation DNA Sequencing Methods. *Annual Review of Genomics and Human Genetics* **9**, 387–402 (2008).

134. Rafiqi, A. M., Lemke, S., Ferguson, S., Stauber, M. & Schmidt-Ott, U. Evolutionary Origin of the Amnioserosa in Cyclorrhaphan Flies Correlates with Spatial and Temporal Expression Changes of *Zen*. *Proceedings of the National Academy of Sciences* **105**, 234–239 (2008).
135. Rafiqi, A. M., Lemke, S. & Schmidt-Ott, U. Postgastrular *Zen* Expression is Required to Develop Distinct Amniotic and Serosal Epithelia in the Scuttle Fly *Megaselia*. *Developmental Biology* **341**, 282–90 (2010).
136. Rafiqi, A. M., Park, C.-H., Kwan, C. W., Lemke, S. & Schmidt-Ott, U. *BMP*-Dependent Serosa and Amnion Specification in the Scuttle Fly *Megaselia abdita*. *Development* **139**, 3373–82 (2012).
137. Panfilio, K. A. Extraembryonic Development in Insects and the Acrobatics of Blastokinesis. *Developmental Biology* **313**, 471–491 (2008).
138. Schmidt-Ott, U. & Kwan, C. W. Morphogenetic Functions of Extraembryonic Membranes in Insects. *Current Opinion in Insect Science* **13**, 86–92 (2016).
139. Gama Sosa, M. A., De Gasperi, R. & Elder, G. A. Animal Transgenesis: An Overview. *Brain Structure and Function* **214**, 91–109 (2010).
140. Berghammer, A., Bucher, G., Maderspacher, F. & Klingler, M. A System to Efficiently Maintain Embryonic Lethal Mutations in the Flour Beetle *Tribolium castaneum*. *Development Genes and Evolution* **209**, 382–389 (1999).
141. Miller, D. E. *et al.* Rare Recombination Events Generate Sequence Diversity Among Balancer Chromosomes in *Drosophila melanogaster*. *Proceedings of the National Academy of Sciences* **113**, E1352–1361 (2016).
142. Lattao, R., Bonaccorsi, S., Guan, X., Wasserman, S. A. & Gatti, M. *Tubby*-Tagged Balancers for the *Drosophila X* and Second Chromosomes. *Fly (Austin)*. **5**, 369–370 (2011).
143. Berghammer, A. J., Klingler, M. & Wimmer, E. A. Genetic Techniques: A Universal Marker for Transgenic Insects. *Nature* **402**, 370–371 (1999).
144. Shaner, N. C. *et al.* Improving the Photostability of Bright Monomeric Orange and Red Fluorescent Proteins. *Nature Methods* **5**, 545–551 (2008).
145. Shaner, N. C. *et al.* Improved Monomeric Red, Orange and Yellow Fluorescent Proteins Derived from *Discosoma sp.* Red Fluorescent Protein. *Nature Biotechnology* **22**, 1567–1572 (2004).
146. Shaner, N. C., Steinbach, P. A. & Tsien, R. Y. A Guide to Choosing Fluorescent Proteins. *Nature Methods* **2**, 905–909 (2005).
147. Hamilton, D. L. & Abremski, K. Site-Specific Recombination by the Bacteriophage P1 *Lox*-Cre System. *Journal of Molecular Biology* **178**, 481–486 (1984).
148. Livet, J. *et al.* Transgenic Strategies for Combinatorial Expression of Fluorescent Proteins in the Nervous System. *Nature* **450**, 56–62 (2007).
149. Wang, S.-Z., Liu, B.-H., Tao, H. W., Xia, K. & Zhang, L. I. A Genetic Strategy for Stochastic Gene Activation with Regulated Sparseness (STARS). *PLoS One* **4**, e4200 (2009).
150. Li, X. *et al.* piggyBac Internal Sequences are Necessary for Efficient Transformation of Target Genomes. *Insect Molecular Biology* **14**, 17–30 (2005).
151. Fraser, M. J., Smith, G. E. & Summers, M. D. Acquisition of Host Cell DNA Sequences by Baculoviruses: Relationship Between Host DNA Insertions and FP Mutants of *Autographa californica* and *Galleria mellonella* Nuclear Polyhedrosis Viruses. *Journal of Virology* **47**, 287–300 (1983).

152. Cary, L. C. *et al.* Transposon Mutagenesis of Baculoviruses: Analysis of *Trichoplusia ni* Transposon IFP2 Insertions within the FP-Locus of Nuclear Polyhedrosis Viruses. *Virology* **172**, 156–169 (1989).
153. Elick, T. A., Bauser, C. A., Principe, N. M. & Fraser, M. J. PCR Analysis of Insertion Site Specificity, Transcription, and Structural Uniformity of the Lepidopteran Transposable Element IFP2 in the TN-368 Cell Genome. *Genetica* **97**, 127–139 (1996).
154. Lorenzen, M. D. *et al.* piggyBac-Mediated Germline Transformation in the Beetle *Tribolium castaneum*. *Insect Molecular Biology* **12**, 433–40 (2003).
155. Kokoza, V., Ahmed, A., Wimmer, E. A. & Raikhel, A. S. Efficient Transformation of the Yellow Fever Mosquito *Aedes aegypti* using the piggyBac Transposable Element Vector pBac[3xP3-EGFPafm]. *Insect Biochemistry and Molecular Biology* **31**, 1137–1143 (2001).
156. Tamura, T. *et al.* Germline Transformation of the Silkworm *Bombyx mori* L. using a piggyBac Transposon-Derived Vector. *Nature Biotechnology* **18**, 81–84 (2000).
157. Peitz, M., Pfannkuche, K., Rajewsky, K. & Edenhofer, F. Ability of the Hydrophobic FGF and Basic TAT Peptides to Promote Cellular Uptake of Recombinant Cre Recombinase: A Tool for Efficient Genetic Engineering of Mammalian Genomes. *Proceedings of the National Academy of Sciences* **99**, 4489–4494 (2002).
158. Schinko, J. B., Hillebrand, K. & Bucher, G. Heat Shock-Mediated Misexpression of Genes in the Beetle *Tribolium castaneum*. *Development Genes and Evolution* **222**, 287–298 (2012).
159. Markwardt, M. L. *et al.* An Improved Cerulean Fluorescent Protein with Enhanced Brightness and Reduced Reversible Photoswitching. *PLoS One* **6**, e17896 (2011).
160. Trauner, J. *et al.* Large-Scale Insertional Mutagenesis of a Coleopteran Stored Grain Pest, the Red Flour Beetle *Tribolium castaneum*, Identifies Embryonic Lethal Mutations and Enhancer Traps. *BMC Biology* **7**, 73 (2009).
161. Mito, T. & Noji, S. The Two-Spotted Cricket *Gryllus bimaculatus*: An Emerging Model for Developmental and Regeneration Studies. *Cold Spring Harbor Protocols*. **2008**, pdb.emo110 (2008).
162. Nakamura, T. *et al.* Imaging of Transgenic Cricket Embryos Reveals Cell Movements Consistent with a Syncytial Patterning Mechanism. *Current Biology* **20**, 1641–1647 (2010).
163. Huiskens, J. & Stainier, D. Y. R. Even Fluorescence Excitation by Multidirectional Selective Plane Illumination Microscopy (mSPIM). *Optics Letters* **32**, 2608–2610 (2007).
164. Preibisch, S., Saalfeld, S. & Tomancak, P. Globally Optimal Stitching of Tiled 3D Microscopic Image Acquisitions. *Bioinformatics* **25**, 1463–1465 (2009).
165. Swoger, J., Huiskens, J. & Stelzer, E. H. K. Multiple Imaging Axis Microscopy Improves Resolution for Thick-Sample Applications. *Optics Letters* **28**, 1654 (2003).
166. Swoger, J., Verveer, P., Greger, K., Huiskens, J. & Stelzer, E. H. K. Multi-View Image Fusion Improves Resolution in Three-Dimensional Microscopy. *Optics Express* **15**, 8029–8042 (2007).
167. Verveer, P. J. *et al.* High-Resolution Three-Dimensional Imaging of Large Specimens with Light Sheet-Based Microscopy. *Nature Methods* **4**, 311–313 (2007).
168. Preibisch, S., Saalfeld, S., Schindelin, J. & Tomancak, P. Software for Bead-Based Registration of Selective Plane Illumination Microscopy Data. *Nature Methods* **7**, 418–419 (2010).
169. Preibisch, S. *et al.* Efficient Bayesian-Based Multiview Deconvolution. *Nature Methods* **11**, 645–648 (2014).

170. Amat, F. & Keller, P. J. Towards Comprehensive Cell Lineage Reconstructions in Complex Organisms using Light Sheet Microscopy. *Development, Growth & Differentiation* **55**, 563–578 (2013).
171. Amat, F. *et al.* Efficient Processing and Analysis of Large-Scale Light Sheet Microscopy Data. *Nature Protocols* **10**, 1679–1696 (2015).
172. Long, F., Zhou, J. & Peng, H. Visualization and Analysis of 3D Microscopic Images. *PLoS Computational Biology* **8**, e1002519 (2012).
173. Udupa, J. K., Hung, H. M. & Chuang, K. S. Surface and Volume Rendering in Three-Dimensional Imaging: A comparison. *Journal of Digital Imaging* **4**, 159–168 (1991).
174. Consortium, F. B. *et al.* Flybase – the *Drosophila* database. *Nucleic Acids Research* **24**, 53–56 (1996).
175. Grumbling, G. & Strelets, V. FlyBase: Anatomical Data, Images and Queries. *Nucleic Acids Research* **34**, D484–8 (2006).
176. Dos Santos, G. *et al.* FlyBase: Introduction of the *Drosophila melanogaster* Release 6 Reference Genome Assembly and Large-Scale Migration of Genome Annotations. *Nucleic Acids Research* **43**, D690–D697 (2015).
177. Davidson, D. *et al.* The Mouse Atlas Database: A Community Resource for Mouse Development. *Trends in Genetics* **17**, 49–51 (2001).
178. Baldock, R. A. *et al.* EMAP and EMAGE: A Framework for Understanding Spatially Organized Data. *Neuroinformatics* **1**, 309–325 (2003).
179. Nagai, T. *et al.* A Variant of Yellow Fluorescent Protein with Fast and Efficient Maturation for Cell-Biological Applications. *Nature Biotechnology* **20**, 87–90 (2002).
180. Siebert, K. S., Lorenzen, M. D., Brown, S. J., Park, Y. & Beeman, R. W. *Tubulin* Superfamily Genes in *Tribolium castaneum* and the Use of a *Tubulin* Promoter to Drive Transgene Expression. *Insect Biochemistry and Molecular Biology* **38**, 749–755 (2008).
181. Schinko, J. B. *et al.* Functionality of the GAL4/UAS System in *Tribolium* Requires the Use of Endogenous Core Promoters. *BMC Developmental Biology* **10**, 53 (2010).
182. Shcherbakova, D. M. & Verkhusha, V. V. Near-Infrared Fluorescent Proteins for Multicolor *in vivo* Imaging. *Nature Methods* **10**, 751–754 (2013).
183. Subach, O. M., Cranfill, P. J., Davidson, M. W. & Verkhusha, V. V. An Enhanced Monomeric Blue Fluorescent Protein with the High Chemical Stability of the Chromophore. *PLoS One* **6**, e28674 (2011).
184. Chen, X.-G., Mathur, G. & James, A. A. Gene Expression Studies in Mosquitoes. *Advances in Genetics* **64**, 19–50 (2008).
185. Labbé, G. M. C., Nimmo, D. D. & Alpey, L. piggyBac- and PhiC31-Mediated Genetic Transformation of the Asian Tiger Mosquito, *Aedes albopictus* (Skuse). *PLoS Neglected Tropical Diseases* **4**, e788 (2010).
186. Brakefield, P. M., Beldade, P. & Zwaan, B. J. Culture and Propagation of Laboratory Populations of the African Butterfly *Bicyclus anynana*. *Cold Spring Harbor Protocols*. **2009**, pdb.prot5203 (2009).
187. Marcus, J. M., Ramos, D. M. & Monteiro, A. Germline Transformation of the Butterfly *Bicyclus anynana*. *Proceedings Of The Royal Society B – Biological Sciences* **271**, S263–S265 (2004).
188. Schulte, C. *et al.* Honeybee Promoter Sequences for Targeted Gene Expression. *Insect Molecular Biology* **22**, 399–410 (2013).

189. Schulte, C., Theilenberg, E., Müller-Borg, M., Gempe, T. & Beye, M. Highly Efficient Integration and Expression of piggyBac-Derived Cassettes in the Honeybee (*Apis mellifera*). *Proceedings of the National Academy of Sciences* **111**, 9003–9008 (2014).
190. Salvemini, M. *et al.* *De novo* Assembly and Transcriptome Analysis of the Mediterranean Fruit Fly *Ceratitis capitata* Early Embryos. *PLoS One* **9**, e114191 (2014).
191. Papanicolaou, A. *et al.* The Whole Genome Sequence of the Mediterranean Fruit Fly, *Ceratitis capitata* (Wiedemann), Reveals Insights into the Biology and Adaptive Evolution of a Highly Invasive Pest Species. *Genome Biology* **17**, 192 (2016).
192. Calla, B., Hall, B., Hou, S. & Geib, S. M. A Genomic Perspective to Assessing Quality of Mass-Reared SIT Flies used in Mediterranean Fruit Fly (*Ceratitis capitata*) Eradication in California. *BMC Genomics* **15**, 98 (2014).
193. Juan-Blasco, M. *et al.* Estimating SIT-Driven Population Reduction in the Mediterranean Fruit Fly, *Ceratitis capitata*, from Sterile Mating. *Bulletin of Entomological Research* **104**, 233–242 (2014).
194. Chen, X.-G. *et al.* Genome Sequence of the Asian Tiger Mosquito, *Aedes albopictus*, Reveals Insights into its Biology, Genetics, and Evolution. *Proceedings of the National Academy of Sciences* **112**, E5907–E5915 (2015).
195. Wang, C. *et al.* Chikungunya Virus Sequences Across the First Epidemic in Nicaragua, 2014–2015. *The American Journal of Tropical Medicine and Hygiene* **94**, 400–403(2015).
196. C Costa, A. C. *et al.* Surveillance of Dengue Vectors Using Spatio-Temporal Bayesian Modeling. *BMC Medical Informatics and Decision Making* **15**, 93 (2015).
197. Boukraa, S. *et al.* Updated Checklist of the Mosquitoes (Diptera:Culicidae) of Belgium. *Journal of Vector Ecology* **40**, 398–407 (2015).
198. Koch, L. K. *et al.* Modeling the Habitat Suitability for the Arbovirus Vector *Aedes albopictus* (Diptera:Culicidae) in Germany. *Parasitology Research* **115**, 957–964 (2015).
199. Cianci, D. *et al.* High Resolution Spatial Analysis of Habitat Preference of *Aedes Albopictus* (Diptera:Culicidae) in an Urban Environment. *Journal of Medical Entomology* **52**, 329–335 (2015).
200. Monteiro, A. Origin, Development, and Evolution of Butterfly Eyespots. *Annual Review of Entomology* **60**, 253–271 (2015).
201. Klingler, M. *Tribolium*. *Current Biology* **14**, R639–640 (2004).
202. Richards, S. *et al.* The Genome of the Model Beetle and Pest *Tribolium castaneum*. *Nature* **452**, 949–955 (2008).
203. Dearden, P. K., Duncan, E. J. & Wilson, M. J. The Honeybee *Apis mellifera*. *Cold Spring Harbor Protocols*. **2009**, pdb.emo123 (2009).
204. Venken, K. J. T. & Bellen, H. J. Genome-Wide Manipulations of *Drosophila melanogaster* with Transposons, FLP Recombinase, and Φ C31 Integrase. *Methods in Molecular Biology* **859**, 203–228 (2012).
205. Masumoto, M., Ohde, T., Shiomi, K., Yaginuma, T. & Niimi, T. A Baculovirus Immediate-Early Gene, *IE1*, Promoter Drives Efficient Expression of a Transgene in both *Drosophila melanogaster* and *Bombyx mori*. *PLoS One* **7**, e49323 (2012).
206. Bajar, B. T. *et al.* Improving Brightness and Photostability of Green and Red Fluorescent Proteins for Live Cell Imaging and FRET Reporting. *Scientific Reports* **6**, 20889 (2016).
207. Patterson, G. H. *et al.* A Photoactivatable GFP for Selective Photolabeling of Proteins and Cells. *Science* **297**, 1873–

- 1877 (2002).
208. Gunewardene, M. S. *et al.* Superresolution Imaging of Multiple Fluorescent Proteins with Highly Overlapping Emission Spectra in Living Cells. *Biophysical Journal* **101**, 1522–1528 (2011).
 209. McKinney, S. A., Murphy, C. S., Hazelwood, K. L., Davidson, M. W. & Looger, L. L. A Bright and Photostable Photoconvertible Fluorescent Protein. *Nature Methods* **6**, 131–133 (2009).
 210. Ando, R., Mizuno, H. & Miyawaki, A. Regulated Fast Nucleocytoplasmic Shuttling Observed by Reversible Protein Highlighting. *Science* **306**, 1370–1373 (2004).
 211. Sarkar, A. *et al.* Insulated piggyBac Vectors for Insect Transgenesis. *BMC Biotechnology* **6**, 27 (2006).
 212. Jacobs, C. G. C., Rezende, G. L., Lamers, G. E. M. & van der Zee, M. The Extraembryonic Serosa Protects the Insect Egg against Desiccation. *Proceedings Of The Royal Society B – Biological Sciences* **280**, 20131082 (2013).
 213. Jacobs, C. G. C. & van der Zee, M. Immune Competence in Insect Eggs Depends on the Extraembryonic Serosa. *Developmental & Comparative Immunology* **41**, 263–9 (2013).
 214. Hilbrant, M., Horn, T., Koelzer, S. & Panfilio, K. A. The Beetle Amnion and Serosa Functionally Interact as Apposed Epithelia. *eLife* **5**, 13834 (2016).
 215. Terskikh, A. V., Fradkov, A. F., Zarskiy, A. G., Kajava, A. V. & Angres, B. Analysis of DsRed Mutants: Space around the Fluorophore Accelerates Fluorescence Development. *Journal of Biological Chemistry* **277**, 7633–7636 (2002).
 216. Boucias, D. G. & Pendland, J. C. Principles of Insect Pathology. 1st edition (Springer, 1998).
 217. Panfilio, K. A., Oberhofer, G. & Roth, S. High Plasticity in Epithelial Morphogenesis during Insect Dorsal Closure. *Biology Open* **2**, 1108–1118 (2013).
 218. Lorenzen, M. D., Brown, S. J., Denell, R. E. & Beeman, R. W. Transgene Expression from the *Tribolium castaneum* Polyubiquitin Promoter. *Insect Molecular Biology* **11**, 399–407 (2002).
 219. Brown, S. J., Parrish, J. K., Denell, R. E. & Beeman, R. W. Genetic Control of Early Embryogenesis in the Red Flour Beetle, *Tribolium castaneum*. *American Zoologist* **34**, 343–352 (1994).
 220. Callaini, G., Dallai, R. & Riparbelli, M. G. Behaviour of Yolk Nuclei during Early Embryogenesis in *Drosophila melanogaster*. *Bollettino di Zoologia*. **57**, 215–220 (1990).
 221. Walker, J. J., Lee, K. K., Desai, R. N. & Erickson, J. W. The *Drosophila melanogaster* Sex Determination Gene *SisA* is Required in Yolk Nuclei for Midgut Formation. *Genetics* **155**, 191–202 (2000).
 222. Koelzer, S., Kölsch, Y. & Panfilio, K. A. Visualizing Late Insect Embryogenesis: Extraembryonic and Mesodermal Enhancer Trap Expression in the Beetle *Tribolium castaneum*. *PLoS One* **9**, e103967 (2014).
 223. Cornett, J. C., Landrette, S. F. & Xu, T. Characterization of Fluorescent Eye Markers for Mammalian Transgenic Studies. *PLoS One* **6**, e29486 (2011).
 224. Quigley, D. A. *et al.* Gene Expression Architecture of Mouse Dorsal and Tail Skin Reveals Functional Differences in Inflammation and Cancer. *Cell Reports* **16**, 1153–1165 (2016).
 225. Zheng, B., Mills, A. A. & Bradley, A. A System for Rapid Generation of Coat Color-Tagged Knockouts and Defined Chromosomal Rearrangements in Mice. *Nucleic Acids Research* **27**, 2354–2360 (1999).
 226. Kawakami, K. Transposon Tools and Methods in Zebrafish. *Developmental Dynamics* **234**, 244–254 (2005).

227. Thummel, R. *et al.* Cre-Mediated Site-Specific Recombination in Zebrafish Embryos. *Developmental Dynamics* **233**, 1366–1377 (2005).
228. Vergunst, A. C., Jansen, L. E., Fransz, P. F., de Jong, J. H. & Hooykaas, P. J. J. Cre/Lox-Mediated Recombination in *Arabidopsis*: Evidence for Transmission of a Translocation and a Deletion Event. *Chromosoma* **109**, 287–297 (2000).
229. Supatto, W., McMahon, A., Fraser, S. E. & Stathopoulos, A. Quantitative Imaging of Collective Cell Migration during *Drosophila* Gastrulation: Multiphoton Microscopy and Computational Analysis. *Nature Protocols* **4**, 1397–1412 (2009).
230. Royer, L. A. *et al.* Adaptive Light Sheet Microscopy for Long-Term, High-Resolution Imaging in Living Organisms. *Nature Biotechnology* **34**, 1267–1278 (2016).
231. Zhu, D., Larin, K. V., Luo, Q. & Tuchin, V. V. Recent Progress in Tissue Optical Clearing. *Laser Photonics Reviews* **7**, 732–757 (2013).
232. Richardson, D. S. & Lichtman, J. W. Clarifying Tissue Clearing. *Cell* **162**, 246–257 (2015).
233. Azaripour, A. *et al.* A Survey of Clearing Techniques for 3D Imaging of Tissues with Special Reference to Connective Tissue. *Progress in Histochemistry and Cytochemistry* **51**, 9–23 (2016).
234. Ke, M.-T., Fujimoto, S. & Imai, T. SeeDB: A Simple and Morphology-Preserving Optical Clearing Agent for Neuronal Circuit Reconstruction. *Nature Neuroscience* **16**, 1154–1161 (2013).
235. Ertürk, A. & Bradke, F. High-Resolution Imaging of Entire Organs by 3-Dimensional Imaging of Solvent Cleared Organs (3DISCO). *Experimental Neurology* **242**, 57–64 (2013).
236. Renier, N. *et al.* IDISCO: A Simple, Rapid Method to Immunolabel Large Tissue Samples for Volume Imaging. *Cell* **159**, 896–910 (2014).
237. Chiang, A.-S. *et al.* Insect NMDA Receptors Mediate Juvenile Hormone Biosynthesis. *Proceedings of the National Academy of Sciences* **99**, 37–42 (2002).
238. Kuwajima, T. *et al.* ClearT: A Detergent- and Solvent-Free Clearing Method for Neuronal and Non-Neuronal Tissue. *Development* **140**, 1364–1368 (2013).
239. Susaki, E. A. *et al.* Whole-Brain Imaging with Single-Cell Resolution using Chemical Cocktails and Computational Analysis. *Cell* **157**, 726–739 (2014).
240. Chung, K. *et al.* Structural and Molecular Interrogation of Intact Biological Systems. *Nature* **497**, 332–337 (2013).
241. Osanai-Futahashi, M. *et al.* A Visible Dominant Marker for Insect Transgenesis. *Nature Communications* **3**, 1295 (2012).
242. Arakane, Y. *et al.* Molecular and Functional Analyses of Amino Acid Decarboxylases Involved in Cuticle Tanning in *Tribolium castaneum*. *Journal of Biological Chemistry* **284**, 16584–16594 (2009).
243. Noh, M. Y., Muthukrishnan, S., Kramer, K. J. & Arakane, Y. Cuticle Formation and Pigmentation in Beetles. *Current Opinion in Insect Science* **17**, 1–9 (2016).
244. Noh, M. Y., Koo, B., Kramer, K. J., Muthukrishnan, S. & Arakane, Y. *Arylalkylamine N-Acetyltransferase 1* Gene (*Tc-AANAT1*) is Required for Cuticle Morphology and Pigmentation of the Adult Red Flour Beetle, *Tribolium castaneum*. *Insect Biochemistry and Molecular Biology* **79**, 119–129 (2016).

245. Gilles, A. F. & Averof, M. Functional Genetics for All: Engineered Nucleases, CRISPR and the Gene Editing Revolution. *Evodevo* **5**, 43 (2014).
246. Gilles, A. F., Schinko, J. B. & Averof, M. Efficient CRISPR-Mediated Gene Targeting and Transgene Replacement in the Beetle *Tribolium castaneum*. *Development* **142**, 2832–2839 (2015).
247. Dai, F. *et al.* Aspartate Decarboxylase is Required for a Normal Pupa Pigmentation Pattern in the Silkworm, *Bombyx mori*. *Scientific Reports* **5**, 10885 (2015).
248. Brown, S. J., Mahaffey, J. P., Lorenzen, M. D., Denell, R. E. & Mahaffey, J. W. Using RNAi to Investigate Orthologous Homeotic Gene Function during Development of Distantly Related Insects. *Evolution & Development* **1**, 11–5 (1999).
249. Bucher, G., Scholten, J. & Klingler, M. Parental RNAi in *Tribolium* (Coleoptera). *Current Biology* **12**, R85–86 (2002).
250. Posnien, N. *et al.* RNAi in the Red Flour Beetle (*Tribolium*). *Cold Spring Harbor Protocols* **2009**, pdb.prot5256 (2009).
251. Sulston, I. A. & Anderson, K. V. Embryonic Patterning Mutants of *Tribolium castaneum*. *Development* **122**, 805–814 (1996).
252. Brown, S. *et al.* Implications of the *Tribolium* Deformed Mutant Phenotype for the Evolution of *Hox* Gene Function. *Proceedings of the National Academy of Sciences* **97**, 4510–4514 (2000).
253. Cerny, A. C., Bucher, G., Schröder, R. & Klingler, M. Breakdown of Abdominal Patterning in the *Tribolium* Krüppel Mutant Jaws. *Development* **132**, 5353–5363 (2005).
254. Berghammer, A. J., Weber, M., Trauner, J. & Klingler, M. Red Flour Beetle (*Tribolium*) Germline Transformation and Insertional Mutagenesis. *Cold Spring Harbor Protocols* **2009**, pdb.prot5259 (2009).
255. Nollmann, F. I. *et al.* A *Photorhabdus* Natural Product Inhibits Insect Juvenile Hormone Epoxide Hydrolase. *ChemBioChem* **16**, 766–771 (2015).
256. Macaya, C. C., Saavedra, P. E., Cepeda, R. E., Nuñez, V. A. & Sarrazin, A. F. A *Tribolium castaneum* Whole-Embryo Culture Protocol for Studying the Molecular Mechanisms and Morphogenetic Movements Involved in Insect Development. *Development Genes and Evolution* **226**, 53–61 (2016).
257. Benton, M. A. & Pavlopoulos, A. *Tribolium* Embryo Morphogenesis: May the Force be with You. *Bioarchitecture* **4**, 16–21 (2014).
258. Horn, T., Hilbrant, M. & Panfilio, K. A. Evolution of Epithelial Morphogenesis: Phenotypic Integration across Multiple Levels of Biological Organization. *Frontiers in Genetics* **6**, 303 (2015).
259. Horn, T. & Panfilio, K. A. Novel Functions for *Dorsocross* in Epithelial Morphogenesis in the Beetle *Tribolium castaneum*. *Development* **143**, 3002–11 (2016).
260. Shingleton, A. W. The Tegulation of Organ Size in *Drosophila*: Physiology, Plasticity, Patterning and Physical Force. *Organogenesis* **6**, 76–87 (2010).
261. Tomer, R., Khairy, K. & Keller, P. J. Shedding Light on the System: Studying Embryonic Development with Light Sheet Microscopy. *Current Opinion in Genetics & Development* **21**, 558–565 (2011).
262. Theiler, K. The House Mouse: Atlas of Embryonic Development. 1st edition (Springer, 1989).
263. Kaufman, M. The Atlas of Mouse Development. 2nd edition (Elsevier, 1992).

264. Wong, M. D., Dorr, A. E., Walls, J. R., Lerch, J. P. & Henkelman, R. M. A Novel 3D Mouse Embryo Atlas based on Micro-CT. *Development* **139**, 3248–3256 (2012).
265. Wong, M. D. *et al.* 4D Atlas of the Mouse Embryo for Precise Morphological Staging. *Development* **142**, 3583–3591 (2015).
266. Kimmel, C. B., Ballard, W. W., Kimmel, S. R., Ullmann, B. & Schilling, T. F. Stages of Embryonic Development of the Zebrafish. *Developmental Dynamics* **203**, 253–310 (1995).
267. Hartenstein, V. Atlas of *Drosophila* Development. 1st edition (Cold Spring Harbor Laboratory Press, 1995).
268. Bassi, A., Schmid, B. & Huisken, J. Optical Tomography Complements Light Sheet Microscopy for *in toto* Imaging of Zebrafish Development. *Development* **142**, 1016–1020 (2015).
269. Meier, P., Finch, A. & Evan, G. Apoptosis in Development. *Nature* **407**, 796–801 (2000).
270. Höckendorf, B., Thumberger, T. & Wittbrodt, J. Quantitative Analysis of Embryogenesis: A Perspective for Light Sheet Microscopy. *Developmental Cell* **23**, 1111–1120 (2012).
271. Reynaud, E. G., Peychl, J., Huisken, J. & Tomancak, P. Guide to Light Sheet Microscopy for Adventurous Biologists. *Nature Methods* **12**, 30–34 (2015).
272. Tweedie, S. *et al.* FlyBase: Enhancing *Drosophila* Gene Ontology Annotations. *Nucleic Acids Research* **37**, D555–D559 (2009).
273. Dönitz, J. *et al.* TrOn: An Anatomical Ontology for the Beetle *Tribolium castaneum*. *PLoS One* **8**, e70695 (2013).
274. Yoder, M. J., Mikó, I., Seltmann, K. C., Bertone, M. A. & Deans, A. R. A Gross Anatomy Ontology for Hymenoptera. *PLoS One* **5**, e15991 (2010).
275. Sulston, J. E., Schierenberg, E., White, J. G. & Thomson, J. N. The Embryonic Cell Lineage of the Nematode *Caenorhabditis elegans*. *Developmental Biology* **100**, 64–119 (1983).
276. Wood, W. B. The Nematode *Caenorhabditis elegans*. 1st edition (Cold Spring Harbor Laboratory Press, 1987).
277. Ashburner, M. *et al.* Gene Ontology: Tool for the Unification of Biology. *Nature Genetics* **25**, 25–29 (2000).
278. Pepperkok, R. & Ellenberg, J. High-Throughput Fluorescence Microscopy for Systems Biology. *Nature Reviews Molecular Cell Biology* **7**, 690–696 (2006).
279. Shamir, L., Delaney, J. D., Orlov, N., Eckley, D. M. & Goldberg, I. G. Pattern Recognition Software and Techniques for Biological Image Analysis. *PLoS Computational Biology* **6**, e1000974 (2010).
280. Duboule, D. Temporal Colinearity and the Phylotypic Progression: A Basis for the Stability of a Vertebrate Bauplan and the Evolution of Morphologies Through Heterochrony. *Dev. Suppl.* **42**, 135–142 (1994).
281. Raff, R. A. The Shape of Life: Genes, Development, and the Evolution of Animal Form. 1st edition (The University of Chicago Press, 2012)
282. Lovtrup, S. On von Baerian and Haeckelian Recapitulation. *Systematic Zoology* **27**, 348–352 (1978).
283. Heliconius Genome Consortium, T. H. G. *et al.* Butterfly Genome Reveals Promiscuous Exchange of Mimicry Adaptations Among Species. *Nature* **487**, 94–98 (2012).
284. Zhan, S., Merlin, C., Boore, J. L. & Reppert, S. M. The Monarch Butterfly Genome Yields Insights into Long-Distance Migration. *Cell* **147**, 1171–1185 (2011).

285. McIntosh, A. H. & Grasele, J. J. Establishment of a Monarch Butterfly (*Danaus plexippus*, Lepidoptera: Danaidae) Cell Line and its Susceptibility to Insect Viruses. *Applied Entomology and Zoology* **44**, 331–336 (2009).
286. Palomares, L. A., Joosten, C. E., Hughes, P. R., Granados, R. R. & Shuler, M. L. Novel Insect Cell Line Capable of Complex N-Glycosylation and Sialylation of Recombinant Proteins. *Biotechnology Progress* **19**, 185–192 (2003).
287. Sadd, B. M. *et al.* The Genomes of Two Key Bumblebee Species with Primitive Eusocial Organization. *Genome Biology* **16**, 76 (2015).
288. Keeling, C. I. *et al.* Draft Genome of the Mountain Pine Beetle, *Dendroctonus ponderosae* Hopkins, a Major Forest Pest. *Genome Biology* **14**, R27 (2013).
289. Yin, C. *et al.* InsectBase: A Resource for Insect Genomes and Transcriptomes. *Nucleic Acids Research* **44**, D801–D807 (2016).
290. Werren, J. H. *et al.* Functional and Evolutionary Insights from the Genomes of Three Parasitoid *Nasonia* Species. *Science* **327**, 343–348 (2010).
291. Barbash, D. A. Ninety Years of *Drosophila melanogaster* Hybrids. *Genetics* **186**, 1–8 (2010).
292. Coyne, J. A. & Orr, H. A. The Evolutionary Genetics of Speciation. *Philosophical Transactions of the Royal Society of London. Series B, Biological Sciences* **353**, 287–305 (1998).
293. Maheshwari, S. & Barbash, D. A. The Genetics of Hybrid Incompatibilities. *Annual Review of Genetics* **45**, 331–355 (2011).
294. Barbash, D. A. & Ashburner, M. A Novel System of Fertility Rescue in *Drosophila* Hybrids Reveals a Link between Hybrid Lethality and Female Sterility. *Genetics* **163**, 217–226 (2003).
295. Braverman, J. M., Goñi, B. & Orr, H. A. Loss of a Paternal Chromosome Causes Developmental Anomalies among *Drosophila* Hybrids. *Heredity (Edinb)*. **69 (Pt 5)**, 416–422 (1992).
296. Mavárez, J. *et al.* Speciation by Hybridization in *Heliconius* Butterflies. *Nature* **441**, 868–871 (2006).
297. Yu, H.-S. *et al.* Evidence of Selection at Melanin Synthesis Pathway Loci during Silkworm Domestication. *Mol. Biol. Evol.* **28**, 1785–1799 (2011).
298. Wade, M. J., Johnson, N. A., Jones, R., Siguel, V. & McNaughton, M. Genetic Variation Segregating in Natural Populations of *Tribolium castaneum* affecting Traits Observed in Hybrids with *T. freemani*. *Genetics* **147**, 1235–1247 (1997).
299. Beukeboom, L. W. & Van Den Assem, J. Courtship and Mating Behaviour of Interspecific *Nasonia* Hybrids (Hymenoptera:Pteromalidae): A Grandfather Effect. *Behavior Genetics* **31**, 167–177 (2001).
300. Pfennig, D. W. Ecological Evolutionary Developmental Biology in Encyclopedia of Evolutionary Biology. 1st edition (Elsevier, 2016).
301. Cato, A. J., Elliott, B., Nayak, M. K. & Phillips, T. W. Geographic Variation in Phosphine Resistance Among North American Populations of the Red Flour Beetle (Coleoptera:Tenebrionidae). *Journal of Economic Entomology* **110**, 1359–1365 (2017).
302. Jones, C. D. The Genetics of Adaptation in *Drosophila sechellia*. *Genetica* **123**, 137–145 (2005).
303. Kuntz, S. G., Eisen, M. B., Lerat, E., Vieira, C. & Carareto, C. *Drosophila* Embryogenesis Scales Uniformly across Temperature in Developmentally Diverse Species. *PLoS Genetics* **10**, e1004293 (2014).

304. Gao, L. *et al.* Non-Invasive Imaging beyond the Diffraction Limit of 3D Dynamics in Thickly Fluorescent Specimens. *Cell* **151**, 1370–1385 (2012).
305. Myers, K. A. & Janetopoulos, C. Recent Advances in Imaging Subcellular Processes. *F1000 Research* **5**, 1553 (2016).
306. Regmi, R., Mohan, K. & Mondal, P. P. High Resolution Light Sheet-Based High-Throughput Imaging Cytometry System Enables Visualization of Intra-Cellular Organelles. *AIP Advances* **4**, 97125 (2014).
307. Kumar, A. *et al.* Dual-View Plane Illumination Microscopy for Rapid and Spatially Isotropic Imaging. *Nature Protocols* **9**, 2555–2573 (2014).
308. Gualda, E. J. *et al.* SPIM-Fluid: Open Source Light Sheet-Based Platform for High-Throughput Imaging. *Biomedical Optics Express* **6**, 4447–4456 (2015).
309. Wu, Y. *et al.* Inverted Selective Plane Illumination Microscopy (iSPIM) Enables Coupled Cell Identity Lineaging and Neurodevelopmental Imaging in *Caenorhabditis elegans*. *Proceedings of the National Academy of Sciences* **108**, 17708–17713 (2011).
310. Wu, J., Li, J. & Chan, R. K. Y. A Light Sheet-Based High Throughput 3D-Imaging Flow Cytometer for Phytoplankton Analysis. *Optics Express* **21**, 14474–14480 (2013).
311. Truong, T. V., Supatto, W., Koos, D. S., Choi, J. M. & Fraser, S. E. Deep and Fast Live Imaging with Two-Photon Scanned Light Sheet Microscopy. *Nature Methods* **8**, 757–760 (2011).
312. Deng, X. & Gu, M. Penetration Depth of Single-, Two-, and Three-Photon Fluorescence Microscopic Imaging through Human Cortex Structures: Monte Carlo Simulation. *Applied Optics* **42**, 3321–3329 (2003).
313. Min Gu & Xiaosong Gan. Penetration Depth in Multi-Photon Fluorescence Microscopy. *The Second Asian and Pacific Rim Symposium on Biophotonics*, 72–73 (2004).
314. Shcherbakova, D. M. & Verkhusha, V. V. Near-Infrared Fluorescent Proteins for Multicolor *in vivo* Imaging. *Nature Methods* **10**, 751–754 (2013).
315. Yu, D. *et al.* An Improved Monomeric Infrared Fluorescent Protein for Neuronal and Tumour Brain Imaging. *Nature Communications* **5**, 3626 (2014).
316. Chernov, K. G., Redchuk, T. A., Omelina, E. S. & Verkhusha, V. V. Near-Infrared Fluorescent Proteins, Biosensors, and Optogenetic Tools Engineered from Phytochromes. *Chemical Reviews* **117**, 6423–6446 (2017).
317. Rodriguez, E. A. *et al.* A Far-Red Fluorescent Protein Evolved from a Cyanobacterial Phycobiliprotein. *Nature Methods* **13**, 763–769 (2016).
318. Fahrbach, F. O. & Rohrbach, A. A Line Scanned Light Sheet Microscope with Phase Shaped Self-Reconstructing Beams. *Optics Express* **18**, 24229 (2010).
319. Vettenburg, T. *et al.* Light Sheet Microscopy Using an Airy beam. *Nature Methods* **11**, 541–544 (2014).
320. Gao, L. Extend the Field of View of Selective Plane Illumination Microscopy by Tiling the Excitation Light Sheet. *Optics Express* **23**, 6102–6111 (2015).
321. Richardson, W. H. Bayesian-Based Iterative Method of Image Restoration. *Journal of the Optical Society of America* **62**, 55–59 (1972).
322. Lucy, L. B. An Iterative Technique for the Rectification of Observed Distributions. *The Astronomical Journal* **79**, 745–754 (1974).

323. Khairy, K., Lemon, W. C., Amat, F. & Keller, P. J. Light Sheet-Based Imaging and Analysis of Early Embryogenesis in the Fruit Fly. Published in *Methods in Molecular Biology – Volume 1189*. 1st edition (Springer, 2015).
324. Stegmaier, J. *et al.* Real-Time Three-Dimensional Cell Segmentation in Large-Scale Microscopy Data of Developing Embryos. *Developmental Cell* **36**, 225–240 (2016).
325. Spahn, P., Reuter, R., Herz, H., Bartoszewski, S. & Schnorrer, F. A Vertex Model of *Drosophila* Ventral Furrow Formation. *PLoS One* **8**, e75051 (2013).
326. Amat, F. *et al.* Fast, Accurate Reconstruction of Cell Lineages from Large-Scale Fluorescence Microscopy Data. *Nature Methods* **11**, 951–958 (2014).
327. Shaw, P. Deconvolution in 3-D Optical Microscopy. *The Histochemical Journal* **26**, 687–694 (1994).
328. Bi, H. & Boerner, G. When Does the Richardson-Lucy Deconvolution Converge? *Astronomy and Astrophysics Supplement Series* **108**, 409–415 (1994).
329. Hsu, P. D., Lander, E. S. & Zhang, F. Development and Applications of CRISPR-Cas9 for Genome Engineering. *Cell* **157**, 1262–1278 (2014).
330. Doudna, J. A. & Charpentier, E. The New Frontier of Genome Engineering with CRISPR-Cas9. *Science*. **346**, 1258096 (2014).
331. Wang, H., La Russa, M. & Qi, L. S. CRISPR/Cas9 in Genome Editing and Beyond. *Annual Review of Biochemistry* **85**, 227–264 (2016).
332. Chen, L., Wang, G., Zhu, Y.-N., Xiang, H. & Wang, W. Advances and Perspectives in the Application of CRISPR/Cas9 in Insects. *Zoological Research* **37**, 220–228 (2016).
333. Taning, C. N. T., Van Eynde, B., Yu, N., Ma, S. & Smagghe, G. CRISPR/Cas9 in Insects: Applications, Best Practices and Biosafety Concerns. *Journal of Insect Physiology* **98**, 245–257 (2017).
334. Gratz, S. J. *et al.* Genome Engineering of *Drosophila* with the CRISPR RNA-Guided Cas9 nuclease. *Genetics* **194**, 1029–1035 (2013).
335. Gratz, S. J., Wildonger, J., Harrison, M. M. & O'Connor-Giles, K. M. CRISPR/Cas9-Mediated Genome Engineering and the Promise of Designer Flies on Demand. *Fly (Austin)*. **7**, 249–255 (2013).
336. Bassett, A. & Liu, J. L. CRISPR/Cas9 Mediated Genome Engineering in *Drosophila*. *Methods* **69**, 128–136 (2014).
337. Meccariello, A. *et al.* Highly Efficient DNA-Free Gene Disruption in the Agricultural Pest *Ceratitis capitata* by CRISPR-Cas9 RNPs. *bioRxiv* doi: 10.1101/127506 (2017).
338. Prakash, A. & Monteiro, A. Apterous A Specifies Dorsal Wing Patterns And Sexual Traits In Butterflies. *bioRxiv* doi: 10.1101/131011 (2017).
339. Kohno, H., Suenami, S., Takeuchi, H., Sasaki, T. & Kubo, T. Production of Knockout Mutants by CRISPR/Cas9 in the European Honeybee, *Apis mellifera* L. *Zoological Science* **33**, 505–512 (2016).
340. Awata, H. *et al.* Knockout Crickets for the Study of Learning and Memory: Dopamine Receptor *Dop1* Mediates Aversive but not Appetitive Reinforcement in Crickets. *Scientific Reports* **5**, 15885 (2015).
341. Gaj, T., Gersbach, C. A. & Barbas, C. F. ZFN, TALEN, and CRISPR/Cas-Based Methods for Genome Engineering. *Trends in Biotechnology* **31**, 397–405 (2013).
342. Barrangou, R. & Horvath, P. A Decade of Discovery: CRISPR Functions and Applications. *Nature Microbiology* **2**, 17092 (2017).

343. Anderson, K. V. & Ingham, P. W. The Transformation of the Model Organism: A Decade of Developmental Genetics. *Nature Genetics* **33**, 285–293 (2003).
344. Hendel, A., Fine, E. J., Bao, G. & Porteus, M. H. Quantifying On- and Off-Target Genome Editing. *Trends in Biotechnology* **33**, 132–140 (2015).
345. Zhang, X.-H., Tee, L. Y., Wang, X.-G., Huang, Q.-S. & Yang, S.-H. Off-target Effects in CRISPR/Cas9-Mediated Genome Engineering. *Molecular Therapy Nucleic Acids* **4**, e264 (2015).
346. Sakaue-Sawano, A. *et al.* Visualizing Spatiotemporal Dynamics of Multicellular Cell-Cycle Progression. *Cell* **132**, 487–498 (2008).
347. Sakaue-Sawano, A. & Miyawaki, A. Visualizing Spatiotemporal Dynamics of Multicellular Cell-Cycle Progressions with FUCCI Technology. *Cold Spring Harbor Protocols* **2014**, pdb.prot080408 (2014).
348. Kaida, A., Sawai, N., Sakaguchi, K. & Miura, M. Fluorescence Kinetics in HeLa Cells after Treatment with Cell Cycle Arrest Inducers Visualized with FUCCI (Fluorescent Ubiquitination-Based Cell Cycle Indicator). *Cell Biology International* **35**, 359–363 (2011).
349. Nakayama, M., Kaida, A., Deguchi, S., Sakaguchi, K. & Miura, M. Radiosensitivity of Early and Late M-Phase HeLa Cells Isolated by a Combination of Fluorescent Ubiquitination-Based Cell Cycle Indicator (FUCCI) and Mitotic Shake-Off. *Radiation Research* **176**, 407–411 (2011).
350. Kaida, A. & Miura, M. Visualizing the Effect of Hypoxia on Fluorescence Kinetics in Living HeLa Cells using the Fluorescent Ubiquitination-Based Cell Cycle Indicator (FUCCI). *Experimental Cell Research* **318**, 288–297 (2012).
351. Abe, T. *et al.* Visualization of Cell Cycle in Mouse Embryos with FUCCI2 Reporter Directed by *Rosa26* Promoter. *Development* **140**, 237–246 (2013).
352. Sugiyama, M. *et al.* Illuminating Cell-Cycle Progression in the Developing Zebrafish Embryo. *Proceedings of the National Academy of Sciences* **106**, 20812–20817 (2009).
353. Zielke, N. *et al.* Fly-FUCCI: A Versatile Tool for Studying Cell Proliferation in Complex Tissues. *Cell Reports* **7**, 588–98 (2014).
354. Snippert, H. J. *et al.* Intestinal Crypt Homeostasis Results From Neutral Competition between Symmetrically Dividing *Lgr5* Stem Cells. *Cell* **143**, 134–144 (2010).
355. Schepers, A. G. *et al.* Lineage Tracing Reveals *Lgr5*⁺ Stem Cell Activity in Mouse Intestinal Adenomas. *Science* **337**, 730–735 (2012).
356. Snippert, H. J., Schepers, A. G., Van Es, J. H., Simons, B. D. & Clevers, H. Biased Competition Between *Lgr5* Intestinal Stem Cells Driven by Oncogenic Mutation Induces Clonal Expansion. *EMBO Reports* **15**, 62–69 (2014).
357. Ritsma, L. *et al.* Intestinal Crypt Homeostasis Revealed at Single-Stem-Cell Level by *in vivo* Live Imaging. *Nature* **507**, 362–365 (2014).
358. Zhang, H. *et al.* Experimental Evidence Showing that no Mitotically Active Female Germline Progenitors Exist in Postnatal Mouse Ovaries. *Proceedings of the National Academy of Sciences* **109**, 12580–12585 (2012).
359. Tabansky, I. *et al.* Developmental Bias in Cleavage-Stage Mouse Blastomeres. *Current Biology* **23**, 21–31 (2013).
360. Komai, Y. *et al.* *Bmi1* Expression in Long-Term Germ Stem Cells. *Scientific Reports* **4**, 6175 (2015).
361. Weissman, T. A. & Pan, Y. A. Brainbow: New Resources and Emerging Biological Applications for Multicolor Genetic Labeling and Analysis. *Genetics* **199**, 293–306 (2015).

362. Weissman, T. A., Sanes, J. R., Lichtman, J. W. & Livet, J. Generating and Imaging Multicolor Brainbow Mice. *Cold Spring Harbor Protocols* **6**, 763–769 (2011).
363. Pan, Y. A., Livet, J., Sanes, J. R., Lichtman, J. W. & Schier, A. F. Multicolor Brainbow Imaging in Zebrafish. *Cold Spring Harbor Protocols* **6**, pdb.prot5546 (2011).
364. Pan, Y. A. *et al.* Zebrawow: Multispectral Cell Labeling for Cell Tracing and Lineage Analysis in Zebrafish. *Development* **140**, 2835–2846 (2013).
365. Hadjiconomou, D. *et al.* Flybow: Genetic Multicolor Cell Labeling for Neural Circuit Analysis in *Drosophila melanogaster*. *Nature Methods* **8**, 260–266 (2011).
366. Hampel, S. *et al.* *Drosophila* Brainbow: A Recombinase-Based Fluorescence Labeling Technique to Subdivide Neural Expression Patterns. *Nature Methods* **8**, 253–259 (2011).
367. Ronaghi, M. Pyrosequencing Sheds Light on DNA Sequencing. *Genome Research* **11**, 3–11 (2001).
368. Adams, M. D. *et al.* The Genome Sequence of *Drosophila melanogaster*. *Science* **287**, 2185–2195 (2000).
369. Consortium, i5K. The i5K Initiative: Advancing Arthropod Genomics for Knowledge, Human Health, Agriculture, and the Environment. *Journal of Heredity* **104**, 595–600 (2013).
370. Ayala, F. J. ‘Nothing in Biology Makes Sense Except in the Light of Evolution’: Theodosius Dobzhansky: 1900–1975. *Journal of Heredity* **68**, 3–10 (1975).
371. Henrick, C. A. Methoprene. *Journal of the American Mosquito Control Association* **23**, 225–239 (2007).
372. Carvalho, G. B., Ja, W. W. & Benzer, S. Non-Lethal PCR Genotyping of Single *Drosophila*. *Biotechniques* **46**, 312–314 (2009).
373. Châline, N., Ratnieks, F., Raine, N., Badcock, N. & Burke, T. Non-Lethal Sampling of Honeybee, *Apis mellifera*, DNA using Wing Tips. *Apidologie* **35**, 311–318 (2004).
374. Perkin, L. C., Adrianos, S. L. & Oppert, B. Gene Disruption Technologies Have the Potential to Transform Stored Product Insect Pest Control. *Insects* **7**, E46 (2016).
375. Scolari, F. *et al.* How Functional Genomics Will Impact Fruit Fly Pest Control: The Example of the Mediterranean Fruit Fly, *Ceratitis capitata*. *BMC Genetics* **15**, Suppl 2, S11 (2014).
376. Benedict, M. Q. & Robinson, A. S. The First Releases of Transgenic Mosquitoes: An Argument for the Sterile Insect Technique. *Trends in Parasitology* **19**, 349–355 (2003).
377. Catteruccia, F., Crisanti, A. & Wimmer, E. A. Transgenic Technologies to Induce Sterility. *Malaria Journal* **8**, Suppl 2, S7 (2009).
378. Nolan, T. *et al.* Developing Transgenic *Anopheles* Mosquitoes for the Sterile Insect Technique. *Genetica* **139**, 33–39 (2011).
379. Baldacchino, F. *et al.* Control Methods against Invasive *Aedes* Mosquitoes in Europe: A Review. *Pest Management Science* **71**, 1471–1485 (2015).
380. Benelli, G. & Mehlhorn, H. Declining Malaria, Rising of Dengue and Zika Virus: Insights for Mosquito Vector Control. *Parasitology Research* **115**, 1747–1754 (2016).
381. Reis, N. N., Silva, A. L. da, Reis, E. P. G., Silva, F. C. E. & Reis, I. G. N. Viruses Vector Control Proposal: Genus *Aedes* Emphasis. *Brazilian Journal of Infectious Diseases* **21**, 457–463 (2017).

382. Ittner, L. M. & Götz, J. Pronuclear Injection for the Production of Transgenic Mice. *Nature Protocols* **2**, 1206–1215 (2007).
383. Cho, A., Haruyama, N. & Kulkarni, A. B. Generation of Transgenic Mice. *Current Protocols in Cell Biology* Chapter 19, Unit 19.11 (2009).
384. Huang, G., Ashton, C., Kumbhani, D. S. & Ying, Q. L. Genetic Manipulations in the Rat: Progress and Prospects. *Current Opinion in Nephrology and Hypertension* **20**, 391–399 (2011).
385. Graf, S. F., Hötzel, S., Liebel, U., Stemmer, A. & Knapp, H. F. Image-Based Fluidic Sorting System for Automated Zebrafish Egg Sorting into Multiwell Plates. *Journal of Laboratory Automation* **16**, 105–111 (2011).
386. Mandrell, D. *et al.* Automated Zebrafish Chorion Removal and Single Embryo Placement: Optimizing Throughput of Zebrafish Developmental Toxicity Screens. *Journal of Laboratory Automation* **17**, 66–74 (2012).
387. Owen, M. D. K. & Zelaya, I. A. Herbicide-Resistant Crops and Weed Resistance to Herbicides. *Pest Management Science* **61**, 301–311 (2005).
388. Collinge, D. B., Lund, O. S. & Thordal-Christensen, H. (Editors). Sustainable Disease Management in a European Context. 1st edition (Springer, 2008).
389. Schuler, T. H., Poppy, G. M., Kerry, B. R. & Denholm, I. Insect-Resistant Transgenic Plants. *Trends in Biotechnology* **16**, 168–175 (1998).
390. Gatehouse, J. A. Biotechnological Prospects for Engineering Insect-Resistant Plants. *Plant Physiol.* **146**, 881–887 (2008).
391. Vasil, I. K. A History of Plant Biotechnology: From the Cell Theory of Schleiden and Schwann to Biotech Crops. *Plant Cell Reports* **27**, 1423–1440 (2008).
392. Qaim, M. The Economics of Genetically Modified Crops. *Annual Review of Resource Economics* **1**, 665–694 (2009).
393. Easwar Rao, D., Divya, K., Prathyusha, I. V. S. N., Rama Krishna, C. & Chaitanya, K. V. Insect-Resistant Plants. Published in *Current Developments in Biotechnology and Bioengineering*. 1st edition (Elsevier, 2016).
394. Wally, O. & Punja, Z. K. Genetic Engineering for Increasing Fungal and Bacterial Disease Resistance in Crop Plants. *GM Crops* **1**, 199–206 (2010).
395. Saharan, V. *et al.* Viral, Fungal and Bacterial Disease Resistance in Transgenic Plants. Published in *Advances in Plant Breeding Strategies: Agronomic, Abiotic and Biotic Stress Traits*. 1st edition (Springer, 2016)
396. Prins, M. Broad Virus Resistance in Transgenic Plants. *Trends in Biotechnology* **21**, 373–375 (2003).
397. Prins, M. *et al.* Strategies for Antiviral Resistance in Transgenic Plants. *Molecular Plant Pathology* **9**, 73–83 (2008).
398. Green, J. C. & Hu, J. S. Editing Plants for Virus Resistance Using CRISPR-Cas. *Acta Virologica* **61**, 138–142 (2017).
399. Stern, C. The Hardy-Weinberg Law. *Science* **97**, 137–138 (1943).
400. Brakefield, P. M., Beldade, P. & Zwaan, B. J. The African Butterfly *Bicyclus anynana*: A Model for Evolutionary Genetics and Evolutionary Developmental Biology. *Cold Spring Harbor Protocols* **2009**, pdb.emo122 (2009).
401. Sanchez, R. ‘Okay, well, sometimes science is more art than science, Morty. A lot of people don’t get that’. *Rick and Morty*, **Season 1**, Episode 6 (2014).

Epilog

Zum Schluss bleiben nur noch ein paar Dinge zu sagen, die nirgendwo anders Platz gefunden haben. Zu allererst wollte ich anmerken, meine Doktorarbeit an einigen Stellen ein paar abstraktere Ansichten enthält – zum Beispiel Insektenembryos als geschlossene physikalische Systeme, Erstellen einer Ontologie auf zellulärer Ebene oder On-Demand versus systematisches Datensammeln – über die ich zwar immer gerne rede, aber für die ich bisher noch kaum Gelegenheit hatte, sie einfach mal schriftlich niederzulegen. Jetzt stehen die meisten gesammelt in meiner Doktorarbeit, einfach damit sie nicht verloren gehen.

Mir ist ebenfalls bewusst, dass meine Dissertation verhältnismäßig viele Querverweise beinhaltet, was bei dem Grad an Heterogenität einfach nicht zu vermeiden ist. Egal, wie ich meine Arbeit thematisch strukturiert hätte, es hätte immer Stellen gegeben, in denen ich – alleine schon um ständige Repetition zu verhindern – andere Kapitel, Abbildungen oder Tabellen ein zweites oder drittes Mal hätte referenzieren müssen. Ich habe viele Alternativen ausprobiert und bin sicher, mich iterativ einer Struktur mit der minimalsten Anzahl an sinnvollen Querverweisen stark angenähert habe.

Zusätzlich wollte ich noch erwähnt haben, dass meine Dissertation nach der Begutachtung durch das Prüfungskomitee noch weiteren Zwecken dienen soll, was den Gesamtstil auch merklich beeinflusst hat. Zum einen soll sie als Nachschlagewerk für nachfolgende Studenten dienen, die die Morphogenese von Insektenembryonen untersuchen wollen, zum anderen allerdings auch als Inspiration für verschiedene wissenschaftliche Texte – die Unpublished Results-Unterkapitel werden, sobald die noch ausstehenden Experimente durchgeführt sind, als Grundlage für Research Articles dienen, die Outlook-Unterkapitel können zu Grant Applications umgeschrieben werden und die Ansichten und Ideen in den Perspective-Unterkapitel sind prädestiniert um Reviews oder Commentaries um sie herum aufzubauen.

Außerdem habe ich aufgehört, einen direkt anwendungsbezogenen Sinn in der Entwicklungsbiologie zu suchen. Das ist, im Vergleich zur vielen anderen Disziplinen, zum Beispiel der Zellbiologie, einfach nicht ihr primärer Sinn und Zweck, und krampfhaft eine Brücke zur Medizin, Wirtschaft oder Ähnlichem zu schlagen um meine Forschung zu rechtfertigen ist einfach nicht mein Stil. Aber das ist vermutlich mehr eine philosophische und auch stark subjektive Sache [401]. Ich bin einfach nur dankbar, dass ich an einem Ort gelandet bin, an dem man sich das Prestige der Grundlagenforschung leisten kann.

Als letztes wollte ich noch kurz anmerken, dass auch mir aufgefallen ist, dass meine Arbeit einen stark methodischen Stil hat. In letzter Zeit behaupte ich zwar immer, dass ich vielleicht in der Biotechnologie besser aufgehoben gewesen wäre – da hat man, wie mir zu Ohren kam, wohl nicht den dogmatischen Anspruch unbedingt einen molekularen Mechanismus aufklären zu müssen um der Arbeit eine gewisse Prägnanz zu verleihen – aber unser Fokus auf die Entwicklung und Verbesserung von Techniken begründet sich auch stark darauf, dass es gerade für uns, die wir wohl eher Quereinsteiger in der Evolutionären Entwicklungsbiologie der Insekten sind, eine Möglichkeit darstellt, den Fuß in die Tür zu bekommen, ohne dass wir in der Luft zerrissen werden, denn Publikationen, die neue Techniken vorstellen, sind meist relativ schwierig angreifbar, oder um es einfach auszudrücken – wenn was funktioniert, dann funktioniert es. Außerdem bin ich überzeugter Verfechter des Sähen-und-Ernten-Prinzips, also erstmal die Methodik polieren und sich anschließend den biologischen Fragestellungen zuzuwenden als sich im Strudel des Nachoptimierens zu verlieren oder sich mit suboptimaler Qualität zufriedenzugeben.

Oder, um es mit den Worten von Jane Oppenheimer zu sagen

‘The greatest progressive minds of embryology have not looked for hypotheses; they have looked at embryos’

**Comparative Embryonic Morphogenesis
of Emerging Insect Model Organisms
• Volume II of III •**

Dissertation

**zur Erlangung des Doktorgrades
der Naturwissenschaften**

**vorgelegt beim Fachbereich 15 – Biowissenschaften
der Johann Wolfgang Goethe-Universität**

**von
Frederic Strobl
aus Frankfurt am Main**

**Frankfurt am Main, 2017
(D30)**

Vom Fachbereich 15 – Biowissenschaften der

Johann Wolfgang Goethe-Universität als Dissertation angenommen.

Dekanin: Prof. Dr. Meike Piepenbring

1. Gutachter: Prof. Dr. Ernst H.K. Stelzer

2. Gutachter: Prof. Dr. Bernd Grünewald

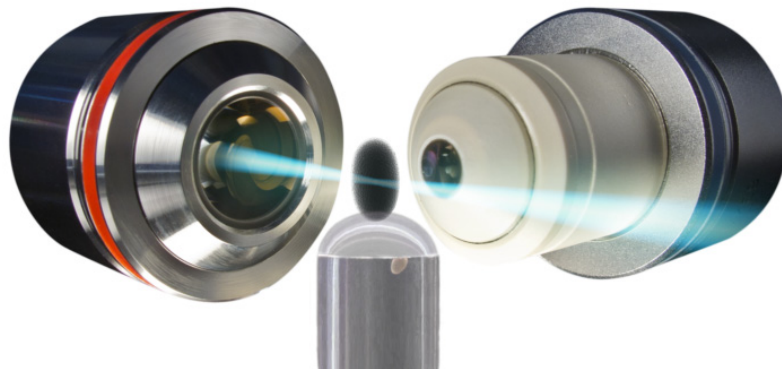
Datum der Disputation:



Buchmann Institute
for Molecular Life Sciences



**Comparative Embryonic Morphogenesis
of Emerging Insect Model Organisms
• Volume II of III •**



Frederic Strobl

Matrikel-Nummer 3326422

Physical Biology / Physikalische Biologie

Buchmann Institute for Molecular Life Sciences

Cluster of Excellence – Macromolecular Complexes

Johann Wolfgang Goethe-Universität – Frankfurt am Main

2012 – 2017

About the Volumes

The style of my PhD thesis is 'publication-based'. Due to the scope, my thesis is divided into three volumes:

- Volume I contains the Extended Summary divided into seven chapters, 1. Summary, 2. Insect Development in a Nutshell, 3. Unpublished Results, 4. Future Trends, 5. Teaching Efforts, 6. Publications and Applications and 7. Trivia.
- Volume II contains the published manuscripts Strobl & Stelzer 2014 (#1), Nollmann *et al.* 2015 (#2), Strobl *et al.* 2015 (#3), Strobl & Stelzer 2016 (#4), Strobl *et al.* 2017A (#5), Strobl *et al.* 2017B (#6) and their respective supplementary material as summarized in Publication Table 1 and Publication Table 2 (Subchapter 6.1) as well as the submitted but not yet accepted manuscripts Strobl *et al.* 2017C (#7), Strobl *et al.* 2017D (#8) and their respective supplementary material as summarized in Publication Table 3 (Subchapter 6.2).
- Volume III contains the submission-ready manuscripts Strobl *et al.* 2017E (#9), Strobl *et al.* 2017F (#10) and their respective supplementary material as summarized in Publication Table 3 (Subchapter 6.2) as well as the patent and grant applications (Subchapter 6.3).

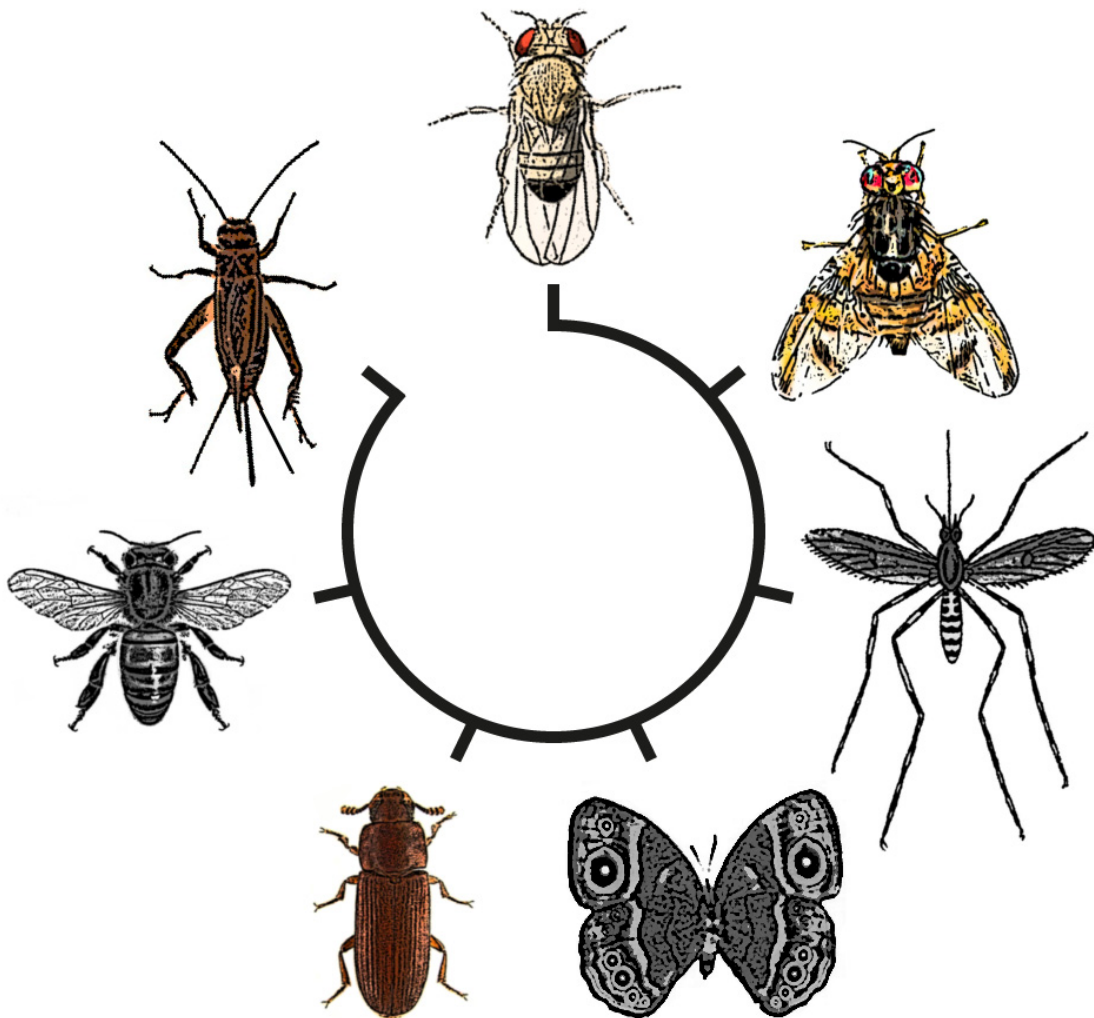


Table of Contents

#1 Non-Invasive long-term live imaging of *Tribolium castaneum* embryos

Frederic Strobl & Ernst H.K. Stelzer
Published in May 2014
Research Article – *Development* – The Company of Biologists
PubMed ID 24803590
Pages 6 – 22

#2 A *Photorhabdus* Natural Product Inhibits Insect Juvenile Hormone Epoxide Hydrolase

Friederike I. Nollmann, Antje K. Heinrich, Alexander O. Brachmann, Christophe Morisseau, Krishnendu Mukherjee, Yngel M. Casanova-Torres, Frederic Strobl, David Kleinhans, Sebastian Kinski, Katharina Schultz, Michael L. Beeton, Marcel Kaiser, Ya-Yun Chu, Long Phan Ke, Aunchalee Thanwisai, Kenan A. J. Bozhiyik, Narisara Chantratita, Friedrich Götze, Nick R. Waterfield, Andreas Vilcinskis, Ernst H.K. Stelzer, Heidi Goodrich-Blair, Bruce D. Hammock & Helge B. Bode
Published in February 2015
Research Article – *ChemBioChem* – Wiley
PubMed ID 25711603
Pages 23 – 55

#3 Live imaging of *Tribolium castaneum* embryonic development using light-sheet-based fluorescence microscopy

Frederic Strobl, Alexander Schmitz & Ernst H.K. Stelzer
Published in September 2015
Research Article – *Nature Protocols* – Nature Publishing Group
PubMed ID 26334868
Pages 56 – 95

#4 Long-term fluorescence live imaging of *Tribolium* embryos: principles, resources, scientific challenges and the comparative approach

Frederic Strobl & Ernst H.K. Stelzer
Published in August 2016
PubMed ID 27939706
Pages 96 – 109

#5 Light Sheet-based Fluorescence Microscopy of Living or Fixed and Stained *Tribolium castaneum* Embryos

Frederic Strobl, Selina Klees & Ernst H.K. Stelzer
Published in April 2016
Research Article – *Journal of Visualized Experiments* – MyJove Corporation
PubMed ID 28518097
Pages 110 – 129

#6 Improving your four-dimensional image: traveling through a decade of light-sheet-based fluorescence microscopy research

Frederic Strobl, Alexander Schmitz & Ernst H.K. Stelzer
Published in May 2017
Review Article – *Nature Protocols* – Nature Publishing Group
PubMed ID 28471459
Pages 130 – 137

#7 Non-lethal genotyping of *Tribolium castaneum* adults using genomic DNA extracted from wing tissue

Frederic Strobl, J. Alexander Ross & Ernst H.K. Stelzer
Submitted in January 2017
Revised and resubmitted in June 2017
Research Article
Pages 138 – 168

#8 A universal vector concept for a direct genotyping of transgenic organisms and a systematic creation of homozygous lines

Frederic Strobl, Anita Anderl & Ernst H.K. Stelzer
Submitted in August 2017
Research Article
Pages 169 – 224

Anmerkung: Nur Publikationen #1, #3 und #4 gingen in die Bewertung der Doktorarbeit mit ein.

Comment: Only publications #1, #3 and #4 were considered for the grade of my PhD thesis.

Non-invasive long-term fluorescence live imaging of *Tribolium castaneum* embryos

Frederic Strobl & Ernst H.K. Stelzer

Insect development has contributed significantly to our understanding of metazoan development. However, most information has been obtained by analyzing a single species, the fruit fly *Drosophila melanogaster*. Embryonic development of the red flour beetle *Tribolium castaneum* differs fundamentally from that of *Drosophila* in aspects such as short-germ development, embryonic leg development, extensive extra-embryonic membrane formation and non-involuted head development. Although *Tribolium* has become the second most important insect model organism, previous live imaging attempts have addressed only specific questions and no long-term live imaging data of *Tribolium* embryogenesis have been available. By combining light sheet-based fluorescence microscopy with a novel mounting method, we achieved complete, continuous and non-invasive fluorescence live imaging of *Tribolium* embryogenesis at high spatiotemporal resolution. The embryos survived the 2-day or longer imaging process, developed into adults and produced fertile progeny. Our data document all morphogenetic processes from the rearrangement of the uniform blastoderm to the onset of regular muscular movement in the same embryo and in four orientations, contributing significantly to the understanding of *Tribolium* development. Furthermore, we created a comprehensive chronological table of *Tribolium* embryogenesis, integrating most previous work and providing a reference for future studies. Based on our observations, we provide evidence that serosa window closure and serosa opening, although deferred by more than 1 day, are linked. All our long-term imaging datasets are available as a resource for the community. *Tribolium* is only the second insect species, after *Drosophila*, for which non-invasive long-term fluorescence live imaging has been achieved.

Published in May 2014

Research Article – *Development* – The Company of Biologists

PubMed ID 24803590

Erklärung zu Autorenanteilen an der Publikation

‘Non-invasive long-term live imaging of *Tribolium castaneum* embryos’

Status: Printed
Zeitschrift: *Development* (Company of Biologists)
Autoren: Frederic Strobl (FS), Ernst H.K. Stelzer (EHKS)

(1) Entwicklung und Planung

FS 50%
EHKS 50%

(2) Durchführung der einzelnen Untersuchungen und Experimente

FS 100%
EHKS 0%

(3) Erstellung der Datensammlung und Abbildungen

FS 100%
EHKS 0%

(4) Analyse und Interpretation der Daten

FS 75% (Verarbeitung Rohdaten, Normalisierungsverfahren, Charakterisierung der Morphogenese)
EHKS 25% (Mikroskop-assoziierte Analyse, Bilddatenverarbeitung)

(5) Verfassen des Manuskriptes

FS 50%
EHKS 50%

Unterschrift Frederic Strobl:

Ort, Datum:

Unterschrift Ernst H.K. Stelzer:

Ort, Datum:

RESEARCH REPORT

TECHNIQUES AND RESOURCES

Non-invasive long-term fluorescence live imaging of *Tribolium castaneum* embryos

Frederic Strobl and Ernst H. K. Stelzer*

ABSTRACT

Insect development has contributed significantly to our understanding of metazoan development. However, most information has been obtained by analyzing a single species, the fruit fly *Drosophila melanogaster*. Embryonic development of the red flour beetle *Tribolium castaneum* differs fundamentally from that of *Drosophila* in aspects such as short-germ development, embryonic leg development, extensive extra-embryonic membrane formation and non-involuting head development. Although *Tribolium* has become the second most important insect model organism, previous live imaging attempts have addressed only specific questions and no long-term live imaging data of *Tribolium* embryogenesis have been available. By combining light sheet-based fluorescence microscopy with a novel mounting method, we achieved complete, continuous and non-invasive fluorescence live imaging of *Tribolium* embryogenesis at high spatiotemporal resolution. The embryos survived the 2-day or longer imaging process, developed into adults and produced fertile progeny. Our data document all morphogenetic processes from the rearrangement of the uniform blastoderm to the onset of regular muscular movement in the same embryo and in four orientations, contributing significantly to the understanding of *Tribolium* development. Furthermore, we created a comprehensive chronological table of *Tribolium* embryogenesis, integrating most previous work and providing a reference for future studies. Based on our observations, we provide evidence that serosa window closure and serosa opening, although deferred by more than 1 day, are linked. All our long-term imaging datasets are available as a resource for the community. *Tribolium* is only the second insect species, after *Drosophila*, for which non-invasive long-term fluorescence live imaging has been achieved.

KEY WORDS: Arthropod development, Coleoptera, *Tribolium castaneum*, Serosa scar, Morphogenesis, Embryogenesis, Light sheet-based fluorescence microscopy, LSFM, DSLM

INTRODUCTION

Research on insect model organisms is an indispensable element in developmental biology (Bodmer and Venkatesh, 1998; Kumar, 2001; Bellen et al., 2010). Although around one million species from the insect order have been described (Patel, 2000), the fruit fly *Drosophila melanogaster* has an almost unchallenged status in the insect developmental biology community. The red flour beetle *Tribolium castaneum* is considered an emerging model organism and has become the second most important insect species after

Drosophila (Klingler, 2004; Schröder et al., 2008; Brown et al., 2009). In contrast to *Drosophila*, *Tribolium* exhibits short-germ development, in which segments are added sequentially to the posterior growth zone (Liu and Kaufman, 2005; Roth and Hartenstein, 2008; Schröder et al., 2008), and embryonic leg development (Grossmann and Prpic, 2012). Other aspects of *Tribolium* development are also considered representative for the insect order, such as extensive extra-embryonic membrane formation (Handel et al., 2005; Panfilio, 2008; Benton et al., 2013; Panfilio et al., 2013) and non-involuting head development (Peel, 2008; Schinko et al., 2008; Posnien and Bucher, 2010). On the methodology side, some molecular biological tools have a higher potency in *Tribolium* than in *Drosophila*, and since the *Tribolium* genome was recently sequenced (Richards et al., 2008), RNA interference (Bucher et al., 2002; Tomoyasu and Denell, 2004; Tomoyasu et al., 2008) has become a very powerful technique for the analysis of gene functions.

A recent approach to study *Tribolium* development has been fluorescence live imaging. First reports have described blastoderm formation, gastrulation, the beginning of germband elongation and dorsal closure by imaging the transgenic EFA-nGFP line or transiently labeled embryos by confocal microscopy (El-Sherif et al., 2012; Sarrazin et al., 2012; Benton et al., 2013; Panfilio et al., 2013). However, no long-term fluorescence live imaging of *Tribolium* embryogenesis has been available until now.

Recently, light sheet-based fluorescence microscopy (LSFM) has emerged as the alternative to confocal fluorescence microscopy and thus constitutes one of the most valuable novel tools in developmental biology (Hell et al., 1994; Stelzer and Lindek, 1994; Huisken et al., 2004; Keller et al., 2008). The complete morphogenesis of *Drosophila* has already been imaged with great success (Keller et al., 2010). In contrast to an epifluorescence arrangement, LSFM uses at least two independently operated lenses. The lenses used in the excitation of the fluorophores are arranged at an angle of 90° relative to those used for the detection of the three-dimensional fluorophore density distribution. Special optical arrangements illuminate only a thin planar section centered on the focal planes of the detection lenses. Hence, true optical sectioning as well as no phototoxic damage and no photobleaching outside a small volume close to the focal plane are intrinsic properties of LSFM. The energy required to excite the fluorophores while recording a three-dimensional stack of images is reduced by two to four orders of magnitude relative to conventional, confocal and two-photon fluorescence microscopy. Since modern cameras are used to record millions of pixels in parallel, tens to hundreds of images with subcellular resolution can be recorded within a few seconds (Keller and Stelzer, 2010).

Here, we describe a novel mounting method for non-invasive long-term fluorescence live imaging of *Tribolium* embryos in LSFM. We show all morphogenetic processes from the rearrangement of the uniform blastoderm to the onset of regular muscular movement

Physical Biology/Physikalische Biologie (IZN, FB 15), Buchmann Institute for Molecular Life Sciences (BMLS), Cluster of Excellence Frankfurt – Macromolecular Complexes (CEF – MC), Goethe University – Frankfurt am Main (Campus Riedberg), Max-von-Laue-Straße 15, Frankfurt am Main D-60348, Germany.

*Author for correspondence (ernst.stelzer@physikalischebiologie.de)

Received 6 February 2014; Accepted 28 March 2014

continuously in the same embryo and in four orientations and provide a comprehensive chronological description of *Tribolium* embryogenesis. As an example of the quality and applicability of our data, we provide evidence that serosa window closure and serosa opening, two processes that occur more than 1 day apart, are functionally linked via a previously undescribed structure, the serosa scar. All of our long-term imaging datasets are available as a resource for the community.

RESULTS AND DISCUSSION

A novel mounting method for *Tribolium* embryos in LSFM

The development of *Tribolium* embryos stops after a few hours when they are embedded in agarose columns, a mounting method that, by contrast, works well with *Drosophila* embryos (Keller et al., 2011). We assume that this is caused by mechanical constraints, reduced gas exchange or a combination of both. Therefore, we developed a novel mounting method in which only a minor fraction of the egg surface is attached to the top of an agarose hemisphere, while the major fraction of the egg surface is exposed to the buffer (supplementary material Fig. S1A). This method allowed us to image *Tribolium* for more than 2 days by LSFM (supplementary material Fig. S1B) until the onset of regular muscular movement (supplementary material Fig. S1C).

Non-invasive long-term fluorescence live imaging of *Tribolium* embryos

With the novel mounting method, we obtained three non-invasive long-term fluorescence live imaging datasets of three embryos from the EFA-nGFP transgenic line (Sarrazin et al., 2012). All three embryos were able to hatch into larvae (supplementary material Fig. S1D), developed into adults that showed no abnormalities, produced healthy and fertile progeny and were still alive at the end of the study. Therefore, we infer that our data were obtained in an as close-to-natural fashion as possible, establishing quality standards that have to be met by future studies.

Our data allow us to summarize nearly the complete course of *Tribolium* embryogenesis from the rearrangement of the uniform blastoderm to the onset of regular muscular movement in a dynamic fashion, including four embryogenesis events that are considered fundamental throughout the insect class – gastrulation, germband elongation, germband retraction and dorsal closure (Fig. 1; supplementary material Movie 1). Furthermore, we created a chronological description of *Tribolium* embryogenesis that links our observations with the current literature (Table 1).

Summary of *Tribolium* morphogenesis

After blastoderm formation, gastrulation begins with the rearrangement of the uniform blastoderm, which differentiates into the serosa and the embryonic rudiment. The serosa migrates over the posterior pole and grows over the embryonic rudiment, initiating the invagination process. The embryonic rudiment condenses and sinks into the yolk (Fig. 1A). Once the serosa window closes, the embryonic rudiment is released into the interior of the serosa, differentiating into the germband, thereby initiating germband elongation. Segments are now added sequentially to the posterior growth zone. The germband tips curl around both poles, migrating dorsally towards each other. Segmentation becomes more prominent in the thoracic region and leg development begins (Fig. 1B). Germband retraction is accompanied by extensive broadening and the germband flanks bend laterally towards the dorsal side. Legs reach their maximum length while pleuropodia develop at the first abdominal segment and the head becomes clearly separated from the

thorax (Fig. 1C). When the germband has retracted completely, dorsal closure begins. After opening, the serosa first migrates over the anterior, then over the posterior pole and turns inside-out on the dorsal side, forming the dorsal organ. Finally, the dorsal organ is incorporated into the dorsal center when both germband flanks close (Fig. 1D). Shortly after dorsal closure, regular muscular movement sets in.

Characteristics of the EFA-nGFP *Tribolium* line in LSFM

In contrast to *Drosophila*, *Tribolium* develops appendices during embryogenesis. We investigated how far these structures can be visualized with LSFM. During dorsal closure, the head performs a $\sim 45^\circ$ turn from an anterior to an anterior-ventral position (Fig. 2A). On the single planes, we were able to resolve and follow structures such as the labial palps and the mandibles over time (Fig. 2B; supplementary material Movie 2). Even deep within the embryo, we could still resolve the trachea as well as the esophagus with its butterfly-shaped inner lumen above the subesophageal ganglion (Fig. 2C; supplementary material Movie 2).

An important issue with long-term fluorescence imaging is photobleaching. If datasets were recorded with an imaging interval of 00:06 h, moderate photobleaching occurred, whereas with an interval of 00:30 h photobleaching was barely visible (supplementary material Fig. S2), maintaining a signal-to-noise ratio that was sufficient to perform volume renderings of the complete dataset (supplementary material Movie 3). Volume rendering visualized certain structures more efficiently; for example, median groove folding during gastrulation or embryonic leg development (Fig. 2D). Furthermore, our LSFM setup was sufficiently sensitive to observe cell proliferation in the EFA-nGFP line. During gastrulation, dividing nuclei could be detected as light gray clouds over a dark gray background (Fig. 2E), and, even beyond gastrulation, sites of massive proliferation could be determined; for example, at the outer rims of the head lobes during germband elongation (Fig. 2F).

Serosa scar formation and serosa opening

As an example of the practical application of our data, we characterized a previously undescribed transient structure that emerges and vanishes again in between serosa differentiation and internalization. After serosa window closure, in many, but not all, instances, the germband rotated slightly around the anterior-posterior axis. This rotation revealed an anterior-ventral cell cluster on the serosa, which we term the serosa scar (Fig. 3A; supplementary material Movie 4). For approximately one-third of embryogenesis, the serosa scar remained quiescent in the same location. Shortly before dorsal closure, the serosa scar was pulled apart in a circular fashion. The pulling redirected dorsally, which led to elimination of the space between the serosa and the germband. This was followed by the migration of the serosa over the anterior pole (Fig. 3B; supplementary material Movie 5).

The cell movement pattern suggests that the serosa scar is established at the end of gastrulation as a predetermined point for the formation of an anterior-ventral serosa opening during dorsal closure once pulling at the dorsal side begins. This view is supported by evidence that the space between the serosa and the germband is eliminated, which indicates a subsequent liquid outflow through the newly formed serosa opening.

Spatiotemporally separated and functionally distinct morphogenetic processes, such as serosa window closure (Handel et al., 2000; Benton et al., 2013) and serosa opening (van der Zee et al., 2005; Panfilio et al., 2013), have been described previously, but were not related to preceding and subsequent processes. Therefore, those investigations had not been able to demonstrate a higher order

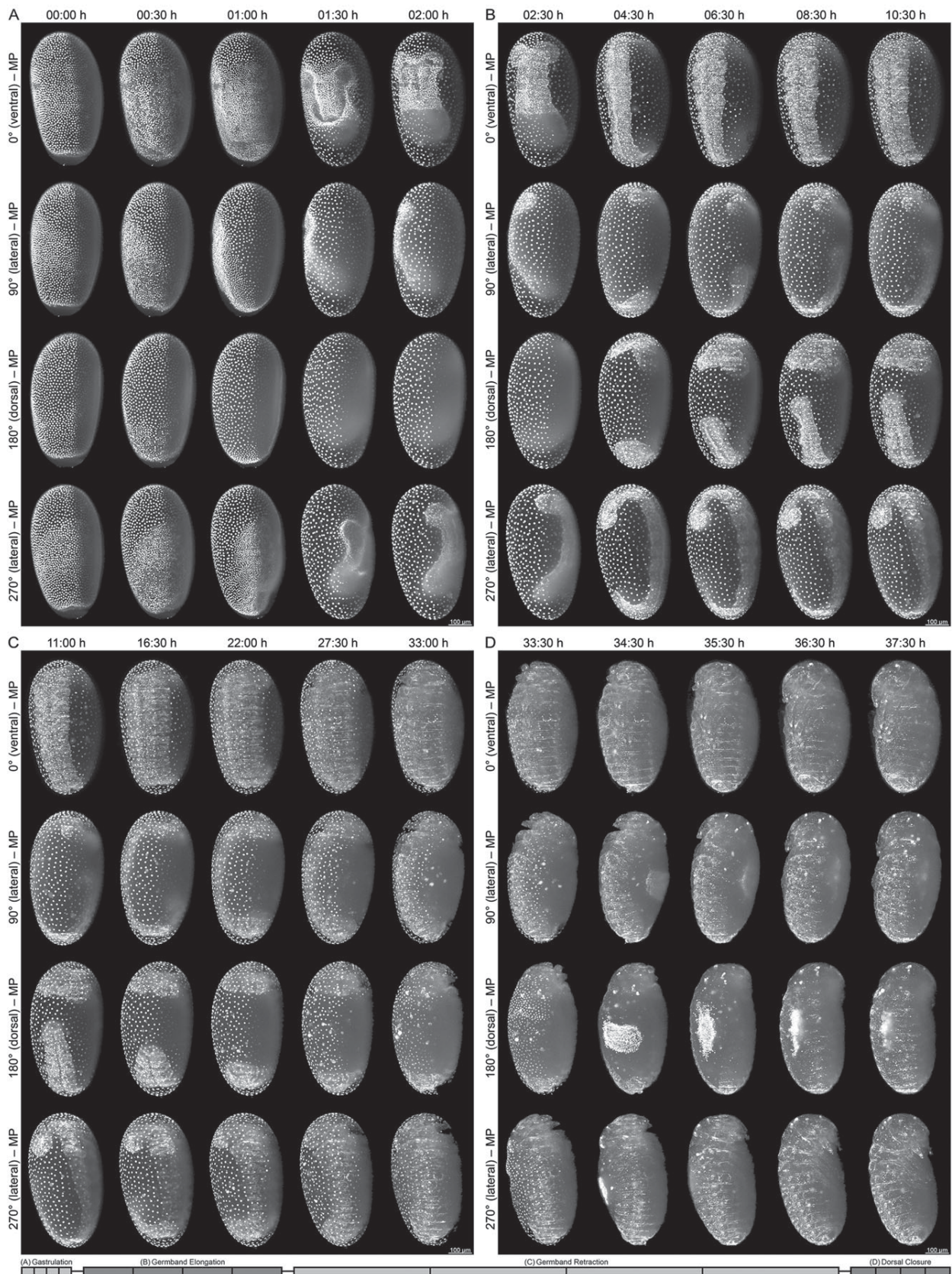


Fig. 1. Overview of *Tribolium* embryogenesis. The four embryogenesis events of (A) gastrulation, (B) germband elongation, (C) germband retraction and (D) dorsal closure of *Tribolium* are shown in four orientations over a period of 37:30 h. The progression bar at the bottom indicates the temporal frame of the images (each black bar represents one time point). MP, maximum projection with image processing.

Table 1. Chronological description of *Tribolium* embryogenesis

Figure and time	Developmental process
Before imaging	<ul style="list-style-type: none"> The twelfth and last synchronous blastodermal proliferation cycle finishes (Handel et al., 2000, 2005; Benton et al., 2013) <ul style="list-style-type: none"> giving rise to the uniform blastoderm (Brown et al., 1994; Handel et al., 2000, 2005; Benton et al., 2013) <p>End of blastoderm formation and beginning of gastrulation</p>
1A – 00:00 h	<ul style="list-style-type: none"> The uniform blastoderm rearranges into the differentiated blastoderm (Brown et al., 1994; Handel et al., 2000; van der Zee et al., 2005; Benton et al., 2013) <ul style="list-style-type: none"> spreading into a dorsally tilted anterior cap (Handel et al., 2000) <ul style="list-style-type: none"> representing the future extra-embryonic tissue clustering into a ventrally tilted posterior cap (Handel et al., 2000; El-Sherif et al., 2012) <ul style="list-style-type: none"> representing the future germband The posterior pole flattens ventrally and forms a plate (Handel et al., 2000) <ul style="list-style-type: none"> usually accompanied by a retraction of the posterior pole from the vitelline membrane (Benton et al., 2013)
1A – 00:30 h	<ul style="list-style-type: none"> The thirteenth asynchronous proliferation cycle finishes laterally (Handel et al., 2000, 2005; El-Sherif et al., 2012; Benton et al., 2013) <ul style="list-style-type: none"> forming the serosa consisting of large and widespread nuclei (Brown et al., 1994; Handel et al., 2000; van der Zee et al., 2005; Benton et al., 2013) forming the median ventral stripe consisting of large and clustered nuclei (Handel et al., 2000, 2005) forming the embryonic rudiment flanks consisting of small and condensed nuclei (Brown et al., 1994; Handel et al., 2000; van der Zee et al., 2005; Benton et al., 2013) The posterior pole invaginates (Handel et al., 2000; Handel et al., 2005; Benton et al., 2013) <ul style="list-style-type: none"> turning the plate at the posterior pole into the primitive pit (Brown et al., 1994; Handel et al., 2000; Handel et al., 2005; van der Zee et al., 2005; Benton et al., 2013)
1A – 01:00 h	<ul style="list-style-type: none"> The median ventral stripe finishes the thirteenth proliferation cycle (Handel et al., 2005) <ul style="list-style-type: none"> turning into the middle plate (Handel et al., 2000) joining both embryonic rudiment flanks The serosa extends to the ventral center around the lateral sides and towards the posterior pole (Brown et al., 1994; Handel et al., 2000; van der Zee et al., 2005; Benton et al., 2013) <ul style="list-style-type: none"> condensing the embryonic rudiment (Brown et al., 1994; Handel et al., 2000, 2005; El-Sherif et al., 2012; Sarrazin et al., 2012; Benton et al., 2013) overgrowing the primitive pit (Brown et al., 1994; Handel et al., 2000; Benton et al., 2013) <ul style="list-style-type: none"> forming the posterior amniotic fold (Handel et al., 2000, 2005; van der Zee et al., 2005; Sarrazin et al., 2012; Benton et al., 2013)
1A – 01:30 h	<ul style="list-style-type: none"> The embryonic rudiment sinks into the yolk (Brown et al., 1994; Handel et al., 2005; Sarrazin et al., 2012; Benton et al., 2013) The middle plate folds into the median groove (Brown et al., 1994; Handel et al., 2000, 2005) The dorsal serosa rotates over the posterior pole (Handel et al., 2000; Benton et al., 2013) The posterior amniotic fold internalizes the embryonic rudiment (Brown et al., 1994; Handel et al., 2005; Sarrazin et al., 2012; Benton et al., 2013) <ul style="list-style-type: none"> rotating the posterior and posterior-lateral amnion inward (Handel et al., 2000; Benton et al., 2013) forming the yolk sac fold (Handel et al., 2000; Benton et al., 2013) The anterior amniotic fold elevates (Brown et al., 1994; Handel et al., 2000; van der Zee et al., 2005; Benton et al., 2013) <ul style="list-style-type: none"> involuting head lobes (Brown et al., 1994) joining subsequently with the posterior amniotic fold (Handel et al., 2000; van der Zee et al., 2005) <ul style="list-style-type: none"> resulting in a combined horseshoe-shaped amniotic fold (Handel et al., 2000; van der Zee et al., 2005; Benton et al., 2013)
1A – 02:00 h	<ul style="list-style-type: none"> The combined amniotic fold gives rise to the serosa window (Handel et al., 2000; van der Zee et al., 2005; Benton et al., 2013) <ul style="list-style-type: none"> changing the horseshoe-shaped amniotic fold into an oval amniotic fold (Benton et al., 2013) bearing slight notches close to the head lobe anlagen rotating the anterior and anterior-lateral amnion inward (Handel et al., 2000) <ul style="list-style-type: none"> allowing the future head lobes to extend below the serosa to the anterior pole (van der Zee et al., 2005) <p>End of gastrulation and beginning of germband elongation</p>
1B – 02:30 h	<ul style="list-style-type: none"> The serosa window closes (Handel et al., 2000; van der Zee et al., 2005; Kittelmann et al., 2013; Sarrazin et al., 2012; Benton et al., 2013) <ul style="list-style-type: none"> separating the serosa from the amnion (Handel et al., 2000; Benton et al., 2013) <ul style="list-style-type: none"> releasing the embryonic rudiment with the affiliated amnion into the interior of the serosa (van der Zee et al., 2005) The embryonic rudiment differentiates into the germband (Brown et al., 1994; Handel et al., 2000; Benton et al., 2013) <ul style="list-style-type: none"> forming the posterior growth zone (Brown et al., 1994; Handel et al., 2005) <ul style="list-style-type: none"> initiating germband elongation (Brown et al., 1994; van der Zee et al., 2005; Sarrazin et al., 2012; Benton et al., 2013) The yolk sac fold retracts (Handel et al., 2000; Benton et al., 2013)
1B – 04:30 h	<ul style="list-style-type: none"> The yolk sac fold levels out (Handel et al., 2000) <ul style="list-style-type: none"> allowing the posterior growth zone to reach the posterior pole (Brown et al., 1994; Handel et al., 2000; Benton et al., 2013) leading to a superficial germband that spans over the complete egg length (Brown et al., 1994; Handel et al., 2000) The head lobes curl around the anterior pole (Brown et al., 1994; Benton et al., 2013) <ul style="list-style-type: none"> extending dorsally towards the posterior pole The posterior growth zone curls around the posterior pole (Brown et al., 1994; Benton et al., 2013) <ul style="list-style-type: none"> extending dorsally towards the anterior pole (Benton et al., 2013) <ul style="list-style-type: none"> resulting in an approaching dorsal movement both germband tips, the head lobes and the posterior growth zone
1B – 06:30 h	<ul style="list-style-type: none"> The head lobes stop migrating dorsally <ul style="list-style-type: none"> leading to a proliferation anterior median region (Kittelmann et al., 2013) <ul style="list-style-type: none"> fusing the head lobes medially (Kittelmann et al., 2013)

Continued

Table 1. Continued

Figure and time	Developmental process
1B – 08:30 h	<ul style="list-style-type: none"> • The mandibular and maxillary segment outlines become visible (Brown et al., 1994; Handel et al., 2005) • The appendage buds become visible (Brown et al., 1994; Handel et al., 2005) • The thorax exhibits a more prominent segmentation (Brown et al., 1994) • The thoracic segments initiate leg development <ul style="list-style-type: none"> ○ pushing the germband slightly into the yolk • The abdomen exhibits a more prominent segmentation • The posterior growth zone spans half of the egg length
1B – 10:30 h	<ul style="list-style-type: none"> • The posterior growth zone spans slightly more than half of the egg length <ul style="list-style-type: none"> ○ allowing the germband to reach the maximal length (Brown et al., 1994; van der Zee et al., 2005) ○ reaching the extended germband stage (Brown et al., 1994) <p>End of germband elongation and beginning of germband retraction</p>
1C – 11:00 h	<ul style="list-style-type: none"> • The germband begins with retraction <ul style="list-style-type: none"> ○ exhibiting massive proliferation at the posterior growth zone
1C – 16:30 h	<ul style="list-style-type: none"> • The germband retracts posteriorly to one-third of the egg length <ul style="list-style-type: none"> ○ broadening parallel to two-thirds of the egg width • At the tip of the posterior growth zone, the hindgut is formed
1C – 22:00 h	<ul style="list-style-type: none"> • The germband retracts posteriorly to one-fifth of the egg length <ul style="list-style-type: none"> ○ broadening parallel to three-quarters of the egg width
1C – 27:30 h	<ul style="list-style-type: none"> • The head becomes clearly separated from the thorax • The germband retracts posteriorly nearly completely <ul style="list-style-type: none"> ○ broadening parallel to the full egg width • The first abdominal segment develops pleuropodia
1C – 33:00 h	<ul style="list-style-type: none"> • The germband flips posteriorly into the posterior pole <ul style="list-style-type: none"> ○ allowing the germband to reach minimal length (Brown et al., 1994) ○ broadening even further (Brown et al., 1994; van der Zee et al., 2005) <ul style="list-style-type: none"> – leading to a lateral bending and the dorsal growth of the germband flanks (Brown et al., 1994; van der Zee et al., 2005) • The serosa is pulled to the dorsal center <ul style="list-style-type: none"> ○ stretching the serosa slightly <p>End of germband retraction and beginning of dorsal closure</p>
1D – 33:30 h	<ul style="list-style-type: none"> • The serosa opens ventrally <ul style="list-style-type: none"> ○ initiating serosa withdrawal (Panfilio et al., 2013) ○ allowing the serosa to migrate over the anterior pole
1D – 34:30 h	<ul style="list-style-type: none"> • The serosa clusters at the dorsal center of the embryo (Panfilio et al., 2013) <ul style="list-style-type: none"> ○ allowing the serosa to migrate over the posterior pole <ul style="list-style-type: none"> – folding over itself (Panfilio et al., 2013) – leading to an inside-out turning of the serosa ○ compacting strongly (Panfilio et al., 2013) <ul style="list-style-type: none"> – reducing the serosa surface area (Panfilio et al., 2013) – forming the dorsal organ (van der Zee et al., 2005; Panfilio et al., 2013)
1D – 35:30 h	<ul style="list-style-type: none"> • The head starts turning from an anterior to an anterior-ventral orientation • The germband flanks extend toward the midline (Panfilio et al., 2013) • The dorsal organ elongates anterior-posteriorly (Panfilio et al., 2013) <ul style="list-style-type: none"> ○ turning the embryo from a dorsally curled position to a ventrally curled position
1D – 36:30 h	<ul style="list-style-type: none"> • The head has reached the anterior-ventral orientation • The dorsal organ sinks into the yolk (van der Zee et al., 2005; Panfilio et al., 2013)
1D – 37:30 h	<ul style="list-style-type: none"> • The dorsal organ becomes completely internalized • The germband flanks begin epidermal zippering (Panfilio et al., 2013) <ul style="list-style-type: none"> ○ initiating midline closure (Panfilio et al., 2013) ○ leaving the dorsal seam behind (Panfilio et al., 2013) <p>End of dorsal closure</p>
Beyond imaging	<ul style="list-style-type: none"> • The germband flanks finish epidermal zippering (Panfilio et al., 2013) <ul style="list-style-type: none"> ○ the dorsal seam closes completely (Panfilio et al., 2013) • The surface exhibits extensive cell proliferation • The embryo exhibits regular muscular movement

We only describe processes for which our data provide evidence. Indentions show associated processes. If applicable, processes are referenced. The references include the majority of current publications, in particular all publications that provide fluorescence live imaging data. We use the original terms suggested in these publications. Please note that some morphogenetic processes can only be seen properly in the supplementary material movies; for example, leg development and serosa stretching.

dynamics of embryogenesis, such as the functional link between serosa window closure and serosa opening that we describe here (Fig. 3C). This example illustrates the importance of non-invasive long-term fluorescence live imaging.

Perspectives

We anticipate that LSFM will become a powerful tool in the analysis of fluorescently labeled transgenic *Tribolium* lines as well as mutants or embryos in which genes have been knocked

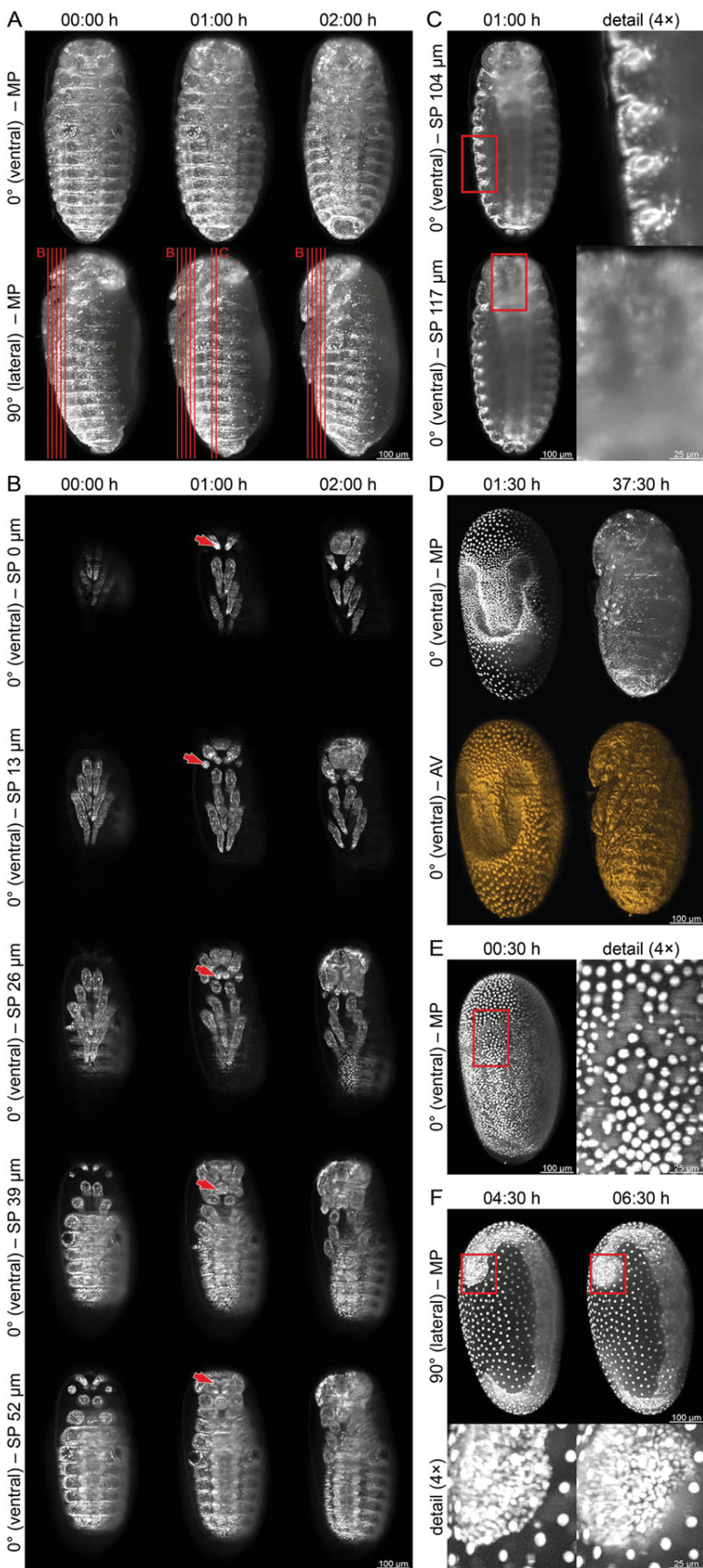


Fig. 2. Characteristics of the EFA-nGFP *Tribolium* line in LSM. (A) Head movement during dorsal closure. The head turns ~45° from an anterior to an anterior-ventral position during dorsal closure. Lines indicate single planes shown in B and C. (B) Ventral optical sectioning during dorsal closure shows head appendices. The first single plane with moderate signal was defined as 0 μm. Because of the head turning, ventrally recorded single planes show details of head development along different head orientations. Arrows mark the antenna at 0 μm, the maxillary palp tip at 13 μm, the labial palps at 26 μm, the labium at 39 μm and the mandibles with the typical Y-shape in between at 52 μm. (C) Ventral optical sectioning during dorsal closure shows structures deep within the embryo. The first single plane with moderate signal was defined as 0 μm. The boxed regions are magnified (4×) to the right. At 104 μm, the tracheae are visible. At 117 μm, the esophagus is cut sagittal, revealing its butterfly-shaped inner lumen. (D) Maximal projections compared with volume rendering. Some structures are better visualized on the volume renderings; for example, the median groove during gastrulation at 01:30 h and the legs during dorsal closure at 37:30 h. (E) Cell proliferation during gastrulation. The boxed region is magnified (4×) to the right. With LSM, it is possible to visualize cell proliferation during early gastrulation, as dividing cells form light gray 'clouds' above a dark gray background. (F) Cell proliferation beyond gastrulation. The boxed regions are magnified (4×) beneath. Beyond gastrulation, LSM can still visualize sites of massive cell proliferation, as shown here for the outer rim of the head lobes during germband elongation. MP, maximum projection with image processing; SP, single plane; AV, Amira-based volume rendering.

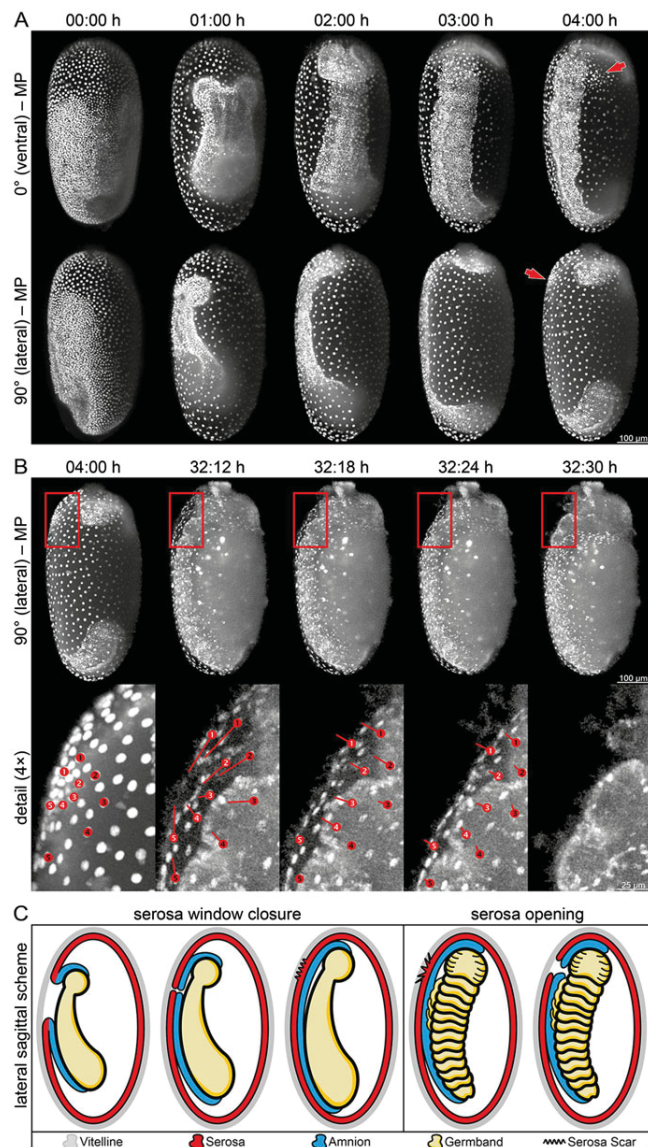


Fig. 3. Serosa scar formation and serosa opening. (A) Serosa window closure and serosa scar formation. During gastrulation, the serosa window emerges and subsequently closes at the anterior-ventral side of the embryo. Then, the germband rotates inside the serosa, exposing a cell cluster at the location where the serosa window closed termed the serosa scar (arrows). (B) Serosa scar quiescence and serosa opening. The boxed regions are magnified (4 \times) beneath. To illustrate serosa movement, ten nuclei were tracked over time, five in close (white numbers) and five in distal (black numbers) proximity to the center of the serosa scar. Upon serosa window closure, the serosa scar remains quiescent for more than 1 day before being pulled apart in a circular fashion. Then, the migration pattern changes as the nuclei migrate dorsally, eliminating the space between the serosa and the germband. (C) Scheme of serosa window closure, serosa scar formation and serosa opening. During gastrulation, the serosa is separated from the amnion/germband as the serosa window closes and the serosa scar is left behind in the location where the window closed. While embryogenesis proceeds, the serosa scar remains quiescent as the germband undergoes elongation and retraction. Shortly before dorsal closure, the serosa scar is pulled apart, the serosa opening is created and the space between serosa and germband is eliminated. MP, maximum projection with image processing.

down, especially in terms of the development of the head, legs and extra-embryonic membranes, in which *Tribolium* differs significantly from *Drosophila*.

With this work, the complete embryogenesis of a second insect species is now documented, which is an important step for comparative studies. We intend to investigate which other morphogenetic concepts exist besides the *Drosophila* paradigm and how they are executed, identifying fundamental principles as well as specialized alterations and thereby providing insights in the fields of developmental, cell and evolutionary biology.

MATERIALS AND METHODS

Tribolium rearing and embryo collection

The *Tribolium castaneum* (Herbst) Vermillion White EFA-nGFP transgenic line was used (Sarrazin et al., 2012). Rearing and embryo collection were performed as described previously (Brown et al., 2009); parameters are provided in supplementary material Table S1.

Mounting

Simultaneous dechoriation of 10-15 embryos was performed as described previously (Benton et al., 2013). An embryo that exhibited reasonable fluorescence emission under a SteREO Discovery.V8 microscope (Carl Zeiss) with filter set 38 (Carl Zeiss) was picked with a small paint brush. A stainless steel pipe with an external diameter of 3 mm and an internal diameter of 1 mm (#R00306, Sawade Edelstahlrohre, Gottmadingen, Germany) was held vertically and filled with agarose from the top until a hemisphere formed and polymerized at the bottom end of the pipe. The hemisphere was then dipped into liquid agarose in order to apply a thin film that was used to mount the dechoriated embryo with the anterior side to the top of the hemisphere. Finally, 2 μ l agarose were added around the gap between the embryo and agarose hemisphere for additional stability (supplementary material Fig. S1). Parameters are provided in supplementary material Table S1.

Microscopy

We used an advanced variant of LSFM termed monolithic digital scanned laser light sheet-based fluorescence microscopy (mDSLML), which is based on DSLM (Keller and Stelzer, 2010). Parameters are provided in supplementary material Table S1. Imaging started immediately after the embryo was inserted into the sample chamber.

Embryo retrieval

When regular muscular movement could be detected (supplementary material Fig. S1C) imaging was stopped. The sample chamber was slowly drained and the agarose hemisphere with the embryo still mounted on top was retrieved and transferred to an object holder. The embryo was dried for 5 min at 35°C, then transferred to a moistening chamber and further incubated at 35°C. After hatching, the larva was transferred to a small glass tube and cultivated as stated above. After the larva had developed into an adult, it was provided with a mating partner. After an appropriate time, progeny production was checked.

Image processing

Image processing was performed with Mathematica (Wolfram). Single planes (SP) were used to calculate the maximum projections. With those projections, two processing steps were performed. (1) Background correction (BC). A brightness threshold was applied that distinguishes the specimen from the background. The background was used to calculate the mean image background and then set to zero. Then, the mean image background was subtracted from the whole image. This led to an overall intensity decrease. (2) Mean transform (MT). For the desired series of images, the brightest and the dimmest images were selected and the mean intensity was calculated. For the desired series, the image closest to that intensity was determined and designated the reference image. All images were normalized to match the intensity of the reference image. This included both increase and decrease of intensities (supplementary material Fig. S3). Images that underwent this procedure are marked as maximum projections with image processing (MP). If necessary, images underwent equal brightness adjustment. Further details of image processing can be provided upon request. Images were cropped to

600×1000 pixels (XD×YD, supplementary material Table S1), maintaining the original line and pixel pitches used during the imaging recording process. Cell tracking in Fig. 3B was performed manually. Amira (FEI Visualization Science Group, Düsseldorf, Germany) was used for volume rendering (AV) in Fig. 2D and supplementary material Movie 3. Meta information about the three long-term imaging datasets is provided in supplementary material Table S1 (the original datasets, associated figures and movies in full quality are available at www.physikalischebiologie.de/bugcube).

Acknowledgements

We thank Andrew Peel and Michalis Averof for the *Tribolium* EFA-nGFP line; the Goethe University workshop for custom hardware; Alexander Schmitz for help with the Mathematica-based image processing; Daniel von Wangenheim for help with the generation of the movies and Amira-based volume rendering; and Isabell Smyrek, Christian Pohl, Anna Gilles and Michalis Averof for comments on the manuscript.

Competing interests

The authors declare no competing financial interests.

Author contributions

F.S. and E.H.K.S. conceived the research and wrote the publication. F.S. performed the experiments.

Funding

This work was supported by the Deutsche Forschungsgemeinschaft (DFG)-funded Cluster of Excellence 'Macromolecular Complexes' [CEF, EXC 115].

Supplementary material

Supplementary material available online at <http://dev.biologists.org/lookup/suppl/doi:10.1242/dev.108795/-/DC1>

References

- Bellen, H. J., Tong, C. and Tsuda, H. (2010). 100 years of *Drosophila* research and its impact on vertebrate neuroscience: a history lesson for the future. *Nat. Rev. Neurosci.* **11**, 514-522.
- Benton, M. A., Akam, M. and Pavlopoulos, A. (2013). Cell and tissue dynamics during *Tribolium* embryogenesis revealed by versatile fluorescence labeling approaches. *Development* **140**, 3210-3220.
- Bodmer, R. and Venkatesh, T. V. (1998). Heart development in *Drosophila* and vertebrates: conservation of molecular mechanisms. *Dev. Genet.* **22**, 181-186.
- Brown, S. J., Parrish, J. K., Denell, R. E. and Beeman, R. W. (1994). Genetic control of early embryogenesis in the red flour beetle, *Tribolium castaneum*. *Am. Zoologist* **34**, 343-352.
- Brown, S. J., Shippy, T. D., Miller, S., Bolognesi, R., Beeman, R. W., Lorenzen, M. D., Bucher, G., Wimmer, E. A. and Klingler, M. (2009). The red flour beetle, *Tribolium castaneum* (Coleoptera): a model for studies of development and pest biology. *Cold Spring Harb. Protoc.* **2009**, ppdb emo126.
- Bucher, G., Scholten, J. and Klingler, M. (2002). Parental RNAi in *Tribolium* (Coleoptera). *Curr. Biol.* **12**, R85-R86.
- El-Sherif, E., Averof, M. and Brown, S. J. (2012). A segmentation clock operating in blastoderm and germband stages of *Tribolium* development. *Development* **139**, 4341-4346.
- Grossmann, D. and Prpic, N.-M. (2012). Egfr signaling regulates distal as well as medial fate in the embryonic leg of *Tribolium castaneum*. *Dev. Biol.* **370**, 264-272.
- Handel, K., Grünfelder, C. G., Roth, S. and Sander, K. (2000). *Tribolium* embryogenesis: a SEM study of cell shapes and movements from blastoderm to serosal closure. *Dev. Genes. Evol.* **210**, 167-179.
- Handel, K., Basal, A., Fan, X. and Roth, S. (2005). *Tribolium castaneum* twist: gastrulation and mesoderm formation in a short-germ beetle. *Dev. Genes. Evol.* **215**, 13-31.
- Hell, S. W., Stelzer, E. H. K., Lindek, S. and Cremer, C. (1994). Confocal microscopy with an increased detection aperture: type-B 4Pi confocal microscopy. *Opt. Lett.* **19**, 222.
- Huisken, J., Swoger, J., Del Bene, F., Wittbrodt, J. and Stelzer, E. H. K. (2004). Optical sectioning deep inside live embryos by selective plane illumination microscopy. *Science* **305**, 1007-1009.
- Keller, P. J. and Stelzer, E. H. K. (2010). Digital scanned laser light sheet fluorescence microscopy. *Cold Spring Harb. Protoc.* **2010**, ppdb.top78.
- Keller, P. J., Schmidt, A. D., Wittbrodt, J. and Stelzer, E. H. K. (2008). Reconstruction of zebrafish early embryonic development by scanned light sheet microscopy. *Science* **322**, 1065-1069.
- Keller, P. J., Schmidt, A. D., Santella, A., Khairy, K., Bao, Z., Wittbrodt, J. and Stelzer, E. H. K. (2010). Fast, high-contrast imaging of animal development with scanned light sheet-based structured-illumination microscopy. *Nat. Methods* **7**, 637-642.
- Keller, P. J., Schmidt, A. D., Wittbrodt, J. and Stelzer, E. H. K. (2011). Digital scanned laser light-sheet fluorescence microscopy (DSLM) of zebrafish and *Drosophila* embryonic development. *Cold Spring Harb. Protoc.* **2011**, 1235-1243.
- Kittelmann, S., Ulrich, J., Posnien, N. and Bucher, G. (2013). Changes in anterior head patterning underlie the evolution of long germ embryogenesis. *Dev. Biol.* **374**, 174-184.
- Klingler, M. (2004). *Tribolium*. *Curr. Biol.* **14**, R639-R640.
- Kumar, J. P. (2001). Signalling pathways in *Drosophila* and vertebrate retinal development. *Nat. Rev. Genet.* **2**, 846-857.
- Liu, P. Z. and Kaufman, T. C. (2005). Short and long germ segmentation: unanswered questions in the evolution of a developmental mode. *Evol. Dev.* **7**, 629-646.
- Panfilio, K. A. (2008). Extraembryonic development in insects and the acrobatics of blastokinesis. *Dev. Biol.* **313**, 471-491.
- Panfilio, K. A., Oberhofer, G. and Roth, S. (2013). High plasticity in epithelial morphogenesis during insect dorsal closure. *Biol. Open* **2**, 1108-1118.
- Patel, N. H. (2000). It's a bug's life. *Proc. Natl. Acad. Sci. U.S.A.* **97**, 4442-4444.
- Peel, A. D. (2008). The evolution of developmental gene networks: lessons from comparative studies on holometabolous insects. *Philos. Trans. R. Soc. Lond. B Biol. Sci.* **363**, 1539-1547.
- Posnien, N. and Bucher, G. (2010). Formation of the insect head involves lateral contribution of the intercalary segment, which depends on Tc-labial function. *Dev. Biol.* **338**, 107-116.
- Richards, S., Gibbs, R. A., Weinstock, G. M., Brown, S. J., Denell, R., Beeman, R. W., Gibbs, R., Bucher, G., Friedrich, M., Grimmelikhuijzen, C. J. et al. (2008). The genome of the model beetle and pest *Tribolium castaneum*. *Nature* **452**, 949-955.
- Roth, S. and Hartenstein, V. (2008). Development of *Tribolium castaneum*. *Dev. Genes Evol.* **218**, 115-118.
- Sarrazin, A. F., Peel, A. D. and Averof, M. (2012). A segmentation clock with two-segment periodicity in insects. *Science* **336**, 338-341.
- Schinko, J. B., Kreuzer, N., Offen, N., Posnien, N., Wimmer, E. A. and Bucher, G. (2008). Divergent functions of orthodenticle, empty spiracles and buttonhead in early head patterning of the beetle *Tribolium castaneum* (Coleoptera). *Dev. Biol.* **317**, 600-613.
- Schröder, R., Beermann, A., Wittkopp, N. and Lutz, R. (2008). From development to biodiversity—*Tribolium castaneum*, an insect model organism for short germband development. *Dev. Genes Evol.* **218**, 119-126.
- Stelzer, E. H. K. and Lindek, S. (1994). Fundamental reduction of the observation volume in far-field light microscopy by detection orthogonal to the illumination axis: confocal theta microscopy. *Opt. Commun.* **111**, 536-547.
- Tomoyasu, Y. and Denell, R. E. (2004). Larval RNAi in *Tribolium* (Coleoptera) for analyzing adult development. *Dev. Genes Evol.* **214**, 575-578.
- Tomoyasu, Y., Miller, S. C., Tomita, S., Schoppmeier, M., Grossmann, D. and Bucher, G. (2008). Exploring systemic RNA interference in insects: a genome-wide survey for RNAi genes in *Tribolium*. *Genome Biol.* **9**, R10.
- van der Zee, M., Berns, N. and Roth, S. (2005). Distinct functions of the *Tribolium* zerknüllt genes in serosa specification and dorsal closure. *Curr. Biol.* **15**, 624-636.

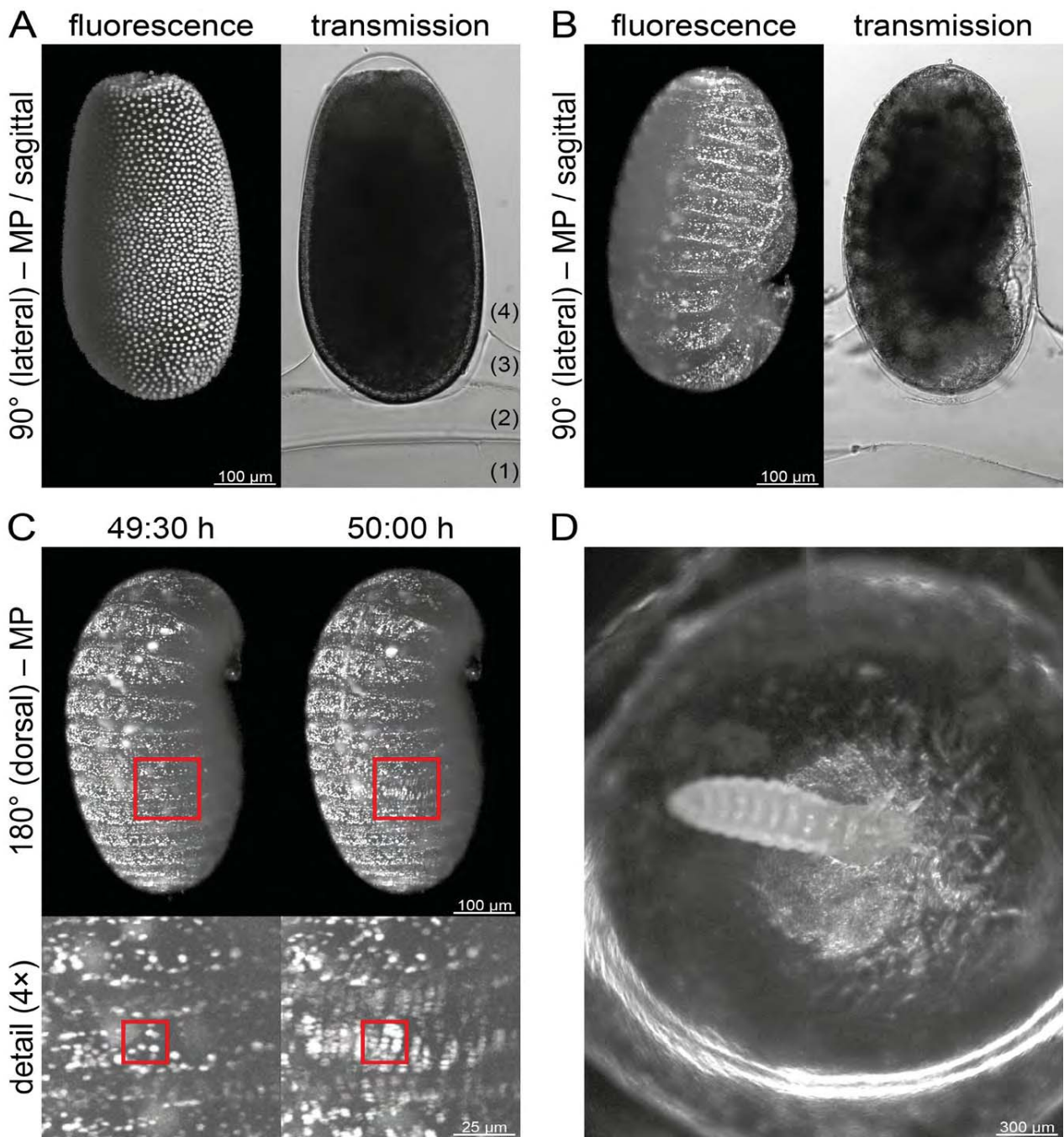


Fig. S1. Methods. (A) Embryo at the beginning of the imaging process, illustrating the sample preparation method. Left the fluorescence image, right the corresponding transmission light image. Upon insertion into the LSFM, embryos were at the stage of the uniform blastoderm. The anterior pole is at the bottom. In the transmission light image, (1) marks the tip of the agarose hemisphere, (2) marks the agarose film that was created by dipping the hemisphere into liquid agarose and that functions as glue, (3) marks the agarose layer that results from adding 2 μl of agarose for additional stability and (4) marks the buffer. Please note that these images are shown with the anterior side of the embryo to the bottom. (B) Embryo at the end of the imaging process when regular muscular movement sets in, after it has spent 50:00 h inside the LSFM under constant imaging. Left the fluorescence image, right the corresponding transmission light image. Please note that these images are shown with the anterior side of the embryo to the bottom. (C) Detection of the onset of regular muscular movement. Imaging at 49:30 h and 50:00 h. The rectangle indicates from where the detail (4x) image was taken. We define the onset of regular muscular movement as the moment when multiple instances of blurring during one recording can be detected. At 49:30 h, the embryo did not move. We marked a group of five nuclei on an abdominal segment. At 50:00 h, we detected those five nuclei twice due to artefactual motion blur resulting from muscular movement. (D) Hatched *Tribolium* larva after long-term imaging. View from the top on the dried-out agarose half sphere. Since the embryo is mounted with the anterior pole at the bottom, the larva stays attached with the anterior part to the agarose hemisphere after hatching. The larvae could be removed without injury from the agarose with a small paint brush. Image taken with a SteREO Discovery.V8 microscope (Carl Zeiss). MP, maximum projection with image processing.

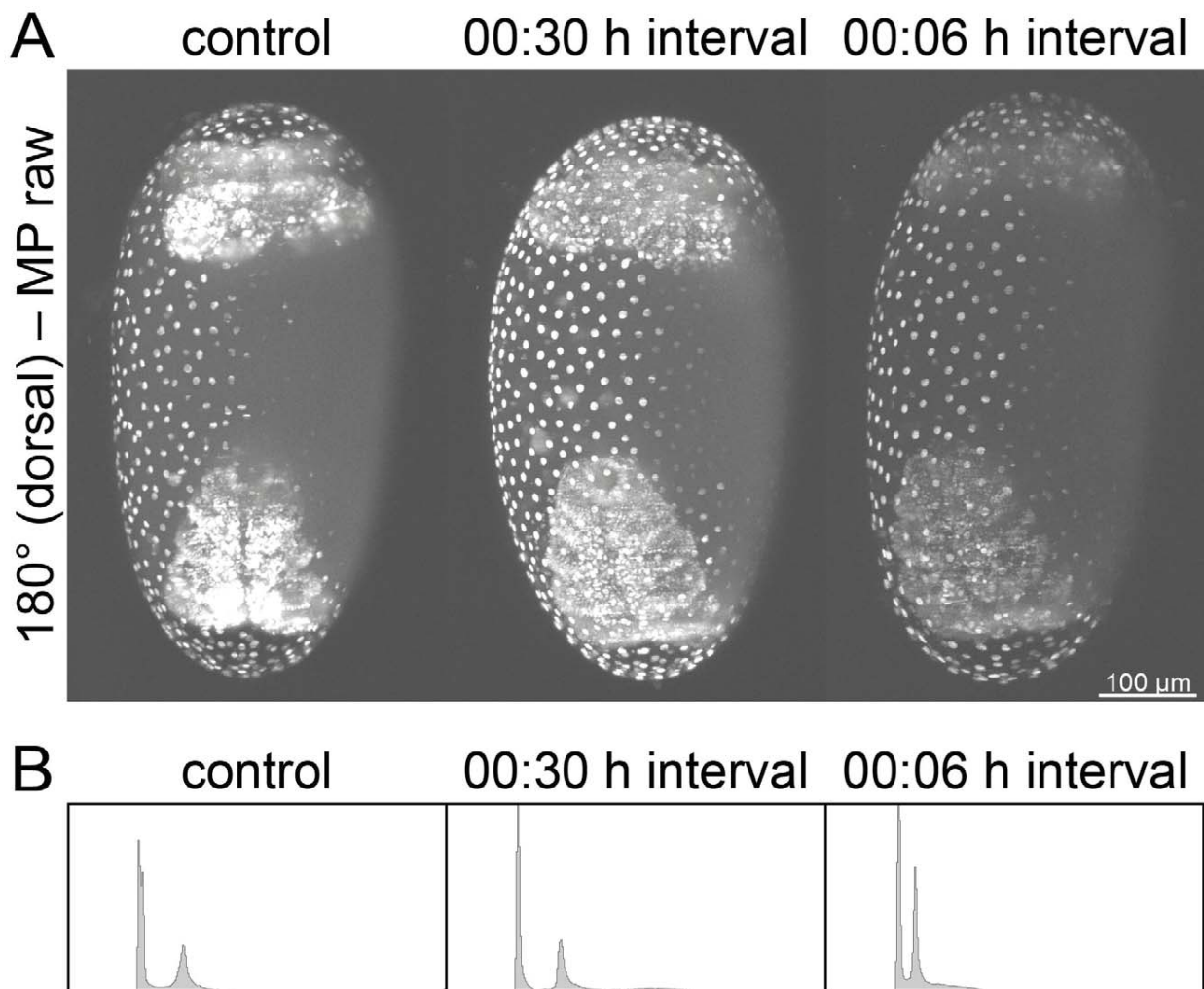


Fig. S2. Photo bleaching. (A) Photo bleaching of the *Tribolium* EFA-nGFP line in LSFM. We compared the signals obtained from an embryo that was imaged with a 00:30 h interval (32 previous time points) and an embryo that was imaged with a 00:06 h interval (158 previous time points) after 16:00 h of constant imaging with a control embryo that was recorded for the first time. The signal obtained from the embryo with the 00:30 h interval appeared to be close to the control while the signal from the embryo with the 00:06 h interval showed a reduction in the signal intensity, which we interpret as photo bleaching. Images shown here are raw data with an equal brightness adjustment for visualization. **(B) Histograms of images in Supplemental Figure 2A.** The histograms consist mainly of a background peak on the left and an object peak with higher intensities on the right. While the histogram of the embryo with the 00:30 h interval is similar to the one of the control embryo, the histogram of the embryo with the 00:06 h interval differs slightly. The object peak is closer to the background peak, higher but narrower compared to the control. MP, maximum projection with image processing.

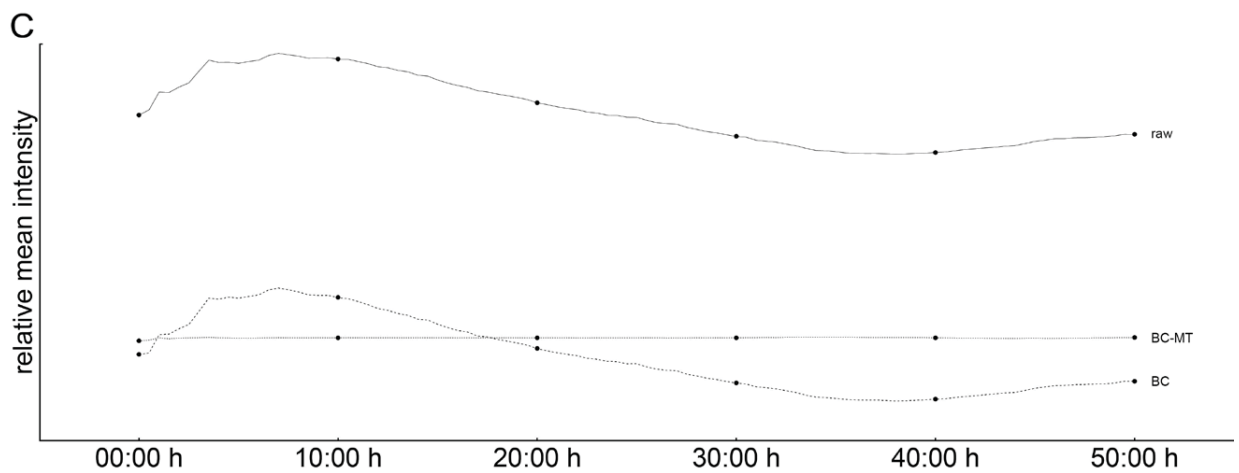
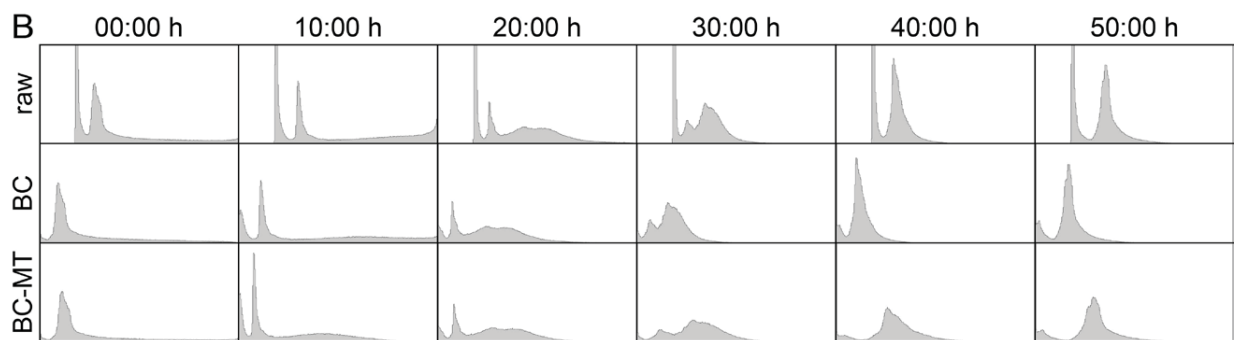
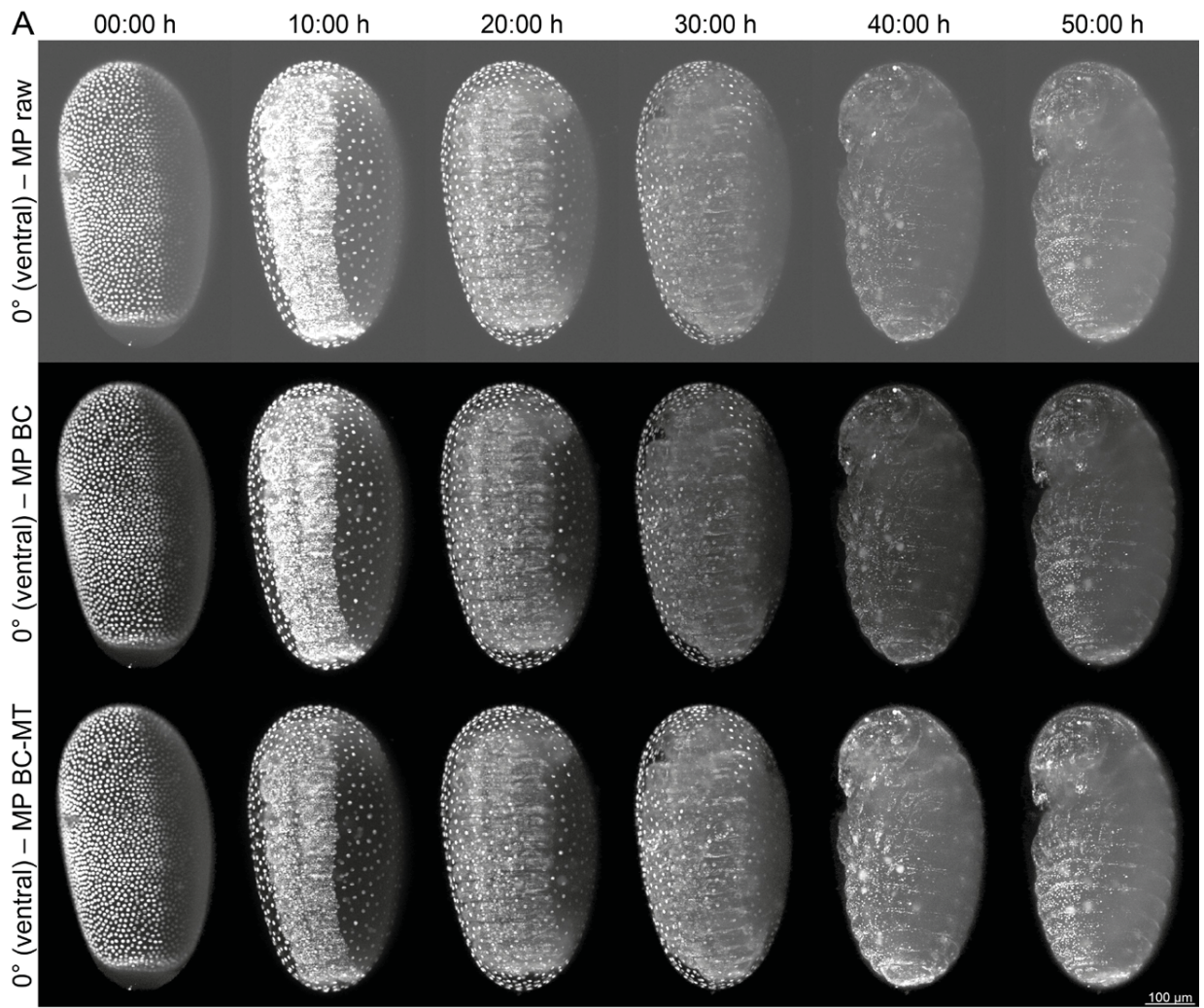


Fig. S3. Image Processing. (A) **Background Correction and Mean Transform in 0° (ventral) views.** The raw images show a background. After background correction (BC), the brightness of all images is reduced. The background is set to zero, while the brightness of the object is reduced by the average background. Background correction and mean transform (BC-MT) adjust the brightness. (B) **Histograms of the eighteen images shown in supplementary material Figure S3A.** The raw image histograms consist mainly of a background peak on the left and an object peak with higher intensities on the right. After BC, the background peak is eliminated and the histogram shifts to the left. After BC-MT, the individual histograms either (i) appear almost identical (for example at 00:00 h), since the values are already close to the mean value, (ii) are compressed (for example at 10:00 h) or (iii) are stretched (for example at 40:00 h). (C) **Relative mean intensity curves over the whole 0° (ventral) series.** The black dots indicate the eighteen images from Supplemental Figure 3A. If the raw data is compared with the data after BC, a consistent mean intensity drop occurs. If the data after BC is compared with the data after BC-MT, equalization can be observed. MP, maximum projection with image processing.



Movie 1. *Tribolium* embryogenesis in four orientations from 00:00 h to 50:00 h with an interval of 00:30 h between the time points. The movie starts with the rearrangement of the blastoderm and ends when regular muscular movement sets in, showing four embryogenetic events that are considered fundamental through the insect class – gastrulation, germband elongation, germband retraction and dorsal closure. Frame rate is 5 frames per second. MP, maximum projection with image processing.



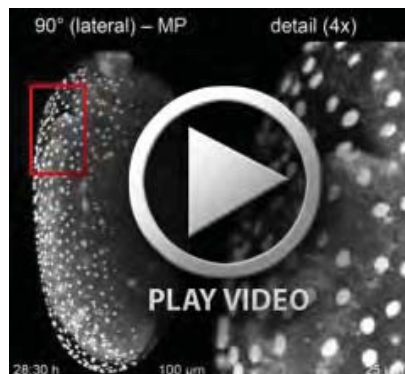
Movie 2. *Tribolium* optical sectioning in the 0° (ventral) orientation at three time points during dorsal closure from -26.0 μm to 309.4 μm with a spacing of 2.58 μm between the single planes. The red bar in the 90° (lateral) maximum projection indicates where the currently shown 0° (ventral) single plane is located. The first single plane with moderate signal was defined as 0 μm. Frame rate is 10 frames per second. MP, maximum projection with image processing; SP, single plane.



Movie 3. *Tribolium* morphogenesis shown as maximum projection in comparison to volume rendering in the 0° (ventral) orientation from 00:00 h to 50:00 h with an interval of 00:30 h between the time points. The movie starts with the rearrangement of the blastoderm and ends when regular muscular movement sets in. Volume rendering visualizes certain structures more efficiently, for example median groove folding during gastrulation or embryonic leg development. Frame rate is 5 frames per second. MP, maximum projection with image processing; AV, Amira-based volume rendering.



Movie 4. Serosa window closure and serosa scar formation during *Tribolium* gastrulation in two orientations from 00:00 h to 06:00 h with an interval of 00:06 h between the time points. After serosa window closure, the germband rotated slightly around the anterior-posterior axis. This rotation revealed a cell cluster that was left behind on the serosa after serosa window closure, the serosa scar, which is marked by arrows. Frame rate is 5 frames per second. MP = maximum projection with image processing.



Movie 5. Serosa window opening at the serosa scar during *Tribolium* dorsal closure in the 90° (lateral) orientation from 28:30 h to 24:30 h with an interval of 00:06 h between the time points. This movie is a sequel to Movie 4, where the serosa scar, which is highlighted inside the box, is shown in more detail. Shortly before dorsal closure, the serosa scar is pulled apart in a circular fashion. The pulling redirects dorsally, which leads to an elimination of the space between the serosa and the germband. This is followed by the migration of the serosa over the anterior pole. Frame rate is 5 frames per second. MP, maximum projection with image processing.

Table S1. Metadata and parameters for the three long-term imaging datasets.

Dataset (DS)	DS0001	DS0002	DS0003
Species	<i>Tribolium castaneum</i> (Herbst) Vermillion White (Coleoptera – Tenebrionidae)		
Line	EFA-nGFP transgenic line (Sarrazin et al., 2012)		
Line Genotype	Unknown		
Stock	~300 adults, not older than 4 month		
Stock Medium	full grain wheat flour (#113061006, Demeter, Darmstadt, Germany) supplemented with 5% (w/w) inactive dry yeast (#62-106, Flystuff, San Diego, CA, USA)		
Stock Conditions	12:00 h light / 12:00 h darkness at 25°C and 70% relative humidity (DR-36VL, Percival Scientific, Perry, IA, USA)		
Egg-Laying Period	01:00 h at 25°C and 70% relative humidity exposed to light		
Pre-imaging incubation	16:00 h at 25°C and 70% relative humidity in darkness		
Dechoriation	~30 seconds in 10% (v/v) sodium hypochlorite (#425044-250ML, Sigma Adlrlich, Taufkirchen, Germany) in PBS pH 7.4 (#10010-023, Gibco Life Technologies GmbH, Darmstadt, Germany)		
Mounting Agarose	1% (w/v) low melt agarose (#6351.2, Carl Roth, Karlsruhe, Germany) in PBS pH 7.4 (#10010-023, Gibco Life Technologies GmbH, Darmstadt, Germany)		
Imaging Buffer	PBS pH 7.4 at 35°C (#10010-023, Gibco Life Technologies GmbH, Darmstadt, Germany)		
LSFM Type	mDSLM based on DSLM (Keller and Stelzer 2010)		
Laser Lines	488 nm diode laser (PhoxX 488-60, Omicron Laserprodukte GmbH, Rodgau-Dudenhofen, Germany)		
Excitation Objective	2.5x NA 0.075 EC Plan Neofluar objective (440310-9903-000, Carl Zeiss, Göttingen, Germany)		
Emission Objective	10x NA 0.3 W N-Achroplan objective (420947-9900-000, Carl Zeiss, Göttingen, Germany)		
Emission Filters	525/50 single-band bandpass filter (FF03-525/50- 25, Semrock/AHF Analysentechnik AG, Tübingen, Germany)		
Camera	High-resolution CCD (Clara, Andor, Belfast, United Kingdom)		
Dataset File Type	TIF 16 bit greyscale (single planes are deposited as multi-plane TIF-files, indicated as SP_ZS_ in the file name)		
Dataset Size	338 Gigabyte	1413 Gigabyte	1454 Gigabyte
Photo Bleaching	low	moderate	moderate
Retrieval	survived, developed to healthy adult, produced fertile progeny	survived, developed to healthy adult, produced fertile progeny	survived, developed to healthy adult, produced fertile progeny
Figures	Figure 1; Figure 2D, E, and F	Figure 3	-
Supplementary Material Figures	Figure S1B and C; Figure S2A (central image); Figure S3A	Figure S1D	Figure S2A (right image)
Supplementary Material Movies	Movie 1; Movie 3	Movie 4; Movie 5	-
Comment	median development time	-	slight movement during imaging
Directions (DR)	4 (DR0001-DR0004)	4 (DR0001-DR0004)	4 (DR0001-DR0004)
DR Orientations	0°, 90°, 180°, 270°	0°, 90°, 180°, 270°	0°, 90°, 180°, 270°
Channels (CH)	1 (CH0001)	1 (CH0001)	1 (CH0001)
CH0001 Excitation Wavelength	488 nm	488 nm	488 nm
CH0001 Power	135 µW (close to the embryo)	135 µW (close to the embryo)	135 µW (close to the embryo)
CH0001 Exposure Time	50 ms	50 ms	50 ms
CH0001 Emission Filter	525/50 single-band bandpass filter	525/50 single-band bandpass filter	525/50 single-band bandpass filter
Single Planes (SP)	311 (SP0001-SP0311)	295 (SP0001-SP0295)	311 (SP0001-SP0295)
SP Spacing	2.58 µm	2.58 µm	2.58 µm
Z-Distance (SP×SP Spacing)	802.4 µm	761.1 µm	761.1 µm
X-Dimensions (XD)	1040 pixels (raw) 600 pixels (cropped)	1040 pixels (raw) 600 pixels (cropped)	1040 pixels (raw) 600 pixels (cropped)
XD Spacing	0.645 µm	0.645 µm	0.645 µm
X-Length (XD×XD Spacing)	670.8 µm (raw) 387.0 µm (cropped)	670.8 µm (raw) 387.0 µm (cropped)	670.8 µm (raw) 387.0 µm (cropped)
Y-Dimensions (YD)	1392 pixels (raw) 1000 pixels (cropped)	1392 pixels (raw) 1000 pixels (cropped)	1392 pixels (raw) 1000 pixels (cropped)
YD Spacing	0.645 µm	0.645 µm	0.645 µm
Y-Length (YD×YD Spacing)	897.8 µm (raw) 645.0 µm (cropped)	897.8 µm (raw) 645.0 µm (cropped)	897.8 µm (raw) 645.0 µm (cropped)

Please note that Figure 2A, B and C, Figure S1A, Figure S2A (left image) and Movie 2 derive from short-term imaging datasets. All datasets can be downloaded at www.physikalischebiologie.de/bugcube.

References

Keller, P. J. and Stelzer, E. H. K. (2010) 'Digital scanned laser light sheet fluorescence microscopy', *Cold Spring Harbor Protocols* 2010(5): pdb.top78.

Sarrazin, A. F., Peel, A. D. and Averof, M. (2012) 'A segmentation clock with two-segment periodicity in insects', *Science* 336(6079): 338-41.

A *Photorhabdus* Natural Product Inhibits Insect Juvenile Hormone Epoxide Hydrolase

**Friederike I. Nollmann, Antje K. Heinrich, Alexander O. Brachmann, Christophe Morisseau,
Krishnendu Mukherjee, Yngel M. Casanova-Torres, Frederic Strobl, David Kleinhans,
Sebastian Kinski, Katharina Schultz, Michael L. Beeton, Marcel Kaiser, Ya-Yun Chu,
Long Phan Ke, Aunchalee Thanwisai, Kenan A. J. Bozhüyik, Narisara Chantratita,
Friedrich Gçtz, Nick R. Waterfield, Andreas Vilcinskas, Ernst H.K. Stelzer,
Heidi Goodrich-Blair, Bruce D. Hammock & Helge B. Bode**

Simple urea compounds (“phurealipids”) have been identified from the entomopathogenic bacterium *Photorhabdus luminescens*, and their biosynthesis was elucidated. Very similar analogues of these compounds have been previously developed as inhibitors of juvenile hormone epoxide hydrolase (JHEH), a key enzyme in insect development and growth. Phurealipids also inhibit JHEH, and therefore phurealipids might contribute to bacterial virulence.

Published in February 2015

Research Article – *ChemBioChem* – Wiley

PubMed ID 25711603

A *Photorhabdus* Natural Product Inhibits Insect Juvenile Hormone Epoxide Hydrolase

Friederike I. Nollmann,^[a] Antje K. Heinrich,^[a] Alexander O. Brachmann,^[a] Christophe Morisseau,^[b] Krishnendu Mukherjee,^[c] Ángel M. Casanova-Torres,^[d] Frederic Strobl,^[e] David Kleinhans,^[e] Sebastian Kinski,^[a] Katharina Schultz,^[a] Michael L. Beeton,^[f] Marcel Kaiser,^[g] Ya-Yun Chu,^[h] Long Phan Ke,^[i] Aunchalee Thanwisai,^[j] Kenan A. J. Bozhüyük,^[a] Narisara Chantratita,^[k] Friedrich Götz,^[h] Nick R. Waterfield,^[l] Andreas Vilcinskas,^[c] Ernst H. K. Stelzer,^[e] Heidi Goodrich-Blair,^[d] Bruce D. Hammock,^[b] and Helge B. Bode^{*,[a, m]}

Simple urea compounds (“phurealipids”) have been identified from the entomopathogenic bacterium *Photorhabdus luminescens*, and their biosynthesis was elucidated. Very similar analogues of these compounds have been previously developed

as inhibitors of juvenile hormone epoxide hydrolase (JHEH), a key enzyme in insect development and growth. Phurealipids also inhibit JHEH, and therefore phurealipids might contribute to bacterial virulence.

Introduction

Natural products have been used in medicine since ancient times, and especially in the past 70 years they have served us

well as anti-infective, anticancer and other therapeutics.^[1,2] Despite their great benefit to human health it is mostly unknown

[a] F. I. Nollmann, A. K. Heinrich, A. O. Brachmann, S. Kinski, K. Schultz, K. A. J. Bozhüyük, Prof. Dr. H. B. Bode
Merck Stiftungsprofessur für Molekulare Biotechnologie
Fachbereich Biowissenschaften, Goethe Universität Frankfurt
60438 Frankfurt am Main (Germany)
E-mail: h.bode@bio.uni-frankfurt.de

[b] C. Morisseau, Prof. Dr. B. D. Hammock
Department of Entomology and Nematology &
UCD Comprehensive Cancer Center, University of California
One Shields Avenue, Davis, CA 95616 (USA)

[c] K. Mukherjee, Prof. Dr. A. Vilcinskas
Department Bioresources
Fraunhofer Institute for Molecular Biology and Applied Ecology (IME)
Winchesterstrasse 2, 35394 Giessen (Germany)

[d] Á. M. Casanova-Torres, Prof. Dr. H. Goodrich-Blair
Department of Bacteriology, University of Wisconsin–Madison
1550 Linden Dr., Madison, WI, 53706 (USA)

[e] F. Strobl, D. Kleinhans, Prof. Dr. E. H. K. Stelzer
Institute for Cell Biology and Neuroscience and
Buchmann Institute for Molecular Life Sciences (BMLS)
Goethe Universität Frankfurt
60438 Frankfurt am Main (Germany)

[f] M. L. Beeton
Cardiff School of Health Sciences
Cardiff Metropolitan University
Llandaff Campus, Western Avenue
Cardiff, CF5 2YB (UK)

[g] M. Kaiser
Swiss Tropical and Public Health Institute
Parasite Chemotherapy, University of Basel
Socinstrasse 57, 4051 Basel (Switzerland)

[h] Y.-Y. Chu, Prof. Dr. F. Götz
Microbial Genetics
Interfaculty Institute of Microbiology and Infection Medicine

University of Tübingen
Auf der Morgenstelle 28, 72076 Tübingen (Germany)

[i] L. Phan Ke
Vietnam National Museum of Nature
Vietnam Academy of Science and Technology
18 Hoang Quoc Viet, Cau Giay, Hanoi (Vietnam)

[j] A. Thanwisai
Department of Microbiology and Parasitology, Faculty of Medical Science
Naresuan University 99 Moo 9
Phitsanulok-Nakhon Sawan Road, Tha Pho Mueang Phitsanulok
65000 Phitsanulok (Thailand)

[k] N. Chantratita
Department of Microbiology and Immunology,
and Mahidol-Oxford Tropical Medicine Research Unit
Faculty of Tropical Medicine
Bangkok 10400 (Thailand)

[l] Prof. N. R. Waterfield
Division of Translational and Systems Medicine
Unit of Microbiology and Infection
Warwick Medical School, University of Warwick
Coventry, CV4 7AL (UK)

[m] Prof. Dr. H. B. Bode
Buchmann Institute for Molecular Life Sciences (BMLS)
Goethe Universität Frankfurt
60438 Frankfurt am Main (Germany)



Supporting information for this article is available on the WWW under <http://dx.doi.org/10.1002/cbic.201402650>.



© 2015 The Authors. Published by Wiley-VCH Verlag GmbH & Co. KGaA. This is an open access article under the terms of the Creative Commons Attribution License, which permits use, distribution and reproduction in any medium, provided the original work is properly cited.

why nature has developed these compounds and what their biological roles are,^[3,4] although examples of natural products acting as virulence factors,^[5] signalling molecules^[6] and antimicrobials^[7] are known. Entomopathogenic bacteria of the genus *Photorhabdus* live in symbiosis with nematodes of the genus *Heterorhabditis*, and together they are able to infect and kill insect larvae. Probably because of the complex bacterial interactions with the nematode host and the insect prey (communication within the bacterial community and between bacteria and nematodes, virulence against the insect prey, defence against food competitors) these bacteria are producers of several natural products.

Here, we describe urea lipid compounds, which we name "phurealipids" (*Photorhabdus* urea lipids) produced by the insect pathogen *Photorhabdus luminescens* to inhibit juvenile hormone epoxide hydrolase (JHEH), a key enzyme in insect development and growth; similar compounds have been developed chemically as insecticides.

Results and Discussion

A detailed HPLC/MS analysis of *P. luminescens* TTO1 showed the presence of four compounds (1–4) with m/z between 215 and 257 $[M+H]^+$ (Table S1 in the Supporting Information). The molecular formulae of 1, 3 and 4 as determined by HR-ESI-MS (Table S1) in addition to their mass fragmentation patterns indicated either a glycine amide or a urea-derived structure; the loss of 57 Da is characteristic for either a glycine or a methyl urea moiety (Figure 1). The structure and nature of the alkyl side chains were confirmed by labelling experiments (Table S1). Briefly, 1–3 were labelled with fully deuterated leucine, thereby indicating the presence of a leucine-derived iso-branched fatty acid; no labelling was observed with deuterated valine (indicative of *iso* even branched amines) or propionic acid (indicative of uneven linear amines) for any compound. A linear, even-numbered side chain similar to that from standard fatty-acid biosynthesis was assumed for 4. Compounds 1, 3 and 4 showed the expected labelling with deuterated L-[methyl-²H₃]-methionine exclusively at the polar moiety and not the side chain (where it could also occur following the biosynthesis of methylated fatty acids), thus confirming a methyl urea moiety (Table S1). This was subsequently proven by chemical synthesis of both glycine amide and the methyl urea derivative of 4 (identical t_R values for synthetic and natural 4). Compound 2 showed a neutral loss of 43 Da, corresponding to the desmethyl derivative of 1 (Figure 2).

Based on the structures of the identified phurealipids (Scheme 1), a biosynthetic pathway was postulated starting from different fatty-acid-derived aldehydes, which are subsequently transformed into the corresponding amines, carbamoylated and finally methylated (Scheme 2). Two carbamoyltransferases were identified in the genome of the producing strain. Gene disruption by plasmid integration (Figure S1 in the Supporting Information) into one of them, *plu2076* (here renamed *pliA* (phurealipid)), led to complete loss of phurealipid production. Disruption of the second carbamoyltransferase, *plu4565*, did not affect phurealipid biosynthesis, although

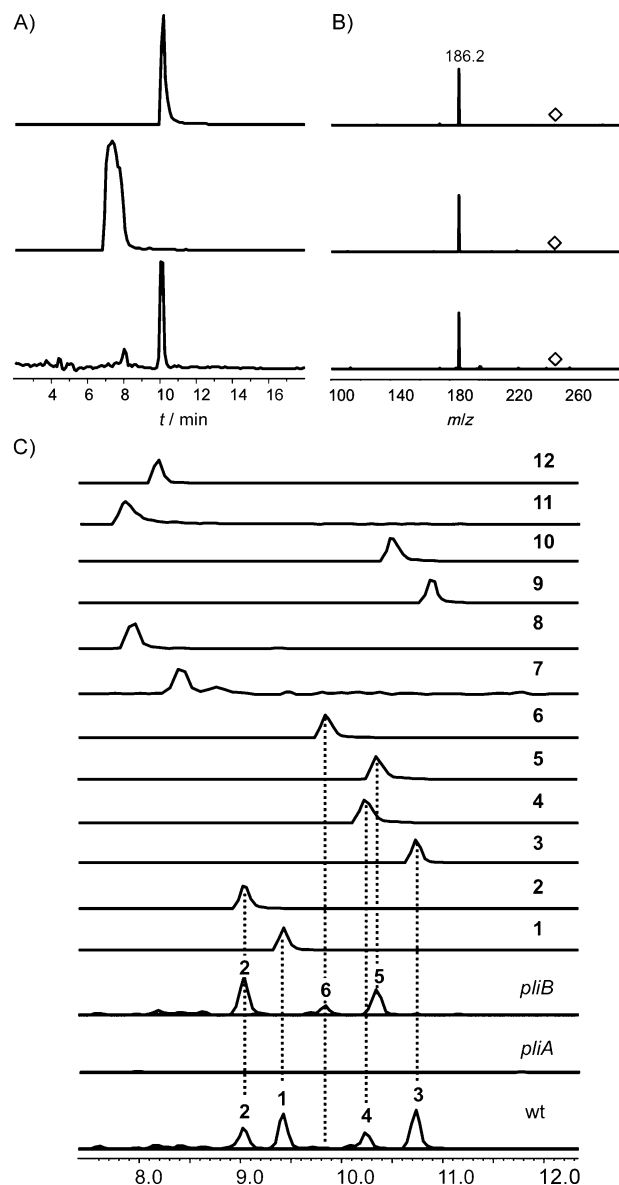


Figure 1. A) Extracted ion chromatograms (m/z 243.2), and B) MS/MS analysis of synthetic 4 (top), the corresponding glycine amide (middle) and natural 4 (bottom); diamond: mother ion. C) Extracted ion chromatograms of the natural phurealipids 1–6 from *P. luminescens* TTO1 (wt and *pliA* and *pliB* mutants) in comparison with the synthesised compounds: m/z 229.2 (1, 6 and 7), m/z 215.2 (2 and 8), m/z 257.2 (3 and 9), m/z 243.2 (4, 5 and 10), m/z 201.2 (11) and m/z 187.2 (12). The dotted lines highlight identical retention times between natural and synthetic compounds. Disruption of *pliA* led to total loss of phurealipid production.

these mutants were no longer able to produce a virulence factor that we termed "Photorhabdus clumping factor" or "PCF",^[8] the structure of which is currently unknown. Despite the fact that more than 15 methyltransferase homologues were identified in the *P. luminescens* genome, comparative genome analysis between different *Photorhabdus* and *Xenorhabdus* strains revealed only *plu2237* to be unique to *P. luminescens* (the only phurealipid producer with a sequenced genome).^[9] Subsequent gene disruption (Figure S1) of *plu2237* (which we renamed *pliB*) led to the biosynthesis of a different

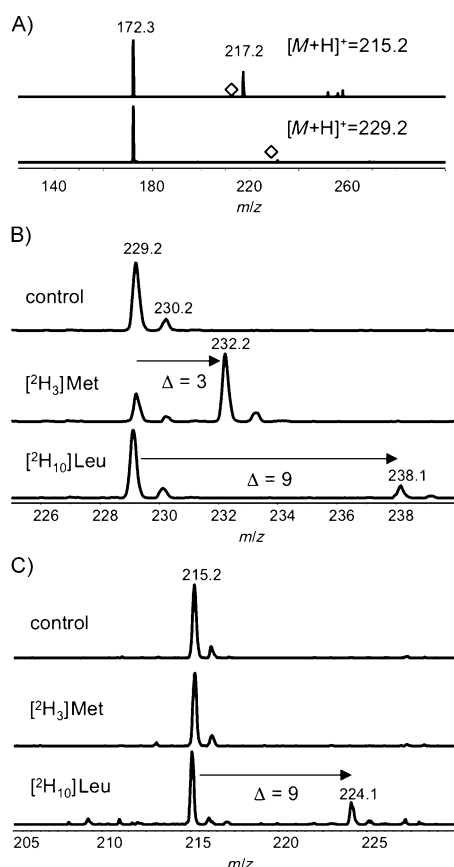
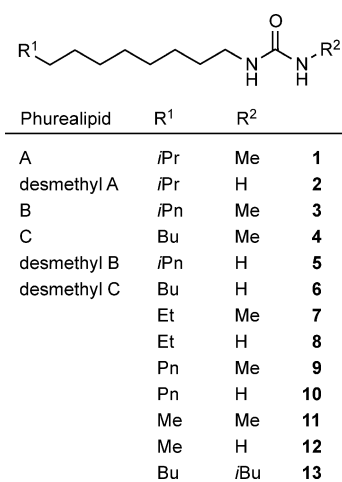
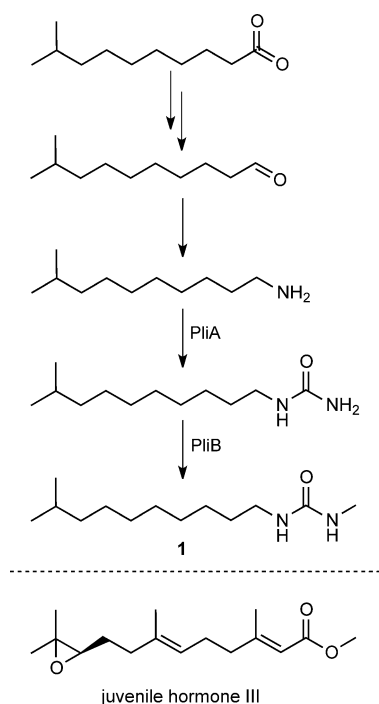


Figure 2. A) MS² data of **1** (bottom) and **2** (top). MS data of **1** and **C** **2** obtained from labelling experiments in strain TTO1 (control with no additives, addition of L-[methyl-²H₃]methionine and L-[2,3,3,4,4,5,5,6,6,6-²H₁₀]leucine (from top to bottom)).



Scheme 1. Natural phurealipids **1–6** and synthetic derivatives **7–13**.

phurealipid profile. Detailed MS and labelling experiments revealed the presence of desmethylphurealipids **B** (**5**) and **C** (**6**; Figure 1, Table S1), whose structures were confirmed by synthesis. A search for additional phurealipid-producing strains in our entomopathogenic bacteria strain collection^[10] based on HPLC/MS analysis of over 250 strains revealed **1** to be wide-

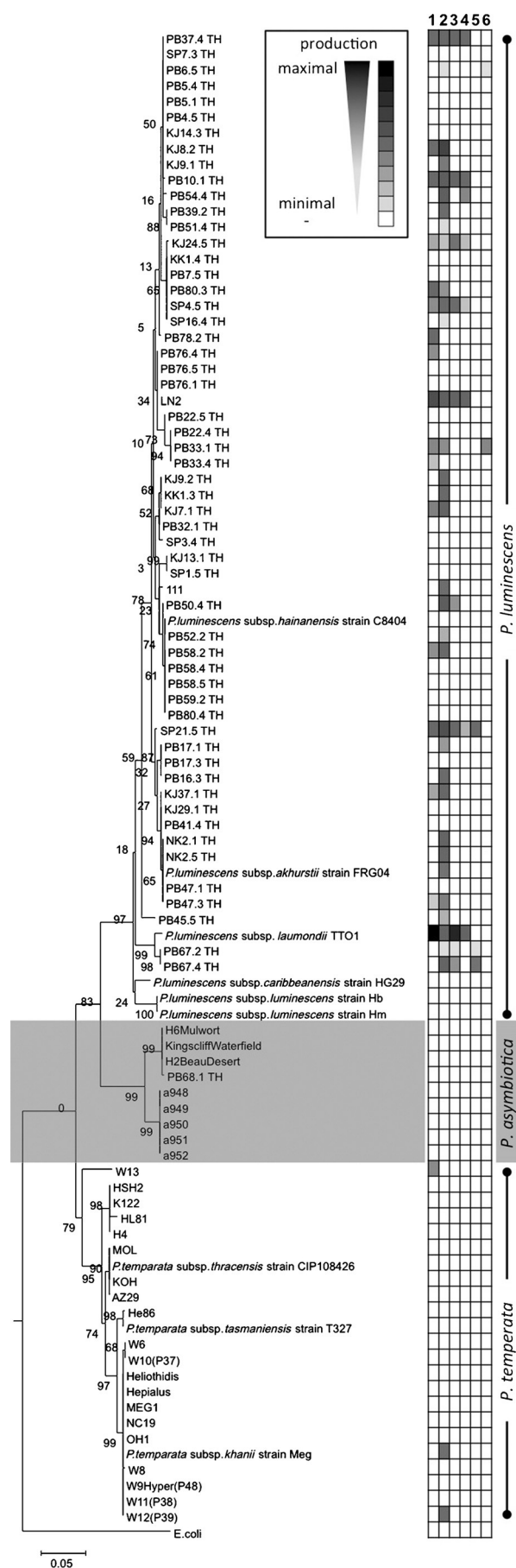


Scheme 2. Proposed biosynthesis of phurealipid A (**1**), and structure of JH III.

spread in *P. luminescens* strains (Figure 3, Figure S2) but very rare in *Photorhabdus asymbiotica* or *Photorhabdus temperata*, consistent with the fact that no *plu2076* homologue could be found in the genome of *P. asymbiotica*.^[11] However, three *Xenorhabdus* strains isolated in Vietnam and related to *Xenorhabdus ehlersii* DSM 16337 showed production of **1** (Figure S3).

In independent research, closely related synthetic compounds have been previously described as inhibitors of insect juvenile hormone epoxide hydrolase (JHEH).^[12–14] In conjunction with juvenile hormone esterase (JHE), JHEH is a key player in the degradation of juvenile hormone (JH), which regulates both growth and development of insect larvae and reproductive functions of adults,^[15] and is also produced by the plant *Cyperus iria* as a defence mechanism against insects.^[16] Importantly, *P. luminescens* phurealipids and the related synthetic insecticides are structurally similar to JH (Scheme 2), thus suggesting a possible mode of action. We tested all phurealipids against JHEH purified from caterpillars of the tobacco hornworm *Manduca sexta* and demonstrated that **1**, **3** and **4** showed IC₅₀ values of 6.5 ± 0.9, 30 ± 4, and 10.7 ± 1.2 μM, respectively. These are in a similar range to that observed for the known synthetic inhibitor **13** (Scheme 1, Table S2; IC₅₀ = 2.3 ± 0.6 μM) and is in agreement with comparable K_i values (1.80 ± 0.30 and 0.35 ± 0.04 μM for **1** and **13**, respectively; Figure S4). Although desmethylphurealipid **B** (**5**) showed weak activity against JHE (IC₅₀ = 25 ± 4 μM), no other derivatives showed activity (> 100 μM) against either JHE or JHEH (Table S2).

Upon infection of *Galleria mellonella* larvae, *P. luminescens* produced phurealipids at up to 200 μM (≈ 44 mg L⁻¹; Figure S5) as determined by HPLC/MS. This would be sufficient to inhibit JHEH and thus might lead to an increase in JH. JH accu-



mulation in *Drosophila melanogaster* inhibits the production of antimicrobial peptides (AMPs), thus indicating that JH acts as a humoral immuno-suppressor.^[17] Hence, manipulation of JH levels influences not only insect development but also the efficacy of the immune response. Taken together, these data suggest that phurealipids contribute to the overall virulence of *P. luminescens* by inhibiting JHEH activity and therefore limiting AMP production.

To test this hypothesis, we used quantitative reverse-transcriptase PCR to measure the RNA levels of certain AMP genes (lysozyme, gallerimycin, moricin and cecropin) in caterpillars of *M. sexta* and the greater waxmoth *G. mellonella* challenged with *Serratia entomophila* or *Salmonella enterica*, respectively, following injection of different urea lipid compounds (Figure S6). The known synthetic inhibitor 13 demonstrated the best activity (lower levels of AMP RNAs relative to the control). Of the natural compounds, desmethylphurealipid A (2) was the most active in this assay but showed no JHEH inhibitory activity in vitro, thus suggesting other or additional JHEH independent activities for phurealipids in vivo.

We also tested whether urea lipids predicted to lead to JH III accumulation by JHEH inhibition influence the embryonic development of the emerging insect model organism *Tribolium castaneum*. As methoprene was described^[18] as a JH III mimic used as insecticide, it was used as positive control for 13 (the most active urea compound inhibiting JHEH). All *T. castaneum* embryos treated with methoprene proceeded through gastrulation, germ band elongation and germ band retraction normally, but failed to internalise the remaining yolk sac during dorsal closure (Figure S7; Supporting Movie 1). The result was significant compared to the PBS and DMSO controls (Figure S7c), thus confirming the insecticidal effect of this compound.^[19,20] In contrast, embryos treated with 13 were able to proceed through dorsal closure normally (Figure S7, Supporting Movie 1), and the percentage of embryos successfully completing development did not differ significantly from those subjected to PBS and DMSO (Figure S7).

JH has been reported to influence gene expression in protozoan termite gut symbionts^[21] and to play a role in Ca^{2+} homeostasis,^[22] in addition to exerting epigenetic control of gene expression.^[23] Based on their structural resemblances, similar activities might exist for phurealipids. Indeed, the desmethyl urea lipids in particular exhibited very strong activity against *Leishmania donovani* and were in fact at least 10 times more active than the methylated derivatives (Table S2). *L. donovani*, the causative agent of leishmaniasis (kala-azar), is not known to employ any JH-like regulatory pathways, but the promising activity of such simple compounds will be studied in more

Figure 3. Phylogenetic tree based on a 646 bp region of *recA* (encoding the highly conserved RecA protein involved in DNA repair) for different *Photobacterium* strains (outgroup: *E. coli*).^[34] The tree was reconstructed by the maximum likelihood approach (ClustalW alignment). Jukes-Cantor (JC69) was used as substitution-model; bootstrap values are based on 1000 replicates. Right: relative production of phurealipids 1–6. All strains were analysed by HPLC/MS; mostly strains of *P. luminescens* produce phurealipids, as identified by retention time and MS/MS data.

detail in the future. Further bioactivity tests revealed neither antibacterial nor antifungal activity for any phurealipid, and although other urea derivatives are quorum quenching compounds in Gram-negative bacteria,^[24] no such activity was observed for phurealipids. In experimental infections of the caterpillar *M. sexta*, no difference in virulence was observed between the *pliA* insertion mutant and the parental wild-type strain. Nevertheless, because of the large redundancy of virulence factors in this bacterium it is likely that the contribution of the phurealipids to the overall virulence is masked. Precedence for this can be seen in the observation that strains lacking the highly potent Mcf1 toxin remain as virulent as the wild type,^[25] and disruption of rhabdopeptide biosynthesis in the related bacterium *Xenorhabdus nematophila* had only a slight effect on overall toxicity whereas the pure compounds showed insecticidal activity.^[26] Moreover, it has been proposed that the “stacking” of multiple virulence factors gives *P. luminescens* a selective advantage during typical suboptimal infection scenarios and in diverse hosts in nature.^[25]

It is interesting that *P. luminescens* produces a small library of phurealipids in similar amounts, as has been observed for other compound classes, such as rhabdopeptides, xentriptideptides and taxllalids.^[26–28] Because the nematode vector shows little insect host specificity,^[29] we propose that this might provide *P. luminescens* with the ability to inhibit diverse JHEHs from a range of insect orders. JHs differing in the presence of methyl or ethyl substituents, degree of saturation and epoxide moieties have been described from different insects, thus making the presence of slightly different JHEHs quite likely.^[30]

The phurealipids offer a rare example of a compound class originally developed by synthetic chemists to address a specific molecular target, but which had in fact already been “developed” by *P. luminescens* much earlier. We can draw parallels with the cultivation and use of antifungal-producing *Streptomyces* by leaf-cutting ants^[31,32] or bark beetles^[33] to protect their fungal gardens against pathogenic fungi, similar to humans using such compounds in antifungal therapy. These examples clearly highlight the value of organisms producing natural product, both as sources of molecules and as inspiration for much-needed novel bioactive compounds.

Acknowledgements

Work in the Bode laboratory was supported by an ERC starting grant under grant agreement no. 311477 and by the European Community's Seventh Framework Program (FP7/2007-2013) under grant agreement no. 602773, which also supported M.K. Isolation and screening of strains (L.P.K., A.T., N.C., N.R.W., H.B.B.) was partially supported by the European Community's Seventh Framework Programme (FP7/2007-2013) within the GameXP consortium (grant agreement no. 223328). K.M. and A.V. are grateful to the LOEWE-Zentrum “ZIB - Zentrum für Insektenbiotechnologie und Bioressourcen” for financial support. This work was partially supported by NIEHS grant no. ES02710 to C.M. and B.D.H. Work in the Goodrich-Blair lab was supported by funding from the

UW–Madison USDA Hatch Multi-state research formula fund WISO1582. Á.M.C.-T. was supported by NIH National Research Service Award T32 GM07215. L.P.K. is grateful to Vietnam's National Foundation for Science and Technology Development (NAFOSTED), the Ministry of Science and Technology (grant no. 106.06.16.09) and the DAAD (grant no. A/08/04969) who funded part of this work including a stay in the Bode lab. N.C. was supported by a Wellcome Trust Career Development award in Public Health and Tropical Medicine, UK (grant 087769/Z/08/Z). A.T. was supported by a scholarship under a PhD Sandwich Program of Commission on Higher Education, Ministry of Education of Thailand.

Keywords: biosynthesis · entomopathogenic bacteria · juvenile hormone epoxide hydrolase inhibitor · natural products · *Photorhabdus*

- [1] G. M. Cragg, D. J. Newman, *Biochim. Biophys. Acta Gen. Subj.* **2013**, *1830*, 3670–3695.
- [2] D. J. Newman, G. M. Cragg, *J. Nat. Prod.* **2012**, *75*, 311–335.
- [3] R. D. Firn, C. G. Jones, *Nat. Prod. Rep.* **2003**, *20*, 382–391.
- [4] J. Davies, G. B. Spiegelman, G. Yim, *Curr. Opin. Microbiol.* **2006**, *9*, 445–453.
- [5] H. Hong, C. Demangel, S. J. Pidot, P. F. Leadlay, T. Stinear, *Nat. Prod. Rep.* **2008**, *25*, 447–454.
- [6] C. M. Waters, B. L. Bassler, *Annu. Rev. Cell Dev. Biol.* **2005**, *21*, 319–346.
- [7] D. Reimer, K. M. Pos, M. Thines, P. Grün, H. B. Bode, *Nat. Chem. Biol.* **2011**, *7*, 888–890.
- [8] A. O. Brachmann, S. Brameyer, D. Kresovic, I. Hitkova, Y. Kopp, C. Manske, K. Schubert, H. B. Bode, R. Heermann, *Nat. Chem. Biol.* **2013**, *9*, 573–578.
- [9] E. Duchaud, C. Rusniok, L. Frangeul, C. Buchrieser, A. Givaudan, S. Taourit, S. Bocs, C. Boursaux-Eude, M. Chandler, J.-F. Charles, E. Dassa, R. Deroose, S. Derzelle, G. Freyssinet, S. Gaudriault, C. Médigue, A. Lanois, K. Powell, P. Siguier, R. Vincent, et al., *Nat. Biotechnol.* **2003**, *21*, 1307–1313.
- [10] A. Thanwisai, S. Tandhavanant, N. Saiprom, N. R. Waterfield, P. Ke Long, H. B. Bode, S. J. Peacock, N. Chantratita, *PLoS One* **2012**, *7*, e43835.
- [11] P. Wilkinson, N. R. Waterfield, L. Crossman, C. Corton, M. Sanchez-Contreras, I. Vlisidou, A. Barron, A. Bignell, L. Clark, D. Ormond, M. Mayho, N. Bason, F. Smith, M. Simmonds, C. Churcher, D. Harris, Nicholas R Thompson, M. Quail, J. Parkhill, R. H. French-Constant, *BMC Genomics* **2009**, *10*, 302.
- [12] C. Morisseau, B. D. Hammock, *Annu. Rev. Pharmacol. Toxicol.* **2005**, *45*, 311–333.
- [13] T. F. Severson, M. H. Goodrow, C. Morisseau, D. L. Dowdy, B. D. Hammock, *Insect Biochem. Mol. Biol.* **2002**, *32*, 1741–1756.
- [14] M. Garriga, J. Caballero, *Chemosphere* **2011**, *82*, 1604–1613.
- [15] M. Jindra, S. R. Palli, L. M. Riddiford, *Annu. Rev. Entomol.* **2013**, *58*, 181–204.
- [16] Y. C. Toong, D. A. Schooley, F. C. Baker, *Nature* **1988**, *333*, 170–171.
- [17] T. Flatt, A. Heyland, F. Rus, E. Porpiglia, C. Sherlock, R. Yamamoto, A. Garbuzov, S. R. Palli, M. Tatar, N. Silverman, *J. Exp. Biol.* **2008**, *211*, 2712–2724.
- [18] M. Jindra, S. R. Palli, L. M. Riddiford, *Annu. Rev. Entomol.* **2013**, *58*, 181–204.
- [19] F. H. Arthur, E. A. Fontenot, *J. Insect Sci.* **2012**, *12*, 95–111.
- [20] L. K. W. Wijayaratne, P. G. Fields, F. H. Arthur, *Pest Manage. Sci.* **2012**, *68*, 217–224.
- [21] R. Sen, R. Raychoudhury, Y. Cai, Y. Sun, V.-U. Lietze, D. G. Boucias, M. E. Scharf, *BMC Genomics* **2013**, *14*, 491.
- [22] A. De Loof, W. De Haes, T. Janssen, L. Schoofs, *Gen. Comp. Endocrinol.* **2014**, *199*, 70–85.
- [23] A. De Loof, B. Boerjan, U. R. Ernst, L. Schoofs, *Gen. Comp. Endocrinol.* **2013**, *188*, 35–45.

- [24] Y.-Y. Chu, M. Nega, M. Wölfle, L. Plener, S. Grond, K. Jung, F. Götz, *PLoS Pathog.* **2013**, *9*, e1003654.
- [25] R. H. ffrench-Constant, A. Dowling, N. R. Waterfield, *Toxicon* **2007**, *49*, 436–451.
- [26] D. Reimer, K. N. Cowles, A. Proschak, F. I. Nollmann, A. J. Dowling, M. Kaiser, R. ffrench-Constant, H. Goodrich-Blair, H. B. Bode, *ChemBioChem* **2013**, *14*, 1991–1997.
- [27] Q. Zhou, A. Dowling, H. Heide, J. Wöhnert, U. Brandt, J. Baum, R. ffrench-Constant, H. B. Bode, *J. Nat. Prod.* **2012**, *75*, 1717–1722.
- [28] M. Kronenwerth, K. A. J. Bozhüyük, A. S. Kahnt, D. Steinhilber, S. Gaudriault, M. Kaiser, H. B. Bode, *Chem. Eur. J.* **2014**, *20*, 17478–17487.
- [29] M. M. A. de Doucet, M. A. Bertolotti, A. L. Giayetto, M. B. Miranda, *J. Invertebr. Pathol.* **1999**, *73*, 237–242.
- [30] W. Goodman, M. Cusson in *Insect Endocrinology* (Ed.: L. I. Gilbert), Elsevier, China, **2012**, pp. 310–365.
- [31] S. Haeder, R. Wirth, H. Herz, D. Spiteller, *Proc. Natl. Acad. Sci. USA* **2009**, *106*, 4742–4746.
- [32] D.-C. Oh, M. Poulsen, C. R. Currie, J. Clardy, *Nat. Chem. Biol.* **2009**, *5*, 391–393.
- [33] J. J. Scott, D.-C. Oh, M. C. Yuceer, K. D. Klepzig, J. Clardy, C. R. Currie, *Science* **2008**, *322*, 63–63.
- [34] F. I. Nollmann, C. Dauth, G. Mulley, C. Kegler, M. Kaiser, N. R. Waterfield, H. B. Bode, *ChemBioChem* **2015**, *16*, 205–208.

Received: November 7, 2014

Published online on February 25, 2015

Supporting Information

A *Photorhabdus* Natural Product Inhibits Insect Juvenile Hormone Epoxide Hydrolase

Friederike I. Nollmann,^[a] Antje K. Heinrich,^[a] Alexander O. Brachmann,^[a]
Christophe Morisseau,^[b] Krishnendu Mukherjee,^[c] Ángel M. Casanova-Torres,^[d]
Frederic Strobl,^[e] David Kleinhans,^[e] Sebastian Kinski,^[a] Katharina Schultz,^[a]
Michael L. Beeton,^[f] Marcel Kaiser,^[g] Ya-Yun Chu,^[h] Long Phan Ke,^[i] Aunchalee Thanwisai,^[j]
Kenan A. J. Bozhüyük,^[a] Narisara Chantratita,^[k] Friedrich Götz,^[h] Nick R. Waterfield,^[l]
Andreas Vilcinskas,^[c] Ernst H. K. Stelzer,^[e] Heidi Goodrich-Blair,^[d] Bruce D. Hammock,^[b] and
Helge B. Bode^{*[a, m]}

cbic_201402650_sm_miscellaneous_information.pdf
cbic_201402650_sm_miscellaneous_information.avi

Supplementary Material

Methods

General. Cultivation of *Photorhabdus luminescens* TT01 and its plasmid integration mutants plu2237::cat and plu2076::cat was performed as described previously ^[1-3] with the appropriate antibiotics in the following concentrations: ampicillin 100 µg/ml, chloramphenicol 20 µg/ml, rifampicin 50 µg/ml. Natural product analysis by HPLC-MS/MS and HRESI-MS/MS ^[4-6], natural product quantification in LB and *Galleria mellonella* ^[3], and inhibition of JHEH ^[7] and JHE ^[8,9] from *Manduca sexta* were performed as described previously. Bioactivity against *Escherichia coli*, *Micrococcus luteus*, *Bacillus subtilis*, *Saccharomyces cerevisiae* was performed as described ^[10]. Quorum quenching assays have also been described previously ^[11]. Phylogenetic analysis of *Photorhabdus* was performed as described ^[12] and all strains listed in Figure 4 were cultivated and analyzed by HPLC/MS as described previously ^[2,3,6]. Feeding experiments ^[3] were performed as follows: L-[2,3,4,4,4,5,5,5-²H₈]valine, L-[2,3,3,4,5,5,5,5',5',5'-²H₁₀]leucine, L-[methyl-²H₃]methionine and [2,2,3,3,3-²H₅]propionic acid were fed to LB medium with Amberlite XAD-16. 5 mL of LB media with 2% XAD-16 in 50 mL Erlenmeyer flasks were inoculated to an OD₆₀₀ of 0.1 with a preculture in the same medium without XAD16. Possible precursors were fed at 0, 24 and 48 h after inoculation to a final concentration of 2 mM. Cultures were harvested after 72 h of cultivation at 30 °C and 180 rpm. To obtain the crude extracts the XAD beads were separated from the supernatant by decanting and for 1 h extracted with 5 ml MeOH. The metabolites in the crude extracts were identified using HPLC/MS analysis.

Analysis of phurealipid production. *Galleria mellonella* larvae were used for the determination of the phurealipid production in insects as described previously ^[3]. The experiment was performed in duplicates and covered a time period of 14 days, samples were taken after 6h, 12h, 24h, 36h, 48h, 3d, 4d, 7d, 10d, and 14d. Each sample comprised ten

larvae that were infected with a suspension of *P. luminescens* TT01 cells. For this, an overnight culture of TT01 was washed with LB and adjusted to an optical density of OD₆₀₀ 1.0 and each larva was injected by syringe in the midabdominal proleg with 5 µl of cell suspension. Aseptic LB medium was used as a control. All infected larvae were dead after 48 hours, while 95% of the control group survived. Each sample was snap-frozen in liquid nitrogen. The frozen larvae were ground to a crude powder using a pestle and mortar. The powder was extracted for 1 hour with 50 mL of a methanol/acetone (1:1) solvent mixture, filtered and evaporated. The crude extract was re-dissolved in 3 mL of methanol and diluted 1:10 before HPLC-MS analysis. Production kinetics were analysed using triplicates in LB broth. *P. luminescens* TT01 was cultivated in 1 L Erlenmeyer flasks containing 100 mL LB using the described cultivation conditions. For each time point 4 mL of culture broth was extracted with the same solvent mixture, filtered and the solvents removed under reduced pressure. The crude extract was then dissolved in 1 mL methanol and without further dilution submitted to HPLC-MS analysis.

Construction of the carbamoyl transferase and the methyl transferase mutants.

Carbamoyl transferase and methyl transferases encoded in the genome of *P. luminescens* TT01 ^[13] were identified using their homology to known enzymes from *E. coli* and by comparison between all *Xenorhabdus* ^[14,15] and *Photorhabdus* ^[13,16] genomes currently available. The genes *plu2076* and *plu2237* were only present in *P. luminescens* and encode a carbamoyl transferase and a methyl transferase, respectively. They were disrupted by plasmid integration as described previously. Briefly, the suicide vector pDS132 ^[17] or pCKcipB (a pDS132 derivative with an additional *Bgl*III recognition site) both carrying a chloramphenicol resistance gene (*cat*) were used. An internal fragment of *plu2237* (*pliB*) was amplified with the following PCR primers: KO_plu2237_PstI_fw (5'-ATATCTGCAGCATATGGAATTTCCACAAGAGG-3') containing a *Pst*I restriction site

(bold) and KO_plu2237_BamHI_rev (5'-ATATGGATCCGAATCTTTGGTTATAATCAAGAGC-3') containing a *Bam*HI restriction side (bold), yielding a product of 534 bp. This amplicon was subcloned into vector pJET1.2 (Thermo Scientific, Fermentas) and subsequently digested with the restriction endonucleases *Pst*I and *Bam*HI (both Fermentas). This restriction fragment was ligated into pCKcipB linearised with *Pst*I and *Bgl*II. The resulting plasmid pDS2237KO was transformed by electroporation into *E. coli* S17-1 λ pir (Tpr Smr *recA thi hsdR* RP4-2-Tc::Mu-Km::Tn7, λ pir phage lysogen). Subsequently this construct was conjugated into a rifampicin-resistant TT01 strain as previously described ^[1].

The plasmid donor strain and the acceptor strain were grown to an OD₆₀₀ of 0.6-0.8 and spotted together (in a ration of 1:3) onto a LB agar plate without any selection marker. Cells were incubated at 37°C for 3 h and another 21 h at 30°C. The cell lawn was harvested using an inoculation loop and resuspended in 2 ml LB medium. For selection of TT01 colonies with acquired chloramphenicol resistance different volumes of the cell suspension (50 μ l, 100 μ l and 200 μ l) were plated on LB agar plates with rifampicin and chloramphenicol. The genotype of the chloramphenicol resistant strain TT01-2237::cat was confirmed by PCR using a plasmid-specific pair of primers pDS132fw (5'-GATCGATCCTCTAGAGTCGACCT-3') and pDS132rv (5'-ACATGTGGAATTGTGAGCGG-3') in combination with a genome-specific pair of primers V_KO_plu2237_fw (5'-GAGCGATTCTGGCTAAATCG-3') and V_KO_plu2237_rev (5'-TTGATGTTTACGGCGATGG-3').

For the generation of the *plu2076* (*pliA*) insertion mutant in *P. luminescens* the same approach was applied: An internal fragment of *plu2076* was amplified with the primers KOplu2076SacI (5'-AATGCTGAGCTCACGTTTTCTGCGAGAGAATAATCCA-3') containing a *Sac*I restriction side (bold) and KOplu2076PaeI (5'-ATATTCGCATGCCATTATCAAATGCTGGCGGTAAC-3') containing a *Pae*I restriction side (bold) which yielded a product of 740 bp that was then subcloned into vector pJET1.2

and subsequently cloned into pDS132 via the *SacI* and *PaeI* restriction sites. The resulting plasmid pDS2076KO was introduced into *E. coli* S17-1 λ pir by electroporation and the *P. luminescens* plasmid insertion mutant TT01-2076::cat was generated as described. The correct plasmid insertion was confirmed by PCR using again the plasmid-specific primers pDS132fw and pDS132rv as well as genomic-specific primers V2076_Fw (5'-TTCGCTAGAAGCACCGCATT-3') and V2076_Rv (5'-TCAGCAAAGTTGCGCAAAGC-3').

Comparison of *in vivo* virulence of *P. luminescens* WT and *pliA* mutant. *P. luminescens* wt and *pliA* mutant were grown overnight in LB broth with shaking at 28°C in the dark. Subcultures were grown to mid exponential phase ($OD_{600} = 0.2-0.4$). Dilutions of bacteria were then injected into first day 5th instar *Manduca sexta* larvae, which were reared as previously described [18]. Briefly, larvae were maintained individually at 25°C under a photoperiod of 17 hours light: 7 hours dark and fed on an artificial diet based on wheat germ. Unless otherwise stated, larvae 1 day after ecdysis to the 5th instar were used for all experiments.

For the two strains approximately 100, 1000 and 10000 viable cells (confirmed by overnight plating) were injected into a cohort of 12 animals each, which were then monitored for mortality (movement and turgidity) by regular physical stimulus over 3 days and again at 7 days.

Determination of antimicrobial peptide transcript levels in *Galleria mellonella* and *Manduca sexta*. Stock solutions of the different phurealipids were prepared by dissolving the compounds separately in 100% ethanol. For injection, 1:100 dilutions of individual compound were used for injection. The concentrations injected were as follows: **1** (46 μ g/ml), **2** (28 μ g/ml), **3** (28 μ g/ml), **4** (31 μ g/ml), **5** (28 μ g/ml), **6** (28 μ g/ml), **7** (22 μ g/ml), **8** (28 μ g/ml), **9** (28 μ g/ml), **10** (28 μ g/ml), **12** (28 μ g/ml), and **13** (44 μ g/ml).

Larvae of *G. mellonella* were reared at 32°C in darkness and on an artificial diet (22% maize meal, 22% wheat germ, 11% dry yeast, 17.5% bees wax, 11% honey, 11% glycerin). Last-instar larvae, each weighing 250–350 mg, were used in all experiments as described previously^[19-21].

To induce immune responses in *G. mellonella* larvae were injected with the entomopathogenic bacterium *Serratia entomophila* obtained from the DSMZ (Deutsche Sammlung von Mikroorganismen und Zellkulturen GmbH) and cultured aerobically in LB medium at 37°C. Overnight cultures were diluted (1:50), and grown till OD-1.0. *S. entomophila* in its exponential phase (10^9 cfu/ ml in 10 ml LB broth) were washed and serially diluted with 1x PBS. For each insect, 10 µl of culture (10^6 cfu/larva) was injected dorsolaterally into the hemocoel of last-instar larvae using 1-ml disposable syringes and 0.4 × 20 mm needles mounted on a micromanipulator. After 1.5 h infected larvae of *G. mellonella* were injected with urea lipid compounds (15 µl/larva). Samples were collected for RNA isolation after incubation for 2 hours at 37°C. The control larvae previously injected with *S. entomophila* were further challenged with 1% ethanol.

For quantitative reverse transcriptase (qRT) PCR in *G. mellonella*, five larvae per injected phurealipid were homogenized in 1 ml Trizol reagent (Sigma Aldrich), and whole RNA was extracted according to the manufacturer's recommendations. Complementary DNA (cDNA) synthesis was performed using the First Strand cDNA synthesis kit (Fermentas). The RNA and cDNA quantity was spectrophotometrically determined and the integrity was confirmed by ethidium bromide gel staining. Quantitative real time RT-PCR was performed with the Biorad real-time PCR system (CFX 96) using the SsoFast EvaGreen Supermix protocol (Biorad). We used 50 ng of cDNA per reaction to amplify genes like moricin, gallerimycin

and lysozyme using the following primers: Gallerimycin-forward (5'-CGCAATATCATTGGCCTTCT-3') and Gallerimycin-reverse (5'-CCTGCAGTTAGCAATGCACTC-3'), Lysozyme-forward (5'-TCCCAACTCTTGACCGACGA-3') and Lysozyme-reverse (5'-AGTGGTTGCGCCATCCATAC-3'), Moricin-like peptide A-forward (5'-GCGATCATTGCCCTCTTTAT-3') and Moricin-like peptide A-reverse (5'-AGTGCCTTCTGTTTTTAATGTGTTC-3'), 18S rRNA-forward (5'-ATGGTTGCAAAGCTGAAACT-3') and 18S rRNA-reverse (5'-TCCCGTGTTGAGTCAAATTA-3').

To examine the impact of phurealipids on *M. sexta* immune responses, they were dissolved in dimethylsulfoxide (DMSO) (Fisher Scientific) and used for insect injection at a final concentration of 10 μ M. Larvae of *M. sexta* (Carolina Biological Supply) were reared on a wheat-germ based artificial diet (MP-Biomedicals, Solon, OH, USA) at 26 °C with daily 18 h/6h light/dark photoperiods. Five 4th instar larvae were injected with *Salmonella enterica* serovar Typhimurium LT2 or PBS and 1.5 hours later were injected with 10 μ M phurealipids 1, 7, 13, or the control solvent DMSO. Whole insects were snap-frozen and homogenized in TRIzol reagent (Invitrogen) 3.5 hours after treatment with phurealipids. For qRT-PCR, 5 μ g of total RNA were treated with RQ1 RNase-free DNase I (Promega). Reverse transcription was performed using the Mg primer: 5-CGGGCAGTGAGCGCAACGTTTTTTTTTTTTTTT-3' (Integrated DNA Technologies) and AMV Reverse Transcriptase (Promega). cDNA was diluted 10-fold and used as template for quantitative real time PCR (qRT-PCR). qRT-PCR was performed with SYBR® Green Supermix (Bio-Rad) on a Bio-Rad iCycler using diluted cDNAs as template. Transcript levels of cecropin, lysozyme and moricin were measured and normalized against rpS3 using the following primers: cecropin-forward (5'-GGTCAAAGGATTCGTGACGC-3') and cecropin-reverse (5'-

TTTGATTGTCCTTTGAAAATGGCG-3'), lysozyme-forward (5'-
TCGACTTGCGCCAAGAAGAT-3') and lysozyme reverse (5'-
ACGATGGGTTTCAGGACTGT-3'), moricin-forward (5'-
TGAATTTTCGCATTATAGGCTGTGT-3') and moricin-reverse (5'-
GAGGTATCATTTTACCCGCCAC-3'), rpS3-forward (5'-
ACTTCTCAGGCAAGGAGTGC-3') and rpS3-reverse (5'-
GTCACCAGGATGTGGTCTGG-3').

Data were analyzed as described previously ^[22]. Briefly, Ct values were normalized by calculating the ratio between the reference gene and the gene of interest and presented as a ratio between infected versus PBS injected larvae. Data were statistically analyzed using Mixed Effect ANOVA with a Dunnett's post-hoc test on normalized Ct values (SAS Software).

***Tribolium castaneum* embryo collection, treatment and fluorescence live imaging.** For this study, the *Tribolium castaneum* (Herbst) Vermillion White EFA-nGFP transgenic line (Sarrazin *et al.*, 2012) was crossed homozygote on one insert and reared on full grain wheat flour (#113061036, Demeter, Darmstadt, Germany) supplemented with 5% (w/v) inactive dry yeast (#62-106, Flystuff, San Diego, CA, USA) at 25°C and 70% relative humidity in a 12:00 h light / 12:00 h darkness cycle (#DR-36VL, Percival Scientific, Perry, IA, USA). For embryo collection, 300-500 adults were transferred to 10 g 405 fine wheat flour (#113061006, Demeter, Darmstadt, Germany) supplemented with 5% (w/w) inactive dry yeast and incubated for 02:00 hours at 25°C. After the incubation period, the embryos were incubated 16:00 hours at 25°C. Simultaneous dechoriation of 80-100 embryos was performed as described previously (Benton *et al.*, 2013). A drop of 300 µl 1% (w/v) low-melt agarose in PBS pH 7.4 was added to each of the inner 60 wells of a 96-well plate before attaching the embryos on top of these drops with a small paint brush one-by-one. Methoprene and HB71

were dissolved in 0.1% DMSO (v/v, #A994.1, Carl Roth, Karlsruhe, Germany) in PBS pH 7.4 (#10010-023, Gibco Life Technologies GmbH, Darmstadt, Germany) to final concentrations of 10 μ M and 100 μ M and 100 μ l of those solutions were added to the respective wells. As controls, PBS pH 7.4 and 0.1% DMSO (v/v) in PBS pH 7.4 were used. Fluorescence live imaging started directly after the addition of the compounds and was performed on a ZEISS Cell Observer SD (Carl Zeiss, Göttingen, Germany). Embryos were illuminated with a 488 nm Argon laser (100 mW initial power, 30%), images were recorded through an EC Plan-Neofluar 10 \times /0.30 M27 objective (#420341-9910-000, Carl Zeiss, Göttingen, Germany) with a Rolera EM-C² camera (#01-ROL-EMC2-R-F-M-14-C, QImaging, Surrey, BC, Canada). Each embryo was imaged in 6 planes with 30 μ m spacing and a 200 ms exposure time. Imaging was performed over a period of 50:00 hours with an interval of 00:15 hours. The stage speed was reduced to 10% of the maximum to prevent embryos from detaching. From the recorded planes per embryo, maximum projections were computed and embryos were rotated with their anterior pole to the top.

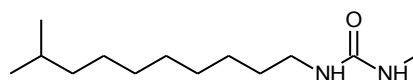
Statistics. Four datasets with 6 PBS control embryos, 6 DMSO control embryos and 12 embryos for each compound/concentration were recorded. Embryos that completed dorsal closure properly were scored as completing the development. Significance was determined by the two-sided student's t-test.

Chemical synthesis of glycine amides and phurealipids. If not noted differently, the chemicals were purchased in the highest purity available.

General synthetic procedure I. 1 eq of the corresponding isocyanides were dissolved in acetone (4 mL/mmol) and 2 eq of the amine were added. The reaction mixture was stirred overnight and the forming precipitate recrystallized.

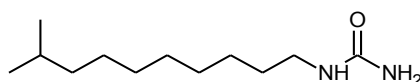
General synthetic procedure II. 1 eq of the free acid was dissolved in benzene (45 mL/mmol) and 6 eq of triethylamine and 3 eq of diphenylphosphoryl azide were added. After refluxing for approximately 1h the reaction mixture was cooled to room temperature, acetone (30 mL/mmol) and ca. 10 eq of methylamine (40% in water) or ammonium hydroxide (28 – 30% in water) were added and the mixture stirred at room temperature overnight. The solvents were removed under reduced pressure and the precipitate purified with normal phase liquid chromatography or recrystallization.

General synthetic procedure III (synthesis of glycine amides). 1 eq of Boc-protected glycine was dissolved in dichloromethane (3 mL/mmol), cooled to 0°C and 1.1 eq of TBTU and 4 eq DIEA were added slowly. After stirring of 10 min at 0°C the reaction mixture was warmed to room temperature and 1.1 eq of the corresponding amine were added and stirred overnight. Upon completion of the reaction the organic phase was washed with a saturated ammonium chloride solution. The resulting aqueous phase was extracted three times with dichloromethane, then the organic phases were combined and dried over sodium sulfate. The solvents were removed under reduced pressure and the precipitate purified with normal phase liquid chromatography. The protecting group was removed quantitatively upon incubation with 4 M hydrochloric acid in dioxane (10 mL/mmol) at 0°C for several hours. Then the solvents were removed under reduced and the target compound was obtained as a hydrochloric salt.



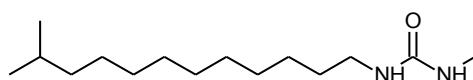
1

***N*-Methyl-*N'*-(9-methyldecyl) urea (1)** was obtained according to the general procedure II. The *iso*-branched fatty acid was purchased with Larodan AB (Limhamn, Sweden). Recrystallization from acetone yielded the white crystalline urea (15 mg, 0.066 mmol, 65% yield). HRMS (m/z): [M+H]⁺ calcd. for C₁₃H₂₉N₂O, 229.2274; found 229.2293; T_m=85°C; ¹H-NMR (400 MHz, CDCl₃): δ 3.16 (t, *J* = 7.1 Hz, 2H) 2.79 (s, 3H), 1.55 – 1.47 (m, 3H), 1.30 - 1.25 (m, 10H), 1.16 (m, 2H), 0.87 (d, *J* = 6.6 Hz, 6H), ¹³C-NMR (125 MHz, CDCl₃): δ 158.9, 40.8, 39.1, 30.2, 29.8, 29.6, 29.3, 27.9, 27.4, 27.3, 26.9, 22.6



2

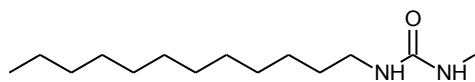
***N*-(9-Methyldecyl) urea (2)** was obtained according to the general procedure II. Recrystallization from acetone yielded the white crystalline urea (111 mg, 0.51 mmol, 86% yield). HRMS (m/z): [M+H]⁺ calcd. for C₁₂H₂₇NO, 215.2117; found 215.2132; T_m=94°C ¹H-NMR (400 MHz, CDCl₃): δ 3.11 (t, *J* = 7.1 Hz, 2H), 1.57 – 1.46 (m, 3H), 1.28 - 1.26 (m, 10H), 1.20-1.15 (m, 2H), 0.90 (d, *J* = 6.6 Hz, 6H) ¹³C-NMR (75 MHz, CDCl₃): δ 160.1, 38.9, 30.8, 30.1, 29.8, 29.5, 29.3, 27.8, 27.5, 27.3, 26.8, 22.5



3

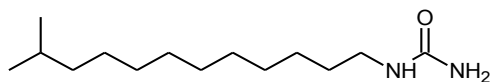
***N*-Methyl-*N'*-(11-methyldodecyl) urea (3)** was obtained according to the general procedure II. The *iso*-branched fatty acid was purchased with Sigma Aldrich (Germany). Recrystallization from acetone yielded the white crystalline urea (4.2 mg, 0.016 mmol, 25% yield). HRMS (m/z): [M+H]⁺ calcd. for C₁₅H₃₃N₂O, 257.2587; found 257.2594; ¹H-NMR

(400 MHz, CDCl₃): δ 3.15 (t, $J = 7.1$ Hz, 2H), 2.79 (s, 3H), 1.57 – 1.45 (m, 3H), 1.33 - 1.26 (m, 14H), 1.18 - 1.13 (m, 2H), 0.88 (d, $J = 6.7$ Hz, 6H)



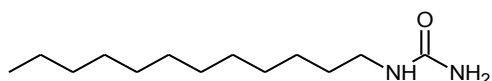
4

***N*-Methyl-*N'*-dodecyl urea (4)** was obtained according to the general procedure II. Recrystallization from acetone yielded the white crystalline urea (31 mg, 0.13 mmol, 52% yield). HRMS (m/z): [M+H]⁺ calcd. for C₁₄H₃₁N₂O, 243.2430; found 243.2465; T_m=81.1°C; ¹H-NMR (400 MHz, CDCl₃): δ 3.14 (t, $J = 7.2$ Hz, 2H), 2.78 (s, 3H), 1.51-1.44 (m, 2H), 1.32-1.25 (m, 18H), 0.89 (t, $J = 6.6$ Hz, 3H); ¹³C-NMR (125 MHz, CDCl₃): δ 159.4, 40.4, 39.8, 31.5, 30.0, 29.2, 29.2, 29.0, 28.9, 26.6, 26.3, 22.2, 13.7



5

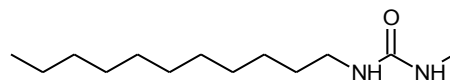
***N*-(11-Methyldodecyl) urea (5)** was obtained according to the general procedure II. The *iso*-branched fatty acid was purchased with Sigma Aldrich. Recrystallization from acetone yielded the white crystalline urea (6.6 mg, 0.027 mmol, 41% yield). HRMS (m/z): [M+H]⁺ calcd. for C₁₄H₃₁N₂O, 243.2430; found 243.2449; ¹H-NMR (400 MHz, CDCl₃): δ 3.15 (t, $J = 7.1$ Hz, 2H), 1.56 – 1.45 (m, 3H), 1.33 - 1.26 (m, 14H), 1.16 (m, 2H), 0.88 (d, $J = 6.6$ Hz, 6H) ¹³C-NMR (125 MHz, CDCl₃): δ 158.5, 45.6, 41.0, 39.1, 30.0, 29.9, 29.7, 29.6, 29.6, 29.3, 28.0, 27.4, 26.8, 22.7



6

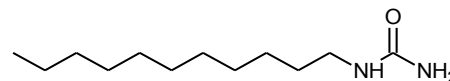
***N*-Dodecyl urea (6)**^[23] was obtained according to the general procedure II. Recrystallization from acetone yielded the white crystalline urea (35.1 mg, 0.164 mmol, 65% yield). HRMS

(m/z): $[M+H]^+$ calcd. for $C_{13}H_{29}N_2O$, 229.2274; found 229.2306; $T_m=105.9^\circ C$; **1H -NMR** (400 MHz, $CDCl_3$): δ 3.16 (t, $J = 7.2$ Hz, 2H), 1.54 – 1.49 (m, 2H), 1.32 - 1.27 (m, 18H), 0.89 (t, $J = 6.6$ Hz, 3H)



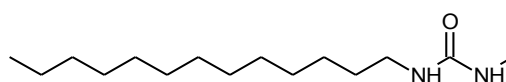
7

N-methyl-N'-undecyl urea (7) was obtained according to the general procedure I. Recrystallization from acetone yielded the white crystalline urea (69 mg, 0.3 mmol, 61% yield). HRMS (m/z): $[M+H]^+$ calcd. for $C_{13}H_{29}N_2O$, 229.2274; found 229.2283; $T_m=88.1^\circ C$; **1H -NMR** (400 MHz, $CDCl_3$): δ 3.14 (t, $J = 7.2$ Hz, 2H), 2.76 (s, 3H), 1.50 - 1.44 (m, 2H), 1.32-1.25 (m, 16H), 0.88 (t, $J = 6.6$ Hz, 3H) **^{13}C -NMR** (125 MHz, $CDCl_3$): δ 159.8, 40.4, 31.9, 30.3, 29.6, 29.6, 29.4, 29.3, 26.9, 26.8, 22.6, 14.0



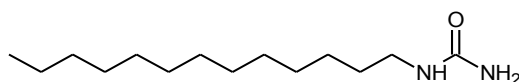
8

N-Undecyl urea (8) was obtained according to the general procedure I. Recrystallization from acetone yielded the white crystalline urea (74 mg, 0.35 mmol, 69% yield). HRMS (m/z): $[M+H]^+$ calcd. for $C_{12}H_{27}NO$, 215.2117; found 215.2137; $T_m=112.3^\circ C$; **1H -NMR** (400 MHz, $CDCl_3$): δ 3.16 (t, $J = 7.2$ Hz, 2H), 1.55 - 1.48 (m, 2H), 1.34-1.27 (m, 16H), 0.89 (t, $J = 6.6$ Hz, 3H) **^{13}C -NMR** (125 MHz, $CDCl_3$): δ 160.6, 41.0, 31.9, 29.6, 29.5, 29.4, 29.3, 29.2, 26.7, 22.7, 14.1



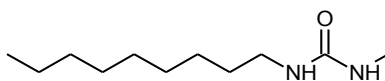
9

***N*-Methyl-*N'*-tridecyl urea (9)** was obtained according to the general procedure II. Recrystallization from acetone yielded the white crystalline urea (12.8 mg, 0.05 mmol, 10% yield). HRMS (m/z): [M+H]⁺ calcd. for C₁₅H₃₃N₂O, 257.2587; found 257.2621; ¹H-NMR (400 MHz, CDCl₃): δ 3.14 (t, *J* = 7.2 Hz, 2H), 2.76 (s, 3H), 1.51 - 1.44 (m, 2H), 1.32-1.25 (m, 20H), 0.88 (t, *J* = 6.6 Hz, 3H)



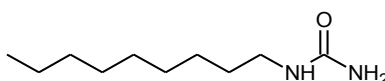
10

***N*-Tridecyl urea (10)**^[24] was obtained according to the general procedure II. Recrystallization from acetone yielded the white crystalline urea (40.4 mg, 0.166 mmol, 34% yield). HRMS (m/z): [M+H]⁺ calcd. for C₁₄H₃₀NO, 243.2358; found 243.2456; T_m=110.4°C ¹H-NMR (400 MHz, CDCl₃): δ 3.15 (t, *J* = 7.2 Hz, 2H), 2.76 (s, 3H), 1.54 - 1.45 (m, 2H), 1.34-1.26 (m, 16H), 0.89 (t, *J* = 6.6 Hz, 3H) ¹³C-NMR (75 MHz, CDCl₃): δ 158.51, 41.0, 31.9, 30.0, 29.7, 29.6, 29.6, 29.6, 29.3, 29.3, 26.8, 22.7, 14.1



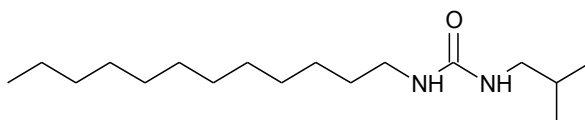
11

***N*-Methyl-*N'*-nonyl urea (11)** was obtained according to the general procedure II. Recrystallization from acetone yielded the white crystalline urea (53.1 mg, 0.065 mmol, 53% yield). ¹H-NMR (400 MHz, CDCl₃): δ 3.15 (t, *J* = 7.1 Hz, 2H), 2.76 (s, 3H), 1.50 - 1.44 (m, 2H), 1.29-1.26 (m, 14H), 0.89 (t, *J* = 6.6 Hz, 3H)



12

***N*-nonyl urea (12)**^[25,26] was obtained according to the general procedure II. Recrystallization from acetone yielded the white crystalline urea (18.5 mg, 0.099 mmol, 19% yield). $T_m=101.1$ °C; **¹H-NMR** (400 MHz, CDCl₃): δ 3.15 (t, $J = 7.1$ Hz, 2H), 1.50 - 1.44 (m, 2H), 1.29-1.26 (m, 12H), 0.89 (t, $J = 6.6$ Hz, 3H)



13

***N*-Dodecyl-*N'*-isobutyl urea (13)** was obtained according to the general procedure I. After recrystallization with *n*-hexane/ethylacetate 112 mg (0.39 mmol, 84%) of the white crystalline urea was obtained. HRMS (m/z): $[M+H]^+$ calcd. for C₁₇H₃₆N₂O, 285.2906; found 285.2898; **¹H-NMR** (500 MHz, CDCl₃): δ 4.36 (sh, 2H), 3.16 (dt, $J = 7.1$ Hz, $J = 6.5$ Hz, 2H), 2.78 (d, $J = 4.7$ Hz, 3H), 1.57 - 1.45 (sh, 3H), 1.35 - 1.25 (sh, 10H), 0.87 (t, $J = 6.6$ Hz, 6H).

References

- [1] H. B. Bode, D. Reimer, S. W. Fuchs, F. Kirchner, C. Dauth, C. Kegler, W. Lorenzen, A. O. Brachmann, P. Grün, *Chem. Eur. J.* **2012**, *18*, 2342–2348.
- [2] A. O. Brachmann, S. A. Joyce, H. Jenke-Kodama, G. Schwär, D. J. Clarke, H. B. Bode, *Chembiochem* **2007**, *8*, 1721–1728.
- [3] A. O. Brachmann, S. Brameyer, D. Kresovic, I. Hitkova, Y. Kopp, C. Manske, K. Schubert, H. B. Bode, R. Heermann, *Nat. Chem. Biol.* **2013**, *9*, 573–578.
- [4] S. W. Fuchs, K. A. J. Bozhüyük, D. Kresovic, F. Grundmann, V. Dill, A. O. Brachmann, N. R. Waterfield, H. B. Bode, *Angew. Chem. Int. Ed. Engl.* **2013**, *52*, 4108–4112.
- [5] S. W. Fuchs, C. C. Sachs, C. Kegler, F. I. Nollmann, M. Karas, H. B. Bode, *Anal. Chem.* **2012**, *84*, 6948–6955.
- [6] D. Reimer, K. M. Pos, M. Thines, P. Grün, H. B. Bode, *Nat. Chem. Biol.* **2011**, *7*, 888–890.
- [7] S. Debernard, C. Morisseau, T. F. Severson, L. Feng, H. Wojtasek, G. D. Prestwich, B. D. Hammock, *Insect Biochem.Mol.Biol.* **1998**, *28*, 409–419.
- [8] S. G. Kamita, M. D. Wogulis, C. S. Law, C. Morisseau, H. Tanaka, H. Huang, D. K. Wilson, B. D. Hammock, *Biochemistry-US* **2010**, *49*, 3733–3742.
- [9] B. D. Hammock, T. C. Sparks, *Anal.Biochem.* **1977**, *82*, 573–579.
- [10] S. W. Fuchs, F. Grundmann, M. Kurz, M. Kaiser, H. B. Bode, *Chembiochem* **2014**, *15*, 512–516.
- [11] Y.-Y. Chu, M. Nega, M. Wölflle, L. Plener, S. Grond, K. Jung, F. Götz, *PLoS Pathog* **2013**, *9*, e1003654.
- [12] A. Thanwisai, S. Tandhavanant, N. Saiprom, N. R. Waterfield, P. Ke Long, H. B. Bode, S. J. Peacock, N. Chantratita, *PLoS ONE* **2012**, *7*, e43835.
- [13] E. Duchaud, C. Rusniok, L. Frangeul, C. Buchrieser, A. Givaudan, S. Taourit, S. Bocs, C. Boursaux-Eude, M. Chandler, J. F. Charles, et al., *Nat. Biotechnol.* **2003**, *21*, 1307–1313.
- [14] J. M. Chaston, G. Suen, S. L. Tucker, A. W. Andersen, A. Bhasin, E. Bode, H. B. Bode, A. O. Brachmann, C. E. Cowles, K. N. Cowles, et al., *PLoS ONE* **2011**, *6*, e27909–.
- [15] A. Lanois, J. C. Ogier, J. Gouzy, C. Laroui, Z. Rouy, A. Givaudan, S. Gaudriault, *Genome Announcements* **2013**, *1*, e00342–13–e00342–13.
- [16] P. Wilkinson, N. R. Waterfield, L. Crossman, C. Corton, M. Sanchez-Contreras, I. Vlisidou, A. Barron, A. Bignell, L. Clark, D. Ormond, et al., *BMC Genomics* **2009**, *10*, 302–302.
- [17] N. Philippe, J. P. Alcaraz, E. Coursange, J. Geiselmann, D. Schneider, *Plasmid* **2004**, *51*, 246–255.
- [18] S. E. Reynolds, S. F. Nottingham, *J.Insect Physiol.* **1985**, *31*, 129–134.
- [19] K. Mukherjee, B. Altincicek, T. Hain, E. Domann, A. Vilcinskas, T. Chakraborty, *Appl. Environ. Microbiol.* **2009**, *76*, 310–317.
- [20] K. Mukherjee, M. A. Mraheil, S. Silva, D. Muller, F. Cemic, J. Hemberger, T. Hain, A. Vilcinskas, T. Chakraborty, *Appl. Environ. Microbiol.* **2011**, *77*, 4237–4240.
- [21] K. Mukherjee, T. Hain, R. Fischer, T. Chakraborty, A. Vilcinskas, *Virulence* **2013**, *4*, 324–332.
- [22] J. C. Castillo, U. Shokal, I. Eleftherianos, *J.Insect Physiol.* **2013**, *59*, 179–185.
- [23] T. F. Severson, M. H. Goodrow, C. Morisseau, D. L. Dowdy, B. D. Hammock, *Insect Biochem.Mol.Biol.* **2002**, *32*, 1741–1756.
- [24] Y. Mido, F. Fujita, H. Matsuura, K. Machida, *Spectrochimica Acta Part A: Molecular Spectroscopy* **1981**, *37A*, 103–112.
- [25] Y. Mido, S. Kimura, Y. Sugano, K. Machida, *Spectrochimica Acta Part A: Molecular Spectroscopy* **1988**, *44*, 661–668.
- [26] C. C. Porter, D. C. Titus, M. J. DeFelice, *Life Sci.* **1976**, *18*, 953–959.

Table S1. Structure elucidation of the phurealipids A, C, D (**1**, **3**, **4**) and the desmethyl phurealipids B, E, F (**2**, **5**, **6**). The desmethyl derivatives **5** and **6** were only produced in the *pliB* mutant. Feeding of deuterated leucine resulted in the expected $^2\text{H}_7$ -shift in **1-3** and **5** from the incorporation of L-[2,3,3,4,5,5,5',5',5'- $^2\text{H}_{10}$]leucine derived isovaleryl unit. Feeding of L-[*methyl*- $^2\text{H}_3$]methionine resulted in labeling of the methylated derivatives **1-3**. No incorporation of L-[2,3,4,4,4,5,5,5'- $^2\text{H}_8$]valine or [2,2,3,3,3- $^2\text{H}_5$]propionate have been observed indicating only acetyl or isovaleryl as starting units.

	$\begin{array}{c} \text{O} \\ \parallel \\ \text{R}^1\text{-NH}-\text{C}-\text{NH}-\text{R}^2 \end{array}$	R ²	R _t [min]	[M+H] ⁺		feeding experiments		
				exp.	theo.	comp.	L-[2,3,3,4,5,5,6,6- $^2\text{H}_{10}$]leucine	L-[<i>methyl</i> - $^2\text{H}_3$]methionine
1		CH ₃	9.6	229.2293	229.2274	C ₁₃ H ₂₉ N ₂ O	+	+
2		H	9.1	215.2132	215.2117	C ₁₂ H ₂₇ N ₂ O	+	-
3		CH ₃	10.8	257.2594	257.2587	C ₁₅ H ₃₃ N ₂ O	+	+
4		CH ₃	10.3	243.2465	243.2431	C ₁₄ H ₃₁ N ₂ O	-	+
5		H	10.4	243.2449	243.2431	C ₁₄ H ₃₁ N ₂ O	+	-
6		H	9.9	229.2306	229.2274	C ₁₃ H ₂₉ N ₂ O	-	-

Table S2. Overview of the biological activities of synthetic and natural phurealipids as well as their occurrence. Activity against juvenile hormone epoxide hydrolase (JHEH) and juvenile hormone esterase (JHE) from *Manduca sexta* as well as activity against *Trypanosoma brucei rhodesiense* (positive control melarsoprol IC₅₀=0.004 µg/mL), *Trypanosoma cruzi* (positive control benznidazole IC₅₀=0.498 µg/mL), *Leishmania donovani* (positive control miltefosine IC₅₀=0.174 µg/mL), and *Plasmodium falciparum* NF54 (positive control chloroquine IC₅₀=0.003 µg/mL) were performed as described previously.

	$\begin{array}{c} \text{O} \\ \parallel \\ \text{R}^1-\text{NH}-\text{C}-\text{NH}-\text{R}^2 \end{array}$	R ²	IC ₅₀ [µM] (% of enzyme inhibition at 100µM)		IC ₅₀ [µg/mL]					occurrence
			JHEH	JHE	<i>T. b. rhod.</i>	<i>T. cruzi</i>	<i>L. don.</i>	<i>P. falc. NF54</i>	L6 cells	
1		CH ₃	6.5 ± 0.9 (81)	> 100 (1)	44.0	16.5	17.6	2.02	34.4	TT01 wt
2		H	> 100 (0)	> 100 (2)	61.8	27.3	6.6	44.3	79.1	TT01 wt
3		CH ₃	30 ± 4 (53)	> 100 (9)	17.8	19.2	10.3	3.3	79.6	TT01 wt
4		CH ₃	10.7 ± 1.2 (67)	> 100 (1)	>100	47.3	94.8	15.1	>100	TT01 wt
5		H	> 100 (9)	25 ± 4 (89)	22.8	17.5	0.9	8.1	61.1	KO <i>pilB</i>
6		H	> 100 (8)	> 100 (5)	49.1	17.0	2.2	10.2	>100	KO <i>pilB</i> and ²³
7		CH ₃	4.3 ± 0.5 (nd)	> 100 (4)	62.5	19.1	18.1	8.0	40.6	synthetic
8		H	nd	nd	25.9	9.4	1.7	12.6	>100	synthetic
9		CH ₃	10 ± 2 (64)	> 100 (4)	40.5	27.1	8.3	3.0	>100	synthetic
10		H	> 100 (2)	> 100 (9)	50.1	43.6	3.5	27.5	>100	synthetic ²⁴
11		CH ₃	> 100 (0)	> 100 (0)	54.6	63.8	>100	>50	>100	synthetic
12		H	> 100 (6)	> 100 (39)	34.3	12.8	3.8	22.8	16.5	synthetic ^{25,26}
13		<i>t</i> Bu	2.3 ± 0.6 (nd)	> 100 (7)	>100	76.7	22.9	3.12	95.8	synthetic

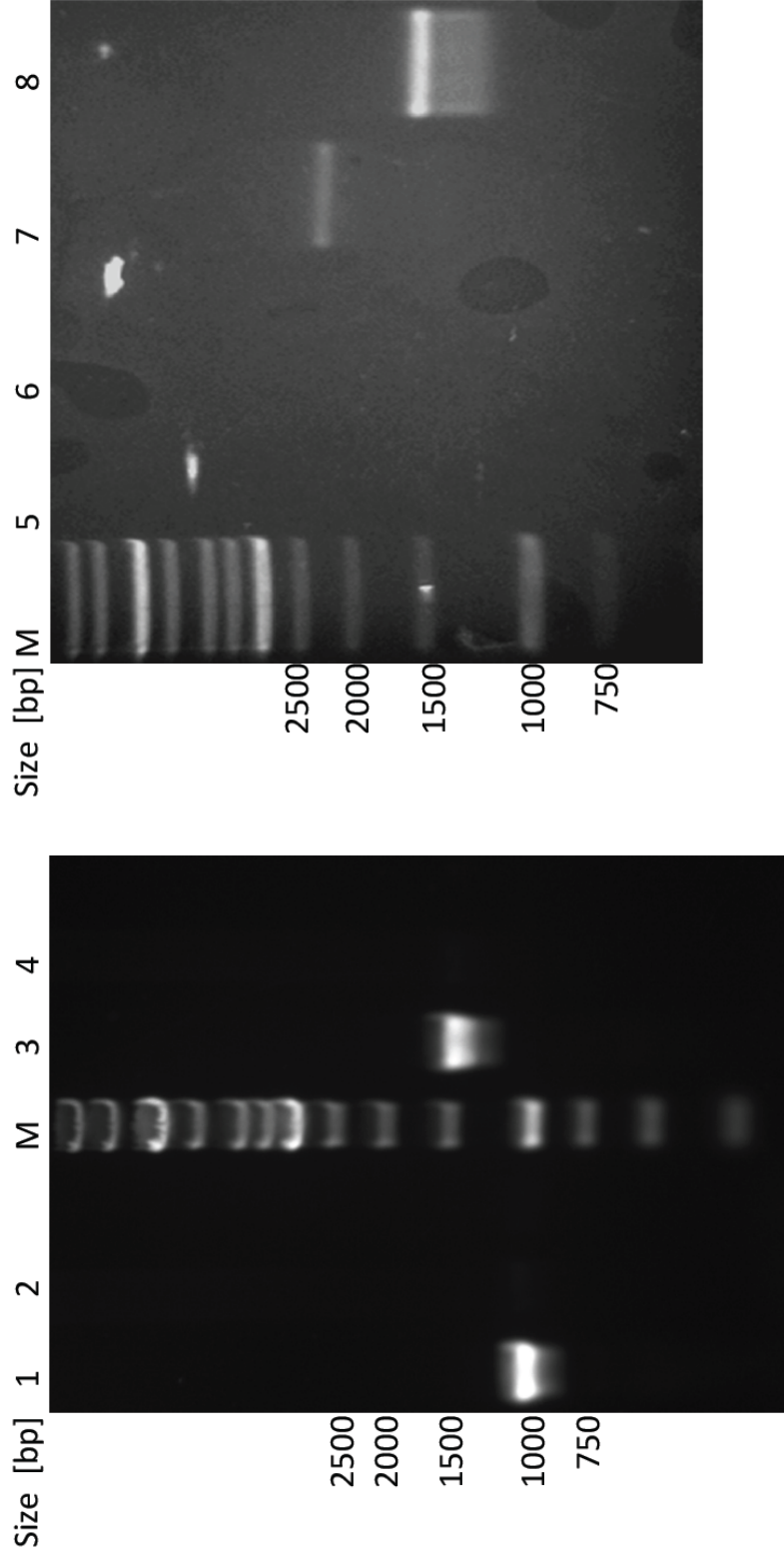


Figure S1. Genotypic Verification of the TT01-2237::cat and the TT01-2076::cat mutants by PCR

M: GeneRuler™ 1kb DNA Ladder,

1 TT01-2237::cat with pDS132fw + V_KO_plu2237_rev (1053 bp);

2 TTO1 WT with pDS132fw + V_KO_plu2237_rev;

3 TT01-2237::cat with V_KO_plu2237_fw + pDS132rv (1525bp);

4 TTO1 WT with V_KO_plu2237_fw + pDS132rv;

5 TTO1 WT with pDS132fw + V2076_Rv

6 TTO1 WT with V2076_Fw + pDS132rv

7 TT01-2076::cat with pDS132fw + V2076_Rv (~2230 bp)

8 TT01-2076::cat with V2076_FW + pDS132rv (~1550 bp)

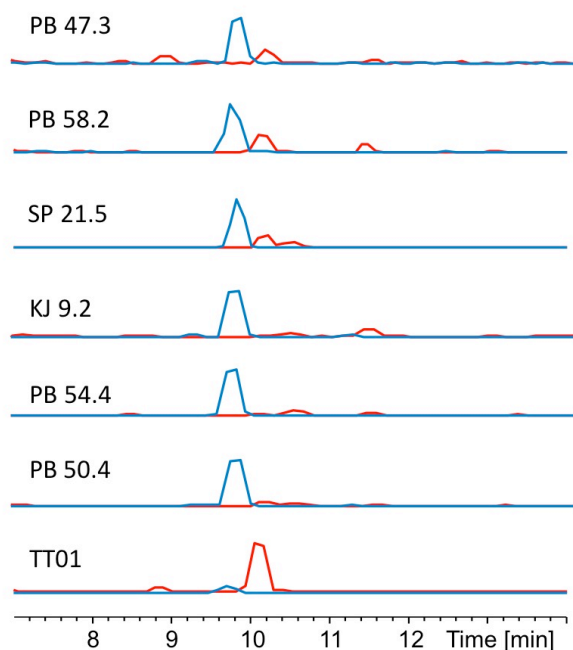


Figure S2. HPLC/MS analysis of selected strains of *P. luminescens* showing the production of different phurealipids. The EICs of **1** (red) and **2** (blue) are shown. In several cases an inversion of the amounts of produced phurealipids **1** and **2** in comparison to TT01 is observed (*Photorhabdus* PB 47.3, *Photorhabdus* PB 58.2 and *Photorhabdus* SP 21.5). Moreover, a total loss in the production of **1** can also be observed (*Photorhabdus* KJ 9.2, *Photorhabdus* PB 54.4 and *Photorhabdus* PB 50.4).

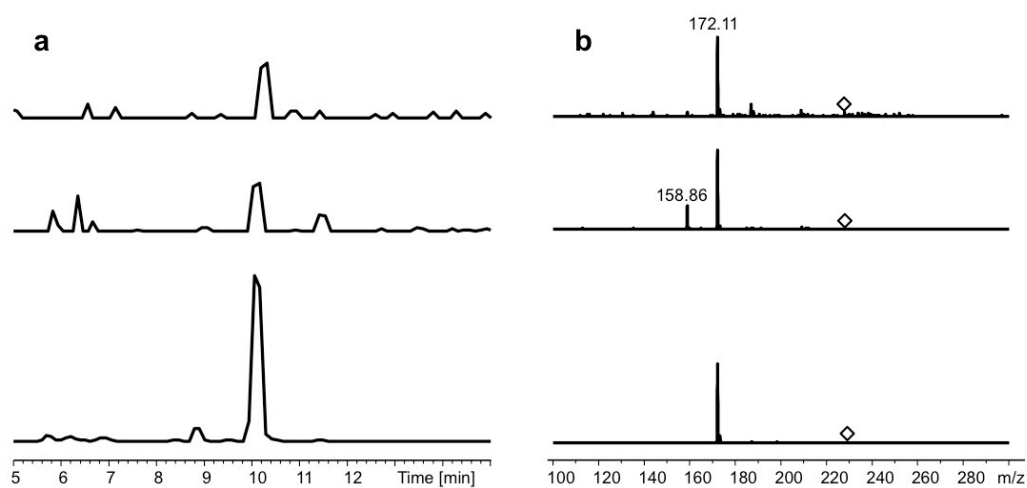


Figure S3. LC-MS/MS analysis of selected *Xenorhabdus* strains isolated from Vietnam (*Xenorhabdus* 1LC 1.2 (top) and *Xenorhabdus* DL13 red (middle)) in comparison to *Photorhabdus luminescens* TT01 (bottom). HPLC/MS chromatogram (a) and MS/MS analysis of the mother ion of **1** (m/z 229 $[M+H]^+$ diamond; b).

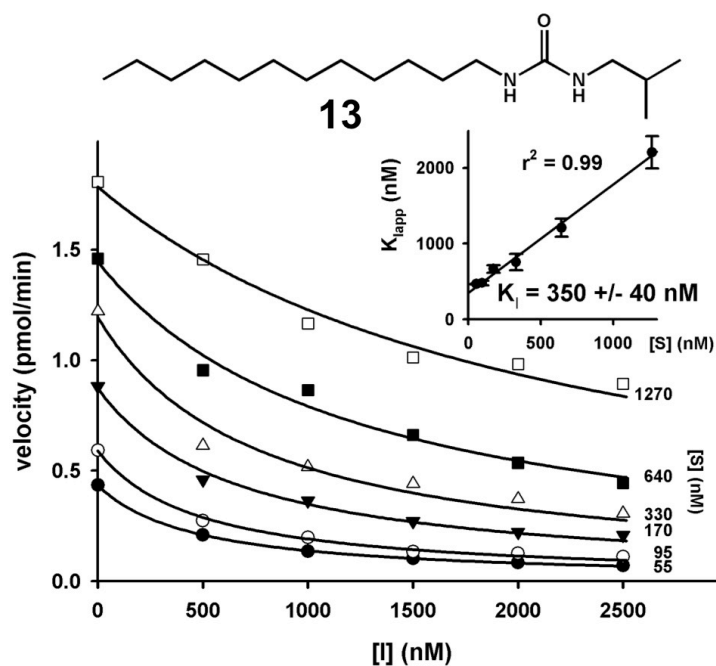
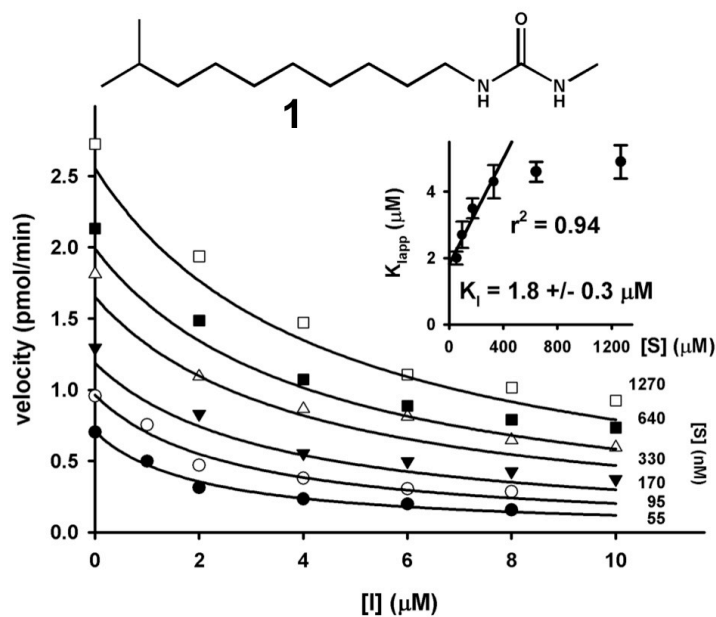


Figure S4. Determination of the K_I of compounds **1** and **13** with *Manduca sexta* JHEH using [^3H]-JH III as substrate. For each substrate concentration (55-1270 nM), the velocity is plotted as a function of **1** concentration (0-10 μM), allowing the determination of an apparent inhibition constant (K_{Iapp}). K_{Iapp} s are plotted as a function of the substrate concentration (insert). For [S] = 0, a K_I value of 1.8 μM was found (top). For each substrate concentration of **13** (55-1270 nM), the velocity is plotted as a function of **13** concentration (0-2.5 μM), allowing the determination of an apparent inhibition constant (K_{Iapp}). K_{Iapp} s are plotted as a function of the substrate concentration (insert). For [S] = 0, a K_I value of 350 nM was found (bottom).

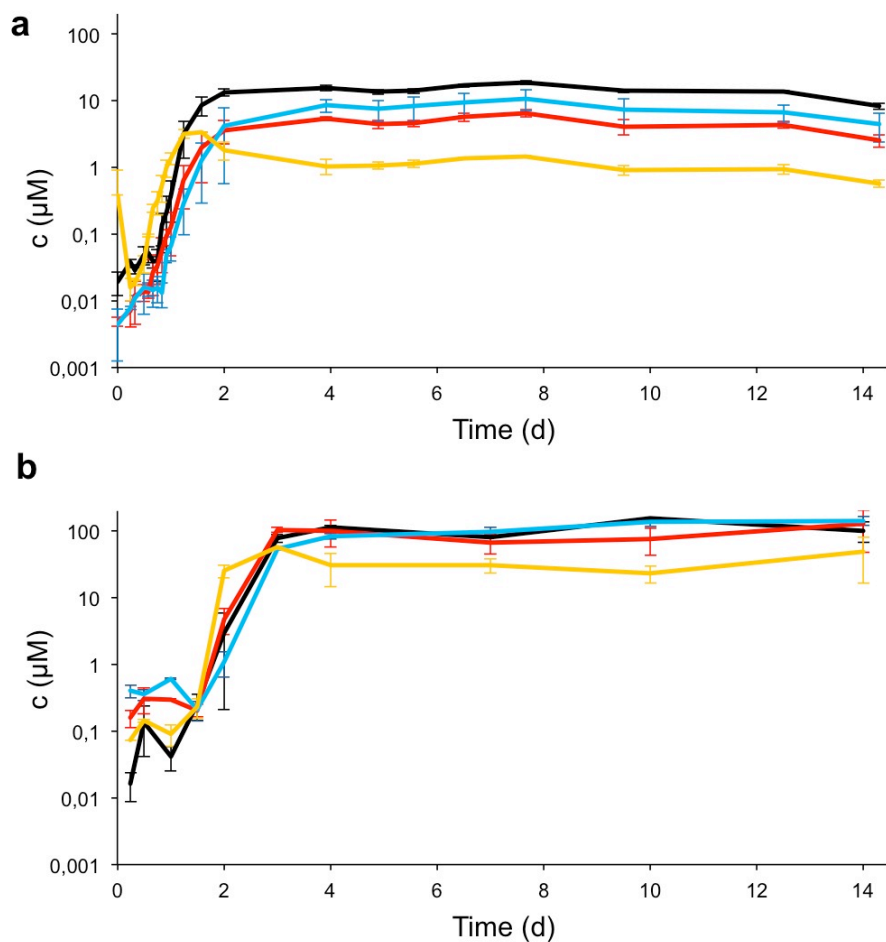


Figure S5. Production kinetics of phurealipids of TT01 cultivated in LB broth (a) and after the injection of the bacteria in larvae of *Galleria mellonella* (b) based on LC-MS measurements. An increase in production of the phurealipids **1** (black), **2** (orange), **3** (blue) and **5** (red) can be observed after the injection in the insect. In order to determine an absolute concentration of the phurealipids, a calibration curve was compiled based on five different concentrations of the synthetically obtained **1** measured as triplicates. The absolute and maximal amount of the main compound **5** in *G. mellonella* was 208 μM . The absolute and maximal amount of the main compound **1** in LB broth was 19 μM .

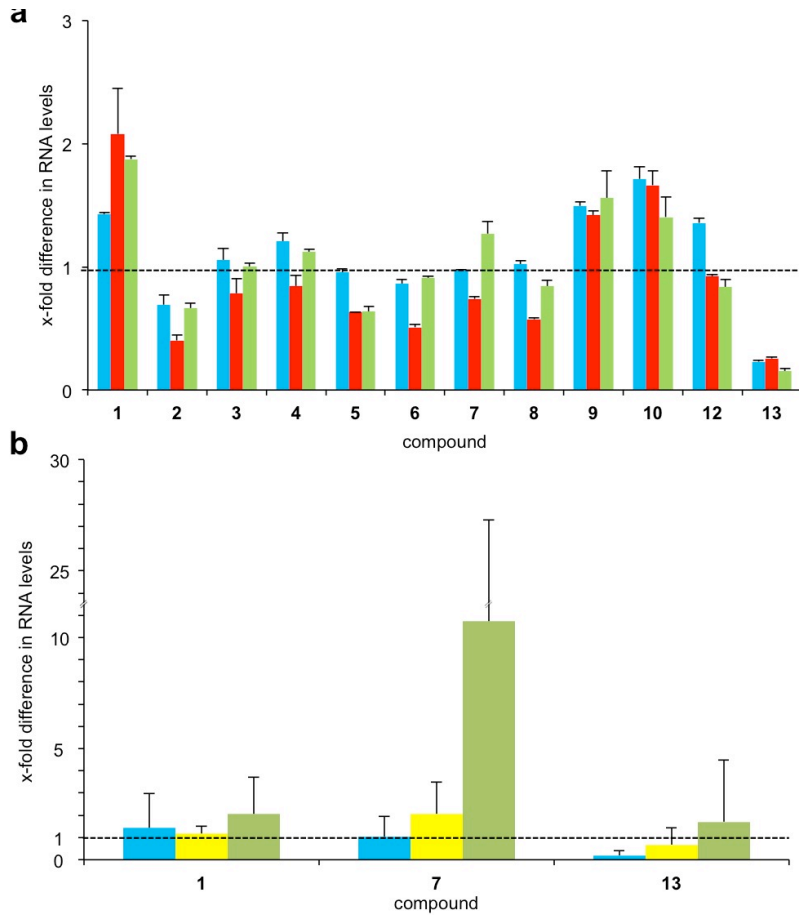


Figure S6. a, Level of transcription of the immune responsive genes responsible for the production of lysozyme (blue), gallerimycin (red) and moricin (green) in *Galleria mellonella* after injection of *S. entomophila* following injection of phurealipids. **b**, Level of transcription (relative to a DMSO control) of the immune responsive genes responsible for the production of lysozyme (blue), cecropin (orange) and moricin (green) in *Manduca sexta* after injection of *Salmonella enterica* serovar Typhimurium following injection of selected phurealipids.

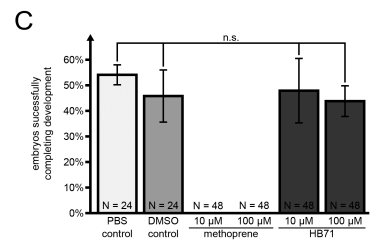
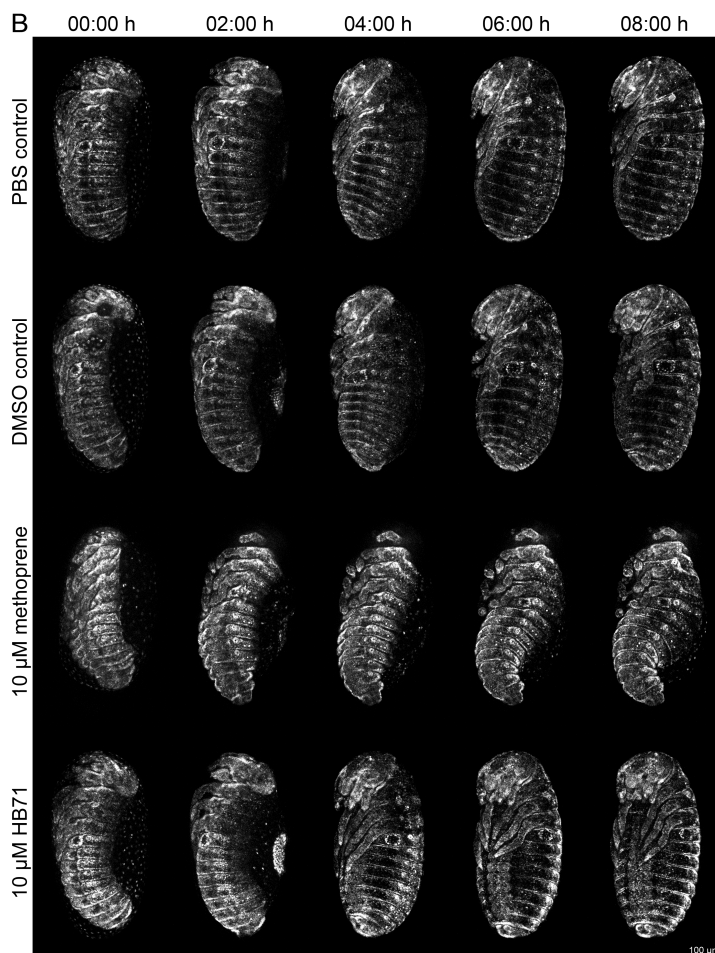
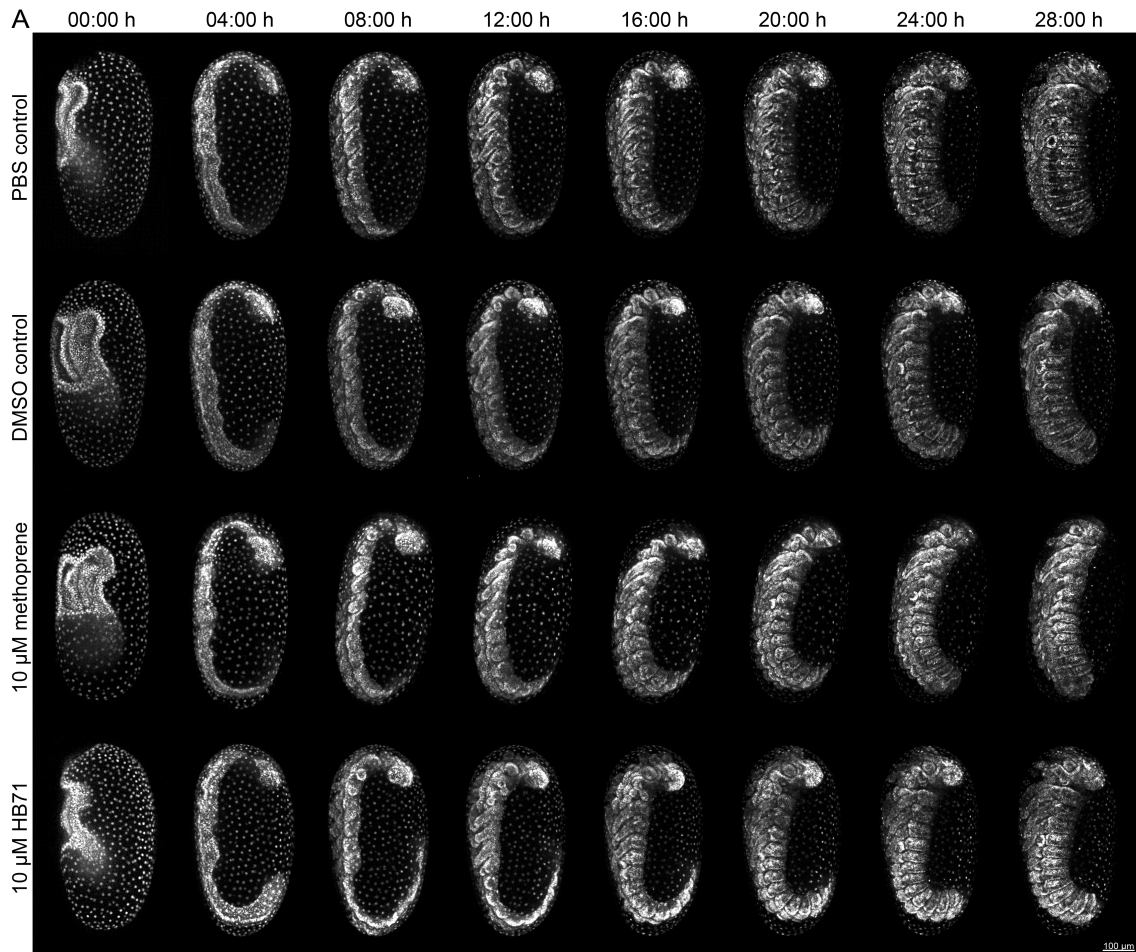


Figure S7. Fluorescence live imaging of *Tribolium castaneum* embryogenesis under the effects of methoprene and **13** (HB71). (A) Gastrulation (00:00 h), germ band elongation (04:00-08:00 h) and germ band retraction (12:00-28:00 h). In this development period, no influence of 10 μ M methoprene and 10 μ M **13** on morphogenesis are visible. (B) Dorsal closure: Embryos treated with 10 μ M methoprene failed to complete dorsal closure properly. **13** did not affect the dorsal closure process, as the embryo does not differ from the control embryos. (C) Quantification of fluorescence live imaging: Approximately half of the embryos in the PBS and DMSO control were able to complete development. Both tested concentrations of methoprene did result completely in development aberrations, while successful development under the two tested concentrations of **13** (HB71) did not significantly differ from the controls. Error bars show S.E.M. n.s., not significant.

Data analysis (in % living *T. castaneum* embryos) of the Fluorescence live imaging experiments. MP (methoprene).

Date	Exp.	PBS	0.1% DMSO	MP (100 μ M)	13 (100 μ M)	MP (10 μ M)	13 (10 μ M)
08.08.	1	50	66.7	0	58.3	0	58.3
12.08.	2	50	50	0	41.7	0	41.7
27.08.	3	50	16.6	0	8.3	0	33.3
05.09	4	66.7	50	0	66.7	0	58.3
Mean		54.1	45.8	0	43.8	0	47.9
S.E.		8.3	21.0	0	25.8	0	12.5

Supplementary Movie 1. *Tribolium castaneum* embryogenesis under the effects of 10 μ M methoprene and 10 μ M **13** (HB71) from 00:00 h to 50:00 h with an interval of 00:15 h between the time points. The embryo treated with 10 μ M methoprene failed to complete dorsal closure properly, resulting in a sigmoid shape. **13** did not affect the dorsal closure process, as the embryo does not differ from the control embryos. Frame rate is 5 frames per second.

(see separate file)

Live imaging of *Tribolium castaneum* embryonic development using light-sheet–based fluorescence microscopy

Frederic Strobl, Alexander Schmitz & Ernst H.K. Stelzer

Tribolium castaneum has become an important insect model organism for evolutionary developmental biology, genetics and biotechnology. However, few protocols for live fluorescence imaging of *Tribolium* have been reported, and little image data is available. Here we provide a protocol for recording the development of *Tribolium* embryos with light-sheet–based fluorescence microscopy. The protocol can be completed in 4–7 d and provides procedural details for: embryo collection, microscope configuration, embryo preparation and mounting, noninvasive live imaging for up to 120 h along multiple directions, retrieval of the live embryo once imaging is completed, and image data processing, for which exemplary data is provided. Stringent quality control criteria for developmental biology studies are also discussed. Light-sheet–based fluorescence microscopy complements existing toolkits used to study *Tribolium* development, can be adapted to other insect species, and requires no advanced imaging or sample preparation skills.

Published in September 2015

Research Article – *Nature Protocols* – Nature Publishing Group

PubMed ID 26334868

Erklärung zu Autorenanteilen an der Publikation

‘Live imaging of *Tribolium castaneum* embryonic development with light-sheet–based fluorescence microscopy’

Status: Printed

Zeitschrift: *Nature Protocols* (Nature Publishing Group)

Autoren: Frederic Strobl (FS), Alexander Schmitz (AS), Ernst H.K. Stelzer (EHKS)

(1) Entwicklung und Planung

FS 33.3%

AS 33.3%

EHKS 33.3%

(2) Durchführung der einzelnen Untersuchungen und Experimente

FS 100%

AS 0%

EHKS 0%

(3) Erstellung der Datensammlung und Abbildungen

FS 100%

AS 0%

EHKS 0%

(4) Analyse und Interpretation der Daten

FS 75.0% (Verarbeitung Rohdaten, Aufnahme-Optionen, Troubleshooting, Bilddatenverarbeitung)

AS 12.5% (Bilddatenverarbeitung, Normalisierungsverfahren)

EHKS 12.5% (Mikroskop-assoziierte Analyse, Bilddatenverarbeitung)

(5) Verfassen des Manuskriptes

FS 33.3%

AS 33.3%

EHKS 33.3%

Unterschrift Frederic Strobl:

Ort, Datum:

Unterschrift Ernst H.K. Stelzer:

Ort, Datum:

Live imaging of *Tribolium castaneum* embryonic development using light-sheet-based fluorescence microscopy

Frederic Strobl, Alexander Schmitz & Ernst H K Stelzer

Physical Biology/Physikalische Biologie (IZN, FB 15), Buchmann Institute for Molecular Life Sciences (BMLS), Cluster of Excellence Frankfurt–Macromolecular Complexes (CEF-MC), Goethe University–Frankfurt am Main (Campus Riedberg), Frankfurt am Main, Germany. Correspondence should be addressed to E.H.K.S. (ernst.stelzer@physikalischebiologie.de).

Published online 3 September 2015; doi:10.1038/nprot.2015.093

***Tribolium castaneum* has become an important insect model organism for evolutionary developmental biology, genetics and biotechnology. However, few protocols for live fluorescence imaging of *Tribolium* have been reported, and little image data is available. Here we provide a protocol for recording the development of *Tribolium* embryos with light-sheet-based fluorescence microscopy. The protocol can be completed in 4–7 d and provides procedural details for: embryo collection, microscope configuration, embryo preparation and mounting, noninvasive live imaging for up to 120 h along multiple directions, retrieval of the live embryo once imaging is completed, and image data processing, for which exemplary data is provided. Stringent quality control criteria for developmental biology studies are also discussed. Light-sheet-based fluorescence microscopy complements existing toolkits used to study *Tribolium* development, can be adapted to other insect species, and requires no advanced imaging or sample preparation skills.**

INTRODUCTION

During the past two decades, the red flour beetle *T. castaneum* has become the second most important insect model organism besides the fruit fly *Drosophila melanogaster*. Similarly to *Drosophila*, *Tribolium* is relatively easy to culture, has a short life cycle and generates a large number of progeny. However, *Drosophila* exhibits many derived developmental and morphological features, whereas *Tribolium* is considered more representative of insects: its embryogenesis is characterized by short-germ band development, extensive embryonic membrane formation, embryonic leg development and non-involuting head morphogenesis^{1–5}. These aspects contribute to its important role in evolutionary developmental biology, insect physiology and genetics. In addition, *Tribolium* is a globally distributed crop pest and therefore also of commercial biotechnological interest^{1,3,4,6}.

The arsenal of molecular biology tools available for *Tribolium* has increased during the last decade, covering areas such as concurrent *in situ* hybridization and antibody staining⁷, germline transformation⁸ and parental RNAi⁹. However, fluorescence live imaging data is still not abundant, with only a handful of studies published since 2012, most of which used confocal fluorescence microscopy^{10–16}. For almost three decades, confocal fluorescence microscopy has been the state of the art in 3D light microscopy. It provides true optical sectioning and an excellent signal-to-noise ratio. However, because it is essentially a sampling device, the image recording speed is fairly low. Its major disadvantage is that the image recording process exposes the specimen to a very high energy level, which can cause detrimental phototoxic effects.

To overcome the limitations of confocal fluorescence microscopy, we established¹⁷ and improved^{18,19} light-sheet-based fluorescence microscopy (LSFM), which we used to publish the first noninvasive long-term fluorescence live imaging study of *Tribolium*²⁰. LSFM uses two independent, azimuthally arranged optical paths to excite the fluorophores in a specimen and to detect the fluorescence emission. The laser beam is channeled through the illumination objective and creates a several micrometer

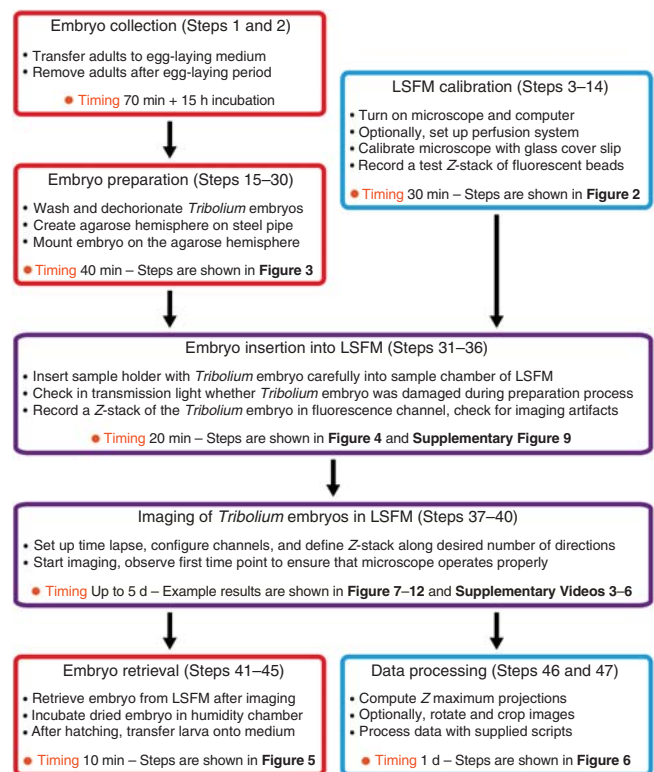
thin light sheet that overlaps with the focal plane of the detection objective^{17,18,21}. In consequence, only a thin volume of the specimen is exposed to the laser, thus providing true optical sectioning²². The benefits are reduced out-of-focus blur and no phototoxicity or photobleaching outside the illuminated volume. Because LSFM uses a low-numerical-aperture illumination objective and a detection objective with an approximately 5–10-times-higher numerical aperture, the depth penetration is usually very good.

The most important differences between confocal fluorescence microscopy and LSFM have been discussed previously²³. One noticeable difference between images produced by conventional and confocal microscopes compared with LSFM is the nature of the ‘shadowing effect’. Light that passes through biological tissue is scattered and absorbed. Hence, the illumination intensity drops along the illumination axis as some objects throw a shadow on the objects that lie behind them. When using conventional and confocal fluorescence microscopes, most users will not notice the shadowing effect, and most users of confocal fluorescence microscopes accept that fluorescent objects are not observable beyond a certain depth. This effect is well-known and has been described in detail²⁴. In LSFM, this shadowing effect is clearly visible (**Supplementary Fig. 1**). The images show a bright side (toward the illumination objective) and a dark and sometimes blurred side, which is more pronounced when optically dense and thick specimens are observed. The final image is a result of the limits of illumination and detection.

Overview of the procedure

Here we provide a comprehensive protocol based on our published work²⁰ which describes all the necessary steps to perform non-invasive *in toto* long-term fluorescence live imaging of *Tribolium* embryos for up to 120 h with LSFM. The procedure starts with the collection of embryos from the appropriate transgenic line and the corresponding background strain as control; we use the

Figure 1 | Flowchart of the procedure. The main steps of the protocol include embryo collection (Steps 1 and 2), LSFM calibration (Steps 3–14), embryo preparation (Steps 15–30), embryo insertion into the LSFM (Steps 31–36), imaging of *Tribolium* embryos in the LSFM (Steps 37–40), embryo retrieval (Steps 41–45) and data processing (Steps 46 and 47). The time required to conduct the steps is indicated and the respective figures, supplementary figures and supplementary videos are referenced. Red boxes refer to embryo handling, blue boxes to technical issues and purple boxes to the data recording process.



EFA-nGFP transgenic line and the vermilion white background strain, respectively. Collected embryos are then incubated at the appropriate temperature until the desired developmental stage is reached; we incubate embryos for 15 h (overnight) at 25 °C so that they reach the uniform blastoderm stage at the start of imaging. During this incubation period, imaging options are selected and the LSFM is calibrated accordingly. We use a two-step approach for calibration. First, a glass coverslip allows the adjustment of all the parameters required to generate and calibrate the light sheet. It aligns it with the focal plane of the detection system and centers the thinnest part of the light sheet on the optical detection axis. Next, an agarose-embedded beads column, which represents the optical properties of a fluorescently labeled biological specimen, is used for test recording of a 3D image volume, which can be regarded as a ground truth for any further 3D image processing steps. When the incubation period for the embryos is complete, they are dechorionated using a sodium hypochlorite solution and mounted onto the sample holder using a modified method designed for optimal recording: briefly, only the anterior end of the embryo is covered in agarose and attached to the sample holder, with the elongated anterior–posterior axis aligned to the rotation axis. The mounted embryos are then placed into the microscope and imaging is started using appropriate settings for time lapse, recording directions, spectral channels and imaging volume. When imaging is complete, embryos are retrieved and allowed to develop into larvae, which can be compared with suitable control larvae. Image data is processed using custom scripts. A flowchart of the procedure is provided in **Figure 1**.

This protocol is primarily designed for LSFM instruments working with a dynamic light sheet created by scanning the illumination laser beam¹⁸, but can be generalized and applied to setups with a static light sheet^{17,25,26}, extended instrumentation such as dual-sided illumination^{27–29} or multiple quasi-parallel views^{28,29} and commercial LSFM setups such as the Lightsheet Z.1 (Carl Zeiss). The application of this protocol requires no special skills and addresses two scientific fields: developmental biology, to answer morphogenesis-related questions with an advanced imaging technology, and optical physics and bioinformatics, in which *Tribolium* can be considered an appropriate model system for improving LSFM and developing algorithms for data analysis. The methodological principles are universal and the procedure should therefore be adaptable to other insect species or even species of other classes; we have successfully used these methods with *Drosophila* embryos (F.S., unpublished data).

Applications

We have shown that noninvasive long-term fluorescence live imaging of *Tribolium* embryos at cellular resolution can be achieved. We assume that our protocol will be of use in the scenarios described below.

Wild-type embryogenesis. Description and analysis of *Tribolium* wild-type embryogenesis by live imaging provides the framework for further studies. On a broader scale, the characterization of *Tribolium* embryogenesis can be approached systematically. Data acquired with LSFM is a key element to establish an image depository and database for *Tribolium*. Similar databases³⁰ have already been established for the fruit fly *D. melanogaster* (<http://flybase.org>)^{31,32} and the nematode *Caenorhabditis elegans* (<http://www.wormatlas.org>, <http://www.wormimage.org>), as well as the two most commonly used vertebrate model organisms, zebrafish (<http://zfatlas.psu.edu>) and mouse (<http://www.emouseatlas.org>)^{33,34}. These projects allow storage and exchange of information, the construction of digital atlases³⁵ and analyses of complex patterns during embryogenesis.

Developmental aberration. As already shown with confocal fluorescence microscopy^{12,13}, imaging embryos with altered gene and protein functions by RNAi gene knockdown provides morphogenetic insights. The iBeetle project (<http://ibeetle-base.uni-goettingen.de>) offers a comprehensive database of RNAi phenotypes in *Tribolium*^{36,37}. In addition, mutant strains and phenotypes induced with chemical compounds also provide observable specimens. Nuclease-based gene editing tools (e.g., CRISPR/Cas9 nuclease^{38–41}) might also be used, as has been shown in *Drosophila*^{42,43}. However, interference with wild-type development may weaken the resistance of the embryo to physical stress and some phenotypes might, therefore, be incompatible with the mounting method presented in this protocol. In such cases, alternative mounting methods should be considered^{44–46}.

Quantitative data analysis. The high recording speed and the optical sectioning capability of LSFM generate high-quality images, from which quantitative information is easily extracted.

PROTOCOL

Only a few simple data processing steps are necessary to perform basic quantitative analyses with the raw data (e.g., the decrease of the serosa window area over time during the transition from gastrulation to germ band elongation can be determined as illustrated in **Supplementary Fig. 2**). In addition, LSFM lends itself to advanced quantitative analyses of cell dynamics in developing multi-cellular organisms, enabling the investigation of complex processes in biological systems. High-quality fluorescence live imaging with LSFM provides the essential data to map individual cell lineages during key developmental processes of tissue formation or even full embryogenesis^{47–49}.

Limitations

Embryo positioning. Our mounting principle is designed to optimize the image recording process, as described in detail in the Experimental design section. This means that only sagittal and coronal optical sections of the embryo benefit from the high lateral resolution, whereas the transverse sections have to be calculated from the raw data and suffer from an axial resolution that is approximately four times lower⁵⁰. To overcome this limitation, the mounting method should be modified, or alternative approaches should be considered^{44–46}.

Throughput. The biggest limitation of our protocol is its low throughput. Currently, a maximum of two long-term imaging experiments per week can be performed at an imaging temperature of 35 °C, and only one experiment per week at room temperature (23 ± 1 °C). An adaptation of the mounting procedure that keeps more than one embryo in one microscope is possible, but it can affect image quality and temporal resolution. Alternatively, multiple microscopes can be used to increase the number of experiments per week. Depending on the overall setup, several components (e.g., a single laser source) can operate in multiple microscopes²⁵. Another option is the use of LSFM variants that are capable of high-throughput imaging by moving object slides or multi-well plates through the light sheet^{51,52}. However, some key features of LSFM, such as sample rotation, might be hampered in such setups. The number of experiments that can be performed is also dependent on the amount of available data storage space, but data volume can be drastically reduced by modern data compression algorithms, as indicated in the Experimental design section.

Experimental design

Generation and/or choice of fluorescent line. The generation and/or choice of the fluorescent transgenic line depends on the experimental question and should be compatible with long-term fluorescence live imaging in LSFM. Currently, the EFA-nGFP line¹⁰ is the only available transgenic line specifically designed for live imaging. However, transformation protocols for the creation of stable transgenic lines exist^{8,53}, and transient labeling of cell compartments can be achieved by mRNA¹² or dye injection¹⁶. In addition, the GEKU project (<http://www.geku-base.uni-goettingen.de>) has resulted in a large number of enhancer trap lines⁵⁴ that can be investigated or chosen appropriately for a diverse number of experiments¹⁴. Multiple criteria should be considered when deciding on an appropriate transgenic line, including:

- **Promoter.** The promoter should drive marker expression in a temporally and spatially relevant set of cells. Previous research has indicated that endogenous promoters are preferable⁵⁵.

Because the *Tribolium* genome has been sequenced⁶, promoter sequences are easily obtained and multiple endogenous *Tribolium* promoters have been characterized, including the ubiquitous α -tubulin 1 promoter⁵⁶, the polyubiquitin promoter⁵⁷ and the heat-shock-inducible HSP68 promoter⁵⁸.

- **Protein localization.** A tag, protein fragment or protein has to be chosen that is responsible for the intracellular localization of the protein. The resulting fusion protein should not cause detrimental effects^{59,60}. Three subcellular localization tags have already been proven to work properly in *Tribolium*: the nuclear localization sequence derived from the SV40 virus¹⁰, the actin-labeling peptide Lifeact derived from *Saccharomyces cerevisiae*¹², and the plasma membrane anchor from the human GAP43 protein¹².
- **Fluorescent protein.** The excitation and emission maxima of the chosen fluorescent protein should be as close as possible to the excitation wavelength of the laser and the transmission window of the emission filter, respectively. Especially for long-term live imaging, the photobleaching characteristics of fluorophores are important. Multiple reviews have summarized the characteristics of a broad arsenal of fluorescent proteins, which span emission wavelengths from the blue to the IR^{60–62}. The Nikon Imaging Center (<http://nic.ucsf.edu/FPvisualization>) provides a comprehensive interactive graph of fluorescent protein properties.
- **Transgenic line genotype.** when working with fluorescent transgenic lines, we recommend a line that is homozygous for one transgene insert. A homozygous transgenic line simplifies culture handling, reduces experimental variability, and should reach a higher fluorophore expression level.

Imaging start point. The egg-laying period and subsequent incubation time (Step 2 of the PROCEDURE) determine the developmental stage of the *Tribolium* embryo at the beginning of the imaging process. Our standard imaging starting point is defined by a 1-h egg-laying period/15 h of incubation at 25 °C and 1 h of preparation at room temperature. This results in embryos that are at the uniform blastoderm stage at the onset of imaging and provides a good starting point for lines that express a fluorophore under the control of a ubiquitous promoter or embryos that were injected with fluorophore-coding mRNA or fluorescent dyes. If a process that occurs later during embryogenesis is imaged, the incubation period is extended accordingly. When lines express a fluorophore only during a temporary limited developmental window, we recommend initiating the imaging process a few time points before the onset of fluorophore expression and to end it is a few time points after fluorophore expression stops. For convenience, we provide a staging table for five important embryogenetic events: gastrulation, germ band elongation, germ band retraction, dorsal closure and the muscular movement phase (**Supplementary Fig. 3**).

Embryo mounting. In the initial LSFM publications, established model organisms such as *D. melanogaster*^{17,19} and zebrafish^{17,18} were used and their embryos were embedded in an agarose column inside a glass capillary. The capillary was inserted into the microscope and the column was partially pushed out of the glass capillary into the imaging buffer. The complete embedding of the sample into agarose has several limitations, which have led to the development of improved sample mounting techniques. For example, embedding in agarose spatially restricts growth at later stages of zebrafish development. This limitation has been

overcome by embedding zebrafish embryos in very low concentrations of agarose inside fluorinated ethylene propylene tubes⁶³. Similarly, explanted mouse embryos cannot be cultured when embedded in conventional agarose columns and instead need to be covered with Reichert's membrane and placed in pockets of an acrylic rod^{64,65}. We have encountered similar problems with *Tribolium* embryos, which we overcame by changing the mounting principle²⁰. The mounting method that we present differs substantially from previous strategies. Instead of completely embedding the embryo in agarose, we mount a minimal portion of the anterior end onto the pole of an agarose hemisphere, leaving the majority of the embryo surface safely exposed to the imaging buffer. This mounting principle reduces the stress on the embryo and maximizes direct contact between the embryo surface and the imaging buffer, thereby facilitating gas exchange while providing unobstructed observation of the embryo *in toto* along arbitrary directions. Due to the intrinsic rigidity of the sample holder, the mechanical stability and thus spatial precision is high even during long-term imaging experiments. In addition, the embryo survives the imaging procedure, is retrieved easily from the microscope and is raised to a fully functional and fertile adult. Our mounting principle was specifically designed to ensure optimal recording. By aligning the elongated anterior–posterior axis with the rotation axis, only the dorso-ventral and lateral axes, which are shorter by approximately a factor of two, are aligned with the detection axis. This is even true for imaging assays that record the embryo along multiple directions. The benefits, especially for *in toto* recordings, are the distances covered by the illumination and excitation light through organic material are minimized, and, as a stack of images is recorded plane by plane along the detection axis by moving the embryo through the light sheet, the thickness of the embryo along the detection axis determines the maximum recording frequency and thus the minimal temporal interval.

Imaging options. Depending on the experiment, different imaging setups can be used (see **Table 1**). The options listed below can also be combined.

- **Temperature.** We image embryos either at 35 °C with the incorporation of a perfusion system, or at room temperature.

Both temperatures were chosen for practical reasons: embryos develop more quickly at 35 °C, thereby maximizing the number of experiments that can be conducted within a given time, whereas imaging at room temperature does not require any additional equipment such as a perfusion system. The following alternative temperature conditions have already been successfully used for *Tribolium* live imaging: 21–25 °C (ref. 13), 23.5 ± 1 °C (ref. 14), 25–32 °C (ref. 13), 26–28 °C (ref. 11), 30 °C (refs. 10,14), and 32 °C (ref. 12). The perfusion system can be used at Step 6 of the PROCEDURE.

- **Illumination.** Embryos can be imaged using uniform illumination or structured illumination. Structured illumination reduces the amount of blur from out-of-focus structures. In dense regions (e.g., the germ band), the application of structured illumination leads to an increased image contrast, allowing a better distinction between individual cell nuclei. The basic idea of incoherent structured illumination in LSM has been described previously⁶⁶. Imposing a sinusoidal pattern on the image during the illumination process allows to estimate the background in the image since the entire range of gray levels is explored. Three to five images are usually recorded and each pixel is replaced by the s.d. of its intensities. The intensities now cover the entire range from zero to the maximum intensity in the original image. Obvious effects are that the contrast improves and featureless blurry sections in an image become dark. Structured illumination can be implemented on the software level and should be considered at Step 39 of the PROCEDURE.
- **Objective/camera combination.** Imaging using a 10× objective/charge-coupled device (CCD) camera combination versus imaging using a 20× objective/scientific complementary metal–oxide–semiconductor (sCMOS) camera combination. Image volumes obtained with a 20× objective and a high-resolution sCMOS camera provide an up to eight-fold higher spatial resolution compared with image volumes recorded with a 10× objective and a CCD camera. This effect is due to the fact that the larger chip size of the sCMOS camera results in a similar field of view when combined with an objective of higher magnification. This option is valuable if subcellular processes are of interest. The choice for the appropriate objective/camera combination is made at Step 4 of the PROCEDURE.

TABLE 1 | Summary of imaging options.

Option	Advantages (+)/disadvantages (-)	Rationale
Imaging at room temperature (Fig. 10)	<ul style="list-style-type: none"> + Higher relative temporal resolution + Higher efficiency of fluorescent proteins⁷⁵ + No perfusion system (or other heating system) required - Duration for embryogenesis approximately tripled^{4,76} - Lower survival rate^{4,56} 	<ul style="list-style-type: none"> • Detailed observation of morphogenesis • Use of short-term imaging • Not recommended for high-throughput long-term imaging
Structured illumination (Fig. 11)	<ul style="list-style-type: none"> + Higher contrast in focal plane¹⁹ + Reduced background in dense regions¹⁹ - Higher laser energy exposure - Longer recording time 	<ul style="list-style-type: none"> • Required for accurate segmentation • Not recommended for high temporal resolution and long-term imaging
20× objective/sCMOS camera combination (Fig. 12)	<ul style="list-style-type: none"> + Higher spatial resolution - Longer recording time - Larger data volume 	<ul style="list-style-type: none"> • Required for accurate segmentation • Not recommended for high temporal resolution and long-term imaging



PROTOCOL

Imaging setup. Multiple parameters must be considered for imaging. The duration and interval of the time lapse have to suit the experimental question. The required number of channels has to be selected, and laser power as well as exposure time have to be adjusted to obtain sufficient signal and minimal photo-bleaching. The number of directions along which Z-stacks are recorded must provide sufficient coverage of the embryo. Refer to **Box 1** for guidelines on how to choose appropriate imaging parameters.

Controls. Especially for long-term imaging, stringent quality controls are indispensable. Therefore, we highly recommend that two important controls (**Supplementary Fig. 4**) be included in each experiment aimed at studying wild-type development (for experiments that disturb development, alternative controls will need to be chosen): non-imaged fluorescent embryos of the same line and genotype as the imaged embryos, taken from Step 15 of the PROCEDURE; and non-imaged wild-type embryos of the same background strain, collected in parallel at Step 1 of the PROCEDURE. Incubation conditions for embryos of both controls should be synchronized with the imaged embryo. After embryo retrieval and hatching, as described from Steps 41 to 44,

the imaged larva (that developed from the imaged embryo) can be compared with both controls. Important points that should be considered are:

- The development time of the imaged fluorescent embryo and the fluorescent control embryos should be identical and hatched larvae should exhibit approximately the same fluorescence intensity. A substantial delay in development time and/or a reduced fluorescence intensity of the imaged larva indicates that the integrated energy load over time was too high.
- The development time between the imaged fluorescent embryo, the fluorescent control embryos and the wild-type control embryos should be identical. A significant delay in the development time of the fluorescent embryos compared with the wild-type control embryo indicates that fluorophore expression during development might decelerate certain processes (e.g., by consuming nutrients or by production of stress factors such as reactive oxygen species).
- After hatching, the morphology of the imaged fluorescent larva, the fluorescent control larvae, and the wild-type control larvae should be similar. A difference in morphology indicates that the energy exposure over time was too high.

Box 1 | Parameters of LSFM and their impact on data set size and the energy exposure of the embryo

- The number of planes (N_{PL}) in a Z-stack depends on the objective/camera combination. A minimum of 125 planes with a 10× objective/CCD camera combination and a minimum of 250 planes with a 20× objective/sCMOS camera are required to cover the complete embryo. We recommend recording at least 25 empty planes as a buffer in front and behind the embryo. For the Z spacing, we use four times the XY spacing (i.e., the pixel pitch) to achieve the maximal axial resolution⁵⁰.
- The number of channels (N_{CH}) depends on the number of labeled structures that are imaged simultaneously and is usually between one and six. Each channel i is characterized by two parameters, the laser power (P_i) and the camera exposure time (T_i). We recommend a camera exposure time between 50 and 100 ms to ensure a high recording speed. The laser power should be set accordingly to obtain a sufficient signal-to-noise ratio.
- The number of directions (N_{DR}) depends on the desired angular coverage of the region of interest. For some experiments, one direction is sufficient. A fair coverage of the whole embryo is achieved by imaging along at least four directions (**Supplementary Fig. 10**).
- The number of time points (N_{TP}) is the total imaging duration divided by the temporal interval between individual recordings plus one. The total imaging duration is set according to the investigated developmental process, whereas the temporal interval defines the temporal resolution. Imaging complete embryogenesis for 120 h at room temperature with a temporal interval of 30 min results in 241 time points.

The parameter settings have two important consequences: first, they determine the total number of acquired images, and second, they account for the energy exposure on the embryo. The total number of images (N) is calculated as:

$$N = N_{PL} \times N_{CH} \times N_{DR} \times N_{TP}$$

For exemplary data set DS0001 (**Supplementary Table 1**) this corresponds to 34,300 images. The total number of images determines the hard disk space that is required. Images recorded with the 10× objective/CCD camera combination results in images with a size of 2.76 Megabytes, and the 20× objective/sCMOS camera combination results in images with a size of 10.5 Megabytes (TIFF, uncompressed).

A biological specimen can only be exposed to a certain amount of light without affecting its viability²³. This has to be considered when performing long-term fluorescence live imaging. As a theoretical maximal limit for the energy exposure (E) on the embryo we get:

$$E = N_{PL} \times \sum_{i=0}^{N_{CH}} P_i T_i \times N_{DR} \times N_{TP}$$

For exemplary data set DS0002 (**Supplementary Table 1**) this corresponds to an energy exposure of <1 J over the course of 120 h. In our experience, embryos can tolerate an up to a tenfold-higher energy amount without affecting viability.

For a final quality control, the imaged larva and multiple fluorescent control larvae are raised until adulthood. The imaged fluorescent adult is afterwards crossed with a fluorescent control adult to check if the imaged fluorescent adult retains its fertility. Fluorescence live imaging is always accompanied with a certain influence (i.e., the energy exposure) on the embryo, especially during long-term fluorescence live imaging. By ensuring healthy development and fertility of the imaged fluorescent adult, the impact of fluorescence live imaging can be considered noninvasive.

Data architecture and processing. The data acquired by long-term live imaging in LSM usually explore many dimensions, and the typical data storage format is the tagged image file format (TIFF). The first (*X*) and second (*Y*) spatial directions are saved as a TIFF file. The number of planes (N_{PL}) represents the third spatial dimension (*Z*) and defines together with the first and second spatial dimensions the imaging volume. For convenience, planes are saved as a *Z*-stack in one TIFF file by using the intrinsic container function. All further dimensions are typically saved as individual files: the number of channels (N_{CH}), the number of directions (N_{DR}) and the number of time points (N_{TP}). For data visualization, we suggest a straightforward processing procedure that simplifies the raw data by removing one spatial dimension (i.e., computation of maximum projections), compensates for fluorescence intensity changes over time, and allows the user to evaluate the assay. The processed data is of publication quality and can be used in post-processing steps such as figure or video production. For advanced qualitative analyses and visualization, standards for LSM data post-processing have been established during the past few years: imaging along multiple directions allows subsequent registration and fusion into a single 3D image^{67,68}, image deconvolution can be applied to improve the resolution^{67,69}, and 3D volume and surface rendering help with data visualization^{20,70}. Depending on the scope of the experiments and the required processing procedures, well-equipped personal computers are suitable to perform all necessary data processing steps. However, depending on the raw data volume and the steps involved, processing can be very time consuming, and some processing steps have to run overnight or even for several days. Because the computer cannot be used for other purposes during processing, laboratories that generate large amounts of

data should invest in high-performance workstations that handle the bulk of data processing. Example hardware setups are provided in the Equipment section.

Data storage. Imaging single embryos with LSM generates data volumes that exceed previous standards (Box 1). The raw data volume can be drastically reduced on different levels:

- Cropping the generated raw data along *X*, *Y* and *Z* to cover solely the region of interest with a sufficient amount of background for subsequent processing steps. For many automated image processing steps (e.g., deconvolution, filtering and segmentation), a certain amount of remaining background information is indispensable.
- It might be sufficient to work with data of reduced dynamic range (i.e., fewer bits). Although the cameras provide a dynamic range of up to 14 or 16 bits, recording the data with a dynamic range of 8 bits or less is often sufficient. As intensity measurements are based on a Poisson process, it also suffices to store the square root of the signal⁷¹.
- TIFF provides the option to perform lossless data compression (e.g., ZIP or LZW).

In our experience, this reduces the data volume to ~40–10%. Moreover, we found that lossy JPEG2000 compression of single planes leads to a considerable reduction to <1% of the raw data volume without disturbing the relevant features of the data. For example, dataset DS0001 could be reduced from a raw data volume of 92 converted to 37 GB (40%) with lossless ZIP and to 0.47 GB (0.5%) with lossy JPEG2000 compression. For the other two example data sets, similar compression rates were obtained (Supplementary Table 1). For recording several long-term data sets of *Tribolium* embryos we suggest a minimum of 12 TB of data storage capacity to store the raw data, the temporarily generated files during processing, and the processed images. However, the capacity should be increased to at least 36 TB for larger laboratories or experiments that need a larger number of conditions or repetitions. The data storage should ideally be connected to: the computer that operates the LSM, high-performance workstations or servers to process the raw data, and personal computers for post processing the data. In addition, many universities and institutions provide a service for long-term archiving of data.

MATERIALS

REAGENTS

- Fluorescent *T. castaneum* line (e.g., the EFA-nGFP transgenic line¹⁰, which expresses nuclear-localized S65T-GFP under control of the elongation factor 1 alpha 1 subunit promoter ubiquitously throughout embryonic development. Alternatively, *Tribolium* embryos can be injected with fluorophore-encoding mRNA or fluorescent dyes (see the Experimental design section)
- Full grain wheat flour (Demeter, cat. no. 113061036)
- 405 fine wheat flour (Demeter, cat. no. 113061006)
- Inactive dry yeast (Flystuff/Genesee Scientific, cat. no. 62-106)
- PBS, pH 7.4 (Gibco Life Technologies, cat. no. 10010-023)
- Sodium hypochlorite (NaOCl, bleach), 12% (wt/vol) active Cl (Sigma-Aldrich, cat. no. 425044-250ML) **! CAUTION** Sodium hypochlorite is corrosive. Wear personal protection such as gloves and goggles. **▲ CRITICAL** The quantity of active chlorite in sodium hypochlorite decreases over time. Solutions should only be used for up to 6 months.
- Low-melt agarose (Carl Roth, cat. no. 6351.2)

- Fluorescent beads, diameter 1.0 μm (Life Technologies, cat. no. T-7282) **▲ CRITICAL** We recommend using beads from this supplier, the quality (shape and size of the beads, concentration, fluorescence intensity) is outstanding and well-suited as the ground truth during LSM calibration.
- Six-well plate (Orange Scientific, cat. no. 4430500)
- Glass coverslips, 5 mm × 5 mm (Gerhard Menzel/Thermo Fisher Scientific, customized)
- Glass capillaries, 125 mm length, external diameter 1.25 mm, internal diameter 0.46 mm, 10 μl volume (Brand, cat. no. 7087 09)
- Object slides, 76 mm × 26 mm (Carl Roth, cat. no. 1879.1)

EQUIPMENT

- LSM, e.g., a DSLM⁷² (see Equipment Setup section), or a Lightsheet Z.1 (Carl Zeiss)
- Data storage system, e.g., a file server with at least 12 TB of storage capacity in RAID 5/6 and a 10 G/s network interface **▲ CRITICAL** For extensive usage of LSM, we recommend a throughput-optimized storage system with even more storage capacity in RAID 10 with SSD caching and



PROTOCOL

multiple ≥ 10 G/s network or fiber channel interfaces connected to one or more image processing servers using multipath I/O.

- Well-equipped personal computer, e.g., a quad-core CPU (Intel Core i7-4er series, Intel Corporation), 16 GB of DDR3 memory, and 2 TB of internal HDD data storage. Additionally, many processing steps can be accelerated using GPU computing. Therefore, we suggest the use of graphics cards with adequate performance (e.g., GeForce GTX 650 (NVIDIA))
- ▲ **CRITICAL** For accelerated data processing, we recommend high-performance workstations, e.g., hexa-core or octa-core CPUs (Intel Core i7-5er series, Intel Corporation), at least 96 GB of DDR3 memory, and 5 TB of internal HDD data storage. Additionally, we suggest the use of high-performance graphics cards (e.g., Quadro K6000 or Tesla K40 (NVIDIA)).
- Stereomicroscope with fluorescence unit, e.g., Discovery.V8 (Carl Zeiss)
- Appropriate filter set for the stereomicroscope, e.g., a GFP filter set (FS38, Carl Zeiss)
- Insect incubator with light/temperature/humidity control (Percival Scientific, cat. no. DR-36VL)
- Sieve, 800- μ m mesh size (VWR International, cat. no. 200.025.222-051)
- Sieve, 710- μ m mesh size (VWR International, cat. no. 200.025.222-050)
- Sieve, 300- μ m mesh size (VWR International, cat. no. 200.025.222-040)
- Sieve, 250- μ m mesh size (VWR International, cat. no. 200.025.222-038)
- Cell strainer, 100 μ m (BD Biosciences, cat. no. 352360)
- Laboratory bottle, 250 ml (neoLab Migge Laborbedarf-Vertriebs, cat. no. E-2058)
- Glass Petri dish, diameter 100 mm \times 20 mm (Corning Soda Lime Silica, Sigma Aldrich Chemie, cat. no. CLS70165102)
- Syringe, 1.0 ml (Injekt-F, B. Braun Medical, cat. no. 9166017V)
- Paint brush, 9-mm length, head diameter 2 mm (VWR International, cat. no. 149-2121)
- Steel cylinder, diameter 3 mm (Presch Edelstahl Service, cat. no. V2A 1.4301/ASTM AISI 304) ▲ **CRITICAL** We recommend steel cylinders made out of inert material such as stainless V2A or V4A steel.
- Steel pipe, external diameter 3 mm, internal diameter 1 mm (Sawade Edelstahlrohre/Edelstahlrohrbogen, cat. no. R00306) ▲ **CRITICAL** We recommend steel pipes made out of inert material such as stainless V2A or V4A steel.
- Thermo mixer (Thermomixer Comfort, Eppendorf)
- Microwave oven, 800 W
- Fiji (<http://fiji.sc/> version 1.48o, or higher)⁷³
- Mathematica (Wolfram Research; <https://www.wolfram.com/>; version 9.0.1, or higher)

REAGENT SETUP

Stock medium preparation Incubate full-grain wheat flour and inactive dry yeast for at least 24 h at -20 °C, then pass both through a sieve with 710- μ m mesh size, and discard leftovers. Supplement sieved full grain wheat flour with 5% (wt/wt) sieved inactive dry yeast. Stock medium can be stored at room temperature; the maximum storage duration complies with the expiry date of the full grain wheat flour and the inactive dry yeast.

Egg-laying medium preparation Incubate 405 fine wheat flour and inactive dry yeast for at least 24 h at -20 °C, then pass both through a sieve with a 250- μ m mesh size, and then discard the leftovers. Supplement sieved 405 fine wheat flour with 5% (wt/wt) sieved inactive dry yeast. Egg-laying medium can be stored at room temperature; the maximum storage duration complies with the expiry date of the 405 fine wheat flour and the inactive dry yeast.

Dechoriation six-well plate preparation Pipette 10 ml of PBS into wells A1, A2, A3 and B3, and 9-ml PBS into B1 and B2, then add 1 ml of sodium hypochlorite to B1 and B2 for a total volume of 10 ml to obtain a 10% (vol/vol) sodium hypochlorite in PBS solution. For each experiment, freshly prepare the dechoriation six-well plate. ▲ **CAUTION** Sodium hypochlorite is corrosive. Wear personal protection such as gloves and goggles.

Mounting agarose preparation Add 1 g of low-melt agarose to a 250-ml laboratory bottle, then pipette 100-ml PBS into the bottle. Heat the mixture for ~ 90 s in a microwave oven at 800 W. Interrupt heating from time to time to swirl the mixture. Fill a 1.5-ml reaction tube with agarose and place it in a thermomixer at 40 °C until required. The remaining mounting agarose in the laboratory bottle will solidify during the cooling process. The solidified agarose can be stored for up to 3 months at room temperature, but should not be reused more than two or three times, as it becomes too viscous.

▲ **CRITICAL** Be sure to completely dissolve the agarose, but not to

overheat the mixture too much, as this causes the water to evaporate and increases the ratio of agarose to liquid.

Agarose-embedded beads column preparation Fill a 1.5-ml reaction tube with 98 μ l of mounting agarose, then add 2 μ l of fluorescent beads to the mounting agarose. Mix at 1,400 r.p.m. in a thermomixer at 40 °C for 10 min. Draw the agarose bead mixture into the glass capillary by using a modified syringe and a rubber hose (see Equipment Setup). Set the capillary aside for 15 min to allow the agarose to solidify. Use the capillary directly or store it in PBS. Agarose-embedded bead columns can be stored in PBS for up to 2 months at 4 °C, but they need to be protected from light.

EQUIPMENT SETUP

T. castaneum stock culture For general *Tribolium* culture handling, please refer to previous literature⁴; the following description serves only as a minimalistic guideline. Working cultures are incubated in stock medium in a 12-h light/12-h darkness cycle at 25 °C and 70% relative humidity. Keep working cultures at sizes of ~ 300 adult beetles, which are ideally not older than 4 months. Change stock medium weekly, ideally 24–48 h before embryo collection. While changing the stock medium, remove dead adults. Keep the removed medium to grow daughter cultures. If the working culture becomes too old, replace it with a daughter culture. Always keep a stock in parallel to the working cultures.

Light-sheet-based fluorescence microscope Our LSM instrument is a monolithic digital scanned laser light-sheet-based fluorescence microscope (mDSLm), which is comparable to the DSLM⁷². A scheme of the DSLM operating principle is provided in **Supplementary Figure 5**. For ease of use, we define three axes as follows: the illumination axis is defined as X, the rotation axis as Y and the detection axis as Z. When appropriate, axes are indicated in relevant figures. The illumination laser light source is a 488-nm/60-mW diode laser (SOLE-3/PhoxX 488-60, Omicron Laserprodukte) with a 488-nm cleanup filter (xX.F488, Omicron Laserprodukte). The laser beam is guided by a single-mode fiber (kineFLEX-P-2-S-405.640-0.7-1.5-P2, Qioptiq Photonics) and scanned with a two-axis piezo scanning mirror (S-334.2SL, Physik Instrumente) through a telecentric pair of f-theta lenses (S4LFT0061/065, Sill Optics) and a tube lens (425308-0000-000, Carl Zeiss) into a 2.5 \times numerical aperture (NA) 0.06 EC Epiplan-Neofluar objective (422320-9900-000, Carl Zeiss), thereby creating the dynamic light sheet that is used for fluorophore excitation. We use two setups for detection: a 10 \times NA 0.3 W N-Achroplan objective (420947-9900-000, Carl Zeiss) with a high-resolution CCD camera (Clara, Andor) or a 20 \times NA 0.5 W N-Achroplan objective (420957-9900-000, Carl Zeiss) with a high-resolution sCMOS camera (Neo 5.5, Andor). In both cases, the emission light is guided through a 525/50 single-band band-pass filter (FF03-525/50-25, Semrock/AHF Analysentechnik) inside a six-slot filter wheel (Compact Wheel 96A351, Ludl Electronic Products) and a tube lens (425308-0000-000, Carl Zeiss).

All objectives are moved via piezo nanopositioners (PIFOC P-725.4CD, Physik Instrumente). Holders are moved along X, Y and Z via three compact micro-translation stages (M-111.2DG, Physik Instrumente) and rotated around Y with a precision rotation stage (M-116.DG, Physik Instrumente). Optical elements and building units have been described previously⁷⁴. The rotation stage is equipped with a clamp mechanism that accepts 3-mm-diameter cylindrical elements (i.e., the holders that are created from the steel cylinder and the steel pipe). Please note that the cylindrical elements have to be trimmed to an appropriate length so that the glass coverslip, the agarose-embedded bead column and the embryo can be positioned in the field of view of the detection objective with the micro-translation stages.

Temperature control Imaging can be performed at room temperature. A perfusion system can be optionally used to adjust the temperature of the PBS (**Supplementary Fig. 6**). The perfusion system should be installed in Step 6 of the PROCEDURE.

Glass coverslip holder The glass coverslip has to be attached to the steel cylinder in order to insert it into the sample chamber and redirect the laser beam in Steps 8–11 of the PROCEDURE. For this, a half cylinder (length 2 mm) is cut out of the steel cylinder (**Supplementary Fig. 7a**). The glass coverslip is glued to the flat rectangular area (**Supplementary Fig. 7b**) to create the glass coverslip holder.

Capillary holder To partially push the agarose-embedded beads column out of the capillary fragment in Step 12 of the PROCEDURE, the steel cylinder is equipped with a short pin (diameter 0.46 mm,

length 4–5 mm) along the cylinder axis to create the capillary holder (Supplementary Fig. 7d, left). The glass capillary should fit tightly onto the pin (Supplementary Fig. 7d, right).

Modified syringe preparation A modified syringe is used to create the agarose hemisphere in Step 24 of the PROCEDURE. A crystal pipette tip and the piston of the syringe are trimmed (Supplementary Fig. 7e). The trimmed pipette tip is inserted into the back opening of the syringe and pushed with the piston into the front opening (Supplementary Fig. 7f, top). A rubber hose attached to the modified syringe (Supplementary Fig. 7f, middle) connects a glass capillary to the syringe. (Supplementary Fig. 7f, bottom). The syringe with the attached rubber hose is used during the agarose-embedded beads column preparation process (see Reagent Setup).

Humidity chamber After its retrieval from the microscope, the embryo is incubated on an object slide in a humidity chamber to monitor embryo survival and hatching (Supplementary Fig. 7g). The humidity chamber consists of a scaffold created from serological pipette fragments in a glass Petri dish that keeps the object slide above the PBS reservoir (Supplementary Fig. 7h).

Data processing hardware and software Batch image processing was performed using custom code written in the open source software FIJI⁷³, version 1.48o and Mathematica, versions 9.0.1, 10.0.0 and 10.0.2. The custom code is provided as Supplementary Scripts 1 and 2; alternatively, it can be downloaded at <https://www.physikalischebiologie.de/bugcube>. The workstation to perform image processing comprises two six-core CPUs (X5650, Intel Corporation), with 96 GB of DDR3 memory and running Windows Server 2012 R2.

PROCEDURE

Embryo collection ● TIMING 70 min + 15 h incubation

1| Pass adult *Tribolium* cultures in whole wheat flour through a sieve with an 800- μ m mesh size to separate adults from the flour. Set up an egg-laying culture by transferring adults into a new culture bottle and covering them with 10 g of egg-laying medium. Allow adults to deposit embryos for 1 h at 25 °C and 70% relative humidity in light.

▲ **CRITICAL STEP** In addition to any fluorescent lines used for imaging, also collect wild-type control embryos from the same background strain as the fluorescent line to enable a comparison of larval morphology after hatching at Step 43. Incubation conditions of the experimental fluorescent embryos and wild-type control embryos should be similar. For further information, see the Experimental design section of the INTRODUCTION.

2| Pass the egg-laying culture through a sieve with an 800- μ m mesh size to separate adults from the medium containing the newly laid embryos. Transfer adults back to the culture bottle. Incubate the embryos for 15 h (overnight) at 25 °C and 70% relative humidity in the egg-laying medium.

▲ **CRITICAL STEP** After a 1-h egg-laying period, 15 h of incubation at 25 °C and 1 h of preparation at room temperature, the embryos have reached the uniform blastoderm developmental stage. The incubation time should be adjusted depending on the experimental setup, e.g., if a specific embryonic event is to be imaged or a fluorescent line with a temporally restricted expression pattern is used. For further information, see the Experimental design section of the INTRODUCTION.

LSFM calibration ● TIMING 30 min

▲ **CRITICAL** The following calibration protocol is suitable for LSFMs with a scanned laser such as the mDSL (Fig. 2a–c, Supplementary Fig. 5), whose construction and technical background have been described previously^{19,72}. The protocol can be adapted to suit other LSFM types. Please be aware that proper LSFM calibration is crucial for obtaining reliable image quality. Therefore, we provide a two-stage calibration routine (visualization of the light sheet and test recording of an agarose-embedded beads column). Steps 3–14 can be performed while the embryos incubate. If any advanced imaging options (e.g., structured illumination, dual-sided illumination) are to be used, we recommend that their functionality is tested at this point.

3| Turn on the microscope and the computer. Start the appropriate software and wait for its initialization.

4| Attach the 2.5 \times objective into the illumination piezo nano-positioner and either the 10 \times or the 20 \times objective into the detection piezo nano-positioner. Install either the CCD or the sCMOS camera, respectively (see Experimental design section and Table 1).

5| Attach the sample chamber to the microscope and fill it with dH₂O to check for leakage (Fig. 2a–c).

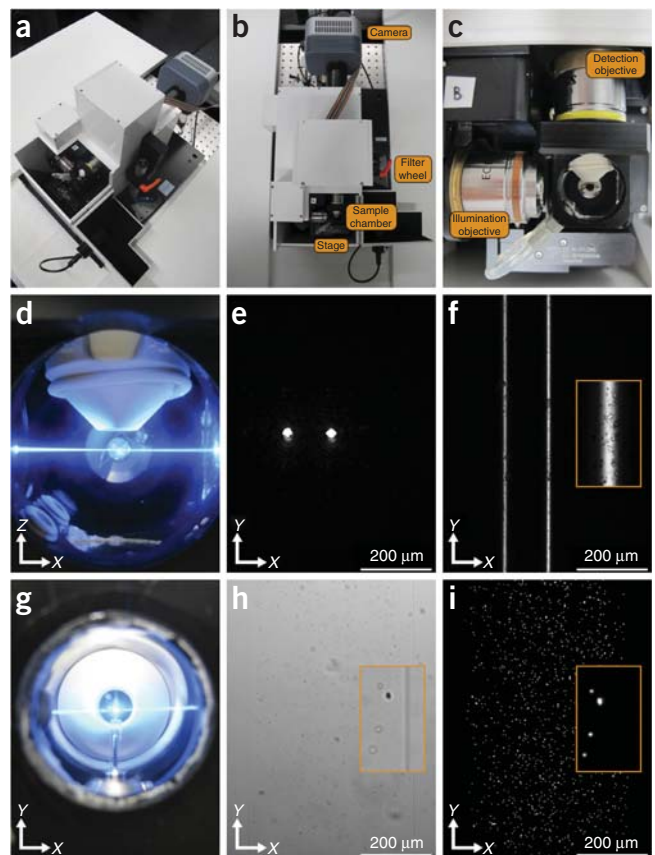
▲ **CRITICAL STEP** If leakage occurs, remove the water, unscrew the chamber, check the sealing and replace it if necessary, and then reattach the sample chamber to the microscope.

6| Remove the dH₂O from the sample chamber and fill it with PBS. Optionally, if an alternative temperature condition should be used, install the perfusion system before filling the sample chamber with PBS (Supplementary Fig. 6).

7| Insert the glass coverslip holder into the sample chamber and align the glass coverslip perpendicular to Z (the detection axis). Turn the laser on, switch to the fluorescence channel and deselect the emission filter.

PROTOCOL

Figure 2 | LSFM instrument calibration. (a) Top front right view of the mDSL. (b) Top view of the mDSL. Important elements are indicated. (c) Detailed top view of the sample chamber. Illumination and detection objectives are indicated. (d) Top view of the sample chamber with glass coverslip holder and laser beam. The glass coverslip holder is rotated by 45° relative to X and Z . A fraction of the laser beam is thus reflected along Z into the detection objective. (e) Laser beam reflection resulting in a static bright dot in the center of the field of view. The second dot (on the left) can be ignored. (f) Dynamic light sheet obtained by activating the scanning mirror. The light sheet height should extend $\sim 20\%$ over the field of view along Y so that the light sheet appears uniform. The width of the light sheet should be minimal, so that the light sheet appears focused along X (see detail). The second light sheet (on the left) can be ignored. (g) Front view of sample chamber with agarose-embedded beads column partially pushed out of the glass capillary fragment. (h) Transmission light image of agarose-embedded beads column. Detail box shows four beads on the right border of the column. (i) Z maximum projection of an agarose-embedded beads column Z -stack. Detail box shows the same four beads as shown in h.



8 | Rotate the glass coverslip holder by 45° around Y (the rotation axis) with the rotation stage (**Fig. 2d**, **Supplementary Fig. 7c**) so that a fraction of the laser beam is reflected along Z in the direction of the detection objective.

9 | Move the glass coverslip holder with the micro-translation stages along X (the illumination axis) until the laser beam is detected as a bright dot by the camera (**Fig. 2e**).

? TROUBLESHOOTING

10 | Move the bright dot with the micro-translation stages along X and with the scanning mirror along Y into the center of the field of view.

▲ CRITICAL STEP Reflection of the laser beam at the glass coverslip usually results in a second, weaker dot, because the beam is reflected twice, first at the PBS/glass transition, and again at the glass/PBS transition. The second dot can be disregarded.

11 | Activate the scanning mirror so that the laser beam forms the dynamic light sheet. Adjust the length of the light sheet until it extends $\sim 20\%$ over the field of view along Y . Minimize the width of the light sheet by moving the illumination objective with the piezo nano-positioners along X , then focus on the surface irregularities of the glass coverslip by moving the detection objective with the piezo nano-positioners along Z (**Fig. 2f**). Remove the glass coverslip holder from the sample chamber.

▲ CRITICAL STEP The second dot mentioned at Step 10 will form a second weaker light sheet, which can be disregarded.

? TROUBLESHOOTING

12 | Insert the capillary holder into the microscope. Take a glass capillary with the agarose-embedded beads column inside and cut off a fragment (length 7–9 mm) before fitting it on the pin (length 4–5 mm) of the capillary holder. The agarose-embedded beads column should be partially (3–4 mm) pushed out (**Fig. 2g**).

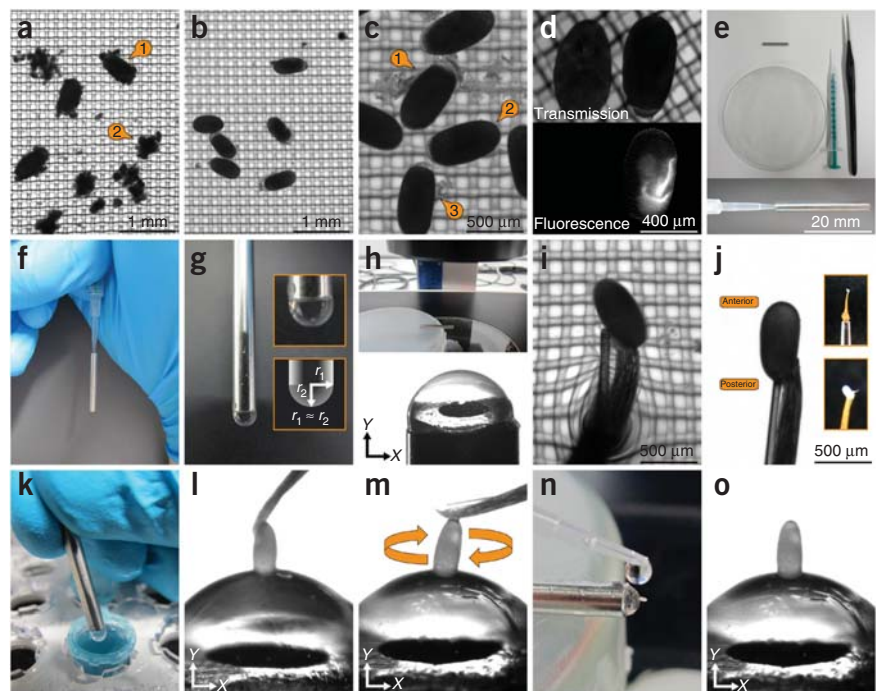
13 | Switch to the transmission light channel and move the column of agarose-embedded beads with the micro-translation stages along X and Y into the field of view. The capillary should not be visible in the field of view. Focus the borders of the agarose-embedded beads column by moving it with the micro-translation stages along Z (**Fig. 2h**).

14 | Switch to the fluorescence channel, select the appropriate emission filter, record a Z -stack, and compute the Z maximum projection (**Fig. 2i**). Optionally, also compute the X and Y maximum projections (**Supplementary Fig. 8**, first column). If imaging artifacts occur, repeat the calibration process from Step 7.

▲ CRITICAL STEP If the embryo is to be imaged along multiple directions, rotate the agarose-embedded bead column around Y using the rotation stage, and record a Z -stack for each respective direction. Check the Z , X and Y maximum projections for imaging artifacts (**Supplementary Fig. 8**).

? TROUBLESHOOTING

Figure 3 | Embryo preparation. (a) Embryos in the cell strainer in well A1 (PBS). After sieving the egg-laying medium (300- μ m mesh size sieve), (1) flour-covered embryos and (2) flour particles are obtained. (b) Embryos in well B1 (dechoriation solution). Flour is removed from the embryos and flour particles are degraded. (c) Embryos in well A3 (PBS). Three cases have to be distinguished: (1) incomplete dechoriation, (2) complete detachment of chorion from embryo and (3) small parts of the chorion still sticking to the embryo. Therefore, the embryos have to be checked carefully. (d) Distinction between non-fertilized (left) and fertilized (right) embryos in transmission light (top) and between non-fluorescent and fluorescent embryos with the respective fluorescence filter set (bottom). (e) Tools for mounting the embryo onto the sample holder (top). Shown are the steel pipe, the modified syringe, a small paintbrush and the Parafilm-covered glass Petri dish. Insertion of modified syringe to the steel pipe (bottom). (f) Preparation of agarose hemisphere. The steel pipe aligned along gravity and filled from the top with liquid agarose to create the hemisphere at the bottom. (g) Detail of the agarose hemisphere on the steel pipe. Top detail box shows the hemisphere. Bottom detail box shows a scheme of the optimal hemisphere geometry. The semi-axes r_1 and r_2 should have similar lengths. (h) Examination of agarose hemisphere. To prevent contamination and damage of the agarose hemisphere, the steel pipe is placed on the Parafilm-covered glass Petri dish and positioned under the stereomicroscope (top). The agarose hemisphere should appear uniformly smooth and transparent (bottom). (i) Picking of embryo with the brush. Submerge the brush into the PBS and carefully approach the embryo from below to reduce the risk of damaging the embryo. (j) Correct positioning of the embryo on brush. Attach the embryo with the posterior end on the tip of the brush so that the anterior end is accessible. Detail boxes show the positioning on a macroscopic level. (k) Creation of the mounting agarose layer. Dip the agarose hemisphere into liquid agarose. (l) Placement of the embryo in mounting agarose layer. Ideally, the embryo should be placed on the pole of the agarose hemisphere. (m) Correction of the embryo position on agarose hemisphere. Gradually correct the position of the embryo on the hemisphere by rotating the steel pipe and carefully brushing along the posterior end of the embryo. (n) Preparation of the stability agarose layer. Form a drop of liquid agarose at the pipette tip and deposit it slowly on the side of the agarose hemisphere. (o) Correctly mounted embryo on the agarose hemisphere. The embryo is positioned upright at the pole of the agarose hemisphere. The major fraction of the embryo surface is not covered by agarose and is in contact with the air and later on with PBS.



Embryo preparation ● TIMING 40 min

- 15|** Pass the embryos in egg-laying medium (from Step 2) through a sieve with a 300- μ m mesh. Retain the embryos and discard the flour. Transfer 25–30 embryos to a 100- μ m cell strainer.
- ▲ CRITICAL STEP** Put aside a few fluorescent embryos as a pre-imaging control to allow a comparison of fluorescence and larval morphology after hatching at Step 43. Incubation temperatures for these embryos should be synchronized to the imaged embryo.
- 16|** Prepare a six-well plate for dechoriation as described in the Reagent Setup section. Steps 17–30 are performed under the stereomicroscope at room temperature and in Steps 17–21; the cell strainer is used to transfer the embryos between the wells.
- 17|** Wash embryos in well A1 (PBS) for 1 min. Examine embryos under the stereomicroscope. The embryos are still partially covered in flour particles (**Fig. 3a**).
- 18|** Transfer embryos to well B1 (10% (vol/vol) sodium hypochlorite in PBS). Shake embryos in this solution for ~30 s to remove flour particles.
- 19|** Wash embryos in well A2 (PBS) for 1 min. Check that flour particles have been removed under the stereomicroscope (**Fig. 3b**).
- 20|** Transfer embryos to well B2 (10% (vol/vol) sodium hypochlorite in PBS). Shake embryos in this solution until the chorion detaches completely (**Fig. 3c**).
- ▲ CRITICAL STEP** Proceed to Step 21 as soon as the chorion detaches. Incubation of embryos for too long in sodium hypochlorite decreases viability drastically.
- 21|** Wash embryos in well A3 (PBS) for 1 min and transfer to well B3 (PBS).

PROTOCOL

22| Remove all non-fluorescent embryos under a stereomicroscope (**Fig. 3d**). These are either non-fertilized or do not carry the transgene for the fluorescent protein. Store remaining embryos temporarily in well B3 (PBS) until required for imaging.

23| Cover a glass Petri dish with Parafilm and place the tools required for embryo mounting alongside it (**Fig. 3e**, top).

24| Load the syringe with liquid agarose and fit the tip into the steel pipe (**Fig. 3e**, bottom). Hold the steel pipe upright and fill it slowly from the top with agarose until a hemisphere forms at its bottom (**Fig. 3f**). The dimensions of the hemisphere should match those of the outer diameter of the steel pipe (**Fig. 3g**). Allow the agarose hemisphere to solidify for 3 min.

25| Place the steel pipe on the Parafilm-covered glass dish to prevent damage or contamination and examine the agarose hemisphere under the stereomicroscope (**Fig. 3h**, top). The hemisphere should be transparent, without dark spots, debris or irregularities (**Fig. 3h**, bottom).

26| Use a brush to carefully pick an embryo (**Fig. 3i**) and re-position it so that only the posterior end is in contact with the tip of the brush and the anterior end is accessible (**Fig. 3j**).

▲ **CRITICAL STEP** Steps 26–30 must be performed within 5 min so that the embryo does not dry out.

27| Dip the agarose hemisphere into liquid agarose to create the mounting layer (**Fig. 3k**), and then place the anterior end of the embryo on the pole of the hemisphere (**Fig. 3l**).

▲ **CRITICAL STEP** Embryo placement has to be done while the mounting layer is still liquid, but cool enough not to damage the embryo. Take care not to damage the embryo with the brush while positioning the embryo on the agarose hemisphere.

28| Carefully adjust the position of the embryo by rotating the steel pipe and brushing lightly against the posterior end of the embryo (**Fig. 3m**). The final positioning of the embryo should be in an upright orientation at the pole of the agarose hemisphere. **? TROUBLESHOOTING**

29| To create the stability layer, drop 2 μ l of liquid agarose on the agarose hemisphere and drag it slowly around the hemisphere as long as it is still partially attached to the pipette tip (**Fig. 3n**).

▲ **CRITICAL STEP** Less than half of the embryo should be covered in agarose, and the flanks of the mounting and stability layers should be as steep as possible. Our experience is that the viability of embryos during long-term imaging decreases if they are more than half covered with agarose.

30| Examine the sample holder with the mounted embryo under the stereomicroscope to ensure that the embryo is properly oriented and stabilized (**Fig. 3o**).

Embryo insertion into LSFM ● **TIMING 20 min**

31| With forceps, insert the sample holder slowly and carefully into the sample chamber (**Fig. 4a**).

▲ **CRITICAL STEP** Be extremely careful when the embryo reaches the PBS surface. Owing to the surface tension of the PBS, the embryo might detach when submerged. If the perfusion system is used, stop the pumps during the embryo insertion process. If the embryo detaches, restart at Step 23.

? TROUBLESHOOTING

Figure 4 | Embryo insertion into the LSFM. (a) Insertion of the sample holder into the sample chamber. At the PBS surface, proceed slowly and steadily to prevent detachment of the embryo. (b) Correct positioning of the embryo in the sample chamber. The embryo is centered in front of the detection objective. The detail boxes show the top and side views of the embryo in the focal plane of the detection objective. (c) Top view of embryo with light sheet. (d) Image of embryo recorded in the transmission light channel. From bottom to top, the different agarose layers (hemisphere, mounting layer and stability layer) and PBS are indicated. Ideally, the flanks of the mounting and stability layers should be as steep as possible. (e) Plane from the center of the embryo recorded in the fluorescence channel. (f) Z maximum projection of a Z-stack recorded in the fluorescence channel. The boundaries of the agarose layers are outlined in green in e and f.

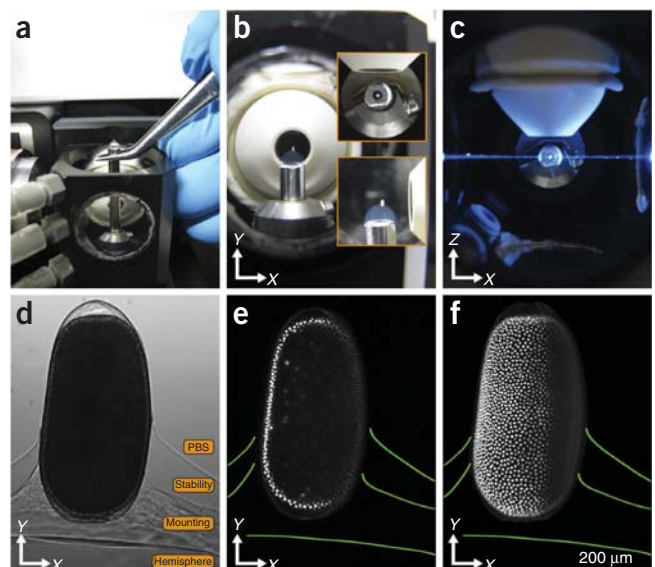
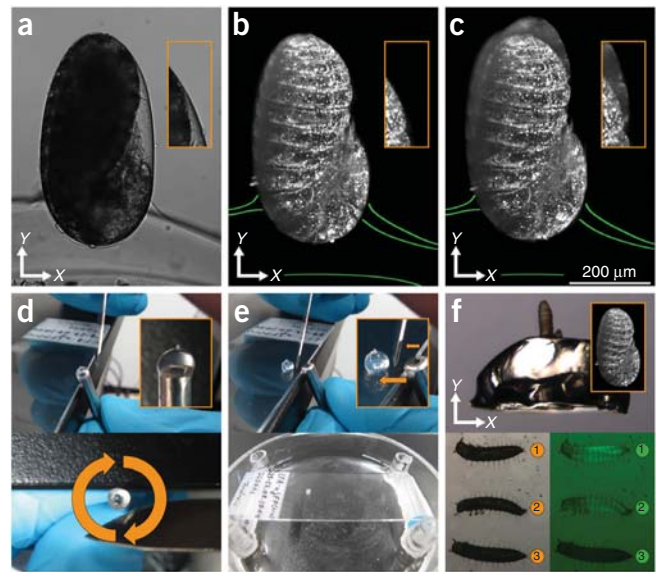


Figure 5 | Embryo retrieval. (a) Transmission light image of embryo at end of long-term imaging. Detail box shows a 2× magnification of the ventral-posterior area of the embryo. (b) Z maximum projection of the same embryo as shown in a. Detail box shows the same 2× magnification as in a. The green lines indicate the agarose–agarose and agarose–medium interfaces. (c) Z maximum projection of the same embryo as shown in b, 1 min later. Motion blur is evident at the posterior end of the embryo. (d) Transfer of the agarose hemisphere to the object slide. To avoid the risk of damaging the embryo, the agarose hemisphere is transferred horizontally by pushing it with a scalpel (top). If the agarose hemisphere sticks to the steel pipe, rotate it gradually and loosen it from the hemisphere with the scalpel (bottom, arrows). (e) Transfer of agarose hemisphere and embryo incubation in humidity chamber. The agarose hemisphere is placed on its flat surface with the embryo still fixed to the pole (top). This should be done by pushing the agarose hemisphere from the side with the scalpel (detail box, arrows). The object slide is then placed in the humidity chamber (bottom). (f) Hatched larva. Transmission light image of hatched larva still attached to agarose hemisphere (top). Detail box shows the embryo from b in the same orientation. Transmission light (bottom left, orange numbers) and GFP filter set (bottom right, green numbers) image of (1) imaged fluorescent larva that was retrieved, also shown are two controls, (2) one larva of the same fluorescent line and (3) one wild-type larva of the same background strain. The imaged fluorescent larva shows approximately the same intensity as the fluorescent control larva and exhibits the same morphology as both control larvae.



32 | Move the embryo with the micro-translation stages along *X* and *Y* in front of the detection objective (**Fig. 4b**).

33 | Turn the laser on and move the embryo with the micro-translation stages along *Z* into the light sheet (**Fig. 4c**), then turn off the laser.

34 | Switch to the transmission light channel and move the embryo with the micro-translation stages along *X* and *Y* into the center of the field of view, then focus on the embryo borders by moving with the micro-translation stages along *Z*. The hemisphere layer, the mounting layer and the stability layer should be clearly visible (**Fig. 4d**). Rotate the embryo with the precision rotation stage around *Y* in 90° steps and inspect it for damage that might have occurred during the mounting process (**Supplementary Fig. 9**, first row).

35 | Switch to the fluorescence channel, turn the laser on and record a plane close to the center of the embryo (**Fig. 4e**). Check whether the signal intensity is sufficient and whether any imaging artifacts occur. Adjust laser power and exposure time as necessary. If the embryo is to be imaged in multiple fluorescence channels, change the laser line and/or emission filter and also adjust the laser power and exposure time as necessary. In addition, test any advanced imaging options (e.g., structured illumination, dual-sided illumination).

36 | Record a *Z*-stack that covers the whole volume of the embryo, compute the *Z* maximum projection and check it for imaging artifacts (**Fig. 4f**).

▲ CRITICAL STEP If the embryo is to be imaged along multiple directions, rotate the embryo with the precision rotation stage around *Y* and record a *Z*-stack for each direction. Check the *Z*, *X* and *Y* maximum projections for imaging artifacts (**Supplementary Fig. 9**, second to fourth row).

? TROUBLESHOOTING

Imaging of *Tribolium* embryos in LSMF ● TIMING up to 120 h

▲ CRITICAL Multiple parameters must be set during the following steps, which have two important consequences: on the one hand, they determine the total number of acquired images, and thus the data volume that is created, and on the other hand, they account for the energy exposure of the embryo. Considerations and guidelines are given in **Box 1**. See also **Supplementary Figure 10**.

37 | Define *Z*-stacks for the desired number of directions. For *Z* spacing, use four times the *XY* spacing⁵⁰.

▲ CRITICAL STEP Leave a few planes in front of and behind the embryo as a buffer along each direction (i.e., record from the dark through the embryo into the dark).

38 | Set up the desired number of channels. For each channel, choose the appropriate laser line, laser power, exposure time and emission filter. Define advanced imaging options for each channel as needed (e.g., structured illumination, dual-sided illumination).

PROTOCOL

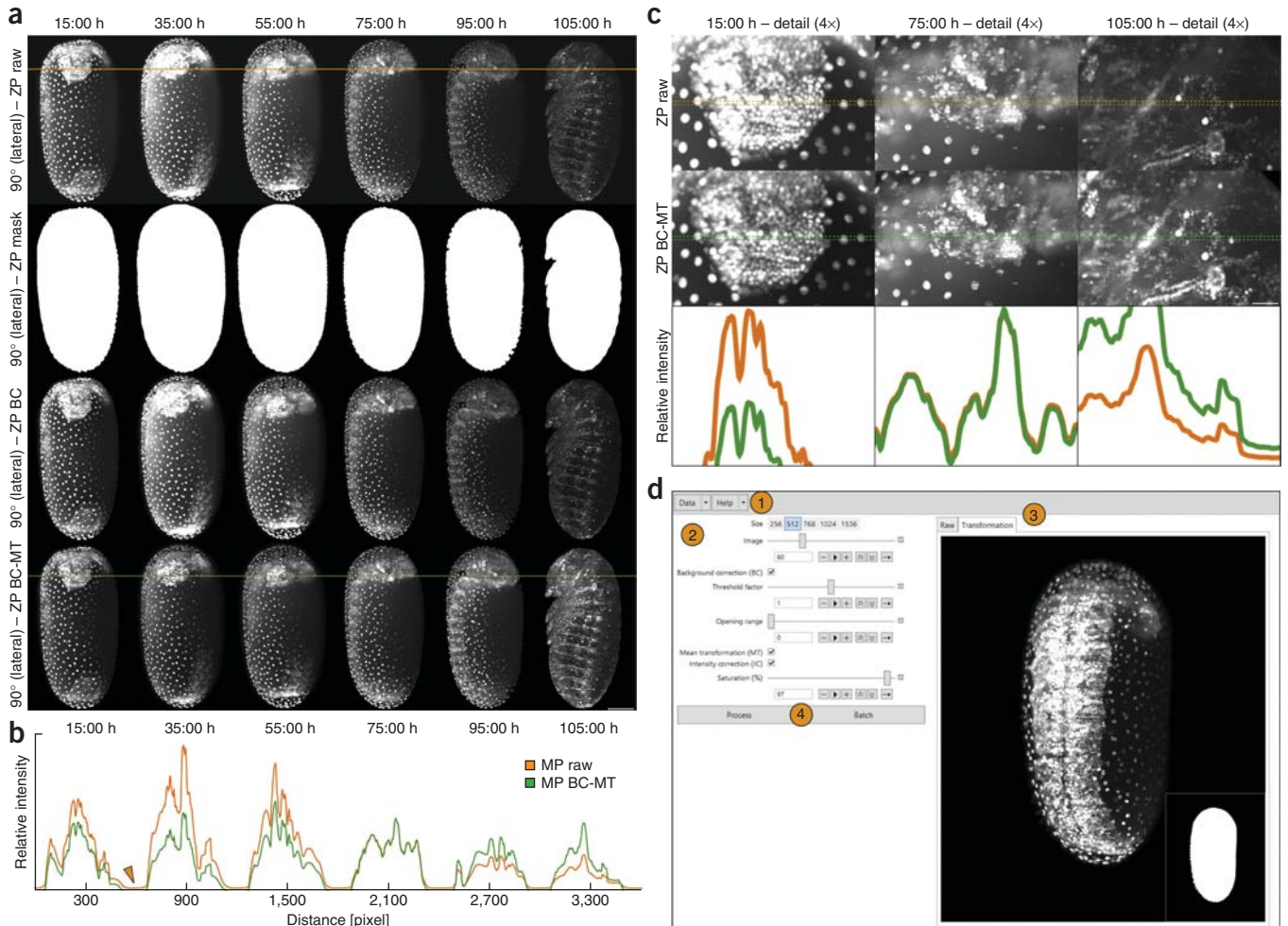


Figure 6 | Data processing. (a) Background correction and mean intensity transformation shown for a time series of six Z maximum projections in 90° (lateral) views. Raw Z maximum projections contain background (ZP raw). The background is distinguished from the object information by applying an automatically determined threshold resulting in a binary object mask (ZP mask). The background is set to zero and the mean background intensity is calculated and subtracted from the object intensity (ZP BC). For Z maximum projection time series, the images with minimum and maximum mean intensity are determined and the mean value is computed. For that series, the image whose mean intensity is closest to that value is defined as the reference image. All images of the time series are adjusted to match the mean intensity of the reference image (MP BC-MT). Scale bar, 100 μ m. (b) Intensity plot along orange line along ZP raw images and along green line along ZP BC-MT in a. The intensity distribution of images in a Z maximum projection time series is either decreased (15:00 h), remains almost unchanged (75:00 h), or is increased (105:00 h). Compared to the intensity profile along ZP raw, the background information along ZP BC-MT is completely removed (see arrowhead). (c) Detail of anterior region along ZP raw, ZP BC-MT and intensity plot along orange and green lines. The image processing procedure has no effect on image features. Scale bar, 25 μ m. (d) Screenshot of Mathematica-based image processing program user interface: (1) data menu to import and export Z maximum projection time series, and Help menu. (2) Settings menu to configure image data processing. Parameter functions are explained in the Help menu. (3) Comparison of raw and transformed image. (4) Buttons to start processing and run batch mode for several files with the chosen settings.

39 | Configure the time lapse.

▲ CRITICAL STEP For long-term imaging, ensure that the sample chamber is filled with enough PBS (cover the opening if necessary).

40 | Start imaging. Observe the first time point of the time lapse to ensure that the microscope is operating properly.

? TROUBLESHOOTING

Embryo retrieval ● TIMING 10 min

41 | When the embryo exhibits regular muscular movement (**Fig. 5a–c** and **Supplementary Videos 1** and **2**), stop imaging. Slowly and carefully drain the PBS from the sample chamber.

▲ CRITICAL STEP Be extremely careful when the PBS surface reaches the embryo on top of the hemisphere, as the surface tension can generate enough force to detach the embryo.

42 | Remove the sample holder from the drained sample chamber. Use a scalpel to transfer the agarose hemisphere with the attached embryo to an object slide (**Fig. 5d**). Wait for ~5 min until the embryo surface is dry.

▲ CRITICAL STEP Do not dry the embryo for too short or too long, as this reduces viability.

Box 2 | Data processing: background correction and mean intensity transformation

1. Preprocess the raw *Z* maximum projections (**Fig. 6a**, first row) using Gaussian filtering. A kernel size of 7×7 pixels is suitable.
2. Compute an intensity threshold for each preprocessed image (e.g., Kittler–Illingworth’s minimum error threshold method^{77,78}). If necessary, adjust the computed threshold by a suitable factor.
3. Fill small background regions in the obtained binary image and optionally perform morphological opening to smooth object boundaries.
4. Select the largest object to represent the object binary mask (**Fig. 6a**, second row).
5. Compute the mean background intensity for raw *Z* maximum projections using the object binary mask.
6. Multiply the object binary masks obtained in step 4 with the raw *Z* maximum projections and subtract mean background intensities (**Fig. 6a**, third row).
7. Determine the two background-corrected *Z* maximum projections with minimum and maximum mean intensity and compute the mean intensity.
8. Find the reference *Z* maximum projection whose mean intensity is closest to the value computed in step 7 and transform all *Z* maximum projections to match the mean intensity of that reference (**Fig. 6a**, fourth row).

43| Place the object slide with the embryo onto the scaffold of the humidity chamber (**Fig. 5e**), fill the bottom of the chamber with 10-ml PBS and incubate at an appropriate temperature until the embryo hatches. If applicable, monitor hatching time. For an approximation of the incubation time, consult **Supplementary Figure 3**.

44| After hatching, remove the larva from the agarose hemisphere with a brush and examine it under a stereomicroscope in the transmission light channel and with the appropriate fluorescence filter set. As a quality control, we recommend comparing fluorescence and larval morphology to a control fluorescent larva and to a wild type larva (**Fig. 5f**).

? TROUBLESHOOTING

45| Transfer the hatched larva to an individual rearing tube and incubate as described for *T. castaneum* stock culture in the Equipment Setup section. Once it has reached its adult stage (after ~6 weeks), provide it with an appropriate mating partner.

Data processing ● TIMING 1 d

46| Using the image data generated in Step 40, compute the *Z* maximum projections. If required, rotate and crop the obtained *Z* maximum projections. This step can be performed using the script ‘Strobl2015A - ProCroRo.ijm’ (provided as **Supplementary Script 1** or available for download at <http://www.physikalischebiologie.de/bugcube>), which extends the open-source image processing software FIJI to enable it to perform common image processing steps for multiple image stacks in batch mode.

47| Apply image processing for background correction and mean intensity transformation (**Fig. 6**) as described in **Box 2**. This step can be performed using the script ‘Strobl2015A - BackCorMeanTra.m’ (provided as **Supplementary Script 2** or available for download at <http://www.physikalischebiologie.de/bugcube>).

? TROUBLESHOOTING

Troubleshooting advice can be found in **Table 2**. The figures in the **Supplementary Note** illustrate many of the problems mentioned in **Table 2**.

TABLE 2 | Troubleshooting table.

Step	Problem	Possible reason	Solution
9	Bright dot is not visible when glass coverslip holder is placed in microscope chamber	Hardware or laser is not switched on, or the light path is blocked	Control the light path at multiple positions (laser source, laser fiber, scanning mirror, illumination objective, sample chamber)
		Glass coverslip holder is not properly positioned or rotated in the sample chamber (Supplementary Note , Fig. A',A'')	Reposition the glass coverslip holder with the micro-translation stages along <i>X</i> and ensure that it is rotated to 45° relative to <i>X</i> and <i>Z</i> (Supplementary Note , Fig. A)

(continued)

TABLE 2 | Troubleshooting table (continued).

Step	Problem	Possible reason	Solution
11	Height of the light sheet is too small along <i>Y</i> (Supplementary Note , Fig. B')	Scanning range of the activated scanning mirror is too small along <i>Y</i>	Readjust the scanning mirror so that the light sheet extends approximately 20% over the field of view along <i>Y</i> (Supplementary Note , Fig. B)
	Light sheet is tilted toward <i>Z</i> relative to the focal plane of the detection objective (Supplementary Note , Fig. B'')	Scanning mirror also scanning slightly along <i>Z</i>	Readjust the scanning mirror so that the light sheet overlaps with the focal plane of the detection objective and is no longer tilted toward <i>Z</i> (Supplementary Note , Fig. B)
	Light sheet appears unfocused along <i>X</i> , the width appears too large, and the intensity appears too dark (Supplementary Note , Fig. C')	Light sheet 'waist' is not positioned in the center of the field of view along <i>X</i>	Move the illumination objective with the piezo nano-positioners along <i>X</i> so that the light sheet is focused along <i>X</i> , the width is minimal, and the intensity is maximal (Supplementary Note , Fig. C)
	Light sheet appears blurry, surface irregularities on the glass coverslip are not clearly recognizable (Supplementary Note , Fig. C'')	Light sheet and the focal plane of the detection objective are displaced along <i>Z</i>	Move the detection objective with the piezo nano-positioners along <i>Z</i> so that the focal plane is in the center of the light sheet (Supplementary Note , Fig. C)
14	Beads are not completely visible over the complete height along <i>Y</i> (Supplementary Note , Fig. D')	Height of the light sheet is too small along <i>Y</i> (Supplementary Note , Fig. B')	Remove the agarose-embedded bead column and place the glass coverslip holder into the sample chamber. Readjust the scanning mirror so that the light sheet extends approximately 20% over the field of view along <i>Y</i> (Fig. 2f and Supplementary Note , Fig. B). Beads should now be visible over the complete height along <i>Y</i> (Supplementary Note , Fig. D)
		Capillary is in the field of view	Switch to the transmission light channel. Remove capillary with the micro-translation stages from the field of view along <i>Y</i>
		Agarose-embedded bead column is too short	Prepare a new column. Check in the transmission light channel that the column spans completely across <i>Y</i> (Fig. 2h)
	Beads appear blurry at the top and/or bottom of <i>Y</i> (Supplementary Note , Fig. D'')	Light sheet is tilted toward <i>Z</i> relative to the focal plane of the detection objective (Supplementary Note , Fig. B')	Remove the agarose-embedded bead column and place the glass coverslip holder into the sample chamber. Readjust scanning mirror so that the light sheet is no longer tilted toward <i>Z</i> (Supplementary Note , Fig. B). Beads should now be focused across the complete field of view (Supplementary Note , Fig. D)
		Light sheet waist is not positioned in the center of the field of view along <i>X</i> (Supplementary Note , Fig. C')	Remove the column and place the glass coverslip holder into the sample chamber. Move the illumination objective with the piezo nano-positioners along <i>X</i> so that the light sheet is focused along <i>X</i> , the width is minimal, and the intensity is maximal (Supplementary Note , Fig. C). Beads should now be focused across the complete field of view (Supplementary Note , Fig. E)
	Beads appear dim and elongated (Supplementary Note , Fig. E')	Light sheet waist is not positioned in the center of the field of view along <i>X</i> (Supplementary Note , Fig. C')	Remove the column and place the glass coverslip holder into the sample chamber. Move the illumination objective with the piezo nano-positioners along <i>X</i> so that the light sheet is focused along <i>X</i> , the width is minimal, and the intensity is maximal (Supplementary Note , Fig. C). Beads should now be focused across the complete field of view (Supplementary Note , Fig. E)
Beads appear blurry in the complete field of view (Supplementary Note , Fig. E'')	Light sheet and focal plane of the detection objective are displaced along <i>Z</i> (Supplementary Note , Fig. C'')	Remove the column and place the glass coverslip holder into the sample chamber. Move the detection objective with the piezo nano-positioners along <i>Z</i> so that the focal plane is in the center of the light sheet (Supplementary Note , Fig. C). Beads should now be focused across the complete field of view (Supplementary Note , Fig. E)	

(continued)

TABLE 2 | Troubleshooting table (continued).

Step	Problem	Possible reason	Solution
28	Difficulties in mounting the embryo on the agarose hemisphere The embryo tends to move on the top of the agarose hemisphere	Misshapen agarose hemisphere (Supplementary Note , Fig. F',F'')	Recreate the agarose hemisphere so that the semi-axes r_1 and r_2 do not become oval (Fig. 3g and Supplementary Note , Fig. F)
		Embryo is oriented with the anterior end on the brush during mounting (Supplementary Note , Fig. G'')	Release the embryo and restart the picking process (Fig. 3i) or turn the embryo around on the brush, so that it can be mounted with the bulgy anterior end to the hemisphere (Fig. 3j,l and Supplementary Note , Fig. G,G')
		Attaching agarose layer is still too liquid	Attach the embryo to the hemisphere when the mounting agarose layer is about to polymerize
		Attaching agarose layer is already dry	Attach the embryo to the hemisphere when the mounting agarose layer is about to polymerize
31	The embryo detaches when the sample holder is inserted into the sample chamber	Insufficient time for the agarose to solidify properly	Wait slightly longer before insertion into the sample chamber
		Agarose is solidified and dried out	Wait less time before insertion into the sample chamber
		Stability layer is not applied properly (Supplementary Note , Fig. H',H'')	Carefully apply the agarose on the gap between the hemisphere and the embryo; check under the stereomicroscope (Fig. 3n and Supplementary Note , Fig. H)
		Sample holder inserted too forcefully	Insert the sample holder slowly but steady. Alternatively, use the micro-translation stages for a steady insertion process
36	Blurred or dark regions at the anterior or posterior part of the embryo (Supplementary Note , Fig. J'')	Not enough agarose in the stability layer (Supplementary Note , Fig. I')	Apply more agarose (Supplementary Note , Fig. I)
		Light sheet is tilted toward Z relative to the focal plane of the detection objective (Supplementary Note , Fig. B'')	Remove the embryo and place the glass coverslip holder into the sample chamber. Readjust the scanning mirror so that the light sheet overlaps with the focal plane of the detection objective along X and is no longer tilted toward Z (Supplementary Note , Fig. B). The embryo should now be visible across the complete height along Y (Supplementary Note , Fig. J)
		Height of the light sheet is too small along Y (Supplementary Note , Fig. B')	Remove the embryo and place the glass coverslip holder into the sample chamber. Readjust the scanning mirror so that the light sheet extends approximately 20% over the field of view along Y (Fig. 2f and Supplementary Note , Fig. B). The embryo should now be visible across the complete height along Y (Supplementary Note , Fig. J)
		Blurred or dark regions on the embryo along one or multiple directions	Embryo is not dechorionated properly
Too much agarose in the light path	Mount the embryo on the pole of the agarose hemisphere (Fig. 3o)		
	Whole embryo appears blurred (Supplementary Note , Fig. K')	Light sheet and the focal plane of the detection objective are displaced along Z (Supplementary Note , Fig. C'')	Remove the embryo and place the glass coverslip holder into the sample chamber. Move the detection objective with the piezo nano-positioners along Z so that the focal plane is in the center of the light sheet (Supplementary Note , Fig. C). The embryo should now be focused across the complete field of view (Supplementary Note , Fig. K).

(continued)



PROTOCOL

TABLE 2 | Troubleshooting table (continued).

Step	Problem	Possible reason	Solution
36	Certain regions of the embryo appear dark (Supplementary Note , Fig. K’')	Embryo is out of the volume of view	Stabilize the embryo such that it is within the volume of view (Supplementary Note , Fig. K)
40	The embryo shows malformations or dies during imaging	Embryo was damaged during the preparation and mounting process	Perform embryo handling with more caution and/or check the embryo in transmission light along multiple directions before imaging (Supplementary Fig. 9)
		Embryo is covered with too much agarose (Supplementary Note , Fig. I’').	Keep the amount of agarose used to mount the embryo minimal (Supplementary Note , Fig. I). Ideally, the flanks of the mounting and stability layers should be as steep as possible
		Energy exposure from the laser is too high (see Box 1)	Use less laser power, reduce exposure time per plane, increase imaging interval and/or reduce the number of views
44	After retrieval, the embryo does not hatch	Embryo is damaged during the retrieval process because it was covered by too much agarose (Supplementary Note , Fig. I’')	Try to keep the amount of agarose used to mount the embryo at a minimum (Supplementary Note , Fig. I)
		Embryo is damaged during the retrieval process as a result of poor handling	Perform retrieval steps with more caution, do not roll but push the agarose hemisphere to the object slide (Fig. 5); check the embryo under a stereomicroscope if it was damaged
		Embryo is dried out or too wet	Dry the embryo on the hemisphere so that the embryo surface is dry, and then incubate it in the humidity chamber under saturated atmosphere but without the formation of condensing drops around the embryo or at the lid

● TIMING

Steps 1 and 2, embryo collection: 70 min + 15 h incubation
 Steps 3–14, LSFM calibration: 30 min (can be performed while the embryos incubate)
 Steps 15–30, embryo preparation: 40 min
 Steps 31–36, embryo insertion into LSFM: 20 min
 Steps 37–40, imaging of *Tribolium* embryos in LSFM: up to 120 h
 Steps 41–45, embryo retrieval: 10 min
 Steps 46 and 47, data processing: 1 d

ANTICIPATED RESULTS

The described protocol allows noninvasive long-term fluorescence imaging of *T. castaneum* embryos. In **Figures 7–12**, we show typical results that can be obtained by following the protocol. All example results were obtained using the EFA-nGFP transgenic line¹⁰. This line expresses nuclear-localized S65T-GFP under control of the elongation factor 1 alpha 1 subunit promoter ubiquitously throughout embryonic development.

In **Figure 7**, we show the development of a *Tribolium* embryo from 5:00 h to 105:00 h along four directions. The full 120:00-h development of this embryo is shown in **Supplementary Video 3**. The images illustrate the embryogenic events gastrulation (05:00 h), germ band elongation (15:00 h–35:00 h), germ band retraction (45:00 h to 95:00 h) and dorsal closure (105:00 h). Structural features of development deep inside the *Tribolium* embryo are unveiled with optical sections as shown in **Figure 8**. Planes of the Z-stacks that were shown in **Figure 7** at 05:00 h as Z maximum projections are depicted in identical orientations up to a depth of 104 μm . The single plane at 26 μm in the 0° (ventral) view reveals the two ridges of

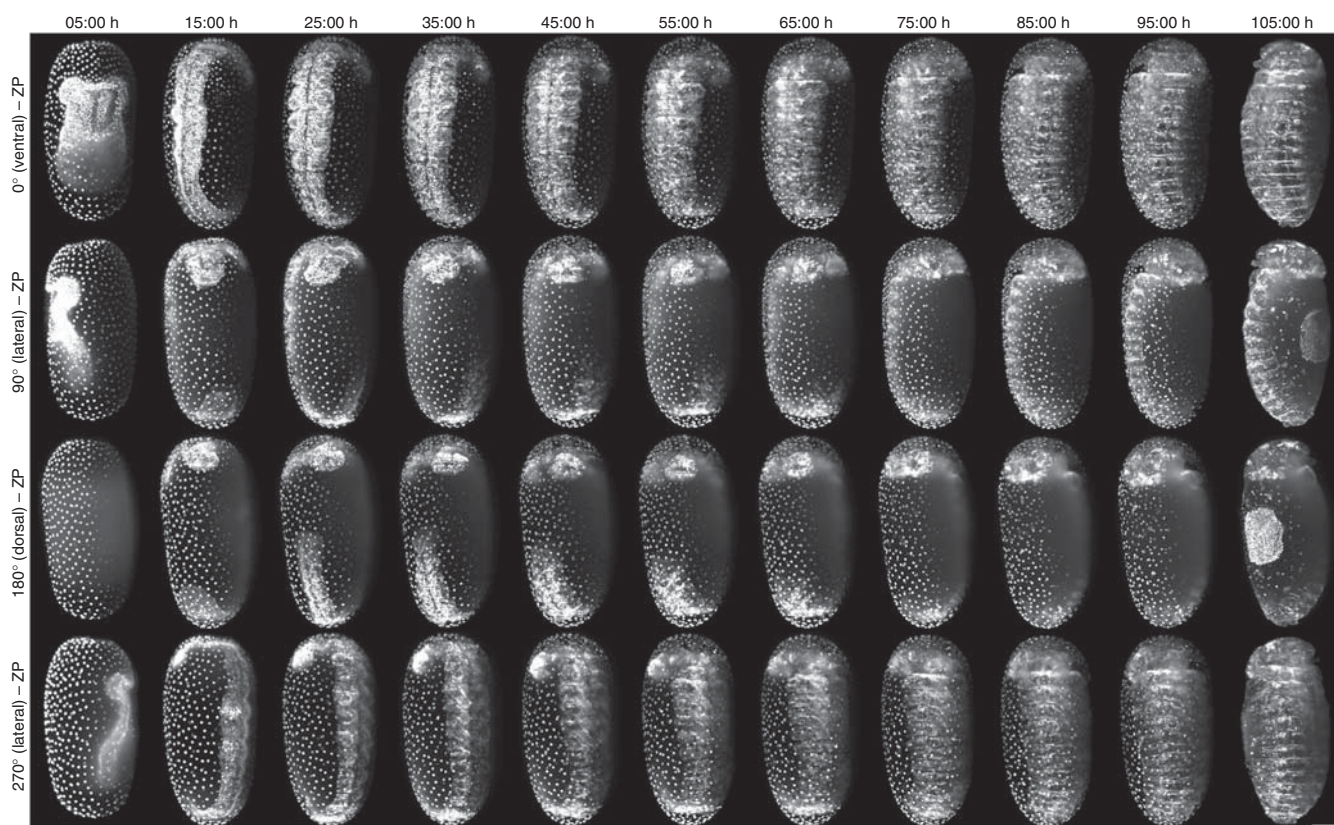


Figure 7 | *Tribolium* embryo imaged over time along four directions. Temporal interval is 10:00 h. ZP, Z maximum projections with image processing. Scale bar, 100 μ m.

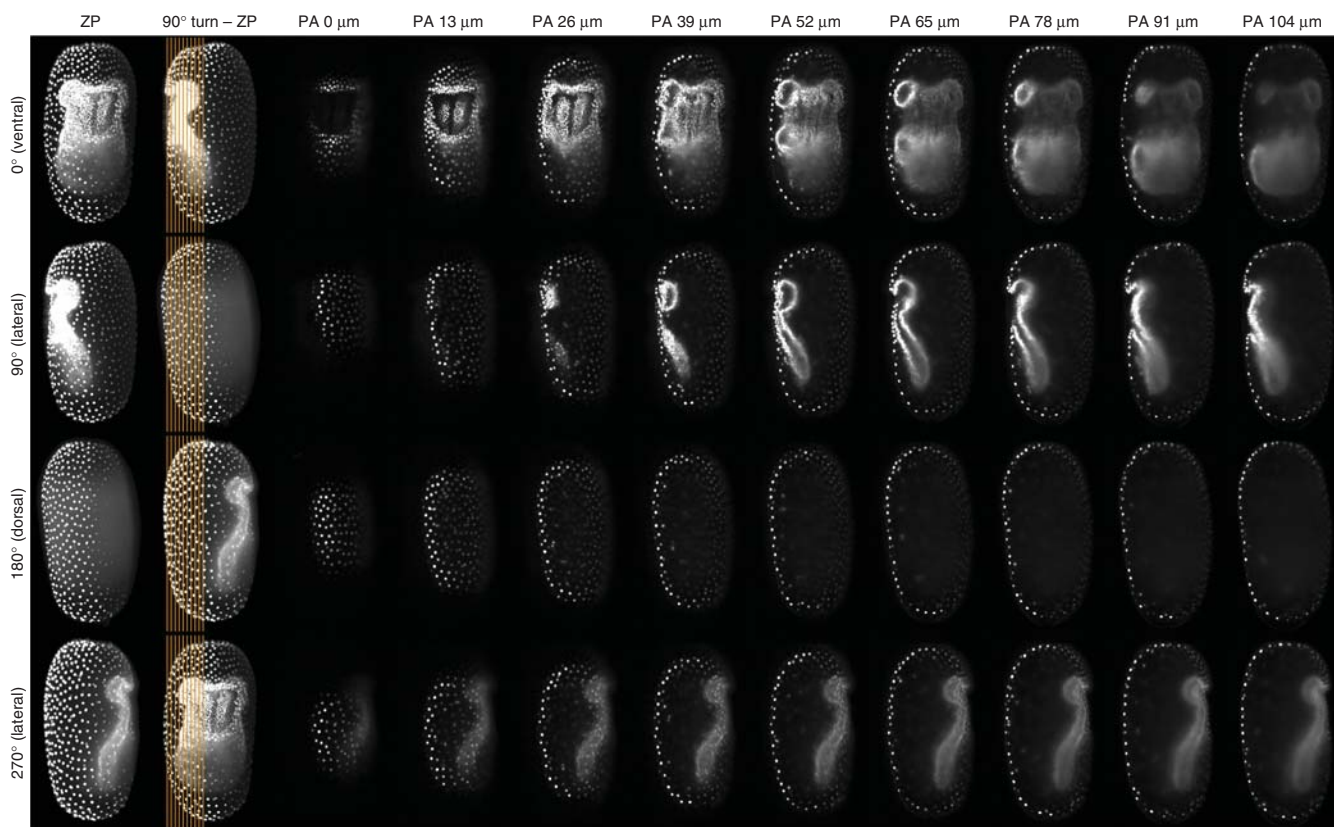


Figure 8 | Optical section of a *Tribolium* embryo along four orientations. Z spacing is 13 μ m. The locations of the planes are indicated by the orange lines. ZP, Z maximum projections with image processing; PA, single plane with intensity adjustment. Scale bar, 100 μ m.

PROTOCOL

Figure 9 | Optical sectioning a *Tribolium* embryo over time. Temporal interval is 10:00 h; Z spacing is 13 μm . The locations of the planes are indicated by the orange lines. ZP, Z maximum projections with image processing; PA, single plane with intensity adjustment. Scale bar, 100 μm .

the folding median groove. The complete optical sectioning is provided as **Supplementary Video 4**. **Figure 9** shows optical sectioning as a function of time. The depicted optical sections of three time points illustrate the process of leg development during germ band elongation. The complete optical sectioning is provided as **Supplementary Video 5**.

To demonstrate the effect of different temperature conditions during imaging, 5 h of *Tribolium* development commencing with the rearrangement of the uniform blastoderm at 35 $^{\circ}\text{C}$ and at room temperature are shown in **Figure 10**. While the embryo imaged at 35 $^{\circ}\text{C}$ has already completed gastrulation and begun germ band elongation at 05:00 h, the serosa window of the embryo imaged at room temperature is not yet closed. In **Figure 11**, the image quality obtained by uniform illumination and structured illumination are compared. Imaging with structured illumination commonly improves image contrast. A complete optical sectioning is provided as **Supplementary Video 6**. Differences between the 10 \times objective/CCD camera combination and the 20 \times objective/sCMOS camera combination are illustrated in **Figure 12**. As indicated in the detail boxes, biological structures such as cell nuclei are better resolved. Metadata, parameters and download information about the data sets that were used for the example results are provided in **Supplementary Table 1**.

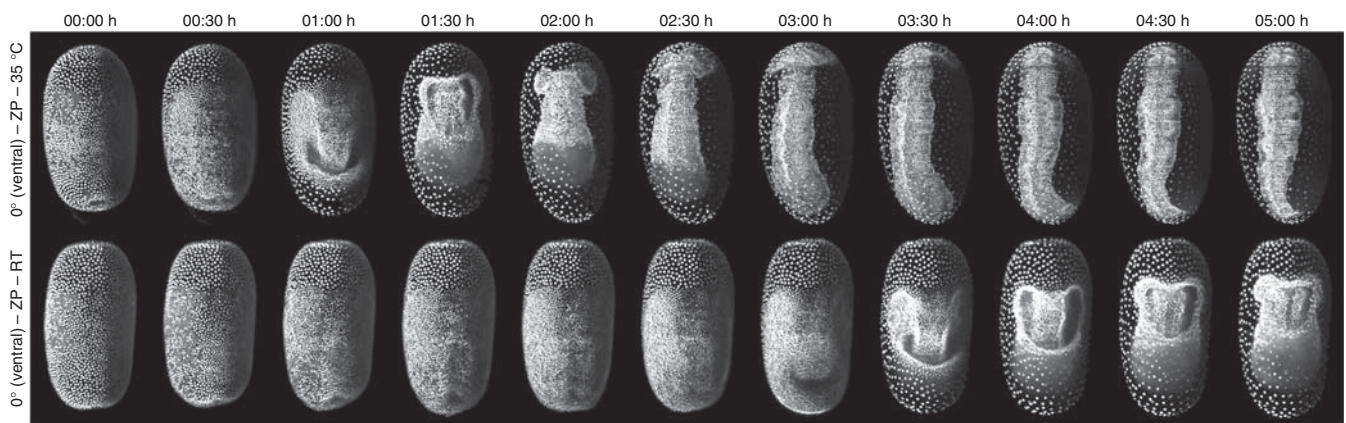
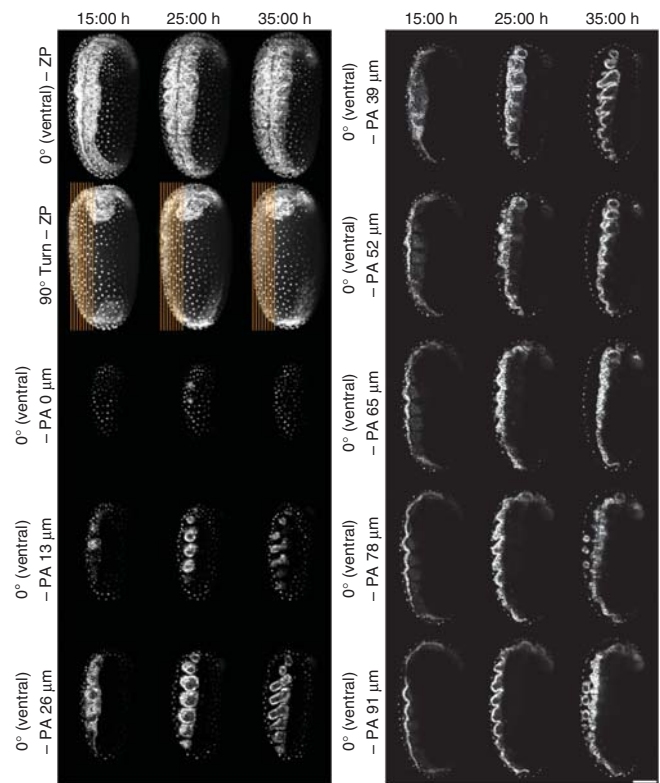


Figure 10 | Comparison of *Tribolium* embryo development at different temperature conditions. Z maximum projection time series imaged at 35 $^{\circ}\text{C}$ (using a perfusion system) and at room temperature. In contrast to imaging at 35 $^{\circ}\text{C}$, a temperature decrease by 12 $^{\circ}\text{C}$ delays embryonic development approximately by a factor of three. ZP, Z maximum projections with image processing; RT, room temperature. Scale bar, 100 μm . Adapted from ref. 23 with permission, Nature Publishing Group.

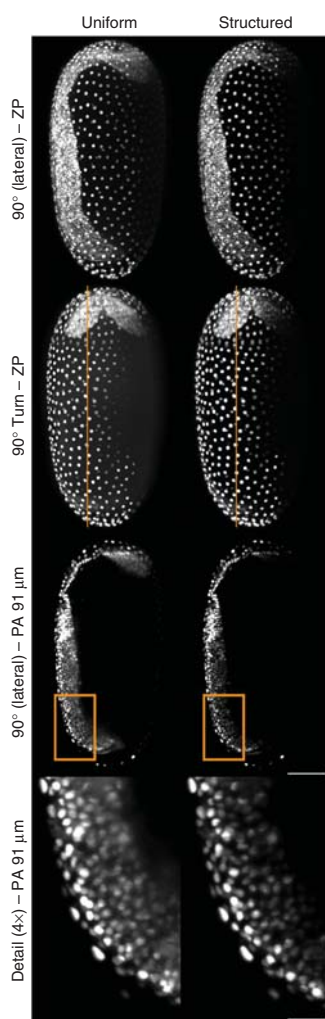


Figure 11 | Comparison of uniform versus structured illumination light-sheet modes. Dense structures such as the germ band might appear blurry using uniform illumination light-sheet mode. Structured illumination light-sheet mode leads to an increased image contrast by eliminating most of the blur from out-of-focus structures. The locations of the planes are indicated by the orange lines. ZP, Z maximum projections with image processing; PA, single plane with intensity adjustment. Scale bar in main image, 100 μm ; in detail image (4 \times) 25 μm .

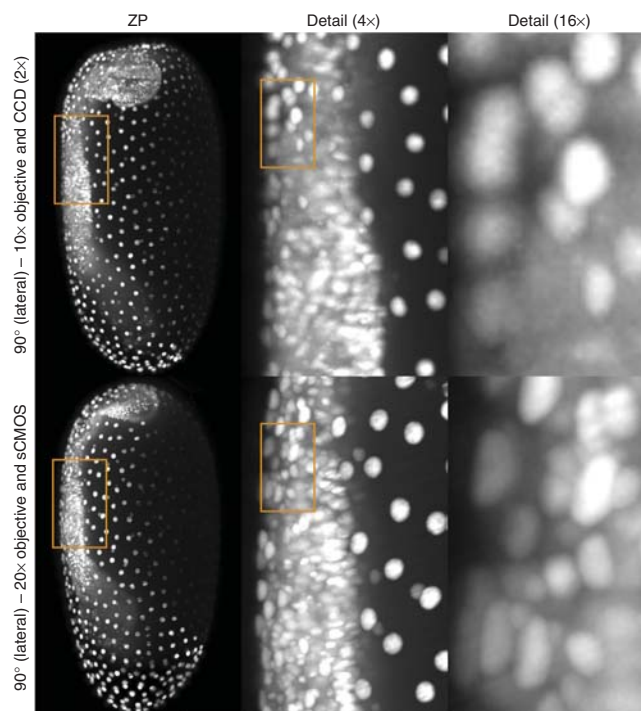


Figure 12 | Comparison of imaging with the 10 \times objective/CCD camera combination versus the 20 \times objective/sCMOS camera combination. Although the field of view remains approximately equal, an eightfold-higher spatial resolution can be obtained by a combination of a 20 \times objective with a sCMOS camera. ZP, Z maximum projections with image processing. Scale bar in main image, 100 μm ; in middle detail image (4 \times) 25 μm , and in right detail image (16 \times) 5 μm .

Note: Any Supplementary Information and Source Data files are available in the online version of the paper.

ACKNOWLEDGMENTS We thank A. Peel (University of Leeds) and M. Averof (Institut de Génomique Fonctionnelle de Lyon) for the *Tribolium* EFA-nGFP line; D. Kleinhans for kindly providing a raw version of the mDSLm principle scheme; D. von Wangenheim for help with the generation of the videos; S. Plath and K. Schmale for technical assistance; and J. Alexander Ross, A. Anderl and S. Fischer for their general support. The research was funded by the Cluster of Excellence Frankfurt for Macromolecular Complexes (CEF-MC, EXC 115) granted to the Buchmann Institute for Molecular Life Sciences (BMLS) at the Goethe University—Frankfurt am Main by the Deutsche Forschungsgemeinschaft (DFG).

AUTHOR CONTRIBUTIONS All authors conceived the research and wrote the publication. F.S. performed the experiments to obtain the example results.

COMPETING FINANCIAL INTERESTS

The authors declare no competing financial interests.

Reprints and permissions information is available online at <http://www.nature.com/reprints/index.html>.

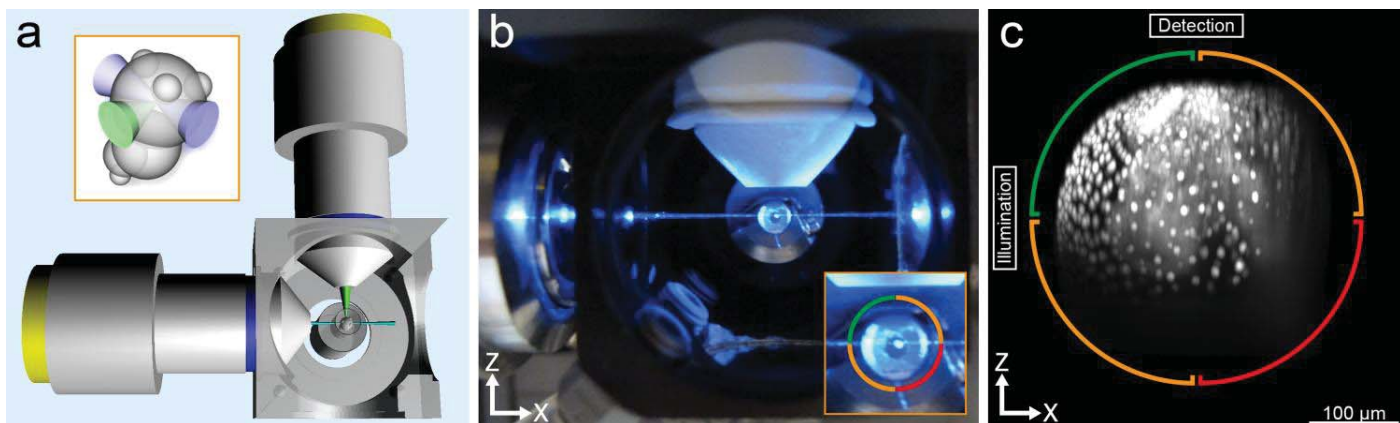
1. Klingler, M. *Tribolium*. *Curr. Biol.* **14**, R639–R640 (2004).
2. Schröder, R., Beermann, A., Wittkopp, N. & Lutz, R. From development to biodiversity—*Tribolium castaneum*, an insect model organism for short germband development. *Dev. Genes Evol.* **218**, 119–126 (2008).
3. Roth, S. & Hartenstein, V. Development of *Tribolium castaneum*. *Dev. Genes Evol.* **218**, 115–118 (2008).
4. Brown, S.J. *et al.* The red flour beetle, *Tribolium castaneum* (Coleoptera): a model for studies of development and pest biology. *Cold Spring Harb. Protoc.* **4** doi:10.1101/pdb.emo126 (2009).
5. Roth, S. & Panfilio, K.A. Development. Making waves for segments. *Science* **336**, 306–307 (2012).
6. Richards, S. *et al.* The genome of the model beetle and pest *Tribolium castaneum*. *Nature* **452**, 949–955 (2008).
7. Shippy, T.D., Coleman, C.M., Tomoyasu, Y. & Brown, S.J. Concurrent *in situ* hybridization and antibody staining in red flour beetle (*Tribolium*) embryos. *Cold Spring Harb. Protoc.* **4**, 968–973 (2009).
8. Berghammer, A.J., Weber, M., Trauner, J. & Klingler, M. Red flour beetle (*Tribolium*) germline transformation and insertional mutagenesis. *Cold Spring Harb. Protoc.* **4** doi:10.1101/pdb.prot5259 (2009).
9. Posnien, N. *et al.* RNAi in the red flour beetle (*Tribolium*). *Cold Spring Harb. Protoc.* **4** doi:10.1101/pdb.prot5256 (2009).



10. Sarrazin, A.F., Peel, A.D. & Averof, M. A segmentation clock with two-segment periodicity in insects. *Science* **336**, 338–341 (2012).
11. El-Sherif, E., Averof, M. & Brown, S.J. A segmentation clock operating in blastoderm and germband stages of *Tribolium* development. *Development* **139**, 4341–4346 (2012).
12. Benton, M.A., Akam, M. & Pavlopoulos, A. Cell and tissue dynamics during *Tribolium* embryogenesis revealed by versatile fluorescence labeling approaches. *Development* **140**, 3210–3220 (2013).
13. Panfilio, K.A., Oberhofer, G. & Roth, S. High plasticity in epithelial morphogenesis during insect dorsal closure. *Biol. Open* **2**, 1108–1118 (2013).
14. Koelzer, S., Kölsch, Y. & Panfilio, K.A. Visualizing late insect embryogenesis: extraembryonic and mesodermal enhancer trap expression in the beetle *Tribolium castaneum*. *PLoS ONE* **9**, e103967 (2014).
15. Nollmann, F.I. *et al.* A photorhabdus natural product inhibits insect juvenile hormone epoxide hydrolase. *Chembiochem* **16**, 766 (2015).
16. Nakamoto, A. *et al.* Changing cell behaviours during beetle embryogenesis correlates with slowing of segmentation. *Nat. Commun.* **6**, 6635 (2015).
17. Huisken, J., Swoger, J., Del Bene, F., Wittbrodt, J. & Stelzer, E.H.K. Optical sectioning deep inside live embryos by selective plane illumination microscopy. *Science* **305**, 1007–1009 (2004).
18. Keller, P.J., Schmidt, A.D., Wittbrodt, J. & Stelzer, E.H.K. Reconstruction of zebrafish early embryonic development by scanned light sheet microscopy. *Science* **322**, 1065–1069 (2008).
19. Keller, P.J. *et al.* Fast, high-contrast imaging of animal development with scanned light-sheet-based structured-illumination microscopy. *Nat. Methods* **7**, 637–642 (2010).
20. Strobl, F. & Stelzer, E.H.K. Non-invasive long-term fluorescence live imaging of *Tribolium castaneum* embryos. *Development* **141**, 2331–2338 (2014).
21. Stelzer, E.H.K. & Lindek, S. Fundamental reduction of the observation volume in far-field light microscopy by detection orthogonal to the illumination axis: confocal theta microscopy. *Opt. Commun.* **111**, 536–547 (1994).
22. Cox, I. Scanning optical fluorescence microscopy. *J. Microsc.* **133**, 149–154 (1984).
23. Stelzer, E.H.K. Light-sheet fluorescence microscopy for quantitative biology. *Nat. Methods* **12**, 23–26 (2015).
24. Hell, S., Reiner, G., Cremer, C. & Stelzer, E.H.K. Aberrations in confocal fluorescence microscopy induced by mismatches in refractive index. *J. Microsc.* **169**, 391–405 (1993).
25. Pitrone, P.G. *et al.* OpenSPIM: an open-access light-sheet microscopy platform. *Nat. Methods* **10**, 598–599 (2013).
26. Gualda, E.J. *et al.* OpenSpinMicroscopy: an open-source integrated microscopy platform. *Nat. Methods* **10**, 599–600 (2013).
27. Huisken, J. & Stainier, D.Y.R. Even fluorescence excitation by multidirectional selective plane illumination microscopy (mSPIM). *Opt. Lett.* **32**, 2608–2610 (2007).
28. Krzic, U., Gunther, S., Saunders, T.E., Streichan, S.J. & Hufnagel, L. Multiview light-sheet microscope for rapid *in toto* imaging. *Nat. Methods* **9**, 730–733 (2012).
29. Tomer, R., Khairy, K., Amat, F. & Keller, P.J. Quantitative high-speed imaging of entire developing embryos with simultaneous multiview light-sheet microscopy. *Nat. Methods* **9**, 755–763 (2012).
30. Tang, B., Wang, Y., Zhu, J. & Zhao, W. Web resources for model organism studies. *Genomics Proteomics Bioinformatics* **13**, 64 (2015).
31. St Pierre, S.E., Ponting, L., Stefancsik, R. & McQuilton, P. FlyBase 102: advanced approaches to interrogating FlyBase. *Nucleic Acids Res.* **42**, D780–D788 (2014).
32. Dos Santos, G. *et al.* FlyBase: introduction of the *Drosophila melanogaster* release 6 reference genome assembly and large-scale migration of genome annotations. *Nucleic Acids Res.* **43**, D690–D697 (2015).
33. Baldock, R.A. *et al.* EMAP and EMAGE: a framework for understanding spatially organized data. *Neuroinformatics* **1**, 309–325 (2003).
34. Davidson, D., Bard, J., Kaufman, M. & Baldock, R. The mouse atlas database: a community resource for mouse development. *Trends Genet.* **17**, 49–51 (2001).
35. Husz, Z.L., Burton, N., Hill, B., Milyaev, N. & Baldock, R.A. Web tools for large-scale 3D biological images and atlases. *BMC Bioinformatics* **13**, 122 (2012).
36. Dönitz, J. *et al.* TrOn: an anatomical ontology for the beetle *Tribolium castaneum*. *PLoS ONE* **8**, e70695 (2013).
37. Dönitz, J. *et al.* iBeetle-Base: a database for RNAi phenotypes in the red flour beetle *Tribolium castaneum*. *Nucleic Acids Res.* **43**, D720–D725 (2014).
38. Cong, L. *et al.* Multiplex genome engineering using CRISPR/Cas systems. *Science* **339**, 819–823 (2013).
39. Ran, F.A. *et al.* Genome engineering using the CRISPR-Cas9 system. *Nat. Protoc.* **8**, 2281–2308 (2013).
40. Gilles, A.F. & Averof, M. Functional genetics for all: engineered nucleases, CRISPR and the gene editing revolution. *EvoDevo* **5**, 43 (2014).
41. Gillies, A.F., Schinko, J.B. & Averof, M. Efficient CRISPR-mediated gene targeting and transgene replacement in the beetle *Tribolium castaneum*. *Development* doi:10.1242/dev.125054 (9 July 2015).
42. Bassett, A.R., Tibbit, C., Ponting, C.P. & Liu, J.-L. Highly efficient targeted mutagenesis of *Drosophila* with the CRISPR/Cas9 system. *Cell Rep.* **4**, 220–228 (2013).
43. Bassett, A.R. & Liu, J.-L. CRISPR/Cas9 and genome editing in *Drosophila*. *J. Genet. Genomics* **41**, 7–19 (2014).
44. Reynaud, E.G., Krzic, U., Greger, K. & Stelzer, E.H.K. Light sheet-based fluorescence microscopy: more dimensions, more photons, and less photodamage. *HFSP J.* **2**, 266–275 (2008).
45. Keller, P.J., Schmidt, A.D., Wittbrodt, J. & Stelzer, E.H.K. Digital scanned laser light-sheet fluorescence microscopy (DSLIM) of zebrafish and *Drosophila* embryonic development. *Cold Spring Harb. Protoc.* **6**, 1235–1243 (2011).
46. Reynaud, E.G., Peychl, J., Huisken, J. & Tomancak, P. Guide to light-sheet microscopy for adventurous biologists. *Nat. Methods* **12**, 30–34 (2014).
47. Khairy, K. & Keller, P.J. Reconstructing embryonic development. *Genesis* **49**, 488–513 (2011).
48. Amat, F. & Keller, P.J. Towards comprehensive cell lineage reconstructions in complex organisms using light-sheet microscopy. *Dev. Growth Differ.* **55**, 563–578 (2013).
49. Amat, F. *et al.* Fast, accurate reconstruction of cell lineages from large-scale fluorescence microscopy data. *Nat. Methods* **11**, 951–958 (2014).
50. Engelbrecht, C.J. & Stelzer, E.H.K. Resolution enhancement in a light-sheet-based microscope (SPIM). *Opt. Lett.* **31**, 1477–1479 (2006).
51. Wu, Y. *et al.* Inverted selective plane illumination microscopy (iSPIM) enables coupled cell identity lineaging and neurodevelopmental imaging in *Caenorhabditis elegans*. *Proc. Natl. Acad. Sci. USA* **108**, 17708–17713 (2011).
52. Kumar, A. *et al.* Dual-view plane illumination microscopy for rapid and spatially isotropic imaging. *Nat. Protoc.* **9**, 2555–2573 (2014).
53. Lorenzen, M.D. *et al.* piggyBac-mediated germline transformation in the beetle *Tribolium castaneum*. *Insect Mol. Biol.* **12**, 433–440 (2003).
54. Trauner, J. *et al.* Large-scale insertional mutagenesis of a coleopteran stored grain pest, the red flour beetle *Tribolium castaneum*, identifies embryonic lethal mutations and enhancer traps. *BMC Biol.* **7**, 73 (2009).
55. Schinko, J.B. *et al.* Functionality of the GAL4/UAS system in *Tribolium* requires the use of endogenous core promoters. *BMC Dev. Biol.* **10**, 53 (2010).
56. Siebert, K.S., Lorenzen, M.D., Brown, S.J., Park, Y. & Beeman, R.W. Tubulin-superfamily genes in *Tribolium castaneum* and the use of a tubulin promoter to drive transgene expression. *Insect Biochem. Mol. Biol.* **38**, 749–755 (2008).
57. Lorenzen, M.D., Brown, S.J., Denell, R.E. & Beeman, R.W. Transgene expression from the *Tribolium castaneum* polyubiquitin promoter. *Insect Mol. Biol.* **11**, 399–407 (2002).
58. Schinko, J.B., Hillebrand, K. & Bucher, G. Heat shock-mediated misexpression of genes in the beetle *Tribolium castaneum*. *Dev. Genes Evol.* **222**, 287–298 (2012).
59. Terasaki, M. & Jaffe, L.A. Labeling of cell membranes and compartments for live cell fluorescence microscopy. *Methods Cell Biol.* **74**, 469–489 (2004).
60. Kremers, G.-J., Gilbert, S.G., Cranfill, P.J., Davidson, M.W. & Piston, D.W. Fluorescent proteins at a glance. *J. Cell Sci.* **124**, 157–160 (2011).
61. Shaner, N.C., Steinbach, P.A. & Tsien, R.Y. A guide to choosing fluorescent proteins. *Nat. Methods* **2**, 905–909 (2005).
62. Chudakov, D.M., Matz, M.V., Lukyanov, S. & Lukyanov, K.A. Fluorescent proteins and their applications in imaging living cells and tissues. *Physiol. Rev.* **90**, 1103–1163 (2010).
63. Kaufmann, A., Mickoleit, M., Weber, M. & Huisken, J. Multilayer mounting enables long-term imaging of zebrafish development in a light sheet microscope. *Development* **139**, 3242–3247 (2012).
64. Ichikawa, T. *et al.* Live imaging of whole mouse embryos during gastrulation: migration analyses of epiblast and mesodermal cells. *PLoS ONE* **8**, e64506 (2013).
65. Ichikawa, T. *et al.* Live imaging and quantitative analysis of gastrulation in mouse embryos using light-sheet microscopy and 3D tracking tools. *Nat. Protoc.* **9**, 575–585 (2014).

66. Breuninger, T., Greger, K. & Stelzer, E.H.K. Lateral modulation boosts image quality in single plane illumination fluorescence microscopy. *Opt. Lett.* **32**, 1938–1940 (2007).
67. Swoger, J., Verveer, P., Greger, K., Huisken, J. & Stelzer, E.H.K. Multi-view image fusion improves resolution in three-dimensional microscopy. *Opt. Express* **15**, 8029–8042 (2007).
68. Preibisch, S., Saalfeld, S., Schindelin, J. & Tomancak, P. Software for bead-based registration of selective plane illumination microscopy data. *Nat. Methods* **7**, 418–419 (2010).
69. Preibisch, S. *et al.* Efficient Bayesian-based multiview deconvolution. *Nat. Methods* **11**, 645–648 (2014).
70. Walter, T. *et al.* Visualization of image data from cells to organisms. *Nat. Methods* **7**, S26–S41 (2010).
71. Stelzer, E.H.K. Contrast, resolution, pixelation, dynamic range and signal-to-noise ratio: fundamental limits to resolution in fluorescence light microscopy. *J. Microsc.* **189**, 15–24 (1998).
72. Keller, P.J. & Stelzer, E.H.K. Digital scanned laser light sheet fluorescence microscopy. *Cold Spring Harb. Protoc.* **5** doi:10.1101/pdb.top78 (2010).
73. Schindelin, J. *et al.* Fiji: an open-source platform for biological-image analysis. *Nat. Methods* **9**, 676–682 (2012).
74. Greger, K., Swoger, J. & Stelzer, E.H.K. Basic building units and properties of a fluorescence single plane illumination microscope. *Rev. Sci. Instrum.* **78**, 023705 (2007).
75. Arpino, J.A.J., Rizkallah, P.J. & Jones, D.D. Crystal structure of enhanced green fluorescent protein to 1.35 Å resolution reveals alternative conformations for Glu222. *PLoS ONE* **7**, e47132 (2012).
76. Sokoloff, A. *The Biology of Tribolium: With Special Emphasis on Genetic Aspects* (Oxford University Press, 1974).
77. Kittler, J. & Illingworth, J. Minimum error thresholding. *Pattern Recogn.* **19**, 41–47 (1986).
78. Cho, S., Haralick, R. & Yi, S. Improvement of Kittler and Illingworth's minimum error thresholding. *Pattern Recogn.* **22**, 609–617 (1989).

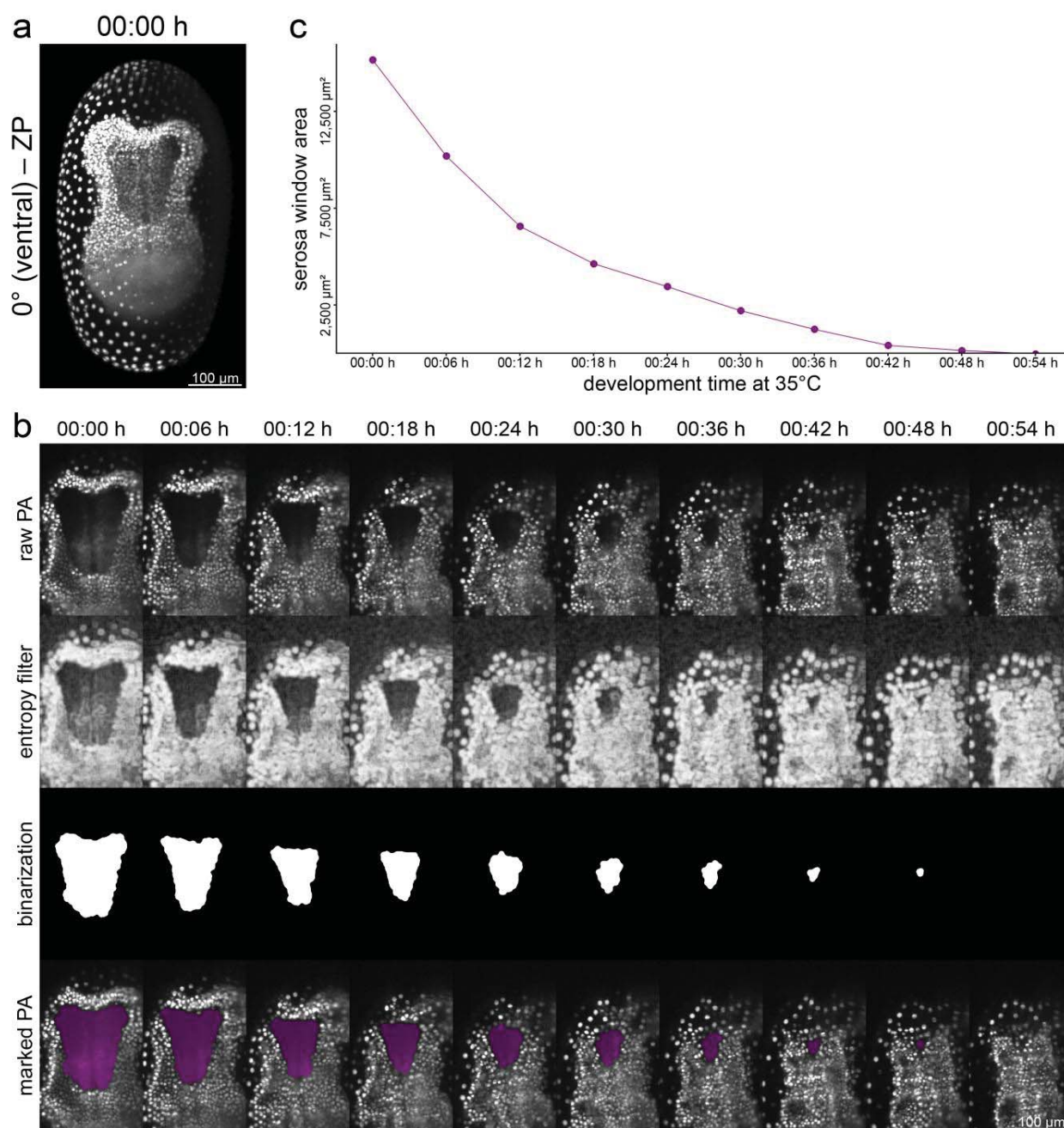




Supplementary Figure 1

Principle effects of LSFM illumination and detection on image quality.

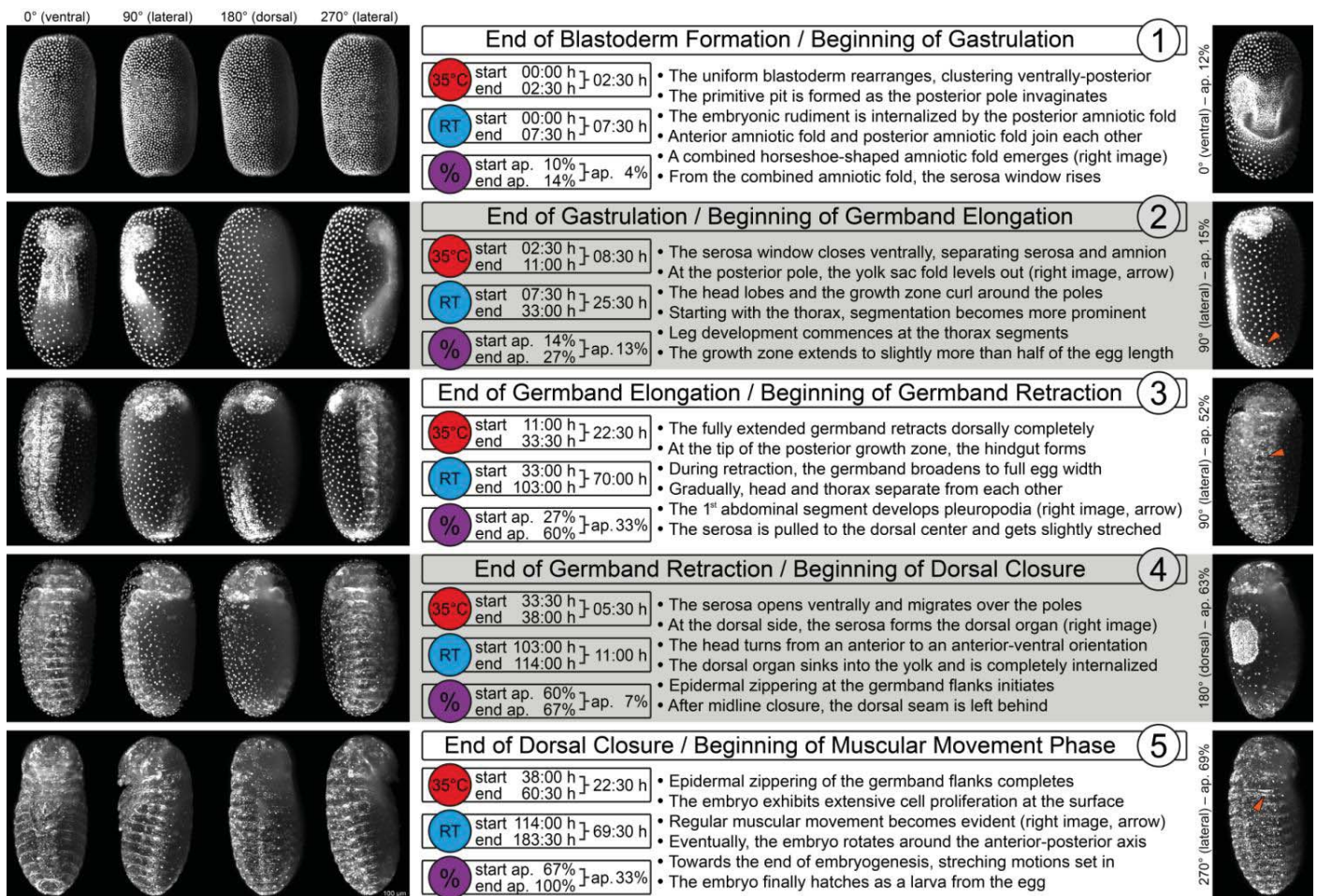
(A) Top view of a scheme showing the arrangement of illumination objective, sample chamber and detection objective in a light sheet-based fluorescence microscope. The inset depicts the illumination and detection of a single line in a specimen. (B) Top view of the objective arrangement in the mDSLIM. In the inset, image quality indicators are provided as colored arcs. The green arc marks the quarter with an expected high quality, the orange arcs the quarters with an expected medium quality and the red arc the quarter with an expected low quality. (C) Y maximum projection of a Z stack with the image quality indicators introduced in B.



Supplementary Figure 2

Example quantification of the serosa window area over time during serosa window closure.

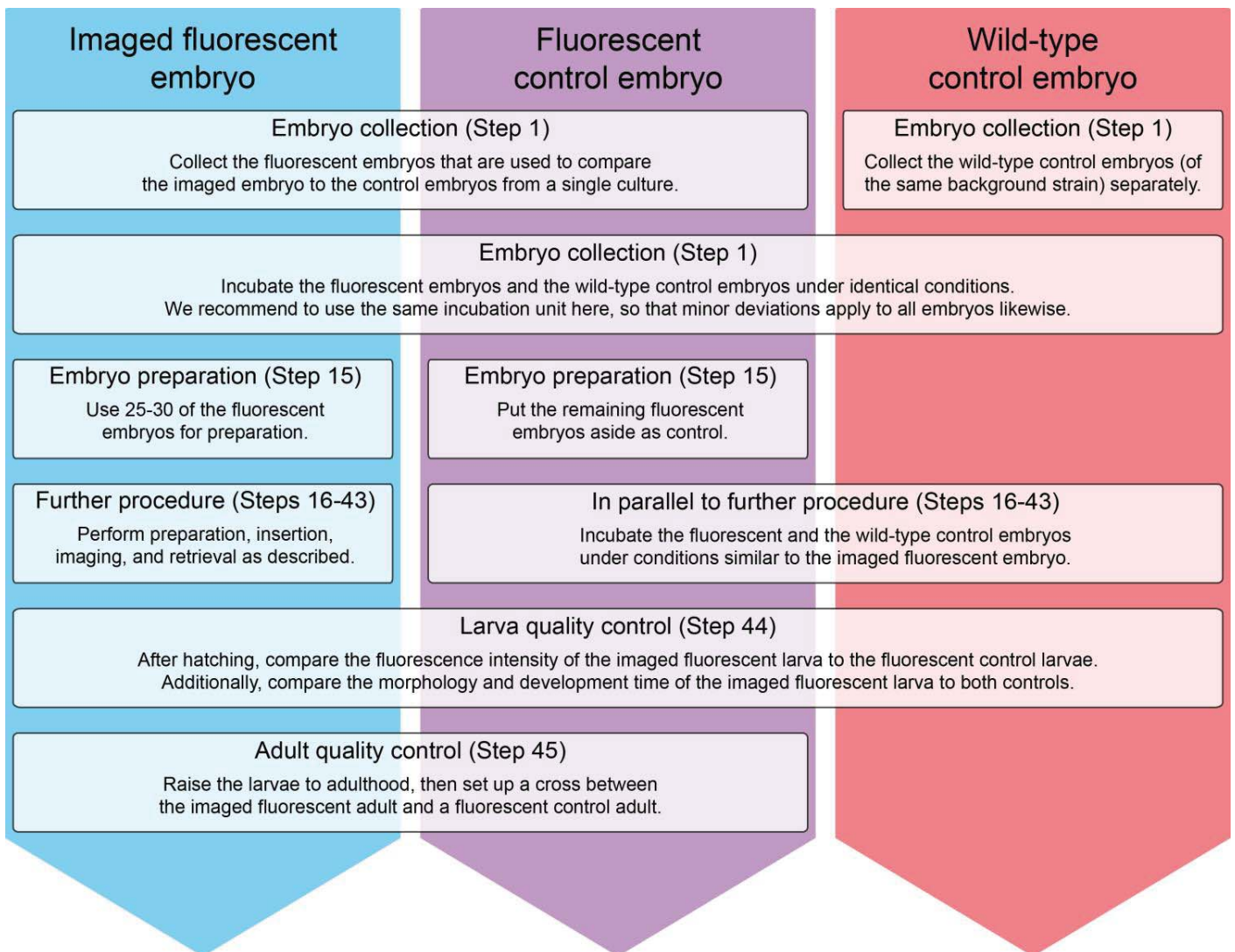
(A) Z maximum projection of a *Tribolium* embryo during gastrulation that commences serosa window closure seen from the ventral side. (B) Time lapse of single planes, 26 µm below the ventral surface of the embryo, showing the process of serosa window closure. The first row depicts the raw planes. In the second row, an entropy filter was applied to the raw planes. Then, an intensity threshold was set to obtain the binary images. The binary images were inverted and further processed by morphological operations to extract the serosa window area in each image, as shown in the third row. The fourth row illustrates the raw planes marked with the extracted serosa window area. (C) A plot of the serosa window area as a function of development time, providing evidence that the serosa window area during serosa window closure follows an exponential decay. ZP, Z maximum projection with image processing; PA, plane with intensity adjustment.



Supplementary Figure 3

Chronological staging table of *Tribolium* embryogenesis.

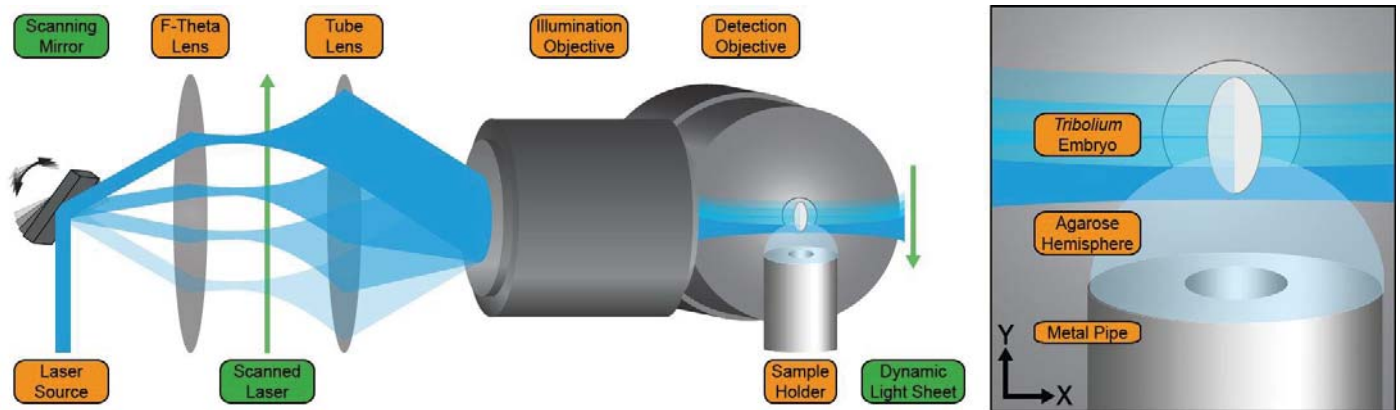
The left column contains Z maximum projections along four orientations (0° (ventral), 90° (lateral), 180° (dorsal), and 270° (lateral)) of a *Tribolium* embryo at the beginning of five major embryogenetic events. In the middle column, an outline of the most important developmental processes with a temporal indication in hours (developments at 35°C and at room temperature) and stage indication in percent of full development. Please note that 00:00 h relates to our standard imaging starting point (that is after a 1 h egg laying period / 15 h of incubation at 25°C and 1 h of preparation at room temperature), whereas the stage indication in percent is provided for the whole of embryogenesis. The right column shows Z maximum projections of developmental processes during the respective embryogenetic events that have been the focus of previous research. Red arrows indicate the location of the process mentioned in the bullet points. RT, room temperature (23±1°C); ap., approximately.



Supplementary Figure 4

Scheme of the recommended control experiments.

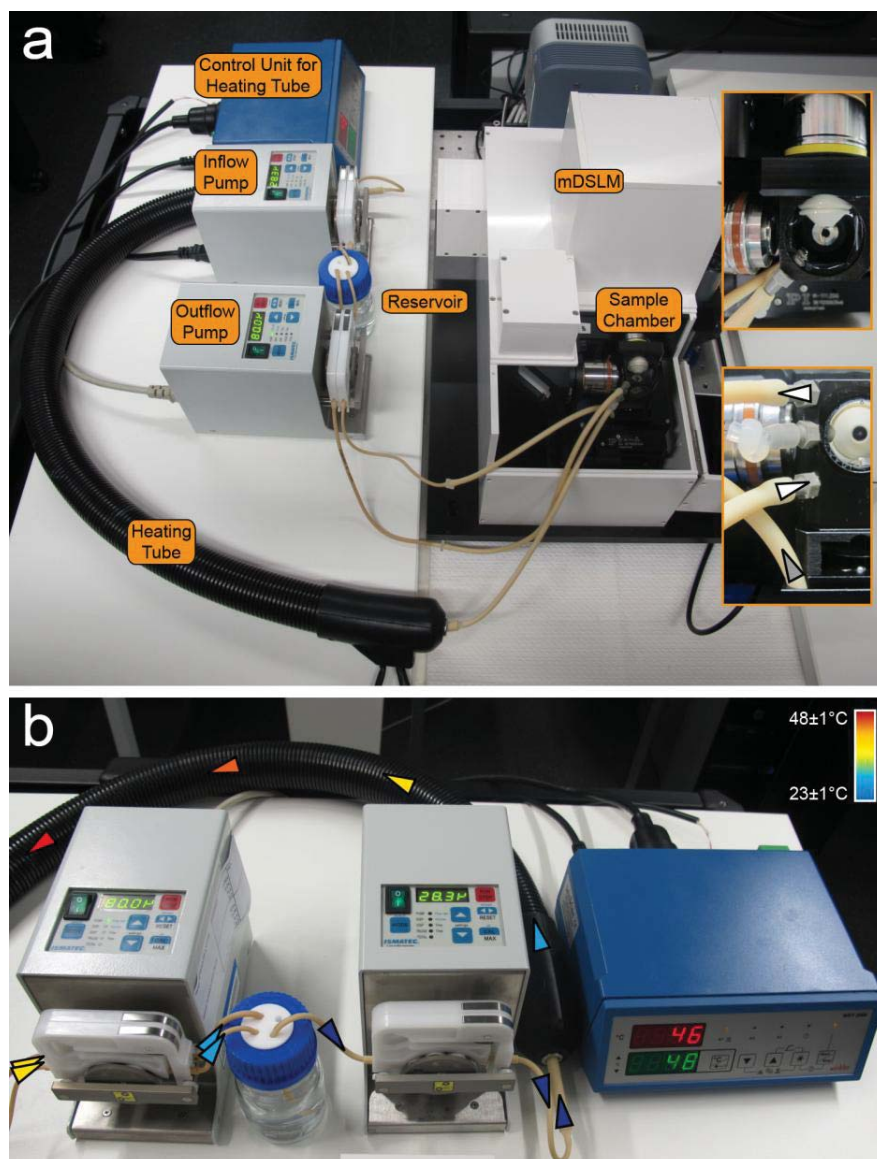
In addition to the imaging procedure of the fluorescent embryo (left column), we suggest two control experiments that can be run in parallel: a fluorescent control embryo (middle column) and a wild type control embryo (right column). All steps in which the control experiments have to be considered are indicated and also mentioned in the Procedure section.



Supplementary Figure 5

Operating principle of the digital scanned laser light sheet-based fluorescence microscope (DSLIM).

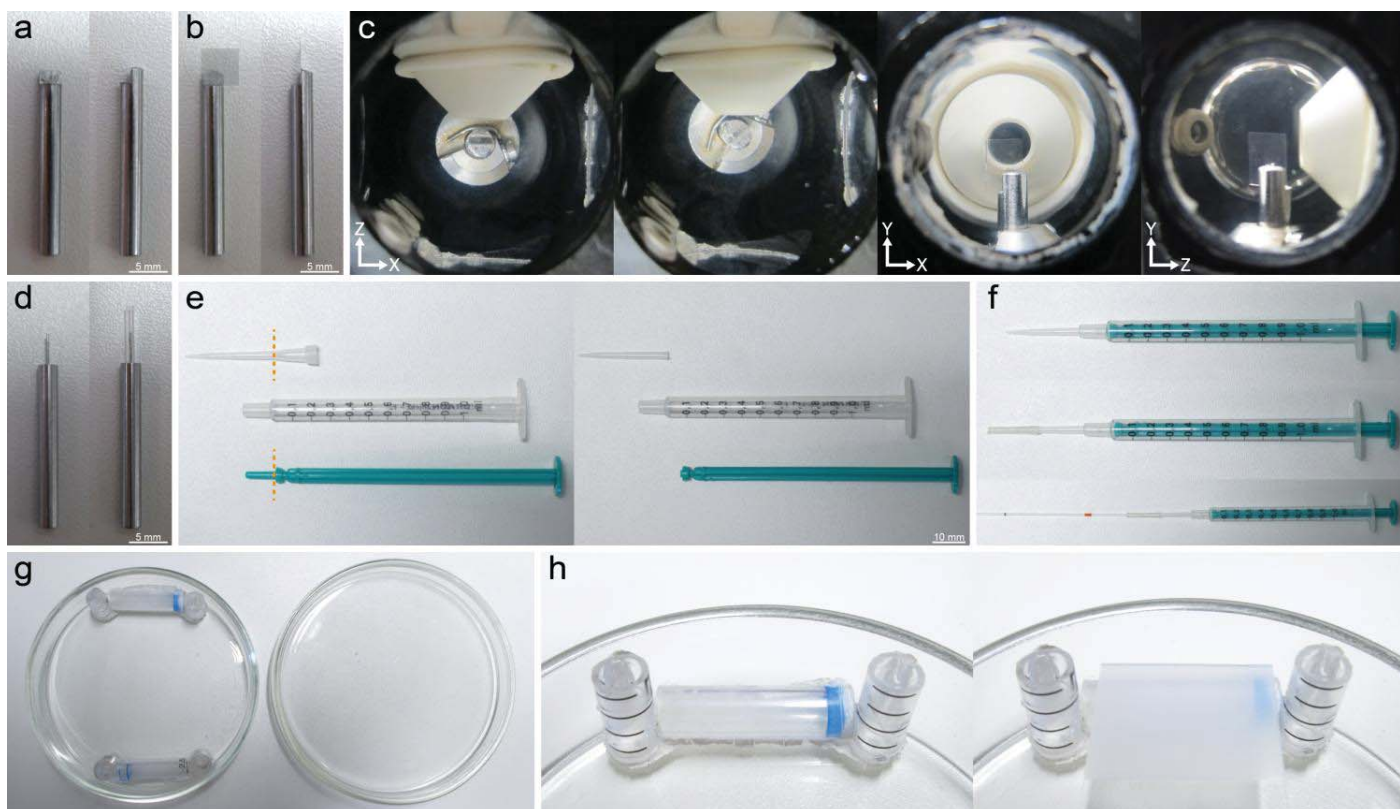
In contrast to other types of light sheet-based fluorescence microscopes, the DSLIM does not have a static light sheet. Instead, a dynamic light sheet is generated by scanning the laser beam with a piezo-driven two-axes scanning mirror (see green annotations). The laser beam, originating from the laser source, is guided by the scanning mirror through an f-theta and a tube lens into the illumination objective. The dynamic light sheet illuminates a thin slice of the *Tribolium* embryo, and the emitted fluorescence is guided by a perpendicularly arranged detection objective through an appropriate filter and a tube lens into the camera. The detail on the right shows the sample holder with the embryo in front of the detection objective. Adapted and modified from ref. 18 with permission, Nature Publishing Group.



Supplementary Figure 6

Perfusion system.

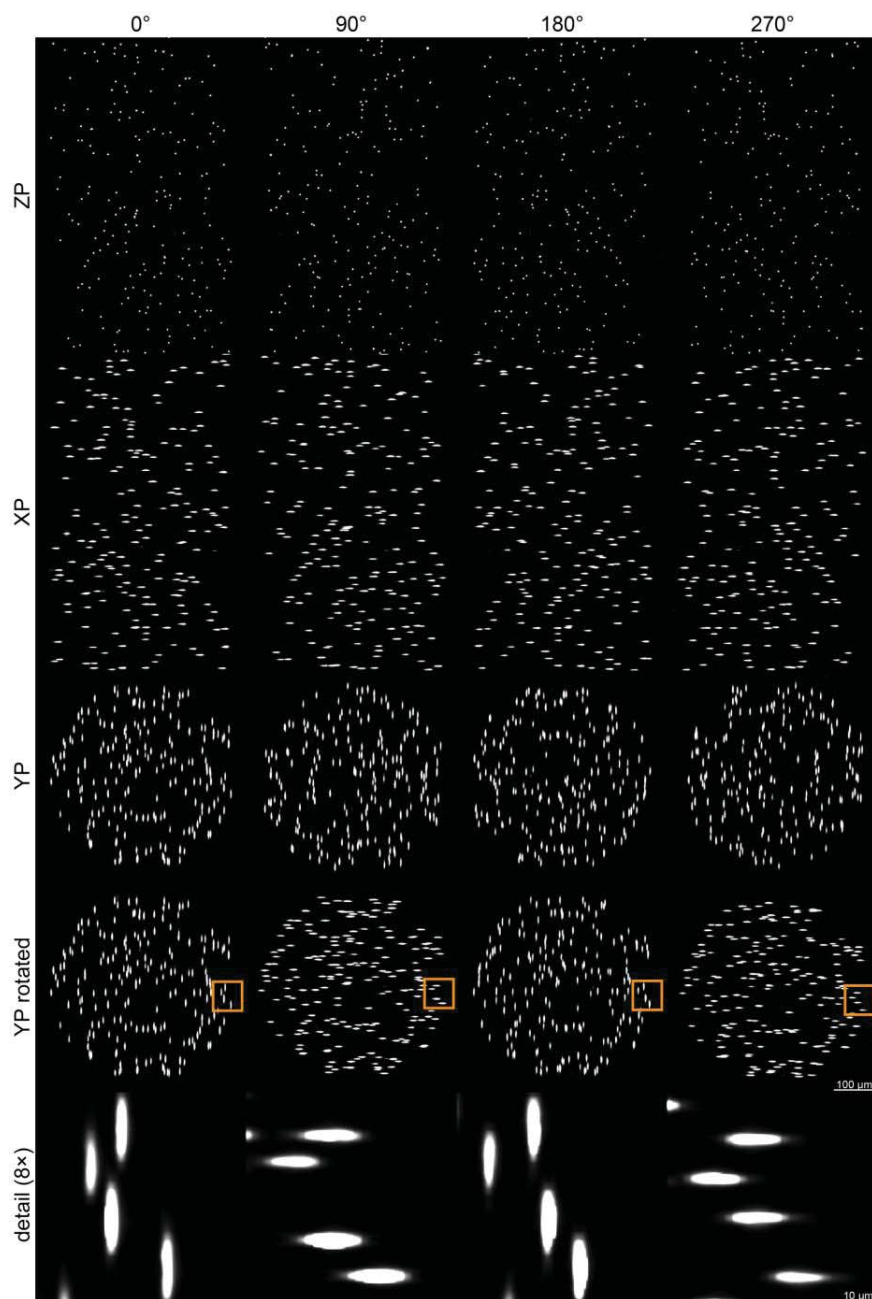
(A) Overview of mDSLIM with connected perfusion system. The main elements of the circulatory perfusion system are labelled. Controlled transfer of PBS from the reservoir is achieved via the inflow pump through the heating tube into the sample chamber. From the chamber, excessive PBS is transferred via the outflow pump back into the reservoir. Upper detail box shows a top view of the sample chamber. The perfusion system connects to the periphery of the sample chamber and, therefore, does not impair the imaging process. Lower detail box shows the front view of the sample chamber with connected inflow and outflow tubes. The inflow tube connects to the lower and the outflow tube to the upper joint of the sample chamber. Therefore, the PBS outflow rate is limited by the inflow rate. Directions of flow are indicated with white arrowheads. A third tube is connected to a catch basin located beneath the sample chamber in case of a leakage, as indicated with a gray arrowhead. (B) Setup and equilibrium of perfusion system. A constant temperature in the sample chamber is maintained via a combination of PBS flow rate and the temperature generated in the heating tube. Prior to the experiment, the perfusion system is given two hours to ensure a stable temperature in the sample chamber. The circulatory flow of PBS and relative warmth are indicated with colored arrowheads.



Supplementary Figure 7

Illustration of equipment setup.

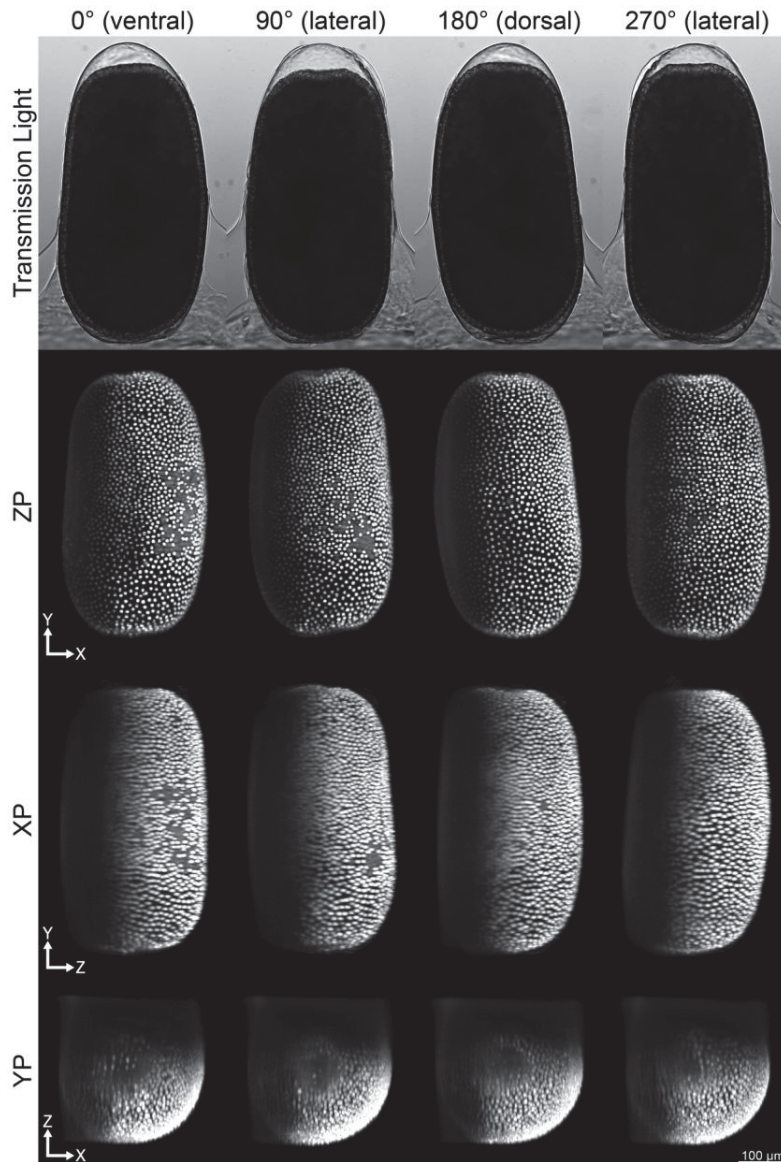
(A) Front (left) and side view (right) of the glass cover slip holder. (A') Front (left panel) and side view (right panel) of the holder in A with attached glass cover slip. (A'') Glass cover slip holder in the LSFM sample chamber. From left to right: top view of glass cover slip holder perpendicular to Z (the detection axis), top, front and side view of the glass cover slip holder rotated by 45° around Y (the rotation axis). (B) Capillary holder (left panel) with capillary attached (right panel). (C) Syringe components with cut lines indicated in orange (left panel). Components with indicated parts cut off (right panel). (C') Assembled syringe (top panel), with rubber hose (middle panel) and capillary (bottom panel) attached. (D) Humidity chamber. (D') Scaffold created from serological pipette fragments without (left panel) and with object slide (right panel).



Supplementary Figure 8

Test recording of agarose-embedded beads column for microscope calibration.

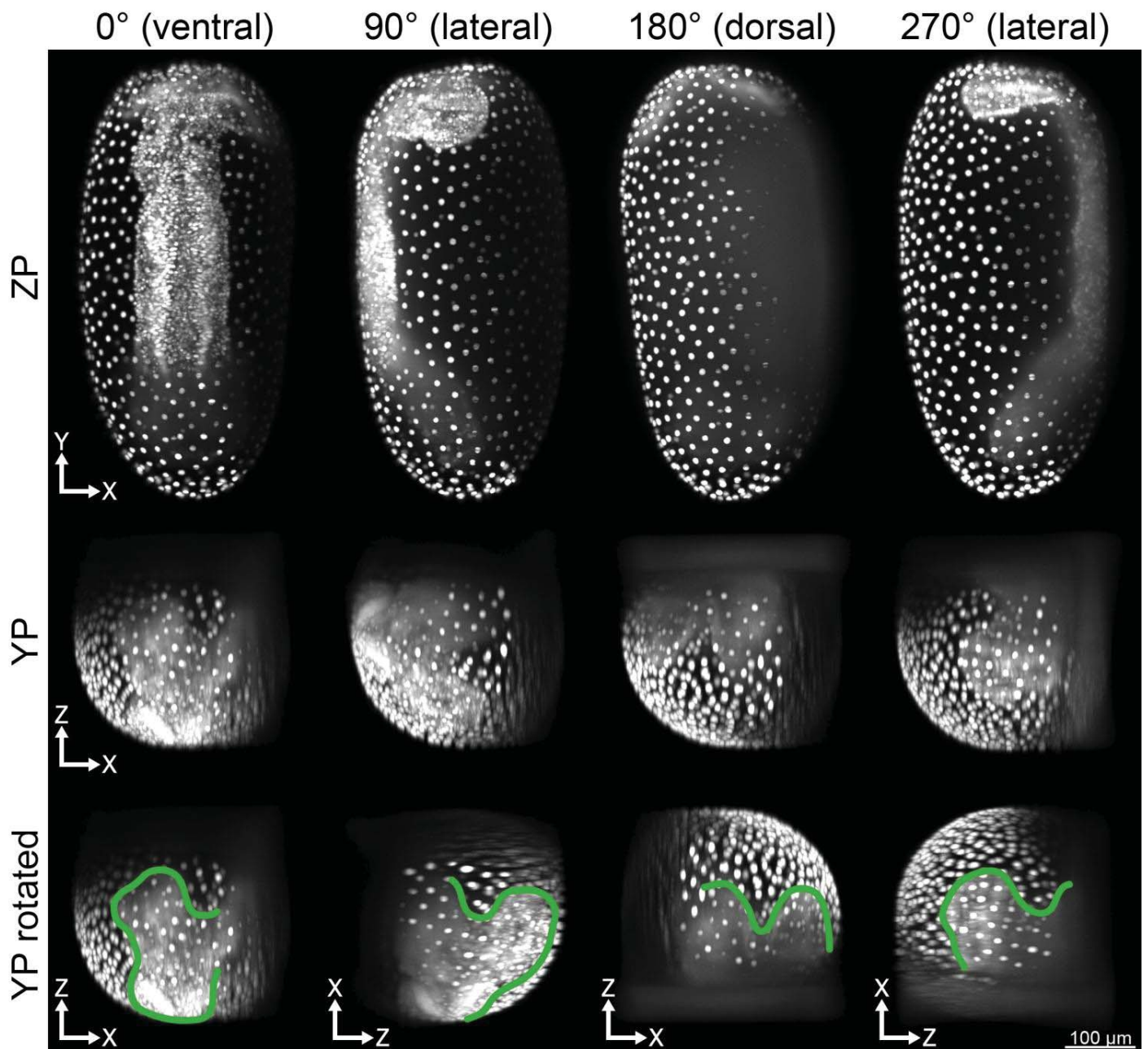
The agarose-embedded beads column is shown along four orientations as a Z (first row), X (second row) and Y (third row) maximum projections. The maximum projections illustrate correct calibration of the microscope without any imaging artifacts. The rotated Y maximum projections (fourth row) demonstrate a correctly set up recording of the bead agarose column. Individual beads can be identified along all directions as shown in the detail images (fifth row). Due to the point spread function, beads are expected to appear as bright, round dots in the Z maximum projection and elongated along X and Y maximum projections. ZP, Z maximum projections with image processing; XP, X maximum projections with image processing; YP, Y maximum projections with image processing.



Supplementary Figure 9

Test recording of the embryo along four directions prior to time lapse imaging.

The embryo is shown in four orientations in the transmission light channel (first row) and as Z (second row), X (third row) and Y (fourth row) maximum projections. The maximum projections illustrate a correctly set up recording along four directions without any imaging artifacts. Some preparation issues and misconfigurations of the imaging setup (e.g. insufficient amount of agarose in the stability layer leading to a drift of the embryo, incorrect Z spacing, incorrect configured volume of view), might be more apparent in X and Y maximum projections than in the Z maximum projections. Indicators for a correctly set up recording are: X and Y maximum projections depict smooth object boundaries and show no motion blur; Z maximum projections and the corresponding X maximum projections exhibit high similarity; and in the Y maximum projections, the shape of the embryo should be roughly circular. ZP, Z maximum projections with image processing; XP, X maximum projections with image processing; YP, Y maximum projections with image processing.



Supplementary Figure 10

Qualitative coverage of the embryo.

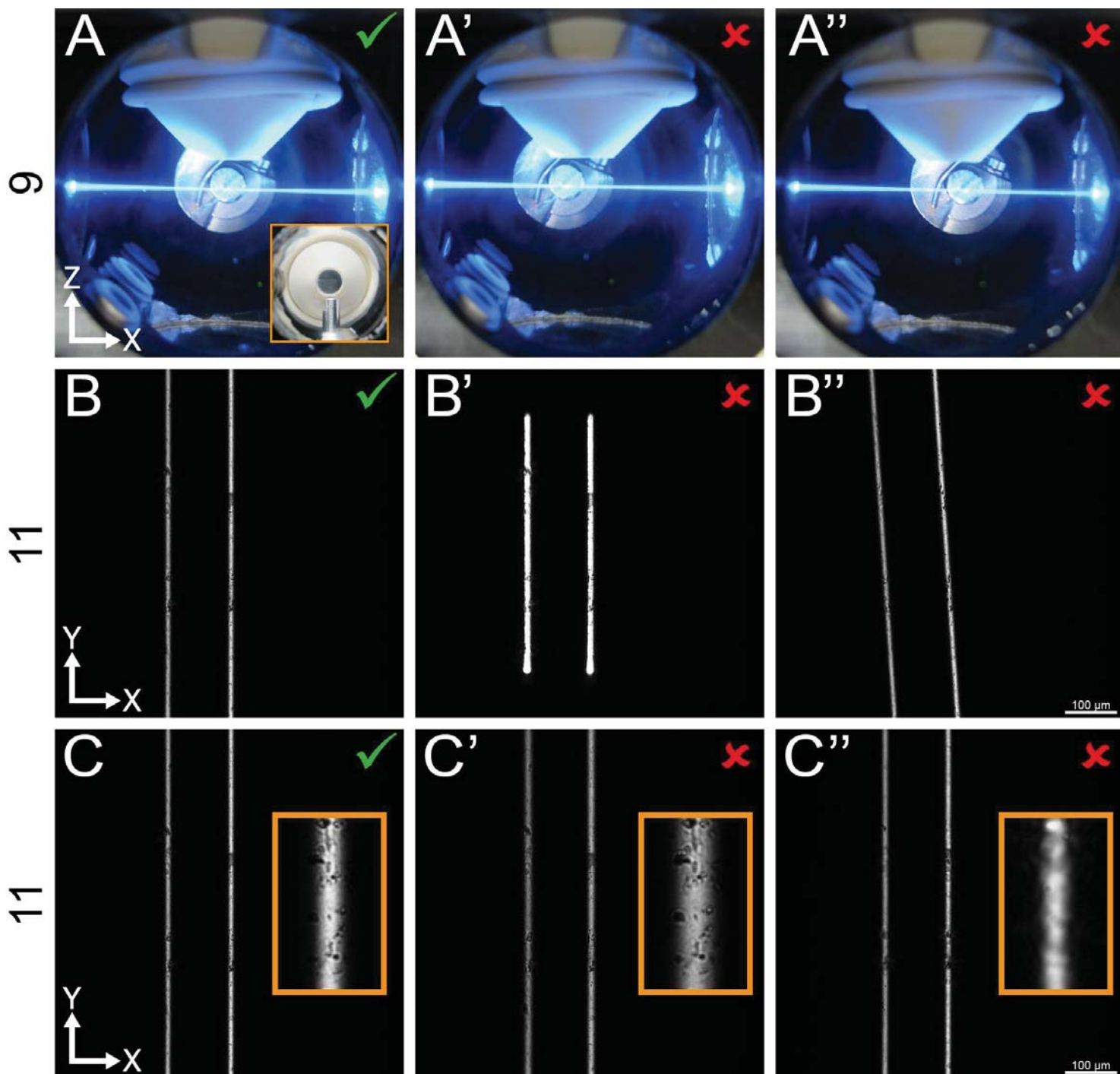
The embryo is shown along four orientations as Z and Y maximum projections. The Y maximum projections (second row) illustrate that the quality of the recording strongly depends on the amount and type of biological material passed by the illumination and emission light paths. If no biological material obstructs the light paths, the resulting image quality is high (lower left area in all orientations). However, if the amount of material that has to be passed increases, the image quality drops (upper left and lower right areas in all orientations). The image quality is worst in areas where both light paths have to pass the complete embryo (upper right areas in all orientations). The rotated Y maximum projections (third row) highlight the fact that features of the embryo might only be partly visible in some orientations. The green lines outline the clearly detectable germ band borders from the respective direction. ZP, Z maximum projections with image processing; YP, Y maximum projections with image processing.

Supplementary Table 1 | Metadata and parameters for the three example datasets.

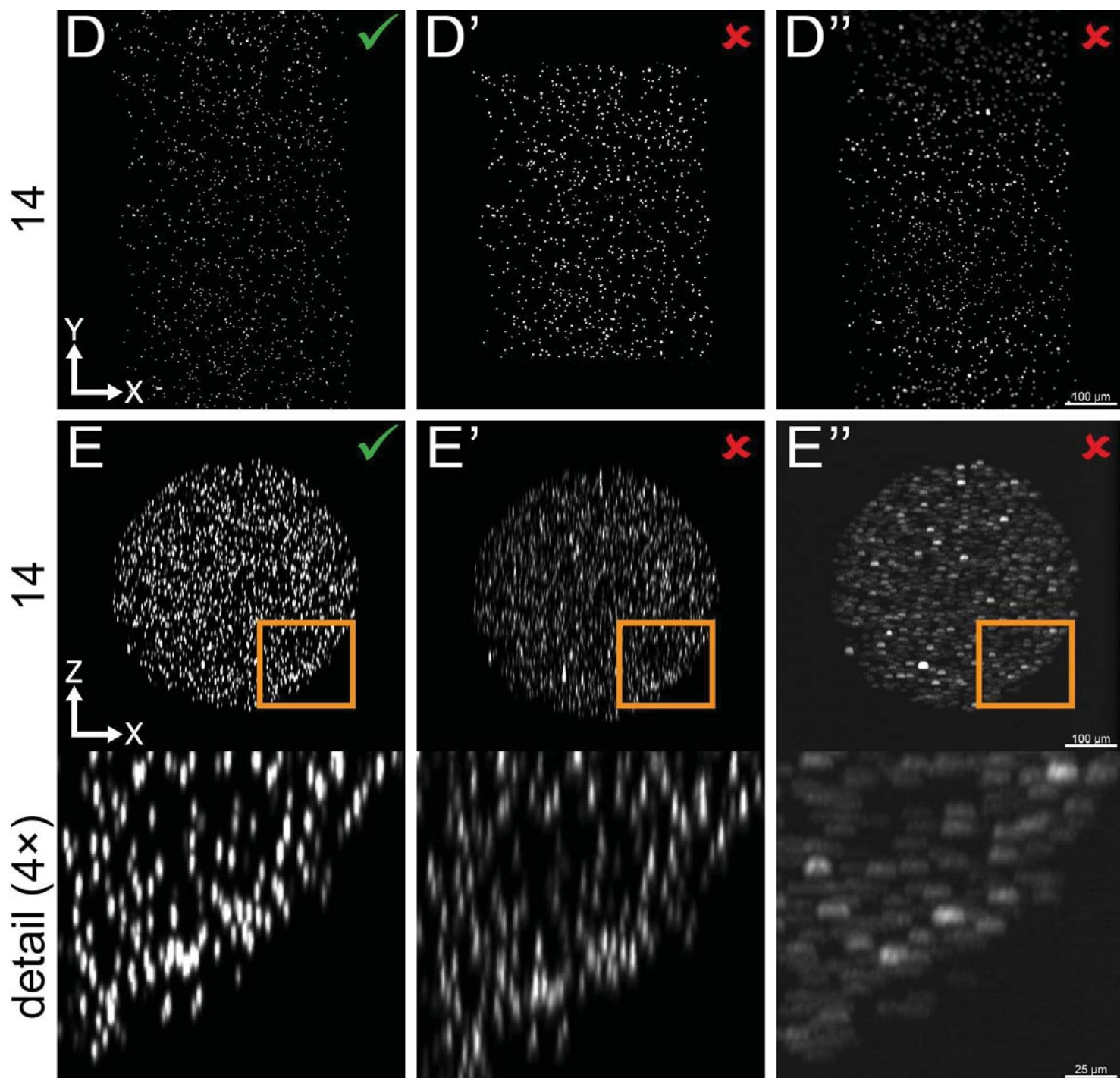
<i>Dataset (DS)</i>	DS0001	DS0002	DS0003
<i>Species</i>	<i>Tribolium castaneum</i> (Herbst) / Arthropoda → Insecta → Coleoptera → Tenebrionidae		
<i>Line</i>	EFA-nGFP transgenic line ¹⁰ (background strain: vermilion white)		
<i>Line Genotype</i>	one insert / homozygote		
<i>Stock</i>	~300 adults, less than 4 months old		
<i>Stock Medium</i>	full grain wheat flour (113061006, Demeter, Darmstadt, Germany) supplemented with 5% (wt/wt) inactive dry yeast (62-106, Flystuff, San Diego, CA, USA)		
<i>Stock Conditions</i>	12:00 h light / 12:00 h darkness at 25 °C and 70% relative humidity (DR-36VL, Percival Scientific, Perry, IA, USA)		
<i>Egg Laying Period</i>	01:00 h at 25 °C and 70% relative humidity exposed to light		
<i>Egg Laying Medium</i>	405 fine wheat flour (113061036, Demeter, Darmstadt, Germany) supplemented with 5% (wt/wt) inactive dry yeast (62-106, Flystuff, San Diego, CA, USA)		
<i>Pre-imaging Incubation</i>	15:00 h at 25 °C and 70% relative humidity in darkness		
<i>LSFM Type</i>	mDSLM based on DSLM ^{18,72} with structured illumination ¹⁹		
<i>Laser Lines</i>	488 nm / 60 mW diode laser (PhoxX 488-60, Omicron Laserprodukte GmbH, Rodgau-Dudenhofen, Germany)		
<i>Excitation Objective</i>	2.5x NA 0.06 EC Epiplan-Neofluar objective (422320-9900-000, Carl Zeiss, Göttingen, Germany)		
<i>Emission Objective</i>	10x NA 0.3 W N-Achroplan objective (420947-9900-000, Carl Zeiss, Göttingen, Germany)		
<i>Emission Filters</i>	525/50 single-band bandpass filter (FF03-525/50- 25, Semrock/AHF Analysentechnik AG, Tübingen, Germany)		
<i>Camera</i>	High-resolution CCD (Clara, Andor, Belfast, United Kingdom)		
<i>Dataset File Type (Raw)</i>	TIFF, 16 bit grayscale (planes are deposited as Z stacks, indicated as PL(ZS) in the file name)		
<i>Dechoriation</i>	~30 s in 10% (vol/vol) sodium hypochlorite (425044-250ML, Sigma Adrich, Taufkirchen, Germany) in PBS pH 7.4 (10010-023, Gibco Life Technologies GmbH, Darmstadt, Germany)		
<i>Mounting Agarose</i>	1% (wt/vol) low-melt agarose (6351.2, Carl Roth, Karlsruhe, Germany) in PBS pH 7.4 (10010-023, Gibco Life Technologies GmbH, Darmstadt, Germany)		
<i>Imaging Buffer</i>	PBS pH 7.4 (10010-023, Gibco Life Technologies GmbH, Darmstadt, Germany)		
<i>Imaging Temperature</i>	35°C (perfusion system)	room temperature (23±1 °C)	room temperature (23±1 °C)
<i>Dataset Size</i>	92 Gigabyte (raw)	642 Gigabyte (raw)	193 Gigabyte (raw)
	37 Gigabyte (ZIP)	273 Gigabyte (ZIP)	77 Gigabyte (ZIP)
	0.47 Gigabyte (JPEG2000)	5.54 Gigabyte (JPEG2000)	1.62 Gigabyte (JPEG2000)
<i>Retrieval</i>	survived, developed to healthy adult, produced fertile progeny	survived, developed to healthy adult, produced fertile progeny	survived, developed to healthy adult, produced fertile progeny
<i>Figures</i>	10 (upper row)	4D-F; 7; 8; 9; 10 (lower row); 12 (upper row)	11
<i>Supplementary Figures</i>	-	2; 3; 9; 10	-
<i>Supplementary Videos</i>	-	3; 4; 5	6

Time Points (TP)	49 (TP0001-TP0049)	241 (TP0001-TP0241)	49 (TP0001-TP0049)
<i>TP Interval</i>	00:30 h	00:30 h	00:30 h
<i>Total Time (TP×TP Interval)</i>	24:00 h	120:00 h	24:00 h
Directions (DR)	4 (DR0001-DR0004)	4 (DR0001-DR0004)	4 (DR0001-DR0004)
<i>DR Orientations</i>	0°, 90°, 180°, 270°	0°, 90°, 180°, 270°	0°, 90°, 180°, 270°
Channels (CH)	1 (CH0001)	1 (CH0001)	2 (CH0001-CH0002)
<i>CH0001 Excitation</i>	488 nm	488 nm	488 nm
<i>CH0001 Power</i>	135 μW (close to the embryo)	135 μW (close to the embryo)	135 μW (close to the embryo)
<i>CH0001 Exposure Time</i>	50 ms	50 ms	50 ms
<i>CH0001 Emission Filter</i>	525/50 single-band bandpass filter	525/50 single-band bandpass filter	525/50 single-band bandpass filter
<i>CH0002 Excitation</i>	-	-	488 nm, structured illumination 50 Hz
<i>CH0002 Power</i>	-	-	270 μW (close to the embryo)
<i>CH0002 Exposure Time</i>	-	-	50 ms
<i>CH0002 Emission Filter</i>	-	-	525/50 single-band bandpass filter
Planes (PL)	175 (PL0001-PL0175)	198 (PL0001-PL0198)	183 (PL0001-PL0183)
<i>Z Spacing</i>	2.58 μm	2.58 μm	2.58 μm
<i>Z Distance (PL×Z Spacing)</i>	451.5 μm	510.8 μm	472.1 μm
X-Dimensions (XD)	1040 pixels (raw) 600 pixels (cropped)	1040 pixels (raw) 600 pixels (cropped)	1040 pixels (raw) 600 pixels (cropped)
<i>X Spacing</i>	0.645 μm	0.645 μm	0.645 μm
<i>X Length (XD×X Spacing)</i>	670.8 μm (raw) 387.0 μm (cropped)	670.8 μm (raw) 387.0 μm (cropped)	670.8 μm (raw) 387.0 μm (cropped)
Y-Dimensions (YD)	1392 pixels (raw) 1000 pixels (cropped)	1392 pixels (raw) 1000 pixels (cropped)	1392 pixels (raw) 1000 pixels (cropped)
<i>Y Spacing</i>	0.645 μm	0.645 μm	0.645 μm
<i>Y Length (YD×Y Spacing)</i>	897.8 μm (raw) 645.0 μm (cropped)	897.8 μm (raw) 645.0 μm (cropped)	897.8 μm (raw) 645.0 μm (cropped)

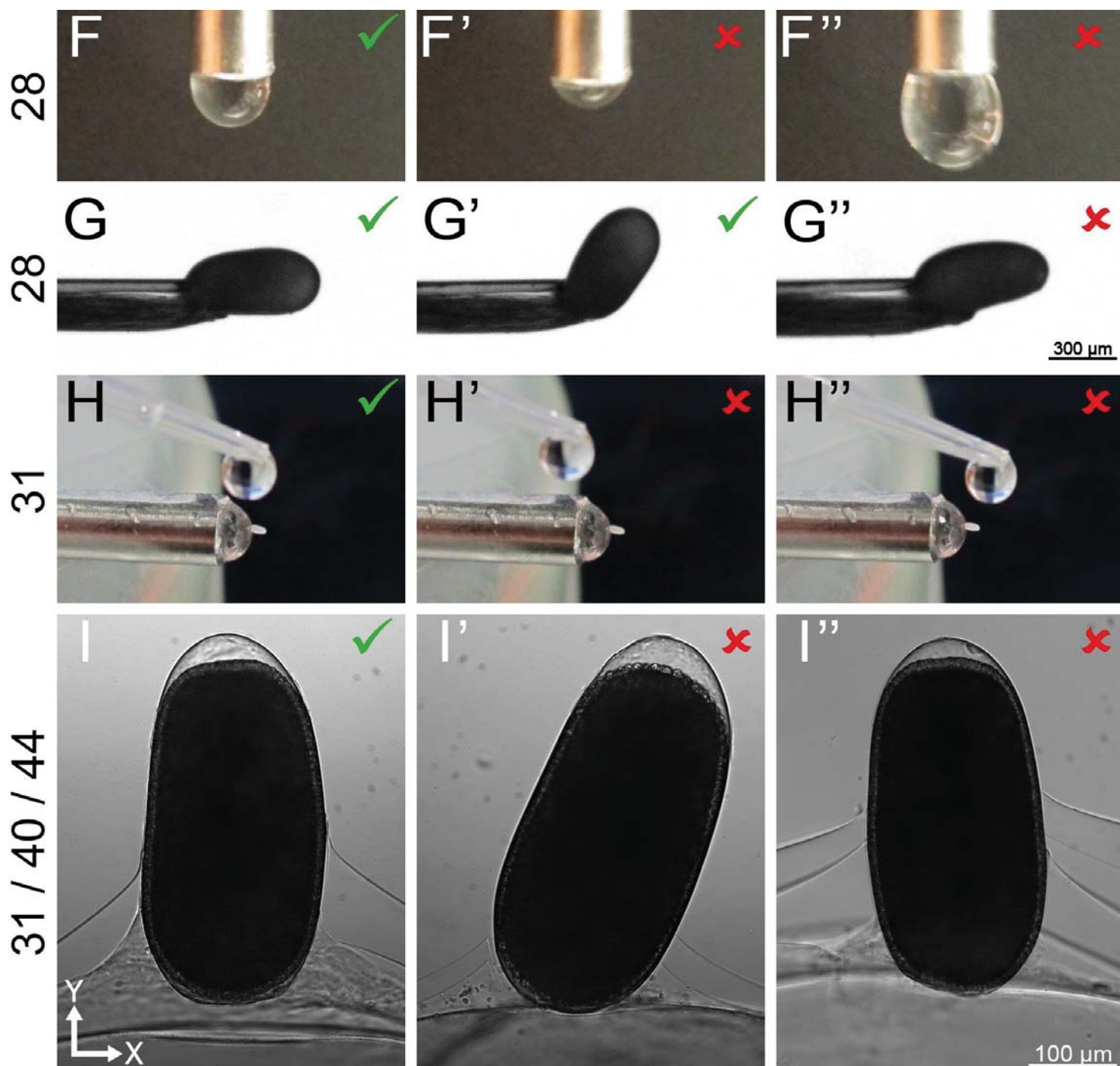
The original datasets, associated figures and videos in full quality are available at www.physikalischebiologie.de/bugcube.



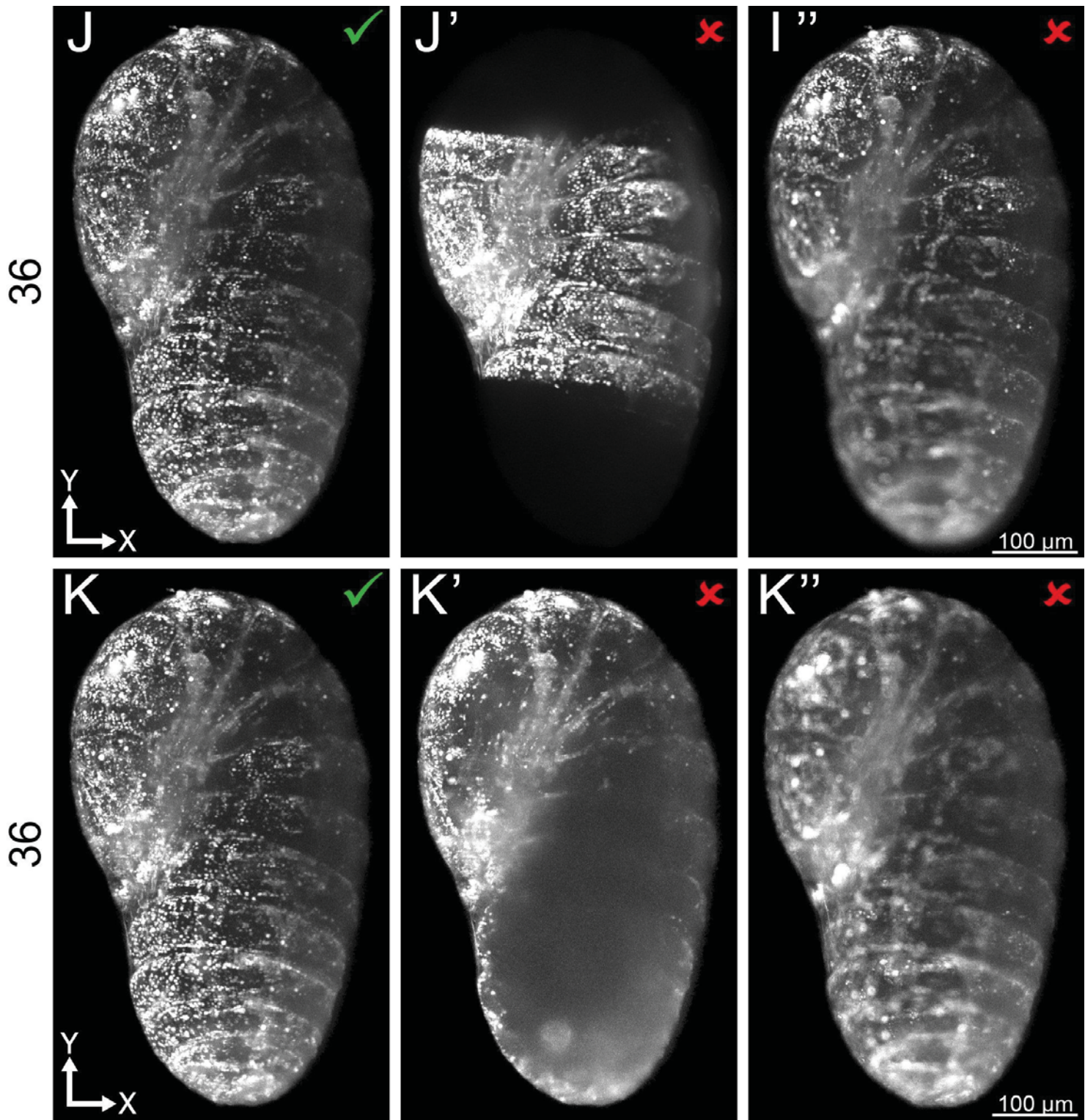
Supplementary Note | Troubleshooting of common problems during LSFM calibration and subsequent imaging processing. Please note that in some figures the problem and in others the reason is shown. A green checkmark in the upper right corner indicates the correct execution, whereas a red cross indicates an incorrect execution. (A-A'') Bright dot not visible when glass cover slip holder is placed in microscope chamber (Step 9). (A) The correct glass cover slip holder position reflects the laser light directly into the detection objective. (A'-A'') Glass cover slip holders that are positioned offset either left (A') or right (A'') cause the reflected laser light to miss the detection objective. Also ensure that the glass cover slip holder is positioned at the correct height (front view in detail box in A). (B-B'') Light sheet does not span straight across the complete field of view along Y (Step 11). (B) The light sheet should extend approximately 20% over the field of view along Y, so that the visible part of the light sheet is homogeneous. (B') If the scanning range of the activated scanning mirror is too small, the light sheet does not span across the complete field of view along Y. (B'') If the scanning mirror is not adjusted correctly, the light sheet is tilted. (C-C'') Light sheet does not appear focused (Step 11). (C) The light sheet should be a straight focused line with minimal width highlighting surface irregularities on the inserted glass cover slip. (C') The light sheet appears broader when the waist is not positioned in the field of view. (C'') It appears blurry when the focal plane is not in the center of the light sheet.



Supplementary Note (continued) | (D-D'') Beads are missing or appear blurry on either end of Y (Step 14). (D) The beads should appear focused and homogeneously distributed along the vertical direction across the full height of the acquired image. (D') If beads are missing on either end or on both ends of the image, the light sheet height has to be readjusted, the glass capillary is in the field of view, or the agarose-embedded beads column is too short. (D'') If beads appear focused in the image center and blurry on the outer edges in the vertical direction, the light sheet is tilted. The light sheet orientation needs to be readjusted using the glass cover slip holder. (E-E'') Beads appear blurry across the complete field of view (Step 14). (E) A circle of homogeneously distributed beads should appear and beads should be focused across the full Z distance of the Y maximum projection. (E') If beads appear dim and elongated, the light sheet waist is not positioned correctly and the position of the illumination objective needs to be readjusted using the piezo nano-positioners. (E'') If beads appear blurry, the light sheet does not overlap with the focal plane. The position of the detection objective needs to be readjusted using the piezo nano-positioners.



Supplementary Note (continued) | (F-F'') Difficulties in mounting the embryo on the agarose hemisphere (Step 28). (F) The semi axes of the agarose hemisphere should be at best identical (see also Figure 3G). (F'-F'') If the pole radius is smaller (F') or greater (F''), the embryo tends to tip over during the mounting procedure. (G-G'') The embryo moves after being placed on the pole of the agarose hemisphere (Step 28). (G-G') During the mounting process, the posterior end of the embryo should be attached to the brush tip, while the anterior end remains accessible. (G'') If the embryo is attached vice versa, either reposition the embryo with a second brush, or release the embryo into the PBS and restart the picking process. (H-H'') Embryo detaches when sample holder is inserted into sample chamber (Step 31). (H) The drop of liquid agarose to fix the embryo has to be correctly placed on the agarose hemisphere. (H') If it is placed on the steel pipe, the agarose does not reach the embryo. (H'') If the drop is positioned directly on the embryo, the embryo might detach. (I-I'') Incorrect amount of agarose for the mounting and stability layers (Steps 31 / 40 / 44). (I) The mounting and stability layers should cover approximately between a quarter and half of the embryo surface at maximum and the agarose flanks should be as steep as possible. The embryo shown here survived the imaging process and developed into a fertile adult. (I') If too little agarose is applied, the embryo detaches during the insertion into the sample chamber. (I'') If too much agarose is applied, the survival chance of the embryo and the imaging quality are decreased. The embryo shown here did not survive the imaging process.



Supplementary Note (continued) | (J-J'') Blurred or dark regions at anterior or posterior regions of the embryo (Step 36). (J) The embryo should be visible and in focus in the complete acquired image. (J') If the light sheet height is insufficient, the embryo is only partially visible. (J'') A tilted light sheet results in blurry regions at the top and bottom along Y. (K-K'') During long-term imaging, the whole embryo appears blurred or certain regions appear dark after some time (Step 36). (K) The embryo should remain focused in the image volume, even during long-term imaging. (K') Insufficient amount of agarose in the stability layer might lead to a drift of the embryo out of the image volume. Besides, the Z stack should be large enough to cover slight movements of the embryo over time. (K'') If the chamber sealing for example generates excessive force on the detection objective, a focus drift may occur over time.

**Long-term fluorescence live imaging of
Tribolium castaneum embryos: principles, resources,
scientific challenges and the comparative approach**

Frederic Strobl & Ernst H.K. Stelzer

Light sheet-based fluorescence microscopy became an important tool in insect developmental biology due to its high acquisition speed, low photo-bleaching rate and the high survival probability of the specimens. Initially applied to document the embryogenesis of *Drosophila melanogaster*, it is now used to investigate the embryonic morphogenesis of emerging model organisms such as the red flour beetle *Tribolium castaneum*. Here, we discuss the principles of light sheet-based fluorescence microscopy and outline *Tribolium* as a model organism for developmental biology. We summarize labeling options and present two custom-made transgenic lines suitable for live imaging. Finally, we highlight studies on *Tribolium* that address scientific questions with fluorescence live imaging and discuss the comparative approach to investigate insect morphogenesis in an evolutionary context.

Published in August 2016

Review Article – *Current Opinion in Insect Science* – Elsevier

PubMed ID 27939706

Erklärung zu Autorenanteilen an der Publikation

**‘Long-term fluorescence live imaging of *Tribolium castaneum* embryos:
principles, resources, scientific challenges and the comparative approach’**

Status: Accepted
Zeitschrift: *Current Opinion in Insect Science* (Elsevier)
Autoren: Frederic Strobl (FS), Ernst H.K. Stelzer (EHKS)

(1) Entwicklung und Planung

FS	50%
EHKS	50%

(2) Durchführung der einzelnen Untersuchungen und Experimente

FS	n/a
EHKS	n/a

(3) Erstellung der Literatursammlung und Abbildungen

FS	100%
EHKS	0%

(4) Analyse und Interpretation der Daten

FS	75%	(Lebendaufnahmen von <i>Tribolium</i> , wissenschaftliche Fragestellungen, vergleichender Ansatz)
EHKS	25%	(Lichtblatt-Fluoreszenzmikroskopie, Schlussfolgerung)

(5) Verfassen des Manuskriptes

FS	50%
EHKS	50%

Unterschrift Frederic Strobl:

Ort, Datum:

Unterschrift Ernst H.K. Stelzer:

Ort, Datum:



Long-term fluorescence live imaging of *Tribolium castaneum* embryos: principles, resources, scientific challenges and the comparative approach

Frederic Strobl¹ and Ernst HK Stelzer²

Light sheet-based fluorescence microscopy became an important tool in insect developmental biology due to its high acquisition speed, low photo-bleaching rate and the high survival probability of the specimens. Initially applied to document the embryogenesis of *Drosophila melanogaster*, it is now used to investigate the embryonic morphogenesis of emerging model organisms such as the red flour beetle *Tribolium castaneum*. Here, we discuss the principles of light sheet-based fluorescence microscopy and outline *Tribolium* as a model organism for developmental biology. We summarize labeling options and present two custom-made transgenic lines suitable for live imaging. Finally, we highlight studies on *Tribolium* that address scientific questions with fluorescence live imaging and discuss the comparative approach to investigate insect morphogenesis in an evolutionary context.

Address

Physical Biology/Physikalische Biologie (IZN, FB 15), Buchmann Institute for Molecular Life Sciences (BMLS), Cluster of Excellence Frankfurt – Macromolecular Complexes (CEF–MC), Goethe Universität – Frankfurt am Main (Campus Riedberg), Max-von-Laue-Straße 15, D-60348 Frankfurt am Main, Germany

Corresponding author: Stelzer, Ernst HK
(ernst.stelzer@physikalischebiologie.de)

¹ www.physikalischebiologie.de/people/frederic-strobl,
www.physikalischebiologie.de/bugcube.

² <http://www.physikalischebiologie.de/people/ernst-hk-stelzer>.

Current Opinion in Insect Science 2016, 18:17–26

This review comes from a themed issue on **Neuroscience/insect phylogenetics**

Edited by **Susan Fahrbach**

<http://dx.doi.org/10.1016/j.cois.2016.08.002>

2214-5745/© 2016 Elsevier Inc. All rights reserved.

Light sheet-based fluorescence microscopy in developmental biology

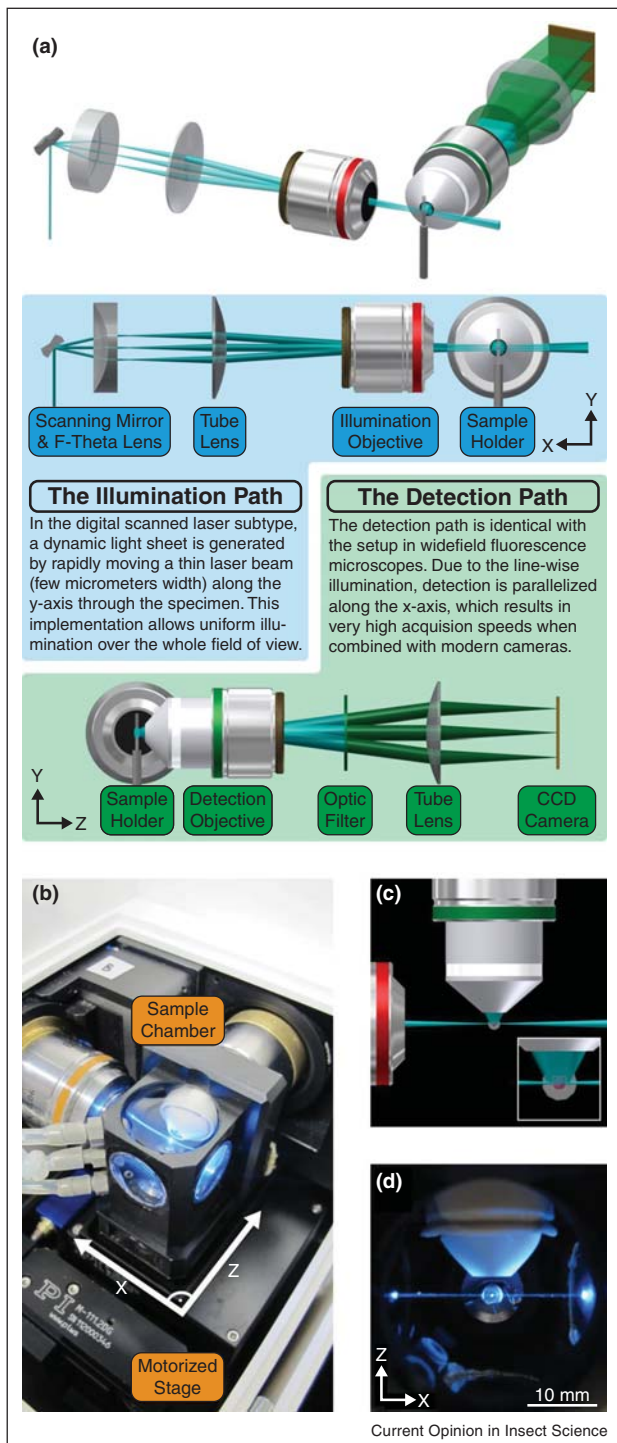
The most important property of fluorescence microscopy is its specificity. Ideally, only the fluorescently labeled targets emit light, while the non-labeled regions remain dark. However, there are several limitations. Firstly, fluorophores bleach with a certain probability upon excitation, that is, the population of fluorophores is consumed.

Secondly, the number of fluorophores is finite and so is the number of photons that can be collected during observation. Thirdly, many endogenous non-fluorescing organic compounds also absorb light, degrade very much like fluorophores and thus become unavailable for vital metabolic processes. Fourthly, life on Earth is adapted to the amount of energy provided by the sun. The solar flux might not serve as a hard limit, but it indicates that the irradiance should not exceed $1 \text{ nW}/\mu\text{m}^2 = 1 \text{ mW}/\text{mm}^2$ when live specimens are observed [1].

In light sheet-based fluorescence microscopy (LSFM), the illumination and detection light paths are decoupled. The illumination path (x) features either a static light sheet by expanding the laser beam one-dimensionally with a cylindrical lens (single/selective plane illumination microscope, SPIM [2]) or a dynamic light sheet, which is generated by rapidly scanning a laser beam (digital scanned laser light sheet-based fluorescence microscope, DSLM [3,4], Figure 1a). In both implementations, the specimen is imaged plane-wise while moving it along the perpendicularly arranged detection path (z) through the light sheet (Figure 1b). LSFM uses objectives with low numerical apertures in the illumination path, which results in light sheets with a relatively thin waist (a few micrometers) along the x -axis that retains this extent over a relatively long distance (several hundreds of micrometers) along the x -axis (Figure 1c,d). This azimuthal optical arrangement [5] allows the massive parallel detection of only the fluorophores that lie within the focal plane, resulting in true optical sectioning and a fast acquisition with a high signal-to-noise ratio and minimal photo-bleaching as well as phototoxicity [1]. Additionally, the specimen can be revolved stepwise around the rotation axis (y), which is pairwise perpendicular to x and z , allowing data acquisition along multiple directions.

LSFM has already been applied successfully in developmental biology, for example, to characterize cell migration paths in early zebrafish [3], chicken [6] and mouse [7] embryos. Also for the fruit fly *Drosophila melanogaster*, large image datasets on wild-type development [8–11], and several publications that have utilized LSFM to investigate gene function [12] or physical interaction of tissues during development [13] are available. Beside *Drosophila*, the scuttle fly *Megaselia abdita* [14] and the red flour beetle *Tribolium castaneum* [15^{••},16^{••}] have been investigated with LSFM.

Figure 1



Principles of light sheet-based fluorescence microscopy. **(a)** Operating principle of a digitally scanned laser light sheet-based fluorescence microscope, a LSFM subtype. The scheme indicates the layouts of the illumination (blue) and detection (green) paths. **(b)** Diagonal view of the sample chamber. In developmental biology, the detection objectives are typically water-immersion lenses, since a specimen chamber is required, which is typically filled with an aqueous medium. Motorized

stages are used to move the specimen along z though the light sheet and the focal plane of the detection objective. Another motor rotates the specimen around y, which allows imaging along multiple directions. **(c)** Illumination and detection shown from above. The inset illustrates the parallelized fluorescence detection. **(d)** Imaging process of a *Tribolium* embryo mounted with the agarose hemisphere method [15[•],32[•]] shown from above.

Fluorescence live imaging of *Tribolium castaneum* embryos

Trailing *Drosophila*, the red flour beetle *Tribolium castaneum* has emerged as the second most important insect model organism due to a broad variety of reasons: (i) the embryonic development principles represent ancestral insect development more appropriately, for example, in terms of embryonic leg development [22] and extensive extra-embryonic membrane formation [23,24], (ii) its genes have a higher degree of similarity to their vertebrate counterparts [25] and (iii) *Tribolium* could be an eligible representative for the Coleopteran order [26].

Beside the biological rationale, a comprehensive experimental toolbox is available, as summarized within the *Emerging Model Organisms* books [27], with highlights such as efficient germ line transformation [28,29], concurrent *in situ* hybridization and antibody staining [30] and double whole-mount *in situ* hybridization protocols [31]. A very recent add-on to the toolbox is non-invasive long-term fluorescence live imaging [15[•],32[•]]. *Tribolium* embryos are well suited for fluorescence live imaging: (i) albeit the embryos typically develop in low humidity environments, submersion in aqueous buffers neither interferes with development nor causes significant delays, (ii) the embryos have an anterior-posterior length of approximately 600 μm and a transversal width of approximately 300 μm , that is, they are more voluminous than *Drosophila* embryos, but can still be imaged *in toto* with typical objective/camera combinations used in LSFM and (iii) the non-cellular biological components such as the vitelline membrane and the yolk exhibit only marginal autofluorescence.

A prerequisite for fluorescence live imaging is the presence of fluorophores within the observed specimen. In *Tribolium*, four approaches have been suggested: (i) mRNA injection, (ii) dye injection, (iii) usage of GEKU enhancer trap lines and (iv) custom-made transgenic lines. Key considerations, including a summary of the

stages are used to move the specimen along z though the light sheet and the focal plane of the detection objective. Another motor rotates the specimen around y, which allows imaging along multiple directions. **(c)** Illumination and detection shown from above. The inset illustrates the parallelized fluorescence detection. **(d)** Imaging process of a *Tribolium* embryo mounted with the agarose hemisphere method [15[•],32[•]] shown from above.

Table 1

Labeling approaches for fluorescence live imaging of *Tribolium* embryos.

Method	Rationale	Advantages and limitations	Required work and time	Resources and references
<ul style="list-style-type: none"> mRNA injection 	<ul style="list-style-type: none"> The respective plasmids carry a viral promoter (typically T7) that allows <i>in vitro</i> transcription of mRNA coding for the respective fluorescence fusion protein. The mRNA is injected into early preblastoderm embryos. 	<ul style="list-style-type: none"> (+) strong and homogenous fluorescence a few hours after injection (+) the <i>in vitro</i> synthesized mRNA should work in a broad variety of insect species (+) co-injection with constructs for RNA interference possible (+) fluorescence protein can be fused to tags or proteins that will lead to a certain intracellular localization (-) embryo manipulation necessary (-) only spatiotemporal ubiquitous labeling possible 	<ul style="list-style-type: none"> Several hours for the preparation and purification of the mRNA and injection of the embryos, fluorescence expression starts a few hours after injection. If new constructs are needed, several days to a few weeks are necessary for cloning. Initial work and time requirements are low (plasmid already available) to medium (molecular cloning is necessary), but live imaging work and time requirements are high (the embryos have to be injected every time an assay should be performed). Few hours for injection of the embryos. Initial work and time requirements are very low (dyes can be purchased), but live imaging work and time requirements are high (the embryos have to be injected every time an assay should be performed). 	<ul style="list-style-type: none"> pT7-H2B-RFP — chromatin/nuclei in red [55] pT7-LifeAct-EGFP — actin in green [55,56] pT7-ABP-tdEosFP — actin, green/red photoconvertible [55] pCS2-GAP43-YFP — Membranes in yellow [55–57]
<ul style="list-style-type: none"> Fluorescent dye injection 	<ul style="list-style-type: none"> The respective caged or fluorescent dye is directly injected into early preblastoderm embryos. 	<ul style="list-style-type: none"> (+) low effort (-) embryo manipulation necessary (-) only spatiotemporal ubiquitous labeling possible (-) only cytoplasmic labeling demonstrated 	<ul style="list-style-type: none"> DMNB-caged fluorescein — cytoplasm, green after photoactivation [58*] Fluoro-ruby — cytoplasm in red [58*] 	
<ul style="list-style-type: none"> GEKU enhancer trap lines 	<ul style="list-style-type: none"> The GEKU screen is a large scale insertional mutagenesis assay in which an enhancer-affine <i>piggyBac</i>-based reporter cassette (EGFP under control of the artificial 3xP3 promoter) was remobilized by crossing a respective reporter cassette donor line against a <i>piggyBac</i> transposase-expressing jumpstarter line. When the reporter cassette reintegrates closely to an enhancer, it adapts (to a certain degree) the enhancer expression pattern. 	<ul style="list-style-type: none"> (+) 505 enhancer trap lines available, which are registered in the GEKU base (http://www.geku-base.uni-goettingen.de/) (+) enhancer trap lines are manually annotated, the database in searchable (+) background information partially known (chromosomal location, homozygote lethality and sterility, stereo microscope images) (+) expression patterns available that are difficult to obtain with custom-made transgenic lines (+) no embryo manipulation necessary (+) continuous production of fluorophores (-) only cytoplasmic labeling (-) fluorescence strength depends on the enhancer and might vary between individuals of the same line 	<ul style="list-style-type: none"> No preparation necessary. The enhancer trap lines might however not be homozygote, therefore curation or homozygote crossing is recommended. Initial work and time requirements are low (the enhancer trap lines can be requested from the respective laboratories). Live imaging work and time requirements are low for homozygote lines, mixed lines should either be crossed homozygote or curated from time to time, homozygote lethal/sterile lines need frequent curation (or an adequate balancer, which is not always available). 	<ul style="list-style-type: none"> Of the 505 enhancer trap lines that are listed for the GEKU screen [40], five have been analyzed with fluorescence live imaging: <ul style="list-style-type: none"> G04609 — mesodermal and sensory domains, serosa [16**,59*] G11410 — mushroom bodies [34**] G12424 — mature serosa, expression begins after serosa window closure [16**,59*] KT650 — mature serosa, expression begins around extended germband stage [16**,59*] HC079 — amnion, expression begins during germband retraction [16**]

Table 1 (Continued)

Method	Rationale	Advantages and limitations	Required work and time	Resources and references
<ul style="list-style-type: none"> • Custom-made transgenic lines 	<ul style="list-style-type: none"> • Donor plasmids typically contain the coding sequence for a fluorescence fusion protein under control of a specific endogenous promoter as well as a transgenesis marker. Both cassettes are inserted into transposase recognition sites, which allows the transfer of the cassette to the genome when the donor plasmid is co-injected with a helper plasmid that expresses the respective transposase (for example <i>piggyBac</i> or <i>Minos</i>). 	<ul style="list-style-type: none"> • (+) fluorescence protein can be fused to tags or proteins that will lead to a certain intracellular localization • (+) spatiotemporal expression control available via promoter choice • (+) no embryo manipulation necessary • (+) continuous production of fluorophores • (-) long and laborious effort to create custom-made transgenic lines 	<ul style="list-style-type: none"> • No preparation necessary. The custom-made transgenic lines might however not be homozygote, therefore curation or homozygote crossing is recommended. • Initial work and time requirements are very high (molecular cloning, injection, screening for founders, further crossing). Live imaging work and time requirements are low for homozygote lines, mixed homozygote or curated from time to time, homozygote lethal/sterile lines need frequent curation (or an adequate balancer, which is not always available). 	<ul style="list-style-type: none"> • EFA-nGFP — expresses nuclear localized GFP under control of the elongation factor 1 alpha 1 subunit promoter [15**,16**,24,32*,33,55,59*,60–62] • FNLL — expresses histone2B-EGFP under control of the elongation factor 1 alpha 1 subunit promoter (this review) • Glia-blue and Glia-red — labels approximately 600 glia cells with ECFP or DsRed, respectively [34**] • Neuron-red — expresses DsRed in neurons under control of the elongation factor 1 alpha B (paralog) promoter [34**] • Brainy — Glia-blue/Neuron-red double transgenic line [34**], this review)

available resources, are outlined in Table 1. Of those four approaches, the lack of custom-made fluorophore-expressing transgenic lines is currently the biggest limitation for fluorescence live imaging. The ‘gold standard’ is the EFA-nGFP line introduced in 2012, which has been featured in nearly every live imaging publication (compare Table 1) over the last four years. The line expresses nuclear-localized GFP under control of the elongation factor 1 alpha 1 subunit promoter ubiquitously through the whole embryonic development [33]. To improve the attractiveness of live imaging as a readout technique, more standard lines are necessary, and two candidates are presented here: Firstly, the recently created FNL line, which expresses a histone2B-EGFP fusion protein

Box 1 Selection of scientific questions in *Tribolium* developmental biology that are addressed with fluorescence live imaging. General studies are mentioned whenever necessary, the live imaging-associated studies are summarized at the end of the paragraph.

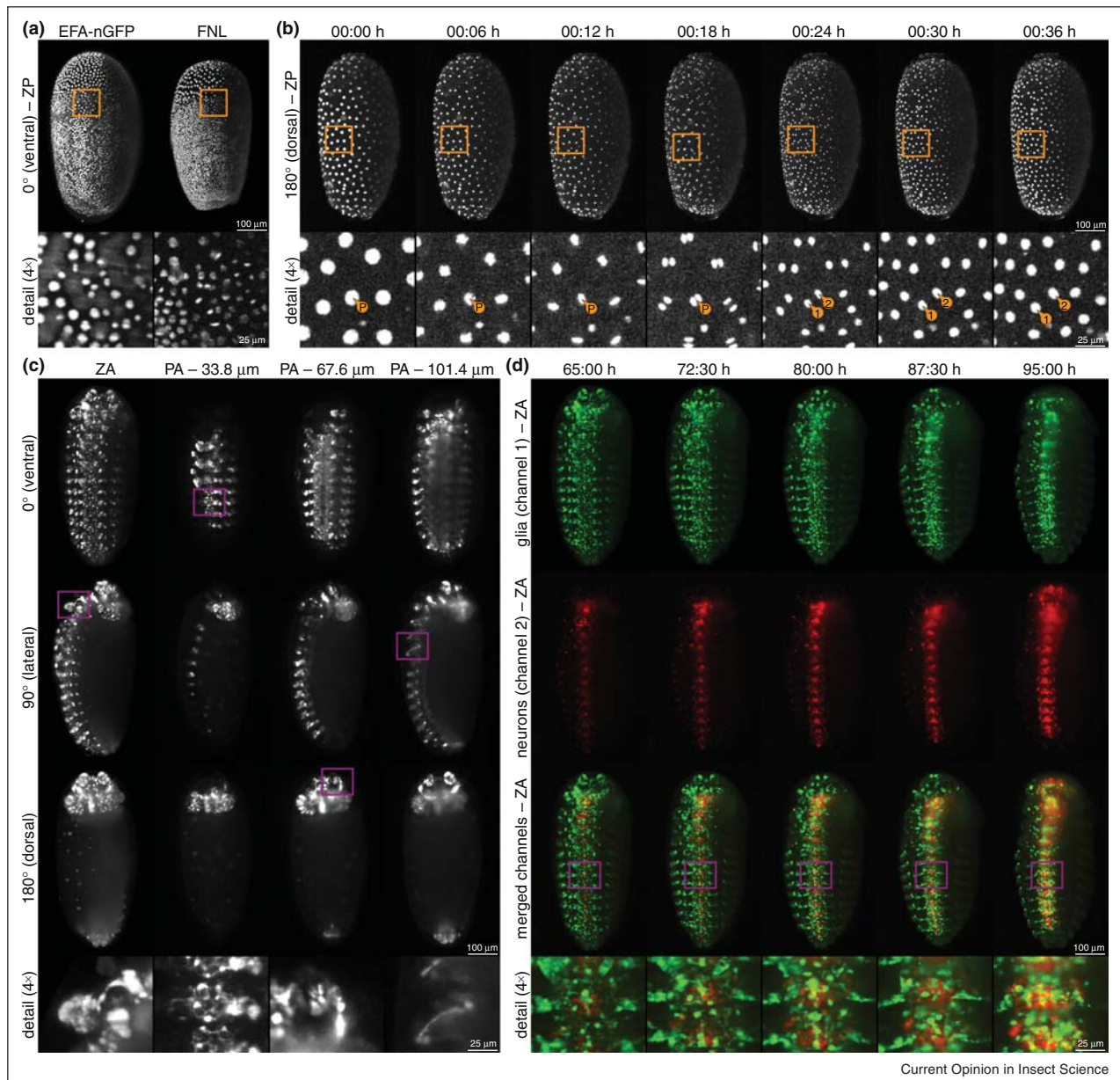
(1) Early embryogenesis: blastoderm formation and gastrulation. Upon blastoderm formation, when all cells are uniformly distributed on the egg surface, gastrulation commences. Gastrulation is an embryogenetic event with massive morphogenetic movements, where the germband condensates and sinks into the yolk while becoming covered by extensive extra-embryonic membranes [63]. Fluorescence live imaging is used to collect the data that can be interpreted to describe the involved processes on the cellular level and to characterize phenotypes, for example, embryos where genes were knocked down via parental RNA interference. Working with advanced fluorescence microscopy also allows the tracking and mapping of individual cells over extended developmental periods [55,56,58*,64].

(2) Formation and degradation of extra-embryonic membranes. In contrast to *Drosophila*, *Tribolium* develops two extra-embryonic membranes during embryogenesis. The inner amnion covers the embryo on the ventral side, whereas the serosa envelops the embryo completely [63,65]. Two purposes have been suggested: protection from desiccation [66] and defense against pathogens [67,68]. The extra-embryonic membranes differentiate during gastrulation, cover the embryo during germband elongation and germband retraction and are finally internalized during dorsal closure. Live imaging was used to investigate the dynamic morphogenetic processes that take place during differentiation, formation, interaction and degradation of those membranes [15**,16**,24,55,59*,64].

(3) The principles of short-germ development. While *Drosophila* follows the principles of long-germ development, where all segments are specified during gastrulation, *Tribolium* belongs to the group of short-germ insects. In this mode, only the minority of (anterior) segments is formed during gastrulation and the ‘missing’ segments are added one-by-one during germband elongation at the posterior end [69]. *Tribolium* utilizes a ‘segmentation clock’, which was shown by following cell positions during germband elongation with fluorescence live imaging [33,60].

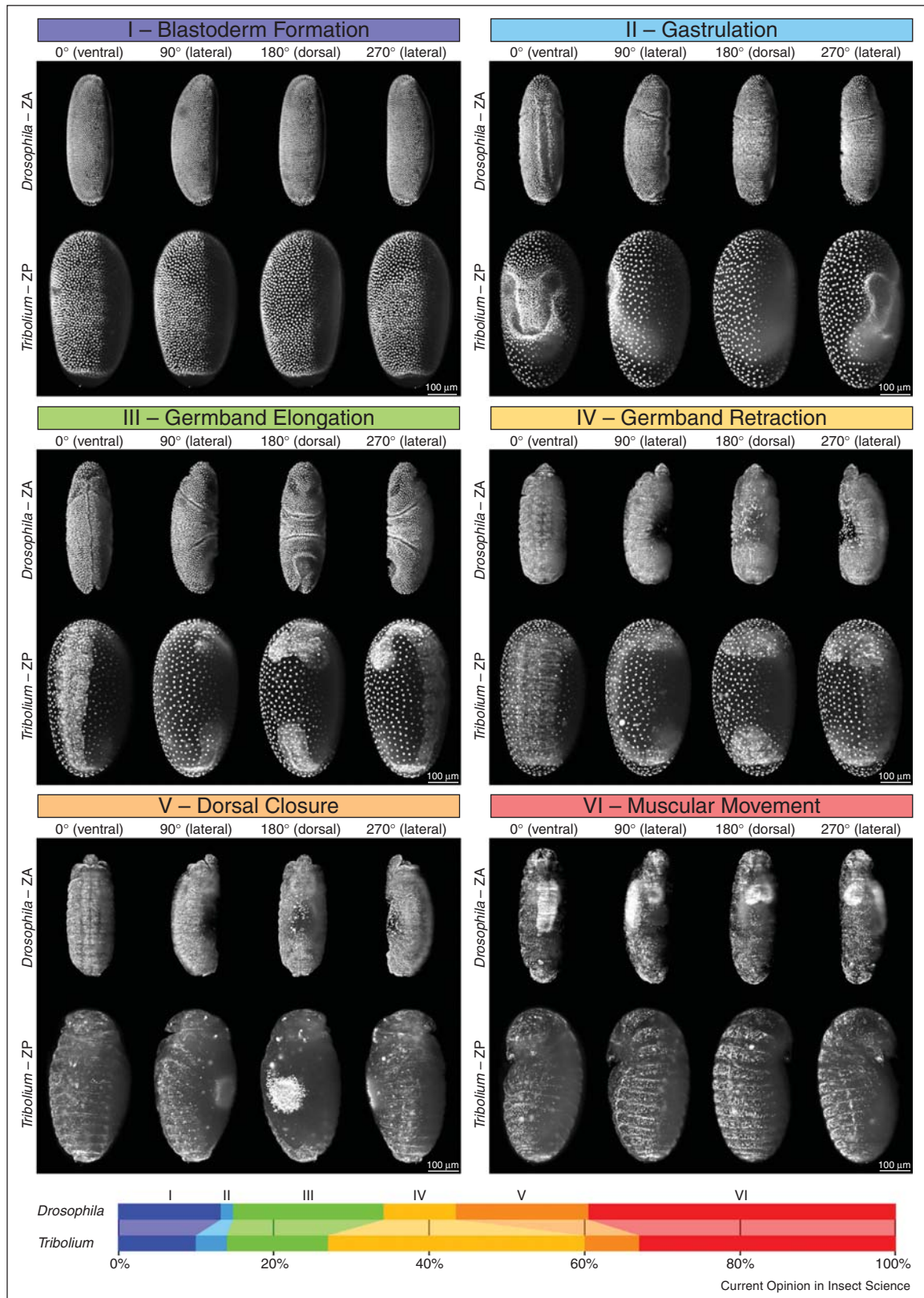
(4) Live imaging methods, protocols and screening assays. Especially for emerging model organisms such as *Tribolium*, the establishment and/or adaption of techniques and protocols is essential for a smooth workflow when addressing biological questions. Fluorescence live imaging is only a recent addition to the *Tribolium* toolbox and, until now, only a few methodically-orientated publications are available [15**,32*,61,62].

Figure 2



Novel transgenic lines for long-term fluorescence live imaging of embryonic development. **(a)** Comparison of the established EFA-nGFP and the novel FNL transgenic lines. Both embryos were recorded with LSMF at comparable conditions and show the onset of gastrulation. During mitosis, the nuclear envelope dissipates and the otherwise concentrated nGFP is distributed throughout the cytosol in the EFA-nGFP line. In the FNL line, the GFP remains bound to the chromatin. The resulting signal exhibits the form of a bright white plate in metaphase that splits during anaphase. **(b)** FNL line embryo imaged over time during blastoderm formation at the 10th synchronous cell division cycle. Transgenic lines with the fluorescence protein linked to a histone subunit allow cell tracking and lineaging even through cell proliferation. The detail images show multiple cell nuclei, including a parent cell (P) that divides into two daughters (1 and 2) over the course of 36 min. **(c)** The Brainsy line during germband retraction imaged along three directions in the glia channel. Single planes for three depths are provided. The first single plane with a moderate signal is defined as 0 μm. Detail images show the developing labium with the left labial palps (first column), single glia cells from the ventral nerve cord (second column), the primordium of the right antennae (third column) and the left leg primordium forming at the third thoracic segment (fourth column). **(d)** The Brainsy line at the transition from germband retraction to dorsal closure imaged in the glia (1) and neurons (2) channel over a period of 30:00 h. Detail images show the third abdominal segment, illustrating the developing ventral nerve cord. The data from the EFA-nGFP line was reproduced [15**], the data for the FNL and Brainsy lines is provided for the very first time with this publication (Supplementary Table 1). ZP, z maximum projections with image processing; ZA, z maximum projections with intensity adjustment; PA, single plane with intensity adjustment.

Figure 3



under control of the elongation factor 1 alpha 1 subunit promoter. In contrast to the EFA-nGFP line, the FNL line allows the tracking of dividing cells and their daughters (Figure 2a,b). Secondly, the double homozygote Brainy line [34**] can be used to visualize glia and neuronal cells in the developing embryo (Figure 2c,d, Supplementary Video 1). In future, several other standards should be added to the repertoire, such as actin or membrane-labeled lines or more advanced systems such as the fluorescent ubiquitination-based cell cycle indicator or Brainbow, which were primarily designed for vertebrates but have already been adapted for *Drosophila* [35,36].

Addressing scientific challenges with fluorescence live imaging

Tribolium live imaging has been and will be applied to address a variety of scientific challenges:

- **Development of wild-type embryos.** A comprehensive characterization of wild-type development is a prerequisite for any further studies. Fluorescence live imaging is the tool of choice to gather the data required for descriptions at any morphogenetic level. While state-of-the-art fluorescence microscopy techniques become available for systematic data acquisition, establishing an image depository similar to *Drosophila* (www.flybase.org) facilitates data sharing and further usage.
- **Enforcement of aberrations.** Expression patterns and/or functions have to be altered to properly understand the roles of genes and proteins during development. Well established techniques are heat shock-mediated mis-expression [37], highly penetrant embryonic gene knockdowns via parental RNA interference [38,39], insertional mutagenesis [40] and genome engineering [41].
- **Systematic quantitative characterization.** The efficient continuous development of microscopy techniques throughout the last years has made it possible to perform exhaustive quantitative studies of the development of whole organisms, as demonstrated with *Drosophila* [42]. Thus, it is not only possible to characterize fundamental properties of structures in a developing organism on the cellular and subcellular level, but it is also feasible to determine quantitative values, such as the relative locations and frequencies of cell proliferations, to track cell migration velocities and

pathways or to characterize spatiotemporal attributes of cell differentiation.

Current specific questions that are addressed with fluorescence live imaging are summarized in Box 1. Most of these questions focus on former embryogenetic events such as blastoderm formation, gastrulation and germband elongation, and studies that investigate processes occurring during the latter embryogenetic events such as germband retraction and dorsal closure, for example, neurulation and brain development, have not yet used fluorescence live imaging as a readout technique. In two recent studies, *six3* [43] and the two *Pax6* orthologues *eyeless* and *twin of eyeless* [44] have been identified as key players for the embryonic formation of the central complex. The underlying experimental strategy has been to knockdown of the respective gene via RNA interference followed by fluorescence imaging of fixed and stained embryos and first instar larvae to characterize the scope of the morphological defects. Follow up studies might consider fluorescence live imaging as a readout, which would also provide cues at which time point/developmental stage the defects arise, and to follow and characterize their course over time.

Comparative approach to morphogenesis

In developmental biology, species are investigated with only limited consideration of their evolutionary lineage. Thus, a phylogenetic classification of specific traits as apomorphic or plesiomorphic is not possible. In contrast, evolutionary developmental biology is based on the comparative approach: similarities and differences in the development of at least two species are analyzed and interpreted within the phylogenetic context. In insect science, the comparative approach has been performed on multiple levels, for example, genomics [45–47], transcriptomics [48,49], morphology [50] and a mixture thereof [51]. Morphogenesis, the alteration of morphology as a function of time, is a dynamic process. Therefore, it provides insights that go beyond the cues drawn from studying morphology alone. This applies in particular to the cellular and sub-cellular levels, when patterns of cell migration, proliferation and differentiation are analyzed. Similar to morphology, the comparative approach can be applied to morphogenesis. However, documenting embryonic morphogenesis is a non-trivial task when fluorescence live imaging is the technique of choice: (i) the recording process must be non-invasive, that is, the

(Figure 3 Legend) Comparative approach: morphogenesis of *Drosophila* and *Tribolium* embryos. Shown are six consecutive embryogenetic events (indexed with Roman numerals) for the *Drosophila* P(His2Av-EGFP.C)2 (Bloomington Stock Center #24163) and the *Tribolium* EFA-nGFP [33] transgenic lines at approximately the same development stage. The *Drosophila* embryo was recorded at room temperature (23 ± 1 °C) for more than one day, while the *Tribolium* embryo was recorded at 35 °C for more than two days. The progression bar below the images shows a temporal comparison relative to the complete embryonic development (data for *Drosophila* derives from www.flybase.org, data for *Tribolium* from [32*]). For example, (IV) germband retraction takes approximately three-and-a-half times as long in *Tribolium* than in *Drosophila*, but (V) dorsal closure proceeds more than twice as fast on this normalized scale. The image data from the EFA-nGFP line were reproduced [15**], the image data from the P(His2Av-EGFP.C)2 line is provided for the very first time with this publication (Supplementary Table 1). ZP, z maximum projections with image processing; ZA, z maximum projections with intensity adjustment.

induced stress must not affect viability and fertility, (ii) the embryo must be observed for long time periods, that is, the majority of its embryogenesis has to be covered, and (iii) the sampling rate has to be sufficiently high to document similar embryogenetic events with significant spatiotemporal resolution. With LFSM, fluorescence microscopes became available that minimize photo-bleaching and phototoxicity, the two crucial factors that have to be avoided during the entire observation period, while providing a high sampling rate due to the parallelized detection principle. To date, non-invasive long-term live imaging data are available for *Drosophila* and *Tribolium*, which allow a side-by-side comparison (Figure 3).

The significance of the comparative approach rises strongly with an increasing number of species. Beside *Drosophila*, which represents the Diptera (flies and mosquitoes), and *Tribolium*, which represents the Coleoptera (beetles), there are two more very species-rich orders within the Holometabola, the Lepidoptera (moths and butterflies), a sister group to the Diptera, and the Hymenoptera (bees, wasps and ants), which are located basally. Comprehensive fluorescence live imaging data from morphogenetic representative members of those orders, for example, *Nasonia vitripennis* for the Hymenoptera [52], could provide information on which morphogenetic processes are ancestral, and which might be derived within the monophyletic group of the Holometabola. The respective cues can then be aligned with non-morphogenetic dynamic data, such as spatiotemporal gene expression patterns.

Conclusions

The application of LFSM in insect developmental biology has just started but already contributes to the move from a single established model organism to a heterogeneous canonic group of model organisms. With about one million described and more than twenty million assumed species [53], insects can be considered the most successful evolutionary class. They inhabit every continent and climate zone, occupy all food niches, exploit all modes of locomotion (walking, flying, swimming and burrowing) and exhibit considerable morphogenetic variations as a consequence of adaptation to their environment. The comparison of multiple insect species with strongly deviating phylogenetic backgrounds is required to understand the fundamentals of how evolution has affected development, while the consolidation of their ecological backgrounds provides insights into the evolution of biological robustness (also known as canalization). The emerging model organism *Tribolium castaneum* is a promising candidate that complements *Drosophila* on multiple levels: (i) the ecological niche is entirely different, (ii) it exhibits moderate similarity in the course of embryogenetic events, but a high degree of variation of specific structures and processes during embryonic development, (iii) the

ever-growing toolbox comprises several techniques that are non-existent in *Drosophila* such as parental RNA interference and (iv) *Tribolium* bridges the 300 million years phylogenetic gap between the Diptera and the Coleoptera [54]. Together with other promising insect model organisms and state-of-the-art microscopy techniques such as LFSM that are continuously improved, insect morphogenesis can be analyzed and understood in an evolutionary context.

Acknowledgements

We thank Franziska Krämer and Selina Klees for their help with image acquisition, Alexander Schmitz for help with data processing and Sven Plath for technical support. The Brainy transgenic line was a kind gift from Gregor Bucher (Göttingen, Germany). The research was funded by the Cluster of Excellence Frankfurt for Macromolecular Complexes (CEF-MC, EXC 115) granted in part to EHKS at the Buchmann Institute for Molecular Life Sciences (BMLS) at the Goethe University – Frankfurt am Main by the Deutsche Forschungsgemeinschaft (DFG).

Appendix A. Supplementary data

Supplementary data associated with this article can be found, in the online version, at [doi:10.1016/j.cois.2016.08.002](https://doi.org/10.1016/j.cois.2016.08.002).

References and recommended reading

Papers of particular interest, published within the period of review, have been highlighted as:

- of special interest
 - of outstanding interest
1. Stelzer EHK: **Light-sheet fluorescence microscopy for quantitative biology.** [Internet]. *Nat Methods* 2015, **12**:23-26.
 2. Huisken J, Swoger J, Del Bene F, Wittbrodt J, Stelzer EHK: **Optical sectioning deep inside live embryos by selective plane illumination microscopy.** [Internet]. *Science* 2004, **305**:1007-1009.
 3. Keller PJ, Schmidt AD, Wittbrodt J, Stelzer EHK: **Reconstruction of zebrafish early embryonic development by scanned light sheet microscopy.** [Internet]. *Science* 2008, **322**:1065-1069.
 4. Keller PJ, Stelzer EHK: **Digital scanned laser light sheet fluorescence microscopy.** [Internet]. *Cold Spring Harb Protoc* 2010. 2010:pdb.top78.
 5. Stelzer EHK, Lindek S: **Fundamental reduction of the observation volume in far-field light microscopy by detection orthogonal to the illumination axis: confocal theta microscopy.** [Internet]. *Opt Commun* 1994, **111**:536-547.
 6. Rozbicki E, Chuai M, Karjalainen AI, Song F, Sang HM, Martin R, Knölker H-J, MacDonald MP, Weijer CJ: **Myosin-II-mediated cell shape changes and cell intercalation contribute to primitive streak formation** [Internet]. *Nat Cell Biol* 2015, **17**:397-408.
 7. Ichikawa T, Nakazato K, Keller PJ, Kajijura-Kobayashi H, Stelzer EHK, Mochizuki A, Nonaka S: **Live imaging of whole mouse embryos during gastrulation: migration analyses of epiblast and mesodermal cells.** [Internet]. *PLoS One* 2013, **8**:e64506.
 8. Keller PJ, Schmidt AD, Santella A, Khairy K, Bao Z, Wittbrodt J, Stelzer EHK: **Fast, high-contrast imaging of animal development with scanned light sheet-based structured-illumination microscopy.** [Internet]. *Nat Methods* 2010, **7**:637-642.
 9. Tomer R, Khairy K, Amat F, Keller PJ: **Quantitative high-speed imaging of entire developing embryos with simultaneous multiview light-sheet microscopy.** [Internet]. *Nat Methods* 2012, **9**:755-763.

10. Krzic U, Gunther S, Saunders TE, Streichan SJ, Hufnagel L: **Multiview light-sheet microscope for rapid in toto imaging.** [Internet]. *Nat Methods* 2012, **9**:730-733.
11. Chhetri RK, Amat F, Wan Y, Höckendorf B, Lemon WC, Keller PJ: **Whole-animal functional and developmental imaging with isotropic spatial resolution.** [Internet]. *Nat Methods* 2015, **12**:1171-1178.
12. Beira JV, Springhorn A, Gunther S, Hufnagel L, Pyrowolakis G, Vincent J-P: **The Dpp/TGF β -dependent corepressor Schnurri protects epithelial cells from JNK-induced apoptosis in *Drosophila* embryos.** [Internet]. *Dev Cell* 2014, **31**:240-247.
13. Lye CM, Blanchard GB, Naylor HW, Muresan L, Huisken J, Adams RJ, Sanson B: **Mechanical coupling between endoderm invagination and axis extension in *Drosophila*.** [Internet]. *PLoS Biol* 2015, **13**:e1002292.
14. Caroti F, Urbansky S, Wosch M, Lemke S: **Germ line transformation and in vivo labeling of nuclei in Diptera: report on *Megaselia abdita* (Phoridae) and *Chironomus riparius* (Chironomidae).** [Internet]. *Dev Genes Evol* 2015, **225**:179-186.
15. Strobl F, Stelzer EHK: **Non-invasive long-term fluorescence live imaging of *Tribolium castaneum* embryos.** [Internet]. *Development* 2014 <http://dx.doi.org/10.1242/dev.108795>.
Introduces a novel and gentle mounting method that allows the observation of fluorescent *Tribolium* embryos over time period of up to 50 h at 35 °C, documenting the whole embryonic morphogenesis from the rearrangement of the uniform blastoderm to the onset of muscular movement.
16. Hilbrant M, Horn T, Koelzer S, Panfilio KA: **The beetle amnion and serosa functionally interact as apposed epithelia.** [Internet]. *Elife* 2016:5.
Hilbrant and colleagues utilize many tools and resources to analyze the principle of extra-embryonic membrane rupture and degradation: four GEKU enhancer trap lines (see also Table 1), parental RNA interference, light sheet-based fluorescence microscopy and cell tracking. They conclude that the amnion functions as the rupture initiator, whereas the serosa acts as the driver for the subsequent withdrawal.
17. Rieckher M: **Light sheet microscopy to measure protein dynamics.** [Internet]. *J Cell Physiol* 2016 <http://dx.doi.org/10.1002/jcp.25451>.
18. Huisken J, Stainier DYR: **Even fluorescence excitation by multidirectional selective plane illumination microscopy (mSPIM).** [Internet]. *Opt Lett* 2007, **32**:2608-2610.
19. Swoger J, Verveer P, Greger K, Huisken J, Stelzer EHK: **Multiview image fusion improves resolution in three-dimensional microscopy.** [Internet]. *Opt Exp* 2007, **15**:8029-8042.
20. Preibisch S, Saalfeld S, Schindelin J, Tomancak P: **Software for bead-based registration of selective plane illumination microscopy data.** [Internet]. *Nat Methods* 2010, **7**:418-419.
21. Preibisch S, Amat F, Stamatakis E, Sarov M, Singer RH, Myers E, Tomancak P: **Efficient Bayesian-based multiview deconvolution.** [Internet]. *Nat Methods* 2014, **11**:645-648.
22. Klingler M: **Tribolium.** [Internet]. *Curr Biol* 2004, **14**:R639-R640.
23. van der Zee M, Berns N, Roth S: **Distinct functions of the *Tribolium zerknullt* genes in serosa specification and dorsal closure.** [Internet]. *Curr Biol* 2005, **15**:624-636.
24. Panfilio Ka, Oberhofer G, Roth S: **High plasticity in epithelial morphogenesis during insect dorsal closure.** [Internet]. *Biol Open* 2013, **2**:1108-1118.
25. Richards S, Gibbs RA, Weinstock GM, Brown SJ, Denell R, Beeman RW, Gibbs R, Bucher G, Friedrich M, Grimmlikhuijzen CJP et al.: **The genome of the model beetle and pest *Tribolium castaneum*.** [Internet]. *Nature* 2008, **452**:949-955.
26. Denell R: **Establishment of tribolium as a genetic model system and its early contributions to evo-devo.** [Internet]. *Genetics* 2008, **180**:1779-1786.
27. Inglis J, Gann A, Crotty D, Janssen K, Smit M (Eds): *Emerging Model Organisms: A Laboratory Manual* [Internet], vol 2. Cold Spring Harbour Laboratory Press; 2010.
28. Lorenzen MD, Kimzey T, Shippy TD, Brown SJ, Denell RE, Beeman RW: **piggyBac-based insertional mutagenesis in *Tribolium castaneum* using donor/helper hybrids.** [Internet]. *Insect Mol Biol* 2007, **16**:265-275.
29. Berghammer AJ, Weber M, Trauner J, Klingler M: **Red flour beetle (*Tribolium*) germline transformation and insertional mutagenesis.** [Internet]. *Cold Spring Harb Protoc* 2009. 2009:pdb.prot5259.
30. Shippy TD, Coleman CM, Tomoyasu Y, Brown SJ: **Concurrent in situ hybridization and antibody staining in red flour beetle (*Tribolium*) embryos.** [Internet]. *Cold Spring Harb Protoc* 2009. 2009:pdb.prot5257.
31. Schinko J, Posnien N, Kittelmann S, Koniszewski N, Bucher G: **Single and double whole-mount in situ hybridization in red flour beetle (*Tribolium*) embryos.** [Internet]. *Cold Spring Harb Protoc* 2009. 2009:pdb.prot5258.
32. Strobl F, Schmitz A, Stelzer EHK: **Live imaging of *Tribolium castaneum* embryonic development using light-sheet-based fluorescence microscopy.** [Internet]. *Nat Protoc* 2015, **10**:1486-1507.
Comprehensive live imaging protocol that also explains proper calibration for custom-built light sheet-based fluorescence microscopes, presents imaging options, outlines simple data processing steps and discusses quality control for live imaging assays. *Tribolium* embryos were recorded at 35 °C and at room temperature for periods of up to 120 h.
33. Sarrazin AF, Peel AD, Averof M: **A segmentation clock with two-segment periodicity in insects.** *Science* 2012, **336**:338-341 80.
34. Koniszewski NDB, Kollmann M, Bigham M, Farnworth M, He B, Büscher M, Hütteroth W, Binzer M, Schachtner J, Bucher G: **The insect central complex as model for heterochronic brain development-background, concepts, and tools.** [Internet]. *Dev Genes Evol* 2016 <http://dx.doi.org/10.1007/s00427-016-0542-7>.
Koniszewski and colleagues suggest a three-species (*Drosophila*, *Tribolium* and *Gryllus bimaculatus*) comparative approach to study brain development and evolution in insects. They also summarize current structural and functional data of the developing *Tribolium* brain and present five transgenic lines for fluorescence live imaging (see also Table 1). They also discuss eight antibodies for brain development-related immunohistochemistry assays.
35. Zielke N, Korzelius J, van Straaten M, Bender K, Schuhknecht GFP, Dutta D, Xiang J, Edgar BA: **Fly-FUCCI: a versatile tool for studying cell proliferation in complex tissues.** [Internet]. *Cell Rep* 2014, **7**:588-598.
36. Hadjieconomou D, Rotkopf S, Alexandre C, Bell DM, Dickson BJ, Salecker I: **Flybow: genetic multicolor cell labeling for neural circuit analysis in *Drosophila melanogaster*.** [Internet]. *Nat Methods* 2011, **8**:260-266.
37. Schinko JB, Hillebrand K, Bucher G: **Heat shock-mediated misexpression of genes in the beetle *Tribolium castaneum*** [Internet]. *Dev Genes Evol* 2012, **222**:287-298.
38. Bucher G, Scholten J, Klingler M: **Parental RNAi in *Tribolium* (Coleoptera).** [Internet]. *Curr Biol* 2002, **12**:R85-R86.
39. Posnien N, Schinko J, Grossmann D, Shippy TD, Konopova B, Bucher G: **RNAi in the red flour beetle (*Tribolium*).** [Internet]. *Cold Spring Harb Protoc* 2009, **2009** pdb.prot5259.
40. Trauner J, Schinko J, Lorenzen MD, Shippy TD, Wimmer EA, Beeman RW, Klingler M, Bucher G, Brown SJ: **Large-scale insertional mutagenesis of a coleopteran stored grain pest, the red flour beetle *Tribolium castaneum*, identifies embryonic lethal mutations and enhancer traps.** [Internet]. *BMC Biol* 2009, **7**:73.
41. Gilles AF, Schinko JB, Averof M: **Efficient CRISPR-mediated gene targeting and transgene replacement in the beetle *Tribolium castaneum*.** [Internet]. *Development* 2015 <http://dx.doi.org/10.1242/dev.125054>.
42. Amat F, Lemon W, Mossing DP, McDole K, Wan Y, Branson K, Myers EW, Keller PJ: **Fast, accurate reconstruction of cell lineages from large-scale fluorescence microscopy data** [Internet]. *Nat Methods* 2014, **11**:951-958.

43. Posnien N, Koniszewski NDB, Hein HJ, Bucher G: **Candidate gene screen in the red flour beetle *Tribolium* reveals six3 as ancient regulator of anterior median head and central complex development.** [Internet]. *PLoS Genet* 2011, **7**:e1002416.
44. Luan Q, Chen Q, Friedrich M: **The Pax6 genes eyeless and twin of eyeless are required for global patterning of the ocular segment in the *Tribolium* embryo.** *Dev Biol* 2014, **394**:367-381.
45. Heffer A, Pick L: **Conservation and variation in *Hox* genes: how insect models pioneered the evo-devo field** [Internet]. *Annu Rev Entomol* 2013, **58**:161-179.
46. Bergman NH: *Comparative Genomics* [Internet]. Humana Press; 2007.
47. Cameron SL: **Insect mitochondrial genomics: implications for evolution and phylogeny** [Internet]. *Annu Rev Entomol* 2014, **59**:95-117.
48. Oppenheim SJ, Baker RH, Simon S, DeSalle R: **We can't all be supermodels: the value of comparative transcriptomics to the study of non-model insects.** [Internet]. *Insect Mol Biol* 2015, **24**:139-154.
49. Roux J, Rosikiewicz M, Robinson-Rechavi M: **What to compare and how: comparative transcriptomics for evo-devo** [Internet]. *J Exp Zool Part B Mol Dev Evol* 2015, **324**:372-382.
50. Chapman RF: *The Insects — Structure and Function*. Cambridge University Press; 2012.
51. Lynch JA, El-Sherif E, Brown SJ: **Comparisons of the embryonic development of *Drosophila*, *Nasonia*, and *Tribolium*.** [Internet]. *Wiley Interdiscip Rev Dev Biol* [date unknown], **1**:16-39.
52. Werren JH, Loehlin DW: **The parasitoid wasp *Nasonia*: an emerging model system with haploid male genetics.** [Internet]. *Cold Spring Harb Protoc* 2009. 2009 pdb.emo134.
53. Patel NH: **It's a bug's life.** [Internet]. *Proc Natl Acad Sci U S A* 2000, **97**:4442-4444.
54. Brown SJ, Denell RE, Beeman RW: **Beetling around the genome.** [Internet]. *Genet Res* 2003, **82**:155-161.
55. Benton MA, Akam M, Pavlopoulos A: **Cell and tissue dynamics during *Tribolium* embryogenesis revealed by versatile fluorescence labeling approaches.** [Internet]. *Development* 2013, **140**:3210-3220.
56. van der Zee M, Benton MA, Vazquez-Faci T, Lamers GEM, Jacobs CGC, Rabouille C: **Innexin7a forms junctions that stabilize the basal membrane during cellularization of the blastoderm in *Tribolium castaneum*.** [Internet]. *Development* 2015, **142**:2173-2183.
57. Benton MA, Pechmann M, Frey N, Stappert D, Conrads KH, Chen Y-T, Stamatakis E, Pavlopoulos A, Roth S: **Toll genes have an ancestral role in axis elongation.** [Internet]. *Curr Biol* 2016 <http://dx.doi.org/10.1016/j.cub.2016.04.055>.
58. Nakamoto A, Hester SD, Constantinou SJ, Blaine WG, Tewksbury AB, Matei MT, Nagy LM, Williams TA: **Changing cell behaviours during beetle embryogenesis correlates with slowing of segmentation.** [Internet]. *Nat Commun* 2015, **6**:6635. Nakamoto and colleagues establish a *Tribolium* dye injection protocol to trace cell populations during blastoderm formation, gastrulation and germband elongation. Subsequently, they compare the fate of anterior and posterior blastoderm cells in wild type and *Tc-eve* knockdown embryos.
59. Koelzer S, Kölsch Y, Panfilio KA: **Visualizing late insect embryogenesis: extraembryonic and mesodermal enhancer trap expression in the beetle *Tribolium castaneum*.** [Internet]. *PLoS One* 2014, **9**:e103967. Koelzer and colleagues exhaustively characterize three extra-embryonic membrane-related enhancer trap lines from the GEKU screen with fluorescence live imaging (see also Table 1).
60. El-Sherif E, Averof M, Brown SJ: **A segmentation clock operating in blastoderm and germband stages of *Tribolium* development.** *Development* 2012 <http://dx.doi.org/10.1242/dev.085126>.
61. Nollmann FI, Heinrich AK, Brachmann AO, Morisseau C, Mukherjee K, Casanova-Torres AM, Strobl F, Kleinhans D, Kinski S, Schultz K et al.: **A phorohabdus natural product inhibits insect juvenile hormone epoxide hydrolase.** [Internet]. *Chembiochem* 2015, **16**:766-771.
62. Macaya CC, Saavedra PE, Cepeda RE, Nuñez VA, Sarrazin AF: **A *Tribolium castaneum* whole-embryo culture protocol for studying the molecular mechanisms and morphogenetic movements involved in insect development.** [Internet]. *Dev Genes Evol* 2016, **226**:53-61.
63. Handel K, Grünfelder CG, Roth S, Sander K: ***Tribolium* embryogenesis: a SEM study of cell shapes and movements from blastoderm to serosal closure.** [Internet]. *Dev Genes Evol* 2000, **210**:167-179.
64. Horn T, Hilbrant M, Panfilio KA: **Evolution of epithelial morphogenesis: phenotypic integration across multiple levels of biological organization.** [Internet]. *Front Genet* 2015, **6**:303.
65. Handel K, Basal A, Fan X, Roth S: ***Tribolium castaneum* twist: gastrulation and mesoderm formation in a short-germ beetle.** [Internet]. *Dev Genes Evol* 2005, **215**:13-31.
66. Jacobs CGC, Rezende GL, Lamers GEM, van der Zee M: **The extraembryonic serosa protects the insect egg against desiccation.** [Internet]. *Proc Biol Sci* 2013, **280** 20131082.
67. Jacobs CGC, van der Zee M: **Immune competence in insect eggs depends on the extraembryonic serosa.** [Internet]. *Dev Comp Immunol* 2013, **41**:263-269.
68. Jacobs CGC, Spaink HP, van der Zee M: **The extraembryonic serosa is a frontier epithelium providing the insect egg with a full-range innate immune response.** [Internet]. *Elife* 2014:3.
69. Schröder R, Beermann A, Wittkopp N, Lutz R: **From development to biodiversity — *Tribolium castaneum*, an insect model organism for short germband development.** [Internet]. *Dev Genes Evol* 2008, **218**:119-126.

Supplementary Table 1 – Metadata and parameter for the long-term live-imaging datasets DS0001-0003.

<i>Dataset (DS)</i>	DS0001	DS0002	DS0003
<i>Species</i>	<i>Tribolium castaneum</i> (Herbst) Arthropoda → Insecta → Coleoptera → Tenebrionidae		<i>Drosophila melanogaster</i> (Meigen) Arthropoda → Insecta → Diptera → Drosophilidae
<i>Line</i>	FNL (expresses H2B-EGFP under control of the EFA promoter)	Brainy (double transgenic) [34]	Bloomington #24163 (w*; P{His2Av-EGFP.C}2 / SM6a)
<i>Line Genotype</i>	one insert / heterozygote	double homozygote	homozygote / balancer
<i>Stock</i>	~300 adults, less than 4 months old		~150 adults, less than 3 weeks old
<i>Stock Medium</i>	full grain wheat flour (113061006, Demeter, Darmstadt, Germany) supplemented with 5% (wt/wt) inactive dry yeast (62-106, Flystuff, San Diego, CA, USA)		Nutri-Fly Bloomington Formulation (66-112, Dominique Dutscher SA, Brumath, France)
<i>Stock Conditions</i>	12:00 h light / 12:00 h darkness at 25°C and 70% relative humidity (DR-36VL, Percival Scientific, Perry, IA, USA)		
<i>Egg Laying Period</i>	01:00 h at 25°C and 70% relative humidity exposed to light		0:10 h at room temperature (23±1°C) exposed to light
<i>Egg Laying Medium</i>	405 fine wheat flour (113061036, Demeter, Darmstadt, Germany) supplemented with 5% (wt/wt) inactive dry yeast (62-106, Flystuff, San Diego, CA, USA)		apple juice (254615, REWE Markt GmbH, Köln, Germany) plates with 1% (wt/vol) agarose
<i>Pre-imaging Incubation</i>	07:00 h at 25°C and 70% relative humidity in darkness, 01:00 h at room temperature (23±1°C)	23:00 h at 25°C and 70% relative humidity in darkness, 01:00 h at room temperature (23±1°C)	00:30 h at room temperature (23±1°C)
<i>LSFM Type</i>	mDSLMM (monolithic digital scanned laser light sheet-based fluorescence microscope) based on DSLM [4]		
<i>Laser Lines</i>	488 nm / 20 mW diode laser (PhoxX 488-20, Omicron Laserprodukte GmbH, Rodgau-Dudenhofen, Germany) 561 nm / 25 mW DPSSL (Cobolt Jive CW 561, Omicron Laserprodukte GmbH, Rodgau-Dudenhofen, Germany)		
<i>Excitation Objective</i>	2.5× NA 0.06 EC Epiplan-Neofluar objective (422320-9900-000, Carl Zeiss, Göttingen, Germany)		
<i>Emission Objective</i>	10× NA 0.3 W N-Achroplan objective (420947-9900-000, Carl Zeiss, Göttingen, Germany)		
<i>Emission Filters</i>	525/50 single-band bandpass filter (FF03-525/50-25, Semrock/AHF Analysentechnik AG, Tübingen, Germany) 607/70 single-band bandpass filter (FF01-607/70-25, Semrock/AHF Analysentechnik AG, Tübingen, Germany)		
<i>Camera</i>	High-resolution CCD (Clara, Andor, Belfast, United Kingdom), 14 bit, 1040×1392 pixel (pitch 6.45 µm)		
<i>Dataset File Type</i>	TIFF, 16 bit grayscale (planes saved as Z stacks in ZIP-compressed container files, indicated as PL(ZS))		
<i>Dechoriation</i>	~60-90 s in 10% (vol/vol) sodium hypochlorite (425044-250ML, Sigma Adrich, Taufkirchen, Germany) in PBS pH 7.4 (10010-023, Gibco Life Technologies GmbH, Darmstadt, Germany)		
<i>Mounting Agarose</i>	1% (wt/vol) low-melt agarose (6351.2, Carl Roth, Karlsruhe, Germany) in PBS pH 7.4 (10010-023, Gibco Life Technologies GmbH, Darmstadt, Germany)		
<i>Imaging Buffer</i>	PBS pH 7.4 (10010-023, Gibco Life Technologies GmbH, Darmstadt, Germany)		
<i>Imaging Temperature</i>	room temperature (23±1°C)	room temperature (23±1°C)	room temperature (23±1°C)
<i>Retrieval</i>	developed to healthy adult		

Supplementary Table 1 – Metadata and parameter for the long-term live-imaging datasets DS0001-0003.

<i>Dataset (DS)</i>	DS0001	DS0002	DS0003
<i>Dataset Size</i>	382.0 Gigabyte (TIFF)	92.4 Gigabyte (TIFF)	20.0 Gigabyte (TIFF)
<i>Figures</i>	2a-b	2c-d	3
<i>Supplementary Videos</i>	-	1	-
<i>Comment</i>	-	-	-
<i>Time Points (TP)</i>	1501 (TP0001-TP1501)	193 (TP0001-TP0193)	168 (TP0001-TP0168)
<i>TP Interval</i>	00:06 h	00:30 h	00:10 h
<i>Total Time (TP×TP Interval)</i>	150:00 h	96:00 h	27:50 h
<i>Directions (DR)</i>	4 (DR0001-DR0004)	4 (DR0001-DR0004)	4 (DR0001-DR0004)
<i>DR Orientations</i>	0°, 90°, 180°, 270°	0°, 90°, 180°, 270°	0°, 90°, 180°, 270°
<i>Channels (CH)</i>	1 (CH0001)	2 (CH0001-CH0002)	1 (CH0001)
<i>CH0001 Excitation</i>	488 nm	488 nm	488 nm
<i>CH0001 Power</i>	135 μW (close to the embryo)	270 μW (close to the embryo)	135 μW (close to the embryo)
<i>CH0001 Exposure Time</i>	50 ms	50 ms	50 ms
<i>CH0001 Emission Filter</i>	525/50 single-band bandpass filter	525/50 single-band bandpass filter	525/50 single-band bandpass filter
<i>CH0002 Excitation</i>	-	561 nm	-
<i>CH0002 Power</i>	-	270 μW (close to the embryo)	-
<i>CH0002 Exposure Time</i>	-	50 ms	-
<i>CH0002 Emission Filter</i>	-	607/70 single-band bandpass filter	-
<i>Planes (PL)</i>	100 (PL0001-PL0150)	150 (PL0001-PL0150)	100 (PL0001-PL0100)
<i>Z Spacing</i>	2.58 μm	2.58 μm	2.58 μm
<i>Z Distance (PL×Z Spacing)</i>	387.0 μm	387.0 μm	258.0 μm
<i>X-Dimensions (XD)</i>	600 pixels (cropped)	600 pixels (cropped)	500 pixels (cropped)
<i>X Spacing</i>	0.645 μm	0.645 μm	0.645 μm
<i>X Length (XD×X Spacing)</i>	387.0 μm	387.0 μm	322.5 μm
<i>Y-Dimensions (YD)</i>	1000 pixels (cropped)	1000 pixels (cropped)	900 pixels (cropped)
<i>Y Spacing</i>	0.645 μm	0.645 μm	0.645 μm
<i>Y Length (YD×Y Spacing)</i>	645.0 μm	645.0 μm	580.5 μm

All datasets can be downloaded at www.physikalischebiologie.de/bugcube.

Light Sheet-based Fluorescence Microscopy of Living or Fixed and Stained *Tribolium castaneum* Embryos

Frederic Strobl, Selina Klees & Ernst H.K. Stelzer

The red flour beetle *Tribolium castaneum* has become an important insect model organism in developmental genetics and evolutionary developmental biology. The observation of *Tribolium* embryos with light sheet-based fluorescence microscopy has multiple advantages over conventional widefield and confocal fluorescence microscopy. Due to the unique properties of a light sheet-based microscope, three dimensional images of living specimens can be recorded with high signal-to-noise ratios and significantly reduced photo-bleaching as well as photo-toxicity along multiple directions over periods that last several days. With more than four years of methodological development and a continuous increase of data, the time seems appropriate to establish standard operating procedures for the usage of light sheet technology in the *Tribolium* community as well as in the insect community at large. This protocol describes three mounting techniques suitable for different purposes, presents two novel custom-made transgenic *Tribolium* lines appropriate for long-term live imaging, suggests five fluorescent dyes to label intracellular structures of fixed embryos and provides information on data post-processing for the timely evaluation of the recorded data. Representative results concentrate on long-term live imaging, optical sectioning and the observation of the same embryo along multiple directions. The respective datasets are provided as a downloadable resource. Finally, the protocol discusses quality controls for live imaging assays, current limitations and the applicability of the outlined procedures to other insect species. This protocol is primarily intended for developmental biologists who seek imaging solutions that outperform standard laboratory equipment. It promotes the continuous attempt to close the gap between the technically orientated laboratories/communities, which develop and refine microscopy methodologically, and the life science laboratories/communities, which require 'plug-and-play' solutions to technical challenges. Furthermore, it supports an axiomatic approach that moves the biological questions into the center of attention.

Published in April 2016

Research Article – *Journal of Visualized Experiments* – MyJove Corporation

PubMed ID 28518097

Video Article

Light Sheet-based Fluorescence Microscopy of Living or Fixed and Stained *Tribolium castaneum* Embryos

Frederic Strobl^{1,2,3}, Selina Klees^{1,2,3}, Ernst H. K. Stelzer^{1,2,3}¹Physical Biology, Buchmann Institute for Molecular Life Sciences (BMLS)²Cluster of Excellence Frankfurt, Macromolecular Complexes³Goethe-Universität Frankfurt am Main – Campus RiedbergCorrespondence to: Ernst H. K. Stelzer at ernst.stelzer@physikalischebiologie.deURL: <https://www.jove.com/video/55629>DOI: [doi:10.3791/55629](https://doi.org/10.3791/55629)Keywords: Developmental Biology, Issue 122, Arthropod, insect, Coleoptera, *Tribolium castaneum*, morphogenesis, embryogenesis, non-invasive long-term fluorescence live imaging, light sheet-based fluorescence microscopy, three-dimensional light microscopy, LSFM, DSLM, SPIM

Date Published: 4/28/2017

Citation: Strobl, F., Klees, S., Stelzer, E.H. Light Sheet-based Fluorescence Microscopy of Living or Fixed and Stained *Tribolium castaneum* Embryos. *J. Vis. Exp.* (122), e55629, doi:10.3791/55629 (2017).

Abstract

The red flour beetle *Tribolium castaneum* has become an important insect model organism in developmental genetics and evolutionary developmental biology. The observation of *Tribolium* embryos with light sheet-based fluorescence microscopy has multiple advantages over conventional widefield and confocal fluorescence microscopy. Due to the unique properties of a light sheet-based microscope, three dimensional images of living specimens can be recorded with high signal-to-noise ratios and significantly reduced photo-bleaching as well as photo-toxicity along multiple directions over periods that last several days. With more than four years of methodological development and a continuous increase of data, the time seems appropriate to establish standard operating procedures for the usage of light sheet technology in the *Tribolium* community as well as in the insect community at large. This protocol describes three mounting techniques suitable for different purposes, presents two novel custom-made transgenic *Tribolium* lines appropriate for long-term live imaging, suggests five fluorescent dyes to label intracellular structures of fixed embryos and provides information on data post-processing for the timely evaluation of the recorded data. Representative results concentrate on long-term live imaging, optical sectioning and the observation of the same embryo along multiple directions. The respective datasets are provided as a downloadable resource. Finally, the protocol discusses quality controls for live imaging assays, current limitations and the applicability of the outlined procedures to other insect species.

This protocol is primarily intended for developmental biologists who seek imaging solutions that outperform standard laboratory equipment. It promotes the continuous attempt to close the gap between the technically orientated laboratories/communities, which develop and refine microscopy methodologically, and the life science laboratories/communities, which require 'plug-and-play' solutions to technical challenges. Furthermore, it supports an axiomatic approach that moves the biological questions into the center of attention.

Video Link

The video component of this article can be found at <https://www.jove.com/video/55629/>

Introduction

The red flour beetle *Tribolium castaneum*, which belongs to the large family of darkling beetles (Tenebrionidae), has a long history within the agricultural and life sciences and is the second best studied model insect organism after the fruit fly *Drosophila melanogaster*. During the last four decades, it became a powerful and popular insect model organism in developmental genetics, in evolutionary developmental biology and, during the last twenty years, in embryonic morphogenesis for a variety of reasons:

Drosophila and *Tribolium* both belong to the Holometabola, but diverged approximately 300 million years ago^{1,2,3,4}. While the embryonic development of *Drosophila* is commonly considered as highly derived, *Tribolium* shows a more ancestral mode of development that is found in a considerably larger proportion of insect species^{5,6,7,8,9}. Firstly, *Tribolium* exhibits non-involuting head development, *i.e.* its mouthparts and antennae emerge already during embryogenesis^{10,11,12,13,14,15}. Secondly, *Tribolium* follows the principles of short-germ development, *i.e.* abdominal segments are added sequentially from a posterior growth zone during germband elongation^{16,17,18,19}. Thirdly, *Tribolium* develops and later degrades two extra-embryonic membranes *i.e.* the amnion, which covers the embryo only ventrally, and the serosa, which envelops the embryo completely^{20,21,22}. Both membranes play a crucial morphogenetic²³ as well as protective role against microorganisms^{24,25} and desiccation²⁶. Fourthly, the embryonically developing legs are fully functional during the larval life stage and serve as the primordia for the adult legs during pupal metamorphosis^{27,28,29,30,31}.

Due to their small size and modest demands, cultivation of *Tribolium* in the laboratory is fairly straightforward. Cultures of wild-type (WT) strains or transgenic lines typically consist of around 100-300 adults and can be kept within one-liter glass bottles (footprint 80 cm²) filled three to four centimeters high (about 50 g) with growth medium that consists of full grain wheat flour supplemented with inactive dry yeast. A water supply is not necessary. This allows even small laboratories to keep dozens of beetle cultures within small- or medium-sized commercially available

insect incubators. Later developmental stages of *Tribolium* (larvae after approximately the fourth instar, pupae and adults) are easily separated from the growth medium by sieving. Synchronized embryos are obtained by incubating adults for short periods on egg-laying medium. For rapid development, beetle cultures are kept at 32 °C (about four weeks per generation), while stock keeping is typically performed at 22-25 °C (about ten weeks per generation).

Within the last decade, many standard techniques have been gradually adapted and optimized for *Tribolium*, as summarized in the *Emerging Model Organisms* books³². Of great importance are advanced genetic methods such as embryonic³³, larval^{34,35} or parental^{36,37} RNA interference-based gene knockdown, germline transformation with either the *piggyBac*^{38,39} or the *Minos*⁴⁰ transposase system and CRISPR/Cas9-based genome engineering⁴¹. Furthermore, the *Tribolium* genome has been sequenced about a decade ago⁴², and is now in the third round of genome assembly release⁴³, which allows efficient and genome-wide identification and systematic analysis of genes⁴⁴ or other genetic elements^{45,46}. Additionally, the genomes of four other coleopteran species are available for comparative genetic approaches^{47,48,49,50}. In association with the sequenced genome, two large-scale genetic analyses have been performed, *i.e.* an insertional mutagenesis screen⁵¹ and a systematic RNA interference-based gene knockdown screen^{52,53}.

Fluorescence live imaging with widefield, confocal or light sheet-based microscopy (LSFM) allows to observe the embryonic morphology of *Tribolium* as a function of time (*i.e.* the morphogenesis) in a multi-dimensional context (**Table 1**). In widefield and confocal fluorescence microscopy, the excitation and emission light is guided through the same objective lens. In both approaches, the entire specimen is illuminated for every recorded two-dimensional plane. Hence, the specimens are subjected to very high energy levels. In LSFM, only the fluorophores in the focal plane are excited due to a decoupling of illumination and detection by using two perpendicularly arranged objective lenses (**Figure 1**). LSFM comes in two canonic implementations – the single plane illumination microscope (SPIM) and the digital scanned laser light sheet-based fluorescence microscope (DSLM, **Figure 2**) – and offers several crucial advantages over traditional approaches: (i) intrinsic optical sectioning capability, (ii) good axial resolution, (iii) strongly reduced level of photo-bleaching, (iv) very low photo-toxicity, (v) high signal-to-noise ratio, (vi) relatively high acquisition speed, (vii) imaging along multiple directions and (viii) deeper tissue penetration due to the usage of low numerical aperture illumination objective lenses^{54,55,56}.

LSFM has already been successfully applied in *Tribolium* to document nearly the entire embryonic morphogenesis⁵⁷ and to analyze the principles of extra-embryonic membrane rupture at the beginning of dorsal closure²³. To raise the attractiveness of LSFM in the *Tribolium* community and for insect science in general, it is of great importance to establish standard operating procedures and to improve the methods, protocols and the pool of resources to a level where the microscope becomes an ease-of-use standard tool in developmental biology laboratories, and the biological questions stay in the center of attention.

This protocol begins with the basics of *Tribolium* cultivation, *i.e.* maintenance, reproduction and embryo collection. Next, two experimental strategies are illustrated: (i) live imaging of custom-made transgenic lines and (ii) imaging of fixed embryos that were stained with fluorescent dyes (**Table 2**). Subsequently, three mounting techniques with slightly different purposes are explained in detail (**Figure 3** and **Table 3**): (i) the agarose column, (ii) the agarose hemisphere and (iii) the novel cobweb holder. The protocol then explains the data acquisition procedure with LSFM. Imaging modalities and key considerations are outlined. Finally, embryo retrieval is explained and suggestions for basic data processing are provided. In the representative results, live imaging data from two novel custom-made and the Glia-blue⁵⁸ transgenic lines are shown and the respective imaging datasets are provided as a downloadable resource. Additionally, image data of fixed embryos that were stained with a variety of fluorescence dyes are presented. The discussion focuses on quality control, current limitations of the live imaging approach and the adaptation of the protocol to other species.

The protocol is written for light sheet-based fluorescence microscopes that are equipped with a sample chamber and a rotatable clamp mechanism for standardized sample holders^{54,59,60}, which are typically cylinder-shaped elements made of metal, plastic or glass with a diameter in the millimeter range. The protocol is also suitable for both canonic implementations, *i.e.* SPIM and DSLM, as well as for setups with two or more illumination and detection arms^{61,62,63}. The representative results show data in two spectral channels, green (illumination with a 488 nm laser, detection through a 525/50 bandpass filter) and red (illumination with a 561 nm laser, detection through a 607/70 bandpass filter), but the protocol can be expanded to three or four spectral channels.

Protocol

1. Husbandry of *Tribolium* Cultures

NOTE: Standard conditions are defined as an incubation temperature of 25 °C and 70% relative humidity in a 12 h bright/12 h dark cycle. For more information on *Tribolium* husbandry, respective guidelines are available⁶⁴. This protocol requires two different flour-based media, which can be prepared in kilogram quantities and stored for several months.

1. Prior to working with flour and inactive dry yeast, store the unopened packages at -20 °C for 24 h and then let them warm up to room temperature. This procedure eliminates potential pathogens.
2. Pass full grain wheat flour and inactive dry yeast through a sieve with 710 µm mesh size, then prepare growth medium by supplementing the sifted full grain flour with 5% (w/w) sifted inactive dry yeast.
3. Pass 405 fine wheat flour and inactive dry yeast through a sieve with 250 µm mesh size, then prepare egg-laying medium by supplementing the sifted 405 fine wheat flour with 5% (w/w) sifted inactive dry yeast.
4. Pass the respective *Tribolium* culture through a sieve with 800 µm mesh size. Discard the leftover growth medium. Transfer the larvae, pupae and adults to a large glass dish.
5. If no progeny culture exists, transfer around 80 larvae and/or pupae to a new glass bottle to establish a new progeny culture. If no larvae and/or pupae are present, take around 40 adults instead. Add 50 g of growth medium and incubate under standard conditions.
6. Collect around 300 adults (500-700 mg) in another new glass bottle to establish the imaging culture. Add 50 g of growth medium and incubate under standard conditions. Allow the imaging culture to settle for at least 24 h in the fresh growth medium before embryo collection.

7. Replace the growth medium of the imaging culture at least every two weeks, which can be done in conjunction with embryo collection (see 3.2). After two to three months, replace the imaging culture completely by new adults from the progeny culture.
8. If a non-homozygous transgenic line is used, curate the progeny cultures frequently by removing non-transgenic animals. Ideally, generate homozygous lines if the respective transgene is not lethal or causes sterility when present on both chromosomes. Homozygous cultures typically have a higher average fluorescence level and the overall experimental conditions are narrower, since only one genotype is present.

2. Microscope Setup and Calibration

NOTE: The *Tribolium* embryo has an anterior-posterior length of about 600-660 μm and a transversal diameter of about 300-330 μm . Most modern CCD cameras have a sensor chip size of about 9 mm x 7 mm, *i.e.* a diameter of 11.4 μm , and a pixel-pixel distance of 6.45 μm . When combined with a 10X magnification objective lens, the embryo can be imaged *in toto* with a pixel pitch of 0.645 μm . Most modern sCMOS cameras have a larger sensor chip size of about 16 mm x 14 mm, *i.e.* a diameter of 21.3 μm , and a pixel-pixel distance of 6.5 μm . When combined with a 20X magnification objective lens, the embryo can be imaged *in toto* with a pixel pitch of 0.325 μm .

1. Attach the illumination and detection objective lenses to the microscope. Ensure that lasers and fluorescence filters match the fluorophore absorption and emission spectra very well.
2. Attach the sample chamber to the microscope. Fill the sample chamber with PBS pH 7.4 or any other appropriate imaging buffer.
3. Switch on and calibrate the microscope. Comprehensive calibration routines and troubleshooting guidelines for custom-built light sheet-based microscopes (more specifically for the DSLM implementation) have been published previously⁶⁵. For commercial devices, follow the manufacturer's instructions very carefully. Mishandling might deplete the sample chamber of the medium and cause havoc to the instrument as well as the specimen.

3. Collection of Transgenic or WT Embryos

1. Pass the imaging colony through a sieve with 800 μm mesh size. Collect adult beetles in a new glass bottle and add 10 g of egg-laying medium. Incubate the egg-laying culture for 1 h at 25 °C and 70% relative humidity in light.
2. Pass the egg-laying culture through a sieve with 800- μm mesh size to separate adults from the egg-laying medium, which contains around 30-100 embryos. Transfer adults to a new glass bottle and add either the old or 50 g of fresh growth medium.
3. If observation should start at the uniform blastoderm stage (example dataset DS0002), incubate the egg-laying medium for 15 h at 25 °C and 70% relative humidity. To start at the beginning of germband retraction (example datasets DS0001 and DS0003), incubate embryos for 23 h at 32 °C and 70% relative humidity. If other developmental stages are desired, refer to the respective literature^{64,65} and adapt incubation time and/or temperature as necessary.

4. Embryo Dechoriation

NOTE: The chorion is the outer layer of the eggshell and consists of proteins and polysaccharides. It is strongly light absorbent but not essential for proper development and can thus be chemically removed.

1. Pass the egg-laying medium through a sieve with 300 μm mesh size. Collect the embryos in a cell strainer with 100 μm mesh size and discard the leftover egg-laying medium.
2. Prepare a 6-well plate as follows: fill the A1, A2, A3 and B3 wells with 10 mL PBS pH 7.4 and the B1 and B2 wells with 9 mL PBS. Then carefully add 1 mL sodium hypochlorite to B1 and B2. Observe the progress of steps 4.3 to 4.8 under the stereo microscope. CAUTION sodium hypochlorite is corrosive.
3. Insert the cell strainer into the A1 well (PBS pH 7.4) and wash the embryos for one minute under gentle agitation. Larger flour particles should detach from the embryos.
4. Transfer the cell strainer to the B1 well (sodium hypochlorite in PBS pH 7.4) and shake the plate vigorously for 30 s. The remaining flour particles should detach completely from the embryos.
5. Transfer the cell strainer to the A2 well (PBS pH 7.4) and wash the embryos for 1 min under gentle agitation.
6. For dechoriation, transfer the cell strainer to the B2 well (sodium hypochlorite in PBS pH 7.4). Shake the plate vigorously until the chorion ruptures and detaches from the embryos. The chorion looks like a thin, semi-transparent membrane with lacerated edges, while dechorionated embryos have a plain silhouette.
7. Transfer the cell strainer to the A3 well (PBS pH 7.4) and wash the embryos for 1 min under gentle agitation. If any chorion fragments are still attached to the embryos after the washing, repeat step 4.6.
8. Store the embryos in the B3 well (PBS pH 7.4). Storage for several hours does not harm the embryos, but keep in mind that development continues.
9. For non-homozygous transgenic lines, remove any non-fluorescent embryos if possible. For fixation and staining of WT or transgenic embryos, continue with step 5. For live imaging of transgenic embryos, continue with step 6.

5. Vitelline Membrane Permeabilization, Fixation, and Staining

NOTE: The vitelline membrane is the inner layer of the eggshell. It is impervious for fluorescent dyes and thus has to be chemically permeabilized before staining.

1. Fill a scintillation vial with fixation/permeabilization solution (1.5 mL 4% (w/v) paraformaldehyde in PBS pH 6.9 and 1.5 mL n-heptane). Transfer embryos with a paintbrush to the vials. Cover vials with aluminum foil to protect fluorophores from light and incubate for 30 min on a rocking platform at 50 rotations per minute. CAUTION paraformaldehyde is toxic and corrosive, n-heptane is flammable and toxic.
2. Remove fixation solution and treat embryos three times for 15 min in 3 mL 0.1% (v/v) Triton X-100 in PBS pH 7.4 and subsequently once for 15 min in 3 mL 1% (v/v) Triton X-100 in PBS pH 7.4 on a rocking platform at 50 rotations per minute. CAUTION Triton X-100 is corrosive.

- Remove permeabilization solution and add 0.5 mL staining solution to the vial. Exemplary staining solutions are provided in **Table 2**. Stain embryos overnight at 4 °C on a rocking platform at 50 rotations per minute. For the dyes proposed in **Table 2**, washing is not necessary.

6. Preparation of Mounting Agarose

- Add 1 g low-melt agarose to 100 mL PBS pH 7.4 and heat the mixture for 2-3 min in a microwave oven at 800 W. If small agarose particles are still present, repeat the heating process in 30 sec intervals until the particles dissolve completely. The mounting agarose does not need to be prepared freshly every time, the solidified agarose can be re-liquefied by heating as described above. This process can be repeated 5-6 times before too much water has evaporated.
- Allow the agarose to cool down to approximately 40-45 °C, then fill two 1.5 mL reaction tubes with the heated agarose and keep those tubes at 35 °C in a thermoblock.

7. Embryo Mounting and Insertion into the Sample Chamber

- Option 1: Agarose column (Figure 3A-C, first column; Table 3, second column)**
 - Fill a 1.0 mL syringe with distilled water and attach it to one of the glass capillary openings by using a small rubber hose. Fill the capillary halfway with distilled water.
 - Pick an embryo with a paintbrush and place it on the inner side of the other glass capillary opening. Proceed quickly to the next step before the embryo dries out.
 - Stick the capillary into the liquid agarose and slowly draw a few μL of liquid agarose alongside the embryo into the capillary. Then quickly increase the drawing force so that the embryo is dragged along with the agarose. In the end, a few μL of agarose should be above and below the embryo. Set the capillary aside for a few minutes and let the agarose solidify.
 - Shorten the capillary with a diamond glass cutter to a length of about 5 mm. The remaining fragment should be completely filled with agarose and the embryo should be within the second quartile.
 - Insert the steel cylinder with the pin into the sample chamber, and then stick the capillary fragment on top of the pin. The agarose column should protrude a few millimeters from the capillary fragment with the part that contains the embryo.
- Option 2: Agarose hemisphere (Figure 3A-C, second column; Table 3, third column)**
 - Draw 200 μL of liquid agarose into a 1.0 mL syringe, then use it to fill the steel pipe from the top with agarose until a hemisphere forms at the bottom opening. The hemisphere diameter should be equal to the pipe diameter. Wait a few minutes until the agarose has solidified.
 - Pick an embryo with a paintbrush and rearrange it on the tip of the brush so that the anterior end becomes accessible. Dip the agarose hemisphere into liquid agarose to cover it with a thin film.
 - Place the embryo with its anterior end upright on the pole of the agarose hemisphere. Turn the steel pipe around and correct the position of the embryo with the brush. If necessary, stabilize the embryo by adding 2 μL agarose to the embryo/hemisphere border. Ideally, less than half of the embryo surface should be covered in agarose and the flanks should be as steep as possible.
 - Insert the steel pipe with the hemisphere and embryo slowly into the sample chamber.
- Option 3: Cobweb holder (Figure 3A-C, third column; Table 3, fourth column)**
 - Pick an embryo with a paintbrush and set it aside.
 - Cover the slotted hole of the cobweb holder with 5-8 μL liquid agarose, then remove most of the agarose until only a thin agarose film remains.
 - Place the embryo onto the agarose film and adjust its position. Carefully move the embryo to the x-axis center of the slotted hole, and align its elongated anterior-posterior axis with the elongated axis of the slotted hole.
 - Insert the cobweb holder with the mounted embryo slowly into the sample chamber. Position the cobweb holder so that it does not interfere with the excitation and emission light, *i.e.* 45° relative to the x- and z-axis.

8. Light Sheet-based Fluorescence Microscopy

- Decide along how many directions (and along which orientations) the embryo should be imaged. Four directions (along the orientations 0°, 90°, 180° and 270°) typically provide a good trade-off between coverage and energy load.
- Set up the number of fluorescence channels. The major parameters for each channel are the laser line, the fluorescence filter, the laser power and the exposure time. For long-term live imaging, it is important that the integrated energy load does not exceed the tolerance of the embryo. An exposure time of 25-50 ms ensures fast imaging, while a laser power between 100 and 300 μW should not affect the viability of the embryo. For fixed samples, exposure time and laser power can be at least doubled.
- For live imaging assays, configure the time lapse. The complete embryogenesis of *Tribolium* takes about seven days at room temperature (23 ± 1 °C) and a little less than three days at 32-35 °C⁶⁴. Define the temporal interval according to the morphogenetic events that should be observed. For short temporal intervals, consider lowering exposure time and laser power (see 8.2).
- Position the embryo in transmission light mode along the x- and y-axes into the center of the field of view without exposing it to the laser. Rotate the embryo by 360° in 90° steps to examine the embryo for any damage that could have occurred during the mounting process.
- Rotate the embryo appropriately around the y-axis to align the embryonic axes with the microscope axes, for example the lateral axis with the x-axis, *i.e.* the dorsoventral axis with the z-axis. When using the cobweb holder technique, alignment might not be possible.
- In the fluorescence mode, define the z-stack for each direction. Add 25-50 μm as spatial buffer in front of and behind the embryo. Including the buffer, the typical z-stack covers around 350-400 μm for a *Tribolium* embryo. Also define the z-spacing, which should be four times the lateral spacing, *i.e.* the spacing along the x- and y-axes⁶⁶.
- If two or more embryos are imaged in parallel, restart at 8.4 with the next embryo.

8. For long-term imaging, ensure that the sample chamber is filled with sufficient PBS pH 7.4 or other imaging buffer. Also cover the sample chamber opening.
9. Start the imaging process. For long-term live imaging, monitor the correct acquisition along all directions in all channels for all embryos. Occasionally check during the next days that the embryos are alive and in the appropriate position.

9. Embryo Retrieval and Quality Control

1. Once imaging has completed, remove the sample holder with the embryos from the sample chamber. Only embryos from live imaging assays have to be retrieved. Fixed and stained embryos can be discarded.
2. If a live imaging assay was performed, transfer the embryo to an object slide. For the agarose column technique, extract the embryos from the surrounding agarose with a scalpel, micro-knife or razor blade. For the agarose hemisphere technique, transfer the hemisphere with the flat side to the object slide. Embryo removal is not necessary. For the cobweb holder technique, gently dismount the embryos from the agarose film with a paintbrush. Incubate the object slide in a small glass dish in saturated humidity atmosphere under standard conditions until the larvae hatch.
3. After hatching, transfer the larvae to individual wells of a 24-well plate and add 500 mg of growth medium to each well. Incubate under standard conditions. Compare the total development time and morphology of the imaged larvae to non-imaged WT and transgenic larvae (see discussion). In assays that characterize WT development, no obvious morphological aberrations should ideally be noticeable.
4. Once the larvae develop to healthy adults, provide them with appropriate WT partners of the same background strain. After two weeks, check for progeny production. Also consider to check the fertility of the progeny by mating them *inter pares*. Only when the imaged embryos develop into fertile adults that produce fertile progeny, the imaging procedure can be considered non-invasive.

10. Image Data Processing

NOTE: For image data processing, the open-source image processing software ImageJ⁶⁷ or its derivate FIJI⁶⁸ are recommended. Both versions as well as comprehensive documentation are found at www.imagej.net. The standard file format for LSFM data is the tagged image file format (TIFF). The intrinsic container option allows the storage of image stacks such as z-stacks or time series of z maximum projections within a single file that can be opened in ImageJ or FIJI via drag-and-drop.

1. If necessary, rotate the z-stacks to align the anterior-posterior axis of the embryo with the y-axis (Image → Transform → Rotate). Please note that the rotation parameters have to be set individually for each direction, but not for the time lapse and the fluorescence channels.
2. Crop the z-stacks along the x-, y- and z-axes so that only minimal background (20 - 40 pixels along the x- and y-axes, 5 - 10 planes along the z-axis) remains (for the x- and y-axes, use the Rectangular Selection Tool, then Image → Crop; for the z-axis, use Image → Stacks → Tools → Slice Keeper). Please note that the cropping parameters have to be set individually for each direction, but not for the time points and the fluorescence channels.
3. Calculate the z maximum projection for each z-stack (Image → Stacks → Z Project, choose Max Intensity). Intensity projection calculations are data simplification procedures that remove one spatial dimension.
4. For long-term live imaging data, consider using an ImageJ or FIJI script that performs processing steps 10.1 to 10.3 for all directions, all time points and all fluorescence channels⁶⁵. Ideally, concatenate all z maximum projections per channel and direction and save them as a time series in one TIFF container. Alternatively, the BigDataViewer⁶⁹ plug-in for FIJI can be used to navigate through Terabyte-large datasets.
5. Depending on the transgenic line and imaging modalities, dynamic intensity adjustments of the time stacks might be desirable due to photo-bleaching and/or fluorophore expression fluctuations. Either the ImageJ- or FIJI-intrinsic Bleach Correction function (Image → Adjust → Bleach Correction, choose Histogram Matching) or dedicated software⁶⁵ are suggested.
6. If the embryo was recorded and/or along multiple directions and in multiple fluorescence channels, horizontal combination of the directions (Image → Stacks → Tools → Combine) and channel merge (Image → Color Merge → Channels) are recommended.
7. Registration and fusion of z-stacks acquired along multiple directions⁷⁰, eventually in combination with deconvolution⁷¹, allows the calculation of superior three-dimensional images of uniform quality and isotropic resolution. Both plug-ins are open source and pre-installed in FIJI, but they require the presence of landmarks (fluorescent microspheres, e.g. beads) around the specimen.
8. Open-source software frameworks for large-scale quantitative data extraction and analysis are also available, for example for segmentation and tracking of cell nuclei⁷² or cell shape recognition⁷³.

Representative Results

This protocol describes an experimental framework for fluorescence imaging of living or fixed and stained *Tribolium* embryos with LSFM. Due to the low levels of photo-bleaching and photo-toxicity, a direct consequence of its optical sectioning capability, LSFM is particularly well suited for long-term live imaging.

The novel AGOC{ATub'H2B-mEmerald} #1 transgenic line expresses a histone2B-mEmerald fusion protein under control of the *alpha-tubulin 1* promoter⁷⁴. It shows an enhancer trap-like expression pattern⁵¹, since the fluorescence signal is mainly obtained from the serosa, the yolk sac and several neuronal cell clusters. Using this line, 66 hr of embryonic development at room temperature (23±1 °C) were recorded, covering germband retraction and dorsal closure (Supplementary Movie 1). This line can be used to visualize neuronal clusters within the head appendages (Figure 4A) and the dynamics of serosa migration during dorsal closure (Figure 4B). The novel AGOC{ATub'H2B-mEmerald} #4 line carries the same transgene as the #1 line, but at a different genomic location. It does not show an obvious enhancer trap pattern, but the fluorescence signal is spatiotemporally ubiquitously detectable as described previously for this promoter⁷⁴. This line was imaged at the transition from gastrulation to germband elongation to demonstrate the optical sectioning capability at two depth levels (Figure 4C). Another feature, especially for live imaging, is the acquisition of z-stacks along multiple directions via sample rotation, which is standard for LSFM setups used in developmental biology. For example, in the Glia-blue⁵⁸ line, sample rotation allows the observation of glia cell reorganization along and around the ventral nerve cord as well as the proliferation dynamics in the left head lobe, which can only be seen properly from the dorsal site, in the same embryo (Figure 4D, Supplementary Movie 2). The live imaging datasets associated with this study are provided as a downloadable resource, meta and access information are found in Supplementary Table 1.

Since the choice of transgenic lines for live imaging is still limited, small fluorescent dyes can be used to specifically label intracellular structures. SYTOX Green binds to cell nuclei and can be visualized in the green channel, while YOYO-1 and BOBO-3 iodide bind to the nuclear envelope and can be visualized in the green or red channel, respectively (Figure 5A). These dyes can be used to highlight certain embryonic structures, such as the serosa scar (Figure 5B, first column), the posterior ventral serosa cells (Figure 5B, second column) or the serosa-amnion-germband tissue tri-layer that emerges during serosa window closure (Figure 5B, third to fifth column). Dual-color staining allows the visualization of two intracellular structures in the same embryo, for example the nuclear envelope together with the actin cytoskeleton, which can be stained with Alexa Fluor-conjugated Phalloidin dyes. For example, YOYO-1 iodide can be combined with Phalloidin 546 (Figure 5C), while BOBO-3 can be combined with Phalloidin 488 (Figure 5D).

It is also convenient to fix and stain transgenic embryos that already express a certain fluorescent protein, since the fixation procedure quenches the intrinsic fluorescence signal only marginally. For example, embryos from the AGOC{ATub'H2B-mEmerald} #4 transgenic line, in which the nuclei are detected in the green channel, can be stained with Phalloidin 546 so that the actin cytoskeleton becomes visible in the red channel (Figure 6).

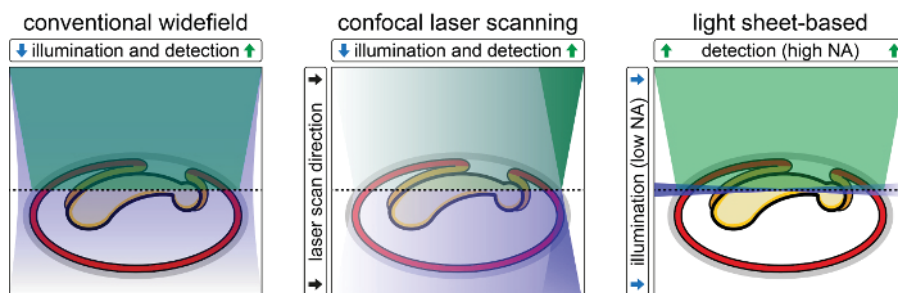


Figure 1: Comparison of Conventional Widefield, Confocal Laser Scanning and Light Sheet-based Fluorescence Microscopy.

Conventional widefield epi-fluorescence microscopy uses xenon arc/mercury-vapor lamps with appropriate filters or high-power light emitting diodes as light sources. For each acquired two-dimensional image, the whole specimen is illuminated with a non-diffraction-limited light cone. In confocal laser scanning fluorescence microscopy, a diffraction-limited Gaussian laser beam is scanned through the specimen and fluorescence is detected incoherently point-by-point. Similarly to conventional widefield epi-fluorescence microscopy, the whole specimen is illuminated for each acquired two-dimensional image. In light sheet-based fluorescence microscopy, a diffraction-limited Gaussian laser beam illuminates the specimen perpendicularly to the detection axis. Fluorescence is detected either plane-by-plane or line-by-line. During the acquisition of a two-dimensional image, only a small volume centered on the focal plane of the detection objective experiences the effects of the excitation light. The remaining volume of the specimen is not illuminated, does not contribute to out-of-focus blur, does not suffer from photo-toxic effects and does not lose fluorophores due to photo-bleaching. [Please click here to view a larger version of this figure.](#)

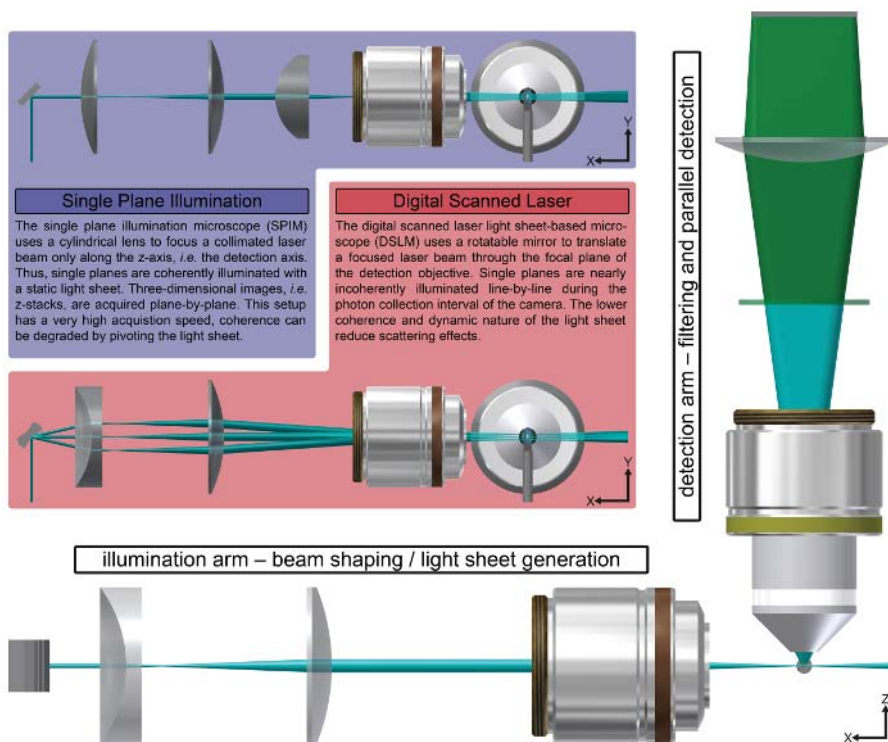


Figure 2: The Principle of Light Sheet-based Fluorescence Microscopy. In LSFM, illumination and detection are split into at least two optical paths. At least one illumination arm is used to generate the light sheet (cyan), while at least one detection arm is equipped with an appropriate filter and a camera for the parallel detection of the fluorescence signal (green). LSFM has two canonic implementations, the single (or selective) plane illumination microscope (blue background) and the digital scanned laser light sheet microscope (red background). By moving the specimen and the light sheet relative to each other, three-dimensional images are acquired. Information along multiple directions is collected by rotating the specimen around the y-axis, which is preferentially oriented along gravity. [Please click here to view a larger version of this figure.](#)

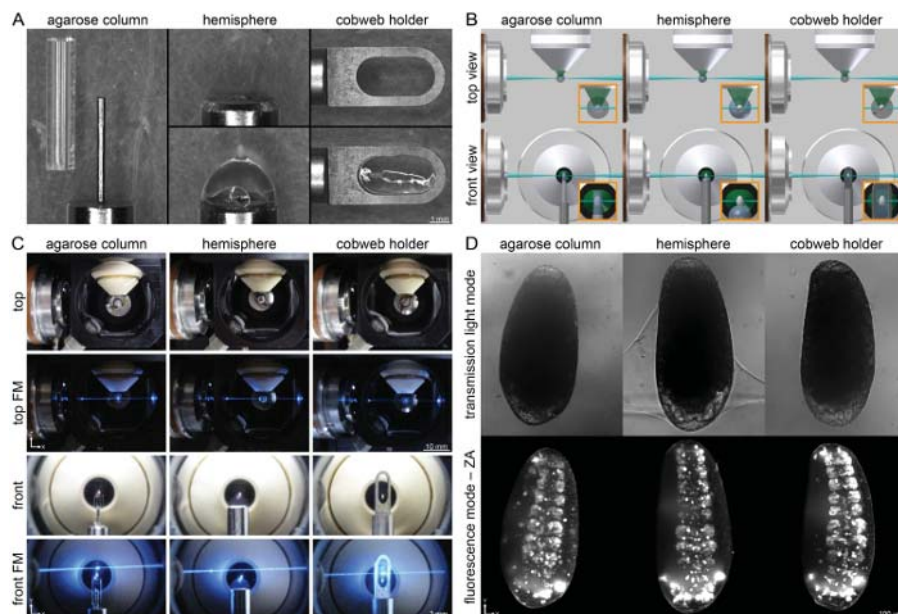


Figure 3: Three Different Mounting Techniques used in the Recording of the Embryonic Development of *Tribolium* with Light Sheet-based Fluorescence Microscopy. (A) The agarose column refers to a steel cylinder with a small pin that pushes the agarose column, in which the embryo is embedded, out of a glass capillary. The agarose hemisphere is mounted on a steel pipe. The embryo is attached to the pole of the hemisphere with a small amount of agarose. The cobweb holder is a sheet of metal with a slotted hole mounted on top of the steel cylinder. The embryo is glued to a thin agarose film that spans the slotted hole. (B) Schemes of the three mounting techniques inside a light sheet microscope. (C) The three mounting techniques applied within a DSLM. (D) Exemplary images from embryos of the Glia-blue transgenic line recorded with the three mounting techniques. The embryos, which are at the onset of germband retraction, are shown with their posterior end orientated towards top to match the transmission light images. FM, fluorescence mode; ZA, z maximum projection with intensity adjustment. [Please click here to view a larger version of this figure.](#)

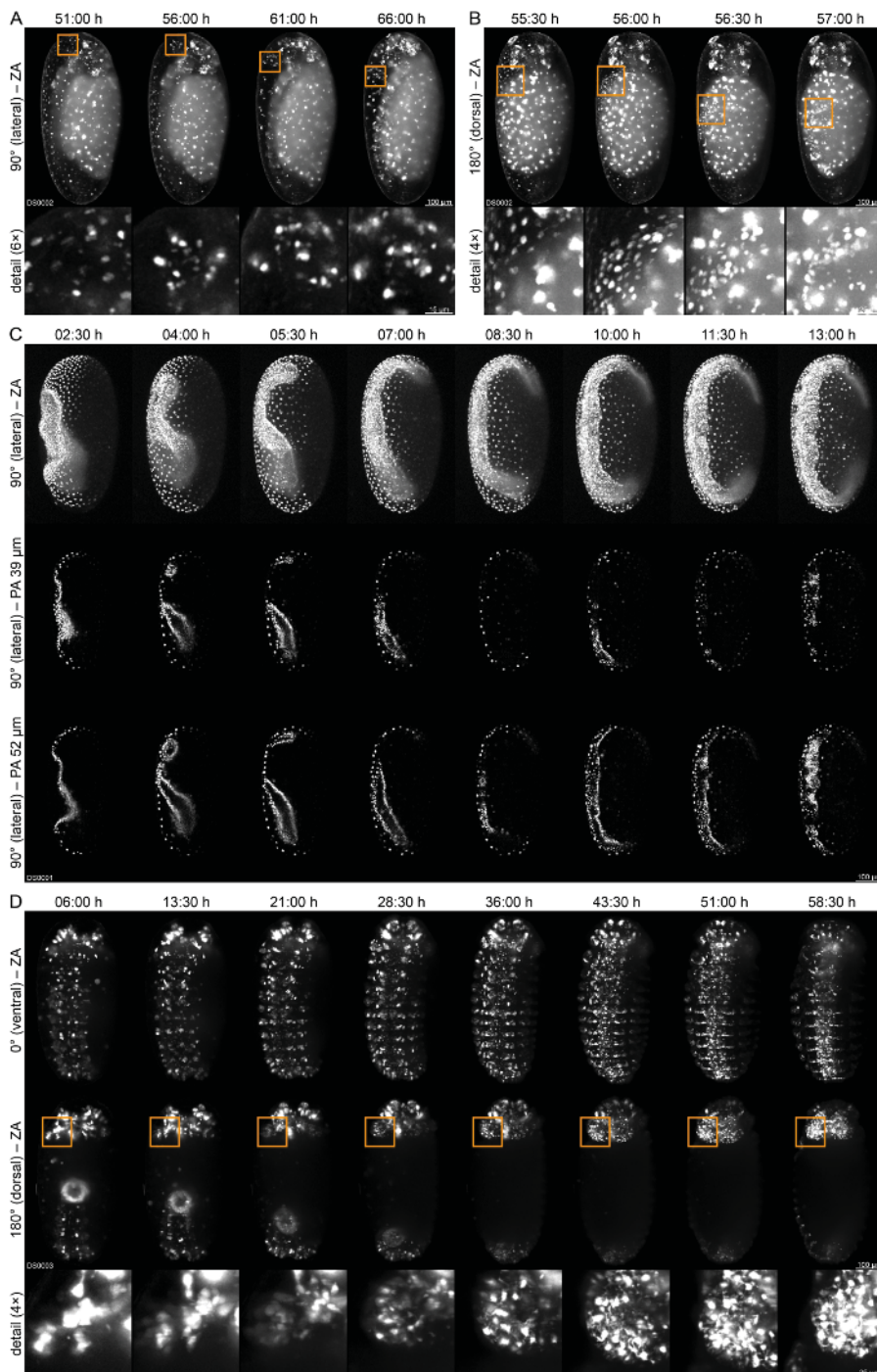


Figure 4: Live imaging of *Tribolium* embryos. (A) An embryo of the AGOC{ATub'H2B-mEmerald} #1 line at the transition from germband retraction to dorsal closure. This line exhibits an enhancer trap expression pattern. The fluorescence signal is mainly found in the serosa, the yolk sac and a few neuronal cell clusters. The embryo is shown over a period of 15 h with an interval of 5 h. The detail images show cell clusters in the head appendages. Initially, the clusters are still covered by serosal cells (first column), upon serosa rupture, the cells follow along with the turning movement of the head. (B) Same embryo shown during dorsal closure for 1:30 h with an interval of 0:30 h. The detail images show the migration of the ruptured serosa over the yolk sac. (C) Top row: An embryo of the AGOC{ATub'H2B-mEmerald} #4 line at the transition from gastrulation to germband elongation. Middle and lower row: Single planes are shown in two depths over a period of 10:30 h with an interval of 1:30 h. (D) An embryo of the Glia-blue line during germband retraction shown over a period of 50:30 h with an interval of 07:30 h. The detail images show the morphogenetic reorganization of the glial cells in the left head lobe. ZA, z maximum projection with intensity adjustment; PA single plane with intensity adjustment. [Please click here to view a larger version of this figure.](#)

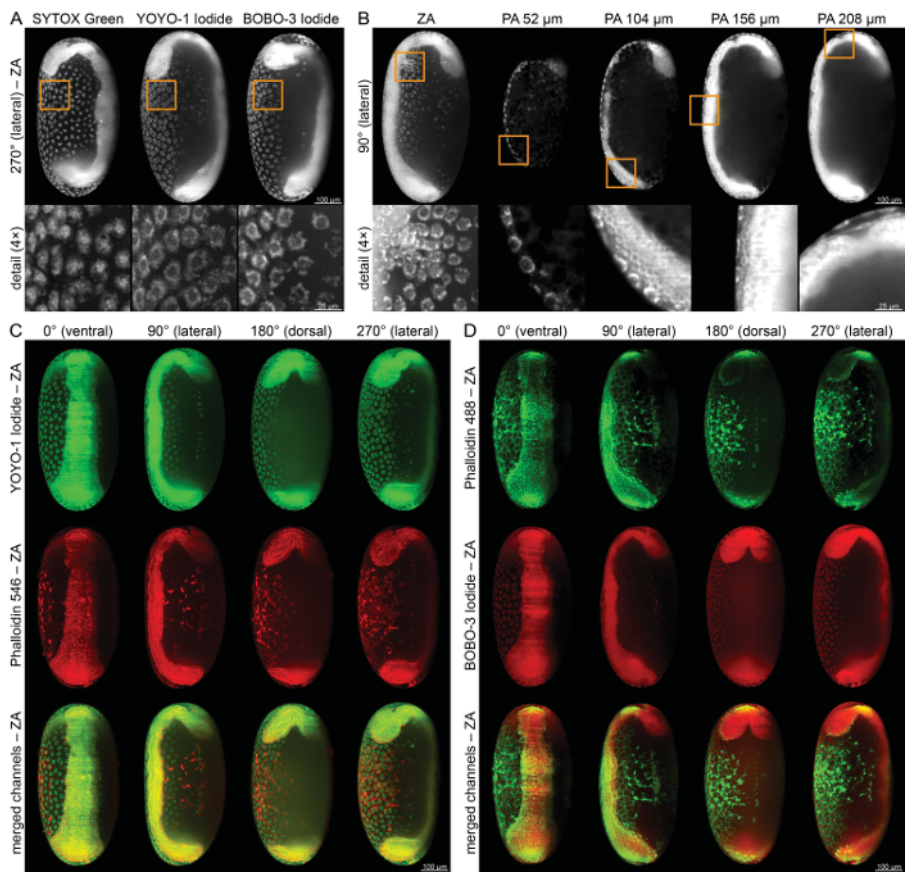


Figure 5: Fixation, Staining, and Imaging of WT Embryos during Germband Elongation. (A) Embryos stained with either SYTOX Green, *i.e.* a fuzzy nuclear stain, or YOYO-1 iodide or BOBO-3 iodide, *i.e.* two nuclear envelope stains. (B) YOYO-1 iodide-stained embryo. Details show the serosa scar (first column), the nuclear envelope of the large posterior-ventral serosa cells (second column) or the three-layered tissue organization of the serosa, the amnion and the actual embryonic tissue (third to fifth column). (C) Dual-color staining with YOYO-1 iodide and Phalloidin 546. (D) Dual-color staining with Phalloidin 488 and BOBO-3 iodide. ZA, z maximum projection with intensity adjustment. [Please click here to view a larger version of this figure.](#)

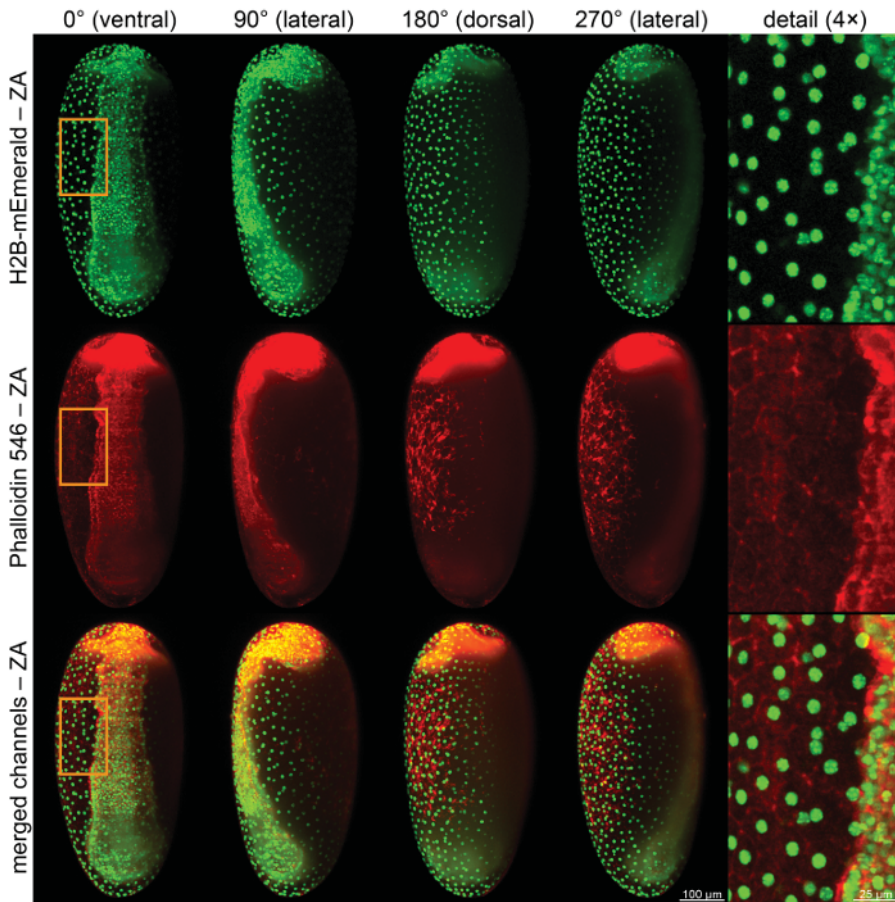


Figure 6: Images of Fixed and Stained Transgenic Embryos from the AGOC{ATub'H2B-mEmerald} #1 line. This transgenic line expresses mEmerald-labeled histone2B (H2B) under control of the *alpha-tubulin 1* promoter, which marks the nuclei/chromatin ubiquitously throughout the whole embryonic development. The embryo was further stained with Alexa Fluor 546 Phalloidin, which labels the actin cytoskeleton/f-actin. ZA, z maximum projection with intensity adjustment. [Please click here to view a larger version of this figure.](#)

criterion	fluorescence microscope type		
	conventional wide field	confocal laser scanning	light sheet-based
objective lens setup	one objective lens, medium-high NA	one objective lens, high NA	two perpendicularly arranged objective lenses, illumination: low NA, detection: high NA
illumination light source	white light source and appropriate filters (e.g. mercury short-arc lamps) or LED-based with clean-up filters	laser with clean-up filter (e.g. diode or DPSS lasers)	laser with clean-up filter (e.g. diode or DPSS lasers)
illumination per two-dimensional image	whole sample	whole sample (typically two-dimensional Gaussian beam scan)	only focal plane (DSLIM: one-dimensional Gaussian beam scan)
detection	parallel (typically CCD or sCMOS camera)	sequential (photomultiplier tube)	parallel (typically CCD or sCMOS camera)
imaging speed	fast (milliseconds per image)	slow (seconds per image)	fast (milliseconds per image)
out-of-focus fluorescence	no discrimination	blocked nearly completely by the pinhole (rejection efficiency depends on diameter)	nearly non-existent (only due to scattering)
spatial dimensions	2 (x / y)	3 (x / y / z)	3 (x / y / z)
further degrees of freedom	2 (time, fluorescence channel)	2 (time, fluorescence channel)	3 (time, fluorescence channel, direction)
lateral resolution	r (0.6 λ / NA)	0.66 r (0.4 λ / NA)	r (0.6 λ / NA)
optical sectioning capability	No	Yes (discrimination in the detection pathway)	Yes (discrimination in the illumination pathway ⁷⁵)
availability and price	predominantly commercial, low cost	predominantly commercial, expensive	commercial, expensive custom-built, moderate ^{54,59,60,75}
live imaging publications covering <i>Tribolium</i> embryos	six ^{44,76,77,78,79,80}	seven ^{23,77,79,81,82,81} (spinning disk confocal) ^{83,84,85}	four ^{23,57,65,86}

Table 1 - Characteristics of Fluorescence Microscopy Techniques used in *Tribolium* live Imaging.

dye	staining	dilution
SYTOX Green	nuclei (fuzzy)	1:10,000 (1:100 in ddH ₂ O and 1:100 in 1% (w/v) BSA in PBS)
YOYO-1 Iodide	nuclear envelope	1:10,000 (1:100 in ddH ₂ O and 1:100 in 1% (w/v) BSA in PBS)
BOBO-3 Iodide	nuclear envelope	1:10,000 (1:100 in ddH ₂ O and 1:100 in 1% (w/v) BSA in PBS)
Alexa Fluor 488 Phalloidin	actin cytoskeleton	1:100 (in 1% (w/v) BSA in PBS)
Alexa Fluor 546 Phalloidin	actin cytoskeleton	1:100 (in 1% (w/v) BSA in PBS)

Table 2 - Staining Solutions.

	agarose column (option 1)	hemisphere (option 2)	cobweb holder (option 3)
rationale	embryo is embedded in an agarose column that is pushed out of a capillary	posterior end of embryo is glued to pole of an agarose hemisphere	embryo is glued to thin agarose film spanning a slotted hole
sample holder	steel cylinder with pin	steel pipe	steel cylinder with slotted hole
directions (orientations)	unlimited (any)	unlimited (any)	four (0°, 90°, 180°, 270°)
required skill level	moderate	high	low
agarose around the embryo	high	low	moderate
number of embryos per session	up to three	one	up to six
embryo retrieval	tricky	easy	easy
disposable equipment	glass capillaries	-	-
recommended for	short-term live imaging, stained embryos	long-term live imaging	long-term live imaging, stained embryos
references	three ^{23,87,88}	two ^{57,65}	this publication

Table 3 - Mounting Methods Advantages and Disadvantages.

aberrational phenotype induction	rationale	step	reference (methodological)
embryonic RNA interference	double-stranded RNA is injected into embryos during the syncytial blastoderm stage to knock-down one or more specific genes	inject embryos after Step 4.8.	two ^{33,81}
parental RNA interference	double-stranded RNA is injected laterally into female pupae between the abdominal segments 3 and 4, which leads to gene knock-down in the progeny	take the pupae from Step 1.5.	two ^{36,37}
recessive embryonic lethal mutant lines	egg-laying cultures that carry a recessive embryonic lethal mutation heterozygous yield about 25% homozygote mutant progeny	cross mutant line into imaging line during Step 1.5.	three ^{39,51,89}
application of extrinsic factors	certain bioactive or toxic factors are extrinsically applied to the embryos by adding them to the imaging buffer	add factor to imaging buffer during Step 2.2.	two ^{83,85}

Table 4 - LSFM Live Imaging of Aberrational Phenotypes

Supplementary Table 1 - Metadata and Parameter for the Long-term Live-imaging Datasets DS0001-0003. [Please click here to download the file.](#)

Supplementary Movie 1 - Live Imaging of a *Tribolium* Embryo from the AGOC{ATub^{H2B-mEmerald}} #1 Transgenic Line.

This line exhibits an enhancer trap expression pattern. The fluorescence signal is primarily found in the serosa, the yolk sac and a subset of neuronal cells. The embryo is shown along four orientations from 00:00 h to 66:00 h with an interval of 00:30 h between the time points. The movie starts at the beginning of germband retraction and ends once dorsal closure is completed. Frame rate is five frames per second. ZA, z maximum projection with intensity adjustment. [Please click here to download the file.](#)

Supplementary Movie 2 - Live Imaging of a *Tribolium* Embryo from the Glia-blue Transgenic Line.

The embryo is shown along four orientations from 00:00 h to 66:00 h with an interval of 00:30 h between the time points. The movie starts at the beginning of germband retraction and ends once dorsal closure is completed. Frame rate is five frames per second. ZA, z maximum projection with intensity adjustment. [Please click here to download the file.](#)

Discussion

Quality control

In live imaging assays, the preparation and recording procedure must be non-invasive, *i.e.* neither the mechanical and chemical handling (collection, dechoriation, mounting onto the sample holder) nor the integrated energy load during the observation should affect the viability of the specimen. For studies that characterize WT development, it is recommended to only use data from experiments in which the embryo

survives the recording process, is retrieved successfully and develops into a healthy adult. The adult should not show any morphological aberrations, should be fertile and its progeny should also be fertile. There are three major reasons for low survival rates, especially in long-term live imaging assays:

Firstly, the embryo surface was covered extensively with agarose during Step 7, which probably hinders ion and gas exchange and constricts the embryo mechanically. Affected embryos, especially when imaged during early embryogenesis, typically develop inconspicuously for several hours, arrest suddenly and lose their fluorescence signal quickly. With some experience, the surface fraction that is embedded in agarose by using the hemisphere technique can be kept below one-third, while with the cobweb holder technique, at most half of the surface is covered by a very thin agarose layer. Secondly, the integrated energy load applied to the embryo exceeds the tolerance. The values given in Step 8.2 serve as a rule of thumb, but the following criteria should be considered: (i) embryos during early embryonic development do not endure laser irradiation as well as embryos during late embryonic development, (ii) although the integrated energy load might be identical, higher laser power with either lower exposure time or longer temporal intervals appears to be more stressful than lower laser power with a high exposure time or shorter temporal intervals, (iii) higher wavelengths are typically better tolerated and (iv) for transgenic lines, the tolerance limit appears to be line-specific, whereas fluorophore expression strength seems to be inversely proportional to the laser irradiation tolerance. Additionally, the design of the fusion protein and/or the intracellular localization also play a role. Thirdly, the embryo is damaged during the mounting process. The most crucial factor here is that the incubation time in the sodium hypochlorite solution is as short as necessary to completely remove the chorion. Longer incubation times might harm the embryos. Care should also be taken to not puncture or squeeze the embryos with the brush and to keep the mounting agarose at an ambient temperature. Damaged embryos can be identified during Step 8.4 before the actual imaging process commences, so that damaged embryos can be replaced with viable ones.

By following those guidelines, typically around 85-90% of the embryos survive the live imaging procedure and hatch. Around 90% of the hatched embryos develop into healthy and fertile adults. The survival ratio appears to be independent from imaging temperature and mounting techniques (when the agarose column is used for imaging periods of not more than half a day), but slightly decreases with elevated levels of laser irradiance. As an additional control, especially during the initial characterization of custom-made transgenic lines for fluorescence live imaging or the framework establishing phase as precursor for a comprehensive experimental sequence, it is recommended to run non-imaged WT and transgenic embryos in parallel to the imaged embryos, which are incubated at the same temperature as the imaged embryo, and compare their development time and morphology⁸⁵.

Furthermore, studies that characterize aberrational phenotypes (**Table 4**) via live imaging should also run a non-affected control embryo in parallel. It is recommended to keep the treatment of both embryos as similar as possible, but this has to be considered individually for each experimental strategy:

Knock-down via RNA interference.

For embryonic RNA interference^{33,81}, embryos that derive from the same egg-laying culture should either be injected with functional or control double-stranded RNA. The differently injected embryos should then be imaged simultaneously in the same LSMF by using either the agarose column or the cobweb holder technique. For parental RNA interference^{36,37}, the imaging culture should be split into two subcultures. Female pupae of one subculture should be injected with the functional double-stranded RNA, while the other subculture should be injected with control double-stranded RNA. Embryo collection should be performed in parallel, and both the experimental and the control embryo can be imaged simultaneously in the same microscope by using the agarose column or cobweb holder technique.

Recessive embryonic lethal mutant lines.

When working with recessive embryonic lethal mutants^{39,89,91,92,93}, an egg-laying culture of heterozygous mutants, which are normally phenotypically inconspicuous, yields theoretically 25% homozygous mutant progeny (but sometimes less due to practical handling issues⁸⁹) and 75% of phenotypically inconspicuous progeny (50% heterozygous mutants and 25% WTs). It is recommended to use the cobweb holder technique to mount several embryos from such an egg-laying culture. The homozygous mutants can be identified throughout the course of imaging by the manifestation of the phenotype, while the normally developing embryos serve as controls. The genotype of the imaged specimens can be determined once imaging and quality control are completed.

Application of extrinsic factors.

If the influence of extrinsic factors within the imaging buffer^{83,85}, e.g. bioactive or toxic substances, on development is investigated, parallel imaging together with a control embryo in the same LSMF is typically not possible. Therefore, imaging has to be performed sequentially. Optimally, the time between subsequent experiments is minimized and the embryos derive from the same imaging culture. Alternatively, two identically constructed and operated LSMFs can be used. In this case, embryos from the same egg-laying period should be used, but it is of great importance that the calibration of both microscope is conducted carefully so that the imaging properties are comparable. By using the cobweb holder technique, multiple embryos for each condition can be imaged at once. With the agarose column technique, the extrinsic factors might be hindered from reaching the embryos.

Current limitations of the LSMF live imaging approach

LSMF is a powerful tool to analyze embryonic morphogenesis non-invasively in multiple broad-scaled dimensions. Standard operation procedures, as proposed in this protocol, will support the process to establish light sheet technology as a standard tool in developmental biology. However, the approach is limited by a number of factors on diverse experimental and organizational levels:

Initially, LSMF was developed to analyze one specimen at a time. All current approaches that image two or more embryos simultaneously in the same microscope by 'stacking' the specimen along the y-axis in the agarose column or the cobweb holder addresses this issue only to a certain degree. Multi-well plate- and coverslip-based setups are available^{94,95,96}. However, they suffer from reduced image quality and sacrifice some of the essential benefits from LSMF, such as imaging along multiple directions. Currently, the best option is to work with multiple microscopes in parallel, which becomes reasonably feasible when costly components, such as the laser, are shared⁶⁰.

With the EFA-nGFP^{57,65,84}, the FNL⁸⁶, the Brainy^{58,86}, the AGOC{ATub'H2B-mEmerald} #1, the AGOC{ATub'H2B-mEmerald} #4 and the Glia-blue⁵⁸, only six custom-made transgenic lines suitable for long-term live imaging are currently available. In addition, the HC079 (amnion), G12424 (serosa) and G04609 (heart) enhancer trap lines⁵¹ have been characterized with LSFM²³. Alternatively, fluorescent embryos can also be generated by mRNA⁸¹ or dye injection⁷⁹, those approaches are relatively straightforward, but also suffer from limitations⁸⁶. Several more standards are still required such as cytoskeletal-, organelle- and membrane-labeled lines or lines that express fluorophores under certain non-ubiquitous promoters to observe only certain organs or tissues. Ideally, those lines are also available with different fluorescent proteins.

Another challenge is the data volume generated by LSFM. Due to acquisition of information in three spatial dimensions and at least three further degrees of freedom (time, direction, fluorescence channel), the size of live imaging datasets can easily reach many Gigabytes to a few Terabytes. Even after three-dimensional cropping and ZIP-based compression of the TIFF containers, the three exemplary datasets associated with this study have sizes of 31.6, 12.6 and 45.1 Gigabytes, *i.e.* 89.3 Gigabyte in total. When working with LSFM, it is necessary to have the respective infrastructure for data storage and processing^{88,97}.

The highest image quality is obtained at the surface of the embryo, but with increasing depth, the fluorescence signal becomes more and more blurry. For example, the posterior end of the germband becomes covered by the yolk sac fold during gastrulation and cannot be properly resolved (**Figure 4C**, first to fifth column). Imaging along multiple directions solves this problem at least partially – high quality information from the surface all around the embryo is available, but the inner regions remain fuzzy. Currently, no satisfying solutions are available, but in the long run, infrared fluorescent proteins⁹⁸, genetic approaches⁹⁹ or microscope setups with adaptive optics¹⁰⁰ could be considered.

Adaptation for other species

By now, LSFM has been used to document the embryonic development of three insect species, *i.e.* the fruit fly *Drosophila melanogaster*^{61,62,101}, the scuttle fly *Megaselia abdita*¹⁰² and the red flour beetle *Tribolium castaneum*⁵⁷. The experimental framework, standard operating procedures and mounting techniques described here should be easily adaptable to other insect species. Germline transformation protocols for many insects that belong to various orders are available¹⁰³, including species of economical and/or medical importance, such as the honeybee¹⁰⁴, several lepidopterans^{105,106} or multiple mosquito species^{107,108,109}. With respective transgenic lines suitable for fluorescence live imaging, the embryonic morphogenesis of insects can be characterized while considering their evolutionary lineages and/or ecological niches. About one million insect species have been described and a further twenty million insect species most likely exist¹¹⁰, covering more than 400 million years of evolution². Only the comparative approach will generate information that in turn provides insights which cannot be obtained by studying the developmental principles of only a single species.

Disclosures

The authors have nothing to disclose.

Author Contributions

FS and EHKS conceived the research. FS generated the transgenic AGOC lines. Light sheet-based fluorescence imaging was performed by FS and SK. FS and EHKS wrote the manuscript with input from SK.

Acknowledgements

We thank Sven Plath for technical support. The Glia-blue transgenic line was a kind gift from Gregor Bucher (Göttingen, Germany). The research was funded by the Cluster of Excellence Frankfurt am Main for Macromolecular Complexes (CEF-MC, EXC 115, speaker Volker Dötsch) granted in part to EHKS at the Buchmann Institute for Molecular Life Sciences (BMLS, director Enrico Schleiff) at the Goethe Universität Frankfurt am Main by the Deutsche Forschungsgemeinschaft (DFG).

References

1. Brown, S. J., Denell, R. E., & Beeman, R. W. Beetling around the genome. *Genet. Res.* **82**, 155-61 (2003).
2. Misof, B. *et al.* Phylogenomics resolves the timing and pattern of insect evolution. *Science*. **346**, 763-7 (2014).
3. Tong, K. J., Duchêne, S., Ho, S. Y. W., & Lo, N. INSECT PHYLOGENOMICS. Comment on "Phylogenomics resolves the timing and pattern of insect evolution". *Science*. **349**, 487 (2015).
4. Kjer, K. M. *et al.* INSECT PHYLOGENOMICS. Response to Comment on "Phylogenomics resolves the timing and pattern of insect evolution". *Science*. **349**, 487 (2015).
5. Klingler, M. *Tribolium*. *Curr. Biol.* **14**, R639-40 (2004).
6. Savard, J., Marques-Souza, H., Aranda, M., & Tautz, D. A segmentation gene in tribolium produces a polycistronic mRNA that codes for multiple conserved peptides. *Cell*. **126**, 559-69 (2006).
7. Yang, X., Zarinikamar, N., Bao, R., & Friedrich, M. Probing the *Drosophila* retinal determination gene network in *Tribolium* (I): The early retinal genes dachshund, eyes absent and sine oculis. *Dev. Biol.* **333**, 202-14 (2009).
8. Peel, A. D. Forward genetics in *Tribolium castaneum*: opening new avenues of research in arthropod biology. *J. Biol.* **8**, 106 (2009).
9. Lynch, J. A., El-Sherif, E., & Brown, S. J. Comparisons of the embryonic development of *Drosophila*, *Nasonia*, and *Tribolium*. *Wiley Interdiscip. Rev. Dev. Biol.* **1**, 16-39 (2012).
10. Schröder, R., Jay, D. G., & Tautz, D. Elimination of EVE protein by CALI in the short germ band insect *Tribolium* suggests a conserved pair-rule function for even skipped. *Mech. Dev.* **80**, 191-195 (1999).
11. Posnien, N., Schinko, J. B., Kittelmann, S., & Bucher, G. Genetics, development and composition of the insect head--a beetle's view. *Arthropod Struct. Dev.* **39**, 399-410 (2010).

12. Posnien, N., Koniszewski, N. D. B., Hein, H. J., & Bucher, G. Candidate gene screen in the red flour beetle *Tribolium* reveals six3 as ancient regulator of anterior median head and central complex development. *PLoS Genet.* **7**, e1002416 (2011).
13. Angelini, D. R., Smith, F. W., Aspiras, A. C., Kikuchi, M., & Jockusch, E. L. Patterning of the adult mandibulate mouthparts in the red flour beetle, *Tribolium castaneum*. *Genetics.* **190**, 639-54 (2012).
14. Coulcher, J. F., & Telford, M. J. Cap'n'collar differentiates the mandible from the maxilla in the beetle *Tribolium castaneum*. *Evodevo.* **3**, 25 (2012).
15. Peel, A. D. *et al.* Tc-knrps plays different roles in the specification of antennal and mandibular parasegment boundaries and is regulated by a pair-rule gene in the beetle *Tribolium castaneum*. *BMC Dev. Biol.* **13**, 25 (2013).
16. Bucher, G., & Klingler, M. Divergent segmentation mechanism in the short germ insect *Tribolium* revealed by giant expression and function. *Development.* **131**, 1729-40 (2004).
17. Handel, K., Basal, A., Fan, X., & Roth, S. *Tribolium castaneum* twist: gastrulation and mesoderm formation in a short-germ beetle. *Dev. Genes Evol.* **215**, 13-31 (2005).
18. Roth, S., & Hartenstein, V. Development of *Tribolium castaneum*. *Development Genes and Evolution.* **218**, 115-118 (2008).
19. Schröder, R., Beermann, A., Wittkopp, N., & Lutz, R. From development to biodiversity--*Tribolium castaneum*, an insect model organism for short germband development. *Dev. Genes Evol.* **218**, 119-26 (2008).
20. Sharma, R., Beermann, A., & Schröder, R. The dynamic expression of extraembryonic marker genes in the beetle *Tribolium castaneum* reveals the complexity of serosa and amnion formation in a short germ insect. *Gene Expr. Patterns.* **13**, 362-71 (2013).
21. Benton, M. A., & Pavlopoulos, A. *Tribolium* embryo morphogenesis: may the force be with you. *Bioarchitecture.* **4**, 16-21 (2014).
22. Horn, T., Hilbrant, M., & Panfilio, K. A. Evolution of epithelial morphogenesis: phenotypic integration across multiple levels of biological organization. *Front. Genet.* **6**, 303 (2015).
23. Hilbrant, M., Horn, T., Koelzer, S., & Panfilio, K. A. The beetle amnion and serosa functionally interact as apposed epithelia. *Elife.* **5**, (2016).
24. Jacobs, C. G. C. C., & van der Zee, M. Immune competence in insect eggs depends on the extraembryonic serosa. *Dev. Comp. Immunol.* **41**, 263-9 (2013).
25. Jacobs, C. G. C., Spaink, H. P., & van der Zee, M. The extraembryonic serosa is a frontier epithelium providing the insect egg with a full-range innate immune response. *Elife.* **3**, (2014).
26. Jacobs, C. G. C., Rezende, G. L., Lamers, G. E. M., & van der Zee, M. The extraembryonic serosa protects the insect egg against desiccation. *Proc. Biol. Sci.* **280**, 20131082 (2013).
27. Lewis, D. L., DeCamillis, M., & Bennett, R. L. Distinct roles of the homeotic genes *Ubx* and *abd-A* in beetle embryonic abdominal appendage development. *Proc. Natl. Acad. Sci. U. S. A.* **97**, 4504-9 (2000).
28. Beermann, A. *et al.* The Short antennae gene of *Tribolium* is required for limb development and encodes the orthologue of the *Drosophila* Distal-less protein. *Development.* **128**, 287-97 (2001).
29. Grossmann, D., Scholten, J., & Prpic, N.-M. Separable functions of wingless in distal and ventral patterning of the *Tribolium* leg. *Dev. Genes Evol.* **219**, 469-79 (2009).
30. Angelini, D. R., Smith, F. W., & Jockusch, E. L. Extent With Modification: Leg Patterning in the Beetle *Tribolium castaneum* and the Evolution of Serial Homologs. *G3 (Bethesda).* **2**, 235-48 (2012).
31. Grossmann, D., & Prpic, N.-M. Egrf signaling regulates distal as well as medial fate in the embryonic leg of *Tribolium castaneum*. *Dev. Biol.* **370**, 264-272 (2012).
32. *Emerging Model Organisms: A Laboratory Manual, Volume 2.* Cold Spring Harbour Laboratory Press. (2010).
33. Brown, S. J., Mahaffey, J. P., Lorenzen, M. D., Denell, R. E., & Mahaffey, J. W. Using RNAi to investigate orthologous homeotic gene function during development of distantly related insects. *Evol. Dev.* **1**, 11-5 (1999).
34. Tomoyasu, Y., & Denell, R. E. Larval RNAi in *Tribolium* (Coleoptera) for analyzing adult development. *Dev. Genes Evol.* **214**, 575-8 (2004).
35. Linz, D. M., Clark-Hachtel, C. M., Borràs-Castells, F., & Tomoyasu, Y. Larval RNA interference in the red flour beetle, *Tribolium castaneum*. *J. Vis. Exp.* e52059 (2014).
36. Bucher, G., Scholten, J., & Klingler, M. Parental RNAi in *Tribolium* (Coleoptera). *Curr. Biol.* **12**, R85-6 (2002).
37. Posnien, N. *et al.* RNAi in the red flour beetle (*Tribolium*). *Cold Spring Harb. Protoc.* **2009**, pdb.prot5256 (2009).
38. Lorenzen, M. D. *et al.* piggyBac-mediated germline transformation in the beetle *Tribolium castaneum*. *Insect Mol. Biol.* **12**, 433-40 (2003).
39. Berghammer, A. J., Weber, M., Trauner, J., & Klingler, M. Red flour beetle (*Tribolium*) germline transformation and insertional mutagenesis. *Cold Spring Harb. Protoc.* **2009**, pdb.prot5259 (2009).
40. Pavlopoulos, A., Berghammer, A. J., Averof, M., & Klingler, M. Efficient transformation of the beetle *Tribolium castaneum* using the Minos transposable element: quantitative and qualitative analysis of genomic integration events. *Genetics.* **167**, 737-46 (2004).
41. Gilles, A. F., Schinko, J. B., & Averof, M. Efficient CRISPR-mediated gene targeting and transgene replacement in the beetle *Tribolium castaneum*. *Development.* **142**, 2832-9 (2015).
42. Richards, S. *et al.* The genome of the model beetle and pest *Tribolium castaneum*. *Nature.* **452**, 949-55 (2008).
43. Kim, H. S. *et al.* BeetleBase in 2010: revisions to provide comprehensive genomic information for *Tribolium castaneum*. *Nucleic Acids Res.* **38**, D437-42 (2010).
44. Stappert, D., Frey, N., von Levetzow, C., & Roth, S. Genome-wide identification of *Tribolium* dorsoventral patterning genes. *Development.* **143**, 2443-54 (2016).
45. Pavlek, M., Gelfand, Y., Plohl, M., & Meštrović, N. Genome-wide analysis of tandem repeats in *Tribolium castaneum* genome reveals abundant and highly dynamic tandem repeat families with satellite DNA features in euchromatic chromosomal arms. *DNA Res.* **22**, 387-401 (2015).
46. Vlahović, I., Glunčić, M., Rosandić, M., Ugarković, Đ., & Paar, V. Regular higher order repeat structures in beetle *Tribolium castaneum* genome. *Genome Biol. Evol.* (2016).
47. Keeling, C. I. *et al.* Draft genome of the mountain pine beetle, *Dendroctonus ponderosae* Hopkins, a major forest pest. *Genome Biol.* **14**, R27 (2013).
48. Vega, F. E. *et al.* Draft genome of the most devastating insect pest of coffee worldwide: the coffee berry borer, *Hypothenemus hampei*. *Sci. Rep.* **5**, 12525 (2015).
49. Cunningham, C. B. *et al.* The Genome and Methylome of a Beetle with Complex Social Behavior, *Nicrophorus vespilloides* (Coleoptera: Silphidae). *Genome Biol. Evol.* **7**, 3383-96 (2015).
50. Meyer, J. M. *et al.* Draft Genome of the Scarab Beetle *Oryctes borbonicus* on La Réunion Island. *Genome Biol. Evol.* **8**, 2093-105 (2016).

51. Trauner, J. *et al.* Large-scale insertional mutagenesis of a coleopteran stored grain pest, the red flour beetle *Tribolium castaneum*, identifies embryonic lethal mutations and enhancer traps. *BMC Biol.* **7**, 73 (2009).
52. Schmitt-Engel, C. *et al.* The iBeetle large-scale RNAi screen reveals gene functions for insect development and physiology. *Nat. Commun.* **6**, 7822 (2015).
53. Dönitz, J. *et al.* iBeetle-Base: a database for RNAi phenotypes in the red flour beetle *Tribolium castaneum*. *Nucleic Acids Res.* **43**, D720-5 (2015).
54. Keller, P. J., & Stelzer, E. H. K. Digital scanned laser light sheet fluorescence microscopy. *Cold Spring Harb. Protoc.* **2010**, pdb.top78 (2010).
55. Weber, M., & Huisken, J. Light sheet microscopy for real-time developmental biology. *Curr. Opin. Genet. Dev.* **21**, 566-72 (2011).
56. Stelzer, E. H. K. Light-sheet fluorescence microscopy for quantitative biology. *Nat. Methods.* **12**, 23-6 (2015).
57. Strobl, F., & Stelzer, E. H. K. Non-invasive long-term fluorescence live imaging of *Tribolium castaneum* embryos. *Development.* 1-8 (2014).
58. Koniszewski, N. D. B. *et al.* The insect central complex as model for heterochronic brain development-background, concepts, and tools. *Dev. Genes Evol.* (2016).
59. Gualda, E. J. *et al.* OpenSpinMicroscopy: an open-source integrated microscopy platform. *Nat. Methods.* **10**, 599-600 (2013).
60. Pitrone, P. G. *et al.* OpenSPIM: an open-access light-sheet microscopy platform. *Nat. Methods.* **10**, 598-9 (2013).
61. Tomer, R., Khairy, K., Amat, F., & Keller, P. J. Quantitative high-speed imaging of entire developing embryos with simultaneous multiview light-sheet microscopy. *Nat. Methods.* **9**, 755-63 (2012).
62. Krzic, U., Gunther, S., Saunders, T. E., Streichan, S. J., & Hufnagel, L. Multiview light-sheet microscope for rapid in toto imaging. *Nat. Methods.* **9**, 730-3 (2012).
63. Chhetri, R. K. *et al.* Whole-animal functional and developmental imaging with isotropic spatial resolution. *Nat. Methods.* **12**, 1171-8 (2015).
64. Brown, S. J. *et al.* The red flour beetle, *Tribolium castaneum* (Coleoptera): a model for studies of development and pest biology. *Cold Spring Harb. Protoc.* **2009**, pdb.emo126 (2009).
65. Strobl, F., Schmitz, A., & Stelzer, E. H. K. Live imaging of *Tribolium castaneum* embryonic development using light-sheet-based fluorescence microscopy. *Nat. Protoc.* **10**, 1486-1507 (2015).
66. Engelbrecht, C. J., & Stelzer, E. H. Resolution enhancement in a light-sheet-based microscope (SPIM). *Opt. Lett.* **31**, 1477-9 (2006).
67. Schneider, C. A., Rasband, W. S., & Eliceiri, K. W. NIH Image to ImageJ: 25 years of image analysis. *Nat. Methods.* **9**, 671-675 (2012).
68. Schindelin, J. *et al.* Fiji: an open-source platform for biological-image analysis. *Nat. Methods.* **9**, 676-82 (2012).
69. Pietzsch, T., Saalfeld, S., Preibisch, S., & Tomancak, P. BigDataViewer: visualization and processing for large image data sets. *Nat. Methods.* **12**, 481-483 (2015).
70. Preibisch, S., Saalfeld, S., Schindelin, J., & Tomancak, P. Software for bead-based registration of selective plane illumination microscopy data. *Nat. Methods.* **7**, 418-9 (2010).
71. Preibisch, S. *et al.* Efficient Bayesian-based multiview deconvolution. *Nat. Methods.* **11**, 645-8 (2014).
72. Amat, F. *et al.* Fast, accurate reconstruction of cell lineages from large-scale fluorescence microscopy data. *Nat. Methods.* **11**, 951-8 (2014).
73. Stegmaier, J. *et al.* Real-Time Three-Dimensional Cell Segmentation in Large-Scale Microscopy Data of Developing Embryos. *Dev. Cell.* **36**, 225-240 (2016).
74. Siebert, K. S., Lorenzen, M. D., Brown, S. J., Park, Y., & Beeman, R. W. Tubulin superfamily genes in *Tribolium castaneum* and the use of a Tubulin promoter to drive transgene expression. *Insect Biochem. Mol. Biol.* **38**, 749-755 (2008).
75. Greger, K., Swoger, J., & Stelzer, E. H. K. Basic building units and properties of a fluorescence single plane illumination microscope. *Rev. Sci. Instrum.* **78**, 23705 (2007).
76. El-Sherif, E., Averof, M., & Brown, S. J. A segmentation clock operating in blastoderm and germband stages of *Tribolium* development. *Development.* (2012).
77. Panfilio, K. a, Oberhofer, G., & Roth, S. High plasticity in epithelial morphogenesis during insect dorsal closure. *Biol. Open.* **2**, 1108-18 (2013).
78. Koelzer, S., Kölsch, Y., & Panfilio, K. A. Visualizing late insect embryogenesis: extraembryonic and mesodermal enhancer trap expression in the beetle *Tribolium castaneum*. *PLoS One.* **9**, e103967 (2014).
79. Nakamoto, A. *et al.* Changing cell behaviours during beetle embryogenesis correlates with slowing of segmentation. *Nat. Commun.* **6**, 6635 (2015).
80. Horn, T., & Panfilio, K. A. Novel functions for Dorsocross in epithelial morphogenesis in the beetle *Tribolium castaneum*. *Development.* **143**, 3002-11 (2016).
81. Benton, M. A., Akam, M., & Pavlopoulos, A. Cell and tissue dynamics during *Tribolium* embryogenesis revealed by versatile fluorescence labeling approaches. *Development.* **140**, 3210-20 (2013).
82. van der Zee, M. *et al.* Innexin7a forms junctions that stabilize the basal membrane during cellularization of the blastoderm in *Tribolium castaneum*. *Development.* **142**, 2173-83 (2015).
83. Macaya, C. C., Saavedra, P. E., Cepeda, R. E., Nuñez, V. A., & Sarrazin, A. F. A *Tribolium castaneum* whole-embryo culture protocol for studying the molecular mechanisms and morphogenetic movements involved in insect development. *Dev. Genes Evol.* **226**, 53-61 (2016).
84. Sarrazin, A. F., Peel, A. D., & Averof, M. A Segmentation Clock with Two-Segment Periodicity in Insects. *Science.* **336**, 338-341 (2012).
85. Nollmann, F. I. *et al.* A photorhabdus natural product inhibits insect juvenile hormone epoxide hydrolase. *Chembiochem.* **16**, 766-71 (2015).
86. Strobl, F., & Stelzer, E. H. Long-term fluorescence live imaging of *Tribolium castaneum* embryos: principles, resources, scientific challenges and the comparative approach. *Curr. Opin. Insect Sci.* **18**, 17-26 (2016).
87. Keller, P. J., Schmidt, A. D., Wittbrodt, J., & Stelzer, E. H. K. Digital scanned laser light-sheet fluorescence microscopy (DSLIM) of zebrafish and *Drosophila* embryonic development. *Cold Spring Harb. Protoc.* **2011**, 1235-43 (2011).
88. Reynaud, E. G., Peychl, J., Huisken, J., & Tomancak, P. Guide to light-sheet microscopy for adventurous biologists. *Nat. Methods.* **12**, 30-4 (2015).
89. Cerny, A. C., Bucher, G., Schröder, R., & Klingler, M. Breakdown of abdominal patterning in the *Tribolium* Krüppel mutant jaws. *Development.* **132**, (2005).
90. Keller, P. J., Schmidt, A. D., Wittbrodt, J., & Stelzer, E. H. K. Reconstruction of zebrafish early embryonic development by scanned light sheet microscopy. *Science.* **322**, 1065-9 (2008).
91. Sulston, I. A., & Anderson, K. V. Embryonic patterning mutants of *Tribolium castaneum*. *Development.* **122**, (1996).
92. Berghammer, A., Bucher, G., Maderspacher, F., & Klingler, M. A system to efficiently maintain embryonic lethal mutations in the flour beetle *Tribolium castaneum*. *Dev. Genes Evol.* **209**, 382-389 (1999).

93. Brown, S. *et al.* Implications of the *Tribolium* Deformed mutant phenotype for the evolution of Hox gene function. *Proc. Natl. Acad. Sci. U. S. A.* **97**, 4510 (2000).
94. Wu, Y. *et al.* Inverted selective plane illumination microscopy (iSPIM) enables coupled cell identity lineaging and neurodevelopmental imaging in *Caenorhabditis elegans*. *Proc. Natl. Acad. Sci.* **108**, 17708-17713 (2011).
95. Kumar, A. *et al.* Dual-view plane illumination microscopy for rapid and spatially isotropic imaging. *Nat. Protoc.* **9**, 2555 (2014).
96. McGorty, R. *et al.* Open-top selective plane illumination microscope for conventionally mounted specimens. *Opt. Express.* **23**, 16142-53 (2015).
97. Amat, F. *et al.* Efficient processing and analysis of large-scale light-sheet microscopy data. *Nat. Protoc.* **10**, 1679-96 (2015).
98. Shcherbakova, D. M., & Verkhusha, V. V. Near-infrared fluorescent proteins for multicolor in vivo imaging. *Nat. Methods.* **10**, 751-4 (2013).
99. Supatto, W., McMahon, A., Fraser, S. E., & Stathopoulos, A. Quantitative imaging of collective cell migration during *Drosophila* gastrulation: multiphoton microscopy and computational analysis. *Nat. Protoc.* **4**, 1397-1412 (2009).
100. Royer, L. A. *et al.* Adaptive light-sheet microscopy for long-term, high-resolution imaging in living organisms. *Nat. Biotechnol.* (2016).
101. Keller, P. J. *et al.* Fast, high-contrast imaging of animal development with scanned light sheet-based structured-illumination microscopy. *Nat. Methods.* **7**, 637-42 (2010).
102. Caroti, F., Urbansky, S., Wosch, M., & Lemke, S. Germ line transformation and in vivo labeling of nuclei in Diptera: report on *Megaselia abdita* (Phoridae) and *Chironomus riparius* (Chironomidae). *Dev. Genes Evol.* **225**, 179-186 (2015).
103. Handler, A. M. Use of the piggyBac transposon for germ-line transformation of insects. *Insect Biochem. Mol. Biol.* **32**, 1211-1220 (2002).
104. Schulte, C., Theilenberg, E., Müller-Borg, M., Gempe, T., & Beye, M. Highly efficient integration and expression of piggyBac-derived cassettes in the honeybee (*Apis mellifera*). *Proc. Natl. Acad. Sci. U. S. A.* **111**, 9003-8 (2014).
105. Tamura, T. *et al.* Germline transformation of the silkworm *Bombyx mori* L. using a piggyBac transposon-derived vector. *Nat. Biotechnol.* **18**, 81-4 (2000).
106. Marcus, J. M., Ramos, D. M., & Monteiro, A. Germline transformation of the butterfly *Bicyclus anynana*. *Proc. R. Soc. B Biol. Sci.* **271**, S263-S265 (2004).
107. Catteruccia, F. *et al.* Stable germline transformation of the malaria mosquito *Anopheles stephensi*. *Nature.* **405**, 959-62 (2000).
108. Grossman, G. L. *et al.* Germline transformation of the malaria vector, *Anopheles gambiae*, with the piggyBac transposable element. *Insect Mol. Biol.* **10**, 597-604 (2001).
109. Labbé, G. M. C., Nimmo, D. D., & Alphey, L. piggybac- and PhiC31-mediated genetic transformation of the Asian tiger mosquito, *Aedes albopictus* (Skuse). *PLoS Negl. Trop. Dis.* **4**, e788 (2010).
110. Patel, N. H. It's a bug's life. *Proc. Natl. Acad. Sci. U. S. A.* **97**, 4442-4 (2000).

Supplementary Table 1 – Metadata and parameter for the long-term live-imaging datasets DS0001-0003.

<i>Dataset (DS)</i>	<i>DS0001</i>	<i>DS0002</i>	<i>DS0003</i>
<i>Species</i>	Tribolium castaneum (Herbst)		
	Arthropoda → Insecta → Coleoptera → Tenebrionidae		
<i>Line</i>	AGOC{ATub'H2B- mEmerald} #1	AGOC{ATub'H2B- mEmerald} #4	Glia-blue ⁵⁸
<i>Line Genotype</i>	one insert / unknown	one insert / unknown	unknown
<i>Stock</i>	~400 adults, less than 2 months old		
<i>Stock Medium</i>	full grain wheat flour (113061006, Demeter, Darmstadt, Germany) supplemented with 5% (wt/wt) inactive dry yeast (62-106, Flystuff, San Diego, CA, USA)		
<i>Stock Conditions</i>	12:00 h light / 12:00 h darkness at 25°C and 70% relative humidity (DR-36VL, Percival Scientific, Perry, IA, USA)		
<i>Egg Laying Period</i>	01:00 h at 25°C and 70% relative humidity exposed to light		
<i>Egg Laying Medium</i>	405 fine wheat flour (113061036, Demeter, Darmstadt, Germany) supplemented with 5% (wt/wt) inactive dry yeast (62-106, Flystuff, San Diego, CA, USA)		
<i>Pre-imaging Incubation</i>	24:00 h at 32°C and 70% relative humidity in darkness, 01:00 h at room temperature (23±1°C)	15:00 h at 25°C and 70% relative humidity in darkness, 01:00 h at room temperature (23±1°C)	24:00 h at 32°C and 70% relative humidity in darkness, 01:00 h at room temperature (23±1°C)
<i>LSFM Type</i>	mDSLMS (monolithic digital scanned laser light sheet-based fluorescence microscope) based on DSLM ^{54,90}		
<i>Laser Lines</i>	488 nm / 20 mW diode laser (PhoxX 488-20, Omicron Laserprodukte GmbH, Rodgau-Dudenhofen, Germany)		
<i>Excitation Objective</i>	2.5× NA 0.06 EC Epiplan-Neofluar objective (422320-9900-000, Carl Zeiss, Göttingen, Germany)		
<i>Emission Objective</i>	10× NA 0.3 W N-Achroplan objective (420947-9900-000, Carl Zeiss, Göttingen, Germany)		
<i>Emission Filters</i>	525/50 single-band bandpass filter (FF03-525/50-25, Semrock/AHF Analysentechnik AG, Tübingen, Germany)		

<i>Camera</i>	High-resolution CCD (Clara, Andor, Belfast, United Kingdom), 14 bit, 1040×1392 pixel (pitch 6.45 μm)		
<i>Dataset File Type</i>	TIFF, 16 bit grayscale (planes saved as Z stacks in ZIP-compressed container files, indicated as PL(ZS))		
<i>Dechoriation</i>	~60-90 s in 10% (vol/vol) sodium hypochlorite (425044-250ML, Sigma Adlrich, Taufkirchen, Germany) in PBS pH 7.4 (10010-023, Gibco Life Technologies GmbH, Darmstadt, Germany)		
<i>Mounting Agarose</i>	1% (wt/vol) low-melt agarose (6351.2, Carl Roth, Karlsruhe, Germany) in PBS pH 7.4 (10010-023, Gibco Life Technologies GmbH, Darmstadt, Germany)		
<i>Imaging Buffer</i>	PBS pH 7.4 (10010-023, Gibco Life Technologies GmbH, Darmstadt, Germany)		
<i>Imaging Temperature</i>	room temperature (23±1°C)	room temperature (23±1°C)	room temperature (23±1°C)
<i>Retrieval</i>	developed to healthy adult, produced fertile progeny	developed to healthy adult, produced fertile progeny	developed to healthy adult, produced fertile progeny

**Improving your four-dimensional image:
traveling through a decade of
light-sheet–based fluorescence microscopy research**

Frederic Strobl, Alexander Schmitz & Ernst H.K. Stelzer

Light-sheet–based fluorescence microscopy features optical sectioning in the excitation process. This reduces phototoxicity and photobleaching by up to four orders of magnitude compared with that caused by confocal fluorescence microscopy, simplifies segmentation and quantification for three-dimensional cell biology, and supports the transition from on-demand to systematic data acquisition in developmental biology applications.

Published in May 2017

Review Article – *Nature Protocols* – Nature Publishing Group

PubMed ID 28471459

Improving your four-dimensional image: traveling through a decade of light-sheet-based fluorescence microscopy research

Frederic Strobl, Alexander Schmitz & Ernst H K Stelzer

Light-sheet-based fluorescence microscopy features optical sectioning in the excitation process. This reduces phototoxicity and photobleaching by up to four orders of magnitude compared with that caused by confocal fluorescence microscopy, simplifies segmentation and quantification for three-dimensional cell biology, and supports the transition from on-demand to systematic data acquisition in developmental biology applications.

Fluorescence microscopy provides high contrast between sample and background, as only specifically labeled cellular components are observed, while all other structures remain dark. There are, however, fundamental issues: first, the excitation light degrades endogenous organic compounds and bleaches fluorophores¹. Second, only a finite number of excitable fluorophores are available, and thus the number of collectable emitted photons is limited. Third, organisms are generally adapted to the solar flux of 1.4 kW m^{-2} , which indicates that the irradiance should not exceed a few milliwatts per square millimeter or nanowatts per square micrometer in live imaging assays². This limits how often live samples can be imaged without too much damage. When medium-magnification objectives and standard cameras are used, one square millimeter equals roughly one field of view, and one square micrometer equals roughly four to nine pixels.

In confocal epifluorescence microscopy, the same objective lens is used for excitation and collection of the emitted light³. Because hardly any light is absorbed, the integrated intensity is constant along the optical axis. Thus, for each acquired two-dimensional image, all fluorophores in the specimen are excited, and a spatial filter (i.e., a pinhole) is necessary to reject out-of-focus light. Hence, the ratio of the sample thickness to the depth of field indicates how many times the fluorophores are exposed to the illumination light during the recording of a three-dimensional stack of images.

Light-sheet-based fluorescence microscopy (LSFM) addresses this limitation by decoupling the excitation and emission light paths. The optical axis of the illumination objective lens is aligned

with the focal plane of the perpendicularly arranged detection objective lens². By design, only the fluorophores around the focal plane are excited for each acquired two-dimensional image. Hence, each fluorophore is exposed only once to the illumination light when a three-dimensional image stack is recorded. This illumination-based optical sectioning property⁴ retains the viability and the fluorescence signal of a living specimen while millions of images are recorded for days or even weeks. The detection path resembles that of a conventional fluorescence microscope, with an objective lens, a spectral filter, a tube lens, and a camera that acquires hundreds of images comprising millions of pixels within a few seconds. Neither a spatial filter nor a dichroic mirror is required. Further benefits of LSFM² are (i) good axial resolution, (ii) the ability to image along multiple directions, (iii) deeper tissue penetration owing to low-numerical-aperture illumination objective lenses, (iv) a high signal-to-noise ratio, and (v) unrestricted compatibility with fluorescent dyes and proteins.

Two basic implementations, many modifications

LSFM comes in two fundamentally different (i.e., canonic) implementations. The selective-plane (or single-plane) illumination microscope (SPIM) uses a cylindrical lens to focus a collimated laser beam along one direction and hence forms a static coherent light sheet⁵. A SPIM illuminates the entire camera field of view globally, and thus has the potential for an extremely high image-acquisition speed⁶. One can minimize striping artifacts by destroying the coherence, for example, by pivoting the light sheet⁷. In contrast, the digital scanned laser light-sheet-based fluorescence microscope (DSLIM) translates a Gaussian beam through the focal plane, forming a dynamic light sheet that illuminates only a few lines in the camera field of view at once⁸. Because its illumination is incoherent and uniform, a DSLIM has by design fewer issues with shadowing effects. Schematic illustrations of light sheets⁹ and a comprehensive tabular comparison¹⁰ have been published previously; some milestones in LSFM development are summarized in Table 1.

Physical Biology/Physikalische Biologie (IZN, FB 15), Buchmann Institute for Molecular Life Sciences (BMLS), Cluster of Excellence Frankfurt–Macromolecular Complexes (CEF–MC), Goethe Universität–Frankfurt am Main (Campus Riedberg), Frankfurt am Main, Germany. Correspondence should be addressed to ernst.stelzer@physikalischebiologie.de.

PERSPECTIVE

TABLE 1 | A selection of LSMF modifications and development milestones from the past decade

Modification (rationale)	Ref.	LSFM	Specimen (labeling/staining/imaging modalities)
Beam-shaping			
Bessel beam (improved penetration depth)	42	DSLIM	<i>Drosophila</i> (fixed; nuclei stained with Sytox)
Airy beam (high contrast and resolution in a larger field of view)	43	DSLIM	Amphioxus (fixed; nuclei stained with propidium iodide; actin cytoskeleton stained with Alexa Fluor 488–phalloidin)
Lattice light sheet (super-resolution imaging at subsecond intervals)	44	DSLIM	Broad variety of biological samples: various vertebrate cell lines, <i>Dictyostelium discoideum</i> , mouse embryonic stem cells, <i>Tetrahymena thermophile</i> , <i>Caenorhabditis elegans</i> embryo, <i>Drosophila</i>
Multiple illumination and detection paths			
Two illumination paths, with pivoting of light sheets (uniform illumination; effective light sheet is thinner; improved axial resolution)	7	SPIM	Zebrafish (H2A–GFP; live imaging)
Two illumination and detection paths (high temporal resolution)	31	DSLIM	<i>Drosophila</i> (H2Av–mCherry; live imaging)
Two illumination and detection paths with two-photon excitation (high temporal resolution)	30	DSLIM	<i>Drosophila</i> (ubiquitous nuclear GFP expression; live imaging)
Four illumination and detection paths (uniform illumination; very high temporal resolution; isotropic spatial resolution)	32	DSLIM	<i>Drosophila</i> (whole-animal functional imaging) Zebrafish (whole-brain functional imaging) <i>Drosophila</i> (His2Av–mRFP1 and Spider–GFP; live imaging)
Parallelization and high throughput			
OpenSPIM microscopy ‘farm’ (multiple-microscope setup in a rack)	45	DSLIM	Zebrafish (H2A–EGFP; live imaging) <i>Drosophila</i> (His–YFP and Csp–sGFP; live imaging)
Light-sheet-based flow cytometer (high-volume throughput combined with high-spatial-content analysis)	46	SPIM	<i>Gambierdiscus</i> sp. (autofluorescence; live imaging) <i>Procentrum</i> sp. (autofluorescence; live imaging)
Multiple-view fusion and deconvolution			
Non-blind, shift-invariant multiple-view fusion (isotropic resolution in transparent samples, and improved uniformity in partially opaque samples)	47	SPIM	Mulberry pollen grain (autofluorescence) <i>Drosophila</i> (fixed; BJ1 immunostained with FITC-labeled IgH and IgL, and Chriz immunostained with TRITC-labeled GAR IgH and IgL) Medaka (fixed; nuclei stained with Sytox–Green and fluorescent <i>in situ</i> hybridization for McF0001MGR–1G19bd1)
Joint deconvolution of data acquired along multiple directions (higher, more isotropic resolution)	48	SPIM	Mulberry pollen grain (autofluorescence) Madin–Darby canine kidney cell cysts (GFP-tagged actin; fixed; nuclei stained with DRAQ5) BxPC3 human pancreatic cancer cell spheroids (nuclei stained with DRAQ5)
Bead-based registration and fusion (generation of superior data sets by fusion of information from multiple directions)	26	SPIM	<i>C. elegans</i> (fixed) <i>Drosophila</i> (fixed; stained with Sytox–Green) <i>Drosophila</i> (His–YFP; live imaging)
Bead-based registration and fusion in conjunction with Bayesian-based multiple-view deconvolution (fusion with substantially increased resolution and contrast)	27	DSLIM	<i>Drosophila</i> (His–YFP; live imaging) <i>Drosophila</i> ovaries (fixed; autofluorescence) <i>Drosophila</i> (histone H2Av–mRFP _{ruby} ; live imaging) <i>C. elegans</i> (PH domain–GFP; live imaging) <i>C. elegans</i> (LMN–1–GFP; fixed; nuclei stained with Hoechst)

(continued)

TABLE 1 | A selection of LSFM modification and development milestones from the past decade (continued)

Modification (rationale)	Ref.	LSFM	Specimen (labeling/staining/imaging modalities)
Combinational approaches			
With fluorescence correlation spectroscopy (more measurements per time period than in confocal-based approaches)	49	DSLIM	Zebrafish (injection of fluorescent microspheres into the blood stream)
With structured illumination ^a (removal of out-of-focus signal and improved contrast)	29	DSLIM	Medaka (fixed; nuclei stained with Sytox-Green) Zebrafish (injection of H2B-RFP and ras-eGFP mRNA; live imaging) <i>Drosophila</i> (H2B-eGFP; live imaging)
With stimulated emission depletion (improved axial resolution)	50	DSLIM	Zebrafish (actin cytoskeleton stained with ATTO647 phalloidin)
With confocal slit detection ^a (background signal rejection of scattered light)	51	DSLIM	Mouse whole brain and hippocampus (Thy1-GFP-M; fixed and cleared) Mouse cerebellum (L7-GFP; fixed and cleared)
With two-photon excitation (reduced scattering; improved depth penetration)	52	DSLIM	<i>Drosophila</i> (His2AV-GFPS65T; live imaging) Zebrafish (Tg(flk1-eGFP); live imaging)
With optical tomography (fluorescence signal is collected in the context of the three-dimensional anatomy of the specimen)	53	SPIM	Zebrafish (Tg(kdrl:rasCherry), Tg(kdrl:GFP), Tg(fli:GFP) and Tg(neurog1:GFP); live imaging)
With reversible saturatable/switchable optical fluorescence transitions (improved axial resolution)	54	SPIM	HIV-1 particles
Other			
Rapid imaging with an electrically tunable lens (high acquisition speed)	6	SPIM	Zebrafish (Tg(kdrl:EGFP, GATA1:dsRed) and Tg(myf7:dsRed, GATA1:dsRed); live imaging)
Hyperspectral light-sheet-based microscopy (spectral unmixing of overlapping fluorophores and spectral removal of autofluorescence)	55	DSLIM	Zebrafish (Tg(h2afva:h2afva-GFP, kdrl:Hsa.HRAS-mCherry) and Tg(kdrl:EGFP,s1013t:Gal4,UAS:Chr2-eYFP); live imaging) Zebrafish (Tg(kdrl:EGFP,s1013t:Gal4,UAS:Chr2-eYFP,ptf1a:dsRed); fixed; nuclei stained with Hoechst, membranes stained with Bodipy) <i>Drosophila</i> (sens-sfGFP; live imaging)

Entries below subheadings are ordered chronologically. ^aFrom a physical point of view, structured illumination and confocal slit detection are similar.

In general, SPIMs and DSLMs rely predominantly on automated operation: cameras replace oculars and visual inspection by eye, and the three-dimensional imaging, multiple channels, multiple views, and high data-recording speeds require processing before humans can comprehend the data. The vision of a microscope that sustains a multitude of naturally maintained specimens and returns dynamic three-dimensionally rendered views¹¹ that are based on full segmentations¹² in real time is quite realistic. Life science laboratories need easily comprehensible, mechanically stable solutions in sophisticated imaging to ensure that the biological questions remain the center of attention, and that imaging restrictions do not determine which experiments can be performed. Four of the major disciplines for LSFM application are plant research¹³, neurosciences¹⁴, cell biology¹⁵, and developmental biology^{9,16}. Below, we outline in more detail how LSFM improves studies of three-dimensional cell and insect developmental biology.

LSFM in three-dimensional cell biology: expanding the quantitative space

Understanding the mechanisms of complex cellular processes requires dynamic investigations under close-to-physiological conditions. For instance, the expression of genes associated with tissue development, cell adhesion, stress response, and pathogenesis differs when cells are grown in three-dimensional aggregates rather than as a monolayer cell culture¹⁷. Multicellular *in vitro* model systems, such as spheroids, mimic *in vivo* scenarios more closely than two-dimensional cell cultures can. Three-dimensional cell biology cannot replace experiments with animals and clinical samples, but it certainly bridges the gap between conventional two-dimensional cell cultures and *in vivo* models¹⁸.

Using state-of-the-art fluorescence microscopy techniques such as LSFM allows one to perform comprehensive quantifications on multiple levels. Initially, data are collected on the cellular and subcellular levels—for example, on cell nuclei, membranes, and

PERSPECTIVE

the Golgi apparatus (Fig. 1a)—and single cells are characterized with a multitude of different parameters. The spheroid can then be described on the multicellular level through the determination of higher-order properties such as the global and local nuclei density (Fig. 1b), total volume, and geometric shape. With quantitative information from different levels, one can obtain insights into more complex structures. For example, on the basis of their molecular profile, T47D cells represent luminal breast cancer tissue¹⁹. Spheroids formed from these cells develop hollow structures (Fig. 1a, right), which are interpreted as acini. Similar histological patterns are found in low-grade breast cancer tumors²⁰. On the basis of the distribution of cell nuclei, the arrangement of membranes, and the absence of the Golgi apparatus, one can calculate the number of acini as well as their volume and shape. With these data, in combination with higher-order information derived from cell-nuclei quantification, the morphological features can be described in detail, including the relative localization and distribution of acini within the spheroid (Fig. 1c), for example, as a function of the distance from the surface. These values can be compared with data acquired from breast tumor xenografts or clinical samples. Acini formation, tumor shrinkage, decreased nuclear size, and cellular dis-cohesion can be used to assess the effects of potential anticancer drugs¹⁵.

LSFM is the technique of choice for such assays, but the image quality and thus the efficiency and precision of postprocessing algorithms for segmentation and quantification benefit strongly

from pre-imaging optimization. We see the future of LSFM in cell biology as lying in a combinatorial approach with advanced sample-preparation techniques. For example, scattering effects are significantly reduced by optical clearing²¹. Although samples are no longer alive when they undergo optical clearing, the significant increase in penetration depth resolves the internal structures of large specimens properly²².

LSFM in insect developmental biology: from on-demand to systematic data acquisition

Most microscopy assays in insect developmental biology are designed to acquire data on demand. The number of images is usually in the range of 10^1 – 10^4 (i.e., several megabytes to a few gigabytes), and thus is restricted to a fraction of the specimen and/or a complete development process. The information is question-specific but otherwise limited, as the observed processes cannot be interpreted within their broader spatiotemporal context. However, thanks to a broad variety of technological advances—particularly the emergence and continuous development of LSFM—live imaging data sets (i.e., three spatial dimensions as a function of time) can now be acquired in a systematic fashion. Such data sets comprise 10^5 – 10^8 images (i.e., many gigabytes to several terabytes) and can provide morphological data on any tissue or organ for any time point during development.

This switch from the acquisition of small data sets on demand to vast data sets in a systematic fashion is comparable

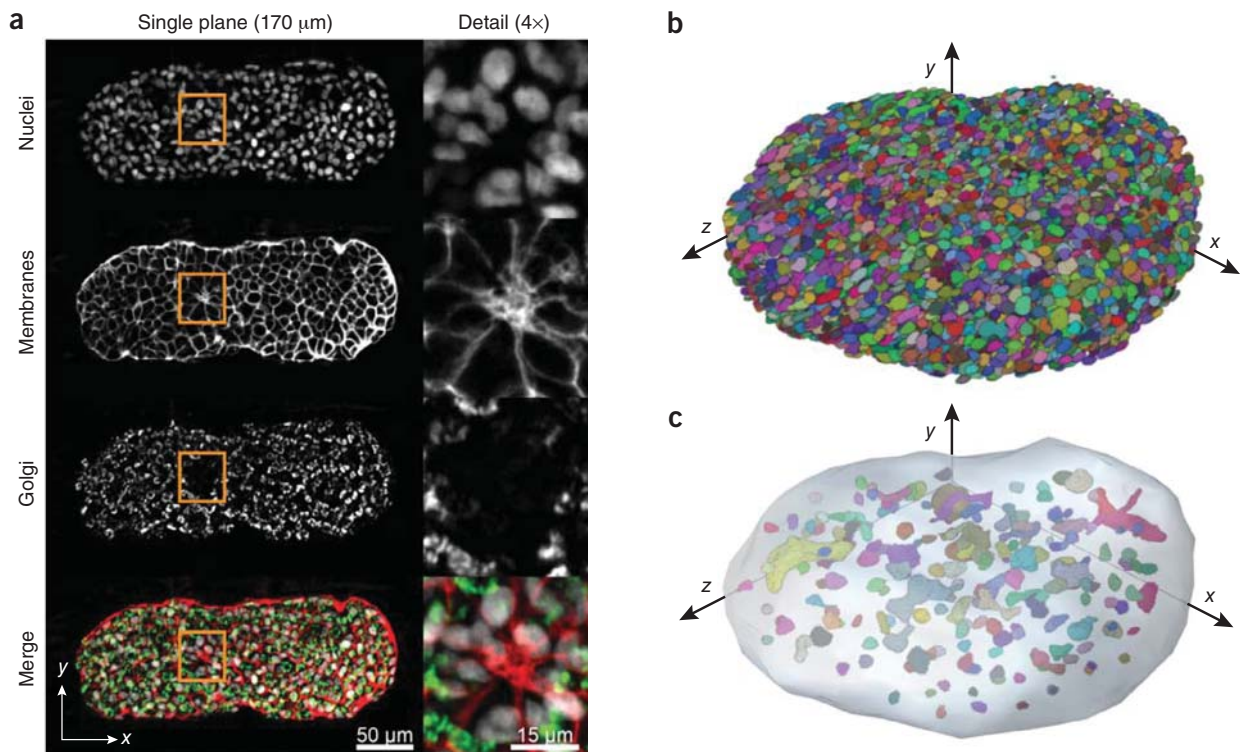


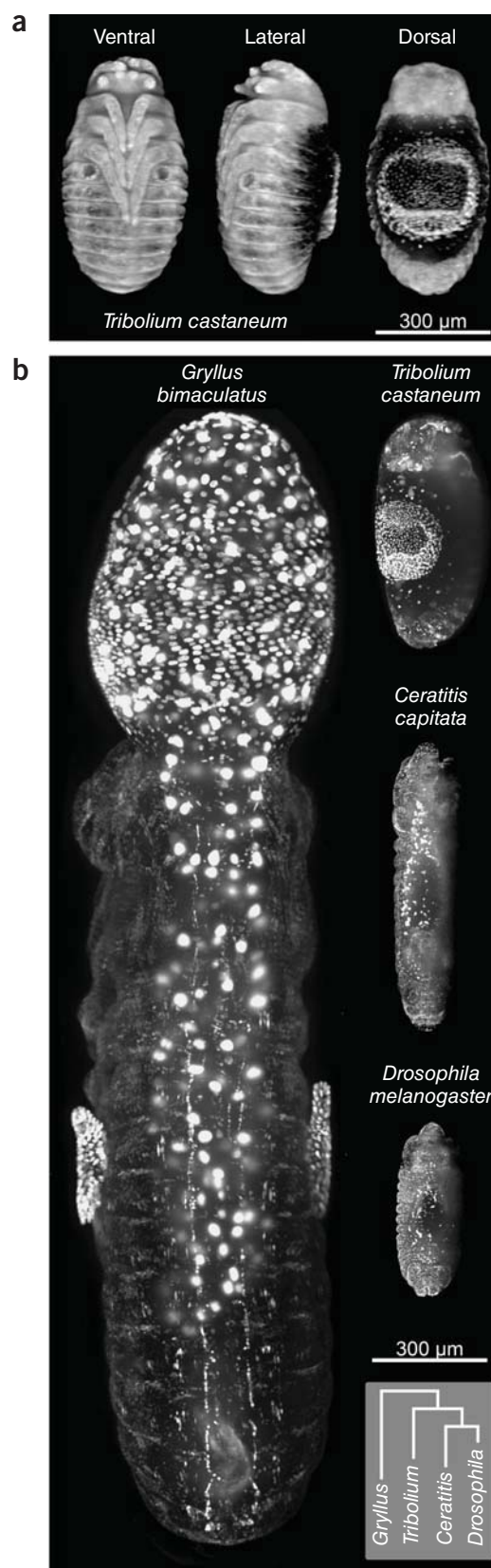
Figure 1 | LSFM in three-dimensional cell biology. (a) Single plane of an optically cleared and triple-stained (nuclei, membranes, and Golgi apparatus) spheroid (2,000 seeded T47D human breast cancer cells; 10-d formation). The spheroid was cleared with a 2:1 mixture of benzyl benzoate and benzyl alcohol, stained with DAPI (DNA and nuclei; gray in the merged image), and immune-labeled with antibodies to β -catenin (adherence junctions and membranes; red in the merged image) and GM130 (cis-Golgi; green in the merged image). The detail images in the right-hand column show an acinus during the initiation phase. (b,c) Segmentation and volume rendering of (b) cell nuclei and (c) acinar structures of the same spheroid. The gray shading in c indicates the approximated surface of the spheroid, based on the cell nuclei segmentation.

Figure 2 | LSFM in insect developmental biology. **(a)** Three volume renderings of a live embryo of a transgenic *Tribolium* specimen that expresses nuclear localized GFP during dorsal closure along three directions. The renderings, generated with Arivis 3D-Vision (Rostock, Germany), derive from a single, superior-quality volume data set that was calculated from eight z-stacks recorded along eight equally spaced orientations. **(b)** Images of live transgenic insect embryos of four different species, shown dorsally as maximum projections during dorsal closure. All specimens expressed either a nuclear-localized fluorescent protein or a histone subunit-linked fluorescent protein under the control of a ubiquitous promoter. For convenience, the phylogenetic relationship is provided in the lower right corner. Whereas the *Tribolium*, *Ceratitis*, and *Drosophila* embryos were acquired *in toto* within a single volume of view, the *Gryllus* embryo was acquired with four vertically continuous volumes of view, which were stitched and fused in three dimensions. Please note that the volume of the *Gryllus* embryo is approximately 80× that of the *Drosophila* embryo. All embryos shown in this figure survived the recording process and could be raised to healthy adults.

to the changes in data acquisition in eukaryotic genomics that commenced in the mid-1990s. The first sequences of genes or gene fragments were 10^2 – 10^3 nucleotides long and were obtained as contributions to well-defined scientific projects²³. Thus, initially data were generated in independent and usually unrelated studies that covered only a fraction of the 10^7 – 10^9 nucleotides in a typical eukaryotic genome. Interpretations in a broader genomic context were therefore impossible. But about two decades ago, technological advances led to the point where entire genomes could be sequenced systematically—the beginning of eukaryotic genomics²⁴.

Systematic data-acquisition approaches follow a different rationale than that of on-demand approaches. Instead of verifying concrete scientific hypotheses, they establish databases that relate previous experiments and substantiate future studies. They have fundamental relevance for the scientific community at large and for many different research areas. However, two important criteria need to be met to ensure high scientific potential for systematically acquired data: (i) a self-contained, reasonable scope and (ii) a high degree of universality, which is typically inversely proportional to the number of experimental parameters. Whole-genome sequencing fulfills both criteria adequately: (i) the experimental scope can be clearly defined²⁵ (ideally from the first base of the first chromosome to the last base on the last chromosome, *de facto* >99%), and (ii) the primary data (i.e., the nucleotide sequences themselves) are entirely independent of the experimental parameters. Similar arguments back Landsat (<https://landsat.gsfc.nasa.gov>) and Envisat's whole-earth environmental surveys (<https://earth.esa.int>).

At first sight, it appears bold to compare systematic data-acquisition approaches in both disciplines, but the similarities are evident. In insect developmental biology, (i) the scope can be properly defined as from the moment of fertilization to the point of hatching, and (ii) a high degree of universality is accomplishable. However, unlike nucleotide sequence data, which are entirely independent of the sequencing method and thus are absolute, microscopy data depend on the experimental circumstances and conditions during the observation. Fortunately, the number of essential parameters is low. As discussed above, the spatiotemporal resolution is limited mainly by the number of collectable photons. However, with LSFM, even when specimens are imaged *in toto*, the three-dimensional spatial resolution is sufficient to provide



subcellular details, and the temporal resolution is more than adequate to sample the embryo a thousand or more times during the complete development period^{9,16}. Thus, the amount of data usually exceeds the 'interest threshold'. In addition, the architecture of the

fluorophore-expressing transgene is another important parameter. Ubiquitous labeling of cell nuclei—for example, via the SV40 nuclear localization sequence or linkage to a histone subunit—is convenient and thus the ‘gold standard’. It allows the identification of tissues, organs, cell clusters, individual cells, and certain organelles, and performs well in LSFM-specific postprocessing algorithms such as multiple-views fusion^{26,27} (Fig. 2a).

Large-scale databases with systematically acquired live imaging data offer a benefit to the insect developmental biology community that is similar to what nucleotide-sequence databases have provided for the genome community²⁸. For the fruit fly *Drosophila melanogaster*^{29–32} and the red flour beetle *Tribolium castaneum*^{33–35}, fractional data are already published; information on other insect species, such as the Mediterranean fruit fly *Ceratitis capitata* and the two-spotted cricket *Gryllus bimaculatus*, will soon become available (Fig. 2b). Again similar to ongoing research in whole-genome sequencing, the systematic observation of many individual insects under varied endogenous and environmental conditions allows scientists to test the robustness of their embryonic morphogenesis³⁶ (better known as canalization) and hence determine what is actually ‘normal’ in insect development. These kinds of data serve as the ground truth for studies that enforce developmental aberrations, or can be used in a comparative morphogenetic approach to interpret divergent developmental strategies in an evolutionary context³⁷.

With confocal fluorescence microscopy, such a systematic live imaging approach is not possible. Because of the high degree of irradiance, a detrimental effect on the specimen cannot be excluded. In contrast, LSFM exposes the live specimen to a very low energy level even when an observation continues for several days. The embryos develop normally, can be raised to adults that show no morphological aberrations, and produce progeny that are also fertile³⁴—a tough but particularly meaningful quality control for all live imaging experiments.

Concluding remarks

Since the invention of SPIMs and DSLMs about 15 years ago³⁸, LSFM has evolved remarkably well. We believe that this trend continues: first, because the detection paths are simple, every contrast and manipulation tool implemented in conventional fluorescence microscopy can be adapted for LSFM. Second, image size, acquisition speed, and data management have always been major issues in microscopy^{34,39}. Although LSFM benefits from the development of larger and faster cameras, data processing remains a limiting factor and provides ample opportunities for the development of sophisticated software. Third, SPIMs and DSLMs purposely lack ergonomic features and allow for simple, efficient, and inexpensive designs. Hence, LSFM is amenable to highly specialized modifications, which laboratories and imaging facilities can employ in large numbers. Fourth, long-term experiments require convenient solutions to maximize the throughput. Parallelization is achieved either on the level of specimen preparation, which calls for dedicated sample holders, or through the use of large numbers of independently operated instruments. High-throughput implementations adapted to standard multiwell plates for cell monolayers and more refined

multispecimen containers for three-dimensional multicellular objects will certainly become available.

Although technological developments seem obvious, many extremely interesting novel directions for biology are founded simply on the basic advantages of LSFM over wide-field and confocal fluorescence microscopy. The reduced phototoxicity and photobleaching provide a particular advantage for experiments that involve live specimens. In LSFM, a volume of view comprises several thousand pixels per line, several thousand lines per plane, and several hundred planes per three-dimensional image stack. Hence, it covers two to three orders of magnitude, and thus several biologically relevant scales. Not only does this allow researchers to reconsider the way they perform biological experiments in cell and developmental biology, as discussed above, but it will also have an impact on more distant disciplines such as ecology. For example, interspecies relationships between small and large organisms, such as symbioses and parasite–host interactions, are highly relevant, but their observation is experimentally challenging. LSFM has already been used to characterize the bacterial colonization dynamics of a zebrafish’s intestine⁴⁰, and given its high tissue-penetration depth, it also rivals confocal microscopes in studies of plant–symbiont relationships, such as with mycorrhizae⁴¹.

In general, novel technologies should provide opportunities to conceive and perform experiments that could not have been imagined before. LSFM has already raised fluorescence microscopy to a new level, but it has by no means reached its full potential yet. The next decade will surely surprise us with sophisticated technological advancements and exciting applications in many different biological disciplines.

ACKNOWLEDGMENTS We thank K. Hötte (Goethe Universität, Frankfurt am Main, Germany) for the T47D spheroid images, S. Fischer for helpful comments on the manuscript, M.F. Schetelig (Justus-Liebig-Universität, Gießen, Germany) for the *Ceratitis* line, and T. Mito (Tokushima University, Tokushima, Japan) for the *Gryllus* line. The research was supported by funding from the Cluster of Excellence–Frankfurt am Main for Macromolecular Complexes (CEF-MC II, EXC 115; speaker: V. Dötsch) granted in part to E.H.K.S. at the Buchmann Institute for Molecular Life Sciences (BMLS; director: E. Schleiff) at the Johann Wolfgang Goethe Universität–Frankfurt am Main by the Deutsche Forschungsgemeinschaft (DFG).

AUTHOR CONTRIBUTIONS F.S., A.S., and E.H.K.S. wrote the manuscript. F.S. and A.S. prepared the display items.

COMPETING FINANCIAL INTERESTS The authors declare no competing financial interests.

Reprints and permissions information is available online at <http://www.nature.com/reprints/index.html>.

Publisher’s note: Springer Nature remains neutral with regard to jurisdictional claims in published maps and institutional affiliations.

- Schneckenburger, H. *et al.* Light exposure and cell viability in fluorescence microscopy. *J. Microsc.* **245**, 311–318 (2012).
- Stelzer, E.H.K. Light-sheet fluorescence microscopy for quantitative biology. *Nat. Methods* **12**, 23–26 (2015).
- Resandt, R.W.W. *et al.* Optical fluorescence microscopy in three dimensions: microtomoscopy. *J. Microsc.* **138**, 29–34 (1985).
- Cox, I.J. Scanning optical fluorescence microscopy. *J. Microsc.* **133**, 149–154 (1984).
- Huisken, J., Swoger, J., Del Bene, F., Wittbrodt, J. & Stelzer, E.H.K. Optical sectioning deep inside live embryos by selective plane illumination microscopy. *Science* **305**, 1007–1009 (2004).

6. Fahrbach, F.O., Voigt, F.F., Schmid, B., Helmchen, F. & Huisken, J. Rapid 3D light-sheet microscopy with a tunable lens. *Opt. Express* **21**, 21010–21026 (2013).
7. Huisken, J. & Stainier, D.Y.R. Even fluorescence excitation by multidirectional selective plane illumination microscopy (mSPIM). *Opt. Lett.* **32**, 2608–2610 (2007).
8. Keller, P.J., Schmidt, A.D., Wittbrodt, J. & Stelzer, E.H.K. Reconstruction of zebrafish early embryonic development by scanned light sheet microscopy. *Science* **322**, 1065–1069 (2008).
9. Weber, M. & Huisken, J. Light sheet microscopy for real-time developmental biology. *Curr. Opin. Genet. Dev.* **21**, 566–572 (2011).
10. Keller, P.J. & Ahrens, M.B. Visualizing whole-brain activity and development at the single-cell level using light-sheet microscopy. *Neuron* **85**, 462–483 (2015).
11. Royer, L.A. *et al.* ClearVolume: open-source live 3D visualization for light-sheet microscopy. *Nat. Methods* **12**, 480–481 (2015).
12. Stegmaier, J. *et al.* Real-time three-dimensional cell segmentation in large-scale microscopy data of developing embryos. *Dev. Cell* **36**, 225–240 (2016).
13. von Wangenheim, D. *et al.* Rules and self-organizing properties of post-embryonic plant organ cell division patterns. *Curr. Biol.* **26**, 439–449 (2016).
14. Keller, P.J., Ahrens, M.B. & Freeman, J. Light-sheet imaging for systems neuroscience. *Nat. Methods* **12**, 27–29 (2015).
15. Pampaloni, F., Chang, B.-J. & Stelzer, E.H.K. Light sheet-based fluorescence microscopy (LSFM) for the quantitative imaging of cells and tissues. *Cell Tissue Res.* **360**, 129–141 (2015).
16. Amat, F. & Keller, P.J. Towards comprehensive cell lineage reconstructions in complex organisms using light-sheet microscopy. *Dev. Growth Differ.* **55**, 563–578 (2013).
17. Zschenker, O., Streichert, T., Hehlhans, S. & Cordes, N. Genome-wide gene expression analysis in cancer cells reveals 3D growth to affect ECM and processes associated with cell adhesion but not DNA repair. *PLoS One* **7**, e34279 (2012).
18. Pampaloni, F., Reynaud, E.G. & Stelzer, E.H.K. The third dimension bridges the gap between cell culture and live tissue. *Nat. Rev. Mol. Cell Biol.* **8**, 839–845 (2007).
19. Kao, J. *et al.* Molecular profiling of breast cancer cell lines defines relevant tumor models and provides a resource for cancer gene discovery. *PLoS One* **4**, e6146 (2009).
20. Rakha, E.A. *et al.* Breast cancer prognostic classification in the molecular era: the role of histological grade. *Breast Cancer Res.* **12**, 207 (2010).
21. Azaripour, A. *et al.* A survey of clearing techniques for 3D imaging of tissues with special reference to connective tissue. *Prog. Histochem. Cytochem.* **51**, 9–23 (2016).
22. Dodt, H.-U. *et al.* Ultramicroscopy: three-dimensional visualization of neuronal networks in the whole mouse brain. *Nat. Methods* **4**, 331–336 (2007).
23. Sanger, F. & Coulson, A.R. A rapid method for determining sequences in DNA by primed synthesis with DNA polymerase. *J. Mol. Biol.* **94**, 441–448 (1975).
24. Ankeny, R.A. Sequencing the genome from nematode to human: changing methods, changing science. *Endeavour* **27**, 87–92 (2003).
25. Lander, E.S. *et al.* Initial sequencing and analysis of the human genome. *Nature* **409**, 860–921 (2001).
26. Preibisch, S., Saalfeld, S., Schindelin, J. & Tomancak, P. Software for bead-based registration of selective plane illumination microscopy data. *Nat. Methods* **7**, 418–419 (2010).
27. Preibisch, S. *et al.* Efficient Bayesian-based multiview deconvolution. *Nat. Methods* **11**, 645–648 (2014).
28. Pandey, A. & Lewitter, F. Nucleotide sequence databases: a gold mine for biologists. *Trends Biochem. Sci.* **24**, 276–280 (1999).
29. Keller, P.J. *et al.* Fast, high-contrast imaging of animal development with scanned light sheet-based structured-illumination microscopy. *Nat. Methods* **7**, 637–642 (2010).
30. Tomer, R., Khairy, K., Amat, F. & Keller, P.J. Quantitative high-speed imaging of entire developing embryos with simultaneous multiview light-sheet microscopy. *Nat. Methods* **9**, 755–763 (2012).
31. Krzic, U., Gunther, S., Saunders, T.E., Streichan, S.J. & Hufnagel, L. Multiview light-sheet microscope for rapid *in toto* imaging. *Nat. Methods* **9**, 730–733 (2012).
32. Chhetri, R.K. *et al.* Whole-animal functional and developmental imaging with isotropic spatial resolution. *Nat. Methods* **12**, 1171–1178 (2015).
33. Strobl, F. & Stelzer, E.H.K. Non-invasive long-term fluorescence live imaging of *Tribolium castaneum* embryos. *Development* **141**, 2331–2338 (2014).
34. Strobl, F., Schmitz, A. & Stelzer, E.H.K. Live imaging of *Tribolium castaneum* embryonic development using light-sheet-based fluorescence microscopy. *Nat. Protoc.* **10**, 1486–1507 (2015).
35. Strobl, F. & Stelzer, E.H. Long-term fluorescence live imaging of *Tribolium castaneum* embryos: principles, resources, scientific challenges and the comparative approach. *Curr. Opin. Insect Sci.* **18**, 17–26 (2016).
36. Siegal, M.L. & Bergman, A. Waddington's canalization revisited: developmental stability and evolution. *Proc. Natl. Acad. Sci. USA* **99**, 10528–10532 (2002).
37. Heffer, A. & Pick, L. Conservation and variation in Hox genes: how insect models pioneered the evo-devo field. *Annu. Rev. Entomol.* **58**, 161–179 (2013).
38. Stelzer, E.H.K., Enders, S., Huisken, J., Lindek, S. & Swoger, J.H. Microscope with a viewing direction perpendicular to the illumination direction. US patent 7554725 B2 (2009).
39. Reynaud, E.G., Peychl, J., Huisken, J. & Tomancak, P. Guide to light-sheet microscopy for adventurous biologists. *Nat. Methods* **12**, 30–34 (2015).
40. Taormina, M.J. *et al.* Investigating bacterial-animal symbioses with light sheet microscopy. *Biol. Bull.* **223**, 7–20 (2012).
41. Rath, M., Grolig, F., Haueisen, J. & Imhof, S. Combining microtomy and confocal laser scanning microscopy for structural analyses of plant-fungus associations. *Mycorrhiza* **24**, 293–300 (2014).
42. Fahrbach, F.O. & Rohrbach, A. A line scanned light-sheet microscope with phase shaped self-reconstructing beams. *Opt. Express* **18**, 24229–24244 (2010).
43. Vetterburg, T. *et al.* Light-sheet microscopy using an Airy beam. *Nat. Methods* **11**, 541–544 (2014).
44. Chen, B.-C. *et al.* Lattice light-sheet microscopy: imaging molecules to embryos at high spatiotemporal resolution. *Science* **346**, 1257998 (2014).
45. Pitrone, P.G. *et al.* OpenSPIM: an open-access light-sheet microscopy platform. *Nat. Methods* **10**, 598–599 (2013).
46. Wu, J., Li, J. & Chan, R.K.Y. A light sheet based high throughput 3D-imaging flow cytometer for phytoplankton analysis. *Opt. Express* **21**, 14474–14480 (2013).
47. Swoger, J., Verveer, P., Greger, K., Huisken, J. & Stelzer, E.H.K. Multi-view image fusion improves resolution in three-dimensional microscopy. *Opt. Express* **15**, 8029–8042 (2007).
48. Verveer, P.J. *et al.* High-resolution three-dimensional imaging of large specimens with light sheet-based microscopy. *Nat. Methods* **4**, 311–313 (2007).
49. Wohland, T., Shi, X., Sankaran, J. & Stelzer, E.H.K. Single plane illumination fluorescence correlation spectroscopy (SPIM-FCS) probes inhomogeneous three-dimensional environments. *Opt. Express* **18**, 10627–10641 (2010).
50. Friedrich, M., Gan, Q., Ermolayev, V. & Harms, G.S. STED-SPIM: stimulated emission depletion improves sheet illumination microscopy resolution. *Biophys. J.* **100**, L43–L45 (2011).
51. Silvestri, L., Brià, A., Sacconi, L., Iannello, G. & Pavone, F.S. Confocal light sheet microscopy: micron-scale neuroanatomy of the entire mouse brain. *Opt. Express* **20**, 20582–20598 (2012).
52. Truong, T.V., Supatto, W., Koos, D.S., Choi, J.M. & Fraser, S.E. Deep and fast live imaging with two-photon scanned light-sheet microscopy. *Nat. Methods* **8**, 757–760 (2011).
53. Bassi, A., Schmid, B. & Huisken, J. Optical tomography complements light sheet microscopy for *in toto* imaging of zebrafish development. *Development* **142**, 1016–1020 (2015).
54. Hoyer, P. *et al.* Breaking the diffraction limit of light-sheet fluorescence microscopy by RESOLFT. *Proc. Natl. Acad. Sci. USA* **113**, 3442–3446 (2016).
55. Jahr, W., Schmid, B., Schmied, C., Fahrbach, F.O. & Huisken, J. Hyperspectral light sheet microscopy. *Nat. Commun.* **6**, 7990 (2015).

Non-lethal genotyping of *Tribolium castaneum* adults using genomic DNA extracted from wing tissue

Frederic Strobl, J. Alexander Ross & Ernst H.K. Stelzer

The red flour beetle *Tribolium castaneum* has become the second most important insect model organism and is frequently used in developmental biology, genetics and pest-associated research. Consequently, the methodological arsenal increases continuously, but many routinely applied techniques for *Drosophila melanogaster* and other insect species are still unavailable. For example, a protocol for non-lethal genotyping has not yet been adapted but is particularly useful when individuals with known genotypes are required for downstream experiments. In this study, we present a workflow for non-lethal genotyping of *T. castaneum* adults based on extracting genomic DNA from wing tissue. In detail, we describe a convenient procedure for wing dissection and a custom method for wing digestion that allows PCR-based genotyping of up to fifty adults in less than an afternoon with a success rate of about 86%. The amount of template is sufficient for up to ten reactions while viability and fertility of the beetles are preserved. We prove the applicability of our protocol by genotyping the white / scarlet gene pair alleles from the black-eyed San Bernadino wild-type and white-eyed Pearl recessive mutant strains spanning four generations. Non-lethal genotyping has the potential to improve and accelerate many workflows: Firstly, during the establishment process of homozygous cultures or during stock keeping of cultures that carry recessively lethal alleles, laborious test crossing is replaced by non-lethal genotyping. Secondly, in genome engineering assays, non-lethal genotyping allows the identification of appropriate founders before they are crossed against wild-types, narrowing the efforts down to only the relevant individuals. Thirdly, non-lethal genotyping simplifies experimental strategies, in which genotype and behavior should be correlated, since the genetic configuration of potential individuals can be determined before the actual behavior assays is performed.

Submitted in January 2017

Revised and resubmitted in June 2017

Research Article

Title

(Full) Non-lethal genotyping of *Tribolium castaneum* adults using genomic DNA extracted from wing tissue

(Short) Non-lethal genotyping of *Tribolium castaneum* adults

Author List

Frederic Strobl¹, J. Alexander Ross¹ and Ernst H.K. Stelzer^{1*}

¹ Physical Biology / Physikalische Biologie (IZN, FB 15)

Buchmann Institute for Molecular Life Sciences (BMLS)

Cluster of Excellence Frankfurt – Macromolecular Complexes (CEF – MC)

Goethe Universität – Frankfurt am Main (Campus Riedberg)

Max-von-Laue-Straße 15 – D-60348 Frankfurt am Main – Germany

* Corresponding author

Email: ernst.stelzer@physikalischebiologie.de

Striking Image



Abstract

The red flour beetle *Tribolium castaneum* has become the second most important insect model organism and is frequently used in developmental biology, genetics and pest-associated research. Consequently, the methodological arsenal increases continuously, but many routinely applied techniques for *Drosophila melanogaster* and other insect species are still unavailable. For example, a protocol for non-lethal genotyping has not yet been adapted but is particularly useful when individuals with known genotypes are required for downstream experiments. In this study, we present a workflow for non-lethal genotyping of *T. castaneum* adults based on extracting genomic DNA from wing tissue. In detail, we describe a convenient procedure for wing dissection and a custom method for wing digestion that allows PCR-based genotyping of up to fifty adults in less than an afternoon with a success rate of about 86%. The amount of template is sufficient for up to ten reactions while viability and fertility of the beetles are preserved. We prove the applicability of our protocol by genotyping the *white / scarlet* gene pair alleles from the black-eyed San Bernadino wild-type and white-eyed Pearl recessive mutant strains spanning four generations. Non-lethal genotyping has the potential to improve and accelerate many workflows: Firstly, during the establishment process of homozygous cultures or during stock keeping of cultures that carry recessively lethal alleles, laborious test crossing is replaced by non-lethal genotyping. Secondly, in genome engineering assays, non-lethal genotyping allows the identification of appropriate founders before they are crossed against wild-types, narrowing the efforts down to only the relevant individuals. Thirdly, non-lethal genotyping simplifies experimental strategies, in which genotype and behavior should be correlated, since the genetic configuration of potential individuals can be determined before the actual behavior assays is performed.

Introduction

During the past century, the fruit fly *Drosophila melanogaster* has become the best understood insect and an established model organism in developmental biology and genetics [1]. However, *D. melanogaster* is a highly specialized species and thus considered non-representative of insects in general. In contrast, the red flour beetle *Tribolium castaneum* (Herbst, 1797), an emerging insect model organism [2,3], is considered more generic since it retained many ancestral features [4,5]. During embryonic development, both species differ remarkably in their principles of body segmentation [6–8], organization of extra-embryonic membranes [9,10] and formation of appendages [11,12]. Since *T. castaneum* is of agricultural and thus also of economic importance [5,13], considerable research focuses on pest control measures [14,15].

For almost two decades, the methodological arsenal for *T. castaneum* has increased steadily [16]. Currently, it covers procedures such as non-invasive long-term live imaging with light sheet-based fluorescence microscopy [17–20], embryonic [21], larval [22] and parental [23,24] RNA interference, comprehensive *in situ* hybridization and antibody staining protocols [25,26], germline transformation with the lepidopteran *piggyBac* [27,28] or the dipteran *Minos* [29] transposon and genome engineering with the CRISPR/Cas9 system [30].

During certain experimental workflows, for example those involving mutant, transgenic or genetically engineered lines, it is usually necessary to determine the genotype of individual beetles. In certain scenarios, the genotype can be identified by (i) the phenotype, (ii) familiarity with the parental genotypes, (iii) test crossing, or (iv) a combination thereof. However, the phenotype typically allows only the partial identification of the genotype, the parental genotypes are not always known and test crossing requires manpower and time and may interfere with the overall experimental strategy. Alternatively, individual beetles can be sacrificed to extract their genomic DNA. This allows an evaluation of the genotype with molecular biology-based assays, but the respective individuals are unavailable for downstream experiments or crossing assays. In summary, both approaches suffer from limitations.

Non-lethal genotyping, which is standard for vertebrate model organisms such as mouse and zebrafish, determines the genotype while retaining the individual. PCR-based genotyping, one of the most commonly performed procedures, requires a small amount of blood or tissue, from which genomic DNA is extracted. Similar protocols for insect model organisms have been developed for *D. melanogaster* [31] and the honeybee *Apis mellifera* [32] by using dissected wing tissue as the DNA source. In both studies, the procedure is invasive, but affected individuals (females and males for *D. melanogaster*, queens for *A. mellifera*) have the same mating success as control animals.

Research on *T. castaneum* is strongly driven by genetic approaches: the genome has been sequenced [13] and massive data from large-scale projects such as insertional mutagenesis [33] and systematic RNA interference gene knockdown [34,35] screens are available. Non-lethal genotyping for *T. castaneum* has not yet been established but is particularly useful for the generation of homozygous lines, to facilitate stock keeping of lines that carry recessive lethal alleles, to identify appropriate founders during genome engineering assays and to preselect candidates with known genotypes in behavior assays.

In this study, we present a convenient workflow for non-lethal genotyping of *T. castaneum* adults by using wing tissue as the genomic DNA source and prove the applicability of our technique in more than one hundred individuals. We explain in detail how wings can be dissected without affecting survival and fertility and outline a custom method for genomic DNA extraction that performs reliably in PCR-based assays. The amount of DNA per wing is sufficient for up to ten reactions and single reactions yield enough PCR product for sequencing. Furthermore, we obtain the nucleotide sequence of the ABC transmembrane transporter *white* from the two prominent laboratory background strains San Bernadino (SB) and Pearl (PrI) and generate respective hybrids to perform a four generation proof-of-principle assay with phenotypic validation. Our method complements the arsenal of molecular biology techniques that are available for *T. castaneum* and can be used to simplify comprehensive workflows.

Materials and Methods

***Tribolium castaneum* rearing and crossing**

The *Tribolium castaneum* black-eyed SB wild-type [36] and the white-eyed Prl recessive mutant [37] strains were used in this study. Rearing was performed as described previously [5]. In brief, stock cultures were kept on full grain wheat flour (113061036, Demeter) supplemented with 5% (wt/wt) inactive dry yeast (62-106, Flystuff/Genesee Scientific) in 1-liter glass bottles at 32°C and 70% relative humidity in a 12-h light/12-h darkness cycle. Individuals were sexed as pupae as described previously [38] and separately reared in single wells of 24-well plates (4430300N, Orange Scientific) until they reached adulthood and were ready for wing dissection. For the fertility assays and the proof-of-principle spanning four generations, single pairs were crossed in separate glass tubes (LC84.1, Carl Roth).

Wing dissection procedure

Individual adults from the Prl strain were transferred from the 24-well plate to the lid of a glass dish that was filled with ice and covered in parafilm. Upon paralysis due to the low temperature, the adult beetles were turned on the side and held in position with forceps. The tip of a micro prober was carefully slid sideward below the distal, slightly bent region of the right elytron to lift it from the abdomen and expose the right wing. Using the forceps, the wing was dragged forth laterally, pressed against the parafilm and cut as proximal as possible with a micro scalpel. If necessary, the left wing was dissected similarly. Subsequently, the adults were transferred to a non-cooled glass dish to recover from paralysis and then returned to their rearing well inside the 24-well plate.

Survival and fertility assays

After eclosure, adults were given two to three weeks to mature. Either one or both wings were dissected from ten individuals (mixed sexes) in five replicates and survival was assayed one week after dissection. The sham control animals were also paralyzed, and the right elytron was also lifted from the abdomen, but the wing was not dissected. All surviving adults, dissected and sham, were provided with a partner of the opposite sex. After two additional weeks, progeny production was checked. A two-sample / two-tailed Student's t-test was performed to determine significance, normal distribution was confirmed by the Shapiro-Wilk normality test [39].

DNA extraction

Commercial kit. Genomic DNA from the whole body, one wing or both wings of individual adults was extracted by using the Blood & Tissue Kit (69504, Qiagen) according to the manufacturer's instructions. Elution volume was 15 μ l. From the eluate, 1 μ l for whole body and 5 μ l for wings were used as a template for the PCR-based genotyping assay.

Custom method. Dissected wings were individually placed in 200 μ l reaction tubes and stored on ice. After the dissection procedure, the wings were frozen at -80°C for 15 min and physically homogenized with a micro mortar. The fragments were covered with 10 μ l of Proteinase K solution (500 $\mu\text{g/ml}$ Proteinase K, 10 nM Tris-Cl, 1 mM EDTA, and 25 mM NaCl in double-distilled H_2O), the mixture was incubated at 37°C for 1 h and then inactivated at 75°C for 20 min. From this solution, 1 μ l was used as a template for the PCR-based genotyping assay.

Molecular biology

Polymerase chain reaction (PCR) assays. All PCRs were performed with the Phusion polymerase (M0530L, New England BioLabs) in 20 μ l reactions. Primer sequences are listed in Supplementary Table 1. PCR products were mixed with 4 μ l $6\times$ DNA gel loading dye (R0611, Thermo Fisher Scientific) and run on a 1% (wt/vol) agarose broad range (T846.3, Carl Roth) gel in TAE buffer at 100 V for 35 min. The GeneRuler DNA Ladder Mix (SM0331, Thermo Fisher Scientific) was used as the molecular weight size marker. A two-sample / two-tailed Student's t-test was performed to determine significance, normal distribution was confirmed by the Shapiro-Wilk normality test [39].

Sequencing of PCR products. PCR products were purified using the NucleoSpin Gel and PCR Clean-up Kit (740609.250, Macherey-Nagel) according to the manufacturer's instructions. Purification was followed by A-tailing using the Recombinant Taq DNA polymerase (10342020, Thermo Fisher Scientific), ligation into the pGEM-T Easy plasmid (A1360, Promega) and transformation into heat-shock competent DH5 α *E. coli*. Plasmids were isolated with the NucleoSpin Plasmid Kit (740588.250, Macherey-Nagel) according to the manufacturer's instructions. Control digestions were performed with NotI-HF (R3189L, New England BioLabs). The digested plasmids were run on a 0.8% (wt/vol) agarose broad range gel in TAE buffer at 100 V for 30 min. Plasmids that showed the correct pattern on the gel were sent for sequencing. Sequencing was performed initially with the T7 and SP6 primers, sequence-specific primers were used to continue sequencing when the initial results became available. The SB *white* allele sequence is provided as Supplementary Sequence 1, the Prl *white* allele sequence is provided as Supplementary Sequence 2.

Results

Wing dissection procedure, survival and fertility

In contrast to *D. melanogaster* and *A. mellifera*, the wings of *T. castaneum* are covered by protective elytra and thus not freely accessible. Therefore, we developed a ‘gentle’ procedure to dissect one or both wings from an adult beetle (Figure 1A-F), which is comprehensively described within the Materials and Methods section. Removal of one or both wings has no significant effect on the survival rate (Figure 1G) and nearly all survivors were fertile after wing dissection (Figure 1H). To ensure that the presented ratios cannot be credited to a high personal skill level of a single experimenter, we compared the survival rate of adult beetles when either one or both wings were dissected by two independent experimenters. No significant difference in the performance was detected (Supplementary Figure 1A-B).

Figure 1

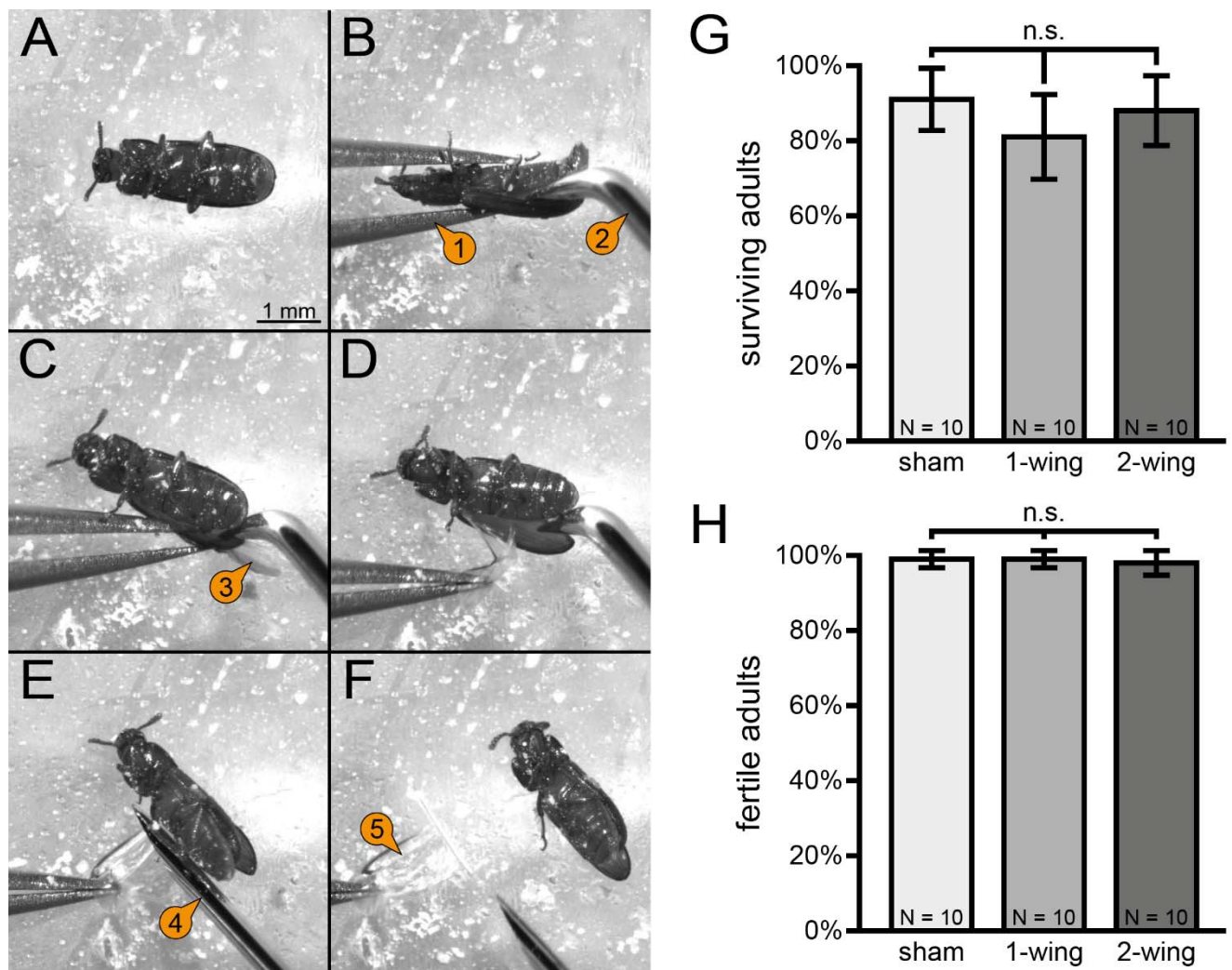


Figure 1 – Wing dissection procedure and impact on survivability and fertility. (A) Adults are paralyzed by incubation on a parafilm-covered lid of a glass dish filled with ice for a few minutes. (B) The adult is held in position with a forceps (1) and a micro prober (2) is used to push the right elytron aside. (C) The micro prober is carefully inserted at the posterior region into the groove between the right elytron and the abdomen to expose the right wing (3). (D) The right wing is pressed onto the parafilm with the forceps. (E) Using a micro scalpel (4), the wing is cut as proximal as possible. (F) The dissected wing (5) is transferred to a 200 μ l reaction tube and stored on ice. (G) Quantification of surviving adults from ten replicates with ten adults after the dissection of one or both wings. The sham control animals were also paralyzed, and their elytra were also lifted from the abdomen, but the wing was not dissected. No significant difference was found. Error bars represent standard deviation. (H) Quantification of fertile adults from ten replicates with the respective number of surviving adults after dissection of one or both wings. No significant difference was found. Error bars represent standard deviation.

Proof-of-principle on the molecular level

First, we assayed whether the amount of template obtainable from one or both wings by using a commercial DNA kit is sufficient for PCR-based genotyping. The primers were designed to target a part of the *alpha-tubulin 1* upstream regulatory sequence [40], which should result in a product with 616 bp length. However, the amount of tissue is about three orders of magnitude less than the recommended starting material and thus, the ratio of successful PCRs was inconveniently low (Supplementary Figure 2). Therefore, we developed a custom method for DNA extraction where either one or both wings were frozen, manually homogenized and digested in the same volume of Proteinase K solution. This approach was more effective in general, but with 86% to 62%, we obtained significantly more successful PCRs when only one wing was used (Figure 2).

Figure 2

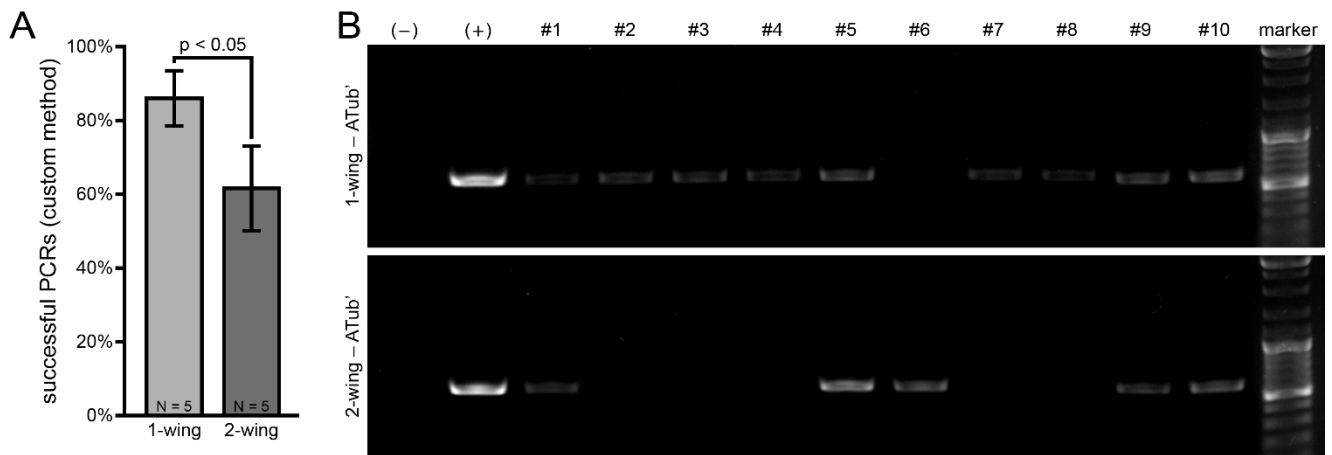


Figure 2 – Successful PCRs on genomic DNA extracted from one or both wings by using the custom method.

(A) Quantification of successful PCRs on the *alpha-tubulin 1* upstream regulatory sequence from five replicates with ten adults each using genomic DNA extracted from one or both wings as template. Significantly more successful PCRs could be performed when only one wing was digested. Error bars represent standard deviation.

(B) Exemplary agarose gel electrophoresis images showing the PCR-based amplification of the *alpha-tubulin 1* upstream regulatory sequence (ATub') for ten individual adults using DNA extracted from either one or both wings. The estimated PCR product size is 616 bp. The bright DNA marker bands (top to bottom) represent 3,000 / 1,000 / 500 bp. In the negative control (-), double-distilled H₂O was used as template and in the positive control (+), DNA extracted from the whole body was used as template.

Sequencing of the San Bernadino and Pearl *white* alleles

Next, we tested whether DNA extracted with the custom method suffices to obtain the nucleotide sequence. We used the black-eyed SB wild-type strain and the white-eyed Prl recessive mutant strain. The current assumption is that the Prl phenotype is caused by a dysfunction of either *white* or *scarlet*, a pair of ABC transmembrane transporter genes that are co-localized in a tail-to-head fashion on chromosome LG9 [41,42]. According to the genomic sequence [13], which derives from the black-eyed GA-2 strain, the *white* gene contains ten exons distributed across a distance of 8,376 bp. We designed primers to amplify the whole coding sequence within two PCRs that cover 4,208 (exon 1-6 primer) and 4,295 bp (exon 6-10 primer), respectively (Figure 3A) and successfully amplified the target sequences from genomic DNA extracted from the whole body and from one wing for both, the SB and Prl strain (Figure 3B). The PCR products obtained for SB and Prl from wing tissue were subsequently sequenced, revealing nearly complete identity through the *white* coding sequence except for several silent mutations and two mutations that lead to an amino acid exchange, Y437V and G573S. However, a high number of insertions, deletions and substitutions were found within introns 2 and 6 (Figure 3C). We also compared the sequencing results from genomic DNA extracted from either the whole body or from one wing, which were nearly identical except for two single nucleotide polymorphisms in both, the SB (Supplementary Figure 3A) and Prl (Supplementary Figure 3B) strain. Additionally, we compared the SB (Supplementary Figure 4A) and Prl (Supplementary Figure 4B) allele sequences to the GA-2 reference [13]. For SB, three amino acid exchanges and comprehensive deviations in intron 6 were found, while for Prl, four amino acid exchanges (three in a similar position as for SB) and comprehensive deviations in introns 2 and 6 were found.

Figure 3

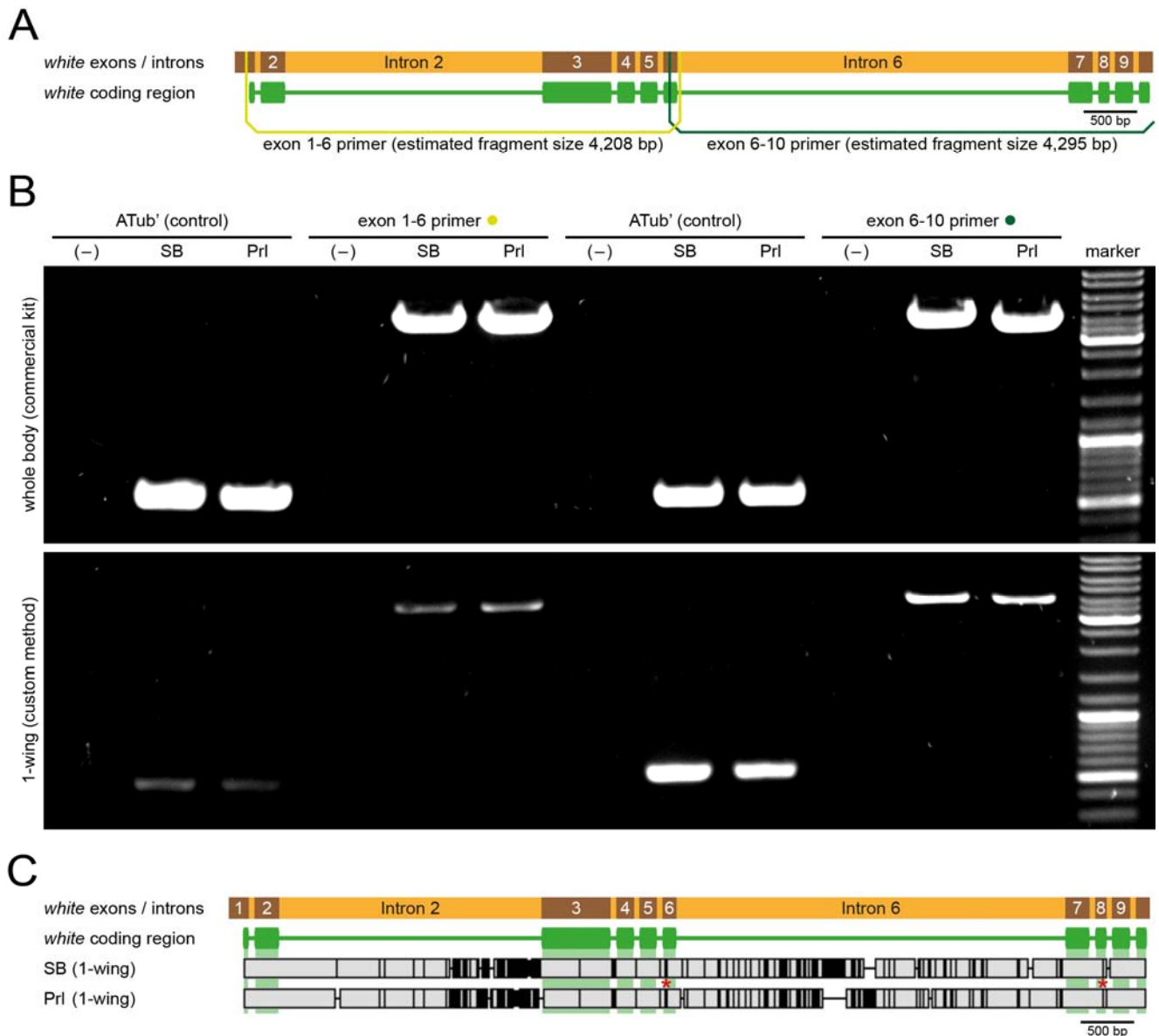


Figure 3 – Sequencing of the SB and Prl *white* allele. (A) Exon / intron structure of the *white* gene (8,376 bp) with respective primer groups for extraction PCRs. (B) Agarose gel electrophoresis image showing the results for the extraction PCRs. Estimated PCR product size is 616 bp for the *alpha-tubulin 1* upstream regulatory sequence control (ATub'), 4,208 bp for the exon 1-6 primer group and 4,295 bp for the exon 6-10 primer group. Bright DNA marker bands (top to bottom) represent 3,000 / 1,000 / 500 bp. In the negative control (-), double-distilled H₂O was used as template. (C) Alignment of the SB and Prl *white* sequences. Vertical black bars represent sequence deviations, horizontal black lines show insertions / deletions. The red asterisks mark the two mutations that lead to amino acid exchanges (Y437V and G573S).

Proof-of-principle spanning four generations

Our sequencing results of the *white* alleles do not properly reveal if the Prl allele is functional or if the white-eyed phenotype results from a lesion close to the C-terminal end in the co-localized *scarlet* gene as proposed by Grubbs *et al.* [42]. However, the obtained sequence data is adequate to design primer groups that allow the genotyping of the *white / scarlet* gene pair alleles for the SB and Prl strains based on the *white* intron 6 insertion / deletion pattern. The primer groups share the same reverse primer that attaches in an identical region, while the forward primers are different. The SB forward primer attaches in a region that is not present in the Prl allele and results in a 577 bp PCR product in the SB allele (Figure 4A, red lines). The Prl forward primer attaches in a region that is not present in the SB allele and result in a 349 bp PCR product on the Prl allele (Figure 4A, blue lines). We crossed a F1 SB female with a F1 Prl male and analyzed the F2 progeny phenotypically and via non-lethal genotyping using DNA extracted from one wing as a template. All F2 individuals showed black eyes and all were identified as SB/Prl heterozygotes (Figure 4B, first block). We crossed two F2 SB/Prl heterozygotes, which resulted in 75% progeny with black eyes. Out of those individuals, 20.8% were genotyped as SB, while 54.2% were genotyped as SB/Prl heterozygotes. The remaining 25% had white eyes and were genotyped as Prl (Figure 4B, second block). With the GF individuals, we performed six different control crosses to confirm the genotyping results of the F3 generation by the F4 eye phenotype (Figure 4B, third block). All experimentally obtained ratios agree with the theoretical Mendelian values, exemplary agarose gel electrophoresis images outlining the genotyping results for F1, F2 and F3 are shown in Figure 4C.

Figure 4

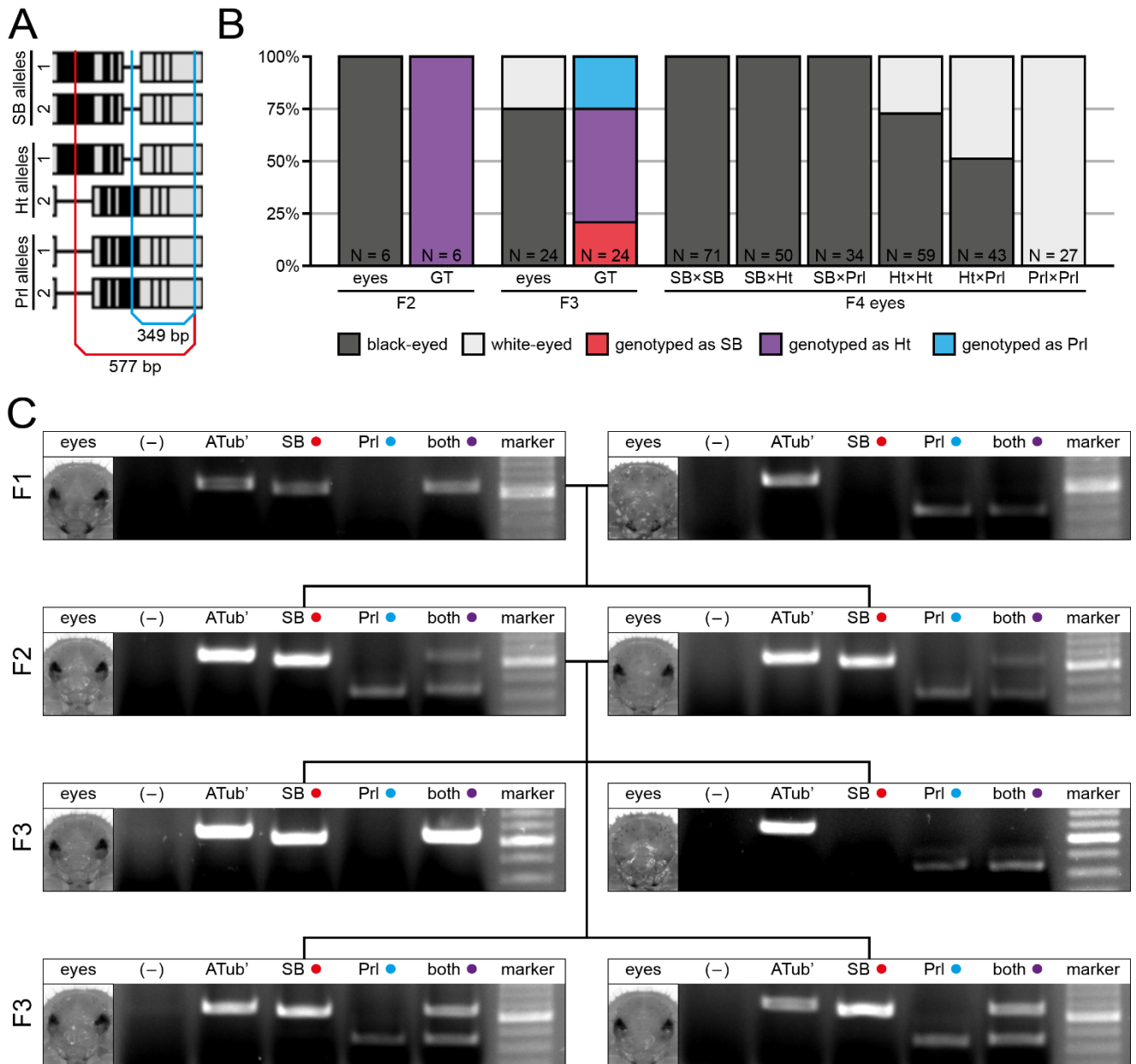


Figure 4 – Proof-of-principle spanning four generations. (A) Primer group design for genotyping of either the SB (red lines) or Prl (blue lines) allele. (B) Eye pigmentation from G2 to G4 and genotyping results from G2 to G3. In the G1, a SB female was crosses with a Prl male, and the progeny was assayed phenotypically and their genotype was determined. (C) Exemplary results from the proof-of-principle assay from the G1 to G3. Estimated PCR product size is 616 bp for the *alpha-tubulin* 1 control (ATub'), 577 bp for the SB primer group, 349 bp for the Prl primer group and 577 as well as 349 bp for the primer group that contains both forward primers. Bright DNA marker band represents 500 bp. The negative control (-) used double-distilled H₂O as template. Ht, heterozygote.

Discussion

In this study, we describe a viable and efficient wing dissection procedure for *T. castaneum* that more than eight out of ten beetles survive. The amount of DNA extracted from one wing performs reliably in PCRs and is sufficient for ten reactions. However, doubling the amount of tissue, *i.e.* digesting two wings in the same volume of Proteinase K solution, decreases the efficiency. We assume that although the amount of DNA template is twice as high, the increase in organic debris as a by-product of the digestion reaction interferes with the subsequent PCR. Even for distances of around 4,000 bp, the amount of PCR product is adequate for sequencing. Thus, our method facilitates all experimental workflows, in which the exact genetic configuration of individual living beetles has to be known. We assume that non-lethal genotyping of *T. castaneum* will be of use in the following scenarios:

- The most trivial solution for stock keeping of non-lethal alleles is the establishment of homozygous cultures. For alleles that induce a dominant phenotype, *e.g.* certain mutants [43], custom-made transgenic lines for applications such as fluorescence live imaging [44], or enhancer trap lines that are result from large-scale assays such as insertional mutagenesis screenings [33], the establishment procedure from a single founder is rather complex. If relevant progeny genotypes have to be identified via test crossing, four generations are necessary to distinguish homozygous from mixed cultures. In contrast, our method allows the identification of homozygous animals after two generations (Figure 5).
- Stock keeping of cultures that carry embryonic recessive lethal alleles is laborious since heterozygous animals are usually phenotypically inconspicuous and appropriate balancers are not always available [4,45]. Respective technical protocols [46] suggest test crossing followed by phenotypical identification of mutant phenotypes within the eggs. With our non-lethal genotyping approach, both steps can be replaced by determining the genotype via molecular biology-based assays.
- Genome engineering with the CRISPR/Cas9 nuclease system has been established for *T. castaneum* [30]. However, respective assays require the screening of a certain number of potential founders to identify appropriately altered alleles. Typically, founders have to be crossed against wild-types and sequence analysis has to be performed with the progeny. With our technique, the sequences of potentially altered alleles can be determined directly in the founders and only the favorable individuals are subsequently crossed against the wild-type to secure the allele.
- Besides developmental biology, genetics and agricultural-related research, *T. castaneum* is also used in behavior experiments [47–49]. The proposed method also improves workflows where genotype and behavior need to be correlated – the genotypes can be determined before the respective individuals are used in assays.

Protocols for non-lethal genotyping by extracting genomic DNA from dissected legs has been shown for *D. melanogaster* [31] and two wasp species [50]. In *T. castaneum*, we consider the wing as the ideal tissue choice for multiple reasons: Firstly, under laboratory culture conditions, adult beetles scarcely fly but primarily scuttle and/or dig tunnels into the flour. Secondly, the dissection wound is properly covered and not exposed to pollutants or pathogens. Thirdly, legs are an essential factor for the mating behavior of *T. castaneum* since males rub their legs against the elytra of the partner during copulation. The oviposition rate of females that were paired with males, which had their tarsi ablated was significantly decreased [51–53]. This is in direct conflict with the primary motivation for our method, *i.e.* genotyped individuals with the desired allele(s) have to produce sufficient progeny. For *D. melanogaster*, quantitative data on the performance of non-lethal genotyping is not available [31], but our ratio of successful PCRs, which is about 86%, is comparable to the 87.5% that have been obtained for *A. mellifera* workers when a similar genomic DNA extraction procedure was used [32]. Due to the protective elytra, the extraction of wing tissue from *T. castaneum* is experimentally slightly more challenging. With some training, the wing dissection time per individual reduces to two to three minutes. Including digestion, PCR and electrophoresis, the complete process for up to fifty adults is completed in less than an afternoon.

The nucleotide sequences of the *white* alleles from the SB wild-type and Prl mutant strains do not provide a clear evidence for the functionality of the respective genes. The coding sequence in both alleles appears intact and severe deviations are only found in the intron sequences. These findings are consistent with the conclusions from Grubbs *et al.* [42], which proposed that not the *white*, but the *scarlet* gene is dysfunctional in the Prl strain. To completely verify this assumption, a complementation assay needs to be performed where functional variants of both, the *white* and the *scarlet* gene, are expressed in the Prl strain via transgenesis.

Non-lethal genotyping is a valuable addition to the methodological arsenal for *T. castaneum* and an adaptation of the proposed procedure for other coleopteran species should be convenient. Compared to the known alternatives, our approach has a high potential to save manpower, consumables and time. However, our approach is invasive, which might interfere with certain experimental strategies. In such scenarios, it may be necessary to establish non-invasive genotyping protocols, for example by extracting genomic DNA from exuviae as shown for *A. mellifera* [54]. Exuviae mainly consist of extra-cellular proteins and polysaccharides, but usually, a few ectodermal cells from the trachea system and the digestive tract detach during the molting process.

Figure 5

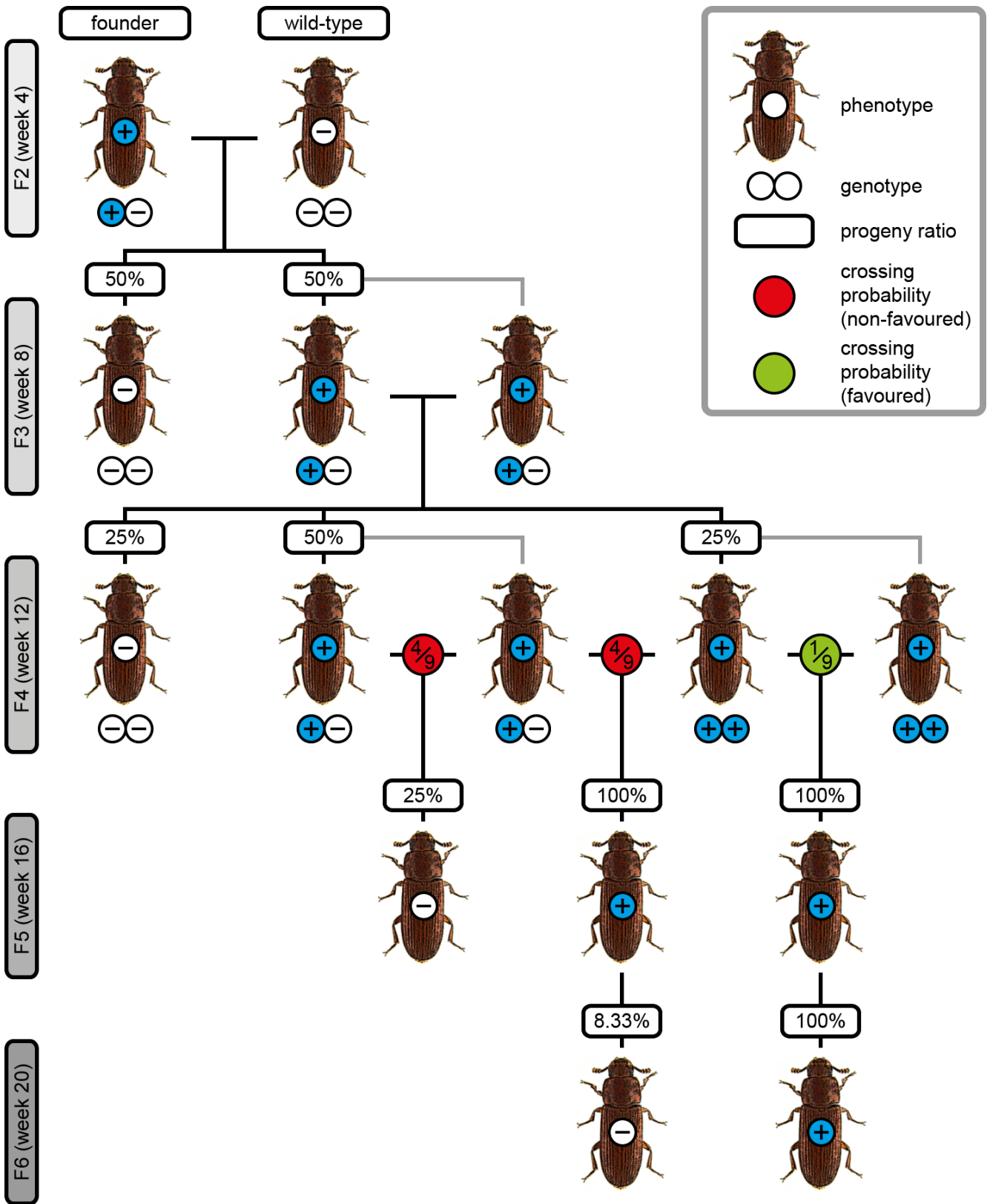


Figure 5 – F2 to F5 crossing procedure for the establishment of homozygous cultures when the respective allele induces a dominant phenotype. F1 (not shown) is either the generation that was irradiated or treated with chemicals (mutants), the generation that was injected and thus has a mosaic-like integration pattern (custom-made transgenic lines) or the donor/helper hybrid generation (insertional mutagenesis screening). To establish a homozygous culture, a heterozygous F2 founder, which shows the respective phenotype, is outcrossed against the wild-type. In the F3, two heterozygous animals are crossed, which results in 25% wild-types, 50% heterozygotes and 25% homozygotes in the F4. Since heterozygotes and homozygotes are usually not distinguishable by the phenotype, individuals are crossed in single pairs without *a priori* knowledge of their allelic configuration and test crossings are performed to determine the genotypes. The genotypes of a F4 heterozygous/heterozygous pair can be identified by the phenotype distribution in the F5, since around 25% wild-types are expected. However, the genotypes of F4 heterozygous/homozygous and homozygous/homozygous pairs cannot be determined by inspecting the F5 since every descendant shows the phenotype. An additional F5 *en masse* cross is necessary to determine the genotypes of the F4 pair – no wild-types among the F6 progeny indicate that both F4 individuals were homozygous. This is a rather cumbersome process since statistically, only one out of nine F4 pairs consists of two homozygotes, and only four of those nine pairs can be discarded by analyzing the F5. Non-lethal genotyping allows to pair only homozygous animals in the F4, thus saving consumables (mainly rearing supplies) and manpower (to set up, cultivate and screen the F5 and F6 generations). Additionally, the process saves time, since awaiting the F5 and F6 is not necessary. At a rearing temperature of 30°C, the generation time is approximately 4 weeks, thus with non-lethal genotyping, homozygous cultures are available about 8 weeks more early.

Acknowledgements

We thank Maarten Hilbrant, Kristen Panfilio, Matthias Teuscher and Michael Schoppmeier for the San Bernadino and Pearl *Tribolium castaneum* strains.

Funding

The research was funded by the Cluster of Excellence – Frankfurt am Main for Macromolecular Complexes (CEF-MC, EXC 115) granted in part to EHKS at the Buchmann Institute for Molecular Life Sciences (BMLS) at the Goethe Universität – Frankfurt am Main by the Deutsche Forschungsgemeinschaft (DFG).

Competing Interests Statement

The authors declare no competing financial interests.

Author Contributions

FS and EHKS conceived the research. FS and JAR performed the experiments. FS and EHKS wrote the publication with input from JAR.

References

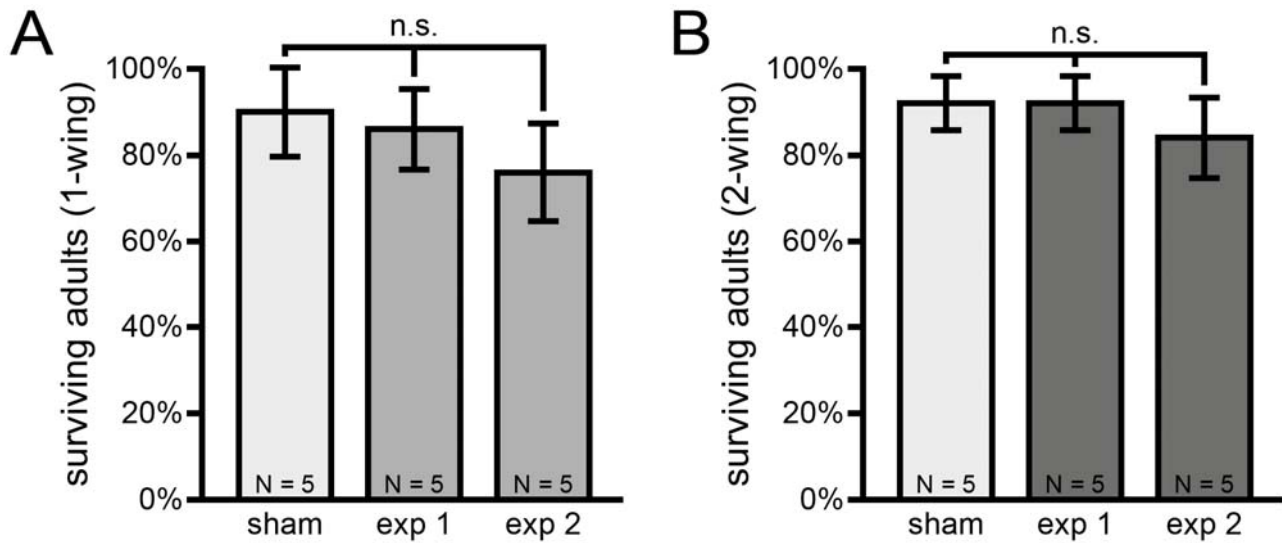
1. Bellen HJ, Tong C, Tsuda H. 100 years of *Drosophila* research and its impact on vertebrate neuroscience: a history lesson for the future. *Nat Rev Neurosci.* 2010;11: 514–522. doi:10.1038/nrn2839
2. Inglis J, Gann A, Crotty D, Janssen K, Smit M, editors. *Emerging Model Organisms: A Laboratory Manual, Volume 1.* 1st Ed. Cold Spring Harbor, New York, NY: Cold Spring Harbour Laboratory Press; 2009.
3. Inglis J, Gann A, Crotty D, Janssen K, Smit M, editors. *Emerging Model Organisms: A Laboratory Manual, Volume 2.* 1st Ed. Cold Spring Harbor, New York, NY: Cold Spring Harbour Laboratory Press; 2010.
4. Klingler M. *Tribolium*. *Curr Biol.* 2004;14: R639-40. doi:10.1016/j.cub.2004.08.004
5. Brown SJ, Shippy TD, Miller S, Bolognesi R, Beeman RW, Lorenzen MD, et al. The red flour beetle, *Tribolium castaneum* (Coleoptera): A model for studies of development and pest biology. *Cold Spring Harb Protoc.* 2009;4. doi:10.1101/pdb.emo126
6. Bucher G, Klingler M. Divergent segmentation mechanism in the short germ insect *Tribolium* revealed by giant expression and function. *Development.* 2004;131: 1729–40. doi:10.1242/dev.01073
7. Roth S, Hartenstein V. Development of *Tribolium castaneum*. *Development Genes and Evolution.* Apr 2008;218: 115–118. doi:10.1007/s00427-008-0215-2
8. Schröder R, Beermann A, Wittkopp N, Lutz R. From development to biodiversity--*Tribolium castaneum*, an insect model organism for short germband development. *Dev Genes Evol.* 2008;218: 119–26. doi:10.1007/s00427-008-0214-3
9. Sharma R, Beermann A, Schröder R. The dynamic expression of extraembryonic marker genes in the beetle *Tribolium castaneum* reveals the complexity of serosa and amnion formation in a short germ insect. *Gene Expr Patterns.* 2013;13: 362–71. doi:10.1016/j.gep.2013.07.002
10. Hilbrant M, Horn T, Koelzer S, Panfilio KA. The beetle amnion and serosa functionally interact as apposed epithelia. *Elife.* 2016;5. doi:10.7554/eLife.13834
11. Grossmann D, Scholten J, Prpic N-M. Separable functions of wingless in distal and ventral patterning of the *Tribolium* leg. *Dev Genes Evol.* Springer; 2009;219: 469–79. doi:10.1007/s00427-009-0310-z
12. Angelini DR, Smith FW, Jockusch EL. Extent With Modification: Leg Patterning in the Beetle *Tribolium castaneum* and the Evolution of Serial Homologs. *G3 (Bethesda).* 2012;2: 235–48. doi:10.1534/g3.111.001537
13. Richards S, Gibbs RA, Weinstock GM, Brown SJ, Denell R, Beeman RW, et al. The genome of the model beetle and pest *Tribolium castaneum*. *Nature.* 2008;452: 949–55. doi:10.1038/nature06784
14. Audsley N, Down RE. G protein coupled receptors as targets for next generation pesticides. *Insect Biochem Mol Biol.* 2015;67: 27–37. doi:10.1016/j.ibmb.2015.07.014
15. Perkin LC, Adrianos SL, Oppert B. Gene Disruption Technologies Have the Potential to Transform Stored Product Insect Pest Control. *Insects.* Multidisciplinary Digital Publishing Institute (MDPI); 2016;7. doi:10.3390/insects7030046
16. Brown SJ, Denell RE, Beeman RW. Beetling around the genome. *Genet Res.* 2003;82: 155–61. Available: <http://www.ncbi.nlm.nih.gov/pubmed/15134194>
17. Strobl F, Stelzer EHK. Non-invasive long-term fluorescence live imaging of *Tribolium castaneum* embryos. *Development.* 2014;141: 2331–2338. doi:10.1242/dev.108795
18. Strobl F, Schmitz A, Stelzer EHK. Live imaging of *Tribolium castaneum* embryonic development using light-sheet-based fluorescence microscopy. *Nat Protoc.* Nature Publishing Group, a division of Macmillan Publishers Limited. All Rights Reserved.; 2015;10: 1486–1507. doi:10.1038/nprot.2015.093
19. Strobl F, Stelzer EH. Long-term fluorescence live imaging of *Tribolium castaneum* embryos: principles, resources, scientific challenges and the comparative approach. *Curr Opin Insect Sci.* 2016;18: 17–26. doi:10.1016/j.cois.2016.08.002
20. Strobl F, Schmitz A, Stelzer EHK. Improving your four-dimensional image: traveling through a decade of

- light-sheet-based fluorescence microscopy research. *Nat Protoc.* 2017;12: 1103–1109. doi:10.1038/nprot.2017.028
21. Brown SJ, Mahaffey JP, Lorenzen MD, Denell RE, Mahaffey JW. Using RNAi to investigate orthologous homeotic gene function during development of distantly related insects. *Evol Dev.* 1999;1: 11–5. Available: <http://www.ncbi.nlm.nih.gov/pubmed/11324015>
 22. Tomoyasu Y, Denell RE. Larval RNAi in *Tribolium* (Coleoptera) for analyzing adult development. *Dev Genes Evol.* 2004;214: 575–8. doi:10.1007/s00427-004-0434-0
 23. Bucher G, Scholten J, Klingler M. Parental RNAi in *Tribolium* (Coleoptera). *Curr Biol.* 2002;12: R85-6. Available: <http://www.ncbi.nlm.nih.gov/pubmed/11839285>
 24. Posnien N, Schinko J, Grossmann D, Shippy TD, Konopova B, Bucher G. RNAi in the red flour beetle (*Tribolium*). *Cold Spring Harb Protoc.* 2009;2009: pdb.prot5256. doi:10.1101/pdb.prot5256
 25. Schinko J, Posnien N, Kittelmann S, Koniszewski N, Bucher G. Single and double whole-mount in situ hybridization in red flour beetle (*Tribolium*) embryos. *Cold Spring Harb Protoc.* 2009;2009: pdb.prot5258. doi:10.1101/pdb.prot5258
 26. Shippy TD, Coleman CM, Tomoyasu Y, Brown SJ. Concurrent in situ hybridization and antibody staining in red flour beetle (*Tribolium*) embryos. *Cold Spring Harb Protoc.* 2009;2009: pdb.prot5257. doi:10.1101/pdb.prot5257
 27. Lorenzen MD, Berghammer AJ, Brown SJ, Denell RE, Klingler M, Beeman RW. piggyBac-mediated germline transformation in the beetle *Tribolium castaneum*. *Insect Mol Biol.* 2003;12: 433–40. Available: <http://www.ncbi.nlm.nih.gov/pubmed/12974948>
 28. Berghammer AJ, Weber M, Trauner J, Klingler M. Red flour beetle (*Tribolium*) germline transformation and insertional mutagenesis. *Cold Spring Harb Protoc.* 2009;2009: pdb.prot5259. doi:10.1101/pdb.prot5259
 29. Pavlopoulos A, Berghammer AJ, Averof M, Klingler M. Efficient transformation of the beetle *Tribolium castaneum* using the Minos transposable element: quantitative and qualitative analysis of genomic integration events. *Genetics.* 2004;167: 737–46. doi:10.1534/genetics.103.023085
 30. Gilles AF, Schinko JB, Averof M. Efficient CRISPR-mediated gene targeting and transgene replacement in the beetle *Tribolium castaneum*. *Development.* 2015;142: 2832–9. doi:10.1242/dev.125054
 31. Carvalho GB, Ja WW, Benzer S. Non-lethal PCR genotyping of single *Drosophila*. *Biotechniques.* NIH Public Access; 2009;46: 312–4. doi:10.2144/000113088
 32. Châline N, Ratnieks F, Raine N, Badcock N, Burke T. Non-lethal sampling of honey bee, *Apis mellifera*, DNA using wing tips. doi:10.1051/apido:2004015>
 33. Trauner J, Schinko J, Lorenzen MD, Shippy TD, Wimmer EA, Beeman RW, et al. Large-scale insertional mutagenesis of a coleopteran stored grain pest, the red flour beetle *Tribolium castaneum*, identifies embryonic lethal mutations and enhancer traps. *BMC Biol.* 2009;7: 73. doi:10.1186/1741-7007-7-73
 34. Schmitt-Engel C, Schultheis D, Schwirz J, Ströhlein N, Troelenberg N, Majumdar U, et al. The iBeetle large-scale RNAi screen reveals gene functions for insect development and physiology. *Nat Commun.* 2015;6: 7822. doi:10.1038/ncomms8822
 35. Dönitz J, Schmitt-Engel C, Grossmann D, Gerischer L, Tech M, Schoppmeier M, et al. iBeetle-Base: a database for RNAi phenotypes in the red flour beetle *Tribolium castaneum*. *Nucleic Acids Res.* 2015;43: D720-5. doi:10.1093/nar/gku1054
 36. Altincicek B, Elashry A, Guz N, Grundler FMW, Vilcinskas A, Dehne H-W, et al. Next Generation Sequencing Based Transcriptome Analysis of Septic-Injury Responsive Genes in the Beetle *Tribolium castaneum*. Mariño-Ramírez L, editor. *PLoS One.* Public Library of Science; 2013;8: e52004. doi:10.1371/journal.pone.0052004
 37. Lorenzen MD, Brown SJ, Denell RE, Beeman RW. Cloning and characterization of the *Tribolium castaneum* eye-color genes encoding tryptophan oxygenase and kynurenine 3-monooxygenase. *Genetics.* 2002;160: 225–234.
 38. Park T. *Observations on the General Biology of the Flour Beetle, Tribolium Confusum.* Q Rev Biol. University of Chicago Press; 1934;9: 36–54. Available: <http://www.jstor.org/stable/2808486>

39. Shapiro SS, Wilk MB. An Analysis of Variance Test for Normality (Complete Samples). *Biometrika*. 1965;52: 591. doi:10.2307/2333709
40. Siebert KS, Lorenzen MD, Brown SJ, Park Y, Beeman RW. Tubulin superfamily genes in *Tribolium castaneum* and the use of a Tubulin promoter to drive transgene expression. *Insect Biochem Mol Biol*. 2008;38: 749–755. doi:10.1016/j.ibmb.2008.04.007
41. Broehan G, Kroeger T, Lorenzen M, Merzendorfer H, Higgins C, Rees D, et al. Functional analysis of the ATP-binding cassette (ABC) transporter gene family of *Tribolium castaneum*. *BMC Genomics*. *BioMed Central*; 2013;14: 6. doi:10.1186/1471-2164-14-6
42. Grubbs N, Haas S, Beeman RW, Lorenzen MD. The ABCs of eye color in *Tribolium castaneum*: orthologs of the *Drosophila* white, scarlet, and brown Genes. *Genetics*. 2015;199: 749–59. doi:10.1534/genetics.114.173971
43. Dawson PS. The “reindeer” mutation and a revision of linkage groups V and X in the flour beetle, *Tribolium castaneum*. *Can J Genet Cytol*. NRC Research Press Ottawa, Canada ; 1984;26: 762–764. doi:10.1139/g84-120
44. Strobl F, Klees S, Stelzer EHK. Light Sheet-based Fluorescence Microscopy of Living or Fixed and Stained *Tribolium castaneum* Embryos. *J Vis Exp*. 2017; doi:10.3791/55629
45. Mocelin G, Stuart JJ. Crossover Suppressors in *Tribolium castaneum*. *J Hered*. Oxford University Press; 1996;87: 27–34. doi:10.1093/oxfordjournals.jhered.a022949
46. Berghammer A, Bucher G, Maderspacher F, Klingler M. A system to efficiently maintain embryonic lethal mutations in the flour beetle *Tribolium castaneum*. *Dev Genes Evol*. Springer-Verlag; 1999;209: 382–389. doi:10.1007/S004270050268
47. Serrano JM, Castro L, Toro MA, López-Fanjul C. The genetic properties of homosexual copulation behavior in *Tribolium castaneum*: Diallel analysis. *Behav Genet*. Kluwer Academic Publishers-Plenum Publishers; 1991;21: 547–558. doi:10.1007/BF01066681
48. Romero SA, Campbell JF, Nechols JR, With KA. Movement Behavior of Red Flour Beetle: Response to Habitat Cues and Patch Boundaries. *Environ Entomol*. 2010;39: 919–929. doi:10.1603/EN09324
49. Martin CM, Kruse KC, Switzer P V. Social Experience Affects Same-Sex Pairing Behavior in Male Red Flour Beetles (*Tribolium castaneum* Herbst). *J Insect Behav*. Springer US; 2015;28: 268–279. doi:10.1007/s10905-015-9498-0
50. Starks PT, Peters JM. Semi-nondestructive genetic sampling from live eusocial wasps, *Polistes dominulus* and *Polistes fuscatus*. *Insectes Soc*. 2002;49: 20–22. doi:10.1007/s00040-002-8272-4
51. Edvardsson M, Göran A. Copulatory courtship and cryptic female choice in red flour beetles *Tribolium castaneum*. *Proc R Soc London B Biol Sci*. 2000;267. Available: <http://rspb.royalsocietypublishing.org/content/267/1443/559>
52. Bloch Qazi MC. A potential mechanism for cryptic female choice in a flour beetle. *J Evol Biol*. Blackwell Science Ltd; 2003;16: 170–176. doi:10.1046/j.1420-9101.2003.00501.x
53. Edvardsson M, Arnqvist G. The Effects of Copulatory Courtship on Differential Allocation in the Red Flour Beetle *Tribolium castaneum*. *J Insect Behav*. Kluwer Academic Publishers-Plenum Publishers; 2005;18: 313–322. doi:10.1007/s10905-005-3692-4
54. Gregory PG, Rinderer TE. Non-destructive sources of DNA used to genotype honey bee (*Apis mellifera*) queens. *Entomol Exp Appl*. 2004;111: 173–177. doi:10.1111/j.0013-8703.2004.00164.x

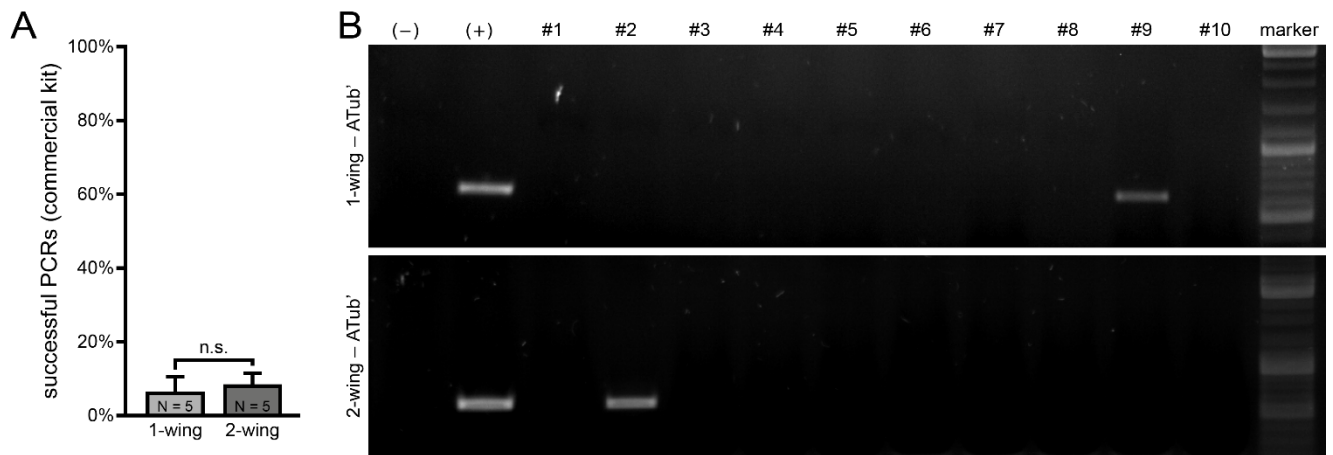
Supplementary Display Items

Supplementary Figure 1



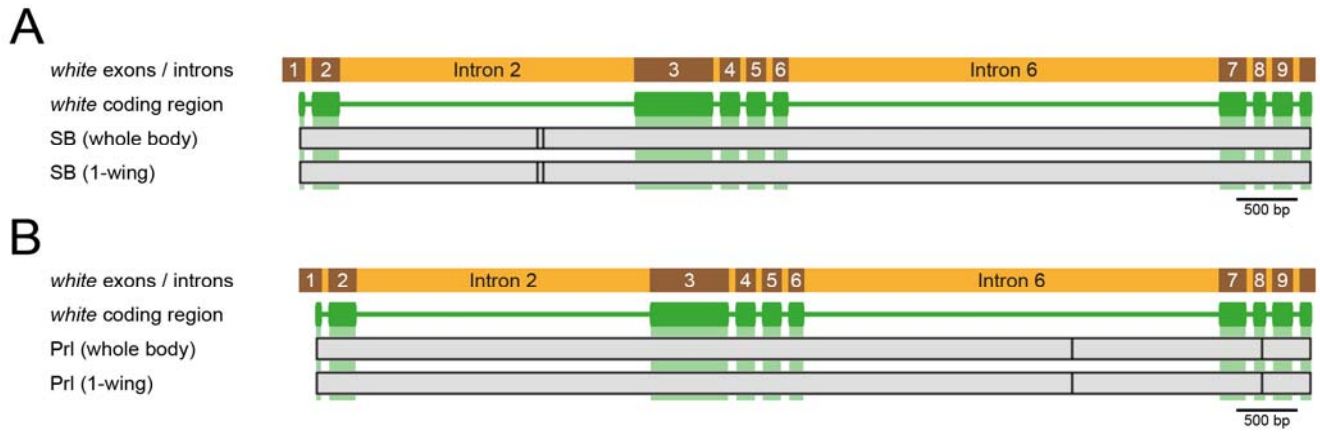
Supplementary Figure 1 – Comparison of survival rate when either one or both wings were dissected by two experimenters. (A) Quantification of surviving adults from five replicates with ten adults after the dissection of one wing. The sham control animals were also paralyzed, and their elytra were also lifted from the abdomen, but the wing was not dissected. No significant difference was found. Error bars represent standard deviation. (B) Quantification of surviving adults from five replicates with ten adults after the dissection of both wings. The sham control animals were also paralyzed, and their elytra were also lifted from the abdomen, but the wing was not dissected. No significant difference was found. Error bars represent standard deviation. Exp, experimenter.

Supplementary Figure 2



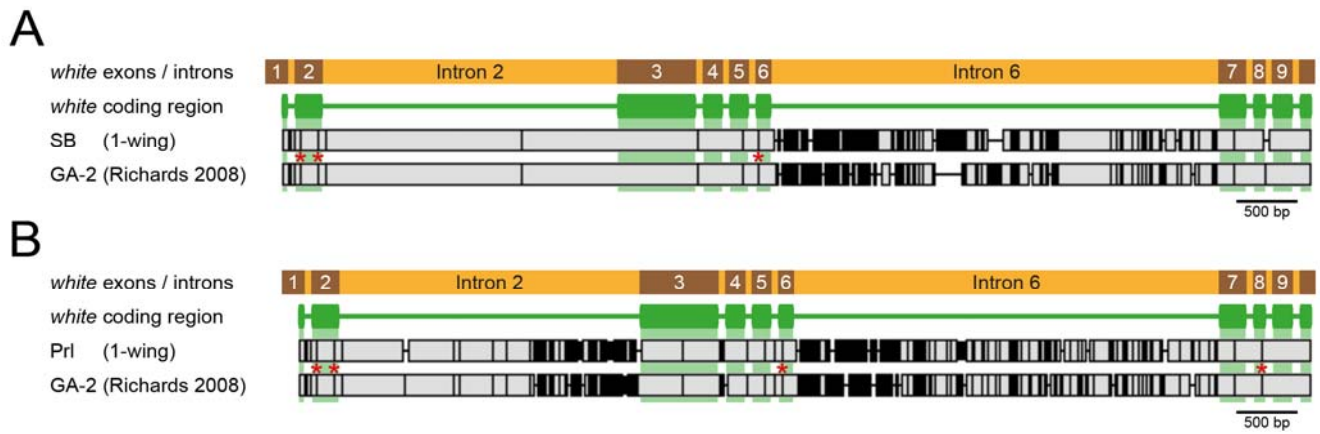
Supplementary Figure 2 – Successful PCRs on genomic DNA extracted from one or both wings by using a commercial DNA extraction kit. (A) Quantification of successful PCRs on the *alpha-tubulin 1* upstream regulatory sequence from five replicates with ten adults each using genomic DNA extracted from one or both wings as template. No significant difference was found. Error bars represent standard deviation. **(B)** Exemplary agarose gel electrophoresis images showing the PCR-based amplification of the *alpha-tubulin 1* upstream regulatory sequence (ATub') for ten individual adults using DNA extracted from either one or both wings. The estimated PCR product size is 616 bp. The bright DNA marker bands (top to bottom) represent 3,000 / 1,000 / 500 bp. In the negative control (-), double-distilled H₂O was used as template and in the positive control (+), DNA extracted from the whole body was used as template.

Supplementary Figure 3



Supplementary Figure 3 – Comparison of sequencing results from genomic DNA extracted either from the whole body or from one wing for SB and Prl. (A) Comparison for the SB strain. Vertical black bars represent sequence deviations. Two deviations were found within intron 2. **(B)** Comparison for the Prl strain. Vertical black bars represent sequence deviations. Two deviations were found, one within intron 6, and one in exon 8. The deviation in exon 8 accounts for the G573S amino acid exchange (Supplementary Figure 4).

Supplementary Figure 4



Supplementary Figure 4 – Comparison of the SB and Prl *white* gene sequences to the GA-2 standard. (A) Comparison for the SB allele. Vertical black bars represent sequence deviations, horizontal black lines show insertions / deletions. Compared to GA-2, the SB *white* allele has multiple insertions, deletions and substitutions mainly within intron 6. The deviations within the coding sequence are primarily silent, except for three amino acid exchanges, T34S, L80F and D437Y, as marked by the red asterisks. **(B)** Comparison for the Prl allele. Vertical black bars represent sequence deviations, horizontal black lines show insertions / deletions. Compared to GA-2, the Prl *white* allele has multiple insertions, deletions and substitutions mainly within introns 2 and 6. The deviations within the coding sequence are primarily silent, except for four amino acid exchanges T34S (similar to SB), L80F (similar to SB), D437V (same position as in the SB sequence, but results in a different amino acid) and G573S (not present for SB), as marked by the red asterisks.

Supplementary Table 1

Supplementary Table 1 – Primer group list. ATub', *alpha tubulin 1* upstream regulatory sequence; ExPCR, primer for extraction PCRs; FD, forward; RV, reverse.

Primer groups	Primer	Sequence	Length	Est. product size	Used
<i>alpha-tubulin 1</i> upstream regulatory sequence (ATub')	ATub' ExPCR FD	5'-AGATGICTATGTATCTCCCGTAAAC-3'	26 bp	616 bp	Figure 2B, Figure 3B, Figure 4C, Supplementary Figure 2B
	ATub' ExPCR RV	5'-GAAATGGGATAAECTTACCATTITGG-3'	25 bp		
<i>white</i> Exon 1-6	White E1-6 ExPCR FD	5'-AATGGACTACAATGTATCAATTTACAAGG-3'	29 bp	4,208 bp	Figure 3B
	White E1-6 ExPCR RV	5'-CACAAAACGTGTAATTTTCATTTCGG-3'	25 bp		
<i>white</i> Exon 6-12	White E6-10 ExPCR FD	5'-GGATGGAGTAATGAACATAAATGGAGTAC-3'	29 bp	4,295 bp	Figure 3B
	White E6-10 ExPCR RV	5'-TTAATAACACCAGATTGAATTCTCGC-3'	26 bp		
SB <i>white</i> allele genotyping	SB Genotyping FD	5'-GCGAATTATGTGATAAATCTTCAATTG-3'	27 bp	577 bp	Figure 4C
	SB and Prl Genotyping RV	5'-GCATCATTTTTTATTAACTCGGAATG-3'	25 bp		
Prl <i>white</i> allele genotyping	Prl Genotyping FD	5'-ACCGAGTTAACGTAACCTCATGG-3'	24 bp	349 bp	Figure 4C
	SB and Prl Genotyping RV	5'-GCATCATTTTTTATTAACTCGGAATG-3'	25 bp		
both (SB and Prl) <i>white</i> allele genotyping	SB Genotyping FD	5'-GCGAATTATGTGATAAATCTTCAATTG-3'	27 bp	577 bp as well as 349 bp	Figure 4C
	Prl Genotyping FD	5'-ACCGAGTTAACGTAACCTCATGG-3'	24 bp		
	SB and Prl Genotyping RV	5'-GCATCATTTTTTATTAACTCGGAATG-3'	25 bp		

Supplementary Sequence 2

Prl white allele (genomic DNA extracted from one wing; 8,372 bp)

```
AATGGACTACAATGTATCAATTTACAAGGTATTTACAAATTCAGACAGCGTCGACAGTTAGCCAAAGTAAACAATCATTTG
TTCCAGATTTTAAATACATAGTACAAAGAGATAAATTTTCATGTGTAAGTCTTTTAAATTTGGTGTATTTGATTAAGT
GTACGTGTAATAAAGTAAAGTAACTGAACCACTTTTACCGGAGTGTATCAAAAATAAAGCGAAATGTAAGACTCAT
TACTTTTCGTTACTGTTTACGAAACATGCGTTTATAGAGTGGCGATAGCACAAGTTCGGCCACTTCTATGATTTATC
ATGTTTCAGAGTTCACAACTATGGGCAACCTTCACCCGACCGCAATTTGGTACCCAGTGTAGCGAAATTAACCTACA
GTTCCAGCGAAATTAACCTTCGCGCAAGTTTCCCTCAAAAACAAATTTTCAATTTTCAAAAACGGAAGTTCCT
CCAGTTCAGAAAAGCCACTTTTGAAGAAGGTATTAAGTACACAACTTTTACCGTAGATGAACCAATGTTGTA
TCGTTAGATTAATAGCCCAAAGTCTAATCCTGAAGCGGGCGATTCGAGACATAAATTTGGGGGGGGGGGATGATG
TTTCCAAAAAATTTAGAAATGGTGAATACTGTGCGGTATGTTGTAATTTTTCATCAAAAACCTCAAAATTTTATTT
CGGAAGATGTTAATAAGCAGATTTAATAAATCTTTAATAAACAACCCCTATATTTTGGTGTGTCATATTTGTTAT
GTATATTTTGGGATTTTGGACATACAGAGTGAATTTAATAAAGCAAGAACTAACCGCCTTATAAATAAAGCAA
AAACCAAAAATAAAGCCTTATATGTTAATATCTATACATTTTGGCCCTTACTTATTTTCTCTTTATGAGTTTT
AAAAACCTATATTTAATTTTACTAGAAAGATAAAGGTAATATCTAGATACTATCAAAAACAGTAAACAAAATGCG
GTTGCTATTTAAAAAATAAATAAGCCTATTTTGAAAAACGAAAGCTCACAAATCTACCTATTTACAAAGATAA
AATCGATCTGTTGAGGATTTTTCGAAAAATGACCTATAGCAGAAATAAATTTTGGCTTACTTCAAACTCAGCCTG
TACATAGTTTTTCAAAATGTTTTTACTAGTAGGTTTTGTTAAGTTTTGAAATAATAGATCTCATGCAAAAAACA
ACACATTTCTTTAAAAAATAAATAAACAACAAGAAATACAACTTCTGTTATTTACTTCCGATAATCTCAATA
TGTATATTTAGCTGTATCAAAACTATAAAGCCCAATGTGCGATTTGACCGAATATCTTTTAAATAATTTGGTAA
CAATGTAACAGGTATAAATGATTAACCTCTCAATAAAACTAATAATGATGAGTTATTTATTTTTTGGAGTGCATGA
ATAATTTAATTTTACAACAACCGTAACTGTAATCTATGCAACAATAATTTGGAGAGAAATGCGACGTTGGCT
TTTAAATTTTAAATGTTTCAATAAAGCACTTATAGGTATTTTAAAAAATTTTGGTCAATGAGCTTTATATGTT
TTTAAAAAATAAATAAATGATGTTGGAGTGGAGAGGCTGGACTTCTGCCCTTCCCTCCCTCCCTGGATCCGCTTTGT
CTCAAGTGCACAGCTGTAATGCGTATATCCCAAAAACCTTTGTAAGCTTTTTCATAAACTTTAATCTTGAAGA
AAGCGTTTACCTTTGATAGCTAAGTTTTCCAGCTTCTATAGAGTTAGGATAATTTTACATAAACAACAAAAGA
TGCCTGGCTTAATCTACATGTTTCAAAAATGTTGTTCACTCAAGTCACTTAAATTTGAACTAACGTCGCGCTTA
GTTTAAATTTGGAATGCTGTAAGTGAAGTTCGTAATAAATGTAAGAAAGCTTCCGATCCGAGATGAAGAATA
CACACAACAAAATCGCGAAATTTATATATATATATATATATATATATATATATATATATATATATATATATAT
TTGAAACAAATTTTCCGAAAAATGCAAAAAAGTGAATAACAGAGAACTATAAAGTCAATTTAGACGAGGCGGATAA
TGAATTTGTTGTCATAAATAGGTGATGAGCAACATTTTGAACAATTTGATCAATTTGACTATATTTAATCA
AATAAATGTTTAAACAAATTAATCAAGAAACAGGAATGCAAACTAAACAGAAACAAAATCAAAATTTTGGTGA
TATATTAAGAAACTAGACTAATATACAAATGACATACAGTGTATCTAATTTTACCAAGTAAATAAATCATCAA
ACAGCAAACTACAACTTTTCTATATAAGCTTTTGAAAAATCTTATTTAATAATTTTCACTGCTTTCCTCTCTTTG
TGTAACCGGATGCTGCTGTTAATAATTTTGGTATAAATAGCAACAATTTTCAATTTGTTGTTTAAATGTTTAAAT
TCCCGTTCTATACAACTAAAATTAATTTGGCGGTATACGTTTCAATGATGTTATCTTTTCCAAATTTAAAGTAAAT
TGGCAATTTTTTATGAAAACCTACAAATAGAAATGTTTATTTGTTGAGCTGTGTTACCTGTTAAAATCAAGACGTA
TTTTCTGATAGCGCTGATATTTTAGTTTCTGTTGAGTAAAGTGAACCAAACTCAGTATAAATTTATTTTGGAAAAGA
AAAAATTTAAGTGTACTTCCAGTGTTTGGGGTGGCTTATCCGGGGAGCTTTTGGCGATCACTGGCTCCAGCGGTGC
CGAAAAACCAACCTCTCAACAACACTAACCTTCCACAGCTTTCGAAATTTGACCGTTCCGGGACTCGGGTGGTAAAG
GAATTCGGGTGCTCGAAAAACCTTGGCAGTCAATCGGCTTATGTTCCACAAGACGACTTATTTATGGGACTTGGAG
GTTTAAAGACTTAATTTTTCAGCTTTTCCAGCTTTCGTAAGTGAACCTGCACTCTACAGCCAGAGATGGCCGAGTCCG
GAAGTATTTTGGATTTGGCTTTGCTAAAGTGTCAAAAACAACCGATTTGGGCGAATTAAGGGGATTTGAG
GTGTTGAAAAGAACGCTCTCTTTTGGCAGCGAAGCTTGCACAAACCCGAACTAATTTTGGGATGAGCCACTTCT
GACCTGACTTCTTCAATGGCGCTGACCTCATGCAAGTCTCAAGGAGTGCATGACCGGAAAACCGTCACTTTGTATC
GATCCATCAACCTTCAAGTGGGTATTTCCATGTTTGAATGTTTGTGTTGATGTTGAGGAGCAACCGGCTTTTGG
GAAGCCGGAAGAGGCGGAAACTTTTCCGGGAGTCACTTTCGAAATTTTGGCCCAATAATGACTCTCACATAAA
TTTTAGGCTTGAAGCCCGGTGTCGCGGAATTAACAACCTGCGGATTTATTCATCAACTTTAGCCATGATCCCGGAA
AGGAGAGTCCGATCGAGTCAAGCAAGCAGTAACTTAATTTGCGACAAATCGAACCTCGAATATCGGGGTTAAATGCACT
GAGGCTGCCACTACTGAAAATCCCGCTGCGTGAAGCTTCCAGATAATTTGGTTTTTCAAGGAGAGAAAGGGGTTAT
CATGATTTTGGATGAGTGGTGAAGTTTTAAAGTCCGTAATAAGCTCGTGTGGGCCAAATCAAGCGCTGTTTTG
CGGTCATTTTGGCGGTTTTTAAAGAACCGCTTTGATTAAGTTCGTTTACTTCAAACTCTGTAAGAAATTTTTAGG
CATAAATTTACAAATTTGATGTTTGGCTTATCAGATCAATTTCCGCTGTTATGAGCGATTTATTTCCGAAAGTTTGA
ACCAGATGGAATGAACATAAATGGAGTACTTTTCTGTTTTCGCAAAATGACATTTCAAAAGCTTTTGGCGTT
ATTAATGTAAGTTTTTCCGAAAGAAATTTACAGTTTTGGGTCAAACTATGAGGAACCAAGTAACTTTTTTATTAAT
TTTTGGTCAAGCTGTTTACTACTTCTTCTGTTTCCGTTTTTCAATTTTATGTAATAAATTAATGATTAAGTAGATA
GACAAAAAATCTTATTTCCGAATAAAGTTCCTTGTGATTTTGAACAGGGGCACTCCCTCGAGATGAATAAAGATAT
GGTGTAAAGCTTTTATAGCTATTTTCTGCAATCAATAATTTATGATGAAGAGAAATAAATAACGTGACTATGTT
TTGAGACTGAATTTTGGTTTTGTTAGCGGTTTTGATGTTTATGAGTATCCCTACTGAAATTTTGTATGTTAATAGCT
CCACTTTAGATTAATAAATAAATAAATAAATAAATAAATAAATAAATAAATAAATAAATAAATAAATAAATAAATA
AAAAAATCTTATGATGGGTATTAAGAAATCCATAACTTTAAAAAATATCTTAAATAATTTAAGCAATAAAGACTT
GGTCCMTTCACTTTTAAATTAATAAAGTATGCTTTTATGTTCTACTACTGAGTGAACCAAGCTCACACTAT
GACTCAAGATCATAGACCACTTCTTCACTGCGGACTATTAATAAATCTATAGAAAATTTACATAGGTTTTTGAAGG
AAATTTAAGTAAAAAGGGTGAACCTTTAAGATTTGATTTGTTTCCCTTAATTTAGTCCAGCTGCTTCAATGCTGTT
AAGTCTTTTTTTTCTGCTCCGCTATAAAGAAAGAAATTTTATATGAAATGAGCATTTTCCGAAAATCTATGA
AAAAAATTTGAGGAAATTTTAAAGTCAAAACCGAATGATATAATTTGAATTAATAAATTTTACTTATTTCCGCGGATTTGA
CGGTAATTTTTTAAATCAGGAATTTGAAACATTTCTGCTTTTATTTGCTTTTCAAAAATAAATAAATAAATAAATAA
TATTATAATTTAGGACCGCTTTACATAAAGTGAATTAAGATTTAATTAATAAATAAATAAATAAATAAATAAATAA
ATTCAAAATGCAATGCAAAATGTTAAGTCAATCGGATTAATAATTTAATGCAATTAATAATGTTCTGTAATCTGGCTCT
AAAAATTCAGTAACTCGGCTTTAATTTGAATTTTATGTTTAAATTTAATTTAATTTAATTTTCTGTTTTTGA
TTAAACTAATTTCTCTCATCTCAGTAAATTTGTCGTTTTTTTGGAAAGTTTAAAGAAATTTTTTGAACATAAATTT
GTTTATCTTTTTCAAAAGATTTGACAATTTATTTAACAATGCTGTACATGATGATTTAGTATAAGAGTACTGACT
GCTTTTTCAAGAAATCAAAAACAGTACAATATATAAATTAATACCATGCAATTTTTTTTTATTTGATCTAGTTATC
TCAGAGTGAATGATTTGGTAAACAACCTTTAGCAACACTTTATCTGCTCAATATGTCAAAATGTTCCAGGAAATAT
TTAGCTAATGGACCGGATTTAAGCTAATCTCATGGATAACTAATCCAAATTTTGGAAAATGCGATGGTCAAGGTTG
ATTAATAATTTTCTATCTAGTAACTTTGAAGAGGTTTTAGTGAJAAAGTTTTAGTGAJAAAGTTTTAGTGAJAAAG
TTGTCAATATTAATAAATCTTTCAAGTTTTTAAATTTAATAAATGCAATTAATTTTAAAGATTTCCCTACTGAGC
AATTAATAATTTACTTTGTCAGAAACACGCTTTATTTCAAGCTTATTTCCGAATTTGAGAGTTAATAAATAAATA
AACAAATTTCTACTTTGCTCCGAGTATAAATAAATGATGCCAACCTGCAATTTACCCATAATTTTTTAATAACG
GTGATAAATAATAAATAGTATGATTTATGATTTAATAACTATCAATGAGAGTCAATTAATACATAGCTATTAAT
TTTTAAGTGCATGAATAAGTATAACATTAATTTGAGAGAGAAATGCGGCTTCTGCTATTTTATGAAAGCTCAATAT
CTGAAAAGCGGATTTTCTGATTTACATAAAGAACTACCATGCGACTAGATAAATCAATTTAATACACTTGTATAA
TAGTATATTTTAAAGATAGGAATAGAAAATTTATATTTTGAACAAAATGAGGGAACAAAATGTTTGTGTTAAACTA
TTGCTTTAAAAAATAGAAAATTTGTTGTTGATAGCTTTTGGAAATTTTGTGTTTAAATGGCGCACTTATGAAAATA
ATATTCGGAATAAATTCAGATAAATTTAATTTACATGTAATCTTCAGATGATAATTTTATACAAAATAAATTTATAA
GTTGCTTTTGAAGAAAGGTTCAACCTGGAGGCTTATCAATGAACTGTTGACTAAATGTTGCTGATTAATAGCTTTT
GCTGATAAAAAGATTTCAATAGACTTTTATTCAGTATTTAATTTGAAACTTAAATTTTGGGGTTTATGTTGCTGATC
TTCAAACTATAGGTAAGTTTTTCAAGTATGTTTGGAGCATTTAAACCTGCAAAATACGTAATGTCGCTCTCATTTT
TGATGTTAGACCAAGATATCTGAAGAAATCATCTTAAATAAATTTGAAGAGAGAAATGTTATTAAGTTAAATGAC
AACAGTATCAGAGACAAAATCAAAACCTTTCTAATGACTAAAAGGCTTAAACAAAATAAAGGACGTTTAAATAGGAA
GGATGTTAATTAAGTGTATAGTGAAGGTTTTGTTCTTGAAGTGGTGTGACTCTCAACAGAACTTCAAAAGTGGG
GATTTATCTTGAACCTCAGAAAGGAAAGGCTGCAATGATGCTTTTCAAGCTTTTCTAGTTTCAATATTTTTTATAGCT
TTCTATTTTCTAATTTGTTTAAAGACTAATAAAGTCAATGATGCTTCAATCAATGATAAAGGTTTAAAGAAAACCTT
GGCTTATAGGGTTTTTGGGCTCAATAAATTTTGGAAATCAATTTTACGTTTTTGGTGTAAAGTCCGCTAATGTTAC
GATTAATTAATCACTTCAATTTGTAATAAAGTCTAATTAATAACACTAGTGCACCTAGATTAAGAGCTTAAATAA
AAAAAATAAATAAATACATGTTTTTGGTTTTTCAAAAACAAAATAAATGTTTCTGTTGCTGTTTTCTCACTTTGG
CTTTGAAACCACTTCAATGCAAAAATGACAGGTTTGAAGGCGAGCTCCCGCTCTCTCCAGGAGCACCGCAACGG
AATGACCGTCCAGATTTTATTTCTCATCAGTAAACGCTCGCCGAATCTCCCAATTTTATAAATAACCGGCTATTTTAA
CATCCGTTGTTATTTCTATGATCGGATTAACCTCACAGGCTTCCGATTTTACATGCTGTTGGGACTCATGATCTGGTT
GCAAAAGTACGATCAGTTTTTGGTAAACCAAAAATGAAAGCAGTCACTCATCCCTCTAATAAATAATTTCAAGTACC
GATATCTGCTGCTCCCGTACGCTTCTATGCTCTGCTCAATCGGACCTCCTTATGTTATCCGTTTTTGGCTGTTTGA
AGCTTCTTCTTAACTGTTAGTACTTGGGGTCAACAGTTACATCAAAAATAAATTTGGGGTTTATGCTGATACCGGA
TTTATTTCAATGTTGCTGTTTCTGCTGTTTCTGCTACGGAATGGGGCTCTGATGATCAACCAAGTGGGAAGTGTG
ACCAACATCAAGTCCCAACCGGATCTGCGTGCCTAAAGACGGGATGTTATTTGGAACCTTCCATTTTCCGGA
GGTCAAAATTAATAATTTGAACAAACCTGATGATTTGCTTTGTTTGGCCGATTTGTAATGGAATGTTGTTATG
TGGCGGCTTATCGTGGATTTGACTGTTGGCTTTTCTGGCATGTTAGTTAAGACTTGGCGTTTTCAAAATGTTGATG
TGTACTTTGTAATTAATAAATTTGGCGAATTTCAATCTGGTGTATTA
```

**A universal vector concept for
a direct genotyping of transgenic organisms and
a systematic creation of homozygous lines**

Frederic Strobl, Anita Anderl & Ernst H.K. Stelzer

Diploid transgenic organisms are either hemizygous or homozygous. Genetic assays are, therefore, necessary to identify the genotype. Our AGameOfClones vector concept uses two phenotypically clearly distinguishable transformation markers embedded in interweaved, but incompatible Lox site pairs. Cre-mediated recombination leads to hemizygous individuals that carry only one marker. In the following generation, heterozygous progeny are identified by the presence of both markers and produce homozygous descendants that are identified by the omission of one marker. We prove our concept in *Tribolium castaneum* by systematically creating multiple homozygous transgenic lines suitable for long-term fluorescence live imaging. Since our approach relies on the universal Cre-Lox system, it works in most diploid model organisms, e.g. rodents, zebrafish, insects and plants. It saves resources, simplifies several aspects of transgenic animal handling and, important for ethical and economic reasons, minimizes the number of wasted animals.

Submitted in August 2017

Research Article

Title

A universal vector concept for a direct genotyping of transgenic organisms and a systematic creation of homozygous lines

Authors

Frederic Strobl, Anita Anderl and Ernst H.K. Stelzer

Affiliations

Frederic Strobl

Physical Biology / Physikalische Biologie (IZN, FB 15)
Buchmann Institute for Molecular Life Sciences (BMLS)
Cluster of Excellence Frankfurt – Macromolecular Complexes (CEF – MC)
Goethe Universität – Frankfurt am Main (Campus Riedberg)
Max-von-Laue-Straße 15 – D-60348 Frankfurt am Main – Germany
frederic.strobl@physikalischebiologie.de (corresponding author)
www.physikalischebiologie.de/people/frederic-strobl ~ www.physikalischebiologie.de/bugcube
Tel: +49 (69) 798 42552

Anita Anderl

Physical Biology / Physikalische Biologie (IZN, FB 15)
Buchmann Institute for Molecular Life Sciences (BMLS)
Cluster of Excellence Frankfurt – Macromolecular Complexes (CEF – MC)
Goethe Universität – Frankfurt am Main (Campus Riedberg)
Max-von-Laue-Straße 15 – D-60348 Frankfurt am Main – Germany
anita.anderl@h-da.de

Ernst H.K. Stelzer

Physical Biology / Physikalische Biologie (IZN, FB 15)
Buchmann Institute for Molecular Life Sciences (BMLS)
Cluster of Excellence Frankfurt – Macromolecular Complexes (CEF – MC)
Goethe Universität – Frankfurt am Main (Campus Riedberg)
Max-von-Laue-Straße 15 – D-60348 Frankfurt am Main – Germany
ernst.stelzer@physikalischebiologie.de (corresponding author)
<http://www.physikalischebiologie.de/people/ernst-hk-stelzer>
Tel: +49 (69) 798 42547, x42545 (Michaela Koller)

Abstract

Diploid transgenic organisms are either hemizygous or homozygous. Genetic assays are, therefore, necessary to identify the genotype. Our AGameOfClones vector concept uses two phenotypically clearly distinguishable transformation markers embedded in interweaved, but incompatible Lox site pairs. Cre-mediated recombination leads to hemizygous individuals that carry only one marker. In the following generation, heterozygous progeny are identified by the presence of both markers and produce homozygous descendants that are identified by the omission of one marker. We prove our concept in *Tribolium castaneum* by systematically creating multiple homozygous transgenic lines suitable for long-term fluorescence live imaging. Since our approach relies on the universal Cre-Lox system, it works in most diploid model organisms, *e.g.* rodents, zebrafish, insects and plants. It saves resources, simplifies several aspects of transgenic animal handling and, important for ethical and economic reasons, minimizes the number of wasted animals.

Main Text

Life sciences, especially cell and developmental biology, rely on model organisms. The most frequently used vertebrates are mouse (*Mus musculus*) and zebrafish (*Danio rerio*). Amongst insects, fruit fly (*Drosophila melanogaster*) and red flour beetle (*Tribolium castaneum*) are the two main species. One of the most important standard techniques is transgenesis, *i.e.* the insertion of recombinant DNA into the genome of the model organism¹. Since model organisms are typically diploid, the genotype has to be considered, which leads to a certain experimental complexity. Usual crossing setups can result in (i) non-transgenic wild-type progeny, (ii) hemizygous transgenic progeny, *i.e.* only the maternal or the paternal chromosome carries the transgene, and (iii) homozygous transgenic progeny, *i.e.* both the maternal and paternal chromosomes carry the transgene. In some cases, the phenotype will reveal the genotype, but usually, either two of the three or even all three outcomes cannot be identified. Transformation markers can be used to separate wild-type from transgenic individuals, but do not allow to distinguish between hemi- and homozygotes. Thus, additional experiments are necessary to determine the genotype, for example genetic assays, which are invasive and require manpower, consumables and time.

In our AGameOfClones (AGOC) vector concept, all genotypes are directly identifiable by purposely produced distinct phenotypes, which permits the systematic creation of homozygous transgenic organisms. The concept relies on two phenotypically clearly distinguishable transformation markers embedded in interweaved, but incompatible Lox site pairs. Cre-mediated recombination results in hemizygous individuals that retain only one of both markers. Thus, they are phenotypically distinguishable from each other and from the wild-type. In the next generation, descendants that express both markers are identified as heterozygous for the transgene. Finally, a cross of two heterozygotes results in homozygous progeny that is selected by the omission of one marker.

Results

Proof-of-principle in the emerging insect model organism *Tribolium castaneum*

The proof-of-principle of the AGOC vector concept relied on the red flour beetle *Tribolium castaneum*, an emerging insect model organism^{2,3}, in conjunction with the piggyBac transposon system^{4,5}, which allows semi-random genomic insertion. We created a piggyBac-based transformation vector termed pAGOC, which contains a mOrange-based⁶ and a mCherry-based⁷ eye-specific⁸ transformation marker, termed mO and mC, respectively. Both fluorescent proteins are spectrally separable by appropriate excitation and emission⁹. Each transformation marker is flanked upstream by a LoxP site¹⁰ and downstream by a LoxN¹¹ site, resulting in interweaved, but incompatible Lox site pairs (Figure 1).

We injected this vector together with a piggyBac transposase-expressing helper vector (pATub'piggyBac) into pre-blastoderm embryos to achieve germline transformation. All survivors, termed F1 potential mosaics, were outcrossed against the wild-type. In six of those crosses, one or more F2 mO-mC hemizygous founder females were found among the progeny, which were outcrossed against wild-type males. The progeny was quantitatively analyzed to confirm that only a single insertion had occurred (Supplementary Table 1) and transgenic progeny was collected to establish six proof-of-principle cultures, which carry the same transgene, but in different genomic locations. These F3 mO-mC pre-recombination hemizygous sublines were termed AGOC #1 to #6. To roughly estimate homozygous viability, two F3 mO-mC pre-recombination hemizygotes were crossed and the progeny was quantitatively evaluated (Supplementary Table 2). Additionally, the insertion location of the transgene was determined in four of the six AGOC sublines (Supplementary Table 3). Until this step, our route did not differ from most standard transgenic organisms establishment procedures.

Systematic creation of homozygous lines

The systematic creation of homozygous transgenic lines (Figure 2, an extensive scheme with all outcomes is provided in Supplementary Figure 1) was performed with all six AGOC sublines and phenotypically documented for #5 and #6 (Figure 3). This procedure is completed within only four further generations.

(1) F3 mO-mC pre-recombination hemizygous females, which carry mO and mC consecutively on the maternal chromosome, were crossed against mCe homozygous helper males of the ICE{HSP68'NLS-Cre} #1 subline (Figure 2 and Figure 3, first row). This subline expresses a nuclear-localized Cre recombinase¹² under control of the *HSP68* promoter¹³ and carries a mCerulean-based¹⁴ eye-specific transformation marker (mCe), resulting in F4 mCe×mO-mC double hemizygotes, in which Cre-mediated recombination occurs (Table 1, 'F3' row). In this hybrid generation, adult beetles show a patchy expression of both markers within their compound eyes (Supplementary Figure 2).

(2) F4 mCe×mO-mC double hemizygous females were outcrossed against wild-type males (Figure 2 and Figure 3, second row). Due to the Cre-mediated recombination in germline cells, this results in F5 mO- and mC-only post-recombination hemizygotes that carry either mO or mC on the maternal chromosome (Table 1, 'F4' row).

(3) F5 mO-only post-recombination hemizygous females were brother-sister crossed against F5 mC-only post-recombination hemizygous males (Figure 2 and Figure 3, third row), resulting in F6 mO/mC heterozygotes, which carry once again both markers (Table 1, 'F5' row). In contrast to the F3 mO-mC pre-recombination hemizygotes, which show the same phenotype but carry both markers consecutively on the maternal chromosome, the F6

mO/mC heterozygotes carry mO on the maternal and mC on the paternal chromosome. This was proven by crossing F6 mO/mC heterozygous females against wild-type males (Table 1, 'F6-S' row).

(4) F6 mO/mC heterozygous females were brother-sister crossed against genotypic identical F6 males (Figure 2 and Figure 3, fourth row), resulting in F7 mO- and mC-only homozygotes that carry either only mO or only mC on both, the maternal and paternal chromosomes (Table 1, 'F6' row). In contrast the F5 mO- and mC-only post-recombination hemizygotes, which show the same phenotype but carry either mO or mC on the maternal chromosome, the F7 mO- and mC-only homozygotes carry the respective marker on the maternal and paternal chromosome (Figure 2 and Figure 3, fifth row). This was proven by crossing F7 mO- and mC-only homozygous females against wild-type males (Table 1, 'F7-O' and 'F7-C' row, respectively). Although some phenotype distributions differed from the theoretical Mendelian values, all expected phenotypes, and thus all expected genotypes, were found in all generations, and both, mO- and mC-only homozygotes, could be obtained for all six AGOC sublines in the F7. The generations and their characteristics are summarized in Supplementary Table 4.

Two controls were performed with the AGOC #5 and #6 sublines to confirm proper functionality of the AGameOfClones vector concept: (i) the F3 to F7 crossing procedure was successfully conducted with inversed genders (Supplementary Figure 3, Supplementary Table 5) and (ii) an alternative mCe helper homozygous subline, ICE{HSP68'NLS-Cre} #2, was used, which carries the same Cre-expressing cassette as the #1 subline, but at a different genomic location (Supplementary Figure 4, Supplementary Table 6).

Systematic creation of functional homozygous AGOC lines and sublines

We expanded the AGOC vector concept by creating three vectors that contain expression cassettes for mEmerald-labeled⁹ Lifeact¹⁵ under control of either the *alpha-tubulin 1* promoter¹⁶, the *zerknüllt 1* promoter¹⁷⁻²¹ or the *actin related protein 5* promoter. Additionally, two vectors were created that contain expression cassettes for either sanyltransferase- or the histone 2B-mEmerald fusion proteins under control of the *alpha-tubulin 1* promoter. With those vectors, five transgenic *Tribolium* lines (with one, three, two, three and four sublines, respectively, *i.e.* thirteen in total) were created, which are primarily designed for fluorescence live imaging of embryonic development. For twelve of the thirteen functional sublines, the systematic creation of homozygous organisms was successful, only the AGOC{ATub'H2B-mEmerald} #4 subline was homozygous sterile (Supplementary Table 7 for the mEmerald-labeled Lifeact sublines, Supplementary Table 8 for the mEmerald-labeled sanyltransferase and histone 2B sublines, see also Supplementary Note).

Live imaging of selected functional homozygous AGOC sublines

We performed long-term fluorescence live imaging of the embryonic development²² with three of the homozygous functional AGOC sublines. We used a digitally scanned laser light sheet-based fluorescence microscope^{23,24} with the previously published sample preparation protocols for *Tribolium*^{25,26}. The AGOC{Zen1'#O(LA)-mEmerald} #2 subline allows the characterization of actin dynamics within the extra-embryonic membranes during gastrulation, visualizing the actomyosin cable that closes the serosa window (Figure 4A, Supplementary Video 1). The AGOC{ARP5'#O(LA)-mEmerald} #1 subline exhibits strong expression in the brain and ventral nerve cord and moderate fluorescence throughout the remaining embryonic tissue (Figure 4B and C, Supplementary Video 2). In contrast, the AGOC{ARP5'#O(LA)-mEmerald} #2 subline does not show any signal in the neuronal system but uniform fluorescence signal during germband elongation, germband retraction and dorsal closure (Figure 4D, Supplementary Video 3).

Discussion

Here, we present the theoretical background of the AGOC vector concept and confirm its functionality in *Tribolium*. The unique feature of our approach is that there are no temporary ambiguities, since all genotypes are directly identified by purposely produced distinct phenotypes. Hence, AGOC-based workflows can be used to systematically generate progeny with relevant genotypes, as exemplarily shown in this study for the creation of homozygous lines within seven generations, *i.e.* with the minimal number of steps. Consequently, our concept confers many advantages that apply not only to *Tribolium* but also to many other model organisms alike: Firstly, our approach saves manpower. For example, genotyping thirty to forty *Tribolium* adults with genetic assays takes about one afternoon²⁷, while processing the same number of individuals under a stereo microscope takes less than ten minutes. Secondly, our concept does not require any further consumables. Thirdly, in genetic assays, the ‘slowest’ individual defines the earliest convenient time point for synchronized genotyping, while our concept also supports desynchronized genotyping. Fourthly, our concept simplifies transgenic organism handling since genotypes are determined directly. Quick and reliable quantification, selection, crossing and/or grouping of organisms can be performed during nearly all developmental stages. Fifthly, our approach is non-invasive and thus favorable when invasive procedures are incompatible with the experimental workflow. It will perform even when sufficient amounts of genomic DNA cannot be obtained without severely injuring or even sacrificing the individual. Sixthly, our approach is straightforward and thus less error-prone than genetic assays. In more than three hundred independent instances, the quantitative evaluation of the progeny always confirmed the phenotypically identified parental genotypes. Seventhly, the insertion location of the transgene does not need to be known. Eighthly, many special cases of transgenesis can be explicitly identified and/or attended (discussed in the Supplementary Note). Ninthly, purposely produced distinct phenotypes foster automation. For example, several approaches for the automated allocation of zebrafish embryos to 96-well plates have been suggested^{28,29}. Automation devices, equipped with a fluorescence detection unit, can be used to sort embryos according to their genotype.

The AGOC vector concept was initially designed for *Tribolium*, but due to the universality of the Cre-Lox system, it should work in most diploid model organisms. These include rodents, zebrafish, various insect species and even plants. Although the 3×P3 promoter is believed to work in a broad variety of animal species⁸, marker adaption is necessary, since fluorophore expression in the visual system is not always a convenient choice. However, many alternatives, such as fur color markers for mouse³⁰, can be considered.

In this study, we used the AGOC vector concept to systematically creating functional homozygous *Tribolium* lines that are designed for fluorescence live imaging of embryonic development. We used transposon-mediated transgenesis with semi-random genomic insertion, but the AGOC vector concept can also be used in insertional mutagenesis knock-out assays. This works independently of whether large-scale transposon-mediated remobilization with subsequent screening is performed³¹, or genes or genetic elements are specifically rendered inoperative, for example by genome engineering techniques such as CRISPR/Cas9, where AGOC-based transgenes can be integrated into targeted genomic locations by utilizing either homology-based repair or non-homologous end-joining^{32,33}.

Studies that utilize genetically manipulated organisms require researchers to maintain their lines for many years. Certain numbers of organisms with known genotypes are required during this period, either to maintain the lines or to use them in experiments. This results in a total demand of hundreds to thousands of organisms. The AGOC vector concept supports well-designed experimental strategies in the following scenarios: Firstly, when generating functional organisms for fluorescence live imaging, transgenic lines are easily maintained as homozygotes since continuous genotyping and curation are not necessary. However, the initial workload following transgenesis necessary to create homozygous lines is typically very high and thus the limiting factor. As shown in this study, those efforts can be significantly reduced by using the AGOC vector concept. Secondly, in knock-out assays of genes that result in homozygous lethality, the respective lines are maintained as hemizygous organisms, which are usually phenotypically inconspicuous. By crossing two hemizygous organisms, one quarter of their progeny is homozygous for the knock-out, half is hemizygous, and one quarter resembles the wild-type. Certain experimental approaches, *e.g.* fluorescence live imaging or transcriptome/proteome analyses, require the researcher to commence with all progeny and to select the homozygous knock-out organisms as soon as discrimination is possible, *i.e.* when the phenotype manifests or when biological material for genetic assays becomes obtainable. By using the AGOC vector concept with appropriate markers, organisms can be selected before the actual experiments are performed. This narrows the efforts down to relevant samples and controls, *i.e.* to one quarter of the currently required number. The AGOC vector concept, broadly adapted to established and emerging model organisms, will contribute significantly to the ethically motivated endeavor to minimize the number of wasted animals.

Materials and Methods

Experimental Design

For transgenesis, the transposase-based piggyBac system³⁴ was chosen, since it is highly active in *Tribolium*. This study utilizes a setup of vectors that are based on *in silico* designed and *de novo* synthesized sequences. This paragraph explains the principal concept of the AGOC system and explains structure and function of the three most important vectors, while the molecular biological procedure is explained in the next section.

All intermediate and transformation vectors used in this study are based on the hypothetical pAVOIAF {#1–#2–#3–#4} vector. This vector is based on the pUC57-Kan vector (GeneBank accession number JF826242.2) and carries an insert in between the AatII and PciI restriction enzyme sites. Only two functional elements from pUC57-Kan remain, the bacterial kanamycin resistance cassette in reverse orientation (neomycin phosphotransferase under control of the beta-lactamase promoter) and the origin of replication. Both elements are necessary for vector propagation in *Escherichia coli*. The insert consists of (i) the piggyBac 3' terminal repeat, (ii) the four-slots (#1 to #4) cloning site and (iii) the 5' piggyBac terminal repeat. The piggyBac terminal repeats have the minimal length (235 bp and 310 bp, respectively) that is necessary for efficient excision and insertion³⁵. The four-slot cloning site consists of four restriction enzyme site pairs. The pairs are XmaI / SpeI for #1, HindIII / XbaI for #2, XhoI / NheI for #3 and AflIII / AvrI for #4. The restriction enzyme sites of each pair are separated by an 18 bp Phe-Arg-Glu-Asp-Asp-Tyr (FREDDY) spacer. For convenience, PmeI restriction enzyme sites are inserted at the beginning and the end of the four-slot multiple cloning site and in between the restriction enzyme pairs. The vector map, with a detailed scheme of the cloning site, is shown in Supplementary Figure 7.

In the pAVOIAF {#1–#2–#3–#4} vector, a mOrange-based eye-specific transformation marker (mO) was inserted into the #3 slot and a mCherry-based eye-specific transformation marker (mC) into the #4 slot, both in reverse orientation. Each marker consists of an expression cassette that is composed of (i) the artificial 3×P3 promoter⁸, (ii) the codon-optimized open reading frames for the respective fluorescence protein, *i.e.* mOrange²⁶ or mCherry⁷, and (iii) the SV40 poly (A) site³⁶. Each marker is flanked upstream by a LoxP site in forward orientation and downstream by a LoxN site in reverse orientation, so that the two transformation markers are embedded in interweaved, but incompatible Lox site pairs¹¹. For convenience, the pAVOIAF {#1–#2–#3–#4} vector that carries mO and mC in the #3 and #4 slot is termed pAGOC. The plasmid map with a detailed scheme of the transformation markers is shown in Supplementary Figure 8. The pAGOC vector was used for transformation to generate proof-of-principle AGOC *Tribolium* lines, but also as an intermediate vector from which other intermediate vectors were evolved by inserting genetic elements into the remaining slots.

We created advanced transformation vectors that enable us to generate functional transgenic *Tribolium* lines for fluorescence live imaging of embryonic development. In the #2 slot of the pAGOC vector, a modular fluorescence protein expression cassette was inserted, which consists of (i) a two-slot subcloning site that is composed of a promoter (#P) slot and an open reading frame (#O) slot, (ii) an 9 bp Ala-Ala-Ala linker, (iii) the codon-optimized mEmerald³⁷ open reading frame and (iv) an elongated variant of the SV40 poly(A) site³⁶. The #P slot can be accessed by the AscI / FseI restriction enzyme site pair, or alternatively scarless by the double BtgZI restriction enzyme site pair. The #O slot carries the open reading frame for the *Saccharomyces cerevisiae* Lifeact peptide¹⁵ per default and can be accessed by the FseI / NotI restriction enzyme site pair. The mEmerald open reading frame can also be accessed by the NotI / SbfI restriction enzyme site pair. For convenience, the pAGOC vector that carries the described fluorescence protein expression cassette in the #2 slot is termed pAGOC {#P'#O(LA)-

mEmerald}. The vector map, with a detailed scheme of the modular fluorescence protein expression cassette, is shown in Supplementary Figure 9. The #P slot can now be filled with any exogenous or endogenous promoter, which determines the spatiotemporal activity pattern of the fluorescence expression cassette during embryonic development. For the #O slot, the Lifeact open reading frame can be replaced with any open reading frame that changes the subcellular localization of the fluorescence protein. If the element is not changed, the default Lifeact peptide will guide the fluorescent protein to the actin cytoskeleton.

Molecular biology

In this study, 24 vectors plus the commercial subcloning vector pGEM-T Easy (A1360, Promega) were used. The vectors are listed in Supplementary Table 12, vector evolution is outlined in Supplementary Figure 10. Three of those vectors were ordered as gene synthesis plasmids that contained *in silico* designed and *de novo* synthesized sequences, two were previously published and obtained from the respective laboratories or from Addgene, four were promoter library vectors (built from genomic DNA and the pGEM-T Easy vector), two were open reading frame (ORF) library vectors (built from cDNA and the pGEM-T Easy vector), while the remaining thirteen vectors derive from the mentioned vectors. For all PCRs, the Phusion High Fidelity DNA polymerase (M0530L, New England BioLabs) was used, and for all ligations the T4 DNA ligase (M0202L, New England BioLabs or provided with the pGEM-T Easy vector). All cloning primers are listed in Supplementary Table 13.

Molecular biology: the promoter and open reading frame library vectors

All library vectors are based on pGEM-T Easy. The four promoter library vectors were created by amplifying the sequences from genomic DNA with the respective extraction PCR primer pairs (C1 for ATub', C2 for Zen1', C3 for ARP5' and C4 for HSP68') and the two open reading frame library vectors were created by amplifying the sequences from cDNA with the respective extraction PCR primer pairs (C5 for 'SiaTr and C5 for 'H2B). Amplification was followed by A-tailing using the Recombinant Taq DNA polymerase (10342020, Thermo Fisher Scientific) and subsequent ligation into pGEM-T Easy. The resulting vectors were termed pTC-ATub'-GEM-T Easy, pTC-Zen1'-GEM-T Easy, pTC-ARP5'-GEM-T Easy, pTC-HSP68'-GEM-T Easy, pTC-'SiaTr-GEM-T Easy and pTC-'H2B-GEM-T Easy and had sizes of 3,633 bp, 4,599 bp, 5,516 bp, 3,778 bp, 4,358 bp and 3,389 bp, respectively. To create the hybrid promoter / open reading frame library vectors, the sequences were amplified from the library vectors or the 6,757 bp pTriEx-HTNC vector¹² with the respective fusion PCR primer pairs (either C7 for HSP68' / 'NLS-Cre, or C8 for ATub' / 'H2B) and fused together in a secondary PCR reaction using both PCR products as a template and the promoter forward primer (C7-1 or C8-1, respectively) and the open reading frame reverse primer (C7-4 or C8-4, respectively). The primers introduce upstream an AscI and downstream a NotI restriction enzyme site or upstream a NheI and downstream a XhoI restriction enzyme site, respectively. The fusion PCR product was then inserted into pGEM-T Easy as described above. The resulting vectors were termed pTC-ATub'H2B-GEM-T Easy and pTC-HSP68'NLS-Cre-GEM-T Easy and had sizes of 4,010 bp and 5,073 bp, respectively. Insert integrity of all library vectors was controlled by sequencing.

Molecular biology: the pUC[AGOC] and pAGOC vectors

The 5,678 bp pUC57[AGOC] vector was ordered as a *de novo* gene synthesis construct (Genewiz). A 3,277 bp insert was inserted into the unique NdeI and PstI restriction enzyme sites of pUC57-Kan, it consists of (i) the 4 bp TTAA 3' piggyBac excision/insertion target sequence, (ii) the 235 bp piggyBac 3' terminal repeat, (iii) the 2,724 bp four-slots (#1 to #4) cloning site, in which the mOrange-based and mCherry-based eye-specific transformation markers (mO and mC, respectively) were already inserted (both in reverse orientation and thus

tail-to-head) into #3 and #4, (iv) the 310 bp 5' piggyBac terminal repeat and (v) the 4 bp TTAA 5' piggyBac excision/insertion target sequence. The insert was amplified with primer pair C9, which introduced upstream an AatII and downstream a PciI restriction enzyme site. The PCR product and pUC57[AGOC] were digested accordingly, and the insert was reintegrated into the vector, reducing the vector size considerably by removing 629 functionless bp. The resulting 5,049 bp vector was termed pAGOC and used (i) for germline transformation to create proof-of-principle lines, and (ii) as an intermediate vector for further cloning operations.

Molecular biology: the pGS[#P'#O(LA)-mEmerald] and pAGOC{#P'#O(LA)-mEmerald} vectors

The 4,111 bp the pGS[#P'#O(LA)-mEmerald] vector was ordered as a *de novo* gene synthesis construct (Thermo Fisher Scientific). A 1,821 bp insert was inserted into the unique SfiI restriction enzyme site of pMK-RQ (Thermo Fisher Scientific), it consists of (i) a 6 bp HindIII restriction enzyme site, (ii) the 107 bp #P'#O two-slot subcloning site, (iii) a 9 bp linker that includes a NotI restriction enzyme site, (iv) the 714 bp codon-optimized mEmerald open reading frame, (v) a 8 bp SbfI restriction enzyme site, (vi) a 983 bp elongated variant of the SV40 poly(A) site and (vii) a 6 bp XbaI restriction enzyme site. The insert was cut from the backbone with HindIII / XbaI and pasted into #3 of the pAGOC vector. The resulting 6,852 bp vector was termed pAGOC{#P'#O(LA)-mEmerald} and used as an intermediate vector for further cloning operations.

Molecular biology: the pAGOC{ATub'#O(LA)-mEmerald}, pAGOC{Zen1'#O(LA)-mEmerald} and pAGOC{ARP5'#O(LA)-mEmerald} vectors

Three transformation vectors were created that allowed the expression of mEmerald-labeled Lifeact (LA) in different spatiotemporal patterns. Therefore, the promoter sequences were amplified from the library vectors with the respective primer pairs (C10 for ATub', C11 for Zen1' and C12 for ARP5'), which introduced upstream an AscI and downstream a BsmBI (ATub') or BsaI (Zen1', ARP5') restriction enzyme site. The PCR product was digested accordingly, and the pAGOC{#P'#O(LA)-mEmerald} vector was digested with BtgZI, which led to compatible overhangs and allowed scarless insertion of the promoter sequences into the #P slot. The resulting vectors were termed pAGOC{ATub'#O(LA)-mEmerald}, pAGOC{Zen1'#O(LA)-mEmerald} and pAGOC{ARP5'#O(LA)-mEmerald}, had sizes of 7,400 bp, 8,367 bp and 9,276 bp, respectively, and were used for germline transformation.

Molecular biology: the pAGOC{#P'SiaTr-mEmerald} and pAGOC{ATub'SiaTr-mEmerald} vectors

One transformation vector was created that allowed the expression of a mEmerald-labeled sialyltransferase ubiquitously throughout the whole embryonic development. The sialyltransferase open reading frame sequence was amplified from the pTC-'SiaTr-GEM-T Easy vector with primer pair C13, which introduced upstream an FseI and downstream a NotI restriction enzyme site. The PCR product and the pAGOC{#P'#O(LA)-mEmerald} vector were digested accordingly and the insert was inserted into the #O slot of the vector. The resulting 8,106 bp vector was termed pAGOC{#P'SiaTr-mEmerald} and used as an intermediate vector for further cloning operations. The alpha-tubulin promoter sequence was amplified from the pTC-ATub'-GEM-T Easy vector with primer pair C10, which introduced upstream an AscI and downstream a BsaI restriction enzyme site. The PCR product was digested accordingly, and the pAGOC{#P'SiaTr-mEmerald} vector was digested with BtgZI, which led to compatible overhangs and allowed scarless insertion of the promoter sequence into the #P slot of the intermediate vector. The resulting 8,654 bp vector was termed pAGOC{ATub'SiaTr-mEmerald} and used for germline transformation.

Molecular biology: the pAGOC{ATub'H2B-mEmerald} vector

One transformation vector was created that allowed the expression of mEmerald-labeled histone 2B subunits ubiquitously throughout the whole embryonic development. The alpha-tubulin promoter / histone 2B open reading frame sequence was cut from pTC-ATub'H2B-GEM-T Easy with AscI and NotI and inserted into the #P'#O slots of the accordingly digested pAGOC{#P'#O(LA)-mEmerald} vector. The resulting 7,718 bp vector was termed pAGOC{ATub'H2B-mEmerald} and used for germline transformation.

Molecular biology: the pAVOIAF{#1-#2-HSP68'NLS-Cre-mC}, pGS[ACOS] and pICE{HSP68'NLS-Cre} vectors

The heat shock protein 68 promoter / NLS Cre recombinase open reading frame sequence was cut from pTC-HSP68'H2B-GEM-T Easy with NheI and XhoI and inserted (in reverse orientation) into the #3 slot of the accordingly digested pAGOC vector, replacing mO. The resulting 5,781 bp vector was termed pAVOIAF{#1-#2-HSP68'NLS-Cre-mC} and used as an intermediate vector for further cloning operations. The 4,928 bp pGS[ACOS] vector was ordered as a *de novo* gene synthesis construct (Thermo Fisher Scientific). A 2,650 bp insert was inserted into the unique SfiI restriction enzyme site of pMK-RQ (Invitrogen), it consists (beside other elements) of a mCerulean-based eye-specific transformation marker (mCe) that is composed of (i) the 283 bp artificial 3×P3 promoter, (ii) the 717 bp codon-optimized open reading frame for mCerulean2¹⁴ and (iii) the 241 bp SV40 poly(A) site. The marker was amplified with primer pair C14, which introduced upstream an AflII and downstream an AvrII restriction enzyme site. The PCR product was digested accordingly and inserted into the #4 slot of the pAVOIAF{#1-#2-HSP68'NLS-Cre-mC} vector, replacing mC. The resulting 5,709 bp vector was termed pICE{HSP68'NLS-Cre} and used for germline transformation to create the Cre recombinase-expressing helper lines.

Molecular biology: the pATub'piggyBac vector

To create the piggyBac transposase-expressing helper vector, the alpha-tubulin 1 promoter and the piggyBac open reading frame fragment were amplified from the pTC-ATub'-GEM-T Easy and the 4,971 bp pBSII-IFP-ORF³⁸ vectors with the C15 primer pairs and fused together in a secondary PCR reaction using both PCR products as a template and the promoter forward primer (C15-1) and the open reading frame reverse primer (C15-4). The primers introduce upstream a Sall and downstream a BglII restriction enzyme site, respectively. The fusion PCR product was digested and then reintegrated into the accordingly digested pBSII-IFP-ORF vector. The resulting 5,511 bp vector was termed pATub'piggyBac and used as the transposase-expressing helper vector during germline transformation.

***Tribolium* strains and rearing**

In this study, the *Tribolium castaneum* Plain-White-As-Snow (PWAS) strain was used in both, as a donor for genomic DNA and mRNA but also to create transgenic lines. This strain derives from the white-eyed Pearl mutant strain³⁹, but also carries the light ocular diaphragm mutation⁴⁰, so that the adult eyes appear completely non-pigmented. Adult animals were kept in groups of 150-500 individuals on growth medium (full grain wheat flour (113061006, Demeter) supplemented with 5% (wt/wt) inactive dry yeast (62-106, Flystuff) in 1 l glass bottles in a 12:00 h light / 12:00 h darkness cycle at 25 °C and 70% relative humidity (DR-36VL, Percival Scientific).

***Tribolium* genomic DNA and mRNA extraction**

Approximately 20 adults (40 mg) were starved for 24 h before genomic DNA was extracted with the Blood and Tissue Kit (69504, Qiagen) according to the manufacturer's instructions. From approximately 10 adults (20 mg), mRNA was extracted with TRIzol Reagent (15596026, Thermo Fisher Scientific) and cDNA was transcribed with the Superscript III reverse transcriptase (12080093, Thermo Fisher Scientific) using random hexamer primers.

Germline transformation

Approximately 500-600 F0 *Tribolium* adults of the PWAS strain were incubated on 405 fine wheat flour (113061036, Demeter, Darmstadt, Germany) supplemented with 5% (wt/wt) inactive dry yeast (62-106, Flystuff, San Diego, CA, USA) at 25°C and 70% relative humidity in light for 2 h. After the incubation period, the adults were removed and the embryos (around 700-900) were extracted from the flour and incubated another hour as stated above. Afterwards, they were transferred to a 100 µm cell strainer (352360, BD Biosciences) and washed in a 6-well plate as follows: (i) in autoclaved tap water for 1 min, (ii) in 10% (vol/vol) sodium hypochlorite (425044-250ML, Sigma Adlrlich) in autoclaved tap water for 10 s, (iii) in autoclaved tap water three times for 1 min and (iv) stored in autoclaved tap water. Next, the embryos were lined up on object slides within the next hour (10 object slides with about 50 embryos each, totaling at approximately 500 embryos per round of germline transformation) with their posterior pole pointing towards the elongated edge of the slide. The embryos were injected with a mixture of 500 ng/µl transformation vector and 400 ng/µl ATub'piggyBac vector in injection buffer (5 mM KCl, 1 mM KH₂PO₄ in ddH₂O, pH 8.8). For injection, a microinjector (FemtoJet, Eppendorf) and 0.7 µm outer diameter capillaries (Femtotips II, Eppendorf) with an injection pressure of 400-800 hPa were used. After injection, the object slides with embryos were placed in Petri dishes on a 5 mm 1% (wt/vol) agarose in tap water 'platform' and incubated at 32°C. After 3 days, hatched larvae, *i.e.* F1 potential mosaics, were collected and raised individually in single wells of 24-well plates as described above. Germline transformation resulted in a total of seven lines with twenty-one sublines, which are summarized in Supplementary Table 14.

Crossing procedure, insert number determination cross and homozygous viability cross

All crossings were single-pair with one female and one male adult. They were performed in small glass vials that were filled with 1.5 g or 2.5 g (F4 cross) of growth medium. The progeny was singularized during the larval or pupal stages, presence of eye markers and gender were determined either in the pupal or adult stage under a fluorescence stereo microscope (SteREO Discovery.V8, Zeiss) with the appropriate filter set (Supplementary Table 15). Eye images in the reflected light or fluorescence channels were taken for each cross in parallel with the controls (Supplementary Figure 11).

F1 potential mosaics were crossed against PWAS wild-type adults, and their F2 progeny was screened for founder individuals. Founder individuals were once again outcrossed against the wild-type to determine the number of inserts by evaluating the ratio of transgenic F3 progeny, whereas a transgene distribution of 60% or less was interpreted as only one insert was present. A homozygous viability cross was performed by crossing two F3 heterozygous adults and subsequent evaluation of the ratio of transgenic progeny, whereas a transgene distribution of 70% or more was interpreted that the line is homozygous viable. The AGOC systematic crossing procedure from the F3 to the F7 is explained within the main text. Beside the procedure-related crosses, F6 mO/mC heterozygous females and F7 mO- and mC-only homozygous females were outcrossed against the wild-type males to determine marker segregation and prove that those individuals are heterozygous or homozygous for the transgene, respectively.

Determination of insertion junction via inverse PCR

To determine the insertion junction of the piggyBac-based transgene, the inverse polymerase chain reaction approach was chosen^{41,42}. At first, inverse PCR was performed for the junction at the 5' piggyBac terminal repeat with the I-5' primer pair (Supplementary Table 16) with up to eight restriction enzymes, and if not successful, also at the 3' piggyBac terminal repeat with the I-3' primer pair (Supplementary Table 16) with up to six different restriction enzymes. PCR products were extracted from the gel, A-tailed, ligated into pGEM-T Easy and sequenced. For each successful inverse PCR, a control PCR at the respective other side was performed (*i.e.* the 3' piggyBac terminal repeat when the 5' inverse PCR was successful or the 5' piggyBac terminal repeat when the 3' inverse PCR was successful). For the control PCR, location-specific primers were used (Supplementary Table 16). Inverse PCR worked in ten out of nineteen lines, for four out of six proof-of-principle lines and six out of thirteen functional lines. The sequencing results were aligned to the *Tribolium* genome⁴³ via the BeetleBase^{44,45} BLAST.

Light sheet-based fluorescence microscopy

Out of the thirteen functional AGOC sublines, three were characterized with long-term fluorescence live imaging. The AGOC{ATub'#O(LA)-mEmerald} #1 subline will be part of another study, the AGOC{ATub'SiaTr-mEmerald} sublines did not exhibit a sufficiently high fluorescence signal, and some AGOC{ATub'H2B-mEmerald} sublines have been analyzed previously⁴⁶. Therefore, we imaged the AGOC{Zen1'#O(LA)-mEmerald} #2 subline, which exhibited the strongest fluorescence signal out of the three sublines, and both AGOC{ARP5'#O(LA)-mEmerald} sublines, since they showed a slightly varying expression pattern. Fluorescence live imaging was performed with digitally scanned laser light sheet-based fluorescence microscopy^{23,24} as described previously for *Tribolium*^{25,26}. In brief, embryo collection was performed with the F7+ continuative mC-only homozygous cultures for one hour at 25°C, and embryos were incubated for 15 hours at 25°C. Sample preparation took approximately one hour at room temperature (23±1°C), so that embryos were at the beginning of gastrulation, when the uniform blastoderm turns into the rearranged blastoderm. Embryos were recorded along four directions (in the orientations 0°, 90°, 180° and 270°) with an interval of 30 minutes for up to four days at room temperature, covering the embryogenetic events gastrulation and germband elongation completely and germband retraction partially. All embryos survived the imaging procedure, developed to healthy and fertile adults, and when outcrossed against the wild-type, produced only transgenic progeny that was also fertile. Metadata for the three datasets is provided in Supplementary Table 17.

References

11. Gama Sosa, M. A., De Gasperi, R. & Elder, G. A. Animal transgenesis: an overview. *Brain Struct. Funct.* **214**, 91–109 (2010).
2. Klingler, M. *Tribolium*. *Curr. Biol.* **14**, R639–40 (2004).
3. Brown, S. J. *et al.* The red flour beetle, *Tribolium castaneum* (Coleoptera): A model for studies of development and pest biology. *Cold Spring Harb. Protoc.* **4**, (2009).
4. Lorenzen, M. D. *et al.* piggyBac-mediated germline transformation in the beetle *Tribolium castaneum*. *Insect Mol. Biol.* **12**, 433–40 (2003).
5. Berghammer, A. J., Weber, M., Trauner, J. & Klingler, M. Red flour beetle (*Tribolium*) germline transformation and insertional mutagenesis. *Cold Spring Harb. Protoc.* **2009**, pdb.prot5259 (2009).
6. Shaner, N. C. *et al.* Improving the photostability of bright monomeric orange and red fluorescent proteins. *Nat. Methods* **5**, 545–51 (2008).
7. Shaner, N. C. *et al.* Improved monomeric red, orange and yellow fluorescent proteins derived from *Discosoma* sp. red fluorescent protein. *Nat. Biotechnol.* **22**, 1567–72 (2004).
8. Berghammer, A. J., Klingler, M. & Wimmer, E. A. Genetic techniques: A universal marker for transgenic insects. *Nature* **402**, 370–371 (1999).
9. Shaner, N. C., Steinbach, P. A. & Tsien, R. Y. A guide to choosing fluorescent proteins. *Nat. Methods* **2**, 905–9 (2005).
10. Hamilton, D. L. & Abremski, K. Site-specific recombination by the bacteriophage P1 lox-Cre system. *J. Mol. Biol.* **178**, 481–486 (1984).
11. Livet, J. *et al.* Transgenic strategies for combinatorial expression of fluorescent proteins in the nervous system. *Nature* **450**, 56–62 (2007).
12. Peitz, M., Pfannkuche, K., Rajewsky, K. & Edenhofer, F. Ability of the hydrophobic FGF and basic TAT peptides to promote cellular uptake of recombinant Cre recombinase: a tool for efficient genetic engineering of mammalian genomes. *Proc. Natl. Acad. Sci. U. S. A.* **99**, 4489–94 (2002).
13. Schinko, J. B., Hillebrand, K. & Bucher, G. Heat shock-mediated misexpression of genes in the beetle *Tribolium castaneum*. *Dev. Genes Evol.* **222**, 287–98 (2012).
14. Markwardt, M. L. *et al.* An improved cerulean fluorescent protein with enhanced brightness and reduced reversible photoswitching. *PLoS One* **6**, e17896 (2011).
15. Riedl, J. *et al.* Lifeact: a versatile marker to visualize F-actin. *Nat. Methods* **5**, 605–7 (2008).
16. Siebert, K. S., Lorenzen, M. D., Brown, S. J., Park, Y. & Beeman, R. W. Tubulin superfamily genes in *Tribolium castaneum* and the use of a Tubulin promoter to drive transgene expression. *Insect Biochem. Mol. Biol.* **38**, 749–755 (2008).
17. van der Zee, M., Berns, N. & Roth, S. Distinct functions of the *Tribolium zerknüllt* genes in serosa specification and dorsal closure. *Curr. Biol.* **15**, 624–36 (2005).
18. Jacobs, C. G. C. C. & van der Zee, M. Immune competence in insect eggs depends on the extraembryonic serosa. *Dev. Comp. Immunol.* **41**, 263–9 (2013).
19. Sharma, R., Beermann, A. & Schröder, R. The dynamic expression of extraembryonic marker genes in the beetle *Tribolium castaneum* reveals the complexity of serosa and amnion formation in a short germ insect. *Gene Expr. Patterns* **13**, 362–71 (2013).
20. Panfilio, K. a, Oberhofer, G. & Roth, S. High plasticity in epithelial morphogenesis during insect dorsal closure. *Biol. Open* **2**, 1108–18 (2013).
21. Hilbrant, M., Horn, T., Koelzer, S. & Panfilio, K. A. The beetle amnion and serosa functionally interact as apposed epithelia. *Elife* **5**, (2016).
22. Strobl, F. & Stelzer, E. H. Long-term fluorescence live imaging of *Tribolium castaneum* embryos: principles, resources, scientific challenges and the comparative approach. *Curr. Opin. Insect Sci.* **18**, 17–26 (2016).
23. Keller, P. J., Schmidt, A. D., Wittbrodt, J. & Stelzer, E. H. K. Reconstruction of zebrafish early embryonic

development by scanned light sheet microscopy. *Science* **322**, 1065–9 (2008).

24. Keller, P. J. & Stelzer, E. H. K. Digital scanned laser light sheet fluorescence microscopy. *Cold Spring Harb. Protoc.* **2010**, pdb.top78 (2010).
25. Strobl, F. & Stelzer, E. H. K. Non-invasive long-term fluorescence live imaging of *Tribolium castaneum* embryos. *Development* **141**, 2331–2338 (2014).
26. Strobl, F., Schmitz, A. & Stelzer, E. H. K. Live imaging of *Tribolium castaneum* embryonic development using light-sheet-based fluorescence microscopy. *Nat. Protoc.* **10**, 1486–1507 (2015).
27. Strobl, F., Ross, J. A. & Stelzer, E. H. K. Non-lethal genotyping of *Tribolium castaneum* adults using genomic DNA extracted from wing tissue. *PLoS One* **12**, e0182564 (2017).
28. Graf, S. F., Hötzel, S., Liebel, U., Stemmer, A. & Knapp, H. F. Image-based fluidic sorting system for automated Zebrafish egg sorting into multiwell plates. *J. Lab. Autom.* **16**, 105–11 (2011).
29. Mandrell, D. *et al.* Automated zebrafish chorion removal and single embryo placement: optimizing throughput of zebrafish developmental toxicity screens. *J. Lab. Autom.* **17**, 66–74 (2012).
30. Zheng, B., Mills, A. A. & Bradley, A. A system for rapid generation of coat color-tagged knockouts and defined chromosomal rearrangements in mice. *Nucleic Acids Res.* **27**, 2354–2360 (1999).
31. Trauner, J. *et al.* Large-scale insertional mutagenesis of a coleopteran stored grain pest, the red flour beetle *Tribolium castaneum*, identifies embryonic lethal mutations and enhancer traps. *BMC Biol.* **7**, 73 (2009).
32. Gilles, A. F. & Averof, M. Functional genetics for all: engineered nucleases, CRISPR and the gene editing revolution. *Evodevo* **5**, 43 (2014).
33. Gilles, A. F., Schinko, J. B. & Averof, M. Efficient CRISPR-mediated gene targeting and transgene replacement in the beetle *Tribolium castaneum*. *Development* **142**, 2832–9 (2015).
34. Handler, A. M. Use of the piggyBac transposon for germ-line transformation of insects. *Insect Biochem. Mol. Biol.* **32**, 1211–1220 (2002).
35. Li, X. *et al.* piggyBac internal sequences are necessary for efficient transformation of target genomes. *Insect Mol. Biol.* **14**, 17–30 (2005).
36. van den Hoff, M. J., Labruyère, W. T., Moorman, A. F. & Lamers, W. H. Mammalian gene expression is improved by use of a longer SV40 early polyadenylation cassette. *Nucleic Acids Res.* **21**, 4987–8 (1993).
37. Tsien, R. Y. The green fluorescent protein. *Annu. Rev. Biochem.* **67**, 509–44 (1998).
38. Yoshida, Y., Takahashi, K., Okita, K., Ichisaka, T. & Yamanaka, S. Hypoxia Enhances the Generation of Induced Pluripotent Stem Cells. *Cell Stem Cell* **5**, 237–241 (2009).
39. Grubbs, N., Haas, S., Beeman, R. W. & Lorenzen, M. D. The ABCs of eye color in *Tribolium castaneum*: orthologs of the *Drosophila* white, scarlet, and brown Genes. *Genetics* **199**, 749–59 (2015).
40. Mocelin, G. & Stuart, J. J. Crossover Suppressors in *Tribolium castaneum*. *J. Hered.* **87**, 27–34 (1996).
41. Triglia, T., Peterson, M. G. & Kemp, D. J. A procedure for in vitro amplification of DNA segments that lie outside the boundaries of known sequences. *Nucleic Acids Res.* **16**, 8186 (1988).
42. Ochman, H., Gerber, A. S. & Hartl, D. L. Genetic applications of an inverse polymerase chain reaction. *Genetics* **120**, 621–3 (1988).
43. Richards, S. *et al.* The genome of the model beetle and pest *Tribolium castaneum*. *Nature* **452**, 949–55 (2008).
44. Wang, L., Wang, S., Li, Y., Paradesi, M. S. R. & Brown, S. J. BeetleBase: the model organism database for *Tribolium castaneum*. *Nucleic Acids Res.* **35**, D476-9 (2007).
45. Kim, H. S. *et al.* BeetleBase in 2010: revisions to provide comprehensive genomic information for *Tribolium castaneum*. *Nucleic Acids Res.* **38**, D437-42 (2010).
46. Strobl, F., Klees, S. & Stelzer, E. H. K. Light Sheet-based Fluorescence Microscopy of Living or Fixed and Stained *Tribolium castaneum* Embryos. *J. Vis. Exp.* (2017). doi:10.3791/55629

Acknowledgements:

We thank J. Alexander Ross, Katharina Hötte, Berit Reinhardt and Sigrun Becker for their valuable support. The pBSII-IFP-ORF vector was a kind gift from M. Fraser (Notre Dame, Indiana, United States).

Funding

The research was funded by the Cluster of Excellence – Frankfurt am Main for Macromolecular Complexes (CEF-MC, EXC 115) granted in part to EHKS at the Buchmann Institute for Molecular Life Sciences (BMLS) at the Goethe Universität – Frankfurt am Main by the Deutsche Forschungsgemeinschaft (DFG).

Competing Financial Interest

F.S. and E.H.K.S. have filed a patent application for the AGOC vector concept (2017061214242700DE).

Author Contributions

F.S. and E.H.K.S. conceived the research. F.S. designed the vector concept, created most of the vectors and transgenic lines, conducted the crossing and control experiments and performed live imaging of two transgenic lines. A.A. created three vectors and four transgenic sublines and performed live imaging of one transgenic subline. F.S. and E.H.K.S. wrote the manuscript, with input from A.A.

Display Items

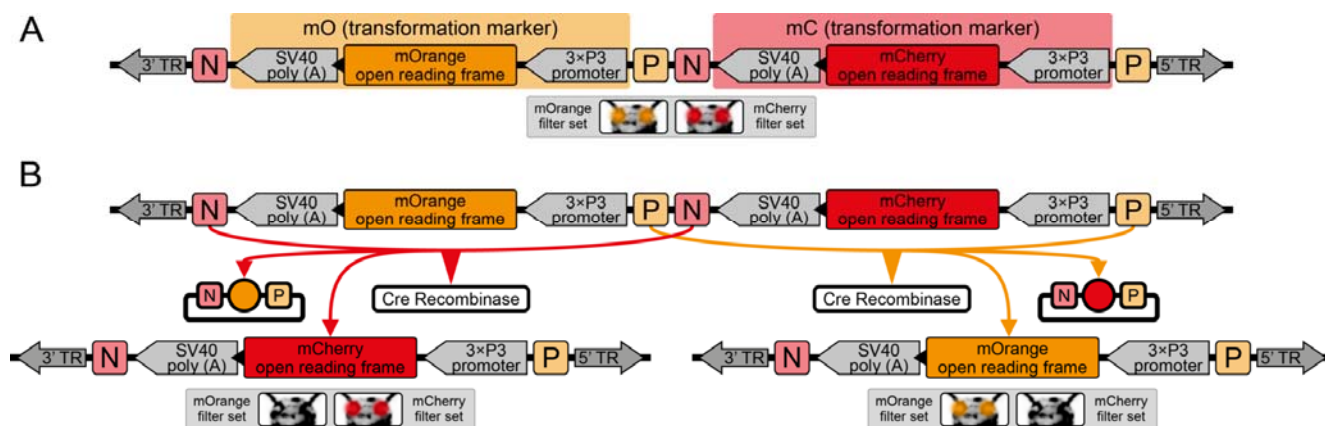


Figure 1 – The AGameOfClones vector concept within the piggyBac-based pAGOC transformation vector for *Tribolium*. (A) Two fluorescence-based transformation markers, mO and mC, which are spectrally distinct, are embedded into a piggyBac-based transformation vector that is characterized by 3' and 5' terminal repeats (TR) necessary for genomic insertion. The markers are based on the artificial 3×P3 promoter, which drives expression in the neuronal system, the open reading frame for the respective fluorescence protein, *i.e.* mOrange or mCherry, and the SV40 poly (A) site. Each transformation marker is flanked upstream by a LoxP and downstream by a LoxN site, which results in interweaved Lox site pairs. In *Tribolium* adults, the fluorescence phenotype is detected in the eyes using appropriate filter sets. (B) Cre-mediated recombination leads to the excision of one of either markers from the genome. When one marker is removed, the other marker remains within the genome, since the two remaining Lox sites, *i.e.* a LoxP and a LoxN site, are incompatible. *Tribolium* adults that underwent recombination give rise to progeny where only one marker is expressed in the eyes.

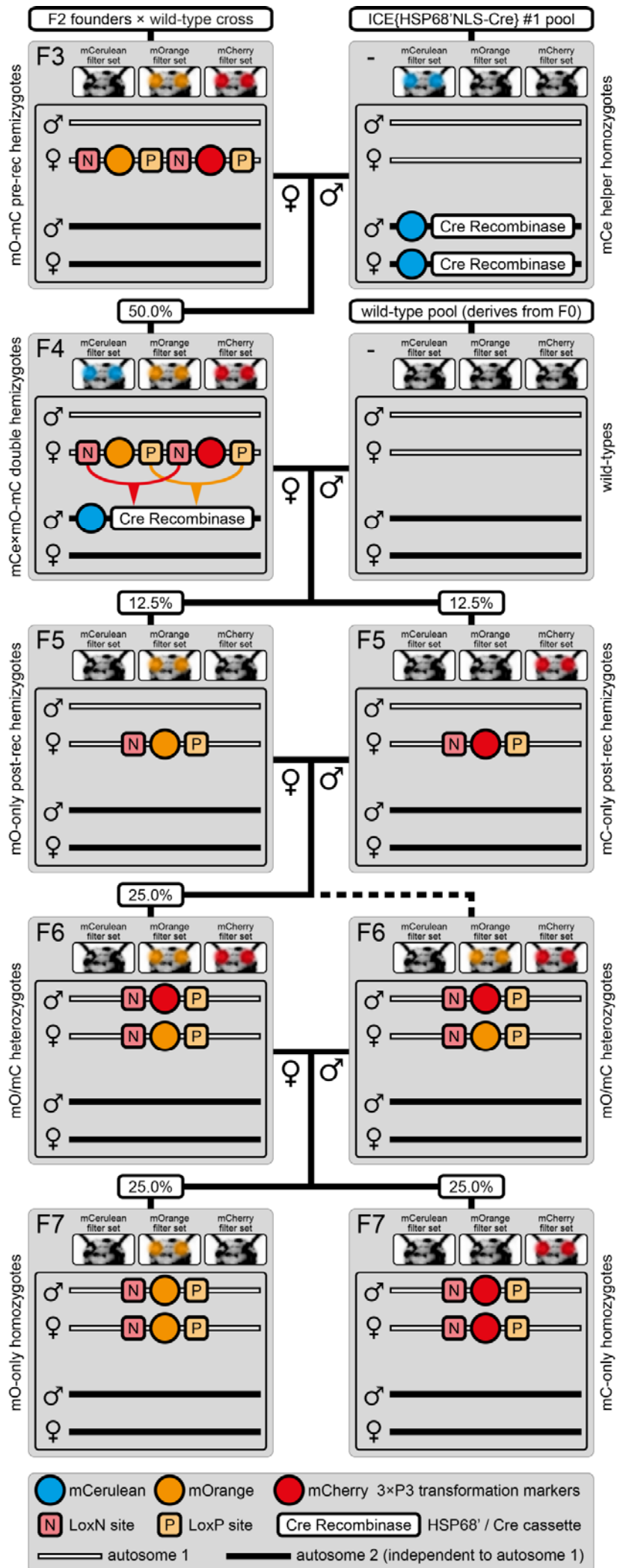


Figure 2 – The AGameOfClones F3 to F7 crossing procedure that allows the systematic creation of homozygous transgenic organisms. The rounded rectangle illustrates the genotype for two independent autosomes, white bars represent the AGOC transgene location and black bars the helper transgene location. A F2 mO-mC founder female \times wild-type male outcross results in F3 mO-mC pre-recombination hemizygotes that carry mO and mC consecutively on one chromosome. A F3 mO-mC pre-recombination hemizygous female \times mCe homozygous helper male cross gives rise to F4 mCe \times mO-mC double hemizygotes, in which one marker is removed through Cre-mediated recombination. A F4 mCe \times mO-mC double hemizygous female \times wild-type male outcross generates F5 mO- and mC-only post-recombination hemizygotes. Next, a F5 mO-only post-recombination hemizygous female \times F5 mC-only post-recombination hemizygous male brother-sister cross results in a certain fraction of F6 mO/mC heterozygous progeny. Finally, a F6 mO/mC heterozygous female \times a F6 mO/mC heterozygous male brother-sister cross generates F7 mO- and mC-only homozygous progeny. The percentage boxes show the theoretical ratio of the progeny that carry the respective genotype.

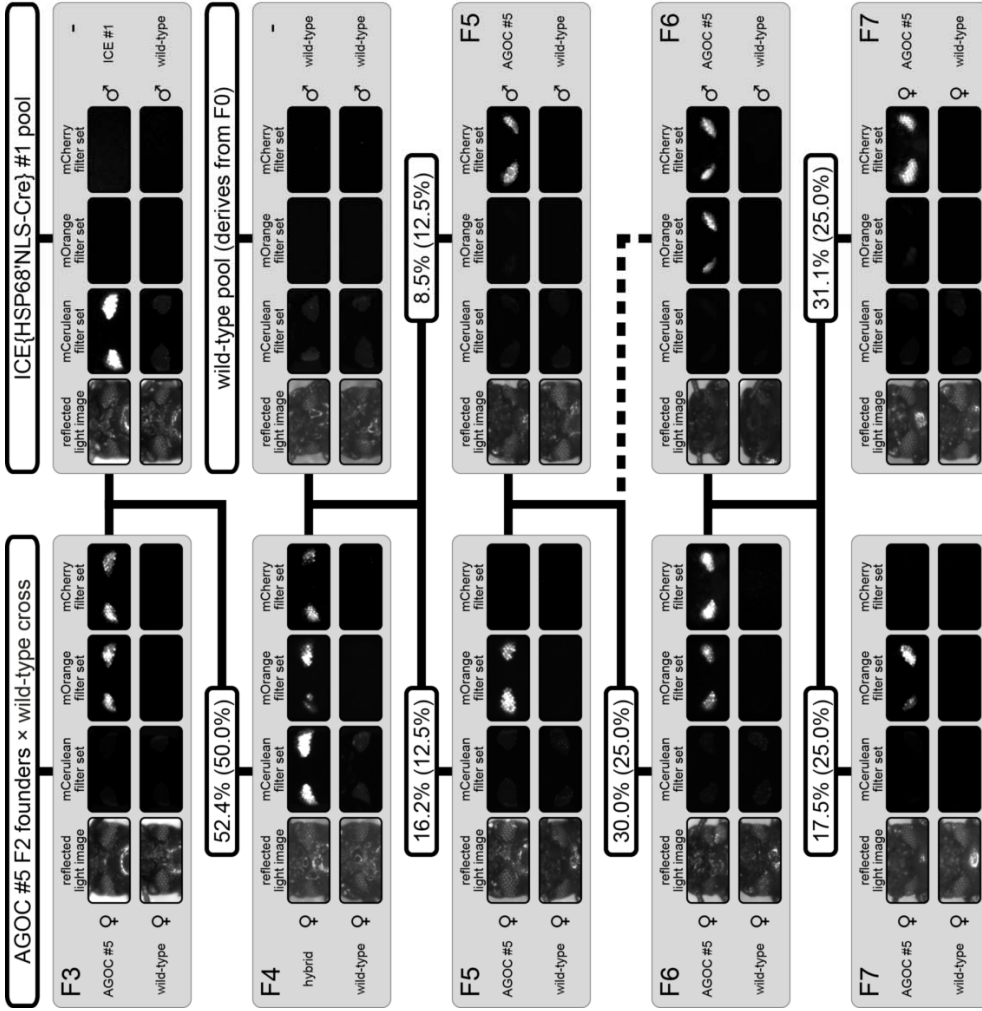
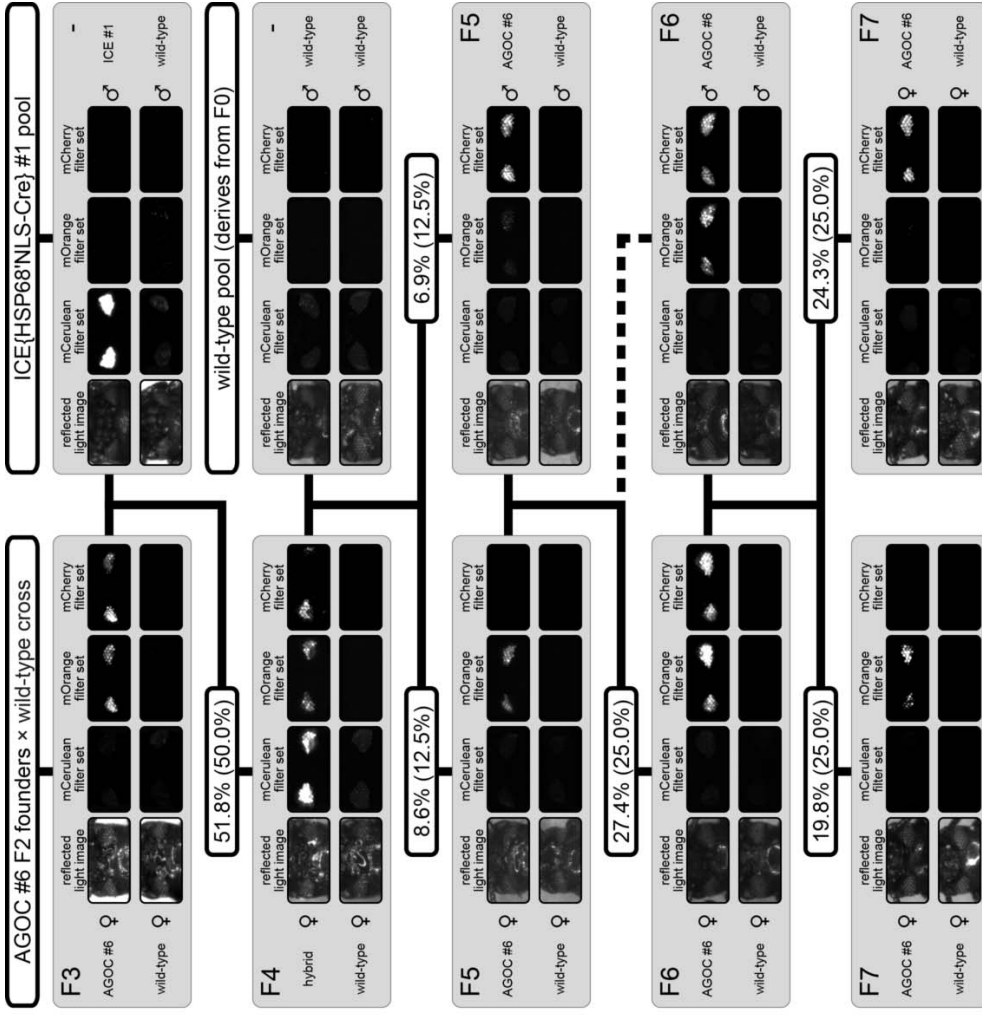


Figure 3 – The AGameOfClones F3 to F7 crossing procedure shown for the AGOC #5 and #6 sublines.

From the F3 to the F7 generation, the genotype was phenotypically determined by monitoring mCe, mO and mC. For both sublines, F7 mO- and mC-only homozygotes were obtained by following the systematic procedure outlined in Figure 2. For each individual, a wild-type control of the same gender is shown. The percentage boxes show the experimental (and theoretical) ratios of the progeny that show the respective phenotype.

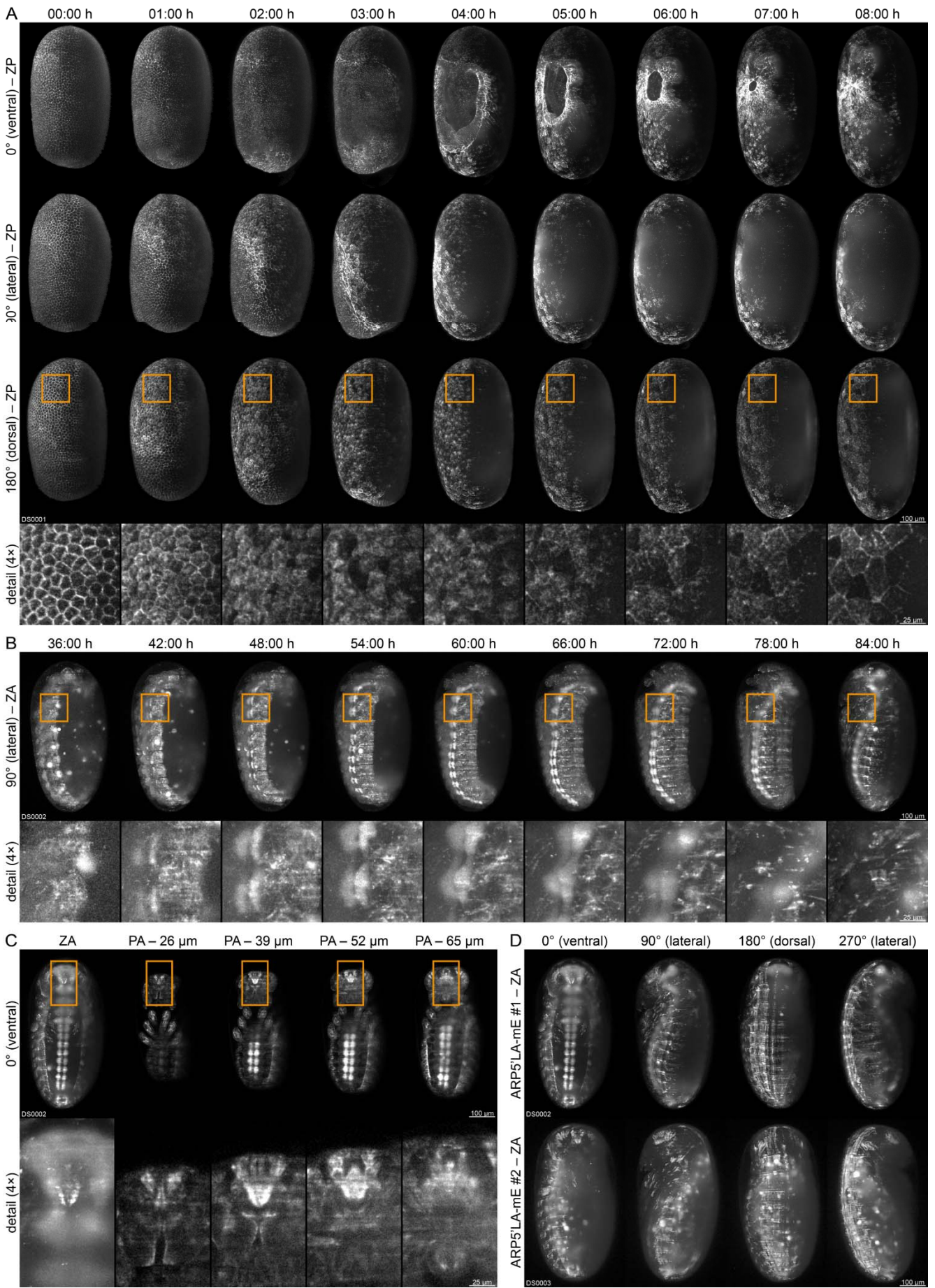


Figure 4 – Fluorescence live imaging of selected homozygous functional AGOC sublines. (A) An AGOC{Zen1^{#O(LA)}-mEmerald} #2 embryo during gastrulation. This subline permits the characterization of actin and actomyosin dynamics that are involved in serosa window closure (first and second row). It can also be used to describe the cytoskeleton rearrangement of the dorsal blastoderm cells and to analyze their appearance change during differentiation to serosa cells (third row and detail images). (B) An AGOC{ARP5^{#O(LA)}-mEmerald} #1 embryo during germband retraction. In this subline, the brain and ventral nerve cord express Lifeact-mEmerald on a high level, permitting the observation of neurulation. Detail images show the forming ganglia of the first and second thoracic segment. (C) Optical sections of an AGOC{ARP5^{#O(LA)}-mEmerald} #1 embryo after dorsal closure. Detail images show the supra- and suboesophageal ganglia. (D) Comparison of embryos from the AGOC{ARP5^{#O(LA)}-mEmerald} #1 and #2 sublines after dorsal closure. In contrast to the expression level in the #1 subline, the Lifeact-mEmerald expression level of the AGOC{ARP5^{#O(LA)}-mEmerald} #2 subline in the nervous system is very low. ZP, z maximum projection with image processing; ZA, z maximum projection with intensity adjustment; PA, single plane with intensity adjustment.

Table 1 – Crossing results for the six proof-of-principle AGOC lines from the F3 to F7 generation. Bold entries mark progeny that was used in the subsequent cross, the F6-S, F7-O and F7-C entries mark control crosses.

Gen	Cross		Subline	Progeny						Total			
	♀	♂		●●●	●●●	●●●	●●●	●●●	●●●				
F3			Theoretical	-	50.0%	-	-	-	-	-	50.0%	100%	
			AGOC #1	-	47.9% (46)	-	-	-	-	-	-	52.1% (50)	100% (96)
			AGOC #2	-	52.4% (44)	-	-	-	-	-	-	47.6% (40)	100% (84)
			AGOC #3	-	55.1% (49)	-	-	-	-	-	-	44.9% (40)	100% (89)
			AGOC #4	-	44.1% (41)	-	-	-	-	-	-	55.9% (52)	100% (93)
			AGOC #5	-	47.6% (39)	-	-	-	-	-	-	52.4% (43)	100% (82)
			AGOC #6	-	48.2% (27)	-	-	-	-	-	-	51.8% (29)	100% (56)
Mean (%)	-	49.2%	-	-	-	-	-	-	50.8%	100%			
F4			Theoretical	25.0%	25.0%	12.5%	12.5%	12.5%	12.5%	-	-	100%	
			AGOC #1	25.6% (30)	34.2% (40)	4.3% (5)	10.2% (12)	6.0% (7)	19.7% (23)	-	-	-	100% (117)
			AGOC #2	27.3% (36)	28.9% (38)	15.1% (20)	8.3% (11)	9.8% (13)	10.6% (14)	-	-	-	100% (132)
			AGOC #3	25.8% (33)	32.8% (42)	13.3% (17)	10.1% (13)	5.5% (7)	12.5% (16)	-	-	-	100% (128)
			AGOC #4 ¹	14.0% (14)	15.0% (15)	20.0% (20)	13.0% (13)	22.0% (22)	9.0% (9)	3.0% (3)	4.0% (4)	-	100% (100)
			AGOC #5	17.1% (20)	40.2% (47)	16.2% (19)	8.5% (10)	10.3% (12)	7.7% (9)	-	-	-	100% (117)
			AGOC #6	33.6% (39)	33.6% (39)	8.6% (8)	6.9% (8)	6.1% (7)	11.2% (13)	-	-	-	100% (116)
Mean (%)	23.9%	30.8%	12.9%	9.5%	9.9%	11.8%	0.5%	0.7%	-	100%			
F5			Theoretical	25.0%	-	25.0%	25.0%	-	-	25.0%	-	100%	
			AGOC #1	27.2% (31)	-	26.3% (30)	23.7% (27)	-	-	-	22.8% (26)	-	100% (134)
			AGOC #2	28.9% (26)	-	33.3% (30)	17.8% (16)	-	-	-	20.0% (18)	-	100% (90)
			AGOC #3	24.8% (30)	-	27.3% (33)	24.8% (30)	-	-	-	23.1% (28)	-	100% (121)
			AGOC #4	19.3% (21)	-	22.9% (25)	37.6% (41)	-	-	-	20.2% (22)	-	100% (109)
			AGOC #5	28.2% (31)	-	29.1% (32)	12.7% (14)	-	-	-	30.0% (33)	-	100% (110)
			AGOC #6	26.2% (22)	-	29.7% (25)	16.7% (14)	-	-	-	27.4% (23)	-	100% (84)
Mean (%)	25.8%	-	28.1%	22.2%	-	-	-	23.9%	-	100%			
F6-S			Theoretical	-	-	50.0%	50.0%	-	-	-	-	100%	
			AGOC #1	-	-	46.4% (39)	53.6% (44)	-	-	-	-	-	100% (84)
			AGOC #2	-	-	50.0% (49)	50.0% (49)	-	-	-	-	-	100% (98)
			AGOC #3	-	-	54.0% (68)	46.0% (58)	-	-	-	-	-	100% (126)
			AGOC #4	-	-	53.8% (50)	46.2% (43)	-	-	-	-	-	100% (93)
			AGOC #5	-	-	51.3% (59)	48.7% (56)	-	-	-	-	-	100% (115)
			AGOC #6	-	-	57.0% (49)	43.0% (37)	-	-	-	-	-	100% (86)
Mean (%)	-	-	52.1%	47.9%	-	-	-	-	-	100%			
F6			Theoretical	-	-	25.0%	25.0%	-	-	50.0%	-	100%	
			AGOC #1	-	-	20.3% (23)	24.8% (28)	-	-	54.9% (62)	-	100% (113)	
			AGOC #2	-	-	21.5% (23)	35.5% (38)	-	-	43.0% (46)	-	100% (117)	
			AGOC #3	-	-	22.9% (27)	22.9% (27)	-	-	54.2% (64)	-	100% (118)	
			AGOC #4	-	-	22.0% (29)	22.7% (30)	-	-	55.3% (73)	-	100% (132)	
			AGOC #5	-	-	17.5% (18)	31.1% (32)	-	-	51.4% (53)	-	100% (103)	
			AGOC #6	-	-	19.8% (22)	24.3% (27)	-	-	55.9% (62)	-	100% (111)	
Mean (%)	-	-	20.7%	26.9%	-	-	52.4%	-	100%				
F7-O			Theoretical	-	-	100%	-	-	-	-	-	100%	
			AGOC #1	-	-	100% (94)	-	-	-	-	-	-	100% (94)
			AGOC #2	-	-	100% (50)	-	-	-	-	-	-	100% (50)
			AGOC #3	-	-	100% (49)	-	-	-	-	-	-	100% (49)
			AGOC #4	-	-	100% (79)	-	-	-	-	-	-	100% (79)
			AGOC #5	-	-	100% (79)	-	-	-	-	-	-	100% (79)
			AGOC #6	-	-	100% (63)	-	-	-	-	-	-	100% (63)
Mean (%)	-	-	100%	-	-	-	-	-	-	100%			
F7-C			Theoretical	-	-	-	100%	-	-	-	-	100%	
			AGOC #1	-	-	-	100% (101)	-	-	-	-	-	100% (101)
			AGOC #2	-	-	-	100% (105)	-	-	-	-	-	100% (105)
			AGOC #3	-	-	-	100% (89)	-	-	-	-	-	100% (89)
			AGOC #4	-	-	-	100% (54)	-	-	-	-	-	100% (54)
			AGOC #5	-	-	-	100% (74)	-	-	-	-	-	100% (74)
			AGOC #6	-	-	-	100% (64)	-	-	-	-	-	100% (64)
Mean (%)	-	-	-	100%	-	-	-	-	-	100%			

¹ in the AGOC #4 subline, incomplete recombination in the F4 mCe×mO-mC double hemizygotes occurred, as we obtained several F5 individuals that still carry both transformation markers (7% in total). We continued the AGOC procedure with the F5 mO- and mC-only post-recombination hemizygous progeny.

Supplementary Material for

A universal vector concept for a direct genotyping of transgenic organisms and a systematic creation of homozygous lines

Authors

Frederic Strobl, Anita Anderl and Ernst H.K. Stelzer

Affiliations

Frederic Strobl

Physical Biology / Physikalische Biologie (IZN, FB 15)
Buchmann Institute for Molecular Life Sciences (BMLS)
Cluster of Excellence Frankfurt – Macromolecular Complexes (CEF – MC)
Goethe Universität – Frankfurt am Main (Campus Riedberg)
Max-von-Laue-Straße 15 – D-60348 Frankfurt am Main – Germany
frederic.strobl@physikalischebiologie.de (corresponding author)
www.physikalischebiologie.de/people/frederic-strobl ~ www.physikalischebiologie.de/bugcube
Tel: +49 (69) 798 42552

Anita Anderl

Physical Biology / Physikalische Biologie (IZN, FB 15)
Buchmann Institute for Molecular Life Sciences (BMLS)
Cluster of Excellence Frankfurt – Macromolecular Complexes (CEF – MC)
Goethe Universität – Frankfurt am Main (Campus Riedberg)
Max-von-Laue-Straße 15 – D-60348 Frankfurt am Main – Germany
anita.anderl@h-da.de

Ernst H.K. Stelzer

Physical Biology / Physikalische Biologie (IZN, FB 15)
Buchmann Institute for Molecular Life Sciences (BMLS)
Cluster of Excellence Frankfurt – Macromolecular Complexes (CEF – MC)
Goethe Universität – Frankfurt am Main (Campus Riedberg)
Max-von-Laue-Straße 15 – D-60348 Frankfurt am Main – Germany
ernst.stelzer@physikalischebiologie.de (corresponding author)
<http://www.physikalischebiologie.de/people/ernst-hk-stelzer>
Tel: +49 (69) 798 42547, x42545 (Michaela Koller)

List of Supplementary Materials

- Supplementary Note
- Supplementary Figure 1 to 11
- Supplementary Table 1 to 18
- Supplementary Video 1 to 3

Supplementary Material

Supplementary Note

The AGOC vector concept in special cases of transgenesis

Transgenesis approaches, especially techniques with random or semi-random genomic insertion, might lead to certain special cases. Below, we discuss four of those cases that occurred during our study:

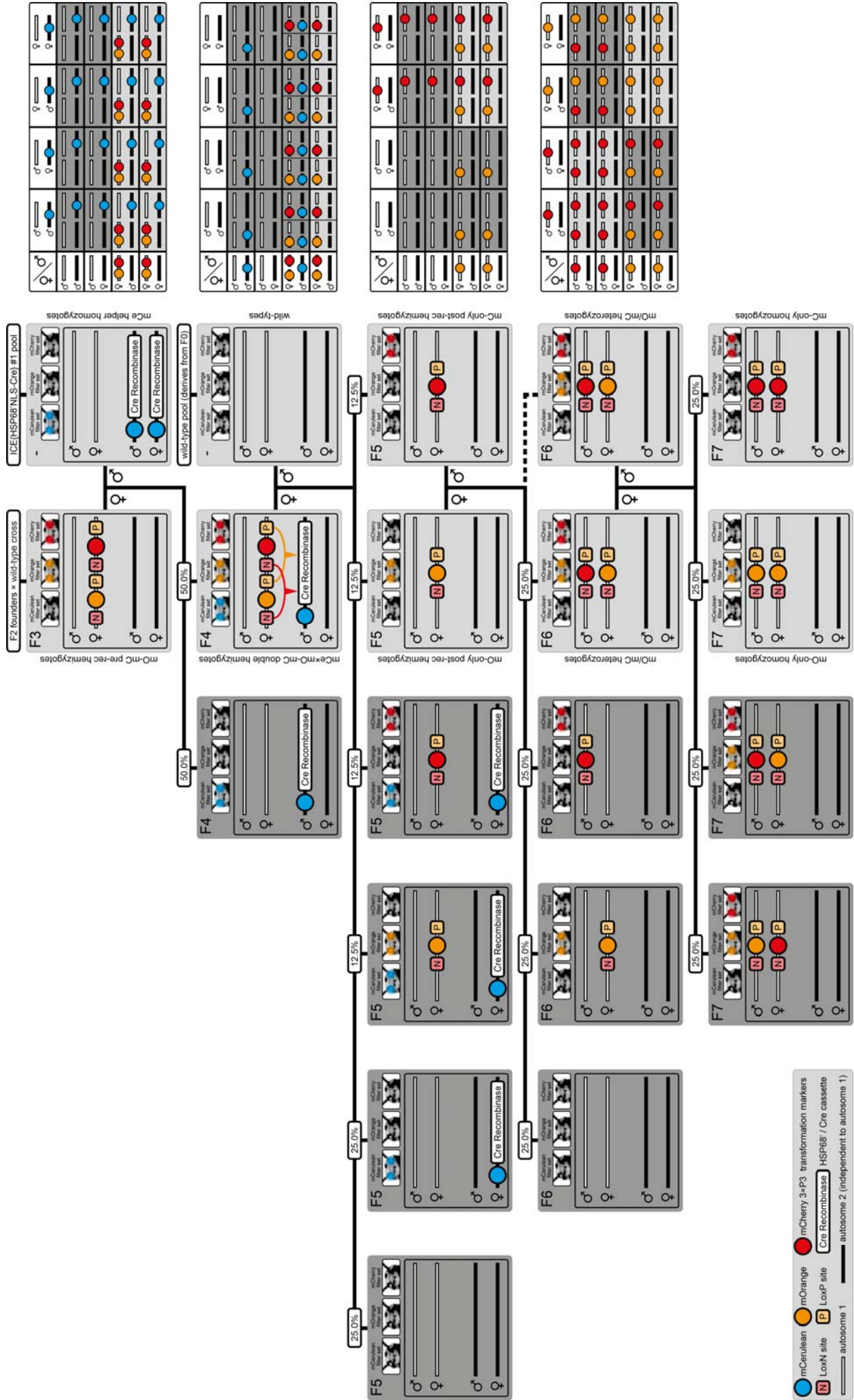
- The homozygous viability crosses indicated that the proof-of-principle AGOC #3, the functional AGOC{ATub' #O(LA)-mEmerald} #1 and the functional AGOC{ATub'H2B-mEmerald} #4 sublines are not homozygous viable (Supplementary Table 2, Supplementary Table 10). However, F6 mO/mC heterozygous individuals could be obtained for all three of those lines and the complete procedure could be carried out successfully with the AGOC #3 and AGOC{ATub' #O(LA)-mEmerald} #1 lines (Table 1, Supplementary Table 7 and Supplementary Table 8). Only for the AGOC{ATub' #O(LA)-mEmerald} #4 subline, the procedure aborted, since the F6 mO/mC heterozygotes were sterile. As the transgene of the proof-of-principle AGOC #3 line might interfere with the sialin-like gene due to its insertion location (Supplementary Table 3), and as both functional lines exhibit a high degree of green fluorescence, we assume that hemizygous transgenic individuals are exposed to a high stress levels, and that this level is even higher in homozygous organisms. Therefore, those transgenic individuals are principally homozygous viable, but a certain degree might fail to develop properly, resulting in biased homozygous viability cross ratios.
- In contrast to homozygous lethality, homozygous sterility cannot be estimated from the homozygous viability crosses, but it can be confirmed by using the AGameOfClones vector concept. The AGOC{ATub'H2B-mEmerald} #4 line was assumed to be homozygous lethal (Supplementary Table 10), but crossing a F5 mO-only post-recombination hemizygous female against a F5 mC-only post-recombination hemizygous male resulted in F6 mO/mC heterozygous progeny. However, by crossing F6 mO/mC heterozygous females against genotypic identical F6 males, no progeny was obtained ($n = 12$). Further, crossing F6 mO/mC heterozygote females and wild-type males did not result in any progeny ($n = 12$). To confirm sterility of both genders, we crossed F6 mO/mC heterozygous males and wild-type females, which did also not result in progeny ($n = 8$).
- All previous considerations discuss only transgenes located on autosomes. Since nine of the ten chromosomes in *Tribolium* are autosomes, this is the most probable scenario. Similarly to most metazoans, *Tribolium* uses the XX and XY allosome gender-determination system to specify female and male individuals, respectively. For transgene insertions into the Y allosome, the genotype can be determined by the phenotype, and females are always wild-types. However, this case is rare, since the number of base pairs in the Y allosome is small compared to the number of base pair in the remaining chromosomes. For transgene insertions into the X allosome, the genotype of males but not of females can be determined by the phenotype. The AGOC vector concept also allows to systematically create homozygous organisms when the transgene is present on the X

allosome. In this case, a slightly different crossing procedure has to be followed to obtain both F7 mO- and mC-only homozygotes (Supplementary Figure 5). For the AGOC{Zen1'#O(LA)-mEmerald} #2 line, which carries the transgene on the X allosome, F7 mO and mC homozygotes were successfully obtained (Supplementary Table 7).

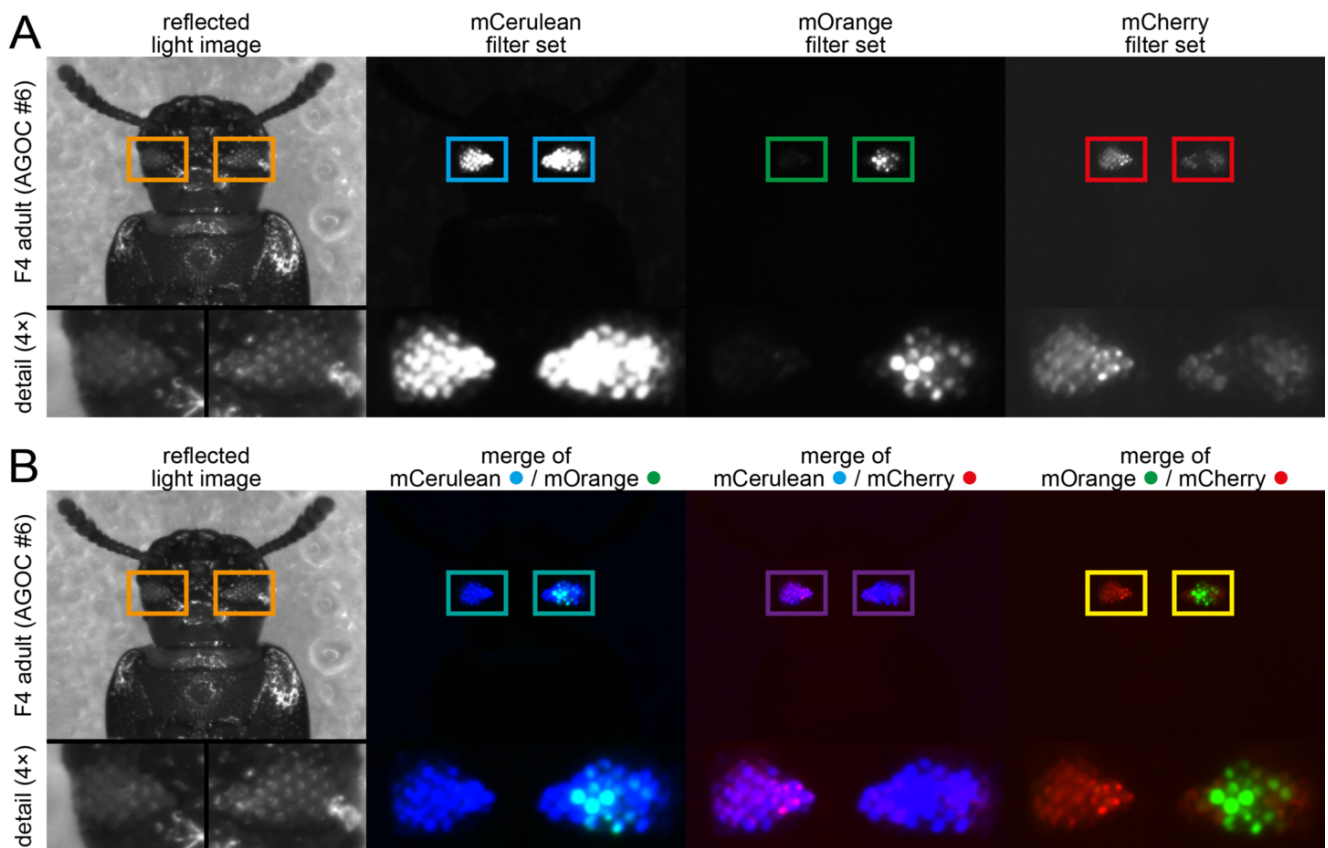
- The piggyBac transposon system is highly efficient in *Tribolium*, which results to a certain degree also from the four bp TTAA target sequence. However, this very short length of the targeting sequence, a certain probability for nested insertions is given, *i.e.* the transgene inserts first into another transformation vector, since also those vectors carry multiple TTAA target sequences. In the AGOC{Zen1'#O(LA)-mEmerald} #3, an insertion of the transgene into the backbone of another vector occurred, and the nested transgene was subsequently inserted into the genome, as revealed by sequencing of the insertion junction (Supplementary Table 11). The AGOC vector concept 'corrects' this rare and undesired case, as within the F4 mCe×mO-mC double hemizygous generation, the Cre recombinase excises nearly one 'stitched equivalent' of the initial transformation vector from the genome (Supplementary Figure 6). The F5 mO- and mC-only hemizygous progeny then carries classically only one copy of either mO or mC.

One of the most obvious special cases, homozygous lethality, did not occur within our study. However, the AGOC vector concept would allow determination of this special case with a high degree of certainty when a F5 mO-only post-recombination heterozygous female is brother-sister crossed against a F5 mC-only post-recombination heterozygous male, and in the F6, none of the progeny carries both, mO and mC. Multiple other transgenesis special cases are possible (*e.g.* female- or male-only homozygous lethality or sterility, nested insertions of transgenes into transgenes, multiple inserts in close proximity on the same chromosome), but are not discussed here due to the very low assumed probability of occurrence.

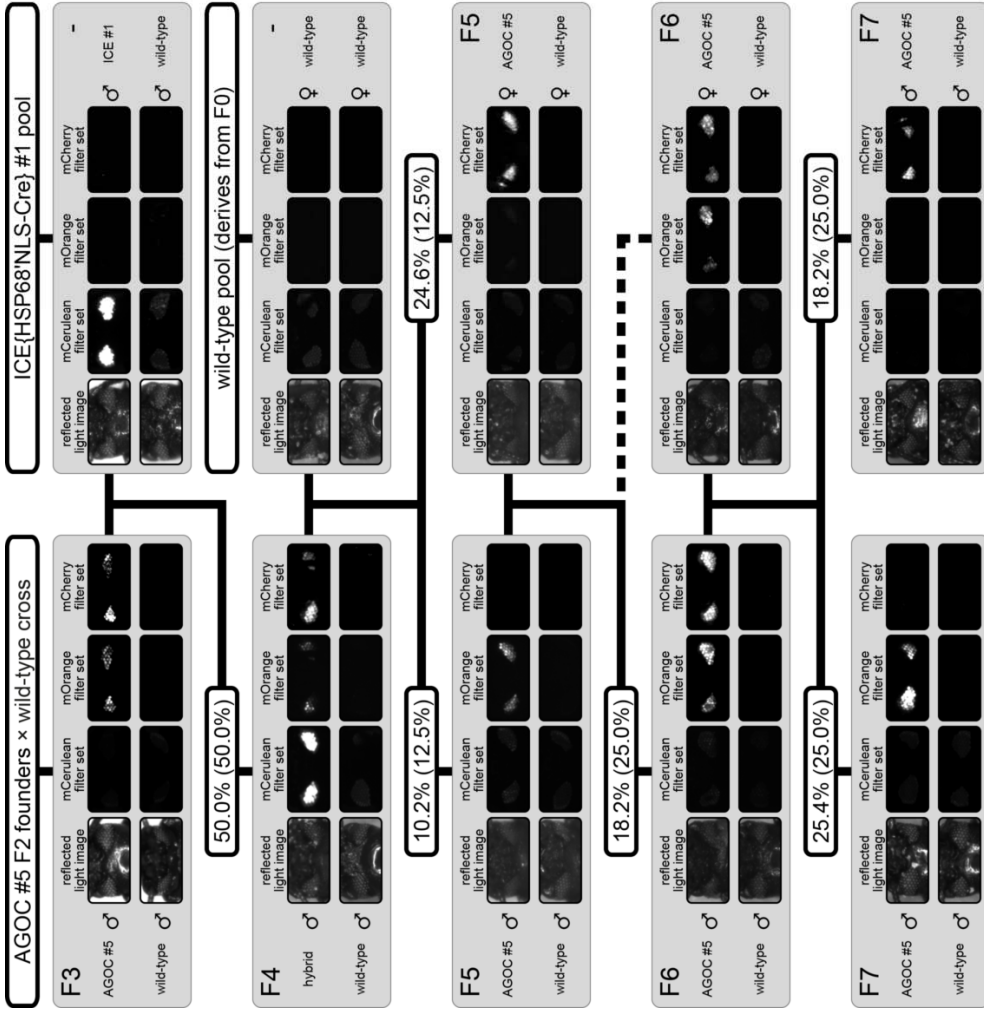
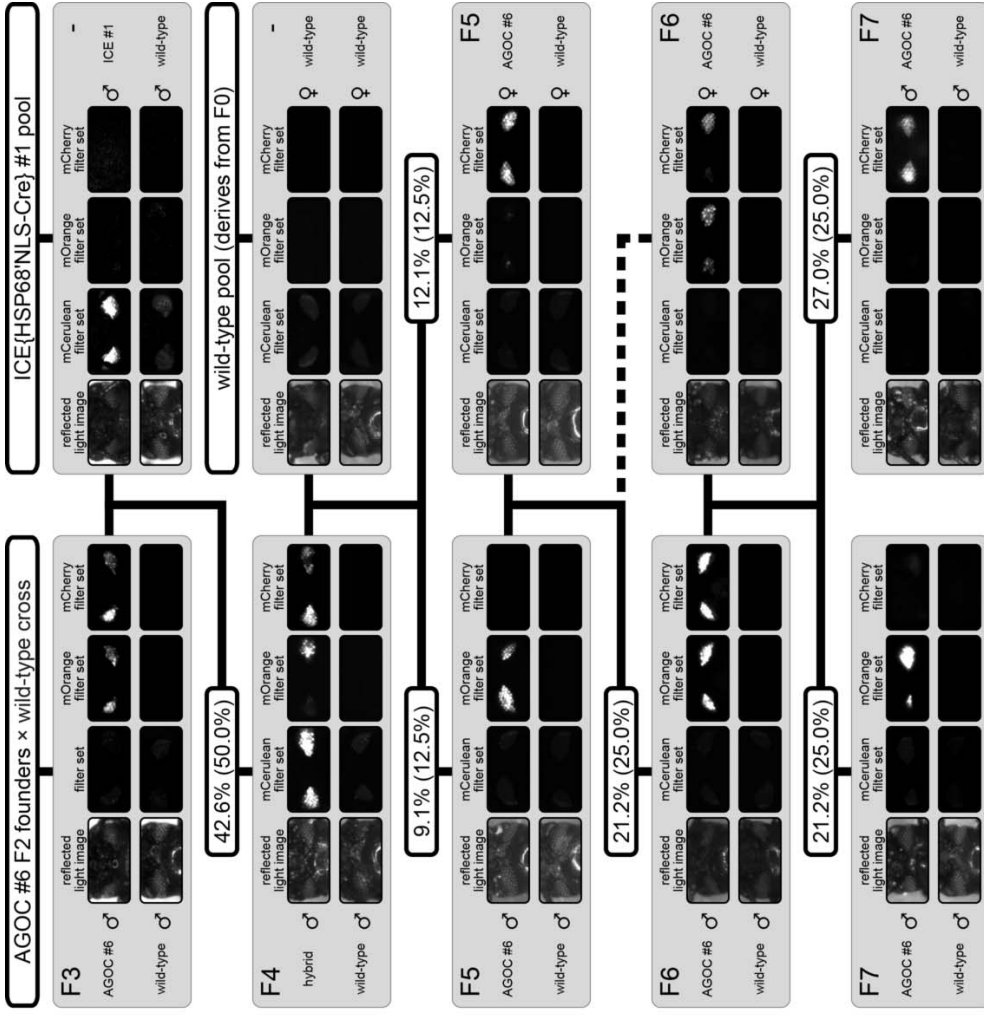
Supplementary Display Items



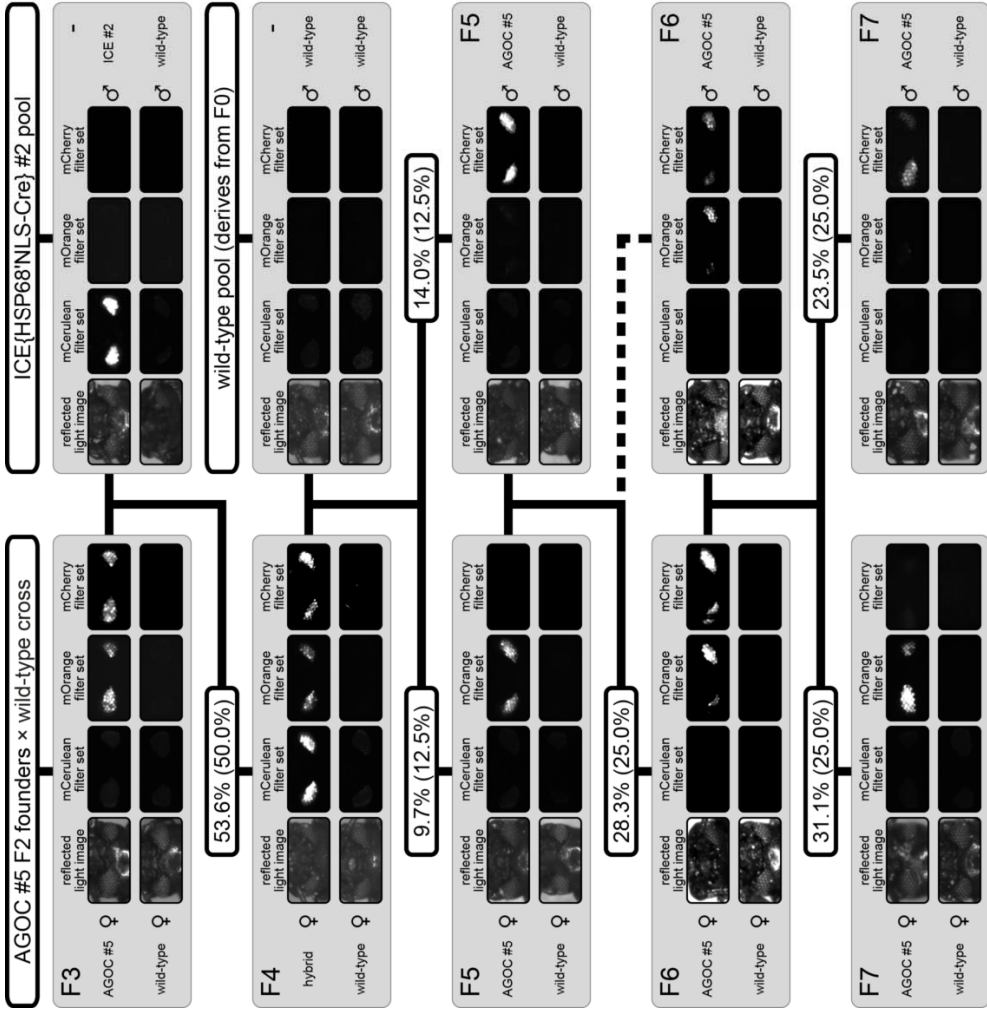
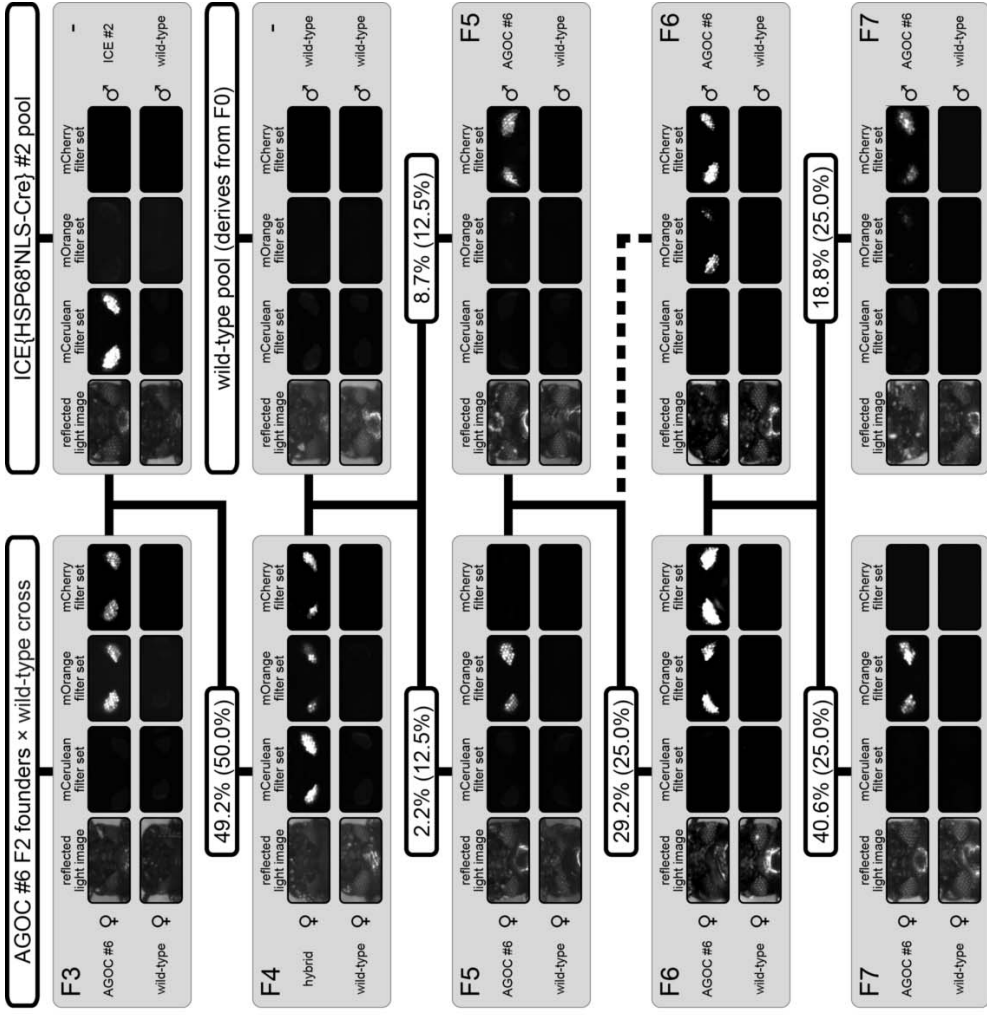
Supplementary Figure 1 – The AGameOfClones F3 to F7 crossing procedure with all outcomes and respective Punnett squares. The light gray background indicates F3 to F6 organisms that are either further used within the procedure or the desired F7 mO- and mC-only homozygotes, while the dark gray background indicates progeny that can be disregarded. The rounded rectangle illustrates the genotype for two independent autosomes, white bars represent the AGOC transgene location and black bars represent the helper transgene location. For convenience, the Punnett squares for the F3 to F6 crosses are provided on the right. A F3 mO-mC pre-recombination hemizygous female \times ICE{HSP68'NLS-Cre} #1 homozygous male cross gives rise to F4 mCe \times mO-mC double hemizygotes, but also mCe helper hemizygotes. A mCe \times mO-mC double hemizygote female \times wild-type male outcross results in F5 mO- and mC-only post-recombination hemizygotes but also in four other combinations (mCe \times mO- and mCe \times mC-only post-recombination double hemizygotes, mCe helper hemizygote and wild-types). Next, a F5 mO-only post-recombination hemizygous female \times F5 mC-only post-recombination hemizygous male brother-sister cross results in a certain fraction of F6 mO/mC heterozygous progeny, but also in three other combinations (hemizygotes that basically represent the genotype of their parents and wild-types). Finally, a F6 mO/mC heterozygous female \times a F6 mO/mC heterozygous male brother-sister cross generates F7 mO- and mC-only homozygous progeny, but also two other combinations (mO/mC heterozygotes, whereas half of the individuals obtain mO maternal and mC paternal, and the other half obtains mO paternal and mC maternal).



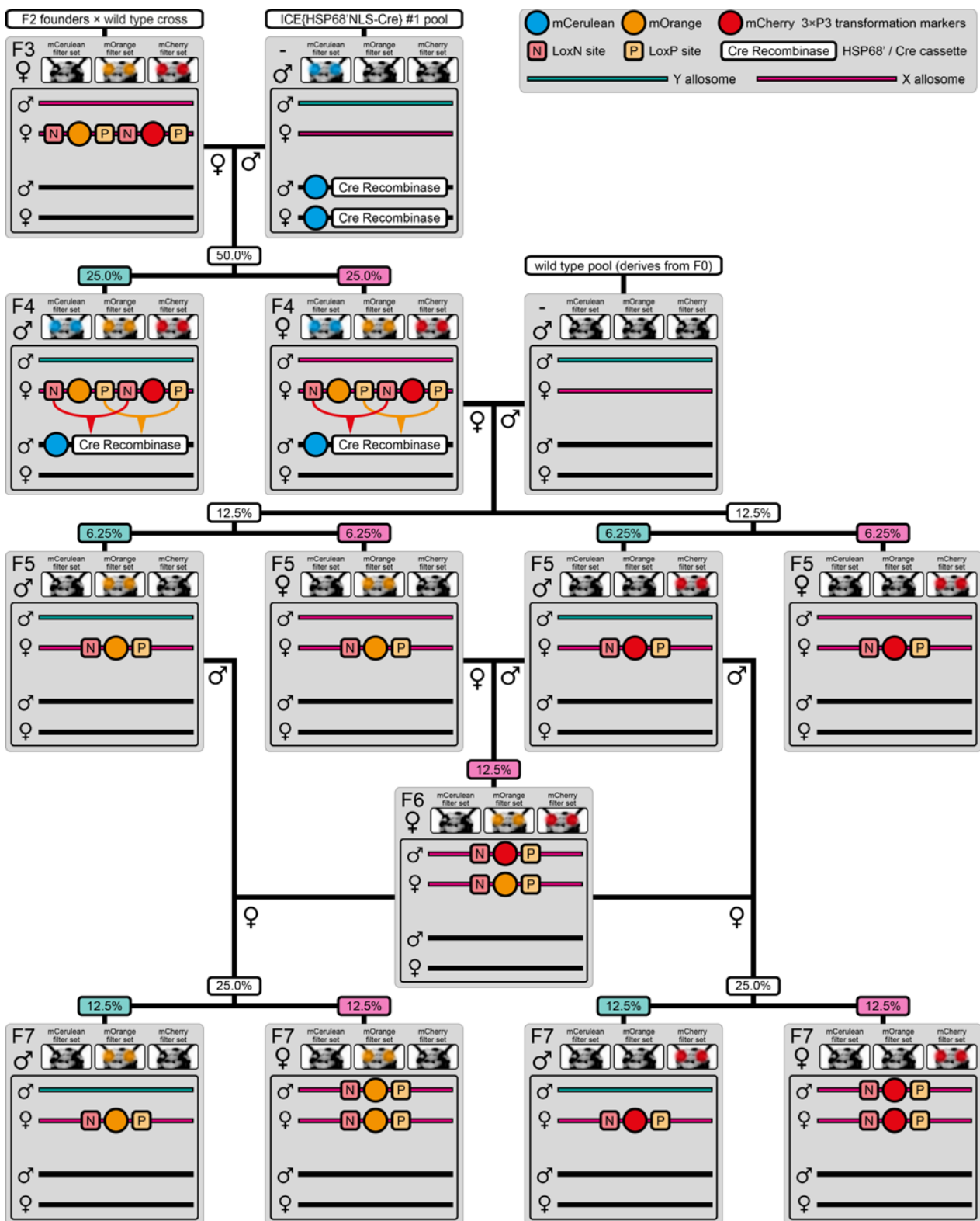
Supplementary Figure 2 – The F4 mCe×mO-mC double hemizygote generation. (A) The F4 hybrids are hemizygous for both the AGOC transgene, which carries both mO and mC embedded into interweaving Lox site pairs, and for the helper transgene, which carries mCe and the Cre recombinase expression cassette. Within this cassette, expression of a nuclear-localized Cre recombinase is driven by the endogenous *HSP68* promoter. During the development of the F4 generation from the zygote to the fertile adult, the *HSP68* promoter exhibits a slight leaky expression. Over time, this leads to recombination in germ cells (*i.e.* the prerequisite for the AGOC vector concept) but also in certain somatic progenitor cells that later on give rise to distinct, typically spatially clustered cell populations. This effect is evident in the compound eyes of adult beetles in all AGOC lines, where certain clusters of ommatidia show either expression of mO or mC. (B) Within the merged images, it becomes evident that most of the ommatidia express either only mO or mC.



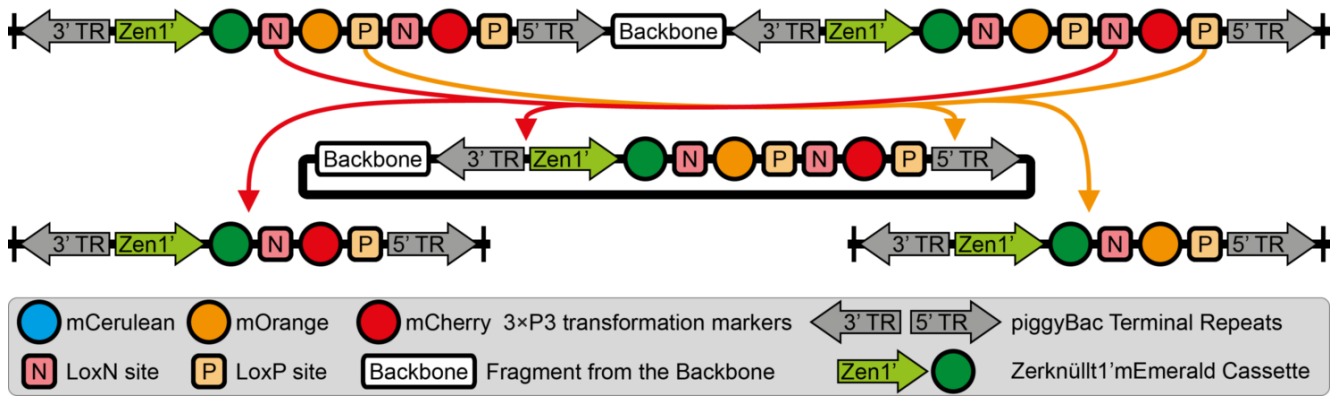
Supplementary Figure 3 – The AGameOfClones F3 to F7 crossing procedure with inversed genders. To prove that the proposed concept is not gender-specific, the F3 to F7 crossing procedure was carried out as described in the main text, but with inversed genders. F3 mO-mC pre-recombination hemizygous males of the AGOC #5 and #6 subline were crossed against mCe helper homozygous females of the ICE {HSP68'NLS-Cre} #1 subline, resulting in F4 mCe×mO-mC double hemizygotes, in which Cre-mediated recombination occurs. F4 mCe×mO-mC double hemizygote males were outcrossed against wild-type females, this results in F5 mO- and mC-only post-recombination hemizygotes that carry either only mO or only mC on the paternal chromosome. F5 mO-only post-recombination hemizygous males were brother-sister crossed against F5 mC-only post-recombination hemizygous females, resulting in F6 mO/mC heterozygotes that carry once again both markers. F6 mO/mC heterozygous males were brother-sister crossed against genotypic identical F6 mO/mC heterozygous females, resulting in F7 mO- and mC-only homozygotes that carry either only the mO or only the mC marker on both, the maternal and paternal chromosomes. Similar to the standard, the procedure could be performed also successfully with inversed genders. For each individual, a wild-type control of the same gender is shown. The percentage boxes show the experimental (and theoretical) ratios of the progeny that show the respective phenotype.



Supplementary Figure 4 – The AGameOfClones F3 to F7 crossing procedure with a different mCe helper subline. To prove that the proposed concept does not rely solely on one Cre recombinase expressing helper subline, the F3 to F7 crossing procedure was carried out as described in the main text, but with the ICE{HSP68'NLS-Cre} #2 helper subline, which carries the same transgene as #1 subline, but at a different genomic location. The subline is homozygous for the transgene. F3 mO-mC pre-recombination hemizygous females of the AGOC #5 and #6 subline were crossed against mCe helper homozygous males of the ICE{HSP68'NLS-Cre} #2 subline, resulting in F4 mCe×mO-mC double hemizygotes, in which Cre-mediated recombination occurs. F4 mCe×mO-mC double hemizygote females were outcrossed against wild-type males, this results in F5 mO- and mC-only post-recombination hemizygotes that carry either only mO or only mC on the paternal chromosome. F5 mO-only post-recombination hemizygous females were brother-sister crossed against F5 mC-only post-recombination hemizygous males, resulting in F6 mO/mC heterozygotes that carry once again both markers. F6 mO/mC heterozygous females were brother-sister crossed against genotypic identical F6 mO/mC heterozygous males, resulting in F7 mO- and mC-only homozygotes that carry either only the mO or only the mC marker on both, the maternal and paternal chromosomes. Similar to the standard, the procedure could be performed also successfully with inversed genders. For each individual, a wild-type control of the same gender is shown. The percentage boxes show the experimental (and theoretical) ratios of the progeny that show the respective phenotype.

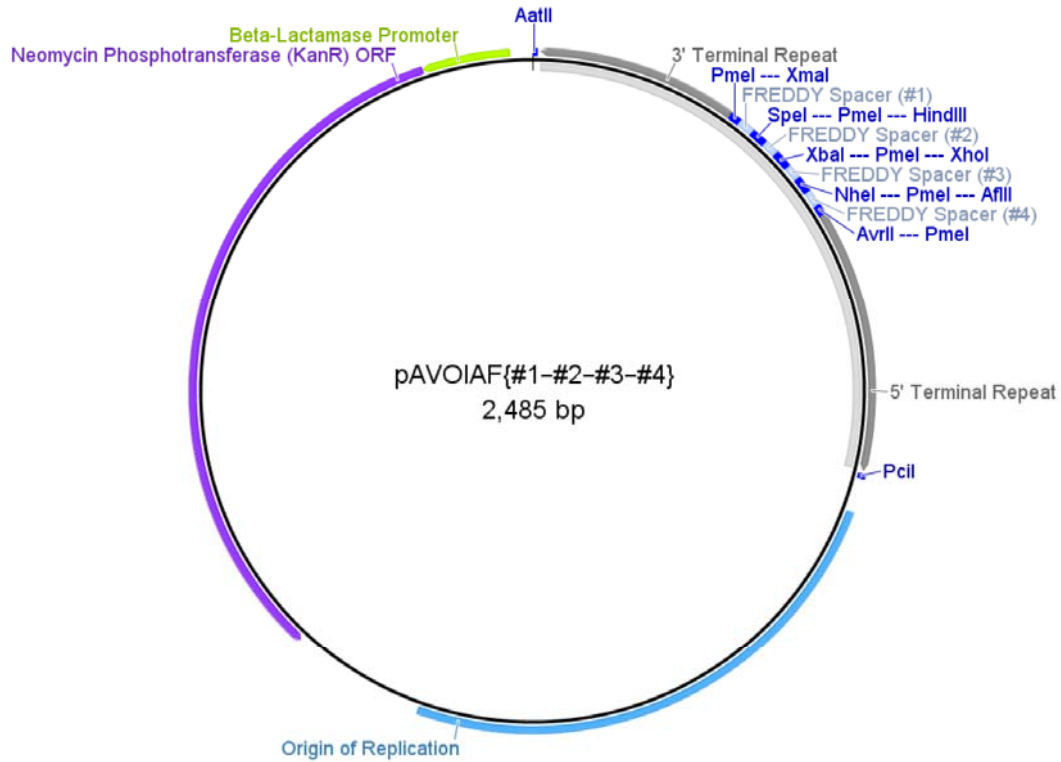


Supplementary Figure 5 – Alternative AGameOfClones F3 to F7 crossing procedure for transgenes located on the X allosome. When the transgene is located on the X allosome instead of one of the nine autosomes, the procedure has to be modified slightly to obtain the F7 mO- and mC-only homozygotes. The rounded rectangle illustrates the genotype for one autosome and both allosomes, pink bars represent the AGOC transgene location on the X allosome, teal bars represent the Y allosome and black bars represent the helper transgene location on an autosome. Until the F6 mO/mC heterozygous generation, the procedure is identical to the standard, but all F6 mO/mC heterozygous individuals are female. Two of those females have to be separately uncle-niece crossed against F5 mO- and mC-only post-recombination hemizygous males, which results in F7 mO- and mC-only homozygous females, respectively. The percentage boxes show the theoretical ratios of the progeny that show the respective phenotype. Pink boxes represent female progeny, teal boxes represent male progeny.

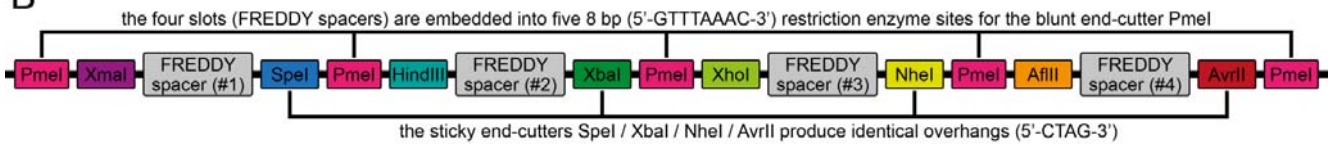


Supplementary Figure 6 – Recombination in the AGOC{Zen1'#O(LA)-mEmerald} #3 line, which carries a nested insert. During the transformation process that led to the AGOC{Zen1'#O(LA)-mEmerald} #3 line, a transgene has inserted into the backbone of another vector. This led to the genomic insertion of a nested construct that also contains a fragment from the backbone (upper scheme). In the F4 mCe×mO-mC double hemizygote generation, the Cre-mediated recombination will 'correct' this issue by excising roughly one 'stitched equivalent' of the initial transformation vector from the genome. The F5 progeny then carries classically only either mO or mC (lower schemes).

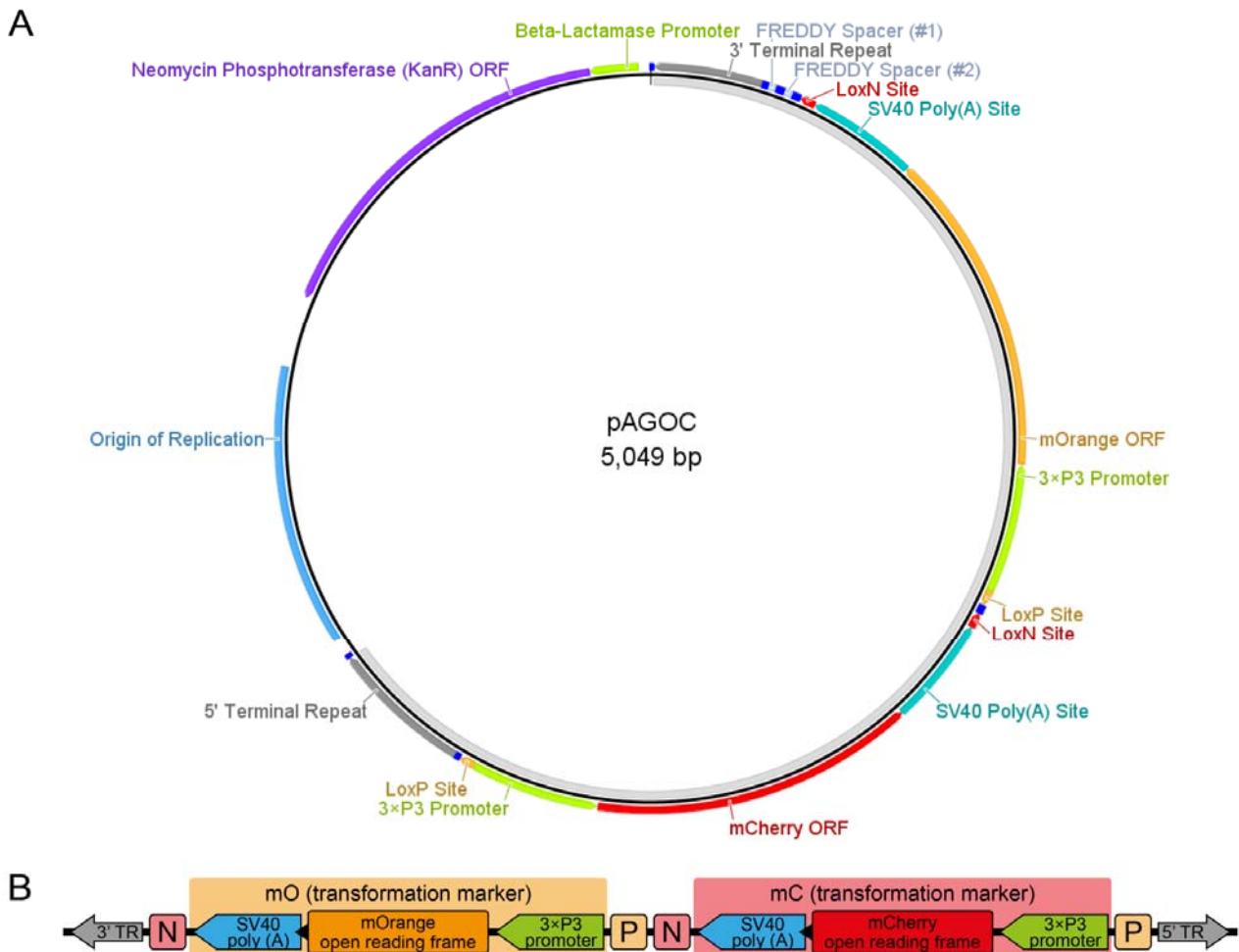
A



B

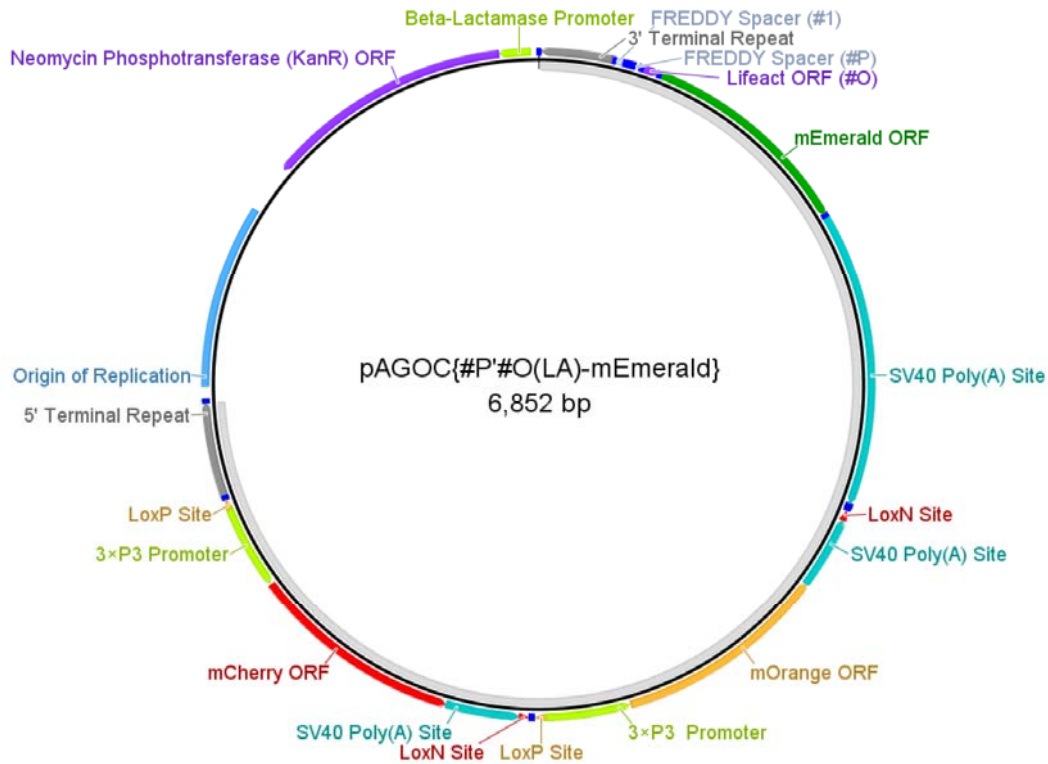


Supplementary Figure 7 – The pAVOIAF{#1-#2-#3-#4} vector. (A) Vector map of pAVOIAF{#1-#2-#3-#4}. The vector is based on the pUC57-Kan vector, from which the kanamycin resistance cassette and the origin of replication derive. The four-slot cloning site together with the 3' and 5' piggyBac terminal repeats is located between the AatII and PciI restriction enzyme sites. The light gray band on the inside indicates the transgene. (B) Scheme of the four-slot cloning site. Each slot consists of an 18 bp spacer that translates into the six amino acids phenylalanine, arginine, glutamic acid, aspartic acid, aspartic acid and tyrosine and thus was called FREDDY spacer. The slots can be accessed individually by unique restriction enzyme site pairs (XmaI/SpeI, HindIII/XbaI, XhoI/NheI and AflII/AvrII for #1, #2, #3 and #4, respectively). They are embedded into five PmeI restriction enzyme sites that allow a simple one-enzyme control digestion to determine the size of the sequences that were inserted into the slots. For convenience, the downstream restriction enzyme sites for each slot (SpeI, XbaI, NheI and AvrII for #1, #2, #3 and #4, respectively) will produce identical sticky ends, facilitating cloning procedures that cannot utilize the suggested restriction enzyme site pairs. Sizes of the genetic elements are not to scale. ORF, open reading frame.

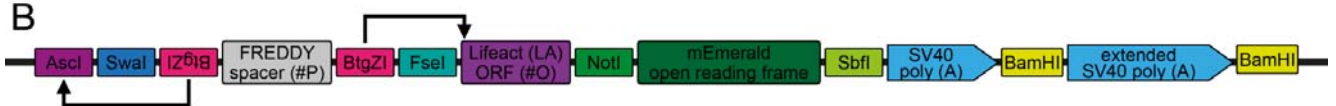


Supplementary Figure 8 – The pAGOC vector. (A) Vector map of pAGOC, which is based on the pAVOIAF[#1–#2–#3–#4] vector (Supplementary Figure 7). In this vector, #1 and #2 remain empty, while mO and mC together with their flanking upstream LoxP and downstream LoxN sites were inserted into #3 and #4, respectively. The non-annotated dark blue boxes represent the same restriction enzyme sites as shown for the pAVOIAF[#1–#2–#3–#4] vector in Supplementary Figure 7. The light gray band on the inside indicates the transgene. (B) Scheme of mO and mC that are embedded into intermeshing but incompatible LoxN and LoxP site pairs. Restriction enzyme sites are not shown. Sizes of genetic elements are not to scale. ORF, open reading frame; TR, piggyBac terminal repeat.

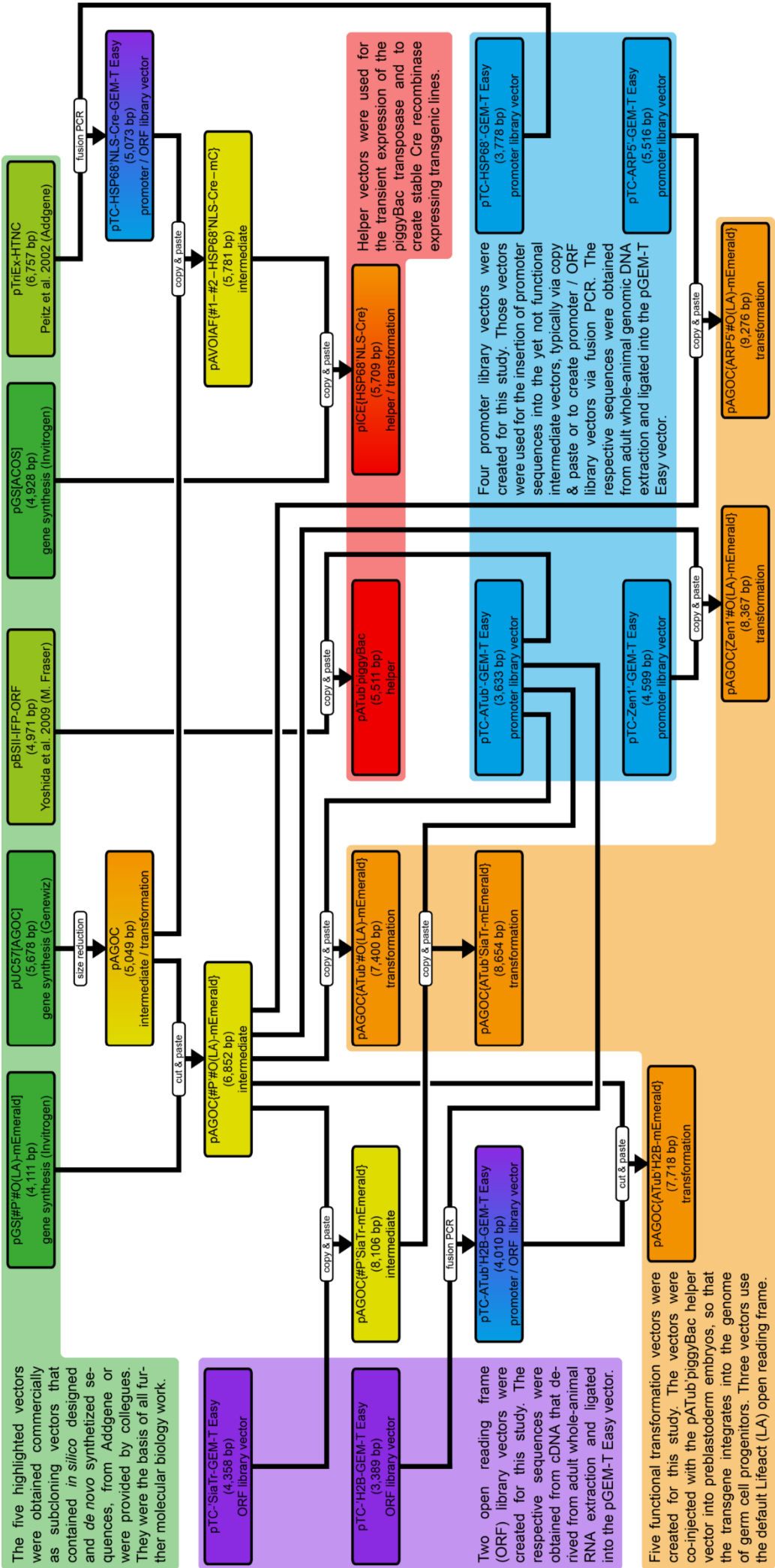
A



B



Supplementary Figure 9 – The pAGOC{#P'#O(LA)-mEmerald} vector. (A) Vector map of pAGOC{#P'#O(LA)-mEmerald}, which is based on the pAGOC vector (Supplementary Figure 8). In this vector, #1 remains empty, while the #P'#O(LA)-mEmerald two-slot cloning site was inserted into #2. The non-annotated dark blue boxes represent the same restriction enzyme sites as shown for the pAVOIAF[#1–#2–#3–#4] vector in Supplementary Figure 7 as well as several new restriction enzyme sites shown in (B). The light gray band on the inside indicates the transgene. (B) Scheme of the #P'#O(LA)-mEmerald two-slot cloning site. To insert a promoter, the #P slot can be accessed by the AscI/FseI restriction enzyme site pair, but alternatively by the double BtgZI restriction enzyme site pair, which flanks a FREDDY spacer. BtgZI is a type I restriction enzyme with a non-palindromic recognition sequence. It cuts the sequence several bp (10/14) downstream, resulting in a 4 bp sticky end. In this vector, the upstream BtgZI restriction enzyme site (in reverse orientation) allows the opening of the AscI restriction enzyme site, while the downstream BtgZI restriction enzyme site (in forward orientation) allows the opening of the Lifeact open reading frame start codon and the first bp of the subsequent codon, which allows scarless insertion of respectively digested promoter sequences (indicated by arrows). The Lifeact (LA) open reading frame, which is in #O per default, can be substituted with another open reading frame to change the intracellular localization by the FseI/NotI restriction enzyme site pair, while the mEmerald open reading frame can be substituted with another fluorescence protein open reading frame by the NotI/SbfI restriction enzyme site pair. ORF, open reading frame.



Five functional transformation vectors were created for this study. The vectors were co-injected with the pATub/piggyBac helper vector into preblastoderm embryos, so that the transgene integrates into the genome of germ cell progenitors. Three vectors use the default Lifeact (LA) open reading frame.

Supplementary Figure 10 – Evolution of the 24 vectors used in this study. Vectors belong either to one or to two types, as indicated by the differently colored backgrounds. Green depicts gene synthesis and previously published vectors, blue depicts promoter library vectors, purple depicts open reading frame (ORF) library vectors, red depicts helper vectors and orange depicts transformation vectors. The ‘copy & paste’ boxes indicate a molecular biology procedure with PCR-based amplification of the insert, while the ‘cut & paste’ boxes indicate that the respective insert was extracted from another vector and inserted into the respective backbone without any amplification. See also the Materials and Methods section.

adult beetle arrangement

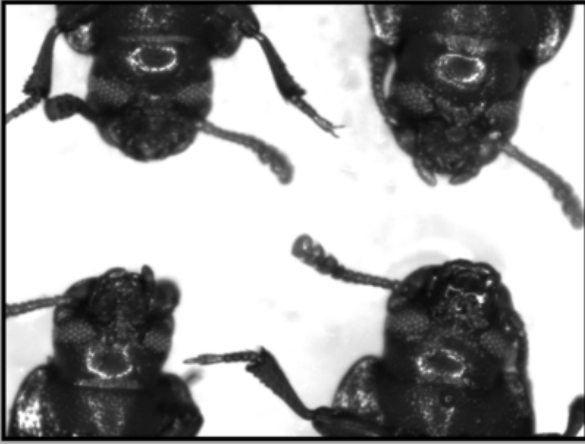
AGOC #5 F3 ♀

ICE{HSP68'NLS-Cre} #1 ♂

wild-type control ♀

wild-type control ♂

reflected light image



mCerulean filter set



mOrange filter set



mCherry filter set



Supplementary Figure 11 – Image acquisition procedure for the eye-specific transformation markers. The images of the adult eyes and the respective markers were carried out in parallel for each cross. In addition, two wild-type controls, a female and a male adult, were used.

Supplementary Table 1 – F2 insert number determination cross for the six proof-of-principle AGOC sublines. F2 mO-mC founder females were crossed against wild-type males and the progeny was quantitatively evaluated. Segregation of mO-mC of 60% or less was defined as the criteria for one insert, no deviants were identified.

Line	●●●	●●●	Total
theoretical – one insertions	50%	50%	100%
theoretical – two insertions ¹	25%	75%	100%
AGOC #1	54.7% (41)	45.3% (34)	100% (75)
AGOC #2	46.2% (30)	53.8% (35)	100% (65)
AGOC #3	61.9% (39)	38.1% (24)	100% (63)
AGOC #4	55.8% (48)	44.2% (38)	100% (86)
AGOC #5	55.1% (27)	44.9% (22)	100% (49)
AGOC #6	56.3% (63)	43.7% (49)	100% (112)

¹ this theoretical value corresponds to the case that the insertions occur on different chromosomes, which is more likely than two independent inserts on the same chromosome.

Supplementary Table 2 – F3 homozygous viability crosses for the six proof-of-principle AGOC sublines. A brother-sister-cross of two F3 mO-mC pre-recombination hemizygotes was performed and the progeny was quantitatively evaluated. Segregation of mO-mC of 70% or more was defined as the criteria for homozygous viability, deviants are marked in bold.

Line	●●●	●●●	Total
theoretical – homozygous viable	25.0%	75.0%	100%
theoretical – homozygous lethal	33.3%	66.7%	100%
AGOC #1	23.7% (27)	76.3% (87)	100% (114)
AGOC #2	29.5% (26)	70.5% (62)	100% (88)
AGOC #3	34.5% (20)	65.5% (38)	100% (58)
AGOC #4	29.3% (36)	70.7% (87)	100% (123)
AGOC #5	17.9% (19)	82.1% (87)	100% (106)
AGOC #6	29.0% (18)	71.0% (44)	100% (62)

Supplementary Table 3 – Insertion locations for four of the six proof-of-principle AGOC sublines. In the Junction column, the piggyBac TTAA insertion/excision target sequence is marked in bold.

Subline	Chromosome	Junction	Neighbors	Inverse primer pair and restriction enzyme, control primer pair
AGOC #1	Unknown (reverse orientation)	5'- AATAGTATTTTCGGTTGAAAAAGTAAGCTTAA GCTGTTTAGACCTAGGTTTTAGCATAG-3'	Cactus (NW_001093503.1), approximately 28,000 bp in 5' with 2 gaps (head-to-head)	1-5' with EcoRI, I1
AGOC #2	Not X or Y	N.A.	N.A.	N.A.
AGOC #3	ChL.G8 (forward orientation)	5'- ACATGTAAATGGGGGGCCCCATCATTCCTTAA AGGTTGATTTATTTGGGTGGGGGAGAA-3'	Intron 1 of Sialin-like (NC_007423.2), approximately 50 bp from Exon 1 (head-to-tail)	1-5' with EcoRI, I2
AGOC #4	Not X or Y	N.A.	N.A.	N.A.
AGOC #5	ChL.G10 (forward orientation)	5'- AAAAAACCCCTCTCCCACTGAACCTCGTTTAA TTGAATCAGCAGAGGAGAGAAAGACAGA-3'	Probable Phenylalanine-tRNA ligase alpha subunit (LOC655993), approximately 33,000 bp in 3' (tail-to-tail)	1-5' with EcoRI, I3
AGOC #6	ChL.G2 (reverse orientation)	5'- GTCGGATCCAGCTGTTGTCGTCGTAACCTTAA AGTGATCTGAATTTTTCAAAATAAAC-3'	Uncharacterized Loc (LOC659067), approximately 4,000 bp in 5' (tail-to-head)	1-5' with BsrGI, I4

Supplementary Table 4 – Generations. In this table, the F0 to F7 and their characteristics are summarized.

Gen	Description / example terminology	Rationale	Crossing
F0	wild-type pool (PWAS strain)	The background line of choice, <i>i.e.</i> PWAS in our study. After a few weeks of adulthood, a replacement F0 is grown from a separate egg collection procedure to keep the line alive.	<i>inter pares / en masse</i>
F1	potential mosaics • AGOC{ATub'#O(LA)-mEmerald} #1 (●●/-) mosaics	Generated via injection of the respective transgenesis construct in conjunction with the ATub'piggyBac helper vector into preblastoderm embryos. Approximately 1-2% of surviving embryos become F1 mosaics. They typically do not show any fluorescence and can only be identified by crossing them against the wild-type and analyzing the progeny.	all surviving embryos, <i>i.e.</i> potential mosaics, are crossed against wild-types
F2	mO-mC hemizygote founders • AGOC{ATub'#O(LA)-mEmerald} #1 (●●/-) founder	The first generation where all cells carry the transgene. For each positive cross among the F1 potential mosaics, one F2 mO-mC founder female is chosen to establish a subline, <i>i.e.</i> lines that carry the identical transgene at different genomic locations. A cross against a wild-type male is necessary to (i) determine the number of inserts, (ii) establish a F3 colony and (iii) generate organisms of both genders for the homozygous viability cross.	wild-type
F3	mO-mC pre-recombination hemizygotes • AGOC{ATub'#O(LA)-mEmerald} #1 (●●/-)	Until this generation, our route does not differ from the standard transgenic animal establishment procedure. Working cultures can be established from the F3 individuals that can be treated like classical transgenic lines and used in (preliminary) experiments. Independently, the AGOC procedure is initiated by crossing F3 mO-mC pre-recombination hemizygous female against the mCe helper homozygote male which express the Cre recombinase.	ICE{HSP68'NLS-Cre}
F4	mCe×mO-mC double hemizygotes (<i>i.e.</i> hybrids) • AGOC{ATub'#O(LA)-mEmerald} #1 (●●/-) × ICE{HSP68'NLS-Cre} (●/-)	The F4 mCe×mO-mC double hemizygotes are hybrids. Within this generation, recombination occurs and one of both markers is excised. This process happens mainly during later stages of development, so that the individuals typically show a patchy transformation marker expression pattern, which is apparent in the adult eyes (Supplementary Figure 2).	wild-type
F5	mO- and mC-only post-recombination hemizygotes • AGOC{ATub'#O(LA)-mEmerald} #1 (●/-) • AGOC{ATub'#O(LA)-mEmerald} #1 (●/-)	In the F5 generation, the Cre-expressing transgene as well as one transformation marker are removed. As the transformation marker is typically excised after most of the germline cells have differentiated, F5 mO- and mC-only post-recombination hemizygotes are obtained from a single cross.	brother-sister crossing of adults with different markers
F6	mO/mC heterozygotes • AGOC{ATub'#O(LA)-mEmerald} #1 (●●)	The F6 mO/mC heterozygotes can be identified as they carry once again both transformation markers, but this times not consecutively on one chromosome, but one marker on the maternal and the other marker on the paternal chromosome. This generation is homozygous for the remaining transgene.	brother-sister crossing of adults with both markers
F7	mO- and mC-only homozygotes • AGOC{ATub'#O(LA)-mEmerald} #1 (●●) • AGOC{ATub'#O(LA)-mEmerald} #1 (●●)	Two types of F7 individuals are obtained that are homozygous, <i>i.e.</i> they carry the transgene with the same transformation marker on the maternal and paternal chromosomes. They are selected by the lack of the other transformation marker. This is the final generation, from which continuous F7+ mO- and mC-only homozygous cultures can be established.	<i>en masse</i> of individuals with the same marker to establish continuous F7+ cultures

Supplementary Table 5 – Crossing results for the two proof-of-principle AGOC #5 and #6 sublimes from the F3 to F7 generation with inversed genders. Bold entries mark progeny that was used in the subsequent cross, the F6-S, F7-O and F7-C entries mark control crosses.

Gen	Cross		Sublime	Progeny								Total		
	♀	♂		●●●	●●●	●●●	●●●	●●●	●●●	●●●	●●●			
F3			Theoretical	-	50.0%	-	-	-	-	-	-	50.0%	100%	
			AGOC #5	-	50.0% (35)	-	-	-	-	-	-	-	50.0% (35)	100% (70)
			AGOC #6	-	57.4% (62)	-	-	-	-	-	-	-	42.6% (46)	100% (108)
			Mean (%)	-	53.7%	-	-	-	-	-	-	-	46.3%	100%
F4			Theoretical	25.0%	25.0%	12.5%	12.5%	12.5%	12.5%	-	-	-	100%	
			AGOC #5	14.4% (17)	39.8% (47)	10.2% (12)	24.6% (29)	4.2% (5)	6.8% (8)	-	-	-	100% (118)	
			AGOC #6	22.7% (30)	35.6% (47)	9.1% (12)	12.1% (16)	8.4% (11)	12.1% (16)	-	-	-	100% (132)	
			Mean (%)	18.5%	37.7%	9.7%	18.3%	6.3%	9.5%	-	-	-	100%	
F5			Theoretical	25.0%	-	25.0%	25.0%	-	-	25.0%	-	100%		
			AGOC #5	29.3% (29)	-	31.3% (31)	21.2% (21)	-	-	18.2% (18)	-	100% (99)		
			AGOC #6	25.0% (26)	-	26.9% (28)	26.9% (28)	-	-	21.2% (22)	-	100% (104)		
			Mean (%)	27.1%	-	29.1%	24.1%	-	-	19.7%	-	100%		
F6-S			Theoretical	-	-	50.0%	50.0%	-	-	-	-	100%		
			AGOC #5	-	-	47.9% (58)	52.1% (63)	-	-	-	-	100% (121)		
			AGOC #6	-	-	53.8% (28)	46.2% (24)	-	-	-	-	100% (52)		
			Mean (%)	-	-	50.8%	49.2%	-	-	-	-	100%		
F6			Theoretical	-	-	25.0%	25.0%	-	-	50.0%	-	100%		
			AGOC #5	-	-	25.4% (14)	18.2% (10)	-	-	56.4% (31)	-	100% (55)		
			AGOC #6	-	-	21.2% (18)	27.0% (23)	-	-	51.8% (44)	-	100% (85)		
			Mean (%)	-	-	23.3%	22.6%	-	-	54.1%	-	100%		
F7-O			Theoretical	-	-	100%	-	-	-	-	-	100%		
			AGOC #5	-	-	100% (58)	-	-	-	-	-	100% (58)		
			AGOC #6	-	-	100% (77)	-	-	-	-	-	100% (97)		
			Mean (%)	-	-	100%	-	-	-	-	-	100%		
F7-C			Theoretical	-	-	-	100%	-	-	-	-	100%		
			AGOC #5	-	-	-	100% (97)	-	-	-	-	100% (97)		
			AGOC #6	-	-	-	100% (72)	-	-	-	-	100% (72)		
			Mean (%)	-	-	-	100%	-	-	-	-	100%		

Supplementary Table 7 – Crossing results for six of the thirteen functional AGOC sublines (Lifect only) from the F3 to F7 generation. Bold entries mark progeny that was used in the subsequent cross, the F6-S, F7-O and F7-C entries mark control crosses.

Gen	Cross		Subline	Progeny								Total		
	♀	♂		●●●	●●●	●●●	●●●	●●●	●●●	●●●	●●●			
F3			Theoretical	-	50.0%	-	-	-	-	-	-	50.0%	100%	
			AGOC{ATub'#O(LA)-mEmerald} #1	-	44.8% (43)	-	-	-	-	-	-	-	55.2% (53)	100% (96)
			AGOC{Zen1'#O(LA)-mEmerald} #1	-	57.4% (20)	-	-	-	-	-	-	-	42.6% (27)	100% (47)
			AGOC{Zen1'#O(LA)-mEmerald} #2 ¹	-	45.9% (45)	-	-	-	-	-	-	-	54.1% (53)	100% (98)
			AGOC{Zen1'#O(LA)-mEmerald} #3	-	48.7% (55)	-	-	-	-	-	-	-	51.3% (58)	100% (113)
			AGOC{ARPS'#O(LA)-mEmerald} #1	-	48.7% (37)	-	-	-	-	-	-	-	51.3% (39)	100% (76)
			AGOC{ARPS'#O(LA)-mEmerald} #2	-	59.4% (38)	-	-	-	-	-	-	-	40.6% (26)	100% (64)
			Mean (%)	-	50.8%	-	-	-	-	-	-	-	49.2%	100%
			F4			Theoretical	25.0%	25.0%	12.5%	12.5%	12.5%	12.5%	-	-
AGOC{ATub'#O(LA)-mEmerald} #1	31.6% (38)	29.2% (35)				15.0% (18)	2.5% (3)	20.0% (18)	1.7% (2)	-	-	-	-	100% (120)
AGOC{Zen1'#O(LA)-mEmerald} #1	32.4% (35)	27.8% (30)				6.5% (7)	14.8% (16)	7.4% (8)	11.1% (12)	-	-	-	-	100% (108)
AGOC{Zen1'#O(LA)-mEmerald} #2 ¹	19.6% (21)	36.4% (39)				5.6% (6)	15.0% (16)	5.6% (6)	17.8% (19)	-	-	-	-	100% (107)
AGOC{Zen1'#O(LA)-mEmerald} #3	40.0% (38)	24.2% (23)				13.7% (13)	6.3% (6)	10.5% (10)	5.3% (5)	-	-	-	-	100% (95)
AGOC{ARPS'#O(LA)-mEmerald} #1	19.6% (21)	33.6% (36)				10.3% (11)	9.4% (10)	12.1% (13)	15.0% (16)	-	-	-	-	100% (107)
AGOC{ARPS'#O(LA)-mEmerald} #2	26.7% (27)	28.7% (29)				18.8% (19)	3.0% (3)	18.8% (19)	4.0% (4)	-	-	-	-	100% (101)
Mean (%)	28.3%	30.0%				11.6%	8.5%	12.4%	9.2%	-	-	-	-	100%
F5						Theoretical	25.0%	-	25.0%	25.0%	-	-	-	25.0%
			AGOC{ATub'#O(LA)-mEmerald} #1	27.2% (31)	-	24.6% (28)	26.3% (30)	-	-	-	-	21.9% (25)	-	100% (114)
			AGOC{Zen1'#O(LA)-mEmerald} #1	26.6% (38)	-	16.8% (24)	33.5% (48)	-	-	-	-	23.1% (33)	-	100% (143)
			AGOC{Zen1'#O(LA)-mEmerald} #2	20.2% (19)	-	31.9% (30)	22.4% (21)	-	-	-	-	25.5% (24)	-	100% (94)
			AGOC{Zen1'#O(LA)-mEmerald} #3	22.7% (27)	-	21.0% (25)	34.5% (41)	-	-	-	-	21.8% (26)	-	100% (119)
			AGOC{ARPS'#O(LA)-mEmerald} #1	25.8% (31)	-	20.9% (25)	28.3% (34)	-	-	-	-	25.0% (30)	-	100% (120)
			AGOC{ARPS'#O(LA)-mEmerald} #2	27.1% (16)	-	15.3% (9)	28.8% (17)	-	-	-	-	28.8% (17)	-	100% (59)
			Mean (%)	24.9%	-	21.8%	29.0%	-	-	-	-	24.3%	-	100%
			F6-S			Theoretical	-	-	50.0%	50.0%	-	-	-	-
AGOC{ATub'#O(LA)-mEmerald} #1	-	-				44.4% (36)	55.6% (45)	-	-	-	-	-	-	100% (81)
AGOC{Zen1'#O(LA)-mEmerald} #1	-	-				43.9% (29)	56.1% (37)	-	-	-	-	-	-	100% (66)
AGOC{Zen1'#O(LA)-mEmerald} #2	-	-				48.8% (41)	51.2% (53)	-	-	-	-	-	-	100% (84)
AGOC{Zen1'#O(LA)-mEmerald} #3	-	-				42.6% (55)	57.4% (74)	-	-	-	-	-	-	100% (129)
AGOC{ARPS'#O(LA)-mEmerald} #1	-	-				55.6% (45)	44.4% (36)	-	-	-	-	-	-	100% (81)
AGOC{ARPS'#O(LA)-mEmerald} #2	-	-				46.8% (37)	53.2% (42)	-	-	-	-	-	-	100% (79)
Mean (%)	-	-				47.0%	53.0%	-	-	-	-	-	-	100%
F6						Theoretical	-	-	25.0%	25.0%	-	-	-	50.0%
			AGOC{ATub'#O(LA)-mEmerald} #1	-	-	27.6% (27)	25.5% (25)	-	-	-	46.9% (46)	-	-	100% (98)
			AGOC{Zen1'#O(LA)-mEmerald} #1	-	-	25.7% (37)	18.1% (26)	-	-	-	56.2% (81)	-	-	100% (144)
			AGOC{Zen1'#O(LA)-mEmerald} #2 ¹	-	-	42.2% (71)	39.3% (66)	-	-	-	18.6% (31)	-	-	100% (168)
			AGOC{Zen1'#O(LA)-mEmerald} #3	-	-	26.8% (22)	26.8% (22)	-	-	-	46.4% (38)	-	-	100% (82)
			AGOC{ARPS'#O(LA)-mEmerald} #1	-	-	14.0% (17)	30.3% (37)	-	-	-	55.7% (68)	-	-	100% (122)
			AGOC{ARPS'#O(LA)-mEmerald} #2	-	-	23.6% (25)	24.5% (26)	-	-	-	51.9% (55)	-	-	100% (106)
			Mean (%)	-	-	23.6%	25.0%	-	-	-	51.4%	-	-	100%
			F7-O			Theoretical	-	-	100%	-	-	-	-	-
AGOC{ATub'#O(LA)-mEmerald} #1	-	-				100% (99)	-	-	-	-	-	-	-	100% (99)
AGOC{Zen1'#O(LA)-mEmerald} #1	-	-				100% (89)	-	-	-	-	-	-	-	100% (89)
AGOC{Zen1'#O(LA)-mEmerald} #2	-	-				100% (77)	-	-	-	-	-	-	-	100% (77)
AGOC{Zen1'#O(LA)-mEmerald} #3	-	-				100% (54)	-	-	-	-	-	-	-	100% (54)
AGOC{ARPS'#O(LA)-mEmerald} #1	-	-				100% (94)	-	-	-	-	-	-	-	100% (94)
AGOC{ARPS'#O(LA)-mEmerald} #2	-	-				100% (106)	-	-	-	-	-	-	-	100% (106)
Mean (%)	-	-				100%	-	-	-	-	-	-	-	100%
F7-C						Theoretical	-	-	-	100%	-	-	-	-
			AGOC{ATub'#O(LA)-mEmerald} #1	-	-	-	100% (64)	-	-	-	-	-	-	100% (64)
			AGOC{Zen1'#O(LA)-mEmerald} #1	-	-	-	100% (101)	-	-	-	-	-	-	100% (101)
			AGOC{Zen1'#O(LA)-mEmerald} #2	-	-	-	100% (63)	-	-	-	-	-	-	100% (63)
			AGOC{Zen1'#O(LA)-mEmerald} #3	-	-	-	100% (67)	-	-	-	-	-	-	100% (67)
			AGOC{ARPS'#O(LA)-mEmerald} #1	-	-	-	100% (98)	-	-	-	-	-	-	100% (98)
			AGOC{ARPS'#O(LA)-mEmerald} #2	-	-	-	100% (91)	-	-	-	-	-	-	100% (91)
			Mean (%)	-	-	-	100%	-	-	-	-	-	-	100%

¹ the AGOC{Zen1'#O(LA)-mEmerald} #2 subline carries the transgene on the X allosome. Thus, two uncle-niece crosses with two F6 mO/mC semi homozygous females were performed, one with a F5 mO-only post-recombination hemizygote male and one with a F5 mC-only post-recombination hemizygote male. For both crosses, 84 individuals were genotyped (168 in total), the values shown are the sums of both crosses. Also, the expected distribution is different: theoretically, 37.5% should be mO-only, 37.5% should be mC-only, and 25.0% should carry mO and mC. In the F6 cross, the subline was left out for the mean calculation. See the Supplementary Note for details.

Supplementary Table 8 – Crossing results for seven of the thirteen functional AGOC sublines (Non-Lifect) from the F3 to F7 generation.

Gen	Cross		Subline	Progeny							Total			
	♀	♂		●●●	●●●	●●●	●●●	●●●	●●●	●●●				
F3			Theoretical	-	50.0%	-	-	-	-	-	50.0%	100%		
			AGOC{ATub'SiaTr-mEmerald} #1	-	57.7% (41)	-	-	-	-	-	-	42.3% (30)	100% (71)	
			AGOC{ATub'SiaTr-mEmerald} #2	-	48.8% (39)	-	-	-	-	-	-	51.2% (41)	100% (80)	
			AGOC{ATub'SiaTr-mEmerald} #3	-	52.0% (39)	-	-	-	-	-	-	48.0% (36)	100% (75)	
			AGOC{ATub'H2B-mEmerald} #1	-	39.3% (22)	-	-	-	-	-	-	60.7% (34)	100% (56)	
			AGOC{ATub'H2B-mEmerald} #2	-	46.7% (28)	-	-	-	-	-	-	53.3% (32)	100% (60)	
			AGOC{ATub'H2B-mEmerald} #3	-	55.0% (55)	-	-	-	-	-	-	45.0% (45)	100% (100)	
			AGOC{ATub'H2B-mEmerald} #4	-	49.4% (44)	-	-	-	-	-	-	50.6% (45)	100% (89)	
			Mean (%)	-	49.8%	-	-	-	-	-	-	50.2%	100%	
			F4			Theoretical	25.0%	25.0%	12.5%	12.5%	12.5%	12.5%	-	-
AGOC{ATub'SiaTr-mEmerald} #1	29.8% (31)	20.2% (21)				23.1% (24)	2.9% (3)	21.1% (22)	2.9% (3)	-	-	-	100% (104)	
AGOC{ATub'SiaTr-mEmerald} #2	24.8% (28)	30.1% (34)				4.4% (5)	19.4% (22)	7.1% (8)	14.2% (16)	-	-	-	100% (113)	
AGOC{ATub'SiaTr-mEmerald} #3	37.9% (36)	25.2% (24)				5.3% (5)	9.5% (9)	15.8% (15)	6.3% (6)	-	-	-	100% (95)	
AGOC{ATub'H2B-mEmerald} #1	29.4% (32)	23.9% (26)				11.9% (13)	16.5% (18)	5.5% (6)	12.8% (14)	-	-	-	100% (109)	
AGOC{ATub'H2B-mEmerald} #2	21.8% (24)	36.4% (40)				22.7% (25)	10.0% (11)	3.6% (4)	5.5% (6)	-	-	-	100% (110)	
AGOC{ATub'H2B-mEmerald} #3	35.8% (34)	25.3% (24)				10.5% (10)	8.4% (8)	14.7% (14)	5.3% (5)	-	-	-	100% (95)	
AGOC{ATub'H2B-mEmerald} #4	21.8% (24)	31.8% (35)				21.8% (24)	13.6% (15)	6.4% (7)	4.6% (5)	-	-	-	100% (110)	
Mean (%)	28.7%	27.6%				14.2%	11.5%	10.6%	7.4%	-	-	-	100%	
F5						Theoretical	25.0%	-	25.0%	25.0%	-	-	-	25.0%
			AGOC{ATub'SiaTr-mEmerald} #1	21.6% (21)	-	26.8% (26)	28.9% (28)	-	-	-	-	22.7% (22)	-	100% (97)
			AGOC{ATub'SiaTr-mEmerald} #2	20.7% (24)	-	30.2% (35)	26.7% (31)	-	-	-	-	22.4% (26)	-	100% (116)
			AGOC{ATub'SiaTr-mEmerald} #3	19.3% (16)	-	30.1% (25)	28.9% (24)	-	-	-	-	21.7% (18)	-	100% (83)
			AGOC{ATub'H2B-mEmerald} #1	29.2% (33)	-	28.3% (32)	23.9% (27)	-	-	-	-	18.6% (21)	-	100% (113)
			AGOC{ATub'H2B-mEmerald} #2	28.6% (30)	-	19.0% (20)	21.0% (22)	-	-	-	-	31.4% (33)	-	100% (105)
			AGOC{ATub'H2B-mEmerald} #3	22.6% (21)	-	25.8% (24)	20.4% (19)	-	-	-	-	31.2% (29)	-	100% (93)
			AGOC{ATub'H2B-mEmerald} #4	26.8% (19)	-	21.1% (15)	26.8% (19)	-	-	-	-	25.3% (18)	-	100% (71)
			Mean (%)	24.1%	-	25.9%	25.2%	-	-	-	-	24.8%	-	100%
			F6-S			Theoretical	-	-	50.0%	50.0%	-	-	-	-
AGOC{ATub'SiaTr-mEmerald} #1	-	-				48.2% (52)	51.8% (56)	-	-	-	-	-	-	100% (108)
AGOC{ATub'SiaTr-mEmerald} #2	-	-				52.8% (28)	47.2% (25)	-	-	-	-	-	-	100% (53)
AGOC{ATub'SiaTr-mEmerald} #3	-	-				44.4% (44)	55.6% (55)	-	-	-	-	-	-	100% (99)
AGOC{ATub'H2B-mEmerald} #1	-	-				40.6% (28)	59.4% (41)	-	-	-	-	-	-	100% (69)
AGOC{ATub'H2B-mEmerald} #2	-	-				48.6% (35)	51.4% (37)	-	-	-	-	-	-	100% (72)
AGOC{ATub'H2B-mEmerald} #3	-	-				50.9% (55)	49.1% (53)	-	-	-	-	-	-	100% (108)
AGOC{ATub'H2B-mEmerald} #4	-	-				-	-	-	-	-	-	-	-	-
Mean (%)	-	-				47.6%	52.4%	-	-	-	-	-	-	100%
F6						Theoretical	-	-	25.0%	25.0%	-	-	-	50.0%
			AGOC{ATub'SiaTr-mEmerald} #1	-	-	27.9% (29)	27.9% (29)	-	-	-	-	44.2% (46)	-	100% (104)
			AGOC{ATub'SiaTr-mEmerald} #2	-	-	28.0% (42)	27.3% (41)	-	-	-	-	44.7% (67)	-	100% (150)
			AGOC{ATub'SiaTr-mEmerald} #3	-	-	20.8% (10)	18.8% (9)	-	-	-	-	60.4% (29)	-	100% (48)
			AGOC{ATub'H2B-mEmerald} #1	-	-	41.1% (23)	12.5% (7)	-	-	-	-	46.4% (26)	-	100% (56)
			AGOC{ATub'H2B-mEmerald} #2	-	-	25.5% (27)	26.4% (28)	-	-	-	-	48.1% (51)	-	100% (106)
			AGOC{ATub'H2B-mEmerald} #3	-	-	28.3% (39)	27.5% (38)	-	-	-	-	44.2% (61)	-	100% (138)
			AGOC{ATub'H2B-mEmerald} #4	-	-	-	-	-	-	-	-	-	-	-
			Mean (%)	-	-	28.6%	23.4%	-	-	-	-	48.0%	-	100%
			F7-O			Theoretical	-	-	100%	100%	-	-	-	-
AGOC{ATub'SiaTr-mEmerald} #1	-	-				100% (57)	-	-	-	-	-	-	-	100% (57)
AGOC{ATub'SiaTr-mEmerald} #2	-	-				100% (51)	-	-	-	-	-	-	-	100% (51)
AGOC{ATub'SiaTr-mEmerald} #3	-	-				100% (59)	-	-	-	-	-	-	-	100% (59)
AGOC{ATub'H2B-mEmerald} #1	-	-				100% (103)	-	-	-	-	-	-	-	100% (103)
AGOC{ATub'H2B-mEmerald} #2	-	-				100% (155)	-	-	-	-	-	-	-	100% (155)
AGOC{ATub'H2B-mEmerald} #3	-	-				100% (103)	-	-	-	-	-	-	-	100% (103)
AGOC{ATub'H2B-mEmerald} #4	-	-				-	-	-	-	-	-	-	-	-
Mean (%)	-	-				100%	-	-	-	-	-	-	-	100%
F7-C						Theoretical	-	-	-	100%	-	-	-	-
			AGOC{ATub'SiaTr-mEmerald} #1	-	-	-	100% (48)	-	-	-	-	-	-	100% (48)
			AGOC{ATub'SiaTr-mEmerald} #2	-	-	-	100% (66)	-	-	-	-	-	-	100% (66)
			AGOC{ATub'SiaTr-mEmerald} #3	-	-	-	100% (73)	-	-	-	-	-	-	100% (73)
			AGOC{ATub'H2B-mEmerald} #1	-	-	-	100% (134)	-	-	-	-	-	-	100% (134)
			AGOC{ATub'H2B-mEmerald} #2	-	-	-	100% (86)	-	-	-	-	-	-	100% (86)
			AGOC{ATub'H2B-mEmerald} #3	-	-	-	100% (71)	-	-	-	-	-	-	100% (71)
			AGOC{ATub'H2B-mEmerald} #4	-	-	-	-	-	-	-	-	-	-	-
			Mean (%)	-	-	-	100%	-	-	-	-	-	-	100%

¹ the AGOC{ATub'H2B-mEmerald} #4 subline did not produce any progeny when F6 mO/mC heterozygotes were crossed (n = 12), when F6 mO/mC heterozygous females and wild-type males were crossed (n = 12), and, as an additional control, when F6 mO/mC heterozygous males and wild-type females were crossed (n = 8). It was therefore assumed that this subline is sterile when both chromosome carry the transgene. In the F6-S, F6, F7-O and F7-C crosses, it was left out of the mean calculations.

Supplementary Table 9 – F2 insert number determination cross for the thirteen functional AGOC sublines.

F2 mO-mC founder females were crossed against wild-type males and the progeny was quantitatively evaluated.

Segregation of mO-mC of 60% or less was defined as the criteria for one insert, no deviants were identified.

Line	●●●	●●●	Total
theoretical – one insertions	50%	50%	100%
theoretical – two insertions ¹	25%	75%	100%
AGOC{ATub'#O(LA)-mEmerald} #1	47.1% (33)	52.9% (37)	100% (70)
AGOC{Zen1'#O(LA)-mEmerald} #1	58.5% (38)	41.5% (27)	100% (65)
AGOC{Zen1'#O(LA)-mEmerald} #2	46.6% (27)	53.4% (31)	100% (58)
AGOC{Zen1'#O(LA)-mEmerald} #3	52.2% (35)	47.8% (32)	100% (67)
AGOC{ARP5'#O(LA)-mEmerald} #1	54.3% (76)	45.7% (64)	100% (140)
AGOC{ARP5'#O(LA)-mEmerald} #2	48.4% (75)	51.6% (80)	100% (155)
AGOC{ATub'SiaTr-mEmerald} #1	51.9% (28)	48.1% (26)	100% (54)
AGOC{ATub'SiaTr-mEmerald} #2	43.5% (30)	56.5% (39)	100% (69)
AGOC{ATub'SiaTr-mEmerald} #3	48.5% (33)	51.5% (35)	100% (68)
AGOC{ATub'H2B-mEmerald} #1	49.2% (31)	50.8% (32)	100% (63)
AGOC{ATub'H2B-mEmerald} #2	64.4% (65)	35.6% (36)	100% (101)
AGOC{ATub'H2B-mEmerald} #3	52.3% (46)	47.7% (42)	100% (88)
AGOC{ATub'H2B-mEmerald} #4	55.2% (48)	44.8% (39)	100% (87)

¹ this theoretical value corresponds to the case that the insertions occur on different chromosomes, which is more likely than two independent inserts on the same chromosome.

Supplementary Table 10 – F3 homozygous viability crosses for the thirteen functional AGOC sublines.

A brother-sister-cross of two F3 mO-mC pre-recombination hemizygotes was performed and the progeny was quantitatively evaluated. Segregation of the mO-mC of 70% or more was defined as the criteria for homozygous viability, deviants are marked in bold.

Line	●●●	●●●	Total
theoretical – homozygous viable	25.0%	75.0%	100%
theoretical – homozygous lethal	33.3%	66.7%	100%
AGOC{ATub'#O(LA)-mEmerald} #1	33.8% (23)	66.2% (45)	100% (68)
AGOC{Zen1'#O(LA)-mEmerald} #1	24.6% (17)	75.4% (52)	100% (69)
AGOC{Zen1'#O(LA)-mEmerald} #2	25.0% (15)	75.0% (45)	100% (60)
AGOC{Zen1'#O(LA)-mEmerald} #3	25.5% (12)	74.5% (35)	100% (47)
AGOC{ARP5'#O(LA)-mEmerald} #1	21.7% (13)	78.3% (47)	100% (60)
AGOC{ARP5'#O(LA)-mEmerald} #2	23.5% (12)	76.5% (39)	100% (51)
AGOC{ATub'SiaTr-mEmerald} #1	28.9% (28)	71.1% (69)	100% (97)
AGOC{ATub'SiaTr-mEmerald} #2	28.4% (19)	71.6% (41)	100% (67)
AGOC{ATub'SiaTr-mEmerald} #3	24.6% (15)	75.4% (46)	100% (61)
AGOC{ATub'H2B-mEmerald} #1	22.4% (19)	77.6% (66)	100% (86)
AGOC{ATub'H2B-mEmerald} #2	23.4% (22)	76.6% (72)	100% (94)
AGOC{ATub'H2B-mEmerald} #3	23.3% (27)	76.7% (89)	100% (116)
AGOC{ATub'H2B-mEmerald} #4	49.7% (73)	50.3% (72)	100% (147)

Supplementary Table 11 – Insertion locations for six of the thirteen functional AGOC sublines. In the Junction column, the piggyBac TTAA insertion/excision target sequence is marked in bold.

Subline	Chromosome	Junction	Neighbors	Inverse primer pair and restriction enzyme, control primer pair
AGOC {ATub#O(LA)-mEmerald} #1	ChLG2 (reverse orientation)	5'-TCTAACGCCACGATACACACAGATAA TTAA AACGCTGATAAATAGGAGAGGCTTCG-3'	Probable JmJc domain-containing histone demethylation protein 2C (NC_007417.2), approximately 13,000 bp in 3' (tail-to-head)	1-3' with SpeI, 15
AGOC {Zen1#O(LA)-mEmerald} #1	ChLG3 (reverse orientation)	5'-ATAGCAAATTAATTTAAGCTTCC TTAA GTTGTTCGTAATTCCTGTTTGAAGA-3'	Activating transcription factor 7-interacting protein 1 (NC_007418.2), approximately 7,000 bp in 5' (head-to-head)	1-3' with AatII, 16
AGOC {Zen1#O(LA)-mEmerald} #2	ChLGX (allosomal) (reverse orientation)	5'-TTTCGACAATGGGTCGTCGACAA TTAA AAAGTCCGATCCTTCTCAGTGCCTAA-3'	GTP-binding protein Rheb (NC_007416.2), approximately 6,000 bp in 5' (tail-to-tail)	1-3' with EciRI, 17
AGOC {Zen1#O(LA)-mEmerald} #3	Not X or Y	N.A. ¹	N.A.	N.A.
AGOC {ARPS#O(LA)-mEmerald} #1	ChLG9 (reverse orientation)	5'-TGAACCCCTTGACATATTTTTGTTAA TTAA ACTTGGCGTAATAATGGCCATAATGGCC-3 ²	Membrane metallo-endopeptidase-like 1 (NC_007424.2), approximately 2,600 bp in 5' (tail-to-head)	1-5' with EagI, control PCR not performed
AGOC {ARPS#O(LA)-mEmerald} #2	Not X or Y	N.A.	N.A.	N.A.
AGOC {ATub/SiaTr-mEmerald} #1	ChLG9 (reverse orientation)	5'-GCTCCAACCACTGTTTCAGCTATTTAA TTAA AGCCATAAATAACGATCGTTATCTCGT-3'	Intron 2 of CUGBP Elav-like family member 1 (NC_007424.2), approximately 3,500 bp from Exon 2 (head-to-tail)	1-5' with SalI, 18
AGOC {ATub/SiaTr-mEmerald} #2	Not X or Y	N.A.	N.A.	N.A.
AGOC {ATub/SiaTr-mEmerald} #3	Not X or Y	N.A.	N.A.	N.A.
AGOC {ATub/H2B-mEmerald} #1	Unknown (forward orientation)	5'-GTCTCACATTTATCAGTCACTTGAAG TTAA AGCTGCTAACATGTTAAAACCTTGACA-3'	No genes within 100,000 bp	1-5' with EcoRI, 19
AGOC {ATub/H2B-mEmerald} #2	Not X or Y	N.A.	N.A.	N.A.
AGOC {ATub/H2B-mEmerald} #3	Not X or Y	N.A.	N.A.	N.A.
AGOC {ATub/H2B-mEmerald} #4	Not X or Y	N.A.	N.A.	N.A.

¹ the AGOC {Zen1#O(LA)-mEmerald} #3 subline has a nested insertion, see Supplementary Note. ² As the control polymerase chain reaction was not performed, the 28 bp upstream of the TTAA site derive from BeetleBase.

Supplementary Table 12 – Vector summary. The 24 vectors used/created in this study are listed in order of their type. Numerical references in the Source/Buildup column refer to the respective vector entry. The rows are colored according to Supplementary Figure 10.

#	Vector	Type	Size	Res	Source / Buildup	Available?
1	pUC57-AGOC	gene synthesis (Genewiz)	2,978 bp	KanR	ordered from Genewiz (3,277 bp <i>de novo</i> synthesized sequence inserted into the pUC57-Kan backbone via NdeI / PstI)	our laboratory
2	pGSI#P#O(LA)-mEmerald	gene synthesis (Invitrogen)	4,111 bp	KanR	ordered from Invitrogen (1,833 bp <i>de novo</i> synthesized sequence inserted into the pMK-RQ backbone via SfiI)	our laboratory
3	pGSI#ACS	gene synthesis (Invitrogen)	4,928 bp	KanR	ordered from Invitrogen (2,650 bp <i>de novo</i> synthesized sequence inserted into the pMK-RQ backbone via SfiI)	our laboratory
4	pBSII-IFP-CDS	previously published	4,971 bp	AmpR	kind gift from Malcolm Fraser, vector described in ³⁸	Malcolm Fraser
5	pTriEx-H1NC	previously published	6,757 bp	AmpR	ordered from Addgene (Catalog #13763), vector described in ⁴²	Addgene (#13763)
6	pTC-ATub-GEM-T Easy	promoter library vector	3,633 bp	AmpR	ATub amplified from genomic DNA with primer pair 3, A-tailed and inserted into pGEM-T Easy (copy & paste)	our laboratory
7	pTC-HSP68-GEM-T Easy	promoter library vector	3,778 bp	AmpR	HSP68 amplified from genomic DNA with primer pair 4, A-tailed and inserted into pGEM-T Easy (copy & paste)	our laboratory
8	pTC-Zen1-GEM-T Easy	promoter library vector	4,599 bp	AmpR	Zen1 amplified from genomic DNA with primer pair 5, A-tailed and inserted into pGEM-T Easy (copy & paste)	our laboratory
9	pTC-ARPS-GEM-T Easy	promoter library vector	5,516 bp	AmpR	ARPS amplified from genomic DNA with primer pair 6, A-tailed and inserted into pGEM-T Easy (copy & paste)	our laboratory
10	pTC-SiaTr-GEM-T Easy	ORF library vector	4,358 bp	AmpR	SiaTr amplified from cDNA with primer pair 7, A-tailed and inserted into pGEM-T Easy (copy & paste)	our laboratory
11	pTC-H2B-GEM-T Easy	ORF library vector	3,889 bp	AmpR	H2B amplified from cDNA with primer pair 8, A-tailed and inserted into pGEM-T Easy (copy & paste)	our laboratory
12	pTC-HSP68-NLS-Cre-GEM-T Easy	promoter / ORF library vector	5,073 bp	AmpR	HSP68 and NLS-Cre amplified from 5 and 7, joined via fusion PCR with primer pair 9, A-tailed and inserted into pGEM-T Easy (fusion PCR)	our laboratory
13	pTC-ATub/H2B-GEM-T Easy	promoter / ORF library vector	4,010 bp	AmpR	ATub and H2B amplified from 6 and 11, joined via fusion PCR with primer pair 10, A-tailed and inserted into pGEM-T Easy (fusion PCR)	our laboratory
14	pATub piggyBac	helper	5,511 bp	AmpR	ATub and a fragment of piggyBac fusion PCR with primer pair 2 and inserted into the unique SalI / BglII sites	Addgene (#####)
15	pBSP68-NLS-Cre	helper / transformation	5,209 bp	KanR	BSP68-NLS-Cre cassette amplified from 3 with primer pair 11 and inserted into the AflI / XbaI sites of 16	Addgene (#####)
16	pAVOIAF#1-#2-HSP68-NLS-Cre-mC	intermediate	5,781 bp	KanR	HSP68-NLS-Cre cassette cut from 12 with NdeI / XhoI and inserted into the respective sites of 19	our laboratory
17	pAGOC #P#O(LA)-mEmerald	intermediate	6,852 bp	KanR	#P#O(LA)-mEmerald cassette cut from 2 with HindIII / XbaI and inserted into the respective sites of 19	Addgene (#####)
18	pAGOC #P#SiaTr-mEmerald	intermediate	8,106 bp	KanR	SiaTr amplified from 10 with primer pair 12 and inserted into the FseI / NotI sites of 17	our laboratory
19	pAGOC	intermediate / transformation	5,049 bp	KanR	AGOC cassette amplified from 1 with primer pair 1 and inserted into up- (AatII) and downstream (PciI) sites of the same vector for size reduction	Addgene (#####)
20	pAGOC {ATub#O(LA)-mEmerald}	transformation	7,400 bp	KanR	ATub amplified from 6 with primer pair 13, digested with AscI / BsmBI and inserted into the respective sites of 17, which was digested with BtgZI	our laboratory
21	pAGOC {ATub/SiaTr-mEmerald}	transformation	8,654 bp	KanR	ATub amplified from 6 with primer pair 13, digested with AscI / BsmBI and inserted into the respective sites of 18, which was digested with BtgZI	our laboratory
22	pAGOC {ATub/H2B-mEmerald}	transformation	7,718 bp	KanR	ATub/H2B cassette cut from 13 with AscI/NotI and inserted into the respective sites of 17	our laboratory
23	pAGOC {Zen1#O(LA)-mEmerald}	transformation	8,367 bp	KanR	Zen1 amplified from 6 with primer pair 14, digested with AscI / BsaI and inserted into the respective sites of 17, which was digested with BtgZI	our laboratory
24	pAGOC {ARPS#O(LA)-mEmerald}	transformation	9,276 bp	KanR	ARPS amplified from 6 with primer pair 15, digested with AscI / BsaI and inserted into the respective sites of 17, which was digested with BtgZI	our laboratory
-	pAVOIAF #1-#2-#3-#4	hypothetical vector	2,485 bp	KanR	vector was designed <i>in silico</i> based on the pUC57 backbone. The four-slot-modular cassette is located between the AatII and PciI sites	

Supplementary Table 13 – Cloning Primers. Primer pairs are listed in order of appearance in the Materials and Methods section. Primer that introduce a restriction enzyme site also carry a 6 bp (5'-AAATTT-3') buffer at the 5' end. ExPCR, extraction polymerase chain reaction; SiRePCR, size reduction polymerase chain reaction; FuPCR, fusion polymerase chain reaction; TrPCR, transfer polymerase chain reaction; FD, forward; RV, reverse.

Primer pair	#	Primer name	Primer sequence	Comment	Length	T _M ¹
C1	C1-1	TC ATub ¹ ExPCR FD	5'-AGATGCTATGTATCTCCCGTGAAC-3'	-	26 bp	59.7°C
	C1-2	TC ATub ¹ ExPCR RV	5'-GAAATGGGATAACTTACCATTITGG-3'	-	25 bp	59.7°C
C2	C2-1	TC Zen1 ¹ ExPCR FD	5'-AAATGCATGATTAACGTACATGTGAC-3'	-	27 bp	61.1°C
	C2-2	TC Zen1 ¹ ExPCR RV	5'-CAAATGGGGAGTAAGACATTTCGTG-3'	-	25 bp	60.8°C
C3	C3-1	TC ARP5 ¹ ExPCR FD	5'-CAACGATTAATCTCCGTGATAACAC-3'	-	26 bp	60.7°C
	C3-2	TC ARP5 ¹ ExPCR RV	5'-CAAGTCTTGAATTCGAGAATITCC-3'	-	25 bp	60.3°C
C4	C4-1	TC HSP68 ¹ ExPCR FD	5'-GAAAGTCGGGACCGAAGGTC-3'	-	20 bp	61.7°C
	C4-2	TC HSP68 ¹ ExPCR RV	5'-CAATACCACTGCCTGGAGATTTCAC-3'	-	25 bp	61.8°C
C5	C5-1	TC 'SiaTr' ExPCR FD	5'-ATGAGAGCTCTAGTGGTATCCATATGG-3'	-	27 bp	60.8°C
	C5-2	TC 'SiaTr' ExPCR RV	5'-CGTCTAAAAATCTACTCCAAAATTTCTC-3'	-	28 bp	61.4°C
C6	C6-1	TC 'H2B' ExPCR FD	5'-ATGCCACCAAGACAAGC-3'	-	18 bp	55.5°C
	C6-2	TC 'H2B' ExPCR RV	5'-CTATTTGAACTTGTGTATTTGGTG-3'	-	25 bp	55.7°C
C7	C7-1	HSP68 ¹ and 'NLS-Cre' FuPCR FD	5'-AAATTTGGCTAGCAAGTCGGGACCGAAGGCTTAATAAAAA-3'	overhang underlined, NheI site in bold	31 bp	66.0°C
	C7-2	HSP68 ¹ and 'NLS-Cre' FuPCR RV	5'-CACTTCCCTCTCTCTTGGGGGCATTTTGGCACTTTGGATTTACTTTG-3'	NLS-Cre ORF overhang underlined, start codon in bold	51 bp	61.8°C
	C7-3	'NLS-Cre and HSP68 ¹ FuPCR FD	5'-AAAGTAAATCCAAAAGTGC AAAAATGGCCCCAAGAAGAAGAGGAGGTGCCAATTTAC-3'	HSP68 ¹ overhang underlined, start codon in bold	61 bp	76.6°C
	C7-4	'NLS-Cre and HSP68 ¹ FuPCR RV	5'-AAATTTCTCGAGTAAGATACATTGATGAGTTTGGACAACCAACACTAG-3'	overhang underlined, XhoI site in bold	40 bp	68.2°C
C8	C8-1	ATub ¹ and 'H2B' FuPCR FD	5'-AAATTTGGCGCGCCAGATGTCTATGTATCTCCCGTGAAC-3'	overhang underlined, AscI site in bold	26 bp	59.7°C
	C8-2	ATub ¹ and 'H2B' FuPCR RV	5'-CGCTTGTCTTGGTGGCATTITGGTAGTTGAGTTTACAAATTAC-3'	H2B ORF overhang underlined, start codon in bold	45 bp	57.8°C
	C8-3	'H2B and ATub ¹ FuPCR FD	5'-GTAAAACCTCAACTACAAAATGCCACCAAGACAAGCGTAAAG-3'	ATub ¹ overhang underlined, start codon in bold	44 bp	66.8°C
	C8-4	'H2B and ATub ¹ FuPCR RV	5'-AAATTTGGCGCGCCCTTTTGAACCTGTGTATTTGGTGAAG-3'	overhang underlined, NotI site in bold	25 bp	60.9°C
C9	C9-1	AGOC SiRePCR FD	5'-AAATTTGACCTGTTAAACCTAGAAAAGATAATCATATTTGTGACGTAC-3'	overhang underlined, AatII site in bold	34 bp	62.6°C
	C9-2	AGOC SiRePCR RV	5'-AAATTTACATGTTTAAACCTAGAAAAGATAGCTGGGTAATTTG-3'	overhang underlined, PciI site in bold	32 bp	63.6°C
C10	C10-1	ATub ¹ TrPCR FD	5'-AAATTTGGCGCGCCAGATGTCTATGTATCTCCCGTGAAC-3'	overhang underlined, AscI site in bold	40 bp	59.7°C
	C10-2	ATub ¹ TrPCR RV	5'-AAATTTCTGCTCACCATTITGGTAGTTGAGTTTACAAATTAC-3'	overhang underlined, BsmBI site in bold	43 bp	60.4°C
C11	C11-1	Zen1 ¹ TrPCR FD	5'-AAATTTGGCGCGCCAAATGCATGATTAACGTATCATGTGAC-3'	overhang underlined, AscI site in bold	41 bp	61.1°C
	C11-2	Zen1 ¹ TrPCR RV	5'-AAATTTGGTCTCACCATTTTCGTCAAAAGTAAGTTTGC-3'	overhang underlined, BsaI site in bold	37 bp	59.6°C
C12	C12-1	ARP5 ¹ TrPCR FD	5'-AAATTTGGCGCGCCCAACGATTAATCTCCGTGATAACAC-3'	overhang underlined, AscI site in bold	40 bp	60.7°C
	C12-2	ARP5 ¹ TrPCR RV	5'-AAATTTGGTCTCACCATTTTGGGGTTAAGTGAC-3'	overhang underlined, BsaI site in bold	40 bp	54.9°C
C13	C13-1	'SiaTr' TrPCR FD	5'-AAATTTGGCGCGCCAAAATGAGAGCTCTAGTGGTATCCATATGG-3'	overhang underlined, FseI site in bold	44 bp	60.8°C
	C13-2	'SiaTr' TrPCR RV	5'-AAATTTGGCGCGCCACATTTAAAATTTTGAACCAAGATTG-3'	overhang underlined, NotI site in bold	43 bp	61.6°C
C14	C14-1	3xP3 ¹ mCerulean TrPCR FD	5'-AAATTTCTTAAGTGTCCACAATGGTAAATTCGAG-3'	overhang underlined, AflII site in bold	35 bp	60.4°C
	C14-2	3xP3 ¹ mCerulean TrPCR RV	5'-AAATTTCTTAGGTAAAGATACATTGATGAGTTGG-3'	overhang underlined, AvrII site in bold	34 bp	50.7°C
C15	C15-1	ATub ¹ and 'piggyBac' FuPCR FD	5'-AAATTTGTGCGACAGATGTCTATGTATCTCCCGTGAAC-3'	overhang underlined, Sall site in bold	38 bp	59.7°C
	C15-2	ATub ¹ and 'piggyBac' FuPCR RV	5'-CTCATCGTCTAAAGAACTACCCATTITGGTAGTTGAGTTTACAAATTAC-3'	piggyBac ORF overhang underlined, start codon in bold	50 bp	57.8°C
	C15-3	'piggyBac' and ATub ¹ FuPCR FD	5'-GTAAAACCTCAACTACAAAATGGGTAGTCTTATAGACGATGAGC-3'	ATub ¹ overhang underlined, start codon in bold	44 bp	59.9°C
	C15-4	'piggyBac' and ATub ¹ FuPCR RV	5'-AAATTTAGATCTAGATCTGACAATGTTCAGTGCAGAG-3'	overhang underlined, BglII site in bold	25 bp	60.7°C

¹ the Applied Biosciences web calculator (www6.appliedbiosystems.com/support/techttools/calc) was used to calculate the melting temperature T_M. In case of primers with overhangs, the T_M was only calculated for the annealing part.

Supplementary Table 14 – Transgenic lines and sublines. In total, seven transgenic lines with twenty-one sublines were created, *i.e.* six proof-of-principle AGOC sublines, thirteen functional AGOC sublines and two helper sublines. Two of the functional AGOC sublines have been analyzed with live imaging previously, live imaging data for three more is proved in this study.

Vector	Subline	Insertion location known	AGOC procedure	Fluorescence	Comment
pAGOC	AGOC #1	Yes (Supplementary Table 3)	Successful	mO/mC – strong	-
	AGOC #2	No	Successful	mO/mC – strong	-
	AGOC #3	Yes (Supplementary Table 3)	Successful	mO/mC – strong	-
	AGOC #4	No	Successful	mO/mC – strong	-
	AGOC #5	Yes (Supplementary Table 3)	Successful	mO/mC – moderate	-
	AGOC #6	Yes (Supplementary Table 3)	Successful	mO/mC – strong (slight enhancer trap pattern)	-
pAGOC{ATub ^{#O(LA)} -mEmerald}	AGOC{ATub ^{#O(LA)} -mEmerald} #1	Yes (Supplementary Table 11)	Successful	mO/mC – strong, mEmerald – strong	-
pAGOC{Zen1 ^{#O(LA)} -mEmerald}	AGOC{Zen1 ^{#O(LA)} -mEmerald} #1	Yes (Supplementary Table 11)	Successful	mO/mC – strong, mEmerald – moderate	-
	AGOC{Zen1 ^{#O(LA)} -mEmerald} #2	Yes (Supplementary Table 11)	Successful	mO/mC – strong, mEmerald – strong	Live imaging in this study
	AGOC{Zen1 ^{#O(LA)} -mEmerald} #3	No	Successful	mO/mC – moderate, mEmerald – weak	Initially a nested insert
pAGOC{ARP5 ^{#O(LA)} -mEmerald}	AGOC{ARP5 ^{#O(LA)} -mEmerald} #1	No	Successful	mO/mC – strong, mEmerald – strong	Live imaging in this study
	AGOC{ARP5 ^{#O(LA)} -mEmerald} #2	No	Successful	mO/mC – strong, mEmerald – strong	Live imaging in this study
pAGOC{ATub ^{SiaTr} -mEmerald}	AGOC{ATub ^{SiaTr} -mEmerald} #1	Yes (Supplementary Table 11)	Successful	mO/mC – strong, mEmerald – not detectable	-
	AGOC{ATub ^{SiaTr} -mEmerald} #2	No	Successful	mO/mC – strong, mEmerald – not detectable	-
	AGOC{ATub ^{SiaTr} -mEmerald} #3	No	Successful	mO/mC – strong, mEmerald – not detectable	-
pAGOC{ATub ^{H2B} -mEmerald}	AGOC{ATub ^{H2B} -mEmerald} #1	Yes (Supplementary Table 11)	Successful	mO/mC – strong, mEmerald – moderate (enhancer trap pattern)	Live imaging data published previously ⁴⁵
	AGOC{ATub ^{H2B} -mEmerald} #2	No	Successful	mO/mC – weak, mEmerald – weak	-
	AGOC{ATub ^{H2B} -mEmerald} #3	No	Successful	mO/mC – strong, mEmerald – moderate	-
	AGOC{ATub ^{H2B} -mEmerald} #4	No	Unsuccessful	mO/mC – strong, mEmerald – strong	Live imaging data published previously ⁴⁵
pICE[HSP68 ^{NLS} -Cre]	ICE[HSP68 ^{NLS} -Cre] #1	No	-	mCe – strong	Line is homozygous
	ICE[HSP68 ^{NLS} -Cre] #1	No	-	mCe – strong	Line is homozygous

Supplementary Table 15 – Stereo microscope filter sets. All components were obtained from AHF Analysentechnik, Tübingen, Germany.

Filter set	Excitation filter	Beam splitter	Emission filter	Comment
mCerulean (for mCe)	436/20 ET Bandpass (F49-436)	455 nm (F48-455)	480/40m ET Bandpass (F47-480)	-
mOrange (for mO)	546/10 ET Bandpass (F49-547)	565 nm (F33-565V20)	575/15 BrightLine HC (F39-575)	Blocks mCherry fluorescence nearly completely
mCherry (for mC)	586/15 BrightLine HC (F37-589)	595 nm (F43-595V20)	645/75 ET Bandpass (F47-645)	Blocks mOrange fluorescence nearly completely

Supplementary Table 16 – Inverse PCR primer. Primer pairs are listed according to their appearance in Supplementary Table 3 and Supplementary Table 11. Several primers have been used in multiple inverse PCRs and are therefore also listed multiple times, as annotated within the Comment column. InvPCR, inverse polymerase chain reaction; ConPCR, control polymerase chain reaction; FD, forward; RV, reverse.

Primer pair	#	Primer name	Primer sequence	Comment	Length	T _M ¹
I-3'	I-3'-1	AGOC 3' TR InvPCR FD	5'-AAAACCTGGTTAAACCCCGGG-3'	-	21 bp	59.9°C
	I-3'-2	AGOC 3' TR InvPCR RV	5'-GCATGATTATCTTTAACGTACGTACAC-3'	-	26 bp	58.9°C
I-5'	I-5'-1	AGOC 5' TR InvPCR FD	5'-CGTATTATAGAAAGAGAGCAATATTTC-3'	-	29 bp	60.4°C
	I-5'-2	AGOC 5' TR InvPCR RV	5'-ICTTGTATAGATATCAGTTTAAACCTAGG-3'	-	31 bp	58.9°C
II	II-1	AGOC #1 ConPCR FD	5'-TACAACAGAAAAGGGGAAGTATATTGG-3'	-	27 bp	60.6°C
	II-2	AGOC #1 ConPCR RV	5'-ATTAATAAAATAAACCTCGATATACAGACCG-3'	Identical with I2-2, I3-2, I4-2, I8-2 and I9-2	30 bp	59.3°C
I2	I2-1	AGOC #3 ConPCR FD	5'-AAAAGTTACAGACCTGTACACAAATG-3'	-	27 bp	59.6°C
	I2-2	AGOC #3 ConPCR RV	5'-ATTAATAAAATAAACCTCGATATACAGACCG-3'	Identical with I1-2, I2-2, I3-2, I4-2, I8-2 and I9-2	30 bp	59.3°C
I3	I3-1	AGOC #5 ConPCR FD	5'-TAAATCGGTTCTTTGTCCGC-3'	-	21 bp	60.9°C
	I3-2	AGOC #5 ConPCR RV	5'-ATTAATAAAATAAACCTCGATATACAGACCG-3'	Identical with I1-2, I2-2, I4-2, I8-2 and I9-2	30 bp	59.3°C
I4	I4-1	AGOC #6 ConPCR FD	5'-GACACCTGTACAACAATTCCAAC-3'	-	24 bp	60.4°C
	I4-2	AGOC #6 ConPCR RV	5'-ATTAATAAAATAAACCTCGATATACAGACCG-3'	Identical with I1-2, I2-2, I3-2, I8-2 and I9-2	30 bp	59.3°C
I5	I5-1	AGOC{ATub#O(LA)-mEmerald} #1 ConPCR FD	5'-GCATGATTATCTTTAACGTACGTACAC-3'	Identical with I6-1 and I7-1	26 bp	58.9°C
	I5-1	AGOC{ATub#O(LA)-mEmerald} #1 ConPCR RV	5'-AATCGAGAATGGTCTTATCAGTG-3'	-	24 bp	59.4°C
I6	I6-1	AGOC{Zen#O(LA)-mEmerald} #1 ConPCR FD	5'-GCATGATTATCTTTAACGTACGTACAC-3'	Identical with I5-1 and I7-1	26 bp	58.9°C
	I6-2	AGOC{Zen#O(LA)-mEmerald} #1 ConPCR RV	5'-TGACAGGACTATGCCTACCTTATAC-3'	-	26 bp	59.7°C
I7	I7-1	AGOC{Zen#O(LA)-mEmerald} #2 ConPCR FD	5'-GCATGATTATCTTTAACGTACGTACAC-3'	Identical with I5-1 and I6-1	26 bp	58.9°C
	I7-2	AGOC{Zen#O(LA)-mEmerald} #2 ConPCR RV	5'-AAACAGCCGCTAAAATCC-3'	-	20 bp	59.1°C
I8	I8-1	AGOC{ATub#Sia1r-mEmerald} #1 ConPCR FD	5'-AATTAATAAAATAAGCTGAACCTTTGATGTAG-3'	-	31 bp	59.0°C
	I8-2	AGOC{ATub#Sia1r-mEmerald} #1 ConPCR RV	5'-ATTAATAAAATAAACCTCGATATACAGACCG-3'	Identical with I1-2, I2-2, I3-2, I4-2 and I9-2	30 bp	59.3°C
I9	I9-1	AGOC{ATub#H2B-mEmerald} #1 ConPCR FD	5'-AGTTGCAAAATAGGCTTGAAGAACTAG-3'	-	27 bp	59.4°C
	I9-2	AGOC{ATub#H2B-mEmerald} #1 ConPCR RV	5'-ATTAATAAAATAAACCTCGATATACAGACCG-3'	Identical with I1-2, I2-2, I3-2, I4-2 and I8-2	30 bp	59.3°C

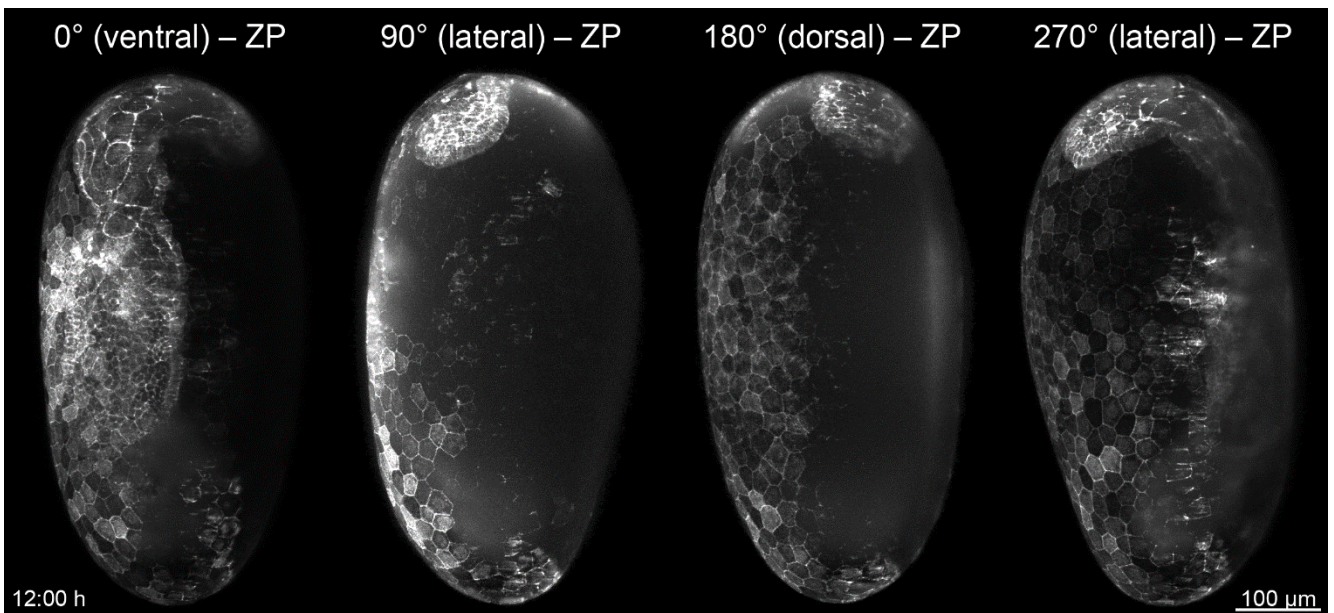
¹ the Applied Biosciences web calculator (www6.appliedbiosystems.com/support/techtools/calc) was used to calculate the melting temperature T_M.

Supplementary Table 17 – Metadata and parameter for the long-term live-imaging datasets DS0001-0003.

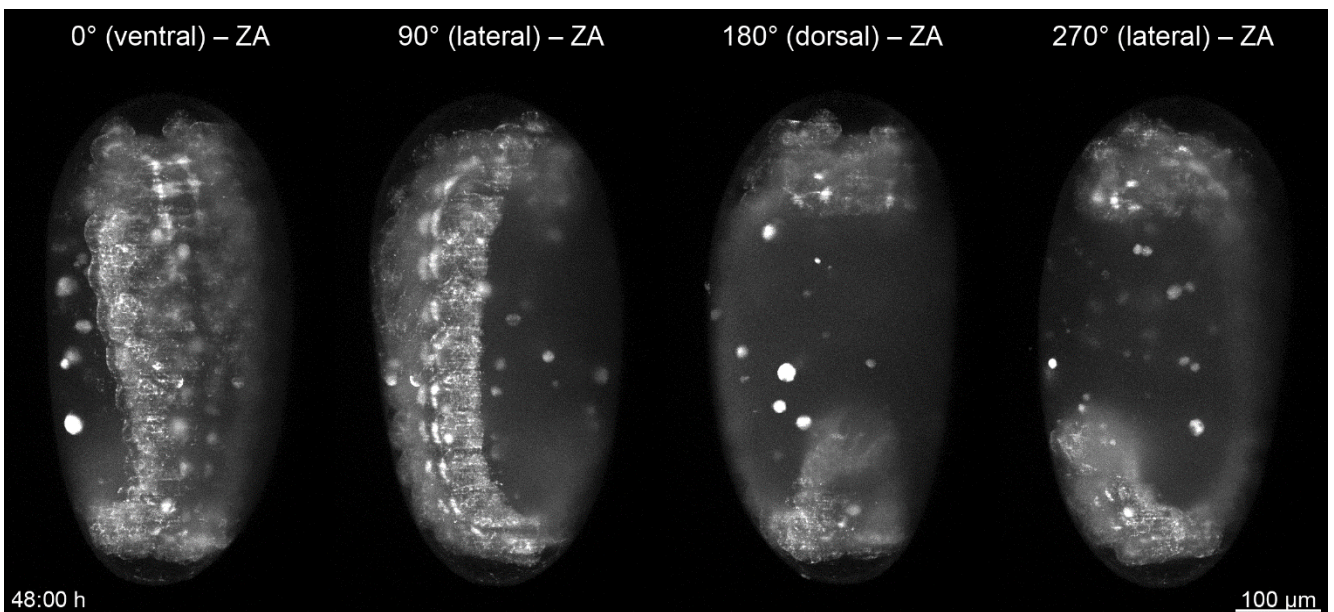
<i>Dataset (DS)</i>	DS0001	DS0002	DS0003
<i>Species</i>	<i>Tribolium castaneum</i> (Herbst) Arthropoda → Insecta → Coleoptera → Tenebrionidae		
<i>Line</i>	AGOC{Zen1' #O(LA)-mEmerald} #1 subline	AGOC{ARP5' #O(LA)-mEmerald} #1 subline	AGOC{ARP5' #O(LA)-mEmerald} #2 subline
<i>Line Genotype</i>	one insert / mC homozygous	one insert / mC homozygous	one insert / mC homozygous
<i>Stock</i>	~500 adults, less than 1 months old		
<i>Stock Medium</i>	full grain wheat flour (113061006, Demeter, Darmstadt, Germany) supplemented with 5% (wt/wt) inactive dry yeast (62-106, Flystuff, San Diego, CA, USA)		
<i>Stock Conditions</i>	12:00 h light / 12:00 h darkness at 25°C and 70% relative humidity (DR-36VL, Percival Scientific, Perry, IA, USA)		
<i>Egg Laying Period</i>	01:00 h at 25°C and 70% relative humidity exposed to light		
<i>Egg Laying Medium</i>	405 fine wheat flour (113061036, Demeter, Darmstadt, Germany) supplemented with 5% (wt/wt) inactive dry yeast (62-106, Flystuff, San Diego, CA, USA)		
<i>Pre-imaging Incubation</i>	15:00 h at 25°C and 70% relative humidity in darkness, 01:00 h at room temperature (23±1°C) – preparation time		
<i>LSFM Type</i>	mDSLm (monolithic digital scanned laser light sheet-based fluorescence microscope) based on DSLM		
<i>Laser Lines</i>	488 nm / 20 mW diode laser (PhoxX 488-20, Omicron Laserprodukte GmbH, Rodgau-Dudenhofen, Germany)		
<i>Excitation Objective</i>	2.5× NA 0.06 EC Epiplan-Neofluar objective (422320-9900-000, Carl Zeiss, Göttingen, Germany)		
<i>Emission Objective</i>	10× NA 0.3 W N-Achroplan objective (420947-9900-000, Carl Zeiss, Göttingen, Germany)		
<i>Emission Filters</i>	525/50 single-band bandpass filter (FF03-525/50-25, Semrock/AHF Analysetechnik AG, Tübingen, Germany)		
<i>Camera</i>	High-resolution CCD (Clara, Andor, Belfast, United Kingdom), 14 bit, 1040×1392 pixel (pitch 6.45 μm)		
<i>Dataset File Type</i>	TIFF, 16 bit grayscale (planes saved as Z stacks in ZIP-compressed container files, indicated as PL(ZS))		
<i>Dechoriation</i>	~60-90 s in 10% (vol/vol) sodium hypochlorite (425044-250ML, Sigma Adlrlich, Taufkirchen, Germany) in PBS pH 7.4 (10010-023, Gibco Life Technologies GmbH, Darmstadt, Germany)		
<i>Mounting Agarose</i>	1% (wt/vol) low-melt agarose (6351.2, Carl Roth, Karlsruhe, Germany) in PBS pH 7.4 (10010-023, Gibco Life Technologies GmbH, Darmstadt, Germany)		
<i>Imaging Buffer</i>	PBS pH 7.4 (10010-023, Gibco Life Technologies GmbH, Darmstadt, Germany)		
<i>Imaging Temperature</i>	room temperature (23±1°C)	room temperature (23±1°C)	room temperature (23±1°C)
<i>Retrieval</i>	developed to healthy adult	developed to healthy adult	developed to healthy adult

<i>Dataset (DS)</i>	DS0001	DS0002	DS0003
<i>Dataset Size</i>	14.1 Gigabyte (TIFF)	57.5 Gigabyte (TIFF)	72.5 Gigabyte (TIFF)
<i>Figures</i>	5A	5B, C, D	5D
<i>Supplementary Videos</i>	1	2	3
<i>Comment</i>	-	-	-
<i>Time Points (TP)</i>	49 (TP0001-TP0049)	193 (TP0001-TP0193)	241 (TP0001-TP0241)
<i>TP Interval</i>	00:30 h	00:30 h	00:30 h
<i>Total Time (TP×TP Interval)</i>	24:00 h	96:00 h	120:00 h
<i>Directions (DR)</i>	4 (DR0001-DR0004)	4 (DR0001-DR0004)	4 (DR0001-DR0004)
<i>DR Orientations</i>	0°, 90°, 180°, 270°	0°, 90°, 180°, 270°	0°, 90°, 180°, 270°
<i>Channels (CH)</i>	1 (CH0001)	2 (CH0001-CH0002)	1 (CH0001)
<i>CH0001 Excitation</i>	488 nm	488 nm	488 nm
<i>CH0001 Power</i>	135 μW (close to the embryo)	270 μW (close to the embryo)	270 μW (close to the embryo)
<i>CH0001 Exposure Time</i>	50 ms	50 ms	50 ms
<i>CH0001 Emission Filter</i>	525/50 single-band bandpass filter	525/50 single-band bandpass filter	525/50 single-band bandpass filter
<i>Planes (PL)</i>	150 (PL0001-PL0150)	150 (PL0001-PL0150)	150 (PL0001-PL0100)
<i>Z Spacing</i>	2.58 μm	2.58 μm	2.58 μm
<i>Z Distance (PL×Z Spacing)</i>	387.0 μm	387.0 μm	387.0 μm
<i>X-Dimensions (XD)</i>	600 pixels (cropped)	600 pixels (cropped)	600 pixels (cropped)
<i>X Spacing</i>	0.645 μm	0.645 μm	0.645 μm
<i>X Length (XD×X Spacing)</i>	387.0 μm	387.0 μm	387.0 μm
<i>Y-Dimensions (YD)</i>	1000 pixels (cropped)	1000 pixels (cropped)	1000 pixels (cropped)
<i>Y Spacing</i>	0.645 μm	0.645 μm	0.645 μm
<i>Y Length (YD×Y Spacing)</i>	645.0 μm	645.0 μm	645.0 μm

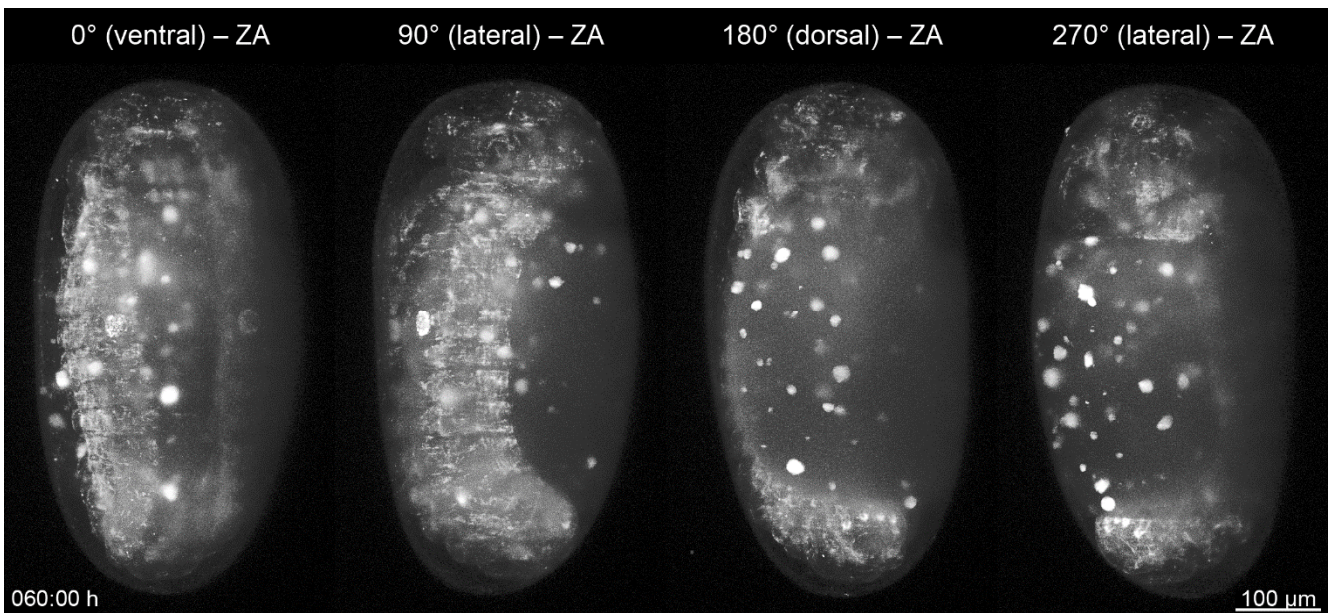
All datasets can be downloaded at www.physikalischebiologie.de/bugcube.



Supplementary Video 1 – Long-term live imaging of a mC-only homozygous *Tribolium* embryo from the AGOC{Zen1^{#O(LA)}-mEmerald} #2 subline. Embryogenesis is shown along four directions from 00:00 h to 24:00 h with an interval of 00:30 h between the time points. The video starts with the rearrangement of the blastoderm and ends during germband retraction. During gastrulation, the ventrally located serosa window is closed by a contracting actomyosin cable that separates the serosa and the amnion. Frame rate is five frames per second. ZP, z maximum projection with image processing.



Supplementary Video 2 – Long-term live imaging of a mC-only homozygous *Tribolium* embryo from the AGOC{ARP5^{#O(LA)}-mEmerald} #1 subline. Embryogenesis is shown along four directions from 00:00 h to 96:00 h with an interval of 00:30 h between the time points. The video starts with the rearrangement of the blastoderm and ends after dorsal closure. This transgenic line exhibits strong fluorophore expression in the ventral nerve cord. Frame rate is five frames per second. ZA, z maximum projection with image adjustment.



Supplementary Video 3 – Long-term live imaging of a mC-only homozygous *Tribolium* embryo from the AGOC{ARP5’#O(LA)-mEmerald} #2 subline. Embryogenesis is shown along four directions from 00:00 h to 120:00 h with an interval of 00:30 h between the time points. The video starts with the rearrangement of the blastoderm and ends after dorsal closure. In contrast to the #1 subline (Supplementary Video 2), this subline does not exhibit strong fluorophore expression in the ventral nerve cord. Frame rate is five frames per second. ZA, z maximum projection with image adjustment.

**Comparative Embryonic Morphogenesis
of Emerging Insect Model Organisms
• Volume III of III •**

Dissertation

**zur Erlangung des Doktorgrades
der Naturwissenschaften**

**vorgelegt beim Fachbereich 15 – Biowissenschaften
der Johann Wolfgang Goethe-Universität**

**von
Frederic Strobl
aus Frankfurt am Main**

Frankfurt am Main, 2017

(D30)

Vom Fachbereich 15 – Biowissenschaften der

Johann Wolfgang Goethe-Universität als Dissertation angenommen.

Dekanin: Prof. Dr. Meike Piepenbring

1. Gutachter: Prof. Dr. Ernst H.K. Stelzer

2. Gutachter: Prof. Dr. Bernd Grünewald

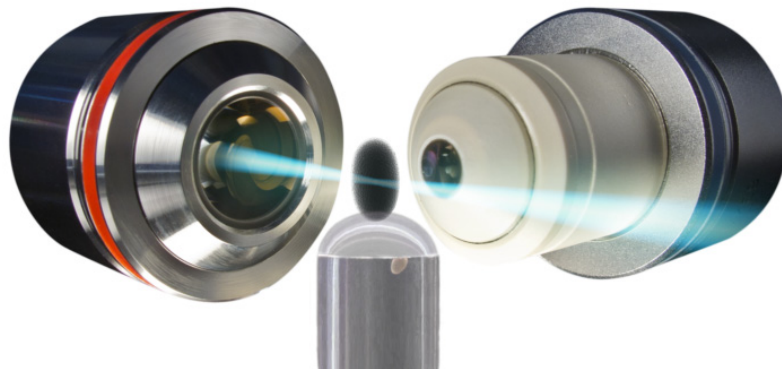
Datum der Disputation:



Buchmann Institute
for Molecular Life Sciences



**Comparative Embryonic Morphogenesis
of Emerging Insect Model Organisms
• Volume III of III •**



Frederic Strobl

Matrikel-Nummer 3326422

Physical Biology / Physikalische Biologie

Buchmann Institute for Molecular Life Sciences

Cluster of Excellence – Macromolecular Complexes

Johann Wolfgang Goethe-Universität – Frankfurt am Main

2012 – 2017

About the Volumes

The style of my PhD thesis is 'publication-based'. Due to the scope, my thesis is divided into three volumes:

- Volume I contains the Extended Summary divided into seven chapters, 1. Summary, 2. Insect Development in a Nutshell, 3. Unpublished Results, 4. Future Trends, 5. Teaching Efforts, 6. Publications and Applications and 7. Trivia.
- Volume II contains the published manuscripts Strobl & Stelzer 2014 (#1), Nollmann *et al.* 2015 (#2), Strobl *et al.* 2015 (#3), Strobl & Stelzer 2016 (#4), Strobl *et al.* 2017A (#5), Strobl *et al.* 2017B (#6) and their respective supplementary material as summarized in Publication Table 1 and Publication Table 2 (Subchapter 6.1) as well as the submitted but not yet accepted manuscripts Strobl *et al.* 2017C (#7), Strobl *et al.* 2017D (#8) and their respective supplementary material as summarized in Publication Table 3 (Subchapter 6.2).
- Volume III contains the submission-ready manuscripts Strobl *et al.* 2017E (#9), Strobl *et al.* 2017F (#10) and their respective supplementary material as summarized in Publication Table 3 (Subchapter 6.2) as well as the patent and grant applications (Subchapter 6.3).

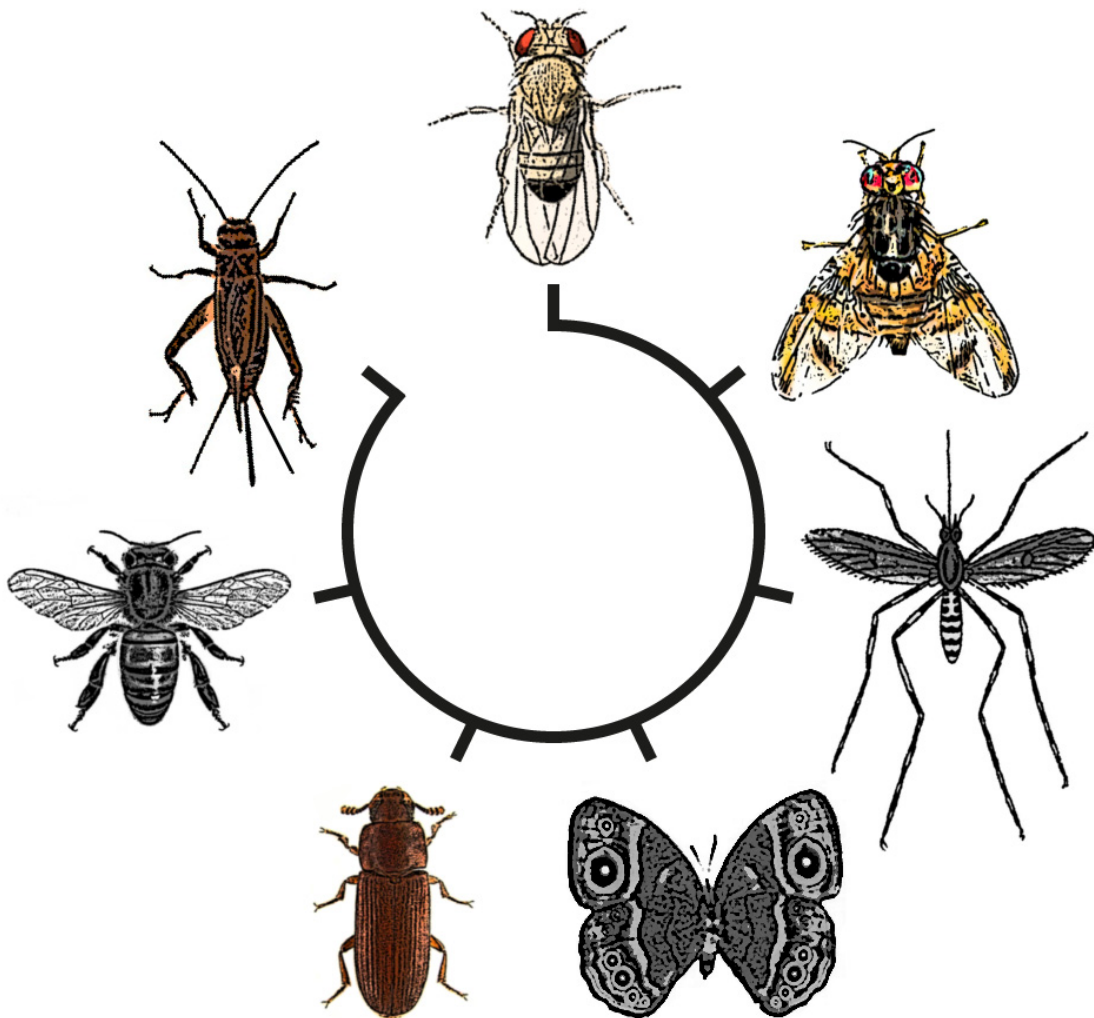


Table of Contents

#9 Nine light sheet-based fluorescence microscopy datasets of *Ceratitis capitata* embryonic development

Frederic Strobl, Alexander Schmitz, Marc F. Schetelig & Ernst H.K. Stelzer

Submission-ready

Research Article

Pages 6 – 45

#10 The embryonic development of the Mediterranean fruit fly *Ceratitis capitata* (Diptera: Tephritidae)

Frederic Strobl, Alexander Schmitz, Marc F. Schetelig & Ernst H.K. Stelzer

Submission-ready

Research Article

Pages 46 – 100

PA Genetic Tools and Procedure for the Phenotypic Identification of the Genotype of Transgenic Diploid Organisms

Frederic Strobl, Ernst H.K. Stelzer & Innovectis GmbH

Submitted in June 2017

Patent Application

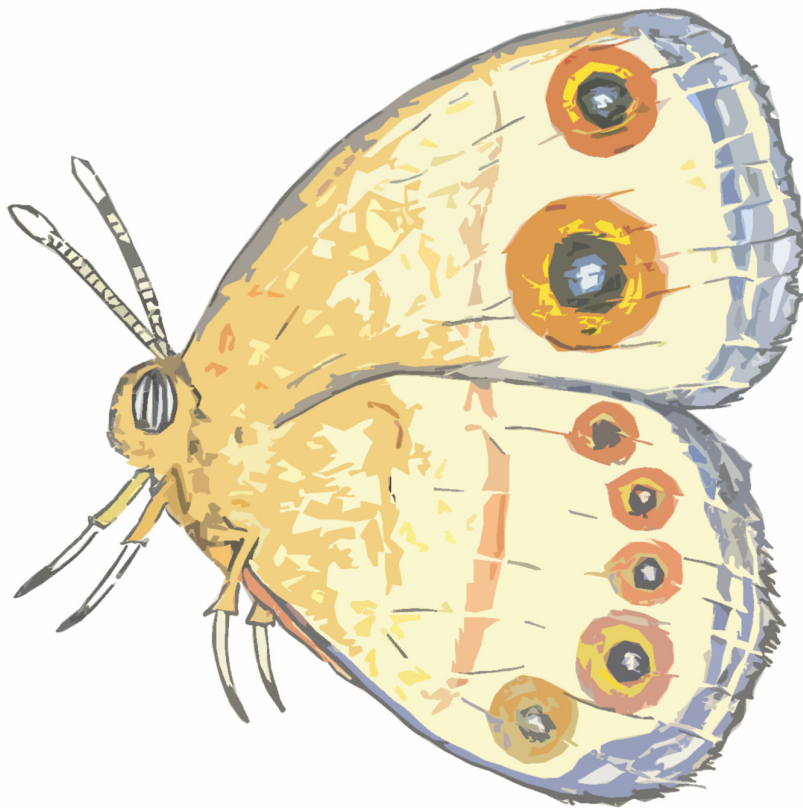
Pages 101 – 156

GA Reinhart Koselleck-Projekt

Morphotypisch-quantitative embryonale Variabilität prominenter Insektennütz- und -schädlinge unter Einfluss ex- und intrinsischer Faktoren

Grant Application

Pages 157 – 181



Nine light sheet-based fluorescence microscopy datasets of *Ceratitis capitata* embryonic development

Frederic Strobl, Alexander Schmitz, Marc F. Schetelig & Ernst H.K. Stelzer

The Mediterranean fruit fly *Ceratitis capitata* is an important model organism in agricultural research and developmental biology. However, no comprehensive morphogenetic information about its embryonic development is yet available. Here, we present nine long-term live imaging datasets acquired with light sheet-based fluorescence microscopy. Six datasets show the embryo *in toto* for more than 60 hours with a temporal interval of 30 minutes along four directions in three spatial dimensions, covering approximately 97% of the whole embryogenetic development. The other three datasets show details of germ cell development and head involution. For quality control, the development of the imaged embryos after hatching was validated. We define a two-level staging system to classify the acquired datasets and thus create a morphogenetic framework for further studies on *Ceratitis*. The data will support research on wild-type or aberrant development, quantitative data analysis, comparative approaches on insect development or pest-associated agricultural studies.

Submission-ready

Research Article

Title

Nine light sheet-based fluorescence microscopy datasets of *Ceratitidis capitata* embryonic development

Authors

Frederic Strobl¹, Alexander Schmitz¹, Marc F. Schetelig² and Ernst H.K. Stelzer¹

Affiliations

¹Physical Biology / Physikalische Biologie (IZN, FB 15)
Buchmann Institute for Molecular Life Sciences (BMLS)
Cluster of Excellence Frankfurt – Macromolecular Complexes (CEF – MC)
Goethe University – Frankfurt am Main (Campus Riedberg)
Max-von-Laue-Straße 15 – D-60348 Frankfurt am Main – Germany

²Justus-Liebig-Universität Gießen
Department of Insect Biotechnology in Plant Protection
Winchesterstraße 2 – D-35394 Gießen – Germany

Corresponding authors:

Frederic Strobl (frederic.strobl@physikalischebiologie.de)

Ernst H.K. Stelzer (ernst.stelzer@physikalischebiologie.de)

Abstract

The Mediterranean fruit fly *Ceratitidis capitata* is an important model organism in agricultural research and developmental biology. However, no comprehensive morphogenetic information about its embryonic development is yet available. Here, we present nine long-term live imaging datasets acquired with light sheet-based fluorescence microscopy. Six datasets show the embryo *in toto* for more than 60 hours with a temporal interval of 30 minutes along four directions in three spatial dimensions, covering approximately 97% of the whole embryogenetic development. The other three datasets show details of germ cell development and head involution. For quality control, the development of the imaged embryos after hatching was validated. We define a two-level staging system to classify the acquired datasets and thus create a morphogenetic framework for further studies on *Ceratitidis*. The data will support research on wild-type or aberrant development, quantitative data analysis, comparative approaches on insect development or pest-associated agricultural studies.

Background & Summary

In insect developmental biology, the comparative approach sheds light on the broad variety of developmental strategies and contributes to our understanding of the evolution of development¹. To study the embryonic morphogenesis on the cellular and subcellular level, light sheet-based fluorescence microscopy (LSFM) became the method of choice. It allows non-invasive live imaging of millimeter-sized specimen for time periods up to several days^{2–8} and has already been successfully applied to analyze the embryogenesis of several insect species such as the fruit fly *Drosophila melanogaster*^{9–15}, the scuttle fly *Megaselia abdita*¹⁶ and the red flour beetle *Tribolium castaneum*^{17–20}. Due to the intrinsic properties of LSFM⁶ – *e.g.* excellent signal-to-noise ratio, nearly no photo-bleaching and supreme depth penetration – the acquired datasets typically provide a profound collection of high quality images with good spatiotemporal resolution. The quantity and quality of the acquired data usually exceeds the requirements for the respective study and in many cases, only a fraction of the acquired data is analyzed. Thus, it is convenient to make the data available as an open resource for the scientific community. Next to classic descriptive and functional studies, technical publications and protocols, also comprehensive publications on datasets should be part of the publication spectrum in the insect development biology community.

Over the past decades, more and more emerging model organisms entered the field of insect developmental biology. The Mediterranean fruit fly *Ceratitis capitata*, which belongs to the Diptera order, has traditionally been investigated as an agricultural pest²¹ but also became a promising model organism in developmental biology. Standard and advanced techniques, such as germline transformation^{22,23} and cryopreservation²⁴, are established and the genome was recently sequenced²⁵. *Ceratitis* and *Drosophila* are both members of the Schizophora section, but belong to different families. Phylogenetic analyses have shown that they diverged approximately 80-100 million years ago^{26–28}. Both species share apomorphic characteristics such as reduced extra-embryonic membrane formation, *i.e.* they generate and degrade only one dorsally located membrane, the amnioserosa²⁹. The closest comprehensively examined model organism is the scuttle fly *Megaselia abdita*³⁰, a member of the Aschiza section, which diverged from *Ceratitis* and *Drosophila* approximately 150 million years ago³¹ and develops two extra-embryonic membranes^{32–34}. *Ceratitis* therefore bridges the phylogenetic gap between *Drosophila* and *Megaselia* and complements the existing pool of dipteran model organisms for evolutionary developmental biology research. Studies on a variety of specific questions have already been published, *e.g.* spatiotemporal gene expression patterns^{35,36}, transcriptomics^{37–39}, oogenesis⁴⁰, larval morphology⁴¹ and antennal lobe structure⁴², but no comprehensive morphogenetic data and staging system for the embryonic development is yet available.

Using a novel, ease-of-use mounting method for insect embryos in LSFM, we recorded nine long-term datasets of the embryogenesis of *Ceratitis*. The embryos typically survived the recording process and developed into functional adults. Six of the datasets cover approximately 97% of *Ceratitis* embryogenesis along four directions at an interval of 30 minutes over periods of more than 60 hours. The remaining datasets focus on specific processes including germ cell formation and head involution. Based on the acquired datasets, we establish a morphogenesis-based two-level staging system that serves as a reference for further developmental studies in *Ceratitis*. The live imaging approach also allows to properly quantify the temporal course of embryogenesis, allowing the calculation of standard deviations for the respective stages. Our recordings provide the first live imaging datasets of *Ceratitis* embryos, which contributes to the insect development comparative approach and might be also of value for the associated pest species research.

Methods

Ceratitis capitata strain and culture

In this study, a homozygous transgenic line of the Mediterranean fruit fly, *Ceratitis capitata* (Wiedemann), was used. The *TREhs43-hid^{Ala5}_F1m2* transgenic line⁴³ expresses nuclear localized EGFP under control of the *Drosophila* polyubiquitin promoter. Adult flies were reared at 25°C, 50% relative humidity in a 12-h bright / 12-h dark cycle (DR-36VL, Percival Scientific, Perry, IA, United States) in transparent acrylic boxes (approximately 15×15×20 cm) in groups of around 80 individuals. The plastic boxes had sideward openings that were covered with fine-meshed gaze, which allows egg deposition. They were fed on 3:1 mixture of refined sugar (524973, REWE Markt GmbH, Köln, Germany) to inactive dry yeast (62-106, Flystuff, San Diego, CA, USA) that was moistened with autoclaved tap water. Additionally, autoclaved tap water was provided in the form of a wet tissue.

Light sheet-based fluorescence microscope

The LSFM we used was a digital scanned laser light sheet-based fluorescence microscope^{3,4}, which creates a dynamic light sheet by rapidly scanning a Gaussian laser beam with a two-axes piezo scanning mirror. For ease of use, we define three axes as follows: the illumination axis as X, the rotation axis as Y, and the detection axis as Z. For convenience, Y is aligned to the gravitational axis. Axes are mentioned in the manuscript or indicated on relevant figures whenever appropriate. As the illumination light source, we use a 488 nm / 20 mW diode laser (PhoxX 488-20, Omicron Laserprodukte GmbH, Rodgau-Dudenhofen, Germany) with a 488 nm cleanup filter (xX.F488, Omicron Laserprodukte GmbH, Rodgau-Dudenhofen, Germany). Whereas we always use a 2.5× NA 0.06 EC Epiplan-Neofluar objective (422320-9900-000, Carl Zeiss AG, Göttingen, Germany) in the illumination pathway, we used either a 10× NA 0.3 W N-Achroplan objective (420947-9900-000, Carl Zeiss AG, Göttingen, Germany) for detection in datasets DS0001-0006 or a 20× NA 0.5 W N-Achroplan objective (420957-9900-000, Carl Zeiss AG, Göttingen, Germany) in datasets DS0007-0009. In both setups, a 525/50 single-band bandpass filter (FF03-525/50-25, Semrock/AHF Analysentechnik AG, Tübingen, Germany) with a high-resolution CCD camera (Clara, Andor, Belfast, United Kingdom) was used for detection. The LSFM is equipped with three compact micro-translation stages (M-111.2DG, Physik Instrumente GmbH & Co KG, Karlsruhe, Germany) that allow to move the sample holder (see below) along X, Y, and Z as well as a precision rotation stage (M-116.DG, Physik Instrumente GmbH & Co KG, Karlsruhe, Germany) that allows to rotate the sample holder around Y.

Cobweb holder

The perpendicular arrangement of the illumination and detection objectives in a LSFM setup (Figure 1A) requires customized mounting techniques. We developed a novel, ease-of-use mounting sample holder for the observation of insect embryos in a LSFM – the so called cobweb holder consists of a slotted hole with an inner diameter of 2 mm along X and 4 mm along Y with a depth of 0.2 mm along Z. A drop of agarose (5-7 µl) is pipetted onto the center of the slotted hole and excessive liquid is removed to create an agarose film with an approximate thickness of around 50 µm. Subsequently, the dechorionated embryo is mounted onto agarose film so that the elongated anterior-posterior axis is aligned to the Y axis of the sample holder (Figure 1B), achieving gentle mounting in less than five minutes. Embryo are only partially embedded into agarose, thus keeping the distance that the laser beam and the emitted fluorescence have to pass through agarose at a minimum while facilitating gas exchange with the imaging buffer.

After insertion into the sample chamber, the cobweb holder is aligned with the respective axes of the microscope (Figure 1C, first column), which we define as the preliminary direction (orientation -45°). This direction serves for moving the embryo into the center of the field of view in transmission light mode. For acquisition of images in fluorescence mode, the cobweb holder is rotated by 45° , which we define as direction 1 (orientation 0°). In this direction, the metal flanks of the cobweb holder do neither block the illumination nor the detection path ((Figure 1C, second and third column). Due to the design of the cobweb holder, the embryos can thus be recorded in both, transmission light (Figure 1D) and fluorescence (Figure 1E) mode. By rotating the cobweb holder around y in steps of 90° , the embryo can be recorded along four directions (in the orientations 0° , 90° , 180° and 270° , Supplementary Figure 1). The dimensions of the slotted hole allow the acquisition of Z stacks with a range of up to $800\ \mu\text{m}$ along all four directions. The cobweb holder keeps the embryo mechanically stable so that a repeated recording sequence (translation along Z while recording a Z stack, rotation and translation along X, Y and Z to reposition the embryo into the field of view after rotation) is performed with high spatial precision for more than 60:00 h. Post-processing steps such as drift correction are not necessary. Additionally, the volume of agarose that is needed to mount the embryo is fairly low, thus allowing for unimpeded gas exchange and minimizing the distance that the laser beam and the emitted fluorescence of the specimen have to pass through agarose. Blurring effects caused by imaging through agarose are therefore reduced.

Embryo preparation

For embryo collection, fly cultures were removed from the incubator and kept at room temperature ($23\pm 1^\circ\text{C}$). Old embryos were removed from the gaze, and the flies were given 00:10 h for embryo deposition. All embryos (typically 5 to 20) that were laid in this time window were transferred to a $100\ \mu\text{m}$ cell strainer (#352360, BD Biosciences, Heidelberg, Germany) with a paint brush. The embryos were moistened in PBS pH 7.4 (10010-023, Gibco Life Technologies GmbH, Darmstadt, Germany), dechorionated for 90 seconds in 10% (vol/vol) sodium hypochlorite with 5-10% active chlorine (425044-250ML, Sigma Adlrlich, Taufkirchen, Germany) in PBS and then washed twice in PBS for 60 seconds. One embryo was picked with a paint brush and carefully transferred to the agarose film of the cobweb holder. The elongated anterior-posterior axis of the embryo was aligned with the Y axis of the slotted hole, so that both will align with Y of the LSM (Figure 1B). Directly after preparation, the embryo was inserted into the sample chamber of the LSM and centered in front of the detection objective before live imaging started.

Cobweb holder

In LSM, the lateral resolution along X and Y exceeds the axial resolution along Z by a factor of four⁴⁴. Using the cobweb holder, either the frontal or sagittal planes of the embryo are aligned with X and Y. To record embryos with the transverse plane aligned along X and Y, an alternative mounting system was used where the embryo was attached with its dorsal side to the pole of an agarose hemisphere (Supplementary Figure 2). The method was used to record DS0009.

Long-term live imaging with light sheet-based fluorescence microscopy

In each plane, the embryo was illuminated with a 488 nm laser beam with a power of $135\ \mu\text{W}$ for 50 ms exposure time. Z stacks, consisting of 100 planes, were acquired with an axial pitch of $2.58\ \mu\text{m}$. Thus, the datasets were acquired with a X:Y:Z resolution ratio of 1:1:4 and 1:1:8 for the $10\times$ objective and the $20\times$ objective, respectively. For datasets DS0001-0008, the embryos were imaged along four directions in the orientations 0° , 90° , 180° and 270° . For dataset DS0009, the embryo was imaged along two directions in the orientations 0° and 90° . The

temporal interval was 00:30 h. In six out of nine datasets (DS0001-0006), the embryo was captured *in toto* under equal conditions for more than 60:00 h, covering approximately 97% of embryogenesis (Supplementary Video 1). In total, nine long-term live imaging datasets of *Ceratitis* were recorded (see Supplementary Table 1 for metadata and the Data records section for download information). The embryo from DS0006 did not develop into a healthy adult and was therefore excluded from further analysis. DS0001 and DS0003 were imaged ventrolateral and dorsolateral, whereas datasets DS0002, DS0004, and DS0005 were imaged ventral, lateral and dorsal. The datasets DS0007-DS0009 cover specific embryonic processes, *i.e.* pole cell formation (DS0007) and head involution (DS0008-DS0009).

Image processing

From the preliminary *Z* stacks, preliminary *Z* maximum projections were calculated. Then, the preliminary *Z* image stacks and preliminary *Z* maximum projections were rotated around *Z* when necessary so that the anterior pole is at the top center of the image and the illumination source is at the left and cropped to a final size of 500 × 1390 pixel, resulting in the raw *Z* stacks and raw *Z* maximum projections. The *Z* maximum projections were finally background corrected, mean transformed¹⁸ and adjusted in brightness and contrast. All images are available for download (see Data records section).

Two-level staging system implementation

For proper temporal quantification of embryogenesis and to provide a general standard for any future studies on *Ceratitis*, a comprehensive staging system is necessary. The proposed staging system consists of two levels, relies on five *in toto* datasets (DS0001-DS0005) that were acquired under equal conditions and is purely based on morphogenetic criteria. For the upper level, we specify six consecutive embryogenetic events, which are denoted with Roman numerals and color-coded for convenience: (I) blastoderm formation is represented in blue, (II) gastrulation in cyan, (III) germband elongation in green, (IV) germband retraction in yellow, (V) dorsal closure in orange and (VI) muscular movement in red. A comparison of event-characteristic structures between DS0001-DS0005 is given in Figure 2, and a comparison of the first time point of each event along three orientations is given in Supplementary Figure 3. The embryogenetic events starting and ending time points for DS0001-DS0005 are summarized in Supplementary Table 2.

For the lower level, due to the high similarity, we adopt the 17 stages from the *Drosophila* staging system⁴⁵ as already done for *Megaselia*³¹ and denote the lower level with Arabic numerals. We align our data from for *Ceratitis* to the given morphologic criteria for *Drosophila* and integrate those stages into the embryogenetic events to create a two-level staging system, where every embryogenetic event consists of one or multiple stages. A comparison of the first time point of each stage between DS0001-DS0005 along one orientation is given in Supplementary Figure 4. Major event and stage identifiers are given in Table 1, a rationale and a comprehensive description is provided within the accompanying descriptive publication (Ref). The stages starting and ending time points for DS0001-DS0005 are summarized in Supplementary Table 3.

Dataset alignment

Of the five datasets (DS0001-DS0005) that captured the embryo *in toto* and under identical conditions, DS0001 was the dataset with the median development time, so DS0002-DS0005 were adjusted and aligned stage-by-stage onto DS0001. When stages in DS0002-DS0005 lasted shorter (or longer) than the respective stage in DS0001, the first and last time point were aligned, resulting in stretching (or compression) of the whole period. As this leads

to non-matching time points, the respective matching time points were interpolated. The interpolation values were used for calculation of the absolute and relative standard deviation. An overview for embryogenetic events and stages is given in Table 1, a comprehensive overview about all time points is given in Supplementary Figure 4.

Data Records

The nine (DS0001-0009) long-term datasets of *Ceratitis* embryogenesis are provided either as JPG2000 files (small size, lossy compression) or as TIFF files (large size, lossless ZIP compression, container function) and explore six degrees of freedom: the three spatial dimensions X, Y and Z, the fluorescence channel, the direction and the time point. Metadata about the datasets is provided Supplementary Table 1 and together with the data files. All nine datasets can be downloaded either as JPEG2000 at www.url.com or as JPEG2000 or TIFF at www.physikalischebiologie.de/bugcube.

Technical Validation

Microscope calibration

Before each imaging assay, the LSFM went through a two-step calibration routine as described previously¹⁸. Thus, typical problems that might occur in LSFM are avoided (*e.g.* light sheet waist not in the center of the field of view, light sheet before or behind the focal plane of the detection objective, light sheet slightly tilted relative to the focal plane of the detection objective). Laser power (see Supplementary Table 1) was measured with an optical power and wavelength meter (OMM-6810B and OMH-6703B, Newport, Irvine, CA, United States) at the exact location where the embryo is positioned during the imaging process.

Quality control

Only by raising the imaged individuals to develop to adults, it can be assured that the imaging procedure, *e.g.* the irradiance by the laser, does not induce any aberrations. The embryos were imaged until they hatched from the egg and were not captured anymore in the volume of view during the recording process. When that happened, imaging was stopped and the larva, which was floating in the imaging buffer of the sample chamber, was retrieved with a plastic Pasteur pipet. The larva was then placed on larval medium⁴⁶ and incubated for several weeks under the same conditions as the described for the adult culture in the Methods section until pupation and emergence as an adult occurred. The embryo in dataset DS0006 did not develop into a healthy adult and was therefore excluded from further analysis. The quality of the image data was validated by manual examination of all Z maximum projections: for each dataset (nine in total), for each time point (up to 126 per dataset), and for each direction (typically four per dataset and time point).

Usage Notes

The nine (DS0001-DS0009) long-term datasets of *Ceratitidis* embryogenesis are provided either as JPEG2000 files (small size, lossy compression) or as TIFF files (large size, lossless ZIP compression, container function) and explore six dimensions: The first (X) and second (Y) spatial dimensions are obtained simultaneously during one camera acquisition period and saved as either JPEG2000 or TIFF files. The third spatial dimension (Z) is represented by the planes that are recorded while the embryo is moved through the light sheet. Together with the first and second spatial dimensions, it defines the volume of view. For JPEG2000, the third spatial dimension (Z) is saved as individual image files (indicated as PL within the file name) in one Z stack subfolder (indicated as PL(ZS) within the subfolder name). For TIFF, the third spatial dimension (Z) is saved as Z stack container files (indicated as PL(ZS) within the file name). The further dimensions are the fluorescence channel (one), the direction (typically four) and the time point (up to 126), which are saved individually in Z stack subfolders for JPEG2000 or Z stack container files for TIFF (indicated as CH, DR or TP within the subfolder or file name, respectively).

For convenience, we also provide Z maximum projections. These are simplifications of the datasets where one spatial dimension (Z) is removed. The projections are provided in two versions, as raw Z maximum projections (indicated as PL(ZM) within the subfolder or file name) or as Z maximum projections with image adjustment (indicated as PL(ZA) within the subfolder or file name). For JPEG2000, the Z maximum projections are saved as individual image files in one Z maximum projection T stack subfolder (indicated as TP(TS) within the subfolder name). For TIFF, the Z maximum projections are saved as Z maximum projection T stack container files (indicated as TP(TS) within the file name).

Additionally, the Z maximum projections with image adjustment are also provided as direction montages along X or Y. For JPEG2000, they are saved as individual image files in Z maximum projection T stack subfolders (indicated as DR(AX) or (AY) within the subfolder name). For TIFF, they are saved as Z maximum projection T stack container files (indicated as DR(AX) or (AY) within the file name).

The JPEG2000 files can be opened with any basic graphic viewer such as IrfanView (freeware, <http://www.irfanview.net/>) or directly used in vector graphic editors such as Inkscape (freeware, <https://inkscape.org/en/>) or Adobe Illustrator (Adobe Systems). However, for both JPEG2000 and TIFF, we recommend ImageJ^{47,48} or its derivate FIJI⁴⁹ as the primary image processing program, which are open source platforms for biological-image analysis. For JPEG2000, the subfolders have to be imported by using the Bio-Formats Importer plugin (which is installed per default), the TIFF container files can simply be opened via drag-and-drop.

Acknowledgements

We thank Maximilian Sandmann and Sven Plath for technical support. FS, AS and EHKS were funded by the Cluster of Excellence Frankfurt for Macromolecular Complexes (CEF-MC, EXC 115) granted to the Buchmann Institute for Molecular Life Sciences (BMLS) at the Goethe University – Frankfurt am Main by the Deutsche Forschungsgemeinschaft (DFG). MFS was funded by the Emmy Noether Program SCHE 1833-1/1 of the German Research Foundation and the LOEWE Center for Insect Biotechnology & Bioresources of the Hessen State Ministry of Higher Education, Research and the Arts.

Author contributions

FS developed the cobweb holder, performed the imaging experiments, and prepared the figures and tables. All authors conceived the research, analyzed the data and wrote the publication.

Competing interests

The authors declare no competing financial interests.

Figures

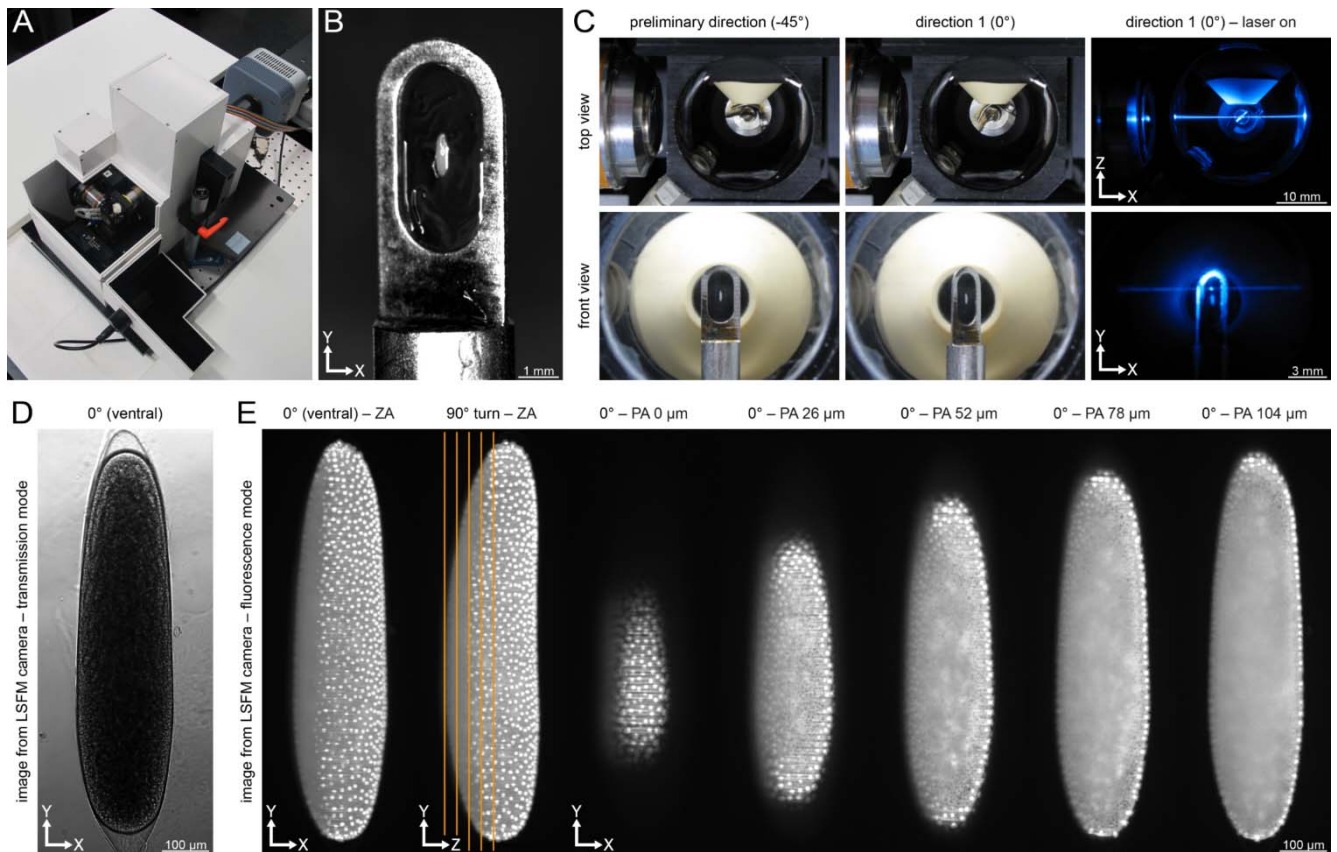


Figure 1 – LSFM setup and mounting of *Ceratitis* embryos to the cobweb holder. (A) Diagonal view of the mDLSM. (B) Cobweb holder with *Ceratitis* embryo embedded into an agarose layer. (C) Top view (upper row) and front view (lower row) of the mDLSM sample chamber. First the embryo is located and centered in x and y in front of the detection objective (first column), which is defined as the preliminary direction (-45°). Afterwards, the embryo is rotated by 45° (second column), which is defined as direction 1 (0°). This setup allows illumination of the embryo with the laser beam and simultaneous acquisition of images with the detection objective (third column). (D) Transmission light image of a *Ceratitis* embryo in the mDLSM. (E) Example fluorescence images of an acquired image stack. Shown are Z maximum projections along two orientations (0° and 90°) and five planes at increasing depth ($0\ \mu\text{m}$ to $104\ \mu\text{m}$, Z spacing $26\ \mu\text{m}$). In the 90° Z maximum projections, the locations of the planes are indicated by orange lines. ZA, Z maximum projection with image adjustment; PA, plane with image adjustment.

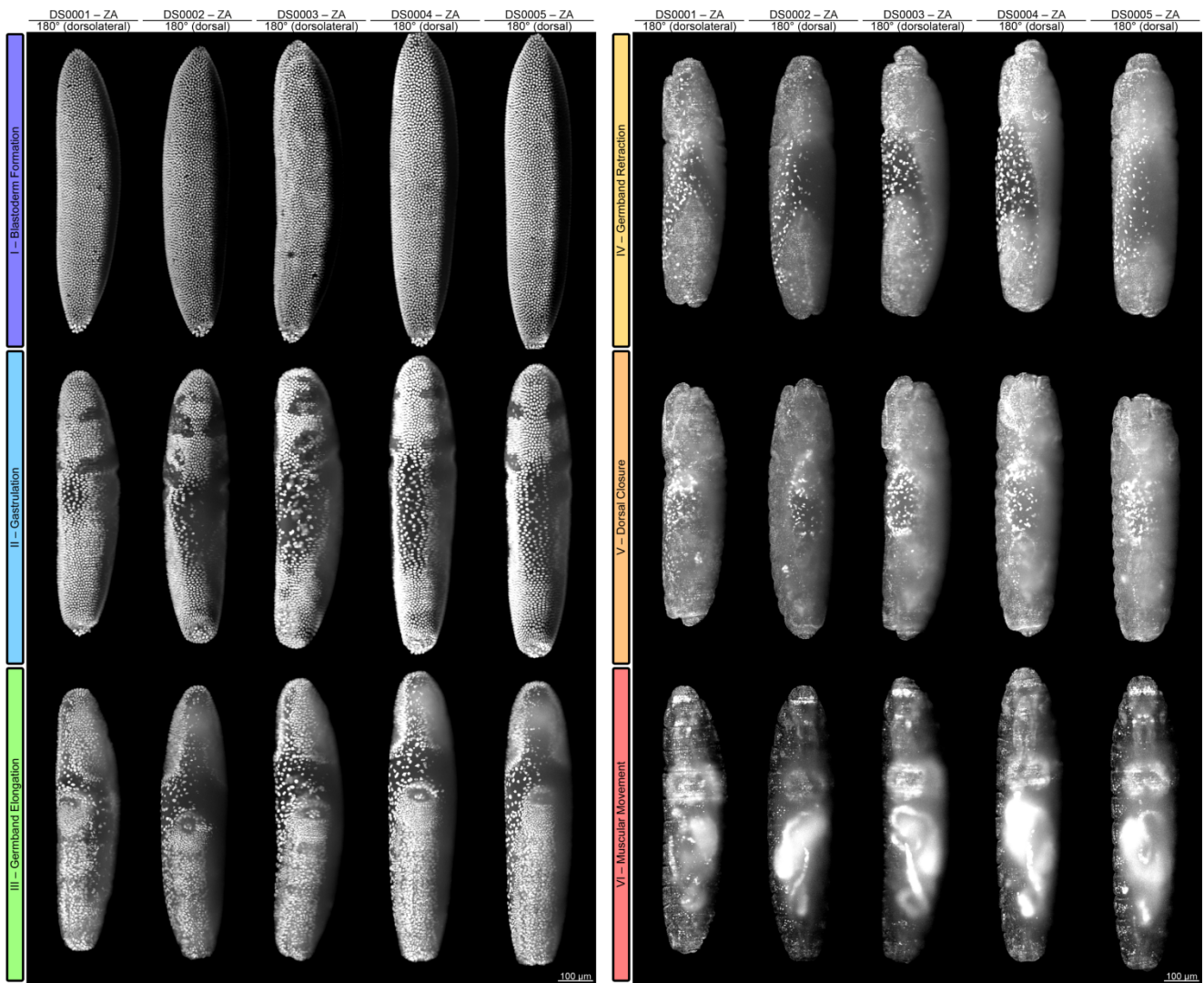
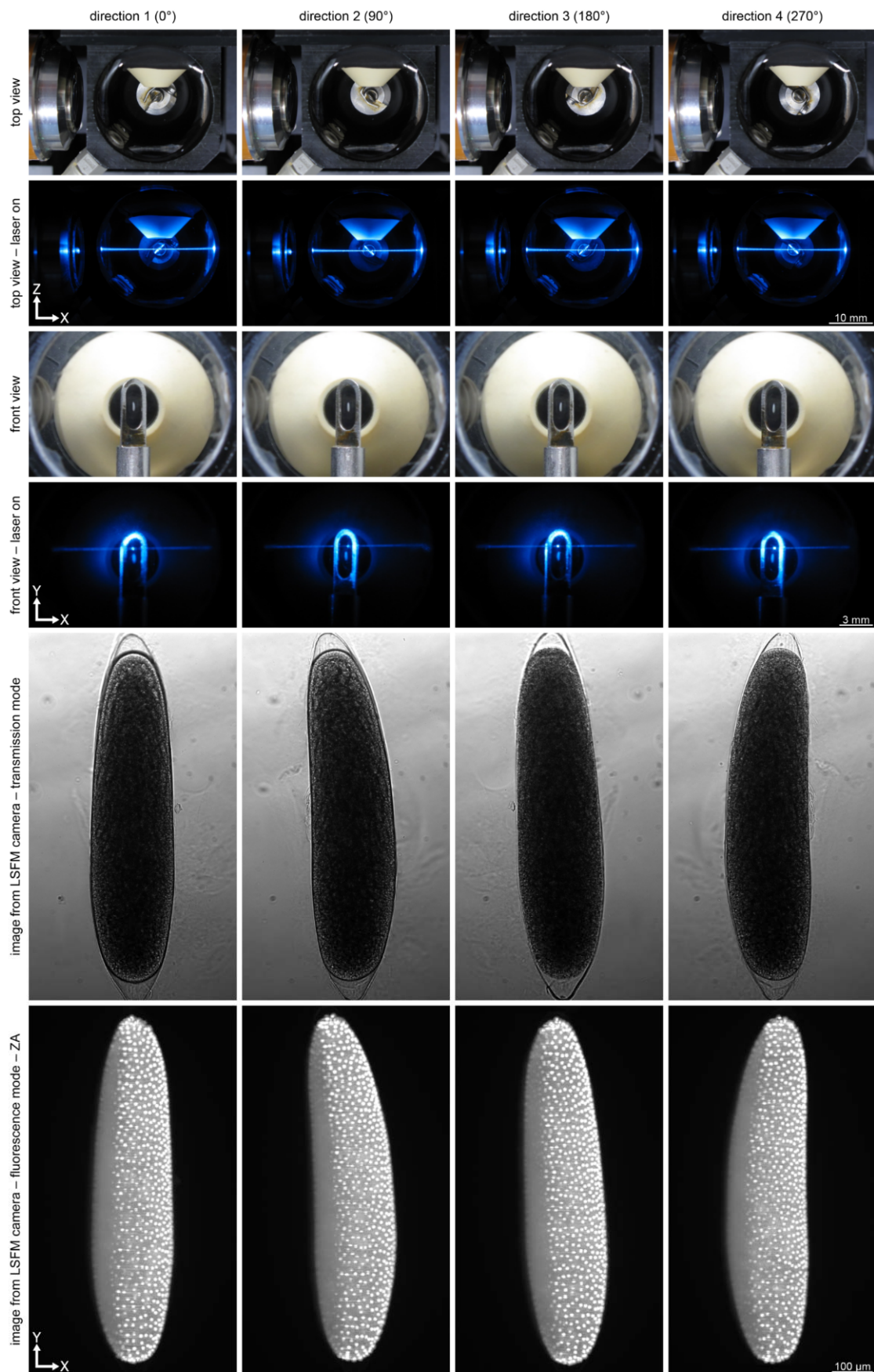
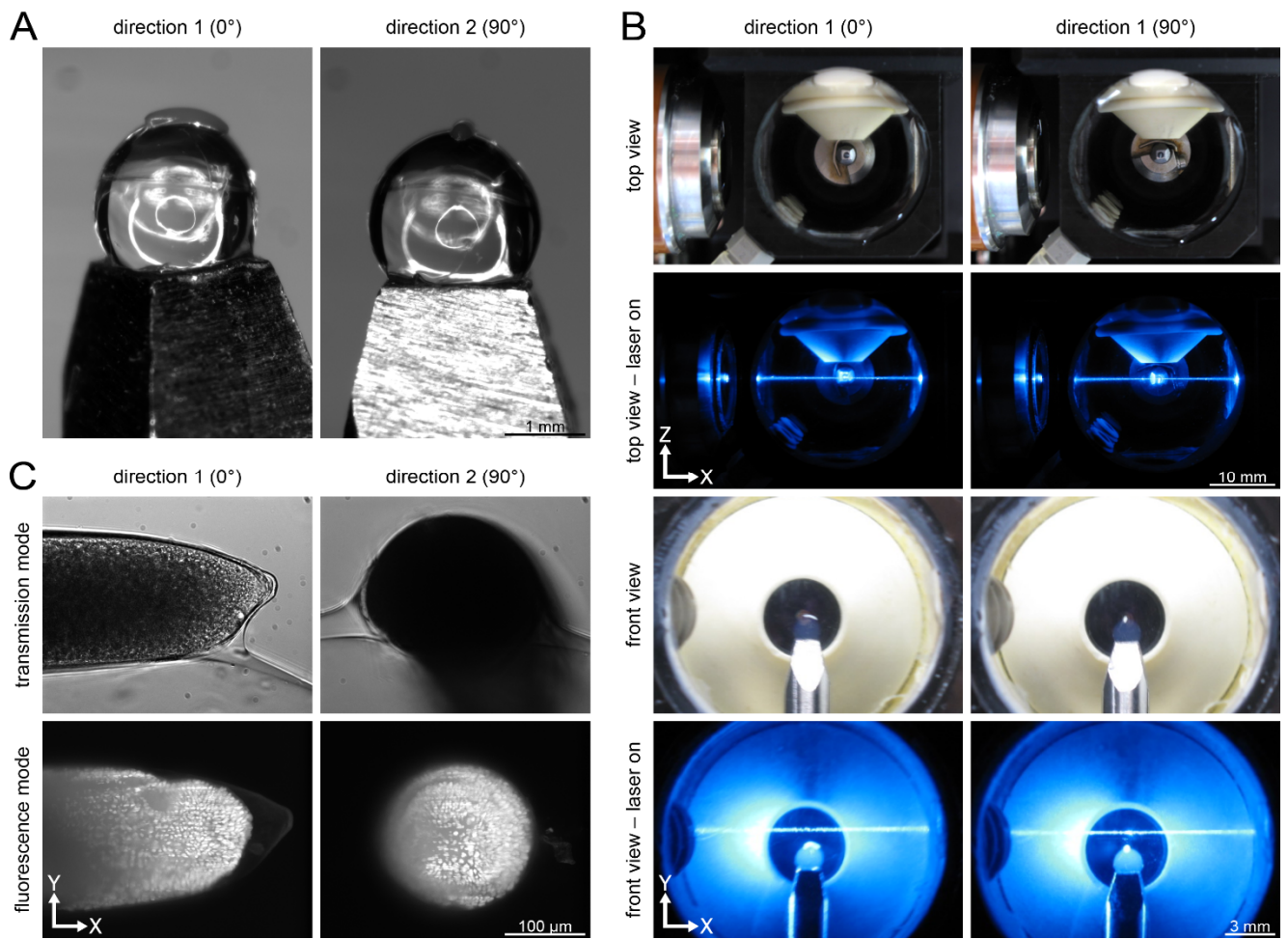


Figure 2 – Comparison of datasets DS0001-005 for the embryogenetic events blastoderm formation, gastrulation, germband elongation, germband retraction, dorsal closure and muscular movement. For this overview, time points were chosen that depict characteristic structures for the respective embryonic event. Datasets DS0001 and 0003 are depicted dorsolateral, whereas DS0002, 0004 and 0005 are depicted dorsal. The embryogenetic events are color-coded (see Methods section). ZA, Z maximum projection with image adjustment.

Supplementary Figures



Supplementary Figure 1 – Illustration of the acquisition process of *Ceratitis* embryos with the cobweb holder along four directions (in the orientations 0°, 90°, 180° and 270°). Top view (first and second row) and front view (third and fourth row) of the mDSLM sample chamber illustrating the illumination process for each direction. Transmission light (fifth row) and fluorescence (sixth row) images of a *Ceratitis* embryo during blastoderm formation acquired along four directions. ZA, Z maximum projection with image adjustment.



Supplementary Figure 2 – Illustration of the acquisition process of *Ceratitis* embryos with an alternative mounting method using an agarose hemisphere. (A) Front and side view of the sample holder with embryo placed on top of the agarose hemisphere. The shown views correspond to the orientations 0° and 90°. **(B)** Top view (first and second row) and front view (third and fourth row) of the mDSLMS sample chamber using the alternative mounting method. **(C)** Transmission light images (upper row) and Z maximum projections (lower row) of the embryo in the mDSLMS.

A

II – Gastrulation

DS0001

DS0002

DS0003

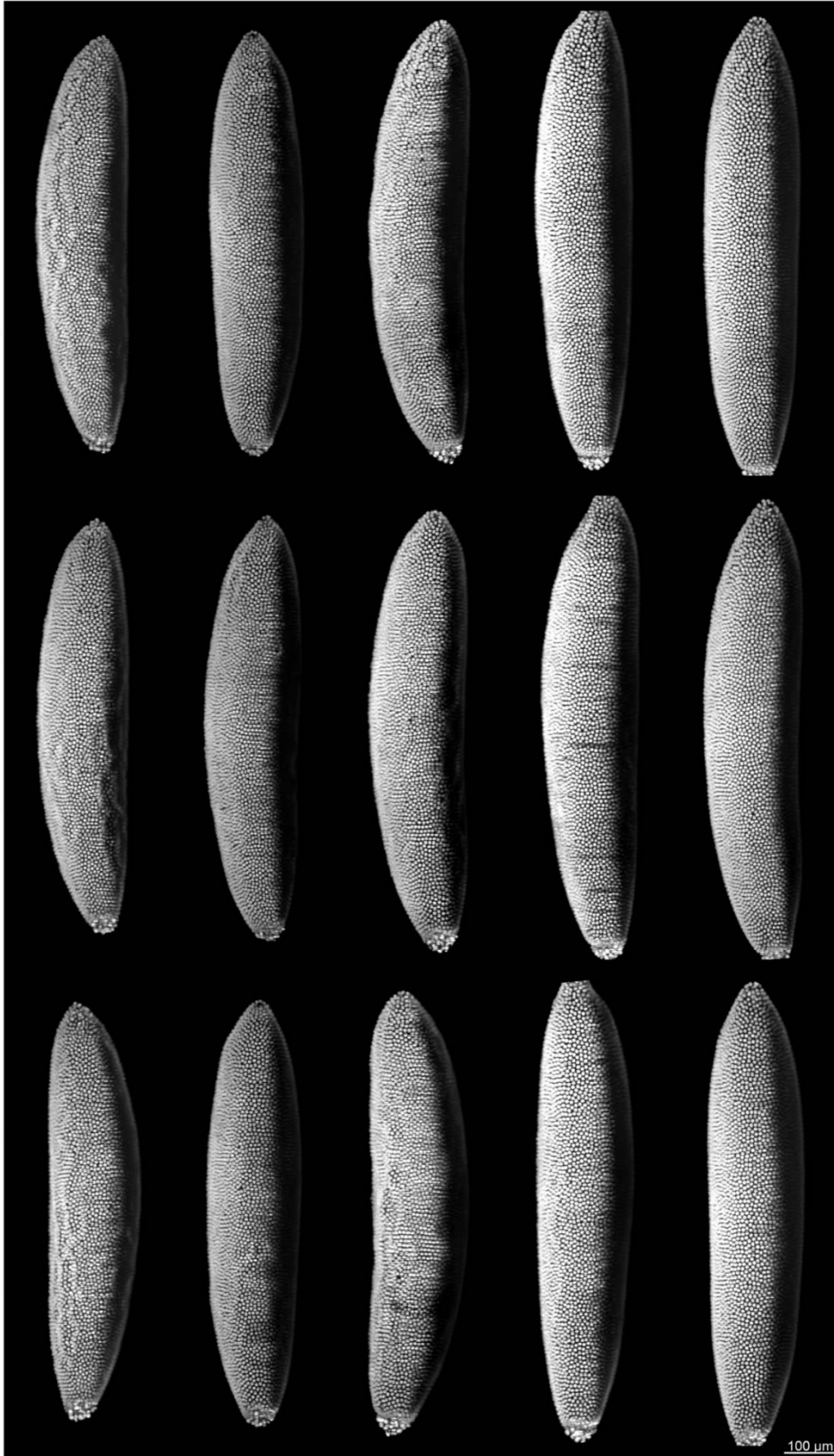
DS0004

DS0005

0° (ventrolateral / ventral) – ZA

90° (dorsolateral / lateral) – ZA

180° (dorsolateral / dorsal) – ZA



B

III – Germband Elongation

DS0001

DS0002

DS0003

DS0004

DS0005

0° (ventrolateral / ventral) – ZA

90° (dorsolateral / lateral) – ZA

180° (dorsolateral / dorsal) – ZA

100 μ m

C

IV – Germband Retraction

DS0001

DS0002

DS0003

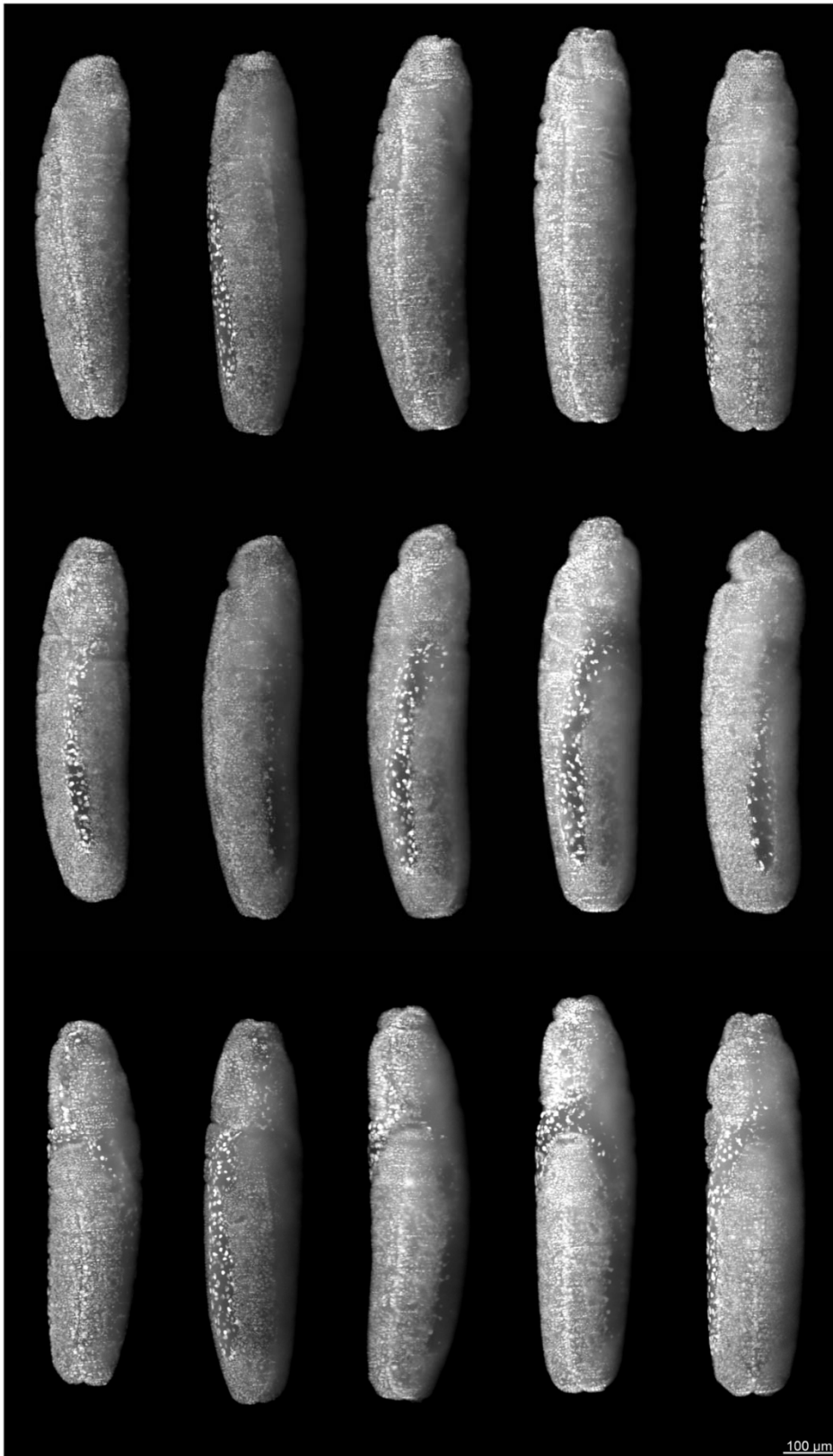
DS0004

DS0005

0° (ventrolateral / ventral) – ZA

90° (dorsolateral / lateral) – ZA

180° (dorsolateral / dorsal) – ZA



100 μ m

D

V – Dorsal Closure

DS0001

DS0002

DS0003

DS0004

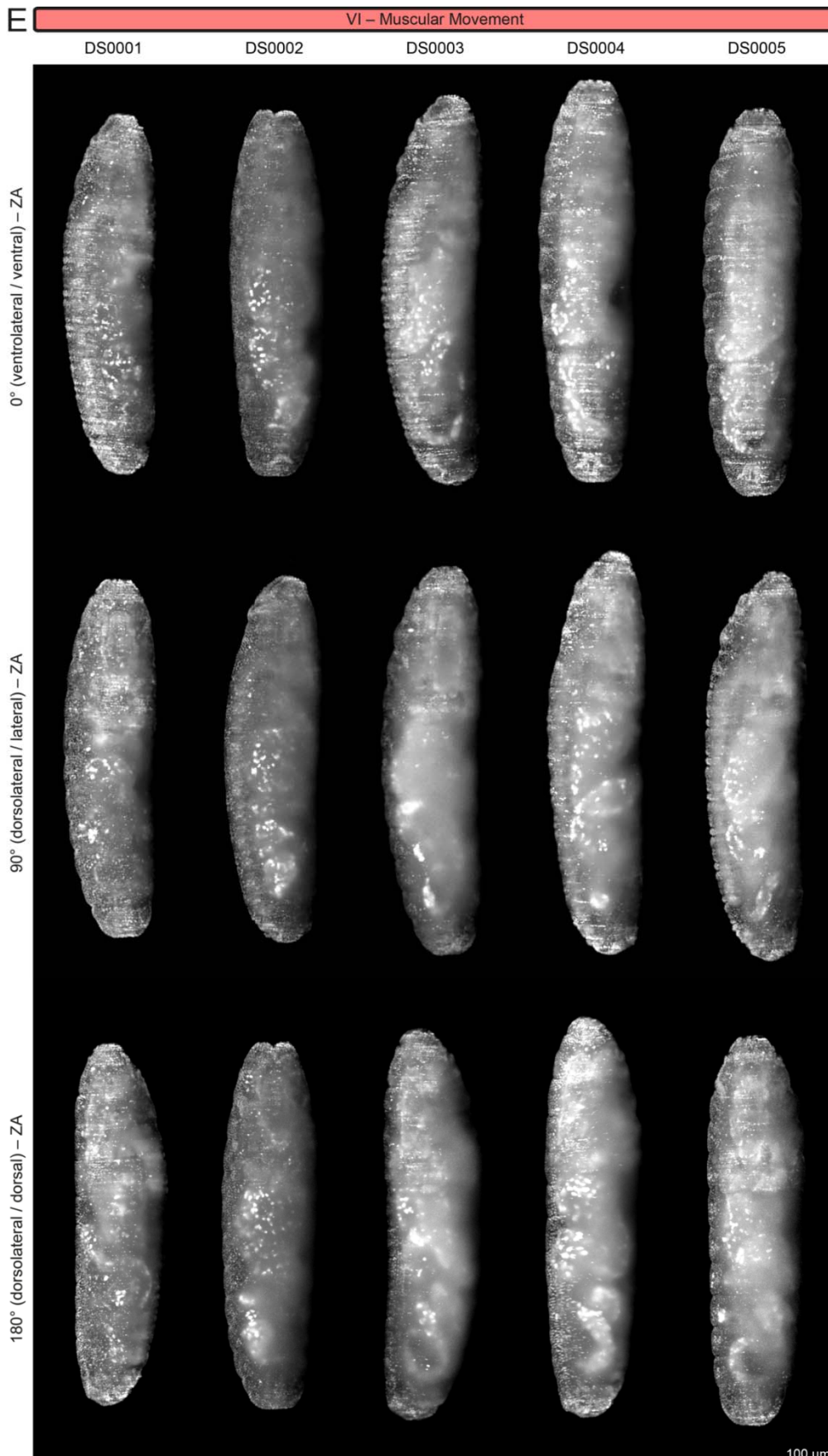
DS0005

0° (ventrolateral / ventral) – ZA

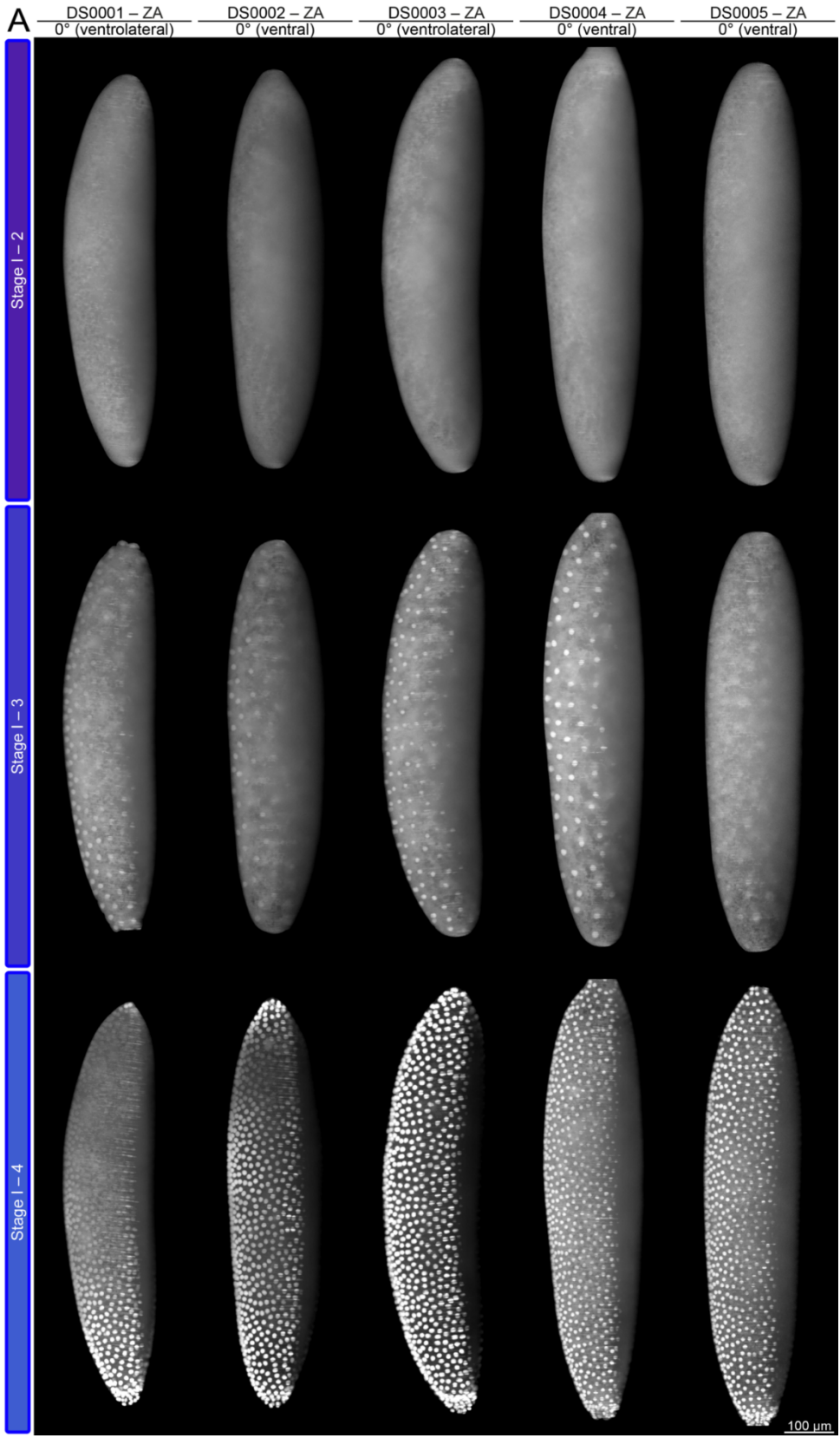
90° (dorsolateral / lateral) – ZA

180° (dorsolateral / dorsal) – ZA





Supplementary Figure 3 – Comparison of datasets DS0001-0005 at the beginning of the embryogenetic events (A) gastrulation, (B) germband elongation, (C) germband retraction, (D) dorsal closure and (E) muscular movement along three directions in the orientations 0°, 90° and 180°. Since recording began after blastoderm formation had started, there is no image data for the beginning of blastoderm formation available. Datasets DS0001 and 0003 are depicted ventrolateral, dorsolateral and dorsolateral, whereas DS0002, 0004 and 0005 are depicted ventral, lateral and dorsal. ZA, Z maximum projection with image adjustment.



B

DS0001 – ZA
0° (ventrolateral)

DS0002 – ZA
0° (ventral)

DS0003 – ZA
0° (ventrolateral)

DS0004 – ZA
0° (ventral)

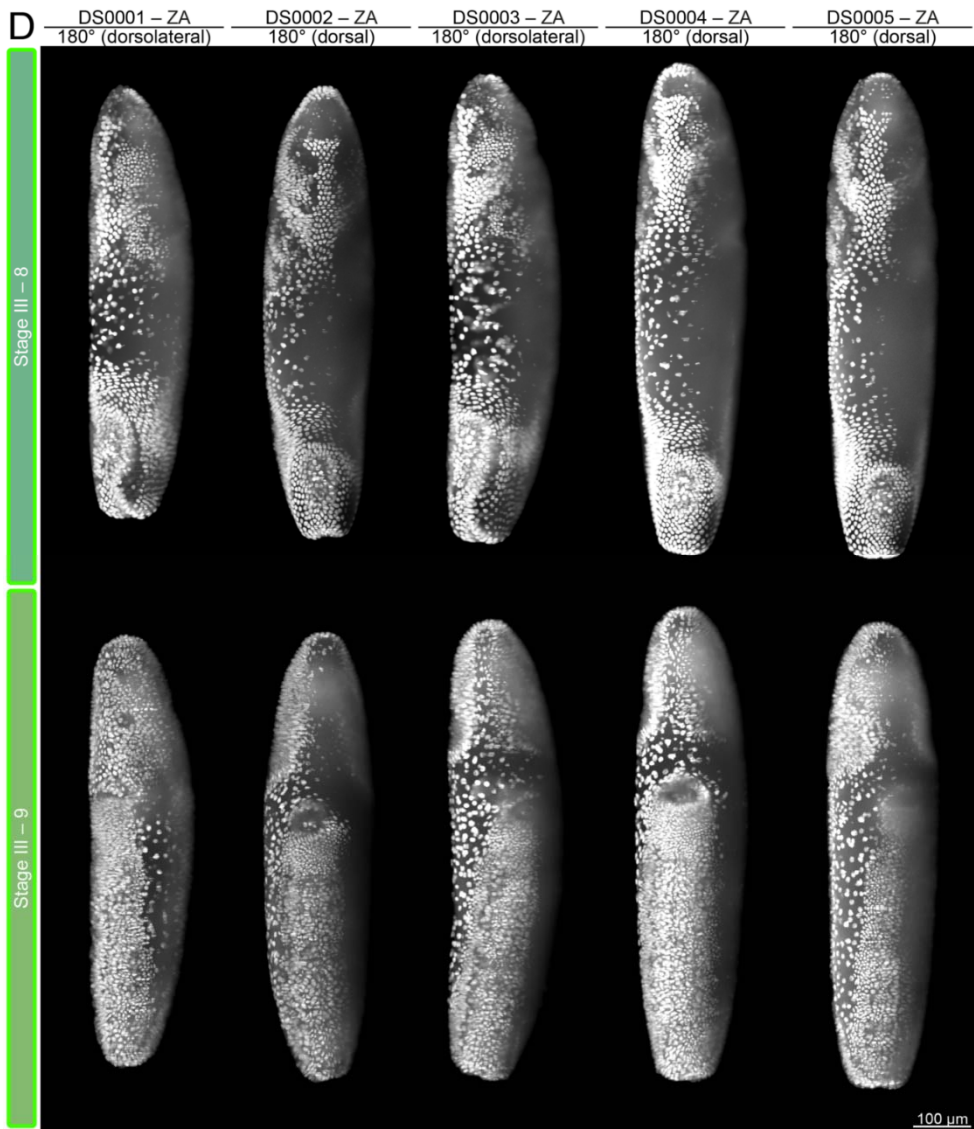
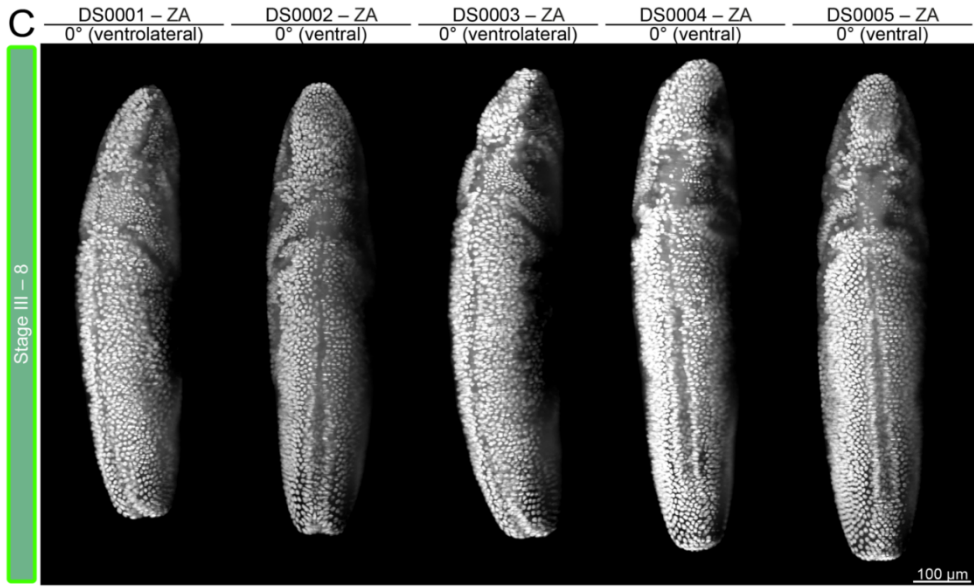
DS0005 – ZA
0° (ventral)

Stage I – 5

Stage II – 6

Stage II – 7





E

DS0001 - ZA
180° (dorsolateral)

DS0002 - ZA
180° (dorsal)

DS0003 - ZA
180° (dorsolateral)

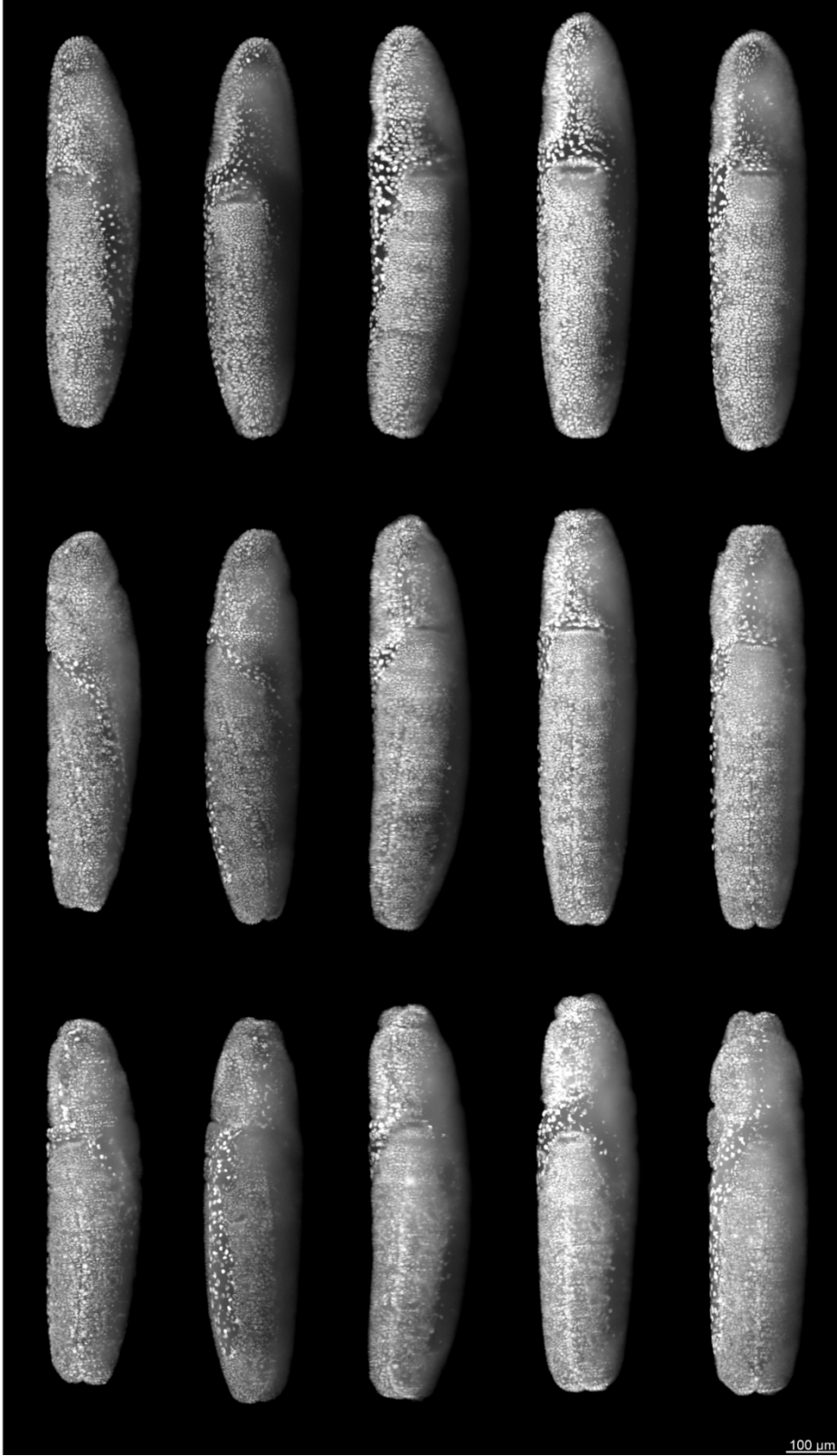
DS0004 - ZA
180° (dorsal)

DS0005 - ZA
180° (dorsal)

Stage III - 10

Stage III - 11

Stage IV - 12

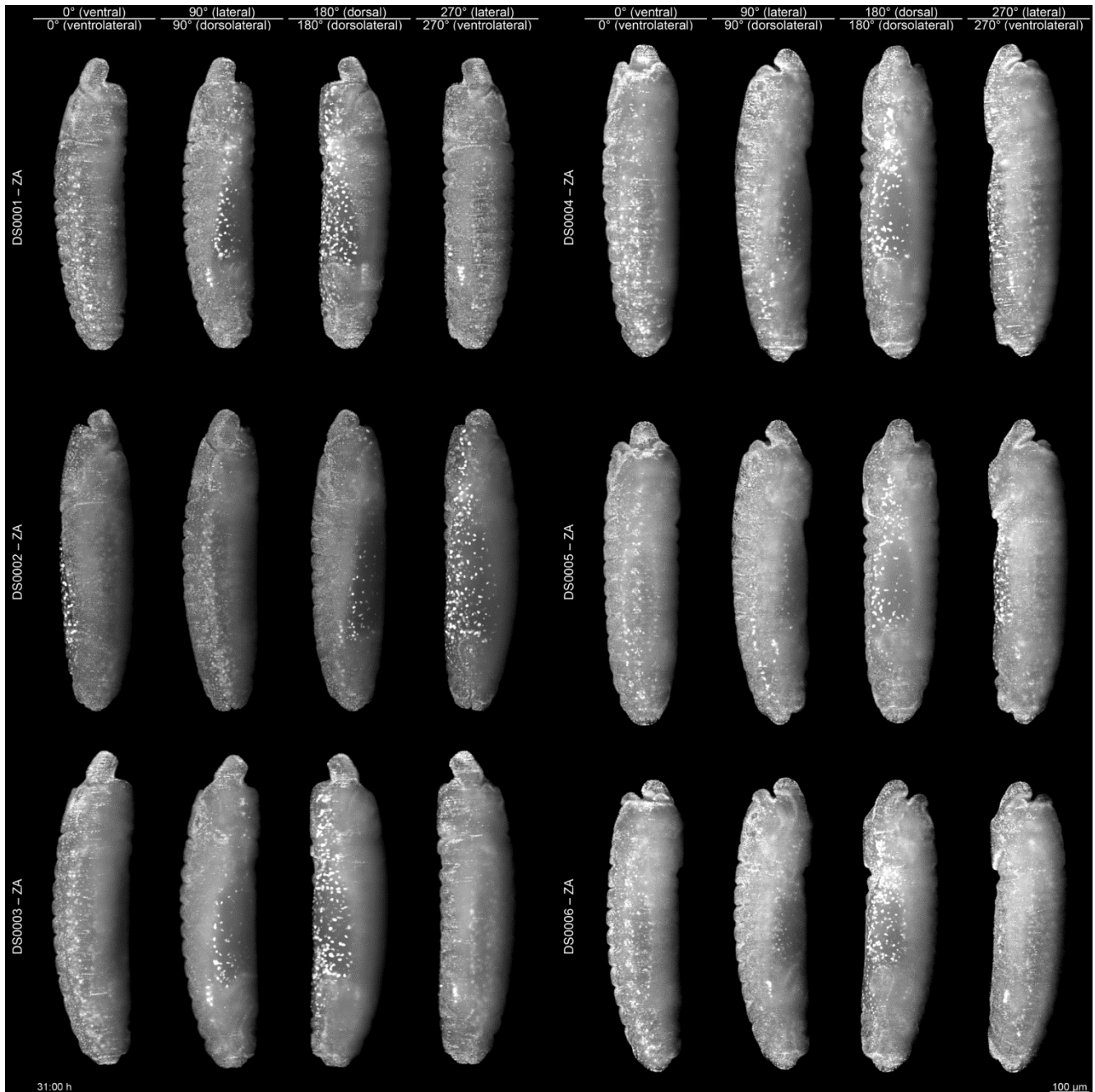


100 μm



Supplementary Figure 4 – Comparison of datasets DS0001-0005 at the beginning of the stages (A) I-2 – I-4, (B) I-5 – II-7, (C) III-8, (D) III-8 – III-9, (E) III-10 – IV-12, (F) IV-12 – V-14, (G) V-15 – VI-17. The shown direction changes throughout the figure (at stage III-8 and IV-12), so that structures that are characteristic for the respective stage can be seen properly. Because recording began after stage I-1 had started, there is no image data for the beginning of stage I-1 available. Datasets DS0001 and 0003 are depicted either ventrolateral or dorsolateral, whereas DS0002, 0004 and 0005 are depicted either ventral, lateral or dorsal. ZA, Z maximum projection with image adjustment.

Supplementary Videos



Supplementary Video 1 – *Ceratitis* embryogenesis for the six in toto datasets (DS0001-0006) along four orientations from 00:00 h to 65:00 h with an interval of 00:30 h between the time points. The video starts at the beginning of stage I-2, when the nuclei move to the surface of the egg and stops at the end of stage VI-17, when the larvae hatch from the egg, showing six embryogenetic events: (I) blastoderm formation, (II) gastrulation, (III) germband elongation, (IV) germband retraction, (V) dorsal closure and (VI) muscular movement. Frame rate is five frames per second. DS0001 and DS0003 show the embryo along the ventrolateral, dorsolateral, dorsolateral and ventrolateral orientations, all other datasets show the embryo along the ventral, lateral, dorsal and lateral orientations. ZA, Z maximum projection with image adjustment.

Tables

Scientific Data Table

Design Type(s)	non-invasive long-term fluorescence live imaging
Measurement Type(s)	three dimensional fluorophore distribution over time in a developing organism
Technology Type(s)	digital scanned laser light sheet-based fluorescence microscopy (DSLIM)
Factor Type(s)	
Sample Characteristics	<i>Ceratitis capitata</i>

Table 1 – Alignment and temporal breakdown of DS0001-0005 into embryogenetic events (Roman numerals) and stages (Arabic numerals). The beginning of each embryogenetic event is color-coded (see Methods section). Imaging typically begins with stage I-2, the values for I-1 are extrapolated. The identifiers are limited on purpose, as a comprehensive documentation of embryogenetic events and stages will be topic of another publication.

Event / Stage	Identifier	DS0001 (median)			DS0002 (longer)			DS0003 (longer)		
		TP	⊕	%	TP	⊕	%	TP	⊕	%
I – 1 Blastoderm Formation	egg fertilization results in the zygote, which consists of the yolk and the zygotic nuclei	-	00:00 h	0.0%	-	00:00 h	0.0%	-	00:00 h	0.0%
I – 2	the yolk begins withdrawing from both poles	0001	02:00 h	3.2%	0001	02:00 h	3.1%	0001	02:00 h	3.2%
I – 3	the yolk withdrawal at both poles reaches a relative maximum and starts reversing	0004	03:30 h	5.6%	0004	03:30 h	5.4%	0004	03:30 h	5.6%
I – 4	the last zygotic nuclei reach the surface	0006	04:30 h	7.2%	0007	05:00 h	7.7%	0006	04:30 h	7.1%
I – 5	the blastoderm nuclei complete the 13th synchronous nuclear division	0010	06:30 h	10.4%	0011	07:00 h	10.8%	0010	06:30 h	10.3%
II – 6 Gastrulation	the blastoderm nuclei complete the synthesis of cell membranes	0020	11:30 h	18.4%	0022	12:30 h	19.2%	0021	12:00 h	19.0%
II – 7	the anterior midgut primordium emerges and invaginates at the anterior tip of the ventral furrow	0024	13:30 h	21.6%	0026	14:30 h	22.3%	0025	14:00 h	22.2%
III – 8 Germband Elongation	the posterior tip of the germband begins anteriad elongation along the dorsal side towards with high speed	0026	14:30 h	23.2%	0027	15:00 h	23.1%	0026	14:30 h	23.0%
III – 9	the posterior tip of the germband continues anteriad elongation along the dorsal side with moderate speed	0030	16:30 h	26.4%	0031	17:00 h	26.2%	0030	16:30 h	26.2%
III – 10	the posterior tip of the germband continues anteriad elongation along the dorsal side with low speed	0033	18:00 h	28.8%	0032	17:30 h	26.9%	0032	17:30 h	27.8%
III – 11	the posterior tip of the germband completes anteriad elongation and remains in a quiescent position	0041	22:00 h	35.2%	0043	23:00 h	35.4%	0038	20:30 h	32.5%
IV – 12 Germband Retraction	the posterior tip of the germband begins posteriad retraction along the dorsal side	0046	24:30 h	39.2%	0048	25:30 h	39.2%	0046	24:30 h	38.9%
V – 13 Dorsal Closure	the posterior tip of the germband completes posteriad retracting	0061	32:00 h	51.2%	0062	32:30 h	50.0%	0059	31:00 h	49.2%
V – 14	the clypeolabrum turns from an antero-dorsal to an antero-ventral orientation	0066	34:30 h	55.2%	0068	35:30 h	54.6%	0066	34:30 h	54.8%
V – 15	the abdomen withdrawal at the posterior pole reaches the absolute maximum	0073	38:00 h	60.8%	0074	38:30 h	59.2%	0071	37:00 h	58.7%
VI – 16 Muscular Movement	the dorsal epidermal primordia complete medial fusion and turn into the dorsal epidermis	0087	45:00 h	72.0%	0084	43:30 h	66.9%	0086	44:30 h	70.6%
VI – 17	the posterior tip of the ventral cord shortens to the 5 th segment of the abdomen	0106	54:30 h	87.2%	0110	56:30 h	86.9%	0104	53:30 h	84.9%
Hatch	the embryo completes embryonic development, hatches and turns into the larva	0122	62:30 h	100.0%	0127	65:00 h	100.0%	0123	63:00 h	100.0%

(continued)

Event / Stage	Identifier	DS0004 (shorter)			DS0005 (shorter)			Standard Deviations	
		TP	⊕	%	TP	⊕	%	⊕	%
I – 1 Blastoderm Formation	egg fertilization results in the zygote, which consists of the yolk and the zygotic nuclei	-	00:00 h	0.0%	-	00:00 h	0.0%	±00:00 h	±0.0%
I – 2	the yolk begins withdrawing from both poles	0001	02:00 h	3.3%	0001	02:00 h	3.3%	±00:00 h	±0.1%
I – 3	the yolk withdrawal at both poles reaches a relative maximum and starts reversing	0004	03:30 h	5.8%	0004	03:30 h	5.7%	±00:00 h	±0.2%
I – 4	the last zygotic nuclei reach the surface	0006	04:30 h	7.5%	0006	04:30 h	7.4%	±00:13 h	±0.2%
I – 5	the blastoderm nuclei complete the 13th synchronous nuclear division	0010	06:30 h	10.8%	0010	06:30 h	10.7%	±00:13 h	±0.2%
II – 6 Gastrulation	the blastoderm nuclei complete the synthesis of cell membranes	0019	11:00 h	18.3%	0019	11:00 h	18.0%	±00:39 h	±0.5%
II – 7	the anterior midgut primordium emerges and invaginates at the anterior tip of the ventral furrow	0023	13:00 h	21.7%	0023	13:00 h	21.3%	±00:39 h	±0.5%
III – 8 Germband Elongation	the posterior tip of the germband begins anteriad elongation along the dorsal side towards with high speed	0024	13:30 h	22.5%	0024	13:30 h	22.1%	±00:40 h	±0.5%
III – 9	the posterior tip of the germband continues anteriad elongation along the dorsal side with moderate speed	0029	16:00 h	26.7%	0029	16:00 h	26.2%	±00:25 h	±0.2%
III – 10	the posterior tip of the germband continues anteriad elongation along the dorsal side with low speed	0031	17:00 h	28.3%	0031	17:00 h	27.9%	±00:25 h	±0.7%
III – 11	the posterior tip of the germband completes anteriad elongation and remains in a quiescent position	0036	19:30 h	32.5%	0038	20:30 h	33.6%	±01:23 h	±1.4%
IV – 12 Germband Retraction	the posterior tip of the germband begins posteriad retraction along the dorsal side	0044	23:30 h	39.2%	0044	23:30 h	38.5%	±00:50 h	±0.3%
V – 13 Dorsal Closure	the posterior tip of the germband completes posteriad retracting	0053	28:00 h	46.7%	0055	29:00 h	47.5%	±01:56 h	±1.8%
V – 14	the clypeolabrum turns from an antero-dorsal to an antero-ventral orientation	0062	32:30 h	54.2%	0062	32:30 h	53.3%	±01:20 h	±0.7%
V – 15	the abdomen withdrawal at the posterior pole reaches the absolute maximum	0069	36:00 h	60.0%	0071	37:00 h	60.7%	±00:58 h	±0.9%
VI – 16 Muscular Movement	the dorsal epidermal primordia complete medial fusion and turn into the dorsal epidermis	0079	41:00 h	68.3%	0082	42:30 h	69.7%	±01:36 h	±2.0%
VI – 17	the posterior tip of the ventral cord shortens to the 5 th segment of the abdomen	0097	50:00 h	83.3%	0101	52:00 h	85.2%	±02:27 h	±1.6%
Hatch	the embryo completes embryonic development, hatches and turns into the larva	0117	60:00 h	100.0%	0119	61:00 h	100.0%	±01:55 h	±0.0%

Supplementary Tables

Supplementary Table 1 – Metadata and parameter for the long-term live-imaging datasets DS0001-0003.

<i>Dataset (DS)</i>	DS0001	DS0002	DS0003
<i>Species</i>	<i>Ceratitis capitata</i> (Wiedemann) / Arthropoda → Insecta → Diptera → Tephritidae		
<i>Line</i>	<i>TREhs43-hid^{Ala5}_F1m2</i> (Schetelig et al. 2009, BMC Biol.)		
<i>Line Genotype</i>	single insertion / homozygous		
<i>Stock</i>	~50-80 adults, less than 4 weeks old		
<i>Stock Medium</i>	refined sugar (524973, REWE Markt GmbH, Köln, Germany) supplemented with 33% (wt/wt) inactive dry yeast (62-106, Flystuff, San Diego, CA, USA)		
<i>Stock Conditions</i>	12:00 h light / 12:00 h darkness at 25°C and 70% relative humidity (DR-36VL, Percival Scientific, Perry, IA, USA)		
<i>Egg Laying Period</i>	eggs were laid under room temperature (23±1°C) for 00:10 h		
<i>Pre-imaging Incubation</i>	embryo mounting procedure, approximately 00:30 h at room temperature (23±1°C), incubation in the sample chamber, approximately 01:30 h at room temperature (23±1°C) resulting in a total of 02:00 h incubation at room temperature (23±1°C)		
<i>LSFM Type</i>	mDSLML (monolithic digital scanned laser light sheet-based fluorescence microscope) based on DSLM		
<i>Laser Lines</i>	488 nm / 60 mW diode laser (PhoxX 488-60, Omicron Laserprodukte GmbH, Rodgau-Dudenhofen, Germany)		
<i>Excitation Objective</i>	2.5× NA 0.06 EC Epiplan-Neofluar objective (422320-9900-000, Carl Zeiss, Göttingen, Germany)		
<i>Emission Objective</i>	10× NA 0.3 W N-Achroplan objective (420947-9900-000, Carl Zeiss, Göttingen, Germany)		
<i>Emission Filters</i>	525/50 single-band bandpass filter (FF03-525/50-25, Semrock/AHF Analysentechnik AG, Tübingen, Germany)		
<i>Camera</i>	High-resolution CCD (Clara, Andor, Belfast, United Kingdom), 14 bit, 1040×1392 pixel (pitch 6.45 μm)		
<i>Dataset File Type</i>	JPEG2000 (planes are deposited as individual image files) TIFF, 16 bit grayscale (planes saved as Z stacks in ZIP-compressed container files, indicated as PL(ZS))		
<i>Dechoriation</i>	~60-90 s in 10% (vol/vol) sodium hypochlorite (425044-250ML, Sigma Adlrich, Taufkirchen, Germany) in PBS pH 7.4 (10010-023, Gibco Life Technologies GmbH, Darmstadt, Germany)		
<i>Mounting Agarose</i>	1% (wt/vol) low-melt agarose (6351.2, Carl Roth, Karlsruhe, Germany) in PBS pH 7.4 (10010-023, Gibco Life Technologies GmbH, Darmstadt, Germany)		
<i>Imaging Buffer</i>	PBS pH 7.4 (10010-023, Gibco Life Technologies GmbH, Darmstadt, Germany)		
<i>Imaging Temperature</i>	room temperature (23±1°C)	room temperature (23±1°C)	room temperature (23±1°C)
<i>Retrieval</i>	developed to healthy adult	developed to healthy adult	developed to healthy adult

Supplementary Table 1 – Metadata and parameter for the long-term live-imaging datasets DS0001-0003.

<i>Dataset (DS)</i>	DS0001	DS0002	DS0003
<i>Dataset Size</i>	0.4 Gigabyte (JPEG2000)	0.3 Gigabyte (JPEG2000)	0.3 Gigabyte (JPEG2000)
	31.1 Gigabyte (TIFF)	31.6 Gigabyte (TIFF)	31.9 Gigabyte (TIFF)
<i>Figures</i>	2 (first column)	2 (second column)	2 (third column)
<i>Supplementary Figures</i>	3 (first column),	3 (first column),	3 (first column),
	4 (first column)	4 (first column)	4 (first column)
<i>Supplementary Videos</i>	1 (first row)	1 (second row)	1 (third row)
<i>Comment</i>	median development time of datasets DS0001-DS0005	-	-
<i>Time Points (TP)</i>	121 (TP0001-TP0121)	126 (TP0001-TP0126)	122 (TP0001-TP0122)
<i>TP Interval</i>	00:30 h	00:30 h	00:30 h
<i>Total Time (TP×TP Interval)</i>	62:00 h	64:30 h	62:30 h
<i>Directions (DR)</i>	4 (DR0001-DR0004)	4 (DR0001-DR0004)	4 (DR0001-DR0004)
<i>DR Orientations</i>	0°, 90°, 180°, 270°	0°, 90°, 180°, 270°	0°, 90°, 180°, 270°
<i>Channels (CH)</i>	1 (CH0001)	1 (CH0001)	1 (CH0001)
<i>CH0001 Excitation</i>	488 nm	488 nm	488 nm
<i>CH0001 Power</i>	135 μW (close to the embryo)	135 μW (close to the embryo)	135 μW (close to the embryo)
<i>CH0001 Exposure Time</i>	50 ms	50 ms	50 ms
<i>CH0001 Emission Filter</i>	525/50 single-band bandpass filter	525/50 single-band bandpass filter	525/50 single-band bandpass filter
<i>Planes (PL)</i>	100 (PL0001-PL0100)	100 (PL0001-PL0100)	100 (PL0001-PL0100)
<i>Z Spacing</i>	2.58 μm	2.58 μm	2.58 μm
<i>Z Distance (PL×Z Spacing)</i>	258.0 μm	258.0 μm	258.0 μm
<i>X-Dimensions (XD)</i>	500 pixels (cropped)	500 pixels (cropped)	500 pixels (cropped)
<i>X Spacing</i>	0.645 μm	0.645 μm	0.645 μm
<i>X Length (XD×X Spacing)</i>	322.5 μm	322.5 μm	322.5 μm
<i>Y-Dimensions (YD)</i>	1390 pixels (cropped)	1390 pixels (cropped)	1390 pixels (cropped)
<i>Y Spacing</i>	0.645 μm	0.645 μm	0.645 μm
<i>Y Length (YD×Y Spacing)</i>	896.6 μm	896.6 μm	896.6 μm

Supplementary Table 1 – Metadata and parameter for the long-term live-imaging datasets DS0004-0006.

<i>Dataset (DS)</i>	DS0004	DS0005	DS0006
<i>Species</i>	<i>Ceratitis capitata</i> (Wiedemann) / Arthropoda → Insecta → Diptera → Tephritidae		
<i>Line</i>	<i>TREhs43-hid^{Ala5}_F1m2</i> (Schetelig et al. 2009, BMC Biol.)		
<i>Line Genotype</i>	single insertion / homozygous		
<i>Stock</i>	~50-80 adults, less than 4 weeks old		
<i>Stock Medium</i>	refined sugar (524973, REWE Markt GmbH, Köln, Germany) supplemented with 33% (wt/wt) inactive dry yeast (62-106, Flystuff, San Diego, CA, USA)		
<i>Stock Conditions</i>	12:00 h light / 12:00 h darkness at 25°C and 70% relative humidity (DR-36VL, Percival Scientific, Perry, IA, USA)		
<i>Egg Laying Period</i>	eggs were laid under room temperature (23±1°C) for 00:10 h		
<i>Pre-imaging Incubation</i>	embryo mounting procedure, approximately 00:30 h at room temperature (23±1°C), incubation in the sample chamber, approximately 01:30 h at room temperature (23±1°C) resulting in a total of 02:00 h incubation at room temperature (23±1°C)		
<i>LSFM Type</i>	mDSLm (monolithic digital scanned laser light sheet-based fluorescence microscope) based on DSLM		
<i>Laser Lines</i>	488 nm / 60 mW diode laser (PhoxX 488-60, Omicron Laserprodukte GmbH, Rodgau-Dudenhofen, Germany)		
<i>Excitation Objective</i>	2.5× NA 0.06 EC Epiplan-Neofluar objective (422320-9900-000, Carl Zeiss, Göttingen, Germany)		
<i>Emission Objective</i>	10× NA 0.3 W N-Achroplan objective (420947-9900-000, Carl Zeiss, Göttingen, Germany)		
<i>Emission Filters</i>	525/50 single-band bandpass filter (FF03-525/50-25, Semrock/AHF Analysetechnik AG, Tübingen, Germany)		
<i>Camera</i>	High-resolution CCD (Clara, Andor, Belfast, United Kingdom), 14 bit, 1040×1392 pixel (pitch 6.45 μm)		
<i>Dataset File Type</i>	JPEG2000 (planes are deposited as individual image files) TIFF, 16 bit grayscale (planes saved as Z stacks in ZIP-compressed container files, indicated as PL(ZS))		
<i>Dechoriation</i>	~60-90 s in 10% (vol/vol) sodium hypochlorite (425044-250ML, Sigma Adlrlich, Taufkirchen, Germany) in PBS pH 7.4 (10010-023, Gibco Life Technologies GmbH, Darmstadt, Germany)		
<i>Mounting Agarose</i>	1% (wt/vol) low-melt agarose (6351.2, Carl Roth, Karlsruhe, Germany) in PBS pH 7.4 (10010-023, Gibco Life Technologies GmbH, Darmstadt, Germany)		
<i>Imaging Buffer</i>	PBS pH 7.4 (10010-023, Gibco Life Technologies GmbH, Darmstadt, Germany)		
<i>Imaging Temperature</i>	room temperature (23±1°C)	room temperature (23±1°C)	room temperature (23±1°C)
<i>Retrieval</i>	developed to healthy adult	developed to healthy adult	did not eclose from the pupa

Supplementary Table 1 – Metadata and parameter for the long-term live-imaging datasets DS0004-0006.

<i>Dataset (DS)</i>	DS0004	DS0005	DS0006
<i>Dataset Size</i>	0.4 Gigabyte (JPEG2000)	0.2 Gigabyte (JPEG2000)	0.2 Gigabyte (JPEG2000)
	31.5 Gigabyte (TIFF)	29.6 Gigabyte (TIFF)	28.3 Gigabyte (TIFF)
<i>Figures</i>	2 (fourth column)	2 (fifth column)	-
<i>Supplementary Figures</i>	3 (fourth column),	3 (fifth column),	-
	4 (fourth column)	4 (fifth column)	-
<i>Supplementary Videos</i>	1 (fourth row)	1 (fifth row)	-
<i>Comment</i>	slightly larger than the volume of view in Y	slightly larger than the volume of view in Y	excluded from statistics
<i>Time Points (TP)</i>	116 (TP0001-TP0121)	118 (TP0001-TP0126)	117 (TP0001-TP0122)
<i>TP Interval</i>	00:30 h	00:30 h	00:30 h
<i>Total Time (TP×TP Interval)</i>	60:00 h	61:00 h	60:30 h
<i>Directions (DR)</i>	4 (DR0001-DR0004)	4 (DR0001-DR0004)	4 (DR0001-DR0004)
<i>DR Orientations</i>	0°, 90°, 180°, 270°	0°, 90°, 180°, 270°	0°, 90°, 180°, 270°
<i>Channels (CH)</i>	1 (CH0001)	1 (CH0001)	1 (CH0001)
<i>CH0001 Excitation</i>	488 nm	488 nm	488 nm
<i>CH0001 Power</i>	135 μW (close to the embryo)	135 μW (close to the embryo)	135 μW (close to the embryo)
<i>CH0001 Exposure Time</i>	50 ms	50 ms	50 ms
<i>CH0001 Emission Filter</i>	525/50 single-band	525/50 single-band	525/50 single-band
	bandpass filter	bandpass filter	bandpass filter
<i>Planes (PL)</i>	100 (PL0001-PL0100)	100 (PL0001-PL0100)	100 (PL0001-PL0100)
<i>Z Spacing</i>	2.58 μm	2.58 μm	2.58 μm
<i>Z Distance (PL×Z Spacing)</i>	258.0 μm	258.0 μm	258.0 μm
<i>X-Dimensions (XD)</i>	500 pixels (cropped)	500 pixels (cropped)	500 pixels (cropped)
<i>X Spacing</i>	0.645 μm	0.645 μm	0.645 μm
<i>X Length (XD×X Spacing)</i>	322.5 μm	322.5 μm	322.5 μm
<i>Y-Dimensions (YD)</i>	1390 pixels	1390 pixels	1390 pixels
<i>Y Spacing</i>	0.645 μm	0.645 μm	0.645 μm
<i>Y Length (YD×Y Spacing)</i>	896.6 μm	896.6 μm	896.6 μm

Supplementary Table 1 – Metadata and parameter for the long-term live-imaging datasets DS0007-0009.

<i>Dataset (DS)</i>	DS0007	DS0008	DS0009
<i>Species</i>	<i>Ceratitis capitata</i> (Wiedemann) / Arthropoda → Insecta → Diptera → Tephritidae		
<i>Line</i>	<i>TREhs43-hid^{Ala5}_F1m2</i> (Schetelig et al. 2009, BMC Biol.)		
<i>Line Genotype</i>	single insertion / homozygous		
<i>Stock</i>	~50-80 adults, less than 4 weeks old		
<i>Stock Medium</i>	refined sugar (524973, REWE Markt GmbH, Köln, Germany) supplemented with 33% (wt/wt) inactive dry yeast (62-106, Flystuff, San Diego, CA, USA)		
<i>Stock Conditions</i>	12:00 h light / 12:00 h darkness at 25°C and 70% relative humidity (DR-36VL, Percival Scientific, Perry, IA, USA)		
<i>Egg Laying Period</i>	eggs were laid under room temperature (23±1°C) for 00:10 h		
<i>Pre-imaging Incubation</i>	embryo mounting procedure, approximately 00:30 h at room temperature (23±1°C), incubation in the sample chamber, approximately 01:30 h at room temperature (23±1°C) resulting in a total of 02:00 h incubation at room temperature (23±1°C)		
<i>LSFM Type</i>	mDSLm (monolithic digital scanned laser light sheet-based fluorescence microscope) based on DSLM		
<i>Laser Lines</i>	488 nm / 60 mW diode laser (PhoxX 488-60, Omicron Laserprodukte GmbH, Rodgau-Dudenhofen, Germany)		
<i>Excitation Objective</i>	2.5× NA 0.06 EC Epiplan-Neofluar objective (422320-9900-000, Carl Zeiss, Göttingen, Germany)		
<i>Emission Objective</i>	10× NA 0.3 W N-Achroplan objective (420947-9900-000, Carl Zeiss, Göttingen, Germany)		
<i>Emission Filters</i>	525/50 single-band bandpass filter (FF03-525/50-25, Semrock/AHF Analysetechnik AG, Tübingen, Germany)		
<i>Camera</i>	High-resolution CCD (Clara, Andor, Belfast, United Kingdom), 14 bit, 1040×1392 pixel (pitch 6.45 μm)		
<i>Dataset File Type</i>	JPEG2000 (planes are deposited as individual image files) TIFF, 16 bit grayscale (planes saved as Z stacks in ZIP-compressed container files, indicated as PL(ZS))		
<i>Dechoriation</i>	~60-90 s in 10% (vol/vol) sodium hypochlorite (425044-250ML, Sigma Adlrlich, Taufkirchen, Germany) in PBS pH 7.4 (10010-023, Gibco Life Technologies GmbH, Darmstadt, Germany)		
<i>Mounting Agarose</i>	1% (wt/vol) low-melt agarose (6351.2, Carl Roth, Karlsruhe, Germany) in PBS pH 7.4 (10010-023, Gibco Life Technologies GmbH, Darmstadt, Germany)		
<i>Imaging Buffer</i>	PBS pH 7.4 (10010-023, Gibco Life Technologies GmbH, Darmstadt, Germany)		
<i>Imaging Temperature</i>	room temperature (23±1°C)	room temperature (23±1°C)	room temperature (23±1°C)
<i>Retrieval</i>	developed to healthy adult	developed to healthy adult	developed to healthy adult

Supplementary Table 1 – Metadata and parameter for the long-term live-imaging datasets DS0007-0009.

<i>Dataset (DS)</i>	DS0007	DS0008	DS0009
<i>Dataset Size</i>	0.4 Gigabyte (JPEG2000)	0.3 Gigabyte (JPEG2000)	0.1 Gigabyte (JPEG2000)
	19.4 Gigabyte (TIFF)	43.0 Gigabyte (TIFF)	12.7 Gigabyte (TIFF)
<i>Figures</i>	-	-	-
<i>Supplementary Figures</i>	-	-	-
<i>Supplementary Videos</i>	-	-	-
<i>Comment</i>	embryo not captured <i>in toto</i> , documents germ cell formation	embryo not captured <i>in toto</i> , documents head involution	embryo not captured <i>in toto</i> , agarose hemisphere mounting
<i>Time Points (TP)</i>	49 (TP0001-TP0049)	127 (TP0001-TP0127)	96 (TP0001-TP0096)
<i>TP Interval</i>	00:30 h	00:30 h	00:30 h
<i>Total Time (TP×TP Interval)</i>	24:00 h	63:00 h	47:30 h
<i>Directions (DR)</i>	4 (DR0001-DR0004)	4 (DR0001-DR0004)	2 (DR0001-DR0002)
<i>DR Orientations</i>	0°, 90°, 180°, 270°	0°, 90°, 180°, 270°	0°, 90°
<i>Channels (CH)</i>	1 (CH0001)	1 (CH0001)	1 (CH0001)
<i>CH0001 Excitation</i>	488 nm	488 nm	488 nm
<i>CH0001 Power</i>	135 μW (close to the embryo)	135 μW (close to the embryo)	135 μW (close to the embryo)
<i>CH0001 Exposure Time</i>	50 ms	50 ms	50 ms
<i>CH0001 Emission Filter</i>	525/50 single-band bandpass filter	525/50 single-band bandpass filter	525/50 single-band bandpass filter
<i>Planes (PL)</i>	100 (PL0001-PL0100)	100 (PL0001-PL0100)	DR0001: 115 (PL0001-PL0115) DR0002: 100 (PL0001-PL0100)
<i>Z Spacing</i>	2.58 μm	2.58 μm	2.58 μm
<i>Z Distance (PL×Z Spacing)</i>	258.0 μm	258.0 μm	DR0001: 296.7 μm DR0002: 258.0 μm
<i>X-Dimensions (XD)</i>	720 pixels (cropped)	720 pixels (cropped)	DR0001: 720 pixels (cropped) DR0002: 1000 pixels (cropped)
<i>X Spacing</i>	0.3225 μm	0.3225 μm	0.3225 μm
<i>X Length (XD×X Spacing)</i>	232.2 μm	232.2 μm	DR0001: 232.2 μm DR0002: 322.5 μm
<i>Y-Dimensions (YD)</i>	1300 pixels (cropped)	1300 pixels (cropped)	720 pixels (cropped)
<i>Y Spacing</i>	0.3225 μm	0.3225 μm	0.3225 μm
<i>Y Length (YD×Y Spacing)</i>	419.25 μm	419.25 μm	232.2 μm

All datasets can be downloaded in the JPEG2000 file format at Dryad and in the JPEG2000 and TIF file format at www.physikalischebiologie.de/bugcube.

Supplementary Table 2 – Embryogenetic events starting and ending time points for DS0001-DS0005. The embryogenetic events are color-coded (see Methods section).

Event	DS0001 (median)			DS0002 (longer)			DS0003 (longer)		
	TP	⊕	%	TP	⊕	%	TP	⊕	%
BF (I)	-	00:00 h	0.0%	-	00:00 h	0.0%	-	00:00 h	0.0%
G (II)	0020	11:30 h	18.4%	0022	12:30 h	19.2%	0021	12:00 h	19.0%
GBE (III)	0026	14:30 h	23.2%	0027	15:00 h	23.1%	0026	14:30 h	23.0%
GBR (IV)	0046	24:30 h	39.2%	0048	25:30 h	39.2%	0046	24:30 h	38.9%
DC (V)	0061	32:00 h	51.2%	0062	32:30 h	50.0%	0059	31:00 h	49.2%
MM (VI)	0087	45:00 h	72.0%	0084	43:30 h	66.9%	0086	44:30 h	70.6%

(continued)

Event	DS0004 (shorter)			DS0005 (shorter)			Standard Deviations	
	TP	⊕	%	TP	⊕	%	⊖ SD	% SD
BF (I)	-	00:00 h	0.0%	-	00:00 h	0.0%	±00:00 h	±0.0%
G (II)	0019	11:00 h	18.3%	0019	11:00 h	18.0%	±00:39 h	±0.5%
GBE (III)	0024	13:30 h	22.5%	0024	13:30 h	22.1%	±00:40 h	±0.5%
GBR (IV)	0044	23:30 h	39.2%	0044	23:30 h	38.5%	±00:50 h	±0.3%
DC (V)	0053	28:00 h	46.7%	0055	29:00 h	47.5%	±01:56 h	±1.8%
MM (VI)	0079	41:00 h	68.3%	0082	42:30 h	69.7%	±01:36 h	±2.0%

Supplementary Table 3 – Stage starting and ending time points for DS0001-DS0005. The beginning of each embryogenetic event is color-coded (see Methods section).

Stage	DS0001 (median)			DS0002 (longer)			DS0003 (longer)		
	TP	⊕	%	TP	⊕	%	TP	⊕	%
I – 1	-	00:00 h	0.0%	-	00:00 h	0.0%	-	00:00 h	0.0%
I – 2	0001	02:00 h	3.2%	0001	02:00 h	3.1%	0001	02:00 h	3.2%
I – 3	0004	03:30 h	5.6%	0004	03:30 h	5.4%	0004	03:30 h	5.6%
I – 4	0006	04:30 h	7.2%	0007	05:00 h	7.7%	0006	04:30 h	7.1%
I – 5	0010	06:30 h	10.4%	0011	07:00 h	10.8%	0010	06:30 h	10.3%
II – 6	0020	11:30 h	18.4%	0022	12:30 h	19.2%	0021	12:00 h	19.0%
II – 7	0024	13:30 h	21.6%	0026	14:30 h	22.3%	0025	14:00 h	22.2%
III – 8	0026	14:30 h	23.2%	0027	15:00 h	23.1%	0026	14:30 h	23.0%
III – 9	0030	16:30 h	26.4%	0031	17:00 h	26.2%	0030	16:30 h	26.2%
III – 10	0033	18:00 h	28.8%	0032	17:30 h	26.9%	0032	17:30 h	27.8%
III – 11	0041	22:00 h	35.2%	0043	23:00 h	35.4%	0038	20:30 h	32.5%
IV – 12	0046	24:30 h	39.2%	0048	25:30 h	39.2%	0046	24:30 h	38.9%
V – 13	0061	32:00 h	51.2%	0062	32:30 h	50.0%	0059	31:00 h	49.2%
V – 14	0066	34:30 h	55.2%	0068	35:30 h	54.6%	0066	34:30 h	54.8%
V – 15	0073	38:00 h	60.8%	0074	38:30 h	59.2%	0071	37:00 h	58.7%
VI – 16	0087	45:00 h	72.0%	0084	43:30 h	66.9%	0086	44:30 h	70.6%
VI – 17	0106	54:30 h	87.2%	0110	56:30 h	86.9%	0104	53:30 h	84.9%
Hatch	0122	62:30 h	100.0%	0127	65:00 h	100.0%	0123	63:00 h	100.0%

(continued)

Stage	DS0004 (shorter)			DS0005 (shorter)			Standard Deviations	
	TP	⊕	%	TP	⊕	%	⊕ SD	% SD
I – 1	-	00:00 h	0.0%	-	00:00 h	0.0%	±00:00 h	±0.0%
I – 2	0001	02:00 h	3.3%	0001	02:00 h	3.3%	±00:00 h	±0.1%
I – 3	0004	03:30 h	5.8%	0004	03:30 h	5.7%	±00:00 h	±0.2%
I – 4	0006	04:30 h	7.5%	0006	04:30 h	7.4%	±00:13 h	±0.2%
I – 5	0010	06:30 h	10.8%	0010	06:30 h	10.7%	±00:13 h	±0.2%
II – 6	0019	11:00 h	18.3%	0019	11:00 h	18.0%	±00:39 h	±0.5%
II – 7	0023	13:00 h	21.7%	0023	13:00 h	21.3%	±00:39 h	±0.5%
III – 8	0024	13:30 h	22.5%	0024	13:30 h	22.1%	±00:40 h	±0.5%
III – 9	0029	16:00 h	26.7%	0029	16:00 h	26.2%	±00:25 h	±0.2%
III – 10	0031	17:00 h	28.3%	0031	17:00 h	27.9%	±00:25 h	±0.7%
III – 11	0036	19:30 h	32.5%	0038	20:30 h	33.6%	±01:23 h	±1.4%
IV – 12	0044	23:30 h	39.2%	0044	23:30 h	38.5%	±00:50 h	±0.3%
V – 13	0053	28:00 h	46.7%	0055	29:00 h	47.5%	±01:56 h	±1.8%
V – 14	0062	32:30 h	54.2%	0062	32:30 h	53.3%	±01:20 h	±0.7%
V – 15	0069	36:00 h	60.0%	0071	37:00 h	60.7%	±00:58 h	±0.9%
VI – 16	0079	41:00 h	68.3%	0082	42:30 h	69.7%	±01:36 h	±2.0%
VI – 17	0097	50:00 h	83.3%	0101	52:00 h	85.2%	±02:27 h	±1.6%
Hatch	0117	60:00 h	100.0%	0119	61:00 h	100.0%	±01:55 h	±0.0%

Supplementary Table 4 – Time point–based alignment of DS0002-DS0005 to DS0001. The beginning of each embryogenetic event is color-coded (see Methods section). As only approximately 97% of embryogenesis were recorded, the first stage does not have time points. Imaging typically begins with stage I-2, the values for I-1 are extrapolated.

Stage	TP	DS0001 (median)		DS0002 (aligned)		DS0003 (aligned)		DS0004 (aligned)		DS0005 (aligned)		Standard Deviation	
		⊕	%	⊕	%	⊕	%	⊕	%	⊕	%	⊕	%
I - 1	-	00:00 h	0.0%	00:00 h	0.0%	00:00 h	0.0%	00:00 h	0.0%	00:00 h	0.0%	±00:00 h	±0.0%
	-	00:30 h	0.8%	00:30 h	0.8%	00:30 h	0.8%	00:30 h	0.8%	00:30 h	0.8%	±00:00 h	±0.0%
	-	01:00 h	1.6%	01:00 h	1.5%	01:00 h	1.6%	01:00 h	1.7%	01:00 h	1.6%	±00:00 h	±0.0%
I - 2	0001	01:30 h	2.4%	01:30 h	2.3%	01:30 h	2.4%	01:30 h	2.5%	01:30 h	2.5%	±00:00 h	±0.1%
	0002	02:00 h	3.2%	02:00 h	3.1%	02:00 h	3.2%	02:00 h	3.3%	02:00 h	3.3%	±00:00 h	±0.1%
	0003	02:30 h	4.0%	02:30 h	3.8%	02:30 h	4.0%	02:30 h	4.2%	02:30 h	4.1%	±00:00 h	±0.1%
I - 3	0004	03:00 h	4.8%	03:00 h	4.6%	03:00 h	4.8%	03:00 h	5.0%	03:00 h	4.9%	±00:00 h	±0.1%
	0005	03:30 h	5.6%	03:30 h	5.4%	03:30 h	5.6%	03:30 h	5.8%	03:30 h	5.7%	±00:00 h	±0.2%
I - 4	0006	04:00 h	6.4%	04:30 h	6.9%	04:00 h	6.3%	04:00 h	6.7%	04:00 h	6.6%	±00:13 h	±0.2%
	0007	04:30 h	7.2%	05:00 h	7.7%	04:30 h	7.1%	04:30 h	7.5%	04:30 h	7.4%	±00:13 h	±0.2%
	0008	05:00 h	8.0%	05:30 h	8.5%	05:00 h	7.9%	05:00 h	8.3%	05:00 h	8.2%	±00:13 h	±0.2%
I - 5	0009	05:30 h	8.8%	06:00 h	9.2%	05:30 h	8.7%	05:30 h	9.2%	05:30 h	9.0%	±00:13 h	±0.2%
	0010	06:00 h	9.6%	06:30 h	10.0%	06:00 h	9.5%	06:00 h	10.0%	06:00 h	9.8%	±00:13 h	±0.2%
	0011	06:30 h	10.4%	07:00 h	10.8%	06:30 h	10.3%	06:30 h	10.8%	06:30 h	10.7%	±00:13 h	±0.2%
	0012	07:00 h	11.2%	07:33 h	11.6%	07:03 h	11.2%	06:56 h	11.6%	06:56 h	11.4%	±00:15 h	±0.2%
	0013	07:30 h	12.0%	08:06 h	12.5%	07:36 h	12.1%	07:23 h	12.3%	07:23 h	12.1%	±00:18 h	±0.2%
	0014	08:00 h	12.8%	08:40 h	13.3%	08:10 h	13.0%	07:50 h	13.1%	07:50 h	12.8%	±00:20 h	±0.2%
	0015	08:30 h	13.6%	09:13 h	14.2%	08:43 h	13.8%	08:16 h	13.8%	08:16 h	13.6%	±00:23 h	±0.2%
	0016	09:00 h	14.4%	09:46 h	15.0%	09:16 h	14.7%	08:43 h	14.5%	08:43 h	14.3%	±00:26 h	±0.3%
	0017	09:30 h	15.2%	10:20 h	15.9%	09:50 h	15.6%	09:10 h	15.3%	09:10 h	15.0%	±00:29 h	±0.3%
	0018	10:00 h	16.0%	10:53 h	16.8%	10:23 h	16.5%	09:36 h	16.0%	09:36 h	15.8%	±00:32 h	±0.4%
II - 6	0019	10:30 h	16.8%	11:26 h	17.6%	10:56 h	17.4%	10:03 h	16.8%	10:03 h	16.5%	±00:35 h	±0.5%
	0020	11:00 h	17.6%	12:00 h	18.5%	11:30 h	18.3%	10:30 h	17.5%	10:30 h	17.2%	±00:39 h	±0.5%
	0021	11:30 h	18.4%	12:30 h	19.2%	12:00 h	19.0%	11:00 h	18.3%	11:00 h	18.0%	±00:39 h	±0.5%
	0022	12:00 h	19.2%	13:00 h	20.0%	12:30 h	19.8%	11:30 h	19.2%	11:30 h	18.9%	±00:39 h	±0.5%
	0023	12:30 h	20.0%	13:30 h	20.8%	13:00 h	20.6%	12:00 h	20.0%	12:00 h	19.7%	±00:39 h	±0.5%
	0024	13:00 h	20.8%	14:00 h	21.5%	13:30 h	21.4%	12:30 h	20.8%	12:30 h	20.5%	±00:39 h	±0.4%
	0025	13:30 h	21.6%	14:30 h	22.3%	14:00 h	22.2%	13:00 h	21.7%	13:00 h	21.3%	±00:39 h	±0.4%
	0026	14:00 h	22.4%	14:30 h	22.3%	14:00 h	22.2%	13:00 h	21.7%	13:00 h	21.3%	±00:40 h	±0.5%
	0027	14:30 h	23.2%	15:00 h	23.1%	14:30 h	23.0%	13:30 h	22.5%	13:30 h	22.1%	±00:40 h	±0.5%
	0028	15:00 h	24.0%	15:30 h	23.8%	15:00 h	23.8%	14:10 h	23.6%	14:10 h	23.2%	±00:35 h	±0.3%
III - 8	0029	15:30 h	24.8%	16:00 h	24.6%	15:30 h	24.6%	14:50 h	24.7%	14:50 h	24.3%	±00:30 h	±0.2%
	0030	16:00 h	25.6%	16:30 h	25.4%	16:00 h	25.4%	15:30 h	25.8%	15:30 h	25.4%	±00:25 h	±0.2%
	0031	16:30 h	26.4%	17:00 h	26.2%	16:30 h	26.2%	16:00 h	26.7%	16:00 h	26.2%	±00:25 h	±0.2%
	0032	17:00 h	27.2%	17:00 h	26.2%	16:45 h	26.6%	16:15 h	27.1%	16:15 h	26.6%	±00:22 h	±0.4%
	0033	17:30 h	28.0%	17:00 h	26.2%	17:00 h	27.0%	16:30 h	27.5%	16:30 h	27.0%	±00:25 h	±0.7%
	0034	18:00 h	28.8%	17:30 h	26.9%	17:30 h	27.8%	17:00 h	28.3%	17:00 h	27.9%	±00:25 h	±0.7%
	0035	18:30 h	29.6%	18:12 h	28.0%	17:51 h	28.3%	17:17 h	28.8%	17:25 h	28.6%	±00:30 h	±0.6%
	0036	19:00 h	30.4%	18:55 h	29.1%	18:12 h	28.9%	17:34 h	29.3%	17:51 h	29.3%	±00:38 h	±0.6%
	0037	19:30 h	31.2%	19:38 h	30.2%	18:34 h	29.5%	17:51 h	29.8%	18:17 h	30.0%	±00:46 h	±0.7%
	0038	20:00 h	32.0%	20:21 h	31.3%	18:55 h	30.0%	18:08 h	30.2%	18:42 h	30.7%	±00:55 h	±0.8%
III - 9	0039	20:30 h	32.8%	21:04 h	32.4%	19:17 h	30.6%	18:25 h	30.7%	19:08 h	31.4%	±01:04 h	±1.0%
	0040	21:00 h	33.6%	21:47 h	33.5%	19:38 h	31.2%	18:42 h	31.2%	19:34 h	32.1%	±01:13 h	±1.2%
	0041	21:30 h	34.4%	22:30 h	34.6%	20:00 h	31.7%	19:00 h	31.7%	20:00 h	32.8%	±01:23 h	±1.4%
	0042	22:00 h	35.2%	23:00 h	35.4%	20:30 h	32.5%	19:30 h	32.5%	20:30 h	33.6%	±01:23 h	±1.4%
	0043	22:30 h	36.0%	23:30 h	36.2%	21:22 h	33.9%	20:22 h	34.0%	21:07 h	34.6%	±01:13 h	±1.1%
	0044	23:00 h	36.8%	24:00 h	36.9%	22:15 h	35.3%	21:15 h	35.4%	21:45 h	35.7%	±01:04 h	±0.8%
	0045	23:30 h	37.6%	24:30 h	37.7%	23:07 h	36.7%	22:07 h	36.9%	22:22 h	36.7%	±00:56 h	±0.5%
	0046	24:00 h	38.4%	25:00 h	38.5%	24:00 h	38.1%	23:00 h	38.3%	23:00 h	37.7%	±00:50 h	±0.3%
	0047	24:30 h	39.2%	25:30 h	39.2%	24:30 h	38.9%	23:30 h	39.2%	23:30 h	38.5%	±00:50 h	±0.3%
	0048	25:00 h	40.0%	25:57 h	39.9%	24:55 h	39.6%	23:47 h	39.6%	23:51 h	39.1%	±00:54 h	±0.4%
IV - 12	0049	25:30 h	40.8%	26:25 h	40.7%	25:21 h	40.2%	24:04 h	40.1%	24:12 h	39.7%	±00:58 h	±0.4%
	0050	26:00 h	41.6%	26:53 h	41.4%	25:47 h	40.9%	24:21 h	40.6%	24:34 h	40.3%	±01:03 h	±0.5%
	0051	26:30 h	42.4%	27:21 h	42.1%	26:12 h	41.6%	24:38 h	41.1%	24:55 h	40.9%	±01:07 h	±0.7%
	0052	27:00 h	43.2%	27:49 h	42.8%	26:38 h	42.3%	24:55 h	41.5%	25:17 h	41.5%	±01:12 h	±0.8%
	0053	27:30 h	44.0%	28:17 h	43.5%	27:04 h	43.0%	25:12 h	42.0%	25:38 h	42.0%	±01:17 h	±0.9%
	0054	28:00 h	44.8%	28:45 h	44.2%	27:30 h	43.7%	25:30 h	42.5%	26:00 h	42.6%	±01:21 h	±1.0%
	0055	28:30 h	45.6%	29:12 h	44.9%	27:55 h	44.3%	25:47 h	43.0%	26:21 h	43.2%	±01:26 h	±1.1%
	0056	29:00 h	46.4%	29:40 h	45.7%	28:21 h	45.0%	26:04 h	43.5%	26:42 h	43.8%	±01:31 h	±1.2%
	0057	29:30 h	47.2%	30:08 h	46.4%	28:47 h	45.7%	26:21 h	43.9%	27:04 h	44.4%	±01:36 h	±1.4%
	0058	30:00 h	48.0%	30:36 h	47.1%	29:12 h	46.4%	26:38 h	44.4%	27:25 h	45.0%	±01:41 h	±1.5%
V - 13	0059	30:30 h	48.8%	31:04 h	47.8%	29:38 h	47.1%	26:55 h	44.9%	27:47 h	45.6%	±01:46 h	±1.6%
	0060	31:00 h	49.6%	31:32 h	48.5%	30:04 h	47.7%	27:12 h	45.4%	28:08 h	46.1%	±01:51 h	±1.7%
	0061	31:30 h	50.4%	32:00 h	49.2%	30:30 h	48.4%	27:30 h	45.8%	28:30 h	46.7%	±01:56 h	±1.9%
	0062	32:00 h	51.2%	32:30 h	50.0%	31:00 h	49.2%	28:00 h	46.7%	29:00 h	47.5%	±01:56 h	±1.8%
	0063	32:30 h	52.0%	33:07 h	51.0%	31:45 h	50.4%	29:00 h	48.3%	29:45 h	48.8%	±01:46 h	±1.5%
	0064	33:00 h	52.8%	33:45 h	51.9%	32:30 h	51.6%	30:00 h	50.0%	30:30 h	50.0%	±01:37 h	±1.2%
	0065	33:30 h	53.6%	34:22 h	52.9%	33:15 h	52.8%	31:00 h	51.7%	31:15 h	51.2%	±01:28 h	±1.0%
	0066	34:00 h	54.4%	35:00 h	53.8%	34:00 h	54.0%	32:00 h	53.3%	32:00 h	52.5%	±01:20 h	±0.7%
	0067	34:30 h	55.2%	35:30 h	54.6%	34:30 h	54.8%	32:30 h	54.2%	32:30 h	53.3%	±01:20 h	±0.7%
	0068	35:00 h	56.0%	35:55 h	55.3%	34:50 h	55.3%	33:00 h	55.0%	33:10 h	54.4%	±01:15 h	±0.6%
V - 14	0069	35:30 h	56.8%	36:20 h	55.9%	35:10 h	55.8%	33:30 h	55.8%	33:50 h	55.5%	±01:10 h	±0.5%
	0070	36:00 h	57.6%	36:45 h	56.5%	35:30 h	56.3%	34:00 h	56.7%	34:30 h	56.6%	±01:06 h	±0.5%
	0071	36:30 h	58.4%	37:10 h	57.2%	35:50 h	56.9%	34:30 h	57.5%	35:10 h	57.7%	±01:03 h	±0.6%
	0072	37:00 h	59.2%	37:35 h	57.8%	36:10 h	57.4%	35:00 h	58.3%	35:50 h	58.7%	±01:00 h	±0.7%
	0073	37:30 h	60.0%	38:00 h	58.5%	36:30 h	57.9%	35:30 h	59.2%	36:30 h	59.8%	±00:58 h	±0.9%
	0074	38:00 h	60.8%	38:30 h	59.2%	37:00 h	58.7%	36:00 h	60.0%	37:00 h	60.7%	±00:58 h	±0.9%
	0075	38:30 h	61.6%	38:50 h	59.8%	37:32 h	59.6%	36:20 h	60.6%	37:23 h	61.3%	±00:59 h	±0.9%
	0076	39:00 h	62.4%	39:11 h	60.3%	38:04 h	60.4%	36:41 h	61.2%	37:46 h	61.9%	±01:00 h	±0.9%
	0077	39:30 h	63.2%	39:32 h	60.8%	38:36 h							

	0077	40:00 h	64.0%	39:53 h	61.4%	39:09 h	62.1%	37:23 h	62.3%	38:32 h	63.2%	±01:04 h	±1.0%
	0078	40:30 h	64.8%	40:13 h	61.9%	39:41 h	63.0%	37:43 h	62.9%	38:55 h	63.8%	±01:07 h	±1.1%
	0079	41:00 h	65.6%	40:34 h	62.4%	40:13 h	63.9%	38:04 h	63.5%	39:18 h	64.4%	±01:09 h	±1.2%
	0080	41:30 h	66.4%	40:55 h	63.0%	40:46 h	64.7%	38:25 h	64.0%	39:41 h	65.1%	±01:13 h	±1.3%
	0081	42:00 h	67.2%	41:16 h	63.5%	41:18 h	65.6%	38:46 h	64.6%	40:04 h	65.7%	±01:16 h	±1.4%
	0082	42:30 h	68.0%	41:36 h	64.0%	41:50 h	66.4%	39:06 h	65.2%	40:27 h	66.3%	±01:20 h	±1.5%
	0083	43:00 h	68.8%	41:57 h	64.6%	42:23 h	67.3%	39:27 h	65.8%	40:50 h	67.0%	±01:23 h	±1.6%
	0084	43:30 h	69.6%	42:18 h	65.1%	42:55 h	68.1%	39:48 h	66.3%	41:13 h	67.6%	±01:27 h	±1.7%
	0085	44:00 h	70.4%	42:39 h	65.6%	43:27 h	69.0%	40:09 h	66.9%	41:36 h	68.2%	±01:32 h	±1.8%
	0086	44:30 h	71.2%	43:00 h	66.2%	44:00 h	69.8%	40:30 h	67.5%	42:00 h	69.7%	±01:36 h	±2.0%
VI - 16	0087	45:00 h	72.0%	43:30 h	66.9%	44:30 h	70.6%	41:00 h	68.3%	42:30 h	69.7%	±01:36 h	±2.0%
	0088	45:30 h	72.8%	44:11 h	68.0%	44:58 h	71.4%	41:28 h	69.1%	43:00 h	70.5%	±01:37 h	±1.9%
	0089	46:00 h	73.6%	44:53 h	69.1%	45:26 h	72.1%	41:56 h	69.9%	43:30 h	71.3%	±01:38 h	±1.8%
	0090	46:30 h	74.4%	45:35 h	70.1%	45:55 h	72.9%	42:25 h	70.7%	44:00 h	72.1%	±01:39 h	±1.7%
	0091	47:00 h	75.2%	46:16 h	71.2%	46:23 h	73.6%	42:53 h	71.5%	44:30 h	73.0%	±01:41 h	±1.6%
	0092	47:30 h	76.0%	46:58 h	72.3%	46:51 h	74.4%	43:21 h	72.3%	45:00 h	73.8%	±01:43 h	±1.6%
	0093	48:00 h	76.8%	47:40 h	73.3%	47:20 h	75.1%	43:50 h	73.1%	45:30 h	74.6%	±01:45 h	±1.5%
	0094	48:30 h	77.6%	48:21 h	74.4%	47:48 h	75.9%	44:18 h	73.8%	46:00 h	75.4%	±01:48 h	±1.5%
	0095	49:00 h	78.4%	49:03 h	75.5%	48:16 h	76.6%	44:46 h	74.6%	46:30 h	76.2%	±01:50 h	±1.4%
	0096	49:30 h	79.2%	49:45 h	76.5%	48:45 h	77.4%	45:15 h	75.4%	47:00 h	77.0%	±01:53 h	±1.4%
	0097	50:00 h	80.0%	50:26 h	77.6%	49:13 h	78.1%	45:43 h	76.2%	47:30 h	77.9%	±01:57 h	±1.4%
	0098	50:30 h	80.8%	51:08 h	78.7%	49:41 h	78.9%	46:11 h	77.0%	48:00 h	78.7%	±02:00 h	±1.4%
	0099	51:00 h	81.6%	51:50 h	79.7%	50:10 h	79.6%	46:40 h	77.8%	48:30 h	79.5%	±02:03 h	±1.4%
	0100	51:30 h	82.4%	52:31 h	80.8%	50:38 h	80.4%	47:08 h	78.6%	49:00 h	80.3%	±02:07 h	±1.4%
	0101	52:00 h	83.2%	53:13 h	81.9%	51:06 h	81.1%	47:36 h	79.4%	49:30 h	81.1%	±02:11 h	±1.4%
	0102	52:30 h	84.0%	53:55 h	82.9%	51:35 h	81.9%	48:05 h	80.1%	50:00 h	82.0%	±02:15 h	±1.4%
	0103	53:00 h	84.8%	54:36 h	84.0%	52:03 h	82.6%	48:33 h	80.9%	50:30 h	82.8%	±02:19 h	±1.5%
	0104	53:30 h	85.6%	55:18 h	85.1%	52:31 h	83.4%	49:01 h	81.7%	51:00 h	83.6%	±02:23 h	±1.5%
	0105	54:00 h	86.4%	56:00 h	86.2%	53:00 h	84.1%	49:30 h	82.5%	51:30 h	84.4%	±02:27 h	±1.6%
VI - 17	0106	54:30 h	87.2%	56:30 h	86.9%	53:30 h	84.9%	50:00 h	83.3%	52:00 h	85.2%	±02:27 h	±1.6%
	0107	55:00 h	88.0%	57:02 h	87.7%	54:06 h	85.9%	50:38 h	84.4%	52:34 h	86.2%	±02:25 h	±1.5%
	0108	55:30 h	88.8%	57:34 h	88.6%	54:42 h	86.8%	51:16 h	85.4%	53:08 h	87.1%	±02:23 h	±1.4%
	0109	56:00 h	89.6%	58:06 h	89.4%	55:18 h	87.8%	51:54 h	86.5%	53:42 h	88.0%	±02:20 h	±1.3%
	0110	56:30 h	90.4%	58:38 h	90.2%	55:54 h	88.7%	52:32 h	87.6%	54:16 h	89.0%	±02:18 h	±1.2%
	0111	57:00 h	91.2%	59:10 h	91.0%	56:30 h	89.7%	53:10 h	88.6%	54:50 h	89.9%	±02:16 h	±1.1%
	0112	57:30 h	92.0%	59:42 h	91.8%	57:06 h	90.6%	53:48 h	89.7%	55:24 h	90.8%	±02:13 h	±1.0%
	0113	58:00 h	92.8%	60:14 h	92.7%	57:42 h	91.6%	54:26 h	90.7%	55:58 h	91.7%	±02:11 h	±0.9%
	0114	58:30 h	93.6%	60:46 h	93.5%	58:18 h	92.5%	55:04 h	91.8%	56:32 h	92.7%	±02:09 h	±0.7%
	0115	59:00 h	94.4%	61:18 h	94.3%	58:54 h	93.5%	55:42 h	92.8%	57:06 h	93.6%	±02:07 h	±0.6%
	0116	59:30 h	95.2%	61:50 h	95.1%	59:30 h	94.4%	56:20 h	93.9%	57:40 h	94.5%	±02:05 h	±0.5%
	0117	60:00 h	96.0%	62:22 h	95.9%	60:06 h	95.4%	56:58 h	94.9%	58:14 h	95.5%	±02:03 h	±0.4%
	0118	60:30 h	96.8%	62:54 h	96.8%	60:42 h	96.3%	57:36 h	96.0%	58:48 h	96.4%	±02:01 h	±0.3%
	0119	61:00 h	97.6%	63:26 h	97.6%	61:18 h	97.3%	58:14 h	97.1%	59:22 h	97.3%	±01:59 h	±0.2%
	0120	61:30 h	98.4%	63:58 h	98.4%	61:54 h	98.3%	58:52 h	98.1%	59:56 h	98.3%	±01:57 h	±0.1%
	0121	62:00 h	99.2%	64:30 h	99.2%	62:30 h	99.2%	59:30 h	99.2%	60:30 h	99.2%	±01:55 h	±0.0%
Hatch	0122	62:30 h	100.0%	65:00 h	100.0%	63:00 h	100.0%	60:00 h	100.0%	61:00 h	100.0%	±01:55 h	±0.0%

References

1. Heffer, A. & Pick, L. Conservation and variation in Hox genes: how insect models pioneered the evo-devo field. *Annu. Rev. Entomol.* **58**, 161–79 (2013).
2. Huisken, J., Swoger, J., Del Bene, F., Wittbrodt, J. & Stelzer, E. H. K. Optical sectioning deep inside live embryos by selective plane illumination microscopy. *Science* **305**, 1007–9 (2004).
3. Keller, P. J., Schmidt, A. D., Wittbrodt, J. & Stelzer, E. H. K. Reconstruction of zebrafish early embryonic development by scanned light sheet microscopy. *Science* **322**, 1065–9 (2008).
4. Keller, P. J. & Stelzer, E. H. K. Digital scanned laser light sheet fluorescence microscopy. *Cold Spring Harb. Protoc.* **2010**, pdb.top78 (2010).
5. Weber, M. & Huisken, J. Light sheet microscopy for real-time developmental biology. *Curr. Opin. Genet. Dev.* **21**, 566–72 (2011).
6. Stelzer, E. H. K. Light-sheet fluorescence microscopy for quantitative biology. *Nat. Methods* **12**, 23–6 (2015).
7. Reynaud, E. G., Peychl, J., Huisken, J. & Tomancak, P. Guide to light-sheet microscopy for adventurous biologists. *Nat. Methods* **12**, 30–4 (2015).
8. Daetwyler, S. & Huisken, J. Fast Fluorescence Microscopy with Light Sheets. *Biol. Bull.* **231**, 14–25 (2016).
9. Keller, P. J. *et al.* Fast, high-contrast imaging of animal development with scanned light sheet-based structured-illumination microscopy. *Nat. Methods* **7**, 637–42 (2010).
10. Tomer, R., Khairy, K., Amat, F. & Keller, P. J. Quantitative high-speed imaging of entire developing embryos with simultaneous multiview light-sheet microscopy. *Nat. Methods* **9**, 755–63 (2012).
11. Krzic, U., Gunther, S., Saunders, T. E., Streichan, S. J. & Hufnagel, L. Multiview light-sheet microscope for rapid in toto imaging. *Nat. Methods* **9**, 730–3 (2012).
12. Rebollo, E., Karkali, K., Mangione, F. & Martín-Blanco, E. Live imaging in *Drosophila*: The optical and genetic toolkits. *Methods* **68**, 48–59 (2014).
13. Beira, J. V *et al.* The Dpp/TGF β -Dependent Corepressor Schnurri Protects Epithelial Cells from JNK-Induced Apoptosis in *Drosophila* Embryos. *Dev. Cell* **31**, 240–7 (2014).
14. Lye, C. M. *et al.* Mechanical Coupling between Endoderm Invagination and Axis Extension in *Drosophila*. *PLoS Biol.* **13**, e1002292 (2015).
15. Chhetri, R. K. *et al.* Whole-animal functional and developmental imaging with isotropic spatial resolution. *Nat. Methods* **12**, 1171–8 (2015).
16. Caroti, F., Urbansky, S., Wosch, M. & Lemke, S. Germ line transformation and in vivo labeling of nuclei in Diptera: report on *Megaselia abdita* (Phoridae) and *Chironomus riparius* (Chironomidae). *Dev. Genes Evol.* **225**, 179–186 (2015).
17. Strobl, F. & Stelzer, E. H. K. Non-invasive long-term fluorescence live imaging of *Tribolium castaneum* embryos. *Development* **141**, 2331–2338 (2014).
18. Strobl, F., Schmitz, A. & Stelzer, E. H. K. Live imaging of *Tribolium castaneum* embryonic development using light-sheet-based fluorescence microscopy. *Nat. Protoc.* **10**, 1486–1507 (2015).
19. Hilbrant, M., Horn, T., Koelzer, S. & Panfilio, K. A. The beetle amnion and serosa functionally interact as apposed epithelia. *Elife* **5**, (2016).
20. Strobl, F. & Stelzer, E. H. Long-term fluorescence live imaging of *Tribolium castaneum* embryos: principles, resources, scientific challenges and the comparative approach. *Curr. Opin. Insect Sci.* **18**, 17–

26 (2016).

21. Scolari, F. *et al.* How functional genomics will impact fruit fly pest control: the example of the Mediterranean fruit fly, *Ceratitis capitata*. *BMC Genet.* **15 Suppl 2**, S11 (2014).
22. Loukeris, T. G., Livadaras, I., Arcà, B., Zabalou, S. & Savakis, C. Gene transfer into the medfly, *Ceratitis capitata*, with a *Drosophila hydei* transposable element. *Science* **270**, 2002–5 (1995).
23. Handler, A. M., McCombs, S. D., Fraser, M. J. & Saul, S. H. The lepidopteran transposon vector, piggyBac, mediates germ-line transformation in the Mediterranean fruit fly. *Proc. Natl. Acad. Sci. U. S. A.* **95**, 7520–5 (1998).
24. Rajamohan, A. *et al.* Cryopreservation of Mediterranean fruit fly embryos. *Cryo Letters* **24**, 125–32
25. Papanicolaou, A. *et al.* The whole genome sequence of the Mediterranean fruit fly, *Ceratitis capitata* (Wiedemann), reveals insights into the biology and adaptive evolution of a highly invasive pest species. *Genome Biol.* **17**, 192 (2016).
26. Pane, A., De Simone, A., Saccone, G. & Polito, C. Evolutionary conservation of *Ceratitis capitata* transformer gene function. *Genetics* **171**, 615–624 (2005).
27. Gabrieli, P. *et al.* Sex and the single embryo: early development in the Mediterranean fruit fly, *Ceratitis capitata*. *BMC Dev. Biol.* **10**, 12 (2010).
28. Misof, B. *et al.* Phylogenomics resolves the timing and pattern of insect evolution. *Science* **346**, 763–7 (2014).
29. Lacy, M. E. & Hutson, M. S. Amnioserosa development and function in *Drosophila* embryogenesis: Critical mechanical roles for an extraembryonic tissue. *Dev. Dyn.* **245**, 558–568 (2016).
30. Rafiqi, A. M., Lemke, S. & Schmidt-Ott, U. The scuttle fly *Megaselia abdita* (Phoridae): A link between *Drosophila* and mosquito development. *Cold Spring Harb. Protoc.* **6**, (2011).
31. Wotton, K. R., Jiménez-Guri, E., García Matheu, B. & Jaeger, J. A staging scheme for the development of the scuttle fly *Megaselia abdita*. *PLoS One* **9**, e84421 (2014).
32. Rafiqi, A. M., Lemke, S., Ferguson, S., Stauber, M. & Schmidt-Ott, U. Evolutionary origin of the amnioserosa in cyclorrhaphan flies correlates with spatial and temporal expression changes of zen. *Proc. Natl. Acad. Sci.* **105**, 234–239 (2008).
33. Rafiqi, A. M., Lemke, S. & Schmidt-Ott, U. Postgastrular zen expression is required to develop distinct amniotic and serosal epithelia in the scuttle fly *Megaselia*. *Dev. Biol.* **341**, 282–90 (2010).
34. Rafiqi, A. M., Park, C.-H., Kwan, C. W., Lemke, S. & Schmidt-Ott, U. BMP-dependent serosa and amnion specification in the scuttle fly *Megaselia abdita*. *Development* **139**, 3373–82 (2012).
35. Ogaugwu, C. E. & Wimmer, E. A. Molecular cloning and expression of nanos in the Mediterranean fruit fly, *Ceratitis capitata* (Diptera: Tephritidae). *Gene Expr. Patterns* **13**, 183–188 (2013).
36. Schetelig, M. F., Schmid, B. G. M., Zimowska, G. & Wimmer, E. A. Plasticity in mRNA expression and localization of orthodenticle within higher Diptera. *Evol. Dev.* **10**, 700–704 (2008).
37. Gomulski, L. M. *et al.* Gene discovery in an invasive tephritid model pest species, the Mediterranean fruit fly, *Ceratitis capitata*. *BMC Genomics* **9**, 243 (2008).
38. Gomulski, L. M. *et al.* Transcriptome profiling of sexual maturation and mating in the Mediterranean fruit fly, *Ceratitis capitata*. *PLoS One* **7**, e30857 (2012).
39. Salvemini, M. *et al.* De novo assembly and transcriptome analysis of the Mediterranean fruit fly *Ceratitis capitata* early embryos. *PLoS One* **9**, e114191 (2014).
40. Vreede, B. M., Lynch, J. A., Roth, S. & Sucena, E. Co-option of a coordinate system defined by the EGFr

and Dpp pathways in the evolution of a morphological novelty. *Evodevo* **4**, 7 (2013).

41. Steck, G. J. & Ekesi, S. Description of third instar larvae of *Ceratitis fasciventris*, *C. anonae*, *C. rosa* (FAR complex) and *C. capitata* (Diptera, Tephritidae). *Zookeys* **540**, 443–466 (2015).
42. Solari, P. *et al.* Morphological characterization of the antennal lobes in the Mediterranean fruit fly *Ceratitis capitata*. *J. Comp. Physiol. A* **202**, 131–146 (2016).
43. Schetelig, M. F., Caceres, C., Zacharopoulou, A., Franz, G. & Wimmer, E. A. Conditional embryonic lethality to improve the sterile insect technique in *Ceratitis capitata* (Diptera: Tephritidae). *BMC Biol.* **7**, 4 (2009).
44. Engelbrecht, C. J. & Stelzer, E. H. Resolution enhancement in a light-sheet-based microscope (SPIM). *Opt. Lett.* **31**, 1477–9 (2006).
45. Campos-Ortega, J. A. & Hartenstein, V. *The Embryonic Development of Drosophila melanogaster*. Springer-Verlag Berlin (1997). doi:10.1007/978-3-662-22489-2
46. Tanaka, N., Steiner, L. F., Ohinata, K. & Okamoto, R. Low-Cost Larval Rearing Medium for Mass Production of Oriental and Mediterranean Fruit Flies. *J. Econ. Entomol.* **62**, (1969).
47. Abramoff, M. D., Magelhaes, P. J. & Ram, S. J. Image processing with Imaje J. *Biophotonics Int.* **11**, 36–42 (2004).
48. Schneider, C. a, Rasband, W. S. & Eliceiri, K. W. NIH Image to ImageJ: 25 years of image analysis. *Nat. Methods* **9**, 671–675 (2012).
49. Schindelin, J. *et al.* Fiji: an open-source platform for biological-image analysis. *Nat. Methods* **9**, 676–82 (2012).

Data Citations

Strobl, F. Dryad DOI.

The embryonic development of the Mediterranean fruit fly

Ceratitis capitata (Diptera: Tephritidae)

Frederic Strobl, Alexander Schmitz, Marc F. Schetelig & Ernst H.K. Stelzer

The fruit fly *Drosophila melanogaster* is a versatile insect model organism and has contributed significantly to our understanding of molecular genetics and embryonic development. However, insights into the evolutionary diversification of developmental strategies can only be obtained with the comparative approach. Thus, more species are necessary to allow the interpretation of similarities and differences in their phylogenetic context. The Mediterranean fruit fly *Ceratitis capitata*, a dipteran that separated from *Drosophila* approximately 80 million years ago, is an established insect model in agricultural- and pest-associated research and also became an emerging model organism for developmental biology. Albeit the genome is sequenced and a broad arsenal of molecular techniques is established, an integrative morphogenetic framework is not yet available. In this study, we present a comprehensive two-level staging system based on nine light sheet-based fluorescence microscopy datasets. The upper level consists of six consecutive embryogenetic events that allow comparison between insect orders, while the lower level consists of seventeen stages that allow comparison within the Diptera. We describe all reasonably identifiable characteristics comprehensively in multiple formats: generally throughout the running text, in a compact stage-based supplementary figure, within a detailed chronologic time table and within two glossary-like tables for structures and most important processes. As one of the most remarkable differences to *Drosophila*, we find that the amnioserosa differentiates and unfolds for the first time already during early gastrulation. This is the first time that a staging system is established on fluorescence live imaging data, which has several advantages compared to traditional approaches – for example, we are able to provide standard deviations for each single developmental time point. Our approach, establishing a two-level staging system on the basis of comprehensive fluorescence live imaging data, serves as a template for futures studies that aim to an integrative morphogenetic framework for other emerging model insect species.

Submission-ready

Research Article

Title

The embryonic development of the Mediterranean fruit fly *Ceratitis capitata* (Diptera: Tephritidae)

Authors

Frederic Strobl¹, Alexander Schmitz¹, Marc F. Schetelig² and Ernst H.K. Stelzer¹

Affiliations

¹Physical Biology / Physikalische Biologie (IZN, FB 15)

Buchmann Institute for Molecular Life Sciences (BMLS)

Cluster of Excellence Frankfurt – Macromolecular Complexes (CEF – MC)

Goethe University – Frankfurt am Main (Campus Riedberg)

Max-von-Laue-Straße 15 – D-60348 Frankfurt am Main – Germany

²Justus-Liebig-Universität Gießen

Department of Insect Biotechnology in Plant Protection

Winchesterstraße 2 – D-35394 Gießen – Germany

Corresponding authors

Frederic Strobl (frederic.strobl@physikalischebiologie.de)

Ernst H.K. Stelzer (ernst.stelzer@physikalischebiologie.de)

Abstract

The fruit fly *Drosophila melanogaster* is a versatile insect model organism and has contributed significantly to our understanding of molecular genetics and embryonic development. However, insights into the evolutionary diversification of developmental strategies can only be obtained with the comparative approach. Thus, more species are necessary to allow the interpretation of similarities and differences in their phylogenetic context. The Mediterranean fruit fly *Ceratitis capitata*, a dipteran that separated from *Drosophila* approximately 80 million years ago, is an established insect model in agricultural- and pest-associated research and also became an emerging model organism for developmental biology. Albeit the genome is sequenced and a broad arsenal of molecular techniques is established, an integrative morphogenetic framework is not yet available. In this study, we present a comprehensive two-level staging system based on nine light sheet-based fluorescence microscopy datasets. The upper level consists of six consecutive embryogenetic events that allow comparison between insect orders, while the lower level consists of seventeen stages that allow comparison within the Diptera. We describe all reasonably identifiable characteristics comprehensively in multiple formats: generally throughout the running text, in a compact stage-based supplementary figure, within a detailed chronologic time table and within two glossary-like tables for structures and most important processes. As one of the most remarkable differences to *Drosophila*, we find that the amnioserosa differentiates and unfolds for the first time already during early gastrulation. This is the first time that a staging system is established on fluorescence live imaging data, which has several advantages compared to traditional approaches – for example, we are able to provide standard deviations for each single developmental time point. Our approach, establishing a two-level staging system on the basis of comprehensive fluorescence live imaging data, serves as a template for futures studies that aim to an integrative morphogenetic framework for other emerging model insect species.

Keywords (6 max)

Insect, Diptera, *Ceratitis capitata*, embryonic development, light sheet-based fluorescence microscopy, LSFM

Introduction

For more than one century, the fruit fly *Drosophila melanogaster* has been the preeminent insect model organism for developmental biology and genetic studies [1–3]. However, only the comparative approach, *i.e.* the identification and classification of similarities and differences between related species [4], provides insights that exceed the limitations of investigating only a single model organism: Firstly, data interpretation with consideration of the phylogenetic lineage allows us to understand the origin and evolutionary diversification of biological structures and processes [5–7]. Secondly, only the comparison of morphological states in conjunction with the respective underlying genetic mechanisms will explain how different outcomes may result from the same ancestral genetic toolkits but also how the a similar outcome is achieved through different strategies on the molecular level [8]. Thirdly, by considering the respective ecological niches, rationales can be found how constant selective pressure led to today's highly diverse pool of species [9].

Throughout the last decades, the number of emerging insect model organisms for evolutionary developmental biology and its associated disciplines has increased steadily, especially for the monophyletic Holometabola: for the basally located Hymenoptera, the honeybee *Apis mellifera* [10] and the jewel wasp *Nasonia vitripennis* [11] are used, for the Coleoptera, the red flour beetle *Tribolium castaneum* [12,13] became popular, and for the Lepidoptera, the squinting bush brown *Bicyclus anynana* [14] is one of the favored organisms. For the Diptera, *Drosophila* remains as the almost unrivaled 'gold standard', but several species such as the scuttle fly *Megaselia abdita* [15] and the moth midge *Clogmia albipunctata* [16] are used as 'phylogenetic links' between *Drosophila* and the mosquitos. However, *Drosophila* diverged from *Megaselia* about 150 and from *Clogmia* about 250 million years ago [17] and thus differs considerably in certain developmental features. One of the most striking examples is the formation and degradation of extra-embryonic membranes – whereas *Drosophila* embryos develop only the dorsally located amnioserosa, *Megaselia* and *Clogmia* embryos are covered ventrally by the amnion and completely engulfed by the serosa [18–22].

Except for several other members of the Drosophilidae family, not many close relatives of *Drosophila* have been investigated in an evolutionary context. The Mediterranean fruit fly *Ceratitis capitata* has been established as a model organism for pest- and agricultural-related research, but is also becoming a promising model organism for developmental biology. *Drosophila* and *Ceratitis* diverged approximately 80-100 million years ago [17,23,24], thus *Ceratitis* shortens the phylogenetic gap between *Drosophila* and *Megaselia*. The spatial or spatiotemporal expression patterns of genes such as *otd* [25], *nos* [26], *slbo*, *grk*, *dpp*, *tkv*, *mirr*, *pip*, *br* [27] or *twit* and other factors of the Ly6 gene family [28] have been documented, multiple transcriptome profiles and analyses with diverse scientific rationales are available [29–32], certain morphological structures of the adult such as the head and abdomen [33] or the copulation site [34], reproductive accessory glands [35] and antennal lobes [36] have been characterized, and the genome has been sequenced recently [37]. The embryonic morphogenesis has been characterized only fragmentally, there is only some information available on the cellularization [38] and germ cell formation [39] processes.

However, especially the studies that work with the embryonic stadia of *Ceratitis* are missing a comprehensive and systematic staging standard to integrate the highly diverse data in a spatiotemporal well-structured context, which is available for some closely related Diptera such as *Drosophila* [40] and *Megaselia* [21], but also for several more distantly related species such as the moth midge *Clogmia albipunctata* [22], the predatory gall midge *Aphidoletes aphidimyza* [41] and the yellow fever mosquito *Aedes aegypti* [42,43]. The value of such a standard

is higher the earlier it becomes available, so that it serves as an integrative framework for as many more specific future studies as possible.

In this study, we rely on previously published fluorescence microscopy data acquired from transgenic *Ceratitis* embryos that express nuclear localized EGFP under control of the *Drosophila* polyubiquitin promoter [44]. The data has been acquired with light sheet-based fluorescence microscopy [45–47], comprises of nine datasets and covers approximately 97% of the whole embryonic development. We refurbish the previously introduced two-level staging system and provide a comprehensive, detailed and well-illustrated description of six general embryogenetic events and seventeen specific stages. We highlight certain developmental processes, such as germ cell formation, the differentiation of the amnioserosa and the morphogenetic movements during head involution. Whenever appropriate, we show quantitative data, for example about total length and volume over time. Due to the fact that the data derive from long-term live imaging assays with distinct temporal interval, we can also provide the spatial and temporal standard deviations throughout the whole embryonic development. Our work is a valuable resource for any further studies on *Ceratitis* embryogenesis and contributes significantly to the morphogenetic aspect of the comparative approach in insect developmental biology.

Materials and Methods

Light sheet-based fluorescence microscopy

All LSFM images shown in this study derive from the homozygous *Ceratitis capitata* (Wiedemann) *TREhs43-hid^{Ala5}_F1m2* transgenic line [44], which expresses nuclear localized EGFP under control of the *Drosophila* polyubiquitin promoter. Data acquisition and processing including the LSFM setup, embryo preparation, microscopy, larva retrieval, image processing and two-level staging system implementation is explained in the accompanying data publication (Ref). For ease of use, we define three microscopy axes as follows: the illumination axis as X, the rotation axis as Y, and the detection axis as Z.

Length and speed measurements

Embryo length as a function of time over the complete embryonic development period was calculated only from datasets DS0001, DS0002 and DS0003 since DS0004 and DS0005 protrude from the volume of view in Y. Z maximum projections for datasets DS0001, DS0002 and DS0003 were slightly rotated such that the embryo length axis is parallel to Y. At each time point the following algorithm is applied to compute the embryo length: Firstly, the image is cropped to the region of interest containing the embryo. Secondly, mean filtering of range 3×3 pixels is applied to smooth the image. Thirdly, a local thresholding algorithm is used to obtain a binary image. Pixel values above the mean intensity computed in a range 150×150 pixels are replaced by 1 and others with 0. Fourthly, the largest region in the obtained binary image is retrieved and the convex hull of this region is computed. Fifthly, the maximum extension of the convex hull along Y is computed as the length of the embryo. The distance and speed of the germband along the dorsal side towards the anterior pole move distance during stages 8, 9, 10 and 11 were determined by manually appointing the posterior tip of the germband in Z maximum projections along the dorsolateral or dorsal orientation in datasets DS0001, DS0002 and DS0003.

Nuclei area and density measurements

The average cell nuclei area and density for three time points during blastoderm formation are determined in the Z maximum projections: Firstly, the embryo is segmented with Otsu's algorithm [48] and the position of the posterior end of the embryo is determined. Secondly, at a distance of 150 pixels from the posterior end of the embryo, a region of 150×150 pixels is extracted from the image. Gaussian filtering with a 2×2 pixel range is applied followed by local thresholding to obtain a rough segmentation of cell nuclei. The local threshold range is set to 15 for the two former time points and to 10 for the latter time point. Thirdly, pixel values above the determined local mean intensity are replaced by 1 and others with 0. Holes in the obtained segmentation are removed using morphological filling. Fourthly, to separate clustered cell nuclei, a seeded immersion watershed algorithm [49,50] is applied to obtain individually labeled cell nuclei. Seed points are detected using a multi-scale Laplacian of Gaussian filtering. The minimum and maximum range of the Laplacian of Gaussian filter are set to 5, 15 for the former two time points and 1, 10 for the latter time point. Fifthly, the immersion watershed algorithm is initialized at the determined seed locations and applied to the inverted Gaussian filtered image. The final cell nuclei segmentation is obtained by multiplying the local thresholding result with the immersion watershed. Objects that are connected to the image border are removed. The number of cell nuclei and the area of each cell nucleus is computed.

Pole cell nuclei counting

The pole cells were counted in the three-dimensional Z stacks of TP0010 in DS0001 and DS0002, of TP0009 in DS0003 and DS0004 and of TP0007 and TP0009 in DS0007: Firstly, the Z stacks were cropped to the region of interest and rotated by -40° for DS0001, -7° for DS0002, $+41^\circ$ for DS0003 and $+13^\circ$ for DS0004 to align the embryonal axes. Secondly, Laplacian of Gaussian filtering with a with a 3×3 pixel range is applied followed by local thresholding to obtain a rough segmentation of cell nuclei. Thirdly, pixel values above the determined local mean intensity are replaced by 1 and others with 0. Holes in the obtained segmentation are removed using morphological filling. Fourthly, to separate clustered cell nuclei, a seeded immersion watershed algorithm [49,50] is applied to obtain individually labeled cell nuclei. Seed points are detected using a multi-scale Laplacian of Gaussian filtering. Fifthly, the immersion watershed algorithm is initialized at the determined seed locations and applied to the inverted Gaussian filtered image. The final cell nuclei segmentation is obtained by multiplying the local thresholding result with the immersion watershed.

Results

Datasets background

The following description and quantitative analyses of *Ceratitis* embryogenesis are based on nine long-term live imaging datasets that were acquired by using light sheet-based fluorescence microscopy [47]. The experimental background, the acquisition procedure, initial data processing and dataset alignment steps have been described previously in the accompanying data publication (Ref). In six out of nine datasets (DS0001-DS0006), the embryo was acquired *in toto* in the orientations 0°, 90°, 180° and 270° under similar conditions for up to 65 hours, covering approximately 97% of the whole embryogenesis period. The embryo from which dataset DS0006 derives did not develop into a functional adult and was excluded from further analysis. The embryos from which datasets DS0001 and DS0003 derive were imaged along the ventrolateral-dorsolateral axes, whereas the embryos, from which datasets DS0002, DS0004 and DS0005 derive were imaged along the ventral-dorsal and lateral axes. The datasets DS0007-DS0009 cover specific embryonic processes, *i.e.* pole cell formation (DS0007) and head involution (DS0008-0009).

A two-level staging system for the embryonic morphogenesis of *Ceratitis*

A reasonable staging system is fundamental for a comprehensive description of the embryonic morphogenesis. The nine datasets were already integrated into a two-level staging system in the accompanying data publication (Ref), this system is further expanded in this study. The rationale for a two-level staging is as follows: The comparative approach, *i.e.* the comparison of the embryonic morphogenesis of multiple species, embeds developmental biology into an evolutionary background and provides insights that are not obtainable when species are analyzed isolated from their phylogenetic lineage. The comparative approach is supported by an increasing number of insect model organisms that have emerged over the last decade. For the distantly species, only general equivalents can be identified, but more closely related species typically exhibit a high degree of similarity even in highly specific processes to the embryonic morphogenesis of *Drosophila*. Thus, a two-level staging system that incorporates general embryogenetic events on the upper level and species-specific stages on the lower level is proposed.

The upper level serves primarily for the morphogenetic comparison of *Ceratitis* with species that belong to different orders, whereas the lower level allows comparison within the Dipteran order. Extensive literature research on morphologic/morphogenetic insect embryogenesis studies published during the last 40 years revealed a set of six prominent consecutive embryogenetic events (Supplementary Table 1

Supplementary Table 1), which we define as the upper level and refer to with Roman numerals: (I) blastoderm formation, (II) gastrulation, (III) germband elongation, (IV) germband retraction, (V) dorsal closure and (VI) muscular movement. The last embryogenetic event, muscular movement, was defined as the period spanning from the end of dorsal closure to the time point when the embryo hatches. These events are not evident in all listed species, but reoccur at high frequency.

The lower level is defined by highly specific morphological states or processes. During the evaluation of the microscopy data, we found many similarities to *Drosophila* (*e.g.* cephalic furrow formation during gastrulation or head involution during dorsal closure) and therefore decided to adopt the 17 stages. An overview of the two-level staging system, including relative and absolute time values, is given in Table 1.

Quantitative analysis

Due to the intrinsic properties of LSM, the respective data is eligible for general and specific quantitative analyses. The alignment of DS0001-DS0005 allow the temporal comparison in means of absolute embryonic development time (Figure 1A) as well as relative completion of embryonic development (Figure 1B), and to calculate the respective deviations. Deviation peaks are found at the transition from stage 10 to stage 11, during of stage 13 and around stage 16 and 17. The aligned datasets also allow for comprehensive quantitative analysis of morphogenetic features.

Furthermore, dataset alignment allowed us to measure the longitudinal extend change of the embryos as a function of time (Figure 1C). The change in length does not follow simple mathematical functions but alter heavily over the course of embryogenesis, resulting in multiple relative maxima and minima. Whenever appropriate, changes and peaks are discussed in the descriptive parts of the result section below.

Description of *Ceratitis* embryogenesis

The aforementioned live imaging datasets form the basis for the description of *Ceratitis* embryogenesis and allow morphogenetic characterization from the first withdrawal of the yolk during blastoderm formation to the moment when the larva hatches from the egg. Description is

- The running text is divided into six sections that relate to the six embryogenetic events. Complex processes that involve multiple structures are described over longer time periods. Only *Ceratitis*-related studies are referenced within the running text.
- Supplementary Figure 1 is a compact stage-based summary of embryogenesis, in which each of the seventeen stages is outlined with a representative image, a temporal breakdown and up to four bullet points highlighting the most important incidents per stage.
- Table 1 provides a time point-based description of the embryogenesis in chronological order with the maximal temporal resolution. For longer lasting processes, beginning and completion are separately indicated.
- Table 2 provides a brief description of all important structures and their precursors and/or successors in alphabetical order. The table also serves as a thoroughly referenced glossary for the terminology – all structural terms that written in italics throughout the publication are defined here.
- Table 3 gives an overview of ten selected higher-level processes in chronological order. It indicates the embryogenetic events during which the respective process occurs and roughly summarizes the morphogenetic sequence. Additionally, the processes are briefly embedded into an evolutionary context.

Summary

(I) Blastoderm formation

Blastoderm formation, embryogenetic event I, starts with egg fertilization and consists of five stages (1 to 5) that are outlined in Table 1 and Figure 2A and B. The *zygote* consist of a vitelline envelope that is mostly filled with *yolk* (Figure 2A, first column). The *zygotic nuclei* are located within the inner regions of the *yolk*, undergo multiple nuclear divisions and form a large syncytium. Cell membranes are yet absent. After the initial nine synchronous nuclear divisions during stage 1 and 2, the first *zygotic nuclei* start protruding towards the surface as part of the *peripheral migration* process and can be reckoned at the end of stage 2 (Figure 2A, second column). Stage 3 begins when the first *zygotic nuclei* reach the surface (Figure 2A, third and fourth column, detail images {3,4}), give rise to the *pole buds* (Figure 2A, fourth column {2}; Figure 2C) and immediately start with the 10th and 11th nuclear division. When the last *zygotic nuclei* have reached the surface and completed the 11th nuclear division, they turn into *blastoderm nuclei*. With the end of the *peripheral migration* process, the *zygote* turns into the *syncytial blastoderm*, which marks the beginning of stage 4. During this stage, the *syncytial blastoderm* undergoes two more parasynchronous nuclear divisions that run exclusively on the surface and proceed in a wave-like fashion from anterior to posterior (Figure 2B, first to fourth column).

The mean nuclei area drops to approximately one-third (Figure 2D) and the relative nuclei density increases by approximately factor four (Figure 2E). The nuclei are now distributed homogenously on the surface, without any apparent differences between particular regions. During stage 5, the *blastoderm nuclei* remain quiescent at their location for about four hours (Figure 2B, fifth column; Figure 3A, first and second column), which indicates that the *cellularization* process takes place during this period [38]. At the end of stage 5, the medioventral *blastoderm nuclei* acquire a wavy appearance (Figure 3A, first and second column, detail images), a preceding for the subsequent comprehensive morphogenetic rearrangements during gastrulation.

During stage 2, the *yolk* begins withdrawing from the anterior and posterior pole as part of the *repeated withdrawal* process (Figure 2C, first column) before reaching its relative maximum distance at the beginning of stage 3 (Figure 2A {1,2}; Figure 2C, second column; cf. Figure 1C {1}). In parallel to the emergence of the *pole buds* at the posterior end of the *zygote*, the withdrawal begins reversing (Figure 2C, third column). Complete reversal is accomplished at the end of stage 3 (Figure 2C, fourth column) and retained during stages 4 and 5 (Figure 2B).

The emergence of the *pole buds* at the posterior pole (Figure 2A, fourth column {2}; Figure 2C) is part of the *germ cell dynamics* process that begins during stage 3 [39]. At the beginning of stage 4, those protuberances pinch off, turn into the *pole cells* (Figure 2B, first column) and become tightly grouped (Figure 2B, second to fifth column {1}). In contrast to the *blastoderm nuclei*, the *pole cells* are already separated by cell membranes [39]. Plane-wise segmentation analysis along the longitudinal axis (Figure 2F) indicated that the *pole cells* undergo asynchronous mitotic division, which results in a total of 27.3 ± 2.6 identifiable *pole cells* at the end of stage 4. A conspicuous spatial organization pattern throughout the embryos was not found (Figure 2G). During stage 5, the *pole cells* remain quiescent.

(II) Gastrulation

Gastrulation, embryogenetic event II, starts when the *blastoderm nuclei* complete the synthesis of cell membranes and consist of two stages (6 and 7) that are summarized in Table 1 and Figure 3A, B and C. With the end of the *cellularization* process, the *syncytial blastoderm* turns into the *cellular blastoderm*, which undergoes considerable

morphogenetic changes in a very short time period (Figure 3C; Figure 3D; Figure 3E). The wavy appearance of the medioventral *blastoderm nuclei* intensifies (Figure 3A, first and second column), resulting in the *ventral furrow*, a longitudinal cleft that arises medioventrally at the beginning of stage 6 (Figure 3A, third column {1,2}; Figure 3B; Figure 3C {1}; Figure 3E {2,3}). The *ventral furrow* is involved the *germ layer specification* process, which occurs during the next few hours. While its anterior tip remains nearly stationary (Figure 3E {2}; Figure 3F), the posterior tip extends posteriad and curls around the posterior pole at the transition from stage 7 to stage 8 (Figure 3E {3}; Figure 3F {1}). During this process, more and more blastodermal cells along the ventral midline are recruited and incorporated. The initial groove width of the *ventral furrow* spans about five to seven cells (Figure 3E, third column), the width of the residual transient gap that remains after invagination is completed spans only about one to two cells (Figure 3E, fifth column). Throughout continuous closure, the *ventral furrow* differentiates into the superficial *ectodermal layer* and the internal *mesodermal layer*. A minor part around the anterior tip (Figure 3E, yellow dashed line; Figure 3F) gives rise to the *anterior midgut primordium*, which is of endodermal origin. At the transition from stage 7 to stage 8, the *anterior midgut primordium* internalizes and undergoes mitotic division (Figure 3F, detail images).

At the end of stage 6, the *cellular blastoderm* withdraws from the anterior and posterior pole (Figure 3B, detail images; cf. Figure 1C {3}). In parallel, the *posterior plate*, to which the *pole cells* adhere, emerges at the flattened posterior tip of the *cellular blastoderm*. At the end of stage 7, the *posterior plate* shifts its position from the posterior pole towards the dorsal side and turns into the *dorsal plate* as part of the *germ cell dynamics* process (Figure 3C, second column; Figure 3H).

Shortly after the *ventral furrow* becomes apparent, symmetrically arranged lateral indentions arise anteromedially, which precede the formation of the *cephalic furrow* (Figure 3B {1}; Figure 3E, second column {1}), leading to a radial alignment of the nuclei in the triangular area between the indentions and the *ventral furrow* at the end of stage 6 (Figure 3E, third column). At the beginning of stage 7, the indentions expand, with moderate anterior inclination, towards the ventral midline and approach the anterior tip of the *ventral furrow* (Figure 3E, fifth and sixth column). This results in a deepening of the *cephalic furrow*, which plays a key role in the differentiation of the *cellular blastoderm* by separating the anterior *head* from the medio-ventral *thorax* (Figure 3C). The *cellular blastoderm* differentiates furthermore into the posterior *abdomen* and the medio-dorsal *amnioserosa* (Figure 3C, red dashed lines). The *head*, the *thorax* and the *abdomen* constitute the *embryo* – the entirety of tissue regions that become part of the larva after hatching – in contrast to the extra-embryonic *amnioserosa* and the *yolk sac*, which become degraded later on. The *head* withdrawal soon reaches a relative maximum and begins reversing (Figure 3C, second column; cf. Figure 1C).

As part of the *extra-embryonic membrane folding* process, the *amnioserosa* extends moderately laterad and strongly posteriad during the next hour (Figure 3C, first column, detail images; Figure 3C, second column; Figure 3D). The cells of the *amnioserosa* do not proliferate, which leads to a sparse distribution of the nuclei over the whole area of the extra-embryonic membrane at the end of stage 7 (Figure 3D, second and third column). Surprisingly, *Ceratitis* does not develop an anterior and posterior transverse fold.

Gastrulation is also characterized by mitotic divisions of four cell clusters within the *head*. At the beginning of stage 7, the *small and large lateral stripes* undergo mitotic division (Figure 3C, first column; Figure 3G, detail images). After both clusters proceed through the telophase and reestablishes their nuclear membranes (Figure 3C, second column {2,3}; Figure 3G, detail images), the cells around those cluster also begin with mitotic division.

After completion at the end of stage 7, the resulting nuclei are significantly small size (Figure 3C, second column, detail images; Figure 3G, detail images) and the *head* has remodeled – while the descendants of the large lateral stripe and its surrounding cells, which are located directly anterior of the *cephalic furrow*, form the postero-ventral *gnathocephalon* (Figure 3C, second column; cf. Figure 4A, first column {2}), the remaining cells constitute the antero-ventral / dorsal *procephalon*. Together with the *thorax* and the *abdomen*, the *gnathocephalon* composes the *germband*.

(III) Germband elongation

Germband elongation starts when the posterior tip of the *germband* begins anteriopad elongation along the dorsal side with high speed and consists of four stages (8 to 11) that are summarized in Table 1 and Figure 4A and B. At the beginning of stage 8, the posterior tip of the *germband* curls around the posterior pole and accomplishes the first 400 μm of anteriopad migration within about two hours (Figure 4A; Figure 4C). The migration speed decelerates two times, once at the beginning of stage 9 and once at the beginning of stage 10, so that the final 100 μm are accomplished within about five and a half hours. When the *germband* is fully elongated, the *amnioserosa* has folded completely and the *yolk sac* has migrated from the surface to the inner regions (Figure 4B, third and fourth column). During stage 11, the posterior tip of the *germband* remains in a quiescent position (Figure 4D; Figure 4E) while the *gnathal protuberances* emerge from the *gnathocephalon* as part of the *metamerization* process (Figure 4B, detail images {1,2,3}).

Shortly after the beginning of stage 8, the *head* withdrawal from the anterior pole reverses completely (Figure 4A, second column; cf. Figure 1C {4}), but begins withdrawing again during stage 10 (Figure 4B, second column; cf. Figure 1C {5}) before reaching a momentary standstill at the beginning stage 11 (Figure 4B, third column; cf. Figure 1C {6}). The *abdomen* withdrawal from the posterior pole reaches a momentary standstill at the end of stage 8 (Figure 4A, second and third column; cf. Figure 1C) and continues withdrawal at the beginning of stage 11 (cf. Figure 1C {6}).

Around the same time as the *germband* begins anteriopad elongation, the *stomodeal cell plate* emerges anteriopad ventrally from the *procephalon* (Figure 4A, first column {1}; Figure 4F, first column). Shortly afterwards, the *stomodeal cell plate* sinks inwards, turns into the *stomodeal invagination* (Figure 4A, second column {2}) and connects with the *anterior midgut primordium* (Figure 4F, second column {1}). At the beginning of stage 9, the *stomodeal invagination* turns into the *stomodeum* (Figure 4A, third and fourth column {3}; Figure 4F, fifth column), which becomes the anteromedial part of the *digestive tract* as part of the *digestive system formation* process. In parallel, the *cephalic furrow* levels out (Figure 4A, third column; Figure 4G, first row of detail images).

During early elongation, the posterior tip of the *germband* carries the *dorsal plate*, to which the *pole cells* adhere (Figure 4A, first column; Figure 4C, detail images {1}; Figure 4H, first to third column). The *dorsal plate* turns into the *posterior midgut primordium* during stage 8 (Figure 4A, second column {5}), which subsequently invaginates, but still carries the *pole cells* (Figure 4C, detail images {2}). The *germ layer specification* process ends, since all components are now allocated to their respective layers. Shortly afterwards, at the posterior tip of the *ventral furrow*, the *ectodermal layer* gives rise to the *amnioproctodeal invagination*, a tubular structure that surrounds the *posterior midgut primordium* (Figure 4A, second column; Figure 4C, second column). As part of the *digestive system formation* process, *amnioproctodeal invagination* differentiates into the *proctodeum* (Figure 4A; cf. Figure 4, detail images, yellow dashed line) and the *proctodeal opening* (Figure 4A, third column; cf.

Figure 4C, detail images, red dashed line) at the beginning of stage 9. The *proctodeal opening* changes from a dorsal to an anterior orientation at the end of stage 9, thus the *pole cells* vanish from sight (Figure 4, fourth column {6}; Figure 4H, fourth column). The *germ cell dynamics* process ends here, since the fate of the *pole cells* cannot be observed anymore.

At the end of stage 8, the *ectodermal layer* differentiates into the *ventral epidermal primordium*, which composes of cells with large nuclei and the *lateral epidermal primordia*, which composes of cells with small nuclei (Figure 4A, first and second column; Figure 4G, detail images). Germband elongation is also the embryogenetic event where neurogenesis begins: Firstly, after the emergence of the *stomodeal cell plate* at the beginning of stage 8, all remaining ventrally and laterally located cells of the *procephalon* undergo mitotic division, sparing a longitudinal stripe of cells with a scraggy outline – the *optic lobe primordium* (Figure 3D, detail images; Figure 4A, first column, red dashed line). The primordium is a shallow groove with a width of around three to four cells and extends along the dorsal midline from the anterior tip of the *procephalon* to the anterior rim of the *amnioserosa*. During stage 8, the *optic lobe primordium* begins multiple cycles of mitotic division that last until the end of stage 10 (Figure 4J). Secondly, in the *thorax* and the *abdomen*, the first *neuroblasts* segregate from the *ventral epidermal primordium* at the beginning of stage 9 (Figure 4G {1,2,3}). Thirdly, the *ventral furrow* levels out at the beginning of stage 9 (Figure 4A, third column; Figure 4I, first column). About two hours later, the *ventral mesectoderm* emerges as longitudinal stripe of mesectodermal cells from the *ventral epidermal primordium* at the same position (Figure 4I, second column). Any further neurodevelopmental processes cannot be properly identified, thus neurogenesis is not described further within this study (Supplementary Table 2).

(IV) Germband retraction

Germband retraction starts when the posterior tip of the *germband* begins posteriad retraction along the dorsal side and consists of one stage (12) that is summarized in Table 1 and Figure 5A. In contrast to germband elongation, which had three periods with high, moderate and low speed of migration, the posterior tip of the *germband* retracts with a relatively constant speed over the next seven and a half hours (Figure 5A, B). The retraction is directly linked to the *extra-embryonic membrane folding* process – the *amnioserosa* unfolds for a second time as part of the *extra-embryonic folding* process and the *yolk sac* protrudes towards the medio-dorsal surface (Figure 5A, second to fourth column). At the end of stage 12, when the retraction process is completed, the *proctodeal opening* is located posterior-dorsally (Figure 5A, fourth column {1}).

Three hours after the beginning of stage 12, the *abdomen* withdrawal reaches a relative maximum and begins reversing (Figure 5A, second and third column; cf. Figure 1C), while the *head* withdrawal remains in a standstill during the whole period of germband retraction (Figure 5; cf. Figure 1C). During this state, two hours after *germband* retraction begins, the *clypeolabrum* emerges antero-dorsally from the *procephalon* (Figure 5A, detail images). Over the next few hours the *clypeolabrum* becomes thinner and more pronounced, but retains its antero-dorsal orientation (Figure 5B, detail images).

During stage 12, the *dorsal epidermal primordia* emerge in an anterior-to-posterior fashion from the *lateral epidermal primordia* (Figure 5B, second to fourth column {1}). Shortly after the *abdomen* withdrawal has reached a relative maximum as part of the *repeated withdrawal* process and begins reversing, the *intersegmental furrows* arise and separate the *thorax* into three (Figure 5B, {2,3,4}) and the *abdomen* into nine segments. Together with

the emergence of the *gnathal protuberances* in the *gnathocephalon* during stage 11, the *germband* is now divided into fifteen segments as part of the *metamerization* process.

(V) Dorsal closure

Dorsal closure starts when the posterior tip of the *germband* completes posteriad retraction and consists of three stages (13 to 15) that are summarized in Table 1 and **Figure 6A** and **B**. As one of the first morphological changes shortly after the beginning of stage 13, the *anterior dorsal gap*, a shallow transversal groove, arises between the *procephalon* and the *amnioserosa* (**Figure 6A**, second column {1}; **Figure 6C**, first to third column). In parallel, the *gnathal protuberances* give rise to the bilateral *dorsal folds* (**Figure 6D**, first column) and subsequently differentiate into the *mandibular buds* (**Figure 6A**, second column {2}; **Figure 6C**, first column {1}; **Figure 6E**, first column {1}; **Figure 6F**, third column), the *maxillary buds* (**Figure 6A**, second column) and the *labial buds* (**Figure 6A**, second column; **Figure 6C**, second column {2}). The *maxillary buds* fuse with the antero-ventral region of the *procephalon* to form the *antennomaxillary complexes* (**Figure 6A**, fifth column {5}; **Figure 6C**, fourth column {3}; **Figure 6E**, third and fourth column {4}; **Figure 6F**, fourth column) while the *labial buds* migrate ventrad and eventually fuse (**Figure 6A**, fifth column {4}; **Figure 6C**, second to fourth column {2}; **Figure 6E**, second to fourth column {2}; **Figure 6F**). The *anterior dorsal gap* is only transient, it levels out during the next few hours (**Figure 6A**, third and fourth column {1}; **Figure 6C**, fourth column {4}).

The *head involution* process begins as the *ventral epidermal primordium* and the *lateral epidermal primordia* (**Figure 6A**, first column, red dashed lines) begin with anteriopad migration to form an envelope around the ventrolateral part of the *head*. Involution of the dorsal part is slightly delayed and does not involve the *dorsal epidermal primordia*. Instead, the *dorsal folds* fuse along the *anterior dorsal gap* and begin with anteriopad migration, covering the *procephalon* and the *clypeolabrum* gradually (**Figure 6D**). The collective anteriopad migration of the epidermal primordia and the *dorsal fold* is accompanied by a co-motion of the bilaterally located *antennomaxillary complexes* (**Figure 6E**, third and fourth column {4}; **Figure 6F**; Supplementary Video 3) and a posteriad counter-motion of the *clypeolabrum* (**Figure 6A**, fifth column; **Figure 6B**; **Figure 6C**, fourth column; **Figure 6E**, third and fourth column; **Figure 6F**, third and fourth column), the *mandibular buds* (**Figure 6A**, fifth column; **Figure 6B**; **Figure 6C**, fourth column {1}; **Figure 6E**, third and fourth column {1}; **Figure 6F**, third and fourth column) and later on also the fused *labial buds* (**Figure 6B**; **Figure 6E**, third and fourth column {2}; **Figure 6F**, third and fourth column), which retract into the inner regions of the *embryo* (Supplementary Video 3).

During dorsal closure, the posterior tip of the *germband* flips into the posterior pole (**Figure 6B**) and the *intersegmental grooves* of the *thorax* and the *abdomen* transiently level out (**Figure 6B**, third column). Anteriorly within the *thorax*, the *anterior midgut primordium* and the *posterior midgut primordium* fuse to form the *midgut* (**Figure 6A**, third column {3}; **Figure 6G**, third column, yellow dashed line), which internalizes the *amnioserosa* and the *yolk sac* at the end of the *extra-embryonic membrane folding* process. The internalization procedure requires the *amnioserosa* to fold for a second time, which seems to be partially mediated by the dorsad migration of both *dorsal epidermal primordia*. This approaching motion marks the beginning of the *dorsal zippering* process – throughout the next several hours, the primordia establish antero- and posteromedially contact and fuse continuously to form a tight seam along the dorsal midline. The anterior leading edge migrates slowly (**Figure 6G**, first to third column {1}), partially covering the *midgut* (**Figure 6G**, third column, yellow dashed line). In contrast, the posterior leading edge migrates slightly faster (**Figure 6G**, first to third column {1}) and covers the *proctodeum* completely (**Figure 6G**, first column, red dashed line). After completion of anterior and posterior

fusion at the beginning of stage 15, the anterior and posterior leading edges continue with median fusion (**Figure 6G**, fourth and fifth column {3,4}).

At the beginning of stage 14, withdrawal of the *head* continues after the momentary standstill (**Figure 6A**; cf. Figure 1C {7}). Both the *head* and the *abdomen* reach their absolute withdrawal maxima during stage 15 (**Figure 6B**; Figure 1C {8}), so that the relative longitudinal extend of the *embryo* has dropped to nearly 90% of its initial value. Withdrawal reverses relatively fast within the next three hours (Figure 1C {9}).

(VI) Muscular movement

Muscular movement starts when the *dorsal epidermal primordia* complete median fusion and turn into the *dorsal epidermis*, thus ending the *dorsal zippering* process and consists of two stages (16 and 17) that are summarized in Table 1 and **Figure 7A**. One of the most remarkable occurrences of this embryogenetic event is the onset of regular muscular movement within the *embryo* (**Figure 7B**). At the beginning of stage 16, both the *ventral epidermal primordium* and the *lateral epidermal primordia* complete their anteriad migration and turn into the *ventral epidermis* and *lateral epidermis*, respectively (**Figure 7A**, first column, red dashed lines; cf. **Figure 6A**, first column, red dashed lines). Slightly later, the fused *dorsal folds* also complete anteriad migration and turn into a pocket-like structure, the *dorsal pouch* (**Figure 7A**; **Figure 7C**, first row of detail images, red dashed lines), which ends the *head involution* process. Of all head appendages, only the anterior, fused part of the *antennomaxillary complexes* is still superficial, while the posterior part, the *clypeolabrum*, the *mandibular buds* and the *labial buds* contribute to form the *atrium*. The *digestive system formation* process ends as the anterior *atrium*, the anteromedial *stomodeum*, the medial *midgut*, the posteromedial *proctodeum* and the posterior *proctodeal opening* consecutively connect to form the *digestive tract*.

At the beginning of stage 17, the withdrawal of the *head* and the *abdomen* nearly completely reverses (**Figure 7A**; cf. Figure 1C). During muscular movement, the posterior tip of the *ventral cord* shortens gradually over a period of several hours until it reaches its final position between the 4th and 5th segment of the *abdomen* (**Figure 7C**, second row of detail images). Ultimately, the *embryo* hatches from the egg and turns into the larva (**Figure 7D**) – the completion of embryonic development and the beginning of the second phase of the life cycle.

Discussion

***Ceratitis capitata* as model organism for evolutionary developmental biology**

In this study, we characterize the whole embryonic morphogenesis of *Ceratitis* qualitatively and quantitatively to provide an integrative framework for future studies. Due to its status as a pest species, *Ceratitis* is primarily a model organism for agricultural-associated research, and has been used only occasionally in developmental biology. Our study shows that *Ceratitis* is well suited as a complementary model organism for evolutionary developmental biology and strengthens the comparative approach.

Extra-embryonic membranes in *Ceratitis* and other insect species

In the evolutionary context, one of the most interesting insights of this study concerns the formation and degradation of extra-embryonic membranes. In strong contrast to *Megaselia* but similar to *Drosophila*, *Ceratitis* develops only one dorsally located amnioserosa. However, in *Ceratitis*, the amnioserosa differentiates during gastrulation as a membrane of widely spaced cells on the dorsal side between the posterior plate and the head during stage II-7. During germband elongation, the amnioserosa cells change their shape – they become dorsally compressed as the germband tip migrates anterior and expand over the lateral flanks of the embryo until the end of stage III-10. During germband retraction, the amnioserosa rearranges in parallel with the retracting germband tip, so that it once again covers a certain dorsal area. The anterior and posterior transverse folds, which are characteristic transient structures for other Diptera [40,51] during gastrulation and early germband elongation, are not found in *Ceratitis*. By contrast, the primordial amnioserosa cells in *Drosophila* are initially clustered in close proximity to the posterior transversal fold during stage 7 and early stage 8, and the subsequent lateral expansion process, which starts at the transition from stage 8 to stage 9, occurs without dorsal compression. The subsequent rearrangement process during germband retraction is similar to *Ceratitis* [40,52].

We hypothesize that a ‘premature’ differentiation process of the amnioserosa during gastrulation, as shown for *Ceratitis*, is an apomorphic trait, since other, more basally located Diptera such as *Megaselia* [18–21] and *Clogmia* [22] appear to morphogenetically specify their extra-embryonic membranes also not before germband elongation. Extra-embryonic membranes in holo- and hemimetabolous insects are currently ambitiously investigated in many insect model organisms [53,54] – also in non-dipteran species such as the red flour beetle *Tribolium castaneum* [55–60] and the milkweed bug *Oncopeltus fasciatus* [61–63] – and our description of the amnioserosa dynamics in *Ceratitis* contributes to the understanding of their structure, function and evolutionary history. However, a comprehensive comparison of further differences between *Ceratitis* and *Drosophila* is beyond the scope of this work and will be analyzed in a study of its own.

Our approach in comparison to traditional strategies

In contrast to similar studies that have analyzed other insect species and established an embryonic staging system (twenty respective publications are summarized in Supplementary Table 1

Supplementary Table 1), our study is based on long-term fluorescence live imaging data. The data was acquired by imaging embryos from a stable homozygote transgenic line that expresses nuclear-localized EGFP ubiquitously with LSFM. Due to its intrinsic characteristics, *e.g.* low photo-bleaching, nearly no photo-toxicity, intrinsic optical sectioning, very good signal-to-noise ratio and imaging along multiple directions, LSFM is a well suited technique for descriptive and analytical studies of insect embryogenesis.

This is the first study that uses fluorescence live imaging to describe the complete embryogenesis of an insect species. In the past, the methods of choice have mainly been fixation and staining with non-fluorescent and fluorescent dyes, mechanical sectioning or scanning electron microscopy. In those approaches, only one time point per specimen can be shown. Therefore, to describe embryogenesis as a whole, many specimens are required, resulting in a high amount of experimental work and, even more crucial, certain statistical errors. For example, it is cumbersome and imprecise to calculate the temporal standard deviations by using fixed and stained samples. Also in traditional approaches, quality control is not properly performable. Our quality criterion is healthy development of the imaged specimen – out of nine imaged embryos, eight (DS0001-0005, DS0007-0009) developed into fully functional adults, and all data that derived from the not properly developing embryo was disregarded.

However, the fluorescence live imaging approach also suffers from several limitations. Firstly, respective transgenic lines are a prerequisite for long-term fluorescence live imaging, and the descriptive quality of structures and processes depends on the available fluorescent labels. In our study, for example, the cellularization process at the end of blastoderm formation (stage I–5) cannot be shown – a membrane labeled transgenic line would be necessary (see also Supplementary Table 2

Supplementary Table 2). Secondly, like with most light microscopy approaches, resolution is limited by the diffraction limit. To identify tinier structures, approaches like electron microscopy have to be used. Thirdly, some structures and processes could not be reliably identified (an overview is given in Supplementary Table 2

Supplementary Table 2) due to limitations in the section capabilities of LSFM, which is very good compared to other fluorescence live imaging methods, but inferior to mechanical section.

Quantitative analyses

Also, traditional approaches for the description of embryonic development typically characterize the structures and processes merely qualitatively (Supplementary Table 2

Supplementary Table 2). Only for established model organisms, such as *Drosophila*, extensive quantitative information is available. This limitation mainly arises from the circumstance that the extraction of quantitative information from data that is obtained by classic methods is labor-intensive, complicated, error-prone or even impossible. One of the major advantages of our approach (i.e. fluorescence live imaging with LSFM) is that the data quality is very high, which allows simple and efficient extraction of a broad spectrum of quantitative data. Due to space restrictions, we have shown only several examples for the extraction of quantitative data in this study. We predict that, also depending on the concrete scientific question, much more qualitative data can be extracted, and that those analytical processes can also be automatized.

Perspective

Our approach – long-term fluorescence live imaging with LSFM – serves as a template for further approaches that characterize the embryonic development of insect model organisms to establish a comprehensive staging system that serves as an integrative framework for future studies. While the initial labor is relatively high due to the requirement of one or more convenient transgenic lines, high quality data can be acquired with only moderate effort when those lines become available. Once long-term fluorescence live imaging data from multiple insect species will be published, morphological structures and the associated morphogenetic processes can be comprehensively analyzed within an evolutionary context. With *Drosophila* [64–67], *Megaselia* [51], *Tribolium*

[68–70] and now *Ceratitis* (Ref), LSM image data for four species are already available to support comparative approach to embryonic morphogenesis of insects.

Tables

Table 1

Table 1 – Detailed description of *Ceratitis* embryogenesis in chronological order. The primary stage identifier is shown in bold. Only time points with substantial morphogenetic changes compared to the previous stages are listed. We only describe processes for which our data provide evidence. Indentions show associated processes, parentheses reference higher-level processes that are summarized in Table 3. Figure references indicate arrows if applicable, figures in which the respective processes can be seen but is not primarily described are referenced in parentheses. Please note that some morphogenetic processes can only be seen properly in the supplementary videos.

stage	time	%	developmental process	figure
I – blastoderm formation – stages 1 to 5 (5 total) – 00:00 h to 11:30 h (11:30 h total) – 0.0% to 18.4% (18.4% total) – Figure 2				
I – 1	00:00 h	0.0%	<ul style="list-style-type: none"> egg fertilization results in the <i>zygote</i>, which consists of the <i>yolk</i> and the <i>zygotic nuclei</i> 	-
I – 2	02:00 h	3.2%	<ul style="list-style-type: none"> the <i>yolk</i> begins withdrawing from both poles (<i>repeated withdrawal</i>) 	2A, C; (1C)
	02:30 h	4.0%	<ul style="list-style-type: none"> the respectively allocated <i>zygotic nuclei</i> begin protruding towards the surface (<i>peripheral migration</i>) 	2A [3]
I – 3	03:30 h	5.6%	<ul style="list-style-type: none"> the <i>yolk</i> withdrawal at both poles reaches a relative maximum and starts reversing (<i>repeated withdrawal</i>) the first <i>zygotic nuclei</i> reach the surface (<i>peripheral migration</i>) the <i>zygotic nuclei</i> begin with the 10th synchronous nuclear division 	2A, C; (1C [1,2]) 2A [3] 2A
	04:00 h	6.4%	<ul style="list-style-type: none"> the <i>zygotic nuclei</i> complete the 10th and begin with the 11th synchronous nuclear division the <i>pole buds</i> emerge at the posterior tip of the <i>zygote</i> from the <i>zygotic nuclei</i> (<i>germ cell dynamics</i>) 	2A 2A [2], C
I – 4	04:30 h	7.2%	<ul style="list-style-type: none"> the last <i>zygotic nuclei</i> reach the surface (end of <i>peripheral migration</i>) the <i>zygotic nuclei</i> complete the 11th synchronous nuclear division and turn into the <i>blastoderm nuclei</i> the <i>blastoderm nuclei</i> begin with the 12th synchronous nuclear division the <i>zygote</i> turns into the <i>syncytial blastoderm</i> (end of <i>peripheral migration</i>) 	2B 2B 2B, D, E 2B
	05:00 h	8.0%	<ul style="list-style-type: none"> the <i>blastoderm nuclei</i> complete the 12th synchronous nuclear division the <i>pole cells</i> derive at the posterior tip of the <i>syncytial blastoderm</i> from the <i>pole buds</i> (<i>germ cell dynamics</i>) 	2B, D, E 2B, F, G
	05:30 h	8.8%	<ul style="list-style-type: none"> the <i>blastoderm nuclei</i> begin with the 13th synchronous nuclear division the <i>pole cells</i> begin with their asynchronous mitotic division (<i>germ cell dynamics</i>) 	2B, D, E 2B [1], F
	06:00 h	9.6%	<ul style="list-style-type: none"> the <i>blastoderm nuclei</i> complete the 13th synchronous nuclear division the <i>pole cells</i> complete their synchronous nuclear division (<i>germ cell dynamics</i>) the <i>yolk</i> withdrawal at both poles completely reverses (<i>repeated withdrawal</i>) 	2B, D, E 2B [1], F 2B; (1C [2])
	06:30 h	10.4%	<ul style="list-style-type: none"> the <i>blastoderm nuclei</i> complete the 13th synchronous nuclear division the <i>blastoderm nuclei</i> begin with the synthesis of cell membranes (<i>cellularization</i>) 	2B, D, E 2B; 3A
I – 5	11:00 h	17.6%	<ul style="list-style-type: none"> the medio-ventral <i>blastoderm nuclei</i> exhibit a slight wavy appearance 	3A
II – gastrulation – stages 6 to 7 (2 total) – 11:30 h to 14:30 h (03:00 h total) – 18.4% to 23.2% (4.8% total) – Figure 3				
II – 6	11:30 h	18.4%	<ul style="list-style-type: none"> the <i>blastoderm nuclei</i> complete the synthesis of cell membranes (end of <i>cellularization</i>) the <i>syncytial blastoderm</i> turns into the <i>cellular blastoderm</i> (end of <i>cellularization</i>) the <i>yolk</i> turns into the <i>yolk sac</i> (end of <i>cellularization</i>) the longitudinal <i>ventral furrow</i> arises medio-ventrally in the <i>cellular blastoderm</i> 	3A 3A 3A 3A [1,2], E [2,3]
	12:30 h	20.0%	<ul style="list-style-type: none"> the <i>cellular blastoderm</i> starts withdrawing from the anterior pole (<i>repeated withdrawal</i>) the <i>ventral furrow</i> starts extending towards both tips of the <i>cellular blastoderm</i> the transversal, antero-ventral / postero-dorsal slightly tilted <i>cephalic furrow</i> arises anteromedially in the <i>cellular blastoderm</i> 	3B, (E); (1C [3]) 3E [2,3] 3B [1], E
	13:00 h	20.8%	<ul style="list-style-type: none"> the <i>ventral furrow</i> completes extending towards the anterior pole of the <i>cellular blastoderm</i> the <i>cellular blastoderm</i> starts withdrawing from the posterior pole (<i>repeated withdrawal</i>) the <i>posterior plate</i>, to which the <i>pole cells</i> adhere, emerges at the posterior tip of the <i>cellular blastoderm</i> (<i>germ cell dynamics</i>) 	3E [2] 3B, (E); (1C [3]) 3B, (E)
II – 7	13:30 h	21.6%	<ul style="list-style-type: none"> the anterior <i>midgut primordium</i> emerges and invaginates at the anterior tip of the <i>ventral furrow</i> (<i>germ layer specification</i>) the <i>cellular blastoderm</i> differentiates into <ul style="list-style-type: none"> the anterior <i>head</i>, the medio-ventral <i>thorax</i> and the posterior <i>abdomen</i>, which constitute the <i>embryo</i> the medio-dorsal <i>amnioserosa</i>, which begins unfolding (<i>extra-embryonic membrane folding</i>) the <i>cephalic furrow</i> deepens laterally the <i>ventral furrow</i> invaginates along the <i>thorax</i> and continues extending towards the posterior tip of the <i>abdomen</i> the <i>small and large lateral cell stripes</i> at the <i>head</i> begin with mitotic division¹ 	3C, E, F 3C, D, (E, G) as above as above 3C, E [1], (F, G) 3C [1], E [2,3], F [1] 3C, (D), G
	14:00 h	22.4%	<ul style="list-style-type: none"> the <i>head</i> withdrawal from the anterior pole reaches a relative maximum and begins reversing (<i>repeated withdrawal</i>) the <i>small and large lateral cell stripes</i> complete mitotic division¹ <ul style="list-style-type: none"> the areas around the <i>small and large transversal cell stripes</i> at the <i>head</i> begin mitotic division² the <i>head</i> remodels into <ul style="list-style-type: none"> the antero-ventral / dorsal non-metameric lobe-like <i>procephalon</i> the postero-ventral <i>gnathocephalon</i>, which constitutes together with the <i>thorax</i> and the <i>abdomen</i> the <i>germband</i> 	3C; (1C) 3C [2,3], (D), G 3C [2,3], (D), G 3C, E, F, G as above as above

			<ul style="list-style-type: none"> the <i>amnioserosa</i> completes unfolding and covers the <i>embryo</i> and the <i>yolk sac</i> medio-dorsally (<i>extra-embryonic membrane folding</i>) the <i>ventral furrow</i> closes along the already invaginated <i>thorax</i> / subsequently invaginating <i>abdomen</i> and differentiates into the superficial <i>ectodermal layer</i> (<i>germ layer specification</i>) the internal <i>mesodermal layer</i> (<i>germ layer specification</i>) the <i>posterior plate</i>, to which the <i>pole cells</i> adhere, turns into the <i>dorsal plate</i> (<i>germ cell dynamics</i>) 	3C, D, (E) 3C, E, F as above as above 3C [4], (D, E, G), H
III – germband elongation – stages 8 to 11 (4 total) – 14:30 h to 24:30 h (10:00 h total) – 23.2% to 39.2% (16.0% total) – Figure 4				
III – 8	14:30 h	23.2%	<ul style="list-style-type: none"> the posterior tip of the <i>germband</i> begins anteriad elongation along the dorsal side towards with high speed <ul style="list-style-type: none"> the <i>amnioserosa</i> begins folding (<i>extra-embryonic membrane folding</i>) the <i>yolk sac</i> begins migration from the medio-dorsal surface to the interior region the <i>stomodeal cell plate</i> emerges antero-ventrally from the <i>procephalon</i> the <i>anterior midgut primordium</i> internalizes (<i>germ layer specification</i>) the areas around the <i>small and large transversal cell stripes</i> complete mitotic division² <ul style="list-style-type: none"> all remaining ventrally and laterally located cells of the <i>procephalon</i> begin mitotic division the <i>optic lobe primordium</i> emerges dorsally from the <i>procephalon</i> 	4A, D, E, H, (3E) 4A, H 4A, H 4A [1], F; (3E) 4A [4]; (3E, F) 4A; (3E, G) 4A; (3D, E, G) 4A; (3D)
	15:00 h	24.0%	<ul style="list-style-type: none"> the <i>head</i> withdrawal reverses completely (<i>repeated withdrawal</i>) all remaining ventrally and laterally located cells of the <i>procephalon</i> complete mitotic division the <i>dorsal plate</i>, to which the <i>pole cells</i> adhere, internalizes and turns into the <i>posterior midgut primordium</i> (end of <i>germ cell dynamics</i> and end of <i>germ layer specification</i>) the <i>stomodeal cell plate</i> sinks inwards and turns into the <i>stomodeal invagination</i> 	4A; (1C [4]) 4A; (3D, E) 4A, C [1,2], H, (J) 4A [2], F; (3E, F)
	15:30 h	24.8%	<ul style="list-style-type: none"> the <i>optic lobe primordium</i> begins with mitotic divisions the <i>stomodeal invagination</i> and the <i>anterior midgut primordium</i> connect the <i>amnioproctodeal invagination</i> emerges at the posterior tip of the <i>ventral furrow</i> and around the invaginating <i>posterior midgut primordium</i> from the <i>ectodermal layer</i> 	4A, J 4F [1] 4A [5]
	16:00 h	25.6%	<ul style="list-style-type: none"> the <i>ectodermal layer</i> differentiates into the <i>ventral epidermal primordium</i> the <i>lateral epidermal primordia</i> the <i>abdomen</i> withdrawal from the posterior pole reaches a momentary standstill (<i>repeated withdrawal</i>) 	4A, (C), G as above as above 4A; (1C)
III – 9	16:30 h	26.4%	<ul style="list-style-type: none"> the posterior tip of the <i>germband</i> continues anteriad elongation along the dorsal side with moderate speed the <i>stomodeal invagination</i> turns into the <i>stomodeum</i>, which becomes the anteromedial part of the <i>digestive tract</i> (<i>digestive system formation</i>) the <i>cephalic furrow</i> levels out the <i>ventral furrow</i> levels out the first <i>neuroblasts</i> begin segregating from the <i>ventral epidermal primordium</i> the <i>amnioproctodeal invagination</i> differentiates into the <i>proctodeum</i>, which starts internalizing and becomes the posteromedial part of the <i>digestive tract</i> (<i>digestive system formation</i>) the <i>proctodeal opening</i>, which becomes the posterior part of the <i>digestive tract</i> (<i>digestive system formation</i>) 	4A, D, E, H, J 4A [3], F 4A, G 4A, (H, I) 4G [1,2,3] 4A, C, (H) as above as above
	17:00 h	27.2%	<ul style="list-style-type: none"> the <i>proctodeum</i> completes internalizing 	4A, H
	17:30 h	28.0%	<ul style="list-style-type: none"> the <i>proctodeal opening</i> changes from a dorsal orientation to an anterior orientation 	4A [6], H, (J)
III – 10	18:00 h	28.8%	<ul style="list-style-type: none"> the posterior tip of the <i>germband</i> continues anteriad elongation along the dorsal side with low speed 	4B, D, E
	19:00 h	30.4%	<ul style="list-style-type: none"> the <i>ventral mesectoderm</i> emerges ventrally along the <i>thorax</i> and <i>abdomen</i> from the <i>ventral epidermal primordium</i> the <i>head</i> begins withdrawing from the anterior pole (<i>repeated withdrawal</i>) 	4I, (J) 4B, J, I; (1C [5])
	21:00 h	33.6%	<ul style="list-style-type: none"> the <i>optic lobe primordium</i> completes mitotic divisions 	4B, J, (I)
III – 11	22:00 h	35.2%	<ul style="list-style-type: none"> the posterior tip of the <i>germband</i> completes anteriad elongation and remains in a quiescent position <ul style="list-style-type: none"> the <i>amnioserosa</i> completes folding (<i>extra-embryonic membrane folding</i>) the <i>yolk sac</i> completes migration from the medio-dorsal surface to the interior regions the <i>head</i> withdrawal from the anterior pole reaches a momentary standstill (<i>repeated withdrawal</i>) the <i>abdomen</i> continues withdrawing after the momentary standstill (<i>repeated withdrawal</i>) 	4B 4B, (H, J, I) 4B, (H, J, I) 4B; (1C [6]) 4B; (1C [6])
	24:00 h	38.4%	<ul style="list-style-type: none"> the <i>gnathal protuberances</i> emerge from the <i>gnathocephalon</i> (<i>metamerization</i>) 	4B
IV – germband retraction – stage 12 (1 total) – 24:30 h to 32:00 h (07:30 h total) – 39.2% to 51.2% (12.0% total) – Figure 5				
IV – 12	24:30 h	39.2%	<ul style="list-style-type: none"> the posterior tip of the <i>germband</i> begins posteriad retraction along the dorsal side <ul style="list-style-type: none"> the <i>amnioserosa</i> begins unfolding again (<i>extra-embryonic membrane folding</i>) the <i>yolk sac</i> begins protruding towards the medio-dorsal surface 	5A 5A 5A
	26:00 h	41.6%	<ul style="list-style-type: none"> the <i>dorsal epidermal primordia</i> emerge laterally from the <i>lateral epidermal primordia</i> 	5A, B [1]
	26:30 h	42.4%	<ul style="list-style-type: none"> the <i>clypeolabrum</i> emerges antero-dorsally from the <i>procephalon</i> 	5A, B
	27:30 h	44.0%	<ul style="list-style-type: none"> the <i>abdomen</i> withdrawal at the posterior pole reaches a relative maximum and begins reversing (<i>repeated withdrawal</i>) 	5A, B; (1C)
	28:30 h	45.6%	<ul style="list-style-type: none"> the <i>intersegmental grooves</i> arise and separate the <i>thorax</i> into three and the <i>abdomen</i> into nine segments (<i>metamerization</i>) 	5A, B [2,3,4]
	30:30 h	48.8%	<ul style="list-style-type: none"> the <i>clypeolabrum</i> becomes thinner and more pronounced the <i>proctodeal opening</i> becomes posterior-dorsally located 	5A, B 5A [1]
	31:30 h	50.4%	<ul style="list-style-type: none"> the <i>amnioserosa</i> completes unfolding and covers the <i>embryo</i> and <i>yolk sac</i> medio-dorsally (<i>extra-embryonic membrane folding</i>) the <i>yolk sac</i> completes protruding towards the medio-dorsal surface 	5A 5A
V – dorsal closure – stages 13 to 15 (3 total) – 32:00 to 45:00 h (13:00 h total) – 51.2% to 72.0% (20.8% total) – Figure 6				
V – 13	32:00 h	51.2%	<ul style="list-style-type: none"> the posterior tip of the <i>germband</i> completes posteriad retracting the <i>ventral epidermal primordium</i> and <i>lateral epidermal primordia</i> of the <i>thorax</i> begin anteriad migration (<i>head involution</i>) the <i>dorsal epidermal primordia</i> begin dorsolaterad migration over the <i>amnioserosa</i> (<i>dorsal zippering</i>) <ul style="list-style-type: none"> the <i>amnioserosa</i> starts folding again (<i>extra-embryonic membrane folding</i>) 	6A 6A, (D) 6A, (D), G 6A, (D), G
	33:30 h	53.6%	<ul style="list-style-type: none"> the <i>anterior dorsal gap</i> arises between the <i>procephalon</i> and the <i>amnioserosa</i> the <i>dorsal folds</i> emerge dorsally from the <i>gnathocephalon</i> 	6A [1], C, D 6D
V – 14	34:30 h	55.2%	<ul style="list-style-type: none"> the <i>clypeolabrum</i> turns from an antero-dorsal to an antero-ventral orientation (<i>head involution</i>) <ul style="list-style-type: none"> the <i>head</i> continues withdrawing after the momentary standstill (<i>repeated withdrawal</i>) 	6A, (D), F 6A, C, D, F; (1C [7])

		<ul style="list-style-type: none"> the <i>dorsal folds</i> fuse along the <i>anterior dorsal gap</i> and begin antieriad migration (<i>head involution</i>) the <i>dorsal epidermal primordia</i> begin with anteromedial and posteromedial fusion (<i>dorsal zippering</i>) the <i>abdomen</i> withdrawal at the posterior pole reaches a relative minimum and begins re-reversing (<i>repeated withdrawal</i>) 	6A, D 6A, G [1,2] 6A, D, G; (1C [7])	
35:00 h	56.0%	<ul style="list-style-type: none"> the <i>stomodeum</i> begins retracting (<i>head involution</i>) the <i>gnathal protuberances</i> migrate anterior and differentiate into <ul style="list-style-type: none"> the <i>mandibular buds</i> (<i>head involution</i>) the <i>maxillary buds</i> (<i>head involution</i>) the <i>labial buds</i> (<i>head involution</i>) 	6A, C, E [3] 6A, C 6A [3], C [1], E [1] 6A 6A	
36:30 h	58.4%	<ul style="list-style-type: none"> the <i>labial buds</i> migrate ventrally (<i>head involution</i>) the <i>midgut</i> originates from the fusion of the <i>anterior midgut primordium</i> and the <i>posterior midgut primordium</i>, which becomes the medial part of the <i>digestive tract</i> (<i>digestive system formation</i>) <ul style="list-style-type: none"> the <i>amnioserosa</i> completes folding and begins internalizing together with the <i>yolk sac</i> into the <i>midgut</i> (<i>extra-embryonic membrane folding</i>) 	6C 6A [2], (G) 6A, (D), G	
37:00 h	59.2%	<ul style="list-style-type: none"> the <i>labial buds</i> fuse ventrally (<i>head involution</i>) 	6A [4], C [2], E [2]	
V – 15	38:00 h	60.8%	<ul style="list-style-type: none"> the <i>abdomen</i> withdrawal at the posterior pole reaches the absolute maximum (<i>repeated withdrawal</i>) <ul style="list-style-type: none"> the posterior tip of the <i>germband</i> begins flipping into the posterior pole the <i>dorsal epidermal primordia</i> complete anteromedial and posteromedial fusion (<i>dorsal zippering</i>) <ul style="list-style-type: none"> the <i>dorsal epidermal primordia</i> begin with medial fusion (<i>dorsal zippering</i>) the <i>antennomaxillary complexes</i> originate from the fusion of the <i>maxillary buds</i> and the antero-ventral region of the <i>procephalon</i> (<i>head involution</i>) <ul style="list-style-type: none"> the <i>clypeolabrum</i> begins retracting (<i>head involution</i>) the <i>mandibular buds</i> begin retracting (<i>head involution</i>) the <i>anterior dorsal gap</i> levels out 	6A; (1C) 6A, B, (D) 6A, G [1,2] 6A, G [3,4] 6A [5], C [3], E [4], F 6A, C, D, E, F, (G) 6A, C [1], E [1], F 6A, C, (D)
	38:30 h	61.6%	<ul style="list-style-type: none"> the fused <i>labial buds</i> begin retracting (<i>head involution</i>) the <i>antennomaxillary complexes</i> begin antieriad migration (<i>head involution</i>) 	6B, C [2], E [2] 6B, E [4], F
	39:30 h	63.2%	<ul style="list-style-type: none"> the fused <i>dorsal folds</i> cover the <i>procephalon</i> and continue antieriad migration (<i>head involution</i>) 	6B, D, E [5]
	40:30 h	64.8%	<ul style="list-style-type: none"> the <i>head</i> withdrawal at the anterior pole reaches the absolute maximum and begin reversing (<i>repeated withdrawal</i>) the <i>abdomen</i> withdrawal at the posterior pole begins reversing (<i>repeated withdrawal</i>) the fused <i>dorsal folds</i> cover the retracting <i>clypeolabrum</i> and continue antieriad migration (<i>head involution</i>) 	6B, D; (1C [8]) 6B, D; (1C [8]) 6B, D
	41:30 h	66.4%	<ul style="list-style-type: none"> the <i>intersegmental grooves</i> of the <i>thorax</i> and the <i>abdomen</i> transiently level out (<i>metamerization</i>) 	6B
	43:30 h	69.6%	<ul style="list-style-type: none"> the <i>head</i> withdrawal at the anterior pole partially reverses (<i>repeated withdrawal</i>) the <i>abdomen</i> withdrawal at the posterior pole partially reverses (<i>repeated withdrawal</i>) 	6B, D; (1C [9]) 6B, D; (1C [9])
	44:00 h	70.4%	<ul style="list-style-type: none"> the <i>dorsal epidermal primordia</i> complete migration dorsolaterally over the <i>amnioserosa</i> (<i>dorsal zippering</i>) <ul style="list-style-type: none"> the <i>amnioserosa</i> completes internalizing together with the <i>yolk sac</i> into the <i>midgut</i> (end of <i>extra-embryonic membrane folding</i>) 	6D 6D
	44:30 h	71.2%	<ul style="list-style-type: none"> the <i>clypeolabrum</i>, the <i>stomodeum</i>, the fused <i>labial buds</i> and the <i>mandibular buds</i> complete retraction (<i>head involution</i>) the <i>antennomaxillary complexes</i> complete antieriad migration (<i>head involution</i>) the posterior tip of the <i>germband</i> completes flipping into the posterior pole <ul style="list-style-type: none"> the <i>proctodeal opening</i> becomes posterior located 	6B 6B 6B 6B
VI – muscular movement – stages 16 to 17 (2 total) – 45:00 h to 62:30 h (17:30 h total) – 72.0% to 100.0% (28.0% total) – Figure 7				
VI – 16	45:00 h	72.0%	<ul style="list-style-type: none"> the <i>dorsal epidermal primordia</i> complete medial fusion and turn into the <i>dorsal epidermis</i> (end of <i>dorsal zippering</i>) <ul style="list-style-type: none"> the <i>ventral epidermal primordium</i> completes antieriad migration and turns into the <i>ventral epidermis</i> (end of <i>head involution</i>) and <i>lateral epidermal primordia</i> complete antieriad migration and turn into the <i>lateral epidermis</i> (end of <i>head involution</i>) the <i>antennomaxillary complexes</i> fuse anterior (end of <i>head involution</i>) the <i>intersegmental grooves</i> arise again (end of <i>metamerization</i>) the posterior tip of the <i>ventral cord</i>, which extends to the 8th segment of the <i>abdomen</i>, begins shortening 	7A, (C) 7A, C 7A, C 7A, C 7A, (B), C 7A, B
	49:00 h	78.4%	<ul style="list-style-type: none"> the fused <i>dorsal folds</i> complete antieriad migration and turn into the <i>dorsal pouch</i> (end of <i>head involution</i>) <ul style="list-style-type: none"> the <i>atrium</i> forms anteriorly through contribution of the <i>clypeolabrum</i>, the fused <i>antennomaxillary complexes</i>, the <i>mandibular buds</i> and the fused <i>labial buds</i> (<i>digestive system formation</i>) the <i>digestive tract</i> originates through consecutive connection of the <i>atrium</i>, the <i>stomodeum</i>, the <i>midgut</i>, the <i>proctodeum</i> and the <i>proctodeal opening</i> (end of <i>digestive system formation</i>) the posterior tip of the <i>ventral cord</i> shortens to the 7th segment of the <i>abdomen</i> 	7C 7A, C 7A, C 7A, C
	52:00 h	83.2%	<ul style="list-style-type: none"> the posterior tip of the <i>ventral cord</i> shortens to the 6th segment of the <i>abdomen</i> 	7A, C
VI – 17	54:30 h	87.2%	<ul style="list-style-type: none"> the posterior tip of the <i>ventral cord</i> shortens to the 5th segment of the <i>abdomen</i> <ul style="list-style-type: none"> the <i>head</i> withdrawal at the anterior pole nearly completely reverses (end of <i>repeated withdrawal</i>) the <i>abdomen</i> withdrawal at the posterior pole nearly completely reverses (end of <i>repeated withdrawal</i>) 	7A, B 7A; (1C) 7A; (1C)
	56:00 h	89.6%	<ul style="list-style-type: none"> the <i>embryo</i> begins with regular muscular movement 	7B
	58:00 h	92.8%	<ul style="list-style-type: none"> the posterior tip of the <i>ventral cord</i> completes shortening between the 4th and 5th segment of the <i>abdomen</i> 	7C
Beyond	62:30 h	100.0%	<ul style="list-style-type: none"> the <i>embryo</i> completes embryonic development, hatches and turns into the larva 	7D

¹begins in DS0002 already during stage 6. Completes in DS0003, DS0004 and DS0005 not until the beginning of stage 8. Proliferation may not be developmentally bound to the emergence of the *anterior midgut primordium*.

²begins in DS0002 already at the beginning of stage 7 and in DS0003, DS0004 and DS0005 not until the beginning of stage 8. Completes in DS0003, DS0004 and DS0005 during stage 8. Proliferation may not be developmentally bound to the emergence of the *posterior plate*.

Table 2

Table 2 – Overview of embryonic structures in alphabetical order. This table also serves as a glossary – all structural terms that written in *italics* throughout the publication are defined in this table. Figure references in parentheses indicate figures in which the respective structure can be seen as a spin-off.

structure	embryogenetic event						description / rationale	figure	reference / comment
<i>abdomen</i>	-	II	III	IV	V	VI	Large tissue region differentiating posteriorly from the <i>cellular blastoderm</i> at the beginning of stage 7. Constitutes together with the <i>head</i> and the <i>thorax</i> the <i>embryo</i> . Composes together with the <i>gnathocephalon</i> and the <i>thorax</i> the <i>germband</i> and becomes divided into nine segments during stage 12 as part of <i>metamerization</i> process.	3C, D, (E), (F), (G); 4A, B, I, (J); 5A, B, 6A, B, D, G; 7A, B, C	Adopted from <i>Drosophila</i> [40,71].
<i>amnioproctodeal invagination</i> (transient)	-	-	III	-	-	-	Tubular structure emerging at the posterior tip of the <i>ventral furrow</i> and around the invaginating <i>posterior midgut primordium</i> from the <i>ectodermal layer</i> during stage 8. Differentiates into the <i>proctodeum</i> and the <i>proctodeal opening</i> at the beginning of stage 9.	4A, C, (H)	Adopted from <i>Drosophila</i> [40,72,73], <i>Megaselia</i> [21,51] and <i>Clogmia</i> [22]. The term ‘proctodeal invagination’ is synonymously used [74,75].
<i>amnioserosa</i> (transient)	-	II	III	IV	V	-	Extra-embryonic membrane differentiating medio-dorsally from the <i>cellular blastoderm</i> at the beginning of stage 7. Unfolds and folds two times without any mitotic division during stages 7 to 14 as part of the <i>extra-embryonic membrane folding</i> process. Internalizes together with the <i>yolk sac</i> into the <i>midgut</i> during stage 15 after the <i>extra-embryonic membrane folding</i> process has ended.	3C, D, (E, G), 4A, B, H, (J, I); 5A; 6A, D, G	Adopted from <i>Drosophila</i> [40,52,73,76]. Common term for the extra-embryonic membrane in cyclorhaphan flies [77].
<i>antennomaxillary complexes</i>	-	-	-	-	V	VI	Bilateral structures originating antero-laterally from the fusion of the <i>maxillar buds</i> and the antero-ventral region of the <i>procephalon</i> at the beginning of stage 15. Fuse at the beginning of stage 16. Contribute to the formation of the <i>atrium</i> during stage 16.	6A [5], B, C [3], E [4], F; 7A, C	Adopted from <i>Drosophila</i> [40,78,79].
<i>anterior dorsal gap</i> (transient)	-	-	-	-	V	-	Transversal groove arising between the <i>procephalon</i> and the <i>amnioserosa</i> during stage 13. Migration starting point for the fused <i>dorsal folds</i> . Levels out during stage 15.	6A [1], C, D	Adopted from <i>Drosophila</i> [40].
<i>anterior midgut primordium</i> (transient)	-	II	III	IV	V	-	Endodermal cell cluster emerging at the anterior tip of the <i>ventral furrow</i> at the beginning of stage 7 as part of the <i>germ layer specification</i> process. Internalizes at the beginning of stage 8. Fuses with the <i>posterior midgut primordium</i> to form the <i>midgut</i> during stage 14.	3C, E, F; 4A [2], F [1]; 6A [3], (G)	Adopted from <i>Drosophila</i> [40,73,80] and <i>Megaselia</i> [19]. The terms ‘anterior midgut rudiment’ and ‘anterior midgut anlage’ are synonymously used [40,81].
<i>atrium</i>	-	-	-	-	-	VI	Mouth cavity forming anteriorly through dorsal contribution of the <i>clypeolabrum</i> , antero-lateral contribution of the <i>antennomaxillary complexes</i> , ventrolateral contribution of the <i>mandibular buds</i> and ventral contribution of the fused <i>labial buds</i> during stage 16 after the <i>digestive system formation</i> process has ended. Is connected to the posteriorly located <i>stomodeum</i> and resembles the anterior region of the fully developed <i>digestive tract</i> .	7A, C	Adopted from <i>Drosophila</i> [40,82]. The term ‘cibarium’ is synonymously used [40]. The term ‘atrium’ is occasionally also used for substructures of the heart [83].
<i>blastoderm nuclei</i> (transient)	I	-	-	-	-	-	Somatic, superficially located and uniformly distributed nuclei deriving from <i>zygotic nuclei</i> at the beginning of stage 4 after the <i>peripheral migration</i> process has ended. Constitute together with the <i>pole buds</i> the <i>syncytial blastoderm</i> .	2B, D, E; 3A	Established for <i>Ceratitis</i> [38,39]. Usage similar for <i>Drosophila</i> [40,84,85]. The term ‘somatic buds’ is synonymously used [40,86].
<i>cellular blastoderm</i> (transient)	-	II	-	-	-	-	Uniform superficial cell layer deriving from the <i>syncytial blastoderm</i> at the beginning of stage 6 after the <i>cellularization</i> process has ended. Envelops the <i>yolk sac</i> . Gives rise to the <i>ventral furrow</i> at the beginning of stage 6 and the <i>cephalic furrow</i> during stage 6. Differentiates into the anterior <i>head</i> , medio-ventral <i>thorax</i> , posterior <i>abdomen</i> and the medio-dorsal <i>amnioserosa</i> at the beginning of stage 7.	3A, B, (E, G)	Established for <i>Ceratitis</i> [25,38,39]. Usage similar for <i>Drosophila</i> [40,84,87,88].
<i>cephalic furrow</i> (transient)	-	II	III	-	-	-	Transversal cleft arising anteromedially in the <i>cellular blastoderm</i> during stage 6. Has a slight antero-ventral / postero-dorsal tilt. Deepens at the beginning of stage 7 and separates the anteriorly located <i>head</i> from the postero-ventrally located <i>thorax</i> and postero-dorsally located <i>amnioserosa</i> . Levels out at the beginning of stage 9.	3B [1], E [1], (F, G); 4A, G	Adopted from <i>Drosophila</i> [40,73,89,90] and <i>Megaselia</i> [21,51].
<i>clypeolabrum</i>	-	-	-	IV	V	VI	Large bulge emerging antero-dorsally from the <i>procephalon</i> during stage 12. Changes from an antero-dorsal to an antero-ventral orientation at the beginning of stage 14. Retracts posteriorly gets covered by the fused <i>dorsal folds</i> during stage 15 as part of the <i>head involution</i> process. Contributes to the formation of the <i>atrium</i> during stage 16.	5A, B; 6A, B, C, D, E, F, (G)	Adopted from <i>Drosophila</i> [40,73,91] and <i>Megaselia</i> [21].
<i>digestive tract</i>	-	-	-	-	-	VI	Large tubular body captivity originating through consecutive connection of the <i>atrium</i> , the <i>stomodeum</i> , the <i>midgut</i> , the <i>proctodeum</i> and the <i>proctodeal opening</i> during stage 16 after the <i>digestive system formation</i> process has ended.	7A, C	Adopted from <i>Drosophila</i> [92,93].
<i>dorsal epidermal primordia</i> (transient)	-	-	-	IV	V	VI	Bilateral superficial ectodermal cell layer emerging laterally from the <i>lateral epidermal primordia</i> during stage 12. Both flanks migrate dorsolaterally over the <i>amnioserosa</i> during stages 13 to 15. Turn into the <i>dorsal epidermis</i> at the beginning of stage 16 after the <i>dorsal zipping</i> process has ended.	5A, B [1]; 6A, D, G [1,2,3,4]; 7A, (C)	Adopted from <i>Drosophila</i> [40,94].

dorsal epidermis	-	-	-	-	-	VI	Large ectodermal cell layer deriving from both flanks of the <i>dorsal epidermal primordia</i> at the beginning of stage 16 after the <i>dorsal zippering</i> process has ended.	7A, (C)	Adopted from <i>Drosophila</i> [40,95,96].
dorsal folds (transient)	-	-	-	-	V	-	Protuberance emerging dorsally from the <i>gnathocephalon</i> at the anterior region of the <i>anterior dorsal gap</i> during stage 13. Migrates over and covers the <i>procephalon</i> and <i>clypeolabrum</i> during stage 14 as part of the <i>head involution</i> process. Turns into the <i>dorsal pouch</i> during stage 16 after the <i>head involution</i> process has ended.	6A, B, D, E [5]; 7C	Adopted from <i>Drosophila</i> [40,97]. The term ‘dorsal ridge’ is sometimes synonymously used in <i>Drosophila</i> [40], <i>Megaselia</i> [21] and <i>Clogmia</i> [22], sometimes it is used to describes the bilaterally emerging primordia of the fold [40].
dorsal plate (transient)	-	II	III	-	-	-	Discoid cell cluster deriving postero-dorsally from the <i>posterior plate</i> during stage 7. Carries the <i>pole cells</i> at the beginning of stage 8 as part of the <i>germ cell dynamics</i> process. Invaginates and turns into the <i>posterior midgut primordium</i> during stage 8 as part of the <i>germ layer specification</i> process.	3C [4], (D, E, G), H; 4A, C [1,2], H	Adopted from <i>Drosophila</i> [40,98], <i>Megaselia</i> [21] and <i>Clogmia</i> [22].
dorsal pouch	-	-	-	-	V	VI	Pocket-like structure deriving antero-dorsally from the fused <i>dorsal folds</i> during stage 16 after the <i>head involution</i> process has ended.	7C	Adopted from <i>Drosophila</i> [40,99].
ectodermal layer (transient)	-	II	III	-	-	-	Superficial cell layer differentiating ventrally at the <i>thorax</i> and <i>abdomen</i> from the <i>ventral furrow</i> during stage 7 as part of the <i>germ layer specification</i> process. Differentiates into the <i>amnioproctodeal invagination</i> , the <i>ventral epidermal primordium</i> and the <i>lateral epidermal primordium</i> during stage 8.	3C, E, F; 4A, (C), G	Adopted from <i>Drosophila</i> [40].
embryo	-	II	III	IV	V	VI	Entirety of the tissue regions differentiating from the <i>cellular blastoderm</i> at the beginning of stage 7 that become part of the larva at the end of stage 17. Consists of the <i>head</i> , the <i>thorax</i> and the <i>abdomen</i> .	3C, D, E, (G); 5A; 7B, D	Adopted from <i>Drosophila</i> [40].
germband	-	II	III	IV	V	VI	Later on metameric part of the <i>embryo</i> . Composes of the <i>gnathocephalon</i> , the <i>thorax</i> and the <i>abdomen</i> .	3C, E, F, G; 4A, B, D, E, H, J; 5A; 6A, B, (D)	Adopted from <i>Drosophila</i> [40,100].
gnathal protuberances (transient)	-	-	-	IV	V	-	Small bulges emerging from the <i>gnathocephalon</i> during stage 12. Differentiate into the anteriorly located <i>maxillary buds</i> , the medially located <i>mandibular buds</i> and the posteriorly located <i>labial buds</i> during stage 14.	4B; 6A, C	Adopted from <i>Drosophila</i> [40,101]. The term ‘gnathal buds’ is synonymously used [40,102].
gnathocephalon	-	II	III	IV	V	VI	Later on metameric subregion forming as the postero-ventral part of the <i>head</i> during stage 7. Composes together with the <i>thorax</i> and the <i>abdomen</i> the <i>germband</i> and becomes divided into three segments during stage 11 as part of <i>metamerization</i> process. Gives rise to the <i>gnathal protuberances</i> during stage 12.	3C, E, F, G; 4B; (6A, C, D)	Adopted from <i>Drosophila</i> [40,103].
head	-	II	III	IV	V	VI	Large tissue region developing anteriorly from the <i>cellular blastoderm</i> at the beginning of stage 7. Constitutes together with the <i>thorax</i> and the <i>abdomen</i> the <i>embryo</i> . Remodels into the non-metameric <i>procephalon</i> and the later on metameric <i>gnathocephalon</i> during stage 7. Internalized during the <i>head involution</i> process.	3C, D, (E), F, (G); 4A, B, J, I; 6A, B, C, D, F; 7A	Adopted from <i>Drosophila</i> [40,104].
intersegmental grooves	-	-	-	IV	V	VI	Transversal grooves arising during stage 12 as part of the <i>metamerization</i> process. Separate the <i>thorax</i> into three and the <i>abdomen</i> into nine segments. Transiently level out during stage 15 and arise again at the beginning of stage 16.	5A, B [2,3,4]; 6B; 7A, (B), C	Adopted from <i>Drosophila</i> [40,105], <i>Megaselia</i> [21] and <i>Clogmia</i> [22]. The term ‘intersegmental furrows’ is synonymously used [40].
labial buds	-	-	-	-	V	VI	Bilateral appendage primordia differentiating from the <i>gnathal protuberances</i> during stage 14. Fuse ventrally before retracting during stage 15 as part of the <i>head involution</i> process. Contribute to the formation of the <i>atrium</i> during stage 16.	6A [4], 6B, C [2], E [2]; (7A, C)	Adopted from <i>Drosophila</i> [40,106].
lateral epidermal primordia (transient)	-	-	III	IV	V	VI	Bilateral superficial ectodermal cell layer differentiating ventrolaterally from the <i>ectodermal layer</i> during stage 8. Comprises of tightly packed cells with small nuclei. Give rise to the <i>dorsal epidermal primordia</i> during stage 13 and turns into the <i>lateral epidermis</i> at the beginning of stage 16.	4A, (C), G; (5A, B [1]); 6A, (D); 7A, (C)	Adopted from <i>Drosophila</i> [107,108]. The term ‘lateral epidermal anlagen’ is synonymously used [40].
lateral epidermis	-	-	-	-	-	VI	Large bilateral ectodermal cell layer deriving from the <i>lateral epidermal primordia</i> at the beginning of stage 16.	7A, (C)	Adopted from <i>Drosophila</i> [40,109,110].
mandibular buds	-	-	-	-	V	VI	Appendage primordia differentiating bilaterally from the <i>gnathal protuberances</i> during stage 14. Retract during the <i>head involution</i> process. Contribute to the formation of the <i>atrium</i> during stage 16.	6A [2], B, C [1], E [1], F; 7A, C	Adopted from <i>Drosophila</i> [40].
maxillary buds	-	-	-	-	V	-	Bilateral appendage primordia differentiating from the <i>gnathal protuberances</i> during stage 14. Fuse with the anteroventrolateral parts of the <i>procephalon</i> to form the <i>antennomaxillary complexes</i> at the beginning of stage 15.	6A [5], C [3], E [4], F	Adopted from <i>Drosophila</i> [40,106].
mesodermal layer	-	II	-	-	-	-	Internal cell layer differentiating ventrally at the <i>thorax</i> and <i>abdomen</i> by invagination of cells along the <i>ventral furrow</i> during stage 7 as part of the <i>germ layer specification</i> process. Involved in mesoderm formation (Supplementary Table X).	3C, E, F	Adopted from <i>Drosophila</i> [40]. The terms ‘mesodermal primordium’ and ‘mesodermal anlage’ are synonymously used [40].
midgut	-	-	-	-	V	VI	Internal endodermal tubular body cavity originating from the fusion of the <i>anterior midgut primordium</i> and the <i>posterior midgut primordium</i> during stage 14. Is connected to the anteriorly located <i>stomodaeum</i> and the posterior	6A [3], (D), (G); (6D); (7A, C)	Adopted from <i>Drosophila</i> [40,73,81,92,93].

							located <i>proctodeum</i> and resembles the medial part of the fully developed <i>digestive tract</i> .		
<i>neuroblasts</i>	-	-	III	-	-	-	Large nuclei segregating from the <i>ventral epidermal primordium</i> at the beginning of stage 9. Involved in neurogenesis (Supplementary Table X).	4G [1,2,3]	Adopted from <i>Drosophila</i> [40,111].
<i>optic lobe primordium</i>	-	-	III	-	-	-	Longitudinal cell layer emerging dorsally at the <i>procephalon</i> during stage 8. Involved in neurogenesis (Supplementary Table X).	(3D); 4A, J, (I)	Adopted from <i>Drosophila</i> [40,112].
<i>pole buds</i> (transient)	I	-	-	-	-	-	Small bulges emerging at the posterior tip of the <i>zygote</i> from the <i>zygotic nuclei</i> during stage 3 as part of the <i>germ cell dynamics</i> process. Turn into the <i>pole cells</i> during stage 4.	2B, C, F, G	No proper term ('cytoplasmic protrusions') in <i>Ceratitis</i> -specific literature [39]. Adopted from <i>Drosophila</i> [40,113,114] and <i>Megaselia</i> [21]. The term 'polar buds' is synonymously used [40,113,115].
<i>pole cells</i> (transient)	I	II	III	-	-	-	Future germ cells deriving at the posterior tip of the <i>syncytial blastoderm</i> from the <i>pole buds</i> and undergo two mitotic divisions during stage 4 as part of the <i>germ cell dynamics</i> process. Adhere to the <i>posterior plate</i> , which forms during stage 6, and to the <i>dorsal plate</i> , which forms during stage 7. Internalize during stage 8 after the <i>germ cell dynamics</i> process has ended.	2B [1], F, G; (3C [4], D, E, G, H); (4A, C [1,2], H)	Established for <i>Ceratitis</i> [39]. Usage similar for <i>Drosophila</i> [40,113,114] and <i>Megaselia</i> [21].
<i>posterior midgut primordium</i> (transient)	-	-	III	IV	V	-	Endodermal cell cluster deriving from the <i>dorsal plate</i> during stage 8 as part of the <i>germ layer specification</i> process. Fuses with the <i>anterior midgut primordium</i> to form the <i>midgut</i> during stage 14 as part of the <i>digestive system formation</i> process.	4A, C [1,2], H; 6A [3], (G)	Established for <i>Ceratitis</i> [39]. Usage similar for <i>Drosophila</i> [40,72,116] and <i>Megaselia</i> [19]. The terms 'posterior midgut rudiment' and 'posterior midgut anlage' are synonymously used [39,40,81].
<i>posterior plate</i> (transient)	-	II	-	-	-	-	Discoid posterior cell cluster to which the <i>pole cells</i> adhere emerging at the posterior tip of the <i>cellular blastoderm</i> during stage 6. Turns into the <i>dorsal plate</i> during stage 7.	3B, C [4], (D, E, G), H	No proper term ('blastoderm cell plate') in <i>Ceratitis</i> -specific literature [39]. Adopted from <i>Drosophila</i> [40,117] and <i>Clogmia</i> [22].
<i>procephalon</i>	-	II	III	IV	V	VI	Non-metameric lobe-like subregion forming as the antero-ventral and dorsal part of the <i>head</i> during stage 7. Gives rise to the <i>clypeolabrum</i> during stage 12 and partially fuses with the <i>maxillary buds</i> to form the <i>antennomaxillary complexes</i> during stage 15.	3C, D, E, F, G; (4A, F); (5A, B); 6A, (B), C, (D), E, F	Adopted from <i>Drosophila</i> [40,118].
<i>proctodeal opening</i>	-	-	III	IV	V	VI	Oval superficial ectodermal opening differentiating at the posterior tip of the germband from the <i>amnioproctodeal invagination</i> at the beginning of stage 9 as part of the <i>digestive system formation</i> process. Changes from a dorsal to an anterior orientation during stage 9. Flips into the posterior pole during stage 15. Is connected to the anteriorly located <i>proctodeum</i> and resembles the posterior part of the fully developed <i>digestive tract</i> .	4A, C, H, (J); (7A, C)	Adopted from <i>Drosophila</i> [40,119].
<i>proctodeum</i>	-	-	III	IV	V	VI	Internal ectodermal tubular body cavity differentiating at the posterior tip of the germband from the <i>amnioproctodeal invagination</i> at the beginning of stage 9 as part of the <i>digestive system formation</i> process. Becomes internalized during stage 9. Is connected to the anteriorly located <i>midgut</i> and the posteriorly located <i>proctodeal opening</i> and resembles the posteromedial part of the fully developed <i>digestive tract</i> .	4A, C, H; (7A, C)	Adopted from <i>Drosophila</i> [40,75,120] and <i>Megaselia</i> [18,121]. The term 'hindgut' and 'future hindgut' are synonymously used [40,122].
<i>small and large lateral cell stripes</i> (transient)	-	II	-	-	-	-	Bilateral cell layers undergoing mitotic division at the lateral sides of the <i>head</i> at the beginning of stage 7.	3C [2,3], (D), G; (4A)	Convenient term.
<i>stomodeal cell plate</i> (transient)	-	-	III	-	-	-	Oval cell layer emerging antero-ventrally from the <i>procephalon</i> at the beginning of stage 8. Turns into the <i>stomodeal invagination</i> during stage 8.	(3E, F); 4A [1], F	Adopted from <i>Drosophila</i> [40]. The term 'stomodeal plate' is synonymously used [73].
<i>stomodeal invagination</i> (transient)	-	-	III	-	-	-	Oval superficial ectodermal opening deriving from the <i>stomodeal cell plate</i> during stage 8. Turns into the <i>stomodeum</i> at the beginning of stage 9.	(3E, F); 4A, F	Adopted from <i>Drosophila</i> [40,73,123,124], <i>Megaselia</i> [21] and <i>Clogmia</i> [22].
<i>stomodeum</i>	-	-	III	IV	V	VI	Internal ectodermal tubular body cavity deriving from the <i>stomodeal invagination</i> the beginning of stage 9 as part of the <i>digestive system formation</i> process. Retracts during stage 14. Is connected to the anteriorly located <i>atrium</i> and the posteriorly located <i>midgut</i> and resembles the anteromedial part of the fully developed <i>digestive tract</i> .	4A, C, E [3], F; 6B; (7A, C)	Adopted from <i>Drosophila</i> [40,73,123,124] and <i>Megaselia</i> [21]. The term 'foregut' is synonymously used [40,124].
<i>syncytial blastoderm</i> (transient)	I	-	-	-	-	-	Uniform superficial nuclei layer deriving from the <i>zygote</i> at the beginning of stage 4 after the <i>peripheral migration</i> process has ended. Envelops the <i>yolk</i> . Undergoes two mitotic division cycles during stage 4. Turns into the <i>cellular blastoderm</i> at the beginning of stage 6 after the <i>cellularization</i> process has ended.	2B, (F), (G); 3A	Established for <i>Ceratitis</i> [25,38,39]. Usage similar for <i>Drosophila</i> [40,125,126].
<i>thorax</i>	-	II	III	IV	V	VI	Large tissue region differentiating medio-ventrally from the <i>cellular blastoderm</i> at the beginning of stage 7. Constitutes together with the <i>head</i> and the <i>abdomen</i> the <i>embryo</i> . Composes together with the <i>gnathocephalon</i> and the <i>abdomen</i> the <i>germband</i> and becomes divided into three segments during stage 12 as part of <i>metamerization</i> process.	3C, D, (E, F, G); (4I, J); 5A, B [2,3,4]; 6A, (D); 7A, C	Adopted from <i>Drosophila</i> [40,127,128].

<i>ventral cord</i>	-	-	-	-	-	VI	Rope ladder-like longitudinal part of the central nervous system becoming visible during stage 16. Spans initially from the third segment of the <i>thorax</i> to the 8 th segment of the abdomen before shortening posteriorly.	7A, B, C	Adopted from <i>Drosophila</i> [40,129]. The term 'ventral nerve cord' is synonymously used [40,129–131].
<i>ventral epidermal primordium</i> (transient)	-	-	III	IV	V	VI	Superficial ectodermal cell layer differentiating ventrally from the <i>ectodermal layer</i> during stage 8. Comprises of loosely arranged cells with large nuclei. Segregates the <i>neuroblasts</i> at the beginning of stage 9. Turns into the <i>ventral epidermis</i> at the beginning of stage 16.	4A, (C), G, (I, J); 6A, (D); 7A, C	Adopted from <i>Drosophila</i> [40]. The term 'ventral epidermal anlagen' is synonymously used [40].
<i>ventral epidermis</i>	-	-	-	-	-	VI	Large ectodermal cell layer deriving ventrally from the <i>ventral epidermal primordium</i> at the beginning of stage 16 after the <i>dorsal zippering</i> process has ended.	7A, C	Adopted from <i>Drosophila</i> [40].
<i>ventral furrow</i> (transient)	-	II	III	-	-	-	Longitudinal cleft arising ventro-medially in the <i>cellular blastoderm</i> at the beginning of stage 6. Involved in the differentiation of the <i>anterior midgut primordium</i> at the beginning of stage 7 as part of the <i>germ layer specification</i> process and the <i>amnioproctodeal invagination</i> during stage 8. Continuous closure of the cleft gives rise to the <i>ectodermal layer</i> and the <i>mesodermal layer</i> at the beginning of stage 8 as part of the <i>germ layer specification</i> process. Levels out at the beginning of stage 9.	3A [1,2], E [2,3]; 3C [1], E [2,3], F [1]; 4A, H, J	Adopted from <i>Drosophila</i> [40,132–135], <i>Megaselia</i> [21,51] and <i>Clogmia</i> [22].
<i>ventral mesectoderm</i>	-	-	III	-	-	-	Longitudinal stripe of mesectodermal cells emerging ventrally along the <i>thorax</i> and <i>abdomen</i> from the <i>ventral epidermal primordium</i> during stage 10. Involved in neurogenesis (Supplementary Table 2).	4I, (J)	Adopted from <i>Drosophila</i> [40].
<i>yolk</i> (transient)	I	-	-	-	-	-	Initial nutrient reservoir of the egg. Constitutes together with the <i>zygotic nuclei</i> the <i>zygote</i> . Becomes enveloped by the <i>syncytial blastoderm</i> at the beginning of stage 6. Turns into the <i>yolk sac</i> at the beginning of stage 6 after the <i>cellularization</i> process has ended.	2A, B, C; 3A	Established for <i>Ceratitis</i> [38,39]. Usage similar for <i>Drosophila</i> [40,73].
<i>yolk sac</i> (transient)	-	II	III	IV	V	-	Nutrient compartmentation deriving from the <i>yolk</i> at the beginning of stage 6 after the <i>cellularization</i> process has ended. Migrates to the interior regions and protrudes back to the surface during stages 11 and 12 as part of the <i>extra-embryonic membrane folding</i> process. Internalizes together with the <i>amnioserosa</i> into the <i>midgut</i> during stage 15 after the <i>extra-embryonic membrane folding</i> process has ended.	3A, (C, D, E); 4A, B, H, (I, J); 5A; 6A, D, G	Established for <i>Ceratitis</i> [38]. Usage similar for <i>Drosophila</i> [40,136].
<i>zygote</i> (transient)	I	-	-	-	-	-	Fertilized egg at the beginning of stage 1. Consists of the <i>yolk</i> and the <i>zygotic nuclei</i> . Turns into the <i>syncytial blastoderm</i> at the beginning of stage 4.	2B, (C)	Adopted from <i>Drosophila</i> [40,137].
<i>zygotic nuclei</i> (transient)	I	-	-	-	-	-	Internal nuclei resulting from the very first mitotic divisions at the beginning of stage 1. Constitutes together with the <i>yolk</i> the <i>zygote</i> . Give rise to the <i>pole buds</i> during stage 3. Turn into <i>blastoderm nuclei</i> at the beginning of stage 4 after the <i>peripheral migration</i> process has ended.	2A [2,3], B, (C)	Adopted from <i>Drosophila</i> [40,138].

Table 3

Table 3 – Overview of ten selected processes of higher importance in chronological order. Figure references in parentheses indicate figures in which the respective process can be seen as a spin-off.

process	embryogenetic event						description / rationale	figure
<i>repeated withdrawal</i>	I	II	III	IV	V	VI	Over the whole course of embryogenesis, first the <i>yolk</i> , later on the <i>head</i> and the <i>abdomen</i> , withdraw and reverse multiple times from the anterior and posterior pole. Withdrawal from both poles occurs sometimes synchronously and sometimes independently from each other, which leads to a non-trivial embryo length-over-time graph (Figure 1C). In some cases, withdrawal is linked to (and maybe also required for the correct execution of) certain processes, for example emergence of the <i>posterior plate</i> during stage 6 (Figure 1C [3]) or the movement of the <i>clypeolabrum</i> during stage 14 (Figure 1C [7]). Withdrawal of both poles reaches an absolute maximum of about 5% of total length for both the <i>head</i> at the anterior and the <i>abdomen</i> posterior pole in parallel during stage 15 (Figure 1C [8]). Withdrawal <i>per se</i> is not a unique feature of <i>Ceratitis</i> development, but happens also in other dipterans [21,22,40] and in more distantly related species such as <i>Tribolium</i> [68,139] or <i>Gryllus</i> [140]. However, the resulting length-over-time graph (Figure 1C) is most probably unique and thus serves as a characteristic curve for <i>Ceratitis</i> .	1C; 2A, B, C; 3B, C, (E); 4A, B, J, I; 5A, B; 6A, B, C, D, F, G; 7A
<i>peripheral migration</i>	I	-	-	-	-	-	After nine synchronous nuclear divisions within the inner regions of the <i>yolk</i> , respectively allocated <i>zygotic nuclei</i> start protruding to the surface during stage 2 (Figure 2A [3]) and immediately proceed through the 10 th and 11 th synchronous nuclear division. Similar to the development of other insect species [40,141], a certain fraction of nuclei remain in the inner regions and become vitellophages (Supplementary Table 2). Once completed, the <i>zygotic nuclei</i> , which have a relatively large size, turn into the <i>blastoderm nuclei</i> , and the <i>zygote</i> turns into the <i>syncytial blastoderm</i> . The general procedure of several synchronous nuclear divisions followed by outward migration is a fundamental feature of insect development, but the quantitative frame may differ between species of different orders (Supplementary Table 1).	2A, B
<i>germ cell dynamics</i>	I	II	III	-	-	-	During stage 3, several zygotic nuclei give rise to the <i>pole buds</i> at the posterior tip of the <i>zygote</i> (Figure 2A [2]). Slightly later, during stage 4, the <i>pole buds</i> pinch off and turn into the <i>pole cells</i> , which undergo synchronous nuclear division (Figure 2B [1]). During stage 6, the <i>pole cells</i> adhere to the emerging <i>posterior plate</i> , which turns into the <i>dorsal plate</i> during stage 7 (Figure 3C). During stages 8, the <i>pole cells</i> stay attached to the <i>posterior midgut primordium</i> which derived from the <i>dorsal plate</i> . Thus, they migrate with the posterior tip of the anterior elongating <i>germband</i> along the dorsal side (Figure 4A [3], C [1]). The <i>pole cells</i> fade from sight as the <i>posterior midgut primordium</i> invaginates and the <i>proctodeal opening</i> changes to an anterior orientation, and their further development cannot be followed anymore (Figure 4A [4]). They remain with the <i>posterior midgut primordium</i> for some more time before formation of gonads	2A, B, C, F, G; 3B, C, (D, E, G), H; 4A, C, H, (J)

							take place [39] and the <i>pole cells</i> turn into germ cells (Supplementary Table 2). The process is very similar to <i>Drosophila</i> [40,142] and <i>Megaselia</i> [21], but in <i>Clogmia</i> [22], and <i>Tribolium</i> [68,141], pole cells are not visible during the early stages of development.	
cellularization	I	II	-	-	-	-	Stage 5 is a long period of morphogenetic quiescence, since the <i>blastoderm nuclei</i> synthesize cell membranes during this time, where almost all changes occur on the sub-cellular level. In brief, the furrow growth is mediated by contracting microfilaments, and the membrane is enlarged by vesicle fusion [38]. Once completed, the <i>blastoderm nuclei</i> are individualized, the <i>syncytial blastoderm</i> has turned into the <i>cellular blastoderm</i> , and instead of nuclear divisions, mitotic divisions occur now. This process is also a fundamental feature of insect development (Supplementary Table 1), but a detailed comparison is not possible since no membrane marker for <i>Ceratitis</i> is available.	2B; 3A
germ layer specification	-	II	III	-	-	-	The ectodermal, mesodermal and endodermal germ layers are allocated under participation of the <i>ventral furrow</i> and the <i>dorsal plate</i> during stages 6, 7 and 8. Once completed, the <i>anterior midgut primordium</i> (Figure 4A [2]), the <i>mesodermal layer</i> , the <i>ectodermal layer</i> and the <i>posterior midgut primordium</i> (Figure 4C [2]) have differentiated. This process is highly similar in closely related dipterans, for example <i>Drosophila</i> [40] and <i>Megaselia</i> [21,51], but it is not yet clear if certain structures, such as the <i>ventral furrow</i> , also arise in more distantly related dipterans such as <i>Clogmia</i> [22]. In <i>Aphidoletes</i> , a sister species to <i>Clogmia</i> , no <i>ventral furrow</i> could be observed [41].	3C, E, F; 4A, C, H, (J)
extra-embryonic membrane folding	-	II	III	IV	V	-	The <i>amnioserosa</i> differentiates medio-dorsally from the <i>cellular blastoderm</i> at the beginning of stage 7 as the only extra-embryonic membrane. It immediately begins to unfold for the first time, covering the <i>embryo</i> and the <i>yolk sac</i> and folds throughout 8, 9, and 10 as the posterior tip of the <i>germband</i> anteriorly elongates along the dorsal side and remains in the conformation during stage 11. During stage 12, it unfolds a second time as the posterior tip of the <i>germband</i> retracts. As the <i>dorsal zippering</i> process proceeds, the <i>amnioserosa</i> folds a second time and finally internalizes together with the <i>yolk sac</i> into the <i>midgut</i> during stage 15. The process of <i>amnioserosa</i> formation and rearrangement differs remarkably from <i>Drosophila</i> [40,52,76,143] and is critically analyzed in the discussion. <i>Megaselia</i> [18–21], <i>Clogmia</i> [22] and more distantly related species such as <i>Tribolium</i> [53] have two extra-embryonic membranes and thus a completely different rearrangement concept.	3C, D, (E), (G); 4A, B, H, (I, J); 6A, (D), G
digestive system formation	-	-	III	IV	V	VI	Formation of the <i>digestive tract</i> is one of the most comprehensive processes in the embryonic development of <i>Ceratitis</i> that involves mainly ectodermal and endodermal tissue that differentiates during the <i>germ layer specification</i> process. In brief, the digestive tract originates through consecutive connection of five structures: (i) the anterior <i>atrium</i> , which forms during stage 16, (ii) the anteromedial <i>stomodeum</i> , which derives from the <i>stomodeal invagination</i> at the beginning of stage 9, (iii) the medial <i>midgut</i> , which originates from the fusion of two endodermal primordia during stage 14 (Figure 6A [3]), (iv) the posteromedial <i>proctodeum</i> , which differentiates from the <i>amnioproctodeal invagination</i> at the beginning of stage 9, and the (v) posterior <i>proctodeal opening</i> , which also differentiates from the <i>amnioproctodeal invagination</i> at the beginning of stage 9. Due to limited resolution within inner regions of the <i>embryo</i> , the mentioned structures cannot be subdivided further as done for <i>Drosophila</i> [40], for example the <i>stomodeum</i> is not subdivided into pharynx, oesophagus and proventriculus. Formation of the <i>digestive tract</i> appears to be very similar to <i>Drosophila</i> [40,92,93] and <i>Megaselia</i> [21], but for other insect species, not enough information for a proper comparison is available (Supplementary Table 1).	4A, C, F, (H); 6A, (G); 7A, C; 5A; 6A, D, G
metamerization	-	-	III	IV	V	VI	During the later stages of embryonic development, the <i>germband</i> becomes subdivided into fifteen segments. Metameres can be recognized first during stage 11, when the <i>gnathal protuberances</i> emerge from the <i>gnathocephalon</i> , and later on also during stage 12, when the <i>intersegmental grooves</i> divide the <i>thorax</i> into three (Figure 5B [2,3,4]) and the <i>abdomen</i> into nine segments. The grooves disappear transiently during stage 15, but reappear at the beginning of stage 16. Due to limited resolution within the inner regions of the <i>embryo</i> , metamerism can only be confirmed for the ectoderm, but similar to <i>Drosophila</i> [40], it can be reasonably assumed that the mesoderm, but not the endoderm is segmentally organized. The number of segments is identical to <i>Drosophila</i> [40] and <i>Megaselia</i> [144].	5A, B; 6B; 7A, (B), C
head involution	-	-	-	-	V	VI	Involution of the <i>head</i> is a complex morphogenetic process that occurs during stages 14, 15 and 16 and can be subdivided into three directed migrations: (i) the <i>ventral epidermal primordium</i> , the <i>lateral epidermal primordia</i> and the <i>antennomaxillary complexes</i> (Figure 6E [4]) migrate anteriorly, (ii) the fused <i>dorsal folds</i> (Figure 6E [5]) cover the <i>procephalon</i> and the <i>clypeolabrum</i> and eventually turns into the <i>dorsal pouch</i> , and (iii) the <i>stomodeum</i> (Figure 6A [3]), the <i>clypeolabrum</i> , the <i>mandibular buds</i> (Figure 6C [1], E [1]) and the fused <i>labial buds</i> retract. Once head involution is completed, the retracted structures and the now fused <i>antennomaxillary complexes</i> have formed the <i>atrium</i> . Head involution proceeds highly similar compared to <i>Drosophila</i> [40], it should however be noted that the <i>clypeolabrum</i> is larger and more pronounced in <i>Ceratitis</i> .	6A, B, C, D, E, F, (G); 7A, C
dorsal zippering	-	-	-	-	V	VI	At the end of stage 12, the <i>embryo</i> is covered dorsally only by the <i>amnioserosa</i> , an extra-embryonic membrane. During stage 13, 14 and 15, the bilateral <i>dorsal epidermal primordia</i> migrate dorsolaterally over the <i>amnioserosa</i> and begin fusing. Thereby, two leading edges emerge anteromedial and posteromedial that gradually approach each other (Figure 6G [1,2,3,4]) and form a tight seam along the dorsal midline. Once completed, the <i>dorsal epidermal primordia</i> have turned into the <i>dorsal epidermis</i> , a continuous cell layer that seals the <i>embryo</i> dorsally. Zippering along the dorsal midline is a conserved process in insects and even in far more distantly related species such as vertebrates [145]. The process is very similar to <i>Drosophila</i> [40,146] and moderately similar to <i>Tribolium</i> [57,68], since <i>Tribolium</i> generates and degrades two extra-embryonic membranes.	6A, D, G; 7A, C

Figures

Figure 1

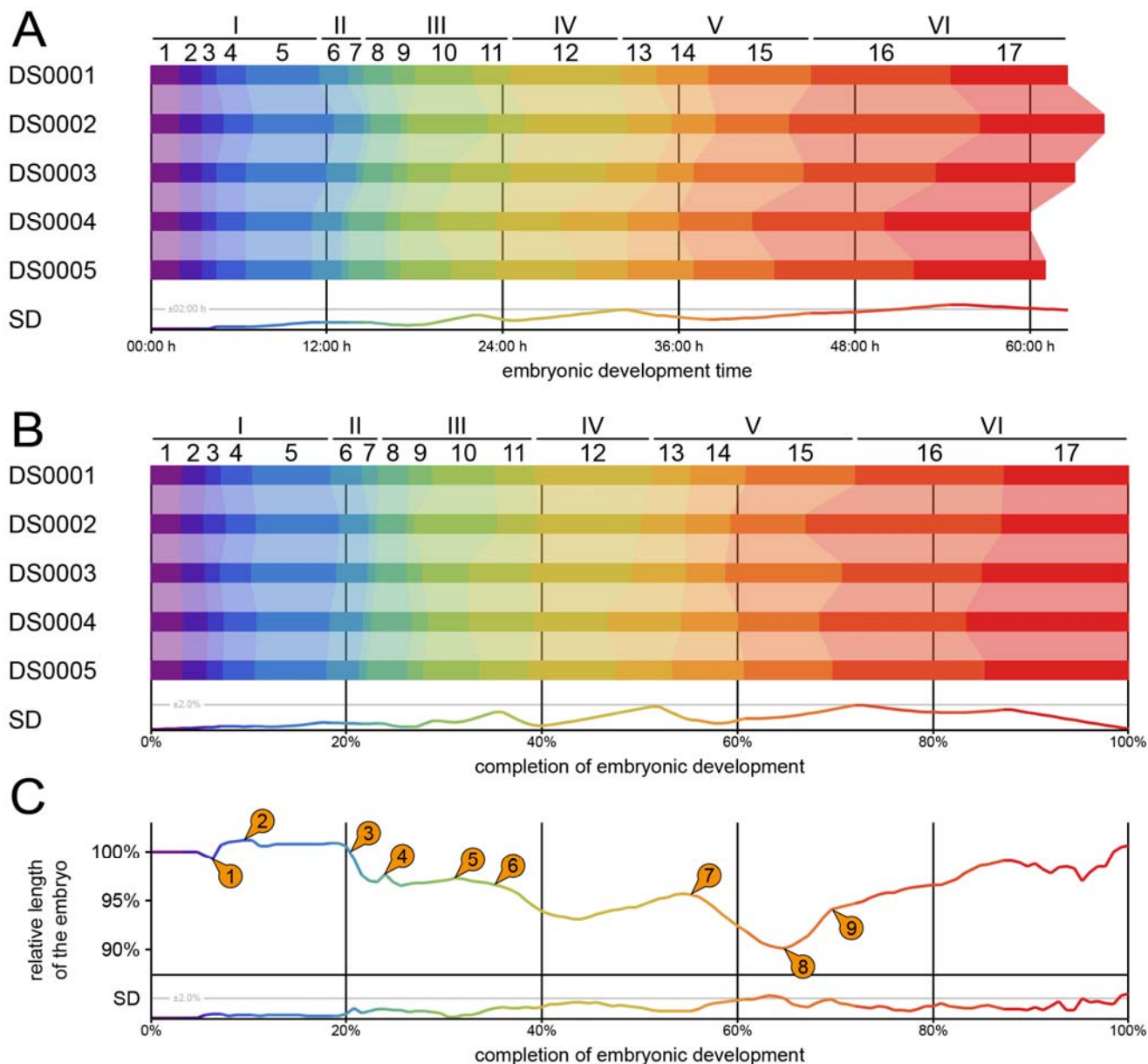


Figure 1 – Staging of *Ceratitidis* embryogenesis and morphological analysis of five datasets. (A) Staging of DS0001-DS0005 as a function of absolute time. **(B)** Staging of DS0001-DS0005 as a function of embryonic development. **(C)** Average relative length with standard deviation for datasets DS0001-DS0003 as a function of embryonic development. The numbered arrows are referred to throughout the running text as well as Table 1 and Table 3. SD, standard deviation.

Figure 2

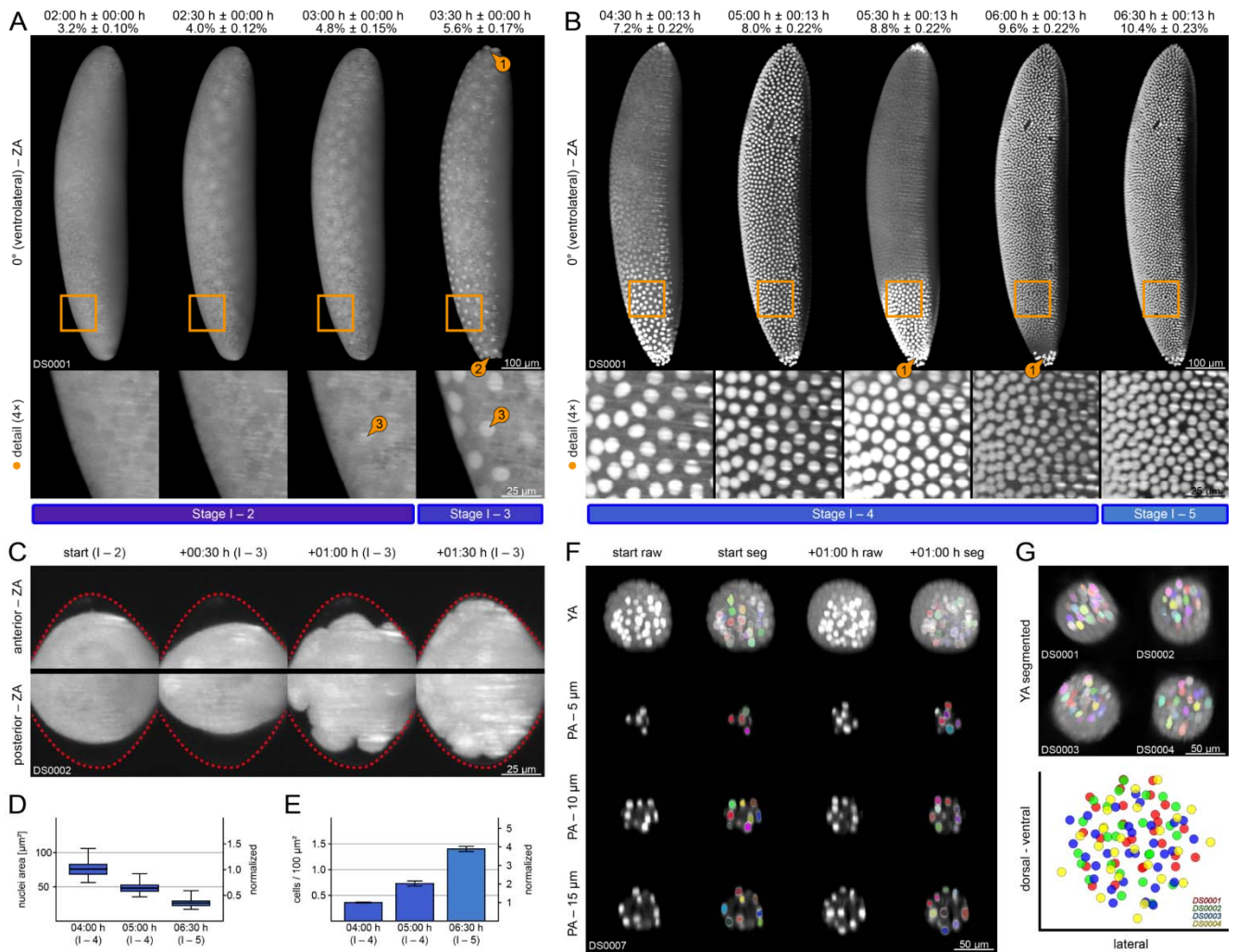


Figure 2 – Blastoderm formation (embryogenetic event I). (A) Stages 2 and 3. Withdrawal of the *yolk* from the anterior {1} and posterior {2} pole, *zygotic nuclei* migration to the surface {3} and emergence of the *pole buds* emerge at the posterior pole {2}. (B) Stages 4 and 5. The 12th and 13th parasynchronous nuclear division of the superficially located *blastoderm nuclei*. The *pole buds* turn into the *pole cells* at the posterior pole and undergo an asynchronous mitotic division {1}. (C) Withdrawal and reversal of the *yolk* from both poles and emergence of the *pole buds* at the posterior pole. (D) Area of the *zygotic nuclei* before the 12th, after the 12th and after the 13th parasynchronous nuclear divisions. (E) Density of the *zygotic nuclei* before, before the 12th, after the 12th and after the 13th parasynchronous nuclear divisions. (F) Segmentation of *pole cells* before and after their asynchronous division. (G) Segmentation and alignment of *pole cells* from four datasets. ZA, Z maximum projection with image adjustment; PA, single plane with image adjustment; seg, segmented.

Figure 3

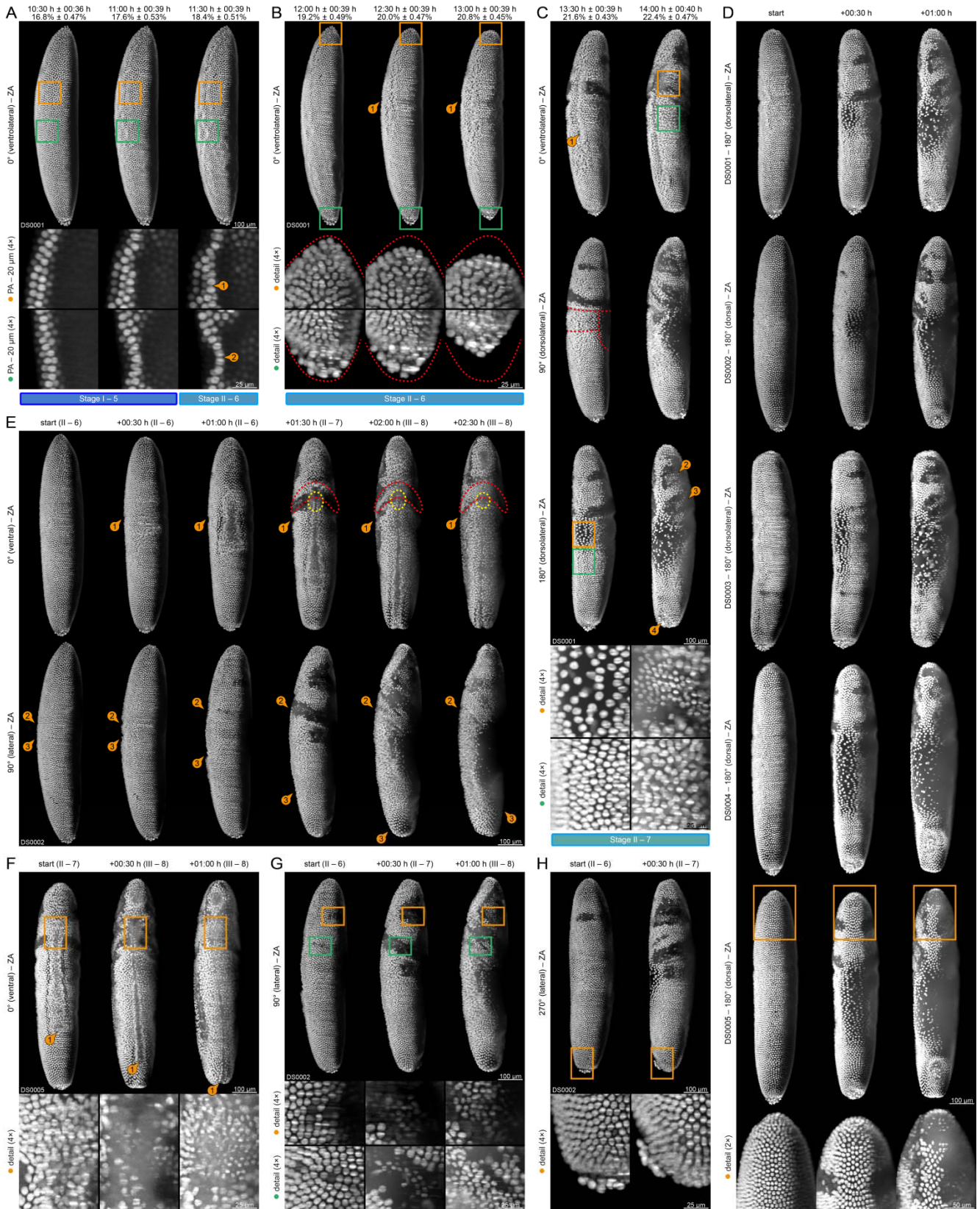


Figure 3 – Gastrulation (embryogenetic event II). (A) Stages 5 and 6. Wavy appearance of *blastoderm nuclei* Arising of the anterior {1} and posterior {2} tips of the *ventral furrow*. (B) Stage 6. Withdrawal of the *head* from the anterior and of the *abdomen* from the posterior pole. Arising of lateral indentions {1} that precede the formation of the *cephalic furrow*. (C) Stage 7. Deepening of the *cephalic furrow*, extension of the *ventral furrow* {1} and mitotic division of the *small and large lateral cell stripes* {2,3}. Differentiation of the *cellular blastoderm* into the *head*, the *thorax*, the *abdomen* and the *amnioserosa* (red dashed lines). Formation of the *gnathocephalon*. The *posterior plate*, which carries the *pole cells*, turns into the *dorsal plate* {4}. (D) Differentiation of the *amnioserosa* shown for five datasets. (E) Arising of the *cephalic furrow* {1} and *ventral furrow* {2,3}, emergence of the *anterior midgut primordium* (yellow dashed line) and formation of the *gnathocephalon* (red dashed line). (F) Emergence of the *anterior midgut primordium* and elongation of the *ventral furrow* {1}. (G) Mitotic division of the *small and large lateral cell stripes*. (H) The *posterior plate*, which carries the *pole cells*, turns into the *dorsal plate*.

Figure 4

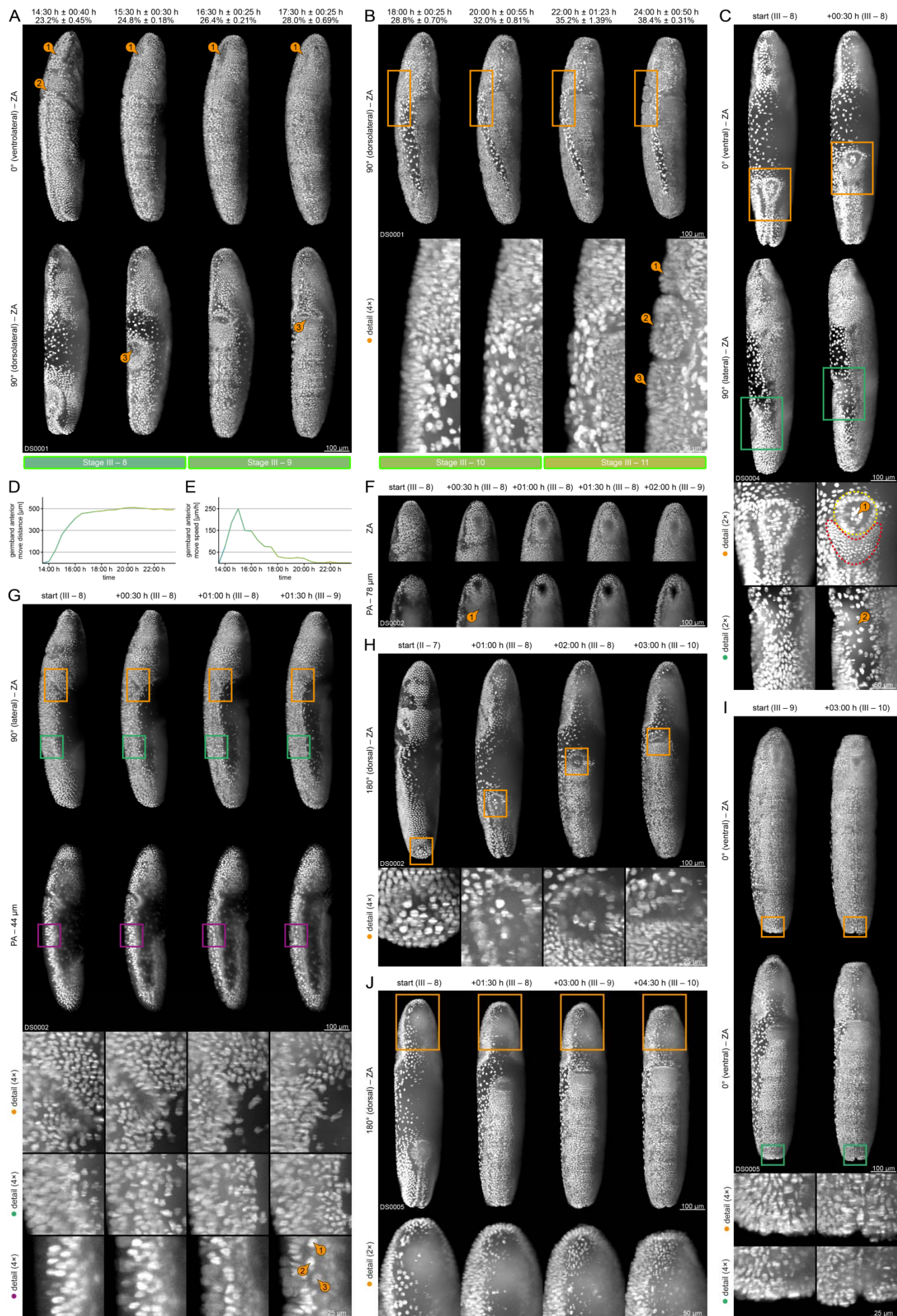


Figure 4 – Germband elongation (embryogenetic event III). (A) Stages 8 and 9. Anteriad elongation of the posterior tip of the *germband*. Emergence of the *stomodeal plate* {1}, which turns into the *stomodeal invagination* {2} and later on into the *stomodeum* {3}. Internalization of the *anterior midgut primordium* {4}. The dorsal plate turns into the *posterior midgut primordium*. Emergence of the *optic lobe primordium* (red dashed line) and the *amnioproctodeal invagination* {5}, which differentiates into the *proctodeum* and the *proctodeal opening* {6}. (B) Stages 10 and 11. Anteriad elongation and quiescence of the posterior tip of the *germband*. Emergence of the *gnathal protuberances* from the *gnathocephalon*, white arrows indicate the respective gnathal segment. (C) Emergence of the *amnioproctodeal invagination* (yellow and red dashed lines) around the *posterior midgut primordium* {2}, which carries the *pole cells* {1}. (D) Move distance of the posterior tip of the *germband* over a period of six hours. (E) Move speed of the posterior tip of the *germband* over the same six hour period. (F) Emergence of the *stomodeal cell plate*, which turns to the *stomodeal invagination*. The *stomodeal invagination* connects to the *anterior midgut rudiment* and turns into the *stomodeum*. (G) Outleveling of the *cephalic furrow*, differentiation of the *ventral epidermal primordium* and the *lateral epidermal primordium* and segregation of *neuroblasts* {1,2,3}. (H) Invagination of the *posterior midgut primordium* as well as differentiation and internalization of the *proctodeum*. (I) Emergence of the *ventral mesectoderm*. (J) Mitotic division in the *optic lobe primordium*.

Figure 5

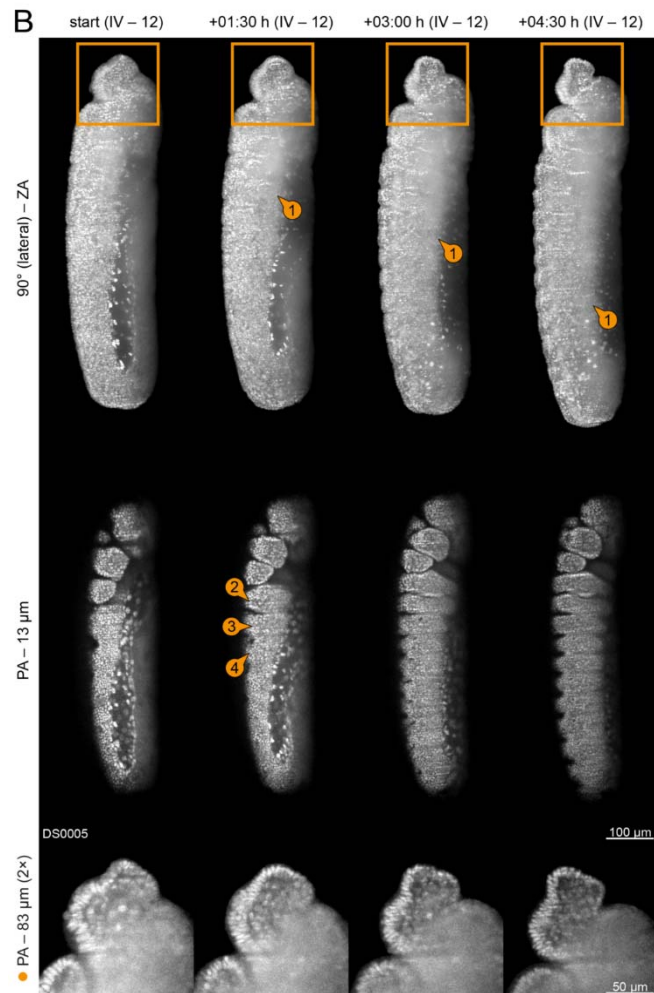
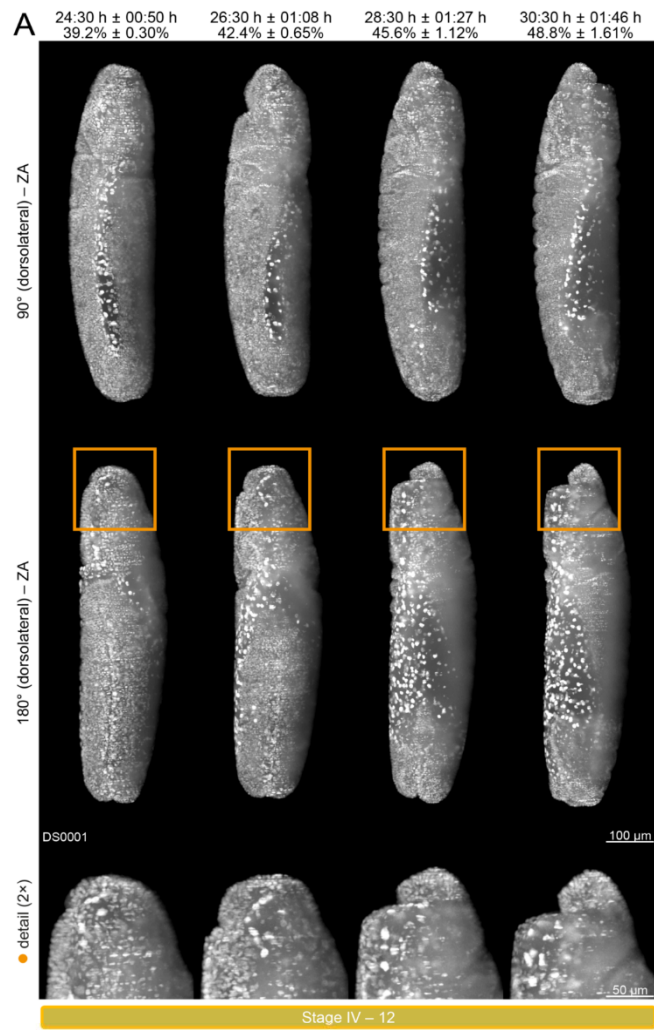


Figure 5 – Germband retraction (embryogenetic event IV). (A) Posterior retraction of the posterior tip of the germband and posterior-dorsally localization of the *proctodeal opening* {1}. Emergence of the *clypeolabrum* and advent of the *intersegmental grooves*. (B) Emergence of the *clypeolabrum* and the *dorsal epidermal primordia* {1}. Advent of the *intersegmental grooves* in the *thorax* {2,3,4} and *abdomen*.

Figure 6

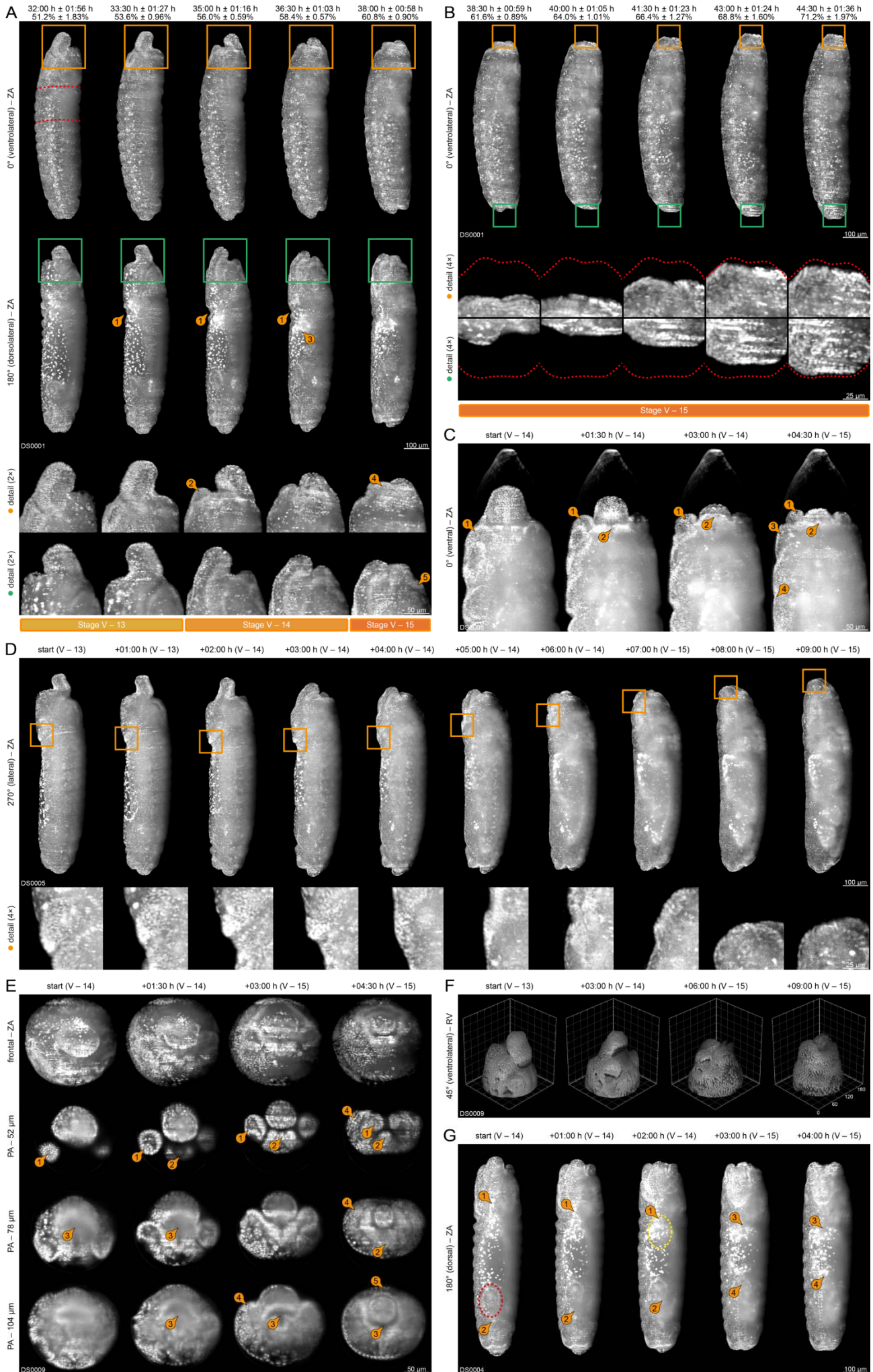


Figure 6 – Dorsal closure (embryogenetic event V). (A) Stages 13, 14 and 15. Anteriad migration of the *ventral epidermal primordium* and the *lateral epidermal primordia* (red dashed lines) as well as dorsolaterad migration and fusion of the *dorsal epidermal primordia*. Advent of the *anterior dorsal gap* {1} and formation of the *midgut* {3}. Morphogenetic change of the *clypeolabrum*. Differentiation of the *mandibular buds* {3}, the *maxillary buds* and the *labial buds*. Fusion of the *labial buds* {4}. Emergence of the *antennomaxillary complex* {5}. (B) Stage 15. Withdrawal of the *head* from the anterior and the *abdomen* from the posterior pole and transient outleveling of the *intersegmental grooves*. Retraction of the *clypeolabrum*, the *mandibular buds* and the fused *labial buds*. (C) Retraction of the *clypeolabrum*, the *mandibular buds* {1} and the fused *labial buds* {2}. Emergence of the *antennomaxillary complex* {3}. Outleveling of the *anterior dorsal gap*. (D) Anteriad migration of the fused *dorsal folds*. (E) Retraction of the *clypeolabrum*, the *mandibular buds* {1}, the fused *labial buds* {2} and the *stomodeum* {3} as well as emergence of the *antennomaxillary complex* {3}. Anteriad migration of the *dorsal fold* {5}. (F) Volume rendering of head involution. (G) Anterior {1} and posterior {2} as well as median {3,4} fusion of the *dorsal epidermal primordia*, which cover the *proctodeum* (red dashed line) and the *midgut* (yellow dashed line).

Figure 7

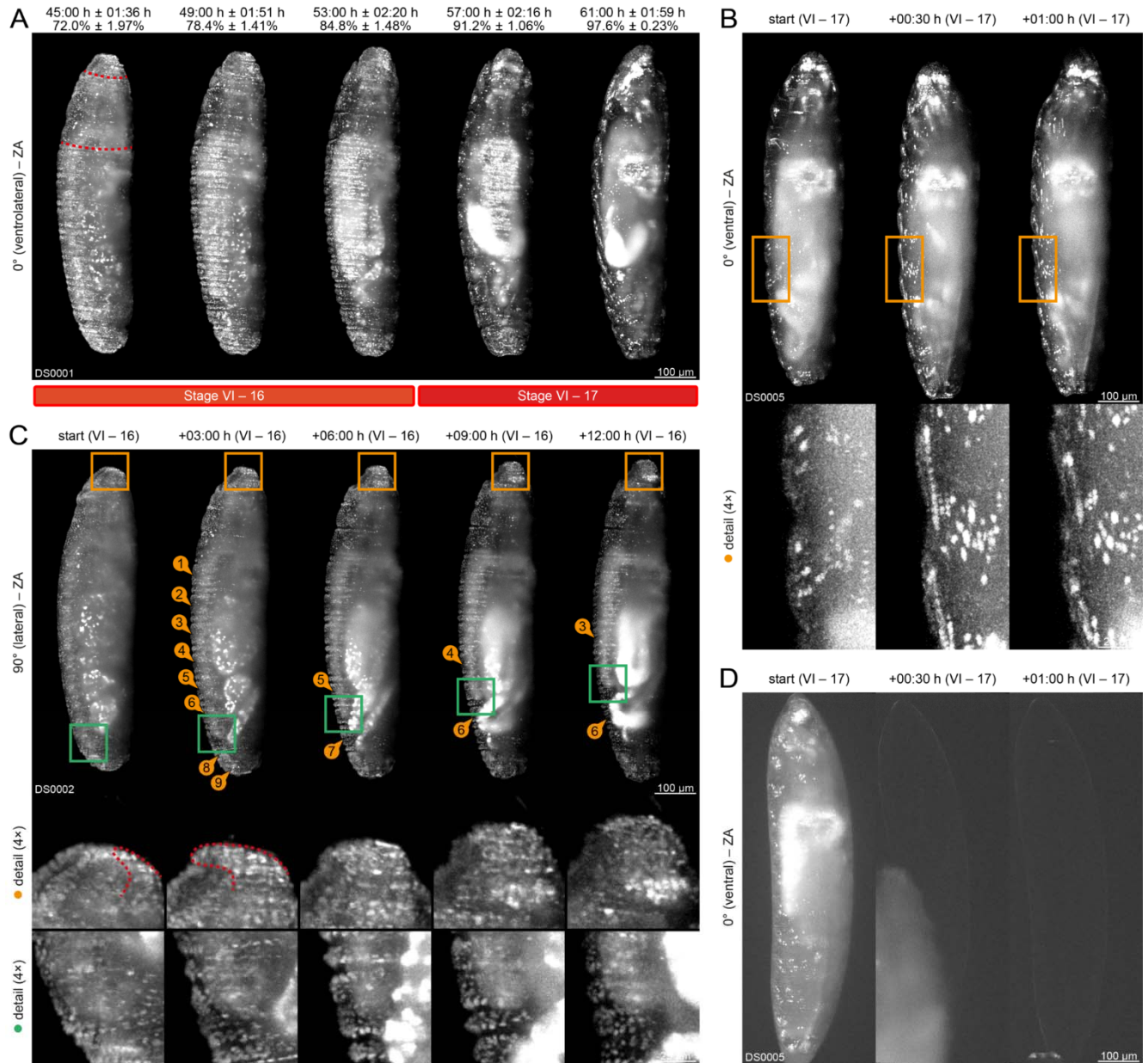
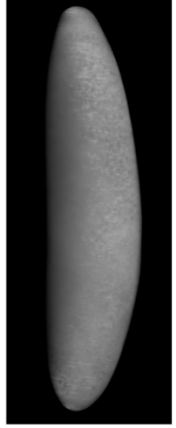


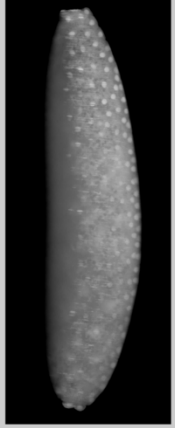


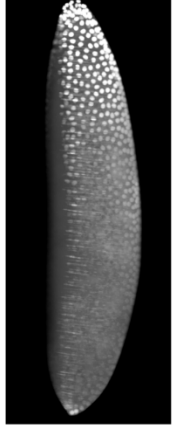


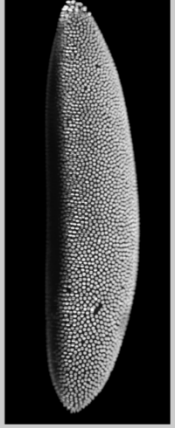


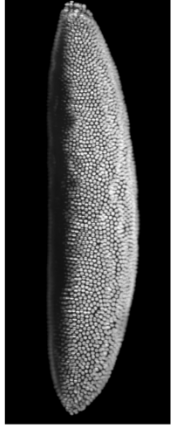





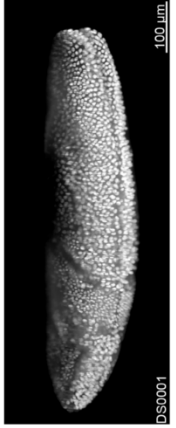


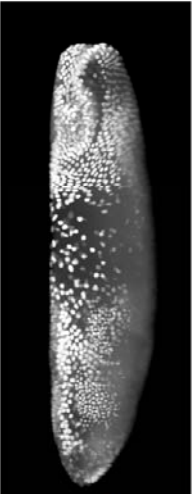


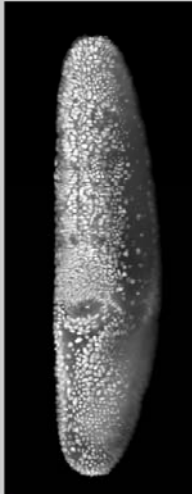


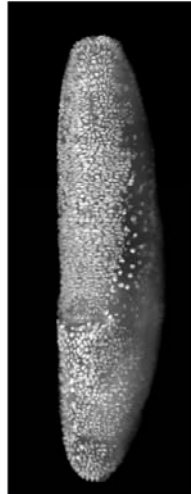


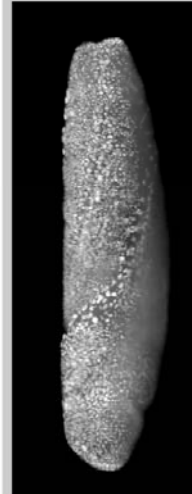


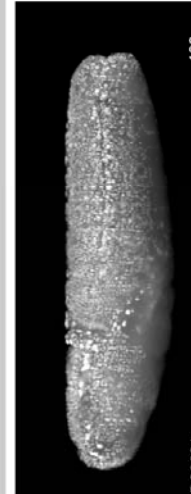




Figure 7 – Muscular movement (embryogenetic event VI). (A) After medial fusion, the *dorsal epidermal primordia* turn into the *dorsal epidermis*. Reemergence of the *intersegmental grooves* and formation of the *atrium*. (B) Onset of regular muscular movement. (C) After migration, the fused *dorsal folds* turn into the *dorsal pouch*. Shortening of the *ventral cord*, white arrows indicate the respective abdominal segment. (D) Hatching of the larva.

Supplementary Figures

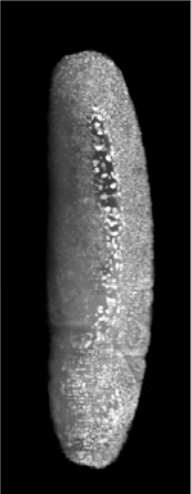


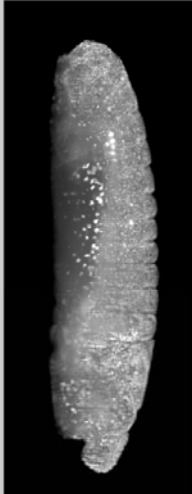


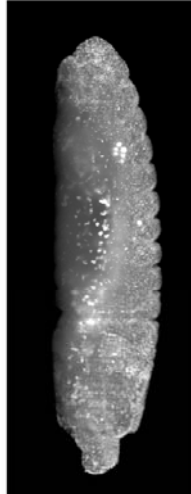


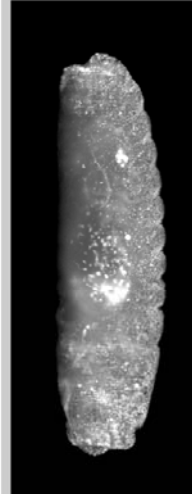


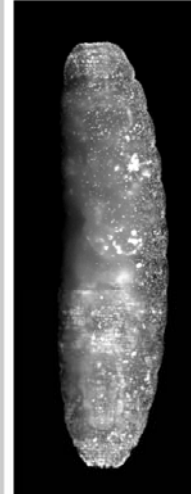


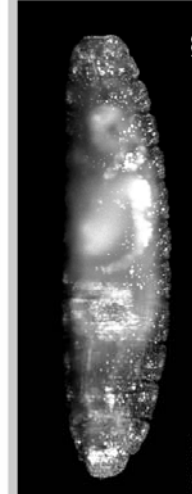


Supplementary Figure 1

stage	0° (ventrolateral) – ZA	timing	description
I-1/2		<div style="display: flex; justify-content: space-between;"> <div>  <p>start 02:00 h end 03:30 h</p> </div> <div>  <p>start 3.2% end 5.6%</p> </div> </div>	<ul style="list-style-type: none"> egg fertilization results in the zygote, which consists of the yolk and the zygotic nuclei the yolk begins withdrawing from both poles (<i>repeated withdrawal</i>) the respectively allocated zygotic nuclei begin protruding towards the surface (<i>peripheral migration</i>)
Figure 2			
I-3		<div style="display: flex; justify-content: space-between;"> <div>  <p>start 03:30 h end 04:30 h</p> </div> <div>  <p>start 5.6% end 7.2%</p> </div> </div>	<ul style="list-style-type: none"> the yolk withdrawal at both poles reaches a relative maximum and starts reversing (<i>repeated withdrawal</i>) the first zygotic nuclei reach the surface (<i>peripheral migration</i>) and undergo two synchronous nuclear divisions the pole buds emerge at the posterior tip of the zygote from the zygotic nuclei (<i>germ cell dynamics</i>)
Figure 2			
I-4		<div style="display: flex; justify-content: space-between;"> <div>  <p>start 04:30 h end 07:00 h</p> </div> <div>  <p>start 7.2% end 11.2%</p> </div> </div>	<ul style="list-style-type: none"> the last zygotic nuclei reach the surface (<i>peripheral migration</i>), turn into blastoderm nuclei and undergo two synchronous nuclear divisions the zygote turns into the syncytial blastoderm (<i>peripheral migration</i>) the pole cells derive at the posterior tip of the syncytial blastoderm from the pole buds (<i>germ cell dynamics</i>)
Figure 2			
I-5		<div style="display: flex; justify-content: space-between;"> <div>  <p>start 07:00 h end 11:30 h</p> </div> <div>  <p>start 11.2% end 18.4%</p> </div> </div>	<ul style="list-style-type: none"> the blastoderm nuclei complete the last synchronous nuclear division and begin with the synthesis of cell membranes (<i>cellularization</i>) the medio-ventral blastoderm nuclei exhibit a slight wavy appearance
Figure 3			
II-6		<div style="display: flex; justify-content: space-between;"> <div>  <p>start 11:30 h end 13:30 h</p> </div> <div>  <p>start 18.4% end 21.6%</p> </div> </div>	<ul style="list-style-type: none"> the blastoderm nuclei complete the synthesis of cell membranes, the syncytial blastoderm turns into the cellular blastoderm (<i>cellularization</i>) the ventral furrow and cephalic furrow arise in the cellular blastoderm the posterior plate, to which the pole cells adhere, emerges at the posterior tip of the cellular blastoderm (<i>germ cell dynamics</i>)
Figure 3			
II-7		<div style="display: flex; justify-content: space-between;"> <div>  <p>start 13:30 h end 14:30 h</p> </div> <div>  <p>start 21.6% end 23.2%</p> </div> </div>	<ul style="list-style-type: none"> the anterior midgut primordium emerges and invaginates at the anterior tip of the ventral furrow (<i>germ layer specification</i>) the cellular blastoderm differentiates into the head, the thorax, the abdomen and the amnioserosa (<i>amnioserosa rearrangement</i>) the ventral furrow differentiates into the superficial ectodermal layer and the internal mesodermal layer (<i>germ layer specification</i>)
Figure 3			
III-8		<div style="display: flex; justify-content: space-between;"> <div>  <p>start 14:30 h end 16:30 h</p> </div> <div>  <p>start 23.2% end 26.4%</p> </div> </div>	<ul style="list-style-type: none"> the posterior tip of the germband begins elongation along the dorsal side towards the anterior pole with high speed the stomodeal cell plate emerges from the procephalon the dorsal plate internalizes and turns into the posterior midgut primordium (<i>germ cell dynamics</i> and <i>germ layer specification</i>)
Figure 4			

stage	180° (dorsolateral – ZA)	timing	description
III–8		<div style="display: flex; justify-content: space-between;"> <div style="text-align: center;">  start 14:30 h end 16:30 h </div> <div style="text-align: center;">  3.2% </div> </div>	<ul style="list-style-type: none"> the stomodeal cell plate turns into the <i>stomodeal invagination</i> the <i>amnioproctodeal invagination</i> emerges around the invaginating posterior <i>midgut primordium</i> from the <i>ectodermal layer</i> the <i>ectodermal layer</i> differentiates into the <i>ventral epidermal primordium</i> and the <i>lateral epidermal primordium</i>
Figure 4			
III–9		<div style="display: flex; justify-content: space-between;"> <div style="text-align: center;">  start 16:30 h end 18:00 h </div> <div style="text-align: center;">  2.4% </div> </div>	<ul style="list-style-type: none"> the posterior tip of the <i>germband</i> continues elongation along the dorsal side towards the anterior pole with moderate speed the <i>stomodeal invagination</i> turns into the <i>stomodeum</i>, which becomes the anteromedial part of the <i>digestive tract (digestive system formation)</i> the <i>amnioproctodeal invagination</i> differentiates into the <i>proctodeum</i> and the <i>proctodeal opening (digestive system formation)</i>
Figure 4			
III–10		<div style="display: flex; justify-content: space-between;"> <div style="text-align: center;">  start 18:00 h end 22:00 h </div> <div style="text-align: center;">  6.4% </div> </div>	<ul style="list-style-type: none"> the posterior tip of the <i>germband</i> continues elongation along the dorsal side towards the anterior pole with low speed the <i>ventral midline</i> emerges ventrally along the <i>thorax and abdomen</i> from the <i>ventral epidermal primordium</i>
Figure 4			
III–11		<div style="display: flex; justify-content: space-between;"> <div style="text-align: center;">  start 22:00 h end 24:30 h </div> <div style="text-align: center;">  4.0% </div> </div>	<ul style="list-style-type: none"> the posterior tip of the <i>germband</i> completes elongation towards the anterior pole and remains in a quiescent position the <i>amnioserosa</i> completes folding (<i>amnioserosa rearrangement</i>) the <i>gnathal protuberances</i> emerge from the <i>gnathocephalon (metamerization)</i>
Figure 4			
IV–12		<div style="display: flex; justify-content: space-between;"> <div style="text-align: center;">  start 24:30 h end 32:00 h </div> <div style="text-align: center;">  12.0% </div> </div>	<ul style="list-style-type: none"> the posterior tip of the <i>germband</i> begins retraction along the dorsal side towards the posterior pole the <i>amnioserosa</i> begins unfolding again (<i>amnioserosa rearrangement</i>) the <i>dorsal epidermal primordia</i> emerge laterally from the <i>lateral epidermal primordia</i>
Figure 4			

DS0001

100 μm

stage	90° (dorsolateral – ZA)	timing	description
IV–12		<div style="display: flex; justify-content: space-around;"> <div style="text-align: center;">  start 24:30 h end 32:00 h </div> <div style="text-align: center;">  start 39.2% end 51.2% </div> </div>	<ul style="list-style-type: none"> the <i>clypeolabrum</i> emerges antero-dorsally from the <i>procephalon</i> and becomes thinner and more pronounced the <i>intersegmental grooves</i> arise and separate the <i>thorax</i> into three and the <i>abdomen</i> into nine segments (<i>metamerization</i>)
Figure 5			
V–13		<div style="display: flex; justify-content: space-around;"> <div style="text-align: center;">  start 32:00 h end 34:30 h </div> <div style="text-align: center;">  start 51.2% end 55.2% </div> </div>	<ul style="list-style-type: none"> the posterior tip of the <i>germband</i> completes retracting the <i>ventral epidermal primordium</i> and <i>lateral epidermal primordia</i> of the <i>thorax</i> begin migration towards the anterior pole (<i>head involution</i>) the <i>dorsal epidermal primordia</i> begin migration dorsolaterally over the <i>amnioserosa</i> (<i>dorsal zipping</i>) the <i>dorsal fold</i> emerges from the <i>gnathocephalon</i> (<i>head involution</i>)
Figure 6			
V–14		<div style="display: flex; justify-content: space-around;"> <div style="text-align: center;">  start 34:30 h end 38:00 h </div> <div style="text-align: center;">  start 55.2% end 60.8% </div> </div>	<ul style="list-style-type: none"> the <i>clypeolabrum</i> turns from an antero-dorsal to an antero-ventral orientation (<i>head involution</i>) the <i>dorsal epidermal primordia</i> begin with fusion (<i>dorsal zipping</i>) the <i>gnathal protuberances</i> differentiate into the <i>mandibular buds</i>, the <i>maxillary buds</i> and the <i>labial buds</i> (<i>head involution</i>)
Figure 6			
V–15		<div style="display: flex; justify-content: space-around;"> <div style="text-align: center;">  start 38:00 h end 45:00 h </div> <div style="text-align: center;">  start 60.8% end 72.0% </div> </div>	<ul style="list-style-type: none"> the <i>abdomen</i> withdrawal at the posterior pole reaches the absolute maximum (<i>repeated withdrawal</i>) the <i>antennomaxillary</i> complexes originate from the fusion of the <i>maxillary buds</i> and the <i>procephalon</i> (<i>head involution</i>) the <i>amnioserosa</i> completes internalizing (<i>amnioserosa rearrangement</i>)
Figure 6			
VI–16		<div style="display: flex; justify-content: space-around;"> <div style="text-align: center;">  start 45:00 h end 54:30 h </div> <div style="text-align: center;">  start 72.0% end 87.2% </div> </div>	<ul style="list-style-type: none"> the <i>dorsal epidermal primordia</i> complete fusion and turn into the <i>dorsal epidermis</i> (<i>dorsal zipping</i>) the posterior tip of the <i>ventral cord</i>, which extends to the eighth segment of the <i>abdomen</i>, begins shortening the <i>dorsal fold</i> turns into the <i>dorsal pouch</i> (<i>head involution</i>) the <i>atrium</i> forms anteriorly (<i>digestive system formation</i>)
Figure 7			
VI–17		<div style="display: flex; justify-content: space-around;"> <div style="text-align: center;">  start 54:30 h end 62:30 h </div> <div style="text-align: center;">  start 87.2% end 100.0% </div> </div>	<ul style="list-style-type: none"> the posterior tip of the <i>ventral cord</i> shortens to the fifth segment of the <i>abdomen</i> the <i>embryo</i> begins with regular muscular movement, completes embryonic development, hatches and turns into the larva
Figure 7			

Supplementary Figure 1 – Chronological staging table of *Ceratitidis capitata* embryogenesis. The first column indicates embryonic event (Roman numerals), stage (Arabic numerals) and references the corresponding figure. The second column shows exemplary Z maximum projections of embryos in a suitable orientation at the given stage. The third column summarizes start, duration and end of the given stage in hours (blue) and in percent of total development (purple). The fourth column outlines up to four developmental actions during the respective stage. ZA, Z maximum projection with image adjustment.

Supplementary Tables

Supplementary Table 1

Supplementary Table 1 – Methodological and structural summary of selected publications that describe the embryogenesis of twenty-three insect species from ten orders. The entries are ordered primarily by phylogenetic distance and secondarily alphabetically.

binominal name	common name	reference	techniques used	embryogenetic events
<i>Drosophila melanogaster</i> (Diptera:Drosophilidae) holometabolous	fruit fly	[40]	non-fluorescence live imaging; fixation, mechanical sectioning and staining with non-fluorescent dyes	I II III IV V VI staging system (17)
<i>Megaselia abdita</i> (Diptera:Phoridae) holometabolous	scuttle fly	[21]	non-fluorescence live imaging; fixation and staining with fluorescent dyes followed by widefield microscopy	I II III IV V VI staging system (17)
<i>Aedes aegypti</i> (Diptera: Culcidae) holometabolous	yellow fever mosquito	[42,43]	fixation, mechanical sectioning and staining with non-fluorescent dyes	I II III IV V VI undergoes blastokinesis; staging system (26, time points)
<i>Aphidoletes aphidimyza</i> (Diptera:Cecidomyiidae) holometabolous	predatory gall midge	[41]	non-fluorescence live imaging	I II III IV V VI staging system (10)
<i>Clogmia albipunctata</i> (Diptera:Psychodidae) holometabolous	moth midge, drain fly	[22]	non-fluorescence live imaging; fixation and staining with fluorescent dyes followed by widefield microscopy	I II III IV V VI staging system (17)
<i>Nemotaulius admorsus</i> (Trichoptera:Limnephilidae) holometabolous	caddis fly	[147]	fixation, mechanical sectioning and staining with non-fluorescent dyes, scanning electron microscopy	I II III IV V VI staging system (10)
<i>Philaniscus plebeius</i> (Trichoptera:Chathamidae) holometabolous	marine caddis fly	[148]	fixation and non-stained observation	I II III IV V VI undergoes blastokinesis; no staging system
<i>Bombyx mori</i> (Lepidoptera:Bombycidae) holometabolous	domestic silkworm	[149]	fixation and staining with fluorescent dyes followed by confocal microscopy	I II III ? ? ? no staging system
<i>Endoclyta signifier</i> and <i>Endoclyta excrescens</i> (Lepidoptera:Hepialodae) holometabolous	primitive moth	[150]	fixation, mechanical sectioning and staining with non-fluorescent dyes	I II ? ? ? ? no staging system
<i>Nemophora albiantennella</i> (Lepidoptera:Adelidae) holometabolous	fairy moth	[151]	fixation and non-stained observation; fixation, mechanical sectioning and staining with non-fluorescent dyes; scanning electron microscopy	I II III IV V VI staging system (12)
<i>Neomicropteryx nipponensis</i> (Lepidoptera:Micropterygidae) holometabolous	primitive moth	[152]	fixation, mechanical sectioning and staining with non-fluorescent dyes	I II III IV V VI staging system (14)
<i>Rhagophthalmus ohbai</i> (Coleoptera:Rhagophthalmidae) holometabolous	glowworm	[153]	fixation, mechanical sectioning and staining with non-fluorescent dyes; scanning electron microscopy	I II III ? ? ? staging system (8, not numbered)
<i>Tribolium castaneum</i> (Coleoptera:Tenebrionidae) holometabolous	red flour beetle	[68]	light sheet-based fluorescence microscopy	I II III IV V VI no staging system
<i>Xyleborus ferrugineus</i> (Coleoptera:Scolytidae) holometabolous	ambrosia beetle	[154,155]	non-fluorescence live imaging	I II III IV V VI staging system (12, time points)
<i>Apis mellifera</i> (Hymenoptera:Apidae) holometabolous	honeybee	[156–158]	scanning electron microscopy	I II - - V VI staging system (6)
<i>Nasonia vitripennis</i> (Hymenoptera:Pteromalodae) holometabolous	jewel wasp	[159]	non-fluorescence live imaging; fixation and staining with non-fluorescent dyes	I II III IV V VI staging system (8)
<i>Acyrtosiphon pisum</i> (Hemiptera:Aphididae) hemimetabolous	pea aphid	[160]	fixation and staining with fluorescent dyes/antibodies followed by confocal microscopy	I II III IV ? VI undergoes blastokinesis; staging system (20)
<i>Galloisiana yuasai</i> (Grylloblattoidea:Grylloblattidae) hemimetabolous	-	[161]	fixation and staining with fluorescent dyes followed by wide field microscopy; fixation, mechanical sectioning and staining with non-fluorescent dyes; scanning electron microscopy; transmission electron microscopy	I II III - V VI undergoes blastokinesis; staging system (11)
<i>Gryllus bimaculatus</i> (Orthoptera:Gryllidae) hemimetabolous	two-spotted cricket	[140]	non-fluorescence live imaging, fixation and non-stained observation, fixation, germband preparation and staining with fluorescent dyes followed by confocal microscopy	I II III - V VI undergoes blastokinesis; staging system (23)
<i>Kamimuria tibialis</i> (Plecoptera:Perlidae) hemimetabolous	stonefly	[162]	fixation, mechanical sectioning and staining with non-fluorescent dyes; scanning electron microscopy	I II III - V VI undergoes blastokinesis; staging system (12)

<i>Rhodnius prolixus</i> (Hemiptera:Redivividae) hemimetabolous	kissing bug	[163]	fixation and staining with fluorescent dyes followed by wide field microscopy; fixation, mechanical sectioning and staining with non-fluorescent dyes; scanning electron microscopy; transmission electron microscopy	<table border="1"> <tr> <td style="background-color: #0000FF; color: white;">I</td> <td style="background-color: #00BFFF; color: white;">II</td> <td style="background-color: #00FF00; color: white;">III</td> <td style="background-color: #CCCCCC; color: white;">-</td> <td style="background-color: #FFA500; color: white;">IV</td> <td style="background-color: #FF0000; color: white;">VI</td> </tr> <tr> <td colspan="6">undergoes blastokinesis; staging system (4, not numbered)</td> </tr> </table>	I	II	III	-	IV	VI	undergoes blastokinesis; staging system (4, not numbered)					
I	II	III	-	IV	VI											
undergoes blastokinesis; staging system (4, not numbered)																
<i>Ephemera japonica</i> (Ephemeroptera:Ephemeridae) hemimetabolous	mayfly	[164,165]	fixation, mechanical sectioning and staining with non-fluorescent dyes; scanning electron microscopy	<table border="1"> <tr> <td style="background-color: #0000FF; color: white;">I</td> <td style="background-color: #00BFFF; color: white;">II</td> <td style="background-color: #00FF00; color: white;">III</td> <td style="background-color: #CCCCCC; color: white;">-</td> <td style="background-color: #FFA500; color: white;">V</td> <td style="background-color: #FF0000; color: white;">VI</td> </tr> <tr> <td colspan="6">undergoes blastokinesis; staging system (13)</td> </tr> </table>	I	II	III	-	V	VI	undergoes blastokinesis; staging system (13)					
I	II	III	-	V	VI											
undergoes blastokinesis; staging system (13)																

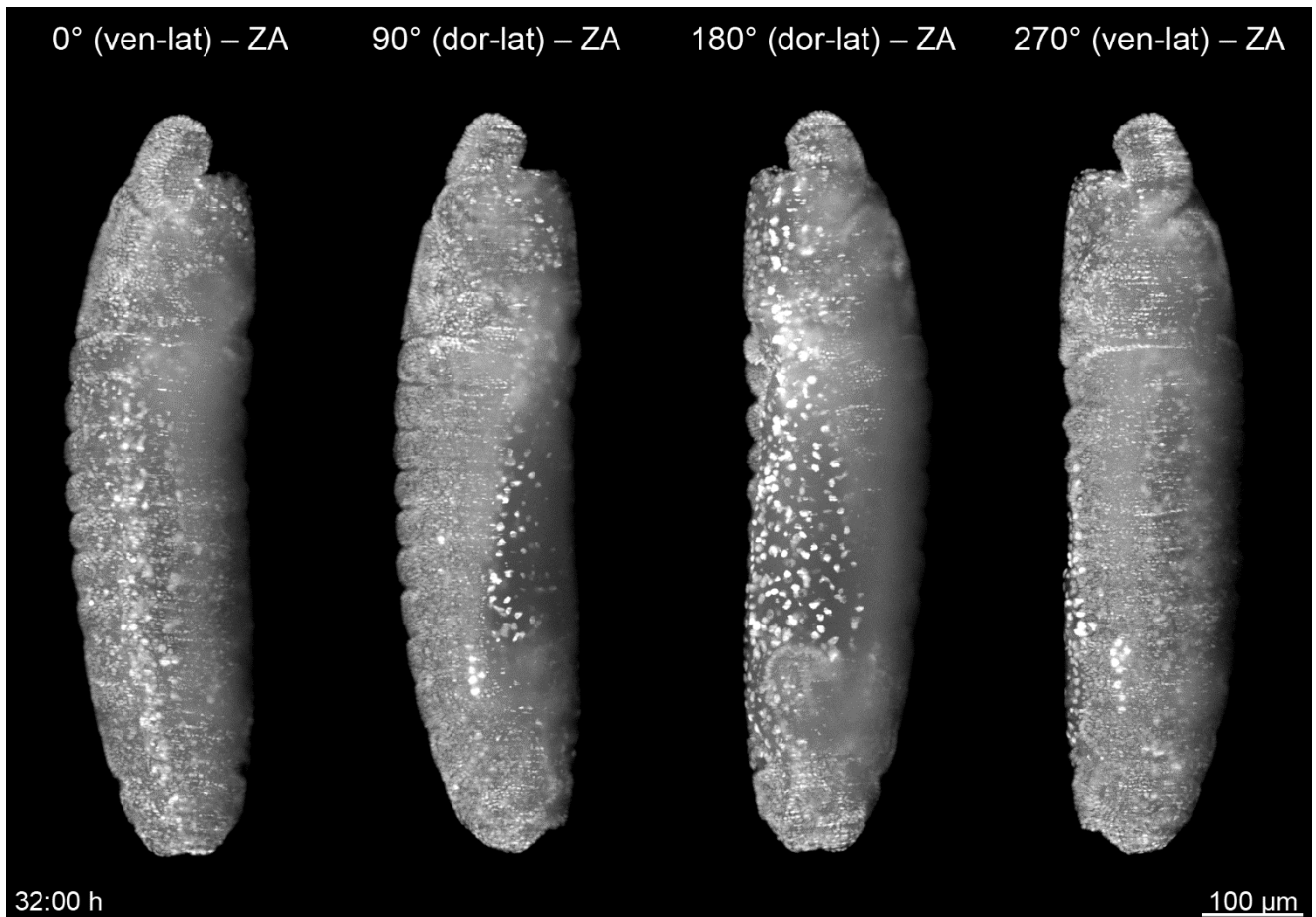
Supplementary Table 2

Supplementary Table 2 – Selection of structures and processes of higher importance that are found in *Drosophila*, but are not described in our study. Our study characterizes the embryogenesis of *Ceratitis* mainly on the tissue and cell level. Thus, we do not describe any subcellular structures and processes with the exception of nuclei.

structure / process	rationale
anterior transversal furrow	Does not arise during <i>Ceratitis</i> embryogenesis (see <i>extra-embryonic membrane folding</i> in Table 3).
apoptosis	Not properly detectable with our method.
epiphysis	Not properly identifiable in our data.
fat bodies	Not properly identifiable in our data.
gastric caeca	Not properly identifiable in our data.
gonads	Not properly identifiable in our data.
macrophages	Not properly detectable with our method.
Malpighian tubes	Not properly identifiable in our data.
mesoderm development	Only differentiation of the <i>ventral furrow</i> into the <i>mesodermal layer</i> and the emergence of the <i>ventral mesectoderm</i> , which gives rise to the mesectoderm, can be properly observed in our data. Thus, any further mesoderm development is not described within this study (see <i>germ layer specification</i> in Table 3).
mitotic divisions	Only mitotic divisions during blastoderm formation (stages I-1 to I-5) and gastrulation (stages II-6 and II-7) can be properly identified in our data. Thus, any further mitotic division is not described within this study.
neurogenesis	Only segregation of <i>neuroblasts</i> from the <i>ventral epidermal primordium</i> , emergence and mitotic division of the <i>optic lobe primordium</i> and shortening of the posterior tip of the <i>ventral cord</i> can be properly observed in our data. Thus, any further neuronal development is not described within this study.
oesophagus	In our study, the <i>stomodeum</i> is not further subdivided into pharynx, oesophagus and proventriculus.
oocyte nucleus	Not properly identifiable in our data. The first nuclei that we describe are the <i>zygotie nuclei</i> .
parasegmental furrows	Not properly detectable in our data. If any parasegmental furrows arise in <i>Ceratitis</i> , they are most probably very faint.
pharynx	In our study, the <i>stomodeum</i> is not further subdivided into pharynx, oesophagus and proventriculus.
posterior transversal furrow	Does not arise during <i>Ceratitis</i> embryogenesis (see <i>extra-embryonic membrane folding</i> in Table 3).
proventriculus	In our study, the <i>stomodeum</i> is not further subdivided into pharynx, oesophagus and proventriculus.
salivary glands	No substructures (placodes, lobes, ducts, tubes) properly identifiable in our data.
spiracles	Not properly identifiable in our data.
tentorium	Not properly identifiable in our data.
tracheal system	No substructures (placodes, pits, tubules) properly identifiable in our data.
vitellophages	Not properly detectable with our method.
yolk granules	Not properly detectable with our method.

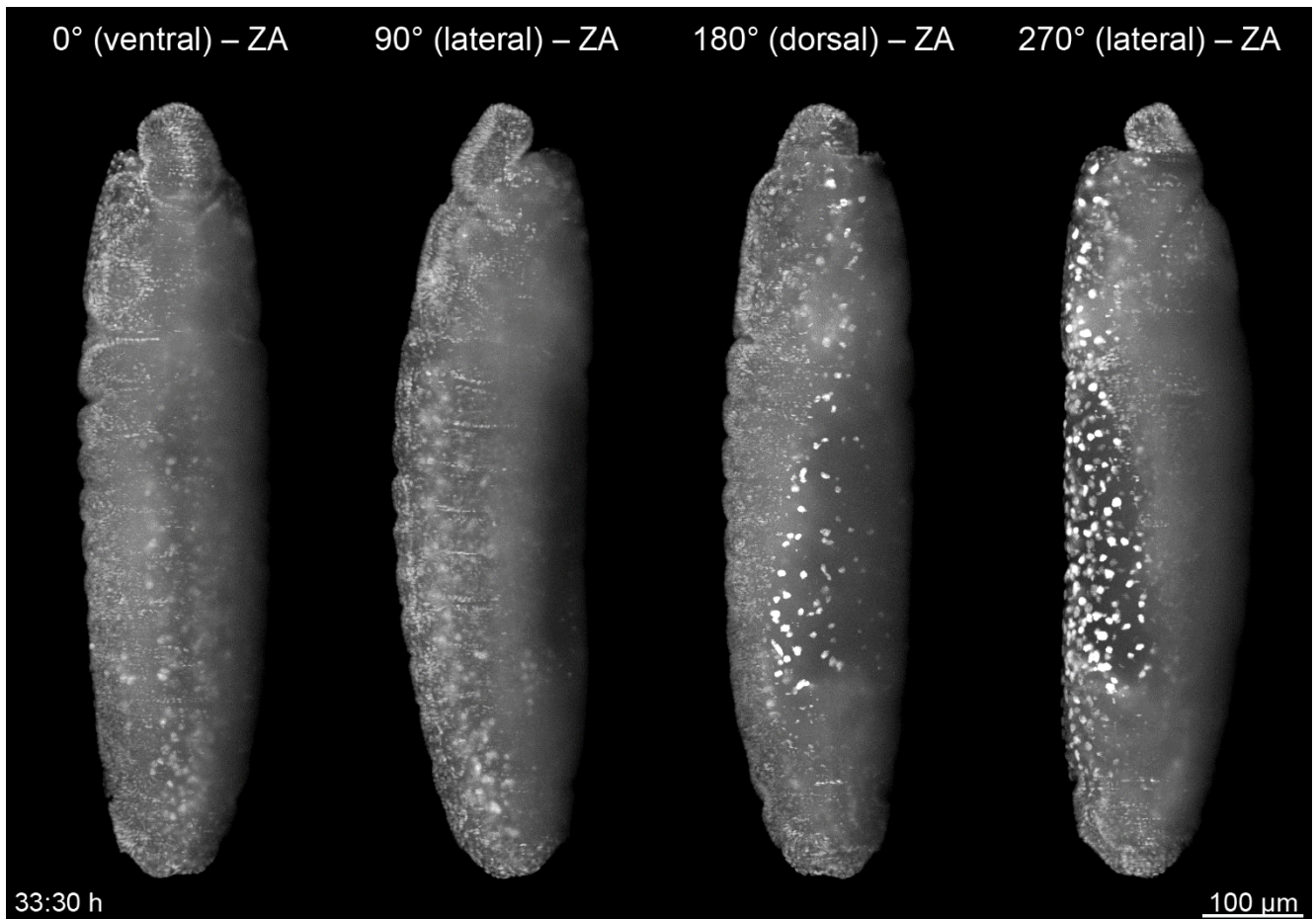
Supplementary Videos

Supplementary Video 1



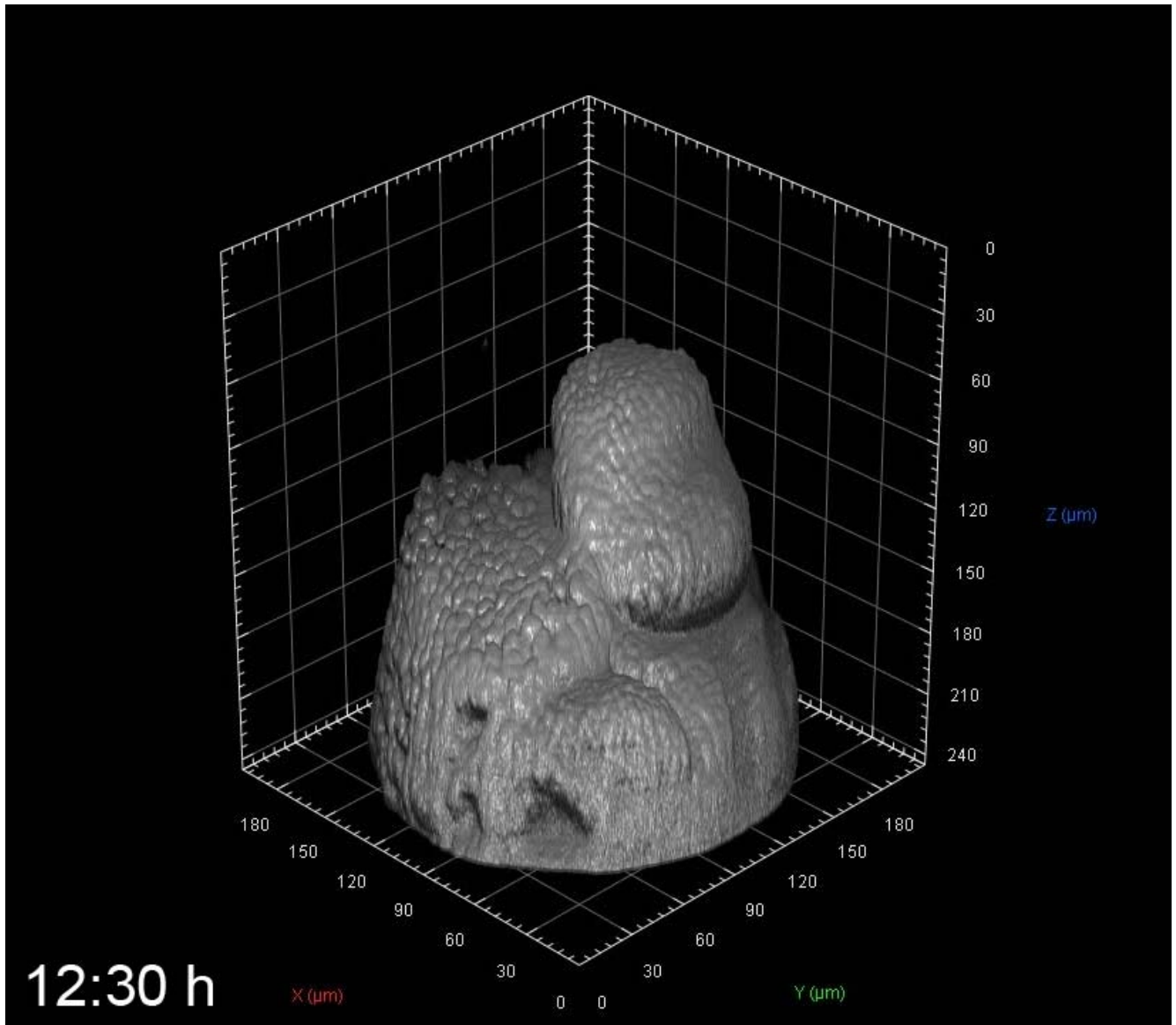
Supplementary Video 1 – *Ceratitis* embryogenesis (dataset DS0001) along four orientations (ventrolateral, dorsolateral, dorsolateral and ventrolateral) from 02:00 h to 62:30 h with an interval of 00:30 h between the time points. The video starts at the beginning of stage I-2, when the nuclei move to the surface of the egg and stops at the end of stage VI-17, when the larvae hatch from the egg, showing six embryogenetic events: (I) blastoderm formation, (II) gastrulation, (III) germband elongation, (IV) germband retraction, (V) dorsal closure and (VI) muscular movement. Frame rate is five frames per second. ZA, Z maximum projection with image adjustment; ven-lat, ventrolateral; dor-lat, dorsolateral.

Supplementary Video 2



Supplementary Video 2 – *Ceratitis* embryogenesis (dataset DS0001) along four orientations (ventral, lateral, dorsal and lateral) from 02:00 h to 62:30 h with an interval of 00:30 h between the time points. The video starts at the beginning of stage I-2, when the *zygotic nuclei* migrate to the surface of the egg and stops at the end of stage VI-17, when the *embryo* completes embryonic development, hatches and turns into the larva. Frame rate is five frames per second. ZA, Z maximum projection with image adjustment.

Supplementary Video 3



Supplementary Video 3 – Arivis-based volume rendering of the *head* (dataset DS0009) along the 0° (ventrolateral) orientation over 25:00 h with an interval of 00:30 h between the time points. The video starts during stage 13, shortly before the *clypeolabrum* turns from an anterior-dorsal to an anterior-ventral orientation and stops during stage 16, shortly after the *head involution* process is completed. Frame rate is five frames per second.

Acknowledgements

We thank Maximilian Sandmann and Sven Plath for technical support

Funding

The research was funded by the Cluster of Excellence Frankfurt for Macromolecular Complexes (CEF-MC, EXC 115) granted to the Buchmann Institute for Molecular Life Sciences (BMLS) at the Goethe University – Frankfurt am Main by the Deutsche Forschungsgemeinschaft (DFG).

Competing Interests Statement

The authors declare no competing financial interests.

Author Contributions

FS designed the figures and tables. FS and AS performed the quantification. All authors conceived the research, analyzed the data and wrote the publication.

References

11. Bodmer R, Venkatesh T V. Heart development in *Drosophila* and vertebrates: conservation of molecular mechanisms. *Dev Genet.* 1998;22: 181–6. doi:10.1002/(SICI)1520-6408(1998)22:3<181::AID-DVG1>3.0.CO;2-2
2. Kumar JP. Signalling pathways in *Drosophila* and vertebrate retinal development. *Nat Rev Genet.* 2001;2: 846–57. doi:10.1038/35098564
3. Bellen HJ, Tong C, Tsuda H. 100 years of *Drosophila* research and its impact on vertebrate neuroscience: a history lesson for the future. *Nat Rev Neurosci.* 2010;11: 514–522. doi:10.1038/nrn2839
4. Abzhanov A, Extavour CG, Groover A, Hodges SA, Hoekstra HE, Kramer EM, et al. Are we there yet? Tracking the development of new model systems. *Trends Genet.* 2008;24: 353–360. doi:10.1016/j.tig.2008.04.002
5. Jenner RA. Unburdening evo-devo: Ancestral attractions, model organisms, and basal baloney. *Development Genes and Evolution.* 2006. pp. 385–394. doi:10.1007/s00427-006-0084-5
6. Jenner RA, Wills MA. The choice of model organisms in evo-devo. *Nat Rev Genet.* 2007;8: 311–319. doi:10.1038/nrg2062
7. Sommer RJ. The future of evo-devo: model systems and evolutionary theory. *Nat Rev Genet.* 2009;10: 416–22. doi:10.1038/nrg2567
8. Heffer A, Pick L. Conservation and variation in Hox genes: how insect models pioneered the evo-devo field. *Annu Rev Entomol.* 2013;58: 161–79. doi:10.1146/annurev-ento-120811-153601
9. Abouheif E, Favé M-J, Ibarrarán-Viniegra AS, Lesoway MP, Rafiqi AM, Rajakumar R. Eco-Evo-Devo: The Time Has Come. *Advances in experimental medicine and biology.* 2014. pp. 107–125. doi:10.1007/978-94-007-7347-9_6
10. Dearden PK, Duncan EJ, Wilson MJ. The honeybee *Apis mellifera*. *Cold Spring Harb Protoc.* 2009;2009: pdb.emo123. doi:10.1101/pdb.emo123
11. Werren JH, Loehlin DW. The parasitoid wasp *Nasonia*: an emerging model system with haploid male genetics. *Cold Spring Harb Protoc.* 2009;2009: pdb.emo134. doi:10.1101/pdb.emo134
12. Klingler M. *Tribolium*. *Curr Biol.* 2004;14: R639-40. doi:10.1016/j.cub.2004.08.004
13. Brown SJ, Shippy TD, Miller S, Bolognesi R, Beeman RW, Lorenzen MD, et al. The red flour beetle,

Tribolium castaneum (Coleoptera): A model for studies of development and pest biology. Cold Spring Harb Protoc. 2009;4. doi:10.1101/pdb.emo126

14. Brakefield PM, Beldade P, Zwaan BJ. The African butterfly *Bicyclus anynana*: a model for evolutionary genetics and evolutionary developmental biology. Cold Spring Harb Protoc. 2009;2009: pdb.emo122. doi:10.1101/pdb.emo122
15. Rafiqi AM, Lemke S, Schmidt-Ott U. The scuttle fly *Megaselia abdita* (Phoridae): A link between *Drosophila* and mosquito development. Cold Spring Harb Protoc. 2011;6. doi:10.1101/pdb.emo143
16. Crombach A, García-Solache MA, Jaeger J. Evolution of early development in dipterans: Reverse-engineering the gap gene network in the moth midge *Clogmia albipunctata* (Psychodidae). Biosystems. 2014;123: 74–85. doi:10.1016/j.biosystems.2014.06.003
17. Misof B, Liu S, Meusemann K, Peters RS, Donath A, Mayer C, et al. Phylogenomics resolves the timing and pattern of insect evolution. Science. 2014;346: 763–7. doi:10.1126/science.1257570
18. Rafiqi AM, Lemke S, Ferguson S, Stauber M, Schmidt-Ott U. Evolutionary origin of the amnioserosa in cyclorrhaphan flies correlates with spatial and temporal expression changes of zen. Proc Natl Acad Sci. 2008;105: 234–239. doi:10.1073/pnas.0709145105
19. Rafiqi AM, Lemke S, Schmidt-Ott U. Postgastrular zen expression is required to develop distinct amniotic and serosal epithelia in the scuttle fly *Megaselia*. Dev Biol. 2010;341: 282–90. doi:10.1016/j.ydbio.2010.01.040
20. Rafiqi AM, Park C-H, Kwan CW, Lemke S, Schmidt-Ott U. BMP-dependent serosa and amnion specification in the scuttle fly *Megaselia abdita*. Development. 2012;139: 3373–82. doi:10.1242/dev.083873
21. Wotton KR, Jiménez-Guri E, García Matheu B, Jaeger J. A staging scheme for the development of the scuttle fly *Megaselia abdita*. PLoS One. Public Library of Science; 2014;9: e84421. doi:10.1371/journal.pone.0084421
22. Jiménez-Guri E, Wotton KR, Gavilán B, Jaeger J. A staging scheme for the development of the moth midge *Clogmia albipunctata*. PLoS One. 2014;9. doi:10.1371/journal.pone.0084422
23. Pane A, De Simone A, Saccone G, Polito C. Evolutionary conservation of *Ceratitis capitata* transformer gene function. Genetics. 2005;171: 615–624. doi:10.1534/genetics.105.041004
24. Gabrieli P, Falaguerra A, Siciliano P, Gomulski LM, Scolari F, Zacharopoulou A, et al. Sex and the single embryo: early development in the Mediterranean fruit fly, *Ceratitis capitata*. BMC Dev Biol. 2010;10: 12. doi:10.1186/1471-213X-10-12
25. Schetelig MF, Schmid BGM, Zimowska G, Wimmer EA. Plasticity in mRNA expression and localization of orthodenticle within higher Diptera. Evol Dev. Blackwell Publishing Inc; 2008;10: 700–704. doi:10.1111/j.1525-142X.2008.00283.x
26. Ogaugwu CE, Wimmer EA. Molecular cloning and expression of nanos in the Mediterranean fruit fly, *Ceratitis capitata* (Diptera: Tephritidae). Gene Expr Patterns. 2013;13: 183–188. doi:10.1016/j.gep.2013.03.002
27. Vreede BM, Lynch JA, Roth S, Sucena E. Co-option of a coordinate system defined by the EGFr and Dpp pathways in the evolution of a morphological novelty. Evodevo. 2013;4: 7. doi:10.1186/2041-9139-4-7
28. Tanaka K, Diekmann Y, Hazbun A, Hijazi A, Vreede B, Roch F, et al. Multispecies Analysis of Expression Pattern Diversification in the Recently Expanded Insect Ly6 Gene Family. Mol Biol Evol. Oxford University Press; 2015;32: 1730–47. doi:10.1093/molbev/msv052
29. Gomulski LM, Dimopoulos G, Xi Z, Soares MB, Bonaldo MF, Malacrida AR, et al. Gene discovery in an invasive tephritid model pest species, the Mediterranean fruit fly, *Ceratitis capitata*. BMC Genomics. 2008;9: 243. doi:10.1186/1471-2164-9-243
30. Gomulski LM, Dimopoulos G, Xi Z, Scolari F, Gabrieli P, Siciliano P, et al. Transcriptome profiling of sexual maturation and mating in the Mediterranean fruit fly, *Ceratitis capitata*. Ouzounis CA, editor. PLoS One. 2012;7: e30857. doi:10.1371/journal.pone.0030857
31. Scolari F, Gomulski LM, Ribeiro JMC, Siciliano P, Meraldi A, Falchetto M, et al. Transcriptional Profiles of Mating-Responsive Genes from Testes and Male Accessory Glands of the Mediterranean Fruit Fly, *Ceratitis capitata*. PLoS One. 2012;7. doi:10.1371/journal.pone.0046812

32. Salvemini M, Arunkumar KP, Nagaraju J, Sanges R, Petrella V, Tomar A, et al. De novo assembly and transcriptome analysis of the Mediterranean fruit fly *Ceratitis capitata* early embryos. Oliveira PL, editor. PLoS One. 2014;9: e114191. doi:10.1371/journal.pone.0114191
33. Steck GJ, Ekesi S. Description of third instar larvae of *Ceratitis fasciventris*, *C. anonae*, *C. rosa* (FAR complex) and *C. capitata* (Diptera, Tephritidae). Zookeys. 2015;540: 443–466. doi:10.3897/zookeys.540.10061
34. Marchini D, Del Bene G, Falso LF, Dallai R. Structural organization of the copulation site in the medfly *Ceratitis capitata* (Diptera: Tephritidae) and observations on sperm transfer and storage. Arthropod Struct Dev. 2001;30: 39–54. doi:10.1016/S1467-8039(01)00018-4
35. Marchini D, Del Bene G, Cappelli L, Dallai R. Ultrastructure of the male reproductive accessory glands in the medfly *Ceratitis capitata* (Diptera: Tephritidae) and preliminary characterization of their secretions. Arthropod Struct Dev. 2003;31: 313–327. doi:10.1016/S1467-8039(03)00003-3
36. Solari P, Corda V, Sollai G, Kreissl S, Galizia CG, Crnjar R. Morphological characterization of the antennal lobes in the Mediterranean fruit fly *Ceratitis capitata*. J Comp Physiol A. 2016;202: 131–146. doi:10.1007/s00359-015-1059-7
37. Papanicolaou A, Schetelig MF, Arensburger P, Atkinson PW, Benoit JB, Bourtzis K, et al. The whole genome sequence of the Mediterranean fruit fly, *Ceratitis capitata* (Wiedemann), reveals insights into the biology and adaptive evolution of a highly invasive pest species. Genome Biol. 2016;17: 192. doi:10.1186/s13059-016-1049-2
38. Callaini G. Cleavage and membrane formation in the blastoderm of the dipteran *Ceratitis capitata* wied. J Morphol. Wiley Subscription Services, Inc., A Wiley Company; 1987;193: 305–315. doi:10.1002/jmor.1051930308
39. Riparbelli MG, Callaini G, Dallai R. Primordial germ cell migration in the *Ceratitis capitata* embryo. Tissue Cell. 1996;28: 99–105. doi:10.1016/S0040-8166(96)80048-6
40. Campos-Ortega JA, Hartenstein V. The Embryonic Development of *Drosophila melanogaster* [Internet]. Springer-Verlag Berlin. 1997. doi:10.1007/978-3-662-22489-2
41. Havelka J, Landa V, Landa V. Embryogenesis of *Aphidoletes aphidimyza* (Diptera: Cecidomyiidae): Morphological markers for staging of living embryos. Eur J Entomol. 2007;104: 81–87. doi:10.14411/eje.2007.013
42. Raminani, L. N.; Cupp EW. Early embryology of *Aedes aegypti* diptera culicidae. Int J Insect Morphol Embryol. 1975;4: 517–528.
43. Raminani LN, Cupp EW. Embryology of *Aedes aegypti* (L.) (Diptera: Culicidae): Organogenesis. Int J Insect Morphol Embryol. 1978;7: 273–296. doi:10.1016/0020-7322(78)90009-0
44. Schetelig MF, Caceres C, Zacharopoulou A, Franz G, Wimmer EA. Conditional embryonic lethality to improve the sterile insect technique in *Ceratitis capitata* (Diptera: Tephritidae). BMC Biol. 2009;7: 4. doi:10.1186/1741-7007-7-4
45. Huisken J, Swoger J, Del Bene F, Wittbrodt J, Stelzer EHK. Optical sectioning deep inside live embryos by selective plane illumination microscopy. Science. 2004;305: 1007–9. doi:10.1126/science.1100035
46. Keller PJ, Schmidt AD, Wittbrodt J, Stelzer EHK. Reconstruction of zebrafish early embryonic development by scanned light sheet microscopy. Science. 2008;322: 1065–9. doi:10.1126/science.1162493
47. Stelzer EHK. Light-sheet fluorescence microscopy for quantitative biology. Nat Methods. 2015;12: 23–6. doi:10.1038/nmeth.3219
48. Zhu N, Wang G, Yang G, Dai W. A fast 2D otsu thresholding algorithm based on improved histogram. Proceedings of the 2009 Chinese Conference on Pattern Recognition, CCPR 2009, and the 1st CJK Joint Workshop on Pattern Recognition, CJKPR. 2009. pp. 319–323. doi:10.1109/CCPR.2009.5344078
49. Malpica N, De Sol??rzano CO, Vaquero JJ, Santos A, Vallcorba I, Garc??a-Sagredo JM, et al. Applying watershed algorithms to the segmentation of clustered nuclei. Cytometry. 1997;28: 289–297. doi:10.1002/(SICI)1097-0320(19970801)28:4<289::AID-CYTO3>3.0.CO;2-7
50. Pinidiyaarachchi A, Wählby C. Seeded watersheds for combined segmentation and tracking of cells. Lecture Notes in Computer Science (including subseries Lecture Notes in Artificial Intelligence and Lecture Notes in Bioinformatics). 2005. pp. 336–343. doi:10.1007/11553595_41

51. Caroti F, Urbansky S, Wosch M, Lemke S. Germ line transformation and in vivo labeling of nuclei in Diptera: report on *Megaselia abdita* (Phoridae) and *Chironomus riparius* (Chironomidae). *Dev Genes Evol.* Springer Berlin Heidelberg; 2015;225: 179–186. doi:10.1007/s00427-015-0504-5
52. Lacy ME, Hutson MS. Amnioserosa development and function in *Drosophila* embryogenesis: Critical mechanical roles for an extraembryonic tissue. *Dev Dyn.* 2016;245: 558–568. doi:10.1002/dvdy.24395
53. Schmidt-Ott U, Kwan CW. Morphogenetic functions of extraembryonic membranes in insects. *Curr Opin Insect Sci.* 2016;13: 86–92. doi:10.1016/j.cois.2016.01.009
54. Horn T, Hilbrant M, Panfilio KA. Evolution of epithelial morphogenesis: phenotypic integration across multiple levels of biological organization. *Front Genet. Frontiers Media SA;* 2015;6: 303. doi:10.3389/fgene.2015.00303
55. van der Zee M, Berns N, Roth S. Distinct functions of the *Tribolium* *zerknüllt* genes in serosa specification and dorsal closure. *Curr Biol.* 2005;15: 624–36. doi:10.1016/j.cub.2005.02.057
56. Sharma R, Beermann A, Schröder R. The dynamic expression of extraembryonic marker genes in the beetle *Tribolium castaneum* reveals the complexity of serosa and amnion formation in a short germ insect. *Gene Expr Patterns.* 2013;13: 362–71. doi:10.1016/j.gep.2013.07.002
57. Panfilio K a, Oberhofer G, Roth S. High plasticity in epithelial morphogenesis during insect dorsal closure. *Biol Open.* 2013;2: 1108–18. doi:10.1242/bio.20136072
58. Koelzer S, Kölsch Y, Panfilio KA. Visualizing late insect embryogenesis: extraembryonic and mesodermal enhancer trap expression in the beetle *Tribolium castaneum*. *PLoS One.* 2014;9: e103967. doi:10.1371/journal.pone.0103967
59. Hilbrant M, Horn T, Koelzer S, Panfilio KA. The beetle amnion and serosa functionally interact as apposed epithelia. *Elife.* 2016;5. doi:10.7554/eLife.13834
60. Horn T, Panfilio KA. Novel functions for *Dorsocross* in epithelial morphogenesis in the beetle *Tribolium castaneum*. *Development.* 2016;143: 3002–11. doi:10.1242/dev.133280
61. Panfilio KA, Liu PZ, Akam M, Kaufman TC. *Oncopeltus fasciatus zen* is essential for serosal tissue function in *katatrepsis*. *Dev Biol.* 2006;292: 226–243. doi:10.1016/j.ydbio.2005.12.028
62. Panfilio KA. Extraembryonic development in insects and the acrobatics of blastokinesis. *Developmental Biology.* 2008. pp. 471–491. doi:10.1016/j.ydbio.2007.11.004
63. Panfilio KA, Roth S. Epithelial reorganization events during late extraembryonic development in a hemimetabolous insect. *Dev Biol.* 2010;340: 100–115. doi:10.1016/j.ydbio.2009.12.034
64. Keller PJ, Schmidt AD, Santella A, Khairy K, Bao Z, Wittbrodt J, et al. Fast, high-contrast imaging of animal development with scanned light sheet-based structured-illumination microscopy. *Nat Methods.* 2010;7: 637–42. doi:10.1038/nmeth.1476
65. Tomer R, Khairy K, Amat F, Keller PJ. Quantitative high-speed imaging of entire developing embryos with simultaneous multiview light-sheet microscopy. *Nat Methods.* 2012;9: 755–63. doi:10.1038/nmeth.2062
66. Krzic U, Gunther S, Saunders TE, Streichan SJ, Hufnagel L. Multiview light-sheet microscope for rapid in toto imaging. *Nat Methods.* 2012;9: 730–3. doi:10.1038/nmeth.2064
67. Chhetri RK, Amat F, Wan Y, Höckendorf B, Lemon WC, Keller PJ. Whole-animal functional and developmental imaging with isotropic spatial resolution. *Nat Methods.* 2015;12: 1171–8. doi:10.1038/nmeth.3632
68. Strobl F, Stelzer EHK. Non-invasive long-term fluorescence live imaging of *Tribolium castaneum* embryos. *Development.* 2014;141: 2331–2338. doi:10.1242/dev.108795
69. Strobl F, Schmitz A, Stelzer EHK. Live imaging of *Tribolium castaneum* embryonic development using light-sheet-based fluorescence microscopy. *Nat Protoc. Nature Publishing Group, a division of Macmillan Publishers Limited. All Rights Reserved.;* 2015;10: 1486–1507. doi:10.1038/nprot.2015.093
70. Strobl F, Stelzer EH. Long-term fluorescence live imaging of *Tribolium castaneum* embryos: principles, resources, scientific challenges and the comparative approach. *Curr Opin Insect Sci.* 2016;18: 17–26. doi:10.1016/j.cois.2016.08.002
71. Rosenberg MI, Lynch JA, Desplan C. Heads and tails: evolution of antero-posterior patterning in insects. *Biochim Biophys Acta. NIH Public Access;* 2009;1789: 333–42. doi:10.1016/j.bbagr.2008.09.007

72. Reuter R. The gene *serpent* has homeotic properties and specifies endoderm versus ectoderm within the *Drosophila* gut. *Development*. 1994;120: 1123–35. Available: <http://www.ncbi.nlm.nih.gov/pubmed/7913013>
73. Kuntz SG, Eisen MB, Lerat E, Vieira C, Carareto C. *Drosophila* Embryogenesis Scales Uniformly across Temperature in Developmentally Diverse Species. Desplan C, editor. *PLoS Genet*. Public Library of Science; 2014;10: e1004293. doi:10.1371/journal.pgen.1004293
74. Colas J-F, Launay J-M, Vonesch J-L, Hickel P, Maroteaux L. Serotonin synchronises convergent extension of ectoderm with morphogenetic gastrulation movements in *Drosophila*. *Mech Dev*. 1999;87: 77–91. doi:10.1016/S0925-4773(99)00141-0
75. Lengyel JA, Iwaki DD. It Takes Guts: The *Drosophila* Hindgut as a Model System for Organogenesis. *Dev Biol*. 2002;243: 1–19. doi:10.1006/dbio.2002.0577
76. Scuderi A, Letsou A. Amnioserosa is required for dorsal closure in *Drosophila*. *Dev Dyn*. 2005;232: 791–800. doi:10.1002/dvdy.20306
77. Schmidt-Ott U. The amnioserosa is an apomorphic character of cyclorrhaphan flies. *Dev Genes Evol*. 2000;210: 373–6. doi:10.1007/s004270050325
78. Higashijima S, Michiue T, Emori Y, Saigo K. Subtype determination of *Drosophila* embryonic external sensory organs by redundant homeo box genes *BarH1* and *BarH2*. *Genes Dev*. 1992;6: 1005–18. Available: <http://www.ncbi.nlm.nih.gov/pubmed/1350558>
79. Fascetti N, Baumgartner S. Expression of *Drosophila* *Ten-a*, a dimeric receptor during embryonic development. *Mech Dev*. 2002;114: 197–200. doi:10.1016/S0925-4773(02)00055-2
80. Nakagoshi H. Functional specification in the *Drosophila* endoderm. *Dev Growth Differ*. 2005;47: 383–392. doi:10.1111/j.1440-169X.2005.00811.x
81. Tepass U, Hartenstein V. Epithelium formation in the *Drosophila* midgut depends on the interaction of endoderm and mesoderm. *Development*. 1994;120: 579–90. Available: <http://www.ncbi.nlm.nih.gov/pubmed/8162857>
82. Younossi-Hartenstein A, Tepass U, Hartenstein V. Embryonic origin of the imaginal discs of the head of *Drosophila melanogaster*. *Roux's Arch Dev Biol*. Springer-Verlag; 1993;203: 60–73. doi:10.1007/BF00539891
83. Wu M, Sato TN. On the mechanics of cardiac function of *Drosophila* embryo. *PLoS One*. Public Library of Science; 2008;3: e4045. doi:10.1371/journal.pone.0004045
84. Mazumdar A, Mazumdar M. How one becomes many: Blastoderm cellularization in *Drosophila melanogaster*. *BioEssays*. 2002;24: 1012–1022. doi:10.1002/bies.10184
85. Luengo Hendriks CL, Keränen SVE, Fowlkes CC, Simirenko L, Weber GH, DePace AH, et al. Three-dimensional morphology and gene expression in the *Drosophila* blastoderm at cellular resolution I: data acquisition pipeline. *Genome Biol*. *BioMed Central*; 2006;7: R123. doi:10.1186/gb-2006-7-12-r123
86. Hunter C, Wieschaus E. Regulated expression of *nullo* is required for the formation of distinct apical and basal adherens junctions in the *Drosophila* blastoderm. *J Cell Biol*. The Rockefeller University Press; 2000;150: 391–401. Available: <http://www.ncbi.nlm.nih.gov/pubmed/10908580>
87. Mahowald AP. Electron microscopy of the formation of the cellular blastoderm in *Drosophila melanogaster*. *Exp Cell Res*. 1963;32: 457–468. doi:10.1016/0014-4827(63)90186-1
88. Karr TL, Kornberg TB. *fushi tarazu* protein expression in the cellular blastoderm of *Drosophila* detected using a novel imaging technique. *Development*. 1989;106: 95–103. Available: <http://www.ncbi.nlm.nih.gov/pubmed/2697548>
89. Vincent A, Blankenship JT, Wieschaus E. Integration of the head and trunk segmentation systems controls cephalic furrow formation in *Drosophila*. *Development*. 1997;124: 3747–54. Available: <http://www.ncbi.nlm.nih.gov/pubmed/9367430>
90. Spencer AK, Siddiqui BA, Thomas JH. Cell shape change and invagination of the cephalic furrow involves reorganization of F-actin. *Dev Biol*. 2015;402: 192–207. doi:10.1016/j.ydbio.2015.03.022
91. Jackson PD, Hoffmann FM. Embryonic expression patterns of the *Drosophila* *decapentaplegic* gene: Separate regulatory elements control blastoderm expression and lateral ectodermal expression. *Dev Dyn*. 1994;199: 28–44. doi:10.1002/aja.1001990104

92. Buchon N, Osman D, David FPA, Yu Fang H, Boquete J-P, Deplancke B, et al. Morphological and Molecular Characterization of Adult Midgut Compartmentalization in *Drosophila*. *Cell Rep*. 2013;3: 1725–1738. doi:10.1016/j.celrep.2013.04.001
93. Lemaitre B, Miguel-Aliaga I. The Digestive Tract of *Drosophila melanogaster*. *Annu Rev Genet. Annual Reviews* ; 2013;47: 377–404. doi:10.1146/annurev-genet-111212-133343
94. Fredieu JR, Mahowald AP. Glial interactions with neurons during *Drosophila* embryogenesis. *Development*. 1989;106: 739–48. Available: <http://www.ncbi.nlm.nih.gov/pubmed/2562666>
95. Bokor P, DiNardo S. The roles of hedgehog, wingless and lines in patterning the dorsal epidermis in *Drosophila*. *Development*. 1996;122: 1083–92. Available: <http://www.ncbi.nlm.nih.gov/pubmed/8620835>
96. Kaltschmidt JA, Lawrence N, Morel V, Balayo T, Fernández BG, Pelissier A, et al. Planar polarity and actin dynamics in the epidermis of *Drosophila*. *Nat Cell Biol. Nature Publishing Group*; 2002;4: 937–944. doi:10.1038/ncb882
97. VanHook A, Letsou A. Head involution in *Drosophila*: Genetic and morphogenetic connections to dorsal closure. *Dev Dyn. Wiley-Liss, Inc.*; 2008;237: 28–38. doi:10.1002/dvdy.21405
98. St Johnston RD, Gelbart WM. Decapentaplegic transcripts are localized along the dorsal-ventral axis of the *Drosophila* embryo. *EMBO J*. 1987;6: 2785–91. Available: <http://www.ncbi.nlm.nih.gov/pubmed/3119329>
99. Zikova M, Da Ponte J-P, Dastugue B, Jagla K. Patterning of the cardiac outflow region in *Drosophila*. *Proc Natl Acad Sci U S A*. 2003;100: 12189–94. doi:10.1073/pnas.2133156100
100. Irvine KD, Wieschaus E. Cell intercalation during *Drosophila* germband extension and its regulation by pair-rule segmentation genes. *Development*. 1994;120: 827–41. Available: <http://www.ncbi.nlm.nih.gov/pubmed/7600960>
101. Davis GK, Jaramillo CA, Patel NH. Pax group III genes and the evolution of insect pair-rule patterning. *Development*. 2001;128: 3445–58. Available: <http://www.ncbi.nlm.nih.gov/pubmed/11566851>
102. Cho NK, Keyes L, Johnson E, Heller J, Ryner L, Karim F, et al. Developmental control of blood cell migration by the *Drosophila* VEGF pathway. *Cell*. 2002;108: 865–76. Available: <http://www.ncbi.nlm.nih.gov/pubmed/11955438>
103. Lynch JA, El-Sherif E, Brown SJ. Comparisons of the embryonic development of *Drosophila*, *Nasonia*, and *Tribolium*. *Wiley Interdiscip Rev Dev Biol*. 2012;1: 16–39. doi:10.1002/wdev.3
104. Schmidt-Ott U, González-Gaitán M, Jäckle H, Technau GM. Number, identity, and sequence of the *Drosophila* head segments as revealed by neural elements and their deletion patterns in mutants. *Proc Natl Acad Sci U S A*. 1994;91: 8363–7. Available: <http://www.ncbi.nlm.nih.gov/pubmed/7915837>
105. Liu X, Lengyel JA. *Drosophila* arc Encodes a Novel Adherens Junction-Associated PDZ Domain Protein Required for Wing and Eye Development. *Dev Biol*. 2000;221: 419–434. doi:10.1006/dbio.2000.9689
106. Pultz MA, Diederich RJ, Cribbs DL, Kaufman TC. The proboscipedia locus of the Antennapedia complex: a molecular and genetic analysis. *Genes Dev*. 1988;2: 901–20. Available: <http://www.ncbi.nlm.nih.gov/pubmed/2850265>
107. Su YC, Treisman JE, Skolnik EY. The *Drosophila* Ste20-related kinase misshapen is required for embryonic dorsal closure and acts through a JNK MAPK module on an evolutionarily conserved signaling pathway. *Genes Dev*. 1998;12: 2371–80. Available: <http://www.ncbi.nlm.nih.gov/pubmed/9694801>
108. Kyriakis JM. Signaling by the germinal center kinase family of protein kinases. *J Biol Chem*. 1999;274: 5259–62. Available: <http://www.ncbi.nlm.nih.gov/pubmed/10026130>
109. Bejsovec A, Martinez Arias A. Roles of wingless in patterning the larval epidermis of *Drosophila*. *Development*. 1991;113: 471–85. Available: <http://www.ncbi.nlm.nih.gov/pubmed/1782860>
110. Fernandez R, Takahashi F, Liu Z, Steward R, Stein D, Stanley ER. The *Drosophila* shark tyrosine kinase is required for embryonic dorsal closure. *Genes Dev. Cold Spring Harbor Laboratory Press*; 2000;14: 604–14. Available: <http://www.ncbi.nlm.nih.gov/pubmed/10716948>
111. Knoblich JA, Schober M, Schaefer M. Bazooka recruits Inscuteable to orient asymmetric cell divisions in *Drosophila* neuroblasts. *Nature. Nature Publishing Group*; 1999;402: 548–551. doi:10.1038/990135
112. Lee KJ, Mukhopadhyay M, Pelka P, Campos AR, Steller H. Autoregulation of the *Drosophila*

- disconnected Gene in the Developing Visual System. *Dev Biol.* 1999;214: 385–398. doi:10.1006/dbio.1999.9420
113. Deshpande G, Calhoun G, Schedl P. The drosophila fragile X protein dFMR1 is required during early embryogenesis for pole cell formation and rapid nuclear division cycles. *Genetics*. Genetics Society of America; 2006;174: 1287–98. doi:10.1534/genetics.106.062414
 114. Dansereau DA, Lasko P. The development of germline stem cells in *Drosophila*. *Methods Mol Biol. NIH Public Access*; 2008;450: 3–26. doi:10.1007/978-1-60327-214-8_1
 115. Deshpande G, Calhoun G, Schedl P. *Drosophila argonaute-2* is required early in embryogenesis for the assembly of centric/centromeric heterochromatin, nuclear division, nuclear migration, and germ-cell formation. *Genes Dev.* Cold Spring Harbor Laboratory Press; 2005;19: 1680–5. doi:10.1101/gad.1316805
 116. Hozumi S, Maeda R, Taniguchi K, Kanai M, Shirakabe S, Sasamura T, et al. An unconventional myosin in *Drosophila* reverses the default handedness in visceral organs. *Nature*. Nature Publishing Group; 2006;440: 798–802. doi:10.1038/nature04625
 117. Beller M, Blanke S, Brentrup D, Jäckle H. Identification and expression of Ima, a novel Ral-interacting *Drosophila* protein. *Mech Dev.* 2002;119: S253–S260. doi:10.1016/S0925-4773(03)00125-4
 118. de Velasco B, Mandal L, Mkrtychyan M, Hartenstein V. Subdivision and developmental fate of the head mesoderm in *Drosophila melanogaster*. *Dev Genes Evol.* 2006;216: 39–51. doi:10.1007/s00427-005-0029-4
 119. Kuziora MA, McGinnis W. Different transcripts of the *Drosophila* Abd-B gene correlate with distinct genetic sub-functions. *EMBO J.* 1988;7: 3233–44. Available: <http://www.ncbi.nlm.nih.gov/pubmed/2903050>
 120. Murakami R, Shigenaga A, Kawakita M, Takimoto K, Yamaoka I, Akasaka K, et al. *aproctous*, a locus that is necessary for the development of the proctodeum in *Drosophila* embryos, encodes a homolog of the vertebrate *Brachyury* gene. *Roux's Arch Dev Biol.* Springer-Verlag; 1995;205: 89–96. doi:10.1007/BF00188847
 121. Kwan CW, Gavin-Smyth J, Ferguson EL, Schmidt-Ott U. Functional evolution of a morphogenetic gradient. *Elife*. eLife Sciences Publications, Ltd; 2016;5. doi:10.7554/eLife.20894
 122. Takashima S, Paul M, Aghajanian P, Younossi-Hartenstein A, Hartenstein V. Migration of *Drosophila* intestinal stem cells across organ boundaries. *Development*. Company of Biologists; 2013;140: 1903–11. doi:10.1242/dev.082933
 123. González-Gaitán M, Jäckle H. Invagination centers within the *Drosophila* stomatogastric nervous system anlage are positioned by Notch-mediated signaling which is spatially controlled through *wingless*. *Development*. 1995;121: 2313–25. Available: <http://www.ncbi.nlm.nih.gov/pubmed/7671798>
 124. Farge E. Mechanical Induction of Twist in the *Drosophila* Foregut/Stomodaeal Primordium. *Curr Biol.* 2003;13: 1365–1377. doi:10.1016/S0960-9822(03)00576-1
 125. Sherlekar A, Rikhy R. *Drosophila* embryo syncytial blastoderm cellular architecture and morphogen gradient dynamics: Is there a correlation? *Front Biol (Beijing)*. SP Higher Education Press; 2012;7: 73–82. doi:10.1007/s11515-011-1160-4
 126. Ali-Murthy Z, Kornberg TB, Schneider M, Frei E, Noll M, Baumgartner S, et al. Bicoid gradient formation and function in the *Drosophila* pre-syncytial blastoderm. *Elife*. eLife Sciences Publications Limited; 2016;5: 605–614. doi:10.7554/eLife.13222
 127. Struhl G. Genes controlling segmental specification in the *Drosophila* thorax. *Proc Natl Acad Sci U S A.* 1982;79: 7380–4. Available: <http://www.ncbi.nlm.nih.gov/pubmed/6961417>
 128. Peña-Rangel MT, Rodriguez I, Riesgo-Escovar JR. A misexpression study examining dorsal thorax formation in *Drosophila melanogaster*. *Genetics*. 2002;160: 1035–50. Available: <http://www.ncbi.nlm.nih.gov/pubmed/11901120>
 129. Cardona A, Larsen C, Hartenstein V. Neuronal fiber tracts connecting the brain and ventral nerve cord of the early *Drosophila* larva. *J Comp Neurol.* NIH Public Access; 2009;515: 427–40. doi:10.1002/cne.22086
 130. Boerner J, Duch C. An average shape standard atlas for the adult *Drosophila* ventral nerve cord. *J Comp Neurol.* 2010;518: NA-NA. doi:10.1002/cne.22346
 131. Gan G, Lv H, Xie W, Technau G, Buxton E. Morphological Identification and Development of Neurite in

Drosophila Ventral Nerve Cord Neuropil. Zhou R, editor. PLoS One. Public Library of Science; 2014;9: e105497. doi:10.1371/journal.pone.0105497

132. Sweeton D, Parks S, Costa M, Wieschaus E. Gastrulation in *Drosophila*: the formation of the ventral furrow and posterior midgut invaginations. *Development*. 1991;112: 775–89. Available: <http://www.ncbi.nlm.nih.gov/pubmed/1935689>
133. Conte V, Ulrich F, Baum B, Muñoz J, Veldhuis J, Brodland W, et al. A Biomechanical Analysis of Ventral Furrow Formation in the *Drosophila Melanogaster* Embryo. Goldstein B, editor. PLoS One. Reden and Vorträgeanlässlich der Emeritierung von Werner Tack (pp. 115–154). Saarbrueken, Germany: University of Saarland Press; 2012;7: e34473. doi:10.1371/journal.pone.0034473
134. Spahn P, Reuter R, Herz H, Bartoszewski S, Schnorrer F. A Vertex Model of *Drosophila* Ventral Furrow Formation. Kabla AJ, editor. PLoS One. Public Library of Science; 2013;8: e75051. doi:10.1371/journal.pone.0075051
135. Polyakov O, He B, Swan M, Shaevitz JW, Kaschube M, Wieschaus E. Passive mechanical forces control cell-shape change during *Drosophila* ventral furrow formation. *Biophys J*. 2014;107: 998–1010. doi:10.1016/j.bpj.2014.07.013
136. Schöck F, Perrimon N. Retraction of the *Drosophila* germ band requires cell-matrix interaction. *Genes Dev*. 2003;17: 597–602. doi:10.1101/gad.1068403
137. Blachon S, Khire A, Avidor-Reiss T. The origin of the second centriole in the zygote of *Drosophila melanogaster*. *Genetics*. Genetics Society of America; 2014;197: 199–205. doi:10.1534/genetics.113.160523
138. Ali-Murthy Z, Lott SE, Eisen MB, Kornberg TB, Ruan J. An Essential Role for Zygotic Expression in the Pre-Cellular *Drosophila* Embryo. Copenhaver GP, editor. PLoS Genet. Public Library of Science; 2013;9: e1003428. doi:10.1371/journal.pgen.1003428
139. Benton MA, Akam M, Pavlopoulos A. Cell and tissue dynamics during *Tribolium* embryogenesis revealed by versatile fluorescence labeling approaches. *Development*. 2013;140: 3210–20. doi:10.1242/dev.096271
140. Donoughe S, Extavour CG. Embryonic development of the cricket *Gryllus bimaculatus*. *Dev Biol*. 2015; doi:10.1016/j.ydbio.2015.04.009
141. Handel K, Grünfelder CG, Roth S, Sander K. *Tribolium* embryogenesis: a SEM study of cell shapes and movements from blastoderm to serosal closure. *Dev Genes Evol*. 2000;210: 167–79. doi:10.1007/s004270050301
142. Tripathy R, Kunwar PS, Sano H, Renault AD. Transcriptional regulation of *Drosophila* gonad formation. *Dev Biol*. 2014;392: 193–208. doi:10.1016/j.ydbio.2014.05.026
143. Lamka ML, Lipshitz HD. Role of the Amnioserosa in Germ Band Retraction of the *Drosophila melanogaster* Embryo. *Dev Biol*. 1999;214: 102–112. doi:10.1006/dbio.1999.9409
144. Stauber M, Taubert H, Schmidt-Ott U. Function of bicoid and hunchback homologs in the basal cyclorrhaphan fly *Megaselia* (Phoridae). *Proc Natl Acad Sci U S A*. National Academy of Sciences; 2000;97: 10844–9. doi:10.1073/pnas.190095397
145. Millard TH, Martin P. Dynamic analysis of filopodial interactions during the zipper phase of *Drosophila* dorsal closure. *Development*. Europe PMC Funders; 2008;135: 621–6. doi:10.1242/dev.014001
146. Jacinto A, Woolner S, Martin P. Dynamic Analysis of Dorsal Closure in *Drosophila*: From Genetics to Cell Biology. *Dev Cell*. 2002;3: 9–19. doi:10.1016/S1534-5807(02)00208-3
147. Kobayashi Y, Ando H. Early embryonic development and external features of developing embryos of the caddisfly, *Nemotaulius admorsus* (trichoptera: Limnephilidae). *J Morphol*. Wiley Subscription Services, Inc., A Wiley Company; 1990;203: 69–85. doi:10.1002/jmor.1052030108
148. Anderson DT, Lawson-Kerr C. The embryonic development of the marine caddis fly. *Philanisus plebeius* Walker (Trichoptera: Chathamidae). *Biol Bull*. 1977;153: 98–105. doi:10.2307/1540693
149. Nagy L, Riddiford L, Kiguchi K. Morphogenesis in the early embryo of the lepidopteran *Bombyx mori*. *Dev Biol*. 1994;165: 137–151. doi:10.1006/dbio.1994.1241
150. Ando H, Tanaka M. Early embryonic development of the primitive moths, *Endoclyta signifer* walker and *E. excrescens* butler (Lepidoptera: Hepialidae). *Int J Insect Morphol Embryol*. 1980;9: 67–77. doi:10.1016/0020-7322(80)90037-9

151. Kobayashi Y. Embryogenesis of the fairy moth, *Nemophora albi antennella issiki* (Lepidoptera, Adelidae), with special emphasis on its phylogenetic implications. *Int J Insect Morphol Embryol.* 1998;27: 157–166. doi:10.1016/S0020-7322(98)00006-3
152. Kobayashi Y, Ando H. The early embryonic development of the primitive moth, *Neomicropteryx nipponensis issiki* (Lepidoptera, Micropterygidae). *J Morphol.* Wiley Subscription Services, Inc., A Wiley Company; 1982;172: 259–269. doi:10.1002/jmor.1051720302
153. Kobayashi Y, Suzuki H, Ohba N. Embryogenesis of the glowworm *Rhagophthalmus ohbai* Wittmer (Insecta: Coleoptera, Rhagophthalmidae), with emphasis on the germ rudiment formation. *J Morphol.* 2002;253: 1–9. doi:10.1002/jmor.1109
154. Beeman SL, Norris DM. Embryogenesis of *Xyleborus ferrugineus* (Fabr.) (Coleoptera, Scolytidae). I. External morphogenesis of male and female embryos. *J Morphol.* 1977;152: 177–219. doi:10.1002/jmor.1051520205
155. Beeman SL, Norris DM. Embryogenesis of *Xyleborus ferrugineus* (Fabr.) (Coleoptera, Scolytidae). II. Developmental rates of male and female embryos. *J Morphol.* 1977;152: 221–227. doi:10.1002/jmor.1051520206
156. Fleig R, Sander K. Blastoderm development in honey bee embryogenesis as seen in the scanning electron microscope. *Int J Invertebr Reprod Dev.* Taylor & Francis Group; 1985; Available: <http://www.tandfonline.com/doi/abs/10.1080/01688170.1985.10510156#.VnFqL-hs3k>
157. Fleig R, Sander K. Embryogenesis of the honeybee *Apis mellifera* L. (Hymenoptera: Apidae): An SEM study. *Int J Insect Morphol Embryol.* 1986;15: 449–462. doi:10.1016/0020-7322(86)90037-1
158. Fleig and Sander. Honeybee morphogenesis: embryonic cell movements that shape the larval body. *Development.* 1988;103: 525–534.
159. Bull AL. Stages of living embryos in the jewel wasp *Mormoniella (Nasonia) vitripennis* (Walker) (Hymenoptera: Pteromalidae). *Int J Insect Morphol Embryol.* 1982;11: 1–23. doi:10.1016/0020-7322(82)90034-4
160. Miura T, Braendle C, Shingleton A, Sisk G, Kambhampati S, Stern DL. A comparison of parthenogenetic and sexual embryogenesis of the pea aphid *Acyrtosiphon pisum* (Hemiptera: Aphidoidea). *J Exp Zool B Mol Dev Evol.* 2003;295: 59–81. doi:10.1002/jez.b.00003
161. Uchifune T, Machida R. Embryonic development of *Galloisiana yuasai* Asahina, with special reference to external morphology (Insecta: Grylloblattodea). *J Morphol.* 2005;266: 182–207. doi:10.1002/jmor.10373
162. Kishimoto T, Ando H. External features of the developing embryo of the stonefly, *Kamimuria tibialis* (Pictet) (Plecoptera, Perlidae). *J Morphol.* Wiley Subscription Services, Inc., A Wiley Company; 1985;183: 311–326. doi:10.1002/jmor.1051830308
163. Kelly GM, Huebner E. Embryonic development of the hemipteran insect *Rhodnius prolixus*. *J Morphol.* Wiley Subscription Services, Inc., A Wiley Company; 1989;199: 175–196. doi:10.1002/jmor.1051990205
164. Tojo K, Machida R. Embryogenesis of the mayfly *Ephemera japonica* McLachlan (Insecta: Ephemeroptera, Ephemeridae), with special reference to abdominal formation. *J Morphol.* 1997;234: 97–107.
165. Tojo K, Machida R. Early embryonic development of the mayfly *Ephemera japonica* McLachlan (Insecta: Ephemeroptera, Ephemeridae). *J Morphol.* 1998;238: 327–335. doi:10.1002/(SICI)1097-4687(199812)238:3<327::AID-JMOR4>3.0.CO;2-J

PA

**Genetic Tools and Procedure for the
Phenotypic Identification of the Genotype of
Transgenic Diploid Organisms**

Frederic Strobl, Ernst H.K. Stelzer & Innovectis GmbH

Diploid transgenic animals are either hemizygous or homozygous. Genetic assays are, therefore, necessary to identify the genotype. Herein disclosed is a novel vector system, referred to as the "AGameOfClones vector system", which uses two transformation markers embedded in interweaved, but incompatible Lox site pairs. Cre-mediated recombination leads to heterozygous progeny that is identifiable by both markers. In the following generation, the omission of one marker indicates homozygous individuals. The inventors prove this concept in *Tribolium castaneum* by systematically creating multiple homozygous transgenic lines suitable for long-term fluorescence live imaging. Since this approach relies on the universal Cre-Lox system, it should work in most diploid model organisms, e.g. rodents, zebrafish, insects and plants. It saves resources, simplifies transgenic animal handling and contributes to the ethically motivated endeavor to minimize the number of wasted animals.

Submitted in June 2017

Patent Application



Benachrichtigung über den Erhalt einer Patentanmeldung:

Dokumenten Referenz-Nr. (DRN): 2017061214242700DE
Anmeldung eingegangen am: 12.06.2017
Anmeldung erhalten von: O=Boehmert und Boehmert,
E=eliese@boehmert.de,
C=de,
CN=Eva Liesegang,
OU=Patentabteilung
Ihr Zeichen: U30735DE
Digitale Signatur
Signaturniveau: fortgeschritten
gültig von: 25.04.2016 02:00:00
gültig bis: 26.04.2021 01:59:59
Eigentümer: CN=David Kутtenkeuler 48794
Seriennummer: 67199115059568803487653713390373509552
Herausgeber: O=European Patent Office,
CN=European Patent Office CA G2

Daten zum vorliegenden Vorgang:

Amtliches Aktenzeichen: 10 2017 112 863.8
Barcode: 
10 2017 112 863.8
Vorgangstyp: Patentanmeldung (DE)
Bestimmungsamt: DPMA
Titel der Patentanmeldung: Genetic tools and procedure for the phenotypic identification of the genotype of transgenic diploid organisms
Anmelder: Johann Wolfgang Goethe-Universität Frankfurt am Main
Theodor-W.-Adorno-Platz 1
60323 Frankfurt am Main
DE



Folgende Dateien sind beim Deutschen Patent- und Markenamt eingegangen und wurden auf korrekte Syntax, Vollständigkeit der Anmeldedaten und zulässige Graphikformate erfolgreich validiert:

Hashwert des Antrags

Specification.pdf (Anmeldung.pdf)
DIRECTDEBIT.XML
DE-REQUEST.XML
BIOSEQUENCE.txt (SEQ ID.txt)
OTHER_01.pdf (Vertreterbeiblatt.pdf)

1A79F84D5C9859C453236744683CDE6FC09AEC9F



Deutsches
Patent- und Markenamt

DPMAdirekt - elektronische Dokumentenannahme

Diese Mitteilung wird signiert und verschlüsselt übertragen und bestätigt den Eingang der oben aufgelisteten Dateien im Deutschen Patent- und Markenamt. Darüber hinaus sind zu diesem Zeitpunkt keine rechtlich verbindlichen Aussagen bezüglich des Inhaltes dieser Dateien möglich. Fragen zu diesem Vorgang richten Sie bitte unter Angabe der DRN, des amtlichen Aktenzeichens und des Eingangsdatums an:

Deutsches Patent- und Markenamt

elektronische Dokumentenannahme

Zweibrückenstr. 12

80297 München

Telefon: 089 / 2195-2500

Fax: 089 / 2195-2221

E-Mail: DPMAdirekt@dpma.de

Die Information in dieser Mitteilung ist vertraulich und rechtlich geschützt. Sie ist ausschließlich für den Gebrauch durch die juristische Person gedacht, an die sie adressiert ist bzw. für diejenigen Personen, die autorisiert sind, diese Information zu erhalten. Sollten Sie nicht der rechtmäßige Empfänger sein, werden Sie hiermit informiert, dass jedwede Bekanntmachung, Vervielfältigung oder Verteilung der Inhalte dieser Mitteilung verboten und ungesetzlich ist. Das Deutsche Patent- und Markenamt übernimmt keinerlei Haftung für jedwede schädliche Software die in oder mit dieser Mitteilung oder als Anhang daran übertragen wird. Weitergehende Informationen erhalten Sie unter: <http://www.dpma.de>



Erfinderbenennung

Die Erfinderbenennung muss auch erfolgen, wenn der Anmelder selbst der Erfinder ist. Ist der Anmelder Miterfinder, so ist er auch mitzubennennen.

Amtliches Aktenzeichen (wenn bereits bekannt)

Platz für Zeichen des Anmelders/Vertreters

U30735DE

Bezeichnung der Erfindung (bitte vollständig)

Genetic tools and procedure for the phenotypic identification of the genotype of transgenic diploid organisms

Erfinder (1)

Vor- und Zuname

Frederic Strobl

Straße, Hausnummer

Nibelungenallee 19A

Postleitzahl

60318

Ort

Frankfurt am Main, DE

Erfinder stellt Antrag auf Nichtnennung (§ 63 Abs. 1 S. 3 PatG)

Erfinder (2)

Vor- und Zuname

Ernst H. K. Stelzer

Straße, Hausnummer

Eschelbronnerstr. 79

Postleitzahl

74909

Ort

Meckesheim, DE

Erfinder stellt Antrag auf Nichtnennung (§ 63 Abs. 1 S. 3 PatG)

Das Recht auf das Patent ist auf den Anmelder übergegangen durch:

(z.B. Erfinder ist/sind d. Anmelder, Inanspruchnahme aufgrd. §§ 6 u. 7 ArbNErfG, Kaufvertrag mit Angabe des Datums, Erbschaft usw.)

zu 1: Inanspruchnahme §§ 6 u. 7 ArbNErfG

zu 2: Inanspruchnahme §§ 6 u. 7 ArbNErfG

Es wird versichert, dass nach Wissen der signierenden Person (Anmelder bzw. dessen Vertreter) weitere Personen an der Erfindung nicht beteiligt sind.

Anmerkung zum Antrag auf Nichtnennung als Erfinder

Nur der Unterzeichner der Erfinderbenennung kann, sofern gleichzeitig Anmelder und Erfinder, einen Antrag auf Nichtnennung als Erfinder stellen. Falls der Erfinder nicht gleichzeitig der Anmelder ist oder mehrere Erfinder nicht genannt werden sollen, so ist der Antrag auf Nichtnennung als Erfinder mit dem Formular P2792 zu stellen (§ 63 Abs. 1 S. 3 PatG). Der Antrag kann jederzeit widerrufen werden. Ein Verzicht des Erfinders auf Nennung ist ohne rechtl. Wirksamkeit (§ 63 Abs. 1 S. 4 u. 5 PatG).

P 2792 - e

GENETIC TOOLS AND PROCEDURE FOR THE PHENOTYPIC IDENTIFICATION OF THE GENOTYPE OF TRANSGENIC DIPLOID ORGANISMS

FIELD OF THE INVENTION

Diploid transgenic animals are either hemizygous or homozygous. Genetic assays are, therefore, necessary to identify the genotype. Herein disclosed is a novel vector system, referred to as the “AGameOfClones vector system”, which uses two transformation markers embedded in interweaved, but incompatible Lox site pairs. Cre-mediated recombination leads to heterozygous progeny that is identifiable by both markers. In the following generation, the omission of one marker indicates homozygous individuals. The inventors prove this concept in *Tribolium castaneum* by systematically creating multiple homozygous transgenic lines suitable for long-term fluorescence live imaging. Since this approach relies on the universal Cre-Lox system, it should work in most diploid model organisms, *e.g.* rodents, zebrafish, insects and plants. It saves resources, simplifies transgenic animal handling and contributes to the ethically motivated endeavor to minimize the number of wasted animals.

DESCRIPTION

Life sciences, especially cell and developmental biology, rely on model organisms. The most frequently used vertebrates are mouse (*Mus musculus*) and zebrafish (*Danio rerio*). Amongst insects, fruit fly (*Drosophila melanogaster*) and red flour beetle (*Tribolium castaneum*) are the two main species. One of the most important standard techniques is transgenesis, *i.e.* the insertion of recombinant DNA into the genome of the model organism (Gama Sosa *et al.*, 2010). Transgenesis is mainly used in two experimental strategies: Firstly, knock-in assays, where the transgene usually contains a functional expression cassette. Secondly, knock-out assays, where endogenous genes or genetic elements are rendered inoperative. Since model organisms are typically diploid, the genotype has to be considered, which leads to a certain experimental complexity. Usual crossing setups can result in (i) non-transgenic wild-type animals, (ii) hemizygous transgenic animals, *i.e.* only the maternal or the paternal chromosome carries the transgene, and (iii) homozygous transgenic animals, *i.e.* both the maternal and paternal chromosomes carry the transgene. In some cases, the phenotype will reveal the genotype, but usually, either two of the three or even all three outcomes cannot be identified. Transformation markers can be used to separate wild-type from transgenic animals, but do not allow to distinguish between hemizygotes and homozygotes. Thus, additional experi-

ments are necessary to determine the genotype, for example genetic assays, which are invasive and require manpower, consumables and time.

In the AGameOfClones (AGOC) vector system, all genotypes are identifiable by purposely produced distinct phenotypes, which permits the systematic creation of homozygous transgenic animals. The concept relies on two phenotypically clearly distinguishable transformation markers embedded in interweaved, but incompatible Lox site pairs. Cre-mediated recombination results in hemizygous animals that retain only one of both markers. Thus, they can be phenotypically distinguished from each other and from the wild-type. In the next generation, individuals that express both markers are identified as heterozygous for the transgene. Finally, a cross of two heterozygotes results in homozygous progeny that is selected by the omission of one marker.

It was therefore an objective of the present invention to provide novel means to facilitate molecular genetic manipulations of organisms, in particular the introduction of sequence alterations such as transgenic sequences into diploid organisms.

The above problem is solved in a first step by a vector system comprising nucleic acid sequences encoding several different transgenes, characterized in that nucleic acid sequences encoding a transgene, each comprise autonomous nucleic acid sequences controlling the expression of the respective transgene,

wherein each nucleic acid sequence encoding a transgene together with its autonomous nucleic acid sequence controlling the expression of the respective transgene comprises donor/acceptor-nucleic acid sequences at the proximal 5'-end and at the proximal 3'-end which can be recognized by a recombination enzyme,

wherein the 5' donor nucleic acid sequence (a) which is located proximally to the 5'-end of the nucleic acid sequence of a first transgene and the 5' acceptor-nucleic acid sequence (c) which is located proximally to the 5'-end of the nucleic acid sequence of a further transgene can be recognized and recombined by a recombination enzyme, and

wherein the 3' donor nucleic acid sequence (b) which is located proximally to the 3'-end of the nucleic acid sequence of a first transgene and the 3' acceptor-nucleic acid sequence (d) which is located proximally to the 3'-end of the nucleic acid sequence of a further transgene can be recognized and recombined by a recombination enzyme.

The vector system of the invention is herein also often referred to as "AGameOfClones vector system". Generally, a vector system of the invention comprises at least one nucleic acid construct having any selection of: expressible sequences, enzyme recognition sites, promoter elements, enhancer elements, transcriptional start sites, and/or gene sequences. The vector

system may also include any sequence element known in the art and used for molecular genetic experimentation. Hence, a “vector system” according to the invention may comprise one more single vector(s), in which in the recited sequence elements of the invention are distributed on the one or more single vector(s).

As used herein, the term “vector” refers to a nucleic acid molecule capable of transporting one or more other nucleic acid sequence(s) to which it has been linked or which was introduced into said vector. One type of vector is a “plasmid”, which refers to a circular double stranded DNA into which additional DNA segments may be cloned. Another type of vector is a viral vector, wherein additional DNA segments may be cloned into the viral genome. Certain vectors are capable of autonomous replication in a host cell into which they are introduced (*e.g.*, bacterial vectors having a bacterial origin of replication and episomal mammalian vectors). Other vectors (*e.g.*, non-episomal mammalian vectors), are integrated into the genome of a host cell upon introduction into the host cell, and thereby are replicated along with the host genome. Moreover, certain vectors are capable of directing the expression of genes to which they are operatively linked. Such vectors are referred to herein as “recombinant expression vectors” or simply “expression vectors”. In general, expression vectors of utility in recombinant DNA techniques are often in the form of plasmids. In the present specification, “plasmid” and “vector” may be used interchangeably, as the plasmid is the most commonly used form of vector. However, the disclosure is intended to include other forms of expression vectors, such as viral vectors (*e.g.*, replication defective retroviruses, adenoviruses and adeno-associated viruses), which serve equivalent functions.

The vector may also contain additional sequences, such as a polylinker for subcloning of additional nucleic acid sequences, or a polyadenylation signal to effect proper polyadenylation of the transcript. The nature of the polyadenylation signal is not believed to be crucial to the successful practice of the methods of the disclosure, and any such sequence may be employed, including but not limited to the SV40 and bovine growth hormone poly-A sites. Also contemplated as an element of the vector is a termination sequence, which can serve to enhance message levels and to minimize readthrough from the construct into other sequences. Additionally, expression vectors typically have selectable markers, often in the form of antibiotic resistance genes, that permit selection of cells that carry these vectors.

In one embodiment of the invention the vector system disclosed herein is characterized in that it comprises the following nucleic acid sequences in 5' to 3' direction:

(i) a recombinase-donor nucleic acid sequence (a) which is located proximally to the 5'-end of a first transgene,

- (ii) a nucleic acid sequence encoding a first transgene and its autonomous expression control sequence (preferably upstream of the first transgene),
- (iii) a recombinase-donor nucleic acid sequence (b) which is located proximally to the 3'-end of a first transgene,
- (iv) a recombinase-acceptor nucleic acid sequence (c) which is located proximally to the 5'-end of a further transgene,
- (v) a nucleic acid sequence encoding a further transgene and its autonomous expression control sequence (preferably upstream of the further transgene), and
- (vi) a recombinase-acceptor nucleic acid sequence (d) which is located proximally to the 3'-end of a further transgene.

In some embodiments the vector system comprises two nucleic acid sequences encoding two different transgenes, wherein preferably the two different transgenes have non-identical sequences. Even more preferably the transgenes encode different (or non-identical) polypeptide sequences.

In some preferred embodiments of the invention the polypeptide sequences are polypeptide sequences of biomarkers. The term “biomarker” shall refer in context of the invention to any polypeptide that when introduced into a diploid organism is detectable by any means. Such biomarkers usually comprise polypeptides that when expressed confer a particular phenotypic change in the organism. Many such genetic markers are known for any given genetic model organisms. A preferred biomarker of the invention is a fluorescent or luminescent or other optically detectable marker. Other examples of genetics markers are fur color markers for mouse (Zheng et al. 1999, Nucleic Acids Research), eye pigmentation marker in *Drosophila melanogaster* (Rubin and Spradling 1982, Science) and *Tribolium castaneum* (Lorenzen et al. 2002, Genetics), cuticle pigmentation markers for insects in general (Osanai-Futahashi et al. 2012, Nature Communications) and beta-glucuronidase-based markers for Plants (George Acquahh, Principles of Plant Genetics and Breeding, Wiley-Blackwell 2007).

The term “recombinase” as used herein refers to a group of enzymes that can facilitate recombination, preferably, site specific recombination, between defined sites, called “recombination sites”, where the two recombination sites are physically separated within a single nucleic acid molecule or on separate nucleic acid molecules. The sequences of the two defined recombination sites are not necessarily identical. Within the group of recombinases there are several subfamilies including “integrase” (for example, like Cre, Cre-like, FLP and λ integrase), “resolvases/invertases” (for example, ϕ C31 integrase, R4 integrase, and TP-901 integrase). The term “recombinase” also includes, but is not limited to, prokaryotic or eukaryotic transposases, viral or *Drosophila copia*-like or non-viral reterotransposons that include

mammalian reterotransposons. Exemplary prokaryotic transposases include transposases encoded in the transposable elements of Tn1, Tn2, Tn3, Tn4, Tn5, Tn6, Tn9, Tn10, Tn30, Tn101, Tn501, Tn903, Tn1000, Tn1681, Tn2901, etc. Eukaryotic transposases include transposases encoded in the transposable elements of *Drosophila mariner*, sleeping beauty transposase, *Drosophila P* element, maize Ac and Ds elements, etc. Retrotransposases include those encoded in the elements of L1, Tol2 Tc1, Tc3, Mariner (Himar 1), Mariner (mos 1), Minos, etc. Transposases may also be selected from Mp, Spm, En, dotted, Mu, and I transposing elements. Preferred is however that the donor-/acceptor nucleic acid sequences can be recognized and recombined by the Cre-recombinase.

As used herein, the term “Cre recombinase” refers to the site-specific DNA recombinase derived from the P1 bacteriophage. Cre recombinase is a 38-kDa product of the cre (cyclization recombination) gene of bacteriophage P1 and is a site-specific DNA recombinase of the nt family (Sternberg, N. et al. (1986) *J. Mol. Biol.* 187:197-212). Cre recombinase recognizes a 34-bp site on the P1 genome called LoxP (locus of X-over P1, LoxP site) and efficiently catalyzes reciprocal conservative DNA recombination between pairs of LoxP sites. The LoxP site comprises two 13-bp inverted repeats flanking an 8-bp nonpalindromic core region. Cre recombinase-mediated recombination between two directly repeated LoxP sites results in excision of DNA between. The Cre recombinase is known in the art. See, for example, Guo et al. (1997) *Nature* 389:40-46; Abremski et al. (1984) *J. Biol. Chem.* 259:1509-1514; Chen et al. (1996) *Somat. Cell Mol. Genet.* 22:477-488; and Shaikh et al. (1977) *J. Biol. Chem.* 272:5695-5702. The Cre recombinase will recognize a number of variant or mutant lox sites relative to the LoxP sequence. Conversely, the LoxP sequence can be recognized by mutants and variants of Cre recombinase. Examples of these variant or mutant Cre recombination sites include, but are not limited to, the LoxB, LoxL and LoxR sites which are found in the *E. coli* chromosome (Hoess et al. (1982) *Proc. Natl. Acad. Sci. USA* 79:3398). Other variant lox sites include: LoxP511 site (5'-ATAACTTCGTATAGTATACATTATACGAAGTTAT-3' (Hoess et al. (1986) *Nucleic Acid Res.* 14:2287-2300)) and LoxC2 site (5'-ACA ACTTCGTATAATGTATGCTATACGAAGTTAT-3' (U.S. Pat. No. 4,959,317)). Also possible is the use of LoxN sites as for example disclosed in Livet J et al: “Transgenic strategies for combinatorial expression of fluorescent proteins in the nervous system” (*Nature*. 2007 Nov 1;450(7166):56-62). Therefore, the term “Cre recombinase” includes Cre recombinase and all mutants and variants thereof with the recombination catalyzing function described above, and the term “LoxP site” includes the 34 bp site described above and any mutants and variants recognizable by the Cre recombinase, including its variants. An alternative recombinase is a FLP recombinase. As used herein, the term “FLP recombinase” refers to a site-specific DNA recombinase derived from yeast, the 2pi plasmid of *Saccharomyces cerevisiae*, that recognizes a 34 base pair DNA sequence, termed the “FRT site” (FLP recombinase target). “FLP”

is a 423 amino acid protein capable of binding to FRT recombination target sites and mediating conservative site-specific recombination between FRT sites. The basic configuration of the FRT site comprises a 48 nucleotide DNA sequence consisting of an 8-base-pair core and three 13-base-pair symmetry elements where two symmetry elements occur in direct orientation on the 5' end of the core sequence and the third element occurs in inverted orientation on the 3' end of the core sequence. The FRT site has also been identified as minimally comprising two 13 base-pair repeats, separated by an 8 base-pair spacer, as follows: 5'-GAAGTTCCTATTC[TCTAGAAA]GTATAGGAACTTC-3'. The nucleotides in the above "spacer" region can be replaced with any other combination of nucleotides, so long as the two 13 base-pair repeats are separated by 8 nucleotides. The actual nucleotide sequence of the spacer is not critical, although those of skill in the art recognize that, for some applications, it is desirable for the spacer to be asymmetric, while for other applications, a symmetrical spacer can be employed. It is also recognized by one skilled in the art that modified forms or mutants of FLP recombinase can recognize the FRT site and its variants. Therefore, the term "FLP recombinase" and "FRT site" includes all variants and mutants carrying out their functions as described above.

In some embodiments it is preferred that the donor-/acceptor nucleic acid sequences which can be recognized and recombined by the Cre-recombinase, are lox sequences.

In some embodiments, the vector system according to the invention is characterized in that the 5' donor nucleic acid sequence (a) which is located proximally to the 5'-end of the nucleic acid sequence of a first transgene and the 5' acceptor-nucleic acid (c) which is located proximally to the 5'-end of the nucleic acid sequence of a further transgene, are lox sequences which are different from the 3' donor nucleic acid sequence (b) which is located proximally to the 3'-end of the nucleic acid sequence of a first transgene and the 3' acceptor-nucleic acid (d) which is located proximally to the 3'-end of the nucleic acid sequence of a further transgene.

In some embodiments, the vector system according to the invention is characterized in that the donor-/acceptor nucleic acid sequences (a) and (c) are either LoxP- or LoxN nucleic acid sequences.

In some embodiments, the vector system according to the invention is characterized in that the donor-/acceptor nucleic acid sequences (b) and (d) are either LoxP- or LoxN nucleic acid sequences.

In some embodiments, the vector system according to the invention is characterized in that the vector system can be introduced/integrated in the germ line.

In some embodiments, the vector system according to the invention is characterized in that it comprises the sequence(s) according SEQ ID NO: 1 or 2.

In some embodiments, the vector system according to the invention is characterized in that it is a shuttle vector system. In other embodiments the vector system of the invention is a vector system for use in a method of establishing a transgenic organism.

In some embodiments of the invention the vector system described herein is characterized in that it comprises a nucleic acid sequence encoding recombinase as described before, preferably a Cre-recombinase.

In some embodiments of the invention the vector system described herein is characterized in that it comprises a nucleic acid sequence encoding a Cre-recombinase, wherein it comprises a further nucleic acid sequence controlling the inducible expression of the Cre-recombinase.

The object of the invention is also solved in an additional aspect by a cell, characterized in that the cell comprises a vector system as disclosed herein. Preferably the cell is a biological cell, such as a eukaryotic cell, most preferably a cell derived from a plant or animal, such as an insect, a fish, a bird or a mammal. A mammal is preferably selected from the group comprising mouse, rat, guinea pig, rabbit, pig, cat, dog, goat, lama, camel, horse and monkey.

In another aspect the invention also provides a multicellular transgenic organism, characterized in that it comprises a vector system as described herein before.

A further aspect then pertains to a method for the generation of a transgenic organism, the method comprising the following steps:

(i) Introduction of a vector system as described herein into an embryo or a germ cell (of said organism),

(ii) Selection of hemizygous organisms expressing at least two of the transgenes which are encoded by the vector system,

(iii) Optionally, crossing of transgenic, non-human, multicellular hemizygous organisms derived from step (ii) with non-human, multicellular organisms expressing a recombinase transgene,

(iv) Selection of descendants/offsprings which have been obtained by crossing of hemizygous organisms according to step (ii) with non-human, multicellular organisms expressing a recombinase transgene, and a subsequent out-crossing against the wildtype, and

which express only one of the at least two transgenes which are encoded by the vector system of the invention,

(v) Crossing of transgenic, non-human, multicellular hemizygous organisms which express only one of the at least two transgenes, with transgenic non-human, multicellular hemizygous organisms which express another of the at least two transgenes,

(vi) Identification of transgenic, non-human, multicellular heterozygous descendants/offsprings, which express two of the transgenes,

(vii) Crossing of transgenic, non-human, multicellular heterozygous organisms which express two of the transgenes, with transgenic, non-human, multicellular heterozygous organisms which express two of the transgenes,

(viii) Identification of transgenic, non-human, multicellular homozygous descendants/offsprings, which express (preferably only) one of the transgenes.

In some embodiments the invention provides the above method, wherein the vector system according to the invention has been introduced into an embryo or a germ cell, which is able to express the Cre-recombinase in step (i), and wherein step (iii) of the method is omitted.

In some embodiments the invention provides the above method, wherein the vector system has been introduced into an embryo or a germ cell in step (i), and wherein the procedure according to step (i), optionally, comprises the induction of the expression of a nucleic acid sequence encoding the Cre-recombinase.

In some embodiments the transgenic organism is a multicellular organism, preferably selected from a group comprising the following classes: plants or animals, such as insects, birds, fish and mammals. A mammal may be selected from a group consisting of the following members: mouse, rat, guinea pig, rabbit, pig, cat, dog, goat, lama, camel, horse and monkey.

Another aspect of the invention then pertains to a transgenic organism obtained or obtainable by a method for the generation of a transgenic organism as described herein before.

Yet a further aspect then pertains to a use of a vector system of the invention, characterized in that it is used for the identification of hemizygous, heterozygous and/or homozygous, non-human, multicellular organisms, who are derived in a method for the generation of a transgenic organism as described herein before.

The present invention will now be further described in the following examples with reference to the accompanying figures and sequences, nevertheless, without being limited thereto. For

the purposes of the present invention, all references as cited herein are incorporated by reference in their entireties. In the Figures:

Figure 1 shows the AGameOfClones vector concept within the piggyBac-based pAGOC transformation vector for *Tribolium castaneum*. (A) Two fluorescence-based transformation markers, mO and mC, which are spectrally distinct, are embedded into a piggyBac-based transformation vector that is characterized by 3' and 5' terminal repeats (TR) necessary for genomic insertion. The markers are based on the artificial 3×P3 promoter, which drives expression in the neuronal system, the open reading frame for the respective fluorescence protein, *i.e.* mOrange or mCherry, and the SV40 poly (A) site. Each transformation marker is flanked upstream by a LoxP and downstream by a LoxN site, which results in interweaved Lox site pairs. In *Tribolium castaneum* adults, the fluorescence phenotype is detected in the eyes using appropriate filter sets. (B) Cre-mediated recombination leads to the excision of one of either markers from the genome. When one marker is removed, the other marker remains within the genome, since the two remaining lox sites, *i.e.* a LoxP and a LoxN site, are incompatible. *Tribolium castaneum* adults that underwent recombination give rise to progeny where only one marker is expressed in the eyes.

Figure 2 shows the AGameOfClones F3 to F7 crossing procedure that allows the systematic creation of homozygous transgenic animals. The rounded rectangle illustrates the genotype for two independent autosomes, white bars represent the AGOC transgene location and black bars the helper transgene location. A F2 mO-mC founder female × wild-type male outcross results in F3 mO-mC pre-recombination hemizygotes that carry mO and mC consecutively on one chromosome. A F3 mO-mC pre-recombination hemizygous female × mCe homozygous helper male cross gives rise to F4 mCe×mO-mC double hemizygotes, in which one marker is removed through Cre-mediated recombination. A F4 mCe×mO-mC double hemizygous female × wild-type male outcross generates F5 mO- and mC-only post-recombination hemizygotes. Next, a F5 mO-only post-recombination hemizygous female × F5 mC-only post-recombination hemizygous male brother-sister cross results in a certain fraction of F6 mO/mC heterozygous progeny. Finally, a F6 mO/mC heterozygous female × a F6 mO/mC heterozygous male brother-sister cross generates F7 mO- and mC-only homozygous progeny. The percentage boxes show the theoretical ratio of the progeny that carry the respective genotype.

Figure 3 shows the AGameOfClones F3 to F7 crossing procedure shown for the AGOC #5 and #6 sublines. From the F3 to the F7 generation, the genotype was phenotypically determined by monitoring mCe, mO and mC. For both sublines, F7 mO- and mC-only homozygotes were obtained by following the systematic procedure outlined in Figure 2. For each individual, a wild-type control of the same gender is shown. The percentage boxes show the experimental (and theoretical) ratios of the progeny that show the respective phenotype.

Figure 4 shows the crossing results for the six proof-of-principle AGOC lines from the F3 to F7 generation. (1) in the AGOC #4 subline, incomplete recombination in the F4 mCe×mO-mC double hemizygotes occurred, as the inventors obtained several F5 individuals that still carry both transformation markers (7% in total). The inventors continued the AGOC procedure with the F5 mO- and mC-only post-recombination hemizygous progeny.

Figure 5 shows the F4 mCe×mO-mC double hemizygote generation. The F4 hybrids are hemizygous for both the AGOC transgene, which carries both mO and mC embedded into interweaving Lox site pairs, and for the helper transgene, which carries mCe and the Cre recombinase expression cassette. Within this cassette, expression of a nuclear-localized Cre recombinase is driven by the endogenous *HSP68* promoter. During the development of the F4 generation from the zygote to the fertile adult, the *HSP68* promoter exhibits a slight leaky expression. Over time, this leads to recombination in germ cells (*i.e.* the prerequisite for the AGOC vector concept) but also in certain somatic progenitor cells that later on give rise to distinct, typically spatially clustered cell populations. This effect is evident in the compound eyes of adult animals in all AGOC lines, where certain clusters of ommatidia show either expression of mO or mC.

Figure 6 shows the AGameOfClones F3 to F7 crossing procedure with inversed genders. To prove that the proposed concept is not gender-specific, the F3 to F7 crossing procedure was carried out as described in the main text (Figure 2), but with inversed genders. F3 mO-mC pre-recombination hemizygous males of the AGOC #5 and #6 sublines were crossed against mCe helper homozygous females of the ICE{HSP68^{NLS}-Cre} #1 subline, resulting in F4 mCe×mO-mC double hemizygotes, in which Cre-mediated recombination occurs. F4 mCe×mO-mC double hemizygote males were outcrossed against wild-type females, this results in F5 mO- and mC-only post-recombination hemizygotes that carry either only mO or only mC on the paternal chromosome. F5 mO-

only post-recombination hemizygous males were brother-sister crossed against F5 mC-only post-recombination hemizygous females, resulting in F6 mO/mC heterozygotes that carry once again both markers. F6 mO/mC heterozygous males were brother-sister crossed against genotypic identical F6 mO/mC heterozygous females, resulting in F7 mO- and mC-only homozygotes that carry either only the mO or only the mC marker on both, the maternal and paternal chromosomes. Similar to the standard, the procedure could be performed also successfully with inversed genders. For each individual, a wild-type control of the same gender is shown. The percentage boxes show the experimental (and theoretical) ratios of the progeny that show the respective phenotype.

Figure 7 shows the AGameOfClones F3 to F7 crossing procedure with a different mCe helper subline. To prove that the proposed concept does not rely solely on one Cre recombinase expressing helper subline, the F3 to F7 crossing procedure was carried out as described in the main text (Figure 2), but with the ICE{HSP68'NLS-Cre} #2 helper subline, which carries the same transgene as #1 subline, but at a different genomic location. The subline is homozygous for the transgene. F3 mO-mC pre-recombination hemizygous females of the AGOC #5 and #6 sublines were crossed against mCe helper homozygous males of the ICE{HSP68'NLS-Cre} #2 subline, resulting in F4 mCe×mO-mC double hemizygotes, in which Cre-mediated recombination occurs. F4 mCe×mO-mC double hemizygote females were outcrossed against wild-type males, this results in F5 mO- and mC-only post-recombination hemizygotes that carry either only mO or only mC on the paternal chromosome. F5 mO-only post-recombination hemizygous females were brother-sister crossed against F5 mC-only post-recombination hemizygous males, resulting in F6 mO/mC heterozygotes that carry once again both markers. F6 mO/mC heterozygous females were brother-sister crossed against genotypic identical F6 mO/mC heterozygous males, resulting in F7 mO- and mC-only homozygotes that carry either only the mO or only the mC marker on both, the maternal and paternal chromosomes. Similar to the standard, the procedure could be performed also successfully with inversed genders. For each individual, a wild-type control of the same gender is shown. The percentage boxes show the experimental (and theoretical) ratios of the progeny that show the respective phenotype.

Figure 8 shows fluorescence live imaging of selected homozygous functional AGOC sublines. (A) An AGOC{Zeni'#O(LA)-mEmerald} #2 embryo during gastrulation.

This subline permits the characterization of actin and actomyosin dynamics that are involved in serosa window closure (first and second row). It can also be used to describe the cytoskeleton rearrangement of the dorsal blastoderm cells and to analyze their appearance change during differentiation to serosa cells (third row and detail images). (B) An AGOC{ARP5'#O(LA)-mEmerald} #1 embryo during germband retraction. In this subline, the brain and ventral nerve cord expresses Lifact-mEmerald on a high level, permitting the observation of neurulation. Detail images show the forming ganglia of the first and second thoracic segment. (C) Optical sections of an AGOC{ARP5'#O(LA)-mEmerald} #1 embryo after dorsal closure. Detail images show the supra- and suboesophageal ganglia. (D) Comparison of embryos from the AGOC{ARP5'#O(LA)-mEmerald} #1 and #2 sublines after dorsal closure. In contrast to the expression level in the #1 subline, the Lifact-mEmerald expression level of the AGOC{ARP5'#O(LA)-mEmerald} #2 subline in the nervous system is very low. ZP, z maximum projection with image processing; ZA, z maximum projection with intensity adjustment; PA, single plane with intensity adjustment.

Figure 9 shows the pAGOC vector. (A) Vector map of pAGOC, which is based on the pAVOIAF[#1-#2-#3-#4] vector. In this vector, #1 and #2 remain empty, while mO and mC together with their flanking upstream LoxP and downstream LoxN sites were inserted into #3 and #4, respectively. The non-annotated dark blue boxes represent the same restriction enzyme sites as shown for the pAVOIAF[#1-#2-#3-#4] vector. The light gray band on the inside indicates the transgene. (B) Scheme of mO and mC that are embedded into intermeshing but incompatible LoxN and LoxP site pairs. Restriction enzyme sites are not shown. Sizes of genetic elements are not to scale. ORF, open reading frame; TR, piggyBac terminal repeat.

Figure 10 shows the pAGOC{#P'#O(LA)-mEmerald} vector. (A) Vector map of pAGOC{#P'#O(LA)-mEmerald}, which is based on the pAGOC vector (Supplementary Figure 8). In this vector, #1 remains empty, while the #P'#O(LA)-mEmerald two-slot cloning site was inserted into #2. The non-annotated dark blue boxes represent the same restriction enzyme sites as shown for the pAVOIAF[#1-#2-#3-#4] vector in Supplementary Figure 7 as well as several new restriction enzyme sites shown in (B). The light gray band on the inside indicates the transgene. (B) Scheme of the #P'#O(LA)-mEmerald two-slot cloning site. To insert a promoter, the #P slot can be accessed by the AscI/FseI

restriction enzyme site pair, but alternatively by the double BtgZI restriction enzyme site pair, which flanks a FREDDY spacer. BtgZI is a type I restriction enzyme with a non-palindromic recognition sequence. It cuts the sequence several bp (10/14) downstream, resulting in a 4 bp sticky end. In this vector, the upstream BtgZI restriction enzyme site (in reverse orientation) allows the opening of the AscI restriction enzyme site, while the downstream BtgZI restriction enzyme site (in forward orientation) allows the opening of the Lifeact open reading frame start codon and the first bp of the subsequent codon, which allows scarless insertion of respectively digested promoter sequences (indicated by arrows). The Lifeact (LA) open reading frame, which is in #0 per default, can be substituted with another open reading frame to change the intracellular localization by the FseI/NotI restriction enzyme site pair, while the mEmerald open reading frame can be substituted with another fluorescence protein open reading frame by the NotI/SbfI restriction enzyme site pair. ORF, open reading frame.

Figure 11 shows nine different genetic options to create an AGOC vector. The first variant is identical to the variant presented in Figure 1. Variant 1 to 5 are based on recombination-excision, while variants 6 to 9 are based on recombination-inversion. Promoter 1 and Promoter 2 resemble two regulatory sequences with a different spatiotemporal expression pattern. G and R resemble two different polypeptide sequences, for example a green and a red fluorescent protein. Pre-R, pre-recombination; Post-R, post-recombination.

EXAMPLES

Materials and Methods

Molecular biology: the pUC[AGOC] and pAGOC vectors

The 5,678 bp pUC57[AGOC] vector was ordered as a *de novo* gene synthesis construct (Genewiz). A 3,277 bp insert was inserted into the unique NdeI and PstI restriction enzyme sites of pUC57-Kan, it consists of (i) the 4 bp TTAA 3' piggyBac excision/insertion target sequence, (ii) the 235 bp piggyBac 3' terminal repeat, (iii) the 2,724 bp four-slots (#1 to #4) cloning site, in which the mOrange-based and mCherry-based eye-specific transformation markers (mO and mC, respectively) were already inserted (both in reverse orientation and thus tail-to-head) into #3 and #4, (iv) the 310 bp 5' piggyBac terminal repeat and (v) the 4 bp TTAA 5' piggyBac excision/insertion target sequence. The insert was amplified with a respective primer pair, which introduced upstream an AatII and downstream a PciI restriction enzyme site. The PCR product and pUC57[AGOC] were digested accordingly, and the insert was reintegrated into the vector, reducing the vector size considerably by removing 629 functionless bp. The resulting 5,049 bp vector was termed pAGOC (Figure 9) and used (i) for germline transformation to create proof-of-principle lines, and (ii) as an intermediate vector for further cloning operations.

Molecular biology: the pGS[#P'#O(LA)-mEmerald] and pAGOC{#P'#O(LA)-mEmerald} vectors

The 4,111 bp the pGS[#P'#O(LA)-mEmerald] vector was ordered as a *de novo* gene synthesis construct (Thermo Fisher Scientific). A 1,821 bp insert was inserted into the unique SfiI restriction enzyme site of pMK-RQ (Thermo Fisher Scientific), it consists of (i) a 6 bp HindIII restriction enzyme site, (ii) the 107 bp #P'#O two-slot subcloning site, (iii) a 9 bp linker that includes a NotI restriction enzyme site, (iv) the 714 bp codon-optimized mEmerald open reading frame, (v) a 8 bp SbfI restriction enzyme site, (vi) a 983 bp elongated variant of the SV40 poly(A) site and (vii) a 6 bp XbaI restriction enzyme site. The insert was cut from the backbone with HindIII / XbaI and pasted into #3 of the pAGOC vector. The resulting 6,852 bp vector was termed pAGOC{#P'#O(LA)-mEmerald} (Figure 10) and used as an intermediate vector for further cloning operations.

Molecular biology: the promoter library vectors

All library vectors are based on pGEM-T Easy (A1360, Promega). The two promoter library vectors were created by amplifying the sequences from genomic DNA with the respective extraction PCR primer pairs. Amplification was followed by A-tailing using the Recombinant Taq DNA polymerase (10342020, Thermo Fisher Scientific) and subsequent ligation into

pGEM-T Easy. The resulting vectors were termed pTC-Zen1'-GEM-T Easy and pTC-ARP5'-GEM-T Easy and had sizes 4,599 bp and 5,516 bp, respectively.

Molecular biology: the pAGOC{Zen1'#O(LA)-mEmerald} and pAGOC{ARP5'#O(LA)-mEmerald} vectors

Two transformation vectors were created that allowed the expression of mEmerald-labeled Lifeact (LA) in different spatiotemporal patterns. Therefore, the promoter sequences were amplified from the library vectors with the respective primer pairs, which introduced upstream an AscI and downstream a BsaI restriction enzyme site. The PCR product was digested accordingly, and the pAGOC{#P'#O(LA)-mEmerald} vector was digested with BtgZI, which led to compatible overhangs and allowed scarless insertion of the promoter sequences into the #P slot. The resulting vectors were termed pAGOC{Zen1'#O(LA)-mEmerald} and pAGOC{ARP5'#O(LA)-mEmerald}, had sizes of 8,367 bp and 9,276 bp, respectively, and were used for germline transformation.

Germline transformation of *Tribolium castaneum*

Approximately 500-600 Fo *Tribolium castaneum* adults of the PWAS strain were incubated on 405 fine wheat flour (113061036, Demeter, Darmstadt, Germany) supplemented with 5% (wt/wt) inactive dry yeast (62-106, Flystuff, San Diego, CA, USA) at 25°C and 70% relative humidity in light for 2 h. After the incubation period, the adults were removed and the embryos (around 700-900) were extracted from the flour and incubated another hour as stated above. Afterwards, they were transferred to a 100 µm cell strainer (352360, BD Biosciences) and washed in a 6-well plate as follows: (i) in autoclaved tap water for 1 min, (ii) in 10% (vol/vol) sodium hypochlorite (425044-250ML, Sigma Adlrch) in autoclaved tap water for 10 s, (iii) in autoclaved tap water three times for 1 min and (iv) stored in autoclaved tap water. Next, the embryos were lined up on object slides within the next hour (10 object slides with about 50 embryos each, totaling at approximately 500 embryos per round of germline transformation) with their posterior pole pointing towards the elongated edge of the slide. The embryos were injected with a mixture of 500 ng/µl transformation vector and 400 ng/µl transposase-expressing helper vector (pATub'piggyBac) in injection buffer (5 mM KCl, 1 mM KH₂PO₄ in ddH₂O, pH 8.8). For injection, a microinjector (FemtoJet, Eppendorf) and 0.7 µm outer diameter capillaries (Femtotips II, Eppendorf) with an injection pressure of 400-800 hPa were used. After injection, the object slides with embryos were placed in Petri dishes on a 5 mm 1% (wt/vol) agarose in tap water 'platform' and incubated at 32°C. After 3 days, hatched larvae, i.e. F1 potential mosaics, were collected and raised individually in single wells of 24-well plates as described above.

Light sheet-based fluorescence microscopy

Three *Tribolium castaneum* sublines were characterized with long-term fluorescence live imaging, the AGOC{Zeni'#O(LA)-mEmerald} #2 subline, which exhibited the strongest fluorescence signal out of the three sublines, and both AGOC{ARP5'#O(LA)-mEmerald} sublines, since they showed a slightly varying expression pattern. Fluorescence live imaging was performed with digitally scanned laser light sheet-based fluorescence microscopy. In brief, embryo collection was performed with the F7+ continuative mC-only homozygous cultures for one hour at 25°C, and embryos were incubated for 15 hours at 25°C. Sample preparation took approximately one hour at room temperature (23±1°C), so that embryos were at the beginning of gastrulation, when the uniform blastoderm turns into the rearranged blastoderm. Embryos were recorded along four directions (in the orientations 0°, 90°, 180° and 270°) with an interval of 30 minutes for up to four days at room temperature, covering the embryogenetic events gastrulation and germband elongation completely and germband retraction partially. All embryos survived the imaging procedure, developed to healthy and fertile adults, and when outcrossed

**Example 1: Proof-of-principle in the emerging insect model organism
*Tribolium castaneum***

The proof-of-principle of the AGOC vector concept relied on the red flour beetle *Tribolium castaneum* (Brown *et al.*, 2009), an emerging insect model organism, in conjunction with the piggyBac transposon system (Lorenzen *et al.*, 2003), which allows semi-random genomic insertion. The inventors created a piggyBac-based transformation vector termed pAGOC, which contains a mOrange-based (Shaner *et al.*, 2008) and a mCherry-based (Shaner *et al.*, 2004) eye-specific (Wimmer *et al.*, 1999) transformation marker, termed mO and mC, respectively. Both fluorescent proteins are spectrally separable by appropriate excitation and emission. Each transformation marker is flanked upstream by a LoxP site (Hamilton and Abremski, 1984) and downstream by a LoxN (Livet *et al.*, 2007) site, resulting in interweaved, but incompatible Lox site pairs (Figure 1).

The inventors injected this vector together with a piggyBac transposase-expressing helper vector (pATub'piggyBac) into pre-blastoderm embryos to achieve germline transformation. All survivors, termed F1 potential mosaics, were outcrossed against the wild-type. In six of those crosses, one or more F2 mO-mC hemizygous founder females were found among the progeny, which were outcrossed against wild-type males. Transgenic progeny was collected to establish six proof-of-principle cultures, which carry the same transgene, but in different genomic locations. These F3 mO-mC pre-recombination hemizygous sublines were termed AGOC #1 to #6. Until this step, this route did not differ from most standard transgenic animal establishment procedures.

The systematic creation of homozygous transgenic animals (Figure 2) was performed with all six AGOC sublimes and phenotypically documented for #5 and #6 (Figure 3). This procedure is completed within only four further generations.

(1) F3 mO-mC pre-recombination hemizygous females, which carry mO and mC consecutively on the maternal chromosome, were crossed against mCe homozygous helper males of the ICE{HSP68'NLS-Cre} #1 subline (Figure 2 and Figure 3, first row). This subline expresses a nuclear-localized Cre recombinase (Peitz *et al.*, 2002) under control of the *HSP68* promoter and carries a mCerulean-based (Markwardt *et al.*, 2011) eye-specific transformation marker (mCe), resulting in F4 mCe×mO-mC double hemizygotes, in which Cre-mediated recombination occurs (Figure 4, 'F3' row). In this hybrid generation, adult beetles show a patchy expression of both markers within their compound eyes (Figure 5).

(2) F4 mCe×mO-mC double hemizygous females were outcrossed against wild-type males (Figure 2 and Figure 3, second row). Due to the Cre-mediated recombination in germline cells, this results in F5 mO- and mC-only post-recombination hemizygotes that carry either mO or mC on the maternal chromosome (Figure 4, 'F4' row).

(3) F5 mO-only post-recombination hemizygous females were brother-sister crossed against F5 mC-only post-recombination hemizygous males (Figure 2 and Figure 3, third row), resulting in F6 mO/mC heterozygotes, which carry once again both markers (Figure 4, 'F5' row). In contrast to the F3 mO-mC pre-recombination hemizygotes, which show the same phenotype but carry both markers consecutively on the maternal chromosome, the F6 mO/mC heterozygotes carry mO on the maternal and mC on the paternal chromosome. This was proven by crossing F6 mO/mC heterozygous females against wild-type males (Figure 4, 'F6-S' row).

(4) F6 mO/mC heterozygous females were brother-sister crossed against genotypic identical F6 males (Figure 2 and Figure 3, fourth row), resulting in F7 mO- and mC-only homozygotes that carry either only mO or only mC on both, the maternal and paternal chromosomes (Figure 4, 'F6' row). In contrast the F5 mO- and mC-only post-recombination hemizygotes, which show the same phenotype but carry either mO or mC on the maternal chromosome, the F7 mO- and mC-only homozygotes carry the respective marker on the maternal and paternal chromosome (Figure 2 and Figure 3, fifth row). This was proven by crossing F7 mO- and mC-only homozygous females against wild-type males (Figure 4, 'F7-O' and 'F7-C' row, respectively). Although some phenotype distributions differed from the theoretical Mendelian values, all expected phenotypes, and thus all expected genotypes, were found in all

generations, and both, mO- and mC-only homozygotes, could be obtained for all six AGOC sublines in the F7.

Two controls were performed with the AGOC #5 and #6 sublines to confirm proper functionality of the AGameOfClones vector concept: (i) the F3 to F7 crossing procedure was successfully conducted with inversed genders (Figure 6) and (ii) an alternative mCe helper homozygous subline, ICE{HSP68'NLS-Cre} #2, was used, which carries the same Cre-expressing cassette as the #1 subline, but at a different genomic location (Figure 7).

Example 2: Creation and live imaging of functional AGOC lines

The inventors expanded the pAGOC vector concept by creating two vectors that contain expression cassettes for mEmerald-labeled Lifeact under control of either the *zerknüllt 1* promoter or the *actin related protein 5* promoter. With those vectors, two transgenic *Tribolium castaneum* lines (with three and two sublines, respectively) were created, which are primarily designed for fluorescence live imaging of embryonic development. For all of those sublines, the systematic creation of homozygous animals was successful. The inventors performed long-term fluorescence live imaging of the embryonic development (Strobl and Stelzer, 2016) with three of the homozygous functional AGOC sublines by using a digitally scanned laser light sheet-based fluorescence microscope (Keller *et al.*, 2008). The AGOC{Zeni'#O(LA)-mEmerald} #2 subline allows the characterization of actin dynamics within the extra-embryonic membranes during gastrulation, visualizing the actomyosin cable that closes the serosa window (Figure 8A). The AGOC{ARP5'#O(LA)-mEmerald} #1 subline exhibits strong expression in the brain and ventral nerve cord and moderate fluorescence throughout the remaining embryonic tissue (Figure 8B and C). In contrast, the AGOC{ARP5'#O(LA)-mEmerald} #2 subline does not show any signal in the neuronal system but uniform fluorescence signal during germband elongation, germband retraction and dorsal closure (Figure 8C).

U30735DE

Claims

1. A vector system comprising nucleic acid sequences encoding several different transgenes, characterized in that nucleic acid sequences encoding a transgene, each comprise autonomous nucleic acid sequences controlling the expression of the respective transgene,

wherein each nucleic acid sequence encoding a transgene together with its autonomous nucleic acid sequence controlling the expression of the respective transgene comprises donor-/acceptor nucleic acid sequences at the proximal 5'-end and at the proximal 3'-end which can be recognized by a recombination enzyme,

wherein the 5' donor nucleic acid sequence (a) which is located proximally to the 5'-end of the nucleic acid sequence of a first transgene and the 5' acceptor-nucleic acid sequence (c) which is located proximally to the 5'-end of the nucleic acid sequence of a further transgene can be recognized and recombined by a recombination enzyme, and

wherein the 3' donor nucleic acid sequence (b) which is located proximally to the 3'-end of the nucleic acid sequence of a first transgene and the 3' acceptor-nucleic acid sequence (d) which is located proximally to the 3'-end of the nucleic acid sequence of a further transgene can be recognized and recombined by a recombination enzyme.

2. The vector system according to claim 1, characterized in that it comprises the following nucleic acid sequences in 5' to 3' direction:

- (i) a recombinase-donor nucleic acid sequence (a) which is located proximally to the 5'-end of a first transgene,

- (ii) a nucleic acid sequence encoding a first transgene and its autonomous expression control sequence,

- (iii) a recombinase-donor nucleic acid sequence (b) which is located proximally to the 3'-end of a first transgene,

- (iv) a recombinase-acceptor nucleic acid sequence (c) which is located proximally to the 5'-end of a further transgene,

- (v) a nucleic acid sequence encoding a further transgene and its autonomous expression control sequence, and

- (vi) a recombinase-acceptor nucleic acid sequence (d) which is located proximally to the 3'-end of a further transgene.

3. The vector system according to claim 1 or 2, characterized in that it comprises two nucleic acid sequences encoding two different transgenes.
4. Vector system according to any one of claims 1 to 3, characterized in that the transgenes encode polypeptide sequences of different biomarkers.
5. Vector system according to any one of claims 1 to 4, characterized in that the 5' donor nucleic acid sequence (a) which is located proximally to the 5'-end of the nucleic acid sequence of a first transgene and the 5' acceptor-nucleic acid (c) which is located proximally to the 5'-end of the nucleic acid sequence of a further transgene, are lox sequences which are different from the 3' donor nucleic acid sequence (b) which is located proximally to the 3'-end of the nucleic acid sequence of a first transgene and the 3' acceptor-nucleic acid (d) which is located proximally to the 3'-end of the nucleic acid sequence of a further transgene.
6. Vector system according to any one of claims 1 to 5, characterized in that the donor-/acceptor nucleic acid sequences (a) and (c) are either LoxP- or LoxN nucleic acid sequences, and/or characterized in that the donor-/acceptor nucleic acid sequences (b) and (d) are either LoxP- or LoxN nucleic acid sequences.
7. Vector system according to any one of claims 1 to 6, characterized in that it comprises a nucleic acid sequence encoding a Cre-recombinase, wherein it comprises a further nucleic acid sequence controlling the inducible expression of the Cre-recombinase.
8. A cell, characterized in that it comprises a vector system according to any one of the preceding claims.
9. The cell according to claim 8, characterized in that it is a eukaryotic cell, for example derived from a plant, an insect, a fish, a bird or a mammal.
10. A non-human multicellular organism, characterized in that it comprises a vector system according to any one of the preceding claims.
11. A Transgenic non-human multicellular organism, characterized in that it has been generated by a method comprising the following steps:
 - (i) Introduction of a vector system according to any one of the claims 1 to 16 into an embryo or a germ cell,

- (ii) Selection of hemizygous organisms expressing at least two of the transgenes which are encoded by the vector system,
 - (iii) Optionally, crossing of transgenic, non-human, multicellular hemizygous organisms derived from step (ii) with non-human, multicellular organisms expressing a recombinase transgene,
 - (iv) Selection of descendants/offsprings which have been obtained by crossing of hemizygous organisms according to step (ii) with non-human, multicellular organisms expressing a recombinase transgene, and a subsequent out-crossing against the wildtype, and which express only one of the at least two transgenes which are encoded by the vector system according to any of the claims 1 to 16,
 - (v) Crossing of transgenic, non-human, multicellular hemizygous organisms which express only one of the at least two transgenes, with transgenic non-human, multicellular hemizygous organisms which express another of the at least two transgenes,
 - (vi) Identification of transgenic, non-human, multicellular heterozygous descendants/offsprings, which express two of the transgenes,
 - (vii) Crossing of transgenic, non-human, multicellular heterozygous organisms which express two of the transgenes, with transgenic, non-human, multicellular heterozygous organisms which express two of the transgenes,
 - (viii) Identification of transgenic, non-human, multicellular homozygous descendants/offsprings, which express one the transgenes.
12. Transgenic, non-human, multicellular organism, characterized in that it has been generated by a method according to claim 22, wherein the vector system according to any of the claims 1 to 7 has been introduced into an embryo or a germ cell, which is able to express the Cre-recombinase in step (i), and wherein step (iii) of the method according to claim 11 is omitted.
13. Use of a vector system according to any of the claims 1 to 7, characterized in that it is used for the identification of hemizygous, heterozygous and/or homozygous, non-human, multicellular organisms, who are derived in a method comprising the mentioned steps of the claims 11 or 12.

U30735DE

ABSTRACT

Diploid transgenic animals are either hemizygous or homozygous. Genetic assays are, therefore, necessary to identify the genotype. Herein disclosed is a novel vector system, referred to as the “AGameOfClones” vector concept, which uses two transformation markers embedded in interweaved, but incompatible Lox site pairs. Cre-mediated recombination leads to heterozygous progeny that is identifiable by both markers. In the following generation, the omission of one marker indicates homozygous individuals. The inventors prove this concept in *Tribolium castaneum* by systematically creating multiple homozygous transgenic lines suitable for long-term fluorescence live imaging. Since this approach relies on the universal Cre-Lox system, it should work in most diploid model organisms, *e.g.* rodents, zebrafish, insects and plants. It saves resources, simplifies transgenic animal handling and contributes to the ethically motivated endeavor to minimize the number of wasted animals.

U30735DE

FIGURES

Figure 1:

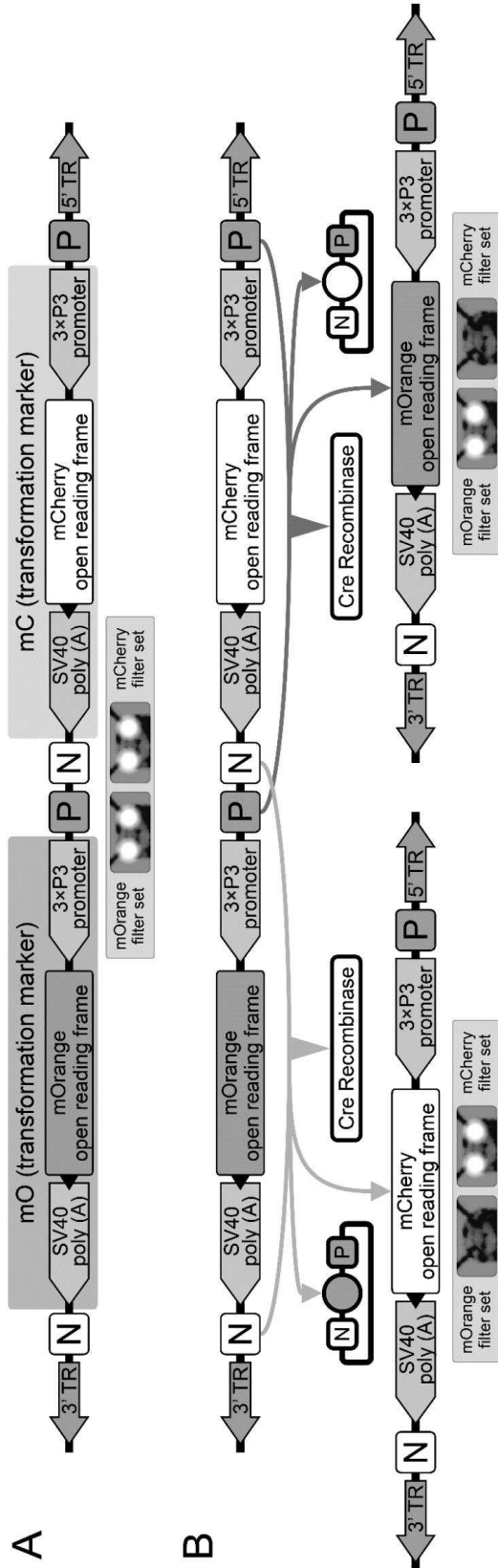


Figure 2:

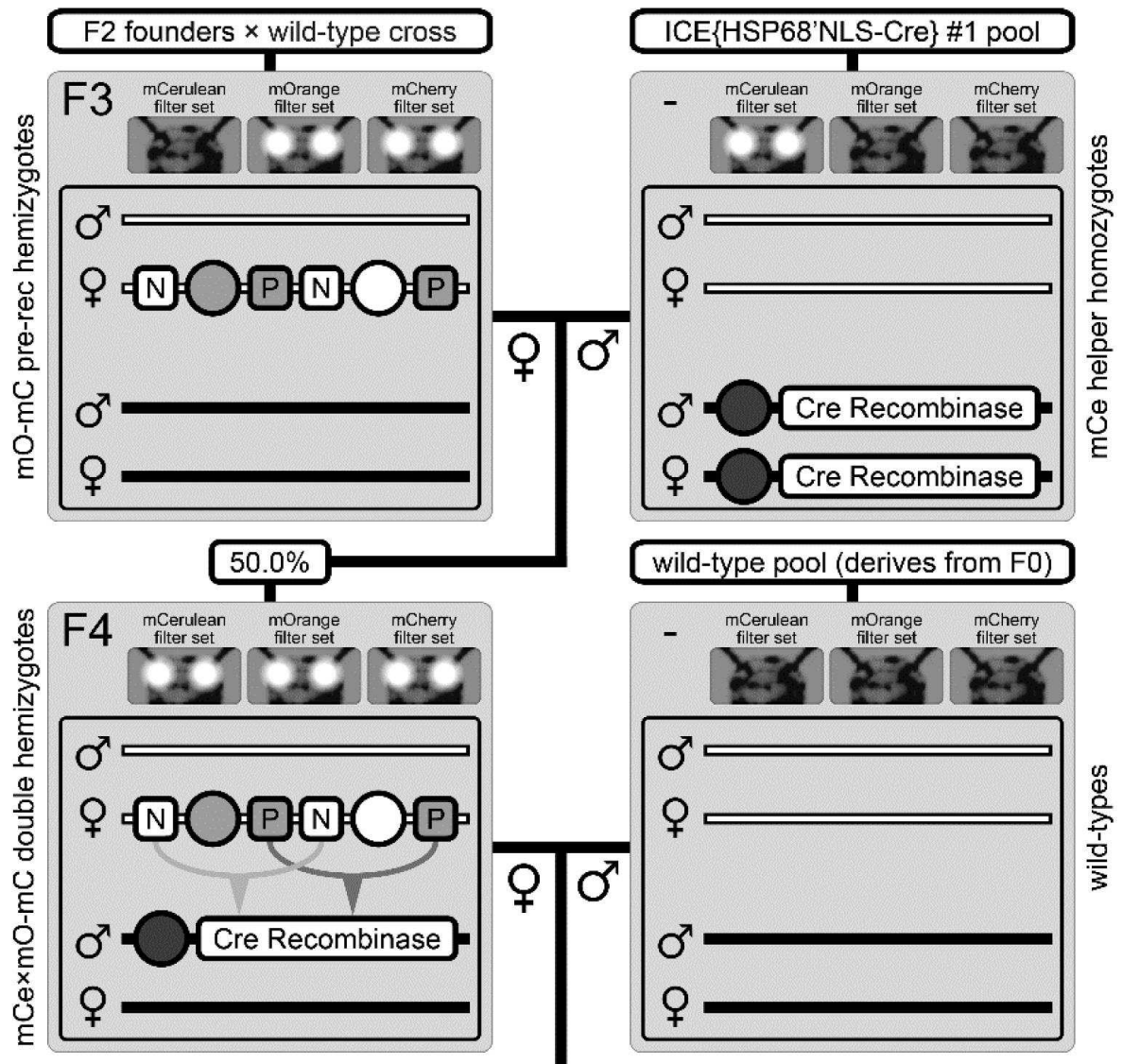


Figure 2 cont:

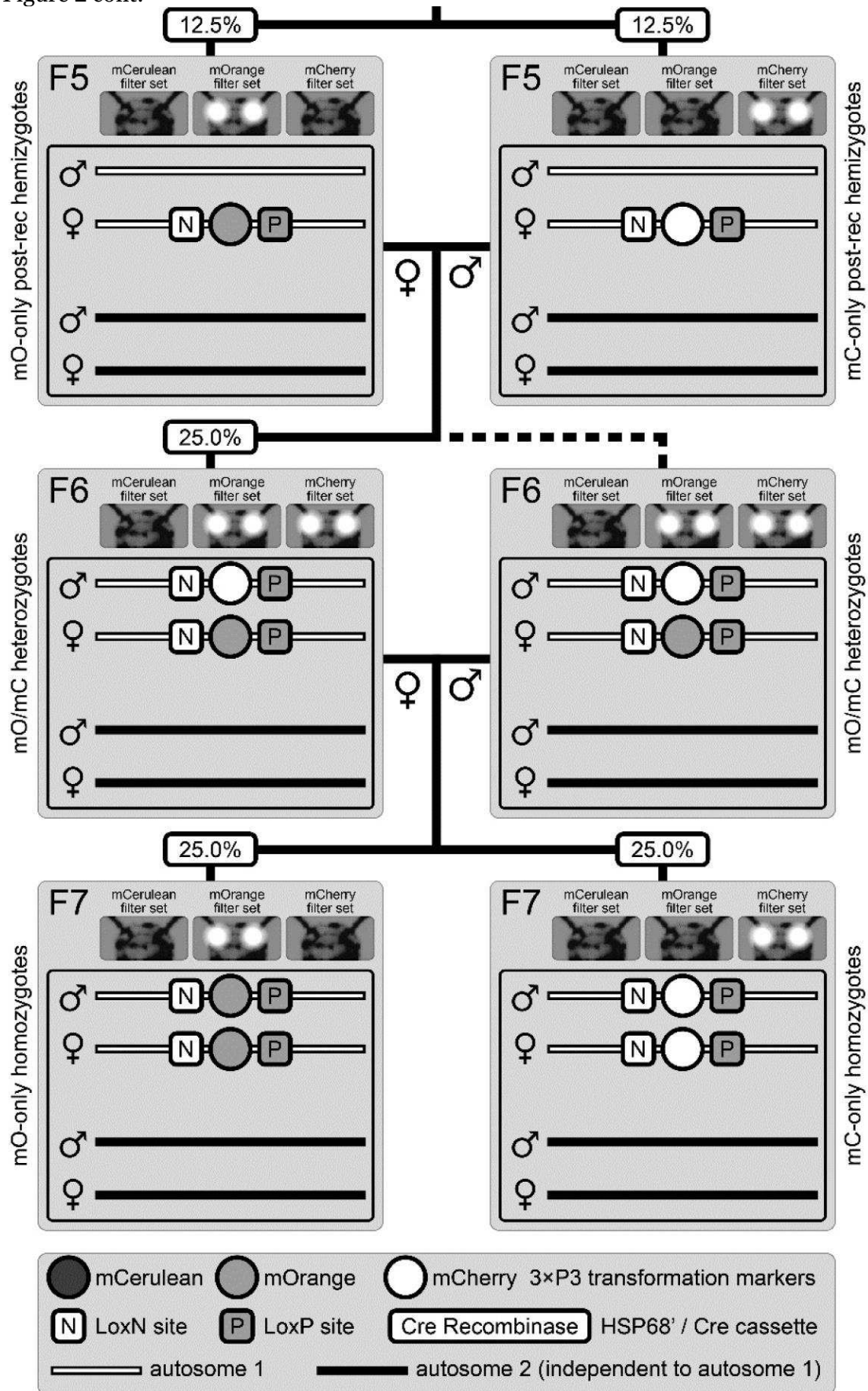


Figure 3:

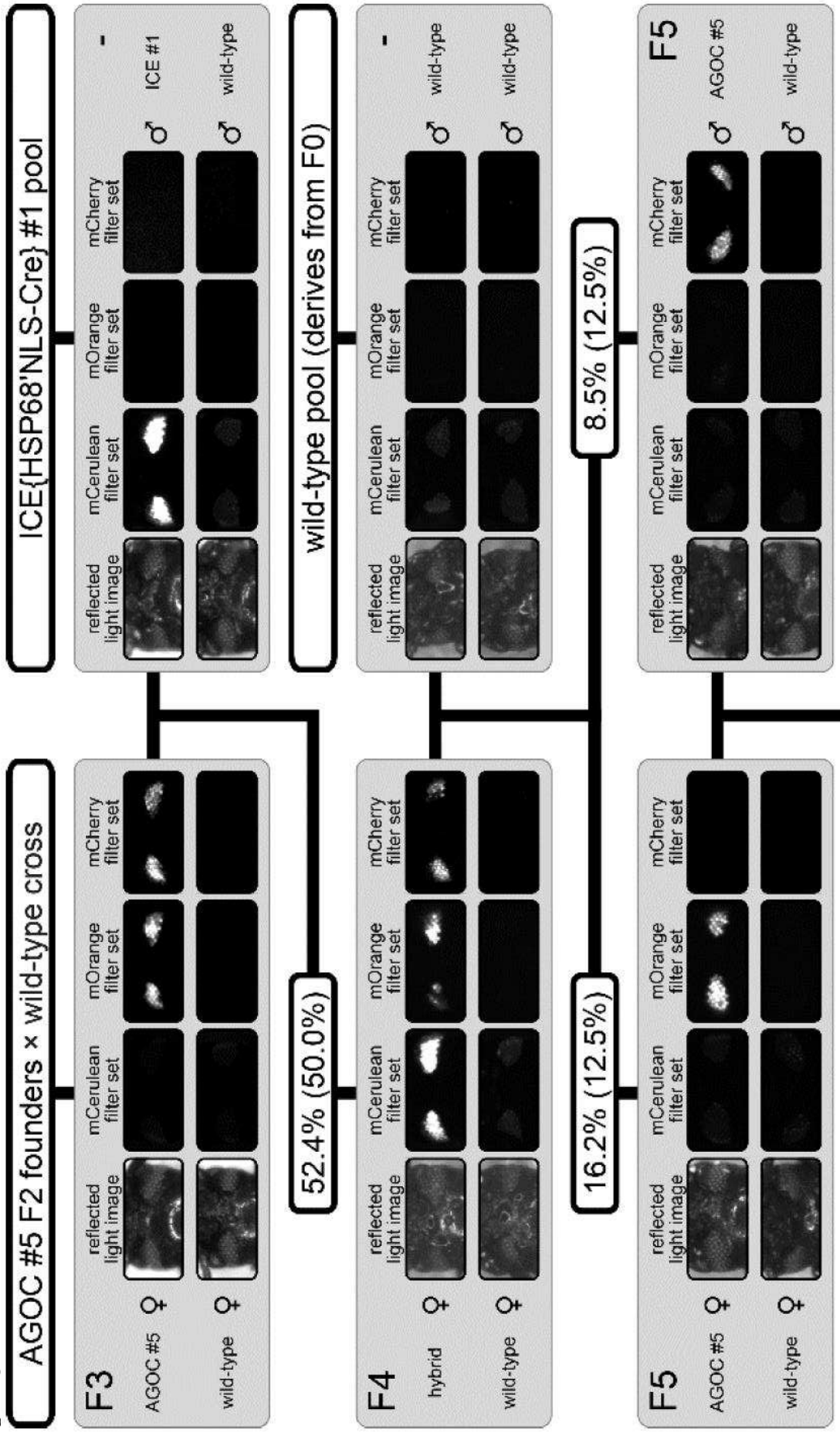


Figure 3 cont.:

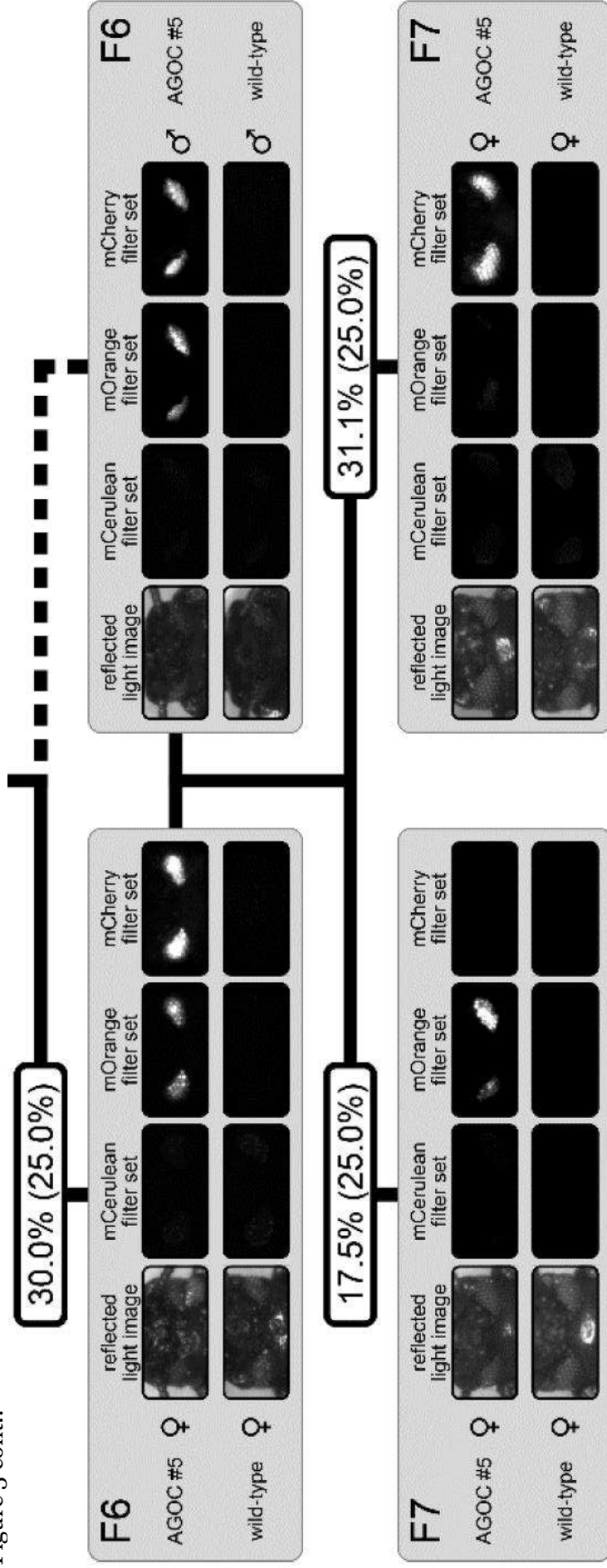


Figure 3 cont.:

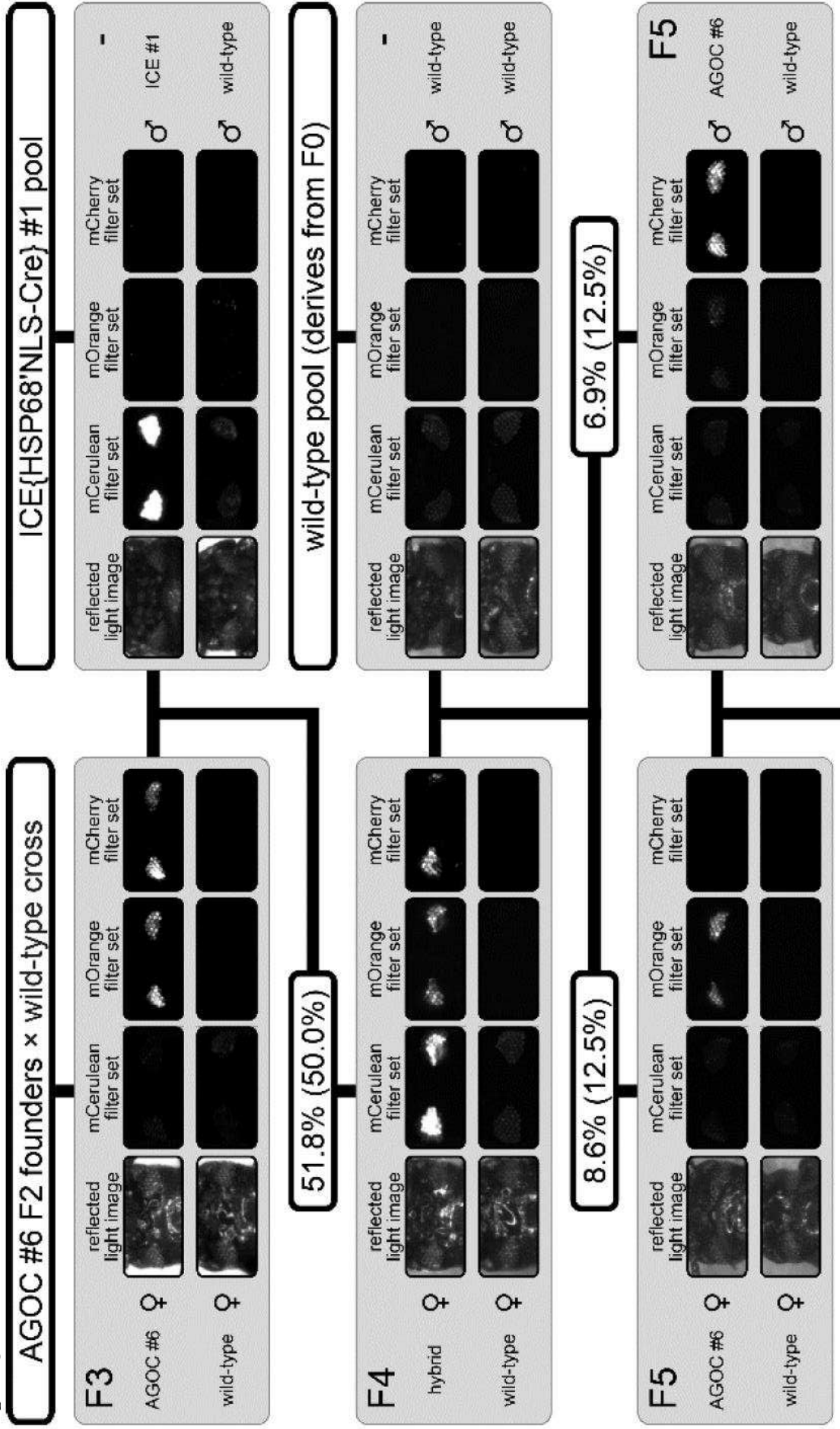


Figure 3 cont:

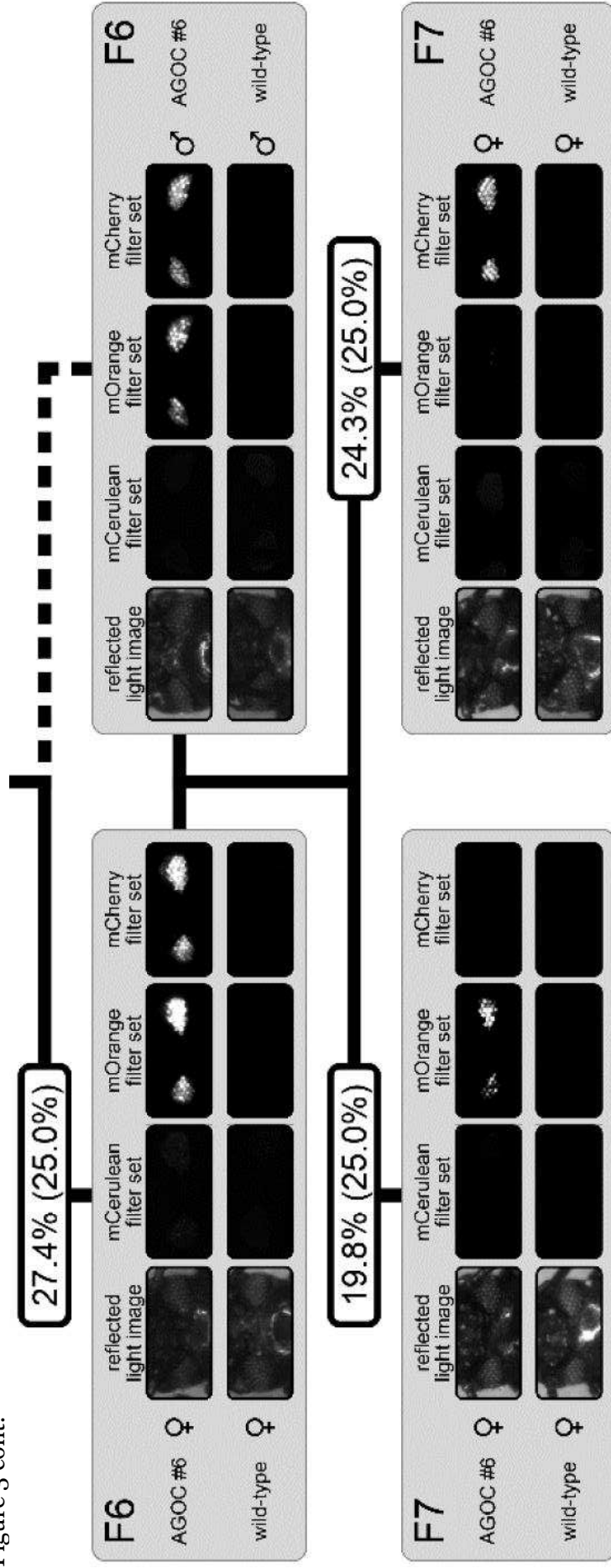


Figure 4:

Gen	Cross		Subline	Progeny						mCe / mO / mC	- / mO / mC	mCe / mO / mC	Total
	♀	♂		- / - / -	mCe / - / -	- / mO / -	- / - / mC	mCe / mO / -					
F3	♂	♀	Theoretical	-	-	-	-	-	-	-	-	50.0%	100%
	♀	♂	AGOC #1	50.0%	34.2% (46)	-	-	-	-	-	-	52.1% (50)	100% (84)
	♂	♀	AGOC #2	-	52.4% (44)	-	-	-	-	-	-	47.6% (40)	100% (89)
	♀	♂	AGOC #3	-	55.1% (49)	-	-	-	-	-	-	44.9% (40)	100% (93)
	♂	♀	AGOC #4	-	44.1% (41)	-	-	-	-	-	-	55.9% (52)	100% (82)
	♀	♂	AGOC #5	-	47.6% (39)	-	-	-	-	-	-	52.4% (43)	100% (56)
	Mean (%)	-	48.2% (27)	49.2%	-	-	-	-	-	-	-	50.8%	100%
F4	♂	♀	Theoretical	25.0%	25.0%	12.5%	12.5%	12.5%	12.5%	12.5%	12.5%	-	100%
	♀	♂	AGOC #1	25.6% (30)	34.2% (40)	4.3% (5)	10.2% (12)	6.0% (7)	19.7% (23)	6.0% (7)	10.6% (14)	-	100% (117)
	♂	♀	AGOC #2	27.3% (36)	28.9% (38)	15.1% (20)	8.3% (11)	9.8% (13)	10.6% (14)	5.3% (7)	12.5% (16)	-	100% (132)
	♀	♂	AGOC #3	25.8% (33)	32.8% (42)	13.3% (17)	10.1% (13)	22.0% (22)	9.0% (9)	3.0% (3)	4.0% (4)	-	100% (128)
	♂	♀	AGOC #4	14.0% (14)	15.0% (15)	20.0% (20)	13.0% (13)	10.3% (12)	7.7% (9)	-	-	-	100% (100)
	♀	♂	AGOC #5	17.1% (20)	40.2% (47)	16.2% (19)	8.5% (10)	10.3% (12)	11.2% (13)	-	-	-	100% (117)
	Mean (%)	23.9%	33.6% (39)	30.8%	30.8%	8.6% (10)	6.9% (8)	9.5%	6.1% (7)	11.8%	0.5%	0.7%	100% (116)
F5	♂	♀	Theoretical	25.0%	-	25.0%	25.0%	-	-	-	-	25.0%	100%
	♀	♂	AGOC #1	27.2% (31)	-	26.3% (30)	23.7% (27)	-	-	-	-	22.8% (26)	100% (114)
	♂	♀	AGOC #2	28.9% (26)	-	33.3% (30)	17.8% (16)	-	-	-	-	20.0% (18)	100% (90)
	♀	♂	AGOC #3	24.8% (30)	-	27.3% (33)	24.8% (30)	-	-	-	-	23.1% (28)	100% (121)
	♂	♀	AGOC #4	19.3% (21)	-	22.9% (25)	37.6% (41)	-	-	-	-	20.2% (22)	100% (109)
	♀	♂	AGOC #5	28.2% (31)	-	29.1% (32)	12.7% (14)	-	-	-	-	30.0% (33)	100% (110)
	Mean (%)	26.2% (22)	25.8%	28.1%	22.2%	29.7% (25)	16.7% (14)	16.7%	22.2%	27.4% (23)	23.9%	-	100% (84)
F6-S	♂	♀	Theoretical	-	-	50%	50%	-	-	-	-	-	100%
	♀	♂	AGOC #1	-	-	46.4% (39)	53.6% (44)	-	-	-	-	-	100% (84)
	♂	♀	AGOC #2	-	-	50.0% (49)	50.0% (49)	-	-	-	-	-	100% (98)
	♀	♂	AGOC #3	-	-	54.0% (68)	46.0% (58)	-	-	-	-	-	100% (126)
	♂	♀	AGOC #4	-	-	53.8% (50)	46.2% (43)	-	-	-	-	-	100% (93)
	♀	♂	AGOC #5	-	-	51.3% (59)	48.7% (56)	-	-	-	-	-	100% (115)
	Mean (%)	-	52.1%	47.9%	-	57.0% (49)	43.0% (37)	-	-	-	-	-	100% (86)

Figure 5:

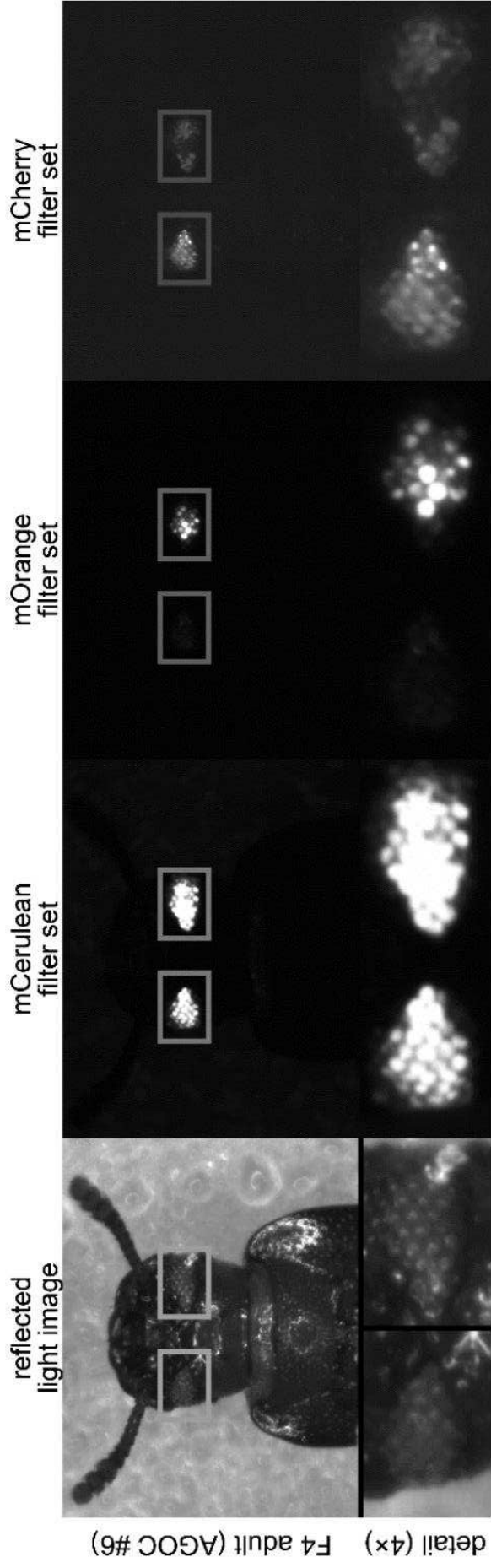


Figure 6:

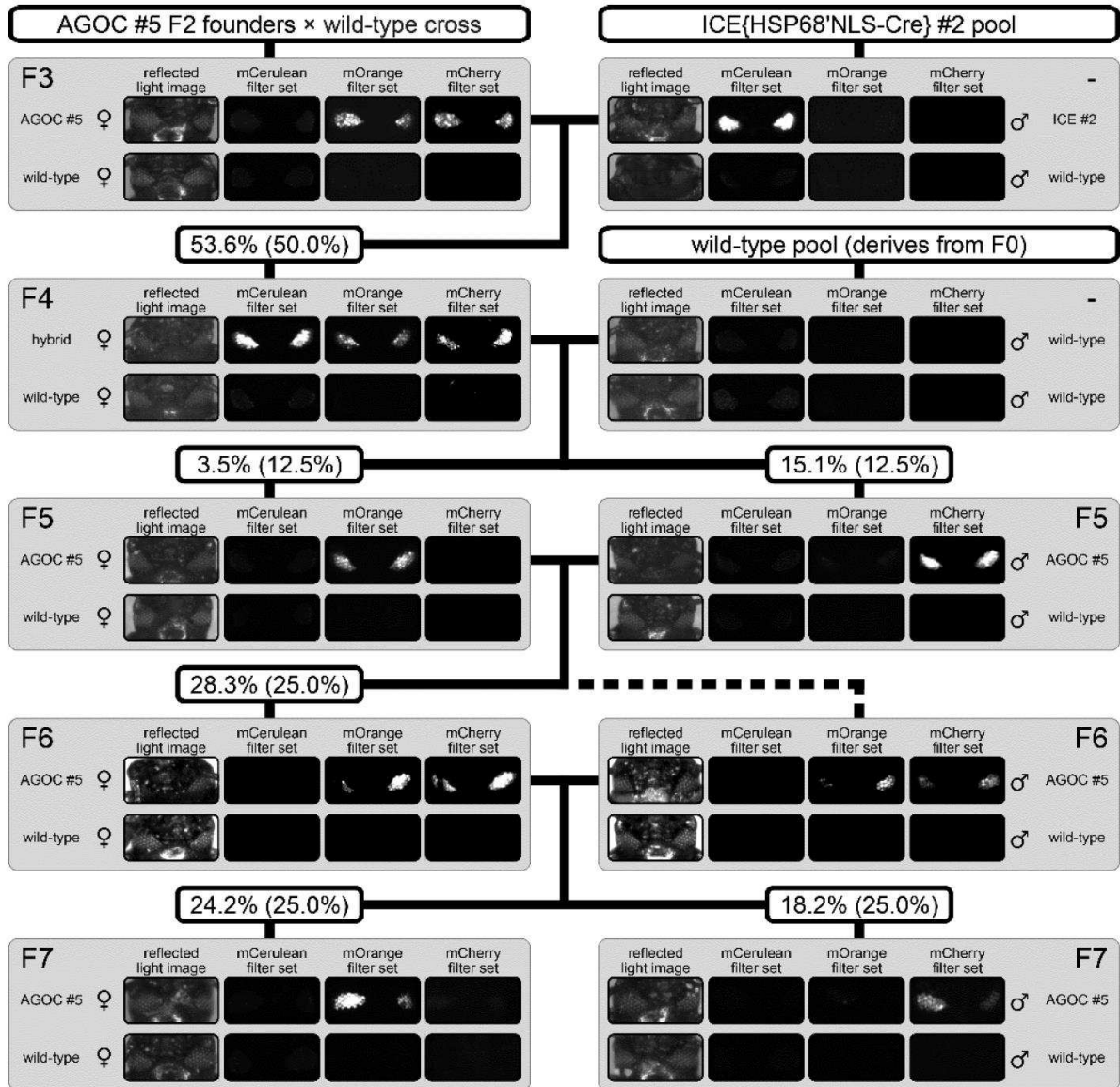


Figure 6 cont.:

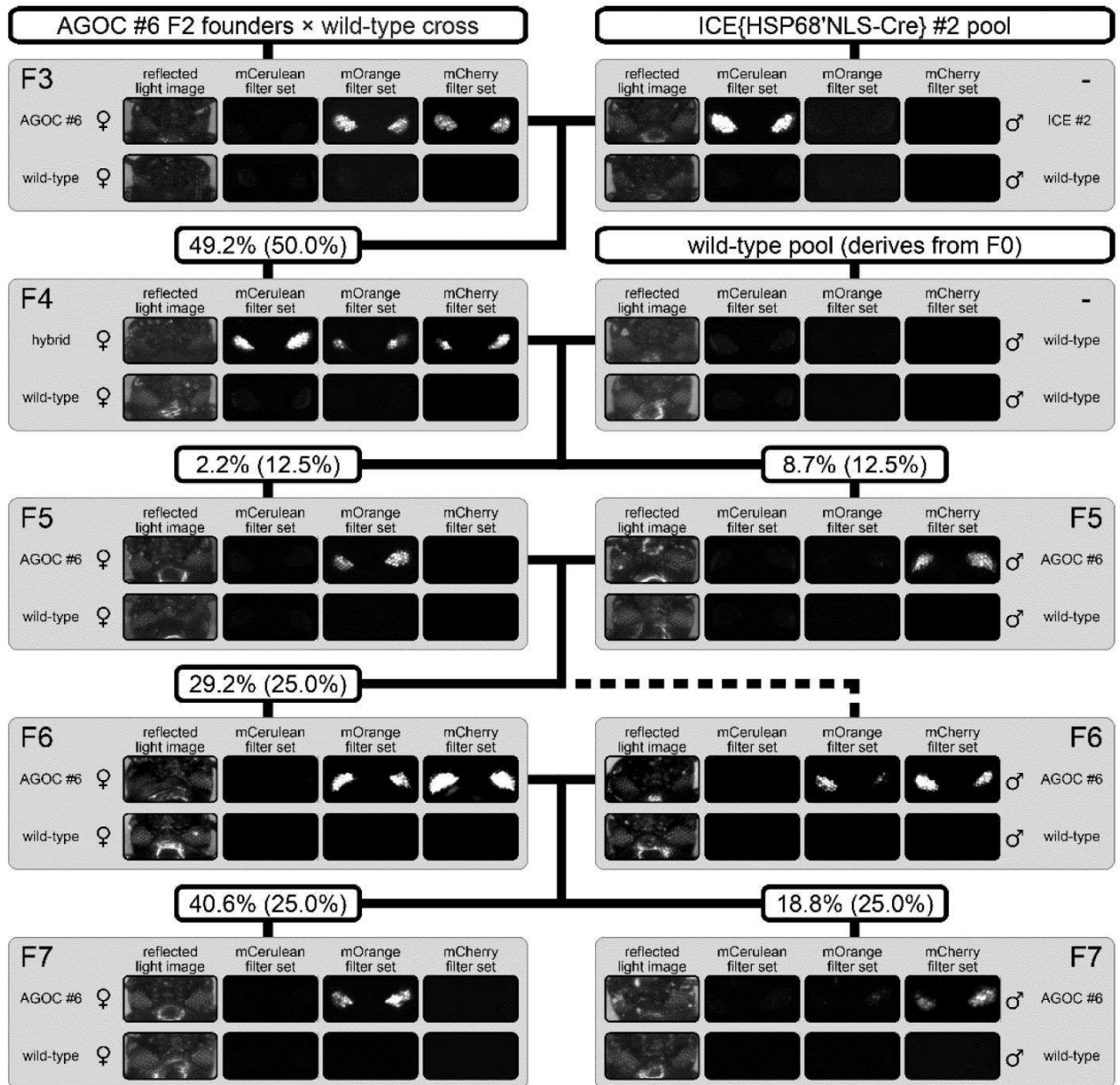


Figure 7:

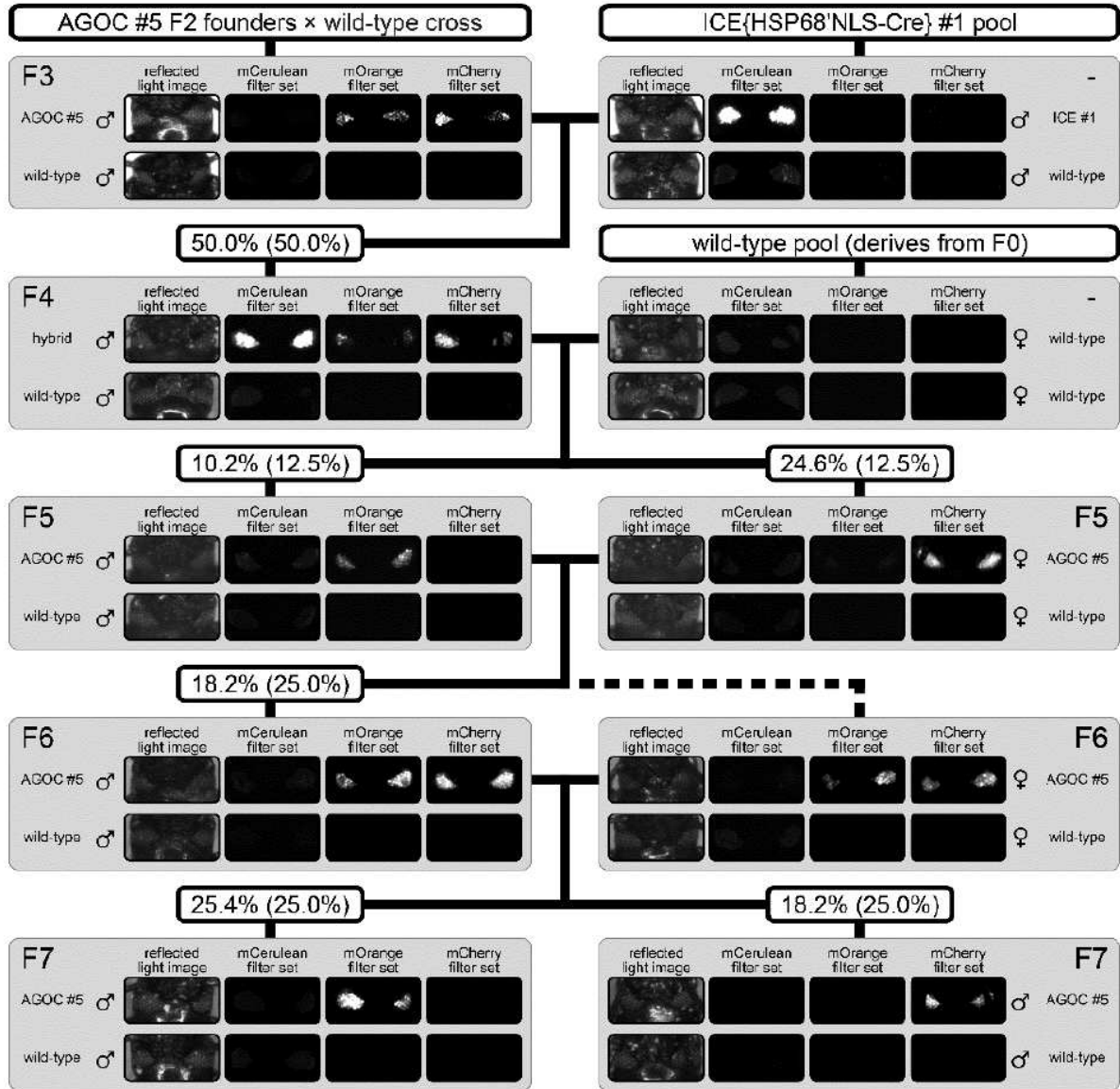


Figure 7 cont.:

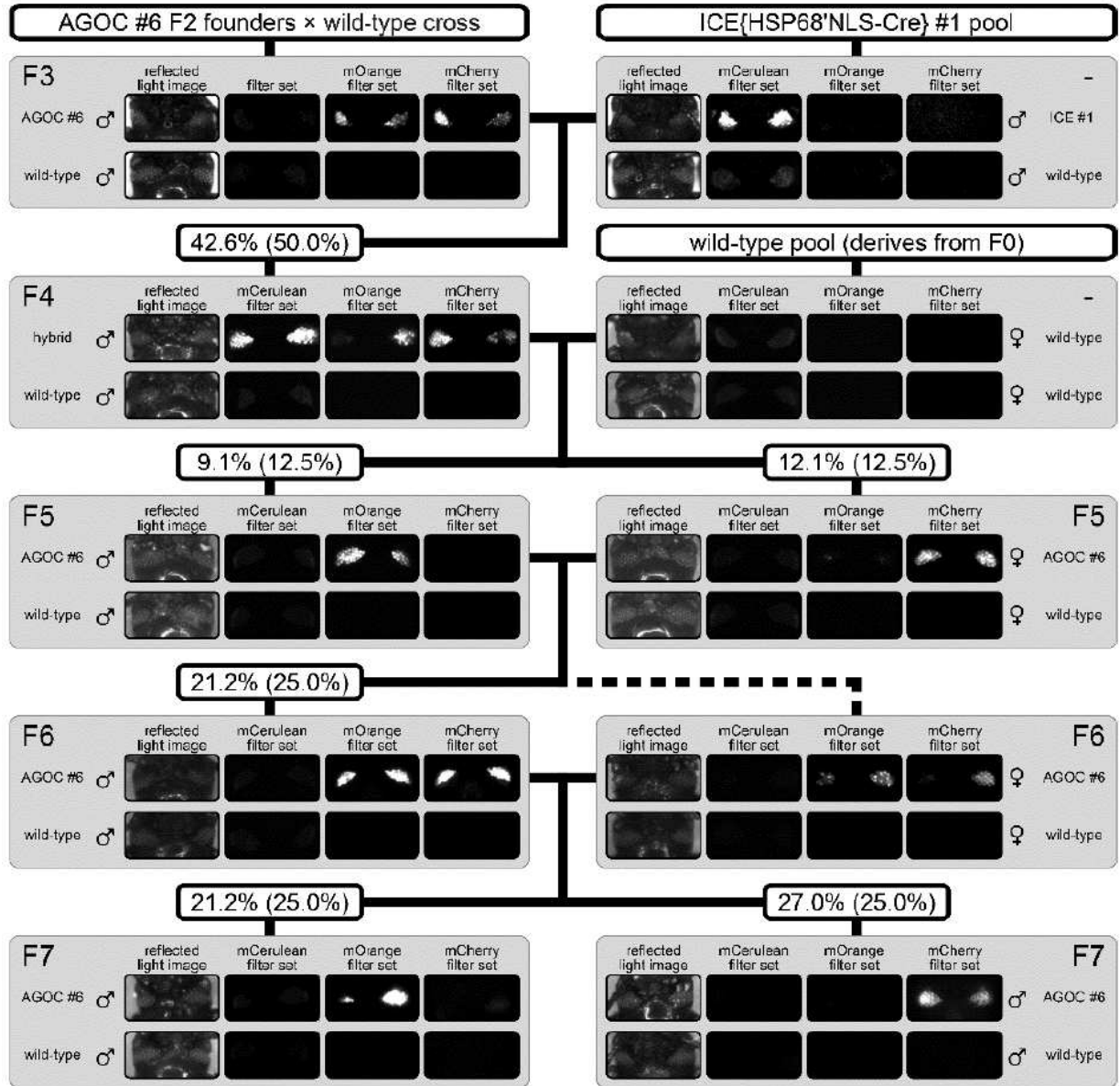


Figure 8:

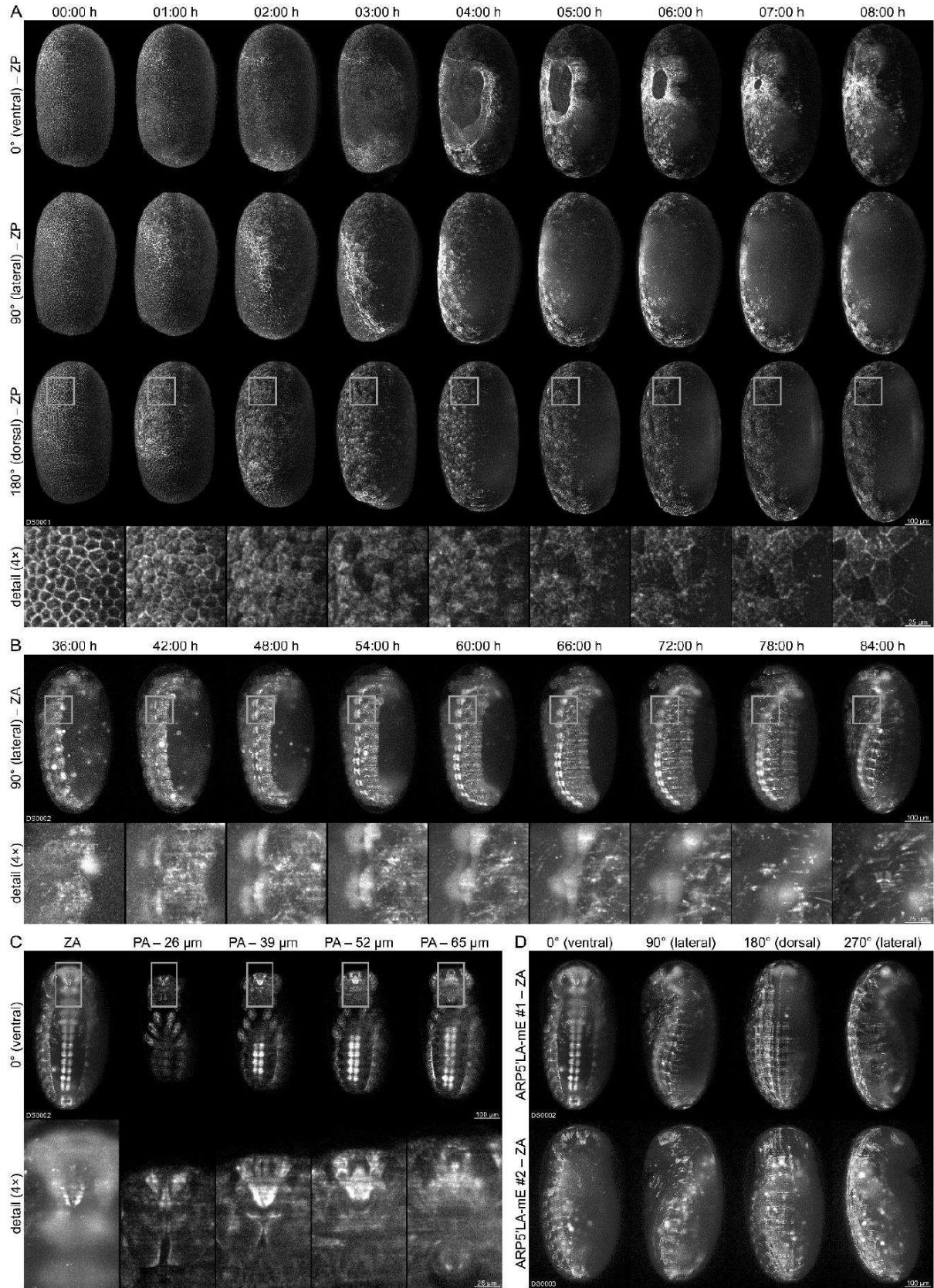
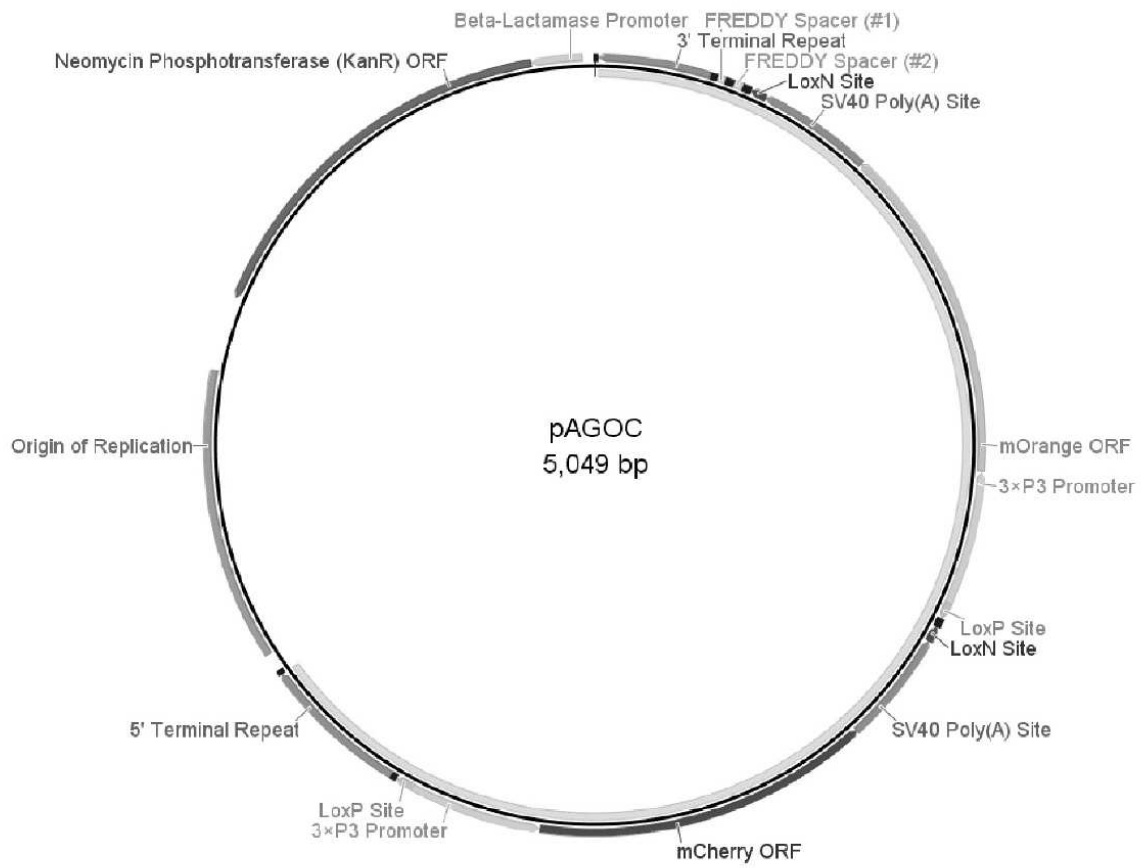


Figure 9:

A



B



Figure 10:
A

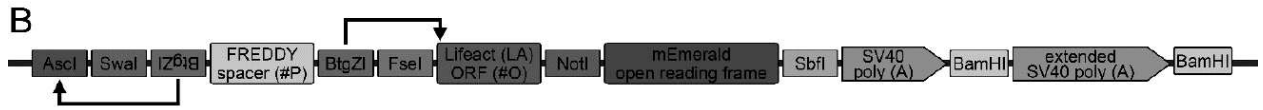
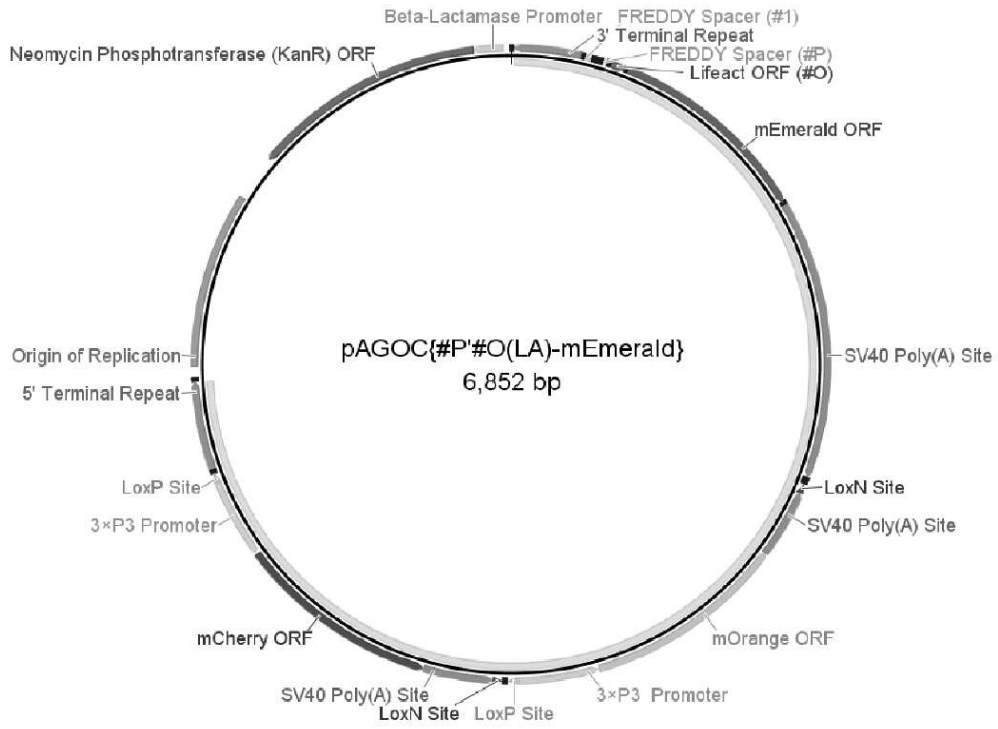
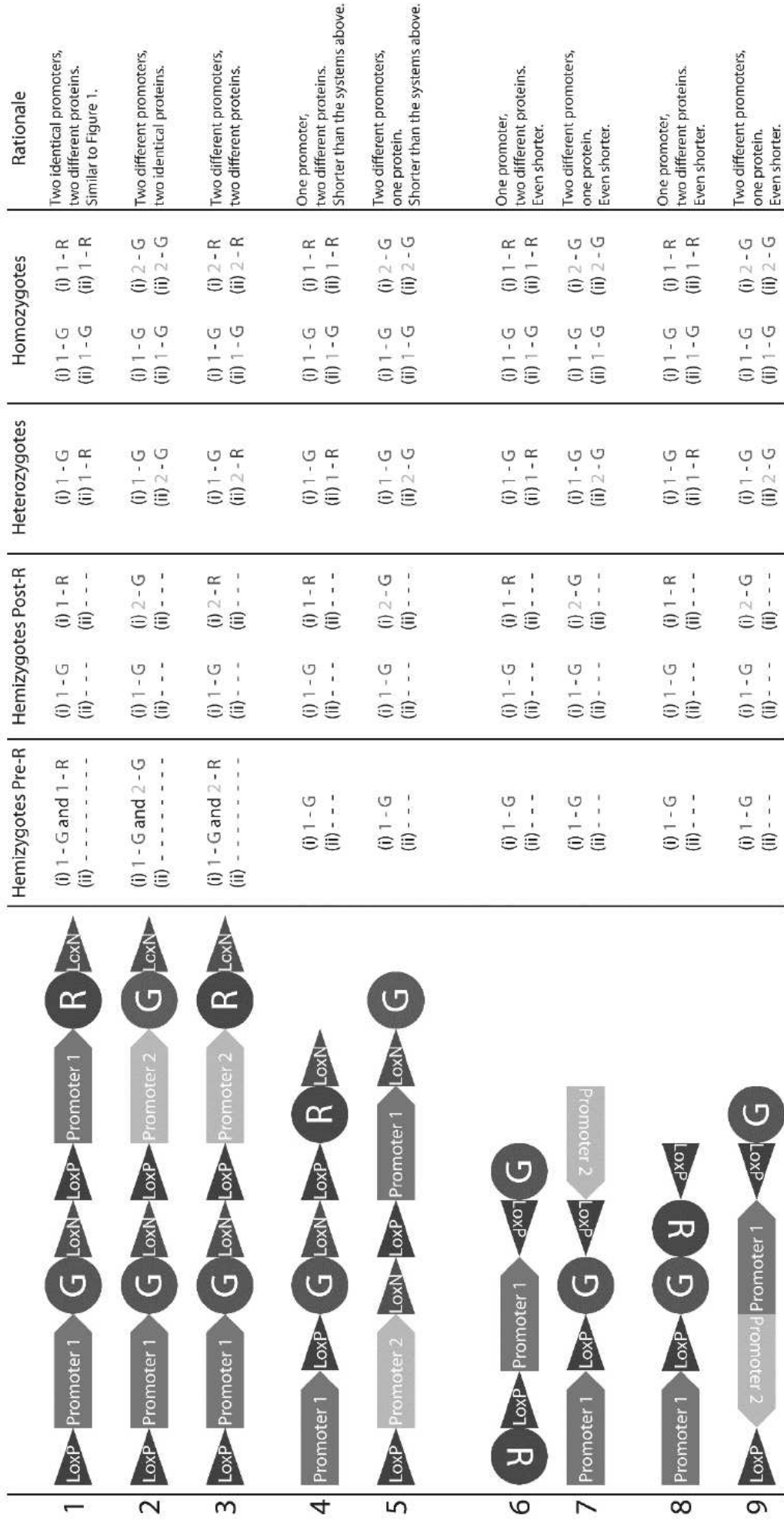


Figure 11:



SEQUENCE LISTING

<110> Johann Wolfgang Goethe-Universitaet Frankfurt am Main

<120> GENETIC TOOLS AND PROCEDURE FOR THE PHENOTYPIC IDENTIFICATION

<130> U30735DE

<160> 2

<170> PatentIn version 3.5

<210> 1

<211> 5049

<212> DNA

<213> artificial

<220>

<223> pAGOC vector (5,049 bps)

<400> 1

gacgtcttaa ccctagaaag ataatcatat tgtgacgtac gttaaagata atcatgcgta 60

aaattgacgc atgtgtttta tcggtctgta tatcgaggtt tatttattaa tttgaataga 120

tattaagttt tattatattt acacttacat actaataata aattcaacaa acaattatt 180

tatgtttatt tatttattaa aaaaaaacaa aaactcaaaa tttcttctat aaagtaacaa 240

aactgtttta aaccccgagg ttagggaaga tgattatact agtgtttaa caagctttt 300

agggaagatg attattctag agtttaaacc tcgagataac ttcgtataag gtatactata 360

cgaagttatg atccagacat gataagatac attgatgagt ttggacaaac cacaactaga 420

atgcagtgaa aaaaatgctt tatttgtgaa atttgtgatg ctattgcttt attgtaacc 480

attataagct gcaataaaca agttaacaac aacaattgca ttcattttat gtttcaggtt 540

cagggggagg tgtgggaggt ttttaaagc aagtaaaacc tctacaaatg tggatggct 600

gattatgac ttattgtac agttcgcca tgccgccggt cgagtcctg ccttcggccc 660

ttcgtattg ttccacaatg gtgtagctt cgttgtgcca ggtaatgtcc agtttaatgt 720

ccacaatgta ggcgccgggc agttgcacgg gtttcttggc tttgtagtg gtttcactt 780

ccgaggtgta gtggccgccc tcttcagtt tcagcctcat ttaattttg ctttcaggg 840

cgccgtcttc ggggtacatc cttccgacg aggcttccca gccatggtt tcttttgca 900

tcacggggcc gtccgagggg aagtgggtgc ccctcagttt cactttgtaa atgaattgc 960

cgtcttgca cgcagagtct tgggtcacgg tcaccacgcc gccgtcttc tagttcatca 1020

cccttccca tttgaagcct tcggggaacg acagtttgaa gtagtcggga atgtcggcgg 1080

ggtgtttcac gtaggcttc gagccgtagg tgaagtgggg cgacagaatg tcccaggcga 1140

agggcagggg gccgccttg gtcacttca gtttggcggg ttggaagcct tcgtagggcc 1200

tgccctgcc ttcgcttca attcgaatt cgtggccgtt caccgagcct tccatcctca 1260

ctttgaacct catgaattct ttaataatgg ccatgtgtt ttcttcgct ttcgacatt 1320

tggtagggc cggtggatcg taccgtcgc tctagcggta ccccgattgt ttagcttgtt 1380

cagctgcgct tgtttattg cttagcttc gcttagcgc gtgttcactt tgcttgttg 1440

aattgaattg tcgctccgta gacgaagcgc ctctattat actccggcgg tcgagggttc 1500

gaaatcgatt agcttgact ctaattgaat tagtctctaa ttgaattag ctctaattga 1560

attagatccc cggccgagct cgaattaacc attgtgggaa cataacttcg tatagcatac 1620

attatacgaa gttatgctag cgtttaaacc ttaagataac ttcgtataag gtatactata 1680

cgaagttatg atccagacat gataagatac attgatgagt ttggacaaac cacaactaga 1740

atgcagtga aaaaatgctt tattgtgaa atttgtgat ctattgctt attgtaacc 1800

attataagct gcaataaaca agttaacaac aacaattgca ttcattttat gtttcaggtt 1860

cagggggagg tgtgggaggt ttttaaagc aagtaaaacc tctacaaatg tggtaggct 1920

gattatgac ttattgtac agttcgtcca tgccgccggg cgagtcctg ccttcggccc 1980

ttcgtattg ttccacaatg gtgtagctt cgttgtgca ggtaatgtcc agtttaatgt 2040

tcacgttgta ggcgccgggc agttgcacgg gtttcttggc tttgtagtg gtttcactt 2100

cggcgctgta gtggccgccc tcttcagtt tcagccttg ttaatttcg ccttcaggg 2160

cgccgtcttc ggggtacatc cttccgacg aggcttccca gcccatggtt ttcttttga 2220

tcacggggcc gtccgagggg aagtgggtgc ccctcagttt cactttgtaa atgaattcgc 2280

cgtcttgacg cgacgagtct tgggtcacgg tcaccacgcc gccgtcttcg aagttcatca 2340

ccctttccca tttgaagcct tcggggaacg acagtttcag gtagtcggga atgtcggcgg 2400

ggtgtttcac gtaggcttc gagccgtaca tgaattgggg cgacagaatg tcccaggcga 2460

agggcagggg gccgccttg gtcactttca gtttgccggt ttgggtgcct tcgtagggcc 2520

tgccttcgcc ttcgcctca atttgaatt cgtggccggt caccgagcct tccatgtgca 2580

ctttgaacct catgaattct ttaataatgg ccatgtgtc ttcttcgct ttcgacatt 2640

tggggcgac cgggtgatcg taccgtcgc tctagcggta ccccgattgt ttagcttgtt 2700

cagctgcgct tgttatttg ctagcttc gcttagcgc gtgttcaatt tgcttgttg 2760

aattgaattg tcgctcgta gacgaagcgc ctctattat actccggcgg tcgagggttc 2820

gaaatcgatt agcttgact ctaattgaat tagtctctaa ttgaattagt ctctaattga 2880

attagatccc cggccgagct cgaattaacc attgtgggaa cataacttcg tatagcatac 2940

attatacgaa gttatcctag ggtttaaact gatatctata acaagaaaat atatatataa 3000

taagtatca cgtaagtaga acatgaaata acaatataat tatcgtatga gttaaatctt 3060

aaaagtcacg taaaagataa tcatgcgtca tttgactca cgcggtcgtt atagttcaaa 3120

atcagtgaca cttaccgcat tgacaagcac gcctcacggg agctccaagc ggcgactgag 3180

atgtcctaaa tgcacagcga cggattcgcg ctatttagaa agagagagca atatttcaag 3240

aatgcatgcg tcaattttac gcagactatc tttctagggt taaacatgtg agcaaaaggc 3300

cagcaaaagg ccaggaaccg taaaaaggcc gcgttgcctg cgttttcca taggetccgc 3360

ccccctgacg agcatcacia aaatcgacgc tcaagtcaga ggtggcgaaa cccgacagga 3420

ctataaagat accagcggtt tccccctgga agctccctcg tgcgctctcc tgttccgacc 3480

ctgccgctta ccgatacct gtccgccttt ctcccttcgg gaagcgtggc gctttctcat 3540
agctcacgct gtaggtatct cagttcgggtg taggtcgttc gctccaagct gggctgtgtg 3600
cacgaacccc ccgttcagcc cgaccgctgc gccttatccg gtaactatcg tcttgagtcc 3660
aaccggtaa gacacgactt atcgccactg gcagcagcca ctggtaacag gattagcaga 3720
gcgaggatg taggcgggtc tacagagttc ttgaagtggg ggcctaacta cggctacact 3780
agaagaacag tatttggtat ctgcgctctg ctgaagccag ttaccttcgg aaaaagagtt 3840
ggtagctctt gatccggcaa acaaaccacc gctggtagcg gtggttttt tgtttgcaag 3900
cagcagatta cgcgcagaaa aaaaggatct caagaagatc cttgatctt ttctacgggg 3960
tctgacgctc agtggaacga aaactcacgt taagggattt tggatcatgag attatcaaaa 4020
aggatcttca cctagatcct tttaaattaa aatgaagtt ttaaataat ctaaagtata 4080
tatgagtaaa ctgggtctga cagttagaaa aactcatcga gcatcaaatg aaactgcaat 4140
ttattcatat caggattatc aataccatat tttgaaaaa gccgtttctg taatgaagga 4200
gaaaactcac cgaggcagtt ccataggatg gcaagatcct ggtatcggtc tgcgattccg 4260
actcgtccaa catcaataca acctattaat ttcccctcgt caaaaataag gttatcaagt 4320
gagaaatcac catgagtgc gactgaatcc ggtgagaatg gcaaaagttt atgcatttct 4380
ttccagactt gttcaacagg ccagccatta cgctcgtcat caaatcact cgcatcaacc 4440
aaaccgttat tcattcgtga ttgcgcctga gcgagacgaa atacgcgac gctgttaaaa 4500
ggacaattac aaacaggaat cgaatgcaac cggcgcagga aactgccag cgcatcaaca 4560
atattttcac ctgaatcagg atatttctt aatacctgga atgctgttt cccagggatc 4620
gcagtgggtga gtaaccatgc atcatcagga gtacggataa aatgcttgat ggtcgggaaga 4680
ggcataaatt ccgtcagcca gtttagtctg accatctcat ctgtaacatc attggcaacg 4740
ctacctttgc catgtttcag aaacaactct ggcgcacatc gcttccata caatcgatag 4800
attgtcgcac ctgattgccc gagattatcg cgagcccatt tataccata taaatcagca 4860

tccatgttgg aatttaacg cggcctagag caagacgttt cccgttgaat atggctcata 4920

ctcttccttt ttcaatatta ttgaagcatt tatcagggtt attgtctcat gacgggatac 4980

atatttgaat gtatttagaa aaataaaca ataggggttc cgcgcacatt tccccgaaaa 5040

gtgccacct 5049

<210> 2

<211> 6852

<212> DNA

<213> artificial

<220>

<223> pAGOC{#P'#O(LA)-mEmerald} vector (6,852 bp)

<400> 2

gacgtcttaa ccctagaaag ataacatat tgtgacgtac gttaaagata atcatgcgta 60

aaattgacgc atgtgttta tcggtctgta tatcgagggt tatttattaa tttgaataga 120

tattaagttt tattatatt acactacat actaataata aattcaaca acaatttatt 180

tatgtttatt tattattaa aaaaaaaca aaactcaaaa tttcttctat aaagtaaca 240

aactgttta aaccccggt ttagggaaga tgattatact agtgtttaa caagcttggc 300

gcgccatta aatcatcgt ttagggaaga tgattatgcg atggccggcc aaaatgggcg 360

tggccgactt gattaaanaa ttcgaatcga ttcgaaaga agaagcggcc gcctcgaaag 420

gcgaagaatt gttcaccggc gtggtgccca ttttgggtga attggacggc gacgtgaacg 480

gccacaaatt ctcggtgtcg ggcgaaggcg aaggcgacgc cacctacggc aaattgacct 540

tgaaattcat ttgtaccacc ggcaattgc cegtgcctg gccaccttg gtgaccacct 600

tgacctacgg cgtgcaatgt ttcgccagg accccgacca catgaaaca cagcattct 660

tcaaatcggc catgcccga ggctacgtgc aagaaaggac cattttctc aaagacgacg 720

gcaactaca aaccagggcc gaagtgaaat tcgaaggcga caccttgggtg aacaggattg 780

aattgaaagg cattgacttc aaagaagacg gcaacatttt gggccacaaa ttggaataca 840

actacaactc gcacaaagtg tacattaccg ccgacaaaca aaagaacggc attaaagtga 900
acttcaaac caggcacaac attgaagacg gctcgggtgca attggccgac cactaccaac 960
aaaacacccc cattggcgac ggccccgtgt tgttgcccga caaccactac ttgtcgacc 1020
aatcgaaatt gtcgaaagac cccaacgaaa agagggacca catggtgttg ttggaattcg 1080
tgaccgccgc cggcattacc ttgggcatgg acgaattgta caataacct gcagggatca 1140
taatcagcca taccacattt gtagaggttt tacttgcttt aaaaaacctc ccacacctcc 1200
ccctgaacct gaaacataaa atgaatgcaa ttgtgtgtg taactgttt attgcagctt 1260
ataatggta caaataaagc aatagcatca caatttcac aaataaagca tttttcac 1320
tgattctag ttgtggttg tccaaactca tcaatgtatc ttatcatgic tggatcccca 1380
ggaagctcct ctgtgtctc ataaacctc acctcctccta cttgagagga cattccaatc 1440
ataggctgcc catccacct ctgtgtctc ctgtaatta ggtcactta caaaaaggaa 1500
attggtagg ggttttcac agaccgcttt ctaagggtaa ttttaaata tctgggaagt 1560
cccttccact gctgtgttc agaagtgtg gtaaacagcc cacaaatgc aacagcagaa 1620
acatacaagc tgtcagcttt gcacaagggc ccaacacct gctcatcaag aagcactgtg 1680
gttgctgtg tagtaatgtg caaacagga ggcacattt cccacctgt gtaggtcca 1740
aaatatctag tgtttcatt ttacttga tcaggaacc agcactccac tggataagca 1800
ttatcctat ccaaacagc cttgtgtca gtgtcatct gctgactgc aactgtagca 1860
tttttgggg ttacagttg agcaggatat ttgtcctgt agtttgctaa cacaccctgc 1920
agtccaaag gttcccacc aacagcaaaa aatgaaaat ttgaccctg aatgggttt 1980
ccagcaccat tttcatgagt ttttgtgtc cctgaatgca agtttaacat agcagttacc 2040
ccaataacct cagtttaac agtaacagct tccacatca aatatttc acaggttaag 2100
tctcattta aaggatcctc tagagttta acctcgagat aacttcgtat aagtatact 2160
atacgaagt atgatccaga catgataaga tacattgatg agtttgaca aaccacaact 2220

agaatgcagt gaaaaaatg ctttattgt gaaattgtg atgctattgc tttattgta 2280

accattataa gctgcaataa acaagttaac aacaacaatt gcattcattt tatgtttcag 2340

gttcaggggg aggtgtggga ggtttttaa agcaagtaa acctctacaa atgtggtatg 2400

gctgattatg atcttattg tacagttcgt ccatgccgcc ggctcgagtgc ctgccttcgg 2460

cccttcgta ttgtccaca atgggtagt cttcgttggt cgaggtaatg tccagtttaa 2520

tgccacaat gtaggcgcc ggcagttgca cgggtttctt ggctttgtag gtggtttca 2580

cttcagagt gtagtgccg ccgtcttca gttcagcct catttaatt tgccttca 2640

gggcgccgc ttcgggtac atccttccg acgaggctc ccagcccatg gtttcttt 2700

gcatcacggg gccgtccgag gggaagtgg tgcccctcag ttcactttg taaatgaatt 2760

cgccgtctg cagcgacgag tcttgggtca cggtcaccac gccgccgtct tcgtagttca 2820

tcacccttc ccattgaag ccttcgggga acgacagtt gaagtagtcg ggaatgctgg 2880

cggggtggtt cacgtaggct ttcagaccg aggtgaagtg gggcgacaga atgtcccagg 2940

cgaagggcag ggggccgcct ttgctactt tcagttggc ggtttgaag ccttcgtagg 3000

gcctgcctc gccttcgct tcaattcga atcgtggcc gttcaccgag ccttccatc 3060

tcactttgaa cctcatgaat tcttaataa tggccatgtt gtttcttcg ccttcgaca 3120

tttggtggc gaccggtgga tcgtaccgtc gactctagcg gtaccccgat tgttagctt 3180

gttcagctgc gctgtttat ttgcttagct ttcgcttagc gacgtgttca cttgcttgt 3240

ttgaattgaa ttgtcgtcc gtagacgaag cgcctctatt tatactccgg cggctcaggg 3300

ttcgaaatcg attagcttg actctaattg aattagctc taattgaatt agtctctaat 3360

tgaattagat cccggccga gctcgaatta accattgtgg gaacataact tcgtatagca 3420

tacattatac gaagtatgc tagcgttaa accttaagat aactcgtat aaggtatact 3480

atacgaagt atgatccaga catgataaga tacattgatg agtttgaca aaccacaact 3540

agaatgcagt gaaaaaatg ctttattgt gaaattgtg atgctattgc tttattgta 3600

accattataa gctgcaataa acaagttaac aacaacaatt gcattcattt tatgtttcag 3660

gttcaggggg aggtgtggga ggtttttaa agcaagtaaa acctctaaa atgtggtatg 3720

gctgattatg atcttattg tacagttcgt ccatgccgcc ggtcgagtgc ctgccttcgg 3780

cccttcgta ttgtccaca atgggttagt cttegtttg cgaggtaatg tccagtttaa 3840

tggtcacgtt gtaggcgcc ggcagttgca cgggtttctt ggctttgtag gtggtttca 3900

cttcggcgtc gtagtggccg ccgtcttca gttcagcct ttgttaatt tcgccttca 3960

gggcgccgtc ttcggggtac atcctttccg acgaggettc ccagcccatg gttttcttt 4020

gcatcacggg gccgtccgag gggaagtgg tgcccctcag tttactttg taaatgaatt 4080

cgccgtcttg cagcgacgag tcttgggtca cggtcaccac gccgccgtct tcgaagtca 4140

tcacccttc ccattgaag ccttcgggga acgacagtt caggtagtcg ggaatgctcg 4200

cggggtgtt cacgtaggct ttcgagccgt acatgaattg gggcgacaga atgtcccagg 4260

cgaagggcag ggggccgcct ttggtcactt tcagtttggc ggtttgggtg ccttcgtagg 4320

gcctgcctc gccttcgcct tcaatttca atcgtggcc gttcaccgag cttccatgt 4380

gcacttgaa cctcatgaat tcttaataa tggccatgt gtcttctcg ccttcgaca 4440

tttgggtggc gaccggtgga tcgtaccgtc gactctagcg gtaccccgat tgttagctt 4500

gttcagctgc gctgtttat ttgcttagct ttcgcttagc gacgtgttca ctttgcttgt 4560

ttgaattgaa ttgtcgtcc gtagacgaag cgctctatt tatactccgg cggtcgaggg 4620

ttcgaaatcg attagcttg actctaattg aattagctc taattgaatt agtctctaat 4680

tgaattagat ccccgccga gctcgaatta accattgtgg gaacataact tcgtatagca 4740

tacattatac gaagtatcc tagggtttaa actgatatct ataacaagaa aatatatata 4800

taataagta tcacgtaagt agaacatgaa ataacaatat aattatcgta tgagttaaat 4860

cttaaaagtc acgtaaaga taatcatgcg tcattttgac tcacgcggtc gttatagttc 4920

aaaatcagt acactaccg cattgacaag cacgcctcac gggagctcca agcggcgact 4980

gagatgtcct aatgcacag cgacggattc gcgctattta gaaagagaga gcaatatttc 5040
aagaatgcat gcgtaattt tacgcagact atctttctag ggtaaacaat gtgagcaaaa 5100
ggccagcaaa aggccaggaa ccgtaaaaag gccgcgttgc tggcgTTTT ccataggctc 5160
cgccccctg acgagcatca caaaaatcga cgctcaagtc agaggtggcg aaacccgaca 5220
ggactataaa gataccaggc gttccccct ggaagctccc tegtgcgctc tctgttccg 5280
accctgccgc ttaccggata cctgtccgcc ttctccctt cgggaagcgt ggcgctttct 5340
catagctcac gctgtaggta tctcagttcg gtgtaggtcg ttegtccaa gctgggctgt 5400
gtgcacgaac cccccgttca gcccgaccgc tgcgccttat ccgtaacta tegtcttgag 5460
tccaacccgg taagacacga cttatcgcca ctggcagcag cactggtaa caggattagc 5520
agagcgaggt atgtaggcgg tgctacagag ttctgaagt ggtggcctaa ctacggctac 5580
actagaagaa cagtatttgg tatctgcgct ctgctgaagc cagttacctt cggaaaaaga 5640
gttgtagct cttgatccgg caaacaacc accgctggta gcggtggtt tttgtttgc 5700
aagcagcaga ttacgcgcag aaaaaagga tctcaagaag atcctttgat ctttctacg 5760
gggtctgacg ctcagtggaa cgaaaactca cgtaaggga tttgttcat gagattatca 5820
aaaagatct tcacctgat cttttaaataaaaaatgaa gttttaaate aatctaaagt 5880
atatatgagt aaacttggtc tgacagttag aaaaactcat cgagcatcaa atgaaactgc 5940
aatttattca taccaggatt atcaatacca ttttttgaa aaagccgtt ctgtaatgaa 6000
ggagaaaact caccgaggca gttccatagg atggcaagat cctggtatcg gtctgcgatt 6060
ccgactcgtc caacatcaat acaacctatt aattccccct cgtcaaaaat aaggttatca 6120
agtgagaaat caccatgagt gacgactgaa tccggtgaga atggcaaaag tttatgcatt 6180
tcttccaga cttgttcaac aggccagcca ttacgctcgt catcaaaate actcgeatca 6240
accaaaccgt tattcattcg tgattgcgcc tgagcgagac gaaatacgcg atcgctgtta 6300
aaaggacaat tacaacagg aatcgaatgc aaccggcgca ggaactgc cagcgcata 6360

acaatattt cacctgaatc aggatattct tctaatacct ggaatgctgt tttcccaggg 6420

atcgcagtgg tgagtaacca tgcacatca ggagtacgga taaaatgctt gatggtcgga 6480

agaggcataa attccgtag ccagtttagt ctgacatct catctgtaac atcattggca 6540

acgtacctt tgccatgttt cagaaacaac tctggcgcac cgggcttccc atacaatga 6600

tagattgtcg cacctgattg cccgacatta tcgcgagccc atttataccc atataaatca 6660

gcatccatgt tggaaattaa tcgcggccta gagcaagacg tttcccgttg aatatggctc 6720

atactcttcc ttttcaata ttattgaagc atttatcagg gttattgtct catgagcgga 6780

tacatattg aatgtattta gaaaaataaa caaatagggg ttccgcgcac atttccccga 6840

aaagtgccac ct 6852

GA

Reinhart Koselleck-Projekt

Morphotypisch-quantitative embryonale Variabilität

prominenter Insektennütz- und -schädlinge

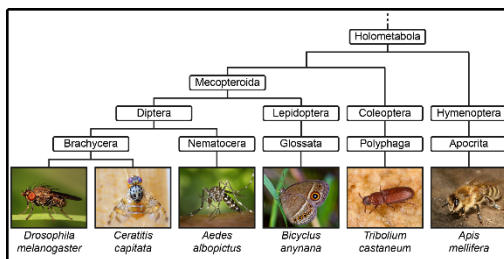
unter Einfluss ex- und intrinsischer Faktoren

Insekten bevölkern die Erde seit 400 Millionen Jahren. Mit einer Million beschriebener Spezies stellen Insekten die Mehrheit tierischer Arten. Sie besetzen alle Futternischen, pflanzen sich überall fort und loten viele unterschiedliche Strategien der Embryogenese aus. Der Parameterraum, der insektenspezifische fundamentale Nischen definiert, wird wesentlich durch das Klima bestimmt. Änderungen des menschlichen Kulturraums (z.B. Landnutzung, Handel, Tourismus) und Klimawandel verschieben regionale Spektren der Insektenspezies kontinuierlich. Ein eindringliches Beispiel ist die Ausbreitung invasiver Stechmücken in Europa. Von epidemiologischer Bedeutung ist zum Beispiel die Asiatische Tigermücke als Überträger für Dengue und Chikungunyaviren. Obwohl eine Million Insekten bekannt sind, werden nur wenige Spezies, meist genetisch motiviert, erforscht. Wir schlagen vor, die Anzahl der Insektenmodellorganismen in einer wissenschaftlich, wirtschaftlich und epidemiologisch fundierten Weise zu erhöhen, verschiedene Umweltbedingungen zu kreieren und die Kanalisierung, d.h. die Robustheit der Embryogenese, zu untersuchen. Das ist möglich, da inzwischen Organelle vieler Insekten mit fluoreszierenden Proteinen markiert werden können. Mit unseren Partnern adressieren wir zunächst konkrete wissenschaftliche Fragen, indem wir der dreidimensionalen räumlichen Verteilung mit Lichtscheibenmikroskopie folgen. Mittelfristig entwickeln wir Methoden, um komplexe ökologische Herausforderungen zu verstehen. Langfristig leisten wir Beiträge zur Insektenbiologie, zur Evolution der Arten und zur Entwicklung eines kanonischen Satzes von Insektenmodellorganismen.

Grant Application

Reinhart Koselleck-Projekt

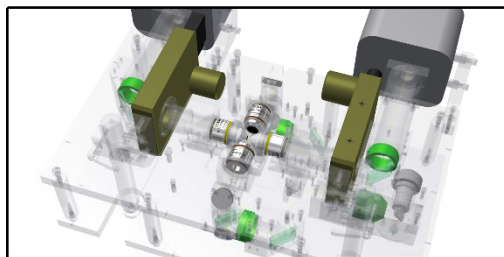
Morphotypisch-quantitative embryonale Variabilität
prominenter Insektennütz- und -schädlinge
unter Einfluss ex- und intrinsischer Faktoren



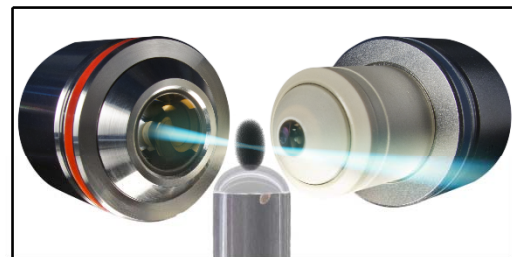
Insektenmodellorganismen



Transgenese von Insekten



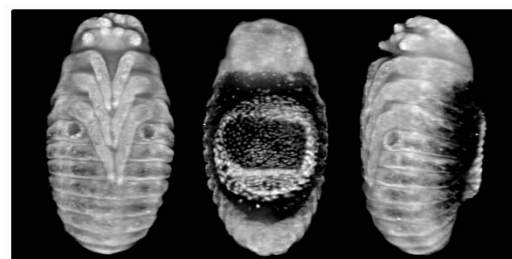
Lichtscheibenmikroskopie



Langzeit-Lebendaufnahmen



Vergleichende Embryogenese



Datenanalyse & Visualisierung

1. Persönliche Daten

Ernst Hans Karl Stelzer

Akademischer Grad	Dr. rer. nat., Diplom-Physiker
Dienststellung	Professor (W3), unbefristet
Geburtsdatum, Nationalität	5. Januar 1959, deutsch
Geschäftszeichen des letzten an die DFG eingereichten Antrags	SPP 2039
Institution / Fachbereich	Institut für Zell- und Neurobiologie, Fachbereich 15 (Biowissenschaften)
Dienstadresse	Physical Biology / Physikalische Biologie (IZN, FB15) Buchmann Institute for Molecular Life Sciences (BMLS) Cluster of Excellence for Macromolecular Complexes (CEF – MC II) Goethe Universität – Frankfurt am Main (Campus Riedberg) Max-von-Laue-Straße 15, D-60438 Frankfurt am Main
Telefon	+49 (69) 798 42547, x42545 (Michaela Koller)
Mobiltelefon	+49 (170) 6357 168
Telefax	+49 (69) 798 42546
E-Mail-Adresse	ernst.stelzer@physikalischebiologie.de
Privatadresse	Eschelbronner Straße 79, D-74909 Meckesheim +49 (6226) 91014

2. Thema

Deutsch: Morphotypisch-quantitative embryonale Variabilität
prominenter Insektennütz- und -schädlinge unter Einfluss ex- und intrinsischer Faktoren

Englisch: Morphotypic-quantitative embryonic variability of
prominent beneficial and detrimental insects influenced by extrinsic and intrinsic factors

3. Fach- und Arbeitsrichtung

Fachgebiet I: Dreidimensionale Fluoreszenzmikroskopie
Arbeitsrichtung: Vergleichende embryonale Morphogenese

Fachgebiet II: Entwicklungsbiologie der Insekten
Arbeitsrichtung: Kanalisierung

4. Gewünschter Beginn der Förderung

Das Projekt und seine Förderung sollen am 01.09.2016 beginnen und zum 31.08.2021 auslaufen.

5. Zusammenfassungen

Zusammenfassung Deutsch

Insekten bevölkern die Erde seit 400 Millionen Jahren. Mit einer Million beschriebener Spezies stellen Insekten die Mehrheit tierischer Arten. Sie besetzen alle Futternischen, pflanzen sich überall fort und loten viele unterschiedliche Strategien der Embryogenese aus. Der Parameterraum, der insektenspezifische fundamentale Nischen definiert, wird wesentlich durch das Klima bestimmt. Änderungen des menschlichen Kulturraums (z.B. Landnutzung, Handel, Tourismus) und Klimawandel verschieben regionale Spektren der Insektenspezies kontinuierlich. Ein eindringliches Beispiel ist die Ausbreitung invasiver Stechmücken in Europa. Von epidemiologischer Bedeutung ist zum Beispiel die Asiatische Tigermücke als Überträger für Dengue- und Chikungunyaviren. Obwohl eine Million Insekten bekannt sind, werden nur wenige Spezies, meist genetisch motiviert, erforscht. Wir schlagen vor, die Anzahl der Insektenmodellorganismen in einer wissenschaftlich, wirtschaftlich und epidemiologisch fundierten Weise zu erhöhen, verschiedene Umweltbedingungen zu kreieren und die Kanalisierung, d.h. die Robustheit der Embryogenese, zu untersuchen. Das ist möglich, da inzwischen Organelle vieler Insekten mit fluoreszierenden Proteinen markiert werden können. Mit unseren Partnern adressieren wir zunächst konkrete wissenschaftliche Fragen, indem wir der dreidimensionalen räumlichen Verteilung mit Lichtscheibenmikroskopie folgen. Mittelfristig entwickeln wir Methoden, um komplexe ökologische Herausforderungen zu verstehen. Langfristig leisten wir Beiträge zur Insektenbiologie, zur Evolution der Arten und zur Entwicklung eines kanonischen Satzes von Insektenmodellorganismen.

Zusammenfassung Englisch

Insects inhabit the earth for about 400 million years. The one million annotated insect species represent the majority of all animal species. Insects occupy all food niches, procreate in all environments and explore many different strategies for embryogenesis. The parameter space defining insect-specific fundamental niches is mainly determined by the climate. Anthropogenic factors (e.g. land usage, global trade, tourism) and climate-change affect these niches and cause a continuous variation in regional spectra of insect species. Particularly striking is the current invasion and spread of mosquitoes in Europe. Of epidemiological importance is the Asian tiger mosquito, the main vector of Dengue- and Chikungunya viruses. Although more than a million different insects are known, only a few species are explored, mostly genetics driven. We propose to increase the number of the insect model organisms in a scientifically, economically and epidemiologically motivated manner, to create different environmental conditions and to investigate canalization, i.e. the robustness of embryogenesis. This is possible, since we can tag arbitrary cellular components (e.g. nucleus, cytoskeleton) with fluorescent fusion proteins. Initially, together with our partners, we address specific scientific questions by following the three-dimensional spatial distribution of the fusion proteins as a function of time with light sheet-based fluorescence microscopy. In the medium term, we develop methods to address complex ecological questions. In the long term, we contribute significantly to insect biology, the evolution of species and the development of a canonical set of insect model organisms.

6. Projektskizze

6.1 Einleitung

Entwicklungsbiologie. Seit einigen Jahren wird angenommen, dass viele entwicklungsbiologische Fragestellungen nicht mit der schwarzbäuchigen Taufliege *Drosophila melanogaster* beantwortet werden können¹. Zum Beispiel entwickelt *Drosophila* embryonal keine Extremitäten und ihre Larven verfügen nur über einen reduzierten, nach innen gestülpten Kopf. Deshalb besteht ein wohlbegründetes Interesse, eine kanonische Gruppe von Insektenmodellorganismen (KIMO) zu definieren, die das Biodiversitätsspektrum, das Insekten zu bieten haben, in seiner vollen Breite abdeckt. Wichtige Zeugen dieses Ansatzes sind die *Emerging Model Organisms* Bände^{2,3}, in denen neun vielversprechende Insektenmodellorganismen vorgestellt werden.

Kanalisation. Insektenarten sind in unterschiedlichem Maß robust gegenüber sich ändernden Umweltbedingungen. Anthropogene Faktoren (globaler Handel, Tourismus, Land- und Wassernutzung, hoher Grad an Industrialisierung, Klimawandel) führen zu einer regionalen Änderung der ökologischen Normbereiche, zum Beispiel bezüglich Temperatur, Einstrahlung von UV-Licht oder pH-Wert sowie Ionenkonzentration in Böden und Gewässern. Die Kanalisation der Entwicklung⁴ kann solche Schwankungen zu einem gewissen Grad kompensieren, doch über ihre Mechanismen, ihren Umfang und ihre Grenzen ist nur wenig bekannt.

Methoden. Bisher ist das Arsenal, d.h. Molekularbiologie, Genetik und Proteomik, das für Untersuchungen zur Verfügung steht, auf spezialisierte Fragestellungen zugeschnitten. Standards, die für *Drosophila* selbstverständlich sind, lassen sich bei vielen anderen Insekten noch nicht anwenden. Eine besondere Lücke weist die Mikroskopie auf, die embryonale Morphogenese ist bisher nur für wenige Insekten dokumentiert.

Lösung. Die embryonale Morphogenese weiterer Insektenarten muss erfasst und miteinander verglichen werden. Dies gilt sowohl für den Wildtyp als auch für abweichende Phänotypen. Konkret bedeutet das, dass eine KIMO anhand wissenschaftlicher, praktischer, wirtschaftlicher und epidemiologischer Kriterien definiert werden muss. Weiterhin müssen Mikroskopie, Datenverarbeitung, Datenanalyse und maschinenbasiertes Lernen etabliert werden.

Projekt. Das vorgeschlagene Projekt gliedert sich in drei Phasen. Die erste Phase ist methodischer Art und hat die Etablierung mehrerer, für die Lebendbeobachtung von Insektenembryonen optimierter, transportabler Lichtscheiben-Fluoreszenzmikroskope (LSFM) und der Herstellung von transgenen Insektenlinien zum Ziel. Dazu definieren wir eine KIMO, die sieben Nütz- und Schädlinge mit abnehmendem Verwandtschaftsgrad zu *Drosophila* beinhaltet, für die Protokolle für die Langzeit-Lebendaufnahme der embryonalen Morphogenese entwickelt werden. In der zweiten Phase liegt der Fokus auf der evolutionären Entwicklungsbiologie, indem Gemeinsamkeiten und Unterschiede der Wildtyp-Embryogenese herausgearbeitet werden. In der dritten Phase wird Entwicklungsbiologie mit ökologischen Fragestellungen kombiniert. Der Einfluss von mehreren Klimawandel-relevanten Umweltfaktoren auf die Morphogenese aller sieben Spezies wird statistisch korrekt erfasst. Ziel ist, die Toleranzgrenzen auszutesten der Kanalisation und damit die Robustheit der Insektenembryogenese zu erforschen. Zusätzlich wird für einige Spezies anhand eines spezifischen Themas erprobt, wie sich LSFM als Methode zur Beantwortung komplexer morphogenetischer Fragestellungen eignet.

6.2 Auswahl der Spezies

Um eine geeignete KIMO mit breiter Relevanz zu bilden, wird die Auswahl der Nütz- und Schädlinge anhand von wissenschaftlichen, ökonomischen, praktischen und epidemiologischen Indikationen getroffen^{2,3}. Neben dem etablierten Modellorganismus *Drosophila* haben wir zunächst sechs weitere Spezies ausgewählt, deren Verwandtschaft zu *Drosophila* in etwa linear abnimmt und meist mindestens eine weitere phylogenetische Gruppierung (Familie, Überfamilie, Teilordnung, Unterordnung oder Ordnung) überbrückt. Abbildung 1A zeigt eine Übersicht in Form eines phylogenetischen Baumes, eine Risikoabschätzung findet sich in Tabelle 1.

6.1.1 Spezies #1 – Mittelmeerfruchtfliege *Ceratitis capitata* (Diptera – Tephritidae)

Einführung. *Ceratitis* ist einer der bedeutendsten Schädlinge im Obstanbau⁵ und außerdem der Hauptvektor des pflanzenpathogenen Bakteriums *Erwinia amylovora*, welches die Feuerbrand-Krankheit (engl. *fire blight*) auslöst⁶. Sie ist daher Gegenstand der Pestizidforschung⁷ und der Entwicklung von genetischen Maßnahmen zur Bestandsverkleinerung⁸⁻¹⁰. **Herausforderungen.** Eine transgene fluoreszente Linie wird von unserem Kollaborationspartner Dr. Marc F. Schetelig (siehe Anhang) zur Verfügung gestellt. Ein Protokoll für die Langzeit-Lebendbeobachtung im LSFM wurde von uns bereits entwickelt (Abbildung 1B) und wird demnächst publiziert. Wir sehen *Ceratitis* als eine der „risikoarmen“ Spezies des Projektes an.

6.1.2 Spezies #2 – Asiatische Tigermücke *Aedes albopictus* (Diptera – Culicidae)

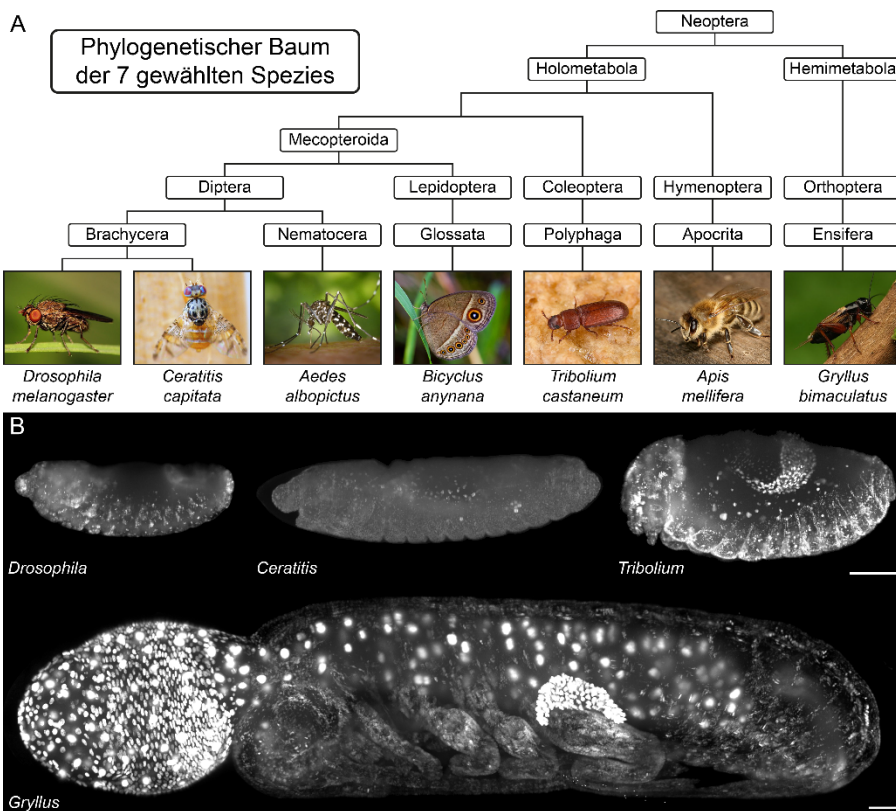
Einführung. Als Überträger von humanpathogenen Viren (Chikungunya^{11,12}, Dengue^{11,13}, Japanische Enzephalitis¹⁴, West-Nil¹⁵) kommt *Aedes* weltweit eine enorme medizinische und sozio-ökonomische Bedeutung zu^{11,16}. Zudem gilt *Aedes* als eine der 100 invasivsten Arten der Welt^{11,16}. Die rapide Ausbreitung, auch in Europa^{17–19}, wird durch die Trockenresistenz der Eier sowie die Kältetoleranz und Diapause-Fähigkeit temperater Populationen stark begünstigt²⁰. **Herausforderungen.** Im Vergleich zu *Drosophila* stellt die Haltung von *Aedes* besondere Anforderungen an Labor und Personal²¹, jegliche Arbeiten müssen unter speziellen Sicherheitsbedingungen durchgeführt werden²². Die Eiproduktion erfordert mindestens eine obligate Blutmahlzeit der weiblichen Individuen (37°C Humanblut, Deutsches Rotes Kreuz)^{21,22}. Um die Arbeiten mit *Aedes* durchführen zu können, kollaborieren wir mit Dr. Ruth Müller (siehe Anhang), welche *Aedes* bereits seit 2010 in Kultur hält und ökologische sowie ökotoxikologische Anpassungsmuster krankheitsübertragender Stechmücken untersucht. Die Herstellung transgener fluoreszenter Linien²³ sowie die Mikroskopieaufnahmen werden direkt am Universitätsklinikum Frankfurt am Main durchgeführt, um unnötige Risiken der Freisetzung während des Transportes von gentechnisch veränderten Organismen zu verhindern.

6.1.3 Spezies #3 – Schielender Busch-Braunling *Bicyclus anynana* (Lepidoptera – Nymphalidae)

Einführung. Schmetterlinge haben sowohl nützliche als auch schädliche Bedeutung. Zum einen helfen sie als Bestäuber und Rohstofflieferanten (z.B. der Seidenspinner), zum anderen sind Schäden durch ihre Raupen in der Land- und Forstwirtschaft gut dokumentiert. Über die embryonale Morphogenese von Schmetterlingen ist wenig bekannt, bisher gibt es nur einige Inselstudien zu *Bombyx mori*^{24,25}, *Bicyclus anynana*^{26,27} und *Heliconius erato*²⁸, in denen man sich auf besondere Ereignisse und fixierte Proben beschränkte. **Herausforderungen.** Für *Bicyclus*, dem wichtigsten Modellorganismus der Schmetterlinge²⁹, ist die Haltung im Labor zwar etabliert, trotzdem stellt diese Spezies im Vergleich zu *Drosophila* höhere Anforderungen³⁰. Unser S1-Insektarium muss entsprechend ergänzt werden, damit wir *Bicyclus* den Standards entsprechend kultivieren können. Die Herstellung transgener fluoreszenter Linien stellt eine weitere Herausforderung dar. Ein Transformationsprotokoll steht zwar zur Verfügung³¹, aber da das Genom nicht sequenziert ist, müssen Promotorsequenzen mit komplexen molekularbiologischen Methoden extrahiert oder exogen ersetzt werden.

Abbildung 1 – (A) Phylogenetischer Baum der sieben gewählten Spezies, die die KIMO bilden sollen.

Neben dem etablierten Modellorganismus *Drosophila* fällt unsere Wahl auf sechs weitere Spezies, deren Verwandtschaft zu *Drosophila* in etwa linear abnimmt, d.h. es kommt jeweils mindestens eine weitere taxonomische Gruppierung (Familie, Ordnung oder Unterordnung) hinzu. Die Auswahl wurde mit Rücksicht auf die bestehende Literatur, die wissenschaftliche Relevanz und die Bedeutung für den menschlichen Kulturraum getroffen. Daher haben wir sowohl Nütz- als auch Schädlinge in unsere Auswahl einbezogen. **(B) Beispielbilder von vier der sieben Insektenspezies, bei denen bereits die Wildtyp-Entwicklung mit dem LSFM dokumentiert ist.** Es handelt sich bei allen vier Spezies um transgene Organismen, die nuklear-lokalisiertes GFP unter Kontrolle eines ubiquitären Promotors exprimieren. Bei allen Spezies



wurde ein vergleichbarer Entwicklungszeitpunkt, der Dorsalschluss, gewählt, bei dem der restliche Dotter vom Embryo inkorporiert wird. Die unterschiedlichen morphogenetischen Strategien sind deutlich zu erkennen. Während Daten von *Drosophila* und *Tribolium* schon mehrfach veröffentlicht wurden, basieren die Bilder von *Ceratitis* und *Gryllus* auf von uns noch nicht publizierten Bildstapeln. *Gryllus* ist im Vergleich zu den drei anderen Spezies achtmal länger, das Bild ist verkleinert dargestellt. Maßstab 100 µm.

6.1.4 Spezies #4 – Rotbrauner Reismehlkäfer *Tribolium castaneum* (Coleoptera – Tenebrionidae)

Einführung. Nach *Drosophila* ist *Tribolium* der zweitwichtigste Insektenmodellorganismus in den Bereichen der vergleichenden Embryologie und der Genetik geworden^{32–34}. *Tribolium* ist außerdem ein wichtiger wirtschaftlicher Schädling, da er in Lagergetreide eindringt^{34,35}. Er repräsentiert die Ordnung der Käfer (Coleoptera). **Herausforderungen.** Entsprechende transgene fluoreszente Linien sind bereits verfügbar³⁶. Außerdem wurde von unserer Gruppe schon eine Methode für die Langzeit-Lebendaufnahme im LSFM entwickelt^{37,38} (siehe Abbildung 1B). Ähnlich wie *Ceratitis* ist *Tribolium* eine „risikoarme“ Spezies des Projektes.

6.1.5 Spezies #5 – Honigbiene *Apis mellifera* (Hymenoptera – Apidae)

Einführung. Nach Rind und Schwein ist *Apis* das drittbedeutendste Nutztier und damit das wichtigste Nutzinsekt weltweit³⁹. Honigbienen sind der wichtigste Bestäuber von Blütenpflanzen in den gemäßigten Breiten, deren Produkte (Honig, Wachs) ebenfalls vom Mensch genutzt werden. Die wenigen morphologischen Studien stammen aus den 1980er Jahren und wurden mit Elektronenmikroskopen durchgeführt^{40,41}. Seither wurde die Embryogenese ausschließlich molekularbiologisch untersucht. In unserem Projekt repräsentiert die Biene die Gruppe der Hautflügler (Hymenoptera). **Herausforderungen.** Bei *Apis* handelt es sich um ein soziales Insekt, welches nicht wie *Drosophila* in Kulturröhrchen gezüchtet werden kann³⁹. Wir arbeiten daher mit Prof. Dr. Bernd Grünewald (siehe Anhang) zusammen. Transformation⁴² und Langzeit-Lebendbeobachtung müssen am Bieneninstitut durchgeführt werden. Außerdem kann im Voraus nur schwer abgeschätzt, welche Bedingungen der Embryo braucht, um sich innerhalb des Mikroskops zu entwickeln. Eventuell muss, ähnlich wie bei *Tribolium*³⁷, von den bislang üblichen Probenpräparationstechniken abgewichen werden.

6.1.6 Spezies #6 – Mittelmeer-Feldgrille *Gryllus bimaculatus* (Orthoptera – Gryllidae)

Einführung. Im Unterschied zu den anderen KMO handelt es sich bei *Gryllus* nicht um ein holometaboles, sondern um ein hemimetaboles Insekt, das also kein Puppenstadium durchlebt⁴³. Unter den hemimetabolen Insekten ist *Gryllus* der wichtigste Modellorganismus, dessen Embryogenese bisher nur mit nicht-fluoreszenter Lichtmikroskopie beschrieben wurde⁴⁴. *Gryllus* repräsentiert die Ordnung der Heuschrecken (Orthoptera), zu denen auch die Feld- und Wanderheuschrecken (Acrididae) gehören, welche vor allem in Afrika und Asien eine wichtige landwirtschaftliche Bedeutung als Schädling haben⁴⁵. **Herausforderungen.** Eine transgene fluoreszente Linie wird uns von Prof. Dr. Taro Mito (Universität Tokushima, Japan) zur Verfügung gestellt⁴⁶. Die Herausforderung bei *Gryllus* besteht in der Größe der Embryonen (Anterior-Posterior-Länge von fast 3 mm). Derzeitige Objektiv- und Kamerakombinationen reichen nicht aus, um einen Embryo mit ausreichender Auflösung in ein einziges Sichtfeld zu bekommen. Daher werden die Embryonen abschnittsweise aufgenommen und im Nachhinein zusammengesetzt werden (Abbildung 1B). Ein Protokoll wird derzeit etabliert.

6.3. Ablauf des Projektes in drei Phasen

Das Projekt ist in drei Phasen unterteilt, die für jede einzelne Spezies erledigt werden müssen. Sie sind modularisiert und müssen zwischen den Spezies nicht synchronisiert werden. Die Phasen sind zeitlich verschoben, um bei experimentellen „Flaschenhälsen“ (z.B. Mikroskopie) keinen Rückstau auftreten zu lassen.

6.1.7 Phase 1 – Vorbereitung (Mikroskope & Insektenmanagement)

Aufbauend auf der Erfahrung der letzten fünfzehn Jahre werden zwei hochwertige LSFMs gebaut, die für die Langzeit-Lebendaufnahmen von Insektenembryonen optimiert sind. Mit ihnen können über mehrere Jahre hinweg qualitativ vergleichbare Aufnahmen gemacht werden. Die Mikroskope sind mit zwei diametralen Beleuchtungseinheiten ausgerüstet, die mit Hilfe eines beweglichen Spiegels dynamische Lichtscheiben erzeugen⁴⁷. Zwei gegenüberliegende Detektionseinheiten nehmen gleichzeitig Bilder vom Embryo auf. Die Probenhalterung ist so konzipiert, dass drei bis fünf Embryonen gleichzeitig aufgenommen werden können. Außerdem sind die Mikroskope kompakt, relativ leicht und transportabel. Die Aufnahmen von *Aedes* und *Apis* können somit in den Laboren unserer Kollaborationspartner gemacht werden (siehe 6.2.2 und 6.2.4).

Außerdem müssen in vier Schritten die molekularbiologische Grundlagen geschaffen werden: Haltung & Zucht der jeweiligen Spezies, Klonieren des Plasmids für die Transformation⁴⁸, Keimbahntransformation und Etablieren einer Methode für die Aufnahme der entsprechenden Spezies im LSFM. Der Arbeitsaufwand ist je nach Spezies unterschiedlich (Tabelle 1). Bei drei Spezies (*Drosophila*, *Ceratitis* und *Tribolium*) haben wir selbst bzw. unsere Kollaborationspartner Vorarbeit geleistet, bei den restlichen vier (*Aedes*, *Bicyclus*, *Apis*, *Gryllus*) sind einige Schritte Hauptherausforderungen des Projektes (siehe 6.2). Die Ergebnisse dieser Phase können unter methodischen Gesichtspunkten publiziert werden.

Tabelle 1 – Benötigte Arbeitsschritte und Risikoabschätzung für Phase 1. Grün markiert Schritte, die als etabliert, d.h. risikoarm, eingeschätzt werden. Gelb markiert Schritte, die unbedingt der Optimierung bedürfen, aber prinzipiell realisierbar sein sollten, d.h. risikobehaftet sind. Rot markiert Schritte, die eine Herausforderung darstellen und deren Durchführungen einen hohen Aufwand erfordern, d.h. riskant sind.

#	Schritt	<i>Drosophila</i>	<i>Ceratitis</i>	<i>Aedes</i>	<i>Bicyclus</i>	<i>Tribolium</i>	<i>Apis</i>	<i>Gryllus</i>
1	Haltung & Zucht	etabliert (unser Labor)	etabliert (Schetelig)	etabliert (Müller)	Protokoll etabliert ³⁰	etabliert (unser Labor)	etabliert (Grünewald)	etabliert (unser Labor)
2	Plasmid	transgene Linie verfügbar (Bloomington)	transgene Linie verfügbar (Schetelig)	Vektoren verfügbar, Erprobung notwendig	nicht verfügbar, Promoter unbekannt	transgene Linie ³⁶ verfügbar (unser Labor)	nicht verfügbar, Promoter bekannt ⁴⁹	transgene Linie ⁴⁶ verfügbar (Mito)
3	Transformation	nicht nötig	nicht nötig	Protokoll etabliert ²³	Protokoll etabliert ³¹	nicht nötig	Protokoll etabliert ⁴²	nicht nötig
4	Methode für LSM	etabliert ^{50–53}	etabliert, noch nicht publiziert	muss etabliert werden	muss etabliert werden	etabliert ^{37,38}	muss etabliert werden	wird z.Z. etabliert (6.2.6)

6.1.8 Phase 2 – Untersuchung der Biodiversität (Embryonalentwicklung aller Spezies)

Mit geeigneten transgenen Tieren kann anschließend die Wildtyp-Embryogenese dokumentiert werden. Hierfür wird eine statistisch aussagekräftige Anzahl an Aufnahmen durchgeführt, um Prozesse auch quantitativ beschreiben zu können. Parallel dazu wird ein Klassifizierungsprogramm (engl. *machine learning*) entwickelt, welches mit Wildtyp-Datensätzen „gefüttert“ wird, um das Entwicklungsstadium automatisch zu bestimmen. Zusätzlich werden Algorithmen entwickelt, um Gemeinsamkeiten und Unterschiede der Morphogenese auf zellulärer Ebene, z.B. Zellmigrations- und Zellteilungsmuster, zwischen den Spezies feststellen. Ergebnisse dieser Phase können unter entwicklungsbiologischen Gesichtspunkten publiziert werden. Wir erwarten in dieser Phase viele neue Erkenntnisse, da Daten zur Embryonalentwicklung vieler Spezies nur bruchstückhaft zur Verfügung stehen. Deshalb messen wir dieser Phase eine hohe Chance für Publikationen bei.

6.1.9 Phase 3 – Einfluss ex- und intrinsischer Faktoren auf die Morphogenese (Kanalisation)

Phase 3 hat zum Ziel, die Toleranzgrenzen der Kanalisation auszuloten und Abweichungen zeitlich und räumlich auf dem quantitativen Level zu erfassen und zu analysieren. Basierend auf ökologischen Kriterien (im Kontext von Umweltverschmutzung und Klimawandel) wird untersucht, wie variable Umweltbedingungen die Morphogenese beeinflussen. Um die Toleranzgrenzen der Embryonen zu definieren und zu vergleichen, werden zunächst vier allgemeine extrinsische Faktoren erprobt: Temperatur, ultraviolette Strahlung, pH-Wert und Salzgehalt (Tabelle 2). Ziel ist es, eine Bilddatenbank vor dem Hintergrund einer mehrdimensionalen Versuchsmatrix (Spezies • Faktor • Varianz des Faktors) zu erstellen. Leitfragen dieser Phase sind:

- In welchen Bereichen verläuft die Entwicklung des Tieres normal, d.h. wie kanalisiert/robust läuft die Embryogenese ab? Sind die Reaktionsnormen breit oder schmal? Gibt es Spezies mit generell eher breiten bzw. schmalen Reaktionsnormen und/oder sind sie faktorabhängig? Verursachen bestimmte Faktoren generell eine breite oder schmale Reaktionsnorm in allen untersuchten Spezies?
- Wie wirken sich die Faktoren auf den zeitlichen Verlauf der Entwicklung aus? Ab wann gibt es morphogenetische Abweichungen? Welcher Abweichungsgrad kann toleriert werden? Ab wann bricht die Robustheit ein bzw. wann treten morphogenetische Schäden auf? Welcher Art sind diese Schäden?
- Sind die Schäden auf beiden Seiten des Bereichs eines Faktors vergleichbar? Haben Schäden, die durch unterschiedliche Faktoren hervorgerufen werden, einen ähnlichen Phänotyp? Gibt es Abstufungen? Sind in verschiedenen Spezies die gleichen Prozesse betroffen? Missbildungen, Infertilität, Letalität?
- Tolerieren manche Spezies extreme Faktoren besser als andere? Wie bezieht sich das auf ihren (zukünftigen) Lebensraum? Begünstigt eine Änderung der Faktoren eher Nütz- oder eher Schädlinge?

Tabelle 2 – Übersicht der allgemeinen Umweltverschmutzung- und Klimawandel-relevanten Faktoren. Zur besseren Einordnung der gewählten Faktoren ist mit jedem ein geläufiges Stichwort verknüpft.

#	Faktor	Stichwort	Antizipierter Bereich
1	Temperatur	„Treibhauseffekt“	Überschneidende Bereiche für alle Spezies; ca. 10°C → 45°C
2	pH-Wert	„saurer Regen“	Änderung des pH mit HCl oder NaOH; pH 3 → pH 11
3	UV-Strahlung	„Ozonloch“	Applikation mit Diode; einige Joule im Laufe der Embryogenese
4	Salzgehalt	„Versalzung“	NaCl, CaSO ₄ , CaCO ₃ ; destilliertes H ₂ O → einige Mol/l

Teil von Phase 3 ist, spezifische Experimente durchzuführen, die sich an aktuellen Fragestellungen unseres Labors und unserer Kollaborationspartner orientieren (Tabelle 3). Die Faktoren sind sowohl ex- als auch intrinsischer Art und breitgefächert aus Gebieten wie angewandter Genetik (*Ceratitis*), Populations- und Verbreitungsökologie (*Aedes*), Genetik der Entwicklung (*Tribolium*) und Ökotoxikologie (*Apis*) gewählt.

Tabelle 3 – Spezifische, an aktuellen wissenschaftlichen Fragestellungen orientierte Faktoren, deren Einfluss auf die entsprechenden Spezies untersucht werden sollen. Bei *Ceratitis*, *Aedes* und *Apis* handelt es sich um Projekte mit unseren Kollaborationspartnern, das *Tribolium*-Projekt ist laborintern.

Spezies	Assay	Rationale
<i>Ceratitis</i> (Anhang)	• Autophagie-Induktion	Besagte Stämme dienen der Bestandskontrolle ^{8,54} , bisher kein Vergleich verschiedener Techniken auf zellulärer Ebene.
<i>Aedes</i> (Anhang)	• Methionin-Deprivation • Länge der Diapause	Methionin-Deprivation und Länge der Diapausen führt zu epigenetischen und reproduktionstoxischen Effekten ²² .
<i>Tribolium</i> (laborintern)	• Knockout von Zen1	Extra-embryonale Membranen sind Thematik unseres Labors, bei Verlust von Zen1 kommt es zur Reorganisation ⁵⁵⁻⁵⁷ .
<i>Apis</i> (Anhang)	• Neonicotinoide • Drohne / Arbeiterin	Neonicotinoide greifen das Nervensystem an ⁵⁸ , Varianz der Morphogenese zwischen Drohne und Arbeiterin unbekannt.

Um die Daten objektiv und automatisch zu bewerten, wird das Klassifizierungsprogramm, das bereits für Phase 2 in 6.3.2 beschrieben wurde, erweitert. Das Programm wird in der Lage sein, zeitliche Abläufe zu vergleichen und morphogenetische Abweichungen zu analysieren und entsprechenden Stadien zuzuordnen.

Die Erwartung an Phase 3 ist, dass die Genauigkeit, mit der Abweichungen von der Wildtyp-Embryogenese beschrieben werden, um mehrere Größenordnungen steigt. Bisher haben Experimente mit geringer bis mittlerer Komplexität (Endpunktaufnahmen oder Anteil überlebender Versuchstiere) kaum Rückschlüsse auf Ort, Beginn, Ausmaß, Verlauf und Varianz der Effekte zugelassen. Außerdem fehlen Aussagen zu mechanistischen Ursachen. Mit dem vorgeschlagenen Ansatz können die beschriebenen Unbekannten präzise bestimmt und Verknüpfungen zwischen Phänotyp und den zu Grunde liegenden biologischen Mechanismen auf zellulärer Ebene gefunden werden. Die Ergebnisse können unter entwicklungsbiologischen und ökologischen Aspekten publiziert werden.

6.4 Besonderheiten des Projekts und Perspektive

Die Besonderheiten des Projektes liegen in der multidisziplinären Herausforderung, dem wissenschaftlichem Potential, der komplementären Zusammenarbeit mit unseren Kollaborationspartnern und dem diversen Spektrum an kurz-, mittel und langfristigen Zielen. Auf der methodischen Seite muss umfassend vertikal interdisziplinär gearbeitet werden, um Elemente der optischen Physik, der Genetik, der Entwicklungsbiologie, der Ökologie und der Bioinformatik zu verknüpfen. Auf der wissenschaftlichen Seite muss horizontal interdisziplinär gearbeitet werden, um die Algorithmen zu entwickeln, mit denen sich Daten, die aus der Analyse von zunächst sieben Spezies gewonnen werden, umfassend vergleichen lassen. Erst dann sind fundierte und signifikante Aussagen zu treffen. Das Projekt stellt auch besondere Anforderungen an die Verantwortung aller Mitarbeiter. Es wird ein besonderes Maß an Sorgfalt, Flexibilität, Erfindergeist und Teamarbeit verlangt. Das Projekt ist durch viele Alleinstellungsmerkmale charakterisiert, die sich aus dem Standort, der Erfahrung und den Arbeitsschwerpunkten der Arbeitsgruppen ergeben. Besonders aufgrund unserer breitgefächerten Auswahl an Spezies und Umweltfaktoren erwarten wir fundierte und weitreichende Ergebnisse unserer Studien. Wir denken, dass wir auf der methodischen Seite die Mikroskopie in der entomologischen Grundlagenforschung auf ein neues Niveau heben können, dass wir einen wichtigen grundlegenden Beitrag zur Entwicklungsbiologie leisten, der eine Basis und einen Rahmen für zukünftige, auch eher angewandte Studien liefert, und dass wir mit unseren umweltbezogenen Analysen einen neuen Blickwinkel und Ansatz für Ökologie und Ökotoxikologie liefern. Auch kann man von diesem Projekt neben den primären Forschungsergebnissen viele sekundäre Gewinne für die entwicklungsbiologische und entomologische Grundlagenforschung erwarten.

Wir antizipieren, dass unsere Methoden und experimentellen Ansätze und Herangehensweisen, gestützt auf ausführliche Protokolle und unterstrichen von gut dokumentierten Anwendungsbeispielen, schnell und effektiv von anderen Arbeitsgruppen adaptiert werden und deren Forschungsansätze maßgeblich beeinflussen. Begründet ist das besonders darin, dass wir auf allen Gebieten (Entwicklung der Mikroskope, Mikroskopieprotokolle, Plasmide, transgene Linien, grundlegende Informationen, z.B. Klassifizierungstabellen, Klassifizierungsprogramme, Datenbanken) Vorarbeiten leisten, die Adaptionaufwände so gering wie möglich halten und die wissenschaftlichen Fragen uneingeschränkt in den Vordergrund stellen.

7. Literaturverzeichnis

1. Abzhanov, A. *et al.* Are we there yet? Tracking the development of new model systems. *Trends Genet.* **24**, 353–360 (2008).
2. *Emerging Model Organisms: A Laboratory Manual, Volume 1.* (Cold Spring Harbour Laboratory Press, 2009).
3. *Emerging Model Organisms: A Laboratory Manual, Volume 2.* (Cold Spring Harbour Laboratory Press, 2010).
4. Stearns, S. C., Kaiser, M. & Kawecki, T. J. The differential genetic and environmental canalization of fitness components in *Drosophila melanogaster*. *J. Evol. Biol.* **8**, 539–557 (1995).
5. Salvemini, M. *et al.* De novo assembly and transcriptome analysis of the Mediterranean fruit fly *Ceratitis capitata* early embryos. *PLoS One* **9**, e114191 (2014).
6. Ordax, M. *et al.* Medfly *Ceratitis capitata* as Potential Vector for Fire Blight Pathogen *Erwinia amylovora*: Survival and Transmission. *PLoS One* **10**, e0127560 (2015).
7. Elleuch, J. *et al.* Characterisation of novel *Bacillus thuringiensis* isolates against *Aedes aegypti* (Diptera: Culicidae) and *Ceratitis capitata* (Diptera: Tephritidae). *J. Invertebr. Pathol.* **124**, 90–7 (2015).
8. Schetelig, M. F., Caceres, C., Zacharopoulou, A., Franz, G. & Wimmer, E. A. Conditional embryonic lethality to improve the sterile insect technique in *Ceratitis capitata* (Diptera: Tephritidae). *BMC Biol.* **7**, 4 (2009).
9. Calla, B., Hall, B., Hou, S. & Geib, S. M. A genomic perspective to assessing quality of mass-reared SIT flies used in Mediterranean fruit fly (*Ceratitis capitata*) eradication in California. *BMC Genomics* **15**, 98 (2014).
10. Juan-Blasco, M. *et al.* Estimating SIT-driven population reduction in the Mediterranean fruit fly, *Ceratitis capitata*, from sterile mating. *Bull. Entomol. Res.* **104**, 233–42 (2014).
11. Chen, X.-G. *et al.* Genome sequence of the Asian Tiger mosquito, *Aedes albopictus*, reveals insights into its biology, genetics, and evolution. *Proc. Natl. Acad. Sci. U. S. A.* **112**, E5907–E5915 (2015).
12. Wang, C. *et al.* Chikungunya Virus Sequences Across the First Epidemic in Nicaragua, 2014–2015. *Am. J. Trop. Med. Hyg.* (2015). doi:10.4269/ajtmh.15-0497
13. C Costa, A. C. *et al.* Surveillance of dengue vectors using spatio-temporal Bayesian modeling. *BMC Med. Inform. Decis. Mak.* **15**, 93 (2015).
14. Nicholson, J., Ritchie, S. A. & van den Hurk, A. F. *Aedes albopictus* (Diptera: Culicidae) as a potential vector of endemic and exotic arboviruses in Australia. *J. Med. Entomol.* **51**, 661–9 (2014).
15. Fortuna, C. *et al.* Evaluation of vector competence for West Nile virus in Italian *Stegomyia albopicta* (= *Aedes albopictus*) mosquitoes. *Med. Vet. Entomol.* **29**, 430–3 (2015).
16. Bonizzoni, M., Gasperi, G., Chen, X. & James, A. A. The invasive mosquito species *Aedes albopictus*: current knowledge and future perspectives. *Trends Parasitol.* **29**, 460–8 (2013).
17. Boukraa, S. *et al.* Updated checklist of the mosquitoes (Diptera: Culicidae) of Belgium. *J. Vector Ecol.* **40**, 398–407 (2015).
18. Koch, L. K. *et al.* Modeling the habitat suitability for the arbovirus vector *Aedes albopictus* (Diptera: Culicidae) in Germany. *Parasitol. Res.* (2015). doi:10.1007/s00436-015-4822-3
19. Cianci, D. *et al.* High Resolution Spatial Analysis of Habitat Preference of *Aedes Albopictus* (Diptera: Culicidae) in an Urban Environment. *J. Med. Entomol.* **52**, 329–35 (2015).
20. Lacour, G. *et al.* When mothers anticipate: effects of the prediapause stage on embryo development time and of maternal photoperiod on eggs of a temperate and a tropical strains of *Aedes albopictus* (Diptera: Culicidae). *J. Insect Physiol.* **71**, 87–96 (2014).
21. Müller, R. *et al.* Appropriate Larval Food Quality and Quantity for *Aedes albopictus* (Diptera: Culicidae). *J. Med. Entomol.* **50**, 668–673 (2013).

22. Kreß, A., Kuch, U., Oehlmann, J. & Müller, R. Impact of temperature and nutrition on the toxicity of the insecticide λ -cyhalothrin in full-lifecycle tests with the target mosquito species *Aedes albopictus* and *Culex pipiens*. *J. Pest Sci.* (2004). **87**, 739–750 (2014).
23. Labbé, G. M. C., Nimmo, D. D. & Alphey, L. piggybac- and PhiC31-mediated genetic transformation of the Asian tiger mosquito, *Aedes albopictus* (Skuse). *PLoS Negl. Trop. Dis.* **4**, e788 (2010).
24. Jingade, A. H. *et al.* Silkworm (*Bombyx mori*) cryopreservation: embryonic development as revealed by microscopic studies. *Cryo Letters* **34**, 90–9
25. Nakao, H. Analyses of interactions among pair-rule genes and the gap gene Krüppel in *Bombyx* segmentation. *Dev. Biol.* **405**, 149–57 (2015).
26. Masci, J. & Monteiro, A. Visualization of early embryos of the butterfly *Bicyclus anynana*. *Zygote* **13**, 139–44 (2005).
27. Tong, X., Hrycaj, S., Podlaha, O., Popadic, A. & Monteiro, A. Over-expression of Ultrabithorax alters embryonic body plan and wing patterns in the butterfly *Bicyclus anynana*. *Dev. Biol.* **394**, 357–66 (2014).
28. Aymone, A. C. B., Lothhammer, N., Valente, V. L. da S. & de Araújo, A. M. Embryogenesis of *Heliconius erato* (Lepidoptera, Nymphalidae): a contribution to the anatomical development of an evo-devo model organism. *Dev. Growth Differ.* **56**, 448–59 (2014).
29. Brakefield, P. M., Beldade, P. & Zwaan, B. J. The African butterfly *Bicyclus anynana*: a model for evolutionary genetics and evolutionary developmental biology. *Cold Spring Harb. Protoc.* **2009**, pdb.emo122 (2009).
30. Brakefield, P. M., Beldade, P. & Zwaan, B. J. Culture and propagation of laboratory populations of the African butterfly *Bicyclus anynana*. *Cold Spring Harb. Protoc.* **2009**, pdb.prot5203 (2009).
31. Marcus, J. M., Ramos, D. M. & Monteiro, A. Germline transformation of the butterfly *Bicyclus anynana*. *Proc. R. Soc. B Biol. Sci.* **271**, S263–S265 (2004).
32. Klingler, M. *Tribolium*. *Curr. Biol.* **14**, R639–40 (2004).
33. Richards, S. *et al.* The genome of the model beetle and pest *Tribolium castaneum*. *Nature* **452**, 949–55 (2008).
34. Brown, S. J. *et al.* The red flour beetle, *Tribolium castaneum* (Coleoptera): A model for studies of development and pest biology. *Cold Spring Harb. Protoc.* **4**, (2009).
35. Ulrich, J. *et al.* Large scale RNAi screen in *Tribolium* reveals novel target genes for pest control and the proteasome as prime target. *BMC Genomics* **16**, 674 (2015).
36. Sarrazin, A. F., Peel, A. D. & Averof, M. A Segmentation Clock with Two-Segment Periodicity in Insects. *Science* **336**, 338–341 (2012).
37. Strobl, F. & Stelzer, E. H. K. Non-invasive long-term fluorescence live imaging of *Tribolium castaneum* embryos. *Development* **141**, 2331–2338 (2014).
38. Strobl, F., Schmitz, A. & Stelzer, E. H. K. Live imaging of *Tribolium castaneum* embryonic development using light-sheet-based fluorescence microscopy. *Nat. Protoc.* **10**, 1486–1507 (2015).
39. Dearden, P. K., Duncan, E. J. & Wilson, M. J. The honeybee *Apis mellifera*. *Cold Spring Harb. Protoc.* **2009**, pdb.emo123 (2009).
40. Fleig, R. & Sander, K. Blastoderm development in honey bee embryogenesis as seen in the scanning electron microscope. *Int. J. Invertebr. Reprod. Dev.* (1985). at <<http://www.tandfonline.com/doi/abs/10.1080/01688170.1985.10510156#.VnFqhL-hs3k>>
41. Fleig, R. & Sander, K. Embryogenesis of the honeybee *apis mellifera* L. (hymenoptera : apidae): An sem study. *Int. J. Insect Morphol. Embryol.* **15**, 449–462 (1986).
42. Schulte, C., Theilenberg, E., Müller-Borg, M., Gempe, T. & Beye, M. Highly efficient integration and expression of piggyBac-derived cassettes in the honeybee (*Apis mellifera*). *Proc. Natl. Acad. Sci. U. S. A.* **111**, 9003–8 (2014).
43. Mito, T. & Noji, S. The Two-Spotted Cricket *Gryllus bimaculatus*: An Emerging Model for

Developmental and Regeneration Studies. *CSH Protoc.* **2008**, pdb.emo110 (2008).

44. Donoughe, S. & Extavour, C. G. Embryonic development of the cricket *Gryllus bimaculatus*. *Dev. Biol.* (2015). doi:10.1016/j.ydbio.2015.04.009
45. Wang, X. *et al.* The locust genome provides insight into swarm formation and long-distance flight. *Nat. Commun.* **5**, 2957 (2014).
46. Nakamura, T. *et al.* Imaging of transgenic cricket embryos reveals cell movements consistent with a syncytial patterning mechanism. *Curr. Biol.* **20**, 1641–7 (2010).
47. Keller, P. J., Schmidt, A. D., Wittbrodt, J. & Stelzer, E. H. K. Digital scanned laser light-sheet fluorescence microscopy (DSLM) of zebrafish and *Drosophila* embryonic development. *Cold Spring Harb. Protoc.* **2011**, 1235–43 (2011).
48. Handler, A. M. Use of the piggyBac transposon for germ-line transformation of insects. *Insect Biochem. Mol. Biol.* **32**, 1211–1220 (2002).
49. Schulte, C. *et al.* Honey bee promoter sequences for targeted gene expression. *Insect Mol. Biol.* **22**, 399–410 (2013).
50. Huisken, J., Swoger, J., Del Bene, F., Wittbrodt, J. & Stelzer, E. H. K. Optical sectioning deep inside live embryos by selective plane illumination microscopy. *Science* **305**, 1007–9 (2004).
51. Keller, P. J. *et al.* Fast, high-contrast imaging of animal development with scanned light sheet-based structured-illumination microscopy. *Nat. Methods* **7**, 637–42 (2010).
52. Tomer, R., Khairy, K., Amat, F. & Keller, P. J. Quantitative high-speed imaging of entire developing embryos with simultaneous multiview light-sheet microscopy. *Nat. Methods* **9**, 755–63 (2012).
53. Krzic, U., Gunther, S., Saunders, T. E., Streichan, S. J. & Hufnagel, L. Multiview light-sheet microscope for rapid in toto imaging. *Nat. Methods* **9**, 730–3 (2012).
54. Ogaugwu, C. E., Schetelig, M. F. & Wimmer, E. A. Transgenic sexing system for *Ceratitis capitata* (Diptera: Tephritidae) based on female-specific embryonic lethality. *Insect Biochem. Mol. Biol.* **43**, 1–8 (2013).
55. van der Zee, M., Berns, N. & Roth, S. Distinct functions of the *Tribolium zerknüllt* genes in serosa specification and dorsal closure. *Curr. Biol.* **15**, 624–36 (2005).
56. Panfilio, K. a, Oberhofer, G. & Roth, S. High plasticity in epithelial morphogenesis during insect dorsal closure. *Biol. Open* **2**, 1108–18 (2013).
57. Jacobs, C. G. C., Spaink, H. P. & van der Zee, M. The extraembryonic serosa is a frontier epithelium providing the insect egg with a full-range innate immune response. *Elife* **3**, (2014).
58. Fischer, J. *et al.* Neonicotinoids interfere with specific components of navigation in honeybees. *PLoS One* **9**, e91364 (2014).

8. Bildquellen

Abbildung Titelseite und 1A:

- *Drosophila* von Agencia Digyt (<http://www.dicyt.com> – 09.03.2016, 09:00 h)
- *Ceratitis* von Daniel Feliciano (<https://en.wikipedia.org/wiki/Ceratitis/> – 09.03.2016, 09:00 h)
- *Aedes* von James Gathany (https://de.wikipedia.org/wiki/Asiatische_Tigermücke/ – 09.03.2016, 09:00 h)
- *Bicyclus* von Leon Molenaar (<https://www.flickr.com/photos/leendert3/8345400683/> – 09.03.2016, 09:00 h)
- *Tribolium* von Peggy Greb (<http://www.uniprot.org/taxonomy/7070/> – 09.03.2016, 09:00 h)
- *Apis* von Richard Bartz (https://de.wikipedia.org/wiki/Kärntner_Biene/ – 09.03.2016, 09:00 h)
- *Gryllus* von Gerd Rossen (<http://www.digital-nature-photography.com/nature/insekten/gryllus-bimaculatus-photos.php> – 09.03.2016, 09:00 h)

9. Beantragte Mittel

Gesamtmittel: 1.249.530 € (1.250.000 €)

Personal, das aus den beantragten Mittel bezahlt werden soll (958.530 €)

Promovierter wissenschaftlicher Mitarbeiter (Projektleiter); 5 Jahre	5	×	68.400 €	=	342.000 €
Promovierter wissenschaftlicher Mitarbeiter (<i>Apis</i> -Teilprojekt); 2 Jahre	2	×	68.400 €	=	136.800 €
Doktorand, biologisch orientiert 65%; 3 ½ Jahre	3 ½	×	41.145 €	=	144.000 €
Doktorand, Bioinformatik 65%; 3 ½ Jahre	3 ½	×	41.145 €	=	144.000 €
Biologisch-technische Assistentin 50% (halbtags); 5 Jahre	5	×	23.550 €	=	117.750 €
Studentische Hilfskräfte 80 Stunden / Monat; 2 Jahre (<i>Aedes</i> -Teilprojekt)	2	×	13.440 €	=	26.880 €
Biologisch-technische Assistentin 50% (halbtags); 2 Jahre (<i>Apis</i> -Teilprojekt)	2	×	23.550 €	=	47.100 €

Gerätschaften (249.000 €)

2 × Ressourcen für den Bau der LSFMs	2	×	90.000 €	=	180.000 €
1 × RAID-Server (Datenspeichersystem) mit 140 Terabyte	1	×	25.000 €	=	25.000 €
3 × leistungsfähige Computer für die Datenverarbeitung	3	×	6.000 €	=	24.000 €
1 × Insekten-Inkubator	1	×	20.000 €	=	20.000 €

Verbrauchsmaterialien und zusätzliche Hilfskräfte (12.000 €)

60 Monate, 200 € / Monat pauschal	60	×	200 €	=	12.000 €
-----------------------------------	----	---	-------	---	----------

Verbrauchsmaterial für Kooperationspartner (30.000 €)

Dr. Marc Schetelig (<i>Ceratitis</i> -Teilprojekt)					5.000 €
Dr. Ruth Müller (<i>Aedes</i> -Teilprojekt)					10.000 €
Prof. Dr. Bernd Grünewald (<i>Apis</i> -Teilprojekt)					15.000 €

10. Sonstige Angaben

a) Der Antragsteller gehört keiner außeruniversitären Einrichtung an, sondern ist ein Mitglied der Goethe Universität Frankfurt am Main.

b) Es werden keine Untersuchungen am Menschen oder an vom Menschen entnommenen Material durchgeführt.

c) Es werden keine genehmigungspflichtigen Tierversuche durchgeführt.

d) Die Genehmigung für gentechnologische Experimente der Stufe 1 (S1) für das Buchmann Institute for Molecular Life Sciences (BMLS) als Teil des Fachbereichs 15 – Biowissenschaften der Goethe Universität Frankfurt am Main wurde am 15.07.2015 vom Regierungspräsidium Gießen unter dem Aktenzeichen 9.99.18/01 IV44-53r.30.03UFM126.13.02 erteilt.

11. Erklärungen

Ich verpflichte mich, mit der Einreichung des Antrags auf Bewilligung eines Reinhart Koselleck-Projekts bei der DFG die Regeln guter wissenschaftlicher Praxis einzuhalten.

Ort, Datum

Prof. Dr. Ernst H.K. Stelzer

Ich habe bei der Antragstellung die Regelungen zu den Publikationsverzeichnissen (III.8.) und zum Literaturverzeichnis (III.6.) beachtet.

Ort, Datum

Prof. Dr. Ernst H.K. Stelzer

12. Anhang

Auf den nachfolgenden Seiten befinden sich die Kollaborationsschreiben unserer wissenschaftlichen Partner. Entsprechende Kontaktinformationen sind den jeweiligen Schreiben zu entnehmen.

- 1. Schreiben von Dr. M. Schetelig (*Ceratitis*-Projekt)
- 2. Schreiben von Dr. R. Müller (*Aedes*-Teilprojekt)
- 3. Schreiben von Prof. Dr. B. Grünwald (*Apis*-Projekt)

Curriculum Vitae / Wissenschaftlicher Lebenslauf

Ernst Hans Karl Stelzer

Akademischer Grad	Dr. rer. nat., Diplom-Physiker
Dienststellung	Professor (W3), unbefristet
Geburtsdatum, Nationalität	5. Januar 1959, deutsch
Geschäftszeichen des letzten an die DFG eingereichten Antrags	SPP 2039
Institution / Fachbereich	Institut für Zell- und Neurobiologie, Fachbereich 15 (Biowissenschaften)
Dienstadresse	Physical Biology / Physikalische Biologie (IZN, FB15) Buchmann Institute for Molecular Life Sciences (BMLS) Cluster of Excellence for Macromolecular Complexes (CEF – MC II) Goethe Universität – Frankfurt am Main (Campus Riedberg) Max-von-Laue-Straße 15, D-60438 Frankfurt am Main
Telefon	+49 (69) 798 42547, x42545 (Michaela Koller)
Mobiltelefon	+49 (170) 6357 168
Telefax	+49 (69) 798 42546
E-Mail-Adresse	ernst.stelzer@physikalischebiologie.de
Privatadresse	Eschelbronner Straße 79, D-74909 Meckesheim ☎ +49 (6226) 91014

Mitgliedschaften

- Deutsche Physikalische Gesellschaft (DPG)
- Optical Society of America (OSA, Washington, USA)
- Society of Photo-Optical Instrumentation Engineers (SPIE, Bellingham, USA)

Ehrungen und Preise

- Ernst Abbe Lecture (1999, Royal Microscopical Society, RMS)
- EMBO Fellow (2009, European Molecular Biology Organisation)
- HMLS Price (2009, Heidelberg Molecular Life Science)
- Boris Balinsky Life Sciences Lecture (2012, The Microscopy Society of Southern Africa)
- Carl Zeiss Lecture (2014, Deutsche Gesellschaft für Zellbiologie, DGZ)
- Honorary Fellow of the Royal Microscopical Society (2014, RMS)
- Protagonist *Nature* Method of the Year 2014 (*Nature Methods*, January 2015, 12(1):23-26)
- Lennart Philipson Award (2016, EMBL-EM)

Ausbildung

1. Juli 1987	Verteidigung (Promotion)
Sep 1983 – Feb 1987	Promotion/Doktorarbeit am European Molecular Biology Laboratory (EMBL) Begutachter: Prof. Dr. Bille (Institut für Angewandte Physik) und Dr. habil. Männer (Physikalisches Institut), in der Gruppe von Dr. Wijnaendts-van-Resandt
23. Mai 1983	Diplomprüfung
Nov 1981 – Nov 1982	Diplomarbeit am Max-Planck-Institut für Biophysik, Frankfurt am Main Begutachter: Prof. Dr. Schlögl (MPI Biophysik) und Prof. Dr. Martienssen (Universität Frankfurt, Experimentelle Physik), in der Gruppe von Dr. Grell
Okt 1977 – Mai 1983	Studium der Physik an der Goethe Universität, Frankfurt am Main
1. Juni 1977	Abitur am Gymnasium Liebigschule, Frankfurt am Main

Professionelle Karriere

Seit März 2011	Professor an der Goethe Universität, Frankfurt am Main Buchmann Institute for Molecular Life Sciences (BMLS) Cluster of Excellence – Macromolecular Complexes (CEF-MC II, EXC 115)
Sommer 2009	Ruf auf eine W3 Professur von der Goethe Universität, Frankfurt am Main
Aug 1989 – Juli 1996	Unbefristete Stelle in der fusionierten Cell Biology and Biophysics Unit (Koordinator: derzeit Jan Ellenberg, vormals Eric Karsenti sowie Kai Simons)
Aug 1987 – Juli 1989	Projektleiter am European Molecular Biology Laboratory (EMBL), Heidelberg im Physical Instrumentation Programme
Juni 1979 – Juli 1983	Assistent am Max-Planck-Institut für Biophysik, Frankfurt am Main

Publikationsverzeichnis zum wissenschaftlichen Lebenslauf

Ernst Hans Karl Stelzer

Reinhart-Koselleck-Projekt „Morphotypisch-quantitative embryonale Variabilität prominenter Insekten-nütz- und -schädlinge unter Einfluss ex- und intrinsischer Faktoren“

- 1) **Optical fluorescence microscopy in three dimensions: microtomoscopy.** Wijnaendts-van-Resandt RW, Marsmann HJB, Kaplan R, Davoust J, Stelzer EH, Stricker R. *Journal of Microscopy*. 1985; 138:29-34.
- 2) **Fundamental reduction of the observation volume in far-field light microscopy by detection orthogonal to the illumination axis: confocal theta microscopy.** Stelzer EH, Lindek S. *Optics Communications*. 1994; 111:536-547.
- 3) **Properties of a 4Pi confocal fluorescence microscope.** Hell S, Stelzer EH. *Journal of the Optical Society of America A / Optics, Image Science, and Vision*. 1996; A9(12):2159-2166.
- 4) **Optical trapping of dielectric particles in arbitrary fields.** Rohrbach A, Stelzer EH. *Journal of the Optical Society of America A / Optics, Image Science, and Vision*. 2001; 18(4):839-853
- 5) **High-resolution three-dimensional imaging of large specimens with light sheet-based microscopy.** Verveer PJ, Swoger J, Pampaloni F, Greger K, Marcello M, Stelzer EH. *Nature Methods*. 2007 Apr;4(4):311-313.
- 6) **Three-dimensional preparation and imaging reveal intrinsic microtubule properties.** Keller PJ, Pampaloni F, Stelzer EH. *Nature Methods*. 2007 Oct;4(10):843-846.
- 7) **The third dimension bridges the gap between cell culture and live tissue.** Pampaloni F, Reynaud EG, Stelzer EH. *Nature Reviews Molecular Cell Biology*. 2007 Oct;8(10):839-845.
- 8) **Light-sheet fluorescence microscopy for quantitative biology.** Stelzer EH. *Nature Methods*. 2015 Jan;12(1):23-26.
- 9) **Rules and Self-Organizing Properties of Post-embryonic Plant Organ Cell Division Patterns.** Von Wangenheim D, Fangerau J, Schmitz A, Smith RS, Leitte H, Stelzer EH, Maizel A. *Current Biology*. 2016 Feb 22;26(4):439-449.
- 10) **csiLSFM combines light-sheet fluorescence microscopy and coherent structured illumination for a lateral resolution below 100 nm.** Chang BJ, Perez Mesa VD, Stelzer EH. *Proceedings of the National Academy of Sciences*. 2017 Apr 24. pii: 201609278.

Projekt- / Themenbezogenes Publikationsverzeichnis

Ernst Hans Karl Stelzer

Reinhart-Koselleck-Projekt „Morphotypisch-quantitative embryonale Variabilität prominenter Insekten-nütz- und -schädlinge unter Einfluss ex- und intrinsischer Faktoren“

- 1) **Optical sectioning deep inside live embryos by selective plane illumination microscopy.** Huisken J, Swoger J, Del Bene F, Wittbrodt J, Stelzer EH. *Science*. 2004 Aug 13;305(5686):1007-1009.
- 2) **Reconstruction of zebrafish early embryonic development by scanned light sheet microscopy.** Keller PJ, Schmidt AD, Wittbrodt J, Stelzer EH. *Science*. 2008 Nov 14;322(5904):1065-1069.
- 3) **Fast, high-contrast imaging of animal development with scanned light sheet-based structured-illumination microscopy.** Keller PJ, Schmidt AD, Santella A, Khairy K, Bao Z, Wittbrodt J, Stelzer EH. *Nature Methods*. 2010 Aug;7(8):637-642.
- 4) **Live imaging of whole mouse embryos during gastrulation: migration analyses of epiblast and mesodermal cells.** Ichikawa T, Nakazato K, Keller PJ, Kajiura-Kobayashi H, Stelzer EH, Mochizuki A, Nonaka S. *PLoS One*. 2013 Jul 8;8(7):e64506.
- 5) **Non-invasive long-term fluorescence live imaging of *Tribolium castaneum* embryos.** Strobl F, Stelzer EH. *Development*. 2014 Jun;141(11):2331-2338.
- 6) **A photorhabdus natural product inhibits insect juvenile hormone epoxide hydrolase.** Nollmann FI, Heinrich AK, Brachmann AO, Morisseau C, Mukherjee K, Casanova-Torres ÁM, Strobl F, Kleinhans D, Kinski S, Schultz K, Beeton ML, Kaiser M, Chu YY, Phan Ke L, Thanwisai A, Bozhüyük KA, Chantratita N, Götz F, Waterfield NR, Vilcinskas A, Stelzer EH, Goodrich-Blair H, Hammock BD, Bode HB. *Chembiochem*. 2015 Mar 23;16(5):766-771.
- 7) **Live imaging of *Tribolium castaneum* embryonic development using light sheet-based fluorescence microscopy.** Strobl F, Schmitz A, Stelzer EH. *Nature Protocols*. 2015 Oct, 20(10):1486-1507.
- 8) **Long-term fluorescence live imaging of *Tribolium castaneum* embryos: principles, resources, scientific challenges and the comparative approach.** Strobl F, Stelzer EH. *Current Opinion in Insect Science*. 2016 Dec; 18:17-26.
- 9) **Light Sheet-based Fluorescence Microscopy of Living or Fixed and Stained *Tribolium castaneum* Embryos.** Strobl F, Klees S, Stelzer EH. *Journal of Visualized Experiments*. 2017 (122), e55629.
- 10) **Improving your four-dimensional image: traveling through a decade of light-sheet-based fluorescence microscopy research.** Strobl F, Schmitz A, Stelzer EH. *Nature Protocols*. 2017 Jun; 12(6):1103-1109.

An
Deutsche Forschungsgemeinschaft
Kennedyallee 40
53175 Bonn

Dr. rer. nat. Marc F. Schetelig
*Head of Emmy Noether and Fraunhofer
Attract Groups*
Justus-Liebig-Universität Gießen
Winchesterstr. 2
D-35394 Gießen
Tel.: +49 (0) 641 99 39504
Email: marc.schetelig@uni-giessen.de

11. März 2016

Kollaborationszusage

Sehr geehrte Damen und Herren,

es ist mir ein Anliegen Herrn Prof. Dr. Ernst Stelzer bei seinem Reinhart Koselleck-Antrag zu unterstützen und auch in Zukunft mit ihm an interdisziplinären Projekten zusammen zu arbeiten.

Meine Arbeitsgruppen am LOEWE Zentrum für Insektenbiotechnologie & Bioressourcen (Emmy Noether und Fraunhofer Attract Programme) arbeiten an der Entwicklung genetischer Bekämpfungsstrategien für Agrarschädlinge und Moskitos. Hier behandeln wir sowohl die Risikoabschätzung von transgenen Tieren als auch die Neuentwicklung von stabilen Systemen um die Sterile Insekten Technik (SIT) zu verbessern und somit neuartige, umweltfreundliche Schädlingsbekämpfung möglich zu machen. Meine Grundausbildung als Entwicklungsbiologie, Biochemiker und Genetiker ermöglicht dabei unsere Grundlagenforschung in anwendungsorientierte Systeme einfließen zu lassen. Die Ergebnisse konnten wir in 30 Publikationen seit 2008 veröffentlichen (u.a. *BMC Biology*, *PNAS*, *Apoptosis*). Unsere Arbeiten an der Mittelmeerfruchtfliege *Ceratitis capitata* und der Gelbfiebermücke *Aedes aegypti* sind sowohl für den Agrar- als auch den Gesundheitssektor von Bedeutung. *C. capitata* ist der Agrarschädling Nummer 1 der Welt und *Ae. aegypti* überträgt das Dengue Virus, das mit geschätzten 390 Millionen Fällen pro Jahr eines der bedrohlichsten Viren unserer Zeit ist.

Elementar wichtig für die Bekämpfung, und speziell für umweltfreundliche Bekämpfung, ist das Verständnis der entwicklungsbiologischen Vorgänge, um die Gemeinsamkeiten und Unterschiede in der Entwicklung besser verstehen zu können. Dies ist mit vorhandenen Methoden nur schwer und zeitlich nur punktuell möglich. In meiner Forschung würde das von Herrn Prof. Stelzer initiierte Projekt die entwicklungsbiologischen Vorgänge in *C. capitata* und Moskitos erstmalig zeitlich aufgelöst beschreibbar und messbar machen. Zusätzlich sehen wir nach dem Grundlagen-Erkenntnisgewinn großes Potential, die Technik für die Entwicklung und ganz dringlich für die Risikoabschätzung von neuen Schädlingsbekämpfungssystemen einzusetzen. So ließen sich z.B. Effekte eines Bekämpfungssystems bei dem gezielt angeschaltete, apoptotische Gene während der Embryonalentwicklung exprimiert werden, über die komplette Embryogenese verfolgen und standardisiert mit anderen Bekämpfungssystemen vergleichen. Ziel solcher Systeme ist das Absterben des Embryos. Jedoch ist es enorm wichtig die genauen zellulären Vorgänge zu

verstehen, um das System zu evaluieren und ggf. zu verbessern. Durch ein *in-vivo* Verfahren wie im Antrag beschrieben, wären erstmals die Auswirkungen solcher Systeme auf Zellstrukturen und eine genaue Darstellung der Defekte in den jeweiligen Entwicklungsprozessen möglich.

Das Projekt würde daher nicht nur meine Forschung voranbringen, sondern einer großen Community von Entwicklungsbiologen, Agrarwissenschaftlern und GVO-Experten zur Forschung und Qualitätskontrolle zur Verfügung stehen.

Ich bin überzeugt davon, dass Prof. Stelzer mit seinem beeindruckenden interdisziplinären Lebenslauf und einzigartigen Expertisen auf dem Gebiet der optischen Physik der ideale Empfänger eines Reinhart Koselleck-Projektes ist und unterstütze seinen besonders innovativen Antrag daher ohne Vorbehalte mit Begeisterung!

Für weitere Fragen stehe ich Ihnen immer gerne zur Verfügung
Vielen Dank für Ihre Zeit
Mit freundlichen Grüßen


Dr. Marc F. Schetelig

An die

Dr. Ruth Müller

Deutsche Forschungsgemeinschaft

Kennedyallee 40
53175 Bonn

Leiterin der Abteilung
Umwelttoxikologie und
Medizinische Entomologie

Institut für Arbeitsmedizin,
Sozialmedizin und Umweltmedizin

Frankfurt, den 09.03.2016

Kollaborationszusage

Sehr geehrte Damen und Herren,

mit größter Begeisterung unterstütze ich Prof. Stelzer in seinem wissenschaftlich sehr spannenden Projektvorhaben, welches im Reinhart Koselleck-Programm beantragt wird.

Der Forschungsgegenstand des Reinhart Koselleck-Antrags von Prof. Stelzer steht in völligem Einklang mit meinen Arbeiten im Bereich medizinischer Entomologie (Abteilung *Umwelttoxikologie und Medizinische Entomologie*) am Universitätsklinikum der Goethe Universität Frankfurt am Main. Das vorgeschlagene Projekt wird innovative Werkzeuge (Lichtscheiben-Fluoreszenzmikroskopie, transgene Insektenlinien) für meine originäre Forschung entwickeln und insbesondere spannende Einblicke in die Embryogenese der Asiatischen Tigermücke *Aedes albopictus* generieren, welche seit 2010 Gegenstand meiner Forschung ist.

Der Krankheitsvektor *A. albopictus*, welcher insgesamt 22 Humanpathogene (u.a. Dengue-, Japanische Enzephalitis-, West-Nil-, Chikungunya- Viren) übertragen kann, ist von enormer medizinischer sowie sozio-ökonomischer Bedeutung, insbesondere im Kontext des Klimawandels. Die weltweit rapide Ausbreitung der Asiatischen Tigermücke, welche zu den 100 invasivsten Arten der Welt gehört, wird erst durch ihre schnelle Anpassungsfähigkeit an neue Klimabedingungen (Überwinterung, Photoperiodik) sowie die Trockentoleranz/Dormanz ihrer embryo-larvalen Stadien verständlich. Meine experimentelle Forschung befasst sich detailliert mit den ökophysiologischen Grundlagen der hohen Stresstoleranz und schnellen Anpassungsfähigkeit von *A. albopictus* an neue Umweltbedingungen und auch an Insektizide (z.B. Oppold et al., 2015, *Ecotoxicology and Environmental Safety*; Dhimal et al. 2014, *PLoS Neglected Tropical Diseases*; Kreß et al. 2014, *Journal of Pest Control*).

Tiefenmorphologische Detailinformationen zur embryonalen Morphogenese von *Ae. albopictus*, insbesondere unter Dormanzbedingungen fehlen bisher leider vollständig, währenddessen die oberflächenmorphologische Entwicklung der im Vergleich großen Pharat-Larven zunehmend in den Fokus entomologischer Publikationen rückt (z.B. Kreß et al. In press, *Journal of Vector Ecology*). Diese Wissenslücke - bedeutend für das Verständnis der *A. albopictus*-Invasion in temperate Gebiete (inkl.

Deutschland) - kann einzig durch die innovative Methodik der Lichtscheiben-Fluoreszenzmikroskopie im vorgeschlagenen Koselleck Projektvorhaben geschlossen werden.

Erst kürzlich gelang es meinem Team, epigenetische Veränderungen und damit mikroevolutionäre Veränderungen der Insektizidtoleranz in *A. albopictus* zu induzieren (Oppold et al. 2015, *Ecotoxicology and Environmental Safety*). Diesen Forschungszweig möchte ich mittelfristig weiter ausbauen (z.B. Methionin-Defizienz-Studien, miRNA – knockdowns). Die Verwendung fluoreszenzmarkierter und transgener Insektenlinien in Kombination mit fortgeschrittenen Lichtmikroskopietechniken würden hierbei sehr nutzbringend sein, insbesondere um bedeutende Einblicke in die morphologische Manifestation von Methionin- und epigenetisch-assoziierten Phänotypen bereits im hoch-sensitiven embryonalen Stadium zu erlangen. Auch langfristig wird eine transgene Stechmücken-Linie in Kombination mit fortgeschrittenen Lichtmikroskopietechniken meine Forschung bereichern, beispielsweise um neue Angriffspunkte für Insektizide (Embryozide) und die horizontale Transmission von Dengue- und Wolbachia-Viren zu untersuchen.

Ich bin vollständig davon überzeugt, dass die von Prof. Stelzer einzigartig zusammengestellte entomologische, bioinformatische und optisch-physikalische Expertise sowie der Einsatz einer außerordentlich innovativen, hochauflösenden und dreidimensionalen Mikroskopietechnik erstmals ermöglichen werden, die phänotypischen Gemeinsamkeiten und Differenzen der Insektenembryogenese aufzuklären und damit eine der wichtigsten grundlegenden entwicklungsbiologischen Fragestellungen im Bereich der Entomologie zu beantworten (vgl. *developmental hourglass model*, Irie und Kuratani 2014, *Development*).

Neben einem großen gemeinsamen Forschungs- und Publikationsinteresse verspricht die bereits intensive und vertrauensvolle Zusammenarbeit mit Prof. Stelzer während der Vorbereitungsphase des Antrags eine zukünftig harmonisch aufeinander abgestimmte Zusammenarbeit sowie eine exzellente Koordination und Durchführung des Projektes. Meine Abteilung stellt deshalb dem beantragten Reinhart Koselleck-Projektvorhaben theoretische sowie praktische medizinisch-entomologische Expertise, ein S1-Insektarium, S1-Labore sowie standardisiertes Moskitomaterial zur Verfügung und offeriert ein interdisziplinäres Netzwerk an der Schnittstelle Entomologie-Medizin-Soziologie für weiterführende Projekte (z.B. nachfolgende entomologisch-virologische Projekte im S3 Insektarium, Dr. Sandra Junglen, Institut für Virologie, Universität Bonn).

Ich wünsche Prof. Stelzer eine positive Begutachtung des vorgeschlagenen Reinhart Koselleck-Projektvorhabens, welches ich mit größtem Enthusiasmus unterstütze. Für weitere Fragen stehe ich Ihnen jederzeit gerne zur Verfügung.

Mit freundlichen Grüßen



Dr. Ruth Müller

Deutsche Forschungsgemeinschaft (DFG)
Kennedyallee 40
D- 53175 Bonn

Prof. Dr. B. Grünewald
Bienenkunde:
Karl-von-Frisch-Weg 2
61440 Oberursel

Campus Riedberg:
Max-von-Laue-Str. 13
60438 Frankfurt am Main
b.gruenewald@bio.uni-frankfurt.de

Oberursel, 08.03.2015

Kollaboration im Rahmen des Koselleck-Antrags von Prof. Dr. Ernst H.K. Stelzer

Sehr geehrte Kollegen,

das Institut für Bienenkunde Oberursel führt Grundlagenforschung und angewandte Forschung durch und unterhält eine moderne, allen Ansprüchen genügende, Bienenhaltung. Das Imkerteam (zwei MeisterInnen, eine Gesellin, drei Auszubildende) hat langjährige Erfahrungen in der Bereitstellung von Bienen und Bienenvölkern für die Forschung. Die handwerklichen Fertigkeiten und die Infrastruktur, die für die langfristige wissenschaftliche Haltung und Pflege von Bienenvölkern notwendig sind, existieren in Oberursel seit vielen Jahrzehnten.

Wir beabsichtigen, mit dem Arbeitskreis Stelzer im Rahmen der Projekte, die in dem eingereichten Koselleck-Antrag zur Embryonalentwicklung von Insekten skizziert sind, zusammen zu arbeiten. Mein Arbeitskreis kombiniert neurobiologische, verhaltensbiologische und zellbiologische Fragestellungen an Honigbienen. Daher sind auch alle Grundlagen, die für Untersuchungen der Embryonalentwicklung notwendig sind, vorhanden. Das Institut für Bienenkunde liegt nur etwa 10km bzw. knapp 15min vom Campus Riedberg entfernt.

Honigbienen sind die weltweit wichtigsten Insekten für die Bestäubung von Pflanzen. Sie sind sowohl ökologisch als auch ökonomisch von überragender Bedeutung. Daher ist die Honigbiene das wissenschaftlich am besten untersuchte **soziale Insekt** und ein Modellorganismus der modernen Biologie. Der Bestand an Honigbienen ist durch zahlreiche Bedrohungen wie viral und bakteriell bedingte Krankheiten, Parasiten, Pflanzenschutzmaßnahmen und Nahrungsmangel gefährdet. Das Institut für Bienenkunde untersucht in diesem Zusammenhang auch die Auswirkungen von Insektiziden auf Nervensystem, Verhalten und Entwicklung von Honigbienen. Es leistet damit einen wichtigen Beitrag zur Versachlichung der derzeit kontrovers geführten öffentlichen und wissenschaftlichen Diskussion der Bedrohungsszenarien von Honigbienen.

Die Embryogenese der Bienen wurde durch verschiedene Arbeitskreise bereits licht- und rasterelektronenmikroskopisch untersucht. Obwohl in diesen Untersuchungen die verschiedenen Phasen der Embryogenese beschrieben werden konnten, haben die bislang verwendeten Methoden klare Grenzen bei der Visualisierung der Zelldifferenzierung und der Gewebebildung. Neue mikroskopische *in vivo* Techniken, wie sie im AK Stelzer entwickelt wurden bzw. werden, bieten völlig neue Einsichten in die frühe Ontogenese von Bienen. Sie erlauben es, die Untersuchungen auf eine präzise morphologische und schließlich auf eine zellulär begründete molekularbiologische Ebene zu legen.


Das Institut für Bienenkunde komplementiert den AK Stelzer durch seine hervorragende Infrastruktur. Zum einen war es an der kürzlich erstmalig erfolgreichen Entwicklung einer transgenen Honigbiene beteiligt. Zum anderen gehört die künstliche Besamung der Königin zu seinen Kernkompetenzen. Schließlich verfügt es über Flugzelte, so dass in Oberursel mit transgenen Bienen gearbeitet werden kann, ohne die Umwelt zu gefährden.

Während der Kooperation sollen neue Erkenntnisse bezüglich einer Reihe exogener Einflüsse (z.B. Temperatur, pH-Wert, UV-Strahlung, Salzgehalt) auf die Entwicklung des Bienenembryos gewonnen werden. Besonders interessiert uns die Temperaturabhängigkeit der Embryonalentwicklung. Die Temperatur im Brutbereich wird vom Bienenvolk sehr präzise auf 35 ± 1 °C gehalten. Welche Auswirkungen Temperaturschwankungen auf den Embryo haben, ist gänzlich unerforscht. Die verschiedenen Unterarten von *Apis mellifera* weisen je nach Ausbreitungsgebiet unterschiedliche Thermoregulationen auf. So wird die Brutraumtemperatur mehr oder weniger schnell ausgeglichen bzw. konstant gehalten. Daher ist davon auszugehen, dass Unterarten verschiedene Entwicklungsgeschwindigkeiten und Temperaturlinien aufweisen. Wir möchten im Rahmen des Projekts, erstens, eine vergleichende Embryogenese zwischen zunächst drei Unterarten von *A. mellifera* (*A. m. mellifera*, *A. m. carnica*, *A. m. ligustica*) erstellen und, zweitens, den Einfluss der Temperatur auf diese Unterarten untersuchen. Drittens, ist es mit der Lichtscheiben-Fluoreszenzmikroskopie möglich, die durch Neonikotinoide hervorgerufenen Brutschäden im frühen Embryonalstadium zu dokumentieren. Zwar sind Effekte von Neonikotinoiden auf die Larvalentwicklung von Honigbienen nachgewiesen, es gibt jedoch keine Publikationen zu Brutschäden während der Embryonalentwicklung. Viertens, möchten wir der Frage nachgehen, ob eine Differenzierung zur männlichen Drohne oder weiblichen Arbeiterin bereits in der Embryogenese stattfindet.

Die Biene als soziales Insekt weist eine hohe Komplexität auf. Die Entwicklung des Volkes, der genetische Hintergrund der Königin, sowie saisonale Aspekte spielen wichtige Rollen in der Bienenhaltung. Das Institut für Bienenkunde in Oberursel besitzt alle Voraussetzungen und die nötige Erfahrung, die für das Kooperationsprojekt notwendig sind. So können Bienenvölker in klimatisierten Flugräumen unter isolierten und künstlichen Licht- und Umgebungsverhältnissen ganzjährig gehalten werden. Für die Königinnenzucht stehen ausgefeilte Besamungsmethoden zur Verfügung. Am Institut können viele Bienenvölker unter ähnlichen und/oder isolierten Bedingungen zu gehalten werden und alle Brutstadien sind zu jeder Jahreszeit verfügbar. S1-Labore stehen meiner Arbeitsgruppe sowohl in Oberursel als auch auf dem Campus Riedberg der Goethe Universität zur Verfügung. Methoden zur *in vitro* Larvenaufzucht von Bienen sind sehr gut etabliert. Die Entwicklung einer Methode zur Herstellung transgener Bienen wurde in Oberursel maßgeblich mit entwickelt.

Das Institut für Bienenkunde gehört zur Goethe Universität Frankfurt am Main und ist eng mit den Landesinstituten der anderen Bundesländer vernetzt. Aktuelle Projekte können im Rahmen studentischer Abschlussarbeiten durchgeführt werden und Imker-Auszubildende können in Forschungsprojekte eingebunden werden. Mit dem Arbeitskreis Stelzer wurden bereits gemeinsame Projekte erfolgreich durchgeführt (gemeinsam betreute Bachelorarbeiten, Teilprojekte von Dissertationen). Im Rahmen seiner Dissertation analysiert Paul Siefert derzeit die Morphologie von Futtersaftdrüsen im Kopf von Ammenbienen, die mit dem Lichtscheiben-Fluoreszenzmikroskop in drei Dimensionen aufgezeichnet wurden. Diese Kooperationen mit Prof. Dr. Stelzer sind aufgrund der räumlichen Nähe der Arbeitskreise auf dem Campus Riedberg besonders erfolgversprechend. Sie ermöglicht einen reibungslosen und kontinuierlichen Austausch von Daten, Material und Informationen.

Mit freundlichen Grüßen



Publikationen mit Bezug zum Kooperationsprojekt:

Schulte C, Lebouille G, Otte M, Grünewald B, Gehne N and Beye M (2013) Honeybee promoter sequences for targeted gene expression. *Insect Mol Biol* 22(4):399-410 doi: 10.1111/imb.12031

Fischer J, Müller T, Spatz A-K, Greggers U, Grünewald B, and Menzel R. (2014) Neonicotinoids Interfere with Specific Components of Navigation in Honeybees. *PLoS ONE* 9(3): e91364. doi:10.1371/journal.pone.0091364

Schild HA, Fuchs SW, Bode HB, Grünewald B. (2014) Low-molecular-weight metabolites secreted by *Paenibacillus larvae* as potential virulence factors of American foulbrood. *Appl Environ Microbiol.* 80(8):2484-2492. doi: 10.1128/AEM.04049-13